SEVENTH INTERNATIONAL SYMPOSIUM ON APPLICATIONS OF LASER TECHNIQUES TO FLUID MECHANICS

VOLUME II

July 11th to 14th 1994
Lisbon, Portugal

SEVENTH INTERNATIONAL SYMPOSIUM ON APPLICATIONS OF LASER TECHNIQUES TO FLUID MECHANICS

VOLUME II

July 11th to 14th 1994
Lisbon, Portugal

PREFACE

The proceedings volumes I and II comprise the papers that were accepted for presentation at the **Seventh International Symposium on Applications of Laser Techniques to Fluid Mechanics** held at *The Calouste Gulbenkian Foundation in Lisbon*, during the period of July 11 to 14, 1994. The prime objective of this Seventh Symposium is to provide a forum for the presentation of the most advanced research on laser techniques for flow measurements, and reveal significant results to fluid mechanics. The applications of laser techniques to scientific and engineering fluid flow research is emphasized, but contributions to the theory and practice of laser methods are also considered where they facilitate new improved fluid mechanic research. Attention is focused on laser-Doppler anemometry, particle sizing and other methods for the measurement of velocity and scalars such as particle image velocimetry and laser induced fluorescence.

The papers comprising the formal record of the meeting, were selected following high standard reviews, by members of the Advisory Committee, from approximately 300 extended abstracts submitted for presentation at this meeting.

Volume I comprises the papers to be presented during the first and second days of the Symposium, namely July 11th and 12th, while *Volume II includes the papers of the following days, Wednesday, July 13th, and Thursday, July 14th.*

We would like to take this opportunity to thank those who assisted us. The assistance provided by the Advisory Committee is highly appreciated. We are highly indebted for the financial support provided by the Sponsoring Organizations that made this Symposium possible. Many thanks are also due to the secretariat of the Symposium, Graça Pereira, Carlos Carvalho, Anabela Almeida and Luísa Martins.

THE ORGANIZING COMMITTEE

ORGANIZING COMMITTEE

- **R.J. Adrian**
  Department of Theoretical and Applied Mechanics
  University of Illinois at Urbana-Champaign
  Urbana, Illinois 61801
  USA

- **D.F. G. Durão**
  Department of Mechanical Engineering
  Instituto Superior Técnico
  Av. Rovisco Pais
  1096 Lisboa Codex
  PORTUGAL

- **F. Durst**
  Lehrstuhl fur Stroemungsmechanik
  University of Erlangen - Nurenberg
  Egerlandstrasse 13
  D-8520 Erlangen
  GERMANY

- **M. V. Heitor**
  Department of Mechanical Engineering
  Instituto Superior Técnico
  Av. Rovisco Pais
  1096 Lisboa Codex
  PORTUGAL

- **M. Maeda**
  Department of Mechanical Engineering
  Keio University
  1-14-1 Hiyoshi, Kohuku
  Yokohama 223
  JAPAN

- **J.H. Whitelaw**
  Imperial College of Science, Technology and Medicine
  Department of Mechanical Engineering
  Exhibition Road
  London SW7 2BX
  ENGLAND

ADVISORY COMMITTEE

SPONSORING ORGANIZATIONS

- Associação para o Desenvolvimento do Instituto Superior Técnico *ADIST*
- Banco Comercial Português, *BCP*
- Câmara Municipal de Lisboa
- Centro de Termodinâmica Aplicada e Mecânica dos Fluídos da Universidade Técnica de Lisboa, *CTAMFUTL*
- DHL
- Direcção Geral de Turismo
- European Research Office: United States Army, Navy and Air Force Departments
- Fundação Luso Americana para o Desenvolvimento *FLAD*
- Fundação Calouste Gulbenkian
- Instituto Superior Técnico, *IST*
- Instituto Tecnológico Para A Europa Comunitária, *ITEC*
- Junta Nacional de Investigação Científica e Tecnológica, *JNICT*
- Air Portugal *TAP*

LIST OF CONTENTS

VOLUME I (SESSION 1-20)

Session 8. DATA PROCESSING I

Session 9. COMBUSTION III

Session 10. ROTATING MACHINES II

Session 11. DATA PROCESSING II

VOLUME II (SESSION 21-39)

Session 21.

Two Phase Flow Instrumentation II

Investigation of Polydisperse Spray Interaction Using an Extended Phase-Doppler Anemometer

G. Brenn, J. Domnick, F. Durst, C. Tropea, T.-H. Xu
Universität Erlangen-Nürnberg, Lehrstuhl für Strömungsmechanik
Cauerstraße 4, D-91058 Erlangen, Germany

Abstract

Interactions between polydisperse sprays commonly occur in many technical processes, such as fuel injection, spray painting, scrubbers or spray drying. The choice or optimization of droplet size distributions in such cases must therefore also consider nozzle placement and orientation, and the variation of the size distribution induced by coalescence. Experimentally, the investigation of spray interaction requires a passive marking of each spray and a suitable measuring technique to distinguish the marker, also in the case of coalescence. In the present study, the refractive index has been chosen as a marker and the Extended Phase-Doppler Anemometer (EPDA) is used as a detector of the marked fluid. The principles of the EPDA have been presented previously, indicating that the velocity, size and refractive index of each droplet can be determined. The present study uses simple hollow-cone nozzles and sugar/water mixtures to carry out EPDA measurements on polydisperse spray interaction.

1 Introduction

Liquid sprays are essential in numerous industrial and technical processes, ranging from spray painting and spray drying to flue gas cleaning in wet scrubbers of power plants, diesel spray generation and rocket fuel injection. In many applications, interactions between the spray cones of neighbouring nozzles are either unavoidable or intentional, where coalescence processes may significantly alter the characteristics of the spray. For investigations aimed at a better understanding of such spray interaction processes, an experimental method is required, which not only yields droplet size and velocity information *(Yurteri et al. (1993))*, but also allows the origin of the droplet and/or the degree of mixing to be recognized. This encompasses both a "marking" of the fluid in each spray and a "detection" of the marker when measuring the droplet size and velocity. The extended Phase-Doppler Anemometry (EPDA) is such a method, providing a measure of the refractive index of individual droplets *(Naqwi et al. (1990), Pitcher et al. (1990))*. The interaction of two sprays can be studied with the EPDA by using two liquids with distinctly different refractive indexes in each of the two spray nozzles. The measured refractive index of individual droplets yields their origin and/or degree of mixing with droplets of the other liquid. The present paper begins with a brief review of the EPDA principles followed by a description of the experimental setup and technique. It is shown that good optical alignment is essential for achieving acceptable accuracy and the alignment techniques devised for this purpose are described. Finally, measurement results from a systematic study of the interaction of two sprays are presented.

2 Principles of Extended Phase-Doppler Anemometry

The basic idea of the extended phase-Doppler anemometry (EPDA) is essentially to operate two PDA receiving units at two different scattering angles simultaneously, yielding redundancy in the size measurement and thus the possibility for determining the refractive index. According to geometrical optics, the relation between the droplet diameter d_p and the measured phase shift Φ_i of the Doppler signals received by two detectors at the scattering angle ϕ_i may be written as

$$\Phi_i = F_i(\alpha, \lambda, m, \psi_{i1,2}, \phi_i) \cdot d_p \qquad (1)$$

for each scattering angle indicated by the subscripts $i = 1, 2$, whereby α is the beam intersection half angle and $\psi_{i1,2}$ are the detector elevation angles. For refraction-dominated light, the ratio of the equations for the two different scattering angles may be written as

$$\frac{\Phi_1}{\Phi_2} = \frac{\sin\psi_1}{\sin\psi_2}\left(\frac{1+\cos\alpha\cos\psi_2\cos\phi_2}{1+\cos\alpha\cos\psi_1\cos\phi_1}\right)^{1/2} \cdot \left(\frac{1+m^2-m[2\,(1+\cos\alpha\cos\psi_2\cos\phi_2)]^{1/2}}{1+m^2-m[2\,(1+\cos\alpha\cos\psi_1\cos\phi_1)]^{1/2}}\right)^{1/2} \qquad (2)$$

giving a relation between the measured phase-shift ratio, the refractive index of the scattering particle and the parameters of the geometrical configuration of the EPDA system. This form of the equation is only valid for a symmetric arrangement of the photodetectors relative to the scattering plane (i.e. $\psi_{i1} = -\psi_{i2}$) and for sufficiently small intersection half angle α and elevation angles ψ. The right-hand side contains as an unknown only the refractive index m of the scattering particle. Resolving the equation with respect to the refractive index and dropping the physically irrelevant solution, one obtains the equation

$$m = -\frac{1}{2}\frac{\sqrt{f_2} - A\sqrt{f_1}}{A-1} + \sqrt{\left(\frac{1}{2}\frac{\sqrt{f_2} - A\sqrt{f_1}}{A-1}\right)^2 - 1} \quad , \tag{3}$$

where

$$f_1 = 2(1 + \cos\alpha\cos\psi_1\cos\phi_1) \tag{4}$$

$$f_2 = 2(1 + \cos\alpha\cos\psi_2\cos\phi_2) \tag{5}$$

$$A = \left(\frac{\Phi_1}{\Phi_2}\frac{\sin\psi_2}{\sin\psi_1}\right)^2 \frac{f_1}{f_2} \quad . \tag{6}$$

This equation provides real solutions only for non-vanishing denominators and positive square-root arguments, thus involving the validation criterion

$$\sqrt{\frac{f_2}{f_1}}\sqrt{\frac{\sqrt{f_2}-2}{\sqrt{f_1}-2}} \leq \frac{\Phi_1}{\Phi_2} < \sqrt{\frac{f_2}{f_1}} \quad . \tag{7}$$

For an optical arrangement with scattering angles $\phi_1 = 60°$, $\phi_2 = 30°$, elevation angles $\psi_{1,2} = \pm 3.69°$, and an intersection half angle of $\alpha = 1.69°$, as used in the present study, these limiting values are

$$0.5663 \leq \frac{\Phi_1}{\Phi_2} < 1.1152 \quad .$$

This configuration was shown by *Naqwi et al. (1990)* to be suitable for applications in liquids with refractive indexes around 1.35.

3 Experimental setup and technique

The setup for the EPDA measurements contains two standard PDA receiving optics units. A sketch of the whole arrangement is shown in Fig. 1. The transmitting side of the optical system was equipped with a 15 mW He-Ne laser. The transmitting optics consisted of a beam splitter, one pair of Bragg cells and a transmitting lens. The diameter of the probe volume generated with this setup was about 290 μm. The Bragg cells in the transmitting optics with a shift frequency difference of 1 MHz facilitated the measurement of

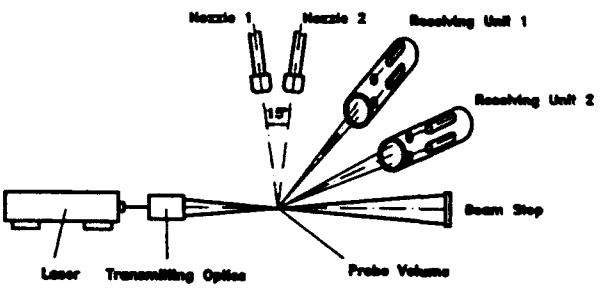

Figure 1: Sketch of the test rig used for the experiments. For preliminary measurements, a monodisperse droplet generator was used instead of the two spray nozzles. The nozzle arrangement is turned by 90° for clarity. The off-axis angles are $\phi_1 = 60°$, $\phi_2 = 30°$.

low droplet velocities. The velocity factor used for the calculation of velocities from measured Doppler frequencies was 10.72 m/s/MHz. Other relevant data of the setup are given in Table 1. For preliminary

Quantity	Value
He-Ne Laser power	$15mW$
Transmitting lens focal length f_t	$372.5mm$
Beam spacing at transm. lens exit	$22mm$
Gaussian beam diameter at lens exit	$0.8mm$
Off-axis angle ϕ receiving unit 1	60°
Off-axis angle ϕ receiving unit 2	30°
Elevation angles ψ on units 1,2	3.69°
Receiving lens focal length	$310mm$

Table 1: Data of the EPDA setup used for the experiments.

measurements, streams of monodisperse droplets produced with a TSI droplet generator were used. In subsequent studies, hollow-cone water and sugar/water sprays were produced by means of domestic oil burner nozzles purchased from DANFOSS Co.. The signal processing was preceded by two band-pass filter units and an 8-bit digitization in a 4-channel transient recorder with data transfer to a personal computer. The frequency and phase shift of the Doppler signals were determined by the software, using the cross-spectral density technique of *Domnick et al. (1988)*. The ratio of the phase shifts measured under different off-axis angles was calculated in a postprocessing procedure; the refractive indexes determined from this ratio were also computed with this software.

4 Measurements in monodisperse droplet streams

Preliminary measurements were carried out with the EPDA system on monodisperse water droplet streams in order to check the accuracy of the measurements and the sensitivity of the system to misalignments. The monodispersed droplets were produced by means of a TSI vibrating orifice generator. The measurements indicated that the relative refractive index m of droplets with a diameter in the range of 60 μm to 110 μm can be measured with an accuracy of 0.6 % and with a normalized standard deviation of about $8 \cdot 10^{-3}$, as indicated in Fig. 2. The occurence of a distribution rather

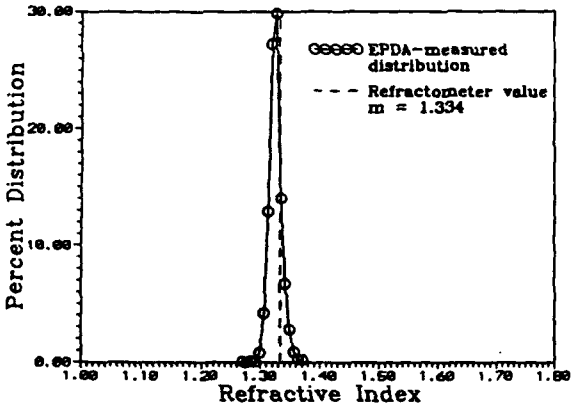

Figure 2: Measured refractive index distribution in a monodisperse water droplet stream (d_P = 71.8 μm). The deviation of the measured mean value of $\bar{m}$ = 1.326 from the refractive index m = 1.334 measured with a refractometer is -0.6%. The normalized standard deviation of the distribution is $8.0 \cdot 10^{-3}$.

than a single peak value is due to slight alignment errors of the receiving optics, inevitable noise in the signals and theoretically verifiable scatter in the phase shift ratio. During these experiments, the alignment of the receiving optics turned out to be the crucial point of the system. It could be shown that even slight errors in the alignment of the APD photodetectors may cause severe errors in the refractive index measurements. For this purpose, correct PDA measurements of the diameter of droplets of known size at both scattering angles were found to be a sufficient condition for good alignment of the receiving optics system, thus the preliminary use of monodispersed droplets.

5 Measurements in polydisperse sprays

Using an EPDA system which was aligned according to the procedure above, measurements in the mixing zone of two polydisperse hollow cone sprays with a nominal spray cone angle of 60° were carried out. The exit hole diameter of these nozzles is 300 μm. The nozzles were traversable in three directions allowing measurements to be carried out at various points in the spray cones. The nozzles were adjusted so that the symmetry lines of the spray cones lay in a plane perpendicular to the plane of the incident laser beams. The intersection angle between the symmetry lines of the nozzles was 15°. The distance between the nozzle exit holes was 14 mm. The arrangement is shown in Figure 3 and also in Figure 1, but there it is turned by 90° for clarity. The x

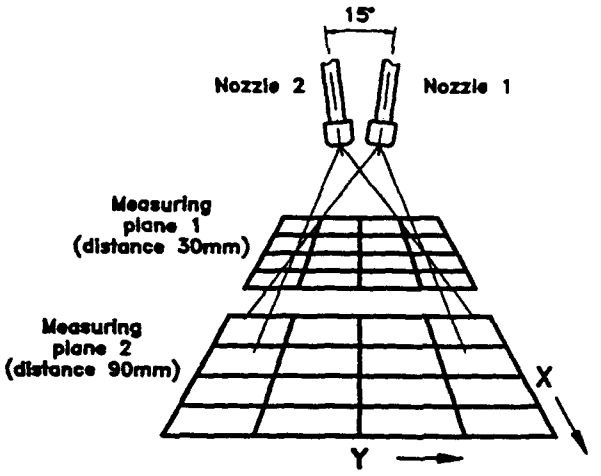

Figure 3: Sketch of the measuring planes in the mixing zone of the sprays. The central grid points have the coordinates (x/y) = (0/0). The positive coordinate directions are indicated by the arrows. The plane of the incident laser beams is the plane y = 0.

axis in Figure 1 is directed from right to left, in the plane of the laser beams.

The liquid was supplied to the nozzles using air-pressurized liquid reservoirs, which were connected to the nozzles by hoses. The use of separate reservoirs for each of the nozzles provided the possibility to run each nozzle with different liquids and pressures. The liquid flow rates through the nozzles were adjusted by choosing the appropriate driving air pressure. In the present section, an overview of the measurements will be given, and the results will be discussed.

5.1 Measurement programme

In order to check the capabilities of the technique, measurements were first carried out in pure water sprays. Measurements were performed on grids of 25 points at two downstream distances from the nozzle exits. The grids are sketched in Fig. 3. The mesh widths at the two distances of 30 mm and 90 mm are 10 mm

and 15 mm respectively. For measurements in mixing two-component sprays, the liquids used were demineralized water (m = 1.334) and a solution of sucrose in demineralized water (m = 1.421). These liquids were chosen in order to achieve a sufficiently large difference between the refractive indexes of the pure liquids without inordenately increasing the viscosity of the fluids. Furthermore, physical properties of the liquids were required which make the merging of colliding droplets possible, in order to have interaction processes similar to those in one-component sprays. Measurements were carried out with constant flow rates of 1.5 l/h and 3.1 l/h for water and sugar/water respectively.

5.2 Measurement results

The results are distributions of mean values of droplet size, droplet velocity, and refractive index over the measurement area and local number distributions of these quantities. The distribution of the number mean diameter in the mixed pure water sprays at the distance of 90 mm is shown in Fig. 4 as a three-dimensional plot in order to show the overall shape

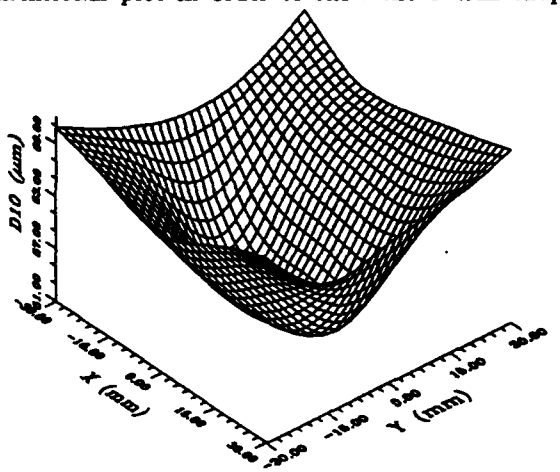

Figure 4: Distribution of the mean diameter D_{10} in the two mixed water sprays (axial distance 90 mm).

of the distribution. The profiles of the distributions along the lines x = 0 and y = 0 are shown in Figs. 5 and 6. From these profiles, the effect of spray interaction resulting in larger droplets is evident. The shapes for the single sprays and those for the sprays of different liquids look very similar and will not be repeatedly shown here.

Fig. 7 shows the same diagram for the distribution of the mean vertical downward velocity component u_{mean} in the two mixed pure water sprays. The distribution exhibits a clear maximum. The maximum value in comparison with the single sprays value is raised by the mixing effects. This effect is clearly displayed in

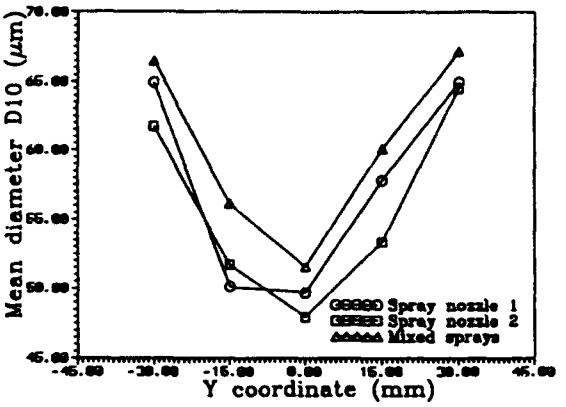

Figure 5: Distribution of the mean diameter D_{10} in the single sprays of nozzles 1 and 2 and in the mixed water sprays along the line x = 0 (axial distance 90 mm).

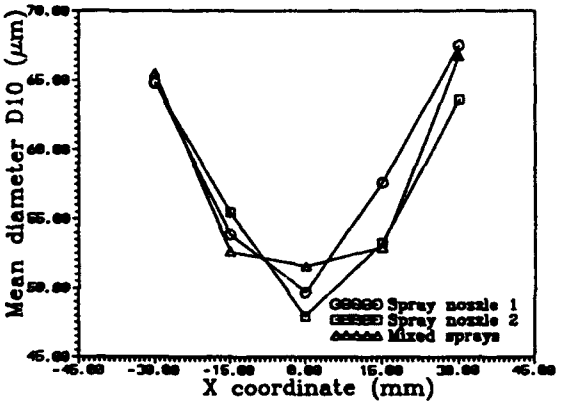

Figure 6: Distribution of the mean diameter D_{10} in the single sprays of nozzles 1 and 2 and in the mixed water sprays along the line y = 0 (axial distance 90 mm).

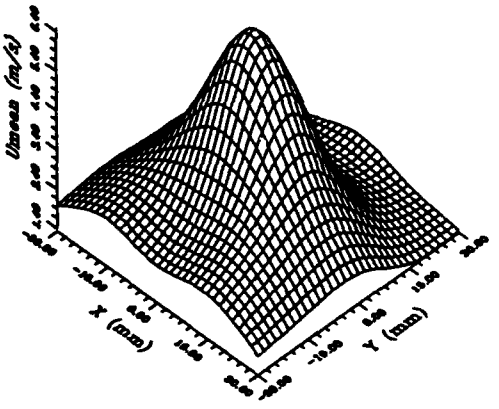

Figure 7: Distribution of the mean velocity component u_{mean} in the two mixed water sprays (axial distance 90 mm).

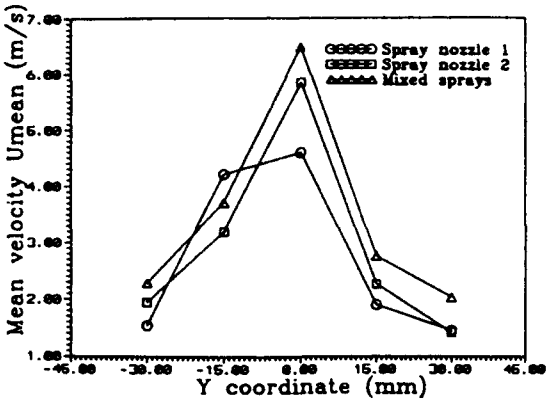

Figure 8: Distribution of the mean vertical downward velocity component u_{mean} in the single sprays of nozzles 1 and 2 and in the mixed water sprays along the line x = 0 (axial distance 90 mm).

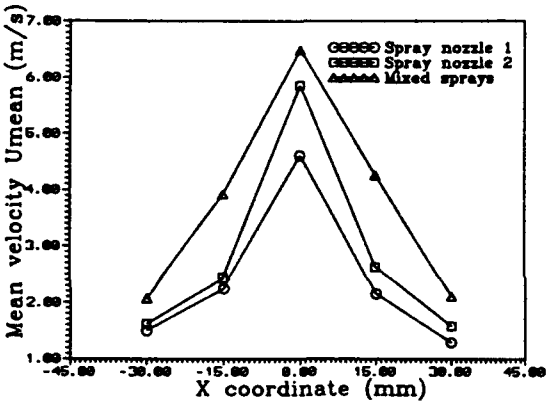

Figure 9: Distribution of the mean vertical downward velocity component u_{mean} in the single water sprays of nozzles 1 and 2 and in the mixed sprays along the line y = 0 (axial distance 90 mm).

the two-dimensional profiles shown in Figs. 8 and 9, where the curves for the single sprays are also shown.

In Fig. 10 the distribution of the mean refractive index measured in the single water spray of nozzle 1 is shown as an example. The deviation of the values from the correct value of $m = 1.334$ varies with the location of measurement in the spray. The minimum of the measured distribution corresponds to the region in the spray where the deviation from the correct value takes the smallest values, i.e. the measured refractive index is too large at all positions due to a systematic error caused by a slight misalignment. The maximum occuring deviation is 1.8 %. The deviation of the measured mean refractive index from the correct value and

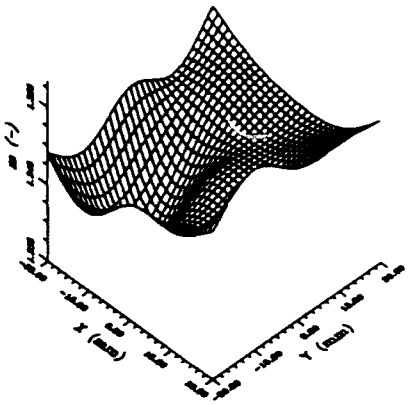

Figure 10: Distribution of the mean refractive index $\bar{m}$ in the pure water spray of nozzle 1 (axial distance 90 mm).

the standard deviation of the measured refractive index distribution both show a negative correlation with the particle size, a result which is not explicitly presented in this paper. Therefore, for a system without the mentioned systematic error, the position of maximum mean value deviation and maximum standard deviation of the measured refractive index coincides with the region of minimum number mean diameter. Maximum normalized standard deviations of the measured refractive index attained values of 6 % for particles with a number mean diameter of about 49 μm. An example of such measured refractive index distributions is shown in Fig. 11. This plot shows the data at the gridpoint (x/y)=(0/0) at an axial distance of 90 mm in the two single and in the mixed water sprays.

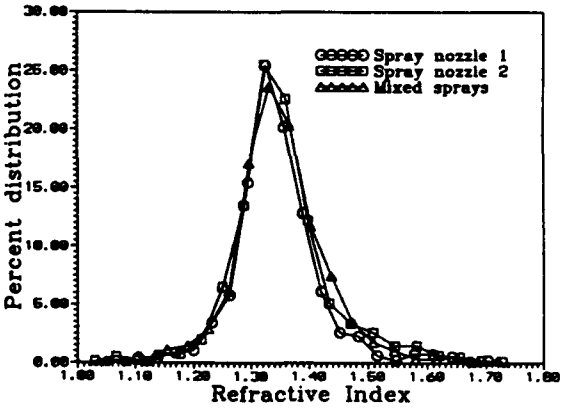

Figure 11: Distribution of the measured refractive index values in the single water sprays of nozzle 1 and 2 and in the two mixed sprays (axial distance 90 mm, central grid point).

The results of the measurements for the case of mixing sprays of different liquids show no significant differ-

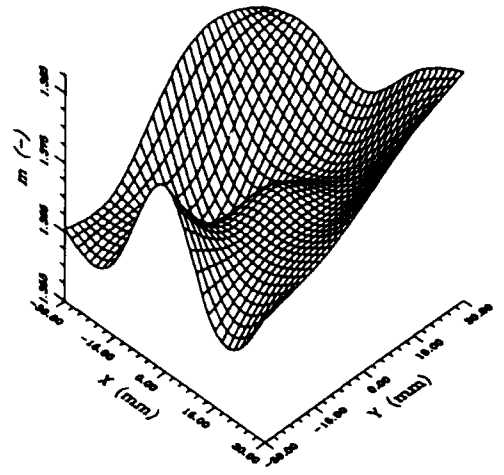

Figure 12: Distribution of the mean refractive index $\bar{m}$ in the mixed water and sugar/water sprays (axial distance 90 mm).

ences to the pure water sprays case discussed above. The only difference worth mentioning occurs in the distribution of the measured mean refractive index, shown in Fig. 12. This diagram clearly shows the regions in the mixing zone of the sprays, where mainly sugar/water droplets are present. Due to some asymmetry in the sugar/water spray, the distribution also is not symmetric. A large sugar/water influence in special occurs in the center of the region around y = -30 mm, and on the opposite side close to y = 30 mm. These zones are characterized by the boundaries of the cone of the sugar/water spray (produced by nozzle 2). In the center of the grid, the measured mean refractive indexes are dominated by the water spray, which exhibited a symmetric hollow cone. Difficulties with the sugar/water spray were mainly due to a slightly too small mass flow rate caused by a limitation in the maximum applicable driving pressure.

A point of special interest are the measured number distributions of the refractive index in the mixing zone of the sprays of different liquids. These distributions in the central point of the measurement grid at the distance of 90 mm are shown in Fig. 13. The curves give the refractive index distributions in the pure water spray, the pure sugar/water spray and in the mixed spray. It can be seen that the peak value of the mixed spray distribution occurs at the point of the pure-water value. Due to the asymmetry in the sprays, no peak of pure sugar/water droplets can be detected at this location in the mixing zone. The distribution for the mixed sprays case, however, is much broader than that of the single spray case, indicating an increased range of re-

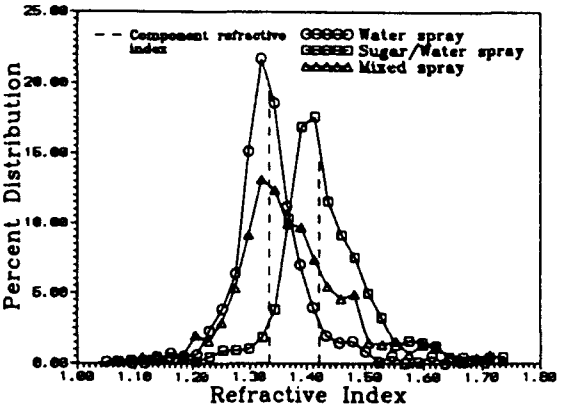

Figure 13: Measured refractive index distributions for the pure water spray, the sugar/water spray and the mixed spray (axial distance 90 mm, point (x/y) = (0/0)).

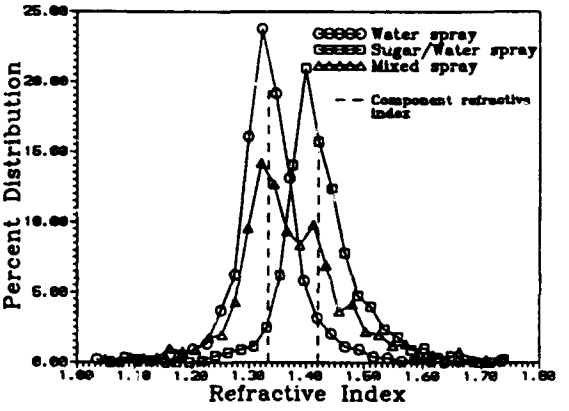

Figure 14: Measured refractive index distributions for the pure water spray, the sugar/water spray and the mixed spray (axial distance 90 mm, point (x/y) = (0/-15 mm)).

fractive indexes occuring in the sprays. At the point (x/y) = (0/-15mm), peaks of the mixed spray refractive index distribution can be detected both at the refractive index of the water and of the sugar/water spray (Fig. 14).

5.3 Fitting of droplet diameter distributions with the three-parameter log-hyperbolic function

The number mean droplet diameter in the center of the mixed spray was found to show only an increase of 6% in comparison with the two single sprays. This small increase has only slight significance for the influence of spray mixing on the droplet diameter distributions. Therefore, the measured distributions were fitted to

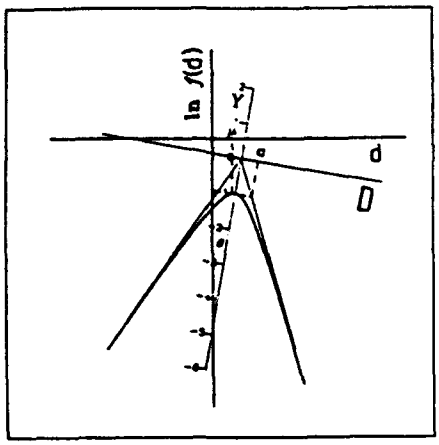

Figure 15: Sketch of the three-parameter log-hyperbolic distribution function. The geometrical significance of the parameters a, ϑ, and μ can be seen from the graph f(d).

the three-parameter log-hyperbolic distribution function. The three parameters of the function were shown to be suitable for characterizing the droplet diameter distributions in polydisperse sprays *(Xu et al. (1993))*. A sketch of the log-hypberbolic function $f(d)$ picturing the geometrical significance of the parameters is shown in Fig. 15. The profiles of the three parameters of the function along the line x = 0 are shown in Figs. 16 through 18. The parameter a shows only

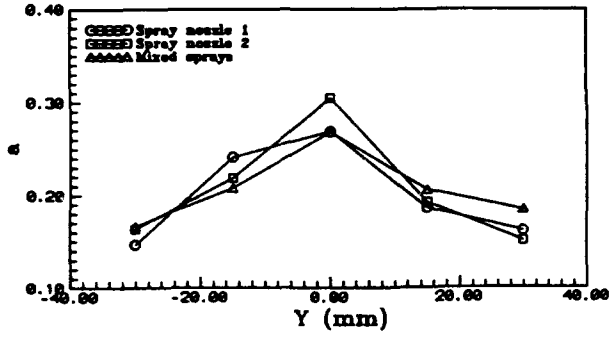

Figure 16: Distribution of the parameter a of the log-hyperbolic distribution function for the pure water sprays of nozzle 1 and nozzle 2 and for the mixed water sprays (axial distance 90 mm, points x = 0).

a small difference between the single sprays and the mixed spray. The parameters ϑ and μ, however, clearly exhibit larger values in the mixing zone of the sprays. These parameters are a measure for the rotation angle of the function graph (ϑ) and for the maximum point

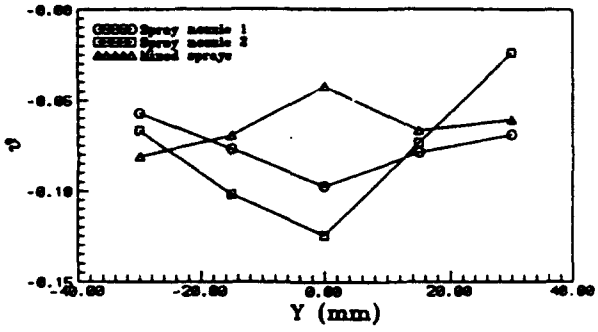

Figure 17: Distribution of the parameter ϑ of the log-hyperbolic distribution function for the pure water sprays of nozzle 1 and nozzle 2 and for the mixed water sprays (axial distance 90 mm, points x = 0).

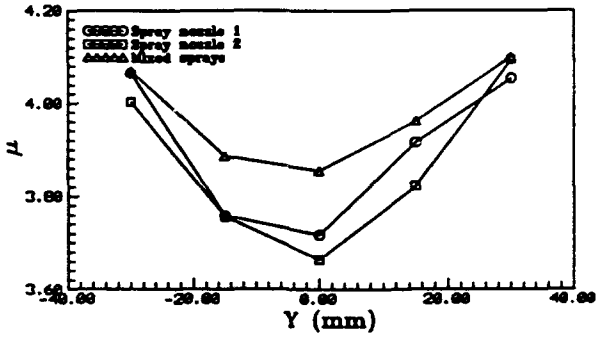

Figure 18: Distribution of the parameter μ of the log-hyperbolic distribution function for the pure water sprays of nozzle 1 and nozzle 2 and for the mixed water sprays (axial distance 90 mm, points x = 0).

location of the function graph (μ), as was pointed out elsewhere *(Xu et al. (1993))*. Therefore, the increased values represent well the increase of the droplet diameters (μ) and the increased percentage of larger droplets (ϑ). The shape of the curve for parameter ϑ in the mixed sprays even changes from concave to convex.

These results show that EPDA together with a fitting procedure to the log-hyperbolic function makes a detailed analysis of mixing processes in interacting spray cones possible and gives better insight into the mixing processes than techniques providing only droplet diameters and velocities.

6 Conclusions

EPDA measurements of the velocity, the diameter and the refractive index of monodisperse droplet streams and of mixing hollow cone sprays of different liquids

at a fixed intersection angle have been carried out. The measurements on monodisperse droplet streams offered a means of alignment for the two receiving optics units of the EPDA system. Using this method, mean refractive index errors as small as 0.6 % and normalized standard deviations of the refractive index distribution of only 0.8 % and even less may be achieved.

Using the EPDA system after this alignment procedure for measurements in polydisperse sprays, refractive index distributions are obtained which are significantly narrower than those presented in earlier measurements by *Naqwi et al. (1990)* (normalized standard deviation of about 6 % or less) and which correctly represent the physical features of the sprays. Thus, in the case of mixing sprays of different liquids, two peaks of the pure liquid droplets are clearly represented. This is the first time, that such results of EPDA measurements have been published.

The mixing zone of the sprays at a distance of 90 mm is characterized by a spray mixing-induced increase of the mean droplet diameter D_{10} by about 3.6 % for the pure demineralized water sprays investigated here, and by 6.0 % for the mixed water and sugar/water sprays. Furthermore, an increase of the maximum downward velocity component in the mixing zone of the sprays by 10 % to 40 % is observed. These effects of increased values of mean quantities may be due to two different phenomena: 1) The values of droplet diameter and velocity really have become larger; 2) The probability of the occurence of larger values has grown due to the presence of a second spray being run simultaneously. These two possible reasons for the increased mean values in the case of the velocity are hard to distinguish, as the maximum velocity of the droplets occuring in the center of the sprays indicates a very high probability density for the occurence of high velocities. In contrary, for the droplet diameter in the center of the spray cones, the probability for the occurence of large droplets is low. The observed increase of the droplet diameters in the mixing zone of the sprays is well represented by the parameters a, μ, and ϑ of the three-parameter log-hyperbolic distribution function, as could be shown here.

In conclusion it can be said that this experimental work shows the feasibility of the EPDA technique for the investigation of multiple interacting sprays. A limitation of the technique, however, comes up due to the effect that uncertainties in the refractive index measurements grow considerably with decreasing droplet diameters. A threshold value for the presently used arrangement is 30 μm. This means that for the purpose of spray interaction studies including the investigation of individual spray droplet coalescence, two liquids with very largely different refractive indexes should be used. The results suggest a desirable minimum difference between these pure component refractive indexes of $\Delta m = 0.2$, which, however, is hard to reach with experimentally workable liquids.

Acknowledgement

The support of the present work by an EC-programme in the JOULE-I framework is gratefully acknowledged.

References

Domnick, J., Ertl, H., & Tropea, C. 1988, Processing of Phase/Doppler signals using the cross-spectral density function. 4th Int. Symp. on Appl. of Laser Techn. to Fluid Mech. Lisbon, paper 3.8.

Naqwi, A., Durst, F., & Liu, X.-Z. 1990, An Extended Phase-Doppler System for Characterization of Multiphase Flows. Proc. 5th Int.Symp. on Appl. of Laser Techn. to Fluid Mech. Lisbon, paper 24.4.

Pitcher, G., Wigley, G., & Saffman, M. 1990, Sensitivity of dropsize measurements by phase-Doppler anemometry to refractive index changes in combusting fuel sprays. Proc. 5th Int.Symp. on Appl. of Laser Techn. to Fluid Mech. Lisbon, paper 14.4.

Xu, T.-H., Durst, F., & Tropea, C. 1993, The three-parameter log-hyperbolic distribution and its application to particle sizing. Atomiz. and Sprays vol. 3, pp. 109 - 124.

Yurteri, C.Ü., Kadambi, J.R., & Arik, E. 1993, Spray characterization and droplet interactions study using particle dynamic analyzer. Proc. 5th Int. Conf. Laser Anemometry Adv. and Appl., Veldhoven (Netherlands), pp. 145 - 152.

THIS PAGE IS MISSING IN ORIGINAL DOCUMENT

21.2.1. & 21.2.2

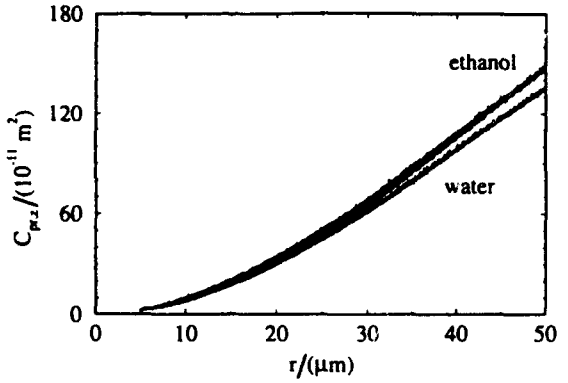

Fig. 3. Radiation pressure cross-sections $C_{pr,z}$ as a function of droplet radius r. The increment between subsequent radii at which $C_{pr,z}$ has been calculated was 0.01 μm. Results are shown for water and ethanol, which have the refractive indices $m = 1.33$ and $m = 1.36$. Here and for all following calculations of radiation pressure cross-sections the waist radius of the laser beam was $w_0 = 100\,\mu m$ and the wavelength was $\lambda = 514.5$ nm.

2.3 Comparison between rainbow position and radiation pressure cross-section

For a comparison of the oscillations of the radiation pressure forces with the oscillations of the rainbow position θ_{RC} calculations with a high resolution in droplet radius were performed for both $C_{pr,z}$ and θ_{RC}. Thirteen different values of refractive indices have been chosen, which correspond to hydrocarbons from pentane to hexadecane and water. With this selection a wide range from $m = 1.333$ to $m = 1.4345$ is covered. In the following two figures the rainbow angle θ_{RC} and the radiation pressure cross-section $C_{pr,z}$ are shown as a function of the droplet radius r. Results for two different radius intervals are presented for water, hexane, and pentadecane. The rainbow angle θ_{RC} is plotted in the upper plot of each figure, whereas the radiation pressure cross-section is shown in the three lower plots. Figure 4 shows results for the radius range from $r = 5\,\mu m$ to $r = 6.5\,\mu m$. In Fig. 5 results for the radius range from $r = 15\,\mu m$ to $r = 16.5\,\mu m$ are shown. The results of $\theta_{RC}(r)$ and $C_{pr,z}(r)$ should be compared for the same refractive index. For the low frequency oscillations of both the rainbow angle and the radiation pressure cross-sections a similar behaviour is found. The period of the lowest frequency of these oscillations -neglecting the sharp peaks- seems to be in the same order of magnitude for θ_{RC} and Cpr,z and for different size ranges and refractive indices. A detailed examination of the period of these oscillations was made using a fast-Fourier transform algorithm (FFT). The FFT algorithm has been applied subsequently to packages of 1024

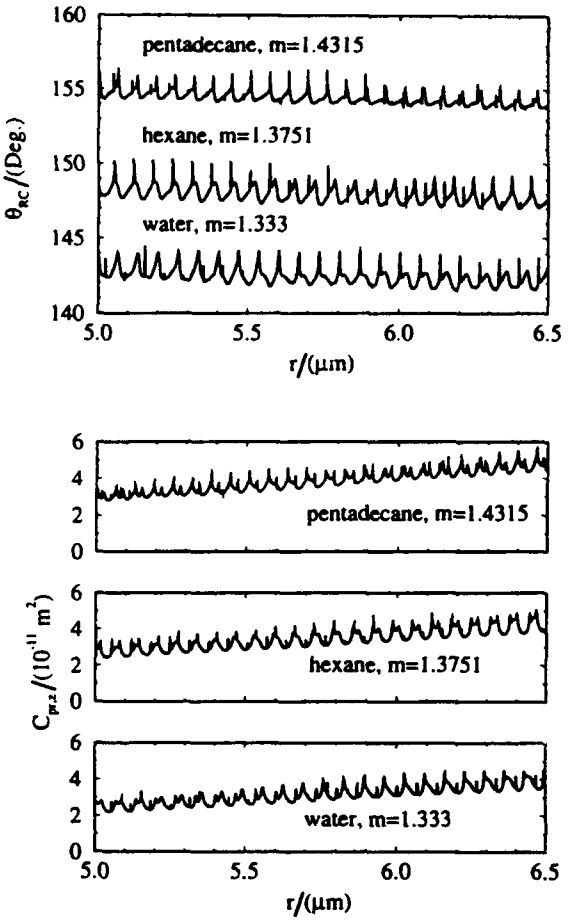

Fig. 4. In the upper diagram the rainbow angle θ_{RC} as a function of droplet radius r is shown. In the three lower diagrams the radiation pressure cross-sections $C_{pr,z}$ is presented in the same size range from $r = 5.0\,\mu m$ to $r = 6.5\,\mu m$. Results are given for water, hexane, and pentadecane. The increment between subsequent radii, at which the values were calculated, is 0.001 μm.

neighbouring points of the droplet radius for which θ_{RC} or $C_{pr,z}$ was calculated. After each FFT the window of 1024 neighbouring points has been shifted by one point. As a results of this procedure one obtains the period p_R for the oscillations of θ_{RC} and the period p_P for the oscillations of $C_{pr,z}$ as a function of the mean radius r_m associated to the 1024 points. Results of this procedure are shown in Fig. 6 and in Fig. 7. There the radius range from $r_m = 10\,\mu m$ to $r_m = 11.5\mu m$ has been evaluated. Again results for water, hexane, and pentadecane are shown. In Fig. 6 the period p_R of the oscillations of the rainbow angle and in Fig. 7 the period p_P of the oscillations of the radiation pressure cross-section is presented. As can be seen from these diagrams the values of

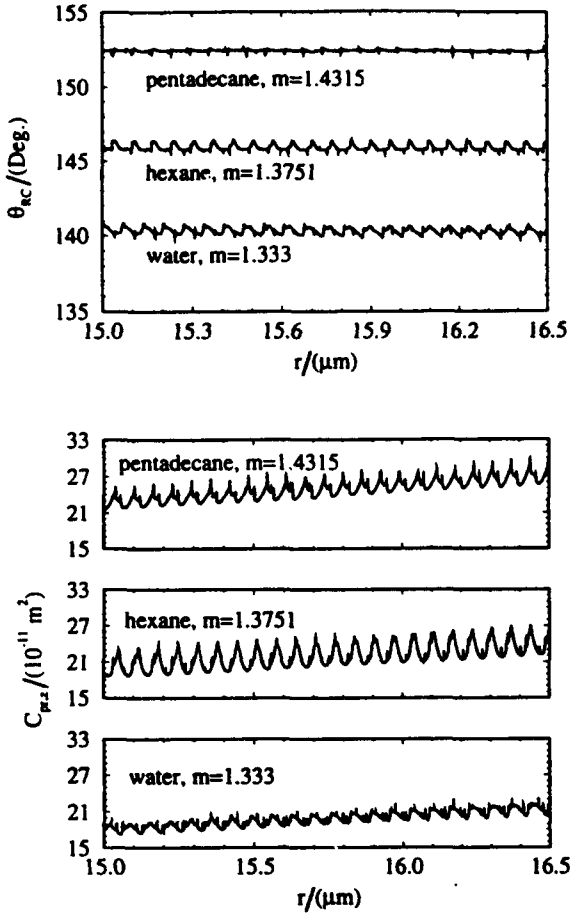

Fig. 5. In the upper diagram the rainbow angles θ_{RC} as a function of droplet radius r is shown. In the three lower diagrams the radiation pressure cross-sections $C_{pr,z}$ is presented for the same size range from $r = 15.0$ μm to $r = 16.5$ μm. Results are given for water, hexane, and pentadecane. The increment between subsequent radii at which the values were calculated is 0.001 μm.

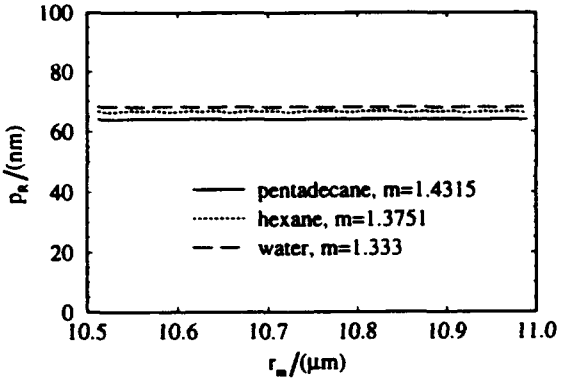

Fig. 6. Period p_R of the oscillations of the rainbow position θ_{RC} as a function of mean radius r_m. Result for water, hexane, and pentadecane are shown in the size range from r = 10.0 μm to r = 11.5 μm.

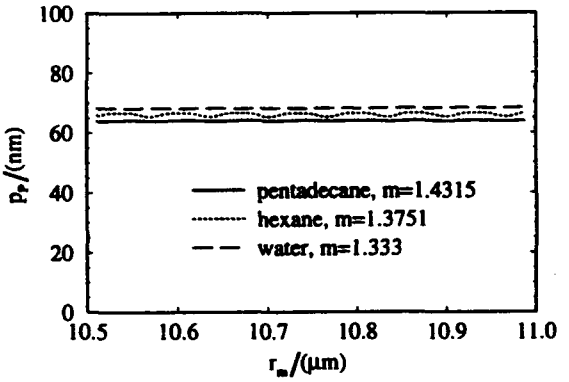

Fig. 7. Period p_P of the oscillations of the radiation pressure cross-sections $C_{pr,z}$ as a function of mean radius r_m. Result for water, hexane, and pentadecane are shown in the size range from 10.0 μm to $r = 11.5$ μm.

period p_R and period p_P are practically the same for equal values of refractive index. Variations with the droplet radius are negligible. A small dependence of the periods p_R and p_P on the refractive index can be found. For the three size ranges from $r_m = 5$ μm to $r_m = 6.5$ μm, from $r_m = 10$ μm to $r_m = 11.5$ μm, and from $r_m = 15$ μm to $r_m = 16.5$ μm the FFT algorithm with the shift of the packages was applied for the data obtained for the refractive indices of the hydrocarbons from pentane to hexadecane and for the refractive index of water. For each size range and for each refractive index the mean values $p_{R,av}$ and $p_{P,av}$ of the periods were calculated. The results are shown in Fig. 8 and Fig. 9 for the average periods $p_{R,av}$ of the oscillations of $\theta_{RC}(r_m)$ and for the average periods $p_{P,av}$ of the oscillations $C_{pr,z}(r_m)$ as a function of the refractive index. It can clearly be seen, that the average periods $p_{R,av}$ and $p_{P,av}$ are practically independent of the droplet radius within the studied size ranges. The values of $p_{R,av}$ and $p_{P,av}$ change very weakly with the refractive index from approximately 68 nm for water with $m = 1.333$ to approximately 64 nm for hexadecane with $m = 1.4345$. The transition from the higher to the lower value becomes more evident in the enlarged view shown in Fig.10. Here the values of the periods $p_{R,av}$ and $p_{P,av}$ are compared for one radius interval. As can be seen in Fig. 10 for refractive indices below $m = 1.36$ a constant value close to 68 nm has been found. For further increasing refractive indices following a transition a constant value close to 64 nm for refractive indices above 1.39 is obtained. Furthermore it should be emphasized that the values of p are identical for both rainbow positions and radiation pressures. In an experiment with evaporation or condensating droplets both the oscillations of the rainbow or the oscillations of the radiation pressure can

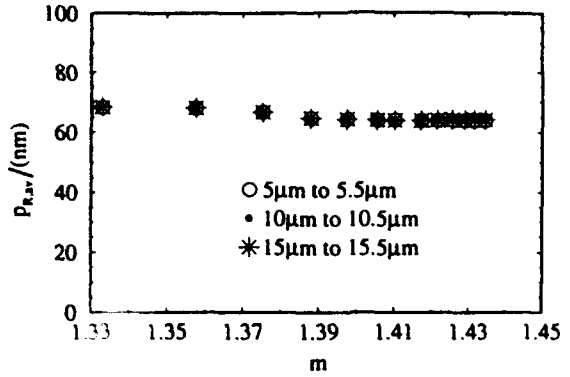

Fig. 8. Averaged period $p_{R,av}$ of the oscillations of the rainbow angle θ_{RC} for the thirteen different refractive indices representing water and the hydrocarbons from pentane to hexadecane. Results are shown for three different size ranges. The averages have been taken over each individual radius interval.

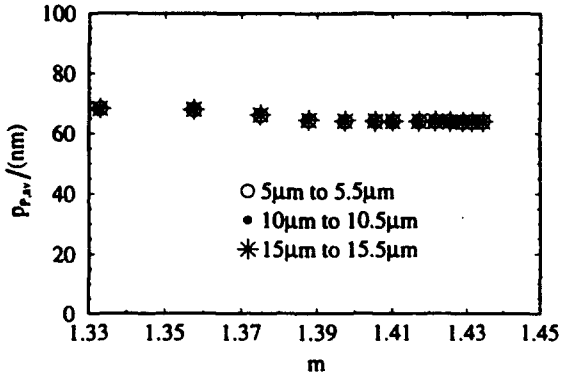

Fig. 9. Averaged period $p_{P,av}$ of the oscillations of the radiation pressure cross-sections $C_{pr,i}$ for the thirteen different refractive indices representing water and the hydrocarbons from pentane to hexadecane. Results are shown for three different size ranges. The averages have been taken over each individual radius interval.

be associated directly with the rate of change of droplet radius $dr/d\tau$ for a range, in which $p(m) \approx$ const.
In this case one has

$$\frac{dr}{d\tau} = p_i f_i \quad , \quad i = R, P \qquad (1)$$

where f_P and f_R are the frequency of the oscillations of radiation pressure or rainbow position respectively. To obtain these values the temporal evolution of one of these values has to be recorded in an appropriate manner. All hydrocarbons

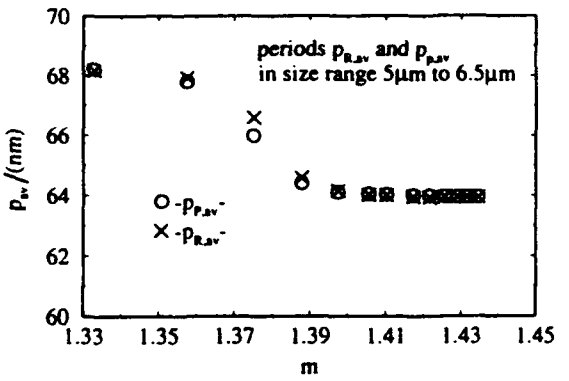

Fig. 10. Averaged period $p_{P,av}$ of the oscillations of the radiation pressure cross-sections $C_{pr,i}$ in comparison with averaged period $p_{R,av}$ of the oscillations of the rainbow angle θ_{RC} for the thirteen different refractive indices representing water and the hydrocarbons from pentane to hexadecane. Results are shown for one size range in an enlarged view.

from octane to hexadecane have refractive indices above 1.39. This gives the basis to examine the evaporation of binary mixtures of these hydrocarbons as p_R and p_P in this range is independent of size and composition.

This theoretical study and the studies of Anders et al. (1993) and Roth et al. (1992) show, that it is possible to measure the refractive index, the droplet size and the evaporation rate in observing and evaluating the scattered light in the region of the first rainbow. This study is the theoretical basis for experimental investigations of evaporation rates of optically levitated droplet. The experimental setup and some experimental results are presented in the following paragraph.

3. EXPERIMENTS

Optical levitation is an appropriate tool to study individual particles. In the work of this paper liquid droplets were levitated optically and stabilized in a vertical laser beam. The technique of optical levitation has been as described in previous papers for instance by Ashkin & Dziedzic (1971). The droplet is observed in a chamber, whose temperature can be adjusted in an appropriate range. Depending on temperature and saturation in the chamber the droplet will evaporate or grow by condensation. The droplet is illuminated by the levitating laser beam of an Ar^+-laser with a wavelength of 514.5 nm. This allows to apply optical non-intrusive measuring techniques to study the droplet behaviour during the evaporation or condensation process.

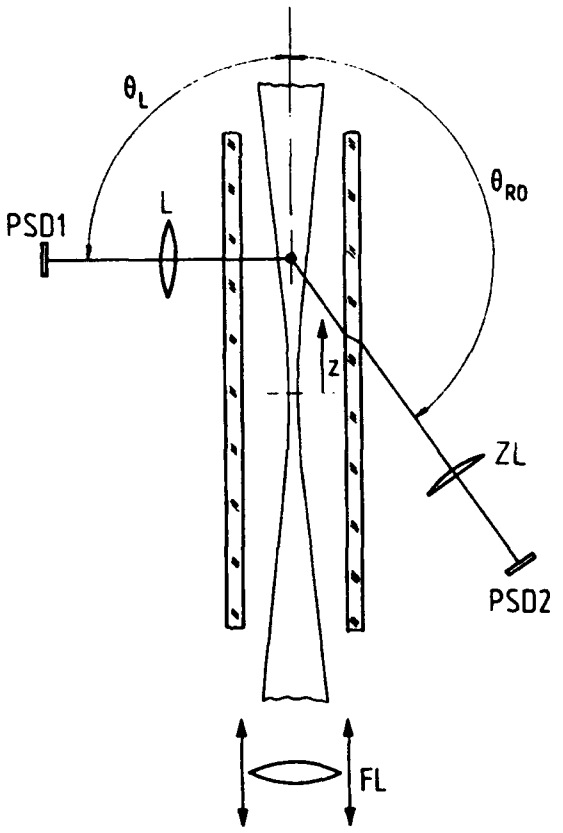

Fig. 11. Schematical view of the experimental setup. The symbols are explained in the text.

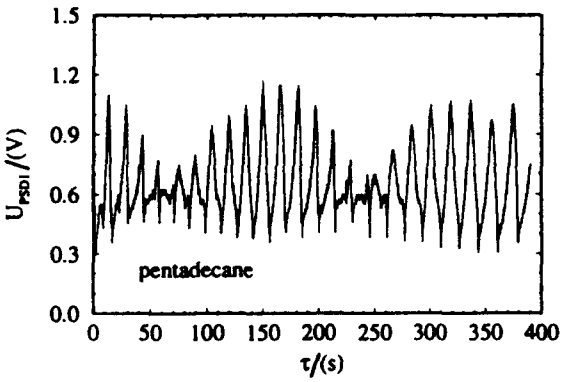

Fig. 12. Output signal U_{PSD1} as a function of time τ of the PSD1, which represents the vertikal droplet position.

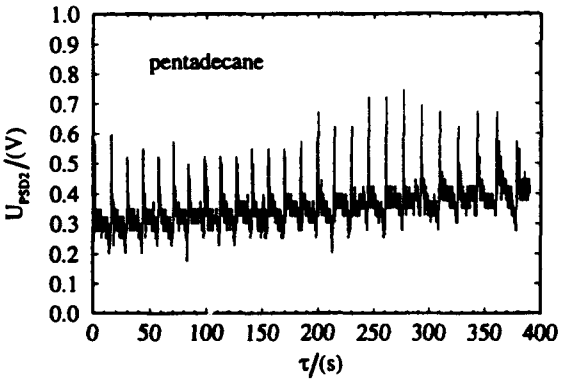

Fig. 13. Output signal U_{PSD2} as a function of time τ of the PSD2, which represents the position of the first rainbow.

The optical set-up used in the experiments of the present paper is shown in Fig. 11. The rate of radius change of a droplet corresponding to the evaporation rate or condensation rate can be determined in evaluating the temporal evolution of the droplet position relative to the focus of the levitating laser beam. This is due to the fact that a droplet with decreasing or increasing radius performs an ocsillatory motion along the axis of the laser beam due to the oscillatory dependence of the light pressure forces on the droplet radius as described in the previous chapter. Light scattered at an angle of 90° is focussed by lens L on the surface of the position sensing detector PSD1. The output signal of this PSD is proportional to the first moment of the light distribution on the sensor surface and is therefore proportional to the position of the light spot on the sensor, which of course corresponds to the position of the droplet. The optical setup is designed to allow the determination of even small changes of the droplet position. An evaporating droplet levitated in a laser beam performs oscillatory motions. These oscillations are detected with PSD1 and recorded by a transient recorder. An example of a record from an evaporating pentadecane droplet is shown in Fig. 12. There the output signal of PSD1 is plotted versus time. The calculations described in the previous chapter showed that to some extend the period length of the oscillations of the radiation pressure as a function of radius are independent of the droplet radius and the refractive index. Therefore the change of droplet radius with time $dr/d\tau$ of a levitated droplet can be determined by evaluating a temporal evolution of the droplet position.

In order to determine the real part of the refractive index the angular position of the first rainbow has to be recorded as described i.e. by Roth et. al. (1991,1993). In the experiments of the present paper the optical arrangement was designed that the rainbow position recorded is not influenced by changes of the positon of the droplet in the laser beam. The light scattered in the rainbow region was imaged by the cylindrical lens ZL on the surface of the position sensing detector PSD2 positioned in the focal plane of the lens. In this case the cylindrical lens

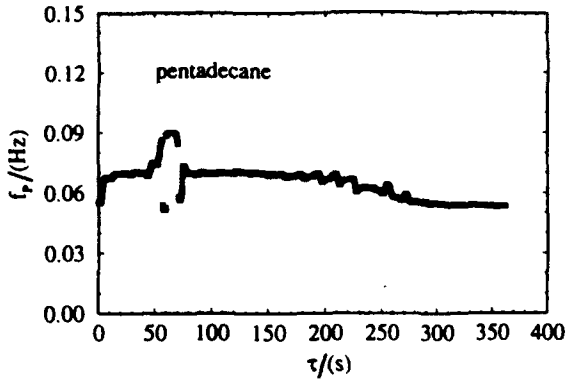

Fig. 14. Temporal evolution of the frequncy f_p of the oscillations of the droplet position. This result has been obtained from the data shown in Fig. 12.

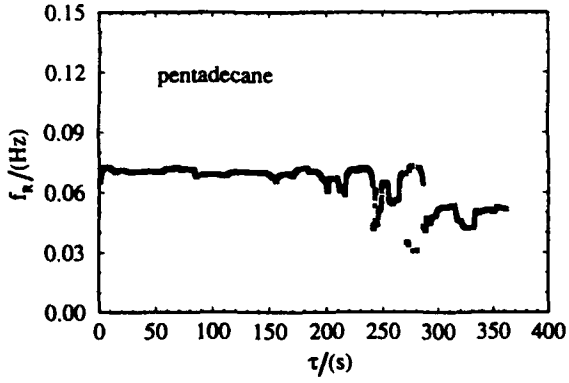

Fig. 15. Temporal evolution of the frequncy f_R of the oscillations of the angular position of the first rainbow. This result has been obtained from the data shown in Fig. 13.

performs an optical Fourier transform of the scattered light; only changes in the angular intensity distributions of the scattered light result in changes of the light distribution on the sensor surface. The application of a PSD to measure rainbow positions was described by Roth et. al. (1993) for monodisperse droplet streams. In the present paper the temporal evolution of the rainbow position for an individual droplet has been examined in detail. The output signal of PSD2 which detects the rainbow position is shown in Fig. 13. This signal has been obtained for the same pentadecane droplet whose position in the laser beam is shown in Fig. 12.

Comparing Fig. 12 and Fig. 13 one can see, that the rainbow position shows peak values occuring with the same frequency as the oscillations of the droplet position, the characteristic of the signal however is quiet different at this particular refractive index. Theoretical calculations with high resolution in radius of the rainbow position applying the correlation algorithm show the same behaviour. This can be clearly seen by comparing Fig. 13 with Fig. 4. By carefully examining the slope between the peaks one can immediately recognize that the droplet is evaporating rather than growing in this case.

In order to get information on the temporal change of droplet radius dr/dτ, which corresponds to the evaporation or condensation rate of the droplet, frequencies of the oscillatory motion of the droplet or of the oscillations of the rainbow position have to be determined. This can be done by applying the FFT-procedure described in chapter 2.3 to the experimental results shown in Fig. 12 and in Fig 13. Results of the FFT procedure are shown in Fig. 14 and in Fig. 15. As expected the frequencies f_p and their temporal evolution obtained for the oscillatory motion shown in Fig. 14 are the same as those obtained for the rainbow positions denoted by f_R and shown in Fig. 14. Only minor deviations can be seen. These can be explained by poor signal quality, for example low amplitude, of the input signal. Applying Eq. (1) the rate $dr/d\tau$ as a function of time can be determined immediately. A slight decrease of the frequencies and therefore for the rate of radius change with increasing time can be observed in both figures. This can be explained by an increasing vapour pressure of pentadecane in the observation chamber in this particular experiment.

4 CONCLUSIONS

In the present paper it has been shown that the rainbow signal can be used to examine the rate of change of droplet radius, corresponding to the evaporation or condensation rate. It has been shown that combining this technique with techniques described in previous papers allows to determine size, refractive index, and evaporation or condensation rate from the intensity distribution in the rainbow region. This gives the possibility to study droplets consisting of binary mixtures. The transient behaviour of the evaporation process of mixtures can be examined by recording the angular rainbow position, which is a measure for the refractive index and therefore for the temperature and composition, and by recording the periodic peaks, which are a measure for the change of radius of the droplet. Furthermore it has been shown theoretically and experimentally that there is a direct relation between fluctuations of the radiation pressure and fluctuations in the rainbow position and that the period of these fluctuations is in a wide range practically independent of droplet size and refractive index.

ACKNOWLEDGMENTS

We gratefully acknowledge the assistance of Dr. G. Gréhan of INSA Rouen/France, who has provided the computer program to calculate radiation pressure cross-sections by GLMT.

REFERENCES

Anders, K., Roth, N., Frohn, A. 1993, Light scattering at the rainbow angle: Information on size and refractive index, Proc. 3rd Int. Congr. on Optical Particle Sizing, Yokokama (Japan), pp.237-242.

Ashkin, A. & Dziedzic, J.M. 1971, Optical levitation by radiation pressure, Appl. Phys. Lett., vol. 19, pp.283-285

Bohren, C.F., Huffman, D.R. 1983, Absorption and scattering of light by small particles, John Wiley & Sons, New York.

Gouesbet, G, Maheu B., Gréhan G 1988, Light scattering from a sphere arbitrarily located in a Gaussian beam, using Bromwich formulation, J.Opt. Soc. Am. A vol. 5, pp1427-1443.

Massoli, P., Beretta, F., D'Alessio, A., Lazzaro 1993, Temperature and size of single transparent droplets by light scattering in the forward and rainbow regions, Appl. Opt., vol.30, pp.3295-3301.

Kai, L., Massoli, P., D'Alesio, A 1993, Studying inhomogeneities of spherical particles by light scattering, Proc. 3rd Int. Congr. on Optical Particle Sizing, Yokokama (Japan), pp.135-143.

Ren, K.F., Gréhan, G., Gouesbet, G.1994, Radiation pressure forces exerted on a particle arbitraily located in a Gaussian beam by using the generalized Lorenz-Mie theory, and associated resonance effects (accepted Opt. Commun.)

Roth, N., Anders, K., Frohn, A. 1988, Simultaneous measurement of temperature and size of droplets in the micrometer range, Proc. 7. Int. Con. on Optical Methods in Flow and Particle Diagnostics ICALEO 88, L.I.A. Vol.67, pp.294-304.

Roth, N., Anders, K., Frohn, A. 1989, Temporal evolution of size and temperature measurements of burning ethanol droplets for different initial temperatures, Proc. Joint Meeting of the German and Italian Sections of the Combustion Institute, Ravello (Italy), pp.2.3.

Roth, N., Anders, K., Frohn, A. 1990, Simultaneous measurements of temperature and size of droplets in the micrometer range, J. Laser Applications, vol. 2, No.1, pp.37-42.

Roth, N., Anders, K., Frohn, A., 1991, Refractive-index measurements for the correction of particle sizing methods, Appl. Opt., vol. 30, No. 33, 4960-4965.

Roth, N., Anders, K., Frohn, A., 1992, Simultaneous determination of refractive index and droplet size using Mie-theory, Proc. 6th Int. Symp. on Application of Laser Techniques to Fluid Mechanics, Lisbon, 15.5.1

Roth, N., Anders, K., Frohn, A., 1993, Measurement of the rainbow positon using a PSD-Sensor, Proc. 3rd Int. Congr. on Optical Particle Sizing, Yokohama (Japan), pp.183-187.

Roth, N. Anders, K., Frohn, A.,1994, Determination of size, evaporation rate, and freezing of water droplets using light scattering and radiation pressure, Part. Part. Syst. Charact., vol.11, (in press), .

Sankar, S.V., Ibrahim, K.M., Buermann, D.H., Fidrich, M.J., Bachalo, W.D. 1993, An integrated phase Doppler/rainbow refractometer system for simultaneous measurements of droplet size, velocity and refractive index, Proc. 3rd Int. Congr. on Optical Particle Sizing, Yokokama (Japan), pp.275-284.

Schneider, M., Hirleman, E.D., Saleheen, H., Chowdhary, D.Q., Hill, S.C. 1993, Rainbows and radially-inhomogeneous droplets, Proc. 3rd Int. Congr. on Optical Particle Sizing, Yokokama (Japan), pp.323-326.

Walker, J. D. 1976, Multiple rainbows from single drops of water and other liquids, Am. J. Phys., vol. 44, pp.421-433.

A New Technique to Measure Refractive Index with Phase Doppler Anemometry

by

Hans-Henrik Benzon, Preben Buchhave
The Technical University of Denmark, Physics Dept.

Thomas Nonn
Dantec Measurement Technology

Abstract

A standard phase-Doppler system was modified to determine the feasibility of refractive index measurements utilizing new optical techniques. With the use of two laser beam systems of different wavelength and a single receiving unit different optical configurations can be explored by varying the scattering, elevation and crossing angles independently for each system. The index of refraction of a droplet can be extracted from the phase-shift ratio of two distinct pairs of apertures. Selecting the proper optical parameters yields a sensitive relationship between phase ratio and refractive index.

For measurements an LDA configuration with two transmitting optics was chosen because of its widespread use and standard components. The two probes were situated 40° relative to each other. This was done to maximize the relationship between the ratio of phase shifts and the refractive index. Tests were conducted on water-glucose mixtures with varying refractive index.

1 Introduction

The fundamental concept behind Phase-Doppler Anemometry (PDA) is that for carefully selected scattering angles a linear relationship can be derived between the phase shift of a particle measured as it passes through an LDA measurement volume and its size. This relationship holds for so long as certain restrictions are enforced (i.e., size range of particles relative to LDA probe volume, dominant scattering mode, polarization) and that the physical properties of the system should remain constant (i.e., refractive index, wavelength of light). In multiphase flows and in sprays where varying temperature environments are experienced, as in combustion, the refractive index of droplets can clearly vary. This variation within the normal PDA operation can add bias to measurements. Several methods have been developed to extend the operation of PDA to include the measurement of refractive index with some success. A two-receiver configuration explored by Pitcher *et al.* [1] and Naqwi *et al.* [2] allude to this. The strength of their method lies in that the dependence of the phase shift on refractive index varies more in the near forward off-axis regions than in the far off-axis regions. Alternatively, Sankar *et al.* [3] utilized the clear dependence of the rainbow angle with refractive index in another instrument configuration. This technique, however, is complex and as indicated by the authors the system is sensitive to high frequency oscillations. An appealing side to refractive index measurement is the ability to confirm different particle types within the same particle distribution. A persistent problem is the existence of multiple modes of light scattering in sprays. Droplets can reflect as well as refract and therefore present a problem when calculating spray statistics. In the standard PDA implementation there is a region of overlap as indicated in Nonn *et al.* [4] between reflecting and refracting particles that lead to ambiguity of some results. Having additional optical information can perhaps help resolve this issue.

2 Theory

The implementation of [1] utilizes the fact that the Doppler-phase is a linear function of diameter and that the refractive index is contained within the proportionality constant for first and higher orders of refraction. This means that the ratio of two phases will be independent of diameter and only dependent on the refractive index of the particle and the parameters that describe the optical configuration. The measurement was accomplished by using two receivers positioned at two different scattering angles. The angles were chosen so that refraction dominated at both angles.

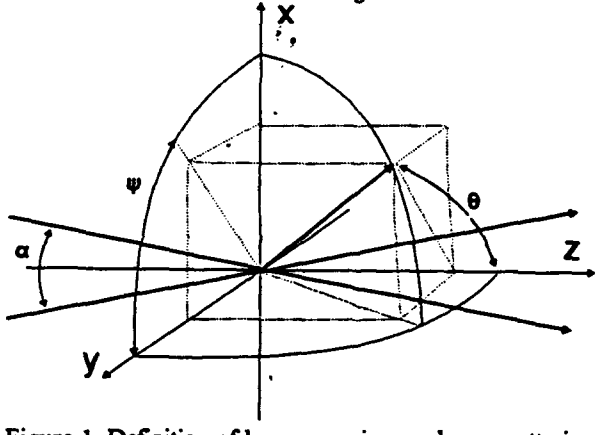

Figure 1. Definition of beam crossing angle α, scattering angle θ and elevation angle ψ

This system is equivelant to one where there are two laser beam systems, for example green and blue, and a single receiver. The light received from this system can then be subsequently separated and analyzed. The advantage of this system is that the three apertures of the receiver can be used for both laser systems. In Figure 1, the reference coordinate system for the green beam system is shown. If we superimpose the blue system and rotate it about the x-axis we get

a system that is equivalent to the system suggested by [1]. The advantage of this method is that one can change the elevation angle and scattering of one beam system independently. The purpose in all this is to maximize the change in the phase ratio.

Rotating the blue system around the z-axis in the reference system has the effect of placing the receiving unit at a different elevation angle. The standard PDA system contains three receiving apertures. In the new system there are three pairs of angularly placed apertures. The index of refraction can be determined from the ratio between the same two aperture pairs for the different beam systems. Having additional apertures also means having more calibration curves for the determination of refractive index, hence data can be verified with different combinations.

The following section will describe the selection of appropriate values for parameters to maximize measurement of the refractive index. To produce a sensitive calibration curve for the refractive index the phase shifts of one of the systems must change more rapidly. The correct choice for optical parameters can be seen in the Table 1. Of the parameters listed the elevation angle is the most sensitive with respect to the phase of the Doppler signal and the wavelength the least.

	Rapidly varying Doppler phase	Slowly varying Doppler phase
Wavelength λ	small (blue)	large (green)
Scattering angle θ	small	large
Crossing angle α	large	small
Elevation angle ψ	large	small

Table 1. Optimum selection of optical parameters.

The overall dynamic range and resolution can be improved by selecting the appropriate calibration curve from the two beam system.

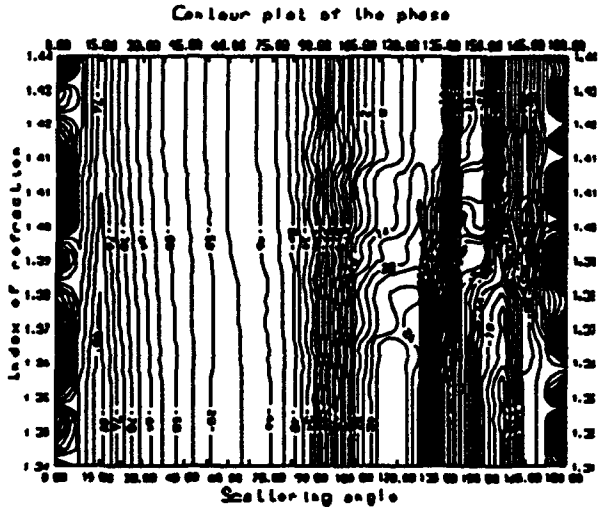

Figure 2. Lorenz-Mie based iso-phase plot as a function of scattering angle and index of refraction.

One gets an idea how the Doppler-phase varies with elevation angle, scattering angle and the refractive index from the iso-plots in Figures 2 and 3. The plots are calculated for a standard PDA system with a crossing angle (α, Fig. 1) of 12.52°, parallel polarization and particle size of 12 μm using Lorenz-Mie theory. The Doppler signal is integrated over the PDA aperture. The scattering angle in the elevation plot is 30°.

From Figure 2 it can be seen that the Doppler phase exhibits more complicated behavior for the back scatter region, as is expected. One could imagine using the second-order refraction to measure in regions where the index of refraction varies little. In the near forward region the Doppler-phase varies rapidly, reaching a maximum change at 20°. As we increase scattering angle the sensitivities decreases. Around a scattering angle of 70° refraction stills dominates but the sensitivity is small. It can be also be inferred from the plots that the Doppler-phase is more sensitive to changes of elevation angle then scattering angle.

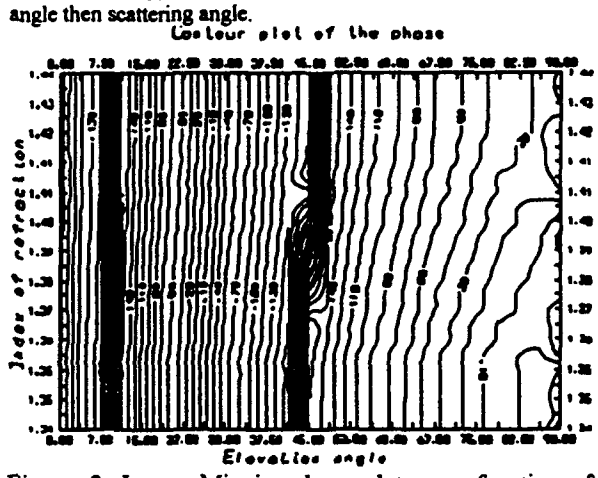

Figure 3. Lorenz-Mie iso-phase plot as a function of elevation angle and refractive index. Scattering angle 30°.

3 Experimental Layout

As indicated earlier a standard Dantec LDA system was used as the test bed for refractive index measurement. To allow for these measurements the standard 57X10 PDA Receiving Optics was modified with three 55X35 color separators. The five photomultipliers were connected to the color separators and routed to a modified Dantec 58N10 PDA signal processor.

The optical layout of the present experiment consisted of the two FiberFlow probes (green and blue) situated at two scattering angles to the receiver, as in Figure 4. The green and blue system were placed 40° with respect to each other, thus making the effective scattering angle with the receiver for the blue and green systems 30° and 70°, respectively. The focal lengths for the transmitting probes were 400 mm, with a beam separation 40 mm, creating a probe volume of diameter 260 μm. The receiver used had a focal length of 310 mm.

In the standard PDA arrangement three phase detectors are used to measure the phase differences between three apertures. An additional phase detector was employed to measure the phase shift from one pair of the apertures of the blue beam system. More detectors could be employed, up to

six, to make a more robust validation. An advantage of using two colors is that the intensity of the beams can be varied independently relative to the receiver. This is useful since the intensity can vary considerably as one goes from the near forward to side scatter.

To ensure proper measurements coincidence between the two pairs of beams is paramount. However, since this configuration also allows for 3-D velocity measurements, this requirement would anyway have to be fulfilled. Alignment was accomplished by first using a 100 μm pinhole, optimizing, and then repeating the procedure with a 50 μm pinhole. The pinholes by themselves were not sufficient to guarantee coincidence, therefore, to maximize overlap of the probe volumes a light sensing diode was placed behind the 50 μm pinhole and the beams manipulated until the maximum beam power was attained at the crossing. The slightest deviation in the alignment had the effect of making the refractive index measurements unusable. In order to get a valid measurement the phases measured from the separate beam systems must correspond to the same particle. Thus, this method makes an excellent test of coincidence for 3D LDA systems.

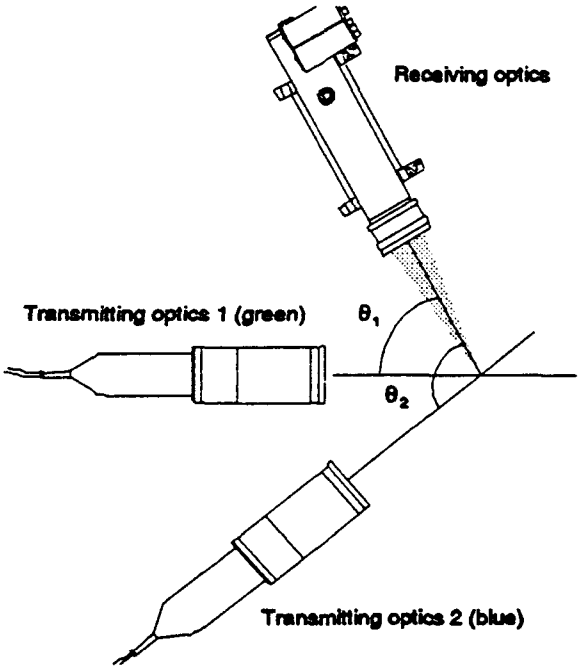

Figure 4. Optical layout with two transmitters situated at 30° and 70° with respect to the receiver.

The test particles were spray droplets made from solutions of water with varying amounts of dissolved glucose. By adding incremental amounts by weight of solid glucose into distilled water one can change the refractive index. The uncertainty in the measurement of glucose dissolved was limited to within 0.01 %.

Figure 5 illustrates the system calibration curve for a 11.9 μm and 12.5 μm particle. The curve is based on the U1-2 phase shift ratio for the green and blue systems. It must be emphasized that the Lorenz-Mie calculations for refractive index are size dependent, that is, each particle size has its own characteristic oscillation. For small particles the oscillations are more pronounced than for larger particles. It was stressed in [1,2] that such oscillatory behavior in small particles would make refractive index measurement difficult if not impossible. A very small spread of particle size will effectively randomize the phase oscillation and average the index measurement. The result will then coincide with the geometric optics calibration curve. To test the robustness of this setup a spray was measured having an effective size distribution of 2-30 μm. It is thought, that a distribution of particles over a range of sizes would tend to average out the effect of the oscillations.

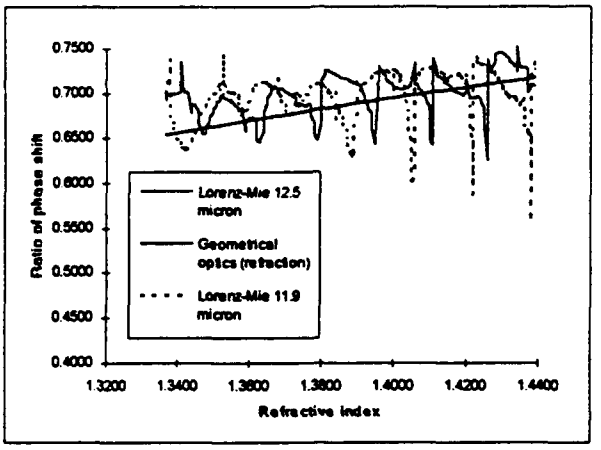

Figure 5. Comparison of Lorenz-Mie and refraction calibration curve for different refractive indexes. Particle diameters were 11.9 μm and 12.5 μm.

4 Measurements

Measurements were made using water droplets issued from an airbrush mixed with glucose in controlled proportions to vary the refractive index. At 20 °C water exhibits a refractive index of 1.334. Adding by percent weight glucose from 0.5% up to 60 % increases the refractive index from 1.337 to 1.439 [5]. Figure 6 displays a typical run with the characteristic peak indicating the dominant phase ratio, corresponding to the refractive index measured.

The accuracy of the measurements over the range of refractive indices tested are listed in table 2 and displayed in Figure 7. The maximum error in the measurement of refractive index was under 2 %. Considering the difficulties implied by the scattering relations and alignment of the system this is a positive result. Though it was not attempted in these tests, an improvement to the sensitivity could be accomplished by choosing an alternate phase ratio; i.e., the ratio between the U1-3 and U1-2 for the two systems. Alternatively, the elevation angle and/or the crossing angle in one of the two systems can be changed.

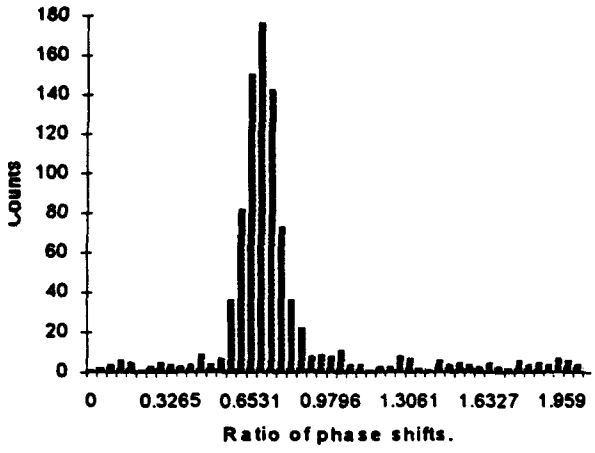

Figure 6. Histogram of phase shift ratio using glucose 40 % by weight.

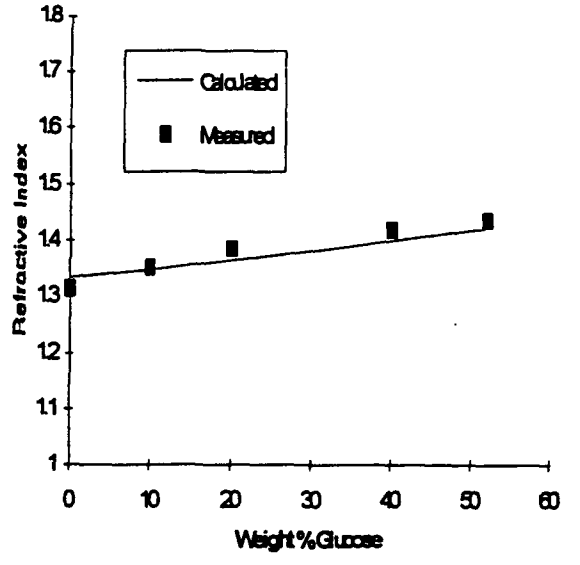

Figure 7. Measured and estimated refractive index as a function of % weight glucose.

% weight glucose	Calculated index	Measured index	Deviation (%)
0	1.334	1.3167	1.2964
10	1.3477	1.353	0.395
20	1.3635	1.3876	1.7683
40	1.3986	1.4222	1.687
52	1.4222	1.4394	1.216

Table 2. Comparison between measured and actual values of refractive index.

5 Conclusion

In this paper we have described a new method for measuring the relative refractive index. This technique has several advantages in that there are many possible permutations of the optical configuration. That is, the elevation angle, scattering angle and crossing angles can be selected independently for each beam system. This means that the phase ratio can be made more sensitive to the index of refraction.

The implementation in this paper shows that a standard PDA system can be easily extended to include the measurement of refractive index. Measurements were made with sprays consisting of droplets of substances with varying index of refraction. The accuracy on average was within 2 % of the estimated value determined from geometrical optics. Furthermore, the refractive ratios that are measured are excellent indicators of coincidence between the beam systems.

The study is preliminary and it is hoped that in future more work will be done to develop this technique and applying it to practical situations.

References

1. Saffman M., G.Pitcher and G.Wigley, "Sensitivity of Dropsize Measurements by Phase Doppler Anemometry to Refractive Index Changes in Combusting Fuel Sprays", Proceedings, *The International Symposium on Applications of Laser Anemometry to Fluid Mechanics*, Lisbon, Portugal, 1990.
2. Naqwi A., F. Durst and X.-Z.Lui, "An Extended Phase-Doppler System for Characterization of Multiphase Flows", Proceedings, *The International Symposium on Applications of Laser Anemometry to Fluid Mechanics*, Lisbon, Portugal, 1990.
3. Sankar S., K.M.Ibrahim, D.H:Buermann, M.J.Fidrich, and W.D. Bachalo, "An Integrated Phase Doppler/Rainbow Refractometer System for Simultaneous Measurement of Droplet Size, Velocity, and Refractive Index", Proceedings, *3rd International Congress on Optical Particle Sizing*, Yokohama, Japan, 1993.
4. Thomas Nonn and Zeev Dagan, "Analysis of Particle Mixtures Exhibiting Different Scattering Modes by Phase Discrimination", Proceedings, *3rd International Congress on Optical Particle Sizing*, Yokohama, Japan, 1993.
5. Weast, "Handbook of Chemistry and Physics", 53rd edition, pg, D-211, CRC Press.

Phase-Doppler Anemometry with Dual Burst Technique for Particle Refractive Index Measurements

F. Onofri[†], G. Gréhan[†], G. Gouesbet[†], T.-H. Xu[††], G. Brenn[††] and C. Tropea[††]

[†] Laboratoire d'Energétique des Systèmes et Procédés
U.R.A. C.N.R.S. 230,
INSA de Rouen, B.P. 08, 76131 Mont-Saint-Aignan, France

[††] Lehrstuhl für Strömungsmechanik
Universität Erlangen-Nürnberg, Cauerstr. 4, D-91058 Erlangen, FRG

Abstract

The principle of the Dual Burst Technique (DBT) based on phase-Doppler Anemometry (PDA) is proposed for simultaneous particle refractive index, size and velocity measurements. This technique uses the trajectory effects in PDA systems to separate the two contributions of the different scattering processes. In the case of forward scattering and refracting particles, it is shown that from the phase of the reflected contribution, the particle diameter can be deduced, whereas from the phase of the refracted contribution the particle refractive index and velocity can be obtained. Simulations based on generalized Lorenz-Mie theory and experimental tests using monodispersed droplets of different refractive indices have validated this technique.

1 Introduction

Phase-Doppler Anemometry is now a well established particle sizing technique in laboratories and industries for studying two-phase flows and sprays. It can provide a particle size distribution correlated with up to three particle velocity components, with a high resolution in time and in space, without being intrusive. The principle, which is now about 20 years old (Durst and Zaré (1975), Bachalo and Houser (1984), Saffman et al. (1984)), is that when a particle is passing through an optical measuring volume defined by the intersection of two laser beams, the phase of the light scattered by the particle carries information about the particle diameter, whereas its frequency provides information about its velocity.

To collect scattered light, a scattering angle should be chosen to ensure that the phase-diameter relationship for each detector pair is linear. This condition can be obtained when the detectors collect light scattered by the particle mainly due to a single scattering process, i.e. reflection, refraction, or 2nd order refraction. It is well known that the scattering angle must be carefully chosen according to the particle refractive index.

As many experimental investigations in the field of two-phase flow, multiphase flow and combustion require simultaneous measurements of individual particle size, velocity and also refractive index, several systems, based on the phase-Doppler technique, have been proposed (Naqwi et al. (1991), Sankar et al. (1993)). Because of the argument in the last paragraph, these system may not suitable for a large measuring range of particle refractive indices. When measurements are performed in a complex flow field e.g. in sprays, the influence of Trajectory Effects (TE) (Sankar et al. 1992, Gréhan et al. (1992), Onofri et al. (1992)) on refractive index measurements has to be considered. Furthermore, these systems require extra receiving units for the refractive index measurements, which increases alignment requirements and costs.

Based on previous works to eliminate TE in PDA systems by Aizu et al. (1993), Xu and Tropea (1994), Tropea et al. (1994) and Gréhan et al. (1994), an innovative PDA technique, called *the Dual Burst Technique* (DBT), is proposed in this paper for refractive index measurements, in addition to particle size and velocity measurements, using a single receiving unit. An obvious advantage of the technique is that it can be easily applied to an existing PDA, with only minimum modifications.

In this paper, after a short review of the newly proposed technique for TE elimination, the principle of DBT is introduced in section 2. Section 3 presents some simulation results using a phase-Doppler code based on the Generalized Lorenz-Mie Theory (GLMT) (see Gouesbet et al. (1991), Gréhan et al. (1991)) and section 4 gives some useful formulae from Geometrical Optics. Section 5 reports the preliminary experimental results of DBT. In section 6 these experimental results are further discussed and points for the future development of DBT are proposed. Finally, section 7 is a conclusion with perspectives.

2 Principle

2.1 TE elimination

Recently two PDA optical geometries and a signal processing procedure have been proposed for TE elimination. The first geometry is a Planar-PDA arrangement (Aizu et al. (1993)), and the second one has been referred to as the Modified Standard geometry (Xu and Tropea (1994), Tropea et al. (1994), Gréhan et al. (1994)). The principle used in these geometries to eliminate TE is briefly reviewed as a basis for introducing DBT.

Referring to Fig.1, the scattering of a laser beam with a Gaussian intensity distribution from a relatively large particle is pictured. In this and for further discussions, scattering in the forward direction and refractive dominated scattering is considered. Since the scattering angle usually exceeds 20°, diffraction can be neglected.

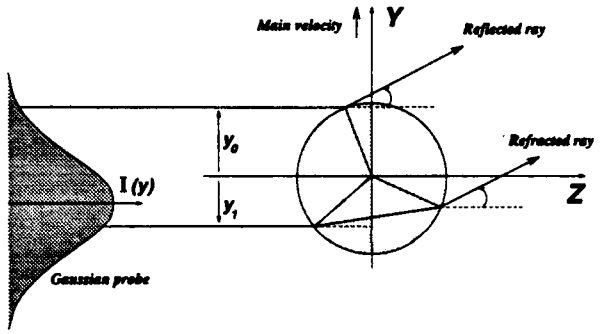

Figure 1: *Simplified scattering processes of a refractive particle in forward scattering, out of the diffraction zone.*

In a standard PDA arrangement, the scattering angle is chosen such that the refractive component dominates. Depending on the trajectory however, the incident light for reflection may greatly exceed that for refraction due to the Gaussian intensity profile $I(y)$, thus altering the received phase. This is the cause of the TE. As shown in Fig. 1, for a given receiving angle the point of the incident light impinging on the particle for the reflection (y_0) is different from the point of that for the refraction (y_1). Therefore when the particle passes through the probe volume along y-axis, there will be a time delay between the intensity maxima of the reflected ray and the refracted ray. In the proposals to eliminate the TE, this time delay is used to separate the refracted contribution from the reflected contribution. Moreover, the signal received from the refractive scattering is much larger in amplitude, allowing a positioning within the burst to insure phase determination corresponding to refractive scattering.

The experimental illustration of this effect in the PDA technique has been first used and reported by Aizu et al. (1993), and afterwards by Xu and Tropea (1994). Hess and Wood (1992), (1993) have also used this effect in their Pulse Displacement Technique, using a thin laser sheet to estimate the particle diameter from the measurement of the time delay between the two intensity maxima from reflection and refraction.

2.2 Dual Burst Technique

In previous work on PDA, this time delay in the different scattering process contributions reaching the detectors was used only to suppress TE by processing the portion of the burst originating from refractive scattering. However, further informations can be extracted by using all portions of the signal. Of the two scattering contributions, i.e. reflection (p=0) and refraction (p=1), only the refracted light is influenced by the material properties of the particle. The basic idea of *the Dual Burst Technique* (DBT) is therefore to use all the phase information contained in the signal bursts for particle material recognition and particle diagnoses (non homogeneity, non sphericity). The present paper is devoted mainly to study the feasibility of the former and the latter will only be briefly discussed.

The principle of DBT for particle material recognition can be given as follows. The phase of the refracted light from a particle is a function of optical setup, particle size and particle refractive index. The phase of the reflected light is, however, only a function of optical setup and particle size, not particle refractive index. From the reflected burst, the particle diameter can be deduced. Knowing this diameter and the optical parameters of the PDA, the particle refractive index can be determined from the phase of the refracted burst.

To use DBT, the beam waist diameter must be reduced compared to typical values in PDA, in order to increase the time delay between the reflected and refracted contributions. Indeed, for a dominant refractive particle the reflected contribution is very low compared to the refracted contribution. Therefore any mixing between the two scattering processes must be avoided. Furthermore, with a smaller measuring volume, the laser power is focussed on a smaller area, which also increases the SNR of the reflected contribution.

3 GLMT Simulations

Numerical simulations, using a phase-Doppler code based on GLMT, have been carried out to investigate DBT. Water droplets were assumed to pass through a 54μm measurement volume ($\lambda = .6328\mu$m) of a Modified Standard PDA with two detectors (see Fig. 2).

The off-axis angle, the elevation angles and the half-beam angle are defined by ϕ, ψ^i, α, and were equal to 30^o, $\pm 3.69^o$, 1.7^o respectively. The receiving aperture shape was rectangular, with an angular aperture defined by $\delta x = \pm 0.277^o$, $\delta y = \pm 2.77^o$.

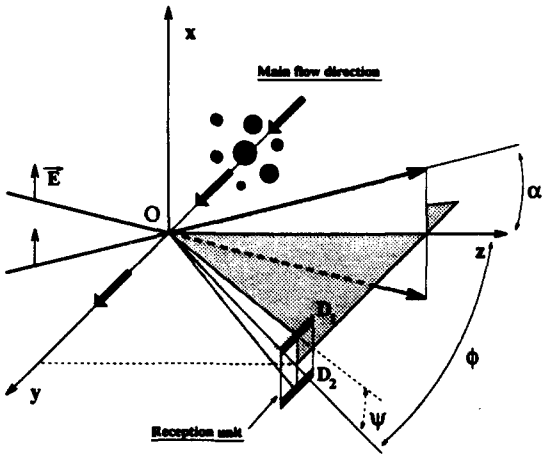

Figure 2: *Optical geometry of a Modified Standard PDA for implementing DBT.*

Fig.3a) displays the simulated phases when the droplets are moving along (OY), whereas Fig.3b) displays the corresponding signal intensity.

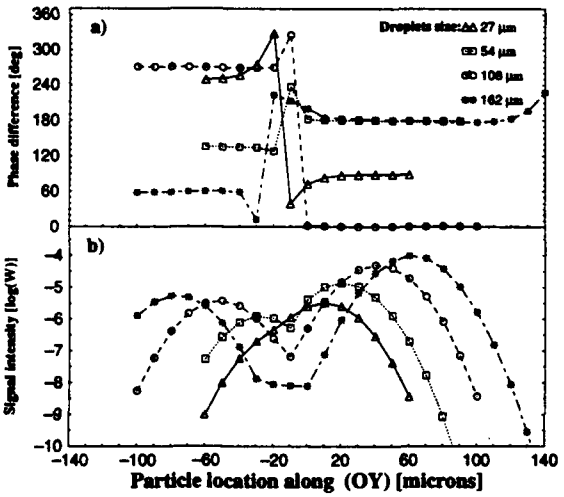

Figure 3: *Dual Burst Technique: Simulated a) Phase difference and b) Signal intensity versus droplet y-location and diameter. Measuring volume diameter* $2\omega_0 = 54\mu m$, *off-axis angle* $\phi = 30^o$, *refractive index* $m = 1.333$.

Both in Fig.3a) and Fig.3b), the two scattering processes ($p = 0$ for $y < 0$, $p = 1$ for $y > 0$) are evident, characterized in Fig.3a) by a flat behavior of the phase evolution, and in Fig.3b) by local maxima for signal intensity. For a $108\mu m$ water droplet for instance, two intensity maxima located at $y \approx -50$ μm and $y \approx 40$ μm can be distinguished. These two locations of intensity maxima correspond to two phase values in the two flat parts of the phase diagrams: $\Phi_0 \approx 270$ *deg* and $\Phi_1 \approx 1$ *deg*. Using these two phases and relations from Geometrical Optics (see next section), the particle diameter and refractive index are determined as 107.7μm and 1.333, respectively. The time delay, expressed here as a space delay between the maxima, decreases with the particle diameter. For the 27μm droplet, the two scattering processes are not well separated, i.e., the first intensity maximum is not clear. Furthermore, the phase difference continues to evolve in the "reflected signal" (as for the TE), demonstrating that there is a mixing of the scattered contributions. The diameter/refractive index deduced as above for the 27μm, 54μm and 162μm water droplets are respectively $24.5\mu m/1.30$, $53.9\mu m/1.328$ and $159.9\mu m/1.330$.

Fig.4 displays the evolution of the signal intensity and the simulated phase difference for the 54μm droplet when its trajectory is still parallel to the fringes as in Fig. 3 but at different x-locations. In the phase

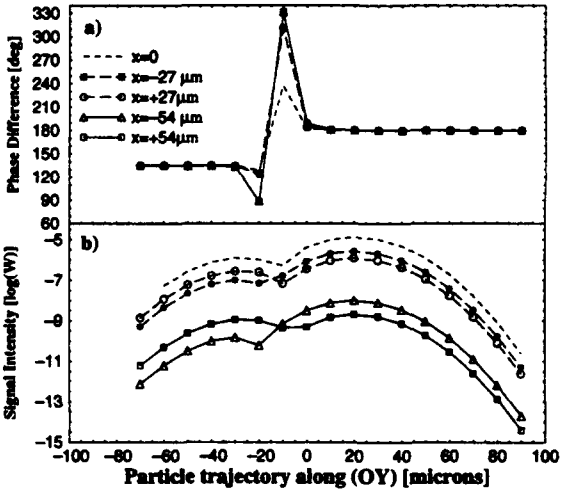

Figure 4: *DBT is free of TE: Simulated a) Phase difference and b) Signal intensity versus droplet y-location for different x-locations. Droplet diameter* $D_p = 54\mu m$, *refractive index* $m = 1.333$, *PDA setup is identical to Fig. 3.*

patterns, only the mixing region evolves with the particle trajectory distance from the probe volume center. The two flat parts are independent of the particle trajectory, i.e., DBT is free of TE.

4 Analytical Expressions from Geometrical Optics

In the current study of DBT, Geometrical Optics was used to determine the particle diameter and refrac-

tive index, because it provides analytical expressions in a simple form. In future it is possible to use look-up tables based on GLMT for a more accurate prediction.

According to Naqwi et al. (1991), the phase conversion factors for reflected light (C_0^i) and for refracted light (C_1^i) can be expressed for a point detector as a function of off-axis angle ϕ and elevation ψ^i:

$$C_0^i = \frac{a^i}{\sqrt{2(1-b^i)}} \quad (1)$$

$$C_1^i = -\frac{m\,a^i}{\sqrt{2(1+b^i)[1+m^2-m\,\sqrt{2(1+b^i)}]}} \quad (2)$$

with

$$\begin{cases} a^i = k\sin(\alpha)\sin(\psi^i) \\ b^i = \cos(\alpha)\cos(\psi^i)\cos(\phi) \end{cases} \quad (3)$$

where $i = 1, 2$ stands for the detector considered, and k for the wave number. For phase-difference measurements, the useful parameters are (with $p = 0,\ 1$)

$$C_p^{12} = C_p^1 - C_p^2 \quad (4)$$

When a particle is passing through the measuring volume, from the detectors $D1$ and $D2$ we get the phase difference Φ_0^{12} from the maximum of the reflected part of the corresponding burst, and the phase difference Φ_1^{12} from the maximum of the refracted part. These phase differences are related to the particle diameter (D_P) and refractive index by

$$\Phi_0^{12} = C_0^{12}\,D_P - n_0\,\pi \quad (5)$$

$$\Phi_1^{12} = C_1^{12}\,D_P + n_1\,\pi \quad (6)$$

Here the even numbers of phase jumps over π, n_0 and n_1 cannot be determined since two detectors have been considered. Nevertheless these parameters are kept in order to check the sensitivity to refractive index measurements with DBT.

Knowing Φ_0^{12} and n_0, the particle diameter can be deduced by

$$D_P = \frac{\Phi_0^{12} + n_0\,\pi}{C_0^{12}} \quad (7)$$

Knowing Φ_1^{12}, n_1, and D_P, the particle refractive index can be simply deduced by solving Eq.(2), yielding

$$m = \frac{\sqrt{2(1+b^1)} + \sqrt{2(1+b^1) - 4x}}{2x} \quad (8)$$

with

$$\begin{cases} x = 1 - \dfrac{2(a^1)^2}{(1+b^1)^2(C_1^{12})^2} \\ C_1^{12} = \dfrac{\Phi_1^{12} + n_1\,\pi}{D_P} \end{cases} \quad (9)$$

5 Experimental Investigations

5.1 Optical setup and procedure

The PDA geometry used in the experiments was the same as in the GLMT simulations, however the detector aperture shape was circular with a cone half-angle equal to 2.77°. The particle stream was in the negative y direction, in contrast to the illustration in Fig.3. For the purpose of achieving a measuring volume with a small diameter and also a small beam-crossing half angle of 1.7°, prisms for setting the beam separation to 4.75 mm and a transmitting lens with a focal length of 80 mm were used. With a 10 mW He-Ne laser, a measuring volume diameter of 54 μm has been achieved. The optical arrangement yields for the reflected light a constant phase factor $C_0^{12} = 4.16°/\mu m$, whereas for refracted light the conversion factor is a function of the particle refractive index. For instance, $C_1^{12} = -3.33°/\mu m$ when m=1.333, using Eqns.(2-4).

Monodispersed droplets produced from a TSI droplet generator have been used for the tests. Water (m=1.333), ethanol (m=1.361) and a sugar-water solution (45% sucrose by weight, m=1.410), were used for different particle refractive indices. The nominal sizes of the droplets, according to the setup of the droplet generator, were $95-98\mu m$ for water, $89-91\mu m$, $100\mu m$ and $125\mu m$ for the sugar-water solution and $25-38\mu m$, $41-45\mu m$ and $54-64\mu m$ for ethanol.

The bursts were stored in a digital oscilloscope and read out to a PC. A zero-crossing procedure and a cross-spectral density algorithm with sliding window (Domnick et al. (1988), Onofri et al. (1994)) were used to compute the phase difference between the bursts coming from the two detectors. A shift frequency of 5 MHz was applied to the laser beams to obtain sufficient cycles in the signal bursts for signal processing.

5.2 Experimental Results

Signal bursts

Fig.5 shows three typical dual bursts from the first detector and the measured phase evolution between signals of the two channels. They were produced by *a)* a $25\mu m$ ethanol droplet, *b)* a $75\mu m$ ethanol droplet, *c)* a $95\mu m$ water droplet, passing through the measuring volume along (OY).

For the large particles *b)* and *c)*, the phase diagrams show two flat zones, separated by a transition zone with a phase jump. These zones correspond to two maxima in the signal amplitude: the refracted burst and the reflected burst (with the lower amplitude). By measuring the phase difference around these maxima, and using Eqns.(7-9) with $n_0 = n_1 = 2$, the droplet size/refractive index deduced are $74.2\mu m/1.354$ and $93.8\mu m/1.316$.

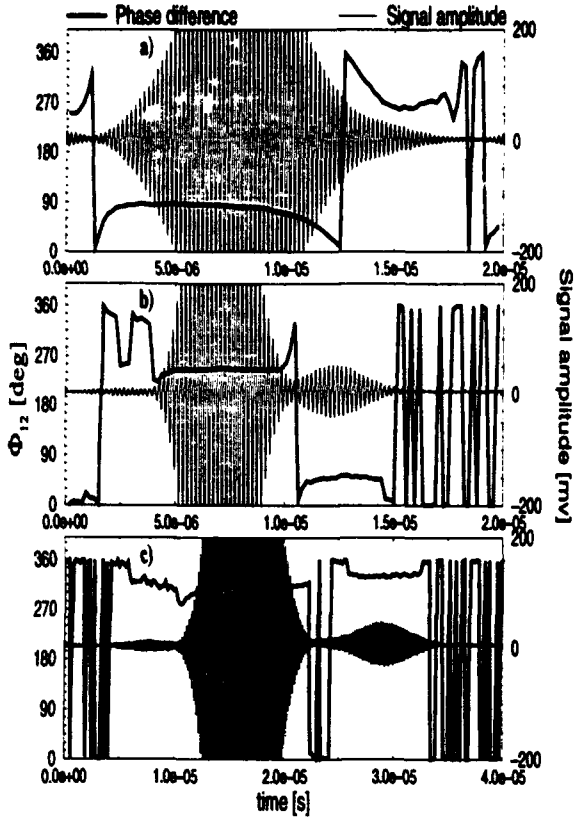

Figure 5: *Dual Burst Technique: experimental bursts.*

In Fig. 5a), a clear separation of the bursts due to the two scattering processes as in Fig. 5b) and c) is not seen. In the phase difference curve, the transition between the two flat parts is smoother compared to cases *b*) and *c*) and the flatness of the curve in the reflection dominated part is reduced. In this case, the droplet size is too small, compared with the beam waist diameter, to avoid mixing between the two scattering processes. In other words, the Gaussian intensity profile with the 54 μm waist diameter is too smooth to separate the two contributions with sufficient time-delay. This phenomenon has been already predicted by simulation in Fig.3, where the behavior of the 27μm droplet is equivalent to case *a*) in Fig. 5. Thus, for this droplet size (about one-half of the probe volume size) and obviously for smaller droplets, the problem is where to extract the phase information for the reflection process in the burst signal to obtain the best accuracy and how to find the required position during signal processing. This problem is still an open problem. Nevertheless some solutions are possible, for example, to make an estimation of the time delay between the maxima of the two contributions, thus enabling the right position in the reflected burst to be found according to the amplitude maximum of the burst (Hess and Wood (1993)). In the current experimental investigation, when the reflected burst from a small particle could not be detected from its amplitude due to the mixing of the two contributions, the phase difference for the reflection was measured at the position where $d^2\Phi_0^{12}/dt^2 = 0$. Using this method, the droplet size/refractive index for case *a*) were estimated as 25μm/1.358.

Measurement results

• First, measurements have been made for different droplet sizes. The accuracy of the size measurements with DBT can thus be checked over a size range.

- In DBT, reflected bursts give directly the particle diameters. Fig. 6 displays the measured diameter from the reflected burst versus the nominal droplet diameter according to the monodispersed droplet generator. Good agreement (within 10%) is seen for large particles, even for particles larger than twice of the probe volume diameter. For small droplets (below 50μm), the diameter estimation is not as good. This point will be discussed later.

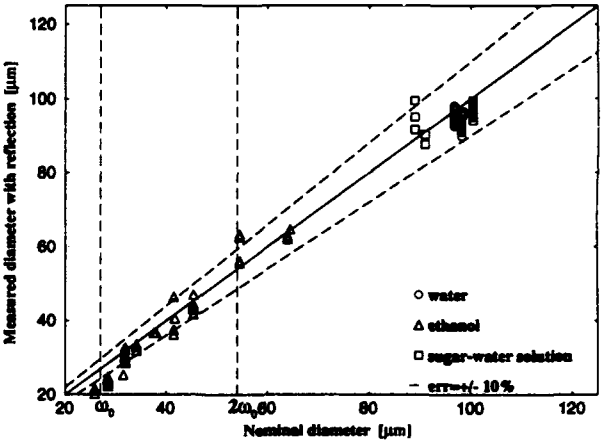

Figure 6: *Size measurements with the reflected contribution.*

- In the present experiments the particle refractive index is known beforehand, thus the droplet diameter can be deduced from the refracted bursts. Fig. 7 shows a comparison of the droplet diameters obtained from the reflected burst and from the refracted burst. The consistency of the information extracted from the two scattering processes is clear: droplet diameters measured from the refracted light and the reflected light agree with an accuracy better than 10% over all the sizes. Note that here for small particles (below 50μm), the agreement is much better than in Fig. 6. It may be doubtful whether the nominal diameters of the small droplets are very accurate, because in the operation of the TSI-3450 droplet generator for producing very small droplets, the flowrate/operating pressure took long time to become stable while the operating

frequency range in which droplets are monodispersed strongly depended on the flowrate.

- Secondly, the results of the simultaneous measurement of droplet diameter and refractive index are displayed in Fig. 8, where the measured droplet refrac- ndex versus the measured diameter is plotted.

.n this plot six groups can be distinguished, as g.ven in Table 1. It is seen in Fig. 8, the measurements of group A60, S100 and W95 are concentrated around the expected value for size and refractive index. The mean refractive index and the standard deviation of these measurements are given in Table 1.

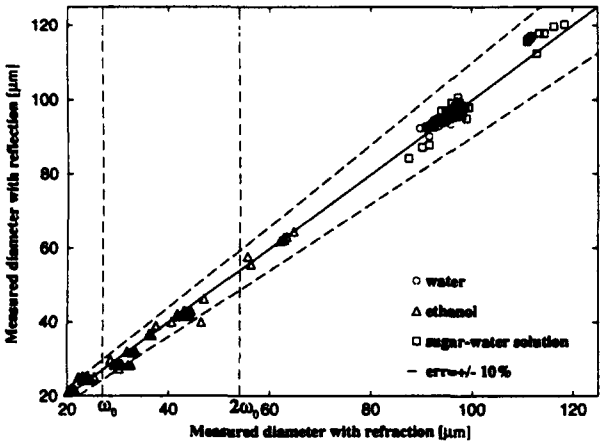

Figure 7: *Measured sizes with the refracted contribution versus the measured sizes with the reflected contribution.*

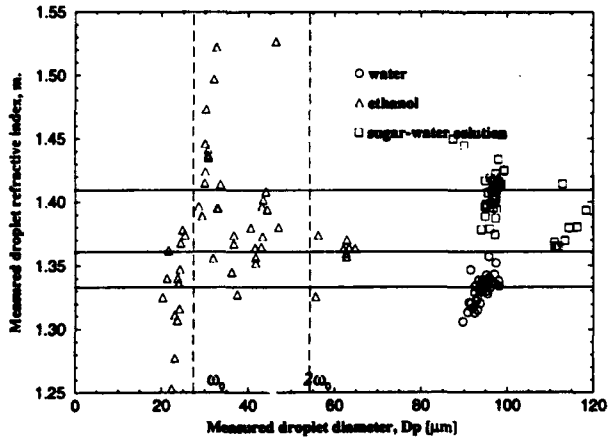

Figure 8: *Dual Burst Technique: Measured droplets diameter versus the corresponding measured refractive index.*

For group A40, results are dispersed leading to non-reliable refractive index measurements. Errors may be due to low SNR and the selection of the portion of the signal for phase estimation.

Errors in measurements of group A30 are abruptly increased compared with the results of group A40.

Group	Material	Nominal dia.(μm)	Mean ref. index	Standard deviation
A30	ethanol	25-34	1.382	0.0636
A40	ethanol	37-45	1.382	0.0441
A60	ethanol	54-64	1.360	0.0147
S100	sugar-water	100	1.407	0.0146
S125	sugar-water	125	1.378	0.0168
W95	water	95	1.331	0.0112

Table 1: *Summary of refractive index measurements.*

Apart from the reasons described above, errors were mainly due to that the distances between droplets were too small in this case. The reflected light from one droplet was thus mixed with the refracted light from another droplet behind it. This was clearly seen in the recorded signals. For the measurements of group S125, a discussion is made in the next section.

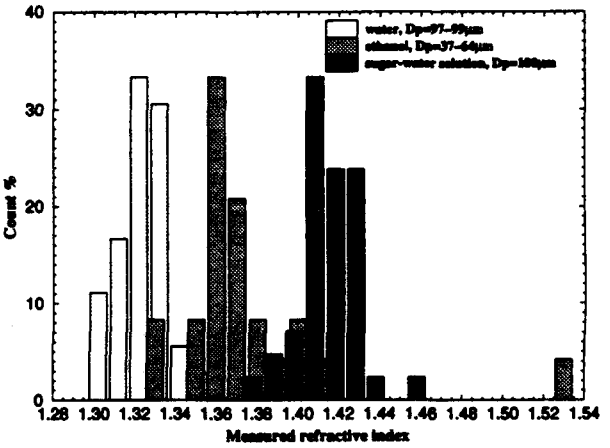

Figure 9: *Distribution of measured refractive index.*

Fig. 9 plots the data of group W95, group A40-A60 and group S100 in a histogram.

6 Discussion

Receiving aperture size and shape

In a conventional PDA it is well known that the receiving aperture size and shape is of great importance to obtain accurate size measurements, see Naqwi and Durst (1990). The aperture size influences directly the signal intensity, whereas the aperture shape determines largely the signal visibility. In DBT, the influence of this last parameter is even more important, because an improper receiving aperture shape may lead to a non-linearity of the calibration curve, especially for large particle sizes, and the tolerance to this deviation for a satisfying refractive index measurement is much smaller than that for a size measurement.

Fig.10 displays the simulated phase and signal evolution for a sugar-water droplet of 125μm diameter. The experimental conditions of group S125 in Fig. 8

have been used with the exception that the receiving apertures have been replaced by thin rectangular apertures ($\delta x = \pm.277°$, $\delta y = \pm 2.77°$). According to geometrical optics (Eqns.(1-6)), the phases in this case should be 160.0° and 24.8° (with a jump of 2π) for reflection and refraction. From GLMT simulations and for the rectangular aperture, using the phases around the intensity maxima, the droplet size/refractive index is predicted to be 125.4μm/1.413. With the exact optical parameters of group S125, including the circular receiving aperture, the results were however 115.9μm/1.363. Regardless of the exact value, this simulation predicted that the use of a circular aperture will result in a negative error in the refractive index measurement. Very good agreement is found with the measured diameter and refractive index for the corresponding particles in Fig. 8 and Table 1.

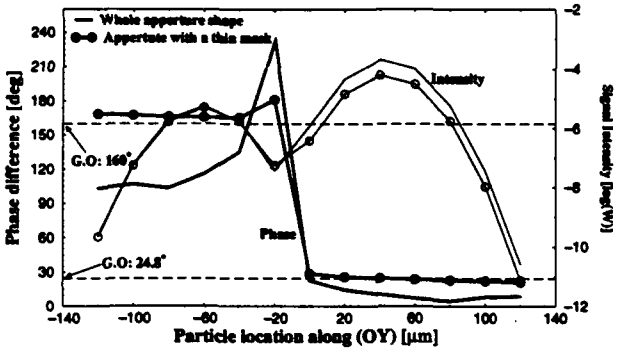

Figure 10: *Influence of the detectors aperture shape.*

Similar simulations have been also made for the optical parameters corresponding to group A64. The results show however, the influence of the aperture shape (rectangular or circular as in Fig. 10) in this case is negligible. These results indicate that the problem is related with the visibility of large particles. When the visibility is very low, the signal phase is deviated from the value predicted by Eqns. (1-6). Note that in Fig. 10, although the area of the circular receiving aperture is as 8 times large as the rectangular aperture, the signal intensity of the reflected contribution in the both cases are about the same.

Scattering angle

A scattering angle of 30° has been chosen for the first experiment on DBT. This angle is the most suitable angle for refractive index measurements in a large range from 1.2 to 1.6, considering the intensity of the other scattering processes (3rd, 4th, 5th order refraction, which have to be minimized). If the required refractive index measuring range is reduced, an optimum scattering angle can be found. For instance, for a refractive index around 1.3, a scattering angle around 70° with a perpendicular polarization can be chosen. In this case the intensity of the reflected contribution is of the same order as the refracted contribution, as predicted with G.O.

With such an arrangement the reflected light would not be dominated by the refracted contribution for small particles, as in the case of group A40 in Table 1.

Signal processing

As shown in Fig. 5, the cross-spectral density algorithm with sliding window can be successfully used in DBT to trace the phase difference evolution. The question is however, as discussed in section 5.2, where to extract the phase information for the reflection process in the burst signal to obtain the best accuracy for small particles and how to find the required position during signal processing. Although in the experiments the phase difference for the reflection was measured at the position where $d^2\Phi_0^{12}/dt^2 = 0$, this method has not been proved to be correct. The scattered measurements of the refractive index for group A40 (see Fig.8 and Table 1) may be partially attributed to this reason. The above proposed optimization on the optical analysis can certainly reduce the difficulty in signal processing. The time-delay method as proposed in section 5.2 may be an effective algorithm in data processing. It may be also useful in burst detection of DBT. When measuring in sprays, it is necessary to distinguish a pair of bursts that are from one particle, or from different particles. This can also be done by checking the arriving time of the two amplitude maxima with the predicted time delay.

For each particle passing through the measuring volume, the phase of the corresponding bursts can be analyzed continuously by the DBT signal processor, although not necessarily. With the actual electronics/computer it is already possible to implement such kind of signal processor. The main advantage is that by tracing the phase evolution inside the dual bursts with DBT, the non-homogeneity (e.g. cenospheres) or non-sphericity of a particle (e.g. a crystal particle) could be recognized.

7 Conclusions

The principle of an innovative technique, the Dual Burst Technique (DBT) has been proposed in this paper. Using this technique, a Phase Doppler Anemometer (PDA) with a single receiving optics is now possible to perform simultaneous refractive index measurements, in addition to particle size, velocity and flux measurements. The results from preliminary experimental investigations and simulations are promising.

The next steps will be to design an optimized DBT system based on the points discussed in this paper. The challenge will be to measure particle refractive index, size and velocity with a single receiving optics, for a size range between one-half to 4 times of the optical probe diameter or larger.

8 Acknowledgments

The authors are grateful to the Commission of the European Communities, the French government (program PROCOPE), the German Ministry of Research and Technology (BMFT), and the Deutsche Forschungsgemeinschaft for providing financial support for this work.

References

Aizu, Y., Durst, F., Gréhan, G., Onofri, F. & Xu, T.H 1993, A PDA system without Gaussian beam defects, *Proc. 3rd Int. Cong. on Optical Particle Sizing, Yokohama (JAPAN)*, pp. 461–470. to be reprinted in ASME Journal of Fluids Engineering.

Bachalo, W.D. & Houser, M.J. 1984, Phase-Doppler spray analyzer for simultaneous measurements of drop size and velocity distributions, *Optical Engineering*, vol 23, pp. 83–590.

Domnick, J. Ertel & H. Tropea, C. 1988, Processing of phase-Doppler signals using the cross-spectral density function, *Proc. 5th Int. Symp. on Application of Laser Techniques to Fluid Mechanics, Lisbon (PORTUGAL), July 20–23*, paper 3.8.

Durst, F. & Zaré, M. 1975, Laser Doppler measurements in two phase flows, *Proc. LDA-Symposium, Copenhagen*, pp. 403–429.

Gouesbet, G., Gréhan, G. & Maheu, M. 1991, Generalized Lorenz-Mie theory and applications to optical sizing, in *Combustion measurements* ed. N. Chigier, pp. 339–384, Hemisphere Publishing Corporation.

Gouesbet, G. 1993, Generalized Lorenz-Mie Theory and Applications, *Proc. 3rd Int. Cong. on Optical Particle Sizing , Yokohama (JAPAN)*, pp. 393–405. *Reprinted in Part. Part. Syst. Charact., vol. 11, pp. 22–34, 1994.*

Gréhan, G., Gouesbet, G., Naqwi, A. & Durst, F. 1991, Evaluation of a phase Doppler system using generalized Lorenz-Mie theory, *Proc. Int. Conf. on Multiphase Flows'91, Tsukuba, Japan*, pp. 291–296.

Gréhan, G., Gouesbet, G., Naqwi, A. & Durst, F. 1992, On elimination of the trajectory effects in phase Doppler systems, *Proc. 5th Euro. Symp. on Particle Characterization (PARTEC 92), Nürnberg, March 24–26*, pp. 309–318.

Gréhan, G., Onofri, F., Girasole, T. & Gouesbet, G. 1994, Measurement of bubbles by phase Doppler technique and trajectory ambiguity, *to be presented at the present Conference.*

Hess, C.F. & Wood, G.P. 1992, Laser technique to measure particle size and velocity in high density applications, *Proc. 6th Int. Symp. on Application of Laser Techniques to Fluid Mechanics, Lisbon (PORTUGAL), July 20–23*, paper 15.6.

Hess, C.F. & Wood, G.P. 1993, The pulse displacement technique — a single particle counter with a size range larger than 1000:1, *Proc. 3rd Int. Cong. on Opticle Partical Sizing, Yokohama (JAPAN)*, pp. 475–482.

Naqwi, A. & Durst, F. 1990, Constraint on the size and shape of the receiving aperture in a phase-Doppler system, *Part. Part. Syst. Charact.*, vol. 7, pp. 113–115.

Naqwi, A., Durst, F. & Liu, X. 1991, Two optical methods for simultaneous measurement of particle size, velocity, and refractive index, *Applied Optics*, vol. 30, pp. 4949–4959.

Onofri, F. & Gréhan, G. 1994, Méthodes de suivi de phase appliquées à la détection des effects de trajectoires dans les granulo-vélocimètres phase Doppler, Rapport Interne LESP URA-CNRS 230, Juin.

Onofri, F., Rozé, C. & Gréhan, G. 1992 Traitement des signaux phase Doppler et ADL sujets aux effets de trajectoire: analyse par ondelettes, *Proc. 9 èmes Journées d'Etudes sur les Aérosols (PARIS), December 8–9*, pp. 81–89.

Saffman, M., Buchhave, P. & Tanger, H. 1984, Simultaneous measurement of size, concentration and velocity of spherical particles by a laser Doppler method, in *Laser Anemometry in Fluid Mechanics-II*, ed. Adrian, Durao, Durst, Mishina & Whitelaw, pp. 85–104, LADOAN-Lisbon.

Sankar, S.V. & Bachalo, W.D. 1991, Response characteristics of the phase Doppler particle analyzer for sizing spherical particles larger than the light wavelength, *Applied Optics*, vol. 30(12), pp.1487–1496.

Sankar, S.V., Inenaga, A. & Bachalo, W.D. 1992, Trajectory dependent scattering in phase Doppler interferometry: minimizing and eliminating sizing error, *Proc. 6th Int. Symp. on Application of laser techniques to fluid mechanics, Lisbon (PORTUGAL), July 20–23*, paper 12.2.

Sankar, S.V., Ibrahim, K.V., Buermann, D.H., Fidrich, M.J. & Bachalo, W.D. 1993, An integrated phase Doppler/rainbow refractometer system for simultaneous measurement of droplet size, velocity, and refractive index, *Proc. 3rd Int. Cong. on Optical Particle Sizing, Yokohama (JAPAN)*, pp. 275–284.

Tropea, C., Xu, T.H., Onofri, F., Gréhan, G. & Haugen, pp. 1994, Dual-Mode phase Doppler Anemometry, *to be presented at the present Conference.*

Xu, T.H. & Tropea, C. 1994, Improving performance of two-component phase Doppler anemometers, *accepted for publication by Measurement Science and Technology.*

SIMULTANEOUS DETERMINATION OF TEMPERATURE AND SIZE OF DROPLETS FROM THE RAINBOW USING AIRY THEORY

J.P.A.J. van Beeck and M.L. Riethmuller

von Karman Institute for Fluid Dynamics, Chaussée de Waterloo 72,
B-1640 Rhode-Saint-Genèse Belgium
Fax: +32 2 3582885 E-mail: vanbeeck@vki.ac.be

ABSTRACT

The anisotropy of laser light scattered by a droplet exhibits a strong dependence on droplet size and temperature. Around the geometrical rainbow angle this dependence is such that it can be used to determine these two parameters. This determination is done with the help of the Airy theory for the rainbow to avoid an extensive calibration of the angular scattered light intensity. A comparison between the Airy and the Mie theories shows that one has to be careful in applying the Airy theory for this purpose. The Airy theory has also been compared with the experimental first order "monochromatic rainbow" created by single falling droplets crossing a laser beam. There is a qualitative good agreement between experiment and theory after the measured rainbow pattern has been properly smoothed.

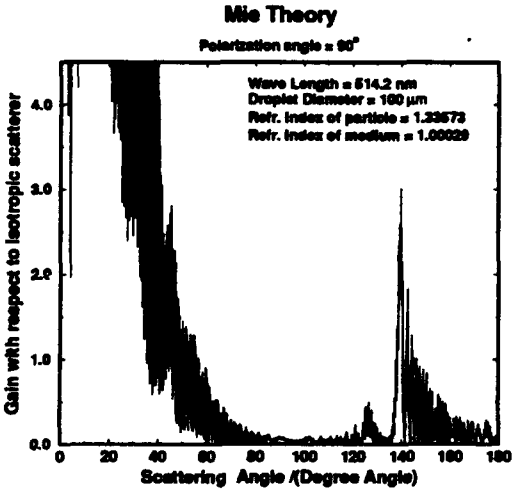

Fig. 1: Gain factor with respect to an isotropic scatterer as a function of the scattering angle according to the Mie theory. The droplet diameter is 100 μm, the refractive index of the particle is 1.33573 and of the medium is 1.00029.

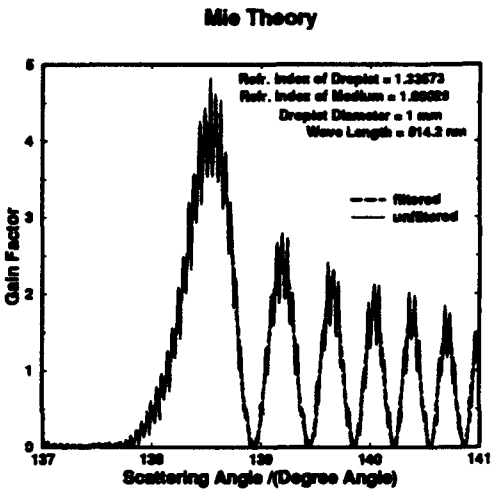

Fig. 2: Filtered and unfiltered first order "monochromatic rainbow".

1. INTRODUCTION

Measurements of droplet velocity and droplet size are nowadays widely performed by optical techniques such as the laser Doppler velocimetry and the Phase Doppler Particle Analysis. Similar well-established non-intrusive techniques do not yet exist for the droplet temperature. Roth et a. (1990) proposed a laser technique which, as for the aforementioned successful techniques, is based on the detection of the scattered laser light. The scattering angle, at which the first order "monochromatic rainbow" is seen, depends on the droplet temperature and the droplet size. The droplet size has been determined from the spatial intensity distribution of the light scattered in the forward hemisphere (see Kōnig et a. (1986)). Once this quantity is known, the temperature can be deduced from the position of the rainbow. In this way two CCD-cameras have to be used, one in the forward and one in the backward hemisphere. The present paper will show that it is possible to deduce the droplet size from the interference pattern that can be seen near the geometrical rainbow angle, thus re-

quiring only one CCD-camera. Therefore, the Airy theory for the rainbow is applied. The applicability of this theory for this new method will be shown by comparing it with the "correct" Mie theory. Finally so-called rainbow patterns, coming from single falling droplets, have been recorded on the CCD-camera and will be presented.

2. THE RAINBOW AS NON-INTRUSIVE MEASUREMENT TECHNIQUE

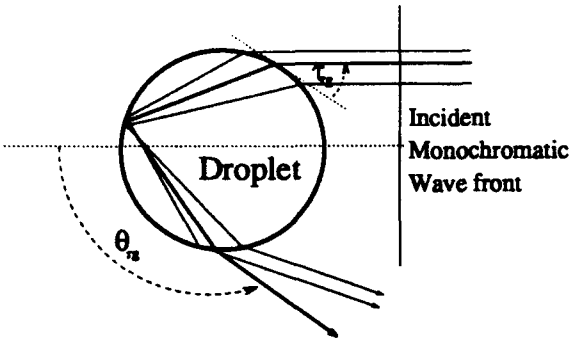

Fig. 3: The geometrical optical rays that form the first order rainbow.

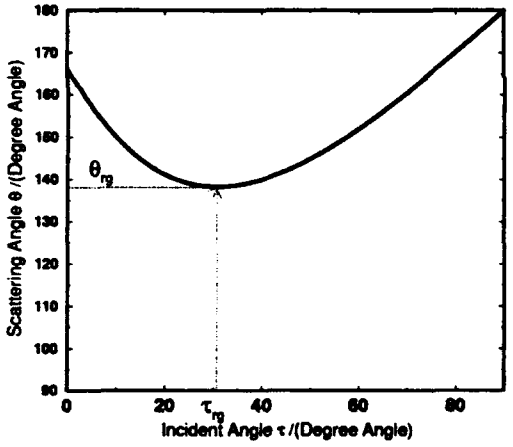

Fig. 4: Scattering angle θ versus incident angle τ for a geometrical ray suffered one internal reflection in a droplet. (Particle and medium refractive index are respectively 1.33573 and 1.00029.)

One could state that by using the rainbow for technical purposes this beautiful phenomenon is deromantized. However, making research on the rainbow shows that also scientifically seen it is a beauty. Just look to figure 1. Herein is depicted the gain factor with respect to an isotropic scatterer as a function of the scattering angle for a droplet being hit by a planar monochromatic electromagnetic wave front. The solution for this problem is given by the Mie theory (see for instance van de Hulst (1957) or Bohren and Huffman (1983) for elaborate descriptions) and is presented here for the particular case of a droplet diameter of $100\,\mu m$, a wave length of the incident light of $514.2\,nm$ and a real refractive index of the particle of 1.33573. The refractive index of the medium is set to 1.00029 and the polarization is perpendicular to the scattering plane.

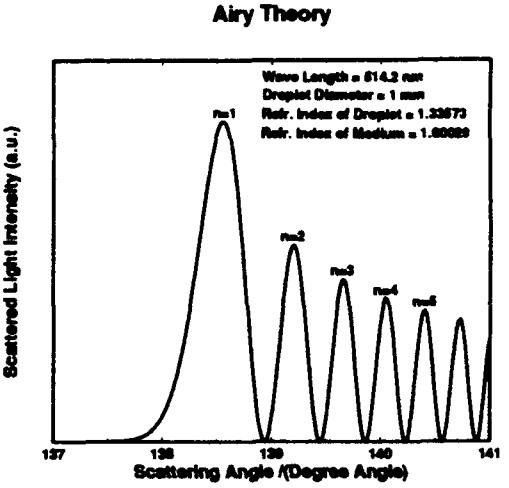

Fig. 5: The rainbow pattern according to the Airy theory.

Near a scattering angle of 140° an interference pattern can be seen that resembles the first order rainbow. Figure 2 shows a close-up of this rainbow pattern for a droplet diameter of $1\,mm$. The pattern, for which the high frequency is filtered out (dashed curve in figure 2), is applied for the optical technique discussed below.

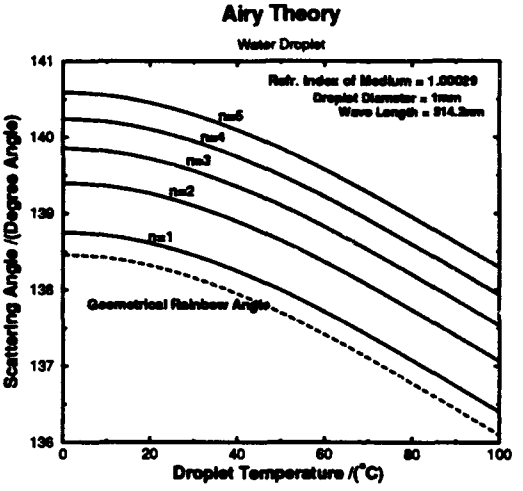

Fig. 6a: Angular positions of the first five extrema in the rainbow pattern as a function of the droplet temperature.

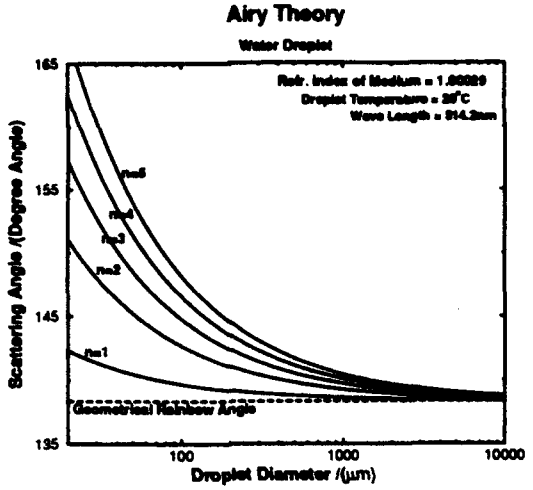

Fig. 6b: Angular positions of the first five extrema in the rainbow pattern as a function of the droplet diameter.

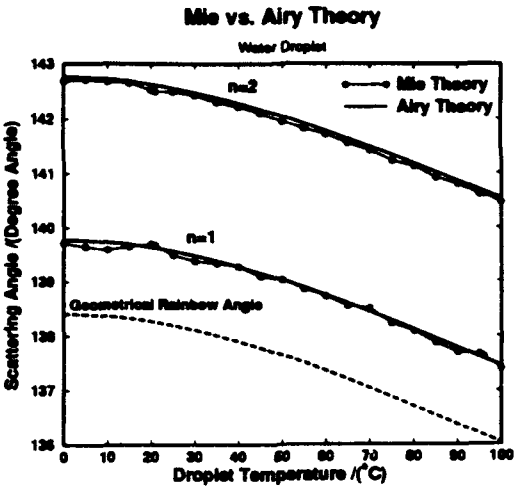

Fig. 7a: Angular positions of the first two extrema in the rainbow pattern as a function of the droplet temperature according to Airy and Mie calculations. ($\lambda = 514.2\,nm$, $D = 100\,\mu m$ and the refractive index of the medium is 1.00029.)

Before explaining this technique it is useful to look to the results of the Airy theory, which is able to predict the filtered interference pattern of figure 2 as well. The advantage of the Airy theory is its simplicity compared to the very complex and computationally expensive Mie theory.

The Airy theory is an extension of geometrical optics based on the Huygens' principle (see Hecht (1987)). Concerning the first order rainbow, the theory deals with rays that have suffered one internal reflection in the drop as is sketched in figure 3. The relationship between the scattering angle θ and the incidence angle τ is given by geometrical optics and is presented in figure 4. The geometrical rainbow angle θ_{rg} is situated at the minimum of the curve. This θ_{rg} depends only on the refractive index of the liquid. The high intensity of the rainbow is due to the fact that a large part of the incident light emerges at a small range of scattering angles θ.

Until so far geometrical optics. The subsidiary maxima are explained as follows. Near τ_{rg}, which is the incident angle of the ray that leaves the droplet at θ_{rg}, there exist rays with different τ's that leave the droplet at the same θ (see sketch in figure 3). These rays are parallel and therefore interfere at infinity, yielding a minimum or maximum in intensity according to their phase shift. The Airy theory computes this phase shift by assuming a cubic wave front near the rainbow (see for instance van de Hulst (1957) about this); thus a pattern as in figure 5 is obtained. It has to be noted that also for the Airy theory the polarization is chosen perpendicular to the scattering plane. For the polarization parallel to the scattering plane the rainbow is hardly visible because the internal angle corresponding (by means of Snell's law) to τ_{rg} is close to the Brewster angle. This is why the polarization perpendicular to the scattering plane is chosen for the optical technique discussed here.

The shape of the Airy's rainbow pattern does not only depend on the refractive index of the liquid but also on the droplet size and the wave length of the laser light. If one uses a laser beam as light source and if the relationship between the refractive index of the liquid and the temperature is well known (see Thormählen et a. (1985) for the refractive index of water), then the rainbow pattern depends on the droplet temperature and size. This dual dependence can be seen in figures 6a and 6b. In figure 6a the scattering angle correponding to the first five maxima in the rainbow pattern, denoted by $n = 1$ to $n = 5$, have been plotted as a function of the temperature for a fixed droplet diameter of $1mm$. Figure 6b depicts the same as a function of the droplet size for a temperature of $20°C$. Note, as mentioned above, that the geometrical rainbow angle does not exhibit any dependence on the droplet size. From these graphs the experimental method can be understood. As the angular difference between the maxima does not depend on the temperature (figure 6a), this spacing can serve to determine the diameter without knowing the temperature before. With this knowledge about the droplet size, the temperature can then be deduced from the scattering angle at which one of the peaks in the rainbow pattern is positioned. In this way, both parameters can be determined from one signal, i.e. the rainbow.

3. COMPARISON BETWEEN AIRY AND MIE COMPUTATIONS

In this section the applicability of the Airy theory for the proposed non-intrusive measurement technique will be discussed. Therefore it will be compared with the "cor-

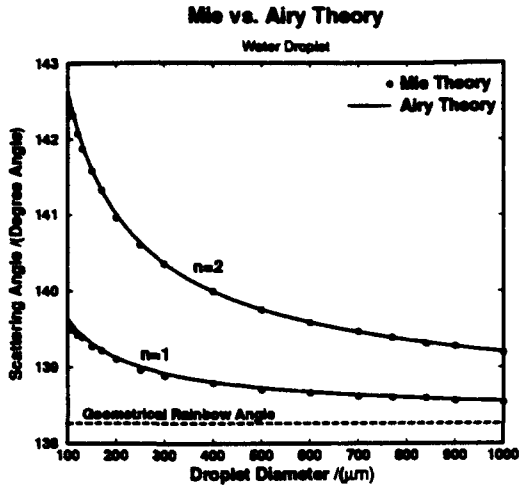

Fig. 7b: Angular positions of the first two extrema in the rainbow pattern as a function of the droplet diameter according to the Mie and Airy theory. ($\lambda = 514.2\,nm$, $T = 20°C$ and the refractive index of the medium is 1.00029.)

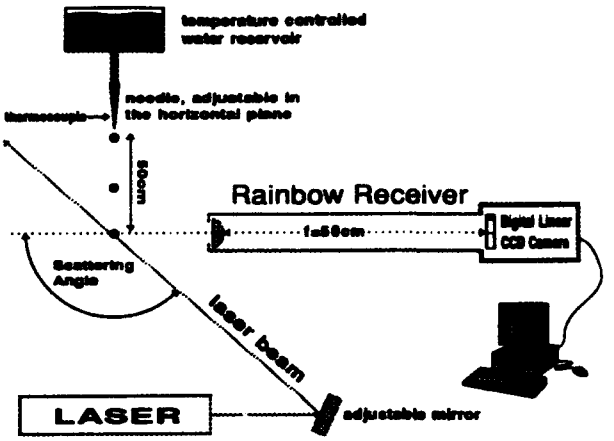

Fig. 8: Experimental setup for the detection of the "monochromatic rainbow".

rect" Mie theory. A comparison between the rainbow given by Mie computations and by the Airy approximation has been carried out by Wang and van de Hulst (1991). Their conclusion was that for the first order rainbow the theories agree with each other for diameters of water droplets down to $0.02\,mm$. Nevertheless, another comparison will be given here which is more suitable to the envisaged application. Namely, similar curves as in figures 6a and 6b have been reproduced by means of the Mie theory. As these calculations are very time consuming, only the first two maxima have been considered. For the comparison the high frequencies in the Mie theory have been filtered out as was done for the dashed curve in figure 2. This leads to the desired comparison between the theories in figures 7a and 7b.

Figure 7a depicts the dependence of the peak positions on the droplet temperature for a droplet diameter of $100\,\mu m$. Remarkable are the wiggles in the curves of the Mie theory. For the first peak this feature even causes an ambiguity for the temperature measurement around $20\,°C$. One could suggest to use the second extremum of the rainbow for the determination of the temperature because for this peak the wiggles have a smaller amplitude. But for the second extremum an angular shift of about 0.1° between both theories can be seen; such a shift corresponds to a temperature change of $2\,°C$. The results of Wang and van de Hulst (1991) indicate that for higher order subsidiary maxima this shift becomes even larger; thus one can also exclude the use of these maxima for the discussed experimental technique. Therefore figure 7a tells us that for droplet sizes around $100\,\mu m$ the use of the Airy theory can lead to errors of several degree Celsius concerning the droplet temperature. Roth et a. (1992) have demonstrated that the amplitude of the wiggles increases for smaller droplets, thus implying that for droplet diameters in the micrometer range certainly the Mie and not the Airy theory has to be used. This, in addition to the fact that for these small droplets more ambiguities occur concerning the droplet temperature determination, makes this technique unfavourable for droplets in the micrometer range.

Figure 7b shows more positive results. Herein is depicted the dependence on the droplet size. The dots produced by the Mie theory coincide well with the curves of the Airy theory except for the droplets near $D = 100\,\mu m$ as has been noticed in the previous paragraph. This means that the wiggles damp out and the angular shift disappears for droplets exceeding $D = 100\,\mu m$! Therefore the Airy theory can applied without any problem for droplets in the millimeter range; the measurements presented in the next section have been performed in this range. But it has to be noted that close study of the presented calculations shows that even for these big droplets the (still present) wiggles lead to an error of several percent concerning the droplet sizing and an error of a fraction of a degree Celsius concerning the temperature determination. If more accurate results are required, the Mie theory itself has to be applied.

4. EXPERIMENTAL RESULTS

The experimental results shown here consist of experimental rainbow patterns arising from single falling droplets in the millimeter range. Such droplets are produced with the setup, outlined in figure 8. The droplets are initiated from the needle of a medical syringe. The hydrodynamic pressure (of several 1000 Pa) in combination with a valve ensures a range of droplet diameters from $1\,mm$ to $4\,mm$. The initial temperature of the droplet is measured with a thermocouple mounted inside the thermally isolated needle. The falling droplet crosses the laser beam which has a diameter of about $5\,mm$ at this cross-

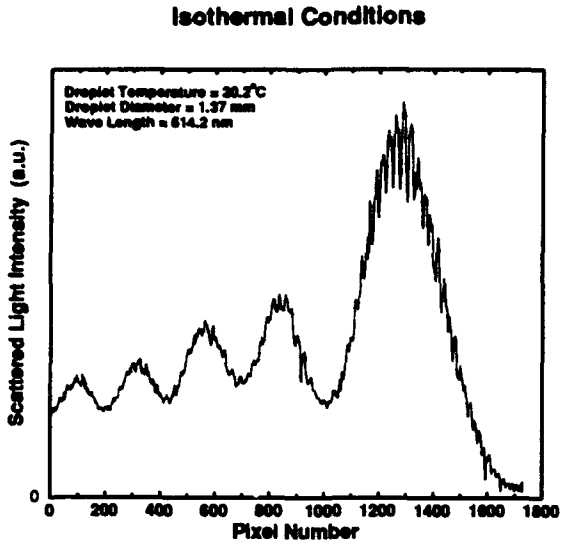

Fig. 9: (Unsmoothed) calibration rainbow pattern recorded in order to relate each pixel number to a scattering angle and to allow the use of the Airy theory.

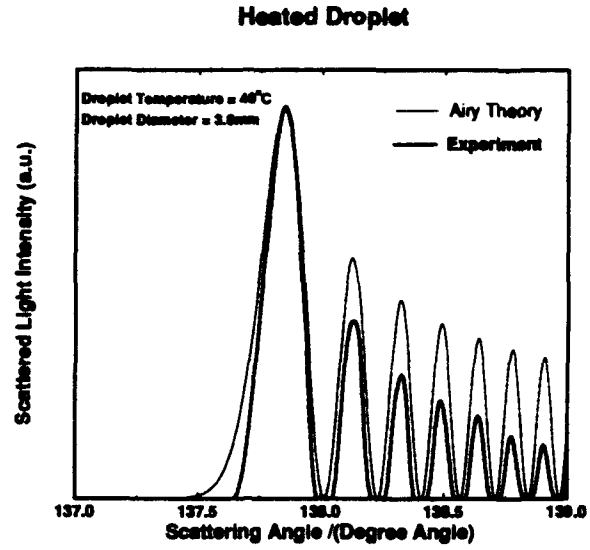

Fig. 10: Typical low pass filtered rainbow pattern and the comparison with the Airy theory.

ing point. The "monochromatic rainbow" is projected on the digital linear CCD-array. The integration time of the camera is chosen such that only one single rainbow pattern is recorded at a time.

A calibration is carried out to relate each pixel number to a certain scattering angle. It avoids the use of a geometrical measurement of the scattering angle. The procedure consists of the detection of a rainbow pattern issued from a droplet at ambient temperature. This calibration rainbow pattern is depicted in figure 9. The droplet size is deduced from the fringe spacing to be $1.37\,mm$. The ambient temperature is given by the thermocouple and equals $20.2°C$. The Airy theory delivers for these parameters the corresponding rainbow pattern so that the desired relation between pixel number and scattering angle can be established. This calibration procedure suffers from the evaporation of the droplet along its path, resulting in a slight change in temperature. This unknown change plus the uncertainty in the determination of the peak positions leads to a total error in the temperature of less than $\pm 1°C$.

After the calibration the temperature and diameter can be determined for any heated droplet. Figure 10 shows a typical experimental low pass filtered signal yielding a "rainbow temperature" of $49°C$. The thermocouple indicated $51°C$ but after a numerical correction for the cooling of the droplet before it crosses the laser beam (given graphically by van Beeck and Riethmuller (1994)), it equals the "rainbow temperature" within $1°C$. The reconstruction of the theoretical rainbow pattern demonstrates a remarkable agreement of the positions of all the peaks which was expected for this droplet size in section 3. As those positions determine the desired parameters the disagreement concerning the peak intensities is just a minor defect.

A final remark concerns the shape of the droplets. For rainbows coming from droplets bigger than $2\,mm$, the "rainbow temperature" suffers largely from the non-sphericity of the oscillating droplets; it is well known that the amplitude of the oscillation increases with the droplet size (see for instance Becker et a. (1991)). The presented Airy theory is only valid for spheres thus yielding incorrect quantities for non-spherical droplets. The reason for the perfect agreement in figure 10 was probably because of the accidental event that an oscillating droplet happened to momentarily have a spherical shape. This has been pointed out by van Beeck and Riethmuller (1994) and definitely requires further study.

5. CONCLUSIONS

The art of using the first order rainbow for the measurement of the droplet temperature has been improved. The droplet size, necessary for this rainbow method, can be deduced from the fringes, visible in the rainbow itself. A comparison between Airy and Mie computations shows that for a droplet diameter bigger than $100\,\mu m$ the Airy theory for the rainbow can be used for the determination of the temperature and diameter provided the signal is properly low pass filtered; the accuracy is several percent concerning the droplet size and a fraction of one degree Celsius concerning the temperature. If higher precision is required, the Mie theory has to be applied.

REFERENCES

Roth, N., Anders, K. & Frohn, A. 1990,
Simultaneous Measurement of Temperature and Size of Droplets in the Micrometer Range,
Journal of Laser Applications, vol. 2, number 1.

König, G., Anders, K. & Frohn, A. 1986,
A New Light Scattering Technique to Measure the Size of Periodically Generated Moving Particles, J. Aerosol Sci., vol. 17, pp. 157-167.

Bohren, C.F. & Huffman, D.R. 1983,
Absorption and Scattering of Light by Small Particles, Wiley, New York.

van de Hulst, H.C. 1957,
Light Scattering by Small Particles, Wiley, New York.

Hecht, Eugene 1987,
Optics, Addison Wesley Publishing Company.

Thormählen, I., Straub, J. & Grigull, U. 1985,
Refractive Index of Water and its Dependence on Wavelength, Temperature and Density,
J. Phys. Chem. Ref. Data, vol. 14, number 4.

Wang, Ru T. & van de Hulst, H.C. 1991,
Rainbows: Mie Computations and the Airy Approximation, Appl. Opt., vol. 30, number 1.

Roth, N., Anders, K. & Frohn, A. 1992,
Simultaneous Determination of Refractive Index and Droplet Size Using Mie Theory,
Proc. Sixth International Symposium on Applications of Laser Techniques to Fluid Mechanics, Lisbon.

van Beeck, J.P.A.J. & Riethmuller, M.L. 1994,
Non-intrusive Measurements of Temperature and Size of Raindrops, submitted to Applied Optics.

Becker, E., Hiller, W.J. & Kowalewski, T.A. 1991,
Experimental and Theoretical Investigation of Large-amplitude Oscillations of Liquid Droplets, J. Fluid Mech., vol. 231, pp. 189-210.

Session 22.
Particle Tracking Velocimetry, PTV

LAGRANGIAN STUDY OF THE CONVECTIVE BOUNDARY LAYER USING THE IMAGE ANALYSIS

A. Cenedese and G.Querzoli

Department of Mechanics and Aeronautics
"La Sapienza" University of Rome, Italy

ABSTRACT

Most of experimental techniques used to investigate the atmospheric turbulence give an Eulerian description of the velocity field. Time histories of the velocity are acquired at one or more fixed points of the field in study. Nevertheless the pollutant dispersion phenomena, are more simply described from the Lagrangian point of view. As a matter of fact, the knowledge of the Lagrangian statistics gives a full description of the behavior of a single particle since it was released from a source; this information is very useful to calibrate the Lagrangian numerical models of dispersion, based on simulations of time histories of the pollutant particles released from a source.

The Particle Tracking Velocimetry has been used to obtain a Lagrangian description of the velocity field. As a consequence, Lagrangian statistics may be directly evaluated without any assumption, rather than heuristically obtained from Eulerian measurements. This technique was applied to the study of the turbulent convection in the atmosphere by means of a laboratory simulation. Lagrangian autocorrelations and integral time scales have been evaluated. Furthermore, the mixing phenomena have been described through the transilient matrix, whose elements represent the fraction of air mixing from one layer to the other in the atmosphere.

1. INTRODUCTION

The study of the convection occurring in the atmospheric boundary layer has been carried out by means of a laboratory model. When the sky is cloud-clear, during the daylight, 10% of the solar radiation is adsorbed by the air. The remaining 90% heats the ground generating a convective layer that grows, since about half hour after sunrise, up to a depth of 500÷1500 m. This layer, called Convective Boundary Layer (CBL), is characterized by intense mixing in a unstable situation where thermals of warm air rise from the ground. Though there is usually wind shear across the top of the CBL, contributing to the turbulence generation, the present study focuses on those situations when the wind is light or not present at all, so that the turbulence is driven only by convection, and the terrain is flat.

Usually, a thermally stable layer at its top (called Capping Inversion), acts as a lid to the thermals, thus restraining the domain of turbulence. The CBL grows by entraining the less turbulent air of the Capping Inversion from above. The presence of the Capping Inversion influence the pollutant dispersion too. As a matter of fact, most of pollutant sources, such as chimney or car exhausts, are located near the ground. Pollutants are dispersed by the convective eddies, therefore the presence of a lid to the turbulence means that pollutants too are trapped within the CBL. These conditions are common in high-pressure regions and, sometimes lead to environmental alerts in the proximity of concentrated sources such as large urban areas (Wyngaard 1985).

The turbulence of the CBL was investigated in the past by means of both laboratory models and field experiments, from the Eulerian point of view(Young 1988a,b,c). This means that the time variability of the velocity is probed at fixed locations or by point probes traversing the investigation area. Unfortunately, the natural frame of reference for the description of the pollutant dispersion phenomena is the Lagrangian one. The turbulent dispersion can be regarded as the result of the behavior of many fluid particles moving in the field, since the pollutant act as a tag of the fluid particles. In the Lagrangian reference frame the time variability of the velocity is given for each fluid particle that is identified by its location at a reference time. Thus all Lagrangian statistics are computed along the particles trajectories rather than at fixed locations.

For the Lagrangian investigation of the field, the Particle Tracking Velocimetry was used: the working fluid was seeded with non-buoyant particles, and their motion was recorded through a video-camera on tape. Then the tapes were analyzed off-line in order to identify the trajectories of the seeding particles. Therefore,

assuming that particles follow closely the motion of the fluid, the measurement results in a time history of the velocity along the trajectories of the fluid particles, i.e. in the Lagrangian reference frame.

Most of techniques used to predict pollutant dispersion in atmosphere, specially in convective conditions, are based on the Lagrangian approach and accept the Lagrangian statistics of the velocity fields as input data (Thomson 1971). This is usually considered a constrain because it is difficult, in general, to state a relationship between the measures Eulerian statistics and the Lagrangian ones. Through the use of the laboratory model and of Particle Tracking Velocimetry, is now possible the direct measurement of these statistics.

2. LABORATORY MODEL AND EXPERIMENTAL PROCEDURES

The CBL is simulated by a parallelepipedal tank filled with water. Its horizontal dimensions are 41.0 cm x 41.0 cm. The side-walls are made of glass whereas the lower surface is a 0.80 cm thick aluminium plate. Under the aluminium plate, an heat exchanger simulates the heating of the earth surface due to the solar radiation. It consists of a copper spiral shaped tube in which hot water flows. The tube is immersed in a 2.5 cm deep chamber filled with water in order to uniformly heat the aluminium plate.

To simulate the Capping Inversion, overlaying the layer in study, the tank is initially filled up to 4 cm with ambient temperature water. Over this layer, a second one of 20 °C higher temperature water is slowly stratified. The upper water surface is thermally insulated by a polystyrene slab floating above the Capping Inversion.

After about half hour of rest, due to the molecular diffusion, a nearly constant vertical temperature gradient is generated, and the heating is applied to the lower surface by letting hot water (20°C higher than ambient temperature) to flow at a 5.0 l/min rate. The acquisition starts 240 s later, when the turbulent convection is fully developed. This instant is considered the origin of the time axis.

3. PARTICLE TRACKING VELOCIMETRY

The aim of the measurements was the detection of long trajectories in order to compute statistics, such as the Lagrangian autocorrelation, at large time lags. Therefore, the traditional multi-exposed technique was not suitable, since not more than 3 or four images can be superimposed without a drop in the trajectory recognition effectiveness. To overcome this constrain, series of images were recorded on tape through a video-camera and processed off-line. Each recording was 500s long and 13 independent experiment were performed. A 3CCD video-camera was placed orthogonal to the light sheet produced by a 1000 W arc lamp, so that it framed a 9.0 cm high, 5.0 cm deep and 12.5 cm wide volume placed in the middle of the tank and tangent to the lower surface. The water was seeded with conifer pollen 200 μm in diameter, having the same density of the water. To increase the length of the recognized trajectories the number of particles present at the same time in the measuring volume was intentionally kept low (80÷90 particles) in order to avoid the ambiguities during the recognition process, though wide tolerance was admitted in the recognizing criteria.

Once the images had been recorded, they were analyzed by a system consisting of a video-recorder, an animation controller, a frame grabber and a personal computer that controlled both frame grabber and video-recorder through the animation controller. Furthermore, the animation controller inserted a frame code during the recording so that, at the processing, each frame was individually identifiable. The original sampling frequency of the recorder was 25 Hz, but only 1 frame every 10 was acquired by the frame grabber and analyzed, in order to have a significant displacement of the seeding particles between one image and the next.

The first step of the processing was the detection of the so called spots, i.e. the images of the particles, and the evaluation of their locations. This task was accomplished by thresholding the images and identifying the islands of lighted pixels (the spots). The islands, to be validated, had to have an area belonging to a given interval.

The resulting list of the particle barycentre locations, together with the time information, were analyzed to recognize the trajectories. The recognition was based relied on two simple criteria:

a) maximum initial velocity;

b) maximum acceleration.

The first one means that the distance between the first and the second spot of a trajectory must be less than an assigned parameter D. The second one means that the difference between two subsequent displacements must be less than another given parameter E (Cenedese and Querzoli 1992).

Finally velocities were computed dividing the particle displacements by the time interval between two images, and the statistics were evaluated.

4. SIMILARITY

Results are presented below in non-dimensional form through the use of the similarity proposed by Deardorff (1970). It rely on the assumption that, when the sky is clear and the wind is light, over a flat terrain the mechanical production of turbulent kinetic energy

can be neglected and phenomena occurring are driven only by the buoyancy. In these conditions the scaling parameters are:

CBL height z_i (length);

convective velocity $w_* = \sqrt[3]{g \cdot \alpha \cdot q_s \cdot z_i}$ (velocity);

convective temperature $\vartheta_* = \frac{q_s}{w_*}$ (temperature);

convective time $t_* = \frac{z_i}{w_*}$ (time).

where g is the gravitational acceleration, α is the thermal expansivity, and q_S is the kinematic heat flux at the surface.

Moreover, phenomena are assumed to be horizontally homogeneous and quasi-steady, that means the CBL is supposed to grow through a succession of steady states. Therefore all normalized statistics may considered time independent.

5. RESULTS

5.1. Probability distributions:

Probability distributions of the vertical velocity component are presented in figure 1 at four levels. The distribution is strongly asymmetric at the lower levels with the most probable value at slightly negative values. This means that cold downdrafts are slower but more probable than the corresponding thermals. This behavior is seen to decrease with height and, close to the to of the CBL (z/zi=0.95) the probability distribution maximum is at zero.

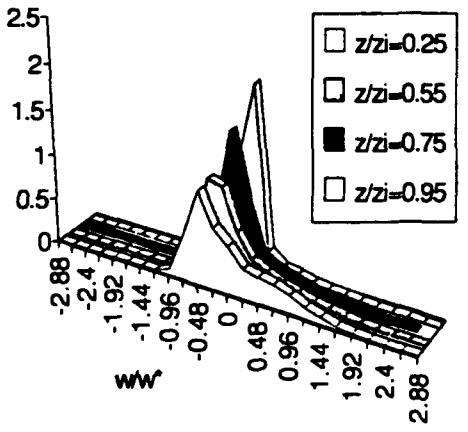

Fig. 1. Vertical velocity probability distribution as functions of the non-dimensional velocity.

Instead, the horizontal velocity component exhibits a symmetrical probability distribution at all the heights (figure 2). The reason is that phenomena occurring within the CBL are horizontally homogeneous and isotropic, thus they do not depend on the orientation of the horizontal axis. The maximum is always placed at zero and the distribution becomes narrower close to the Capping Inversion, where the variance is very low (Hibberd and Sawford 1994).

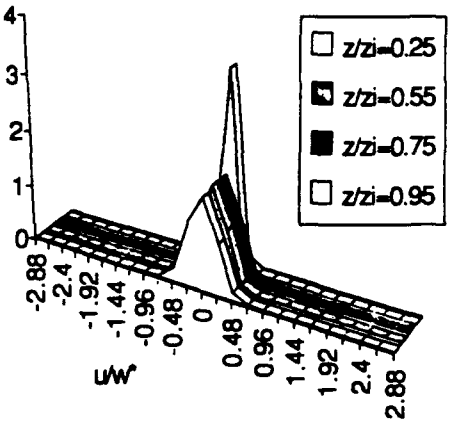

Fig. 2 Probability distribution of the horizontal velocity component.

5.2. Lagrangian autocorrelations:

The vertical velocity autocorrelation (figure 3) is seen to decrease to a minimum at a (1÷1.5)t* time lag. The large negative autocorrelation values means that this is the time taken by most of particles to run along half of the typical convective cycle from the bottom to the top of the CBL and vice-versa.

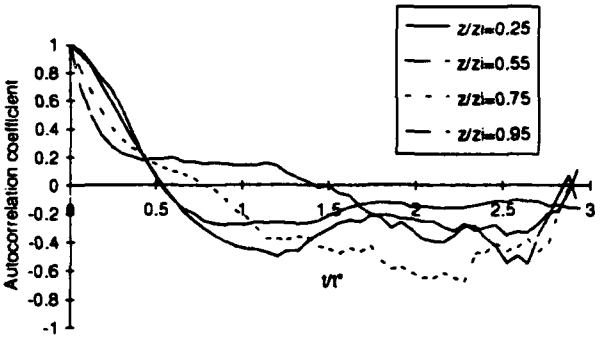

Fig. 3 Autocorrelation coefficient of the vertical velocity component as a function of the non-dimensional time lag.

The autocorrelation of the horizontal velocity is shown in figure 4. Though its initial slope varies with height at which it is evaluated, all the curves approach very slowly the time axis, without a well defined 0-crossing and without any pronounced anti-correlation. Therefore, it seems that the convective structures, though strongly organized in the vertical direction, are not characterized by a typical pattern in the horizontal plane. This is due to the interaction between the adjacent convective structures that deforms one with the other in the horizontal plane, while all of them extend for all the CBL height.

Finally, it should be noticed that the statistics ensemble on which the autocorrelations are computed, at a give time lag t_0, includes all trajectories long enough to "live" during a t_0 time interval. As a consequence, at the larger time lags, the ensemble is reduced and the behavior of the autocorrelations are more affected by the variations due to single trajectories and their trend becomes uncertain.

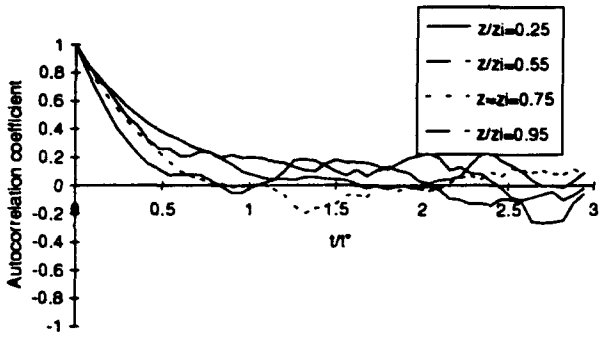

Fig. 4 Autocorrelation coefficient of the horizontal velocity component as a function of the non-dimensional time lag.

5.3. Lagrangian time scales:

In order to represent the Lagrangian integral time scale, the 1/e scale is chosen (e.g. the time lag at which the autocorrelation coefficient drop to the value 1/e). As a matter of fact, both its proper definition and the zero-crossing scale are not suitable for these experimental data: it is not possible to evaluate the time scale by integration of the autocorrelation function because it does not stably approach the horizontal axis at the measurable time lags, while the zero-crossing is not well defined for the horizontal velocity autocorrelations (Hanna 1981).

The vertical profile of the horizontal and vertical velocity 1/e time scale is shown in figure 5. The horizontal velocity scale is large at the levels where the main motion is parallel to the surface, that is in the proximity of the ground ($z/z_i \cong 0.3$) and the CBL top, whereas it decrease in the middle of the CBL where fluid particles are mainly rising or descending.

The 1/e scale of the vertical velocity is seen to decrease from the bottom to the top of the CBL, with small oscillations opposite to the variations of the horizontal scale.

5.4. Transilient matrix:

The transilient matrix is a useful tool both for the detailed description of the mixing processes and for the numerical modelling of non-local phenomena in horizontally homogeneous turbulent fields (Stull, 1993).

Consider the CBL over a homogeneous surface, and a discretization of the field with a grid whose cells are equispaced horizontal layers. Let $C(t,\Delta t)$ be the transilient matrix describing the mixing of the CBL in study, the element $c_{i,j}(t,\Delta t)$ represents the fraction of air mixed from the grid cell j into the destination cell i, during a time interval from t to $t,\Delta t$.

The physical meaning of the transielient matrix is more clear displaying it with the row in reverse order so that destinations near the bottom of the CBL correspond to lower elements of the matrix, and vice-versa. In general, elements in the upper left corner of the matrix represent rapid upward mixing while elements in the lower corner represent the rapid downward mixing. Moreover, the main diagonal elements $c_{i,i}$, represents the fraction of mass of the i-th cell that is not involved with mixing process.

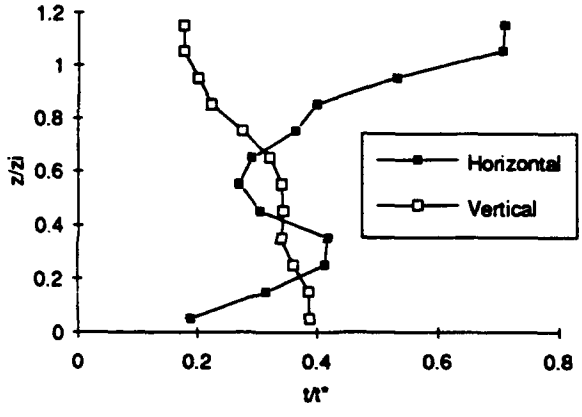

Fig. 5 1/e Lagrangian time scale normalized by the convective time vs. non-dimensional height.

The transilient matrix can be also used for the numerical simulation of horizontally averaged mixing phenomena. let S(t) be a vector representing the vertical profile of the state of a passive scalar (e.g. the pollutant concentration), the vertical profile of the same quantity after a Δt time interval is:

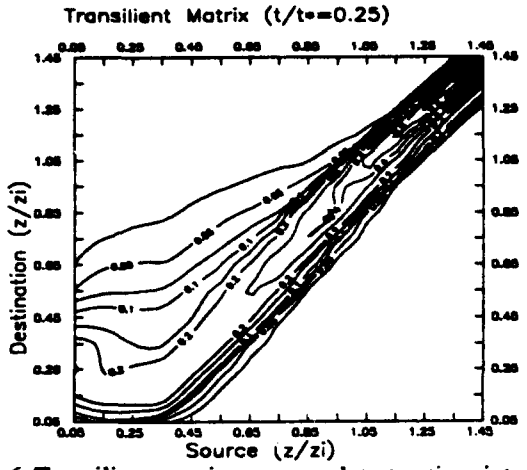

Fig. 6 Transilient matrix contour plot at a time interval t=0.25t*

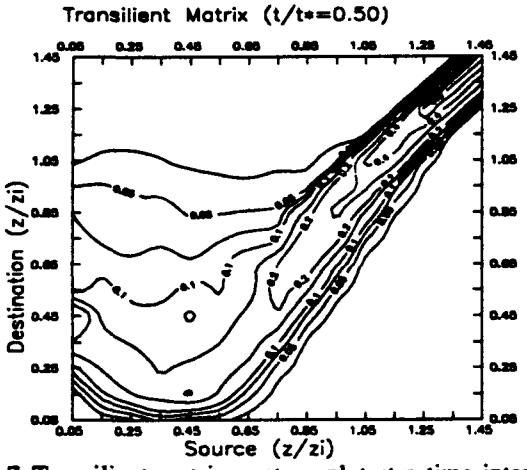

Fig. 7 Transilient matrix contour plot at a time interval t=0.50t*

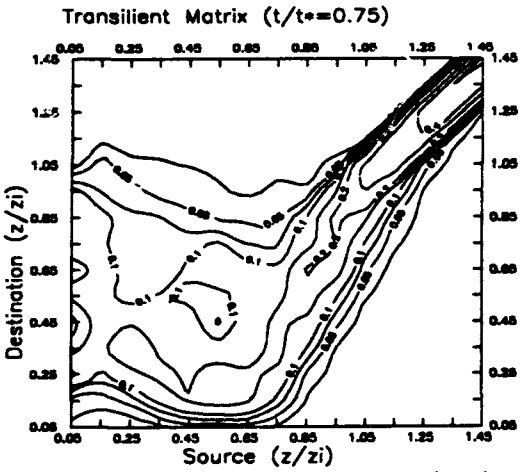

Fig. 8 Transilient matrix contour plot at a time interval t=0.75t*

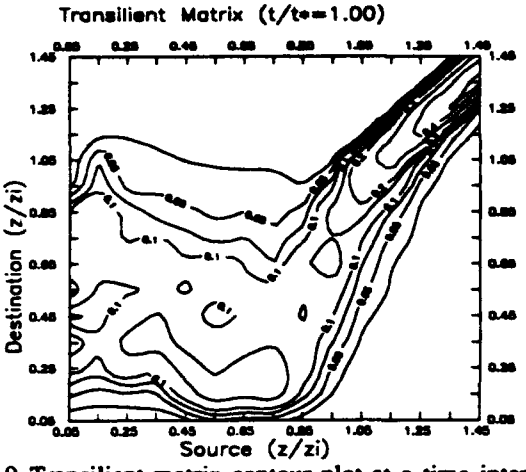

Fig. 9 Transilient matrix contour plot at a time interval t=1.00t*

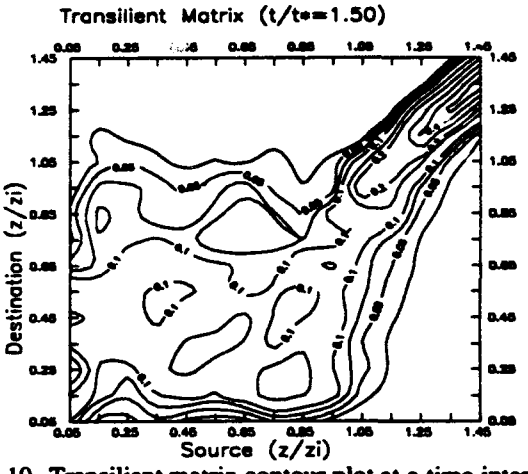

Fig. 10 Transilient matrix contour plot at a time interval t=1.50t*

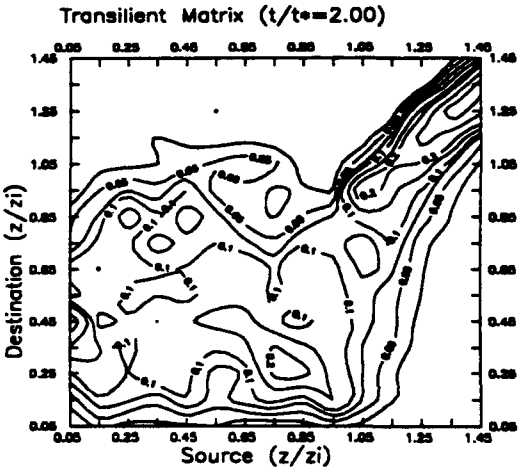

Fig. 11 Transilient matrix contour plot at a time interval t=2.00t*

$$S(t,\Delta t) = C(t,\Delta t)\, S(t).$$

As a consequence, once the transilient matrix is known, the evolution of many characteristics of the CBL can be numerically predicted.

In figures 6-11, the contour plots of the transilient matrix are shown at time intervals from 0.25 t_* to 2.0 t_*. The axis represents non-dimensional source and destination height. Over short time intervals the fluid disperse little from its starting levels, resulting in large elements near the main diagonal (from top right to bottom left). At larger time intervals, the high values spread from the main diagonal to the opposite corners, with a maximum in the lower part of the left border of the transilient matrix, representing the slow downward motion. This behavior is in agreement with the probability distribution of the vertical velocity.

Instead, within the region corresponding to the Capping Inversion (destination and source greater than 1.0) the higher values remain close to the main diagonal because of the thermal stability inhibits the mixing processes.

6. CONCLUSIONS

The convection phenomena of the atmospheric boundary layer has been investigated from the Lagrangian point of view by means of a dedicated PTV system. Through the use of a videorecorder controlled by a personal computer, the seeding particles were tracked during 3÷4 integral time scales as they moved within the simulation tank. As a consequence the Lagrangian statistics have been evaluated. The convective layer of the atmosphere was simulated in an improved aspect ratio (z_i/tank width = 10) with respect to the former measurements (Cenedese and Querzoli 1992), but the Rayleigh number seems to decrease too much (R_a order of 10^7) for the phenomena to be completely independent on it. In addition, some preliminary results on the experimental determination of the transilient matrix have been presented. From this matrix the behaviour of the convective layer may be easily modeled as a two-dimensional phenomenon.

REFERENCES

Cenedese A. & Querzoli G. 1992. PIV for Lagrangian Scale Evaluation in a Convective Boundary Layer, in Flow Visualization VI, Tanida Y. & Miyashiro H. (eds.), Springer-Verlag

Hanna S.R. 1981. Lagrangian & Eulerian timescale relations in the day-time boundary layer, J. Applied Met., vol. 20, pp. 242-249

Hibberd M.F. & Sawford B.L. A saline laboratory model of the planetary convective boundary layer, Boundary-Layer Meteorol., vol. 67, pp. 229-250

Thomson D.J. 1971. Numerical Calculation of Turbulent Diffusion, Quart. J. of Roy. Met. Soc., vol. 97, pp. 93-98

Wyngaard J.C. 1985. Structure of the planetary boundary layer & implications for its modelling, J. Climate Appl. Meteorol., vol. 41, pp. 1959-1969

Young G.S. 1988a. Turbulence structure of the convective boundary layer. Part I: Variability of normalized turbulence statistics, J. Atmos. Sci., vol. 45, pp. 720-726

Young G.S. 1988b. Turbulence structure of the convective boundary layer. Part II: Phoenix aircraft observations of thermals & their environment, J. Atmos. Sci., vol. 45, pp. 727-735

Young G.S. 1988c. Turbulence structure of the convective boundary layer. Part III: The vertical velocity budget of thermals & their environment, J. Atmos. Sci., vol. 45, pp. 2039-2049

FLOW MEASUREMENTS CLOSE TO THE FREE AIR/SEA INTERFACE

Jochen Dieter, Roland Bremeyer, Frank Hering

Institute for Environmental Physics, University of Heidelberg
Im Neuenheimer Feld 366, D-69120 Heidelberg, Germany
Phone: (49) 06221-56-3403, email: jdieter@dali.uphys.uni-heidelberg.de

Bernd Jähne

Scripps Institution of Oceanography, PORD
La Jolla, CA 92093-0230, USA
and
Interdisciplinary Center for Scientific Computing
Im Neuenheimer Feld 368, D-69120 Heidelberg, Germany

ABSTRACT

Two 2D flow visualization techniques for measurement of wind induced flow beneath the water surface are presented. Both use a light sheet illumination parallel to the main wave propagation and image processing techniques for the determination of flow fields. With one technique the layer influenced by wave motion and wind-induced turbulences is observed using Particle Tracking Velocimetry (PTV). Lagrangian vector fields are computed. The second focuses on the viscous boundary layer. Eulerian vector fields are processed by Particle Image Velocimetry (PIV).

1 INTRODUCTION

The study of wind-induced small-scale transport processes across the air-sea interface requires detailed measurements of the turbulent shear flow on both sides of the interface. The presence of wind waves make the physical processes complex and measurements difficult. Thus it is not surprising that knowledge of the micro-turbulence close to free interfaces and its interaction with waves is still very superficial and even basic parameters have not been measured up to date.

Except for some early pioneering Japanese work (*Okuda* [10]), hardly any direct measurements of the shear stress at the water surface and the mean and local vertical velocity profiles in the viscous boundary layers on both sides of the interface are available. Other important scientific issues include the enhancement of turbulent dissipation by waves, the generation and characterization of turbulent patches induced by wave instabilities (so-called 'micro-scale wave breaking') and the interaction between wave motion and the turbulent shear layer.

Flow close to a wavy free interface can hardly be measured with any kind of probes including laser doppler anemometers. Thus non-invasive techniques using quantitative flow visualization techniques seem to be promising. However, these techniques require special adoption to the flow conditions close to free interfaces. The basic difference is that a much larger range of spatial scales are involved. The largest scale of interest is the penetration depth of the wave motion. For typical wind/wave tunnel studies, this scale is in the order of 10 cm. The smallest scales are the tiny residual velocity fluctuations within the water-sided viscous boundary layer which is only about one millimeter thick. It is obvious that a single flow visualization technique cannot span this wide range of scales.

Therefore, a two-scale approach was adopted. The first technique focuses on the wind-wave related scales in the order of centi- to decimeters, the second on the flow within the viscous boundary layer. In order to study wave-influenced transport processes it is important to obtain both Eulerian and Lagrangian flow fields. Consequently, we decided to use particle tracking velocimetry (PTV) and optimized it to track particles over long sequences covering several wave periods.

A PTV technique is less suitable for high-resolution flow measurements within the boundary layer. Because of the small image sector, particles stay only a few frames within the image sector. Thus a particle imaging velocimetry (PIV) is used in this case.

Both techniques are described in this paper. The experimental setup is outlined in section 2 and the image processing techniques for the PTV and PIV techniques are discussed in sections 3 and 4, respectively. Results from both techniques are reported in section 5.

2 EXPERIMENTAL SETUP

2.1 Particle Tracking

Particle Tracking Velocimetry (PTV) was chosen as a tool for the investigation of wave generated turbulences and turbulent transport. The flow field was visualized by small polystyrol particles in a light sheet illumination. The particles are imaged by a CCD camera as streaks. By tracking individual particle streaks from one frame to the next the Lagrangian vector field is extracted.

Experiments were conducted at the circular wind/wave facility (perimeter 11.6 m, width 0.3 m, water depth 0.3 m) of the Institute for Environmental Physics of the University of Heidelberg (Germany). A 1-3 cm thick light sheet parallel to the main wave propagation direction is used to illuminate small (50-150 μm in diameter) polystyrol (LATEX) seeding particles. The depth of the light sheet was chosen such that the particles stay in the illuminated area long enough to enable tracking. The light sheet is generated from below of the channel by Halogen lamps. An area of typically $14.0 \times 10.0\,\mathrm{cm}^2$ is imaged by a standard 60 Hz CCD camera (Pulnix TM-740 and Sony

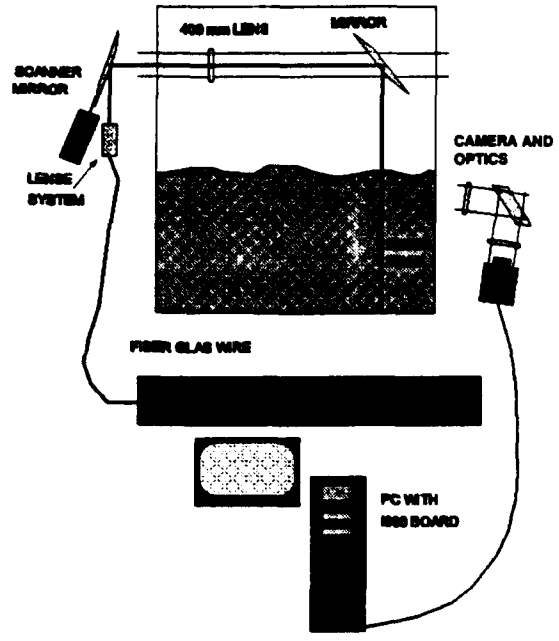

Fig. 1: *The light sheet is generated by a scanning the laser beam over the observation area (PIV-setup).*

XC75) with a spatial resolution of 512 by 480 pixels. Due to the movement of the particles during the exposure time of $16\frac{2}{3}$ ms, they are imaged as streaks. The image sequences are stored on a Laser Video Disc (Sony LVR 5000) for later processing.

2.2 Particle Image Velocimetry

The setup for the high-resolution flow visualization in the aqueous viscous boundary layer is also realized at the Heidelberg facility. Because velocities up to 20 cm/s are expected, a high-speed non-interlaced camera with a frame rate of 200 frames/sec and 256×256 pixel is chosen (Dalsa CA-D1). In order to achieve sufficient spatial resolution of the flow visualization in the viscous boundary layer an image sector of $4 \times 4\,\mathrm{mm}^2$ is selected. A 1 to 1 projection is realized by two 200 mm achromatic lenses, yielding a resolution of 16 μm and a depth of focus of 400 μm. At low wind speeds, (smaller than 2 m/s) wave amplitudes are smaller than the image sector.

The camera is connected to a digital camera interface of a Hyperspeed XPI-i860 board. The images are stored in the RAM of the board during the measurement. 128 MByte RAM allow 1800 pictures ($\equiv$ 9 s) to be taken consecutively.

Seeding particles are produced by electrolysis. Hydrogen bubbles are generated on the cathode, of a tungsten wire of 50 μm diameter. A potential of 60 V lies across the wire and the anode at 10 cm distance at the flume wall. Since the flume is filled with deionized water, 0.15 g/l $NaSO_4$ is added to enable electrolysis [9].

The hydrogen bubbles have the disadvantage that their density is lower than water. Buoyancy changes the vertical component of the vector field.

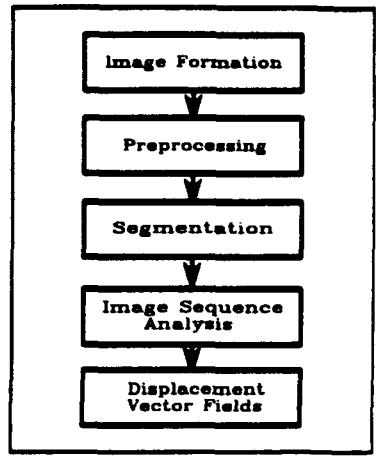

Fig. 2: *An overview over the different steps of image processing, required for the evaluation of the vector field.*

To evaluate the accuracy of the measurements with the bubbles, a campaign with acrylic seeding particles filled with dyed liquid is planned.

For illumination a TEM00 1W argon ion laser (American Laser Corp., model 909) with a wavelength of 488 nm is used. The light is guided through a fiber glas wire. A lens system at the end of the wire and an additional 400 mm lens enable an adjustable beam diameter between 60 μm and 2 mm. Corresponding to the depth of focus of 400 μm a beam diameter of about 300 μm is used. A scanner mirror generates a light sheet, which is directed by a second mirror into the water (see Fig. 1). The scanner mirror is driven by a sinusoidal signal. Every period of the sine signal is sent to the camera for synchronization. This yields two dots for every particle in one image frame. The light sheet is chosen larger than the picture frame. Intensity is lost, but a nearly linear laser beam velocity in the picture area is gained. Due to the movement of the particles the time intervals between two illuminations are not constant. This results in a small error correlated to the velocity.

3 IMAGE PROCESSING : PTV

Several image processing steps are required for the extraction of the flow field from the image sequences (see also Fig. 2). After digitization of the images with a frame grabber, each picture is broken down into its two image fields. Then a specially developed segmentation technique for identifying individual particles from the background follows. Each object is labeled and finally the correspondence problem of identifying the same object in the next image frame is solved by calculating its streak overlap. Repeating this algorithm will track segmented particles through the image sequence. Details can be found in *Hering et al.* [5].

3.1 Preprocessing

An image taken with a standard CCD camera at a frequency of 60 Hz (NTSC-norm) actually consists of two consecutive fields with only half vertical resolution. Therefore it is required to split the original gray value image g(x,y) into its two fields; one field $g_1(x,y)$ being the odd and the second field $g_2(x,y)$ being the

even rows of g(x,y):

$$g_1(x,y) = g(x,2y'+1) \quad \text{and} \qquad (1)$$

$$g_2(x,y) = g(x,2y') \quad \text{where} \quad y' \in \{1...240\} \,. \qquad (2)$$

Both fields are interpolated to their original size of 480 × 512 pixels by a cubic interpolation.

3.2 Segmentation

The histogram (Fig. 3) of a a streak image shows two distinct maxima, at the low gray values being faint particle streaks and the background and at high gray values being reflections at the water surface and bright particles. Therefore the intensity of the streaks ranges from the very low to the very high gray value. Simple pixel based segmentation techniques cannot be chosen as the streak images do not show a true bimodal distribution in the histogram. A region growing algorithm was developed for the discrimination of individual particles from the background. Regions with similar features are to be identified and merged together to a connected object.

Firstly the image g(x,y) is scanned through for local maxima in the intensity, as the location of streaks is well approximated by a local maximum $g_{max}(x,y)$ (Fig. 3). A minimum search horizontally and vertically from $g_{max}(x,y)$ enables the calculation of the peak height:

$$\Delta g = \min(g_{max} - g_{min,i}) \,, \qquad (3)$$

$g_{min,i}$ being the minima revealed by the minimum search. In addition the half width is measured. Both peak height and half width are required to lie above a threshold to prevent random noise being a seeding point for the region growing. After these germ points are identified the growing algorithm segments the object following two rules: Firstly, a pixel is accepted as an object point only when its gray value is higher than an adaptive threshold, which is calculated from $g_{min,i}$ by interpolation. For details regarding computation the threshold see [4]. Secondly only those pixels forming a connected object are considered. A result of the described segmentation algorithm is shown in Fig. 4. Each object identified by the segmentation is then labeled with a flood fill algorithm borrowed from computer graphics. The size of each object can then be determined, and thereby large objects (reflections at the water surface) removed.

3.3 Image Sequence Analysis

After segmentation, the correspondence problem of identifying the same particle in the next image frame is solved, by calculating its image field streak overlap: Some cameras (e.g the Pulnix TM640) show a significant overlap θ of the exposure in two consecutive fields of the same frame. The overlap of the exposure time yields a spatial overlap of the two corresponding streaks from one image to the next (Fig. 5). An AND operation between two consecutive segmented fields calculates the overlap fast and efficiently [4]. In addition as the temporal order of the image fields is known, the sign of the vector is also known and no directional ambiguity has to be solved. However most cameras do not show such a temporal overlap in the exposure time. In these cases corresponding particles will only overlap due to their expansion in space. Arti-

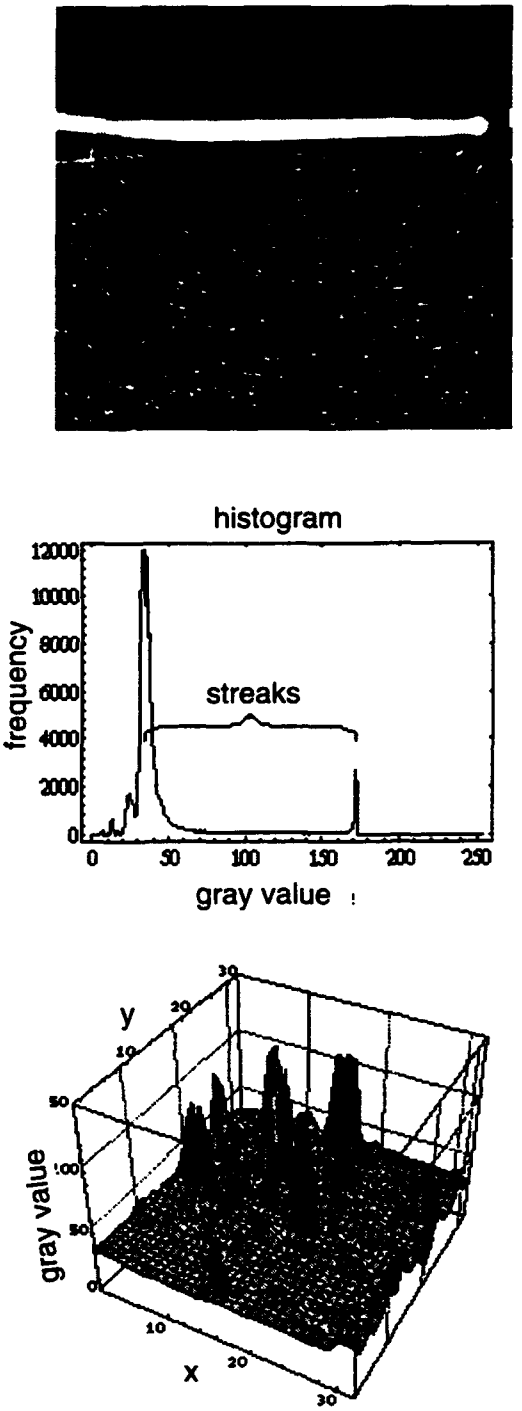

Fig. 3: *Top: Original gray value image of polystyrol seeding particles beneath the water surface. An area of 14.0 × 10.0 cm² is imaged. Middel: Histogram of the above streak image. Although appearing to show a bimodal distribution, particles cannot be segmented by a threshold. Bottom: Pseudo 3d-plot of 32 × 32 pixels of the original streak image. Streaks can clearly be identified as local maxima in the gray value distribution.*

Fig. 4: *Segmented image of original gray value picture (Fig. 3 top). 501 objects were found. The reflections at the water surface were eliminated by the labeling algorithm.*

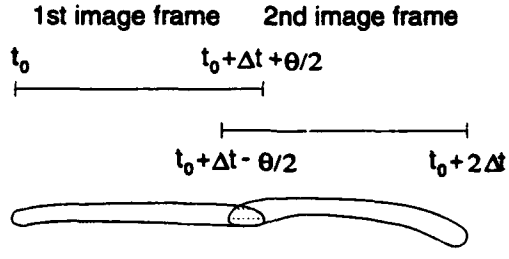

Fig. 5: *The temporal overlap θ of the exposure time in two consecutive fields of the same frame yields a spatial overlap of corresponding streaks.*

ficially this expansion can be increased by the use of a morphological dilation operator. The binary dilation operator of the set of object points $\mathcal{O}$ by a mask M is defined by:

$$\mathcal{O} \oplus M = \{p:\ M_p \cap \mathcal{O} \neq \emptyset\}\ , \qquad (4)$$

where M_P denotes the shift of the mask to the point p, in that way that p is localized at the reference point of the mask. The dilation of $\mathcal{O}$ by the mask M is therefore the set of all points, where the intersecting set of $\mathcal{O}$ and M_P is not empty. This operation will enlarge objects and typically smooth their border. For more details see [6]. To avoid unnecessary clustering of the objects the dilation is not calculated simultaneously for all objects in an image but for each object individually. In most cases, in particular for low particle concentration($\leq$ 300 particles/image), each particle shows only the overlap with the corresponding particle in the next frame. At higher particle concentration, particles however show overlap with up to typically four particles in the next frame. Therefore additional features are required to minimize false correspondences. Ideally the sum of gray values for each streak in the image series should be constant, due to the equation of continuity for gray values [4]:

$$\sum_{x,y \in \mathcal{O}} g(x,y) \ = \ const.\ . \qquad (5)$$

This implies a particle at low speed is visualized as a small bright spot. The same particle at higher speed is imaged as a fainter object extending over a larger area. The sum of gray values in both cases should be identical. Deviations from this ideal situation are caused by segmentation errors. Better results are therefore gained by normalizing the sum of gray values with the segmented area. The normalized sum of gray values being G_n^1 for the first frame and G_n^2 for the second are required to lie above a threshold of the confidence interval C:

$$C \ = \ 1 - \frac{|G_n^1 - G_n^2|}{|G_n^1 + G_n^2|} \ \longmapsto \ [0,1]\ . \qquad (6)$$

A similar expression can be derived for the area of the objects. Finally the expected position of a particle is predicted by interpolation, from the vector field of previous time steps [12]. A χ^2-test evaluates the probability that a pair of particles match. Minimizing χ^2 will maximize the likelihood function.

3.4 Calculation Of The Displacement Vector Field

Wierzimok and *Hering* [12] showed that the center of gray value $\vec{x}_c$ of an isotropic object represents the timely averaged two dimensional location $\langle \vec{x} \rangle_{\Delta t}$, thus:

$$\vec{x}_c = \langle \vec{x} \rangle_{\Delta t}\ , \qquad (7)$$

where $\vec{x}_c$ is calculated from the sum of all n segmented pixels of a streak:

$$\vec{x}_c = \left(\frac{\sum_{i=1}^{n} x_i g(x_i,y_i)}{\sum_{i=1}^{n} g(x_i,y_i)}\ ,\ \frac{\sum_{i=1}^{n} y_i g(x_i,y_i)}{\sum_{i=1}^{n} g(x_i,y_i)} \right)\ . \qquad (8)$$

Now the knowledge of the location of the same particle in the previous frame (at the time $t-1$) enables the first-order approximation the velocity field $\vec{u}(t)$:

$$\vec{u}(t) \approx \frac{\vec{x}_c(t) - \vec{x}_c(t-1)}{\Delta t}\ . \qquad (9)$$

Repeating the described algorithm will automatically track all encountered seeding particles from one frame to the next. The segmentation and tracking algorithms have been implemented on an i860 board to achieve maximum performance. Typical evaluation time of one image including digitization, segmentation and tracking is 10 s. Long image sequences (200-1000) images can therefore be processed. Individual particles can be tracked up to a concentration of 1000 particles/image.

4 IMAGE PROCESSING : PIV

PIV is based on the idea to interpret particles in an interrogation window as a pattern. This window is matched with the next image of the same sequence.

The spatial shift of that pattern to the sequential image yields the mean displacement vector of the particles [1]. This is the major difference to PTV, where single particles are tracked from frame to frame.

Typically an area of 32×32 is chosen as the matching window [11]. The spatial shift of the pattern is computed via a two dimensional discrete cross correlation C(i,j,t,Δt) of the two sampled areas g(i,j,t),h(i,j,t+Δt), where g(i,j,t), h(i,j,t+Δt) denotes the gray value at the position i,j at the time t respectively t+Δt, Δt being the time interval between two images:

$$C(i,j,t,\Delta t)=\frac{\sum_{m=-\infty}^{\infty}\sum_{n=-\infty}^{\infty} g(m+i,n+j,t)h(m,n,t+\Delta t)}{\sum_{m=-\infty}^{\infty}\sum_{n=-\infty}^{\infty} g(m,n,t)\sum_{m=-\infty}^{\infty}\sum_{n=-\infty}^{\infty} h(m,n,t+\Delta t)} \quad (10)$$

In other words, the first picture area g(i,j,t) is shifted pixelwise over the second h(i,j,t+Δt), multiplied to the corresponding gray values, summed up and normalized. The result is stored in the cross correlation function C(i,j,t,Δt) corresponding to the shifting vector (i,j). The correlation function is in the interval [0, 1], 1 being the value for perfectly matching patterns, and 0 for non matching ones. The coordinates of the maximum of the cross correlation function equals therefore to the most probable spatial shift vector. It is however inconvenient to calculate the cross correlation function in the above described way, due to the enormous processing time. Similar to the convolution, which is a multiplication in the Fourier space, the cross correlation is the complex conjugated multiplication in Fourier space. Therefore the picture areas are both Fourier transformed and the first multiplied with the complex conjugated of the second.

$$\widehat{C}(u,v) = \widehat{g}(u,v)\,\widehat{h}^{*}(u,v)\,, \quad (11)$$

$\widehat{C}(u,v)$,$\widehat{g}(u,v)$ and $\widehat{h}^{*}(u,v)$ being the Fouriertransformed of C,g,h with the wavenumbers u,v.

The back transformation of $\widehat{C}(u,v)$ yields the cross correlation function of the interrogation windows. On digital images the discrete Fourier transformation is realized by a fast fourier algorithm FFT, requiring fewer processing steps, thus saving processing time.

The detection of the peak in the cross correlation is often difficult, because of noise in the correlation function. In addition the peak tends to broaden, due to the gaussian form of the particles and from velocity gradients in the picture area. On the other hand this broadening is used for sub pixel accuracy processing via a center of mass algorithm. The noise results from:

- noise in the picture areas,
- three dimensional movement in and out of the light sheet,
- two dimensional movement of particles through the boarders of the picture,
- other particle patterns that randomly match up with the sampled picture area.

In other words the detected peak correlates not always to the real displacement vector. The quotient of the highest peak with the second is used as a measure of confidence for the results [7]. Displacements larger than half the interrogation window can not be separated from displacements in the opposite direction after back transformation of $\widehat{C}(u,v)$ (Nyquist theorem).

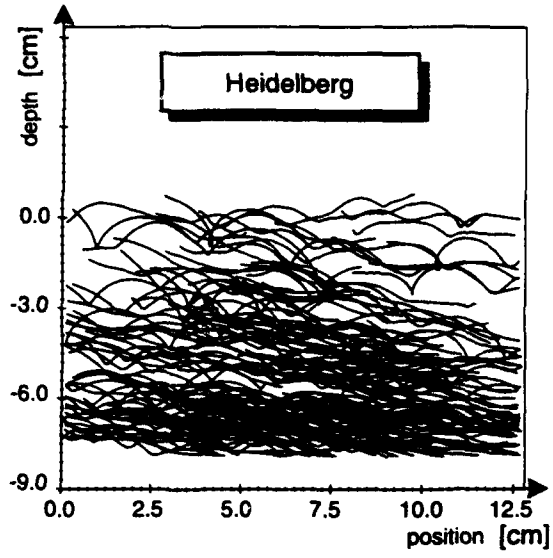

Fig. 6: *Trajectories of seeding particles beneath wind induced water waves.*

Corresponding to the relatively high velocities of 20 cm/s in the boundary layer spatial displacements up to 64 pixels are expected. In order to enable the evaluation of these pictures a multi grid algorithm was developed [3]. It divides the processing in two steps. First an estimate of the displacement vector is evaluated. This estimate is used to shift the second window over the first in such a way that they overlap as good as possible. The estimate is obtained on higher levels of a gaussian pyramid and by taking neighbouring vectors into account [6]. Processing on the higher levels of the pyramid saves processing time. The algorithm was developed on the second level of the pyramid, enabling the detection of displacements up to 32 pixel.

5 RESULTS

Fig. 6 shows a typical result of trajectories beneath water waves at a wind speed of 4.2 m/s. 100 images were processed. For presentation only a fraction of the trajectories were plotted. Only trajectories tracked over 90 image frames (3 s) were considered. Many particles can be tracked from the moment entering into the light sheet until leaving the area of observation.

First results for the boundary layer are available for low velocities (see Fig. 7). The results yield a nearly exponential decrease of velocity with water depth as expected. The boundary layer thickness of 2 mm was estimated from the tangential curves on the drift velocity profiles. This result is in good agreement to measurements of [8]. *Münsterer* measured the aqueous mass boundary layer thickness with a laser-induced fluorescence (LIF) technique.

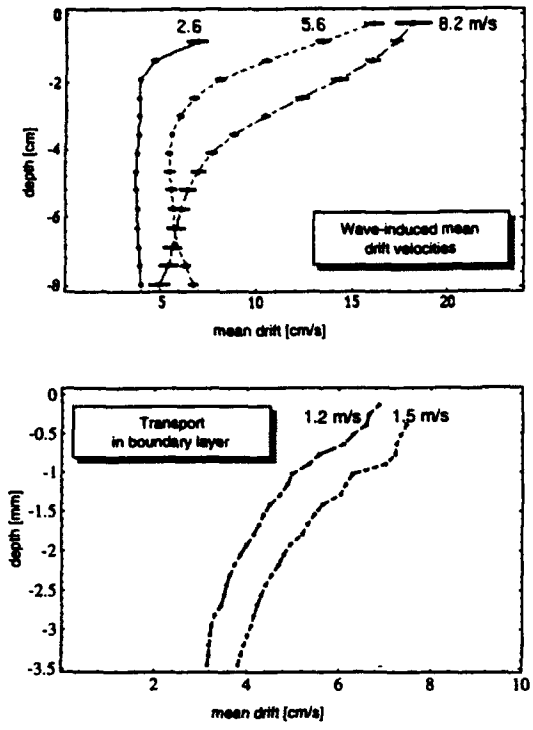

Fig. 7: *Top: Turbulent velocity profile in the first 10 cm beneath water waves at three different wind speeds. Bottom: High resolution profile in the viscous boundary layer.*

In addition the friction velocity u_* can be calculated from the drift velocity gradient (Fig. 7 bottom):

$$u_* = \sqrt{\nu \frac{\partial u}{\partial z}}, \qquad (12)$$

ν being the kinematic viscosity of water. Friction velocities of $u_* = 0.14\,cm/s$ for $1.2\,m/s$ wind speed and $0.16\,cm/s$ for $1.5\,m/s$ are found. *Bösinger* [2] measured friction velocities of $u_* = 0.15\,cm/s$ for $1.2\,m/s$ wind speed and $0.18\,cm/s$ for $1.5\,m/s$ derived from the bulk velocities.

6 OUTLOOK

At higher wind speeds, when the wave amplitude gets larger than the imaged sectors, a wave follower has to be used. Such a system suitable for flow visualization is currently developed. Additional flow-visualization in the air-sided viscous boundary layer is planned.

7 ACKNOWLEDGEMENTS

Financial support for this research by the German Science Foundation DFG (Wi 1029/2-1, Wellen-Turbulenz-Wechselwirkung) and the National Science Foundation (OCE91 15994 and OCE92 17002) is gratefully acknowledged.

REFERENCES

[1] Adrian R.J. 1991, Particle-Imaging Techniques for Experimental Fluid Mechanics, Ann. Rev. Fluid Mech. vol. 23, pp. 261-304

[2] Bösinger, R. 1986, Messungungen zur Schmidtzahlabhängigkeit des Gasaustausches, Diploma thesis, Institute for Environmental Physics, University of Heidelberg, Germany

[3] Dieter J. 1991, Strömungsvisualisierung in der laminaren Grenzschicht, Diploma thesis, Institute for Environmental Physics, University of Heidelberg, Germany

[4] Hering F. 1992, Messung von Transportgeschwindigkeiten in winderzeugten Wasserwellen mittels Digitaler Bildfolgenanalyse, Diploma thesis, Institute for Environmental Physics, University of Heidelberg, Germany

[5] Hering F., Merle M., Wierzimok D. and Jähne B. 1994, Particle Tracking in Space Time Sequences, IAPR, 12th International Conference on Pattern Recognition, Jerusalem, Israel

[6] Jähne B. 1993, Digital Image Processing, Concepts, Algorithms and Scientific Applications, pp. 289-293 and 200-205 2nd edition, Springer-Verlag, Berlin

[7] Keane D. K. and Adrian R.J. 1990, Optimization of particle image velocimetres. Part 1: Double pulsed systems Meas. Sci. Technol vol. 1, pp. 1202-1215

[8] Münsterer T. and Jähne B. 1993, A Fluorescence Technique to Measure Concentration Profiles in the Aqueous Mass Boundary Layer, Proceedings, Air-Sea Interface Symposium, Marseille, to be published

[9] Oertel H. sen. and Oertel H. jun. 1989, Strömungsmesstechnik, pp. 413-415 G. Braun Karlsruhe

[10] Okuda K. 1982, Internal Flow Structure of Short Wind Waves, Part 1. On the Internal Vorticity Structure Journal of the Oceanographical Soc. of Japan, pp. 28-42

[11] Willert, C and Gharib, M. 1991, Digital particle image Velocimetry, Exp.in Fluids vol. 10, pp. 181-193

[12] Wierzimok D. and Hering F. 1993, Imaging in Transport Processes, Athens, Begell House Publisher, Quantitative Imaging of Transport in Fluids with Digital Particle Tracking Velocimetry, pp. 297-308

PTV Measurement on a Rotating System Using Semiconductor Laser and CCD camera.

Tomomasa UEMURA*, Kazuyuki Fujimura**, Hyung-Jin SUNG***,
Jae-Min HYUN***, and Hideharu Koyama**.

* Department of Industrial Engineering,
Kansai University, Japan.
** Department of Mechanical Engineering,
Tokyo Denki University, Japan.
*** Department of Mechanical Engineering,
Korea Advanced Institute of Science and Technology, Korea.

ABSTRACT

Authors have developed a new imaging system for quantitative flow visualization utilizing infrared lasers and compact CCD video cameras, which occupies a small space with the least increase of mass. Applying the system to the measurement of the rotating flows in a cylindrical vessel, velocity distributions and locations of vortex-breakdown were measured quantitatively at both steady states and transient procedures. The binary-image correlation method, which is a method of particle tracking velocimetries, was applied to the measurement of velocity distributions in a horizontal cross section.

1. INTRODUCTION

The spin-down and spin-up processes of the flow in a cylindrical vessel has been interested in many aspects in the field of fluid and heat transfer engineering field. A steady circulating flow appears in a closed cylindrical vessel, when an upper end-wall is rotated about its axis. Rotating about the axis, the fluid circulates also in a vertical direction going upward along the axis. The flow exceeds a critical Reynolds number, a stagnation point appears on the axis and a local recirculation is formed at the upper side. This phenomenon is called a vortex breakdown. Vogel(1968) had studied the vortex breakdown experimentally, and showed the stability boundaries, i.e. domains where vortex breakdown can be observed on a plane expressed by the Reynolds number versus the aspect ratio of the vessel. Later, Escudier(1984) had studied the flow precisely by using both approaches of experimental and numerical analysis. Although his experimental study have been made in the wide Reynolds number range and for various aspect ratios, his quantitative velocity measurements have been limited within steady states. Lopez(1990) showed numerical results for the phenomena during a transient procedure of spin-up, in which the rotation rose up instantaneously.

Authors have attempted to measure transient flows at the Reynolds number up to 20000 using a particle tracking velocimetry(PIV). Experimental measurement of velocity distributions in a rotating vessel is not easy even in steady states. Especially, in the case of transient flow, quantitative measurements of a instantaneous velocity distribution had been almost impossible before the techniques of quantitative flow visualization have been developed. The present study is planed not to supplement Escurdier's steady state experiments but to extend quantitative measurements to the transient flow.

In order to measure and observe the flow relative to the vessel, the measuring system have to be installed on the turn table. From an experimental point of view, lighter components in the measuring system are preferable, because strong centrifugal forces may causes many difficulties in the experiments. Recent advancement in the micro-electronics technologies have solved the problem by offering light weight and compact instruments, which can be installed on the turn table without serious increase of the force.

2. EXPERIMENTAL AND MEASURING SYSTEM

When a cylindrical vessel is rotated about the vertical axis, the flows in the vessel exhibit very interesting behavior. One of the objects of the present study is to measure the transient flows during the spin-up and spin-down process quantitatively. The structure of the experimental system is shown in figure 1.

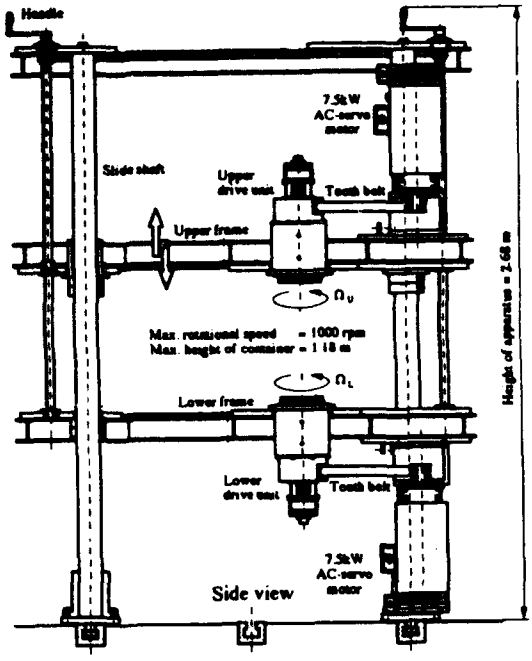

Figure 1. Structure of the experimental system.

A CCD camera and an illuminating system are set on a turn table together with the cylindrical vessel which is filled with viscous liquid. The dimensions of the vessel is 142.7 mmID and 330 mm height. A video camera is installed at the bottom of a hollow conical shaft to observe the flow in a horizontal plane from the axial direction as shown in figure 2. An upper shaft can be driven either synchronously with the lower shaft or independently. An additional camera can be installed in the upper shaft when the flow relative to the shaft is observed. As shown in the figure, signals and electrical power are transferred and fed via slip-rings. Figure 3 shows the experimental setups schematically .

In order to illuminate a horizontal plane of the vessel from both sides, beams of two infrared laser diodes are converted to 2mm-thickness light sheets. Each diode emits 780 nm infrared light and its nominal output is 30 mW. A infrared-cut filter in front of the image sensor is removed to obtain the maximum sensitivity of the CCD camera.

A small amount of fluorescent dye is introduced from a center of the bottom to visualize flow patterns, from which the location of vortices are measured. Instantaneous velocity distributions are measured using the binary-image correlation method(BCM), which is developed by Uemura et al(1991) as one of the techniques of particle tracking velocimetry(PTV), and is able to analyze video pictures of moving particles efficiently. Small plastic spheres are dispersed as tracers for the PTV.

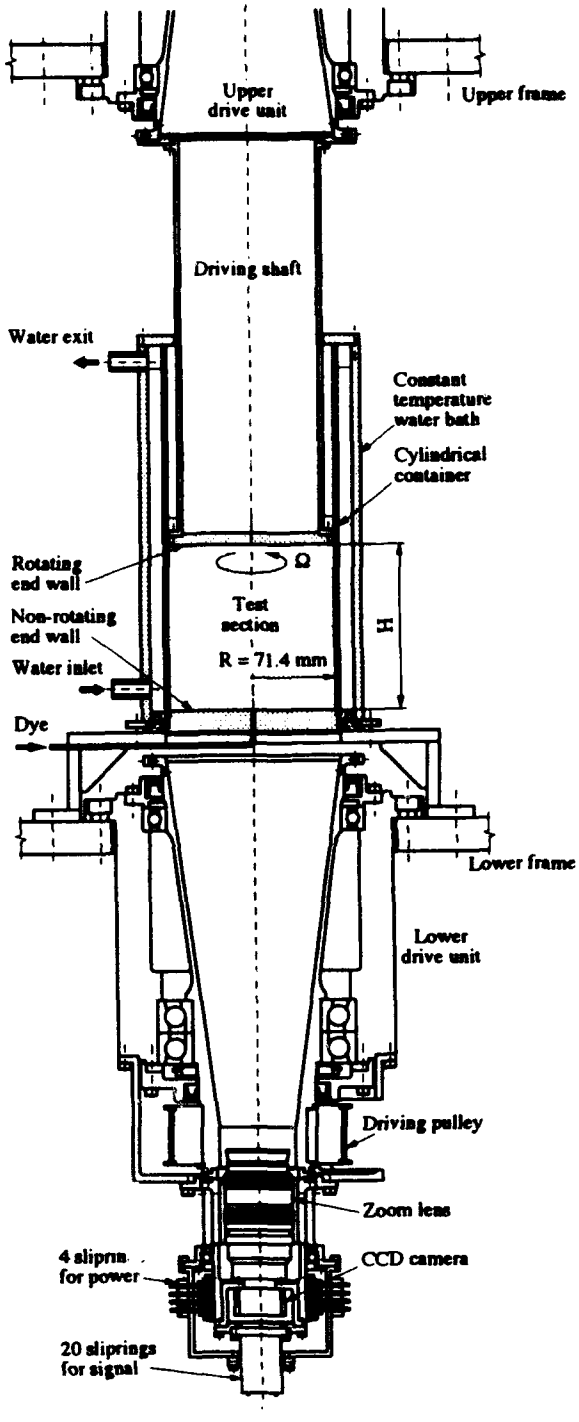

Figure 2.Detailed structure of the experimental apparatus.

The primary parameters of the experiments are the Reynolds number(*Re*) and the aspect ratio(*A*) of the vessel. They are defined in equation (1) and (2), respectively.

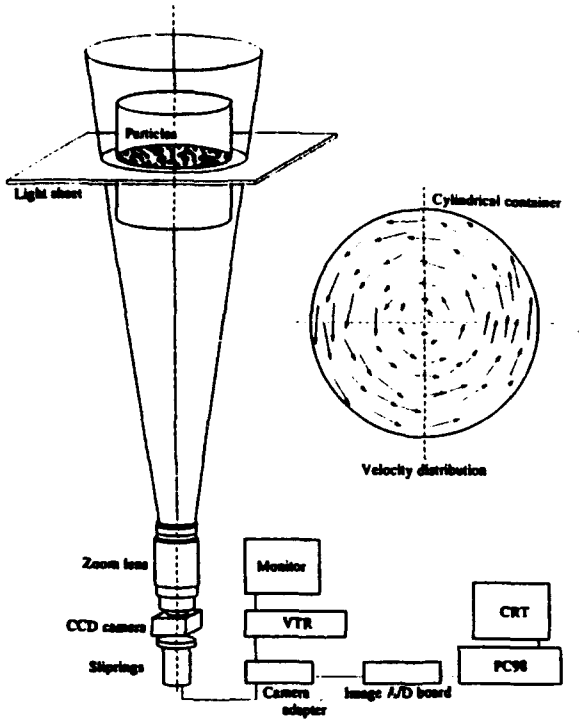

Figure 3. Schematic overview of experimental settings.

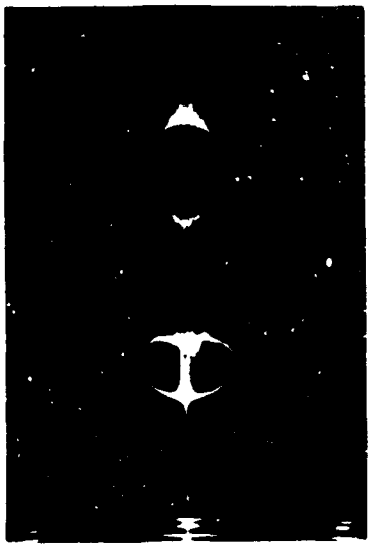

Figure 4. An example of flow patterns in a vertical plane in the steady state.

$$Re = R\omega^2/\nu \qquad (1)$$

$$A = H/R \qquad (2)$$

where, R denotes a radius of the vessel, ω is the angular velocity, and H is the depth of the liquid.

3. EXPERIMENTS

In order to examine the new experimental system, two series of experiments have been done for two different boundary conditions. In the first series of the experiments, the vessel with an open surface was rotated. In the second series, the surface of the vessel is closed by a circular disk. And the disk drives the liquid in the vessel by rotating about the axis. Viscosity of the liquid is increased by adding cane sugar to water(15 wt%).

In order to measure the location of the vortices, the flow is visualized by fluorescent dye, which is introduced from the center of the bottom. Figure 4 is an example of flow pattern exhibiting two vortices(double vortex breakdown) in a vertical plane of the closed surface vessel at steady equilibrium state at Re=2000. Flow patterns in the vertical axial plane and horizontal cross sections are pictured not only in the steady state, but also during the spin-up and spin-down processes. In the spin-up process, the system is rotated suddenly and accelerated from rest to 30 rpm in a short time. In the spin-down process, the rotation is stopped instantaneously from 30 rpm to rest.

Velocity distributions in horizontal planes are measured using the binary-image correlation method. In the velocity measurement, spherical polystyrene beads are used as tracers which diameter is about 0.9 mm and density is 1.04. The tracer particles can be observed clearly as shown in figure 5.

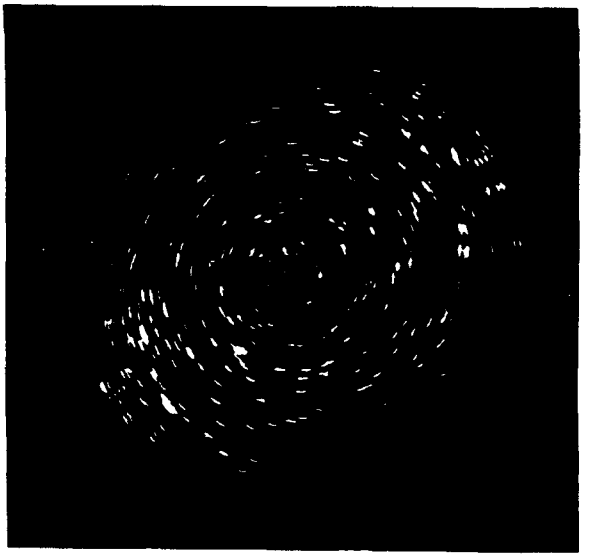

Figure 5. A picture of spherical polystyrene beads with diameter 0.9 mm and density 1.04.

4. EXPERIMENTAL RESULTS

Figure 6 shows an example of instantaneous velocity distribution in the middle horizontal plane in the open surface vessel rotating at 30 rpm. The square frame in the figure shows dimensions the measuring window. In the correction process of the PTV measurement, those vectors which have relatively large difference to neighbouring vectors have been regarded as erroneous and removed.

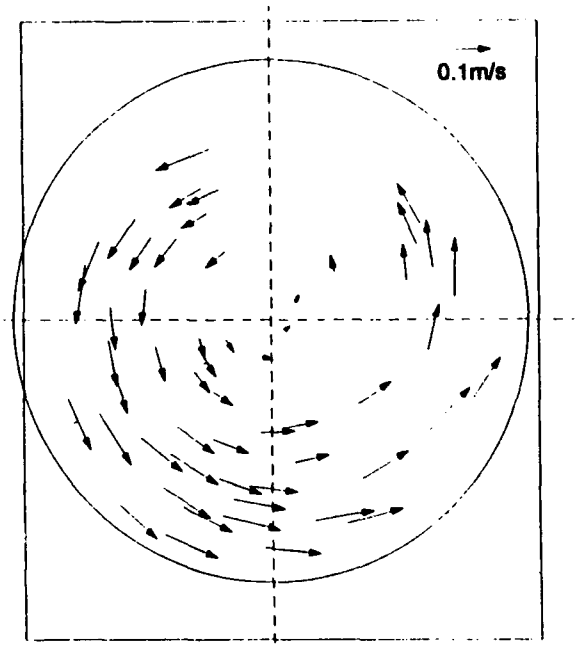

Figure 6. An instantaneous velocity vectors measured in the middle horizontal plane in the open surface vessel rotating at 30.34 rpm.

Some results of velocity measurements are shown in Figure 7 and 8 . In the figure 7, some correlations between tangential components of velocities and radial distances during the spin-up process are shown. The straight diagonal line shows a solid rotation for a reference. Although those plots are rather scattered, the timewise variations of the velocity distributions can be recognized.

Figure 8 shows decay of velocity distributions during the spin-down procedure at the similar experimental conditions. By comparing these two figures, it is quantitatively recognized that the spin-down process can calmed down from the center and the wall sides. And in the spin-up procedure, fluids around the center stays unmoved rather long time.

In the case of the surface of the vessel is closed by a circular plate, the ceiling disk rotates at 150 rpm and drives the fluid instead of the vessel. An experimental result measured under the condition at the Reynolds number Re=1767 and the aspect ratio H/R=1.75 is shown in figure 9, which shows a velocity distribution in a horizontal plane, which slices a bubble vortex on a axis. The velocity vectors are obtained by analysing consecutive sixteen pictures of one half second. A inner circle in the figure exhibits an estimated vortex region. Correlations between the tangential velocities and the radial distances are shown in figure 10, in which R_B is a radius of the vortex bubble measured by the fluorescent dye visualization. There found two different distribution for inside and outside the vortex bubble. And the velocity distribution inside the bubble is not linear.

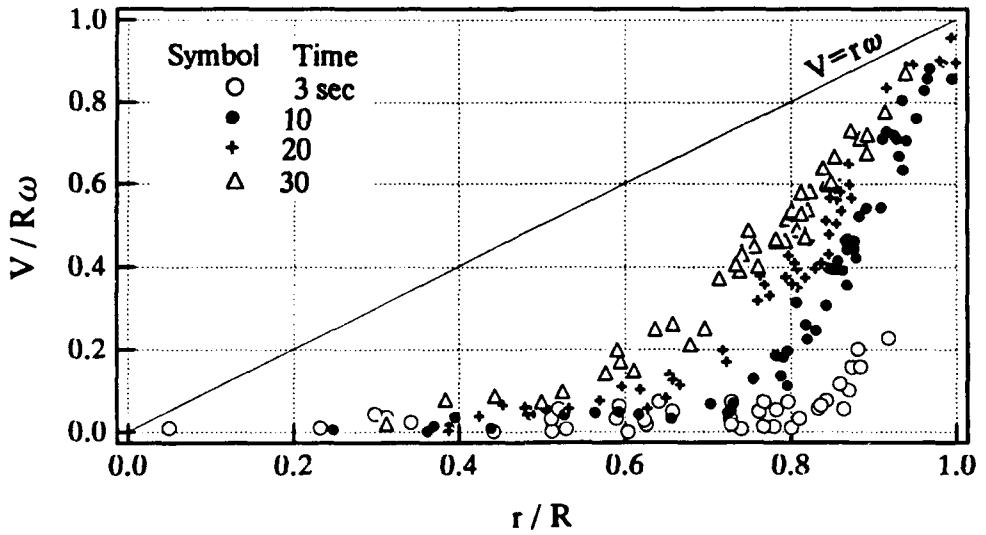

Figure 7. Correlations between tangential components of velocities and radial distances during the spin-up process.

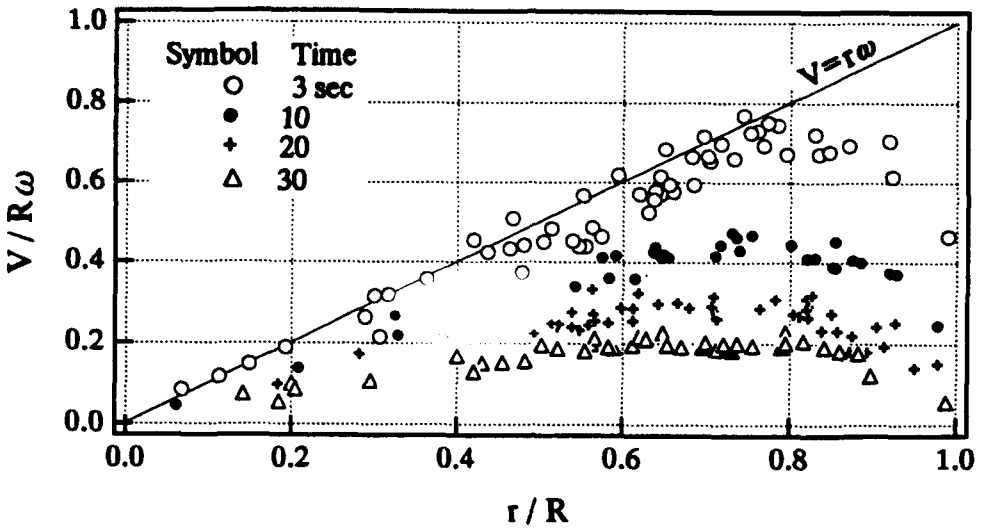

Figure 8. .Correlations between tangential components of velocities and radial distances during the spin-down process.

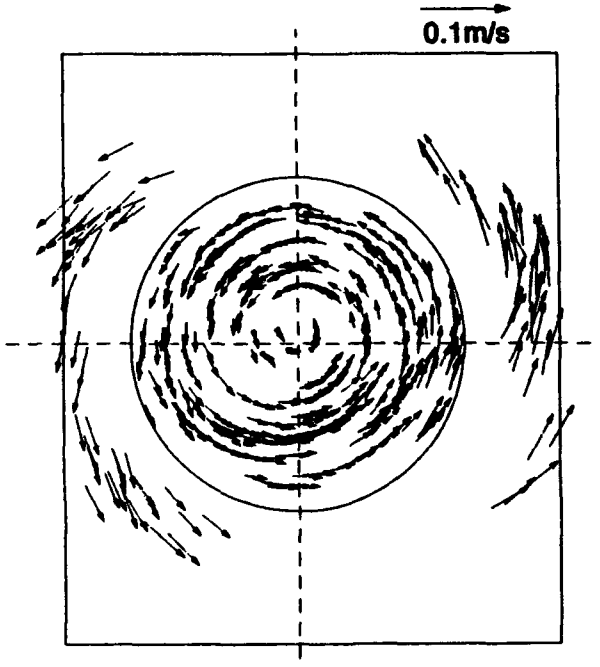

Figure 9. Velocity distribution in a horizontal plane containing a bubble vortex. Mesured from sixteen consecutive pictures. Re=1767, H/R=1.75.

5. CONCLUSIONS

The compact system for a quantitative flow visualization utilizing infrared laser diodes combined with a IR sensitive CCD camera and IR film is confirmed to be a useful tool to investigate the rotating system. By using the system, both spin-down and spin-up process are measured quantitatively for two different the vessels with a closed surface and a open surface.

6. ACKNOWLEDGEMENT

This work was supported by Research Institute for Technology, Tokyo Denki University and also in part by a grant-in-ade for Japan-Korea cooperative research projects from the Japan Society for the Promotion of Science.

7. REFERENCES

Escudier,M.P. 1984, Observations of the flow produced in a Cylindrical Container by a rotating endwall, Experiments in Fluids, 2, pp.189-196.

Lopez,J.M. 1990, Axisymmetric Vortex Breakdown. Part1. Confined Swirling Flow, J. Fluid Mech., Vol.221, pp.533-552.

Uemura,T., Yamamoto, F., Ohmi, K. 1991, Mixing Flow in a Cylindrical Vessel Agitated by a Bubbling Jet, Application of Laser Techniques to Fluid Mechanics, pp.512-536, Springer-Verlag.

Vogel, H.U., 1968, Experimentelle Ergebnisse über die laminare Strömung in einem Zylidrischen Gehäuse mit darin rotierender Scheibe. Max Plank Institut für Strömungsforschung Bericht, 6.

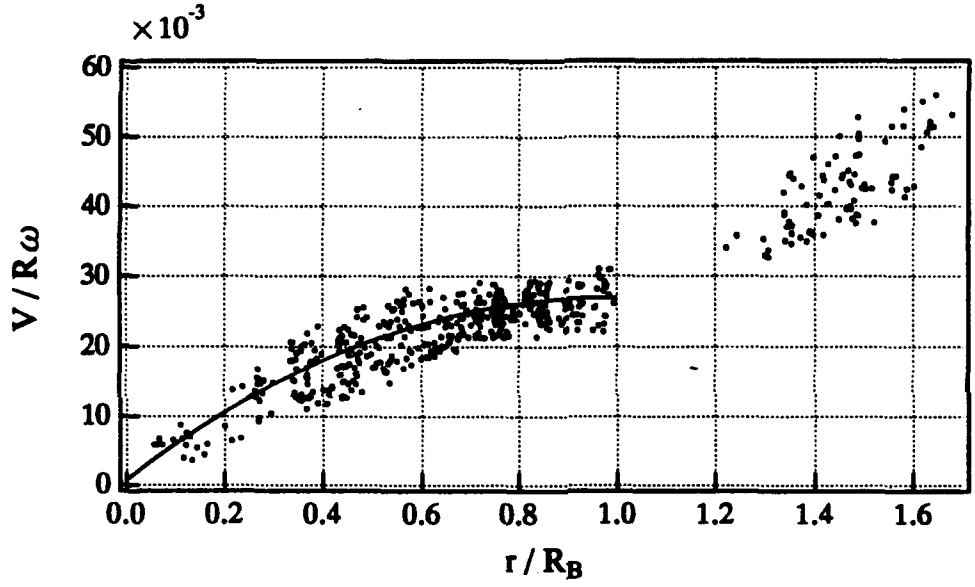

Figure 10. Correlations between tangential velocities and the radial distances for same data in figure 9. R_B is a radius of a vortex bubble.

QUANTITATIVE VISUALIZATION OF VELOCITY DISTRIBUTIONS IN FLOW

Isao SHIMIZU*, Kenji SUZUKI* and Norio AKINO**

* Dep. of Mechanical Engineering, Ibaraki College of Technology
866 Nakane, Katsuta-Shi, Ibaraki-Ken 312 Japan
** Japan Atomic Research Institute, Tohkai-Mura, Ibaraki-Ken

ABSTRACT

A new technique visualizing quantitative velocity distributions of flow has been developed by using Multiplexed Matched Spatial Filtering method for image processing of particle displacement loci in flow. At the present, particle image displacement(PID) method is used for quantitative visualization of two dimensional velocity distributions. In this method, many image pairs of the seeded particles in the multiphase flow are photographed on the negative film by double exposure. The direction and the magnitude of velocities are measured from the direction and space of the Young's interference patterns, which are scattered from the negative film illuminated by the coherent laser beam. The map of equal velocity distribution is reconstructed by the partial light of Young's interferogram passing through a pinhole set at an arbitrary angle and distance from the center of the beam axis on the back focal plane of a Fourier transform lens. The technique using a pinhole set at the back forcal plane has the shortcomings that the image of visualization is inaccurate and dark because of using partial light from Young's interferogram and that the orientation of flow can not be identified. Therefore, a new technique using the Multiplexed Matched Spatial Filtering(MMSF) method is proposed to overcome these defects. Being illuminated the seeded particles suspended in the flow with a double exposed sheet light in a short time and a long time, loci of particle images in the flow like as letter "i" are taken for a photograph on the negative film. The orientation of image pattern "i" which is the locus of particle displacement shows the orientation of flow. The orientation and magnitude of flow velocities can be identified by a MMSF constructed from the diffraction patterns depending on the orientation and the length of the reference image pairs which are loci of particle displacement in the modefied double exposure time.

The direction of plus or minus in velocity of flow can be immediately discriminated by this technique. Image processing is done in real time and the accuracy of the measured velocity is very high in this method.

1. INTRODUCTION

On the quantitative visualizing method for the velocity distributions of flow, there are two methods, those are, the digital correlation method which determine the velocity derived from the distance of displacement of seeded particles in flow in unit time[1], and the analogous correlation method that is the laser speckle method called Particle Image Displacement(PID) method[2].

In the digital correlation method, the techniques which determine the vector of velocity derived from the distance of two images for the same particle taken on the each two photographs at small time difference, and derived from the correlation of two image groups of plural particles on the two photographs are there.

On PID method, the seeded particles suspended in the flow are taken on a photograph with double exposure of sheet light, the image loci of particles are taken on photograph in a negative film. The image pairs of particle displacement taken on a negative film being irradiated by a parallel coherent laser beam, the diffracted light scattered from the speckle pair forms the interference pattern named Youngs interference pattern at the back focal plane of the convex lens.

The velocity and its direction of flow can be determined from the space and direction of the Yongs interference pattern. In the PID method there are two technigues which can determine the local velocity and the velocity contour map in flow. That is, Youngs intereference pattern method (the technigue measuring local velocity) derived from the displacment of local speckel pairs on the negative film, and the quantitative visualizing technique making contour map of equal velocity vectors, which sets the pinhole at the Fourier transform plane, takes only the same magnitude and direction of vector of flow, foms images of speckle pairs corresponding to a certain component of flow velocity at the imaging plane, and foms the contour map of equal velocity vectors of flow in the all of the view. With comparison of these methods, digital correlation methed has a defects which take a lot of time and devote the labor to determine the vectors of displacement of many particles, the time correlation method which takes the correlation with changing positions of particles in a time in flow have defects that the measured values are different with the size change of the compared area measuring the particle images in a shearing time, and that a lot of calculating time with a large computer is needed to process the data.

In the comparison with those methods, the PID method that is analogous technique, has the advantage that the digital techniques can not have, these are applicable to measuring velocity in high dense particle image pairs and to rapidity of data processing, and high precise on measured values. Therefore, at present, to measure the two dimensional distributions of velocities in flow, people pay attention to the PID method.

Nevertheless, following defects are there in the PID method. Those are, in the measuring local sp when Youngs interference pattern is formed from the speck irs irradiated by laser beam, Youngs interference pattern doe ot appear in case of high density of speckle pairs, the enormous time and immense labor are

needed to measure the velocity in all of view with the technique measuring locally because reading out a lot of spaces and directions of Youngs patterns at all point in flow. Other defects are there in the PID method to measure equalvelocities contour map. Laser beam for reconstruction irradiating to the complexed speckle pairs, the bright spots forming the equal velocity contour map at the imaging plane of lanse can not show the correct equal velocity contour map, because Youngs interference patterns in all sizes and directions are constructed around at the center of the beam axis and the parts of each Youngs interference pattern passes through a pinhole set at the Fourier transform plane, respectively.

As above mentioned, a lot of things have to be improved are there in the techniques measuring two dimensional flow velocities. Moreover, the technique adequately determining the direction of plus and minus in flow velocity has not been developed in the present techniques. Since, a new measuring technique of the flow velocity using Multiplexed Matched Spatial Filter (MMSF) has been developed to distinguish the direction of plus and minus of flow velocity, and to determine and display the velocity in local and equal velocities contour map in the all of view immediately, moreover to develop the technique being able to separate parallel and display immediately the contour maps of the different velocities, respectively.

2. PARALLEL IMAGE PROCESSING FOR VISUALIZING THE CONTOURS OF EQUAL VELOCITIES IN FLOW

The method which can simultaneously, precisely and rapidly discriminate a certain length and direction of loci of particles in flow by the Multiplexed matched Spatial Filter[3] has been examined by authours[4]. In Fig. 1, the schematic diagram of the optical data processing system which can correctly discriminate the loci of particles for each velocity components in flow and simultaneously display their contours by a MMSF is shown. The negative film on which the loci of flow particles photographed being set at the frontal focal plane P1 of Fourier transform lens L1, the diffraction patterns scattered from the loci of flow particles being filtered by a MMSF set at the back focal plane P2 of lens L1, the auto-correlation peaks discriminating the same loci of flow particles as the reference loci aligned on the MMSF appear at the back focal plane P3 of imaging lens L2. Now, the MMSF is constructed on a holographic plate from the pattern optically interfered by both the diffraction patterns of reference loci set at the plane P1 and the reference parallel beam.

A 50 mW He-Ne laser was used as the light source. The Fourier transform lens L1 and imaging lens L2 had the focal length of f1=f2= 200 mm and the diameter of 100 mm. An interferometer was incorporated in forming an optical Matched Filter. The diameter of both reference beam and object beam was 40 mm in the constructing MMSF, while the diameter of reserved region for pattern recognition could be reduced to 20 mm. The loci of particle images recorded on a plate, KONIKA HRP N-II, were employed as references and the loci of particle images in flow, recorded on a

mini-copy film HR-II, were used as input objects. A composition of the input objects could be positioned within the beam width 20 mm. The output correlation peaks at plane P3 were recorded on the photographic film or were fed into a frame memory via CCD camera. A micro-computer then performed an optical intensity level processing. The Agfa-Holotest emulsion 8E75 was used in forming a Matched Filter, using D-19 for developing.

Four rectangles were used as the reference patterns of the filter. An example is depicted in Fig.2(a) for the composition of reference patterns and in Fig.2(b) for the composition of input objects. The four sorts of rectangles implying four different velocities could be distinguished from the length of particle loci lying in the X and Y directions, as shown in Fig.3. In Fig.2, (a) and (b) imply the location of reference figures of particle locus, the measured loci of particle image displacement, respectively. In the four measuring fields in Fig.3(a) corresponding to the field of each reference locus shown in Fig.2(a), the bright spots show the signals distinguished the same locus in the measured field shown in Fig.2(b). The auto-correlation signals processed by a certain threshold level of light intensity which show the discriminated results are displayed in Fig.3(b). These signals appear, in each measuring field shown in Fig.2(a), skew-symmetrically to the positions of measured particles shown in Fig.2(b).

3. VISUALIZING CONTOUR MAPS OF EQUAL VELOCITY INCLUDING DIRECTION OF VECTOR IN FLOW

A new technique processing special PID data with a MMSF has been developed to discriminate the direction and magnitude of flow velocity vectors simultaneously and to visualize the equal velocity contour maps instantaneously. Being illuminated the seeded particles suspended in the flow with a double exposed sheet light in a short time and long one, loci of particle images in the flow lika as letter "i" are taken for a photograph on a negative film. The orientation and magnitude of flow velocities can be identified by a MMSF constructed from the diffraction patterns of letters "i". The map of the quantitative visualizing velocity distributions by a MMSF is shown in Fig.4. In Fig.4, (a) shows the composition of reference velocity patterns constructing a MMSF, (b) shows a distribution of measured loci of flow particles, and (c) shows maps of the output correlation peaks (auto-correlation peaks) implying maps of four equal velocities, appearing at the plane P3. The experimental results show that the direction of plus and minus in velocity of flow can be immediately and simultaneously discriminated by this technique. Auto-correlation peaks discriminating the velocity vectors in direction of X and Y axies or plus and minus are displayed; at left hand side and right hand side: six auto-correlation peaks and each five auto-correlation peaks in a double line, respectively, at top right and bottom left: seven peaks and each five peaks in a triple row, respectively.

Using the optical image processing technique and special double exposed PID method, components of vortexes can be determined. In

Fig.5, the experimental result determining the model components of vortex is shown. In the figure, (a) shows the composition of reference circular loci impling model velocity components of double-exposed vortex, (b) shows the distribution of measured model loci, and figure (c) shows the output signals of auto-correlation.

Fig.6 shows the experimental result for identification test investigating the precision of the measurement of flow velocities visualized with one reference velocity pattern. In Fig.6, figure (a) shows the reference pattern, (b) shows the size distribution of measured flow patterns, (c) shows the output correlation peaks at plane P2. For the same size of measured pattern, auto-correlation peak can be seen strongly in figure(c). In response to lowering the threshold level of the intensity of correlation peaks, size difference identified as the same size for the reference pattern increases as long as 5 % difference.

The special PID pais in flow is taken on a negative film in experiment as shown in Fig.7(b). Special PID pairs are discriminated using a MMSF of which reference patterns are composed as shown in Fig.7(a). The distributions of discriminated signals (distributions of auto-correlation peaks) by a MMSF are shown in Fig.7(c).

These experimental results indicated that the new technique double-exposing particle image displacement asymmetrically and discriminating loci of particles optically by a MMSF, is available to determine the magnitude and direction of velocity vectors of flow and to visualize the equal velocity contour maps simultaneously and instantaneously.

4. CONCLUSION

A new technique which takes the particle image displacements on a photograph with a special double-exposure sheet light to discriminate the direction of plus or minus and the magnitude of velocity vectors, and which process the loci of particle image displacements simultaneously and instantaneously, has been developed to visualize the equal velocity contour in flow quantitatively. The experimental results show that the direction of plus and minus in velocity in flow can be immediately and simultaneously discriminated by the technique, and that the equal velocity contour maps of flow in all of view can be constructed simultaneously and instantaneously by a Multiplexed Matched Spatial Filter. It is clarified that the precision of measurement of flow velocities has been kept in response to the threshold level of the intensity of correlation peaks. The experimental results indicate that the new technique is available to determine the magnitude and direction of velocity vectors of flow and to visualize the equalvelocity contour maps simultaneously and instantaneously, for actual flow.

ACKNOWLEDGEMENT

Some parts of this work were financially supported by a Grant

in Aid for Scientific Research from Ministry of Education, Science and Calture in Japan; A Grant under the Monbusho International Scientific Research Program (University to University Cooperative Research): (Project number 06045061), Optical neuro computing system with intelligent sensor.

REFERENCES

1)Merzkirch, W. : "Flow visualization and digital image processing", Von Karman Institute for Fluid Dynamics, Lecture Series 1986-09, (1986) 1-21

2)Meynart, R. : "Equal velocity fringes in a Rayleigh-Benard flow by a speckle method", Appl. Opt. 19(9) (1980) 1385-1386

3)Shimizu, I., Asakawa, S. and Yang, W.-J. : "Simultaneous and instantaneous measurement of the shape, size and position of particles by a Multiplexed Matched Spatial Filter", Proc. of the 2nd Intern. Congress on Optical Particle Sizing (1990) 221-230

4)Shimizu, I. and Akino, N. : "Quantitative visualization of velocity distributions in Multi-Phase flow", Imaging in Transport Processes, Sideman, S. and Hijikata, K. (Eds), Begell House Inc. Publishers, (1993) 343-349

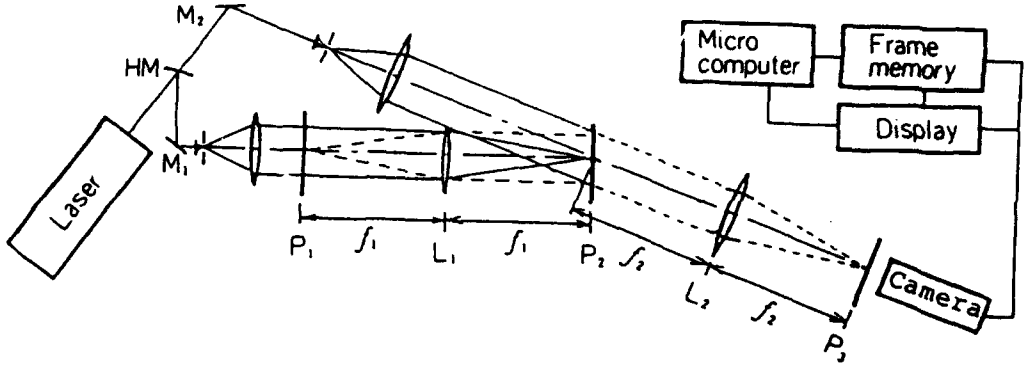

Fig. 1 Optical image processing system for the reconstruction of verocity distribution

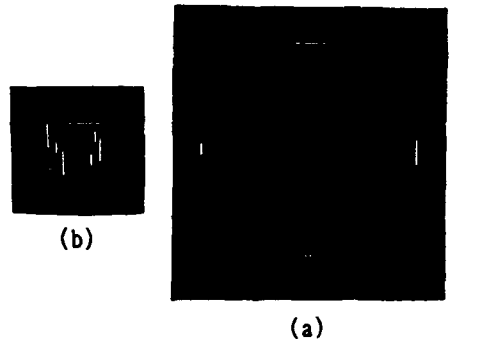

Fig. 2 (a): location of reference figures of particles locus, (b): loci of particle image displacement

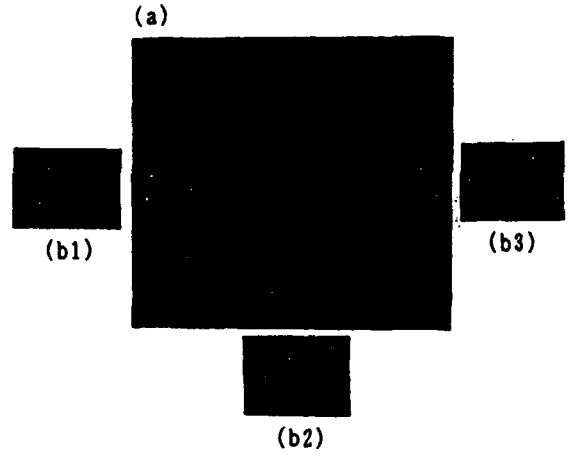

Fig. 3 Experimental result discriminating the loci of particles

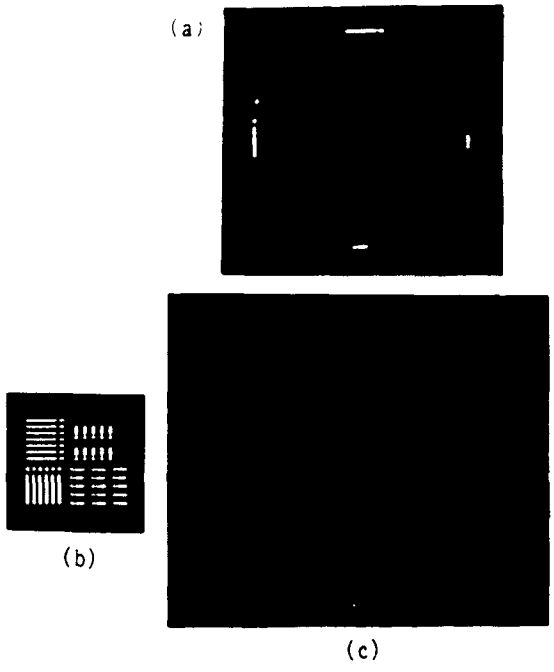

Fig. 4 The maps of the quantitative visualizing velocity distributions by MMSF. (a):location of reference velocity patterns, (b):distribution of measured loci of flow particles, (c):the maps of equal velocities shown by auto-correlation peaks

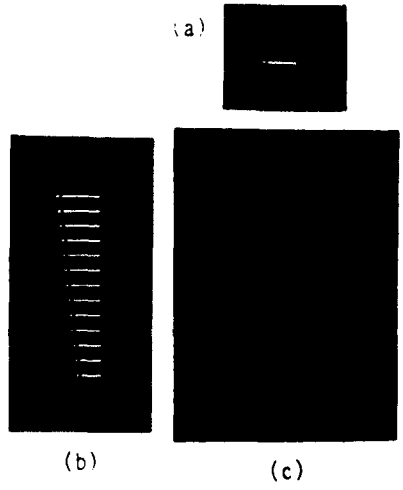

Fig. 6 The identification test investigating the precision of the measurement of flow velocities visualized with one reference velocity pattern. (a):reference pattern, (b):size distribution of flow patterns, (c):output correlation peaks at P_3

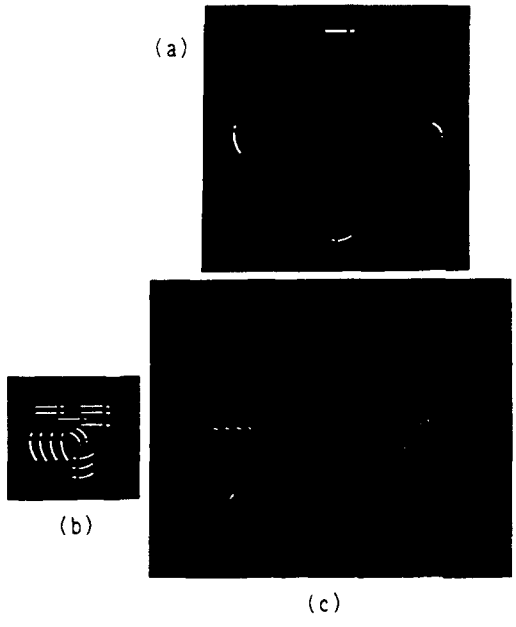

Fig. 5 (a):location of reference circular loci double exposured, (b):distribution of measured loci, (c):output signals of auto-correlation

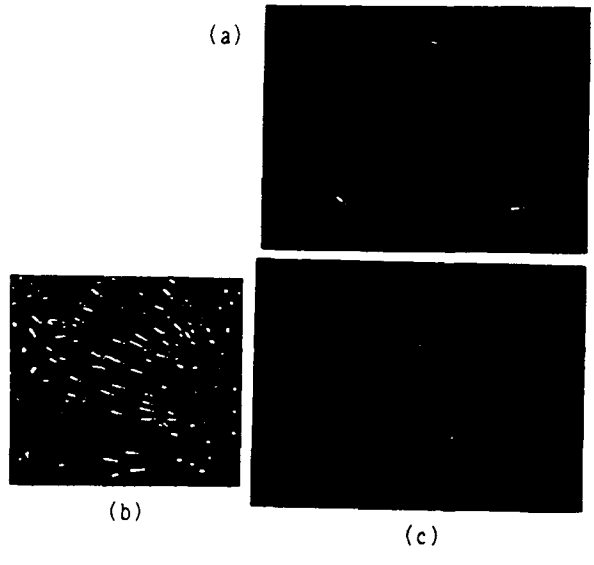

Fig. 7 Determination of orientation and velocity of flow. (a):location of reference loci of particles double exposured, (b) distribution of measured loci of flow particles, (c):output signals of auto-correlation

FLOW TAGGING IN WATER USING PHoto-Activated Nonintrusive Tracking Of Molecular Motion (PHANTOMM)

Walter R. Lempert,* Scott Harris,* Kevin Magee,* Christopher L. Burcham,**
Dudley Saville,** Richard B. Miles,* Kyle R. Gee,† and Richard P. Haugland†

*Department of Mechanical & Aerospace Engineering

† Department of Chemical Engineering
PRINCETON UNIVERSITY
Princeton, New Jersey 08544 U.S.A.

† MOLECULAR PROBES, INC.
Eugene, Oregon 97402 U.S.A.

1. INTRODUCTION

Flow tagging velocimetry is a relatively new time-of-flight optical diagnostic inwhich a spatially continuous pattern is "written" into a fluid by means of an optical resonance. The displacement of the original pattern is subsequently "interrogated" by means of Laser-Induced Fluorescence imaging. The displacement which occurs during the elapsed time interval between the two optical resonances constitutes a measurement of velocity. Examples of flow tagging include Raman Excitation plus Laser-Induced Electronic Fluorescence (RELIEF) [Miles, et. al. (1989)], which has been used recently for fundamental turbulence studies in subsonic air jets [Miles, et. al. (1993)] and multiphoton dissociation of water vapor, followed by hydroxyl radical LIF, which has been demonstrated in supersonic combustion flows by Boedeker (1989), and by Chen, et. al. (1992).

In this paper, we present new results using a flow tagging approach recently developed for water which uses caged dye Photo-Activated Fluorophores (PAF's) [McCray and Trentham (1989)], and which we have termed PHoto-Activated Nonintrusive Tracking Of Molecular Motion (PHANTOMM). Caged dye PAF's are nominally fluorescent dyes which have been rendered nonfluorescent by strategic attachment of a chemical caging group. As illustrated in Fig. 1, the caging group is photolytically cleaved upon absorption of ultraviolet light, generally from a laser. After photolysis, the original dye is recovered, and can subsequently be tracked for a period limited only by mass diffusion using laser sheet imaging approaches [Dahm and Dimotakis (1990)]. The PHANTOMM approach is similar in many respects to Laser-Induced Photochemical Anemometry (LIPA) techniques, based on the use of either photochromic [Popovich and Hummel (1967); Falco and Chu (1987)] or phosphorescent [Stier and Falco (1994)] tracer materials. Photochromic materials exhibit a reversible change in reflectance when activated by ultraviolet light, typically from either a nitrogen or excimer laser. Using back-lighting, the temporal evolution of the initial reflectance pattern can be tracked. Photochromic materials have been used almost exclusively in nonpolar solvents, although, recently, Yurechkov and Ryazantsev (1991) have reported measurements in water. Phosphorescent tracers are materials which absorb light and then re-emit with a relatively long spontaneous radiative lifetime. Stier and Falco (1994) have recently reported measurements in a simulated internal combustion engine using a water-soluble tracer with a lifetime of between 0.30 and 0.80 msec. LIPA has been recently reviewed by Falco and Nocera (1993).

2. EXPERIMENTAL

Two caged dye PAF's, dextran carboxy fluorescein and 8-hydroxypyrene-1,3,6-trisulfonic acid, were used for this work. Figure 2 shows the caged and fluorescent forms of the two dyes. The chemical and optical properties of these compounds has been presented in some detail previously [Lempert, et. al. (1993)]. The caging group is photolyzed upon absorption of a single UV photon in the region of 0.350 microns (characteristic of benzene-like compounds). The uncaged dextran behaves essentially identically to ordinary fluorescein dye, with strong absorption in the region of 0.490 microns (blue) and subsequent fluorescence in the region 0.520 to 0.620 microns. The uncaged trisulfonic acid behaves similarly, but with absorption shifted to the vicinity of 0.450 microns, and fluorescence at wavelengths exceeding 0.480 microns.

The basic optical configuration is illustrated schematically in Fig. 3. The tagging is performed using the third harmonic of a Q-switched Nd:YAG laser at 0.355 microns. Single pulse energies between 2 and 100 mJ were used, depending upon the experiment. The interrogation was performed with either a pulsed, flashlamp-pumped dye laser or a cw argon-ion laser, depending upon flow velocity. The dye laser was capable of pulse outputs between 50-400 mJ, with a pulse duration of approximately 2 microseconds and spectral bandwidth of approximately 1 nm. The cw argon-ion laser was operated on the 0.488 micron transition, with single line output between 0.020 and 1.0 Watts. The tagging beam is focused to "write" a line (or cross) between 50 and 500 microns in diameter. The interrogation beam is formed into a thick sheet using lens combinations which depend upon the experiment. For the experiments to be discussed below, the interrogation sheet thickness varied between approximately 0.1 to 1.0 cm, and sheet height between approximately 1.0 to 7.5 cm. Both a household color camcorder and a COHU monochrome CCD (Model 4800) camera were used for the imaging. A Schott OF475 or OG515 long-pass glass filter was used to separate the fluorescence from background laser scattering. The images were stored on videotape and post-processed using a computer-based framegrabber system.

3. CAGED DYE CHARACTERIZATION

A detailed discussion of experiments designed to characterize the critical optical and chemical properties of caged dye PAF's, as well as to compare them to

phosphorescent and photochromic tracers has been given by Lempert, et. al. (1993), and we will, therefore, only summarize here.

The most fundamental distinction between caged dye PAF's and other tracer compounds is that the photochemical change is permanent. This permits measurement of even very low speed phenomena, such as the electrohydrodynamic flows to be described below, to high accuracy. There is, however, a minimum time delay which can be utilized, due to the finite kinetic rate of the cage-cleaving process. Kinetic rise-time studies have been performed for both PAF's employed to-date. Figure 4 shows a ln-ln plot of the fluorescence (interrogation) intensity, as a function of the time delay between tag and interrogation. For this data, a series of images were obtained by writing a line into a test tube containing a 0.40×10^{-7} M solution of the trisulfonic acid caged dye. The flashlamp-pumped dye laser was used for the interrogation, and the images were digitized with the video frame-grabber. The dye in the test tube was changed after every pair of tag and interrogation pulses. It can be seen that the rise appears to be exponential, with a finite offset at zero time delay. This is due to background fluorescence from uncaged dye impurity. Experiments such as this, using realistic pulse energies and optical collection geometry, have resulted in the general conclusion that the minimum usable time delay for these caged dye PAF's is on the order of 100 microseconds.

A second feature of caged dye PAF's is that signal levels are quite high, even at relatively low concentration. This is due to the fact that the fluorescence radiative lifetime (order nsecs) is much shorter than the duration of the integration laser pulse (order microseconds), therefore enabling hundreds of photons to be extracted from a single uncaged dye molecule. Typical concentrations employed for the images presented below are between 10^{-6} and 10^{-7} M. This permits lines of almost arbitrary length to be written, since absorption of the laser beam is insignificant.

4. FLOW FIELD RESULTS

The potential of the PHANTOMM technique was demonstrated using several model flow fields. The first was a simple benchtop pipe (poiseulle) flow at a centerline velocity between 4.5 cm/sec (R_e = 315 based on pie diameter) and 12 cm/sec (R_e = 840). The pipe was constructed from approximately 1 cm ID quartz tubing and was contained within a rectangular Plexiglas box which was filled with water to provide partial index matching. One-inch diameter quartz windows provided access for the 0.355 micron tagging beam, although ordinary BK-7 optical glass would have sufficed. The tagging was performed with a single, approximately 25 mJ energy pulse, and the interrogation was performed with the cw argon-ion laser. The color camcorder was used to obtain the images.

A 1 mgm/liter solution of the caged fluorescein PAF probe was used for all cases. Figure 5 shows a pair of representative images. The left-hand image corresponds to a maximum flow velocity of 4.5 cm/sec, and exhibits a characteristic laminar profile. The right-hand image corresponds to a maximum velocity of 12 cm/sec and exhibits a more "top-hatted" profile, corresponding to a laminar flow which has not yet fully developed.

As a second illustration, we have written a cross into an approximately 150 mm diameter ordinary laboratory beaker, inwhich swirl was introduced with a magnetic stirring bar. The tagging was performed by splitting a 40 mJ/pulse tagging beam into two pieces, each of which was focused with a simple plano-convex lenses. Figure 6 shows an interrogation sequence, resulting from a single tagging pulse obtained with an approximately 1 cm thick sheet from the pulsed dye laser. The upper left-hand image was obtained with a time delay of 12 msec between tag and interrogation, and, essentially, corresponds to the initial orientation of the cross. The subsequent images are obtained at time delays of 1, 2, and 3 secs, respectively. The rotation of the crossing point, roughly 1/8th of a revolution/sec, counter-clockwise, is clearly evident.

In order to demonstrate potential in large-scale flows, measurements have also been performed in a 5,000 gallon research water channel facility,. The facility test section is 8.2 m long, 1.5 m wide, and operates with a free stream velocity of 10 cm/sec. Measurements were performed by writing a line through the center of rotation of a characteristic tip vortex, shed by an elliptical sail tip model. Figure 7 shows a 50 laser shot average (left), and a single shot (right), cross-sectional image of the tip vortex using ordinary fluorescein sheet visualization. The fluorescein dye was injected from a copper tube positioned just upstream of the leading edge of the model. The principal flow axis is out of the plane of the paper, toward the reader. The fluorescence was captured parallel to the principal flow axis by placing a large, 90° turning mirror in the facility, approximately 0.80 m downstream for the laser sheet.

PHANTOMM images were obtained by replacing the ordinary fluorescein dye with either a 2 mgm/liter solution of the caged pyrene tirsulfonic acid PAF or a 5 mgm/liter solution of the caged dextran PAF. (The concentrations were increased, relative to those used in other measurements, due to a combination of dilution of the seeded fluid by the bulk flow and the flow collection efficiency of the optics. Similar quality images were obtained from both materials.) Figure 8 shows a collage of single-shot images with time delays of 1, 10, 40, 100, 150, and 195 msec, respectively. The lines are continuous since they are only written at the intersection of the tagging beam and the seeded fluid. After 195 msec, the core has rotated by approximately 180° (16 radians/sec), whereas the outer fluid has rotated by less than 90°.

Finally, we have very recently initiated a program to explore the potential of the PHANTOMM approach for quantitative measurement of internal circulation in droplets, including both free-falling droplets and stationary droplets which have been drawn into specific geometrical configurations by application of an external electric field. Figure 9 shows a simplified schematic of the cell employed for the electrohydrodynamic studies. A pair of flat plate electrodes is immersed into a bath of silicon oil, contained within an approximately 5 cm x 5 cm x 5 cm rectangular glass cell. A droplet of a second fluid is attached to the center of one electrode, and its shape subsequently distorted by application of the electric field. In the case of water, we have "stretched" the originally semi-spherical drop into a Taylor cone [Vizika and Saville (1992); Wilson and Taylor (1924)] by application of a 3.5 kV/cm field. The resulting cone has a triangular cross section, approximately 3 mm in diameter at the base. An approximately 100 micron diameter line is written into the cone using a 1 meter focal length lens and 1-2 mJ of third harmonic output from the tagging Nd:YAG laser. Approximately 50 mWatts of output from the cw argon-ion interrogation laser is formed into 2 cm high by 1 mm thick sheet. Figure 10 shows a collage of images obtained from a

single "tag" of the cone at time delays of < 1 sec, 10 sec, 30 sec, and 50 sec, respectively (from top right to bottom left).

Figure 11 shows a preliminary image obtained from an approximately 2 mm diameter free-falling water droplet, produced with a simple laboratory pipette. The image was obtained by tagging with the Nd:YAG laser, operating at a 10 Hz repetition rate. The interrogation is, again, performed using the cw argon-ion laser. The droplet in Fig. 11 has been tagged twice, with a 100 msec temporal separation. The second tagged fluid element (located approximately in the center of the droplet) is translating downward at relatively high velocity, and the resulting image is smeared due to the 16.67 msec video field integration time. The profile, however, can be seen to be quasi-parabolic. The tagged fluid from the previous (in time) YAG laser firing has wrapped up into a pair of characteristic counter-rotating vortices. The left-hand vortex appears brighter due to focusing of the interrogation sheet by the droplet.

5. CONCLUSIONS

We have demonstrated the utility of flow tagging velocimetry based upon caged dye PAF's in a variety of applications ranging from studies of internal circulation in droplets, to tip vortex shedding in full-scale hydrodynamic facilities. Critical optical characteristics, relevant to the diagnostic, have also been investigated.

6. ACKNOWLEDGMENTS

The authors wish to acknowledge Profs. Daniel Nosenchuck and Paul Ronney for several stimulating discussions, and Thomas Frobose and Philip Howard for providing technical support. Preliminary electrohydrodynamic droplet studies were performed by Tania Cendejas and Juan Mier, as part of their Princeton University senior independent thesis. The work was sponsored by ARPA, G. Jones, technical monitor, the National Science Foundation, Robert Powell, technical monitor, and NASA Microgravity Science and Applications Program.

7. REFERENCES

Boedeker, L.R. (1989) Velocity measurement with enhanced OH flow tagging. Opt. Lett. 14, 473-475.

Chen, T.; Schommer, D.; and Goss, L. (1992) Laser diagnostics for velocity measurements in supersonic combusting environments. Paper #AIAA-92-0008, 30th Aerospace Sciences Meeting, Reno, NV.

Dahm, W.J.A.; and Dimotakis, P.E. (1990) Mixing at large Schmidt number in the self-similar far field of turbulent jets. J. Fluid Mech. 217, 299-300.

Falco, R.E. and Chu, C.C. (1987) Measurements of two-dimensional fluid dynamic quantities using a photochromic grid tracing technique. Proceedings of SPIE 814, 706-710.

Falco, R. and Nocera, D. (1993) Quantitative multi-point measurements and visualization of dense liquid-solid flows using laser-induced photochemical anemometry (LIPA). In Particulate Two-Phase Flow (ed. Roco, M.C.) pp. 59-126, Boston: Butterworth-Heinemann.

Lempert, W.R., Magee, K., Gee, K.R., and Haughland, R.P. (1993) Flow tagging velocimetry in incompressible flow using PHoto-Activated Nonintrusive Tracking Of Molecular Motion (PHANTOMM). Submitted to Exp. in Fluids.

McCray, J.A. and Trentham, D.R. (1989) Properties and uses of photoreactive caged compounds. Annu. Rev. Biophys. Chem. 18, 239-270.

Miles, R.B.; Connors, J.J.; Markovitz; E.C.; Howard, P.J.; and Roth, G.J. (1989) Instantaneous profiles and turbulence statistics of supersonic free shear layers by Raman excitation plus laser-induced electronic fluorescence (RELIEF) velocity tagging of oxygen. Exp. in Fluids 8, 17-24.

Miles, R.B.; Zhou, D.; Zhang, B.; Lempert, W.R.; and She, Z.-S. (1993) Fundamental turbulence measurements by RELIEF flow tagging. AIAA J. 31, 447-452.

Popovich, A.T. and Hummel, R.L. (1967) Light-induced disturbances in photochromic flow visualization. Chem. Engrg. Sci. 29, 308-312.

Stier, B. and Falco, R.E. (1994) New developments in laser-induced photochemical anemometry (LIPA). To be published in Proceedings of SPIE Symposium on Optics, Imaging and Instrumentation, San Diego, CA, July 1993.

Vizika, O. and Saville, D.A. (1992) The electrohydrodynamic deformation of drops suspended in liquids in steady and oscillatory electric fields. J. Fluid, Mech., 239, pp. 1-21.

Wilson, C.T.R. and G.I. Taylor (1924). The bursting of soap bubbles in a uniform electric fields. Proc. Camb. Phil. Soc., 22, p. 728.

Yurechko, V.N. and Ryazantsev, Yu.S. (1991) Fluid motion investigation by the photochromic flow visualization technique. Expt'l. Thermal and Fluid Sci. 273-288.

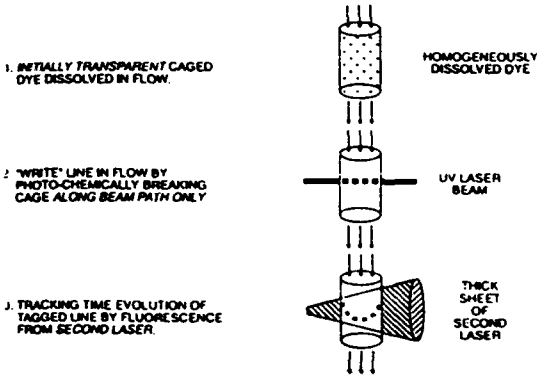

Figure 1. Illustration of PHANTOMM concept.

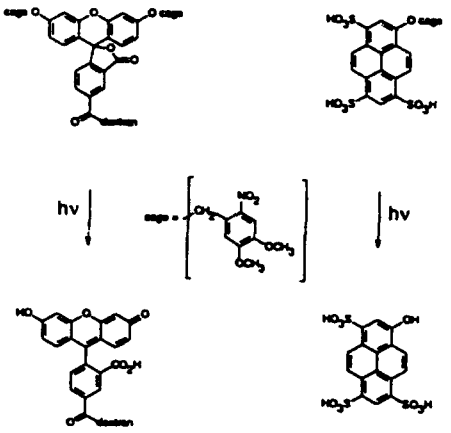

Figure 2. Caged and fluorescent forms of PAF's used in this work.

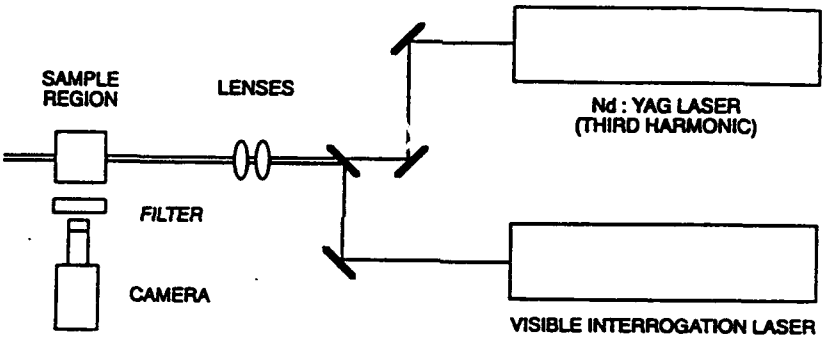

Figure 3. Basic Optical Configuration for PHANTOMM Measurements

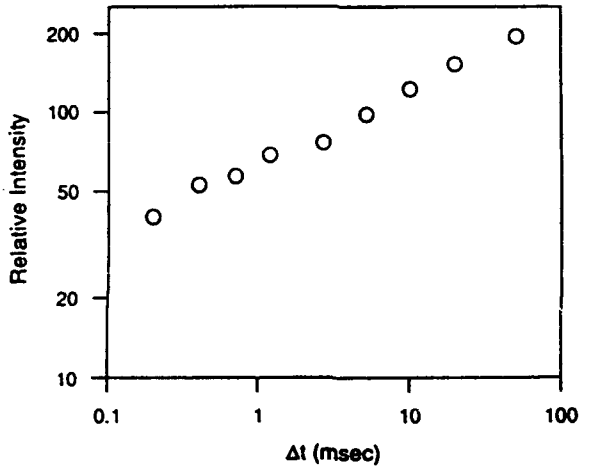

Figure 4. Ln-ln plot of fluorescence intensity as function of time delay between tag and interrogation.

Figure 5. Sample PHANTOMM images from pipe flow at R_e=315 (left) and R_e=840 (right). Flow is from top-to-bottom.

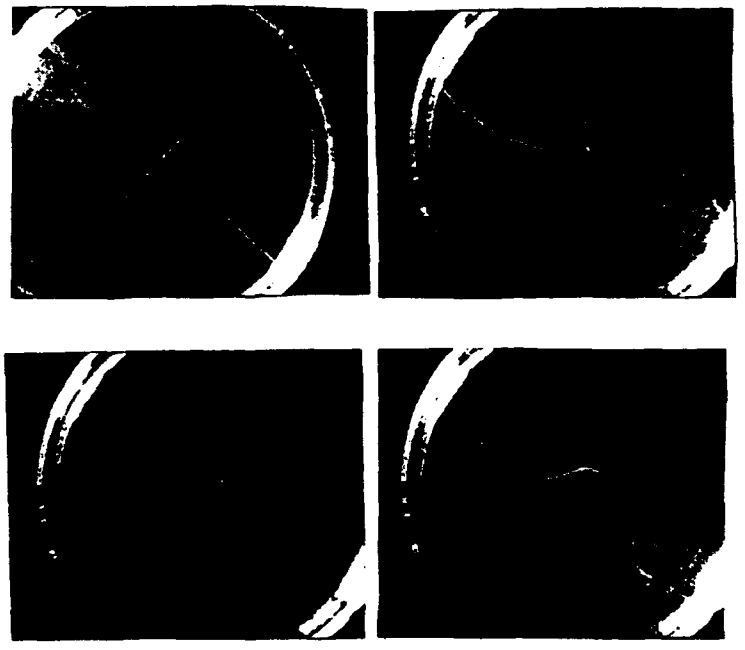

Figure 6. Representative images of rotating cross in water. Time delay between tag and interrogation is 12 msec, 1, 2, and 3 sec, respectively, top left to bottom right. Flow is counter-clockwise.

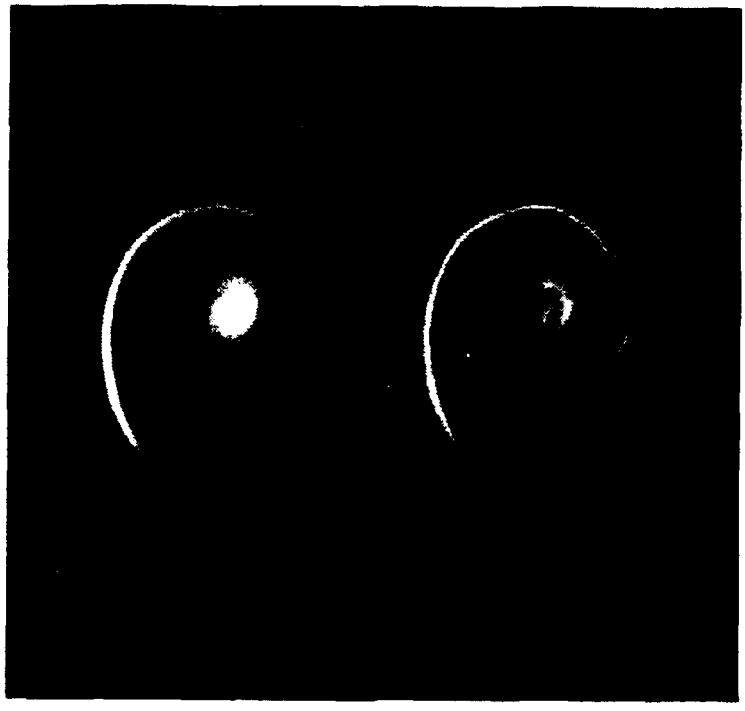

Figure 7. Fifty (50) laser shot average (left) and instantaneous (right) ordinary dye visualization planar image of tip vortex. Principal flow axis is out-of-plane of paper towards reader.

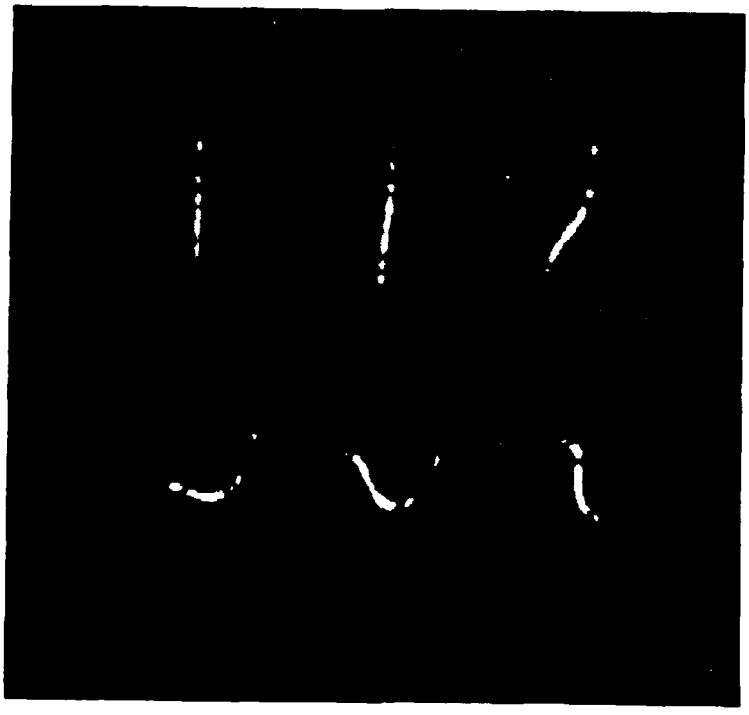

Figure 8 Collage of PHANTOMM images from tip vortex Time delays are 1, 10, 40, 100, 150, and 195 msec, respectively, from top left to bottom right.

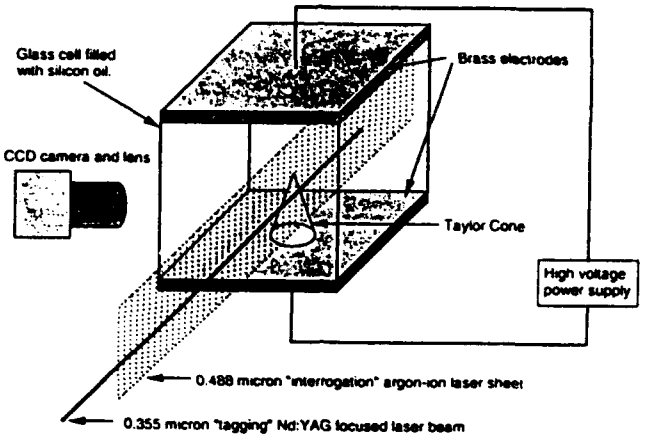

Figure 9. Schematic Diagram of electrohydrodynamic flow apparatus.

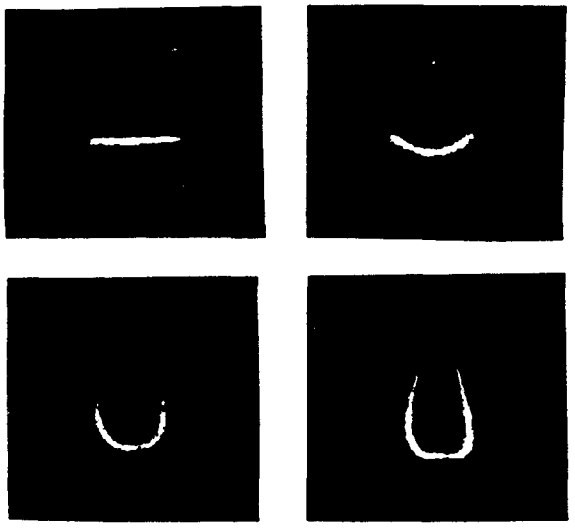

Figure 10. Collage of images from single tag Taylor cone. Time delays are < 1, 10, 30, and 50 secs, respectively, from top left to bottom right.

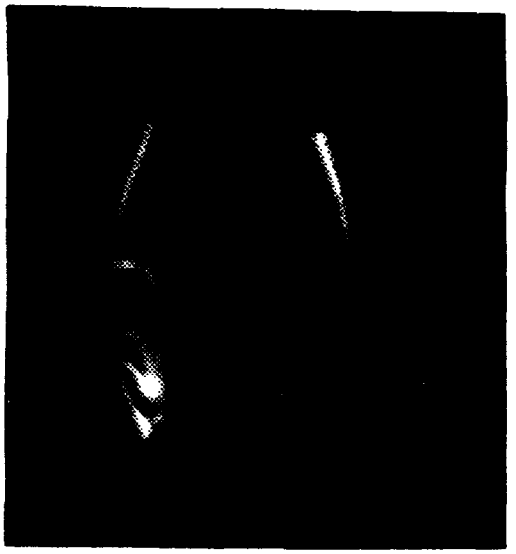

Figure 11. Image of doubly-tagged water droplet falling from pipette. Tagged line is initially horizontal.

Session 23.
Data Processing III

Application of Kalman Reconstruction to Laser-Doppler Anemometry data for estimation of turbulent velocity fluctuations

H.R.E. van Maanen and H.J.A.F Tulleken

Koninklijke/Shell-Laboratorium, Amsterdam (Shell Research B.V.)

Badhuisweg 3, 1031 CM Amsterdam, the Netherlands

1 Introduction

In turbulence studies, Laser-Doppler Anemometry (LDA) [1] has never reached the level of Hot-Wire Anemometry (HWA), which produces a continuous-time record of the turbulence with high Signal-to-Noise ratio (S/N). The inherent advantages of LDA are counteracted by discontinuous measurements being randomly distributed in time, by velocity bias due to increasing data-rate with increasing velocity and inhomogeneous distribution of tracer particles, and by noise which obscures individual velocity estimates. This is illustrated in Fig. 1. Continuous-time information can be obtained with a reconstruction scheme. A hardware solution has been applied in trackers (zero-order track-and-hold) which, however, leads to a significant noise contribution in the reconstructed signal. For the determination of the turbulence power spectrum, two independent measurement channels can be used and processed with a cross-correlation technique [2]. This does not yield direct information on actual velocity fluctuations for the investigation of turbulence and its mechanisms. To this end best estimate for the *actual velocity at any instant*, based on the *available individual measurements* must be determined.

2 Properties of LDA for velocity signal reconstruction

Measurement-time intervals are (approximately) exponentially distributed as can be demonstrated with LDA measurement data. Fig. 2 shows an excellent fit, except for intervals shorter than the dead-time of the processor. The noise contributions in individual measurements are assumed to be identically, independently Gaussian distributed, with zero mean and deviation σ, independent of the velocity. The causes of noise will be discussed in Appendix A; in our discussion any deviation of the estimation from the actual velocity is regarded as noise. Bias has been the subject of numerous publications and there is little agreement on the amount [3]. Here the bias is assumed not to influence the time interval distribution.

3 Simulation of turbulence signals

The influence of the steps in the measurement process and dataprocessing on reconstruction results can be analyzed with simulation. We created 13 "turbulence" signals of 20 seconds at a sampling frequency of 1000 Hz and spectral properties of the Bessem power spectrum [4]:

$$S(f) = \frac{S(0)}{1 + (f/f_1)^{5/3} \cdot [1 + (f/f_2)^4]^{4/3}}$$

with simulation values $S(0) = 1$, $f_1 = 1$ Hz and $f_2 = 50$ Hz. The "experimental" power spectrum, retrieved from these simulated signals is shown in Fig. 3.

4 Slotting technique

The slotting technique is often used for the estimation of the auto-correlation function (ACF) of the turbulence with random sampled data [5, 6]. Its disadvantages are that the estimate variance is higher than with sample/hold techniques [3, 7], and velocity bias leads to systematically incorrect estimates [6]. Fig. 4 shows the ACF's of the simulated turbulence with and without bias. The rise above 1 in the biased case is conflicting with the theory of signal processing [8] - [11]. The simulation correctly predicts this error. Fourier Transformation (FT) of the ACF of Fig. 4 yields the power spectral density in Fig. 5. With bias the low-frequency level, corresponding to the large eddies, is increased. In both cases the small eddies (related to high frequencies) are obscured by noise. Note that this noise is solely caused by the data-processing, the individual velocity estimates are exact in this simulation!

5 Signal reconstruction

The required data-rate for reconstruction should at least be 2π times the highest frequency present in the turbulence, see Appendix B. A technique which assumes that the velocity estimates are exact is unsuitable in the presence of noise, because it obscures the small eddies. Simple reconstruction techniques can be used for the elimination of bias and for periodic re-sampling of the signal, so common signal processing can be applied, including cross-correlation techniques [2]. The high data-rate means that many independent velocity estimates are available. This creates the possibility to use a statistical algorithm, such as Kalman filtering, which takes into account that the velocity estimates are noisy.

6 Kalman-filtered reconstruction

Kalman filtering was originally developed for dynamic system estimation and control purposes. Based on the current information, it constructs optimal estimates of internal ("state") variables, taken into account that the information is accompanied by noise. The noise level(s) need to be known and a dynamic model is required to describe the behaviour of the system under study. In this paper, turbulence is the system of investigation.

6.1 Assumptions

Signal reconstruction can easily become a "self fulfilling prophecy". Unavoidable assumptions should be checked against experimental evidence and/or knowledge of turbulence. For the Kalman reconstruction scheme, three assumptions are made:

1. The power spectrum can be approximated by that of first-order (low-pass) filtered noise (Fig. 11). This assumption means that the turbulence power has a "constant" level below and is proportional to ω^{-2} above a cut-off frequency. It comes close to a slope of -1.67 (on a log/log plot) which is often reported in literature for the inertial subrange [16] and the slope of -2.5 for developing flows [17]. This is related to the situations were the accelerations of the fluid are limited by inertial and frictional forces. The turbulence cut-off frequency can be estimated from the power spectrum (e.g. from a FT of the slotted ACF). In case of bias, the ACF could be obtained from a first-order signal reconstruction scheme.

2. The turbulence generating accelerations and the (measurement) noise contributions in the velocity estimates are neither correlated with each other nor with the velocity. Fig. 9 shows an ACF using the slotting technique with a clear δ-peak at $\tau = 0$. The correlation of the noise contribution is thus only one slot wide. The clear distinction between noise and turbulence in this ACF allows to determine S/N, which is an input parameter of the Kalman reconstruction scheme. The absence of correlation between noise and velocity is valid for several, but not all processors.

6.2 Turbulence Model

The following simple dynamic model for the evolution of the velocity $v(t)$ over time $t \geq t_0$, of a particle with mass m in turbulent flow is being used (Newton's law):

$$\frac{\mathrm{d}}{\mathrm{d}t}v(t) = -\bar{\lambda}/m\ v(t) + \zeta(t)/m = -\lambda v(t) + \xi(t) \qquad (1)$$

where the driving acceleration term $\xi(t)$ is assumed to be equivalent to a Gaussian distributed *continuous-time white* noise signal with intensity σ^2. The term $-\lambda v(t)$ models the frictional de-acceleration, with parameter $\lambda \geq 0$. The velocity $v(t)$ can be measured at stochastic, Poisson distributed times t_k (the innovations $t_k - t_{k-1}$ being identically, independently exponentially distributed), yielding

$$v_k^{\mathrm{obs}} = v(t_k) + \eta_k \quad ; \quad k = 0, 1, 2, \ldots \qquad (2)$$

where η_k is assumed to be a Gaussian distributed *white* noise sequence with variance ρ^2, i.e. $\eta_k \sim \mathcal{N}(0, \rho^2)$ and $\mathbb{E}[\eta_k \eta_\ell] = 0$ for all $k \neq \ell$.

6.3 Design of the Kalman Filter

It is wellknown (see [18] for the system-theoretic setting, or [19] for a concise statistical treatment in discrete time) that the optimal state-estimation problem leads to a Kalman filter design. Let x be the dynamic state (vector) of the system $\dot{x} = Ax + \xi$ with observation equation $y = Cx + \eta$ over time t. Then the optimal prediction $\hat{x}(t)$ of x is a (deterministic) vector which equals the conditional expectation $\mathbb{E}[x(t)|y(s); s \leq t]$. This prediction can be shown to minimize the squared prediction error $\int_0^t \mathbb{E}\|\hat{x}(\tau) - x(\tau)\|^2 \mathrm{d}\tau$ in the class of all linear filters. It can be calculated from

$$\frac{\mathrm{d}}{\mathrm{d}t}\hat{x}(t) = A\hat{x}(t) + L(y(t) - C\hat{x}(t)) \qquad (3)$$

Here the Kalman *filter gain (matrix)* equals

$$L = \Lambda C' \Pi^{-1} \qquad (4)$$

where the (positive definite) matrix Λ is the solution to a Riccati equation:

$$\Lambda A + A'\Lambda - \Lambda C' \Pi^{-1} C \Lambda + \Sigma = 0 \qquad (5)$$

and Σ and Π are the covariance matrices of ξ and η respectively. If one applies the results (3) through (5) to (1) and (2) (with $A = -\lambda$, $C = 1$, $\Pi = \rho^2$ and $\Sigma = \sigma^2$), the optimal filter gain is seen to be

$$L = \lambda + \sqrt{\lambda^2 + \sigma^2/\rho^2} \qquad (6)$$

Note that in this application L is scalar. If $\lambda = 0$ then

$$L = \sigma/\rho$$

depending only upon the ratio of the deviations of the turbulence generating accelaration η and the measurement noise ξ. In the sequel this ratio will be used instead of the more general value (6) although it can be replaced without complication if λ should be non-zero. Furthermore, using (3) it follows that the filter dynamics behave according to

$$\frac{\mathrm{d}}{\mathrm{d}t}\hat{v}(t) = \frac{\sigma}{\rho}(v^{\mathrm{obs}}(t) - \hat{v}(t)) \quad ; \quad \hat{v}(t_0) = v_0^{\mathrm{obs}} \qquad (7)$$

Since $\sigma/\rho \geq 0$, the filter is stable in the bounded input, bounded output sense. There is one structural difficulty, namely that the specific continuous-time Kalman filter (7) requires continuous measurements of the velocities $v^{\mathrm{obs}}(t)$, $t \geq t_0$. As only discrete-time measurements (2) are available, some assumption on the intermediate behaviour has to be formulated. We will use *first-order* interpolation, i.e. for $k = 0, 1, 2, 3, \ldots$ and $t_k \leq t \leq t_{k+1}$:

$$\begin{aligned} v^{\mathrm{obs}}(t) &= \alpha_k t + \beta_k \\ \alpha_k = \frac{v_{k+1}^{\mathrm{obs}} - v_k^{\mathrm{obs}}}{t_{k+1} - t_k} \quad ; \quad \beta_k &= \frac{t_k v_{k+1}^{\mathrm{obs}} - t_{k+1} v_k^{\mathrm{obs}}}{t_k - t_{k+1}} \end{aligned} \qquad (8)$$

With this "measurement" signal, the differential equation (7) can be analytically solved. For $t_k \le t \le t_{k+1}$ with $k = 0, 1, 2, 3, \ldots$, its solution can be recursively calculated:

$$\hat{v}(t) = (\hat{v}_k - \alpha_k(t_k - \frac{\rho}{\sigma}) - \beta_k)\exp\left(-\frac{\sigma(t-t_k)}{\rho}\right) + \alpha_k(t - \frac{\rho}{\sigma}) + \beta_k \quad (9)$$

with α_k and β_k as in (8). This shows that the filter update terms are subject to an (unavoidable) time delay ρ/σ. In order to correct for the effects of this "phase shift", one can apply bidirectional Kalman filtering if the measured data are limited in size with final measurement time t_N and corresponding velocity measurement v_N^{obs}. In other words, one additionally constructs the *backwards* filtered prediction $\bar{v}(t)$, by processing the data in reverse order using the "initial" velocity $\bar{v}(t_N) = v_N^{obs}$. This gives for $k = N-1, N-2, \ldots, 1, 0$:

$$\bar{v}(t) = (\bar{v}_{k+1} - \alpha_k(t_{k+1} + \frac{\rho}{\sigma}) - \beta_k)\exp\left(-\frac{\sigma(t_{k+1}-t)}{\rho}\right) + \alpha_k(t + \frac{\rho}{\sigma}) + \beta_k \quad (10)$$

The "overall" *bidirectional* prediction can be taken as the average of forward and backward predictions. Consequently it is phaselag-free as can be seen from

$$v^{pr}(t) = \frac{\hat{v}(t) + \bar{v}(t)}{2} = \underbrace{\alpha_k t + \beta_k}_{\text{interpolation data } v^{obs}(t)} + \underbrace{\frac{1}{2}(\hat{v}_k - \alpha_k(t_k - \frac{\rho}{\sigma}) - \beta_k)\exp(-\frac{\sigma(t-t_k)}{\rho})}_{\text{forward estimation term}} + \underbrace{\frac{1}{2}(\bar{v}_{k+1} - \alpha_k(t_{k+1} + \frac{\rho}{\sigma}) - \beta_k)\exp(-\frac{\sigma(t_{k+1}-t)}{\rho})}_{\text{backward estimation term}}$$

using (9) and (10). The Kalman scheme performance depends on the quality of the estimated ratio σ/ρ, where σ^2 is the intensity of the continuous-time white noise that models the turbulence generating accelarations, whereas ρ^2 is the variance of the measurement noise at the discrte points in time. An example of behaviour of one quality measure, i.e. the average prediction error $\sqrt{\frac{1}{N+1}\sum_{k=0}^{N}(v_k^{obs} - v_k^{pr})^2}$ over discrete-time simulation data, is given in Fig. 10 as a function of filter gain. It clearly shows that a significant improvement of the quality of the data can be realized. In this example a reduction of about 50 % of the total error is recorded. Of course, this percentage varies from one specific data set to another.

7 Applications

7.1 Simulation Results

Fig. 12 shows the result of the Kalman reconstruction on the simulated signal itself whereas Fig. 13 shows the power spectra of the simulated turbulence after random sampling and with 20 % noise added (S/N = 5) for three different reconstruction schemes: zero-order, first-order and the Kalman reconstruction scheme. The latter produces superior estimates. Note that the change in the slope of the power spectrum above 50 Hz is only shown by the Kalman reconstruction scheme, although this has not been introduced in the assumptions. This illustrates that the Kalman reconstruction scheme is reproducing more than the original assumptions and that good estimation of the velocity fluctuations is obtained with this approach.

7.2 Experimental data

Fig. 14 shows the result of Kalman reconstruction on turbulence signals, obtained in the jet of a stirred vessel. The improvement is also illustrated by the distribution of accelerations before (Fig. 15) and after Kalman velocity signal reconstruction (Fig. 16). The extreme values (above 2 km/s^2) have disappeared and the distribution shows a normal behaviour with more realistic values.

Fig. 17 shows the velocity distributions before and after the application of the Kalman reconstruction algorithm. Due to bias, the distribution before application shows an increase for higher velocities, which is removed after application. This elimination of bias is an additional important advantage of signal reconstruction. Fig. 18 shows the turbulence power spectrum measured in the jet of a stirred vessel. Curve *a* results from the slotting technique, curve *b* using the Kalman reconstruction scheme, cf. Fig. 11.

8 Discussion

The Kalman reconstruction scheme is no "miracle cure". The best results are obtained if the input data are as accurate as possible (high S/N of the Doppler signals) and have a high data rate [13]. This has consequences for the different components of an LDA system.

Consequences for optical systems. In most cases, the requirements can only be fulfilled in forward scatter LDA systems. The use of a small measurement volume results in a high local light intensity, which allows smaller tracer particles -reducing the noise due to beam distortion [12]- and allows higher seeding concentrations, leading to an increase of the data-rate.

Consequences for Doppler-signal processors. Some processors use only a fraction of the Doppler signal, arguing that its S/N is not constant due to its amplitude modulation. Using only the central part seems reasonable, but the other parts still contain information. The best estimate is obtained when all the information in the Doppler signal is used [13] and weighed according to its S/N. This might be achieved by a wavelet transform based processor.

Consequences for data-processing. The current approach is to regard all velocity estimates as equivalent, although some are more accurate than others. It would be better to store the S/N of each estimate and to use it as a weighting factor in the Kalman reconstruction.

9 Future developments

The required parameters for the Kalman reconstruction scheme can be retrieved from the raw velocity data. As a next step, the results of the Kalman reconstruction scheme can be used for more accurate estimation of the required parameters, even repeatedly. With a two-channel approach the remaining noise in the reconstructed signals can be reduced further using the cross correlation technique [2].

A further extension is to introduce a more sophisticated power spectrum in the reconstruction algorithm. This can e.g. be the Bessem spectrum, which is determined by three parameters (Fig. 4), to be determined from the cross-power spectrum. It is then important to reduce the correlated noise contributions (which show up in both channels identically, like due to fringe gradients) as much as possible. This power spectrum can then be used in an extended Kalman reconstruction scheme to retrieve the best estimate for the velocity fluctuations. In this way the need for assumptions about the turbulence is circumvented as much as possible.

10 Conclusions

The Kalman reconstruction scheme is an extension to the data-processing of Laser-Doppler Anemometry which increases its level to that of hot-wire anemometry. It uses very little assumptions and those which are used have a solid foundation on experimental and theoretical grounds. Further extension and improvement is possible by the use of iteration and crosscorrelation techniques, which require no additional assumptions. The reconstruction of the velocity fluctuations requires sufficient individual velocity estimates per unit time, Doppler signals with a high signal-to-noise ratio, an optimised seeding, a high spatial resolution and a proper alignment to reduce fringe gradients as much as possible. These requirements can in practice only be fulfilled by forward scattering systems. The requirements for the Kalman reconstruction scheme point the way for future developments of optical systems, processors and data-processing algorithms for the study of turbulence.

References

[1] F. Durst, A. Melling and J.H. Whitelaw, "Principles and Practice of Laser-Doppler Anemometry", Academic Press 1976.

[2] H.R.E. van Maanen, K. van der Molen and J. Blom, "Reduction of Ambiguity Noise in Laser-Doppler Velocimetry by a Crosscorrelation Technique", Proc. of LDA-Symposium Copenhagen 1975, pp. 81-89.

[3] L.H.J. Absil, W. Steenbergen and D.M. Passchier, "Time and spatial correlation measurements in the turbulent wake of a circular cylinder using laser Doppler anemometry", Applied Scientific Research (July 1990), vol. 47, no. 3, pp. 247-271.

[4] J.M. Bessem and H.R.E. van Maanen, "Procedure for minimum distortion and minimum storage needs for digitized random analog data", Proc. of the Fifth Intern. Conf. on Laser Anemometry, Advances and Applications, Veldhoven, 23rd-27th August 1993, pp. 43 -51.

[5] W. Mayo, M. Shay and S. Riter, "Digital estimation of turbulence power spectra from burst counter LDV data", Proceedings of the second intern. workshop on laser velocimetry, Purdue University, March 1974, pp. 16-26.

[6] J.B. Roberts and D.B.S. Ajmani, "Spectral analysis of randomly sampled signals using a correlation based slotting technique", IEE Proc. F (Comm. Radar and Signal Proc.), April 1986, vol. 133, no. 2, pp. 153-162.

[7] W. Mayo, "A discussion of limitations and extensions of power spectrum estimation with burst-counter LDV systems", Proc. of the second intern. workshop on laser velocimetry, Purdue Univ., March 1974, pp. 90-104.

[8] V. Čižek, "Discrete Fourier Transforms and their Application", Adam Hilger Ltd., Bristol (1986)

[9] A. Papoulis, "The Fourier Integral and its Applications", McGraw-Hill, New York (1962)

[10] A. Papoulis, "Signal Analysis", McGraw-Hill, New York (1984)

[11] J.S. Bendat and A.G. Piersol, "Random Data, Analysis and Measurement Procedures", John Wiley, New York (1986)

[12] B. Ruck and B. Pavlovski, "Limited accuracy of turbulence measurement in laser Doppler anemometry", Proc. of the Fifth Intern. Conf. on Laser Anemometry: Advances and Applications, Veldhoven, 23rd-27th August 1993, pp. 25-35.

[13] R. Booij and J.M. Bessem, Report on Workshop "User's Needs for Laser Doppler Anemometry", Supplement to the Proceedings of the Fifth Intern. Conf. on Laser Anemometry, Veldhoven, 23rd-27th August 1993, pp. 13-50.

[14] R. Adrian and C. Yao, "Power spectra of fluid velocities measured by LDV", Experiments fluids, Vol. 5 (1987), pp. 17-28.

[15] W.K. George and J.L. Lumley, "The laser velocimeter and its applications to the measurement of turbulence", Journal of Fluid Mechanics, Vol. 60 (1973), pt. 2, pp 321-362

[16] H. Tennekens and J.L. Lumley, "A First Course in Turbulence", MIT Press, Cambridge, 1972.

[17] K. van der Molen and H.R.E. van Maanen, "Laser-Doppler Measurements of the Turbulent Flow in Stirred Vessels to Establish Scaling Rules", Chemical Engineering Science, Vol. 33 (1978), pp. 1161-1168

[18] Kwakernaak H. and R. Sivan, "Linear Optimal Control Systems", Wiley Interscience, New York, 1972.

[19] Singpurwalla, N.D. and R.J. Meinhold, "Understanding the Kalman Filter", the American Statistician, Vol. 37, 1985, pp. 123-127.

Appendix A: Noise in Laser-Doppler Anemometry

Noise in the individual velocity estimates of an LDA data can be divided into several groups:

1. Transmission optics (including light source).

   The light intensity variations of the laser also influence the intensity of the scattered light. If these fluctuations contain frequencies in the range of the frequencies of the Doppler signals, these show up as a noise contribution. Transportation of the laser light through optical fibers reduces the coherence and polarisation of the laser light, leading to a lower "fringe visibility", reducing the S/N of the Doppler signal. If the transmission optics are not perfectly aligned or the beams influenced by e.g. curved walls, so-called "fringe gradients" exist in the measurement volume [1]. The conversion factor from velocity to frequency then becomes dependent on the actual position where the tracer particle traverses the measurement volume. This gives rise to an additional uncertainty in the estimation -and thus noise- of the velocity.

2. Receiving optics.

   The scattered light is quantized, leading to quantisation noise in the photodetector signal. The lower the light intensity is, the lower the S/N of the Doppler signal is. The forward scattering mode is therefore to be preferred.

3. Doppler signal processing (amplification, filtering).

   The photodetector adds noise by itself, e.g. due to dark current and internal amplification. The Doppler signal processing, like amplification and filtering, also generates noise.

4. Frequency (and thus velocity estimation) of the Doppler signal.

   The estimation of the frequency of the Doppler signal and thus the velocity of the tracer particle, is done by a processor, which has a limited accuracy. The inaccuracies of the frequency estimation are reflected in the velocity and are noise.

5. Errors and inaccuracies in the arrival time of the Doppler signal.

   An incorrect placement in time of the velocity estimate causes an additional error due to the changes of the velocity due to turbulence. This can happen as is shown in Fig. 6 which shows the time interval distribution with an arrival time resolution of 100 μs and a t_0 of 600 μs. This is undesirable and the resolution should be improved. We expect that the resolution should be less that 5 % of the t0 to be on the safe side.

6. Velocity data-processing (including algorithms to cope with the bias and random sampling contributions).

   The random sampling creates discontinuities in the velocity trace with unknown values in between. This hampers the estimation of the flow parameters and can thus be regarded as a noise source. Noise thus occurs in the Doppler signal and this causes an uncertainty in the estimation of the frequency no matter how accurate the processor is [12, 13]. Therefore a noise contribution to the individual velocity estimates is an unavoidable fact of life. By optimisation of the design of the LDA system this can be reduced as much as possible, yet the dynamic range of a turbulence power spectrum is usually limited to 3 decades or less, except when a cross correlation technique [2] is applied. However, this technique does not reduce the noise at the instantaneous velocity estimates and is therefore only useful for the estimation of statistical properties. To upgrade an LDA to the level of HWA a reconstruction approach is required.

Appendix B: Minimal required data-rate

A minimal data-rate, related to the frequencies, present in the turbulence signal will be required for reconstruction. In literature only heuristic ratio's for data-rate over highest frequency were used [14], ratio ≈ 5. A better estimate can be found from signal reconstruction: Imagine a laminar flow which is sampled randomly (see Fig. 2) with a time constant t_0 and a Gaussian distributed, uncorrelated noise in the velocity estimates. This could be regarded as a "turbulent" flow. The spectrum of the fluctuating components can be found by calculation of the ACF after zero-order reconstruction. This reconstruction introduces correlation in the fluctuations over a period, which is equal to the time between two successive samples. After this time no correlation exists because the noise contributions are uncorrelated. The ACF is therefore equal to an exponential decaying function with the same t_0 as the time interval distribution. This is illustrated in Fig. 7, which shows the results of a simulation and an analytical curve. The ACF of first order (RC) low-pass filtered white noise has the same shape [9, 10, 11] and the random sampling can thus be described as a first order low-pass filter with a cut-off frequency of $1/(2\pi t_0)$. This is confirmed by the FT of the ACF of Fig. 7, which is shown in Fig. 8. Therefore it can be stated that the data-rate needs to be at least 2π time the highest frequency, present in the turbulent fluctuations. Identical results have been obtained with first order reconstruction and the application to the simulated turbulence.

Figure 1: The velocity estimates of the LDA system, indicated by +, are Poisson distributed in time and are accompanied by noise.

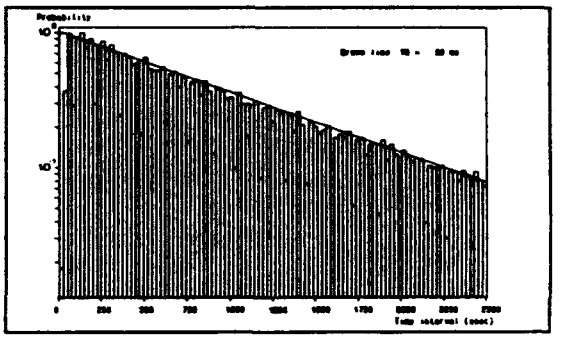

Figure 2: Histogram of interarrival time distribution. Average data-rate was approximately 1 kHz.

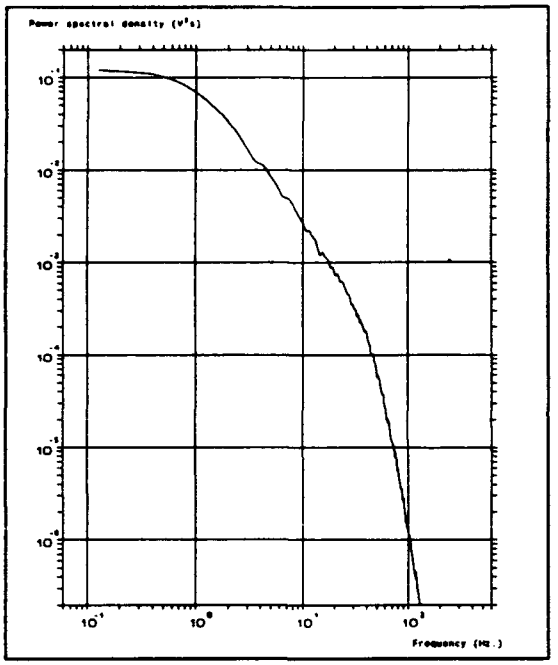

Figure 3: The Bessem turbulence power spectrum after 260 sec. averaging.

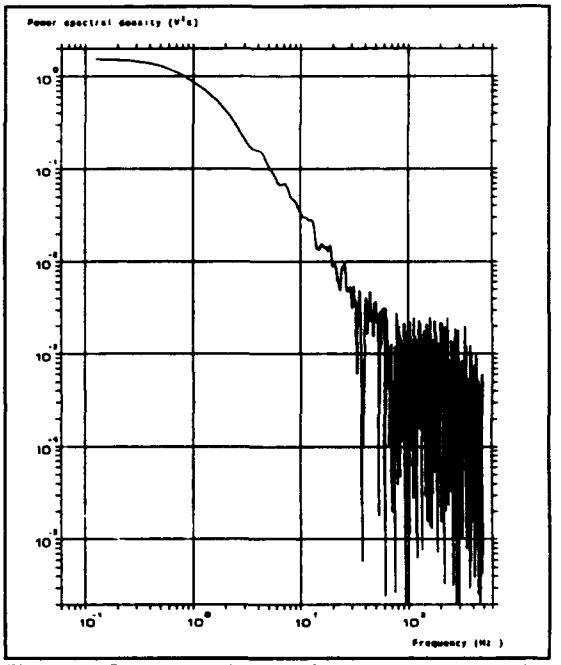

Figure 5: Spectrum calculated from the auto correlation function, determined using the slotting technique, without bias.

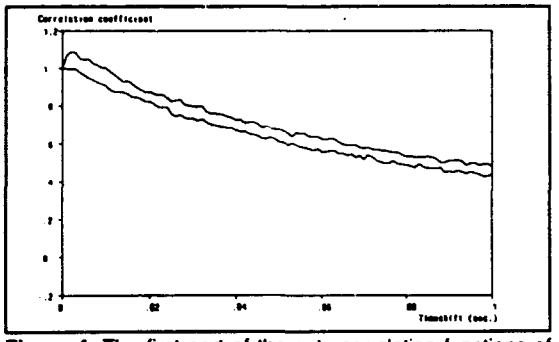

Figure 4: The first part of the auto correlation functions of simulated turbulence with and without bias.

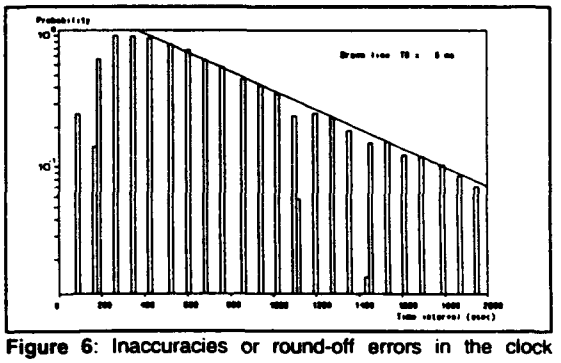

Figure 6: Inaccuracies or round-off errors in the clock introduce another source of noise.

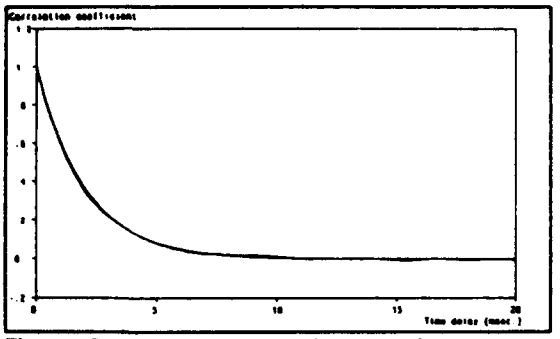

Figure 7: Auto correlation function of zero order reconstructed noise signal. Poisson distributed sampling of 500 Hz. average data-rate.

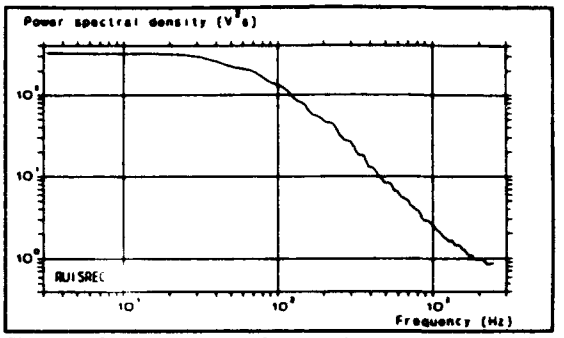

Figure 8: Power spectrum of zero order reconstructed noise signal. Note the decay of the spectrum from 500/2π Hz.

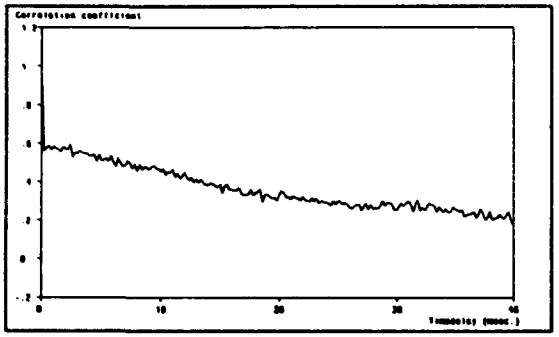

Figure 9: The part close to $\tau = 0$ of a slotted auto correlation function, which clearly shows that the noise contribution to the auto correlation function is limited to the first slot.

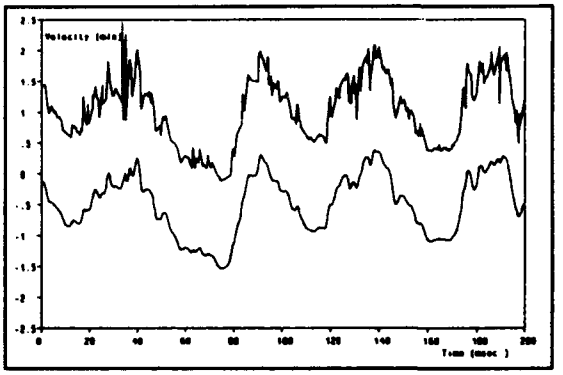

Figure 14: Raw and Kalman reconstructed velocities.

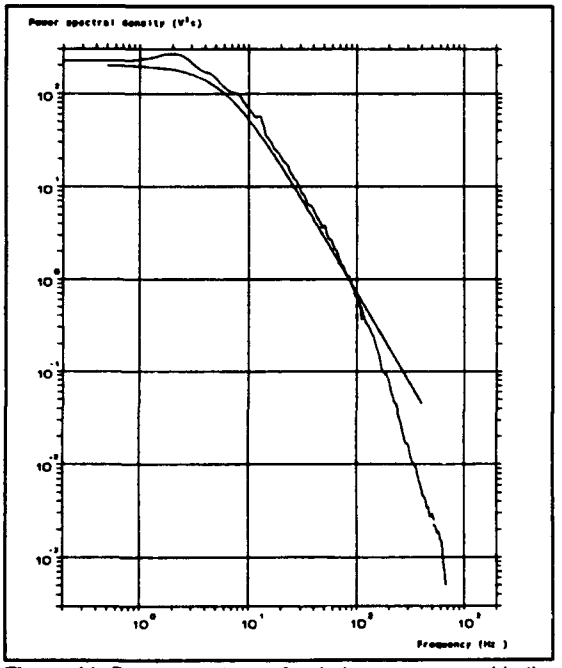

Figure 11: Power spectrum of turbulence, measured in the jet of a stirred vessel using trackers and the cross correlation technique. Also shown first order low-pass filter.

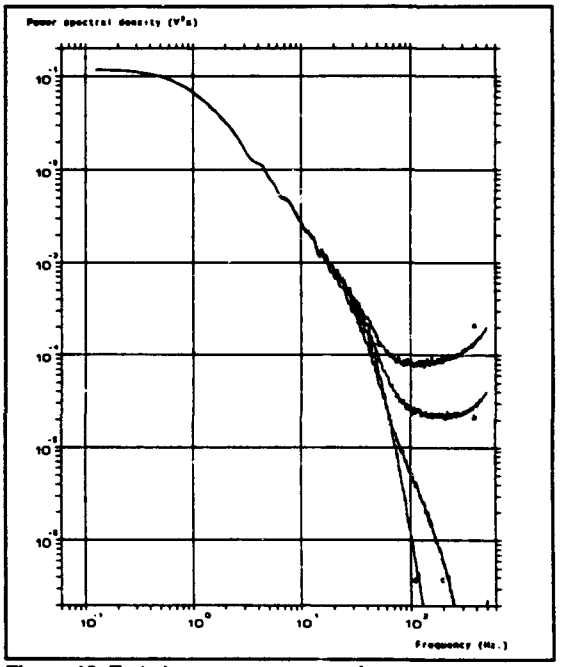

Figure 13: Turbulence power spectra from simulation using different reconstructions. a = zero order, b = first order, c = Kalman scheme, d = original spectrum. 20 % noise.

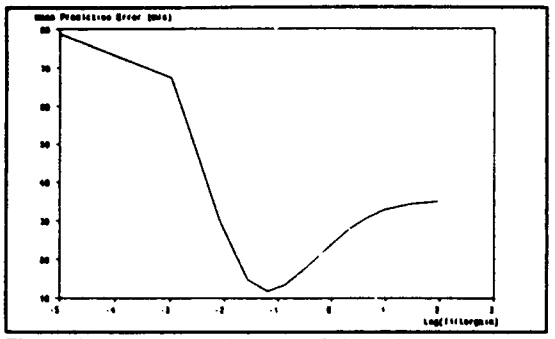

Figure 10: Mean prediction error of bidirectional reconstruction scheme as function of filtergain.

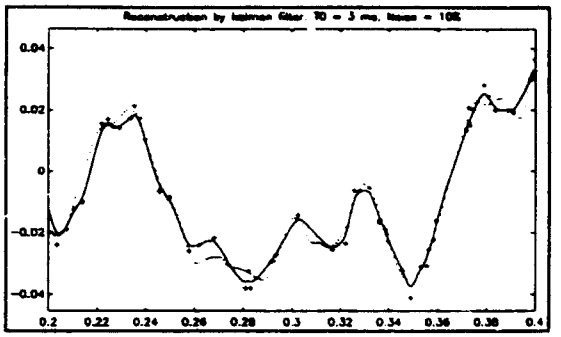

Figure 12: Kalman reconstruction of simulated turbulence. Dotted line input signal, drawn line reconstructed signal. + indicates measurement.

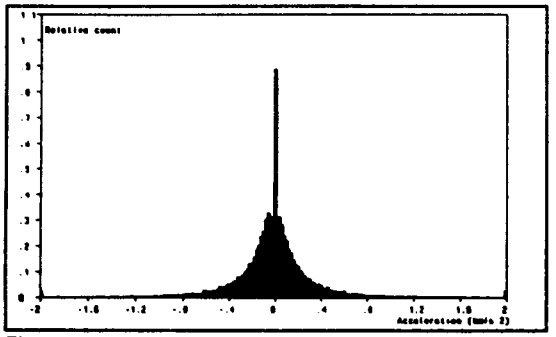

Figure 15: Histogram of the accelerations derived from the raw data. Note the occurrence of accelerations above ± 2 km/s^2.

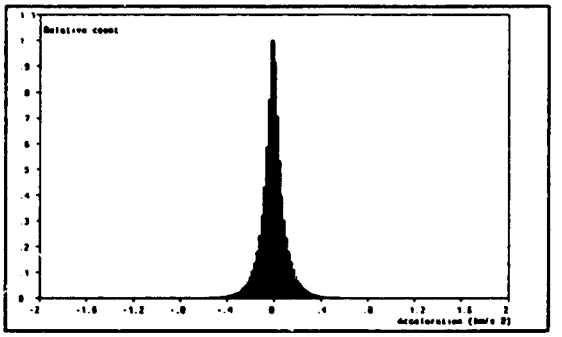

Figure 16: Histogram of accelerations derived from the Kalman reconstructed data.

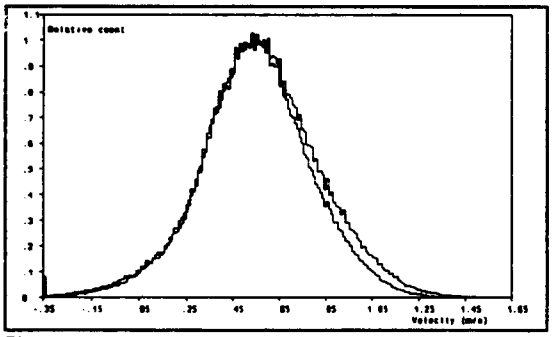

Figure 17: Histograms of the raw data (upper trace) and the Kalman reconstructed velocity signal.

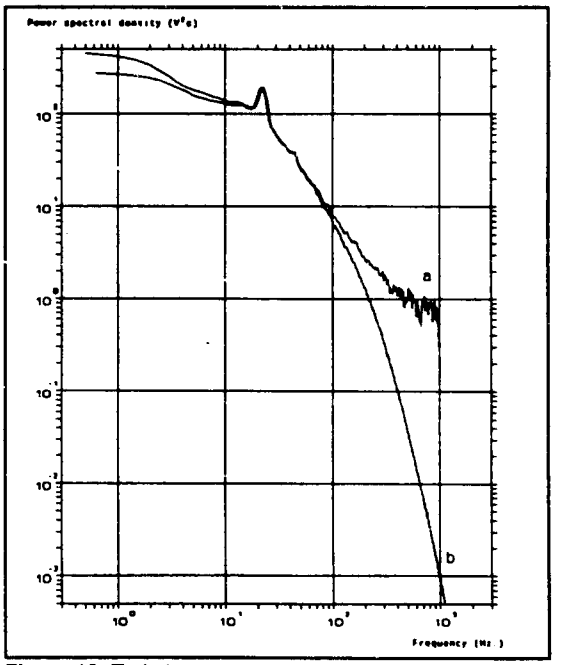

Figure 18: Turbulence power spectrum obtained using the slotting technique (curve a) and using the Kalman reconstruction scheme (curve b). Compare with figure 10.

LDA Signal Reconstruction: Application to Moment and Spectral Estimation

E. Müller, H. Nobach, C. Tropea*

FB Elektrotechnik, University of Rostock

* Lehrstuhl für Strömungsmechnik, University of Erlangen

Abstract

The reconstruction of an LDA signal refers to the interpolation of the measured velocity values obtained at random times, resulting in a velocity signal continuous in time. In particular, this paper deals with the bias and variance of several moment and spectral estimators based on reconstructed LDA signals. In addition to conventional reconstruction techniques, two more recent methods are investigated, including *projection onto convex sets* and *fractal reconstruction*. Both simulations and experiments have been used to evaluate the suitability of the various reconstruction techniques as a function of the flow and seeding parameters.

1 Introduction

Flow velocity information is obtained with an LDA at irregular time intervals, corresponding to random particle arrivals in the control volume. Whereas the information content of data obtained by equidistant sampling of a continuous process is well defined by Shannon theorem [16], there currently exists no equivalent statement for randomly sampled signals. Furthermore, the probability density function of the sample intervals is dependent on the instantaneous velocity magnitude. These properties of LDA signals must be considered in formulating moment and spectral estimators to avoid bias errors [2, 5, 7].

Considerable attention has been directed to extracting moment and spectral information from LDA signals, usually with the intuitively acceptable conclusion that a higher mean particle rate will lead to better estimates. Parameter estimation customarily takes one of two approaches. Either estimates are based directly on the available velocity samples, their arrival times and possibly further information such as residence time; or an interpolation of the velocity signal between the measured values is performed, followed by an estimation based on the reconstructed signal, often using an equidistant sampling of the reconstructed signal.

One may ask why such a myriad of data processing approaches exist and what the motivation for pursuing novel approaches can be. Three interesting situations can be cited for which improvements can be envisioned.

1. At present, direct spectral estimation of LDA signals is basically a trade-off between bandwidth and variability[10]. At higher frequencies, spectral estimates become less certain. This behaviour is well documented and is not likely to change in principle even with improved estimators [15, 17, 20]. However, the estimator variability may decrease for some estimators, especially if physically plausible information regarding the spectrum of turbulent fluctuations can be entered into the estimation *a priori*. A reconstruction model may be capable of achieving this and thus extend the bandwidth or improve the variability of the estimate.

2. There exist several frequently encountered measurement situations in which the seeding density is not homogeneous and may be correlated with the measured velocity. Mixing layers originating from two different flow sources, or combustion systems in which the detection of the seeding particles is influenced by the combustion are examples. In such situations unbiased moment or spectral estimators are difficult to formulate and here again, a reconstruction of the signal may offer an acceptable alternative [21].

3. The third situation concerns spectral estimation of short time records, necessary when analysing transient flows. One such example is length scale estimation in an internal combustion engine. The validity of Taylor's hypothesis put aside, rough length scale estimates are often only available through a spectral analysis of single point velocity measurements in an engine. Clearly, length scales vary dramatically throughout the cycle so that an estimation must be made on relatively short time records. Conventional spectral methods are unsuited to this task, as is well documented by the increasing number of methods developed for speech processing [11].

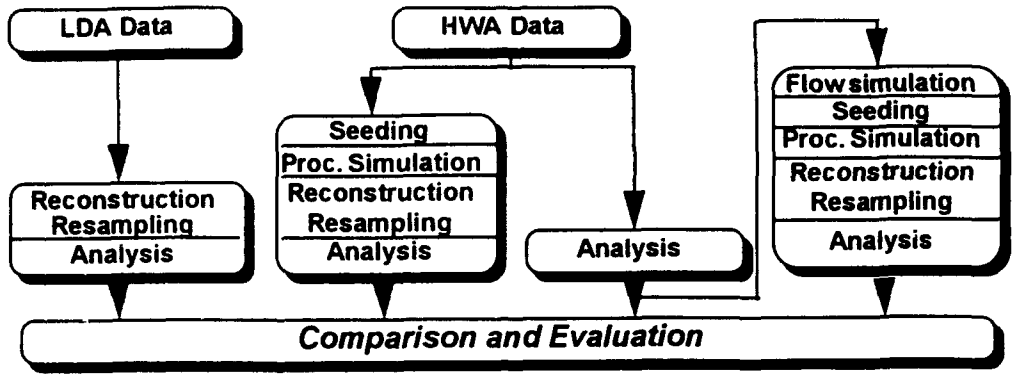

Figure 1: Schematic representation of how experimental data was used to verify results of the simulation program.

The present paper does not attempt to derive a theoretical statement about what information is actually contained in LDA data. Rather it uses an empirical approach to compare various suggestions which have been put forward in the literature, and to investigate under what conditions these estimation schemes perform well. But even with this more modest approach, it is essential that the evaluation of the result is accurate enough to recognize possible differences or improvements between estimators. This has been achieved by a combination of simulation and experiment as summarized in Fig. 1 and described briefly below.

The study of reconstructed LDA signals builds on previous work involving the simulation of LDA data of given statistical properties using a trivariant autoregressive process [8, 9]. The simulated LDA data can then be processed and compared with the known signal properties. In the present study this approach has been refined by also obtaining data from a flowfield. Both LDA and hot-wire data (HWA) were taken from various positions in a flow. Direct comparisons could be obtained between an analysis of the LDA data and the continuous HWA data. Furthermore, the HWA data could be used both directly and indirectly to simulated the LDA data and to obtain a further reasssurance that the simulation results were realistic. Finally, purely simulated results provided the flexibility to investigate situations in which an equivalent experiment would be difficult to perform.

2 Description of Reconstuction Models

This section is purposely kept concise because the models used are taken from the literature and described elsewhere in detail [14].

2.1 Polynomial Interpolation

A zero order and first order polynomial have been used for interpolation. The zero order interpolation corresponds to the well-documented sample and hold (**S+H**) or arrival time weighted estimator[1, 6, 23]. The first order interpolation will be referred to as a **linear** interpolation.

2.2 'Shannon' Reconstruction (SR)

First introduced by Clark *et al.*[4] and applied to LDA data by Veynante and Candel[21], this approach stretches the time axis such that the velocity samples lie at equally spaced time intervals. Shannon reconstruction[16] can then be applied to interpolate intermediate points. After the stretched-signal reconstruction, the inverse of the stretching transformation can be used to resample the signal at the times corresponding to equal intervals prior to the stretching. This approach will be strictly valid only for the case that the *time-stretched* signal is band-limited to half the sampling frequency.

2.3 Fractal Reconstruction (FR)

It is important to note that the fractal reconstruction discussed in [18, 19] uses equally spaced samples. In [3] and this study, a time-stretching transformation similar to that used for the Shannon reconstruction has therefore been used prior to the fractal reconstruction. Note that the fractal reconstruction can be implemented in different ways. Strahle used target points (mid-points) to close the system of mapping equations. In the present study with non-equally spaced data, this method was very unstable and very sensitive to the smallest variation of velocity value, a property not desirable in light of the noise expected to accompany LDA measurements. Results presented by Chao and Leu[3] using target points appear promising, however it is not clear that their data set reflected the true particle arrival statistics of LDA,

since they first artificially reduced the data rate, possibly preferentially, although unintentionally. Therefore in the present study, the fractal reconstruction was implemented using a fixed d_n coefficient in the defining relation

$$\begin{pmatrix} \tau_{new} \\ h_{new} \end{pmatrix} = \begin{pmatrix} a_n & 0 \\ c_n & d_n \end{pmatrix} \begin{pmatrix} \tau_{old} \\ h_{old} \end{pmatrix} + \begin{pmatrix} e_n \\ f_n \end{pmatrix}$$

where τ is the abscissa of the time-stretched coordinate system and h is the transformed velocity. The other transform coefficients were determined by demanding collocation on every interpolation interval. An obvious weak point of this reconstruction method for LDA data is that the essence of the technique, namely the similarity in scales, is not preserved after the reverse time transformation.

2.4 Projection onto Convex Sets (POCS)

Interpolation through POCS has been applied in a variety of fields in which a finite bandwidth B of the underlying process exists and is known. A function $g(t)$ which, through digital filtering (rectangular) satisfies this criteria, i.e. $G(\omega) = 0$ for $\omega > 2\pi B$, is then interatively matched to the measured velocities $u(t_i)$ using the iteration algorithm

$$g^{(k+1)}(t) = g^{(k)}(t) + \lambda_i \frac{u(t_i) - u_r(t_i)}{||\vec{h}(t_i)||} \vec{h}(t_i)$$

where λ_i is a relaxation factor,|| || is the L_2-norm and $u_r(t_i) = \vec{h}(t_i)g(t)$. Again there are several approaches to implementation, all of which are very computationally intensive. Principally however, the spectrum of the interpolation is band-limited according to the filter applied to $g(t)$. In the present study $g^o(t)$ was a low-pass filtered linear interplation of the LDA data, repressented by discrete values at interals of $1/2B$. The one-dimensional vector $\vec{h}(t_i)$ is defined for this implementation of $g(t)$ as:

$$[si(2\pi B(\tau_1 - t_i)), \ldots, si(2\pi B(\tau_M - t_i))]$$

where τ_i are equidistant sampled points of $g(t)$. Note that this method is not necessarily collocative, depending on the termination criteria of the interation.

Previously, this method has only been applied by Lee and Sung[12] to LDA data, with apparent success, extending the cut-off limits of the spectrum by 5-6 times over S+H. Unfortunately, they do not provide information on their choice of B and in fact, their good agreement with the target spectrum may well be fortuitous, the true deviation being compensated by aliasing. More details are required of their implementation technique to be conclusive.

2.5 Direct Spectral Estimation

For comparison purposes a direct spectral estimation has also been performed. This estimator is similar to that proposed by Roberts *et al.*[15] with an additional weighting of the individual velocity values $w(t_i)$, in this case with the residence time:

$$S(f) = T \frac{\left[\left|\sum u(t_i)w(t_i)d(t_i)e^{-2\pi j f t_i}\right|^2 - \sum u^2(t_i)w^2(t_i)d^2(t_i)\right]}{\left[\sum w(t_i)\right]^2}$$

where $d(t_i)$ is a window function. In [13] this estimator was shown to be superior to an estimator without residence time weighting, in terms of turbulence-induced velocity bias.

3 Description of Simulation and Experimental Data Sets

3.1 Test Signals

Two test signals were used to illustrate the reconstruction schemes in time domain, as shown in Fig 2. The first is an exponentially modulated cosinus of the form

$$y_1(t) = e^{\frac{t-15s}{12s}} \cos(\pi t/1s)$$

The second is a simulated (1D) flow field with a mean of zero, a variance of 1 m^2/s^2 and an integral time scale of 1s. The particle density was chosen to yield a mean particle rate of 1 particle per integral time scale.

3.2 Simulation Data Sets

In addition to the two test signals previously mentioned, several other simulated data sets were investigated, all with a mean velocity of 10 m/s, an integral time scale of 0.1s, a first order autoregressive spectral distribution and a primary generation of 100 samples per time scale. The turbulence intensity was varied between 10% and 100% using both 1D and 3D flowfield simulations. All simulated data sets extended over 10,000 integral time scales. The particle number depended on the seeding density, which was varied to yield an average date density (particles per integral time scale) of $\alpha = 10$, 1 or 0.1. Residence times were generated for each particle passage using measurement volume dimensions of 20μm x 20μm x 100μm. Upon reconstruction, further processing continued only after a resampling at equidistant intervals of 0.01s. Full details of the simulation technique can be found in previous publications [8, 9].

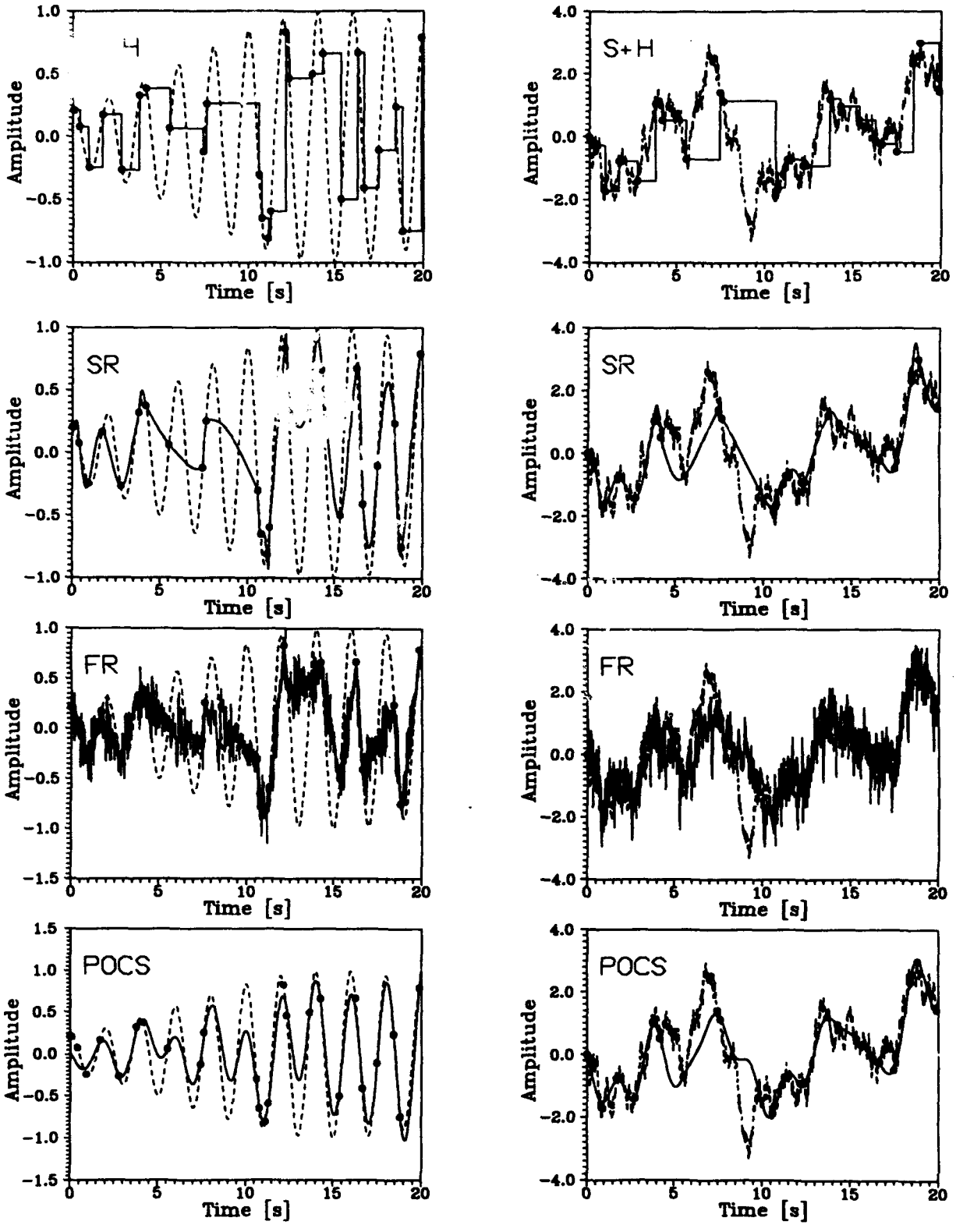

Figure 2: Reconstructed test signals using **S+H**, **SR**, **FR** and **POCS** interpolation: _ _ _ test signal; • LDA sample points; ——— reconstruction

3.3 Experimental Data Sets

Flow velocity measurements were performed behind a wall-mounted obstacle, allowing variation of the turbulence intensity. Hot-wire measurements and LDA measurements were performed at identical positions, the former without seeding. Only the measurement point 1 will be used in this study, the statistics of which are summarized in Table 1. As indicated in Fig.1, the HWA data was used also for indirect simulation studies, whereby the statistical values shown in Table 1 were used as a basis.

The primary purpose of including an experiment in this investigation was to verify the simulation procedure. This is illustrated in Fig. 3. In this figure the spectrum measured using the LDA, employing Shannon reconstruction is compared to the spectrum obtained directly from the hot-wire signal and with the simulated LDA signal using the hot-wire signal as a primary series in the simulation. This comparison shows that the simulation procedure yields a spectrum very similar to that which was actually measured with LDA, indicating that the numerical seeding procedure is trustworthy. Further reference to the hot-wire and LDA measurements will not be made.

HWA					LDA
ϑ_u[s]	$\overline{u}$[m/s]	σ_u^2[m^2/s^2]	D_o[-]	Tu[%]	$\dot{N}$[Hz]
0.003	8.156	0.141	1.67	4.6	212

Table 1: Statistics of measurement point 1

4 Results and Discussion

Already the interpolations viewed in time domain (Fig. 2) indicate that the success of any scheme will depend largely on the input signal. The band-limited test signal $y_n(t)$ is excellently approximated by **POCS**, since this

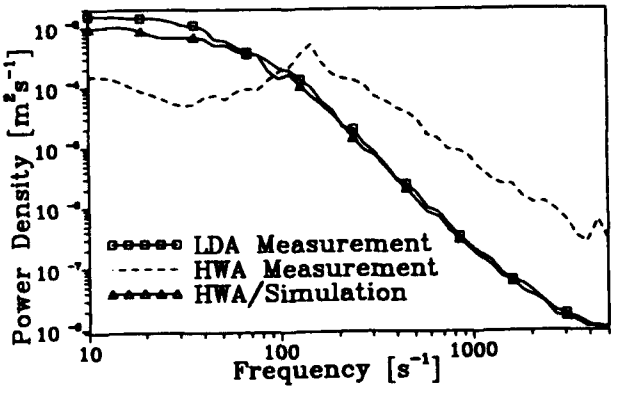

Figure 3: Verification of simulation procedure using HWA signal as primary series. A Shannon reconstruction was used for spectral estimation.

is a prerequisite for such an interpolation. Further evaluation of the reconstruction schemes however, can only be on the basis of more precise statistical measures. For this purpose the normalized error of the first two moments, using arithmetic averaging of the reconstructed signal, has been computed and presented in Fig. 4 for the **S+H**, **linear** and the **SR** reconstruction schemes. Also shown is the percent error expected for a free-running processor[7]. Note that the abscissa is now the data density, i.e. the data rate($\dot{N}$) times by the integral time scale(ϑ_u).

As expected, the normalized errors decrease with increasing data density. The first moment error of all estimators follows very closely the **S+H** error, which has also been theoretically derived and is shown in Fig. 4[23]. From these measures alone, no scheme can be strongly favoured over the other. Examining the normalized variance error indicates that the linear interpolation exhibits significantly lower variance estimates. The **SR** estimates lie between the **linear** and **S+H** values.

Spectral estimates based on a resampling of the reconstructed signal are shown in Fig. 5 for two data densities, $\alpha = 10$ and 0.1, corresponding to data rates of 100 ad 1 Hz respectively. They are compared to the expected spectrum, computed directly from the primary simulation series. All interpolation based estimators are expected to exhibit a low-pass filter characteristic, the cut-off frequency being related to the data density. This calls for great caution in appraising estimators, since typical turbulent spectra, and also the simulation models, resemble closely first order filters. For the **S+H** reconstruction, Adrian and Yao[1] have given the cut-off frequency as the data rate divided by 2π. This corresponds to 16 and 0.16 Hz for the two simulations respectively.

From Fig. 5 it is clear that the linear reconstruction and the Shannon reconstruction behaves more like a second order filter, falling off more rapidly than the **S+H** reconstruction. This also explains the lower variance observed in Fig. 4 for the linear reconstruction. The high variability of the direct estimation at high frequencies, as derived by Gastor and Roberts[10], is confirmed in Fig. 5. At low data densities all estimators resemble the **S+H** result, showing an increase of power at low frequencies, attributed to step noise in [1], and a decrease at higher frequencies due to the filter effect. In fact, the residence time weighted direct spectrum appears to be overall the most efective estimator from these data. Again it must be emphasized that the fact that the **S+H**, **Linear** and **SR** spectra fall off at higher frequencies have less to do with the fact that they estimate the flow fluctuations well, rather this is the *particle rate* filter effect. If the filter effect were computationally removed, these spectra would resemble the flatness of the direct estimate, but with significantly larger bias.

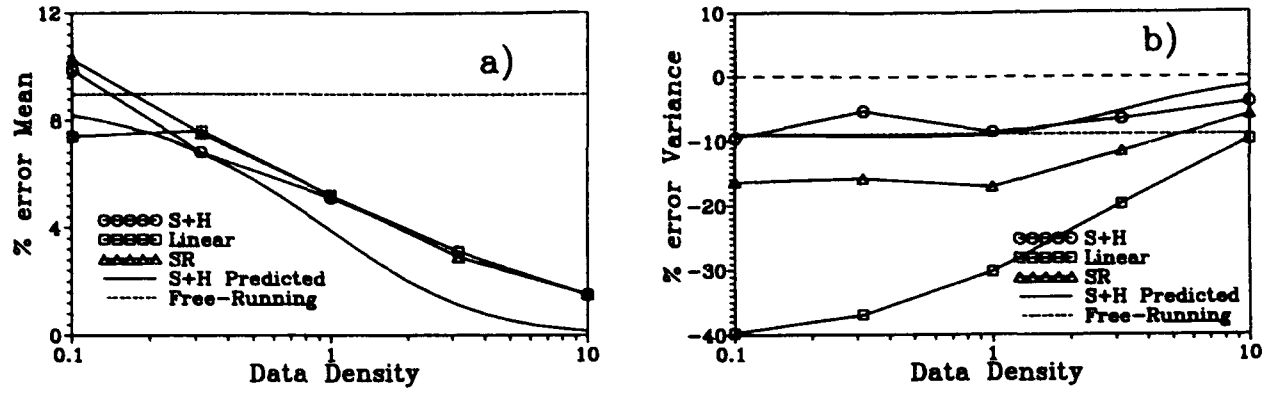

Figure 4: Percent error of a) mean and b) variance when arithmetically averaged over reconstructed signal. A 1D simulation with 30% turbulence level was used.

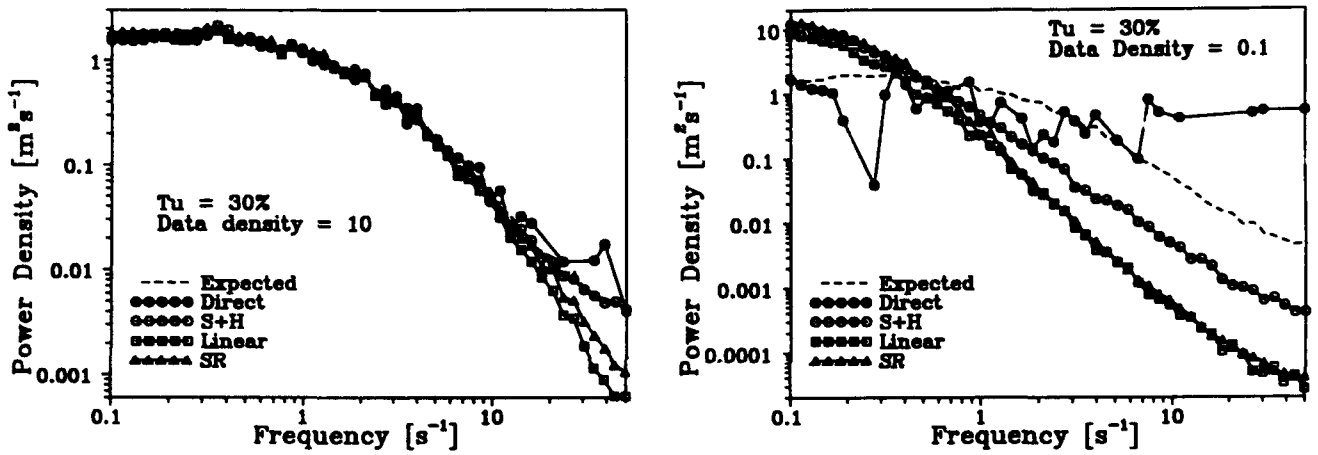

Figure 5: Spectral estimates from a 1D flow simulation with 30% turbulence and two data densities.

The estimate based on the Shannon reconstruction typically lies between the **S+H** and the linear reconstruction. In [21] this reconstruction scheme appeared to be superior to others, a behaviour which is surely attributable to the bandwidth limitation of the three sinusoids used as a test signal. In a second presentation of spectral estimates from Shannon reconstruction, no direct comparison to other techniques were explicitly given[22]. Note that one assumption in applying this technique is the bandwidth limitation of the time-stretched signal, a feature which by no means has been demonstrated for typical LDA signals. Originally this technique was applied only to regularily sampled signals with some jitter on the sample times, a considerably different situation to LDA data[4].

The difficulty in applying fractal reconstruction to LDA data is illustrated well in Fig. 6a, showing the dependence of the mean and variance bias on the choice of d_n. Although a value of 0.17 appears to be quite effective in minimizing bias errors of the variance, this is not known beforehand and furthermore the optimal value will also depend on turbulence level and data density. The mean bias does not reach zero even for a d_n value of 0.4.

Using the fixed value $d_n = 0.17$, the spectra for $\alpha =$ 10 and 0.1 using the fractal reconstruction are shown in Fig. 6b. At high data densities the fractal reconstruction lies between the **S+H** and **SR** in the upper frequency range. At low data densities the **FR** estimate agrees well with the **linear** and **SR** estimates, i.e. it exhibits a stronger filter effect than the **S+H** estimate.

These results do not support the optimism of [3] in applying **FR** to LDA data. Possible refinements to improve the **FR** spectral estimation are: application of **FR** without the time-stretching transformation; estimation of the fractal dimension (D_o) from randomly sampled points and; formulation of some relation between D_o and d_n.

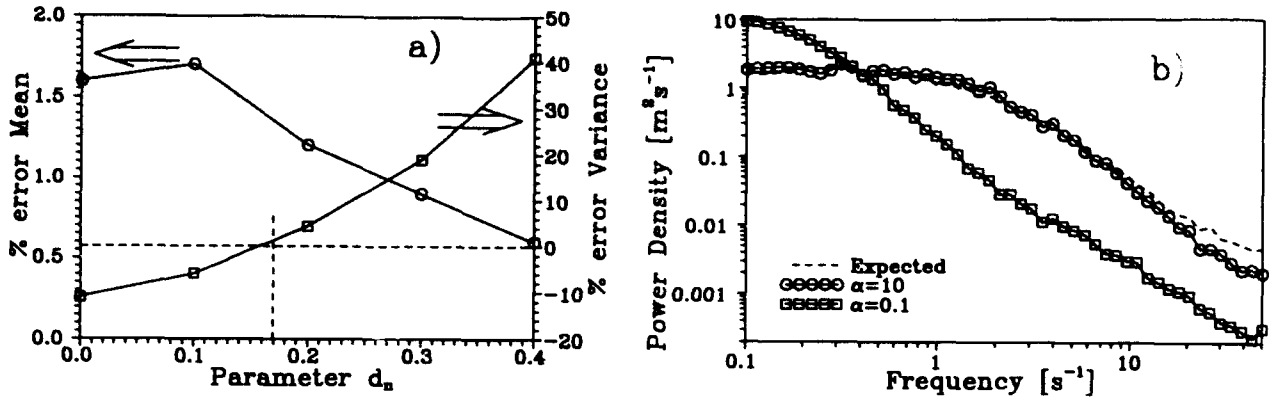

Figure 6: a) Influence of d_n on mean and variance bias of reconstructed signal; b) spectral estimates using fractal reconstruction with $d_n = 0.17$.

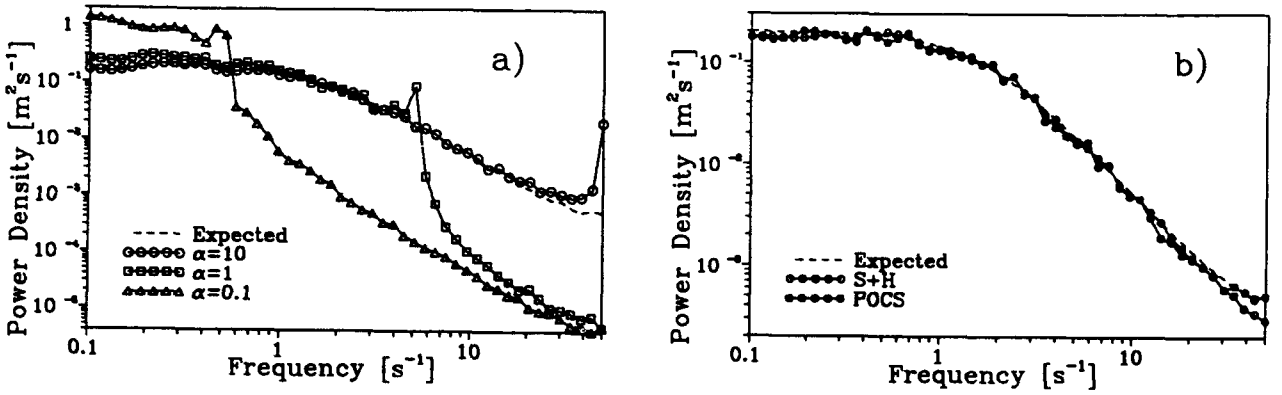

Figure 7: Spectral estimates using a **POCS** reconstruction: a) $B = \alpha/2$; b) $B = \alpha/1.6$, α=10.

Finally the results of applying the **POCS** interpolation are presented in Fig. 7. In Fig. 7a the effect of data density at a bandwidth of B=$1/2\alpha$ is demonstrated. Here the filter influence is much more severe than with other interpolation schemes, exhibiting in addition an oscillation corresponding to the applied boxcar filter (Gibb's phenomenon). If B is increased beyond $\alpha/2$, the spectrum estimate can closely approach the expected spectrum, as shown in Fig. 7b for α=10, however the correct choice of B is not known beforehand. Furthermore, if B is increased still further, the **POCS** spectrum will asymptotically approach the **Linear** estimate, because the linear interpolation was used as a start value for $g(t)$. These results indicate that the **POCS** estimation is not a promising alternative in the present implementation, at least without some scheme for choosing B.

5 Final Remarks

The possibility of improving parameter estimation for LDA data through the use of signal reconstruction techniques has been investigated. Several reconstruction techniques have been considered, some of which have been reported on previously in the literature, usually together with promising results. The results of the present study however, have shown that of those techniques considered, none can unconditionally be considered superior to a residence time weighted direct estimation.

The implementation of the time-stretching transformation in the fractal reconstruction is unsatifactory, since the similarity of scales is not preserved. A refinement in this regard could bring improvements, although some doubt exists whether previously reported performance can be achieved with actual LDA data.

While the present results cannot clearly recommend a signal reconstruction as an alternative to the direct estimation, other conclusions may be obtained for the case of non-homogeneously seeded flows, as was examined in [21]. This will be the topic of future work.

The simulation techniques used in this study were developed with the financial assistance of the VW Foundation under contract I/66 487, for which the authors are grateful. The numerous and valuable discussions with Dr. W. Fuchs are also thankfully acknowledged. Dr. M. Stieglmeier was of great assistance in performing the experimental studies.

References

[1] Adrian, R.J. & Yao, C.S. 1987, Power Spectra of Fluid Velocities Measured by Laser Doppler Velocimetry, *Exp. in Fluids*, vol. 5, pp. 17-28.

[2] Buchhave, P., George, W.K.Jr., Lumley, J. 1979, The Measurement of Turbulence with the Laser Doppler Anemometer, in *Ann. Rev. of Fluid Mech.* pp. 442-503, Ann. Reviews Inc., Palo Alto, CA.

[3] Chao Y.C., Leu J.H. 1992, A Fractal Reconstruction Method for LDV Spectral Analysis, *Exp. in Fluids*, vol. 13, pp. 91-97.

[4] Clark J.J., Palmer M.R., Lawrence P.D. 1985, A Transformation Method for the Reconstruction of Functions from Nonuniformly Spaced Samples, *IEEE Trans. of Acoust., Speech, and Signal Proc.*, vol. ASSP-33, No. 4, pp. 1151-1165.

[5] Edwards, R.V. (Ed.) 1987, Report of the Special Panel on Statistical Particle Bias Problems in Laser Anemometry, *ASME J. Fluids Engg.*, vol. 109, pp. 89-93.

[6] Edwards, R.V., Jensen, A.S. 1983, Particle-Sampling Statistics in Laser Anemometers: Sample-and-Hold Systems and Saturable Systems, *J. of Fluid Mech.*, vol. 133, pp. 397-411.

[7] Erdmann, J.C., Tropea, C. 1982, Statistical Bias of the Velocity Distribution Function in Laser Anemometry, *Proc. Int. Symp. on Appl. of LDA to Fluid Mech.*, LADOAN, Lisbon.

[8] Fuchs, W., Albrecht, H., Nobach, H., Tropea, C., Graham, L. 1992, Simulation and Experimental Verification of Statistical Bias in Laser Doppler Anemometry including Non-Homogeneous Particle Density, *Proc. 6th Int. Symp. of Appl. of Laser Techn. to Fluid Mechanics*, LADOAN, Lisbon.

[9] Fuchs,W., Nobach,H. Tropea, C. 1994, The Simulation of LDA Data and its Use to Investigate the Accuracy of Statistical Estimators, *AIAA Journal*, accepted for publication.

[10] Gaster, M. & Roberts, J.B. 1975, Spectral Analysis of Randomly Sampled Signals, *J. Inst. Maths Applics.* vol. 15, pp. 195-216.

[11] Kay, S.M. & Marple, S.L.Jr. 1981, Spectrum Analysis - A Modern Perspective, *Proc. IEEE*, vol. 69, no. 11, pp. 1380-1419.

[12] Lee, D.H. & Sung, H.J. 1992, Turbulent Spectral Bias of Individual Realization of LDV, *Proc. 6th Int. Symp. of Appl. of Laser Techn. to Fluid Mechanics*, LADOAN, Lisbon.

[13] Nobach, H. 1993, Simulationen zum Einfluß von Teilchen-Seeding und Prozessoreigenschaften auf die Ergebnisse konventioneller Methoden zur Turbulenzspektumbestimmung beim Laser-Dopper-Anemometer, Großer Beleg, Universität Rostock.

[14] Nobach, H. 1994, Signalrekonstruktion in der Laser-Doppler-Anemometrie, Diplomarbeit, Universität Rostock.

[15] Roberts, J.B., Downie, J., Gastor, M. 1980, Spectral Analysis of Signals from a Laser Doppler Anemometer Operating in the Burst Mode, *J. Phys. E.: Sci. Instrum*, vol. 13, pp. 977-981.

[16] Shannon, C.E. 1948, A Mathematical Theory of Communication, *The Bell System Technical Journal*, vol. 27, pp. 379-423.

[17] Srikanataiah, D.W. & Coleman, H.W. 1985, Turbulence Spectra from Individual Realization Velocimetry Data, *Exp. in Fluids*, vol. 3, 35-44.

[18] Strahle W.C. & Jagoda J.I. 1988, Fractal Geometry Applications in Turbulent Combustion Data Analysis, *22nd Int. Symp. on Combustion*, The Combustion Institute, pp. 561-568.

[19] Strahle, W.C. 1991, Turbulent Combustion Data Analysis Using Fractals, *AIAA Journal*, vol. 29, no. 3, pp. 409-417.

[20] Tropea C. 1987, Turbulence-induced Spectral Bias in Laser Anemometry, *AIAA Journal*, vol. 25, pp. 306-309.

[21] Veynante D. & Candel S.M. 1988, Application of Nonlinear Spectral Analysis and Signal Reconstruction to Laser Velocimetry, *Exp. in Fluids*, vol. 6, pp. 534-540.

[22] Veynante D. & Candel S.M. 1988, A Promising Approach in Laser Doppler Velocimetry Data Processing: Signal Reconstruction and Nonlinear Spectral Analysis, *Signal Processing*, vol. 14, pp. 295-300.

[23] Winter, A.R., Graham, L.J.W., Bremhorst, K. 1991, Effects of Time Scales on Velocity Bias in LDA Measurements using Sample and Hold Processing, *Exp. in Fluids*, vol. 11, pp. 147-152.

HETERODYNING AND QUADRATURE SIGNAL GENERATION: ADVANTAGEOUS TECHNIQUES FOR APPLYING NEW FREQUENCY SHIFT MECHANISMS IN THE LASER DOPPLER VELOCIMETRY

H. Müller, J. Czarske *, R. Kramer, H. Többen, V. Arndt, H. Wang, D. Dopheide

Physikalisch-Technische Bundesanstalt (PTB)
Laboratory for Fluid Flow Measuring Techniques
Bundesallee 100, D-38116 Braunschweig

*Institut für Meßtechnik im Maschinenbau
Nienburgerstraße 17, D-30167 Hannover

ABSTRACT

LDV systems with directional discrimination usually involve frequency shift techniques. As the LDV measuring signal consists of the frequency shift and the Doppler shift, conventional LDV signal processing techniques are based on a high stability and a small bandwidth of the generated frequency shift.

The requirements on the frequency shift can be reduced drastically if the resulting carrier frequency is exclusively used as auxiliary carrier which is eliminated when a quadrature signal pair in the baseband containing the directional information is generated.

Using heterodyning and quadrature signal processing techniques novel frequency shift generation concepts can be realized in directional LDV-systems.

1. INTRODUCTION

Conventionally used techniques for directional discrimination in the laser Doppler velocimetry are based on the generation of a frequency shift between the laser beams being focussed into the measuring volume (Drain, 1986).

By means of the frequency shift the measuring signal is a carrier frequency signal which consists of the carrier frequency and the Doppler frequency. The carrier frequency is given by the frequency shift between the laser beams and the Doppler frequency by the measuring effect. For the determination of the magnitude and sign of the Doppler frequency the carrier frequency has to be well known. Therefore, frequency shift techniques usually require carrier frequencies having a high stability and a small bandwidth.

Since the frequency shift, based on the application of conventional frequency shift techniques (Oldengarm *et al* (1976), Durao and Whitelaw (1975) and Jones *et al* (1984)), is exclusively given by the electronic drivers for the optoelectronic components generating the frequency shift, a high stability of the carrier frequency can be achieved. Therefore, conventional LDV signal processing techniques are generally designed for the evaluation of Doppler signals having a stable carrier frequency with a bandwidth which is neglectable in comparison with the bandwidth given by the measuring effect.

That may be the reason why other frequency shift techniques generating unstable frequency shifts with high bandwidths have not been taken into account for directional LDV systems.

Especially if new frequency shift techniques based on the application of different laser sources or frequency shift processes for each LDV beam are considered, the stability and linewidth of each LDV beam enter directly into the stability and bandwidth of the resulting shift frequency (Müller *et al*, 1993). As consequence one has to evaluate signals with frequency bandwidths and frequency shift fluctuations which can lie in the 100 MHz range. Utilizing signal processing techniques for LDV signals which are able to evaluate small Doppler shifts, even if the bandwidths of the detected signals are higher in orders of magnitudes, new frequency shift techniques can be introduced for manifold LDV applications.

It will be shown that transferring heterodyne and quadrature signal processing techniques to the laser Doppler velocimetry, new frequency shift concepts can be employed even for large carrier frequency bandwidths provided that they lie within the detection bandwidth of the photodetectors.

It has to be pointed out that in contrast to commonly used LDV systems the resulting carrier frequency is exclusively used as auxiliary carrier which is eliminated when generating a quadrature signal pair in the baseband containing the directional information.

The advantages of the described technique which mainly consist in

- the avoidance of any frequency shift adaptation over an increased velocity range from "zero" up to "high velocities",
- the utilization of fluctuating frequency shifts without deteriorating the measuring accuracy,
- the applicability of new frequency shift techniques with shift frequency bandwidths up to 100 MHz

will be demonstrated at several examples of innovative LDV systems based on novel frequency shift techniques using the optical frequency difference of

- two orthogonally polarized modes of a micro crystal laser,
- stimulated Stokes waves in different optical fibres,
- different laser sources such as monomode laser diodes or Nd:YAG-ring lasers

as frequency shift.

The aim is to present heterodyning and quadrature signal generation in the baseband as low cost signal processing techniques which allow to realize directional LDV systems with reduced requirements on the frequency shift generation.

The combination of the described signal processing techniques and novel frequency shift techniques will allow to realize promising compact and low cost directional LDV systems.

2. METHOD

2.1 Heterodyning and quadrature signal generation

In order to utilize new frequency shift techniques in the laser Doppler velocimetry, measuring signals with instable carrier frequencies and high bandwidths have to be evaluated. A method of eliminating shift frequency influences on the evaluation of the measuring information is the simultaneous detection of the measuring signal and a reference signal. A reference signal can easily be generated by optical heterodyning of the LDV beams and detected as beat signal on a PIN photodetector.

Frequency fluctuations and bandwidth influences in both carrier frequency signals, the measuring signal and the reference signal, are correlated so that their influence on the measuring information, the Doppler frequency, can be eliminated by correlation techniques. Whereas the correlation of the carrier frequency signals in the range of some ten MHz with bandwidths up to some MHz can be carried out by transient recorder techniques (Kramer *et al*, 1994), the evaluation of measuring signals with carrier frequencies and bandwidths in the 100 MHz range requires analogous correlation techniques. In this case the correlation can be performed by electronical heterodyning using conventional mixer and filter units (see Figure 1).

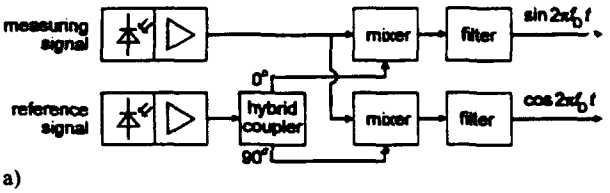

a)

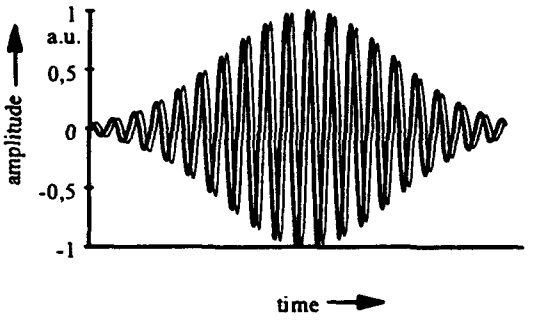

b)

Fig. 1 a) Block diagram of the correlator (mixer-filter) unit
b) Typical burst signal pair as output quadrature signal pair

To retain the directional information when eliminating the shift frequency with all its fluctuations by the mixer stage, quadrature signals have to be generated (Agrawal, 1984). For the generation of quadrature signals the reference signal with the carrier frequency determined by the frequency shift is given to the input of a broadband hybrid coupler. At the outputs of the coupler one gets two signals having the same amplitudes but a phase shift of 90 degrees against each other. By mixing the measuring signal with the reference quadrature signal pair one gets a burst signal pair in the baseband ("carrier frequency equal zero") containing only the Doppler frequency and the directional information.

The correlation by electronical heterodyning and the quadrature signal generation may be illustrated in the following explanations. With the expressions:

f_{Sh}	:	shift frequency (carrier frequency)
f_{FI}	:	shift frequency fluctuation
f_D	:	Doppler frequency (measuring information)
$\Phi(t)$	:	phase fluctuations determining the carrier frequency bandwidth
I	:	signal amplitude

the measuring signal can be described by:

$$I_M \sin(2\pi(f_{Sh} + f_{FI,M} + f_D)t + \Phi_M(t))$$

and for the reference signal pair follows equivalently:

$$I_R \sin 2\pi((f_{Sh} + f_{FI,R})t + \Phi_R(t)),$$
$$I_R \cos 2\pi((f_{Sh} + f_{FI,R})t + \Phi_R(t)).$$

As the frequency and phase fluctuations in both carrier frequency signals are highly correlated one can write:

$$f_{FI,M} = f_{FI,R} = f_{FI},$$
$$\Phi_M(t) = \Phi_R(t) = \Phi(t).$$

By mixing the measuring signal with the reference signal pair one gets the two mixing products:

$$\tfrac{1}{2} I_M I_R (\cos 2\pi f_D t - \left[\cos(2\pi(2f_{Sh} + 2f_{FI} + f_D)t + 2\Phi(t)\right],$$
$$\tfrac{1}{2} I_M I_R (\sin 2\pi f_D t + \left[\sin(2\pi(2f_{Sh} + 2f_{FI} + f_D)t + 2\Phi(t)\right],$$

where the expression [...] can be neglected after low pass filtering of the mixer output signals. The correlator output signals are then given by the quadrature signal pair:

$$\tfrac{1}{2} I_R I_M \cos 2\pi f_D t,$$
$$\tfrac{1}{2} I_R I_M \sin 2\pi f_D t.$$

The resulting quadrature burst signal pair is obviously free of shift frequency influences, the remaining measuring information f_D gives the magnitude of the velocity and the phase relationship of the quadrature signal pair the sign (see Fig. 1b and chapter 2.3).

The efficacy of the heterodyne technique for the evaluation of measuring signals with instable carrier frequencies caused by fluctuating frequency shifts will be demonstrated at several novel LDV-systems starting with shift frequency bandwidths in the kHz-range and shift frequency drifts in MHz range using the optical frequency difference of two separable modes of a micro crystal laser (see chapter 3.1) up to carrier frequency bandwidths in the 100 MHz-range using the optical frequency difference of two frequency stabilized monomode laser diodes (see chapter 3.3).

2.2 Heterodyning for the realization of directional multicomponent systems

By generating frequency shifts for the directional discrimination in LDV systems, one gets carrier frequency signals. The carrier frequency is given by the frequency shift and can be eliminated by a correlator unit (see Figure 1a)) while retaining the directional information in the phase relationship of the quadrature signal pair resulting in the baseband. This concept allows the use of any frequency shift higher than the occurring Doppler shifts without having an influence on the evaluation of the measuring information. In consequence different arbitrary frequency shifts can be used for a channel separation to realize directional multicomponent LDV systems. Therefore, three laser beams of slightly different light frequencies have to be focussed into the measuring volume.

For the generation of the frequency shifts any frequency shift technique, especially the novel frequency shift techniques described in the chapters 3.2 and 3.3, can be employed. To realize adjustment insensitive systems and to make the reference signal generation as easy as possible, the application of fibre optics seems to be advantageous. Using pigtailed laser sources, pigtailed PIN-photodiodes and fibre couplers for the generation of the reference signals by optical heterodyning, pigtailed gradient index lenses for focussing the laser beams into the LDV measuring volume and a conventional backscatter optic for the detection of the LDV-measuring signal, it is possible to realize a compact LDV-system.

Instead of using wavelength stabilized laser sources, one laser source for each laser beam, it would also be possible to use different stimulated Brillouin waves as described in chapter 3.2.

In any way, one gets only one measuring signal containing different carrier frequencies corresponding to the different velocity components to be measured. For each velocity component one carrier frequency reference signal has to be generated. Each carrier frequency is determined by the corresponding shift frequency and can therefore be detected as the beat signal of fractional intensities of both LDV beams in each LDV beam pair. The separation of the different components can then be realized by an extended mixer/correlator unit as shown in Figure 2.

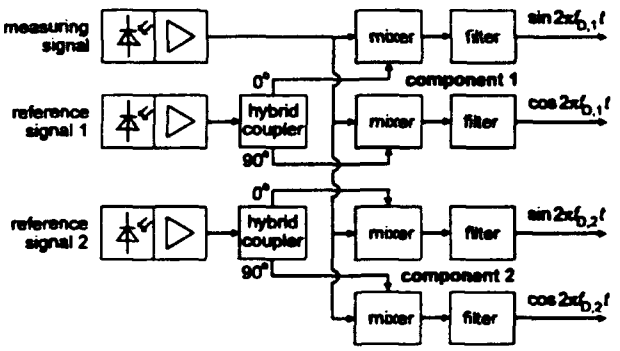

Fig. 2 Correlator unit for a directional two component LDV-system

2.3 Evaluation of the quadrature signals

Due to the mixing process of the carrier frequency signals, the low pass filtered mixing products in the baseband look like band-pass filtered signals without any offsets caused by the Gaussian intensity profile in the measuring volume (see Fig. 1b). The evaluation of the quadrature signal pairs resulting in the baseband can be performed by employing conventional transient recorders as well as quadrature demodulation techniques (Czarske *et al*, 1993 and 1994) or directional counters. By employing transient recorder techniques it is possible to determine the amount of the velocity by evaluating the burst frequencies with FFT algorithms or the zero crossings in each burst signal and the sign of the velocity by evaluating the phase relationship in the quadrature signal pair. The discrimination of the velocity sign is illustrated in the Figures 3a) and 4a) which show the first halves of typical burst signals for opposite velocity directions. The determination of which channels leads the other, gives the directional information.

Each burst signal pair can also be represented in a x-y-plot as a spiral which is given by a rotating phasor. Each rotation of the phasor corresponds to one burst signal period and the direction of the rotation to the sign of the velocity (see Figures 3b and 4b). As each rotation of the phasor corresponds to one burst signal period and each burst signal period to one fringe spacing in the measuring volume, the variation in time of the phase angle of the phasor directly gives the path-time curve of a particle passing through the measuring volume. The Figures 3c) and 4c) show the periodical phase angle time functions for different velocity directions. Considering the periodicity by adding 2π for each phase jump (phase unwrapping) one gets the phase angle time functions represented in the Figures 3d) and 4d). For particles passing through the measuring volume with a constant velocity, the resulting phase angle time functions are straight lines corresponding to the path-time curves of the particles. Consequently the amount and sign of their slope directly determine the amount and sign of the velocity to be measured.

Caused by the linear interrelationship between the phase angle, given by the quotient of the quadrature signal pair and the place of the tracer particle in the measuring volume, the evaluation of the phase angle time function directly allows to investigate quasistatic processes with velocities even to zero.

Furthermore the phase angle time function given by the measured time series of the phase angle values allows to perform a burst frequency estimation by the use of the least-squares method. A linear regression of the phase angle values makes it directly possible to analyse the averaged tracer particle velocity in the measuring volume, which is proportional to the center frequency of the burst signal, given by the slope in the graphs shown in Fig. 3d and Fig. 4d. The accuracy of the phase angle values, given by the standard deviation depends upon the signal-to-noise-ratio. Changes in the momentary frequency within one signal burst (e.g. in turbulent flows) can be evaluated by fitting non-linear polynomials.

As heterodyning is employed to eliminate the shift frequency with all its fluctuations and quadrature signal processing allows to evaluate burst signals in the baseband over a wide frequency range inclusively the directional information, the described signal processing technique is a powerful tool for the signal evaluation in LDV systems with arbitrary frequency shifts and frequency shift bandwidths provided that they lie in the photodetector bandwidths.

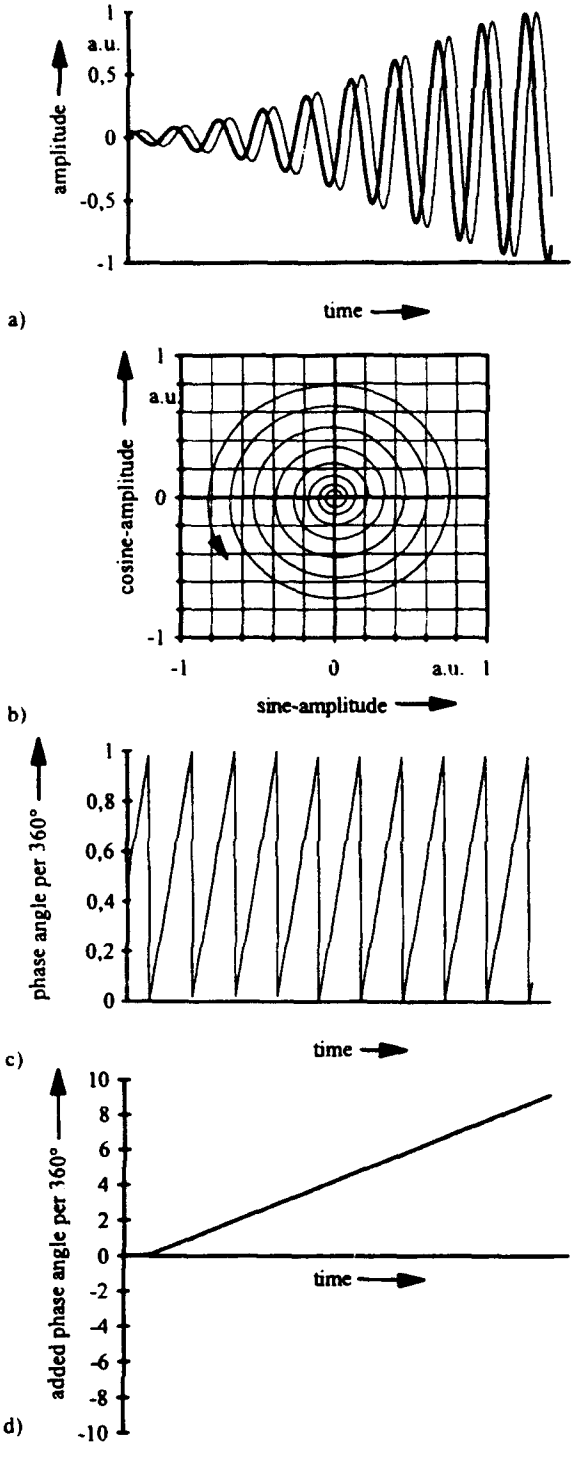

Fig. 3 First half of a typical quadrature burst signal pair resulting in the baseband
a) time function of the quadrature signal pair
b) spiral described by the phasor defined by the quadrature signals
c) phase angle time function given by the rotating phasor
d) continuous function considering the 2π phase jumps

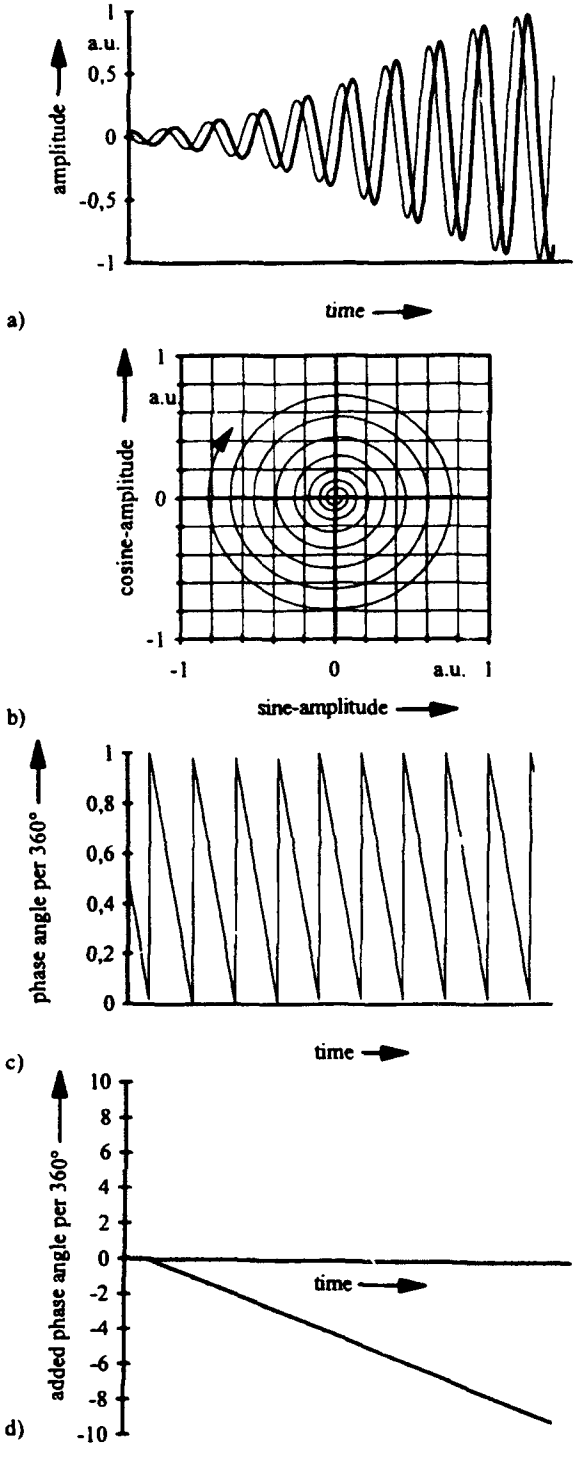

Fig. 4 First half of a typical quadrature burst signal pair for the opposite velocity direction as shown in Fig. 3
a) time function of the quadrature signal pair
b) spiral described by the phasor defined by the quadrature signals
c) phase angle time function given by the rotating phasor
d) continuous function considering the 2π phase jumps

3. NOVEL FREQUENCY SHIFT LDV TECHNIQUES AND EXPERIMENTAL RESULTS

3.1 Use of two separable modes of a micro crystal laser

The application of Nd:YAG micro crystal lasers allows to realize LDV-systems with a frequency shift between the LDV-beams which is directly generated in the laser resonator (Schmidt *et al*, 1993). By inducing local birefringence in the crystal of the laser resonator which is as short that only one lasing mode can be amplified in the gain bandwidth of the lasing medium, a single line emission in two orthogonally polarized modes can occur. Due to the optical frequency difference of the two orthogonally polarized states of the single lasing mode, two frequency shifted LDV beams can easily be generated by the use of polarizing beam splitters.

Applying micro crystal lasers for the Doppler velocimetry compact low cost directional velocimeters can be realized without needing conventionally used optoelectronic components for the generation of a frequency shift between the LDV beams being focussed into the measuring volume (Kramer *et al*, 1994).

A set-up of a LDV system based on a micro crystal laser is shown in Fig. 5. A quarter wave plate in the output beam of the micro crystal laser generates two almost linear polarized orthogonal light waves which are separated and splitted up by a Wollaston prism into two frequency shifted orthogonal polarized laser beams. Behind the first lens, where the laser beams are parallel, a half wave plate is introduced into one beam path to provide the same polarization for the two beams being focussed into the measuring volume by a second lens.

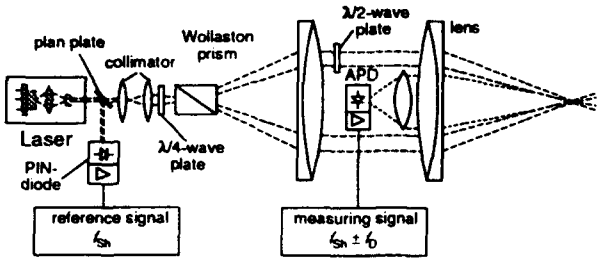

Fig. 5 Set-up of the realized LDV system based on a micro crystal laser

The scattered light of the particles passing through the measuring volume is detected in backward direction and focussed onto an avalanche photo diode (APD) which generates the measuring signal. For the generation of a reference signal a plan plate in the output beam of the micro crystal laser reflects a fractional part of the beam onto a PIN photodetector, where the two orthogonal laser modes are superimposed to produce a beat signal.

Whereas the small linewidth of the beat signal would allow to employ conventional signal processing techniques, precise velocity measurements require a simultaneous detection of the measuring and a reference signal due to the drift effects of the shift frequency depending on, for example, the crystal temperature with a coefficient of about 1 MHz/K.

Figure 6 shows the spectra of the simultaneously detected measuring and the reference signal in the set-up being represented in Figure 5. The bandwidth of the signals is small enough that the spectra can be evaluated in the conventional way. The peaks of the spectra corresponding to the burst frequency of the measuring signal are higher or lower than the frequency of the reference signal depending on the sign of the velocity.

Figure 7 shows an interval of a typical quadrature burst signal pair resulting in the baseband by applying the described signal processing technique which has been discussed in chapter 2. The frequency of the resulting quadrature burst signal pair determines the amount and the rotation direction of the spiral the sign of the velocity to be measured. The shift frequency was 22 MHz but this this is insignificant for the heterodyne and quadrature signal processing technique.

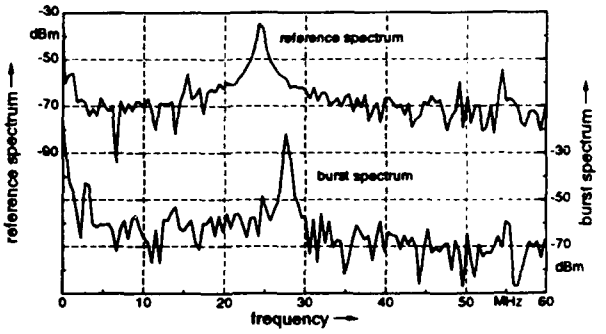

Fig. 6 Spectra of the simultaneously detected reference and measuring signal with the set-up shown in Fig. 5.

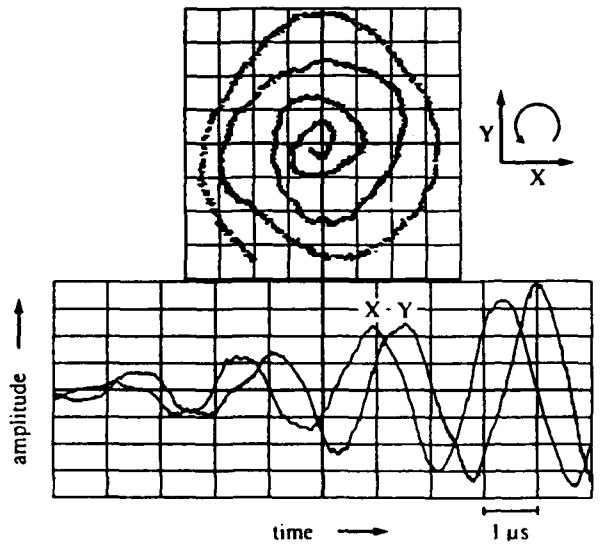

Fig. 7 First half of a measured quadrature signal pair with the LDV set-up shown in Fig. 5. The rotation direction of the phasor described by the spiral respectively the discrimination which channel leads the other gives the directional information.

3.2 Use of stimulated Brillouin scattering as frequency shift mechanism

To realize an adjustment insensitive fibre optical LDV system for directional velocity measurements without needing additional components for the frequency shift generation, stimulated Brillouin scattering (SBS) occurring in the core of an optical fibre can be used as frequency shift mechanism (Többen *et al*, 1994).

The incident wave of a narrow linewidth 1319 nm Nd:YAG laser pumps an acoustic wave which scatters it. The backscattered Brillouin wave is downshifted in frequency by an amount equal to the acoustic frequency in the 13 GHz range. To get a frequency shift in a lower frequency range, the optical frequency difference of two stimulated Brillouin waves was used:

$$f_{Sh} = f_{A,1} - f_{A,2}$$

where $f_{A,1}$ and $f_{A,2}$ are the frequency shifts of the stimulated Brillouin waves generated by one laser source in two differently doped silica fibers. By correlating the measuring signal with the beat signal of the two Brillouin waves as reference signal, the Doppler shift and the directional information can be evaluated independent of frequency shift instabilities.

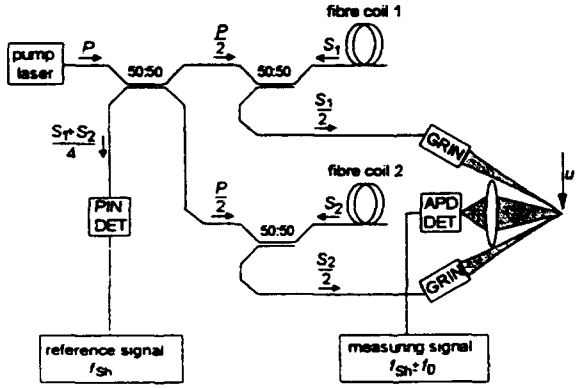

Fig. 8 Experimental set-up of a frequency shift LDV based on stimulated Brillouin scattering as frequency shift mechanism

The experimental configuration shown schematically in Fig. 8 was used to generate two stimulated Brillouin waves S_1 and S_2 in two differently doped monomode fiber coils. Via fused fiber couplers half of the intensity of the stimulated Brillouin waves was focussed into the measuring volume by two gradient index (GRIN) lenses. The beat frequency of the stimulated Brillouin waves S_1 and S_2 gave the reference signal for the detection of the momentary frequency shift. Figure 9 shows the frequency spectrum of the reference signal having a shift frequency of about 257 MHz and frequency fluctuations over a range of 15 MHz.

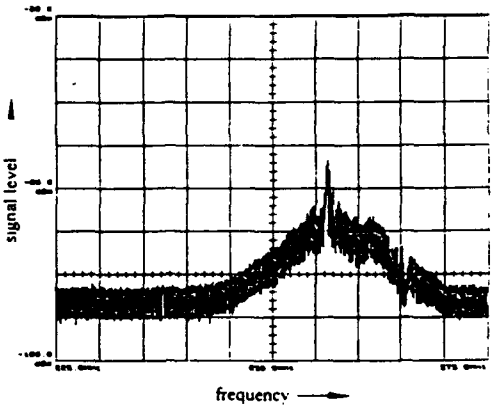

Fig. 9 Frequency spectrum of the reference signal of the Brillouin frequency shift LDV shown in Fig. 8

It is obvious that conventional LDV signal processing techniques would fail when evaluating fluctuating carrier frequency signals in the 250 MHz range. Employing the heterodyning and quadrature signal processing technique one gets quadrature burst signals in the baseband containing the Doppler frequency and the directional information. Figure 10 shows an example of a typical burst signal of the Brillouin frequency shift LDV by employing the described signal processing technique.

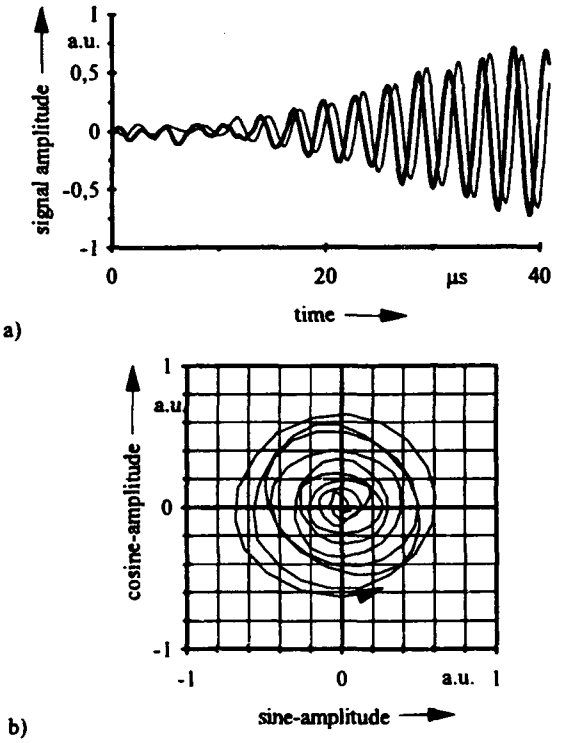

Fig. 10 First half of a detected and downmixed LDV quadrature signal pair. The determination of which channel leads the other gives the directional information requested.

3.3 Use of the optical frequency difference of two monomode laser diodes

The generation of a frequency shift by using the optical frequency difference of two stabilized monomode laser diodes allows on principle the realization of simple and low cost directional LDV set-ups (see Figure 11 and Müller and Dopheide, 1993). Therefore, two laser diodes with almost equal emission frequencies are required.

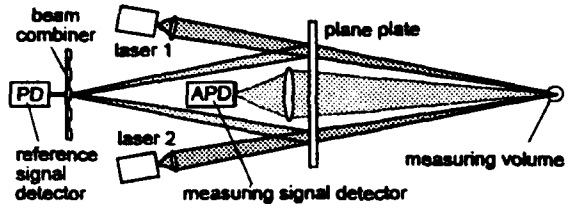

Fig. 11 Principle of a frequency shift LDV set-up using the optical difference frequency of two stabilized monomode lasers

The selection of appropriate monomode laser diodes requires the measurement of their spectral characteristics depending on the current and the temperature of the laser diodes. The resulting mode charts allow to choose the exact operating parameters for the laser diodes. Employing 40 mW Hitachi monomode laser diodes of the HL 8318 type and evaluating the mode charts a typical dependence of the emission frequency within one mode is given by 4.4 GHz/mA for the diode current and by 19.6 GHz/K for the diode temperature. Almost equal emission wavelengths (830.800 nm for example) can be achieved by adjusting the temperatures of both laser diodes and by tuning the laser diode current of one laser diode of the pair. Experiments have shown that the resulting frequency fluctuations were less than 100 MHz/s within a frequency range of about one GHz without any shift frequency control unit. Using laser diodes of the HL 8318 type typical carrier frequency bandwidths in the 100 MHz range were observed (see Figure 12).

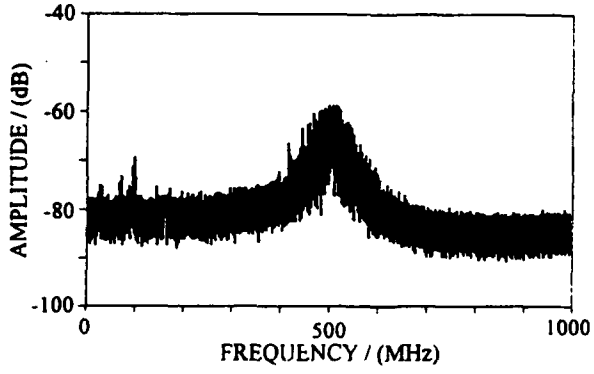

Fig. 12 Beat signal of two stabilized HL 8318 laser diodes as reference signal corresponding to the resulting shift frequency

Although the bandwidth of the detected carrier frequency signals are higher in orders of magnitudes than the Doppler frequencies which have to be evaluated, the described signal processing technique allows a precise evaluation of the amount and sign of the velocities to be measured. Figure 13 shows an example of the first half of a typical quadrature burst signal pair in the baseband.

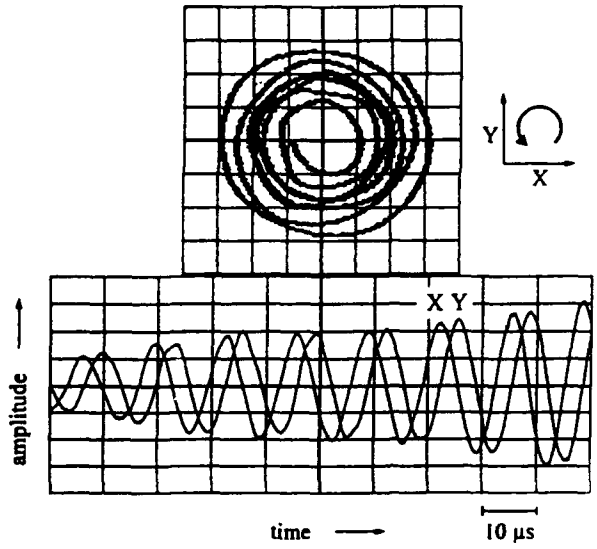

Fig. 13 Measured LDV quadrature signal pair for the directional velocity measurement with the LDV set-up in Fig. 11.

By employing conventional commercially available monomode laser diodes for the described frequency shift LDV using one laser diode for each LDV beam it is possible to realize low cost directional LDV systems with increased power in the measuring volume and without needing additional optoelectronic components for the frequency shift generation. The only disadvantage is the necessity of selecting appropriate monomode laser diodes by evaluating the measured mode charts.

To avoid selection problems in finding appropriate monomode laser diodes with almost equal emission frequencies and overlapping tuning ranges without mode hopping, DFB (distributed feed back) laser diodes can be applied. In contrast to conventional laser diodes having a Fabry-Perot resonator structure, these laser diodes employ a phase grating structure in the laser resonator which guarantees a dynamic single mode operation and allows to adjust the emission frequency without mode hopping by varying the current or temperature of the laser diode.

Furthermore the linewidths of these laser diodes are reduced to a few MHz. To enlarge the tuning range of the DFB laser diode a special TTG (tuneable twin guide) laser diode structure has been developed (Amann, 1991) which additionally allows to adjust the emission wavelength by the current of a tuning diode.

Corresponding to the reduced linewidths it is possible to reduce the bandwidth of the shift frequency significantly if such lasers are implemented in LDV set-ups using one tuneable laser diode for each LDV beam.

By the development of DFB and TTG laser diodes with increased output powers, these laser diodes will be very interesting for the new LDV concept using one laser diode for each LDV beam, especially if multicomponent LDV-systems are considered.

4. CONCLUSIONS

The heterodyning and quadrature signal processing technique has been verified in several novel frequency shift LDV systems with different frequency shifts, frequency shift fluctuations and frequency shift bandwidths. As this technique can work with nearly arbitrary frequency shifts and frequency shift bandwidths, provided that they lie in the bandwidth of the signal processing chain, no adaptation of the frequency shift to the velocities to be measured is required. Another advantage is that the quadrature signals which have to be evaluated are offset free signals in the baseband which allow to apply conventional signal evaluation techniques, such as transient recorders or directional counters. Furthermore the heterodyning and quadrature signal generation can be realized with conventional electronic components being used in the high-frequency engineering so that the described technique is a low cost concept for LDV systems with arbitrary shift frequencies without deteriorating the measuring accuracy over an increased measuring range.

5. REFERENCES

Agrawal, Y. C. 1984, Quadrature demodulation in laser Doppler velocimetry, Appl. Opt., vol 23, pp 1685-1686

Amann, M. Ch. 1991, Wavelength tuneable single mode laser diodes, Advances in Solid State Physics vol 31, pp. 201-218

Czarske, J., Hock, F. & Müller, H. 1993, Quadrature demodulation - A new LDV - Burstsignal Frequency Estimator, Proc. 5th Int. Conf. Laser Anemometry - Advances and Applications, Koningshof, Veldhoven, SPIE VOL. 2052, pp. 79-86

Czarske, J., Hock, F. & Müller, H. 1994, Minimierung der Meßunsicherheit von Laser-Doppler-Anemometern, tm - Technisches Messen vol. 61 no. 4, pp. 168-182

Drain, L. E. 1986, The laser Doppler technique, pp. 156-181, John Wiley & Sons

Durao, D. F. G. & Whitelaw, J. H. 1975, The performance of Acoustooptic cells for Laser Doppler Anemometry, J.Physics E: Scientific Instr. vol. 8, pp. 776-780

Jones, J. D. C., Chan, R.K Y., Corke, M., Kersy, A. D. & Jackson, D. A. 1984, Fibre optic laser Doppler Velocimetry, SPIE VOL. 468 Optics '84, pp. 232

Kramer, R., Müller, H., Dopheide, D., Czarske, J. & Schmidt, N.P. 1994, LDV-system with frequency shift using two modes of a Nd:YAG micro crystal laser, Proc. 7th Int. Symp. Applications to Fluid Mechanics, Lisbon, Portugal, July 11-14, 1994

Müller, H. & Dopheide, D. 1993, Direction sensitive Doppler velocimeter using the optical frequency shift of two stabilized laser diodes, Proc. 5th Int. Conf. Laser Anemometry - Advances and Applications, Koningshof, Veldhoven, SPIE VOL. 2052, pp. 323-330

Müller, H., Kramer, R. & Dopheide, D. 1993, Neue Verfahren zur Erzeugung einer Frequenzshift in der Doppler-Anemometrie mit abstimmbaren Festkörperlasern, PTB Mitteilungen vol. 103 no. 1, pp. 3-17

Oldengarm, J., van Krieken, A. H. & Raterink, H. J. 1976, Development of rotating diffraction gratings and their use in laser anemometry, Optics and Laser Technologie vol. 9, pp. 69-71

Schmidt, N. P., Peuser, P, Heinemann, S. & Mehnert, A. 1993, A model describing the single and multiple spectra of tuneable microcrystal lasers, Optical and Quantum Electronics vol. 25, pp. 527-544

Többen, H., Müller, H. & Dopheide, D. 1994, Brillouin frequency shift LDA, Proc. 7th Int. Symp. Applications to Fluid Mechanics, Lisbon, Portugal, July 11-14, 1994

A Comparison between two different Laser Doppler Anemometer Processors in the low Turbulence Regime

by

Chr. Caspersen

Dantec Measurement Technology

Abstract

The Burst Spectrum Analyzer and the Flow Velocity Analyzer are two very commonly used signal processors in modern laser Doppler Anemometer systems. The BSA is based on a Fourier Transform of each individual burst giving the frequency spectrum followed by a search for the dominating frequency. The FVA is based on correlating the signal with itself after a delay and in this way find the frequency of the signal. There has been performed many both analytical and simultaneous investigations on the two principles in the literature, but there are few comparisons between their performance under realistic measurement conditions. The reason for this can be the many varieties of requirements to a laser Doppler Anemometer processor. In this paper a special area of interest has been investigated, namely the low turbulent regime. There are few investigations in this area, although it is important in the understanding of how correct the LDA is working in terms of estimating the turbulence statistics in all measurement condition. A correct estimation of the turbulence intensity depends on a correct setting of the processor. In most cases there will be an overestimation of the turbulence intensity as the inherent noise is added to the real fluctuating value. The estimation of the added noise can be very difficult, so a number of procedures are generated in the paper in order to find the correct estimate for the turbulence intensity.

In order to have a second reference for the measurement of turbulence intensity, a hot-wire measurement is done under the same conditions. The disturbance from the hot-wire is neglectible in this set-up due to the dimensions. The hot-wire will not suffer from the sources for variance in the LDA-system such as limited transit time, imperfections in the optical configuration in terms of unparallel fringes and noise in the detection system.

The paper will conclude to which lower limit in determination of turbulence intensity an LDA can be used combined with the two processors under investigation.

Introduction

Although LDA has been used in numerous applications where velocity fields are recorded and where turbulence has been measured, it is difficult to find references on analysis of limitations for LDA measurements in low turbulence. The Hot-Wire has always been the dominating device in these applications. For the same reason there are few papers on measurements on turbulence spectra, and they are all very limited in range. This paper will not give an entire analysis of the limitations but focus on the comparison between the Hot-Wire as the reference instrument, and the LDA system supplied with two different processors.

One method to get a correct estimation of the turbulence intensity is to calculate the turbulence spectrum and estimate the noise level from this. In most cases the noise level is easily seen as a point where the spectrum takes a constant value. The total area under the spectrum is an estimation of the fluctuation and the noise, while the area below the noise-level is the added noise. By a simple subtraction, the noise can be reduced significantly. The correct turbulence intensity can now be found by a low-pass filtering of the signal before the RMS-value is calculated.

In this paper the flow from a low-turbulent nozzle is measured both with a BSA and an FVA. A direct estimation of the turbulence intensity is compared with the values achieved from the spectrum. The correction for the additional noise is performed, and the two estimates from the processors are compared.

The contributions to variance in the LDA data

Most of the elements in an LDA system will contribute to an increase in variance in the data coming from the system. These elements are:

1. Inaccurate alignment of the optics. This will always increase the variance. If the beams are not intersecting exactly in the beamwaist position, the fringespacing will be different from one end of the measurement volume to the other. This is demonstrated in fig. 1.

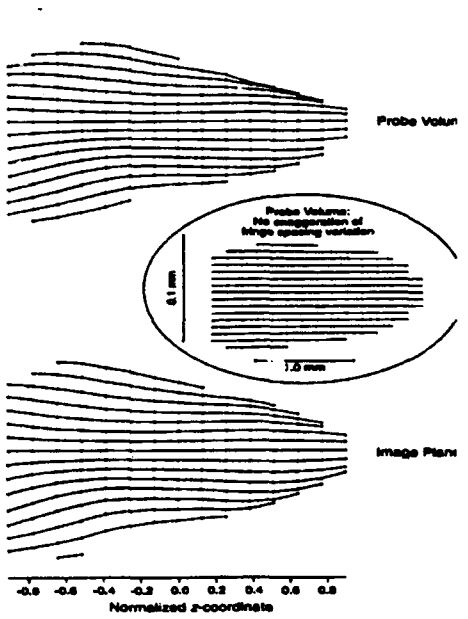

fig. 1 from ref. 1

The influence is a function of the degree of misalignment. However it is not a linear function. It has a maximum with a relatively small misalignment. To a certain degree, this effect is reduced by the fact, that the intensity also has a distribution over the volume, and particles passing the center of the volume with the highest intensity will scatter more light, and in that way have a higher probability to be included in the statistics. As this variance is common to both processors, it is possible to identify the magnitude.

2. Noise from scattering from a background, optical particle interference, ref. 2 and statistical noise from the receiving PM tubes and amplifiers will be treated differently be the two processors. In the comparison, it was intended to adjust the SNR in order to see the noise suppression effect in the two processors. However the SNR remained extremely high during the entire experiment, so this effect is not described further. In general there is a high requirement to the signal to noise ratio, when low turbulence intensities are measured. These noise sources will always add to the variance of the data.

3. Quantization noise from the data output from the processor. Although this can give a significant variation on the individual sample, the influence on the statistics is marginal, as it will be proved in the comparison test, where one processor has a much finer discretization than the other one. The quantization noise is estimated in the section "The theoretical limitations due to quantization".

4. One element that erroneously might reduce the variance, and in that way give an underestimation of the turbulence intensity is particle lag, in the case that large particles are used in flows with large gradients. However in these measurements, this effect is insignificant.

Although all processors are supplied with some kind of validation scheme, there is a general trend, that higher gain will produce more data, also validated data, but the variance is increased. It is therefore relevant to investigate the variance as a function of data-rate. However, due to the high data-rate and high SNR, this is not done in this work. In some references the variance is plotted against signal to noise ratio. Ref. 4. In fig. 2 an example is given on how the different noise sources are contributing to the variance.

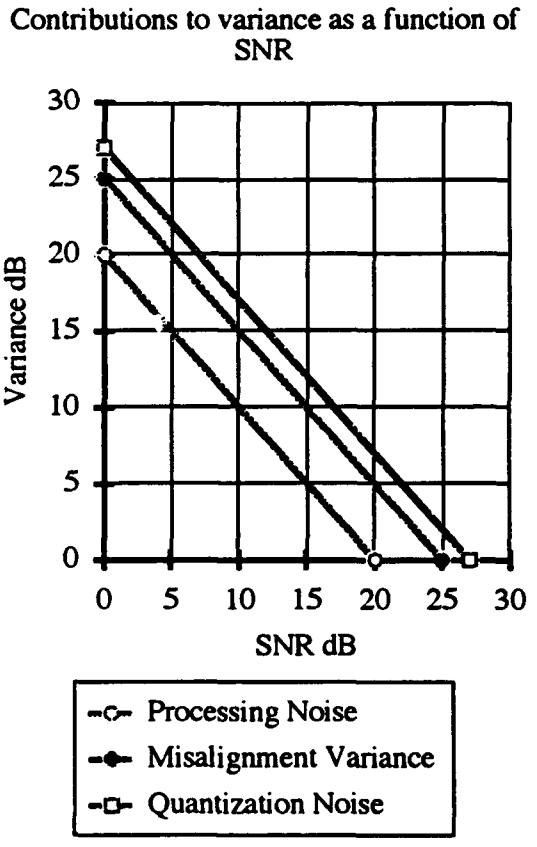

fig. 2

The generation of a Low Turbulence Jet

A low turbulence jet is used for all the measurements in this paper. The reason for the selection of this device is the possibility to achieve the lowest possible level of turbulence, and at the same time have possibilities to increase the turbulence level, both by moving the measurement point in the axial direction or by adding additional turbulence by introducing a grid on the outlet of the nozzle. In order to minimize the influence from blowers and acoustical effects, the nozzle is mounted on the top of a large settling chamber with soft walls. This results in a turbulence structure, that is uninfluenced by the rotation frequency of the blower, or the individual blade frequencies from the blower. The contraction ratio in the nozzle is 13.44:1 and the diameter of the nozzle is 30 mm. This diameter is sufficient in relation to the geometry of the hot-wire and the size of the optical measurement volume. The velocity is the output of the nozzle is close to 5 m/sec. The basic turbulenceintensity is 0,4 %. The entire configuration and the nozzle is shown in fig. 3.

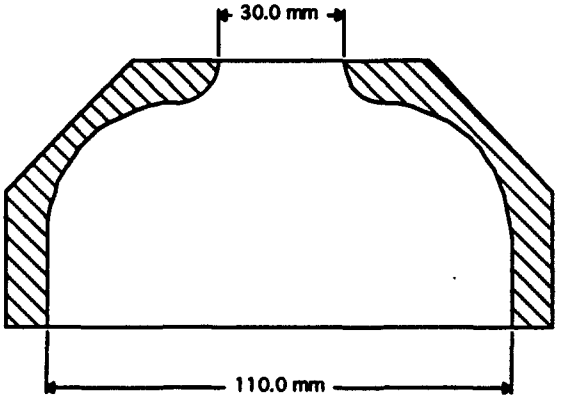

fig.3

The Hot-Wire System

The Hot-Wire system used is the Dantec Streamline System with a 5μ probe P 01. This probe is the most commonly used hot-wire probe for general purpose turbulence measurements. The Streamline System described in ref. 5 includes both the bridge and a signal conditioner for suitable amplification and filtering of the signal.

Included in the system is a calibration system, to assure accurate and stable calibration of the probe before and after the measurement.

The Hot-Wire system is operating completely with analog circuitry. The signal is transmitted to an A/D converter board in a PC.

There are no special means for traversing the probe. This is done manually on a fixture. The Hot-Wire system is shown in fig. 4.

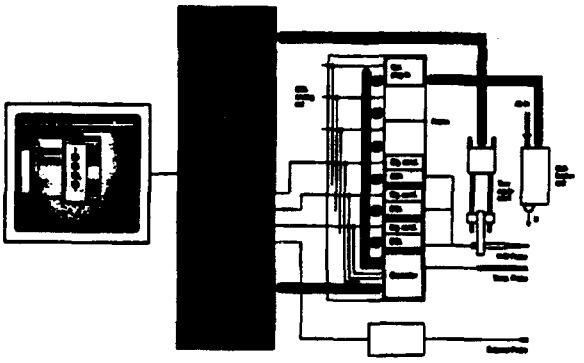

fig. 4

Measurement of the mean velocity and turbulence level using Hot-Wire

The Hot-Wire is positioned in the center of the jet in the outlet plane. This position is regarded as the reference position for all the measurements. In this position the intensity of the turbulence has the lowest value. In order to make measurements with a higher degree of turbulence intensity, the Hot-Wire is traversed to a number of stations along the centerline of the jet. The positions have a distance of 0,5 D, where D is the diameter of the nozzle. The final measurement position is in a distance of 2 D from the nozzle. The results of the mean and RMS measurements are in fig. 5

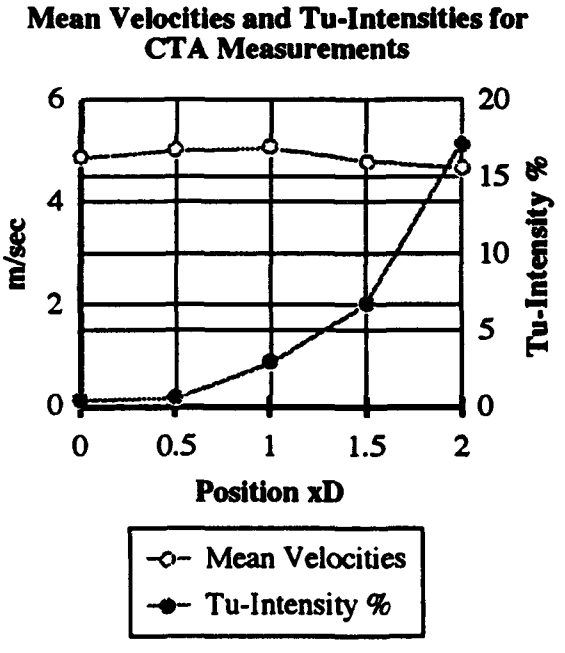

fig. 5

The LDA System

An LDA System is established to measure the vertical component of the flow. It consists of a 85 mm diameter 41X820 Dantec FiberFlow Probe mounted with a 55X29 Beamtranslator and a 55X12 Beamexpander. The probe is able to measure two components of the flow, but only one component is used. The probe is receiving the laser light from a 60X40 Transmitter Box. The focal length is selected to 310 mm and the beamseparation to 64 mm. This will give a calibration factor of 2.504 m/sec/MHz. The laser is an aircooled Ar-Ion laser running at 100 mW. Due to the low laser power, the set-up has facilities to measure in both forward and back scatter. In the forward scatter set-up a receiving system normally used in Particle Dynamic Analyzer is used in order to obtain a large receiving aperture. As the purpose of this work is to map the measured turbulence intensity against turbulence intensity measured by a Hot-Wire, and to compare different processors, forward scatter has advantages in terms of better signal quality and therefore less added noise to the signals.

The two Processors

The two processors under discussion the BSA and the FVA are very different in operating principle. The BSA is based on a Fourier transform of each individual burst, including an advanced validation system, while the FVA is determining the covariance on the same signal with a time delay. As they are operating on the same signal a number of the sources for variance mentioned in section 1 will be identical for both processors, while differences in processing results will be clearly envisioned by this procedure.

The BSA

The BSA and in the new version the Enhanced BSA has since it's introduction been used in a large number of difficult applications. In this context the application is simple as the SNR is high. On the other hand an increase in variance on the data will lead to increased values in the turbulence intensity measured.

The operating principle in the BSA is described in fig. 6. The signal is filtered in a band-pass filter which is selected by the user. After the filtering the signal is amplified and splitted into two signals. The advantage in this is the possibility to use a complex FFT on the signal. The two signals are multiplied by an oscillator signal with a 90 degree phaseshift. The signals are now seen as a complex signal with a real and an imaginary part. In order to eliminate higher harmonics both parts are low pass filtered. This is followed by an A/D conversion in four bits. A more detailed discussion on the selection of four bits are given in the paper in ref. 7. "Quantization of LDA/PDA signals:How many bits are needed ?" by Knud Andersen and Anders Høst-Madsen. presented at this conference.

The digitized information is stored in the input buffer in order

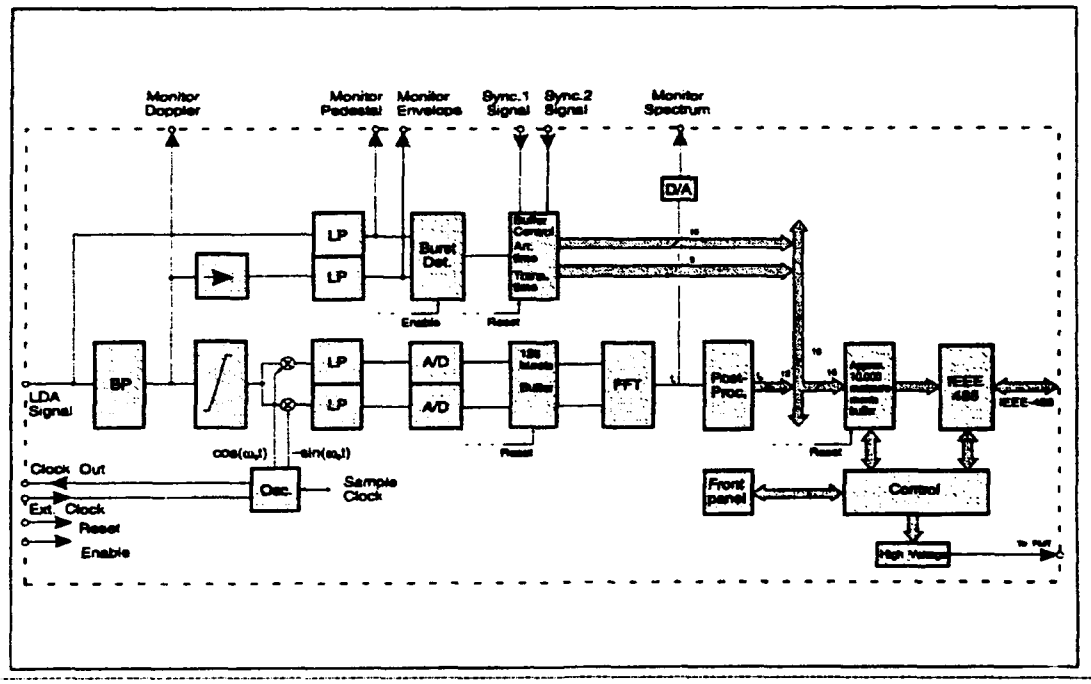

fig. 6

to balance out the uneven arrival of signals. After the input buffer the FFT takes place.

After the FFT process, a post validation system based upon an evaluation of the spectrum is used to remove signals without a significant spectrum.

In parallel to this process the signal is validated in the burst detector in order to select the signals from the background noise. This detection system is the dynamic burst detection system described in ref. 9.

The entire information including the information on arrival time and transit time is collected in the output buffer before it is transmitted to the connected computer in most cases a PC running the dedicated software package BurstWare. For further information on the processor ref. 9 is describing the functions in details, while ref. 4 is discussing the operating principle.

The FVA

The FVA is based upon a method for accurate determination of phasedifference between two different signals. This is very suitable for the application the FVA originally was intended for , namely the Particle Dynamic Analyzer, where phase measurement is the most important issue, in order to measure particle size.

The principle diagram for the FVA is simple, it is shown in fig. 7.

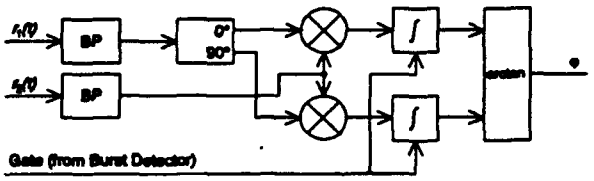

fig. 7

If the two signals are described as:

$$S_1 = A_1 \cdot \cos(\omega t)$$
$$S_2 = A_2 \cdot \cos(\omega t + \varphi)$$
$$S_1^1 = A_1 \cdot \cos(\omega t)$$
$$S_1^2 = A_1 \cdot \sin(\omega t)$$
$$P_1 = S_1^1 \cdot S_2 = A_1 \cdot A_2 [\cos(\omega t) \cdot \cos(\omega t + \varphi)]$$
$$P_2 = S_1^2 \cdot S_2 = A_1 \cdot A_2 [\sin(\omega t) \cdot \cos(\omega t + \varphi)]$$
$$P_1 = \tfrac{1}{2} A_1 A_2 [\cos(-\varphi) + \cos(2\omega t + \varphi)]$$
$$P_2 = \tfrac{1}{2} A_1 A_2 [\sin(2\omega t + \varphi) + \sin(\varphi)]$$
$$\int P_1 = \tfrac{1}{2} A_1 A_2 \cos(\varphi)$$
$$\int P_2 = \tfrac{1}{2} A_1 A_2 \sin(\varphi)$$
$$\varphi = a\tan\left[\frac{\int P_2}{\int P_1}\right]$$

Two signal with the same frequency, but with different phases are passed to a bandpass filter to eliminate noise. One of the signals is splitted up in two signals with a phase difference of 90^o. The unshifted and 90^o shifted signals are led to two mixers, where the other signal is multiplied. This will give two signals representing the cosine and the sine part of the phase information.

If the two signals are the same signal with a known delay the phasedifference is identical to the frequency after a division with the imposed time delay.

In ref. 6 a more detailed description of the principle is given.

The theoretical limitations in the accuracy of the results based upon the resolution of the processor

This aspect is discussed in details in the paper "The Limitations in High Frequency Turbulence Spectrum Estimation using the Laser Doppler Anemometer" which is also presented at this conference. The conclusion from that paper is , that an output with more than 4 bits will be sufficient for the kind of measurements under discussion.

Measurement of turbulence level and measurement of turbulence spectra using the FVA

The FVA is adjusted to optimize the situation with a mean velocity around 5 m/sec. and a low turbulence intensity. However due to the limited selection of settings, the Bandwidth must be set at 4 MHz in order to fit the meanvelocity. One interesting aspect by using the FVA is the resolution on the output of the processor.

For measurements where turbulence spectra are extracted, one million samples are used inorder to have a reasonably low variance on the spectrum

A significantly lower number, between 50.000 and 100.000 are used if only mean and RMS-values are calculated. With the data-rate on 13 - 14 kHz, a record on 50.000 will span 3 sec, a time significantly longer than the time scales in the flow. With the low turbulence level the different weightning methods on the mean and RMS will give identical results.

Measurement of turbulence level using the BSA

The optimal setting of the processors in relation to measurement of turbulence is selected. In this case the selection is simple and uncritical, as the SNR is very high. The span can be selected to the lowest possible value without infringing the turbulence measurement. In this case, with an almost constant mean value at 5 m/sec, the center frequency is set to 2 MHz and the span to 2 MHz. Although in principle independent of bandwidth, an increase in bandwidth, even at the high SNR will result in an increase in variance.

The Turbulence Spectrum

The turbulence spectrum is calculated on all the measurement stations. A characteristic spectrum for the probe positioned in the outlet of the nozzle is in fig. 8. The spectrum is not very significant. It is dominated by the frequency generating the turbulence. This frequency is close to 100 Hz. There are some peaks found at higher frequencies both with the CTA and the FVA, however, it has not been possible to find and specific explanation on these peaks.

As another example, the spectrum is calculated at the 2D position. In this case the spectrum is in fig. 9. This spectrum has the characteristics of turbulence spectrum, and it is indicating to which limit it is possible to obtain spectral information using an LDA system. The entire discussion on limitations in spectral estimation is given in the paper "The Limitations in High Frequency Turbulence Spectrum Estimation using the Laser Doppler Anemometer" presented at this conference, and given as ref. 8.

Results

The results are shown in fig. 10 and 11. The two LDA processors are giving the same mean-values with maximum variation of 1%, while the Turbulence intensities are determined within 0.5%. This is indicating an accuracy, that easily can be obtained by processors operating on the same signal from the optical set-up although the measurements are not recorded simultaneously. Both processors are giving a turbulence intensity at 0.7% at the outlet of the nozzle. The CTA is measuring a lower value 0.4%. As the seeding is removed when the LDA measurements are done, it is not absolutely comparable. However there are reasons to believe, that the CTA is better to resolve the extremely low turbulence levels in the outlet.

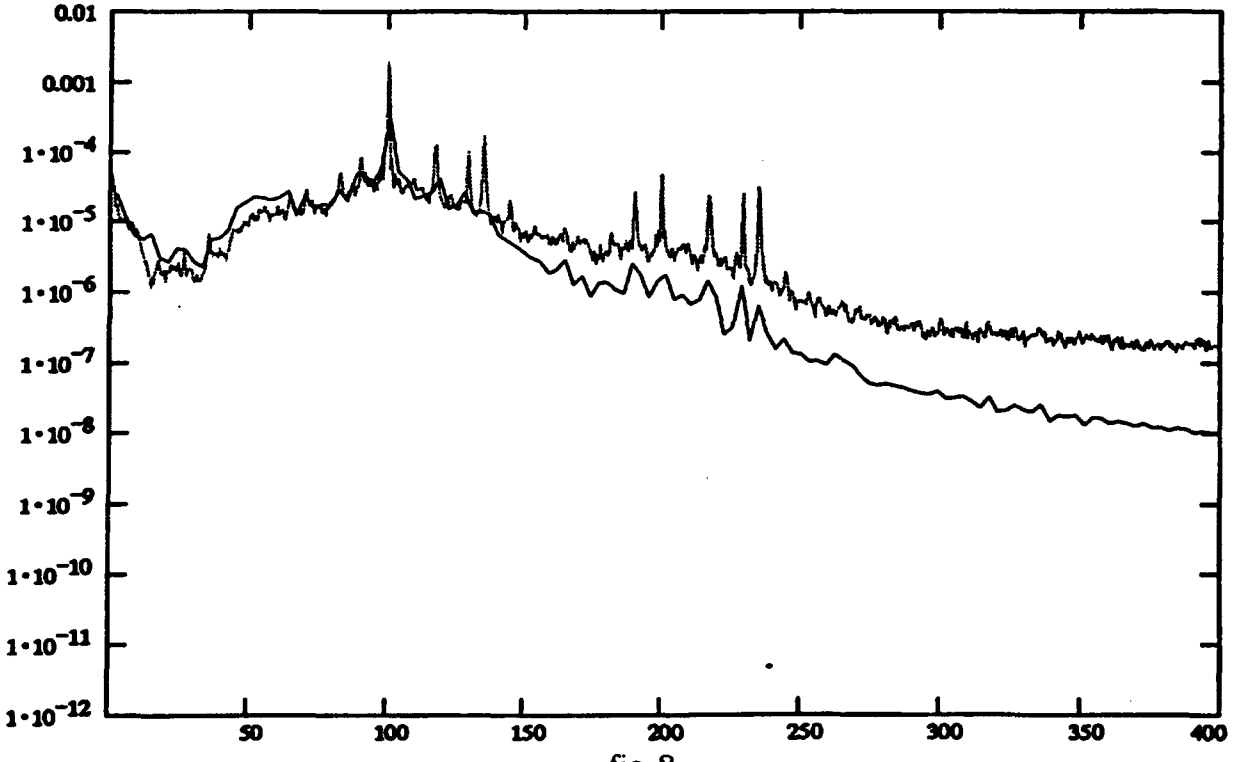

fig. 8

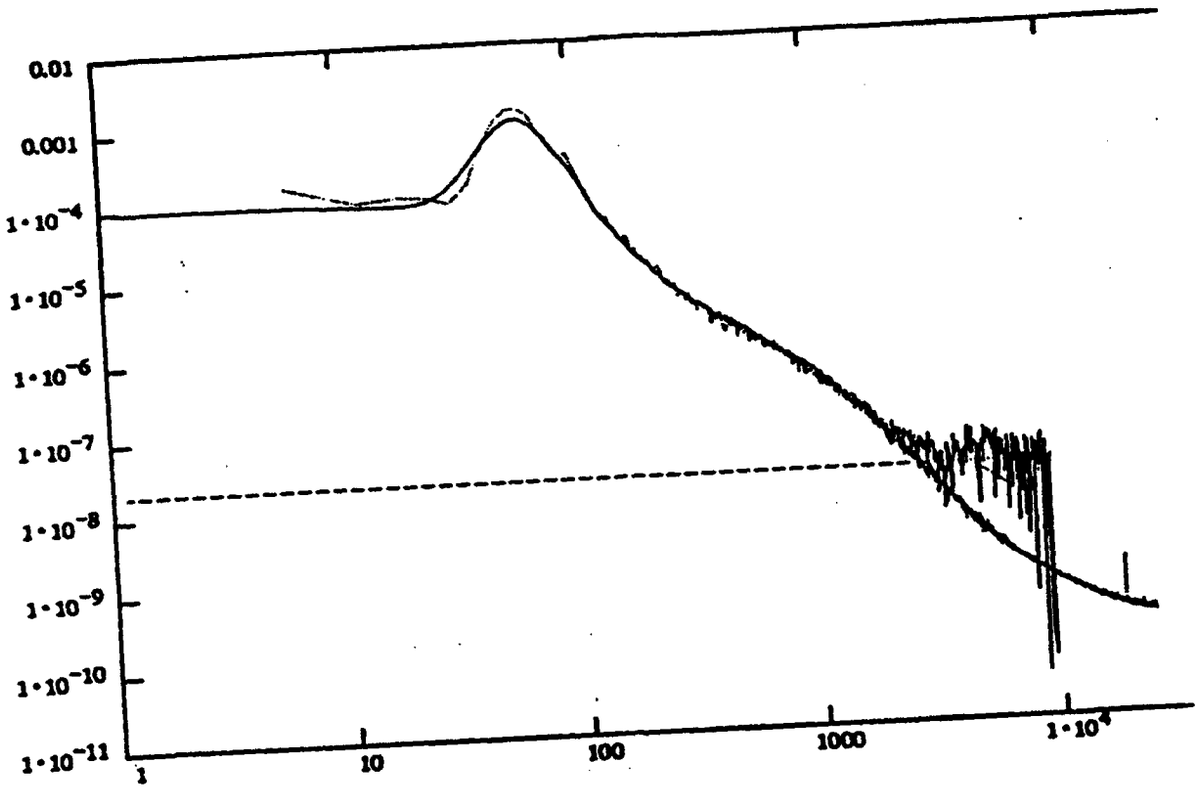

fig. 9

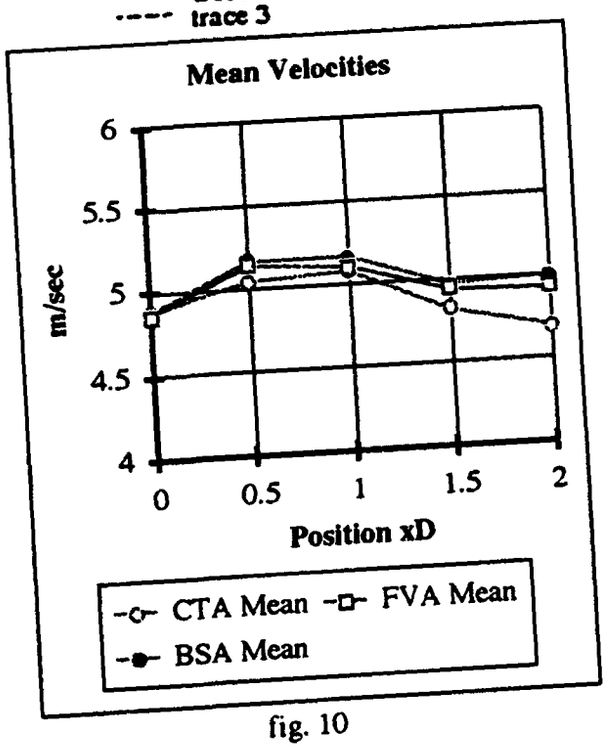

fig. 10

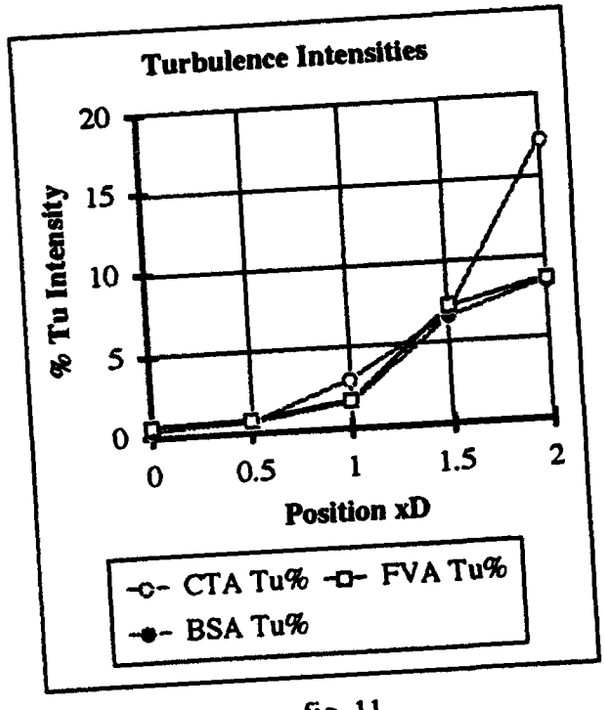

fig. 11

Summery and Conclusion

Two processors with different operating principles have been described and used to measure in the low turbulent regime. The processors are exhibiting very similar results and results comparable to a CTA system. The following conclusions can be drawn:

1. The comparison of the processors

As seen from the results, the two processors are giving extremely similar results, even at the very low degrees of turbulence. Except for the lowest value, the FVA is indicating a slightly higher turbulence, however the difference to the BSA is extremely small. The conclusion is therefore, that in this experiment, the two processors will give the same result. However it must be kept in mind that the SNR is extremely good in this experiment. If that is changed the comparison must be repeated in order to verify the limitation of the two processors .

2. Comparison to CTA measurements

As expected the CTA is able to detect turbulence at a lower level than the LDA system is able to. However more optimization could be done in order to improve the LDA measurements further. The comparison is also clearly indicating, that the CTA has a sensitivity for fluctuations in other components, than the one the LDA is measuring. The conclusion is therefore, that the CTA is still a very valuable instrument for measurement of low turbulence, while higher degree of turbulence will require a more advanced probe, like the X-wire. With a degree of turbulence above 1% the LDA will give a correct prediction of the turbulence if a proper processor is used and a sufficient number of samples are recorded.

References

1.

Fringe field quantification in an LDV probe volume by use of a magnified image

P. C. Miles, P. O. Witze

Experiments in Fluids 16, 330 - 335

Springer Verlag 1994

2.

Limited accuracy of turbulence measurements in laser Doppler anemometry

B. Ruck, B. Pavlowski

Proceedings from the Fifth International Conference on Laser Anemometry

23 - 27 August 1993

Koningshof, Veldhoven, The Netherlands

3.

Three-component LDA Measurements

P. Buchhave

DISA Information No. 29

January 1984

4.

Spectrum Analysis of LDA Signals

L. Lading

Proceedings of an International Specialists Meeting on

The Use of Computers in Laser Velocimetry

ISL May 18-20 1987

5.

StreamLine, The Operation Manual

Dantec 1994

6.

Burst Detection in Phase/Frequency Processors

Knud Andersen and Lars Lading

Proceedings from the Fourth International Conference on Laser Anemometry, Advances and Applications

Cleveland, Ohio

August 5 - 9, 1991

7.

Quantization of LDA/PDA signals:How many bits are needed

Knud Andersen and Anders Høst-Madsen

Proceedings from the seventh International Symposium on Applications of Laser Methods to Fluid Mechanics

11 - 14 July 1994, Lisbon

8.

The Limitations in High Frequency Turbulence Spectrum Estimation

Anders Høst-Madsen and Chr. Caspersen

Proceedings from the seventh International Symposium on Applications of Laser Methods to Fluid Mechanics

11 - 14 July 1994, Lisbon

9.

A new Processing Method for Near Wall LDA Measurements

Chr. Caspersen

Proceedings from the Near-Wall Turbulent Flows Conference

15 - 17 March 1993 Tempe Arizona

Session 24.
Two Phase Flow Instrumentation III

A rigorous procedure for design and response determination of phase Doppler systems

Amir Naqwi and Rajan Menon

Fluid Mechanics Instruments Division, TSI Inc., P.O. Box 64394, St. Paul, MN 55164, USA

1 Introduction

A three-step procedure is described for selecting the critical parameters of a phase Doppler system and for determining the transfer function of the instrument. This procedure covers all possible values of the material properties for homogeneous spherical particles and has the potential to be transformed into an *expert system* for setting up phase Doppler instruments and preparing look-up tables to convert measured phases into particle diameters.

The first step of the design is based on geometrical optics. The PDA designers' chart introduced earlier [1] is divided into 15 domains representing certain combinations of particle refractive index and scattering angle. Within each domain, scattering characteristics are fairly consistent for a given state of polarization and a given level of light attenuation through the particle. Charts are provided, so that the PDA user can select a state of polarization and a range of scattering angles for his/her application. At this stage, an estimate of required beam angle and elevation angle is available for a standard layout. Also, the beam angle for a planar layout can be estimated at this level.

In the second step, due attention is given to the particle trajectory effects. As shown by Naqwi [2], the trajectory effect becomes more and more severe with the increasing dynamic range and concentration of the particles and leads to narrower choices of scattering angles. For transparent particles in a rarer medium, charts are provided to select the scattering angles that would minimize the trajectory effect.

In the third step of design, a choice between planar and standard (or orthogonal) optical layout [2,3] is made. The newly introduced Adaptive Phase/Doppler Velocimeter (APV) can be configured as a standard or a planar system.

Subsequently, size and shape of the receiving apertures are determined. After selection of the optical parameters, Mie scattering theory is used to compute the phase-diameter relationship, provided that the level of confidence regarding the proposed geometrical scattering mechanism is low. Usually, this relationship is not strictly monotonic and may exhibit oscillations with high (submicron) or low periodicity. A smoothing procedure is outlined that transforms the Mie response curve to the nearest nonlinear monotonic function. This procedure results in smaller errors and uncertainties than the commonly used linear regression technique. A look-up table is subsequently generated that allows conversion of phase into particle diameter. The authors prefer to use look-up tables as opposed to conversion factors, even if the phase-diameter relationship is strictly linear. The look-up tables enable faster processing of the data.

2 Identification of Operating Regime

Phase Doppler systems were originally analyzed using the geometrical theory of light scattering, which indicates that the relationship between the phase shift and the particle diameter is linear, provided that a single geometrical scattering mode is dominant. One of the first three modes of geometrical scattering is usually employed for particle sizing. These modes may be described as (i) reflection of light from particle surface, (ii) refraction of light through the particle, and (iii) emergence of light rays from the particle after one internal reflection.

The conditions under which one of these scattering modes are applicable, have been discussed in literature, but only with reference to special cases. A considerable number of cases are discussed by Naqwi & Durst [1 & 4], who also introduced PDA designers' chart, shown in Fig. 1. In this chart, areas covered by horizontal and vertical lines represent the presence of refracted and internally reflected light respectively. The spacing between the vertical lines is reduced to half and one-third in some regions in order to indicate the presence of double and triple contributions of the internally reflected rays. Furthermore, several critical scattering angles, such as those representing the Brewster conditions for surface reflections and internal reflections as well as rainbow angles are included.

The governing equations for some higher order angles are not given in Ref. 1. These mathematical relationships are provided below:

Brewster condition for the first internal reflection:

$$\cos\theta = \left(m^2-1\right)\left(m^4-14m^2+1\right)\Big/\left(m^2+1\right)^3, \qquad (1)$$

where θ and m represent the scattering angle and the refractive index of the particle relative to the surrounding medium.
Second rainbow:

$$\cos\theta = \left(m^8+4m^6+270m^4-972m^2+729\right)\Big/32m^6 \quad (2)$$

Brewster condition for second internal reflection:

$$\cos\theta = \left(-m^8+28m^6-70m^4+28m^2-1\right)\Big/\left(m^2+1\right)^4 \quad (3)$$

The introduction of the designers' chart has enabled us to devise *generalized criteria* for determining the applicability of individual geometrical scattering modes, instead of restricting the discussion to a few special cases. In this context, four independent variables are considered in the present work, i.e. refractive index of the particle relative to the surrounding medium, attenuation coefficient of the particle material, scattering angle of the receiving optics and polarization of the incident light.

The designers' chart is divided into 15 domains based on the values of scattering angle and the refractive index, as shown in Fig. 2. The rationale for the domains in Fig. 2 is provided by the critical angles depicted in Fig. 1, which strictly represents non-absorbing particles. Subsequently a measure of light attenuation is incorporated in the above scheme of classification. An attenuation parameter is introduced as below:

$$a = \chi d_{p\max} = 4\pi n\kappa d_{p\max}/\lambda_0 . \qquad (4)$$

where $d_{p\max}$ is the largest particle diameter and χ is 1/e-attenuation coefficient, which is related to the imaginary part $n\kappa$ of the refractive index and the wavelength of light in vacuum λ_0 as shown above.

Parameter a represents the fraction of the incident light absorbed in the largest particle during its transmission through the particle. A very large range of this parameter may be encountered in practice. Based on the numerical value of this parameter, the light absorbing character of particles may be classified as follows:

1. Very weak attenuation: $a \le 0.005$
2. Weak attenuation: $0.005 < a \le 0.05$
3. Moderate attenuation: $0.05 < a \le 500$
4. Strong attenuation: $500 < a \le 4000$
5. Very strong attenuation: $a > 4000$

In the case of weak attenuation, scattering mechanism is not significantly affected by light absorption. However, some caution is required unless attenuation is qualified as 'very weak'. Similarly, strong attenuation means that only reflected light will be dominant at all the scattering angles. However, the designer should proceed cautiously, unless attenuation is designated as 'very strong', which typically pertains to metallic particles. In the case of moderately absorbing particles, none of the geometrical scattering mechanism is generally applicable.

Based on above considerations, *scattering mode charts* of Fig. 3 are generated. For the 15 domains and 5 levels of attenuation, dominant scattering modes are indicated. Separate charts are given for parallel and perpendicular polarization. The differences between the two charts arise from the fact that various Brewster conditions are met only in the case of parallel polarization. The dominant scattering modes are represented by circles, triangles and squares that depict reflection, refraction and internal-reflection respectively. The closed and open symbols signify whether the level of confidence in the corresponding geometrical mechanism is high or low respectively. The symbol × is used to indicate that none of the three geometrical scattering modes is expected to dominate.

If the level of confidence is high, a linear relationship between phase and diameter is expected and geometrical scattering theory can be used to determine phase-diameter conversion factor with an accuracy of 5%. If the confidence level is low, Mie scattering theory should be used to obtain the phase-diameter relationship. Nevertheless, a low level of confidence should not be interpreted as likelihood of poorer measurements. It simply means that a single geometrical mode of scattering is not fully dominant. However, accurate phase Doppler measurements may be possible.

Deviations from linearity in phase-diameter relationship may exhibit as (i) fluctuations (non-monotonic behavior) and/or (ii) monotonic non-linear behavior. If the latter trend is dominant, then a spectral domain smoothing of the Mie response curve, as illustrated in Sec. 5, is appropriate for obtaining a phase-to-diameter conversion table. Otherwise, the *joint probability method*, as explained in Ref. 2, should be employed.

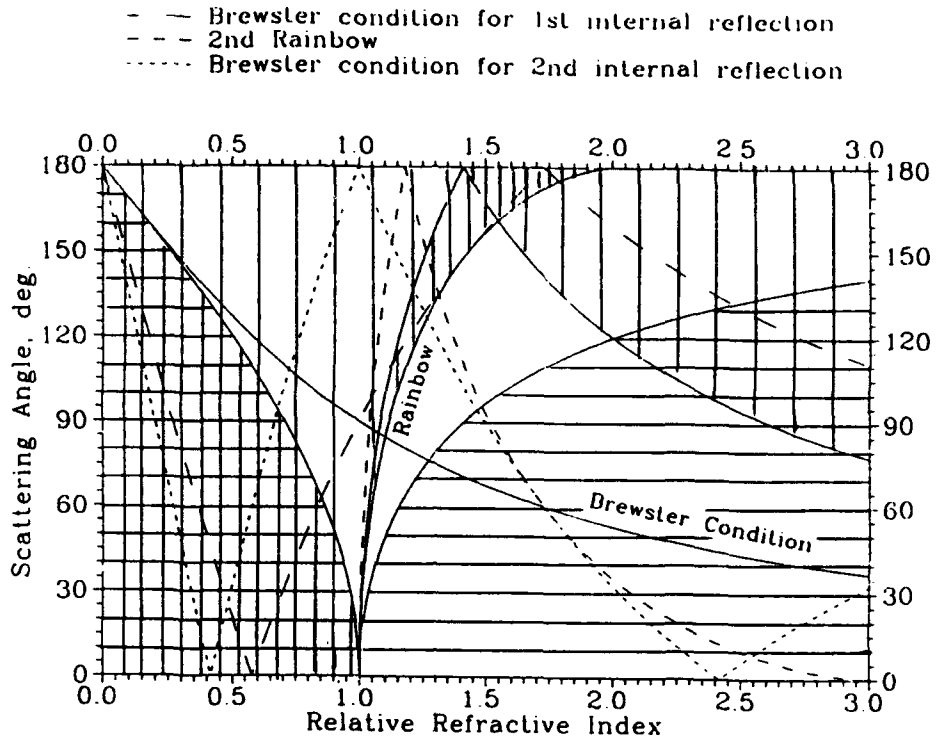

Figure 1: Critical scattering angles as a function of refractive index

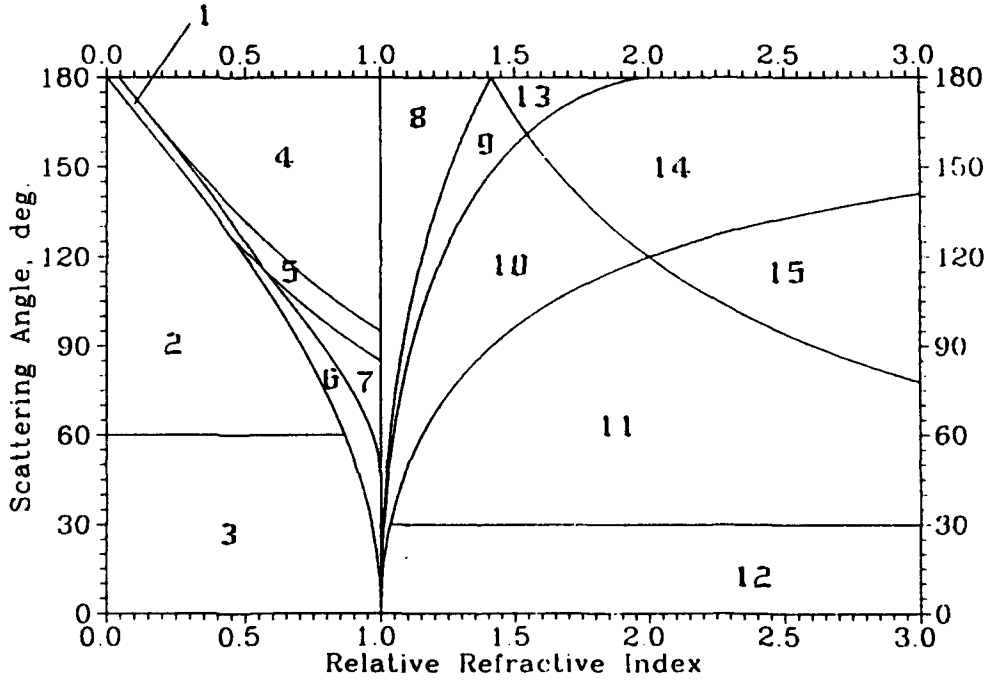

Figure 2: Scattering domains based on refractive index and scattering angle

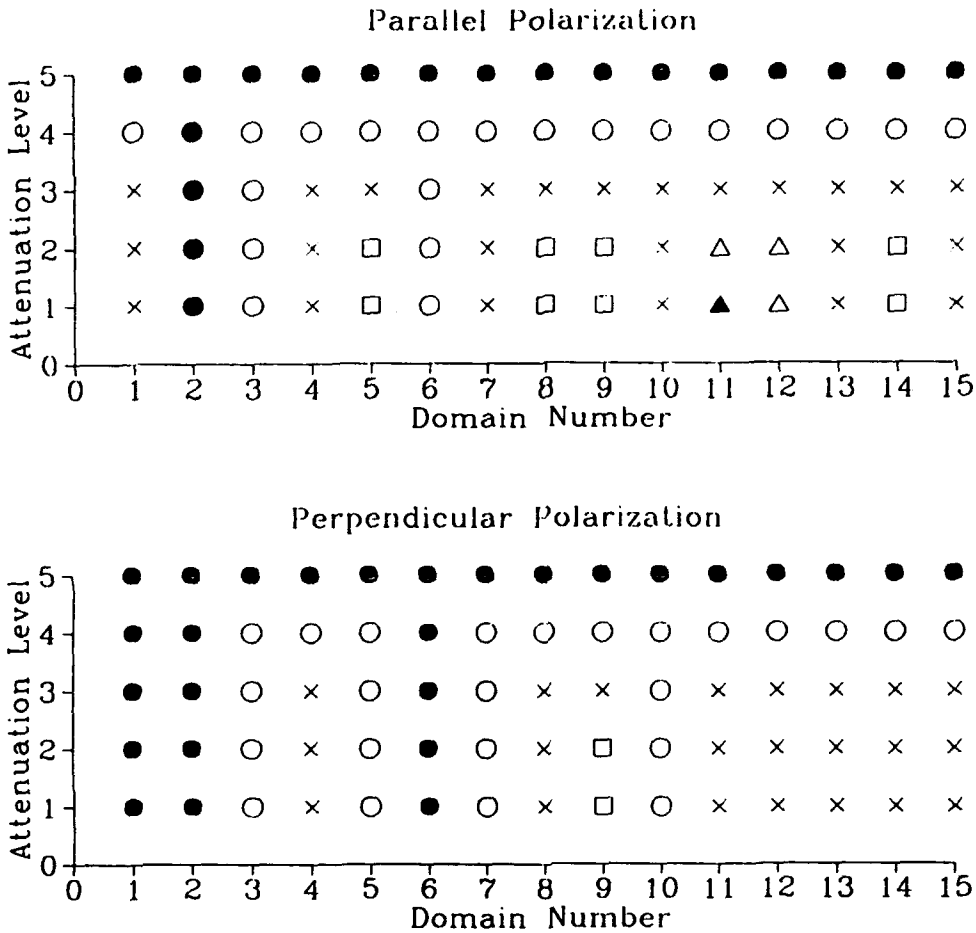

Figure 3: Scattering mode charts

3. A Consideration of Trajectory Effects

The measuring volume diameter is set by default to be comparable to the largest particle diameter in order to suppress the adverse effects of the Gaussian intensity profile. In the case of transparent particles with refractive indices larger than 1, the charts of Fig. 4 & 5 are consulted for further optimizing the scattering geometry in respect of the Gaussian profile effect. Figure 4 receives two inputs: (i) the measuring volume to particle diameter ratio, and (ii) the particle dynamic range.

A large dynamic range requires a low enough trigger level, so as to register the weak signals from small particles. This also means that a large particle will generate signals from a large volume, including the undesirable regions of the illuminating field. Figure 4 provides a measure of the non-uniformity of particle illumination. The light rays reaching a detector after reflection and refraction enter the particle at different locations. The separation between these two incidence locations is conservatively estimated as particle diameter itself. The output of Fig. 4, i.e. the ordinate (maximum incidence ratio: refraction to reflection), indicates how much the intensity of incident light at the incidence point of refraction — which is presumably the dominant scattering mechanism — could be smaller than that at the incidence point of reflection, under the worst conditions.

Figure 5 shows the ratio of reflected to refracted light in the scattered field (scattering ratio: reflection to refraction) for uniform illumination. The abscissa and ordinate of Fig. 5 represent 100 × refractive index and the scattering angle respectively. The latter should be chosen appropriately, so that the output of the second

chart is smaller than that of the first chart. This condition ensures that the refracted light signal dominates the reflected light signal. This condition suffices to ensure that correct size measurements are obtained, at least in the neighborhood of critical particle diameters introduced in Ref. 2.

Figures 4 & 5 are based on geometrical optics but are validated using generalized Lorenz-Mie theory [5] that fully takes into account the Gaussian structure of the laser beam.

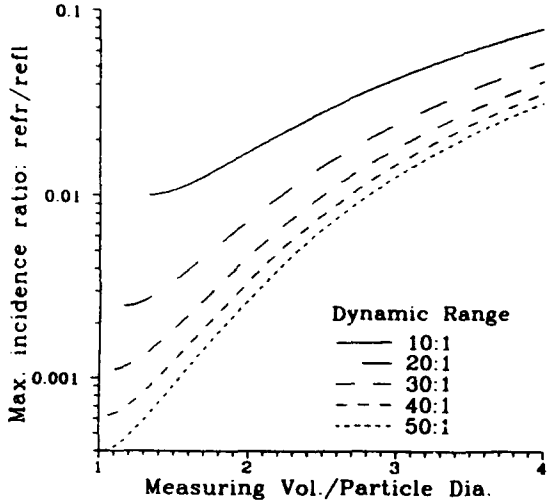

Figure 4: Non-uniformity of particle illumination

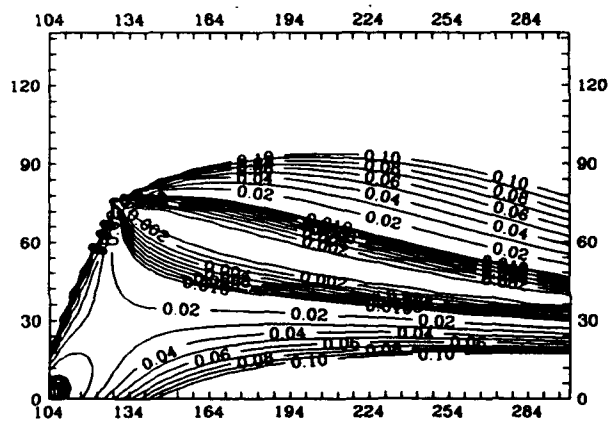

Figure 5: reflection/refraction ratio in the scattered field

4. Type of Layout and Receiver Geometry

For a given particle size range Δd_p, some key design parameters of the system can be selected using the scattering angle θ and the corresponding geometrical scattering mode determined through the procedures of Sec. 2 & 3. These parameters ascertain the elevation angle and the beam angle in the case of a standard phase Doppler system. As shown in Refs. 1 & 4, the phase factor is approximately proportional to $\sin\alpha\sin\psi$, which in turn depends primarily upon the beam spacing s_b, spacing between centroids of the receivers s_r, the receiver spacer angle β and the focal lengths of the transmitting and the receiving units given by f_t and f_r respectively. These parameters are illustrated in Fig. 6 for a typical APV layout and are related as below:

$$\frac{s_b}{f_t}\left(\frac{s_r}{f_r}+\beta\right) \le \frac{\lambda}{\Delta d_p} F_s(\theta,m). \qquad (5)$$

The function F_s takes the following form for a reflecting particle,

$$F_s = 4\sin(\theta/2). \qquad (6)$$

For a refracting particle,

$$F_s = \frac{4\cos(\theta/2)\sqrt{1+m^2-2m\cos(\theta/2)}}{m}. \qquad (7)$$

The above equations follow from Eqs. (60) & (63) of Ref. 1. For particles with internal reflection as the dominant scattering mechanism, an explicit analytical expression for F_s does not exist and the function is computed using an iterative method.

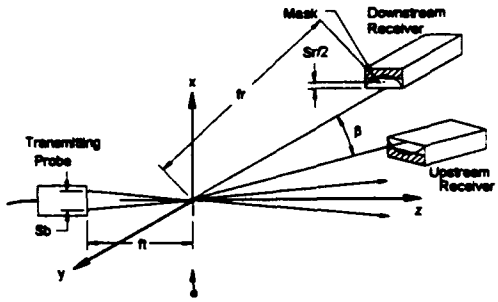

Figure 6: APV design parameters

Adherence to Eq. (5) ensures that the optical parameters are selected to cover a size range $\Delta d_p = d_{p\max} - d_{p\min}$, where $d_{p\min}$ may have a non-zero value. It may be reminded here that conventional approaches to phase Doppler design are based on the presumption that the smallest particle diameter is always nearly zero, which results in an unnecessary loss of sensitivity in the case of narrow size distributions with $\Delta d_p/d_{p\max} << 1$. APV hardware obviates this restriction and provides maximum sensitivity in the case of narrow size distributions by using separate receivers, whose angular spacing β can

be increased to match a narrow size range. This is not possible with conventional PDA receivers, where detector spacing is severely limited by the numerical aperture of the receiver lens.

It is also obvious from Eq. (5) that for very small particles or very small size ranges, the right-hand side of this equation would become so large that it would not be possible to obtain adequate sensitivity even if the largest practical value of β is employed. For such applications, planar layouts are useful.

In a planar arrangement, scattering angle is represented effectively by the elevation angle ψ, whereas off-axis angle is zero. Invoking these conditions in Eqs. (60) & (63) of Ref. 1, the appropriate hardware settings of a planar layout are determined through

$$\frac{s_b}{f_t} \le \frac{\lambda}{\Delta d_p} F_p(\theta, m), \tag{8}$$

where

$$F_p = \frac{1}{\cos(\theta/2)} \tag{9}$$

for reflecting particles and

$$F_p = \frac{\sqrt{1+m^2-2m\cos(\theta/2)}}{m\sin(\theta/2)} \tag{10}$$

for refracting particles. Usually planar layout provides adequate sensitivity to measure particle diameters as small as a fraction of the light wavelength.

5 Final Remarks

Once a complete specification of the optical hardware is achieved, Mie scattering calculations may be conducted. If the level of confidence in the scattering mechanism is high, then these calculations are not necessary for obtaining phase-diameter relationship but if they are conducted for other reasons, large intervals of particle diameter, e.g. 5 μm, may be employed. Otherwise, small increments, such as 0.1 or 0.2 μm, should be used.

If necessary, the phase-diameter relationship based on the Mie theory, may be made monotonic using smoothing in the spectral domain. Subsequently, a lookup table would be generated for converting measured phases into particle diameters.

Figure 7 illustrates the smoothing process. The results based on Mie calculations are shown by a solid line, whereas dotted line represents the relationship after smoothing, which is the basis for the look-up table. It is clear from this figure that smoothing procedure would provide better accuracy than linear regression, which is usually employed for obtaining PDA transfer function.

References

1. A. Naqwi & F. Durst, "Light scattering applied to LDA and PDA measurements, Part 1: Theory and numerical treatments", Part. Part. Syst. Charact. 8 (1991) 245–258.
2. A. Naqwi, "Innovative phase Doppler systems and their applications", Part. Part. Syst. Charact. 11 (1994) 7–21.
3. A. Naqwi & M. Ziema, "Extended phase Doppler anemometer for sizing particles smaller than 10 μm", J. Aerosol Sci. 23 (1992) 613–621.
4. A. Naqwi & F. Durst, "Light scattering applied to LDA and PDA measurements, Part 2: Computational results and their discussion", Part. Part. Syst. Charact. 9 (1992) 66–88.
5. G. Gréhan, G. Gouesbet, A. Naqwi and F. Durst, "Trajectory ambiguities in phase Doppler systems: use of polarizers and additional detectors to suppress the effect", Proc. 6th Intl. Symp. on Applications of Laser Techniques to Fluid Mechanics, Lisbon (1992) Paper # 12.1.

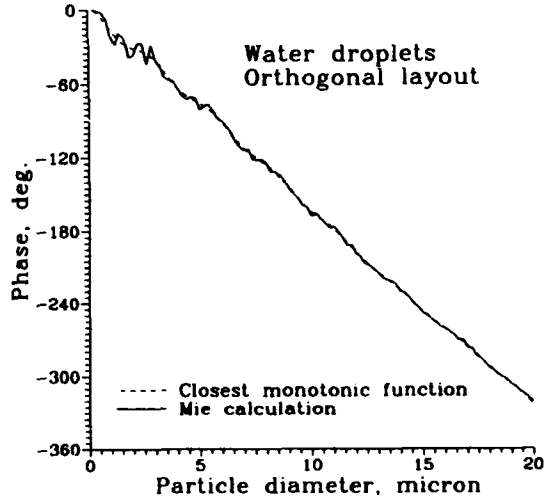

Figure 7: Mie response curve and the nearest monotonic function

Experimental and theoretical studies of the sources of uncertainties in a phase Doppler system

Michael Seidel†, Maris Ziema†, Amir Naqwi* and Franz Durst†

†*Lehrstuhl für Strömungsmechanik, University of Erlangen, Federal Republic of Germany*

*Fluid Mechanics Instruments Division, TSI Inc., St. Paul, MN 55164, USA

1 Introduction

The present study is concerned with two physical effects that need to be taken into account in the selection of a phase Doppler layout in order to obtain accurate results. The first phenomenon considered here is the multiple scattering effect, i.e. modification of the light scattering pattern of the particle under investigation, due to presence of other particles in the laser beam. Since phase Doppler is a single-particle technique, it is understood that the quality of the measurement would deteriorate if more than one particle is present in the measuring volume. However, it is demonstrated herein that due to multiple scattering effect, the signal quality may also degrade even if there is only one particle in the measuring volume. This effect is commonly encountered, when a large particle crosses one of the laser beams *outside* the measuring volume and at a location closer to the laser source than the measuring volume. The light scattered by this particle has a secondary scattering from the primary particle within the measuring volume. The size and velocity information about the measured particle may be affected adversely by this phenomenon. Ruck [1] has examined this effect in connection with LDV applications.

In the present study, the multiple scattering effect was produced by using two independent units of vibrating orifice droplet generator (TSI Model 3450). The first droplet generator was used to maintain a steady chain of drops through the measuring volume of a phase Doppler system. The second droplet generator was employed to create a shower of freely falling secondary drops that intersected the laser beams ahead of the measuring volume. Phase Doppler signals with and without the secondary droplets are presented and analyzed for estimating the associated errors. The measured effects are explained using geometrical optics. Limits on measurable particle concentration, imposed by multiple scattering, are estimated.

The second phenomenon considered in this article is the particle trajectory effect in PDA. It is well-known that the phase signal of a transparent particle may have a strong dependence on the trajectory of the particle through the measuring volume. Obviously, this effect is not desirable and several authors have proposed different schemes for its elimination. Recently, Naqwi [2] has identified a *critical particle diameter* for which the trajectory effect manifests itself only as uncertainties in the signal visibility, without affecting the phase of the signal. The knowledge of the critical diameter helps in optimizing the optical layouts, so as to minimize the trajectory effect in a particular application.

In the present work, the existence of the critical diameter is verified experimentally.

2 Experimental Setup

The transmitting optics consisted of a He-Ne laser with 633 nm wavelength and 15 mW laser power. The collimated laser beam had a $1/e^2$-diameter of 0.9 mm and was split into two parallel beams with a spacing of 20 mm. An achromatic doublet with focal length of 250 mm and diameter of 80 mm was used to focus the laser beams into a measuring volume with diameter 220 µm. This measuring volume diameter was large enough to suppress the effect of particle trajectory, so that pure multiple scattering effect could be examined.

For studies of the trajectory effect, the laser beam was expanded to 2.2 mm and hence, focused to a diameter of 90 µm in the measurement volume.

The receiving optics were located at an off-axis angle of 30° and consisted of two avalanche photodiodes (APD), positioned at elevation angles of ±3.69°. Both the APDs received light scattered by the particle within a half-cone angle of 2.77°.

The output signals from the APDs were bandpass filtered (0.5–2 MHz) and transferred to a transient recorder for digitization and further on to a plug-in PC board for processing.

Two vibrating orifice generators were employed to produce droplets of diethyl-phathalate (DP). This spray liquid was chosen because of its high viscosity and lower surface tension, which results in a stable operation of the droplet generator. The droplet streams of DP were found to be more stable than water or alcohol.

The refractive index of DP at 20 °C is 1.502, which results in a sensitivity of 3.82°/μm for the PDA system.

The head of the primary droplet generator was attached to a two-axis translator, so that the droplet stream could be positioned arbitrarily in the plane of the fringes, i.e. *yz*-plane, as illustrated in Fig. 1. For examining the multiple scattering effect, the droplet stream was located at the center of the measuring volume, whereas several drop locations, esp. along *y*-axis, were covered for studies of the trajectory effect.

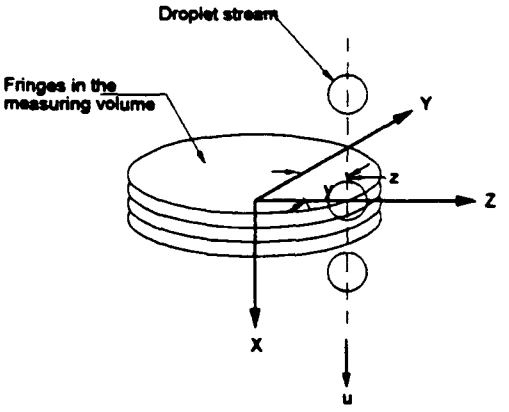

Fig. 1: Primary drops in the measuring volume.

The second droplet generator was used to produce freely falling drops as shown in Fig. 2. Most of these drops were collected by a liquid trap and only drops following a certain trajectory were allowed to cross the laser beams ahead of the measuring volume. The spacing ℓ between the primary and the secondary drop could be adjusted between 3 mm and 15 mm. A detector was arranged to collect the light scattered by the secondary drops as they crossed the upper laser beam. This light signal was used to trigger the measurements of the primary drops crossing the measuring volume. Typically, 200 signals were collected after each triggering event.

Since the secondary drops moved significantly slower than the primary ones, the former could be considered stationary for a given phase Doppler signal.

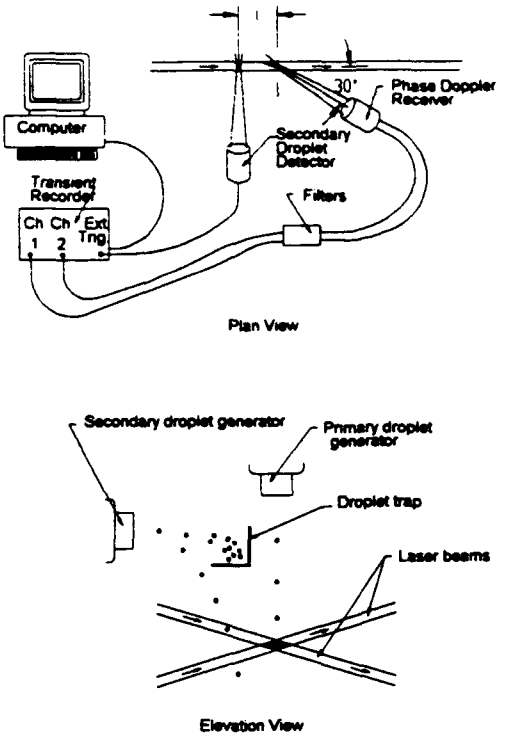

Fig.2: Experimental setup for examining multiple scattering in PDA

3 Multiple Scattering Effect

Investigation of the multiple scattering effect was based on a primary drop diameter of 50 μm and secondary drops of diameters 60, 80 and 100 μm. A range of inter-drop spacing ℓ was employed and associated errors in signal frequency and phase were measured. Also the signal-to-noise ratio was recorded. The measured data are presented below and their impact on the accuracy of phase Doppler measurements is discussed.

3.1 Experimental Results

A series of Doppler bursts generated by primary drops are shown in Fig. 3. These bursts correspond to a secondary drop of diameter 80 μm and an inter-drop spacing of 6 mm. The amplitude of filtered signals dropped twice due to crossing of the individual beams by the secondary drop. The first, twelfth and eighteenth bursts are enlarged. The twelfth burst shows a significant increase in the frequency and the eighteenth burst exhibits an envelop which deviates substantially from a Gaussian shape that characterizes undisturbed signals.

Signal frequency and phase are plotted in Fig. 4 for individual bursts. They show a decrease as the secondary drop enters the first beam, an increase as it leaves the beam and a recovery of

the original phase and frequency when the drop is between the two beams. The above events are repeated, when the drop crosses the second beam.

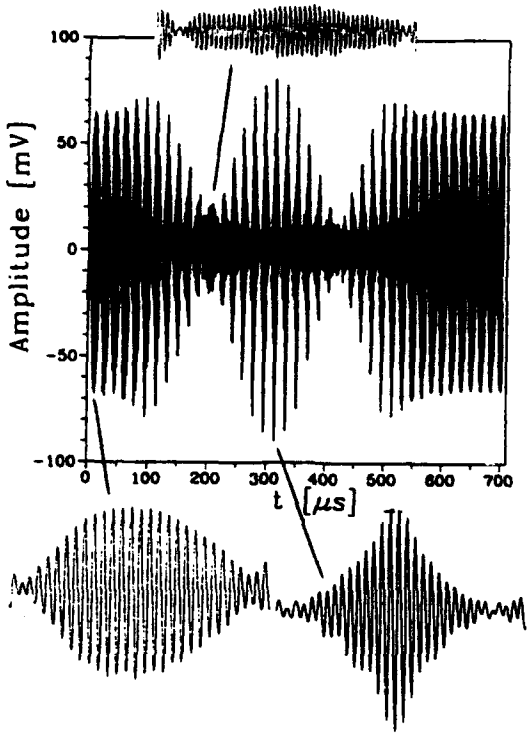

Fig. 3: Effect of a secondary drop on PDA signals

The largest errors in phase for different diameters of the secondary particle are shown in Fig. 5. These data are based on averages of 21 events of the kind considered in Figs. 3 & 4, for each drop size. The largest inter-drop spacing ℓ_m, for which multiple scattering effect is significant, may be estimated from this figure. This parameter increases with the drop size, however, the largest phase error within ℓ_m is larger for smaller drops.

Present work has also shown that in the presence of multiple scattering effect it is necessary to select a large sample for processing. As illustrated in Fig. 6, 64-point FFT and 256-point FFT give comparable accuracy of phase measurements as long as secondary particle is not present. However, in the presence of the secondary particle, significantly better phase measurements are obtained with longer samples. In the present measurements, 64 and 256 point sample lengths correspond to 5 and 20 cycles of Doppler burst respectively.

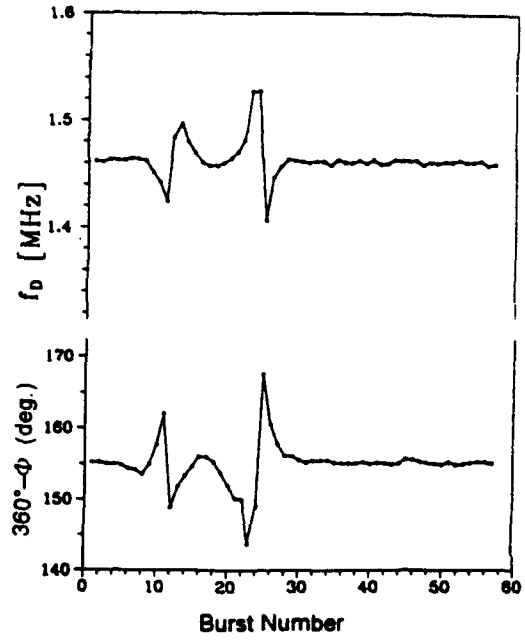

Fig. 4: Influence of secondary drop on signal frequency and phase.

Fig. 6 pertains to a 100 μm secondary particle at 3 mm from the measuring volume.

The results concerning the multiple scattering effect, presented herein, are based on 256 samples, unless otherwise stated.

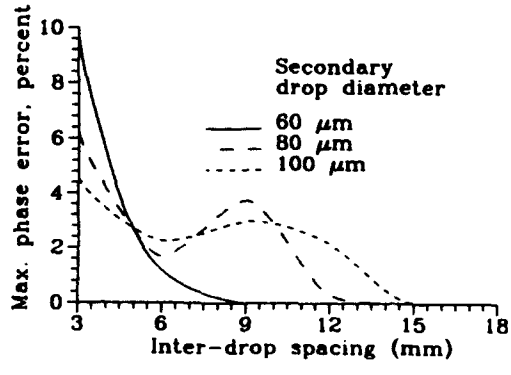

Fig. 5: Phase error versus inter-drop spacing

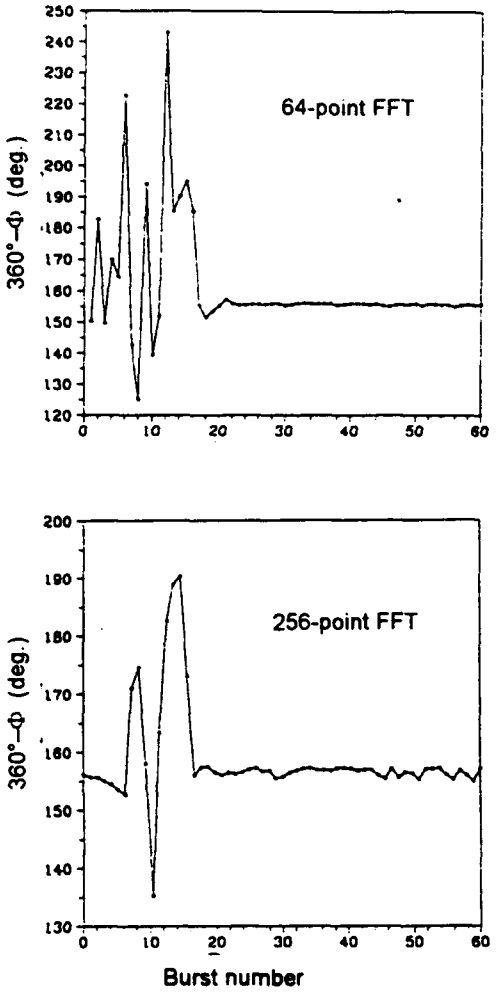

Fig. 6: Phase fluctuations with 64 & 256 samples

3.2 Interpretations based on Geometrical Optics

The variations of phase and frequency shown in Fig. 4 may be explained by considering the deflection of individual laser beams by the transparent drop as illustrated in Fig. 7. As the droplet enters the upper beam, it causes an effective upward deflection of this beam due to refraction, resulting in a decreased beam angle and an increased fringe spacing. This obviously leads to a decrease in the signal frequency as well as the phase. As shown in Fig. 7, the above effect is reversed when the secondary drop begins to leave the upper beam.

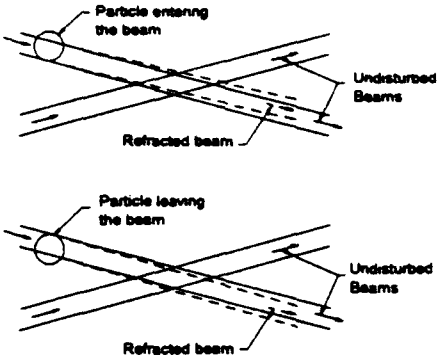

Fig. 7: Interpretation of multiple scattering effect.

It may appear surprising that the light diffracted by the secondary drop — which is normally stronger than the refracted light — does not play an important role. However, this behavior is explicable as the phase of scattered light is generally very uniform over most of the diffracted lobe and undergoes a rather abrupt change of 180° near its edges.

Since the intensity of refracted light in the measuring volume is directly proportional to d_p^2 and — in the far-field — inversely proportional to ℓ^2, the limiting distance ℓ_m should vary linearly with d_p. According to the data in Fig. 5, increase in ℓ_m with d_p is slower than linear, manifesting the near-field effect. Nevertheless, a reasonable estimate of the limiting inter-particle spacing is provided by the correlation,

$$\ell_m = 150 d_p . \qquad (1)$$

The effect of measuring volume diameter d_m on the above correlation was not examined in this study. However, the order of magnitude of the proportionality constant in Eq. (1) is not expected to change in typical phase Doppler systems. Hence, for complete elimination of the multiple scattering effect, there should be a single particle in a volume represented by two interpenetrating cylinders — aligned with the two laser beams — with diameter d_m and length ℓ_m. Typically, this volume will be two orders of magnitude larger than the volume defined by the laser waist and image of the slit used in the receiving optics. Hence, particle concentration should be two orders of magnitude smaller than the recommended values in order to completely eliminate the multiple scattering effect. However, as shown in Fig. 5, the relative errors caused by the multiple scattering effect are small and higher concentrations can be used at the

expense of some broadening of the measured size distribution.

4 Particle Trajectory Effect

Trajectory ambiguity is encountered in the case of transparent particles if the location of receiving optics is substantially different from the position where the Brewster condition is satisfied, so that both refracted and reflected light is present in the scattered signal. Normally, refracted light dominates, but the contribution of reflection becomes significant if the particle size is comparable to the measuring volume diameter and the particle is located in the half of the measuring volume opposite to the detectors.

As discussed in Ref. 2, a phase Doppler signal in such an application, may be considered as a superposition of a reflected and a refracted signal. There exist *critical particle diameters*, at which the reflected and refracted signals are either in-phase or completely out-of-phase. For a symmetric dual- detector PDA receiver, the critical diameter is given as

$$d_{pc} = \frac{360n}{f_{rfr} + f_{rfl}}, \qquad (2)$$

where f_{rfr} and f_{rfl} are the phase-diameter conversion factors in deg./μm for pure refraction and pure reflection respectively. The refracted and reflected signals are out-of-phase for n=1,3,5, ... and in-phase for n=2,4,6, ...

If reflection and refraction are out-of-phase, then the phase of the combined signal agrees with pure refraction, as long as refracted signal is slightly stronger than the reflected signal. Only signal visibility is deteriorated due to strong reflections. The knowledge of these critical diameters is very useful in optimizing system layouts for specific applications, in order to *minimize trajectory effects*.

In the present arrangement, two critical drop diameters, i.e. 38.2 μm and 76.4 μm, exist within the measurable size range [0,94 μm]. The refracted and reflected signals are out-of-phase at 38.2 μm and in-phase at 76.4 μm. A range of droplet diameters, in the vicinity of the second critical diameter was used for experimental verification reported herein.

The results of measurements are given in Fig. 8 and compared with simulations based on generalized Lorenz-Mie theory (GLMT). In this figure, the droplet diameters are reduced by 5 μm in comparison to their values based on the droplet generator settings. This measure appears to account for evaporation of drops in a satisfactory manner and leads to an excellent agreement between theory and measurements.

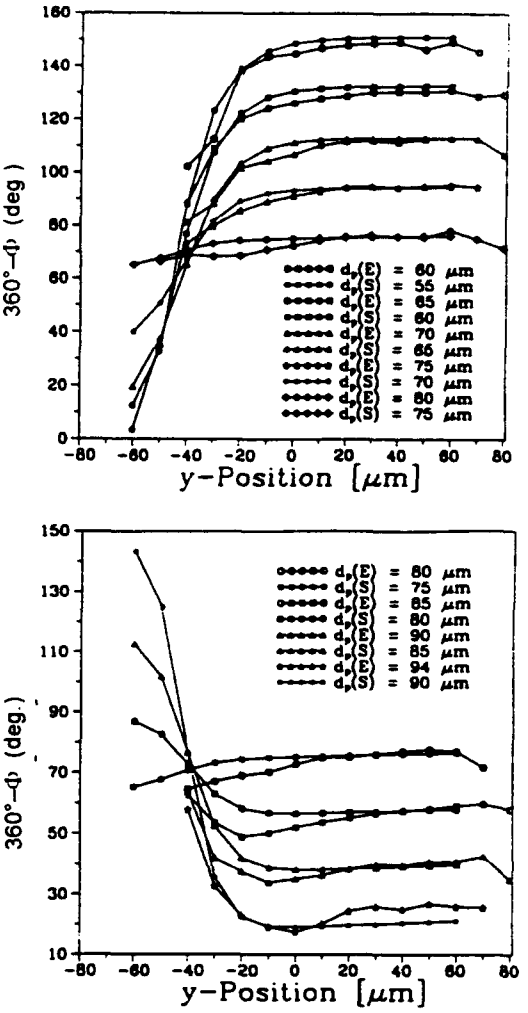

Fig. 8: Experimental (E) and simulated (S) data of phase as a function of drop location

5 Conclusions

Two phenomena that may severely affect the performance of a phase Doppler system are examined. Multiple scattering, in the case of submillimeter particles, may be modelled as a refraction of the entire laser beams. The limiting values of particle concentrations for PDA that are specified in the existing literature are based solely on the dimensions of the measurement volume and ignore the multiple scattering effect. If accurate measurements for *individual* particles are desired then the limiting concentrations are as much as two orders of magnitude smaller than the specified values.

However, multiple scattering causes only a broadening of the measured size distribution without severely affecting the mean particle diameter. Furthermore, it should be possible to

deconvolve the effect of multiple scattering as the phenomenon conforms fairly well to a rather simple model based on geometrical optics. The future work will aim at corrections of the measured distribution to offset the multiple scattering effect.

It is also important to recognize that the multiple scattering effect is rather demanding for the signal processor. The optimal settings of a processor for single scattering are *not* applicable in the presence of multiple scattering. In the present work, 256-point FFT was needed in the presence of multiple scattering, as opposed to 64-point FFT for single scattering.

The second phenomenon of present interest is the particle trajectory effect. Although various elaborate schemes are now available to eliminate this effect, the simplest solution in the case of single-component phase Doppler involves adjustment of optical parameters, i.e. off-axis angle, detector spacing, beam angle etc., in order to minimize the influence of particle trajectories on the measured phase. For this purpose, Ref. 2 provides a rigorous method utilizing the concept of critical particle diameters as well as illumination and scattering ratios for reflection and refraction. An experimental verification of the critical diameters is given herein, which substantiates the above method.

Acknowledgements

The GLMT code for simulation of phase Doppler technique, used in this work was developed through collaboration between author Naqwi and and Dr. G. Gréhan of INSA de Rouen, France, with kind advices from Prof. G. Gouesbet. The authors are grateful to their partners from INSA for this very valuable contribution.

References

1. B. Ruck, "Distortion of LDA fringe pattern by tracer particles", Experiments in Fluids 10 (1991) 349–354.
2. A. Naqwi, "Innovative phase Doppler systems and their applications", Part. Part Syst. Charact. 11 (1994) 7–21.
3. G. Gréhan, G. Gouesbet, A. Naqwi and F. Durst, "Trajectory ambiguities in phase Doppler systems: use of polarizers and additional detectors to suppress the effect", Proc. 6th Intl. Symp. on Applications of Laser Techniques to Fluid Mechanics, Lisbon (1992) Paper # 12.1.

IMPROVING THE ACCURACY OF PARTICLE SIZING TECHNIQUES USING THE LIGHT SCATTERED FROM SINGLE PARTICLES

M.F.J. Bohan and T.C. Claypole

University College of Swansea, Wales

ABSTRACT

The sizing of particles by laser light scattering techniques assumes the particles are smooth and spherical. When sizing materials such as coal and char, this assumption is far from valid as the particles are faceted and non-spherical. The development of a technique for removing spurious measurements caused by facets and other areas of non-uniformity has been developed. Individual particles within a size range between 40μm and 150μm were rotated in a laser beam and the signals from two and three detectors simultaneously compared. This has lead to a technique producing an improvement in the reliability of the measurements by up to 75%.

1.0 INTRODUCTION

Many industrial processes involve flows of powders or sprays in a fluid medium. Information about particle parameters such as velocity, size and concentration are of value in the control of such processes. Well developed non invasive optical techniques exist for the measurement of velocity, e.g. Drain (1986). Several different techniques have been developed for the measurement of particle size using the light scattered from individual particles. These include the use of intensity, visibility and phase Doppler. However, the measurement of irregular particles remains an area of considerable difficulty, despite the widespread occurrences of such particles. A signal validation technique has been developed to improve the accuracy of the sizing of irregularly shaped particles for visibility / intensity based techniques. This first required an understanding of the scattering of light from irregular particles.

2.0 LIGHT SCATTERING FROM IRREGULAR PARTICLES

A short discussion of the processes involved in light scattering from particles would help in the understanding of the experimental program. The scattering of light from spherical particles has been thoroughly researched and is now well understood, van de Hulst (1957), Bohren and Huffman (1983). The use of the spherical particle results in the scattered light intensity distributions being predictable for any particle orientation. Therefore, it is possible to relate the scattered light intensity (and visibility) to the size of the particle.

For particles of diameter much greater than the wavelength of light, three main processes dominate the light scatter. These are reflection, refraction and diffraction. The amount of light scattered by these processes is dependant on the wavelength of the illuminating light, the particle size, shape and material, and on the angle between the incident light and the collection angle.

The particles analysed were coal with nominal diameters varying between 50μm and 200μm. For these particles, the contribution due to refraction is negligible due to their high light absorbtion. The contribution due to diffraction will reduce dramatically outside the main diffraction lobe. For a spherical particle of 50 microns, the main diffraction lobe is approximately one degree off axis. The irregularity of the scattering particle will not significantly effect this angle, but make the diffracted light profile non-symmetric. Therefore, outside this region ($\theta > 1^0$) the majority of the scattered light is due primarily to reflection from the particle surface.

Reflection from spherical particles is a relatively simple problem, but is useful in highlighting the light scatter process. Consider a particle of radius R illuminated by a collimated beam of light. Suppose the scattered light is collected by a lens of diameter d and focal length f. It can be shown that the intensity of the scattered light I, is given by

$$I = k \left| \frac{R}{f / d} \right|^2 \quad \ldots 1$$

or any angle of incidence provided that the collection aperture is small. This relationship will remain good for larger apertures provided the collection angles are away from the forward direction.

Now consider an irregular particle. The primary change in the analysis is that the radius that appears in Equation 1 is replaced by the local radius of curvature of the particle. This is no longer constant but depends on the particle orientation. For a spherical particle this is equivalent to the particle diameter. However, this is not the case for non-spherical

diameter. However, this is not the case for non-spherical particles. The extent to which measurements of radius of curvature of the particle will provide a means of measuring the particle size will depend on the degree of irregularity of the particle. Therefore, as the local radius of curvature increases, there would be a tendency for the scattered light intensity to increase.

2.1 PRELIMINARY INVESTIGATION INTO LIGHT SCATTERING FROM IRREGULAR PARTICLES

Due to the complexity of the scattering from an irregular particle, the light scatter from these particles was investigated experimentally. In a free flow the particles would randomly pass through the laser beam in any orientation. A series of experiments were undertaken with particles suspended on stalks. This allowed each of the particles to be individually characterised. The particles were slowly rotated about their axis in the centre section of an illuminating laser beam to simulate the different orientations the particle would pass through a measurement volume. The scattered light was then collected at different collection angles that varied between five and ninety degrees. Coal was selected for the investigation as this provided an irregular particle for which there was a commercial interest regarding the validity of the size information obtained from the current investigation. The size range of interest varied between 40μm and 160μm in r.m.s diameter.

The experimental arrangement is shown in Figure 1. The mounted particles were rotated about their axis centrally in a laser beam. In this section of the laser beam, the intensity was approximately even. The scattered light was then collected using photomultiplier tubes. The first set of collection optics remained fixed at 5 degrees to the laser beam and the second set were rotated about the particle to collect the scattered light at 90^0, 60^0 and 30^0 to the laser beam. A repeat set measurements were taken at 90^0 to ensure experimental consistencey. The signals were transferred to computer via a set buffer interfaces. A typical response from a single rotating coal particle is shown in Figure 2, for collection angles of five and ninety degrees. The dominant light scattering process for these particles is reflection. The high intensity regions in the signals (A, B and C) correspond to facets (flat areas) on the particle surface. At certain orientations these can give rise to localised flashes of high intensity light. It was found that as the collection angle is increased the intensity of these flashes will increase. These flashes can lead to large errors in particle sizing if conventional laser based systems are used (only 50% of the measurements are within ±25% of the nominal particle size).

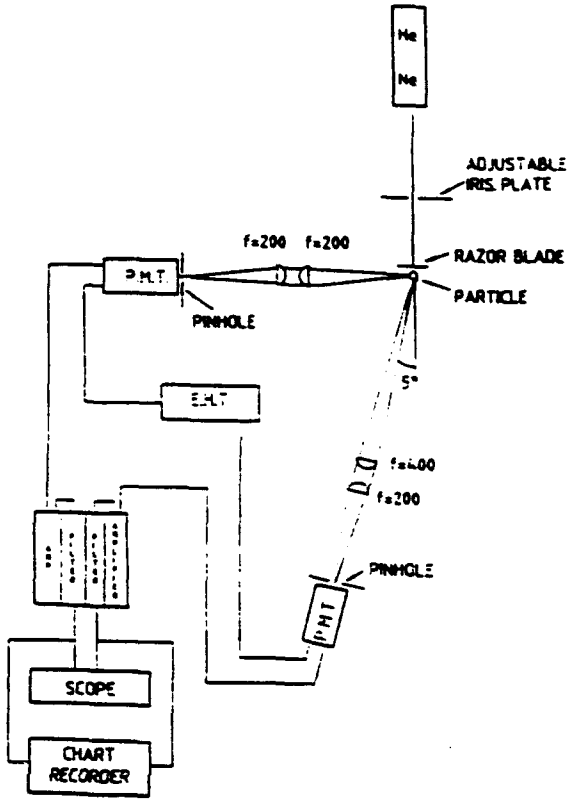

Figure 1 Plan view of the experimental arangement, collection optics set at 5 and 80 degrees

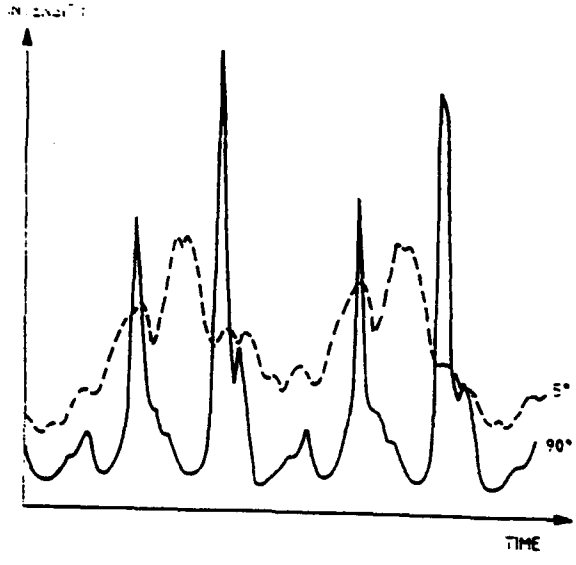

Figure 2 Signal fluctuations for a collection angle of 5 and 90 degrees

3.0 SIGNAL VALIDATION TECHNIQUE USING TWO DETECTORS

The previous section has shown how facets on the particle section can give rise to localised flashes of intense light, depending on the particle orientation. Using this feature, a differencing technique has been developed to remove these flashes. The initial evaluation of the signal validation technique was carried out using coal particles. The method is based on using two spatially separated collection apertures and comparing the two signals received.

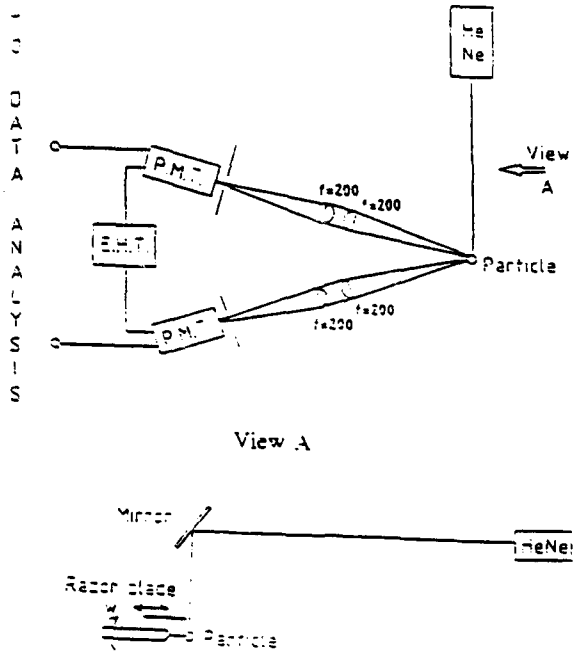

Figure 3 Experimental arrangement using two detectors

The experimental arrangement is shown in Figure 3. The particles are rotated in the central section of a laser beam with two identical sets of collection optics being used to collect the scattered light. These were aligned at 90 degrees to the laser beam, with an internal separation of 20 degrees. The coal particles used were mounted on 9 micron tungsten wires. This allowed for a tight control over the type of particles examined. Particles were only selected that had aspect ratios between 0.6 and 1.0. This meant that the changes in intensity would primarily be functions of the particle surface and not the changing apparent particle size. Figure 4 (i) shows the signal fluctuations from a 100 micron coal particle. The flashes tend not to be detected by both the photomultipliers simultaneously as they are fairly localised. If the two signals are compared, Figure 4 (ii), it can be seen that the in regions where there are high intensity flashes, these will result in there being a large difference between the signals. If a limit is applied to this difference to validate the signals, then those signals due to the facets on the particle surface (flashes) can be removed. The use of this technique results in a 35% improvement in the prediction of the particle size (approximately 72% of the measurements are within ±25% of the nominal particle size), see Table 1.

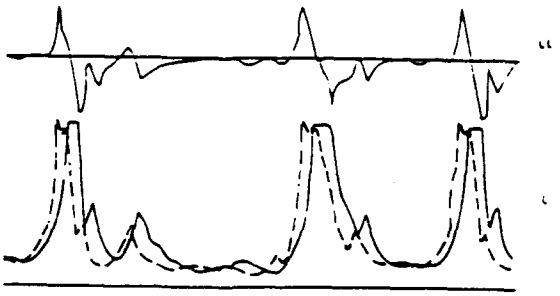

Figure 4 Signal fluctuations and differencing for a 100 micron coal particle

Particle Type	Percentage of correct estimations			
	Original Signal		Difference Signal	
	±15%	±25%	±15%	±25%
Coal	35.9	53.6	53.2	72.2
Char	34.6	53.1	50.0	71.8

Table 1 Average percentage of correct estimations for coal and char particles

The work was extended to include different particle surface characteristics by the use of char. The experimental techniques were similar to those applied to the coal particles. The light is scattered differently from the char when compared with the coal, Figure 5. This can be attributed to the char structure which has been formed by the driving off of volatiles from a coal particle. The resulting structure does not possess such well defined facets and tends towards a roughened surface. This results in the flashes from the char particles not being as intense or as localised as those from the coal particles. The differencing technique when applied to these particles increased the accuracy to a similar degree to that observed with the coal, Table 1.

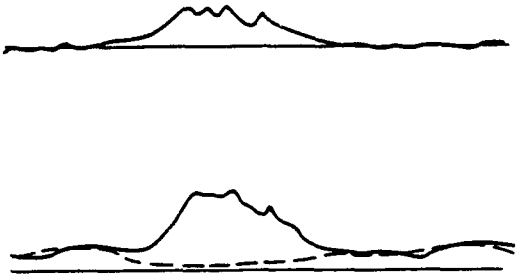

Figure 5 Signal fluctuations and differencing for a 64 micron char particle

4.0 THE USE OF THREE DETECTORS FOR SIGNAL VALIDATION

Study of these results indicated that the accuracy of the technique could be further increased by the use of three detectors. The scattered light was collected at three spatially separated apertures. The signals received from the 72μm particle are shown in Figure 5. The three signals detected again illustrate the effects of facets with the flash L being different between all three signals. The differences between the signals Δ_{AB}, Δ_{AC} and Δ_{BC} can be used for validation. The improvement obtained when only one set of limits are applied (Δ_{AB} or Δ_{AC} or Δ_{BC}) is increased to 72%, which is in good agreement with the earlier findings. This allows the results from the three detector work to compared with two detector findings.

The use of a minimum of two limits (Δ_{AB}&Δ_{AC} or Δ_{AB}&Δ_{BC} or Δ_{AC}&Δ_{BC}) to validate the signal significantly increases the average percentage of correct estimations and change due to the application of the validation technique. The average number of correct estimations within ±25% of the particle size is improved from 52% for the original signal to 71% with one limit being applied and to 92% with the use of all three limits being used to validate the signal.

The further improvement in the percentage of correct estimations with the use of three detectors can be explained by referring to the signal fluctuations, Figure 6. At position X, there is the start of a flash caused by a facet. The response of detectors A and B to the start of this is similar. This is caused by the faceted area being situated nominally midway between the two collection angles. This results in the signals from the faceted area being validated. However, the response from detector C is completely different in both amplitude and shape. Therefore, the resulting signals are not validated using this detector as they are outside the difference limit. The use of three detectors will also eliminate signals that are validated as the transitional response from the two detectors coincide. This may happen as the response of one is increasing as a result of the faceted area as the other is decreasing.

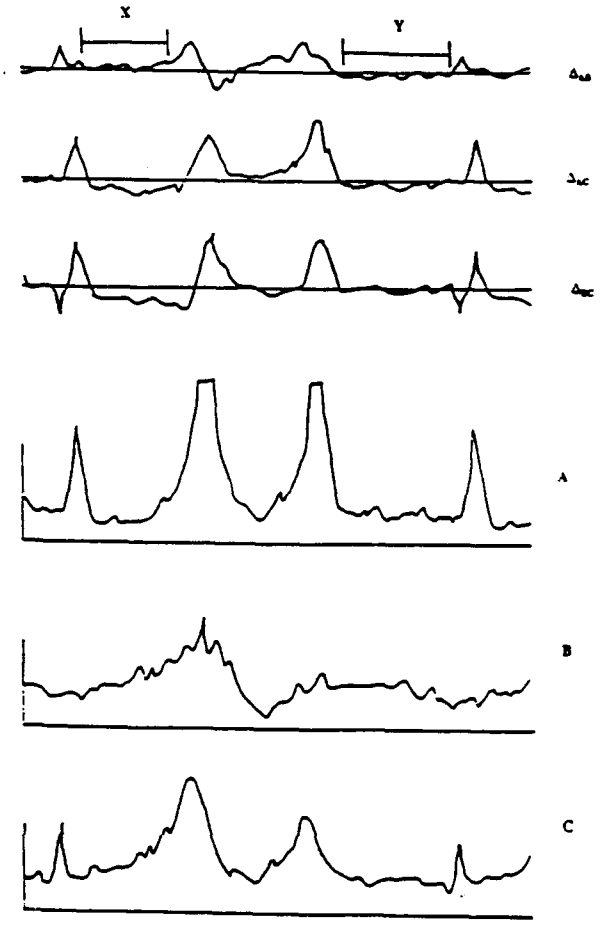

Figure 6 Signal fluctuations and differencing for three detectors using a 72 micron and particle

5.0 CONCLUSIONS

The results have shown that the sizing of irregular particles on the assumption that they are spherical is dangerous as it can give rise to large errors. These are dependent on the particle surface characteristics and size. If the signal validation technique described is applied to a set of two signals the accuracy of the measurement can be increased. This can be further increased if three detectors are used.

ACKNOWLEDGEMENTS

The authors wish to acknowledge the assistance of M.L. Yeoman and D.M. Livesley of A.E.A. Culham throughout the duration of this project. This work has been supported by the S.E.R.C. and the underlying research program of the U.K.A.E.A.

REFERENCES

C.F. Bohren and D.R. Huffman 1983, "Absorption and scattering of light by small particles", Wiley, New York

L.E. Drain 1986, "The laser Doppler technique", John Wiley and Sons

H.C. van de Hulst 1957 "Light scattering by small particles", Wiley, New York

INTEGRAL DOPPLER SPECTRA DUE TO THE PARTICLES SIZE-VELOCITY CORRELATION IN TWO-PHASE FLOWS

V.L. Kononenko

N.N. Semenov Institute of Chemical Physics,
Russian Academy of Sciences, Russia

B.S. Rinkevichius

V.A. Fabrikant Physics Department,
Moscow Power Engineering Institute (Technical University), Russia

ABSTRACT

A common situation is the polydispersity and the slippage of particles in two-phase flows. If the Doppler spectrum of two-phase flow is registered in accumulation mode, then a broad spectrum is obtained instead of a single Doppler line. The complex shape of this spectrum reflects the distributions of particles velocities and scattering properties due to polydispersity of particles system and to variation of the flow velocity in space and time. Thus, by solving an inverse problem, one may hope to reconstruct some of the distribution functions characterizing the particles system or the flow itself from the shape of the integral Doppler spectrum. Such procedure can be convenient when the tracking of particles or the scanning of a flow are complicated. The aim of this paper is to develop the theory and to show characteristic examples of the integral Doppler spectra of two-phase laminar flows with the size-velocity correlation in a particles system.

1. BASIC CONCEPT OF THE INTEGRAL DOPPLER ANEMOMETRY (IDA)

In many fields of laser Doppler anemometry (LDA) the final goal of investigation is some distribution function of the object, e.g. the flow velocity profiles or the particles size distribution function (Durst *et al* (1976), Rinkevichius (1990)). To reach these goals, it is natural to employ the integral approach (Kononenko (1993a)), trying to register the whole spectrum ofparameter values simultaneously, and to obtain the relevant distribution function from a single measured curve.

The general formulation of the integral approach in LDA of laminar flows is as follows. Let us consider a fluid or gas flow containing particles of various size. Let $\vec{v}_p(\vec{r},a,t)$ be the particle velocity, $C(\vec{r},a,t)$ be the time-average particles concentration, both functions depending on coordinate $\vec{r}$, time t, and particle radius a. Let $\sigma(a)$ be the appropriate cross-section of laser light scattering by a particle (Rinkevichius (1990)). The Doppler spectrum corresponding to a single particle can be described (neglecting any broadening) by a delta-function centered at the Doppler frequency of a particle $\omega_D=\vec{q}\cdot\vec{v}_p(\vec{r},a,t)$, $\vec{q}$ being the scattering wavenumber. A time-average amplitude of this Doppler line is proportional to the

particles concentration and to the scattering cross-section of a particle squared. If the integral Doppler spectrum $S(\omega)$ is registered instead of a single Doppler line, then this line's position and intensity should be integrated over all relevant parameters, i.e., over space, time, and particle radius:

$$S(\omega) = const \cdot \iiint \sigma^2(a) \cdot C(\vec{r},a,t) \cdot \cdot \delta[\vec{\omega}-\vec{q}\cdot\vec{v}_p(\vec{r},a,t)]\, d\vec{r}\, da\, dt \quad (1)$$

Formula (1) is the general expression for the integral Doppler spectrum. It connects the shape of this spectrum with the characteristic functions of the flow and the particles system in a flow. Using this connection and employing special algorithms, one may hope to reconstruct these functions from the Doppler spectra. Thus, the problem is formulated as an inverse one. It is known, that problems of this kind can be solved correctly, i.e., the unique solution can be obtained for the integrand functions, provided some additional *a priory* information exists on their functional form. First of all, that means that functions entering (1) should depend on a single variable only. This demand means the possibility of several branches of the Integral Doppler Anemometry (IDA), depending on the physical characteristics of the object being studied and on the measuring conditions (Kononenko (1993a)). The main of these branches are the following ones: 1) the spatial IDA (Kononenko (1992), (1993a), and (1993b)), which can be used in the case of time-independent, spatially-varying flows with particles velocities following the local flow velocity: $\vec{v}_p=\vec{v}_F(\vec{r})$, $C=C(\vec{r},a)$; 2) the time-scale IDA, which can be applied to the time-dependent flows and time-dependent particles systems without spatial dependence or measured locally: $\vec{v}_p=\vec{v}(t,a)$, $C=C(t,a)$; 3) the IDA of multiphase flows with size-velocity correlation of carried particles, which can be used for investigation of polydisperse multivelocity systems of particles in stationary flows without spatial dependence or measured locally: $\vec{v}_p=\vec{v}_p(a)$, $C=C(a)$.

Of these three branches, only the spatial IDA is developed at the present time as a practical measuring technique, and it was applied successfully to investigations of the narrow channel flows (Kononenko (1993b)).

2. IDA OF POLYDISPERSE MULTIVELOCITY SYSTEMS

The particles in multiphase flows are usually polydisperse, and their velocities may differ from the local flow velocity v_F depending on the size, shape and physical parameters of particles. The typical examples are the sedimentation of aerosols and particles in a fluid, or the inertia slip of particles in hypersonic flows (Rinkevichius *et al* (1974), Rinkevichius (1990)). The multiphase flows may, in general, have the spatial dependence of flow velocity also. Thus, to avoid the mixture of the spatial and the polydisperse-multivelocity integral effects, it is necessary to register the spectrum locally. The shape of IDA spectrum in this case is given by the integration in (1) for $\vec{r}, t=const$:

$$S(\omega) = const \cdot \sigma^2[a(\omega)] \cdot C[a(\omega)] \cdot \cdot \left|\frac{da}{dv_p}(\omega)\right| \cdot \Theta(\omega-\omega_1) \cdot \Theta(\omega_2-\omega) \quad (2)$$

The function $a(\omega)$ in (2) is defined by the equation $|\vec{q}\cdot\vec{v}_p(a)|=\omega$, and the boundaries ω_1 and ω_2 of the integral spectrum are defined by the particles size distribution boundaries according to this equation.

The spectral equation (2) shows two measuring possibilities in the IDA of polydisperse-multivelocity systems of particles. The first one is the reconstruction of the size (or other parameter)

distribution function $C(a)$, knowing the dependence $v_p(a)$ of particle velocity on this parameter (the slippage law). The second one is the determination of the slippage law $v_p(a)$ if the distribution function $C(a)$ is known beforehand or measured independently. The situation has a formal similarity with the spatial IDA considered by Kononenko and Shimkus (1992). The difference is that the reconstruction algorithms should take into account the $\sigma(a)$ dependence, which can be taken from the theory of light scattering by small particles.

Let us consider two limiting cases then $\sigma(a)$ can be expressed by simple formulae: the Rayleigh-Gans approximation valid for the optically "soft" particles of arbitrary size, and the large (compared with the light wavelength) particles approximation, when the diffraction component dominates in the scattered light. If a particle is illuminated by two linearly polarized plane waves simultaneously, as it is done in the dual-beam LDA arrangement, then it can be characterized by the usual (single-beam) scattering cross-sections σ_1 and σ_2 refered to each beam, and by the coherent (dual-beam) scattering cross-section σ_{12} (Rinkevichius (1990)). For a spherical particle in Rayleigh-Gans approximation the differential scattering cross-sections have the form:

$$\frac{d\sigma_1}{d\Omega} = \frac{\pi}{4}\,\frac{|\hat{m}-1|^2 ka^3}{\left(\sin\frac{\theta_1}{2}\right)^3}\, f_1(\theta_1,\varphi_1)\, J^2_{\frac{3}{2}}\left(2ka\cdot\sin\frac{\theta_1}{2}\right)$$

$$f_1(\theta_1,\varphi_1) = \sin^2\varphi_1 + \cos^2\varphi_1\cdot\cos^2\theta_1$$

$$\frac{d\sigma_{12}}{d\Omega} = \frac{\pi}{4}\,\frac{|\hat{m}-1|^2 ka^3\cdot f_2(\theta_1,\varphi_1)}{\left(\sin\frac{\theta_1}{2}\right)^{3/2}\cdot\left(\sin\frac{\theta_2}{2}\right)^{3/2}}\cdot$$

$$\cdot J_{3/2}\left(2ka\cdot\sin\frac{\theta_1}{2}\right)\cdot J_{3/2}\left(2ka\cdot\sin\frac{\theta_2}{2}\right)$$

$$f_2(\theta_1,\varphi_1) = \sin(\varphi_1)\cdot\sin(\varphi_2) + \cos(\varphi_1)\cdot$$

$$\cdot\cos(\varphi_2)\cdot\cos(\theta_1)\cdot\cos(\theta_2),$$

$$i=1,2. \qquad (3)$$

In the large particles approximation:

$$\frac{d\sigma_1}{d\Omega} = a^2 J_1^2(ka\cdot\sin\theta_1)\cdot\sin^{-2}\theta_1\ , \quad i=1,2$$

$$\frac{d\sigma_{12}}{d\Omega} = a^2\cdot\frac{J_1(ka\cdot\sin\theta_1)\cdot J_1(ka\cdot\sin\theta_2)}{\sin\theta_1\cdot\sin\theta_2}\cdot$$

$$\cdot f_3(\theta_1,\varphi_1)\ ;$$

$$f_3(\theta_1,\varphi_1) = \sin(\varphi_1)\cdot\sin(\varphi_2) +$$

$$+ \cos(\varphi_1)\cdot\cos(\varphi_2)\ . \qquad (4)$$

Here $\hat{m}$ is the relative complex refractive index of a particle substance, $k=2\pi/\lambda$ is the wavenumber and λ is the wavelength of light in the medium, θ is the scattering angle, φ is the angle between the electric vector of the incident wave and the plane of scattering, $J_{3/2}(x)$ and $J_1(x)$ are the Bessel functions. The inequality $2ka|\hat{m}-1|\ll 1$ is supposed to be fulfilled in (3). Formulae (3), (4) are written for the scattering direction lying in the plane of the incident beams. The scattering cross-sections σ entering formulae (1), (2) are the integrals of the expressions (3) or (4) taken within the aperture solid angle $\Delta\Omega$ of receiving optics (a cone with the apex angle $\beta\ll\theta$). Fig.1 shows the particle size dependence of the corresponding cross-sections.

The analytical expressions (1)-(4) for the shape of IDA spectra can be used both for computation and for comprehensive analysis of this shape. As these expressions and Fig.1 show, the oscillatory behavior of σ_{12} for large particles may result in a series of minima and maxima in IDA spectrum of polydisperse particles system in a flow, even in the case of smooth size distribution function of these particles.

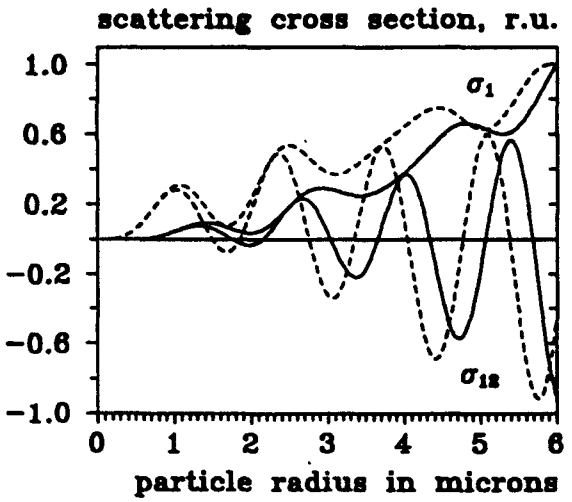

Fig.1. Dependences of single-beam scattering cross-section σ_1 and dual-beam (coherent) cross-section σ_{12} on particle radius in Rayleigh-Gans (solid curves) and large particles (dashed curves) approximations for differential LDA arrangement. $\theta_1=\theta_2=10^0$, $\beta=2^0$, $\lambda=(0.63/1.33)$ μm.

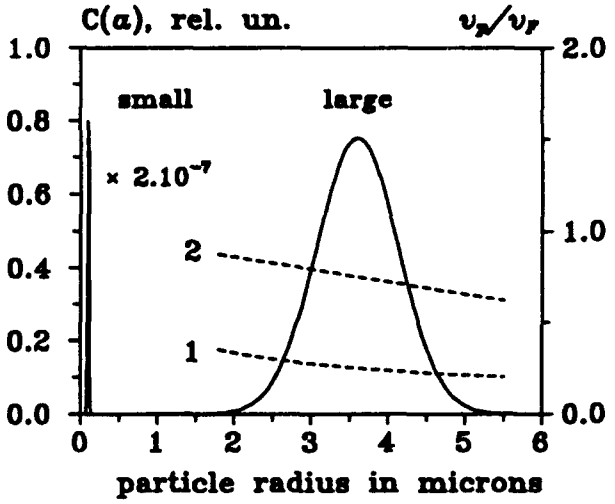

Fig.2. Size distribution in a model mixture containing two fractions with the normal distributions: small particles with $a_0=0.1$ μm, $\delta=0.06$ μm and large particles with $a_0=3.6$ μm, $\delta=0.53$ μm. Dashed lines: size-velocity correlation for large particles at small (1) and large (2) distances for $u_0=0.25\ v_F$.

3. DIFFERENTIAL LDA OPTICAL ARRANGEMENT

Let us consider the shape of polydispersial IDA spectrum for the differential optical arrangement of LDA, using the fringe model of Doppler anemometer (Durst *et al* (1976), Rinkevichius (1990)) and the stochastic analysisprocedure (Kononenko (1993*b*)). Each particle moving with a flow through the fringe pattern near the beams intersection generates a time-dependent signal of the registering photodetector. A total signal can be considered as a random succession of pulses, the shape of a pulse being determined by the profile $I(x,y,z,a)$ of the scattered light intensity taken along the particle's trajectory with particular lateral coordinates y, z. The power spectrum of this signal is given by:

$$S(\omega)=2\int_{a_{min}}^{a_{max}}\iint v_p(y,z,a)\cdot C(y,z,a)\cdot \cdot|F(\omega,y,z,a)|^2\,dy\,dz\,da + + 4\pi\overline{i}^2\delta(\omega)\ . \quad (5)$$

Here $F(\omega,y,z,a)$ is the Fourier transform of the pulse shape $I[x(t),y,z,a]$ with $x(t)=v_p(y,z)\cdot t$, and $\overline{i}^2$ is the time-average photocurrent. The $F(\omega,y,z,a)$ expression for the differential LDA arrangement is given by Kononenko and Rinkevichius (1993).

The formula (5) is the general expression for the shape of IDA spectrum, which describes both the spatial and polydispersial integral effects in LDA of stationary two-phase flows taking into account the instrumental function of the optical arrangement of Doppler

anemometer. To consider the polydispersial IDA spectra only, the integration should be done in (5) over y and z.

4. TYPICAL IDA SPECTRA OF TWO-PHASE FLOWS

Let us consider a system of spherical solid particles with the normal size distribution, which are introduced with zero initial velocities into a high-speed gas flow. It can be shown, that for high values of particle's Reynolds number the size-velocity correlation in this system is described by $v_p(a) \approx u_0(x) \cdot (a_0/a)^{1/2}$ for small distances x from the injection point, and by $v_p(a) \approx v_F - u_0(x) \cdot (a/a_0)$ for large distances close to the equilibration distance. Here a_0 is the distribution-average radius of particles, δ is the distribution width, $u_0(x)$ is the particle's velocity corresponding to a_0. Fig.2 shows the size distribution function $C(a)$ of a model system consisting from two fractions of particles. It is supposed, that at two characteristic observation points downstream the flow small particles has already acquired the flow velocity, while large particles are still slipping in a flow according to above-written laws. Fig.3 shows the IDA spectra of such two-phase flow, calculated using the equation (5) with the corresponding scattering cross-sections σ_1, σ_2, σ_{12} obtained by integrating (3) within the receiving aperture cone (see Fig.1). The main feature of these spectra is the line structure of the spectral curve corresponding to the fraction of large particles. As it can be seen from equations (2), (3) and Figs.1,2, this structure originates from the oscillatory behavior of the differential scattering cross-section $\sigma_{12}(a)$ for $a>1$ μm.

Let us consider another characteristic and practically important example of polydispersial integral effects in LDA, namely, the Doppler spectra of polydisperse particles system with the normal size distribution, which settle in a still medium. In this case $v_p(a) = u_0 \cdot (a/a_0)^2$, $u_0 = 2(\rho_1 - \rho_2) g a_0^2 / 9\eta$. Here $\rho_1 > \rho_2$ are the densities of particles material and medium, correspondingly, g is the acceleration of gravity, η is the medium viscosity. We assume that the light scattering by these particles can be described either by Rayleigh-Gans approximation (3), or by large particles

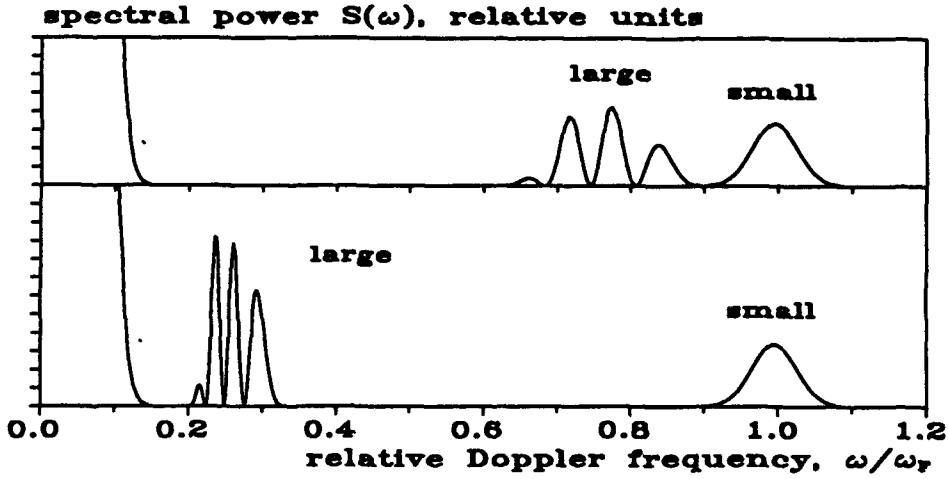

Fig.3. Integral Doppler spectra of bimodal polydisperse particles system (Fig.2) carried along by a high-speed gas flow, calculated for small (bottom) and large (top) distance from the injection point. $u_0(x) = 0.25\ v_F$, $\theta_1 = \theta_2 = 10^0$, $\beta = 2^0$.

approximation (4). Fig.4 shows the changes of the Doppler spectrum of this particles system when the mean particle radius a_0 is increased but the relative width δ/a_0 of the size distribution function is kept constant. The latter ensures the constant shape of the spectral envelope $C[a(\omega)]\cdot[da(\omega)/d\omega]$. For small a_0 the spectrum shape is determined by a smooth contour of the size distribution $C(a)$. With the increase of a_0 the modulation of the spectral envelope by the oscillations of the scattering cross-section $\sigma_{12}[2ka(\omega)\cdot sin(\vartheta/2)]$ (Rayleigh-Gans) or $\sigma_{12}[ka(\omega)\cdot sin(\vartheta)]$ (Large Particles) begins to manifest itself. This process can be easily understood by comparing Fig.4 with Fig.1. The curve $\sigma_{12}(a_0,\omega)$ moves gradually to the left with the increase of a_0, and the transformations of Doppler spectra shape at Fig.4 evidently reflect this movement.

Fig.5 shows the shape of IDA spectrum of settling particles being discussed, calculated using Rayleigh-Gans approximation for various angles 2ϑ between the probing beams. As formulae (3), (4) show, the particle's radius-dependent oscillations of σ_{12} become less frequent with the decrease of ϑ. As a consequence, the Doppler spectrum of large particles acquires the shape characteristic of the spectrum of small particles. Thus, decreasing the angle between the beams, one may transit to the region of "effectively small" particles, where the spectral shape processing and the reconstruction procedure are more simple.

5. CONCLUSIONS

The theory of a new type of the object-integral effects in LDA is developed. The physical basis of these effects is the combination of the polydispersity of particles with their slip relative to a flow, the slip velocity depending on the particle parameters. The characteristic

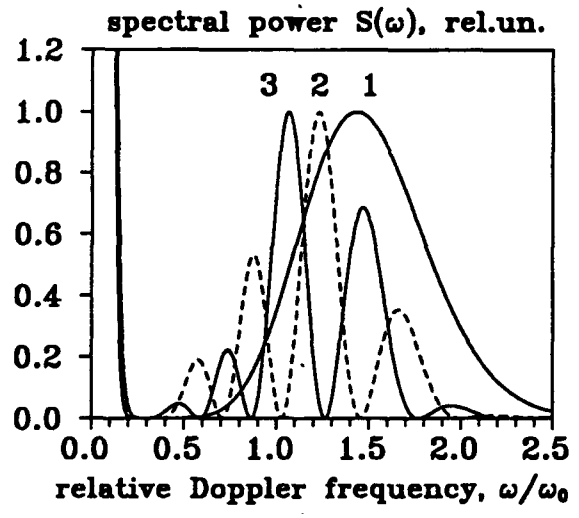

Fig.4. Doppler spectra of settling particles system with the normal size distribution, calculated in Rayleigh-Gans (1,2) and Large Particles (3) approximations for $a_0/\delta=7$, $a_0=0.1$ μm (1), $a_0=3.6$ μm (2,3). $\vartheta_1=\vartheta_2=10^0$, $\beta=2^0$.

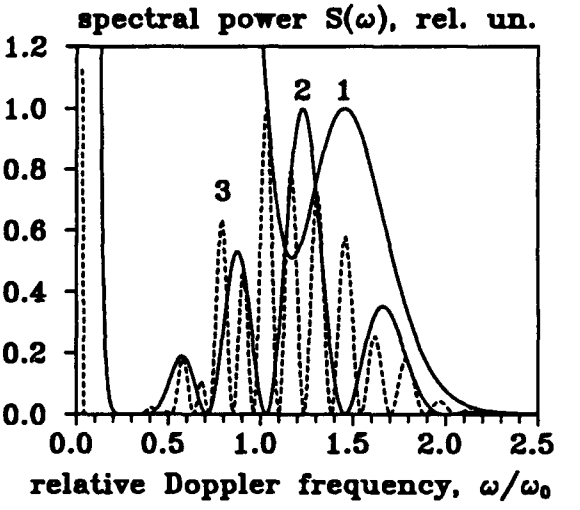

Fig.5. Doppler spectra of settling particles system with the normal size distribution, calculated in Rayleigh-Gans approximation for $a_0=3.6$ μm, $a_0/\delta=7$, and $2\vartheta = 8^0$ (1), 20^0 (2), 60^0 (3). $\vartheta_1=\vartheta_2$, $\beta=2^0$.

features of Doppler spectra registered in such conditions are the following: a large spectral width conditioned by the width of the parameter distribution function $C(a)$ and by the particles slippage law $v_p(a)$; a possible mismatch between the position of the spectral contour maximum and the local Doppler frequency ω_F of a flow ; a complicated shape of a spectrum with the possible line structure due to the oscillatory behavior of the coherent scattering cross-section $\sigma_{12}(a)$ for sufficiently large particles. As Figs.3-5 demonstrate clearly, the size-velocity correlation in large particles system in a flow may result in Doppler spectra which look like those of discrete set of particles fractions, even if the actual size distribution function of particles is a smooth curve. The line structure in such spectra strongly depends on the angular parameters of the registration of the scattered light, namely, on the angle 2θ between the probing laser beams, the observation angles θ_1, θ_2, and aperture angle β of receiving optics. Thus, the polydisperse-multivelocity integral effects may lead to serious metrological errors in LDA, if did not taken into account or misinterpreted. On the other hand, if handled properly, they can be used for determination of some characteristic distribution functions of two-phase flows from the shape of the integral Doppler spectrum.

REFERENCES

Durst, F., Melling, A. & Whitelaw, J.M. 1976, Principles and Practice of Laser Doppler Anemometry, Academic Press, London.

Kononenko, V.L. 1992, Integral Transit-Time Anemometry, Soviet Technical Physics Letters, Vol. 18, pp.693-694.

Kononenko, V.L. 1993a, The integral approach in laser anemometry, Optical Engineering Bulletin SPIE/Russia, N.1, pp.15-18.

Kononenko, V.L. 1993b, Integral Doppler anemometry: a new technique for the measurements of flow velocity profiles and particles concentration profiles in a flow, in Laser Anemometry: Advances and Applications. Proceedings of the Fifth International Conference, ed. J.M. Bessem, R. Booij, H.W.H.E. Godefroy, P.J. de Groot, K. Krishna Prasad, F.F.M. de Mul, E.J. Nijhof, Proceedings of SPIE, Vol. 2052, pp. 605-612.

Kononenko, V.L. & Rinkevichius, B.S. 1993, Aerosols characterization using integral effects in laser Doppler anemometry, in CIS Selected Papers, Optical Monitoring of the Environment, ed. N.N. Belov and E.I Akopov, SPIE Volume 2107, pp.385-399.

Kononenko, V.L. & Shimkus, J.K. 1992, Methods and metrological aspects of Integral Doppler Anemometry, Measurement Techniques, Vol. 35, pp. 933-940.

Rinkevichius, B.S. 1990, Laser Diagnostics in Fluid Mechanics. ed. V.A. Fabrikant, MPEI Publication, Moscow (in Russian).

Rinkevichius, B.S., Tolkachev, A.V., & Kharchenko, V.N. 1974, Measurement of the velocity field of a hypersonic flow by a laser Doppler velocimeter, Bulletin of the Academy of Sciences of the USSR, Fluid and Gas Mechanics series, N.2, pp.559-562.

A MINIATURIZED INSTRUMENT IMPLEMENTING PULSE DISPLACEMENT TO MEASURE PARTICLES FROM 2 μm TO 5,000 μm

Craig P. Wood and Cecil F. Hess

MetroLaser, Inc.
18006 Skypark Circle, Suite 108
Irvine, California 92714
USA

ABSTRACT

This paper describes a miniaturized particle sizing velocimeter built by MetroLaser, highlighting the optical probe containing an integrated transmitter and receiver. The instrument is the first of its kind to utilize the pulse displacement technique (PDT) to measure particle size. PDT is based on the detection of scattered refraction and reflection pulses which sweep past a detector at different times as a particle traverses a narrow laser sheet. In conjunction with the I_{max} particle sizing technique and a time-of-flight velocity measuring technique, the instrument will measure the size, velocity, and concentration of particles with diameters ranging from a few microns to several millimeters. An overview of the features and specifications of the instrument are presented, followed by a brief review of the optical techniques employed. The optical probe is then described in detail. Finally, the data processing hardware and the algorithms developed to sort and identify all reflection and refraction pulses are described. Several challenges and innovations associated with the instrument are addressed, including the use of an optical fiber bundle integrated with two multimode fibers to allow measurements over both a small probe volume (in the measurement of sizes from 2 to 100 μm) and a large probe volume (in the measurement of particle diameters up to several millimeters) without any modification to the optical probe.

1. INTRODUCTION

Single particle counters typically use illuminating laser beams with dimensions on the same order of magnitude or larger than the size of the measured particles (see, for example, Bachalo and Houser (1984); Chu and Robinson (1977); Durst and Zaré (1975); Hess (1984); and Holve (1980)) and are characterized by size ranges of about 35:1 for a given configuration. These features can present a serious limitation in many two-phase flows which are characterized by a large size range and a high particle concentration.

Recently, however, several publications (Hess and Wood (1992); Lading and Hansen (1992); Hess and Wood (1993); and Hess and Wood (1994)) have described the pulse displacement technique (PDT) which has the potential of measuring the size of particles over a range exceeding 1000:1. Unlike earlier techniques, PDT illuminates a particle with a laser beam or sheet that is typically smaller than the particle diameter. This results in resolved refraction and reflection pulses scattered by a particle as it traverses the beam or sheet. At a fixed index of refraction and scattering angle of detection, the time between the refracted and reflected pulses is a function of the size and velocity of the particle. Therefore, knowledge of the velocity and the time between the refraction and reflection pulses leads directly to a measurement of size.

2. INSTRUMENT OVERVIEW

Figure 1 presents a schematic drawing of the miniaturized particle sizing velocimeter. The instrument consists of:

- a miniaturized optical probe with integrated transmitter and receiver;
- an argon ion laser with a laser-mounted fiber optic coupler;
- a flexible, water-proof conduit containing single- and multi-mode optical fibers and a fiber bundle;
- a rack-mounted opto-electronic interface module containing the photodetector assembly and probe heater controller; and
- an IBM-compatible microcomputer containing two digital signal processing boards.

The instrument will measure particle sizes in two ranges without the need for realignment. The first range, from 2 to 100 μm, utilizes PDT and I_{max} together. The second range, from 100 to 5000 μm, utilizes only PDT. When changing size ranges, the optics within the probe do not require reconfiguring so the probe can be left undisturbed at the point of measurement while the operator makes simple changes at the front panel of the opto-electronic interface module (OEIM). For example, if the size range of interest falls between 100 and 5000 μm, the output of a custom fiber optic bundle (described in detail in Section 4.2) is connected to the front panel of the OEIM. If the size range of interest falls between 2 and 100 μm,

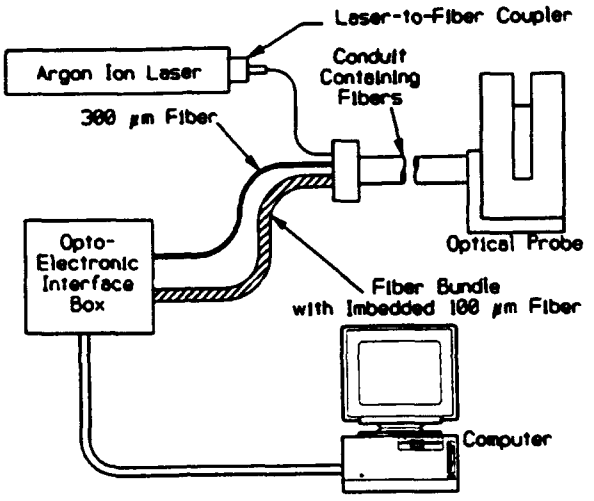

Figure 1. Miniaturized Particle Sizing Velocimeter

the output of a 100 μm fiber, imbedded within the fiber bundle, and a separate 300 μm fiber are connected to the OEIM.

The instrument will measure particle velocities from less than 0.1 m/s to more than 150 m/s. In its present configuration, the optical probe is constrained to measure particles which enter the probe volume at an angle of ± 30° from the normal to the sheets. This constraint is imposed to keep the interior of the optical probe dry in a wet experimental environment. It is not a limitation of PDT, which can be implemented to measure the velocity of particles entering the sheets from either side over a wide range of trajectory angles.

The optical probe is designed to operate in harsh environments characterized by high levels of noise and/or vibration, elevated humidity (from fog to rain), and low ambient temperatures. The inner structure of the optical probe, containing all optics and mounting hardware, is constructed of Invar, an iron/nickel alloy with a low coefficient of expansion. The dimensional stability of Invar, along with thermocouple-controlled flexible heaters attached to the inside of the optical probe, ensures that the probe will operate from below 0°C to well above room temperature without the need for realignment.

The optical probe is separated from the laser, computer, photodetectors, and system electronics by 25 meters of optical fibers to allow the instrument operator to perform all required instrument adjustments in an environmentally controlled area apart from the optical probe. For example, the coupling efficiency of the laser-to-fiber coupler can be monitored visually with a panel meter on the OEIM. This meter receives an electrical signal from a photodiode mounted inside the optical probe. The photodiode monitors the beam emerging from the probe volume to allow the operator to, in real-time, adjust laser-to-fiber launching efficiency or correct for beam obscuration in dense sprays. In addition, the operator can change the photomultiplier tube gains via system software using a custom high voltage control card mounted within the computer.

The instrument employs a 2 watt argon ion laser (Lexel Model 95-2) operating in the multiline mode between 0.4579 and 0.5145 μm. Laser light is launched into 25 meters of Fujikura SM 48-P single-mode optical fiber using a laser-to-fiber coupler (OZ Optics Model HPUC-23-500-P-1) mounted directly onto the laser head. Approximately 0.8 watts of power is delivered to the optical probe.

The optical probe, described in detail in Section 4, consists of a transmitter and receiver integrated into a single package. The transmitter contains optics to a) produce a collimated beam from the light emerging from the single-mode fiber, b) separate the resulting multiwavelength beam into individual monochromatic beams, and c) produce parallel, focused sheets separated by 100 μm at wavelengths of 0.4880 and 0.5145 μm.

Light scattered by particles traversing the probe volume is collected by the receiver and is focused onto a fiber bundle or individual multi-mode optical fibers (depending on the size range chosen) for transmission to a photodetector assembly located in the OEIM. The photodetector assembly consists of three photomultiplier tubes (PMTs), each mounted on a custom preamp card. Two of the PMTs are fitted with either an 0.4880 μm or an 0.5145 μm interference filter. The third PMT acts as a particle trajectory validator and accepts scattered light of all wavelengths.

The output from the preamps is sent to a pair of digital signal processors (Signatec Model DASP100A), housed within the system computer, for digitization and data reduction. The function of the digital signal processors is described in detail in Section 5.

The instrument is controlled by proprietary computer software which allows the operator to a) define important experimental parameters (sheet waist dimensions, sheet separation, desired size and velocity ranges, etc.), b) set important data acquisition parameters (memory size, signal digitization rate, PMT high voltage levels, electronic threshold levels, etc.), and c) perform a wide range of post-experiment data processing functions (calculate size/velocity/time correlations, spline multiple data sets, calculate liquid water content, etc.).

3. OPTICAL TECHNIQUES EMPLOYED

The miniaturized particle sizing velocimeter integrates two optical particle sizing techniques: the pulse displacement technique and the I_{max} technique. Both techniques, as specifically implemented in the present instrument, are briefly described in this section. For a more detailed discussion of PDT, the reader is referred to Hess and Wood (1993) and Hess and Wood (1994). For a

more detailed discussion of the I_{max} technique, the reader is referred to Hess (1984).

PDT is implemented here using a single off-axis receiver which measures the intensity of scattered light from a particle sequentially traversing two parallel laser sheets with wavelengths of 0.5145 and 0.4880 μm. This is shown schematically in Figure 2. The laser sheets have waists of 20 μm, smaller than the diameter of the particles being measured by PDT. As a particle traverses either sheet, laser light is first refracted and then reflected by the particle, resulting in a set of double pulses. This is shown schematically in Figure 3. The temporal separation of either the two refraction pulses or the two reflection pulses is inversely proportional to the velocity, U, of the particle normal to the two sheets. (This time-of-flight method of measuring velocity was chosen because it can be implemented over the entire size range measured by the instrument. In contrast, laser Doppler velocimetry will exhibit a significant loss of visibility, or frequency modulation, at large sizes, making it unsuitable for this instrument.) The temporal separation of the refraction and reflection pulses (each of the same wavelength) is proportional to the diameter, d, of the particle once the velocity is known.

The second of the two techniques, the I_{max} technique, can measure particle diameters smaller than PDT. The I_{max} technique requires that a laser beam be elongated in one dimension to form a sheet where the intensity along the central portion of the sheet is essentially constant. For particles smaller than the width of the laser sheet, each traverse through the central portion of the sheet produces a single pulse of scattered light composed of merged refraction and reflection pulses whose peak scattered intensity is proportional to diameter as predicted by Mie scattering theory. As with PDT, particle velocity is measured from the time-of-flight between the two sheets.

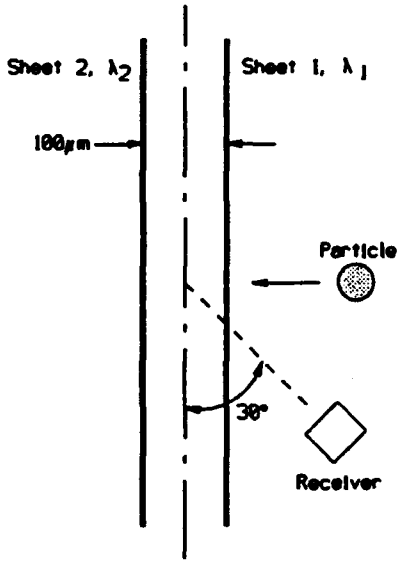

Figure 2. Single Receiver, Dual Wavelength Configuration

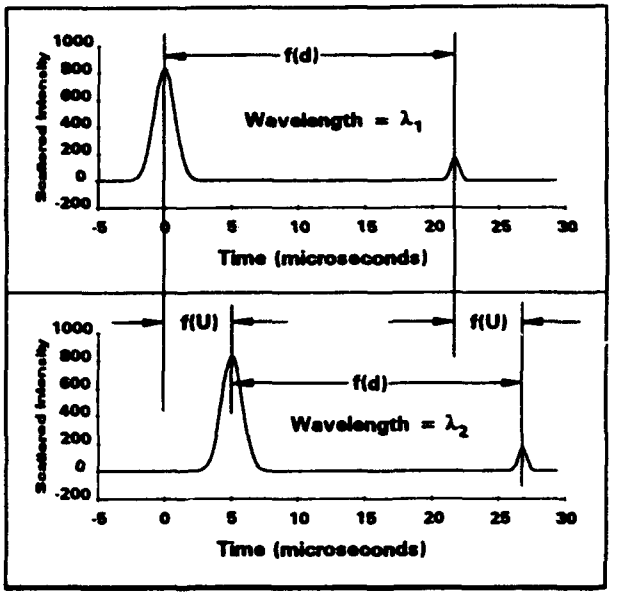

Figure 3. Simulated Refraction and Reflection Pulses Measured with the Single Receiver, Dual Wavelength Configuration. Particle diameter = 500 μm.

Combining the PDT and the I_{max} techniques allows particle sizes to be measured which are both smaller and larger than the laser sheet width. In the current instrument, I_{max} is used to measure diameters from 2 to 45 μm and PDT is used for diameters of 30 μm and greater. This provides an overlapping region from 30 to 45 μm to calibrate the photodetector gains for the I_{max} technique, correcting for fluctuations in probe volume intensity resulting from beam obscuration in dense sprays or a changing laser-to-fiber coupling efficiency.

4. DESCRIPTION OF THE OPTICAL PROBE

A photograph of the optical probe of the miniaturized particle sizing velocimeter is reproduced in Figure 4. The probe consists of a stainless steel L-shaped mounting bracket at the base of the probe; a phenolic thermal insulator; a transmitter arm (shown on the left side) and a receiver arm (shown on the right side); and an anodized aluminum shell (the shell has been removed from the probe in Figure 4 to provide a detailed view of the interior). All fiber optic and electrical feed-through occurs at the lower left side. The overall dimensions of the assembled probe, including the mounting bracket, thermal insulator, and aluminum shell, are 14.9 cm x 4.4 cm x 22.2 cm (L x W x H).

The inner structure of the probe consists of eight parallel Invar rods (four for the transmitter and four for the receiver) and various optical and fiber optic mounts and supports. With the exception of two aluminum light shields, all interior parts are made of Invar.

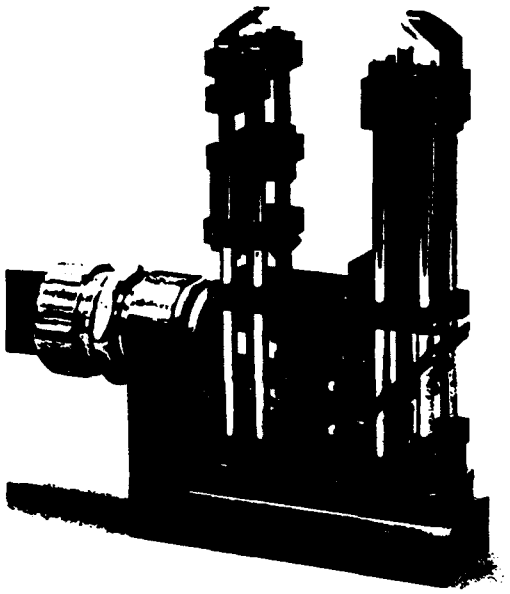

Figure 4. Optical Probe with Aluminum Shell Removed

Size and velocity measurements are made within a probe volume midway between the transmitter and receiver arms and approximately 2.2 cm from the top of the probe. The probe is designed to be completely immersed within the flow field being measured, and to face the oncoming flow (i.e., the transmitter and receiver arms must point into the flow) so that particle-laden air enters the probe volume at the top of the probe and moves downward as oriented in Figure 4. The flow is then divided by a sharp wedge in the aluminum shell as it moves downward beyond the probe volume (i.e., toward the mounting bracket). The results of CFD calculations (Modarress and Hoeft (1993)) show that a velocity deficit of less than 2% occurs at the probe volume for 2 μm particles (which is within the accuracy requirements of the measurement) while the velocity deficit is negligible for particles greater than 10 μm in diameter.

When operating in a wet environment, the interior of the probe is kept dry using a combination of a) baffles and purge air at the apertures where the laser beam exits the transmitter arm and scattered light enters the receiver arm, b) o-ring seals, and c) by imposing a $\pm$ 30° constraint on particle trajectory.

The optical layout of the probe is shown schematically in Figure 5 with each numbered part itemized in Table 1. Items 1 through 8 comprise the transmitter, and items 9 through 15 comprise the receiver.

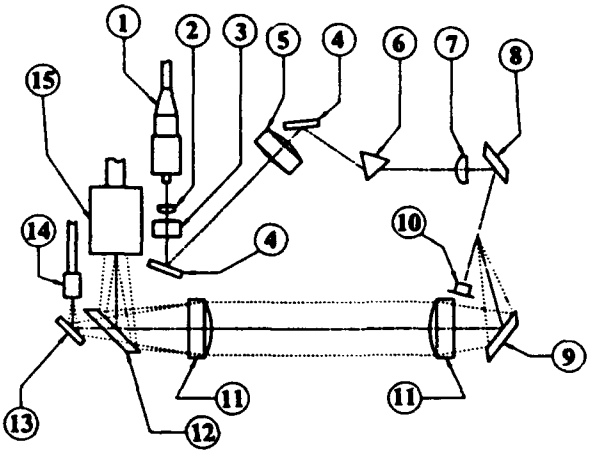

Figure 5. Optical Schematic of Probe

Table 1. List of Probe Optics Referenced in Figure 5.

Item No.	Description
1	Single-mode fiber with FC connector
2	10 mm f.l. achromatic lens
3	44 mm f.l. achromatic lens
4	Mirror
5	31 mm f.l. achromatic lens
6	Quartz dispersion prism
7	37 mm f.l. cylindrical lens
8	Elliptical mirror
9	Elliptical mirror
10	Photodiode
11	60 mm f.l. achromatic lens
12	Elliptical beamsplitter
13	Mirror
14	300 μm optical fiber
15	Fiber bundle with 100 μm optical fiber

4.1 The Transmitter

The transmitter optically conditions the output of the single-mode fiber to produce two parallel laser sheets at wavelengths of 0.4880 and 0.5145 μm. The sheets are focused to 20 μm waists at the point of measurement centered between the transmitter and receiver arms of the probe. To accomplish this task, the multiwavelength laser light emerging from the single-mode fiber is passed through a telescope to produce a collimated beam having a $1/e^2$ diameter of 1.2 mm. The beam is then directed into a quartz prism as depicted in Figure 6. The refractive index of the quartz is a function of wavelength and splits the multiwavelength beam into individual monochromatic beams traveling on divergent paths through the quartz. (This effect is greatly exaggerated in Figure 6.) Each monochromatic beam is turned at a slightly different angle

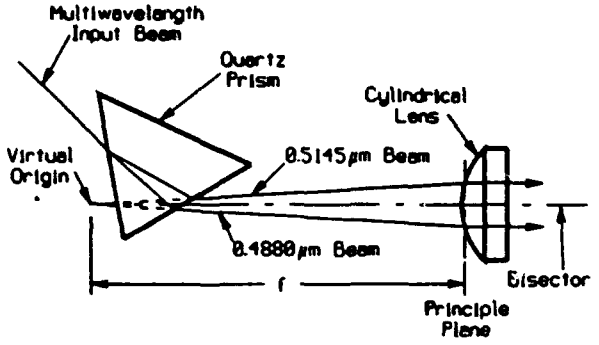

Figure 6. Monochromatic Beams from a Prism

upon emerging from the output face of the prism. The angle of incidence of the multiwavelength beam to the input face of the prism and the angle of the input face of the prism to the geometrical axis of the transmitter are carefully chosen so that the bisector of the 0.4880 and 0.5145 μm beams emerging from the prism is parallel to the geometrical axis of the transmitter.

If the divergent paths of the 0.4880 and 0.5145 μm beams emerging from the prism are extrapolated back into the prism, they appear to originate from a common point - a virtual origin. Therefore, a 37 mm f.l. cylindrical lens is located one focal length from this virtual origin. The 0.4880 and 0.5145 μm beams emerging from the prism intercept the cylindrical lens, resulting in the following:

a) the two beams are made parallel to each other with a separation of 100 μm;
b) each beam is focused in one dimension only to a sheet waist 1.2 mm high by 20 μm wide; and
c) the sheet waists are located one focal length (37 mm) from the cylindrical lens.

The parallel sheets emerging from the cylindrical lens are then reflected by a mirror and directed toward the probe volume. The mirror is placed to locate the waists of the sheets mid-way between the transmitter and receiver arms and 2.2 cm from the forward end of the probe.

4.2 The Receiver

The receiver collects light scattered by particles traversing the probe volume and focuses this light onto a fiber bundle or two individual multi-mode optical fibers (depending on the size range chosen). The scattered light is then transmitted to the photodetector assembly located in the OEIM where only the 0.4880 and 0.5145 μm wavelengths are used.

Scattered light is first reflected by a turning mirror placed at the front of the receiver arm and is then collected and collimated by a 60 mm f.l., f/3 lens. The nominal collection angle is 30°. The collimated light, now directed toward the rear of the probe, is focused by a second 60 mm f.l., f/3 lens onto the face of a rectangular 2 x 8 mm fiber bundle, containing a 100 μm multi-mode fiber imbedded at its center, and a separate 300 μm multi-mode fiber adjacent to it using a 45° beamsplitter. The pair of 60 mm f.l. lenses results in a 1:1 image of the probe volume at the face of the fiber optics irrespective of the size range chosen.

The design and use of the fiber bundle greatly simplifies the optical design of the receiver and allows the measurement of particle sizes from 2 to 5000 μm without altering the optical configuration of the receiver. The fiber bundle is composed of thousands of 50 μm glass multi-mode fibers together with a single 100 μm fused silica multi-mode fiber. At the termination within the probe, the 50 μm glass fibers are bundled into a 2 x 8 mm rectangular aperture with the 100 μm fused silica fiber positioned at the geometrical center of the rectangular aperture. At the other end of the bundle (the end which feeds light to the photodetector assembly in the OEIM), the 50 μm glass fibers and the 100 μm fused silica fiber are bifurcated from each other, allowing the fiber bundle and the 100 μm fiber to be mounted separately on different PMTs within the OEIM.

The fiber bundle is mounted within the optical probe so that the length of the laser sheets imaged onto the bundle is parallel to the 8 mm dimension of the rectangular aperture, and the height of the laser sheets is parallel to the 2 mm dimension. Furthermore, the fiber bundle and the 300 μm fiber adjacent to it are precisely aligned so that the image of the probe volume seen by the 100 μm fiber (centered in the fiber bundle) is exactly centered within the image of the probe volume seen by the 300 μm fiber.

When measuring particle diameters between 2 and 100 μm, the 300 μm fiber acts as a signal aperture and the 100 μm fiber acts as a trigger aperture for trajectory validation. Light collected by the fiber bundle is not used. As explained in more detail in Hess and Wood (1994), only scattering events with a trajectory validation (i.e., only particle trajectories recorded by the signal fiber and the trigger fiber) are processed. This ensures that the particle has traversed the center of the probe volume. A trajectory through the edge of the probe volume can result in scattered pulses which are both a) diminished in intensity, leading to size errors when using I_{max}, and b) skewed in time, leading to size errors when using PDT and to velocity errors when using either I_{max} or PDT.

When measuring particle diameters between 100 and 5000 μm, the 100 and 300 μm fibers are disconnected from the OEIM and the light they collect is not used. Instead, only the fiber bundle is connected to the photodetector assembly within the OEIM. (This is the only change made to the instrument.) In this large particle configuration, the receiver is now imaging a 2 x 8 mm area centered on the sheet waists at the front of the probe.

Unlike the small particle configuration described earlier, the use of the fiber bundle when measuring particle diameters between 100 and 5000 μm does not require a trigger aperture for trajectory validation. Although a traverse through the edge of the probe volume can still result in a decrease in intensity and a shift in the arrival time of a scattered pulse, these phenomena do not result in significant size and velocity errors. First, a decrease in intensity resulting from a particle grazing the edge of the field of view is inconsequential for a measurement of size with PDT, which derives size from the time between pulses. Also, at the low end of the size range, the field of view (2 x 8 mm) is many times larger than particle diameter. Therefore, random traverses of the probe volume will result in a very small fraction of particles traversing the edges, minimizing the number of pulses with shifted arrival times and the resulting errors in velocity. Third, for particles near the high end of the size range, the sheet separation (100 μm) is many times smaller than particle diameter, and a traverse of the edge of the probe volume will result in an equal amount of shift in the pulse arrival time from each sheet, minimizing or eliminating any error in measured velocity.

5. ANALYSIS OF SCATTERED PULSES

Critical to the success of the instrument was the development of robust and accurate algorithms to sort and identify all reflection and refraction pulses to minimize potential errors and data loss. This section will describe the flow of data received in a typical I_{max}/PDT experiment and will discuss how the instrument hardware and software process these data to arrive at accurate results.

Data collected with the miniaturized particle sizing velocimeter consists of two channels of digitized light pulses (one channel each for the 0.4880 and 0.5145 μm wavelengths) containing size, velocity, and arrival time information for each particle traversing the probe volume. The pulses vary in number, intensity, and temporal spacing depending on the size and velocity of the particle. In addition, pulse intensity is a function of particle trajectory through the probe volume in the large particle configuration where PDT is used exclusively. As a result, each sheet traverse may generate one pulse to be analyzed by an I_{max} algorithm, two pulses to be analyzed by both I_{max} and PDT algorithms, or two pulses to be analyzed by a PDT algorithm only, depending on the size of the particle. Because each particle must traverse two sheets to calculate velocity, one or two pulses are generated at each of two wavelengths for a total of two or four pulses per valid traverse. Furthermore, the reflection pulse generated by a particle larger than the sheet width is usually much less intense than the corresponding refraction pulse and must not be mistaken for the merged reflection and refraction pulses of a particle smaller than the sheet width. In addition, trajectory effects may eliminate one or both pulses from one or both sheet traverses requiring care in the pairing of pulses for analysis. Lastly, although not a concern in the present instrument, a particle entering the probe volume from one side will generate a refraction and reflection pulse detected in a specific order with one wavelength pair initiated before the other, but a traverse from the opposite side will result in both the pulse order and the wavelength order being reversed.

As depicted schematically in Figure 7, the particle sizing velocimeter uses two identical digital signal processors, designated $DSP_{\lambda 1}$ and $DSP_{\lambda 2}$, in a master/slave configuration. These processors are used with either two or three PMTs (designated $PMT_{\lambda 1}$, $PMT_{\lambda 2}$, and PMT_{TV}) to collect and process the pulses described above. The specific hardware configuration and the specific algorithms employed depend on the size range being measured.

5.1 The Small Particle Configuration

In the small particle configuration, scattered light is collected by the 300 μm signal fiber and is separated by wavelength within the photodetector assembly. Pulses of wavelength λ_1 = 0.5145 μm are detected by $PMT_{\lambda 1}$ and digitized by $DSP_{\lambda 1}$ (channel 1). Pulses of wavelength λ_2 = 0.4880 μm are detected by $PMT_{\lambda 2}$ and digitized by $DSP_{\lambda 2}$ (channel 2). The clocking circuitry on the master board ($DSP_{\lambda 1}$) controls signal digitization on both boards. Using an OR gate on $DSP_{\lambda 1}$, both digitizers are turned on or off simultaneously when the trigger input on either board crosses a preset threshold voltage. This allows the timing of events recorded by either processor to be correlated with the other to within ± 0.1 μsec. Digitization ends after a preset time interval, called a time-out, following the return of the signal intensity below the threshold voltage. This contiguous sequence of digital

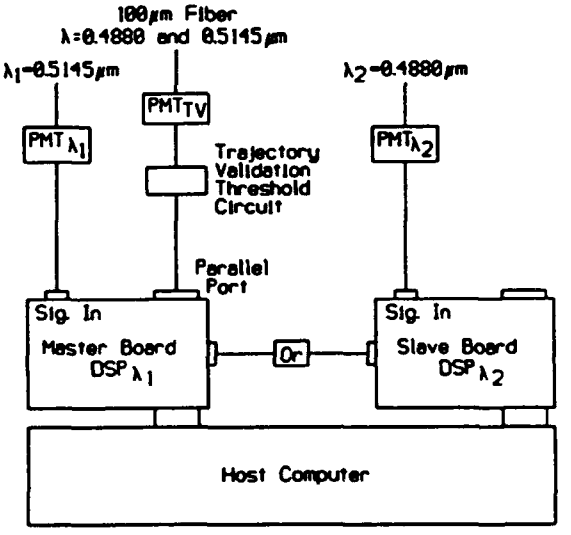

Figure 7. Hardware Configuration for Data Processing

intensity values, bounded in time by the initial upward threshold crossing and the end of the time-out, is called a record and is stored in on-board memory along with its respective start time. Both processors are quiet (i.e., no signal digitization occurs) between the end of a time-out and the next threshold crossing.

Trajectory validation (i.e., validation that a particle has crossed the central, constant intensity portion of the probe volume) is achieved by tagging the start time of each valid record with specific information. The 100 μm trigger fiber (imaging the central portion of the probe volume) receives scattered light of both wavelengths λ_1 and λ_2. This light is delivered to PMT_{TV} as depicted in Figure 7. The output signal from PMT_{TV}, after amplification by a preamplifier, is then passed to a trajectory validation threshold circuit. If the threshold is exceeded at any time during the creation of a data record, the output of the circuit goes high and generates an interrupt which sets the most significant bit of the arrival time to 1, tagging the record as valid.

When the allocated memory onboard either processor is full, data collection stops and the memory contents of $DSP_{\lambda 1}$ and $DSP_{\lambda 2}$ are analyzed. During analysis, each record is scanned from beginning to end for intensity maxima. A record may contain one pulse if the particle was sufficiently small (i.e., the refraction and reflection pulses are merged) or the particle was large and traveling at a slow velocity (i.e., the time out ended before the second pulse occurred, putting the second pulse in the following record), or it may contain two pulses. In either case, a software table is constructed which contains for each pulse a) the peak intensity, b) the time of arrival of the pulse centroid (i.e., the time at which half of the integrated pulse intensity has occurred), and c) a flag indicating whether or not the original record was tagged for trajectory validation.

The next step is to correctly pair the pulses in both channels. First, data for the first pulse in channel 1 is retrieved from the channel 1 software table. Then data for the first pulse in channel 2 with a time greater than the channel 1 pulse is retrieved from the channel 2 software table. This will result in one of three cases:

a) Neither pulse is tagged - In this case, the pulse information from channel 1 is discarded, data for the next channel 1 pulse is retrieved from the software table, and the analysis starts anew.

b) Only one of the pulses is tagged - In this case, the intensity of the single tagged pulse is compared with benchmark intensities to determine whether a second pulse should be retrieved from each channel to perform a PDT size calculation either alone or in addition to an I_{max} size calculation. (An I_{max} calculation alone is not meaningful since both pulses must be tagged to determine an accurate velocity.)

c) Both pulses are tagged - In this case, the average intensity of the two tagged pulses is compared with benchmark intensities to determine whether a) the pulse pair can be analyzed by an I_{max} algorithm only, or b) a second pulse should be retrieved from each channel to perform a PDT size calculation either alone or in addition to an I_{max} size calculation.

Analysis by Imax alone. Both pulses must be tagged and the pulse intensities must be sufficiently small to warrant analysis by I_{max} alone. The velocity is determined from the temporal separation of the pulses (one from each channel), and the particle diameter is determined from the average of the absolute intensities of the pulses.

Analysis by PDT alone. If the intensity in question is sufficiently large to warrant analysis by PDT alone, data for the next pulse in both channels 1 and 2 are retrieved from the software tables. Data for the four pulses (two from channel 1 and two from channel 2) are considered to accurately represent a valid particle traverse if all of the following criteria are met:

a) Three of the four pulses are tagged. (Three pulses are sufficient to determine size and velocity using PDT.)

b) The temporal spacing between the first pulses in each channel must be equal to the temporal spacing between the second pulses in each channel to within a sufficiently small interval, chosen by the operator. This is a check for equivalent velocity. If the time separation between the appropriate pulses is not equal, then the velocities are not equal.

c) The average velocity, calculated from step b, must be less than the velocity maximum set by the instrument operator.

d) The average particle diameter, calculated from the temporal spacing of the refraction and reflection pulses in channels 1 and 2, must be smaller than the diameter maximum set by the operator.

If any one of the above criteria are not met, data for the first pulse just analyzed in channel 1 is discarded, the second pulse just analyzed in channel 1 takes its place, and the analysis starts anew.

If all criteria are met, the scattering event is valid and the diameter and velocity are stored. Data for the next unanalyzed pulse in channel 1 is retrieved from the software table, data for the first pulse in channel 2 with a time greater than the new channel 1 pulse is retrieved from the channel 2 software table, and the analysis starts anew.

Analysis by both PDT and Imax. If the intensity in question is of the appropriate magnitude to warrant analysis by both PDT and I_{max}, the data is first analyzed by the PDT algorithm described above to calculate velocity and diameter, d_{PDT}. The diameter is then calculated a second time from the absolute intensity (i.e., using the I_{max} algorithm) to determine d_{Imax}. A calibration factor, equal to d_{PDT} / d_{Imax}, is calculated and stored along with the velocity and diameter information.

At the conclusion of an experiment, all of the individual calibration factors are averaged to achieve a single global calibration factor. All "I_{max} only" diameter results are then multiplied by the global calibration factor and displayed with the remaining results. The implementation of the global calibration factor can be

turned off at the discretion of the operator. In addition, the operator is provided with the standard deviation of all correction factors and the fraction of all particles with a calculated diameter in the PDT/I_{max} overlap region.

5.2 The Large Particle Configuration

In the large particle configuration, scattered light is collected by the fiber bundle. The detection and digitization of incoming signals is the same as performed for the small particle configuration described in Section 5.1 with one exception: Because trajectory validation is unnecessary, the third PMT used in the small particle configuration (PMT_{TV}) is not used here. Therefore, all pulses detected in the large particle configuration lack a trajectory validation tag.

Data processing in the large particle configuration is performed as in the small particle configuration with only several exceptions. First, PDT is used exclusively because a) the refraction and reflection pulses are fully resolved in this size range and b) the large field of view relative to the dimensions of the laser sheets results in pulse intensities which are trajectory dependent, precluding the use of I_{max}. Second, the time-out period at the end of a scattering event is relatively short to ensure that there is only one pulse per record.

Because particle diameter in this size range can be large relative to the sheet width, the refraction and reflection pulses can be of relatively long duration. In this case, the exact time of maximum pulse intensity may not correspond to the temporal center of the pulse. To minimize errors in determining arrival times for broad pulses, pulse intensity is integrated over the entire duration of the pulse to calculate the temporal location, or arrival time, of the pulse centroid. (The arrival time of the pulse centroid is used when calculating size and velocity with PDT in both the large and small particle configurations.)

ACKNOWLEDGMENTS

The authors gratefully acknowledge Mr. Thomas Hoeft of Physical Research, Inc., for his extensive contribution to the design of the optical probe, and Mr. Matt Tonge and Mr. John Tonge for helpful discussions regarding the data processing hardware configuration and software algorithms.

REFERENCES

Bachalo, W.D. & Houser, M.J. 1984, Phase/Doppler Spray Analyzer for Simultaneous Measurements of Drop Size and Velocity Distributions, Opt. Eng., Vol. 23, No. 5, pp. 583-590.

Chu, W.P. & Robinson, D.M. 1977, Scattering from a Moving Particle by Two Crossed Coherent Plane Waves, Appl. Opt., Vol. 16, No. 3, pp. 619-626.

Durst, F. & Zaré, M. 1975, Laser Doppler Measurements in Two-Phase Flows, Proceedings of the LDA-Symposium, Copenhagen, pp. 403-429.

Hess, C.F. 1984, Nonintrusive Optical Single-Particle Counter for Measuring the Size and Velocity of Droplets in a Spray, Appl. Opt., Vol. 23, No. 23, pp. 4375-4382.

Hess, C.F. & Wood, C.P. 1992, Laser Technique to Measure Particle Size and Velocity in High Density Applications, Sixth Int. Symposium on Applications of Laser Techniques to Fluid Mechanics, Lisbon, 20-23 July.

Hess, C.F. & Wood, C.P. 1993, Pulse Displacement Technique to Measure Particle Size and Velocity in Large Number Density Applications, in Laser Techniques and Applications in Fluid Mechanics, eds. Durau, Durst, Heitor, Maeda, Whitelaw, and Raufelder, Springer-Verlag.

Hess, C.F. & Wood, C.P. 1994, The Pulse Displacement Technique - A Single Particle Counter with a Size Range Larger than 1000:1, Part. Part. Syst. Charact., Vol. 11, pp. 107-113.

Holve, D.L. 1980, In Situ Optical Particle Sizing Technique, J. Energy, Vol. 4, No. 4, pp. 176-183.

Lading, L. & Hansen, B.H. 1992, A Complementary Method for Simultaneous Measurement of Size and Velocity, Sixth Int. Symposium on Applications of Laser Techniques to Fluid Mechanics, Lisbon, 20-23 July.

Modarress, D. & Hoeft, T. 1993, Evaluation of Flow Field with CFD, Physical Research, Inc., Interim Report, April.

MEASUREMENT OF SIZE AND VELOCITY OF ARBITRARY SHAPED PARTICLES BY LDA BASED SHADOW IMAGE TECHNIQUE

Hiroshi Morikita, Koichi Hishida and Masanobu Maeda

Department of Mechanical Engineering
Keio University, Yokohama, JAPAN

ABSTRACT

An instrument based on an imaging technique and laser Doppler velocimetry (LDV) was developed for sizing particles of arbitrary shape. The signal of a particle was detected by a 32 channel linear diode array focused on the measuring volume, and the image was reconstructed from 'sliced' images of the particle provided by temporal outputs from the detector. The present instrument, which consists of a multi-channel transient recorder and independent LDV processor, was used to measure size, velocity, shape and trajectory information of particles ranging from 30 to 250 μm with velocity up to 10.0 m/s; the size of a particle was obtained from the area of the shadow image and the trajectory was inferred by cross-correlation between two images projected by two incident beams of the conventional LDV. The accuracy of the average size for spheres was less than 3.0 % compared with that measured by a microscope. The size distribution of non-spherical particles showed similar shape with microscopic measurement, and maximum error of average diameter was 10 % approximately.

1. INTRODUCTION

The sizing of arbitrary shaped particles is of technical interest and accurate determination of their equivalent diameter is important, because many particles in industrial processes are non-spherical. For sizing spheres, many laser-based techniques, such as the phase Doppler anemometer [e.g. Domnick et al., 1993, Kobashi et al., 1992] and an imaging based system [Hovenac et al., 1985], have been developed. Although these instruments are accurate and robust, they can not be used for sizing non-spherical particles since the methods rely on the light scattering from a sphere. The diffraction amplitude method [Orfanoudakis & Taylor, 1993, Morikita et al., 1993] or the other methods based on light scattering [e.g. Bottlinger and Umhauer, 1988] are suitable instruments for this purpose, however extreme care has to be taken to align the optical probe to avoid uncertainty caused by the non-uniform irradiance distribution of the incident laser beam. A recent method proposed by Kaye et al. [1991] resulted in higher accuracy than the single detector system, however it requires large optical benches surrounding the test volume.

Imaging based techniques [Knollenberg, 1970 and 1976, Bertollini et al., 1985] have an advantage for sizing non-spherical particles because two-dimensional images can eliminate problems arising from the non-sphericity of particles. The Shadow Doppler technique, which is an instrument for sizing irregularly shaped particles developed by the authors [Hardalupas et al., 1993], is based on the imaging method. In this instrument, the images were projected by a pair of beams of a conventional LDV, and the prototype system has been evaluated and shown to provide an accuracy of sizing to 10 μm. The primary advantage of the method is that less care in alignment is necessary compared with intensity based methods and can provide velocity and size information at relatively lower cost than a high speed camera system.

The purpose of this study is the evaluation of accuracy of the instrument by measuring the area-equivalent diameter and velocity of arbitrary shaped particles in free-falling and accelerating flows. The signal processing which provides velocity, size, shape and trajectory of the particle is also introduced and assessed. In the following section, the instrument and method are described, and experimental results of sizing can be found in section 3. Section 4 presents a method to determine the size distribution which eliminates the biasing effect caused by size-dependence of the effective area of the measuring volume.

2. OPTICAL SETUP AND SIGNAL PROCESSOR

2.1 Principle of Shadow Doppler method

The optical arrangement, which includes the transmitting and receiving modules of a conventional LDV system, is illustrated in Figure 1. A laser beam of 514.5 nm wavelength (green), radiated by an Argon-ion laser (NEC, GLG-3262), was used as light source and formed a measuring volume with an intersection angle of 4.936 degrees. The transmitting optics consists of beam expander, beam-splitter, a pair of acousto-optic modulator (AOM) cells and focusing lens. A pair of cylindrical lenses were used to form the incident beam in an elliptical cross-section to increase the effective energy

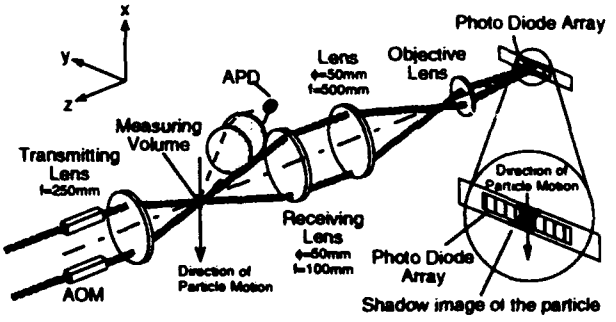

Figure 1 Principle of the method and arrangement of receiving optics. The direction of the particle motion was perpendicular to the axis of the photodiode array

density in the area detected by the linear diodes. The measured diameters of the ellipse were approximately 500 and 250 μm with the major axis coinciding with the axis of the linear diodes. Frequency shift of 50 to 500 kHz was provided by the AOM component to avoid fluctuation of the sizing signals: when the frequency shift is too low compared with the sampling rate of the transient recorder, interfered fringes in the measuring volume derive large fluctuation in the sizing signals.

Two independent receiving probes for size and velocity measurement were used, as shown in figure 1, for ease of alignment. The image of a particle in the measuring volume was focused on the array detector by relay lenses, with a magnification ratio between 75 and 120, and the Doppler signal from the same scatterer was detected, via focusing lenses and a spatial filter (pinhole), by an avalanche photo diode (RCA, C30902E). The sampling space of the APD was aligned to have larger area than that for the sizing.

Signal detection of the particle size and shape was achieved by a 35 channel linear diode (Hamamatsu S4114-35) which is focused on the measuring volume. As a particle passed through the volume, the magnified shadow image moved across the detector in the direction of particle motion; thus the output amplitudes of the detector varied, as shown in figure 2(a). Taking into account the velocity measured by the single photo diode for LDV, a two dimensional image of the particle was reconstructed from the time-series output of the detector.

Since the shadow images are from both of the two beams, the appearance of the images depend on the trajectory of the particle. Figure 2 (a), (b) and (c) show various patterns of projected shadows on the detector plane by a particle without and with 'defocus', i.e. the distance between the particle and the focal plane of the measuring volume. When the particle trajectory was in the focal plane of the relay lenses, the shadow images projected by the two beams coincided precisely and the output signals had two levels of amplitude, as shown in figure 3(a); the marking a-a' denotes the line in figure 2 and the plateau at the lower voltage level corresponds to the central dark part of the particle image. Those two images separate gradually with increasing defocus distance and the signals became tri-state (figure 3 (b)) because the irradiance of the region which lies in the shadow of the particle illuminated by only one beam is half as much as that of the region illuminated by both, unblocked beams. If the particle is out of the measuring volume, the overlapping area and the dark shadow disappear.

In all the cases described above, the equivalent size, d_a, based on the average area of the projected shadow is defined by figure 2(b) and the following equation:

$$d_a = \sqrt{\frac{4\,(2S_L + S_H)}{2\pi}} \qquad (1)$$

The sizing accuracy of the presented method, therefore, relies on the quality of the image and the size of the projected shadow is affected by large defocus distance because the image becomes less sharp. However, the error caused by defocus is small in the vicinity of the focal plane and the quality of the image can be kept almost as good as that of in-focus [Hardalupas et al, 1993]. Thus, suitable signal triggering and data rejection are necessary in order to avoid erroneous size information. For this purpose, the trigger level was set at a normalized amplitude level between 0.2 and 0.3 so as to avoid capturing particles with large defocus (figure 2(c)). Also, an effective data validation scheme is described in section 2.3.

In contrast, when a particle was in the path of the laser beam but outside of the measuring volume, it was not triggered,

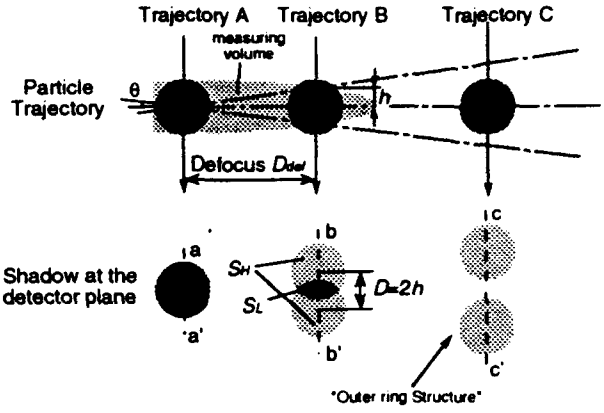

Figure 2 Shadow images of a particle focused on the photodiode array and trajectory dependence on their appearance, A) in-focus, B and C) out-of-focus.

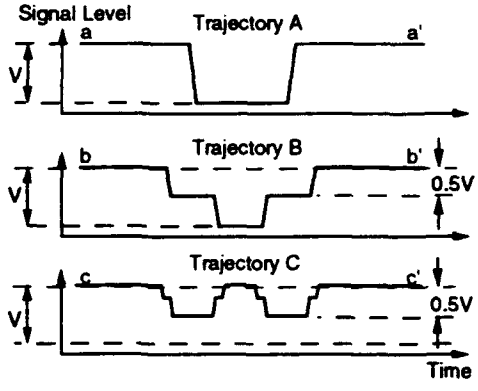

Figure 3 Idealized output signals from the photodiode array with trajectories defined in figure 2.

because relatively short depth field of the relay lenses makes such signals untriggerable.

The novel features of the method are summarized as follows: the signal level is independent of size, material and refractive index of the particle, because the amplitude is determined by the presence of a shadow; hence, no biasing due to size dependence of the signal amplitude arises, and transparent media, such as water or glass, can be measured without changing optical configurations. The instrument can provide not only the size but also the trajectory of the particle by estimation of defocus distance. In addition, the required dynamic range of the detector is small and low intensity resolution is acceptable, relatively to intensity-based methods.

2.2 Signal processor

For the data acquisition of the output signals from the array diodes with appropriately high sampling rate, a computer-controlled transient-recorder system was employed. Figure 4 illustrates a block diagram of the processor. The system consists of a head module including the diode array and multi-channel transient recorder for sizing, and an APD module and single channel recorder for velocity measurement. All the operating procedures were controlled by a personal computer (IBM 486-33 compatible).

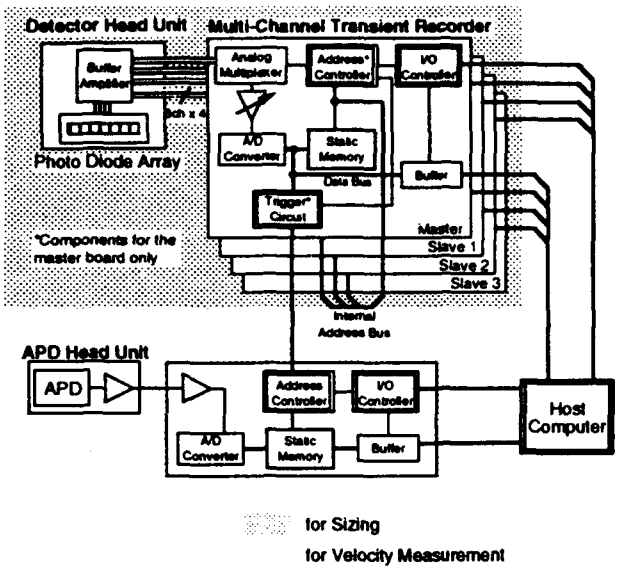

Figure 4 Signal processor including two head-units of the detectors for sizing and velocimeter.

The linear array detector had 35 diode segments and 32 of them were used as active channels to simplify the design of the transient recorder. Each diode had a 0.9 mm width x 4.4 mm height and a slit aperture with 1 mm height was fitted on the detector to increase the spatial resolution; thus each diode had 1 x 1 mm active size, which corresponds to 10 x 10 μm of the measuring volume given the magnification ratio, G, of 100 of the collection optics.

The multi-channel recorder comprised a master and three slave boards. Signals detected by the array diodes were transferred to the recorder through buffer amplifiers and distributed to 8 analog multiplexers (Analog Devices AD9300) which each had four inputs and one output. Two multiplexers on one board were connected to one A/D converter (Fujitsu MB40568) of 8 bit resolution and the converted results were stored in static RAM with 32 kByte on each board. The maximum conversion rate was 8 MHz from the system clock, which corresponded to 1 MHz total sampling rate. For more detailed information of the hardware, see Hardalupas et al. (1993) and Kobashi et al. (1992).

The trigger level was set at around 20 % of the normalized amplitude, as mentioned in the previous subsection; therefore, particles with defocus required a pre-triggering function [Kobashi et al., 1992] to obtain the whole signal corresponding to the leading negative-edge (figure 3(b)). In order to accomplish that, the address generator on the master board was designed to be able to control the address pointer flexibly.

For velocity measurement, a single channel recorder with 128 kByte storage memory was also provided. The clock of this board was synchronized with system clock of the multi-channel recorder with a sampling frequency up to 20 MHz. No trigger circuitry was incorporated on the board because the function was operated by the master board.

Stored signals were transferred to the host computer through an interface module connected on the ISA-bus and processed. The data processing and validation functions are described in the next subsection.

2.3 Software processing

The digitized data, which were stored in static RAM, were transferred to the host computer and processed to construct a 'pseudo-image' of the particle. In this subsection, the procedure to infer velocity, area-based size, defocus distance and trajectory direction is described.

a. Velocity calculation

First of all, the Doppler burst signal detected by the APD was analyzed to obtain velocity information from a fast Fourier transform (FFT) using an adjusted Gaussian interpolation [Kobashi et al, 1990] scheme in frequency space. The applied validation routine was described in Kobashi et al. and the maximum error was estimated at 0.2% of the fundamental frequency of the spectrum. If the triggered signal was recognized as erroneous, it was rejected and another iteration of sampling was started.

b. Normalization

The peak amplitude of the signals from the diode array varies along the detector due to the Gaussian intensity distribution of the incident laser. Hence, amplitude normalization was required to adopt fixed level thresholding for all diodes. Since the amplitude was dependent on the presence or the absence of the particle image, the minimum level was

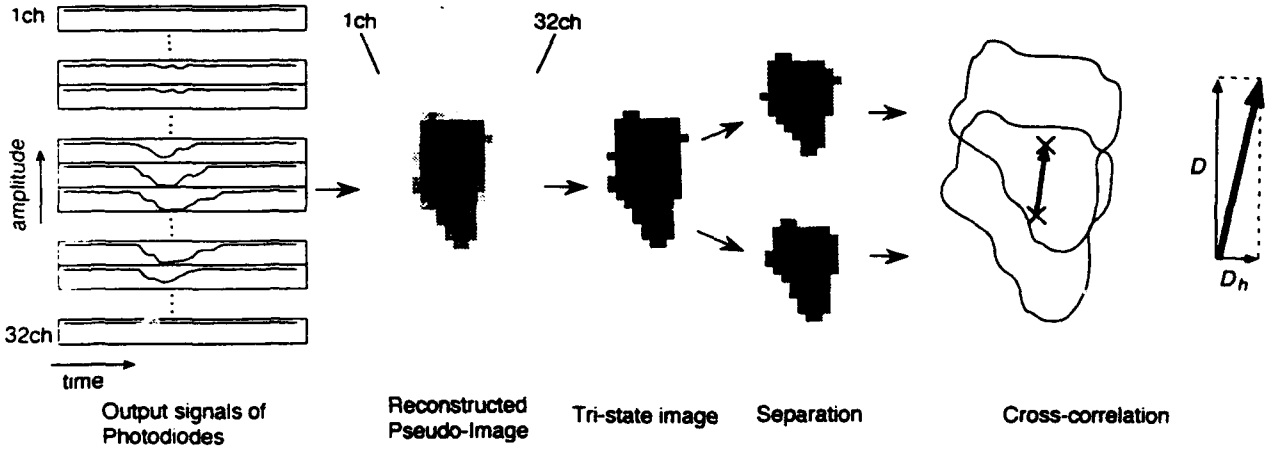

Figure 5 Procedure of the reconstruction of a 'pseudo-image', validation of the signal and determination of the defocus distance

equal to the ground level and the maximum level was equal to the amplitude of the incident laser illumination in the absence of particles. The normalized amplitude of diode channel i at time t, $r_{norm}(i,t)$, was, hence, defined by the following equation,

$$r_{norm}(i,t) = \frac{r(i,t) - r_{min}(i)}{r_{max}(i) - r_{min}(i)} \quad (2)$$

where $r_{max}(i)$ and $r_{min}(i)$ are the maximum and minimum amplitudes of each channel. Figure 5 shows an example of the normalized signal.

c. Temporal Windowing

To construct a two-dimensional pseudo-image of a particle, time averaging of the temporal signals was necessary to convert these to a pixel image. The distance over which a particle, with velocity U [m/s], moved within one sampling period of the recorder, $1/f$ [s], was equal to U/f, and the pitch distance between each detector of the array was 1.0 mm, which corresponded to $10^{-3}/G$ [m] in the measuring volume of the LDV. Thus, the number of the samples which corresponds to the channel pitch of the detector, N, is

$$N = \frac{10^{-3}}{GU} \quad (3)$$

Consequently, sampled signals must be averaged over batches of N samples. In the present instrument, this was implemented using N integer where $N \geq 2.0$, and linear interpolation was applied where $N < 2.0$. However, it should be noted that a test showed that the effect of this averaging resulted in negligibly small error compared with that caused by other factors.

d. Thresholding

In order to determine the boundary of the particle, thresholding with two fixed levels were adopted. Figure 5 shows the example of a tri-state image. The threshold levels were empirically set at normalized amplitudes of 0.4 and 0.75 as recommended in our previous work. The projected area was evaluated by a 'painting' routine to remove the shadow image of any other particles existing in the measuring volume at the same time. The resultant area was substituted into equation 1 to calculate equivalent diameter.

e. Separation of Image and Cross-correlation

There are mainly three purposes in this process: first, to determine the defocus distance of the particle; second, to estimate trajectory direction; third, to eliminate 'multiple scattering' which can cause serious error in sizing. Tri-state image was separated by pattern recognition routine into two binary images, which correspond to shadows from each of the two incident beams. These separated images were used for calculation of cross-correlation to determine the displacement (lag) between two images. As shown in figure 2 and 6, the vertical component of the displacement, D, is proportional to the defocus distance. Thus, the defocus distance, D_{def}, can be obtained by,

$$D_{def} = \frac{D}{2\tan(\theta)} \quad (4)$$

where θ is the beam intersection half angle. When the defocus distance is comparable to, or larger than, the focal depth of the receiving optics, quality of the image becomes poor. To eliminate this effect, the defocus was limited at between 300 to 800 μm.

Similarly, the horizontal displacement is proportional to the particle movement in horizontal direction D_h; hence, the trajectory direction, φ, of the particle can be described by the following equation.

$$\varphi = \tan^{-1}\left(\frac{D_h}{D}\right) \quad (5)$$

This equation allows us to acquire an 'approximate' two dimensional velocity measurement by use of a single channel LDV, although the accuracy decreases with decreasing defocus distance. This angle was also used for determination of the correct size distribution described in section 4.

When the two binary images have the same shape and area, the number of the correlated pixels agrees with the area of the projected shadows; therefore, the maximum value of the correlation function directly quantified the correspondence between two images and was used in the validation of the image of multiple scattering. The tolerance of the correspondence was set at around 30% which was decided empirically. This function, for binary data, was performed with logical, rather than arithmetic, multiplication because it is economical of computation time.

3. RESULTS OF VELOCITY, SIZE AND DEFOCUS DISTANCE MEASUREMENTS

3.1 Spheres in an accelerating flow

Figure 6 shows the size-velocity correlation of polyethylene spheres (Flowbeads, Sumitomo Seika, colored black) which was measured in an accelerating flow, produced by the suction flow induced by an inlet nozzle of 30 mm diameter set vertical with maximum velocity approximately 4.0 m/s. The particles were released 100 mm above the nozzle entrance and were measured at 50 mm above the nozzle on the axis. The sampling frequency and magnification ratio, G, were 312.5 kHz and 116, respectively.

At the measurement point, the particle velocity varied with size because of inertia. The velocity was correlated to the measured size, and the maximum rms value of the size in each velocity class was about 10%. It should be noted that the flow was carefully controlled, so that the scatter seemed to be caused by fluctuation of the flow. This result, therefore, confirms the precision of the size measurement.

3.2 Free fall particles of arbitrary shape

In order to evaluate the accuracy of the measurement, the velocity and size of particles with various shape were tested by sizing particles in free-fall condition to provide direct assessment of sizing accuracy and comparison with the aerodynamic diameter.

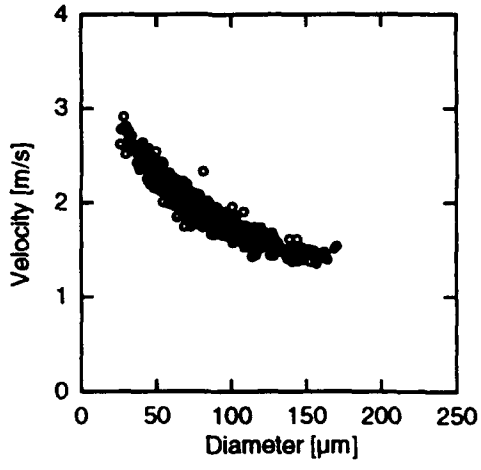

Figure 6 Size-velocity correlation of polyethylene spheres accelerated in the suction flow. Defocus distance is limited at 800 μm.

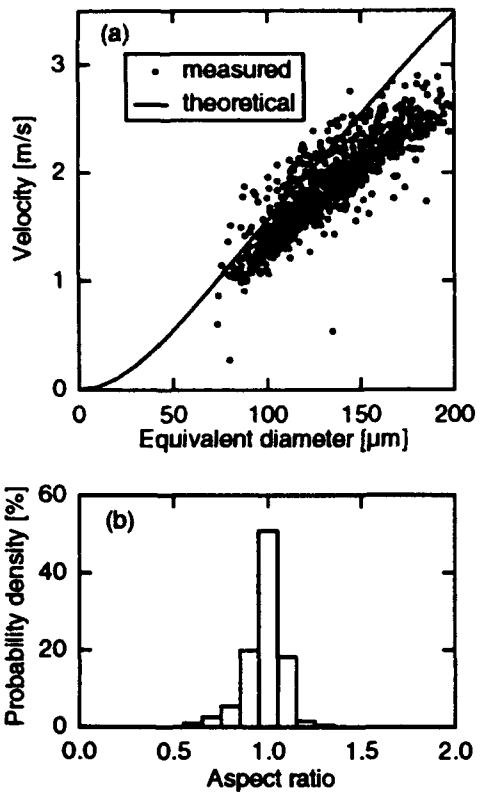

Figure 7 Size-velocity correlations (a) and distribution of aspect-ratios (b) of copper spheres. Defocus distance was limited at 800 μm.

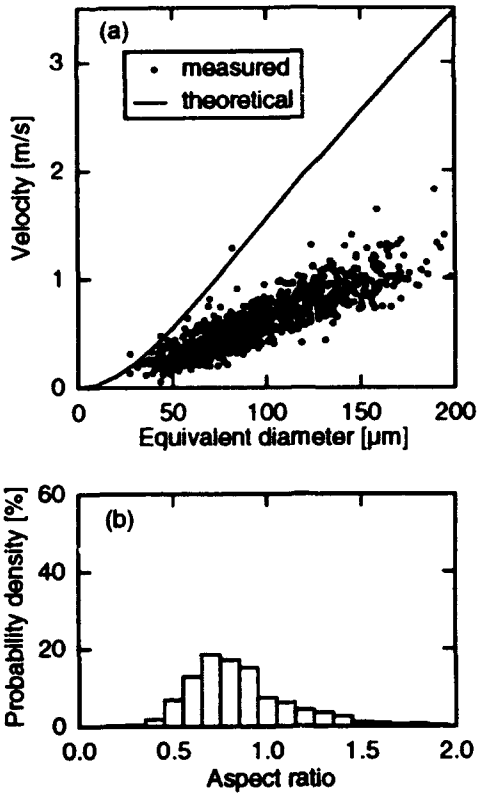

Figure 8 Size-velocity correlations (a) and distribution of aspect-ratios (b) of irregularly shaped copper particles. Defocus distance was limited at 800 μm.

Scatter plots in figure 7 (a) and 8 (a) show resultant size-velocity correlations of spherical and non-spherical copper particles with defocus limit set at 800 μm. For comparison, the terminal velocity of a sphere is shown by solid lines. The measurements were performed with a flow channel of 100 x 100 mm cross-section which was equipped with a particle feeder driven by an acoustic vibrator. The measuring volume was positioned 1.0 m downstream of the feeder at the bottom of the channel. Particles ranging up to 150 μm were estimated to reach their terminal velocities. The sampling frequency and magnification ratio were set at 250 kHz and 105, respectively.

The terminal velocity defines the aerodynamical diameter (Stokes diameter [Clift et al. 1978]), and the area-based diameter of spheres coincide with the Stokes diameter. The velocity measurement was reliable and accurate, therefore, the result for the spheres in figure 7(a) allows us to evaluate sizing accuracy of the method. The velocity of a particle was linearly related to its diameter for the whole size range and the rms value of the size distribution at 2.0 m/s was 10 μm approximately. The size tended to be overestimated by about 15% in contrast with the results of our previous work which resulted in 10% underestimation. This is likely to have been caused by error in determination of the magnification ratio, since it is obvious that the error was systematic. The plots show wider scatter than that of polyethylene in figure 6, because the flow was influenced by the particles.

The shape of a particle also provides useful information, such as the aspect ratio of the projected shape. The ratio was defined by the ratio of the maximum sizes (Ferret diameters) relative to normal and parallel axes of the photodiode array. Figure 7(b) is the pdf of the aspect ratio from copper spheres which shows a narrow distribution around unity ratio. Thus, this gives us confidence that the temporal windowing was accomplished correctly.

The velocity of non-spherical particles, under the same condition, showed smaller values as compared with the spheres in figure 8(a). The motion of the particles depends on their orientation because the drag force from the surrounding air can vary with the shape and orientation. At relatively low Reynolds number, the orientation especially tends to be such that the maximum cross section is aligned normal to the direction of the motion [Clift et al. 1978]. Figure 8(b) shows that the 'alignment' of orientations was clearly observed. Since the plots showed *monotonic increase of size with velocity, this result confirmed* that qualitative measurement is at least possible and suggests that the projected area is statistically related to the Stokes diameter.

4 CORRECTION OF BIAS ERRORS FOR DETERMINATION OF ACCURATE SIZE DISTRIBUTION

For practical applications involving a dispersed phase in a flow, it is often necessary to determine the size distribution at each measuring point with high spatial resolution. For this purpose, particle sampling should be unbiased over the size range, that is large particles should not, for example, be easier to detect than small ones. The sampling bias was mainly caused by the dependence of the effective sampling space on particle size, defocus and shape; in order to eliminate this effect, data correction based on the determination of particle trajectory was

attempted as described below.

4.1 Area of measuring volume

Figure 9 presents the size dependence of the effective size of the sampling space and its width (area) over which the instrument can be triggered. For simplicity, in-focus spheres are shown. The triggerable width, d_w, is equal to the diameter of the particle because only the 17th channel of 32 available was used for triggering; therefore, the triggerable width increased with increasing particle diameter.

For determination of the area-equivalent size, the whole projected image must be recorded and the last channels at both edges of the array, i.e. channels 1 and 32, were used to detect the condition at the edge of the image. If the diameter of the particle exceeds the effective width of the array, the triggerable width is limited and hence decreases with increasing particle size; therefore, the maximum diameter of a particle was equal to the width of 30 segments of the diodes.

At the same time, the effective area of the sampling space varied with defocus distance due to reduction of the overlapped area of triggering as shown in figure 10; the effective sampling area of the measuring volume remains elliptical for all particle sizes but its width, d_t, is dependent on the particle size. Figure 11 shows an example of the size of the sampling space for spheres with magnification ratio of 75 approximately, and the blocked and open symbols correspond to the area without defocus limit, and with limit at 400 µm, respectively. In principle, the effective area was proportional to square of the particle diameter, however, the right side of the graph is limited by the effects of the image exceeding the edge of the detector.

The overlap area can vary with particle shape, so that the sampling space is also a function of the shape. If the particle shape is so complex that the area of the sampling space is not a monotonic function of the defocus distance, correct measurement would require some suitable algorithm to estimate the effective area. In the present study, an equivalent ellipse, defined to have the same projected-area and same aspect-ratio of 'fixed axis' Feret diameter as the particle to be measured, was used to represent its shape in order to simplify the calculations. The reconstructed image of the particle was converted to an ellipse and the size bias correction was implemented using the axis of the ellipse parallel to that of the array.

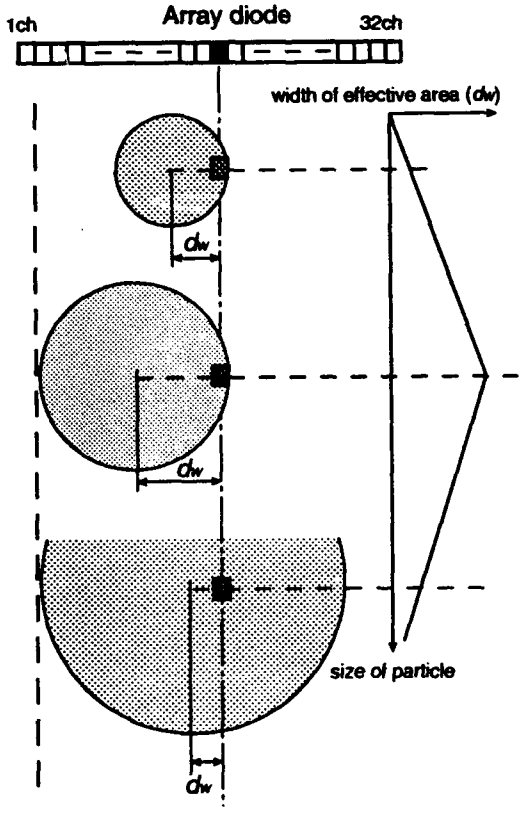

Figure 9 Effective width of the sampling space depending on the particle size. d_w denotes the valid width of triggering for spheres of in-focus condition.

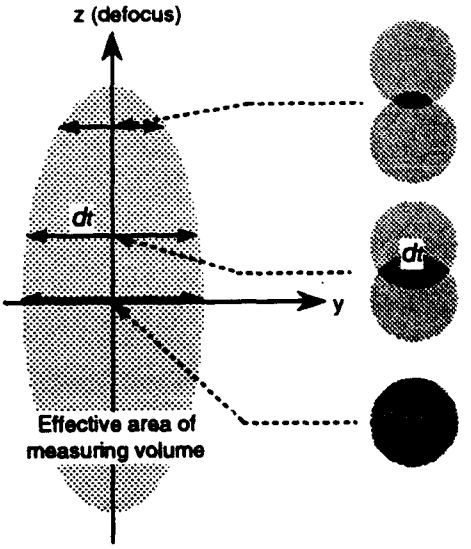

Figure 10 Relationship between defocus distance and effective area of the sampling space.

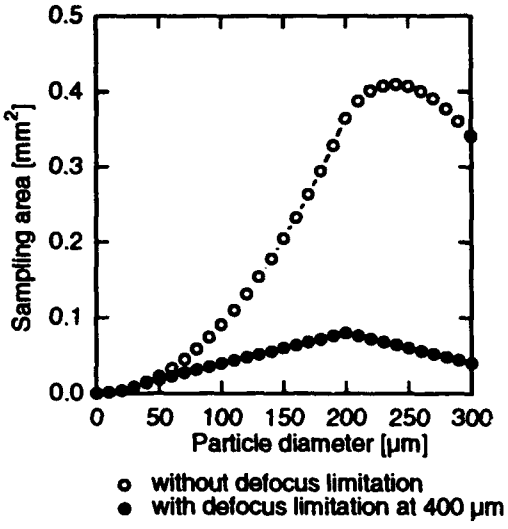

Figure 11 Example of effective size of the sampling space as a function of particle size.

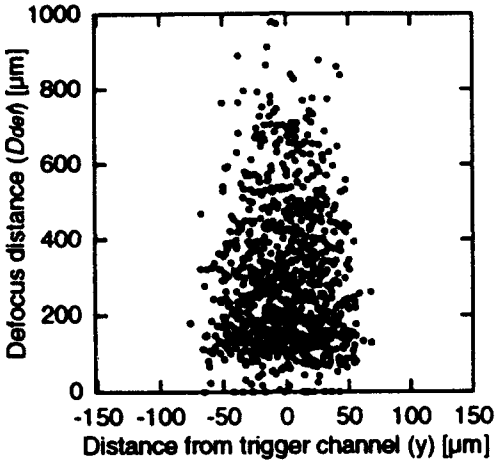

Figure 12 Distribution of particle trajectories of non-spherical copper particles.

Figure 12 shows the distribution of particle positions in the bisector plane of the incident beams which was inferred by the procedure described in section 2. Each plot corresponds to one particle and the total number of samples was 1000. It should be noted that positive and negative values of defocus are not distinguished; i.e., particles which are at a defocus distances of 200 and -200 μm were plotted at the same ordinate.

The distribution was elliptical, corresponding to the shape of the sampling space, but the density of the distribution was not uniform because the triggerable area depends on the particle size. The empty region between defocus distances of 0 and 100 μm was caused by finite responsiveness of the photodetector, and particles there were estimated to be around d=100 μm which corresponded to one pixel displacement of the two projected images.

4.2 Correction of size distribution

Figure 13 compares the size distribution of polyethylene spheres with area-based diameter obtained from microscopic measurement. The bias error was effectively removed with the method based on the sampling area described above. The results showed higher stability and reproducibility, as compared with amplitude based method, because the fluctuation of the laser power or the temperature drift of the detector did not influence the accuracy. The maximum error of average diameter was about 3.0 %.

The corrected size distributions of non-spherical copper and stainless-steel particles are shown in figure 14 and 15, respectively, and compared with microscopic and Stokesian diameter obtained from the terminal velocities. The distributions agree well with the results from microscopic, rather than Stokesian, diameters and with better accuracy than the intensity-based methods; microscope occasionally measure particles with large error. The maximum difference of average diameter was approximately 10 % compared with microscopic measurement, and the distribution tended to be biased to smaller diameter as we expected: particles were likely to present their largest area to the observer when measuring by microscope and, hence, the distribution was biased to larger diameter than that from the present instrument.

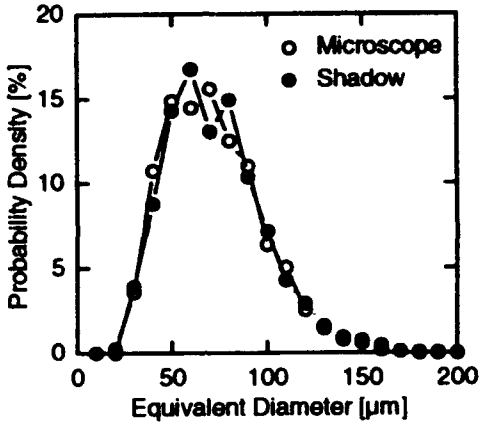

Figure 13 Size distribution of polyethylene spheres measured by a microscope (open) and shadow Doppler velocimeter (blocked).

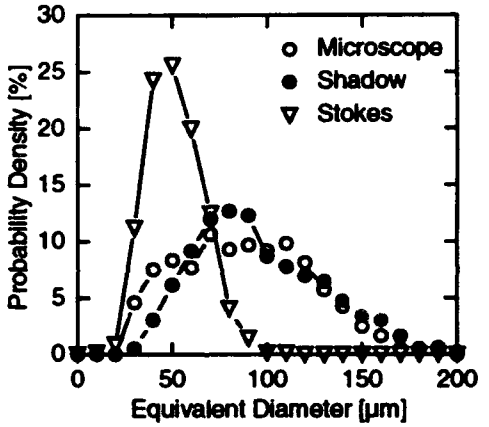

Figure 14 Size distribution of non-spherical copper particles measured by microscope and shadow Doppler velocimeter.

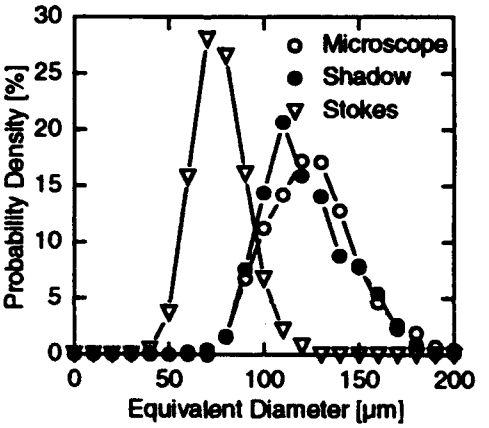

Figure 15 Size distribution of non-spherical stainless-steel particles measured by a microscope and shadow Doppler velocimeter.

5. CONCLUSION

In this study, performance of shadow Doppler instrument was assessed with irregularly shaped particles in fundamental flows. Novel results are summarized as follows:

1. A signal processing method for shadow Doppler velocimetry has been demonstrated using computer controlled hardware. The procedure, which comprised temporal windowing, pattern recognition and correlation of the image, successfully provided information of area-equivalent size, shape and trajectory direction of the particles.

2. Simultaneous measurement of size and velocity of irregularly shaped particles has been achieved in an accelerating flow and quiescent air. Measurement of defocus distance allowed us to identify the erroneous data which was caused by poor images of particles with large defocus distance. Polyethylene particles in the suction flow resulted in about 10 % precision, including the fluctuation of the flow.

3. The size distribution of the particles was obtained using a correction scheme based on the effective size of the measuring volume. The resultant size distribution of polyethylene spheres agreed with the microscopic measurement within 3.0 μm error of arithmetic average. For irregularly shaped particles, the size information inferred from the two-dimensional projected image showed greater similarity with the distributions from the microscopic measurement, rather than that of Stokes diameter.

6. ACKNOWLEDGEMENT

The authors are grateful to Prof. J. H. Whitelaw, Dr. A. M. K. P. Taylor and Dr. Y. Hardalupas for their advice, and Mr. K. Kobashi for their help on construction of the hardware. We also thank Mr. Y Takubo and Mr. K Ishida for their assistance with the experiments.

7. REFERENCES

Bertollini, G. P., Oberdier, L. M. and Lee, Y. H.: Image processing system to analyze droplet distributions in sprays, Opt. Eng., Vol. 24, No. 3, 1985.

Bottlinger, M. and Umhauer, H: Scattered light particle size counting analysis: influence of shape and structure, Optical Particle Sizing: Theory and Practice, G. Gouesbet and G. Gréhan Eds., Plenum Press, New York, 1988, pp. 363-369.

Clift, R., Grace. J. R. and Weber, M. E.: Bubbles, Drops, and Particles, Academic Press, 1978.

Domnick, J., Durst, F., Melling, A., Qiu, H. -H., Sommerfeld, M. and Ziema, M.: A new generation of phase-Doppler instruments for particle velocity, size and concentration measurements, 3rd Int. Cong. Optical Particle Sizing, Yokohama, pp. 407-414,.1993.

Hardalupas, Y., Hishida, K., Maeda, M., Morikita, M., Taylor, A. M. K. P. and Whitelaw, J. H.: A Shadow Doppler technique for sizing particles of arbitrary shape, 3rd Congress on Optical Particle Sizing, Yokohama, Japan, 1993.

Hovenac, E. A., Hirleman, E. D. and Ide, R. F.: Calibration and sample volume characterization of PMS optical array probes, proc. of ICLASS, London, U.K, 1985.

Kaye, P. H., Eyles, N. A., Ludlow, I. K. and Clark, J. M.: An instrument for the classification of airborne particles on the basis of size, shape, and count frequency, Atmospheric Environment, Vol. 25A, No.3/4, pp. 645-654, 1991.

Knollenberg, R. G.: The Optical Array: An Alternative to Scattering or Extension for Airborne Particle Size Determination, J. of Appl. Meteorology, vol. 9, pp. 86-103, 1970.

Knollenberg, R. G.: The use of low power lasers in particle size spectrometry, SPIE, Vol. 92, Practical applications of low power lasers, 1976, pp. 137-152.

Kobashi, K., Hishida, K. and Maeda, M.: Measurement of Fuel Injector Spray Flow of I.C. Engine by FFT Based Phase Doppler Anemometer, in *R. J. Adrian, D. F. G. Durao, F. Durst, M. Maeda, J. H. Whitelaw* (Eds.) Applications of Laser Technique to Fluid Mechanics, Springer-Verlag, 1990, pp. 268-287.

Kobashi, K., Hishida, K. and Maeda, M.: Multi-Purpose High Speed Signal Processor for LDA/PDA Using DSP Array, 1992, Sixth International Symposium Applications of Laser Techniques to Fluid Mechanics, 21.6.1-21.6.6.

Morikita, H., Hishida, K. and Maeda, M.: Simultaneous Measurement of Velocity and Equivalent Diameter of Non-spherical Particles, Proc. 3rd Int. Cong. Optical Particle Sizing, Yokohama, pp. 29-36.1993.

Orfanoudakis, N G, Taylor, A M K P.: Evaluation of a sizing anemometer and application to a small scale swirl stabilized coal burner, *Second International Conference on Combustion Technologies for a Clean Environment*, 19 - 22 July 1993, Lisbon.

Session 25.
Free Flows

THREE-COMPONENT LDA MEASUREMENTS OF MEAN TURBULENCE QUANTITIES, TIME- AND SPATIAL CORRELATION FUNCTIONS IN THE WAKE OF A FLAT PLATE IN AN ADVERSE PRESSURE GRADIENT

M. J. Tummers[1], D. M. Passchier[1] and P. A. Aswatha Narayana[2]

[1]Faculty of Aerospace Engineering, Delft University of Technology
Kluyverweg 1, 2629 HS Delft, The Netherlands
[2]Department of Applied Mechanics, Indian Institute of Technology
Madras-600 036, India

ABSTRACT

This paper presents the results of an investigation of the turbulent wake of a flat plate subjected to a severe adverse pressure gradient. The measurements were performed with a three-component laser Doppler velocimeter, and include all three components of the mean velocity, the Reynolds stresses and temporal correlation functions. Spatial correlation functions were also measured to obtain estimates of the dissipation length scales.

1. INTRODUCTION

The flow-field around a multi-element airfoil is very complicated. One aspect is the development of the wake of the main element in adverse pressure gradients, induced by a flap. In the present investigation, this phenomenon is simulated by the wake of a flat plate developing in an adverse pressure gradient, induced by a two-dimensional diffuser. In this flow there is only a streamwise pressure gradient, so the effects of for example streamline curvature are not taken into account.

The investigation is part of a project related to high-lift configuration turbulence modeling, comprising trailing edge flows, boundary layers and wakes in adverse pressure gradients.

2. TEST CONFIGURATION

The experiments were conducted in the wake of a flat plate. The plate has a 600mm chord, and a thickness of 18mm. The last 110mm of the plate were tapered to form a sharp trailing-edge. The plate was placed at zero angle of attack in the test section (400x400mm^2) of an open-type wind tunnel, see figure 1. The boundary layers on the plate were tripped with wires positioned at 6% chord. The wind tunnel was operated at a free stream velocity of approximately 10m/s, which corresponds to a chord based Reynolds number of 4.10^5.

A two-dimensional diffuser was connected to the test section to create a strong adverse pressure gradient. To prevent boundary layer separation from the diffuser walls, the walls were equipped with 2mm suction slots, and a gauze was placed at the exit of the wind tunnel. The gauze created an overpressure inside the channel, which caused the boundary layers to be removed at the slots, thereby taking care of natural boundary layer control.

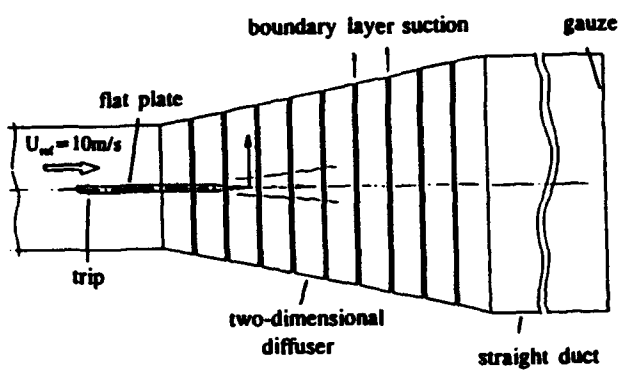

Figure 1: Flow configuration.

3. MEASUREMENT GRID

The complete measurement grid for the flow-field measurements is shown in figure 2. It consists of nine traverses, starting at the trailing-edge. The traverse furthest downstream is at 230mm behind the trailing-edge. All traverses consist of approximately 55 stations, resulting in a total number of about 495 grid points. The present paper reports the results of the six traverses from x=17mm up to x=175mm.

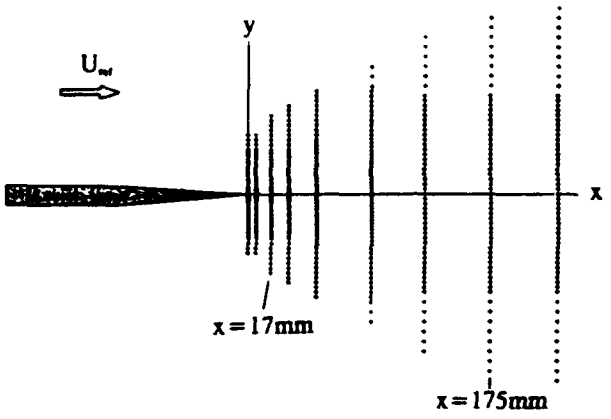

Figure 2: Measurement grid for the flow-field measurements.

4. INSTRUMENTATION

The measurements were performed with a three-component, dual beam LDA system. The green (514.5nm), blue (488.0nm) and violet (476.5nm) colours of a 5W Argon ion laser were used to measure the three components of the velocity simultaneously.

The transmitting optics were arranged such that three nearly orthogonal fringe patterns were created. The measurement volume width was approximately 0.12mm. To collect light only from the overlap region of the three measurement volumes, the receiving directions were almost perpendicular to the transmitting optical axes. Small pinholes mounted in front of the photomultipliers reduced the effective length of the measurement volumes to 0.2mm.

To measure instantaneous flow reversal, Bragg-cell frequency shifters were used in all channels, together with electronic downmixing. The photomultiplier output signals were processed by three Burst Spectrum Analysers. The processors were operated in the 'hardware' coincident mode, which means that a signal is required on all three channels simultaneously. After acquisition, the data was processed using a 'software' coincidence window of 15μs.

Two different optical configurations were ... Figure 3a shows set-up 1, which was used to measure single-point statistics (mean velocities, Reynolds stresses, triple products and time correlation functions). To measure spatial correlation functions, a slightly different set-up was used, see figure 3b. The main difference between the two set-ups is that in set-up 2 the third component could be traversed independently of the other two. With this set-up simultaneous measurements were performed at two different locations in the flow. The third component could be arranged in different orientations, such that either u, v or w is measured.

The flow was seeded with small oil droplets with a mean diameter of 1μm. The particles were injected into the flow upstream of the fan, thereby ensuring a homogeneous distribution in space.

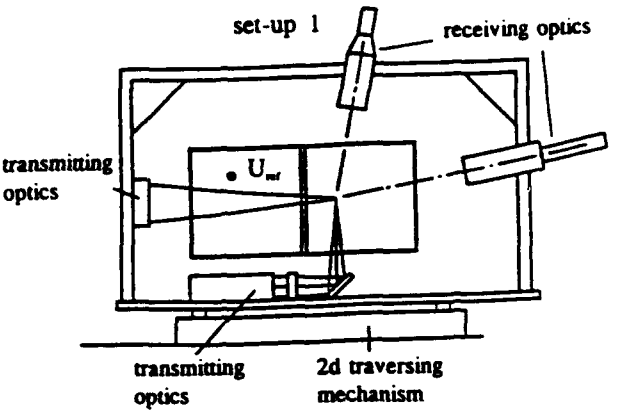

Figure 3a: Set-up to measure single-point statistics.

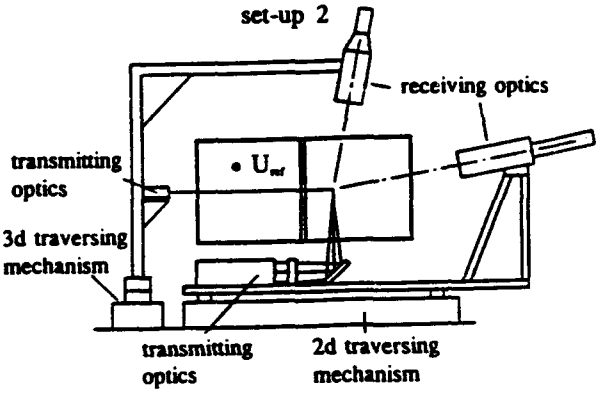

Figure 3b: Set-up to measure two-point statistics.

5. MEAN-FLOW CHARACTERISTICS

Figure 4 presents the three components of the mean velocity measured at station x=53mm. Although the velocity defect is very large, there is no mean flow reversal at this station. Outside the wake, the transverse mean velocity increases in positive y-direction, which is a consequence of the fact that the flow develops in a diffuser. The spanwise mean velocity is small compared to the other two components, suggesting good two-dimensionality of the mean flow. From figure 4 it can be concluded that, within the experimental uncertainty, the flow-field is symmetric.

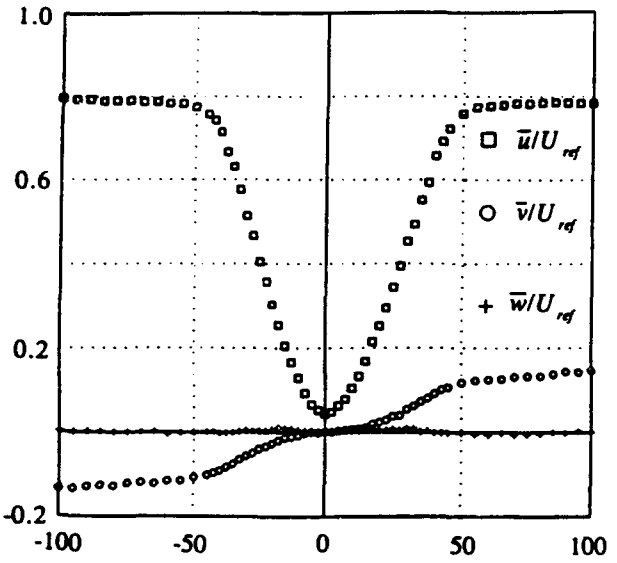

Figure 4: The three components of the mean velocity measured at station x=53mm.

The development of the x-component of the mean velocity is shown in figure 5. It can be seen that the width of the wake increases dramatically. The value of the displacement thickness increases from 44mm at the first station to 91mm at the furthest downstream station. The velocity defect increases in downstream direction. Between stations x=85mm and x=130mm, the mean velocity on the wake centre line changes sign. Downstream of this location, there is a region of mean flow reversal near the centre of the wake.

The development of the kinetic energy of the velocity fluctuations, $k=\frac{1}{2}(\overline{u'^2}+\overline{v'^2}+\overline{w'^2})$, is presented in figure 6. The distributions grow in both height and width when moving downstream. The location of the peak values occurs near the point of inflexion of the mean velocity profiles, and moves away from the centre line.

Figure 7 gives the contribution of $\overline{u'^2}$, $\overline{v'^2}$ and $\overline{w'^2}$ to the kinetic energy for seven stations on the wake centre line. The contribution of the streamwise component, $\overline{u'^2}$,

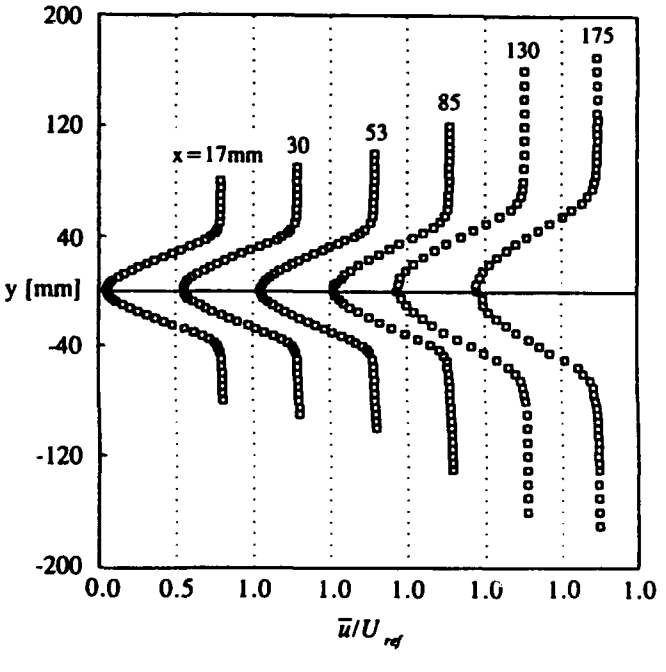

Figure 5: Development of the x-component of the mean velocity.

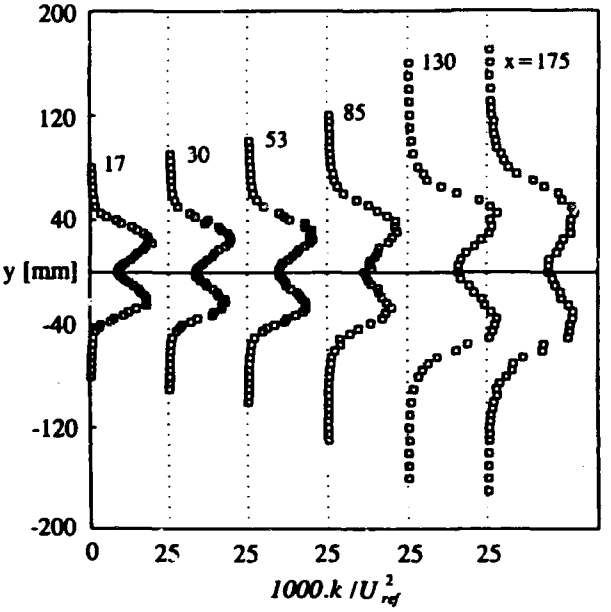

Figure 6: The development of the kinetic energy of velocity fluctuations.

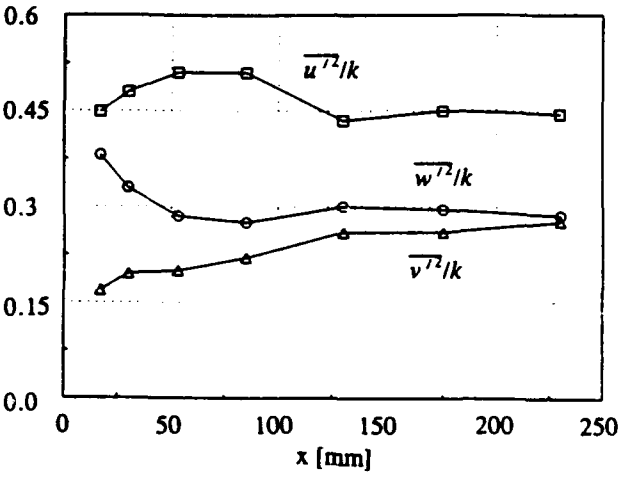

Figure 7: Contribution of $\overline{u'^2}$, $\overline{v'^2}$ and $\overline{w'^2}$ to the kinetic energy.

is much larger than the other two at all stations. At the first station, x=17mm, the contribution of $\overline{v'^2}$ is the smallest. However, at the furthest downstream station the values of $\overline{v'^2}$ and $\overline{w'^2}$ are almost equal.

The development of the turbulent shear stress $\overline{u'v'}$ is shown in figure 8. The triple products $\overline{u'q'} = \overline{u'^3}+\overline{u'v'^2}+\overline{u'w'^2}$ and $\overline{v'q'} = \overline{v'u'^2}+\overline{v'^3}+\overline{v'w'^2}$ were also measured. These terms represent the diffusion of kinetic energy by velocity fluctuations. Figures 9a and b show the development of $\overline{u'q'}$ and $\overline{v'q'}$ in the downstream direction. The main contributor to $\overline{u'q'}$ is $\overline{u'^3}$. The remaining terms show a similar behaviour, but they are much smaller. The value of $\overline{u'q'}$ at the wake centre line increases in the downstream direction, and changes sign between stations x=85mm and x=130mm. The individual components $\overline{v'u'^2}$, $\overline{v'^3}$ and $\overline{v'w'^2}$ of the term $\overline{v'q'}$ give approximately equal contributions to the overall value of $\overline{v'q'}$ at all traverses.

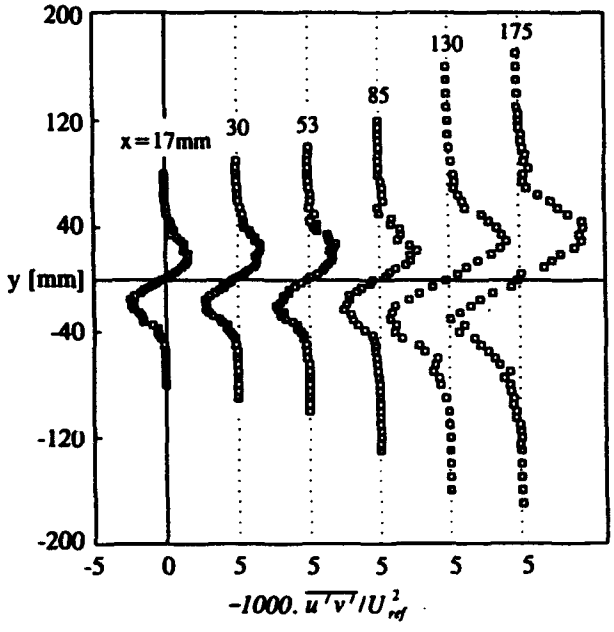

Figure 8: The development of the turbulent shear stress.

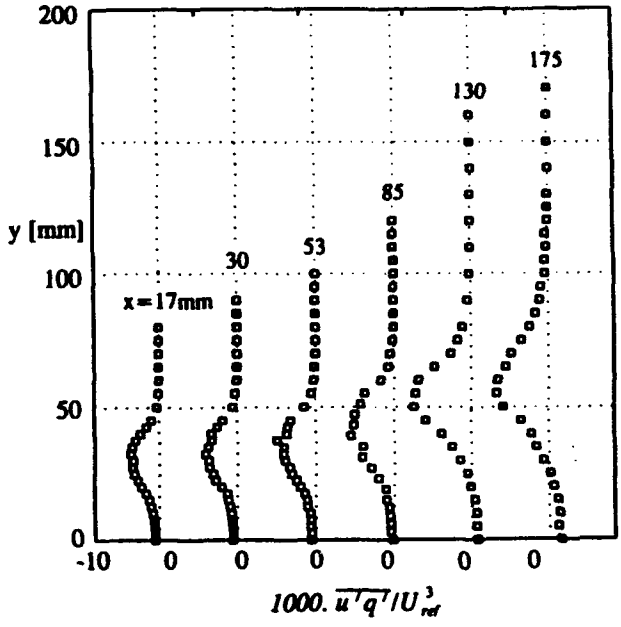

Figure 9a: Profiles of triple-product $\overline{u'q'}$.

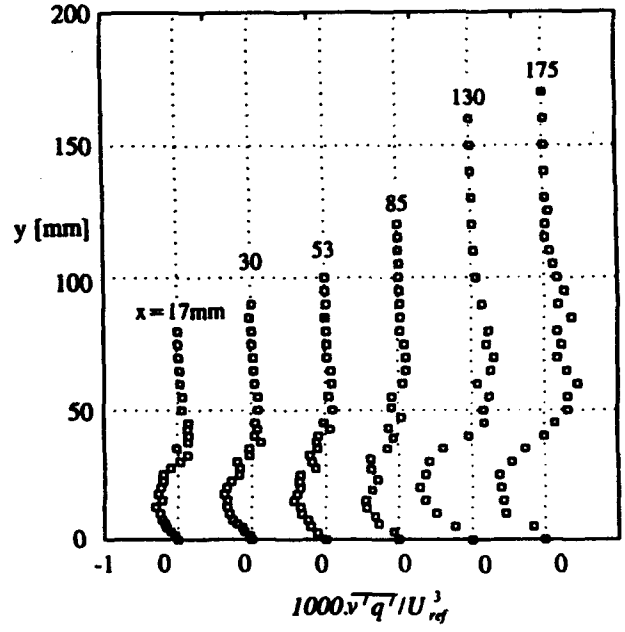

Figure 9b: Profiles of triple-product $\overline{v'q'}$.

6. TIME CORRELATION FUNCTIONS

At a number of locations in the flow auto correlation functions (acf's) of the streamwise velocity component were measured. The acf's were calculated from the LDA data with the 'slotting technique'. This technique can be described by the following algorithm, see e.g. Mayo *et al* (1974):

$$\rho(\tau) = \frac{\{\sum\sum u'(t_i)u'(t_j)\}(k\Delta\tau)}{H(k\Delta\tau)\ \ \frac{1}{N}\sum_{i=1}^{N} u'(t_i)^2} \qquad k=1,2,\ldots,M \qquad (1)$$

where $\{\sum\sum u'(t_i)u'(t_j)\}(k\Delta\tau)$ is the sum of all cross products of velocity fluctuations $u'(t_i)u'(t_j)$ separated by a time lag within the range $(k-\frac{1}{2})\Delta\tau \le t_i-t_j \le (k+\frac{1}{2})\Delta\tau$, $H(k\Delta\tau)$ is the number of cross products within a slot, $\Delta\tau$ is the width of a time slot, and N is the number of velocity samples.

Figures 10a and b shows six acf's measured at station x=30mm. At each location 10^5 samples were used, which were acquired at an average data rate of approximately 1000Hz. The acf's were calculated for a maximum time lag of 1500ms, [illegible] width of 10ms. Near zero time lag the slot [illegible] decreased to 2ms to show more detail.

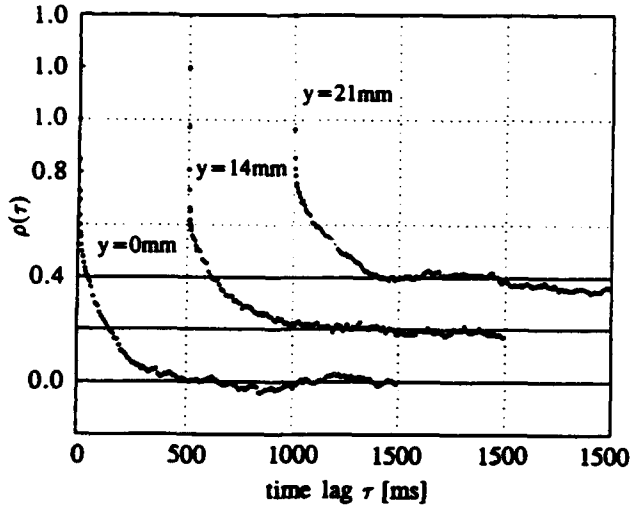

Figure 10a: Auto correlation functions measured at x=30mm for various y-locations.

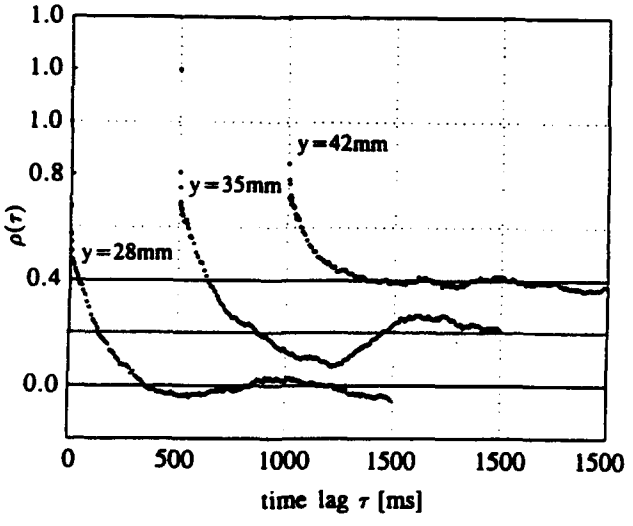

Figure 10b: Auto correlation functions measured at x=30mm for various y-locations.

To calculate the acf at very small time lags, a slightly different algorithm was used in which the denominator in (1) was replaced by:

$$\{\sqrt{\sum u'(t_i)^2}\ \sqrt{\sum u'(t_j)^2}\}(k\Delta\tau) \qquad k=1,2,\ldots,M \qquad (2)$$

This means that for every time slot a separate estimate of the variance of the velocity fluctuations is made, in which only velocities are used that also contribute to the cross products in that slot. At very small time lags, this estimator has a much lower variance than (1), and facilitates the calculation of the small time lag part of the acf.

Figure 11 shows a detailed view of the acf's near zero time lag. The functions were calculated using the same data records as the acf's in figure 10, but with much smaller values of the slot width, 20μs, and the maximum time lag, 1ms. A striking aspect of figure 11 is the very small discontinuity at zero time lag. This indicates that the influence of uncorrelated noise was small during the measurements.

To estimate the Taylor micro time scale, an attempt was made to fit a parabola to each acf at zero time lag, using a method suggested by Zhu *et al* (1992). First, the measured correlation values were replotted as $1-\rho(\tau)$ versus $\Delta\tau^2$. Then a straight line through a number of data points near $\Delta\tau=0$ was constructed. The intersect of this line with the $\Delta\tau^2=0$ axis, gave an indication of the

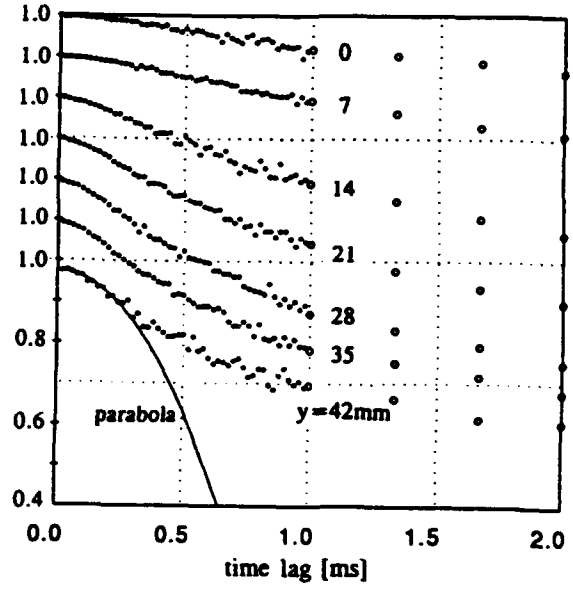

Figure 11: A detailed view of the auto correlation functions near zero time lag.

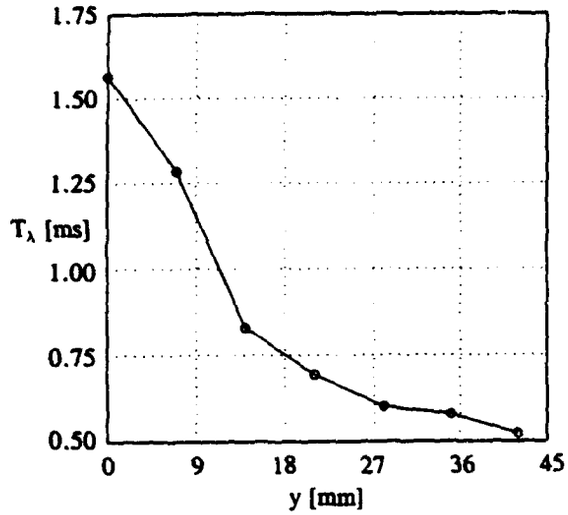

Figure 12: Variation of the Taylor micro *time* scale across the wake at x=30mm.

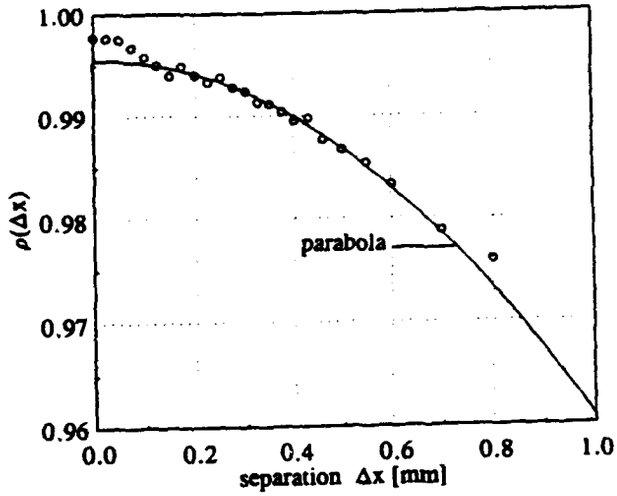

Figure 13: Measured small scale spatial correlation function at station x=175mm, y=47mm.

discontinuity of the acf at zero time lag. After removal of the discontinuity, a parabola was fitted to the selected data points. The resulting values of the Taylor micro time scale are given in figure 12. It can be seen that the Taylor micro time scale decreases when moving away from the wake centre line.

7. SPATIAL CORRELATION FUNCTIONS

At several locations in the flow, spatial correlation functions (scf's) were measured with set-up 2. To obtain information on the Taylor micro length scales, attention was focused on the correlation at very small spatial separation. The measurement volumes were aligned such that the streamwise velocity component was measured simultaneously at two different locations in the flow.

Starting at zero separation, one of the measurement volumes was traversed in streamwise direction in steps of 25μm. For every separation 3.10^4 velocity pairs were acquired at an average data rate of approximately 25Hz. The spatial correlation coefficient was estimated from:

$$\rho(\Delta x) = \frac{\sum_{i=1}^{N} u_i(x)\,u_i(x+\Delta x)}{\sqrt{\sum_{i=1}^{N} u'^2_i(x)}\,\sqrt{\sum_{i=1}^{N} u'^2_i(x+\Delta x)}}$$

Figure 13 gives a typical result measured at station x=175mm, y=47mm. A striking aspect of this scf is the high correlation value at zero separation. This indicates that both channels measured almost identical instantaneous velocities, i.e. errors due to uncorrelated noise were very small.

Another aspect is the presence of a small bump at separations of less than approximately 0.1mm. This has also been observed by Absil *et al* (1990). In this region the measured spatial correlation coefficient is biased towards higher values due to the partial overlap of the measurement volumes. The processors only acquire data when a signal is present on all channels simultaneously. This requirement is most likely met when a particle transits the overlap region of the measurement volumes. However, in that case the effective spatial separation is zero. Therefore, the measured spatial correlation coefficients do not correspond to the true values, as long as there is a partial overlap.

Information on the small scale scf is obtained only when the measurement volumes are completely separated. In this set-up the width of the measurement volumes is 0.12mm, so it is to be expected that the measured correlation values are valid only at separations larger than approximately 0.12mm.

8. TAYLOR'S HYPOTHESIS

Figure 14 shows measurements of the spatial correlation coefficient, together with the auto correlation coefficient with time lag converted to distance using the local mean velocity, according to Taylor's hypothesis. For small separation the two curves practically coincide upto Δx=0.5mm, corresponding to a time lag of about 0.1ms. This coincidence behaviour has also been observed by Cenedese *et al* (1991).

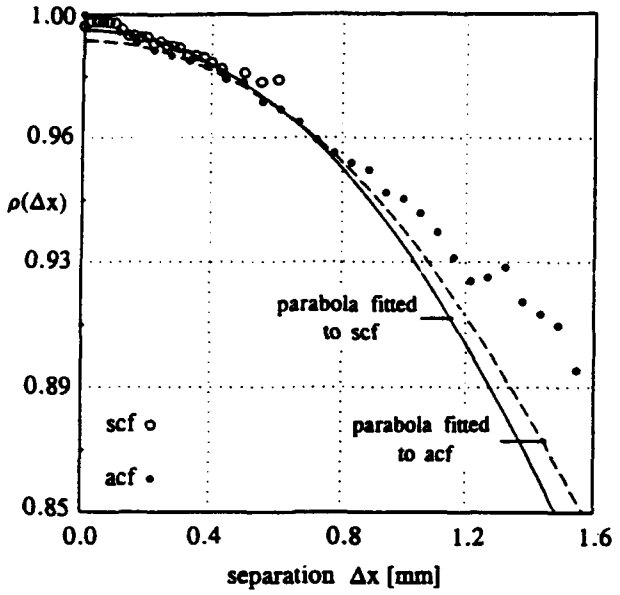

Figure 14: Comparison between the spatial correlation coefficients and the converted auto correlation coefficients.

Parabolas fitted independently to both curves, yielded Taylor micro scales of L_λ=2.75mm (from the spatial correlation function), and uT_λ=2.94mm(from the auto correlation function). In this particular case the application of Taylor's hypothesis gives reasonably accurate results.

9. CONCLUDING REMARKS

The measurements described above are the first results of a continuing project. Experiments performed at the present time include measurements of as many as possible terms contributing to the dissipation, and providing starting conditions for numerical exercises in the flat plate boundary layer.

REFERENCES

Absil, L., Steenbergen, W., and Passchier, D. 1990, Time and Spatial Correlation Measurements in the Turbulent Wake of a Circular Cylinder using LDA, Applied Scientific Research, no. 47, pp. 247-271.

Cenedese, A., Romano, G., Di Felice, F. 1991, Experimental Testing of Taylor's Hypothesis by LDA in Highly Turbulent Flow, Experiments in Fluids, no. 11, pp.351-358.

Mayo, W., Shay, M. and Riter, S. 1974, Digital Estimation of Turbulence Power Spectra from Burst Counter LDV Data, Proceedings of the second international workshop on laser anemometry, vol.1, pp.16-26.

Zhu, Y., Antonia, R. and Kim, J. 1993, Velocity and Temperature Derivative Measurements in the Near-Wall Region of a Turbulent Duct Flow, Near-Wall Turbulent Flows, pp549-561.

AN LDA BASED METHOD FOR ACCURATE MEASUREMENTS OF THE DISSIPATION RATE TENSOR WITH APPLICATION TO A CIRCULAR JET

Gunnar Johansson* and Jens Klingmann**

* Department of Thermo and Fluid Dynamics, Chalmers University of Technology, S-412 96 Göteborg, Sweden
** Department of Heat and Power Technology, Lund Institute of Technology, Box 118, S-221 00 Lund, Sweden

ABSTRACT

We report on the development of an LDA based method by which all the different terms in the dissipation rate tensor can be measured. It is shown that the homogenous part of this tensor can be expressed as a sum of two terms, the second derivative of the two point correlation tensor with respect to the separation between the points and the second derivative with respect to position of the Reynolds stress tensor. The inhomogenous part contains mixed derivatives of the same quantities. An error analysis is performed which shows that the dominating errors are due to the uncertainty in the determination of the distance between the measuring points and to misalignment of the laser beams. The method is applied to the study of a low Reynolds number circular air jet with Kolmogorov microscale of the order of 100 μm and, except for a region close to the outlet nozzle, the error is shown to be of order 5 - 10%. Some results from the measurements are also presented.

1. INTRODUCTION

Reynolds stress modelling of turbulent flow fields requires that an accurate and general model of the dissipation rate tensor is available. A number of such models have been proposed, but direct experimental verification of them is very difficult. For a discussion of these and related matters see e.g. George & Taulbee (1990). In the Reynolds stress equations the terms associated with dissipation usually appears as

$$D_{ij} = D_{ij}^h + D_{ij}^n \tag{1}$$

$$D_{ij}^h = 2\nu \overline{\frac{\partial u_i}{\partial x_k}\frac{\partial u_j}{\partial x_k}} \tag{2}$$

$$D_{ij}^n = \nu \frac{\partial}{\partial x_k}\left(\overline{u_i \frac{\partial u_k}{\partial x_j}}\right) + \nu \frac{\partial}{\partial x_k}\left(\overline{u_j \frac{\partial u_k}{\partial x_i}}\right) \tag{3}$$

where ν is the kinematic viscosity of the fluid, u_i is the velocity vector and x_i is co-ordinate direction. The overbar denotes an unbiased ensemble average. The terms appearing in equation (3) are sometimes written in slightly modified forms, but the way of expression used in equation (3) is best adopted to our way of measurement.

It must be noted that the upper index, h or n appearing in equations (1)-(3), are not tensor indices. h is used to indicate the homogenous part of the tensor and n the non-homogenous part. This convention is also followed for other quantities appearing as superscripts in this paper.

One of the main difficulties in experimental studies of dissipation is that they require that measurements are obtained in two nearby points, without the measurement in one of the points disturbs the measurement in the other, and that the small difference in velocity between the two points is well resolved. In addition to this the effective measuring control volume must be very small, of the order of the Kolmogorov microscale, to avoid that the velocity may vary noticeably across the measuring control volume or that the distance between the measuring points may not be accurately known.

The laser Doppler anemometer has for a long time been considered attractive for this kind of measurements, since it automatically solves one of the most severe of these problems; it measures without disturbing the flow. The size of the measuring control volume can also be made very small by using expanded laser beams and side scattering. It has however some severe drawbacks, in particular the influence of a rather high noise level, usually of the order of 1 percent, and influence of imperfect beam alignment.

We report here on the development of an LDA technique which solves these problems, thus making accurate direct measurements of all the elements in the dissipation rate tensor possible. Some results on a circular jet are included.

2. THE DISSIPATION RATE TENSOR

2.1 Homogeneous part of the dissipation rate tensor

To try to measure the various terms appearing in the homogenous dissipation rate tensor by direct measurements of the velocity in two points simultaneously and forming the average of the product of their difference would lead to unacceptable error levels. This is due to the fact that the calibration constants of the two systems can not be determined accurately enough to permit the small difference in velocity between the two measuring points to be measured accurately. We therefore have to transform the expression (2) to a form that will permit more accurate measurements to be performed. We write

$$\frac{\partial u_i}{\partial x_k}\frac{\partial u_j}{\partial x_k} = \lim_{\Delta x_k \to 0} \frac{u_i(\mathbf{x}_a)-u_i(\mathbf{x}_b)}{\Delta x_k} \times \frac{u_j(\mathbf{x}_a)-u_j(\mathbf{x}_b)}{\Delta x_k}$$

$$= \lim_{\Delta x_k \to 0} \left(\frac{u_i u_j(\mathbf{x}_a) + u_i u_j(\mathbf{x}_b)}{\Delta x_k^2} - \frac{u_i(\mathbf{x}_a)u_j(\mathbf{x}_b) + u_i(\mathbf{x}_b)u_j(\mathbf{x}_a)}{\Delta x_k^2} \right) \quad (4)$$

where we have written

$$u_i(\mathbf{x}_a) = u_i\left(\mathbf{x}_0 + \frac{\Delta x_k}{2}\right) \quad (5)$$

$$u_i(\mathbf{x}_b) = u_i\left(\mathbf{x}_0 - \frac{\Delta x_k}{2}\right) \quad (6)$$

and we, thus, have made a symmetric separation of the two points around the centre point x_0.

The first term on the right hand side of equation (4) contains only one-point correlations. By expanding them in a Taylor series around x_0 we obtain after some algebra

$$u_i(x_a)u_j(x_a) + u_i(x_b)u_j(x_b) = 2R_{ij} + \frac{\Delta x_k^2}{4}\frac{\partial^2 R_{ij}}{\partial x^2} + O\left(\Delta x_k^4\right) \quad (7)$$

where

$$R_{ij} = u_i u_j \quad (8)$$

and it is understood that all terms on the right hand side of (7) are to be evaluated at the point x_0.

The second term on the right hand side of equation (4) is of a different nature. It consists of products of velocity components obtained in two different points. If we write it in the form

$$u_i(x_a)u_j(x_b) + u_i(x_b)u_j(x_a) = u_i\left(x_0 + \frac{\Delta x_k}{2}\right)u_j\left(x_0 - \frac{\Delta x_k}{2}\right) + u_i\left(x_0 - \frac{\Delta x_k}{2}\right)u_j\left(x_0 + \frac{\Delta x_k}{2}\right) \quad (9)$$

we see that it is symmetric in Δx. We will now consider each term in (9) as a two-point function, denoted by Q_{ij}, of the separation Δx_k. Due to the symmetry we thus have

$$u_i(x_a)u_j(x_b) + u_i(x_b)u_j(x_a) = Q_{ij}(x_0, \Delta x_k) + Q_{ij}(x_0, -\Delta x_k) \quad (10)$$

where

$$Q_{ij}(x_0, \Delta x_k) = u_i\left(x_0 + \frac{\Delta x_k}{2}\right)u_j\left(x_0 - \frac{\Delta x_k}{2}\right) \quad (11)$$

Expanding this in a Taylor series around $\Delta x_k=0$ gives

$$u_i(x_a)u_j(x_b) + u_i(x_b)u_j(x_a) = 2R_{ij}(x_0) + \Delta x_k^2 \frac{\partial^2 Q_{ij}}{\partial \Delta x_k^2} + O\left(\Delta x_k^4\right) \quad (12)$$

If equations (7) and (12) now are entered into equation (4) and an ensemble average is taken of the resulting expression we obtain

$$D_{ij}^h = 2\nu \overline{\frac{\partial u_i}{\partial x_k}\frac{\partial u_j}{\partial x_k}} = 2\nu\left(\frac{1}{4}\frac{\partial^2 \overline{R_{ij}}}{\partial x_k^2} - \frac{\partial^2 \overline{Q_{ij}}}{\partial \Delta x_k^2}\right) \quad (13)$$

It must be noted that the first term on the right hand side of equation (13) is the second derivative of a one-point correlation, $\overline{R_{ij}}$, with respect to the co-ordinate x_k, while the second term is the derivative of a two-point correlation, $\overline{Q_{ij}}$, with respect to the separation between the two points.

2.2 Inhomogenous part of the dissipation rate tensor

The primary expression to be considered when evaluating the inhomogenous dissipation rate tensor is according to equation (3)

$$u_i \frac{\partial u_k}{\partial x_j}$$

This can be expressed as

$$u_i \frac{\partial u_k}{\partial x_j} = \lim_{\Delta x_j \to 0} \frac{u_i\left(x_0 + \frac{\Delta x_j}{2}\right) + u_i\left(x_0 - \frac{\Delta x_j}{2}\right)}{2} \times \frac{u_k\left(x_0 + \frac{\Delta x_j}{2}\right) - u_k\left(x_0 - \frac{\Delta x_j}{2}\right)}{\Delta x_j}$$

$$= \lim_{\Delta x_j \to 0} \frac{R_{ik}\left(x_0 + \frac{\Delta x_j}{2}\right) - R_{ik}\left(x_0 - \frac{\Delta x_j}{2}\right)}{2\Delta x_j} - \lim_{\Delta x_j \to 0} \frac{Q_{ik}\left(x_0, \Delta x_j\right) - Q_{ik}\left(x_0, -\Delta x_j\right)}{2\Delta x_j} \quad (14)$$

where R_{ik} and Q_{ik} is defined by equations (8) and (11) respectively. Note again that R_{ik} is a quantity defined in one point, while Q_{ik} is a two-point quantity.

If we expand the terms in equation (14) which contain R_{ik} in a Taylor series around x_0 we obtain

$$R_{ik}\left(x_0 + \frac{\Delta x_j}{2}\right) - R_{ik}\left(x_0 - \frac{\Delta x_j}{2}\right) = \Delta x_j \frac{\partial R_{ik}}{\partial x_j} + O\left(\Delta x_j^2\right) \quad (15)$$

Similarly, if we expand the terms containing Q_{ik} in equation (14) in a Taylor series around $\Delta x_j=0$, keeping x_0 constant, we obtain

$$-Q_{ik}(x_0,\Delta x_j)+Q_{ik}(x_0,-\Delta x_j)=-2\Delta x_j\frac{\partial Q_{ik}}{\partial \Delta x_j}+O(\Delta x_j^2) \quad (16)$$

If the last two expressions are entered into equation (14) and an ensemble average is formed on the resulting expression we obtain

$$\overline{u_i\frac{\partial u_k}{\partial x_j}}=\frac{\partial \overline{R_{ik}}}{\partial x_j}-2\frac{\partial \overline{Q_{ik}}}{\partial \Delta x_j} \quad (17)$$

The non-homogenous dissipation rate tensor can thus be expressed as

$$\begin{aligned} D_{ij}^n &= \nu\frac{\partial}{\partial x_k}\left(\overline{u_i\frac{\partial u_k}{\partial x_j}}+\overline{u_j\frac{\partial u_k}{\partial x_i}}\right) \\ &= \nu\frac{\partial}{\partial x_k}\left(\frac{\partial \overline{R_{ik}}}{\partial x_j}+\frac{\partial \overline{R_{jk}}}{\partial x_i}-2\left(\frac{\partial \overline{Q_{ik}}}{\partial \Delta x_j}+\frac{\partial \overline{Q_{jk}}}{\partial \Delta x_i}\right)\right) \end{aligned} \quad (18)$$

It is thus clear that the primary quantities to measure in order to obtain a measurement of the dissipation rate tensor are the Reynolds stress tensor, $\overline{R_{ik}}$, and the two-point correlation tensor, $\overline{Q_{ik}}$.

3. EXPERIMENT

3.1 Measurement technique

The basic requirement of an instrument used to measure the dissipation rate tensor is an ability to measure in two different points simultaneously. We accomplish this by using four fibre optic probes operating in pairs, see figure 1. One probe in each pair is used to emit the laser beams and the other to collect the scattered light at 90° collection angle. With this arrangement it is possible to reduce the measuring control volume considerably. Its diameter decreases in proportion to

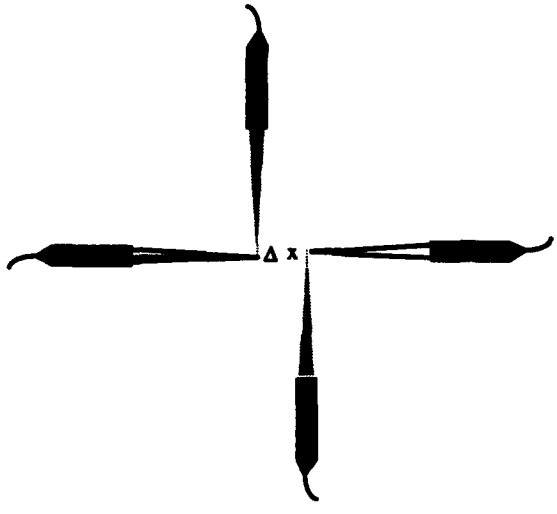

Figure 1. Probe configuration.

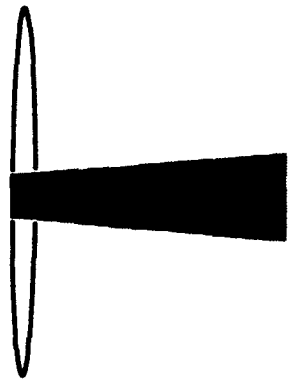

Figure 2. The measuring control volume.

the reciprocal of the F-number of the emitted beams, which is given by the optics used and can be reduced by beam expansion modules. The length of the measuring control volume, see figure 2, is determined by the receiving optics. In our case, we use Dantec probes and the length of the measuring control volume is then approximately 80% larger than the diameter of the beam waists. We obtain a diameter of 45 μm and a length of 80 μm.

Each pair of the probes are traversed symmetrically about a centre point. In this way a number of error terms directly proportional to the distance between the measuring control volumes vanish identically (as opposed to a case when only one of the probe volumes would be traversed). The probes are brought to measure the velocities in the two points at five different separation distances in turn and the correlation coefficient and the rms values of the measured velocity components are computed. These data are then fitted to a fourth order polynomial

$$\overline{C_{ij}}=p_{0,ij}+p_{2,ij}(\Delta x)^2+p_{3,ij}(\Delta x)^3+p_{4,ij}(\Delta x)^4 \quad (19)$$

(if i = j, $p_{3,ij}$ = 0) and the parameter $p_{2,ij}$ is evaluated. The second derivative of $\overline{C_{ij}}$ with respect to Δx as Δx goes to zero is equal to twice the value of this parameter. In this way the second derivative of the correlation function at zero separation is properly obtained. The procedure is then repeated for separation in the other two co-ordinate directions.

One of the probe pairs is always used to measure the velocity in the main flow direction, even in cases when we do not need to measure this component to obtain a particular element of the dissipation rate tensor In this way we are always able to perform a speed weighting of our data, thus permitting us to compensate for particle statistical bias.

The Reynolds stresses were measured using one of the probe pairs in a conventional set up to measure all three velocity components simultaneously.

3.2 The jet flow rig

A simple experiment has been carried out. An air jet with a speed of 10 m/s at the outlet of a nozzle with a diameter d=8 mm entered into a chamber 70×70 cm in cross section and 1.2 m high, see figure 3. The nozzle was made as a part of the bottom wall of the chamber and was turned in the shape of a

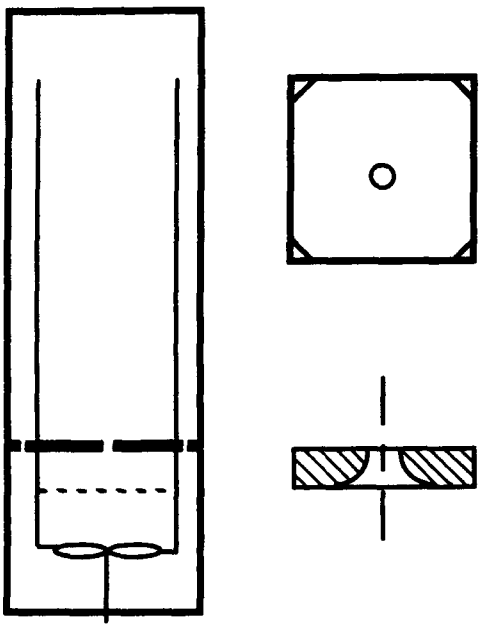

Figure 3. The jet flow rig.

circular arc, see inset in figure 3. The walls of the chamber were made of glass to permit the laser beams to enter into the chamber from the probes which were placed outside the chamber. The flow returned through triangular channels at the corners of the chamber. The flow was driven by a carefully regulated fan. Between the fan and the nozzle a number of screens were placed to reduce the disturbance level of the air stream entering the nozzle. The outlet velocity profile had a top hat shape with very constant velocity across the nozzle and a low turbulence level.

4. ERROR ESTIMATES

Our method to measure the different terms in the dissipation rate tensor involves the use of two separate LDA systems. The Doppler frequency measured by one of the systems (I) in point x_a at the particular instant of time x^1 is given by

$$f_D^I(x_a,t^I)=\overline{f_D^I}(x_a,t^I)+f_D^I(x_a,t^I)+f_n^I(x_a,t^I) \qquad (20)$$

$$\overline{f_D^I}(x_a,t^I)=c^I\mathbf{s}^I\cdot\overline{\mathbf{V}}(x_a,t^I) \qquad (21)$$

$$f_D^I(x_a,t^I)=c^I\mathbf{s}^I\cdot\mathbf{v}(x_a,t^I) \qquad (22)$$

where we have split the velocity vector V into its average $\overline{\mathbf{V}}$, and its fluctuation $\mathbf{v}$. Note that the overbar denotes a non-biased average. Further, c^I is the "calibration" constant of the system I, giving the ratio of the detected Doppler frequency of the projection of the velocity vector V in the direction $\mathbf{s}^I$ (unit vector), which points in the direction of the bisector to the two emitted beams of system I. f_n^I is the noise contribution to the detected Doppler frequency. Analogous formulas are of course available for the measurement in the point x_b using system II.

To carry the analysis further using general expressions would make our formulas very cluttered. We therefore choose to proceed by developing the expressions only for a certain specific choice of combination of velocity components and to imply the others by way of analogy. We will also confine ourselves to an analysis of the $\overline{Q_{ij}}$ - terms and leave the $\overline{R_{ij}}$ - terms since these are much smaller than the two point correlations and varies with position at a much smaller rate than $\overline{Q_{ij}}$ and thus contribute very little to the final error estimates.

Each system is, at a certain phase of the experiment, used to measure the velocity component in the direction of one of the co-ordinate axis. The unit vectors in which we measure are therefore always one of the following

$$\mathbf{s}_x^I=\left(\sqrt{1-\left(\varepsilon_y^I\right)^2-\left(\varepsilon_z^I\right)^2},\ \varepsilon_y^I,\ \varepsilon_z^I\right) \qquad (23)$$

$$\mathbf{s}_y^I=\left(\varepsilon_x^I,\ \sqrt{1-\left(\varepsilon_x^I\right)^2-\left(\varepsilon_z^I\right)^2},\ \varepsilon_z^I\right) \qquad (24)$$

$$\mathbf{s}_z^I=\left(\varepsilon_x^I,\ \varepsilon_y^I,\ \sqrt{1-\left(\varepsilon_x^I\right)^2-\left(\varepsilon_y^I\right)^2}\right) \qquad (25)$$

with analogous expressions for system II. ε_x^I, ε_y^I and ε_z^I are small components of the unit vectors due to some inescapable misalignment of the laser beams.

We now consider the specific example of obtaining Q_{12}. With the aid of the above expressions and equation (10) we obtain

$$\begin{aligned}Q_{12}&=u(x_a)v(x_b)\\&=\frac{\dfrac{f_D^I(x_a)-f_n^I(x_a)}{c^I}-\varepsilon_y^I v(x_a)-\varepsilon_z^I w(x_a)}{\sqrt{1-\left(\varepsilon_y^I\right)^2-\left(\varepsilon_z^I\right)^2}}\\&\times\frac{\dfrac{f_D^{II}(x_b)-f_n^{II}(x_b)}{c^{II}}-\varepsilon_x^{II}u(x_b)-\varepsilon_z^{II}w(x_b)}{\sqrt{1-\left(\varepsilon_x^{II}\right)^2-\left(\varepsilon_z^{II}\right)^2}}\end{aligned} \qquad (26)$$

where we have implicitly assumed that system I is measuring in position x_a and system II in position x_b. In addition to this we have also here written the velocity vector as (u, v, w).

The directional errors, ε, are often of the order of~0.01. This implies that they can safely be neglected compared to 1 in the square roots in the denominator of equation (24). We further assume that the noise terms, f_n^I and f_n^{II}, are uncorrelated with all other terms except when correlated with themselves. Forming a non-biased average of Q_{12} based on a large number of samples we then get

$$\overline{Q_{12}} = \frac{\overline{f_D^I(x_a) f_D^{II}(x_b)}}{c^I c^{II}} - \frac{\varepsilon_x^{II}}{c^I}\overline{f_D^I(x_a)u(x_b)} - \frac{\varepsilon_z^{II}}{c^I}\overline{f_D^I(x_a)w(x_b)} - \frac{\varepsilon_y^I}{c^{II}}\overline{f_D^{II}(x_b)v(x_a)} - \frac{\varepsilon_z^I}{c^{II}}\overline{f_D^{II}(x_b)w(x_a)} \quad (27)$$

When deriving this expression we have also neglected term which contain products of directional errors. These term are of order 10^{-4} times smaller than the dominating terms. In this specific example (Q_{12}) we note that all noise terms have been cancelled since no terms where they were correlated with themselves were present.

If we further note that $f_D^I/c^I = u(x_a)$ and $f_D^{II}/c^{II} = v(x_b)$ we find that the last three terms in equation (27) representing the error in the measurement of $\overline{Q_{12}}$ leads to relative errors of order 0.01 since all correlations $\overline{u_i u_j}$ are of the same order of magnitude and the ε:s are of order 0.01. This error is thus of the order of a few percent. Note that signal noise does not contribute to this error.

It turns out that the scatter in the $\overline{Q_{12}}$ data is larger than the scatter in the corresponding correlation coefficient, which is defined as

$$\overline{C_{12}} = \frac{\overline{Q_{12}}}{\sqrt{\overline{u^2(x_a)}}\sqrt{\overline{v^2(x_b)}}} \quad (28)$$

When taking the second derivative of $\overline{Q_{12}}$, as is required to obtain the homogenous dissipation rate tensor according to equation (13), this is of importance, and we thus prefer to work with the correlation coefficient.

The rms values $\sqrt{\overline{u^2(x_a)}}$ and $\sqrt{\overline{v^2(x_b)}}$ can be computed from equations (20) - (22) in a way analogous to the derivation of equation (27). We find

$$\sqrt{\overline{u^2(x_a)}} = \frac{\sqrt{\overline{\left(f_D^I(x_a)\right)^2}}}{c^I}\left(1+\alpha_u\right) \quad (29)$$

$$\sqrt{\overline{v^2(x_b)}} = \frac{\sqrt{\overline{\left(f_D^{II}(x_b)\right)^2}}}{c^{II}}\left(1+\alpha_v\right) \quad (30)$$

where

$$\alpha_u = \frac{1}{2}\frac{\overline{\left(f_n^I(x_a)\right)^2}}{\left(f_D^I(x_a)\right)^2} - \varepsilon_y^I\frac{\overline{u(x_a)v(x_a)}}{\left(u(x_a)\right)^2} - \varepsilon_z^I\frac{\overline{u(x_a)w(x_a)}}{\left(u(x_a)\right)^2} \quad (31)$$

$$\alpha_v = \frac{1}{2}\frac{\overline{\left(f_n^{II}(x_b)\right)^2}}{\left(f_D^{II}(x_b)\right)^2} - \varepsilon_x^{II}\frac{\overline{u(x_b)v(x_b)}}{\left(v(x_b)\right)^2} - \varepsilon_z^{II}\frac{\overline{v(x_b)w(x_b)}}{\left(v(x_b)\right)^2} \quad (32)$$

If these expressions are entered into equation (28) we find after considerable algebra

$$\overline{C_{12}} = \frac{\overline{f_D^I(x_a) f_D^{II}(x_b)}}{\sqrt{\left(f_D^I(x_a)\right)^2}\sqrt{\left(f_D^{II}(x_b)\right)^2}}\left(1-\alpha_C(x_k)\right) - \beta_C(\Delta x_k) \quad (33)$$

where

$$\alpha_C = \frac{1}{2}\frac{\overline{\left(f_n^I(x_a)\right)^2}}{\left(f_D^I(x_a)\right)^2} + \frac{1}{2}\frac{\overline{\left(f_n^{II}(x_b)\right)^2}}{\left(f_D^{II}(x_b)\right)^2} - \varepsilon_x^{II}\frac{\overline{u(x_b)v(x_b)}}{v(x_b)^2} - \varepsilon_z^{II}\frac{\overline{v(x_b)w(x_b)}}{v(x_b)^2} - \varepsilon_y^I\frac{\overline{u(x_a)v(x_a)}}{u(x_a)^2} - \varepsilon_z^I\frac{\overline{u(x_a)w(x_a)}}{u(x_a)^2} \quad (34)$$

$$\beta_C = \varepsilon_x^{II}\frac{\overline{u(x_a)u(x_b)}}{\sqrt{u(x_a)^2}\sqrt{v(x_b)^2}} + \varepsilon_z^{II}\frac{\overline{u(x_a)w(x_b)}}{\sqrt{u(x_a)^2}\sqrt{v(x_b)^2}} + \varepsilon_y^I\frac{\overline{v(x_b)v(x_a)}}{\sqrt{u(x_a)^2}\sqrt{v(x_b)^2}} + \varepsilon_z^I\frac{\overline{v(x_b)w(x_a)}}{\sqrt{u(x_a)^2}\sqrt{v(x_b)^2}} \quad (35)$$

When deriving equations (29) - (35) we have as before neglected terms which contain products of directional errors, correlations of noise terms with anything except themselves and products of noise and directional errors

The α- terms contain only one-point data, which changes very slowly compared to two-point terms. The terms are small, of the order of 0.01, and the second derivative of these terms can safely be neglected. A word of warning is however in place, since the noise terms may, due to spurious effects, vary also over short distances.

The second term, β_C, in equation (33), contain terms which are also small, of the order of 0.01. However, they, contain two-point data, which are expected to vary in space at approximately the same speed as the dominating term in equation (33). This implies that they will contribute an error term to the homogenous dissipation rate, which is of the same order as their contribution to the correlation term.

The homogenous dissipation rate is finally computed as

$$D_{12}^h = 2\nu\overline{\frac{\partial u}{\partial x_k}\frac{\partial v}{\partial x_k}} = 2\nu\left(\frac{1}{4}\frac{\partial^2\overline{R_{12}}}{\partial x_k^2} - \frac{\partial^2\overline{Q_{12}}}{\partial\Delta x_k^2}\right) = 2\nu\left(\frac{1}{4}\frac{\partial^2\overline{R_{12}}}{\partial x_k^2} - \frac{\partial^2}{\partial\Delta x_k^2}\left(\sqrt{\overline{u^2(x_a)}}\sqrt{\overline{v^2(x_b)}}\,\overline{C_{12}}\right)\right) \quad (36)$$

We have demonstrated that the relative errors due to noise and misalignment in $\overline{Q_{12}}$, $\sqrt{\overline{\left(u(x_a)\right)^2}}$ and $\sqrt{\overline{\left(v(x_b)\right)^2}}$ are all of the order of a few percent. The errors involved in the measurement of $\overline{R_{12}}$ is of the same nature and thus of the same order of magnitude. Moreover, the second derivative of $\overline{R_{12}}$ is to be obtained with respect to x_k, while the derivative of $\overline{Q_{12}}$ is to be evaluated with respect to Δx_k. The variation in space of

any quantity with respect to x_k is an order of magnitude slower than the variation with respect to Δx_k, and, thus, the error in D_{12}^h is dominated by the error in $\overline{Q_{12}}$. In the following we will therefore neglect all errors except those in $\overline{Q_{12}}$.

We have so far considered errors due to signal noise and misalignment of the laser beams. There are however some additional errors that must be considered. These are

a) Statistical uncertainty in the measurement of $\overline{Q_{12}}$.
b) Errors in the determination of c^I, C^{II}.
c) Error due to the finite size of the measuring control volumes.
d) Errors in the determination of the effective distance between the two measuring points.
e) Particle statistical bias.
f) Particle density bias.

The statistical uncertainty, in the measurement of $\overline{Q_{12}}$, has been investigated experimentally. In a certain point and for a certain separation we measured $\overline{Q_{12}}$ 20 times. From this ensemble of $\overline{Q_{12}}$-values, the mean and rms values could be calculated. The central limit theorem then tells us that this ensemble can be modelled as having a Gaussian distribution, and thus the uncertainty in the determination of the mean value of $\overline{Q_{12}}$ can be estimated as $\frac{1.96\sigma}{\sqrt{20}}$ at 95% confidence, where σ is the rms value of the ensemble. We found that if each measurement of $\overline{Q_{12}}$ was based on 2.5 minutes integration time, the error was less than 1%. We thus concluded that if we based our estimates of $\overline{Q_{12}}$ on 50 minutes records the corresponding error should be of this order or less.

Errors in c^I and C^{II} enters in the computation of the rms-values multiplying the two-point correlation coefficient in equation (36). These quantities can usually be determined within 1%, and thus contributes to the relative error in the homogenous dissipation tensor with the same value.

The measurement of dissipation is essentially a measurement of the variances of spatial derivatives of the velocity components. It is thus clear that the measuring control volumes must have a linear dimension significantly smaller than a distance over which the instantaneous velocity changes noticeably. This distance is the Kolmogorov microscale. In our experiment this scale varied from about 70 to 180 μm. Our measuring control volumes had a shape like a circular cylinder with diameter 45 μm and length 80 μm. This is considered to be a sufficient spatial resolution to make the error due to the finite size of the measuring control volume negligible.

Errors due to the uncertainty in the determination of the effective distance between the two measuring points can be evaluated as follows. There are three sources of this error, an imperfection in the determination of the position where the two measuring points coincide, Δ_0, an error due to the fact that scattering particles cross the measuring control volume at varying positions, Δ_p, and an error in the traversing of the two measuring control volumes, Δ_t.

The first error, Δ_0, was evaluated during the adjustment of the measuring control volumes. We found that the coincident data rate changed noticeably when we moved one of the measuring control volumes a distance of 5 - 10 μm. This turns out to be the dominating error in the determination of the effective distance between the measuring control volumes. This is thus our estimate of the zero position error.

The particles cross the measuring control volumes at arbitrary positions. The separations were such that the main flow direction had one of the relations to the measuring control volume depicted in figure 4.

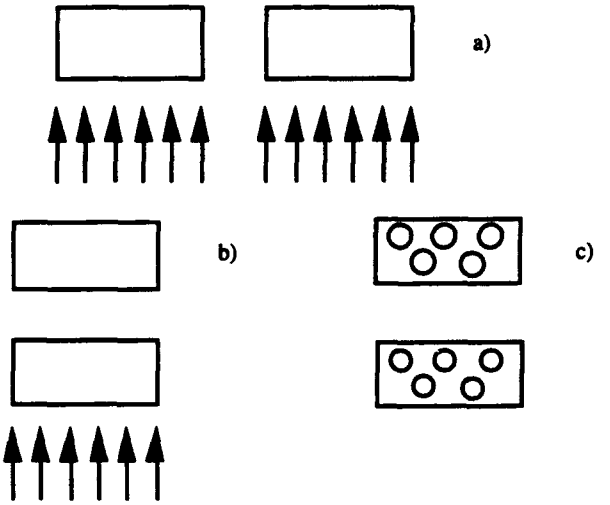

Figure .4 The possible relations between the inflow of particles to the measuring control volume and their separation.

In figure 4a) the measuring control volumes are separated along their longest dimension and the main flow direction is from below. In b) the measuring control volumes have been separated in the main flow direction and in c) they are separated sideways such that the main flow is coming out of the paper. It is immediately realised that in cases a) and c) the influence of the randomness in position of the particles do not change the effective distance. In case b) we examine the cases that the particles give samples of equal probability either anywhere in the two measuring control volumes or anywhere in the lower halves of them. In either case we obtain the result that the effective distance between the two measuring control volumes is unaffected by the randomness of the particle position.

The third position error, Δ_t, due to imperfect translation of the probes is believed to be very small. The mechanical devices used for the translation was very stable and the scales used to read the translations were accurate to within 2 μm. A check on the translation error was performed by returning the probes to zero distance every time the measurements at the longest translation was finished. We were in all cases able to recover the original correlation coefficient very closely

The errors in the primarily measured quantities $\overline{Q_{ij}}$ and $\overline{R_{ij}}$ due to the uncertainty in the determination of the effective distance between the two measuring volumes is dominated by the zero position error Δ_0. In order to estimate the error in the homogenous dissipation rate tensor, D_{ij}^h, due to this error a numerical simulation was performed. The parameter $p_{2,ij}$ in equation (19) was evaluated for three sets of

separation distances, corresponding to Δ_0 =-10μm, Δ_0 =0 and Δ_0 =+10 μm. In our particular case we found that $p_{2,ij}$ varied between 2 - 6% at different position at the centreline in our jet flow.

Two possible sources of bias errors are at hand, particle density bias and particle statistical bias. The first of these is due to the fact that only the flow coming out of the jet was seeded. The flow was however recirculated and the flow was seeded at short time intervals, which indicates that the seeding level should be fairly uniform. Although we cannot give a quantitative estimate of the error due to this effect we believe that it is smaller than or at the most of the same order of magnitude as the averaging error, i.e. of the order of 1%.

It is well established that the particle statistical bias is caused by the increased probability to obtain a sample when the volume flow rate through the measuring control volume is high. One can correct for this effect in single point measurements by weighting each sample with the reciprocal of the volume flow rate, see e.g. McLaughlin & Tiederman (1973) or Buchhave et al (1979). In two point measurements the situation is slightly more complicated, but in our case it is simplified by the fact that, due to the short distance between the measuring control volumes, the volume flow rate is very nearly the same in both points. The proper weighting factor is then again the reciprocal of the volume flow rate through either of the measuring control volumes. In all our measurements we have measured the longitudinal velocity component in at least one of the measuring points, i.e. even when the primary interest was to measure the two radial or the two tangential velocity components. In this way we were able to correct properly for the particle statistical bias effect in all measurements.

We have thus found that two sources of error dominates, the error due to misalignment of the laser beams and the error due to the zero position offset. Our analysis shows that the total error in the homogenous dissipation rate tensor thus can be estimated to be of the order of 5 - 10%.

5. SOME RESULTS AND DISCUSSION

We shall show some examples of our results obtained along the centreline of the jet and limit ourselves to the diagonal elements of the homogenous dissipation rate tensor. At the centre line all the off-diagonal elements are zero. Figure 5 shows the two-point correlation coefficient C_{22} at x_1/d=60, for separations in the three co-ordinate directions. It can be seen that C_{22} decreases roughly twice as fast in the x_1-direction as in the x_2-direction. In isotropic turbulence this is expected, but we would also have expected that $C_{22}(\Delta x_1)=C_{22}(\Delta x_3)$ which clearly is not the case in our measurements.

A clearer impression of the second derivatives of the correlation coefficients is obtained by plotting it versus the square of the separation distance. This is done for i=j=1 in figure 6. The open symbols show C_{11} versus $(\Delta x_2/x_1)^2$ at x_1/d=20, 40 and 60. It can be seen that C_{11} drops with a constant slope down to approximately 0.95. The dominating terms in the series expansion, equation (19), are thus $p_{0,11}$ and $p_{2,11}$, the latter being half the second derivative of C_{11} with respect to Δx_2. The estimated values of $p_{2,11}$ shown in the figure are obtained by fitting the data to the polynomial (19) including the $(\Delta x_2)^4$-term, but no higher order terms. Included in the plot is a measurement of C_{11} versus $(\Delta x_3/x_1)^2$

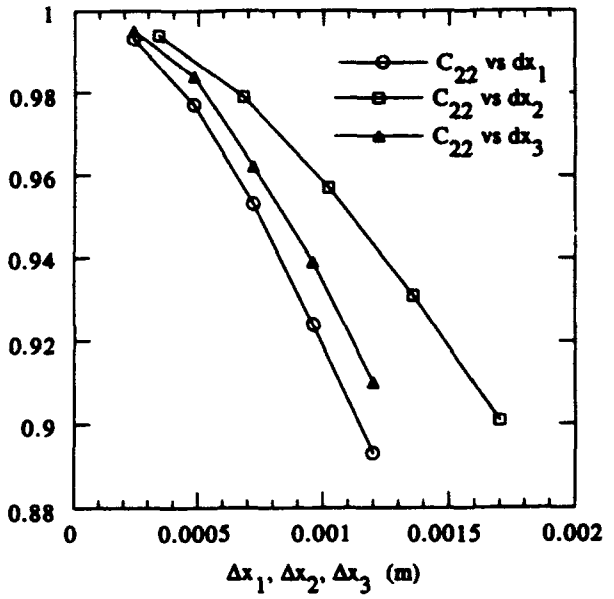

Figure 5. The two point correlation coefficient $\overline{C_{22}}$ for separation of the measuring points in the three co-ordinate directions at the centre-line, 60 diameters downstream of the nozzle.

at x_1/d=40 (filled squares), which should be identical to the measurements for separation in the x_2-direction. Although the measurements differ slightly at large separations the estimated values of $p_{2,11}$ are very close.

A sensitivity analysis of the influence of the zero position error was made using these data. It was found that a position error of 10 μm changed the estimated value of p_2

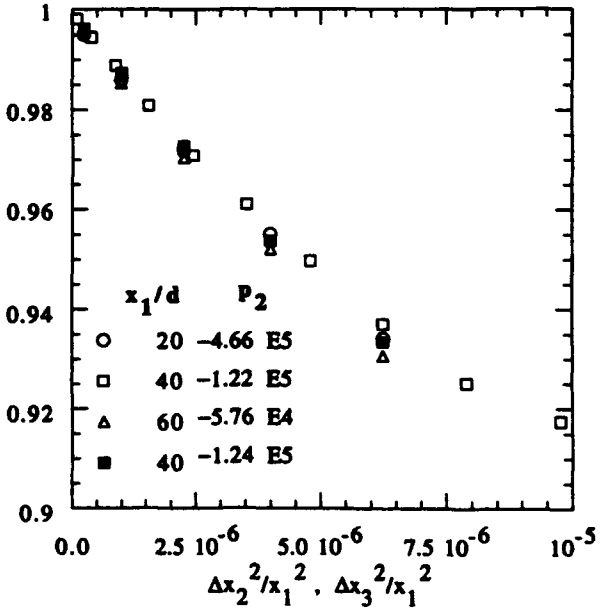

Figure 6. $\overline{C_{11}}$ on the centre-line, 20, 40 and 60 diameters downstream of the nozzle.

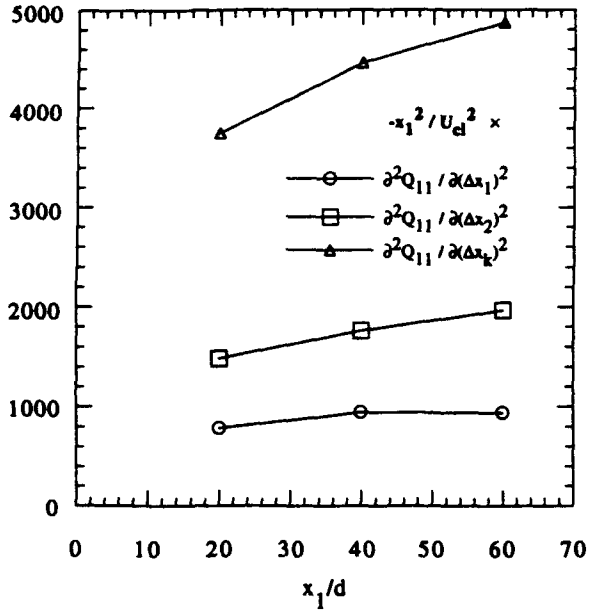

Figure 7. Normalised second derivatives of $\overline{Q_{11}}$.

with about 6% at $x_1/d=20$, decreasing to about 2% at $x_1/d=60$.

At the centre-line $\sqrt{\overline{u_i^2(x)}}$ was found to be very close to a constant, why $\partial^2\overline{Q_{ii}}/\partial(\Delta x_k)^2$ becomes $\overline{R_{ij}}\partial^2\overline{Cij}/\partial(\Delta x_k)^2$, for i=j. This sum over k, and its elements are shown in figure 7, normalised with $-x_1^2/U_{cl}^2$. Note that $\partial^2\overline{Q_{11}}/\partial(\Delta x_3)^2$ is equal to $\partial^2\overline{Q_{11}}/\partial(\Delta x_2)^2$due to symmetry.

Figure 8 shows $\partial^2\overline{Q_{ii}}/\partial(\Delta x_k)^2$ and its components

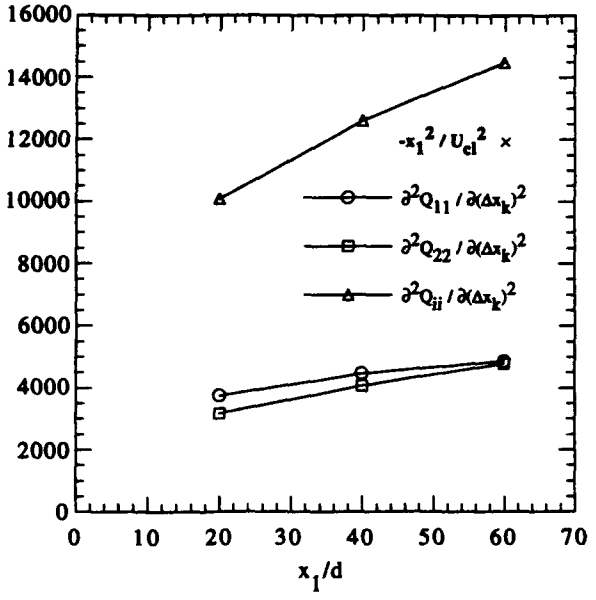

Figure 8. $\partial^2\overline{Q_{ii}}/\partial(\Delta x_k)^2$and its elements normalised with $-x_1^2/U_{cl}^2$.

from the different two-point correlations, once again normalised by $-x_1^2/U_{cl}^2$. If the first term on the right hand side of equation (36) is neglected, this represents $D_{ii}^h/2\nu$, and its components.

All quantities shown in figures 7 and 8 should go to zero near the nozzle and become independent of x_1/d if the jet was self similar.

The normalised value of the scalar dissipation, $D_{ii}/2$, can be obtained from figure 8, if the inhomogenous part is neglected. Normalising the kinematic viscosity with $z_1 U_{cl}$ yields $z_1 D_{ii}/2U_{cl}^3$=0.255 at x_1/d=60. A number of estimates of this value have been published, preferably in the self similar region and at higher Reynolds numbers. Maybe the best comparison is made with Panchapakesan & Lumley (1993), who obtained the value of 0.174 (32% lower) from an energy balance in an air-jet at Re = 11 000.

6. CONCLUSIONS

We have here reported on a method by which all the elements in the dissipation rate tensor can be measured directly. This is accomplished by putting the expressions for the dissipation rate tensor into a form which contains second derivatives of the two point correlation with respect to the separation between the points and second derivatives for the Reynolds stresses with respect to the position for the homogenous part of the dissipation rate tensor and mixed second order derivatives of the same quantities for the inhomogenous part.

The method works for flows with Kolmogorov microscale of the order of 100 μm or larger. It should be possible to extend this to higher Reynolds number flows by using more expanded beams and very stable high precision mechanical traversing.

It has been shown that error bounds can be computed for the different elements of the dissipation rate tensor. It turns out that an accuracy of the order of 5-10% is attainable.

The method has one severe drawback; it is extremely time consuming. To obtain the complete dissipation rate tensor in one point will typically require several days of measurements.

REFERENCES

Buchhave ,P., George, W.K. & Lumley, J.L. 1979, The measurement of turbulence with the laser-Doppler anemometer, in Ann. Rev. Fluid. Mech., eds. van Dyke, M., Wehausen, J.V. & Lumley, J.L., vol. 11, pp. 443-503.

George, G.W. & Taulbee, D.B. 1990, Designing Experiments to Test Closure Hypothesis. In Proc. Int. Symp. on Engineering Turbulence Modelling and Experiments, eds. Rodi, W. and Ganic, pp. 383-397, Elsevier, New York.

McLaughlin, D.K. & Tiederman, W.G. 1973, Biasing correction for individual realization of laser anemometer measurements in turbulent flows, Phys. Fluids, vol. 16, pp. 2082-2088.

Panchapakesan, N.R.& Lumley, J.L. 1993, Turbulence measurements in axisymmetric jets of air and helium. Part 1.. Air jet, J. Fluid Mech., vol. 246, pp. 197-223.

LASER SHEET TOMOGRAPHY OF JET FLOWS

P.S.Larsen, L.Böhme and E.Andreesen*

Department of Fluid Mechanics, Building 404,
Technical University of Denmark, DK-2800 Lyngby, Denmark
*Now at ICCH, DK-2970 Hørsholm, Denmark

ABSTRACT

The mixing process of a single jet in a parallel flow and in a cross-flow has been studied experimentally by a quantitative visualization method. The jet gas was seeded with micron-sized particles whose scattered light in a laser sheet was video recorded. Subsequent image processing, including calibration data for geometrical distortion and the distribution of light intensity, produced quantitative distributions of concentration. The distributions of mean concentration for the jet in a parallel flow show good agreement with similarity solutions.

1. INTRODUCTION

Injection of jets of gas into a channel flow provides for a simple and often effective mixing process. Its purpose may be either to cool the near-wall flow or to establish a controlled chemical reaction in the bulk flow. A single jet, or an array of jets, injected into a cross-flow, are deflected and develop secondary vortex flows with thin shear layers and strong entrainment, which is assumed to contribute to effective mixing. The effectiveness and rate of mixing, the latter being important in many chemically reacting mixtures, depend on nozzle type, initial jet velocity, possible swirl, and the spacing of jets in an array. To experimentally determine the mixing characteristics and select optimal configurations it would be expedient to use a full field technique such as light sheet tomography.

The literature on velocity distributions is fairly complete for the single round jet into a stagnant fluid (see, e.g. Schlichting 1968). For round jets in a cross-flow, a number of studies have been made on both the single jet (Patrick 1967; Le Grivès 1978; Andreopoulos & Rodi 1984) and for a row of jets (Kim & Benson 1993). The study of scalar mixing processes include velocity and temperature distributions in jets (Schlichting 1968), concentration distributions for different gas densities by gas chromatographic analysis of samples (Era & Saima 1977) or by infrared imagery (Gorge & Page 1993). Other techniques include elaborate schemes of Mie-scattering and laser-induced flourescence (Messersmith & Dutton 1992), beam deflection tomography (Cohat et al 1992), and pulse laser visualization (Zhang & Bray 1992), which is required to resolve detailed structures needed for the statistics of flame wrinkling.

The present experimental study pursues the idea of a simple visualization technique which was presented in a preliminary study by (Andreesen et al 1993). This study has demonstrated the feasibility of obtaining quantitative concentration distributions in planes intersected by a laser sheet in the mixing zone of a single jet or arrays of jets in a cross-flow. The jet gas was seeded with 0.5-3 μm diameter glycerol droplets from an atomizer and the image of the laser sheet section with the flow was

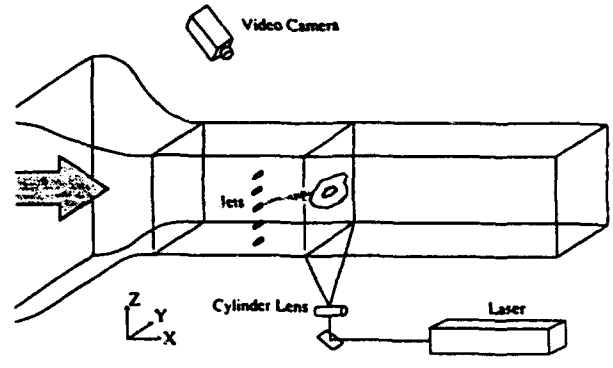

Fig. 1 Experimental setup (schematic)

recorded on video tape. Subsequent image analysis, using also calibration records of scattered intensity over the view

field and correcting for projection geometry, gray-scale iso-concentration contours were resolved. The calibration records of scattered intensity relied on calcul-ated Mie-scattering intensity variations over the field of view combined with measured incident intensity obtained by use of an inclined plate of polyacetate. The present study, on the other hand, relies on a single direct calibration record, obtained after filling the wind tunnel with a uniform concentration of seeding particles. In addition, results are presented on the statistics of mixing processes for jets in parallel flow and mean fields have been compared to theoretical predictions.

2. EXPERIMENT

2.1 Flow System

Visualization experiments were carried out in a 0.2×0.2 m by 1.0 m long test section of a wind tunnel (Figure 1), having 3 sides made from float glass and one side from PVC in which nozzles for jets could be mounted. Using a blower placed downstream, air was drawn through an inlet section with screens giving a uniform bulk flow of U_∞ = 0.8 m/s or 1.1 m/s, as determined from the calibrated flowmeter.

Two jet arrangements were studied: a single axisymmetric jet in parallel flow, and 1 (or 3) jets in a cross-flow. The axesymmetric jet issued at the centerline of the test section from an L-shaped stainless steel tube (3.2/2 0 mm dia.) mounted in the PVC-wall, 70 mm upstream of the jet exit. Two jet velocities were considered, U_o = 57.3 m/s and 28.7 m/s, corresponding to Re = $d_j U_o/\nu$ = 7600 and 3800. Jets in cross-flow issued from convergent nozzles (2.0 mm dia. at exit) mounted flush in the PVC-wall of the test section. One jet was located in the midplane while jet spacing was 50 mm in case of 3 jets. Only the low jet velocity of U_o = 28.7 m/s was employed for jets in cross-flow, and at U_∞ = 1.1 m/s, implying a momentum flux ratio of $[(\rho U^2)_{jet}/(\rho U^2)_{bulk}]^{1/2}$ = 26.1 .

The jet flows were seeded with 0.5-3 μm diameter glycerol droplets (density 1260 kg/m^3 and index of refraction 1.4746) generated in an atomizer. The flow was determined from the pressure measured in a chamber upstream of an orifice plate through which the flow was critical.

2.2 Optical System

A plane light sheet, oriented perpendicular to the direction of bulk flow and covering the full flow area of the test section, was generated by an air cooled argon-ion laser (Uniphase 2013), fitted with a standard fiber optics of 40° sheet angle (Dantec 9060×5001).

The light scattered from the seeding droplets of the jet flow was viewed by a monochrome video camera (Cohu 6510). The camera head contains a 1/2 inch-format CCD image sensor and related support circuits. The active imaging area is 6.4 mm by 4.8 mm, with an array of 739 horizontal by 484 vertical picture elements, each of 256 grey levels. The camera control unit (CCU) allows manual gain control and adjustments to ensure a linear response. These features were essential to yield quantitative data.

The camera signals were stored on SVHS video tapes at a framing rate of fifty half-pictures per second. The exposure time of each frame was about 1/60 s. Individual pictures were captured from the video tape by a frame grapper. These digitized pictures have a resolution of 512 by 512 picture elements with 256 grey levels.

2.3 Image Processing

All recorded images were corrected for geometric distortion and for nonuniform scattering intensity, so as to provide quantitative results of concentration distributions of the seeded jet flows.

The geometrical distortion is shown i Figure 2 (top) for a plate with a reference square grid placed at the location of the light sheet. The optical axis of the camera was aligned with the midplane of the test section and viewed the light sheet at a scattering angle of 32°. Given also the solid angle of view of the camera, however, the transformation of the recorded image to one viewed in the direction of the normal to the light sheet can be readily calculated from geometric optics (see Andresen et al 1993 for equations). This transformation was applied to each recorded image. Figure 2 (bottom) shows the reference grid after such a transformation, as well as the superposed square grid of +marks, spaced 25 mm apart, which were inserted as part of the image processing. The transformation is accurate to within about 2 mm over the 200×200 mm flow area.

At any small volume in the light sheet, the recorded intensity of scattered light from seeding particles is proportional to the local concentration of particles. the intensity of incident light, and the scattering angle. This is true also for particles that are not monodisperse as long as their size distribution is the same at all locations. But the incident intensity is not constant, due to divergence of the laser sheet, and the scattering angle varies over the field of view. These latter effects were calibrated out by recording the light scattered from the laser sheet when the bulk flow was seeded uniformly with the same particles. The result, after correction for the geometric distortion, is shown in Figure 3. Here, as in final images presented below, a cyclic grey scale processing has been introduced to merely facilitate interpretation of the black-and-white

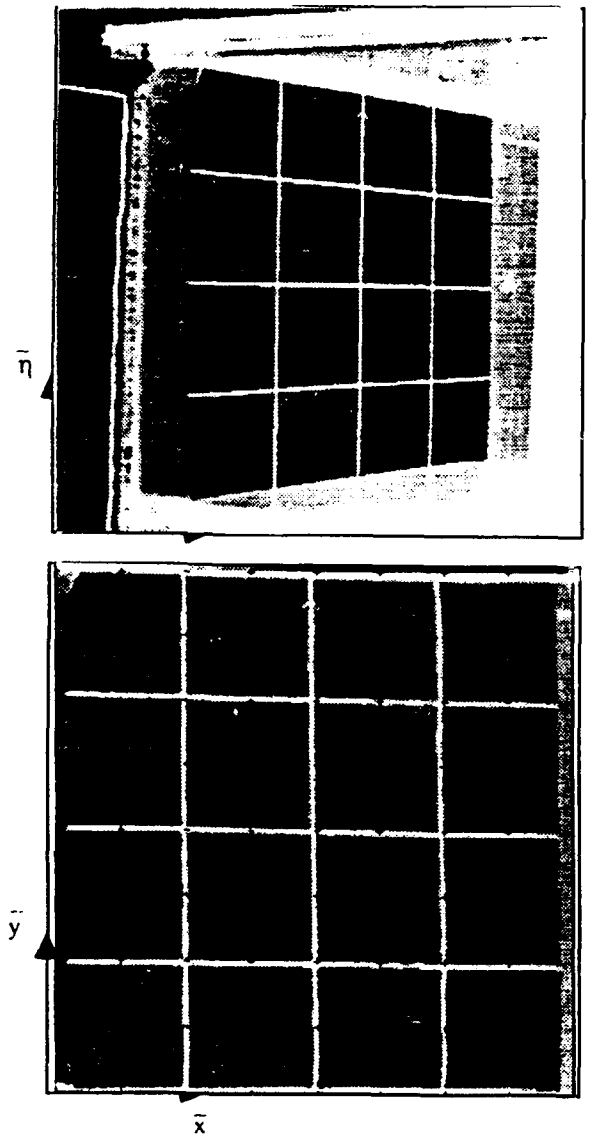

Fig. 2 Image of reference grid, as recorded (top) and after transformation (bottom)

reproduction. The grey scale bar at the top of the image gives here 7 cycles, starting from the lowest intensity (to the left) and increasing to the right. As seen, the light sheet enters the picture from the right.

All images were thus processed for geometric distortion and variation of scattered light intensity. The resulting image was then inverted and the grey scale was scaled to represent relative concentration by equating the concentration at the jet exit to unity. At the top of each image this is shown as the right most (black) grey scale, while zero relative concentration corresponds to the left most (white) grey scale. Distributions of mean concentration were obtained by averaging 16 single frames

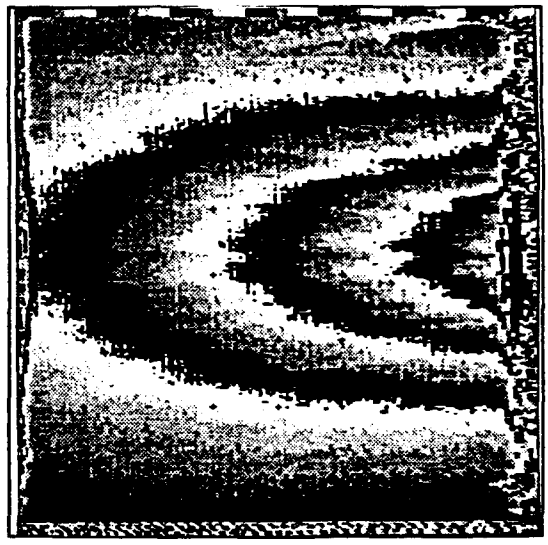

Fig. 3 Image of scattered light intensity distribution for uniform seeding of bulk flow

digitally. This fairly low number of frames is due to the fact that each captured frame takes up 0.25 MB of memory. Alternatively, the averaging can be done over long period in the camera before an image is digitized by the frame grapper. This feature was not utilized since only half-frames were used to ensure positional accuracy.

3. RESULTS

In each test series, after establishing steady flow condition, a series of short video recordings were made at selected axial position downstream of the jet exit at x = 0 mm.

3.1 Single Jet in Parallel Flow

Successive half-frames in a record at x = 80 mm (Figure 4) show moderate differences in structure, while the 16-frame average is representative of the mean concentration. The velocity at x = 80 mm is estimated to be about 5 m/s at the centerline, hence an about 20 mm diameter by about 80 mm long column will have swept through the light sheet during the exposure time of about 1/60 s. The single frames therefore represent an averaging of all small spatial scales and only large scales of the mixing process can be resolved. As the velocity of the jet decreases downstream, smaller and smaller scales can be resolved.

Figure 5 shows the axesymmetric development of mean concentration for 4 axial locations. According to the cyclic grey scale, the relative concentration at the

centerline has dropped to about 0.4 at x = 100 mm, for example.

Figure 6 shows line plots of concentration profiles along one (horizontal) diameter at 8 axial position. The quality of this data could be improved by using a less coarse grey scale and averaging several diametrical sections at each axial postion, but this was not done.

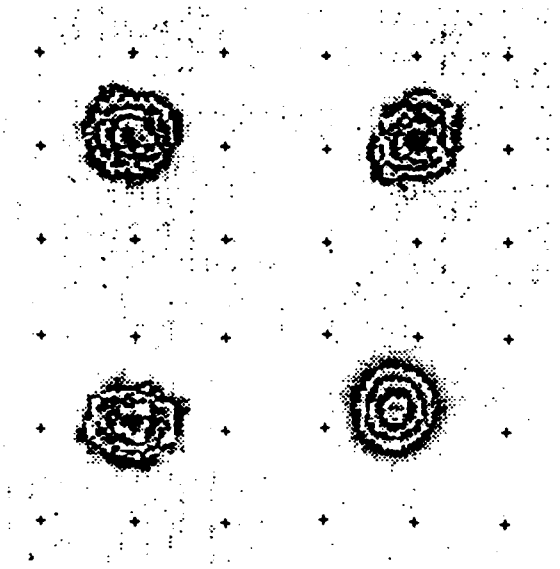

Fig. 4 Single jet in parallel flow, x = 80 mm. 3 successive frames and the mean of 16 frames (lower right). Cyclic grey scale as in Fig.4 for x = 60 and 100 mm

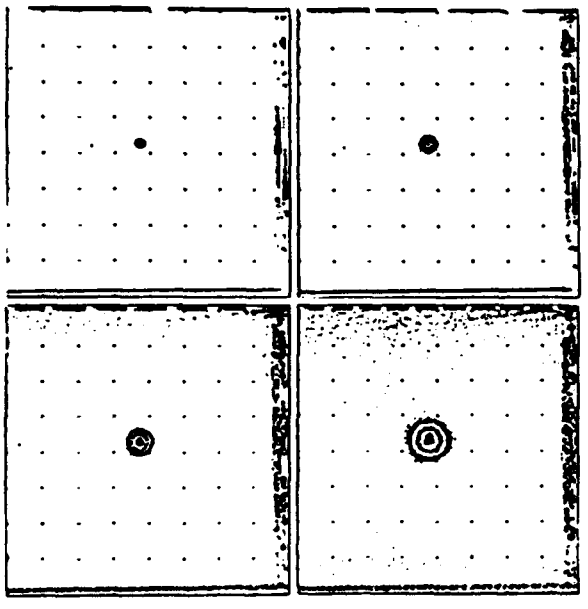

Fig. 5 Single jet in parallel flow. Mean concentration distributions at x = 20, 40, 60 and 100 mm

From the data, the axial development of jet half-width $b_{0.5}$ and centerline concentration C_c/C_0 could be obtained, as shown in Figure 7. The least squares fit to the data can be expressed as

$$b_{0.5} = 0.0847\,x\,, \quad C_c/C_0 = 25.41\,x^{-0.972}\,, \qquad (1)$$

where x and $b_{0.5}$ are in units of mm.

3.2 Jets in Cross-Flow

Successive half-frames in a record at x = 80 mm (Figure 8) show large differences in the structures resolved, while the 16-frame average is again representative of the distribution of mean concentration. The velocity distribution was not measured locally, but is estimated to be close to the bulk velocity of U_∞ = 1.1 m/s. Hence, scales larger that about 10-20 mm should be resolved. The effectiveness of the mixing process in cross-flow, as compared to that of a jet in parallel flow, is clearly seen by comparing Figures 8 and 4.

Figure 9 shows sections, at 8 axial positions, of the single jet in cross-flow, revealing the well-known development of two counter rotating vortices. The ratio of jet to bulk volume flow was about 0.8%, but the momentum flux of the jet sets up secondary flows contributing to the mixing process. As the jet gas spreads downstream to fill the wind tunnel, wall effects were observed to appear, drawing the jet gas closer to one wall.

Using 3 wall jets, with the center jet seeded (not shown), suppresses sideways dispersion and secondary flows but increases the penetration due to increased

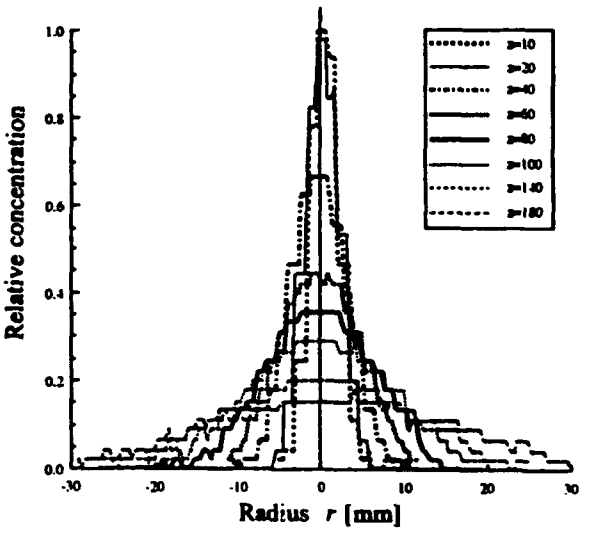

Fig. 6 Distributions of relative concentration along diametral section at various axial positions of single jet in parallel flow

momentum flux and entrainment. For further data on multiple jets, we refer to the earlier study by Andresen et al (1993).

4. ANALYSIS OF SINGLE JET IN PARALLEL FLOW

The classical similarity solution to the velocity distribution of the turbulent, free, round jet issuing into a stagnant fluid is based on the simple eddy viscosity model, $\nu_t \approx b_{0.5} U_c$ = constant, where $b_{0.5}$ is the half-width and U_c the centerline velocity. This simple algebraic model is consistent with the experimentally observed approximate relations, see also (1),

$$b_{0.5} \approx x \; ; \; U_c \approx x^{-1} \; , \tag{2}$$

where x denotes axial position. Ignoring the molecular diffusivity and taking the pressure to be uniform, the velocity field is governed by the thin shear-layer approximation

$$\partial u/\partial x + (1/r)\partial/\partial r(rv) = 0 \; , \tag{3}$$

$$u\partial u/\partial x + v\partial u/\partial r = (\nu_t/r)\partial/\partial r(r\partial u/\partial r) \; , \tag{4}$$

subject to

$$\partial u(x,0)/\partial r = 0; \; v(x,0) = 0; \; u(x,\infty) = 0 \; , \tag{5}$$

which accepts a similarity transformation in terms of

$$\eta = r/x; \; u = (\nu_t/x)f'(\eta)/\eta; \; v = (\nu_t/x)(f' - f/\eta), \tag{6}$$

and transforms into the ordinary differential equation

$$ff'/\eta^2 - (f')^2/\eta - ff''/\eta = (f'' - f'/\eta)' \; , \tag{7}$$

$$f(0) = 0; f'(0) = 0 \; ,$$

where a prime signifies differentiation with respect to η. The remaining boundary condition is related to the total momentum of the jet, $K = J/\rho = (\pi/4)d_j^2 U_0^2$, or the centerline velocity u_c, and may be expressed as

$$\lim_{\eta \to \infty}(f'/\eta) = u_c x/\nu_t = (3/8\pi)K/\nu_t^2 \approx 460.5 \; , \tag{8}$$

according to the experiments of Reichard (see, Schlichting 1968), using the empirical value $\nu_t/K^{1/2} = 0.0161$. For a jet in parallel uniform flow, the velocity u equals the excess velocity over that of the bulk flow.

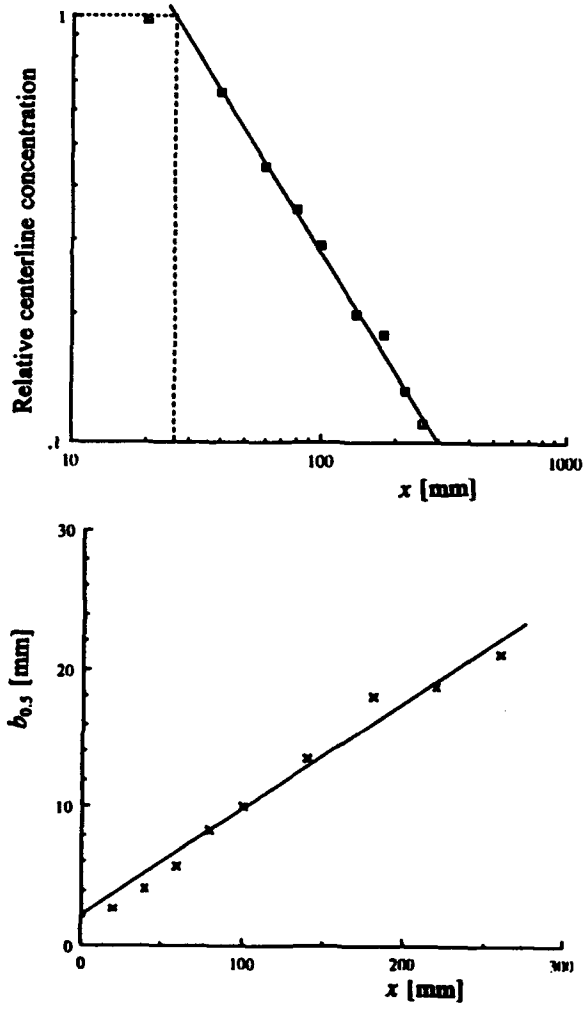

Fig. 7 Axial variation of centerline concentration (top) and half-width (bottom) of single jet in parallel flow

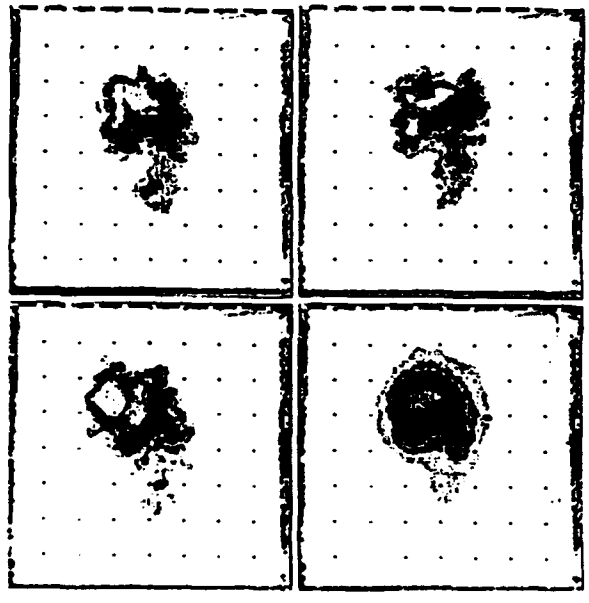

Fig. 8 Single jet in cross-flow, x = 80 mm. 3 successive frames and the mean of 16 frames (lower right)

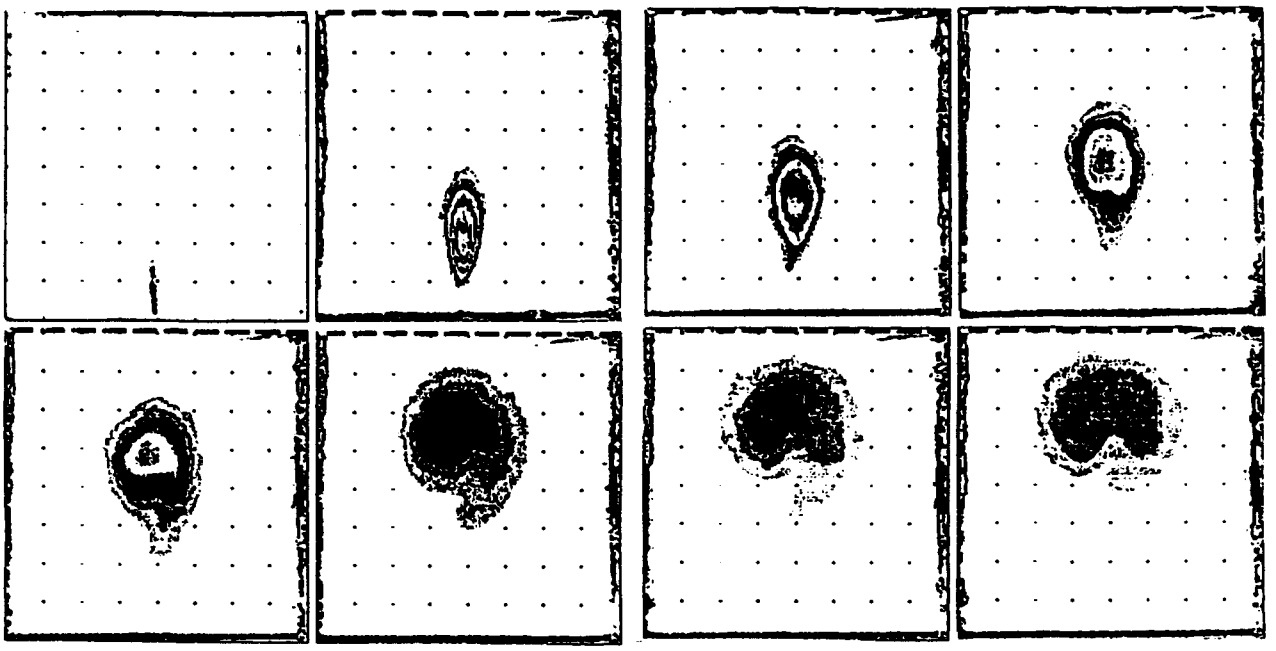

Fig. 9 Single jet in cross flow. Mean concentration at x = 0, 10, 20, 40, 60, 100, 120 and 140 mm

The concentration distribution of jet gas, assuming local analogy between mass and momentum transport, hence a constant eddy diffusivity $D_t = \nu_t/\mathrm{Sc}$, where Sc denotes the Schmidt number, is governed by

$$u\partial c/\partial x + v\partial c/\partial r = (D_t/r)\partial/\partial r(r\partial c/\partial r) ,$$
$$c(0,r) = C_0;\ \partial c(x,0)/\partial r = 0;\ c(x,\infty) = 0 . \qquad (9)$$

It accepts the similarity transformation (6) and

$$c(x,r)/C_0 = g(\eta;\mathrm{Sc})l_c/x , \qquad (10)$$

l_c being a reference length, and transforms into

$$\eta g'' + (1 + \mathrm{Sc}\, f)g' + \mathrm{Sc}\, f'g = 0 ,$$
$$g(0) = 1;\ g(\infty) = 0 . \qquad (11)$$

Note, that (11) reduces to (7) for $g \approx f'/\eta$ at Sc = 1.

Numerical integration of (7) and (11) gives velocity distribution and, for a given value of Sc, concentration distribution, both of which are functions of η and may be normalized to unity centerline values. However, to compare to normalized experimental data on distributions of concentration, the relation between $r/b_{0.5}$ and η must be known. Since the velocity distributions were not measured, the empirical boundary condition (8) was used, yielding the value $\eta_{0.5} = 0.0848$ at the velocity half-width. This gives the relation $r/b_{0.5} = \eta/0.0848$, which was used to plot numerical solutions for Sc = 1 and Sc = 1.2 shown in Figure 10. After testing a number of values, the value Sc = 1.2 was found to be the best estimate, implying an expected lower diffusivity of micron-sized particles.

5. DISCUSSION AND CONCLUSIONS

The present study has demonstrated the utility of a simple visualization method that gives full field, quantitative concentration distributions of a mixing process. In the method, one stream is seeded with micron-sized particles whose concentration is assumed to represent the concentration of this stream. The light scattered from a laser sheet intersecting the flow at selected planes is recorded on video for susequent image analysis. Calibration for geometric distortion of the recorded image and the nonuniform scattering intensity is required, but is readily achieved.

The results obtained for the single jet in a parallel flow validate the method in regard to giving quantitative results for distributions of mean concentration. Also, an estimate of the turbulent Schmidt number for the micron-sized particles used (Sc $\approx$ 1.2) was obtained. Therefore, flows with more complex mixing processes, such as jets in a cross-flow (Figure 9), may be readily studied and interpreted in light of computational results on the assumption that the Schmidt number remains unchanged.

TWO - DIMENSIONAL LASEROPTICAL CONCENTRATION MEASUREMENT IN A LARGE SUBSONIC WIND TUNNEL

Bernd Leitl

Technical University of Dresden
Fluid Mechanics Dept.
Subsonic Wind Tunnel

ABSTRACT

The present study was carried out in the subsonic wind tunnel of the Technical University of Dresden. A modified two-dimensional laseroptical concentration measurement technique for measuring within large planes has been developed. Using laser light sheet, light scattering by small glycerine-water-droplets and digital image processing, concentrations can be measured within a plane of a flow field nonintrusively. The light scattered by particles moved within the light sheet is be recorded using a CCD-camera. Using the developed software package OPTOKONZ the recordings can be corrected corresponding to the actual recording conditions without questionable "calibrating images". Both time averaged concentrations and temporary recordings can be converted to concentration fields. The resulting data have the advantage of being both quantitative and visually interpretable. First results and comparisons with conventional concentrations measurements agree quite well.

1. MOTIVATION

Due to the increasing influence of people on environment, investigations on problems of air pollution and dispersion of pollutants become important in applied aerodynamics research. Beside numerical models, wind tunnel tests are often used to determine the effects of buildings and topographie on gas dispersion in the atmospehric boundary layer. Up till now, wind tunnel modeling is the most appropriate method for figuring out dispersion of pollutants and wind comfort in complex urban areas. Even air pollution by cars or heavier than air gas dispersion may be modeled in a boundary layer wind tunnel. In a boundary layer wind tunnel, essential parameters (like mean velocity profile, turbulence intensity, turbulence length scale ...) of the atmospheric boundary layer are modeled correctly. At the subsonic wind tunnel of the Technical University of Dresden several projects concerning flow and diffusion in atmospheric boundary layers are going on.

When modeling problems of air pollution in a boundary layer wind tunnel, concentration measurements are required frequently. Not only for studies on emission or imission of gases or dyes, tests with tracer gases must be carried out. Tracer gas measurements are also useful for test runs, concerning the ventilation of cities. The conventional way of concentration measurement is the following. At positions, where emissions should be simulated within the model, a mixture of tracer gases and air is emitted into the flow. The tracer gas concentrations in the modeled area may be measured by sampling and analysing a sample. Using today's equipment, it is possible to measure fluctuating concentrations with sampling rates up to 200 Hz [HFR 400, Combustion Ltd.]. The pros and cons of conventional concentration measurement techniques are wellknown.

On one hand the accuracy of tracer gas measurements is very high. On the other hand, much time is needed to handle many points of measurement. A large number of measurements is required to get a sufficient resolution of the investigated concentration field when using single point measurement techniques. Multi point measurements are costly when using conventional instrumentations. In order to better understand processes of dispersion of pollutants in urban areas or in the natural wind it is very useful to measure concentrations in a plane. Thus, it would be possible to pursue the spreading of pollutants not only in time at one point but also in space. In several papers the benefits of 2d-laseroptical concentration measurements using the laser light sheet method, light scattering by small particles and digital image processing are described [see lit.]. Mostly, the instrumentations used for laseroptical concentration measurements are developed for single use in a specific experimental arrangement at particular measuring conditions. To prevent unfavorable conditions of light scattering, small measuring planes are realized. Uneven light distributions in the light sheet are corrected by so-called "calibrating images". The attenuation of laser light due to the light scattering by particles is usually neglected for small measuring planes. Therefore the described instrumentations cannot be applied without restrictions on large measuring planes that are typical of a large wind tunnel. So a modified instrumentation was developed to carry out effective two-dimen-

sional laseroptical concentration measurements in rectangular measuring planes with more than 400 mm's length in each direction. The modified instrumentation is easy to operate and independent of restrictions like above mentioned experimental arrangements or the need to use "calibrating images".

2. BASICS

Two-dimensional laseroptical concentration measurements base on the laser light sheet method for flow visualization. A flow field is being seeded with small scattering particles, which follow the flow without "slip". If these particles pass a thin light plane placed in the flow field, light will be scattered out of the light plane (see **Figure 1**). In general, the intensities of light scattered from the particles are proportional to the local particle density in the light sheet (see *van de Hulst 1981*). If the seeded gas mixes with the unseeded air into the wind tunnel, the number of scattering particles in each unit volume of the flow field will be reduced and the intensity of scattered light will diminish proportionally. When mixing the seeded gas with unseeded air in a boundary layer wind tunnel the dispersion of particles represent the turbulent mixing mechanism only. Because the dispersion of gases in the natural boundary layer is determined principaly by the turbulent motion of the flow, the mixing of gases due to the molecular agitation (Brownian diffusion) can be neglected. The Lorenz/Mie scattering (i.e., scattering from particles with sizes on the order of the wavelength of light used for generating the light sheet) is used for the instrumentation to be presented here. Using Lorenz/Mie scattering, the intensities of scattered light are much stronger than using laser induced fluorescence.

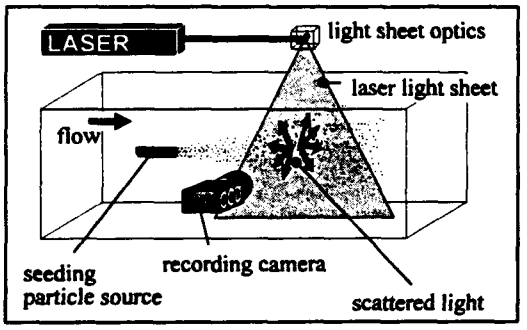

Figure 1: Light scattering by particles moved within a laser light sheet (schematically).

The spatial concentration field can be dicerned in two dimensions at a moment, using a CCD camera system. An image can be digitized and stored using an image processing system. Depending on the available video memory of the image processing system short series of images can be grabbed. It is possible to calculate time averaged images from many snap shots. After digitizing the images there are discrete grey values within the image that represent the intensities of the recorded light.

To calculate particle or gas concentrations from the grey values, some essential factors, the recorded grey values are depending on, must be considered. First of all the light intensities within the unseeded light sheet are not uniform. Depending on the kind of creating the light sheet there are several kinds of light distributions like Gaussian intensity profiles when using an "ideal cylindrical lens". In "real" light sheet systems using cylindrical lenses, it is difficult to describe the light intensity within the light sheet because of the non-Gaussian laser beam, the contamination of the lenses and their distortion. The non-uniform distribution of light can only be considered using so-called "calibrating images". That is why in the present study a rotating mirror is used to form an appropriate light sheet. Using a rotating mirror the light intensity E is a function of the angular velocity, of the radial distance r from the axis of rotation (Eq. 1) and of the attenuation of laser light within air (Eq. 2).

$$E = \frac{E_0}{r} \qquad (1)$$

$$E = E_0 \cdot e^{-\beta \cdot \Delta r} \qquad (2)$$

If one side of the recorded image is long and the rotating mirror is placed near this side, the angle of reflection at the rotating mirror must be considered. Typical measured reflection degrees at the silver mirror used in this work are shown in **Figure 2.**

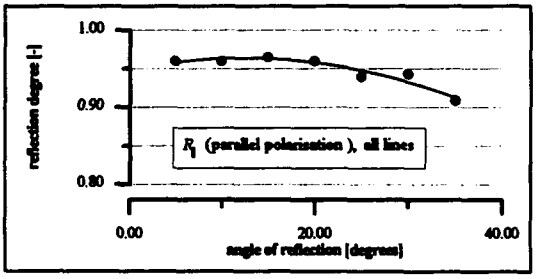

Figure 2: Reflection degrees at the mirror (laser light, parallel polarization).

When carrying out concentration measurements in a seeded flow, the light distribution within the light sheet will be affected by the particles moved within the light sheet. Due to the scattering process by particles closer to the rotating mirror laser light is getting lost for scattering by particles distant from the rotating mirror. For maximum seeded flows the attenuation of laser light can be measured and the coefficient of attenuation β^* can be derived. Assuming a linear behavior between scattered light, particle concentration and the attenuation of laser light, it is possible to calculate local attenuation coefficients β^* within a seeded light sheet.

Using a modified form of equation 2, it will be possible to calculate and correct the non-uniform light distribution due to scattering and attenuation of laser light by particles (Eq. 3).

$$E = E_0 \cdot e^{-\beta' \cdot \Delta r} \qquad (3)$$

Additional important factors, the recorded grey values depend on, are the influence of the line of sight of the recording camera and the angle of view of the camera lens. Because of the visibility of the light sheet within groups of obstacles, light sheet images must often be taken under oblique angles. First, oblique lines of sight leads to geometrical distortions of the recorded objects. Such distortions may be sufficiently corrected, using standard-algorithms of digital image processing (see *Leitl 1992*). Furthermore the intensities of light scattered by small particles (MIE-scattering) depend on the angle of scattering. **Figure 3** shows the typical results of computing the scattered light intensity for glycerine-water-droplets with a diameter of two and four microns (computational code: STREU, author: Dr. A. Napwi).

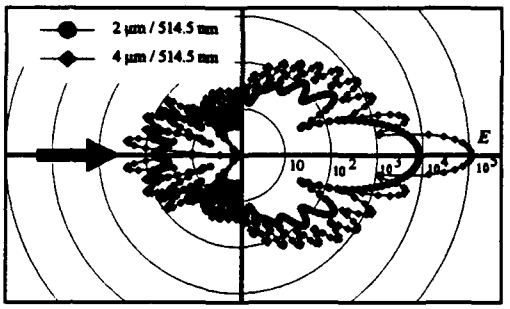

Figure 3: Polar diagramm of scattered intensities for gylcerine-water-droplets.

For depicted groups of particles respectively a particle spectrum applied to 2d-laseroptical concentration measurements, the relative intensity of scattered light can be measured using a small light plane and a CCD to collect the light scattered into different directions (see **Fig. 4**). Typical results of such intensity measurements are shown in **Figure 5**. The structured distribution of scattered intensities that is characteristic for MIE-scattering at a single particle (**Fig. 3**) will be smoothed when observing clouds of particles formed by a particle spectrum.

The mapping properties of the objective lenses used with the recording camera (particularly their shading) must be taken into consideration too. For the lens used in the present study the extenuation of the recorded light intensities near the edges of image plane was measured. In **Figure 6** the results are compared with the cosine-law (Eq. 4).

$$E = E_0 \cdot \cos^4 w' \qquad (4)$$

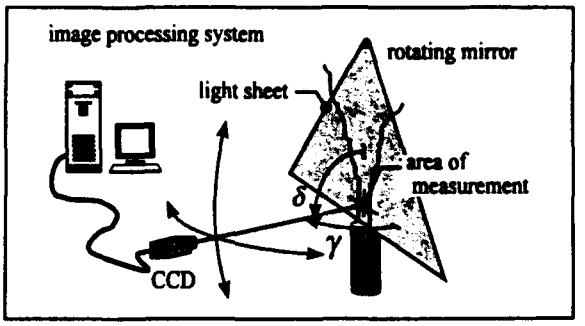

Figure 4: Experimental setup for measuring scattered light intensities by an CCD.

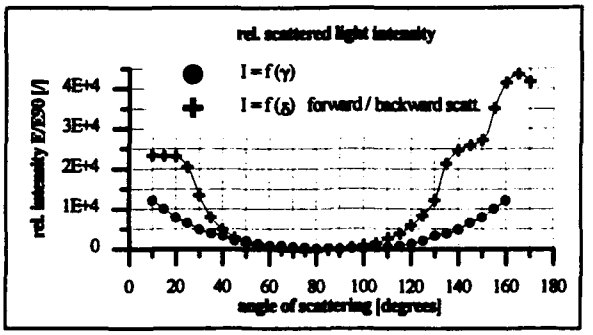

Figure 5: Measured light intensity for scattering by clouds of particles.

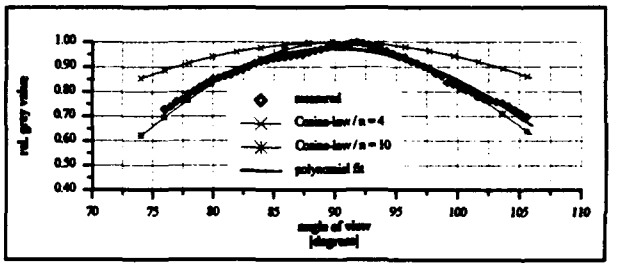

Figure 6: Vignetting of the objective lens COMPUTAR TV 8mm.

In contrast to the exponent $n = 4$ at naturally vignetting, an exponent $n \approx 10$ describes to the investigated objective lens (COMPUTAR TV 8mm). Problems dealing with image recording, digitizing images and digital image processing should not be discussed in this paper. Due to the optimum adjustment of the CCD-camera (COHU 6710) to the image processing system (KONTRON IMCO 10), a range of around 230 usable grey values could be realized. A fine tuning of the camera signal leads to a noise level of one up to two grey values only.

3. OPTOKONZ - SOFTWARE PACKAGE

Based on the ideas mentioned above, a computational code for digitizing and correcting images of grey values as well as their conversion into concentrations was created. The software package named "OPTOKONZ" consists of several independent programs (see also **Figure 7**) for Personal Computer.

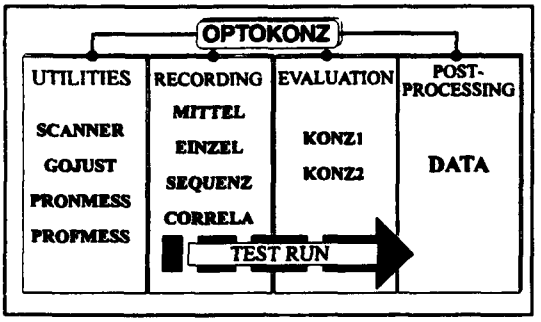

Figure 7: Parts of the software package OPTOKONZ.

Using a first group of programs, the rotating mirror can be synchronized to the camera clock to perform the defined exposure of image frames (program SCANNER). The programs GOJUST, PRONMESS and PROFMESS optimize the recording conditions like laser power, as well as gain and offset of the CCD. By means of the second group of programs the recording of images can be carried out. Both single images and series of images can be digitized and stored real-time. It is possible to calculate time averaged grey values too. According to the size of the video memory and the current image dimensions, a real-time block-averaging algorithm is used. In order to correct the current grey values and to calculate concentrations from the corrected grey values, the third group of programs (KONZ) may be used. In these programs the corrections corresponding to the relations described above are carried out. Performing corrections pixel by pixel, each grey value will be corrected relative to the angle of view (~ respectively the intensity of the scattered light) the vignetting of the objective lens, the attenuation of the rotating laser beam due to the radial distance of pixels from the rotating mirror as well as due to the scattering process by small particles. The whole correcting algorithm must be carried out iteratively because of the dependency of the grey value on the coefficient of attenuation. When the grey values are corrected, concentrations can be assigned to the grey values assuming a linear relation between grey value and concentration. Two significant reference concentrations can be used: the concentration at the particle source release (~ 100%) and the "zero concentration". Reference concentrations measured with conventional techniques can be used too. Also the concentrations or grey values may be transferred from one image to an other when recording overlapping images.

To ease the handling of a large number of measured concentrations within a recorded image, OPTOKONZ was extended by an algorithm for extracting profiles or groups of profiles from complete "concentration images".

4. CONCENTRATION MEASUREMENTS USING OPTOKONZ

4.1 Experimental Setup

The experimental setup is shown schematically in **Figure 8**. In the present study glycerine-water-droplets are used for light scattering. Such particles can be formed using an atomizer.

The light sheet is formed by a rotating mirror, reflecting the principal wavelengths (514.5 nm / 488 nm) of a 6.5 W cw argon-ion laser. To adjust the thickness of the light sheet to about 1 mm a collimator is placed in the path of the beam. In order to synchronize the rotating mirror with the CCD camera, the rotating mirror is powered by a stepper motor. The frequency for the stepper motor can be derived from the camera clock using a plug-in-timer/counter-board for PC. In order to expose each of the half frames of a video image, the revolution of the rotating mirror is fixed to about 50 Hz.

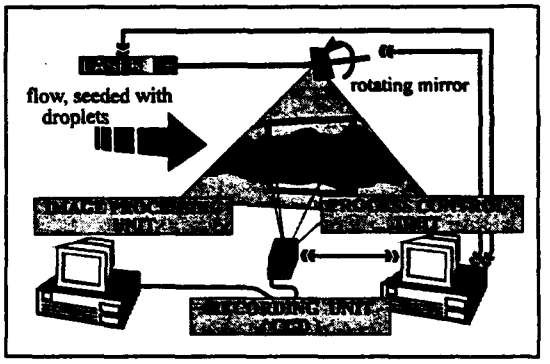

Figure 8: General experimental setup used for laser-optical concentration measurements.

The camera used in the experiments was a CCD-camera COHU 6710 (single CCD using frame transfer method) with a 1/2-inch image area and 699 x 576 active pixel cells. Mostly the camera is used with fixed gain and standard integration time (1/50 sec.). A linear correlation between light intensity and grey value within a digitized image was fixed. The output signals of the camera were digitized with 8 bit resolution that corresponds to 256 grey levels. An atomizer was used to produce small glycerine-water-droplets with diameters from about 0.6 microns up to 4 microns. The main diameter of the aerosol was about 2 microns. The maximum seeding leads to maximum particle concentrations of 800...1400 particles per cubic millimeter.

The image processing system used in the present study was a PC-based system with 3 MB real time video memory (IMCO 10, Kontron Munich). Depending on the size of the recorded

images it was possible to digitize and store up to 12 images in real time. To measure significant mean concentrations more than 1000 images were averaged in groups of 10 images. Because the sampling frequency is comparatively low when using the European video standard (25 images or 50 half frames per second), only "slow dispersion" of particles or rather gases can be pursued in real time (~ up to 10 m/s, depending on the image size). It is possible to speed up the video frequency as a matter of principle when using a video system, which is independent of the limitation due to the standard video frequency. An extension of OPTOKONZ to pursue "faster gas dispersion" is in process.

4.2 Concentration Measurement within an Open Jet

A first set of 2d-laseroptical concentration measurements were made in a wind tunnel with closed test section (see **Figure 9**). The aerosol generated by the atomizer described above was lead through a duct to form a horizontal open jet within the wind tunnel. The CCD-camera and the rotating mirror were mounted at a traversing system out of the wind tunnel. The laser was placed at the top of the wind tunnel. The light sheet as well as a sampling unit for conventional concentration measurements was guided in the test section using a small slot at the upper wall of the wind tunnel. To allow for a side view of the light sheet the wind tunnel was equipped with a pane at one side.

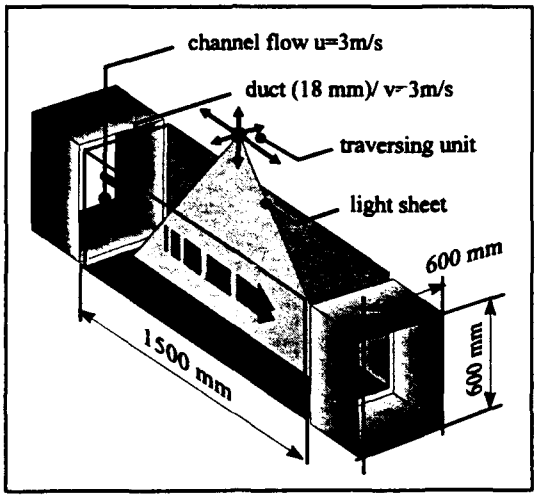

Figure 9: Experimental arrangement - open jet flow.

Figure 10 represents grey values (normally the grey values will be color coded) within the center plane of the jet, as an average of about 1280 video images. The image dimensions are 467 mm x 187 mm respectively 650 x 256 pixels. This uncorrected image was further processed using the program KONZ to correct the actual recording conditions as well as to calculate concentrations from the corrected grey values. Calibrating images are not necessary because the correcting algorithm is based on the simple relations already mentioned. The particle or gas concentrations within the measuring plane that results from the converted grey values are shown in **Figure 11**. Due to the slot at the top of the wind tunnel the concentration profiles are not symmetrical on the right. For verifications of the laseroptical measuring analogous conventional concentration measurements were carried out. The laseroptical and conventional measurements are compared in **Figure 12**. A good correspondence between the results can be detected. Also a distinct difference in quality and quantity can be seen when comparing concentration profiles calculated from uncorrected or corrected grey values.

Figure 10: Recorded grey values - center plane of the jet.

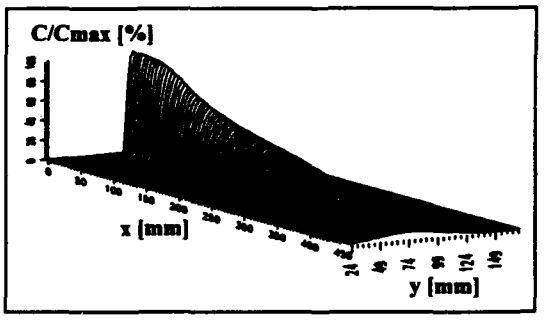

Figure 11: Concentrations measured by OPTOKONZ.

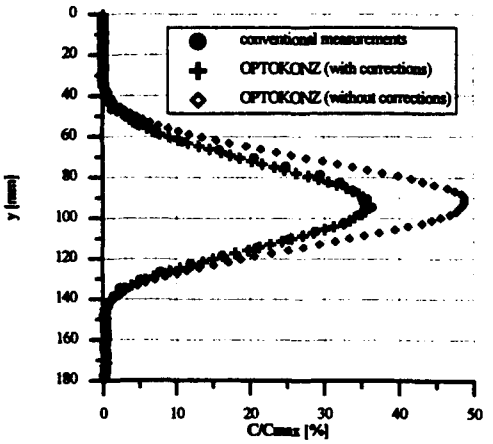

Figure 12a : Comparison between OPTOKONZ and conventional concentration measurements.

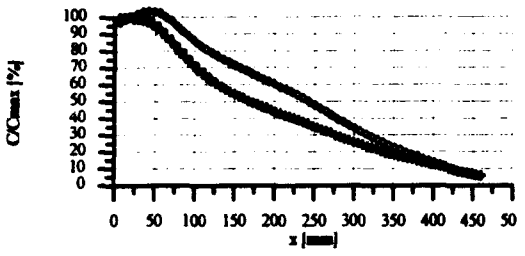

Figure 12b : Comparison between OPTOKONZ and conventional concentration measurements.

4.3 Laseroptical Concentration Measurements within the Model of a Street Canyon

Beside the verification of the laseroptical technique OPTOKONZ was applied for several investigations on gas dispersion within models of urban areas. The experiments were carried out in the large subsonic wind tunnel of the Technical University of Dresden, a return-flow tunnel Göttinger type, with a jet diameter of two or three meters (optional) and an open test section. To simulate the atmospheric boundary layer the wind tunnel is equipped with a turbulence grid and an appropriate surface roughness. A line source for simulating the emissions of cars and the model of a street canyon was placed in the test section. A sketch of the experimental setup in the large subsonic wind tunnel is given in **Figure 13**.

Besides velocity measurements, concentration measurements by means of OPTOKONZ and a hydro carbon analyzer were carried out. Using OPTOKONZ the advantages of 2d-laseroptical concentration measurements become very clear. On one hand it is possible to see the turbulent gas dispersion immediately by observing groups of particles moving within the light plane.

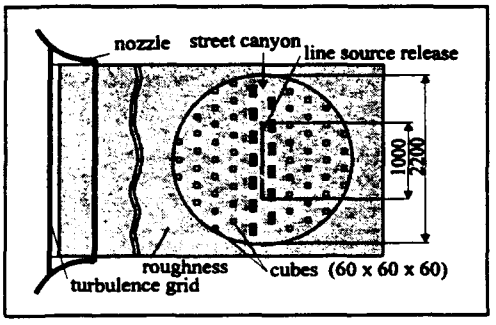

Figure 13: Experimental setup within the test section of the large subsonic wind tunnel (bird's view - schematicaly).

On the other hand due to the easy handling of OPTOKONZ working without difficult and laborious calibrations during the measurements, the laseroptical concentration measurements can be carried out very reliable and fast. Because of the costs of time in a large wind tunnel, the factor of efficiency should not be neglected. Using OPTOKONZ it was possible to study and measure a lot of types of street canyons in a few hours. Some typical results are shown in **Figure 14a and Figure 14b**. In both cases a bird's view on a horizontal measuring plane is represented (≈ 350 mm x 350 mm). The laseroptical measurements are compared with measurements using a hydro carbon analyzer (also flame ionization detector - FID) in this case too. **Figure 15** shows measured concentration profiles along a line between the line source and the upstream row of buildings (pedestrian area). A good correspondence between laseroptical and FID measurements can be detected again. The small differences result from the varied experimental setup when using FID or OPTOKONZ.

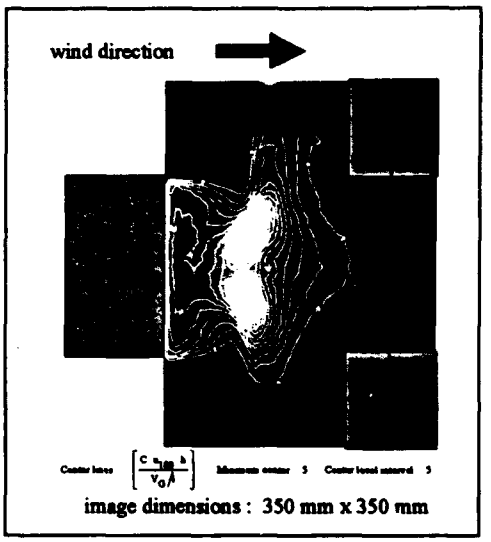

Figure 14a: Grey values and lines of equal concentrations within a street canyon.

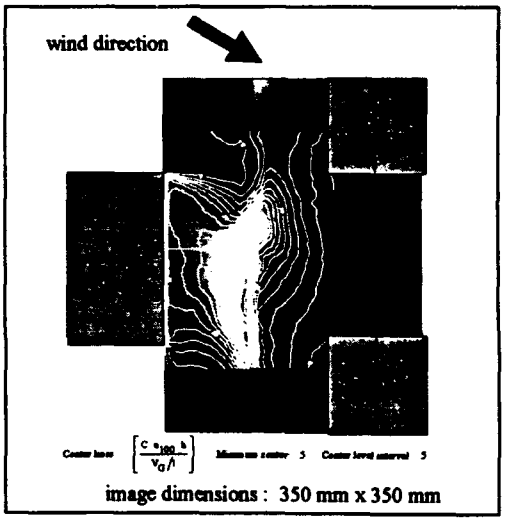

Figure 14b: Grey values and lines of equal concentrations within a street canyon.

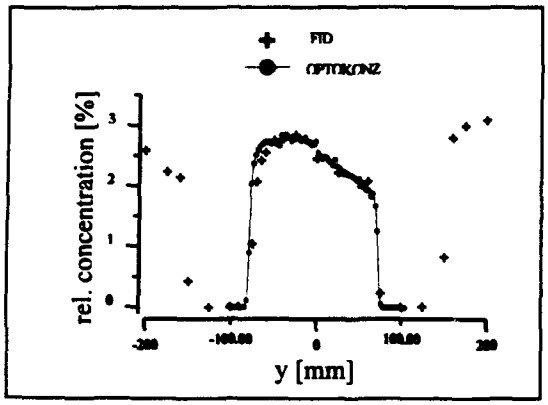

Figure 15: Comparison between concentrations measured by OPTOKONZ and by FID.

5. CONCLUSIONS

A modified technique for 2d-laseroptical concentration measurements "OPTOKONZ" has been developed. It could be shown that laseroptical concentration measurements within large planes are possible without difficult and laborious calibrations. It was shown that the recorded grey values must be corrected before converting them to concentrations. The concentration profiles calculated from the corrected grey values compare favorably well with the concentration measurements by FID.

Beside the effectiveness the laseroptical technique yields to a better understanding of the physics of gas dispersion because of the "visual control" of the concentration fields. In contrast to the conventional techniques the simultaneous measurement at many points within a plane allows to use some other methods for the evaluation of testing data such as multi point correlations.

6. ACKNOWLEDGEMENT

The present study was supported by the DFG (Deutsche Forschnungsgemeinschaft) from 1992 until 1993.

7. REFERENCES

Trucco, R.; Tamagno, J. (1993): Time averaged images of hydrogen fuel plumes by Mie scattering. SPAE Conference Optical Diagnostics in Fluid and Thermal Flow, San Diego

Huber, N.; Qiu, H.-H.; Sommerfeld, N. (1992): Laser light sheet studies by digital image processing compared to particle concentration measurements by PDA in pneumatic conveying. 6th International Symposium on Applications of Laser Techniques to Fluid Mechanics, Lisbon, Portugal

Shaughnessy, E. J.; Morton, J. B. (1977): Laser light-scattering measurements of particle concentrations in a turbulent jet. J. Fluid Mechanics, Vol. 80, part. 1

Rosensweig, E.; Hottel, H. C.; Williams, G. C. (1961): Smoke-scattered light measurement of turbulent concentration fluctuations. Chem. Eng. Science, Vol. 15

Long, M. B.; Chu, B. T.; Chang, R. K. (1981): Instantaneous two-dimensional gas concentration measurements by light scattering. AIAA Journal 19

Long, M. B.; Webber, B. F.; Chang, R. K. (1978): Instantaneous two dimensional concentration measurements in a jet flow by Mie scattering. Applied Physics Letters, Vol. 34

Schon, J. P. (1984): Instantaneous concentration and velocity measurements through laser visualization associated with a digital processing system. Lecture Series 1984-03, von Karman Institute for Fluid Dynamics, Digital Image Processing in Fluid Dynamics

Huber, A. H. (1988): Video Images of Smoke Dispersion in the Near Wake Flow of a Model Building, Part I, J. Wind Eng. Ind. Aerodyn. 31

Ereaut, P. R.; Shand, A. M. (1990): Laser sheet illumination for combusting and high speed flows. 5th International Symposium on Applications of Laser Techniques to Fluid Mechanics

van de Hulst, H. C. (1957): Light Scattering by Small Particles. Reprint 1981, Dover Publications Inc., New York

Mie, G. (1908): Beiträge zur Optik trüber Medien, speziell kolloidialer Metallösungen. Annalen der Physik (4) 25

Leitl, B. (1992): Geometrische Kalibrierung von Aufnahmekonfigurationen zur Rücktransformation digitalisierter Lichtschnittaufnahmen, Mitteilung der Deutschen Forschungsgesellschaft für Luft- und Raumfahrt, DLR-Mitt. 92-04

CONTACT

Bernd Leitl
Technische Universität Dresden
01062 Dresden - Germany
Phone : +49 - 0351 - 4579 - 258
FAX : +49 - 0351 - 4579 - 298
Email : leitl@rmhs2.urz.tu-dresden.de

CONCERNING TAYLOR TIME AND LENGTH SCALE ESTIMATES MADE FROM COUNTER-PROCESSED AUTOCORRELATION MEASUREMENTS IN GAS FLOWS

L. H. Benedict, P. R. Yearling and R. D. Gould
Mechanical and Aerospace Engineering
North Carolina State University
Raleigh, NC 27695

ABSTRACT

An investigation was performed in grid-generated turbulence to test the capacity for making accurate microscale estimates from discrete autocorrelation measurements made in a gas flow using a laser Doppler velocimeter (LDV) with counter-based signal processing. Comparison was made to hot-wire results and the theoretical growth laws determined by the decay of turbulent energy. The chief concern was the presence of a spike in the measured autocorrelation functions at $t = 0$. It was found that renormalising the autocorrelation to a value at $t = 0$ determined by "backfitting" a quadratic equation to the slots near $t = 0$ allowed for accurate determination of microscales. Microscale estimates from the LDV measurements showed the same trend as the decay law and agreed within experimental uncertainty with those determined using a hot-wire. Additionally the paper presents practical guidelines for performing accurate autocorrelation measurements by LDV.

1. INTRODUCTION

As the laser Doppler velocimeter (LDV) becomes a more common tool in the study of turbulent flow phenomena, researchers are rapidly moving on from the measurement of simple means and variances of velocity and are attempting increasingly complex measurements. As might be expected, additional problems usually must be overcome whenever more advanced measurements are undertaken.

One such advanced statistic is the discrete Eulerian autocorrelation function, *i.e.*

$$R_B(\tau) = \frac{\overline{u'(t)u'(t+\tau)}}{\overline{u'^2(t)}} \qquad (1)$$

In reality a simple statistic, used for decades by hot-wire practitioners in studies of turbulent flows, it's accurate measurement by LDV is complicated by the random arrival times of the measurements and – as will be shown here – the lower (relative to good hotwires) signal to noise ratio of the instrument.

Although LDV measurements were initially made using analog frequency tracking units, the development of counter-processors in the late sixties and early seventies allowed for successful discrete measurements in gas flows. Before discrete autocorrelation measurements could be made however, it was necessary to develop techniques for constructing discrete lag products from data with poisson arrival statistics. Early papers concerned with the development and use of discretised autocorrelation algorithms for the LDV are those of Mayo *et al.* (1974), Scott (1974), Smith and Meadows (1974), and Wang (1975). Mayo is usually given credit for the so-called "slotting algorithm" which has become the standard autocorrelation algorithm for LDV measurements and was the technique used in this investigation. In the slotting technique, a discretised estimate $R(k\Delta\tau)$ of $R_B(\tau)$ is made by summing lag products over M equi-spaced slots of interval $\Delta\tau$. Lag products of all points up to a specified maximum lag time are accumulated in appropriate bins. The average of all the auto-products falling in each bin is assumed to be the value of the discrete autocorrelation function at the midpoint of the bin. The algorithm may be summarised as:

$$R(k\Delta\tau) = \frac{\mathrm{SUM}(k\Delta\tau)}{\mathrm{H}(k\Delta\tau)} \quad k = 1, 2, ..., M, \qquad (2)$$

where $\mathrm{SUM}(k\Delta\tau)$ is the sum of all cross products $u(t_i)u(t_j)$ separated by lag times $(k-\frac{1}{2})\Delta\tau < |t_j - t_i| < (k+\frac{1}{2})\Delta\tau$, and $\mathrm{H}(k\Delta\tau)$ is the number of lag products falling within this slot.

These early efforts were geared toward spectral analysis; however, historically, dating back to the early homogeneous isotropic turbulence studies of the thirties, autocorrelation measurements have been used to estimate the Eulerian integral time scale, defined as the integral of the autocorrelation function,

$$\mathcal{T}_B = \int_0^\infty R_B(t)dt \qquad (3)$$

and the Eulerian dissipation (micro)scale, defined in terms of a Taylor series expansion of the autocorrelation curve near $t = 0$. In practice the microscale is often determined by the point at which an osculating parabola fitted to the autocorrelation function near $t = 0$ crosses the time axis. The equation for this curve is given by (Hinze, (1975)):

$$R_B(t_1) \approx 1 - \frac{t_1^2}{\tau_B^2} \qquad (4)$$

The integral and micro-length scales may then be determined from their respective time scales by applying Taylor's hypothesis. Taylor's hypothesis, which is valid only

if the flow field has uniform mean velocity, $\bar{U}$, and small turbulence intensity, gives a relationship between temporal and spatial quantities(i.e. $x = \bar{U}t$). If Taylor's hypothesis applies the relations, $\Lambda_f = \bar{U}\tau_B$ and $\lambda_f = \bar{U}\tau_B$, result. Note that only the longitudinal length scales can be estimated with Taylor's hypothesis.

In the late seventies, Barnett and Giel (1976) and Lau *et al.* (1979) noticed while making measurements in jet flows that the LDV predicted consistently higher turbulence intensities than corresponding measurements made using a hot-wire. In follow-up work, Lau (1980) and Lau *et al.* (1981) traced the source of the discrepancy to the squaring of uncorrelated noise in the LDV signal when the variance of velocity is calculated. The noise level was found to be roughly constant for given LDV settings such that the deviation from the hot-wire results was most grievious at low turbulence intensities. This discovery was aided by concurrent autocorrelation measurements which revealed a large spike at $t = 0$ due to the sero-lag products, *i.e.* the variance of the velocity. The spike was obviously unnatural in a jet flow autocorrelation and thus helped solidify the theory that signal noise superimposes an added variance to the measured velocity. Additionally, these correlation measurements showed that for all practical purposes signal noise is uncorrelated and does not affect lag products other than the sero-lags in discrete autocorrelation measurements. It should be mentioned that hot-wire signals also have a noise component; however, usually it is so small as to go unnoticed unless the turbulence intensity is very low and the sampling rate very high.

Lau further claimed that the spike caused by the sero lag products could be eliminated by the cross correlation of two photomultiplier tube signals responding to the scattered light from the same particles. Unfortunately Lau's work did not receive the attention it deserved, considering its implications for LDV measurement accuracy. Admittedly, at that point autocorrelation measurements made using an LDV were only being attempted by a few researchers. It was not until the late eighties that Lau's claims were further investigated. Absil *et al.* (1990) made discrete autocorrelation measurements in the wake of a cylinder 2 mm in diameter in air at a free stream velocity of 10 m/s. The turbulence intensities for their measurement locations were below 5% and the Kolmogorov scales were rather large thus allowing for adequate resolution of the autocorrelation curve near $t = 0$. The low turbulence intensities ensured that any noise would be well indicated in the autocorrelation measurements. Their research did much to substantiate Lau's work and more clearly showed the spiking effects caused by the squaring of uncorrelated noise in the sero-lag products. Cross-correlation measurements from two photomultiplier tubes were also attempted to eliminate the noise spike, but the effect was only to reduce the noise, not eliminate it. Absil *et al.* noted that the presence of the spike severely inhibits the estimation of microscales from LDV autocorrelation measurements. The present author's experience indicates that in flows with turbulence intensities below 10 percent, the ignoring of noise effects could cause microscale estimates to be a full order of magnitude low, if not further. Integral length scale estimates are less affected by such noise effects, however they may also be greatly underestimated unless the noise is accounted for.

Absil *et al.* focused mainly on the accuracy of turbulence intensity measurements and the general measurement of autocorrelations using LDV. Their work also did not receive proper attention as evidenced by the lack of papers citing their work in the recent literature.

As researchers begin taking simple turbulence intensity measurements for granted and move on towards spatial correlation measurements and spectral estimates, it seems important to put the practical art of making accurate autocorrelation measurements on a firm footing. This paper then attempts to summarise what knowledge has been gained by the authors in the course of making extensive autocorrelation measurements in various gas flows for the purpose of estimating integral and micro length scales.

2. EXPERIMENTAL APPARATUS

It was felt that an important element lacking in previous work in this area was comparison with agreed standards. This is especially important for length scale estimates which can be consistent but still inaccurate. The difficulty of validating most LDV measurements is a lack of certainty in the accuracy of any other data used for comparison. Agreement with hot-wire results is a frequent benchmark test, but in many flows hot-wire results are even less reliable than LDV data. It was decided in this work that comparison would be made with hot-wire results in grid-generated turbulence. This decision was made with deference to the vast amount of well documented research done by able investigators in this area and to the fact that the energy equation in grid-generated turbulence requires that the squares of the microscales vary linearly with distance from the grid (Batchelor (1953)):

$$\lambda_f^2 = \frac{20\nu M}{n\bar{U}}\left(\frac{x}{M} - \frac{x_0}{M}\right) \tag{5}$$

where the constant, 20, follows from Hinze's (1975) definition of λ_f^2, *i.e.*

$$\frac{1}{\lambda_f^2} = -\frac{1}{2}\left[\frac{\partial^2 f}{\partial r^2}\right]_{r=0} \tag{6}$$

and n is the exponent from the decay law for the turbulent energy given below.

$$\frac{\overline{U^2}}{\overline{u^2}} = \alpha\left(\frac{x}{M} - \frac{x_0}{M}\right)^n \tag{7}$$

This implies that the microscales are functions only of distance from the grid with slope determined by the mean velocity, $\bar{U}$ and viscosity, ν. Thus, checks can be made for each instrument with theoretical predictions as well as against one another. Additionally, the low turbulence intensities present in grid-generated turbulence assured the significant presence of noise effects as well as elimination of velocity bias as an issue in this investigation.

To carry out the work, a low speed wind tunnel was built consisting of a blower, a 1.2 m on a side cubical

plenum chamber with a 1.2 m long entrance section to a converging nozzle. The entrance section was 54 cm by 54 cm in cross section with the nozzle feeding to a test section 15.24 cm by 10.16 cm in cross section and 61 cm in length. The test section was fabricated from aluminum in such a way as to allow for complete optical access from all four sides. Basically the walls were all glass windows. This allowed for the possibility of signal collection from any direction. Honeycomb and screens were placed in the entrance section reducing the free stream turbulence levels (without the grid) to between .2 and .3% for the velocities used in this investigation.

The grid was of the bi-plane round rod variety with 6.35 mm between rod centers and a rod diameter of 1.5875 mm. Thus $M/d = 4$ for this grid and the solidity ratio was .4375. This solidity ratio should be low enough to avoid vortex shedding effects from the individual rods which can cause the flow to remain inhomogeneous far downstream of the grid. The grid is also geometrically similar to the M = 25.4 mm grids used by Corrsin and his co-workers, and of equal mesh size to the smallest grid used by Batchelor. The LDV used for these experiments was a two component dual-beam system, operating in forward scatter mode. Only a single component was used in this study as only the axial velocity statistics were of interest. The 514.5 μm laser line from a Model 168B 2 Watt Spectra Physics argon ion laser was used to make the measurements. The beam half angle for this system is 6.261° and the fringe spacing is 2.359 μm. Bragg cells were used to shift the frequency of both beams by 45 and 35 MHz, respectively, in opposite directions causing the fringes to move at 10MHz in the upstream direction (approximately 4 m/s). The LDV employs 3.0× beam expansion optics and gives a probe volume approximately 100 μm in diameter and 1000 μm in length. A TSI Model 1990C counter processor was used in the data collection and processing system. High and low pass filters were set to 1 MHz and 20 MHz. The processor was set to sample in a single measurement per burst mode (multiple measurements per burst not allowed), count 32 fringes and use a 1 % comparator. Data (one velocity and the running time for each realisation) were transferred through a Dostek LDV interface to an intel based 486 66 MHz personal computer for storage and analysis.

To fully resolve the small scales in the flow downstream of the grid, it was realised that very high data rates would be necessary. To this end, 4 custom built seeder units roughly following the design of Liu and Lee (1975) were fabricated and mounted to supply seed particles straight into the blower inlet. This method of seeding ensured a constant seed density throughout the test section. The seeders generated vegetable oil particles in the 1 μm size range. At 12 m/s, single measurement per burst average data validation rates of up to 60 kHz were possible although at lesser speeds this maximum average data rate decreased.

The hot-wire equipment used in this investigation consisted of a TSI 1054 anemometer with a TSI platinum P2 sensor. The sensor diameter was 5 μm and the length 1.25 mm. The linearised output of the anemometer was sampled digitally using a MetraByte DAS20 12 bit A/D converter interfaced to an Intel based 386 computer. The frequency response at the velocities used in this investigation was approximately 50 kHz.

3. EXPERIMENTAL PROCEDURE

All flow conditions were maintained at near constant values throughout the testing procedure. Two inlet centerline velocities were considered, $U_{cl} = 6.15$ m/s and , $U_{cl} = 11.80$ m/s giving $Re_M = 2586$ and 4962 based on upstream centerline velocity and grid size.

Hotwire velocity statistics and autocorrelations were formed by using 10 sets of 4096 individual realisations at each axial measurement location. Good reduction of run to run variance was achieved by using the 10 sets of data, and repeatability of the measurements was high. LDV data were acquired in segments of 60000 samples. Variance of LDV autocorrelation measurements formed using the slotting technique is known to follow the formula (Scott, (1974), Benak *et al.*, (1993)):

$$VAR[R_B(k\Delta\tau)] \leq \frac{R_B^2(0) + R_B^2(k\Delta\tau)}{H(k\Delta\tau)} + \frac{4}{T}\int_0^\infty R_B^2(\mu)d\mu \tag{8}$$

where k is the slot number ($k\Delta\tau$ represents a lag time), $H(k\Delta\tau)$ is the number of lag products falling in the kth slot and T is the total sampling time. The first term may be thought of a variance based on the number of lag products accumulated per slot. High data rates help to accumulate large numbers of lag products per slot as the expected number of products per slot is given by (Mayo, (1974), Absil, (1990)):

$$E[H(k\Delta\tau)] = N\nu\Delta\tau \tag{9}$$

if $T \gg M\Delta\tau$ where ν is the average data rate and $\Delta\tau$ is the slot width. Thus, the first term is reduced by a high data rate; however the second term may be thought of as run to run variance and is increased by a high average data rate. Thus when increasing data rate in an attempt to resolve small scales it becomes necessary to take a great deal of data.

Several combinations of run number and sample size were investigated to determine what the most efficient method of taking data would be. In general it was found to be most advantageous to take as many small sets of data as possible keeping in mind that the condition $T \gg \mathcal{T}_B$ must be maintained for each individual data set. This conclusion was realised somewhat late in the investigation such that the LDV data were taken somewhat inefficiently. A single set of 60000 data points was acquired at each measurement location. The 95 % confidence interval according to Scott's formula for the uncertainty of autocorrelation estimates acquired in such a fashion proved to be typically on the order of 2 %, however this did not guarantee accurate microscale estimates.

In computing statistical parameters, a two step process suggested by Meyers (1988) was used to eliminate noise from the data. All velocity measurements deviating more

than 3 standard deviations from the mean are thus eliminated. For a properly operating LDV system less than 1 % of the data should be discarded. In this investigation this was true in all cases.

4. EXPERIMENTAL RESULTS

4.1 Previous Work

Before reporting the results of the grid experiments, some previous results pertinent to this investigation should be reported. In Figure 1, typical autocorrelation functions measured at 6 step heights downstream ($x/H = 6$) and 2 step heights ($r/H = 2$) from the axis of an axisymmetric expansion are presented. The facility and equipment used in this experiment has been described in Gould and Benedict (1992) The discrete autocorrelations, shown in Figure 1, were obtained using a slot width of 50 μs. Note that there is still some scatter in the data even though 50,000 samples were used to build the autocorrelation functions. A mean data validation rate of approximately 12,000 per second was used here with a free running processor (possibility of multiple measurements per burst). This scatter is statistical in nature and is due to too few lag products in each slot which causes some variance in the data (each bin contained approximately 30,000 lag products). Interestingly, although sero-lag products were not included in the first slot of the discrete autocorrelation function, a severe spike results at the origin (bottom curve). This spike represents those lag products falling between $t = 0$ and $t = \frac{\Delta\tau}{3}$ which in this case were used to normalise the autocorrelation as opposed to the sero-lags products. If the slot size is decreased further the spiking effect carries into the next few slots after the first as well. This particular spiking effect is caused by the continuous sampling of the LDV system. Continuous sampling allows for multiple measurements to be made on a single Doppler burst. In such a situation, a slow moving particle can be sampled more than once as it passes through the probe volume. This first slot thus contains mostly the squared fluctuating velocities of particles moving at velocities much less than the mean. They thus make a large contribution to the discrete correlation estimate at this time lag and serve to bias the autocorrelaion as a whole.

An algorithm was employed to remove multiply sampled velocity measurements from the data set. Basically, the data set was searched for successive measurements which had velocity-time between data products less than the probe volume diameter. If this occurred, these measurements were assumed to have come from the same particle. After eliminating these redundant measurements, a new autocorrelation function was calculated and is also shown in Figure 1 (top curve). One may observe that this new autocorrelation function displays the expected parabolic behavior near the origin without any spiking. From such an autocorrelation function the Taylor microscale may be easily estimated. It should be noted however that the correction algorithm cannot be certain of removing only multiple realisation samples as there may be particles which have traversed only a small portion of the probe volume thus allowing the processor to reset quickly

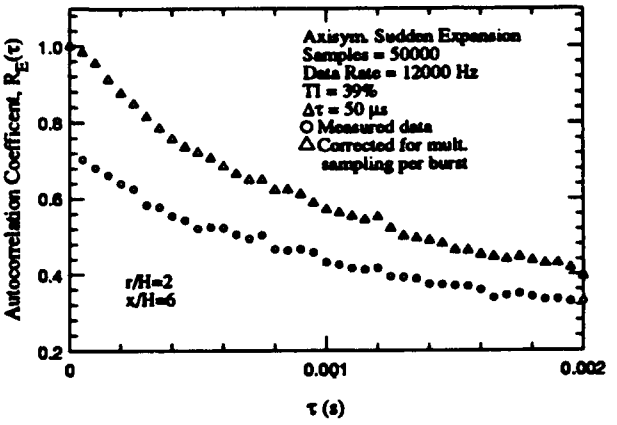

Figure 1. Effect of continuous sampling.

and make another measurement a short time later. For this reason continuous sampling promotes haphasard discrete autocorrelation estimates.

These results clearly support the use of single measurement per burst mode when making autocorrelation measurements in order to prevent biasing of the autocorrelation function as described above. This puts a tremendous burden on seeding requirements; however, since investigators frequently make use of continuous sampling processor settings to boost data validation rates. It was this reasoning which led to the multiple seeder arrangement used in this investigation.

4.2 Grid Results

Absil reported that the noise spike in LDV autocorrelation measurements varies with the data rate, although, in general, the noise effects come from several sources including photomultiplier shot noise and heterodyning of signals from several particles simultaneously at the detector. This noise evidently manifests itself as a variation of the Schmidt trigger signaling the processor when to begin counting fringe crossings in the Doppler burst. It had been noted by the present authors that processor settings had a great influence on turbulence intensity measurements and so a series of autocorrelations were performed to determine if fringe-count settings had a significant impact on the signal to noise ratio. Figure 2 shows correlations made under the same conditions except for a variation in the number of fringes required for validation of a Doppler signal. It can be seen that the parameter N (number of fringes) has a significant affect on the mean square of the velocity. Note that all curves are normalised to one at $t = 0$ and the immediate drop in $R_{B\tau}$ is this "spiking" effect.

It would seem from the figure that the greater the number of fringes the better, but even with frequency shifting it is probable that some form of fringe bias (Edwards, (1987)) is taking place when 128 fringes are required to validate a measurement. Also there is a severe penalty in average data rate for chosing $N = 128$ so that a compromise solution is justified in choice of fringe-count settings. Setting $N = 32$ proved to be the best compromise between noise and data rate in this investigation and may

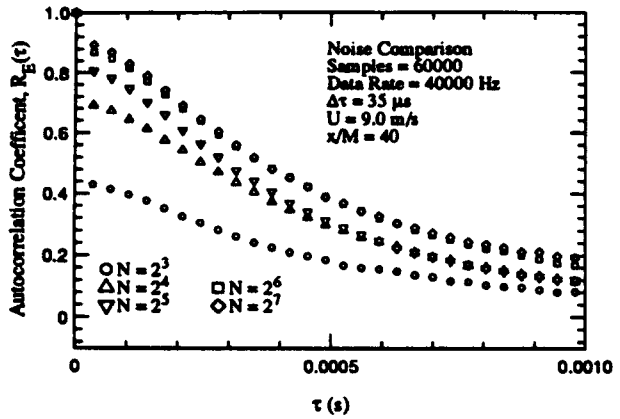

Figure 2. Noise as a function of fringe setting.

be globally applicable for LDV's with frequency shifting, but researchers are encouraged to evaluate the optimum combination for their systems.

As first suggested by Lau, the autocorrelation measurements may be corrected for noise by some form of curve fitting back to the $t = 0$ axis (*i.e.* the spike was discarded as erroneous). In this work, quadratic fits between the second and third slots were using to "backfit" a parabolic variation to $t = 0$. Figure 3 shows the corrected discrete autocorrelations exhibiting good agreement although there is some variance caused by the finite time sampling discussed above in connection with Scott's formula.

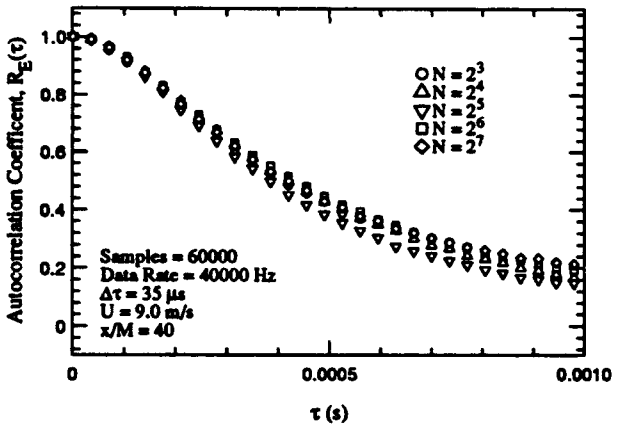

Figure 3. Noise-corrected LDV results.

Figure 4 shows that hot-wires also have a characteristic RMS noise level (approximately 9 mV in this work) although the signal to noise ratio tends to be much greater than that of the LDV. The hot-wire equipment used in this investigation was on loan and somewhat out-dated. It may be that this is an unrealistically high level of noise for state-of-the-art hot-wire equipment but it is strange that little if any mention was made of such effects in some of the classic hot-wire studies. In such studies, wind tunnels were often used with free stream turbulence intensities of 0.02 %. Surely noise effects would be evident under such circumstances. As a check to be sure the spiking matched with the noise level measured during the experiment, the spiking was predicted for a given voltage level from the apparent RMS noise level of 9 mV. After converting to velocity, the predictions agreed well with the spiking seen in the autocorrelation measurements. Thus, there was confidence that the hot-wire displays similar behavior to the LDV albeit to a lesser extent. All hot-wire measurements were therefore corrected as was done with the LDV measurements.

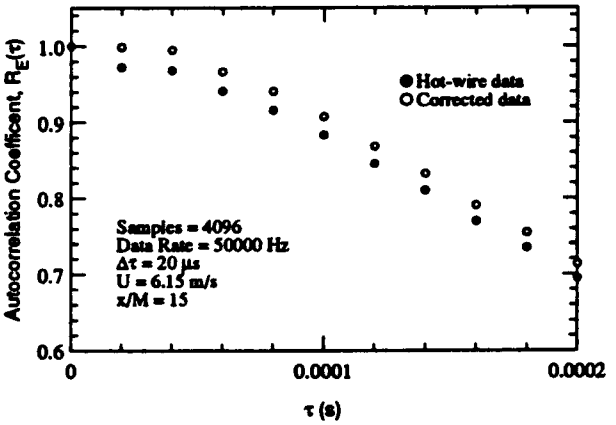

Figure 4. Measured and corrected hot-wire results.

The measured and corrected decay curves for the normalised turbulence energy at $\overline{U} = 6.15$ m/s and $\overline{U} = 11.80$ m/s are shown in Figures 5 and 6. The Kolmogorov frequencies in this flow range from 29 kHs to 16 kHs at $\overline{U} = 6.15$ m/s and 91 kHs to 52 kHs at $\overline{U} = 11.80$ m/s. In both cases, hot-wire measurements were made at 50 kHs while the maximum LDV sampling rates were dependent on the mean velocity. At 11.80 m/s rates over 50 kHs were attained with the LDV, however data rates of only roughly 25 kHs could be attained at the lower velocity. It was noticed at the lower velocity however, that the continuous data rate was on the order of 110 kHs. Since the hot-wire data indicated that a 60 μm slot size was sufficient to make accurate microscale estimates at this lower velocity, an attempt to use a "controlled processor" to make equal time sampled autocorrelation measurements with the LDV at 16.7 kHs from the continuous running average data rate of 110 kHs according to the technique investigated by Gould *et al.* (1989) was made. To the authors knowledge this technique has not yet been applied to autocorrelation measurements as it would seldom be feasible under normal measuring conditions. (Note that this type of use of a *controlled processor* is not the same as using all of the data from a free running processor, although in both cases the counter is set to *continuous* measurement mode.) The LDV measurements at 11.80 m/s were made in a data ready fashion.

The decay data was fitted according to the technique described in some detail by Gad-el-Hak and Corrsin (1974). The data were first plotted in logarithmic coordinates and a virtual origin, x_0, determined. The slope of the line then determined n and the vertical position, α. The constants

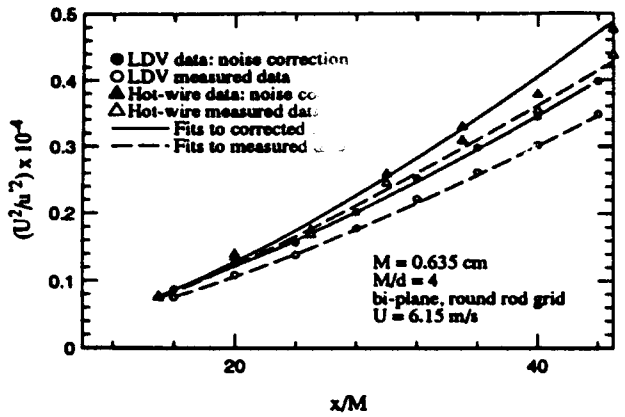

Figure 5. Decay curves for U = 11.80 m/s.

in the decay law (Eq. 7) for data taken at both $\overline{U}$ = 6 m/s and $\overline{U}$ = 11.80 m/s are summarised in Tables 1 and 2.

Table 1. Decay law constants, (measured data).

Instr.	$\overline{U}$ (m/s)	α	n	x_0
Hot-wire	6.15	39.5	1.27	-5.0
LDV	6.15	13.5	1.47	-0.5
Hot-wire	11.80	39.0	1.23	-5.0
LDV	11.80	57.0	1.05	-6.0

Table 2. Decay law constants, (corrected data).

Instr.	$\overline{U}$ (m/s)	α	n	x_0
Hot-wire	6.15	18.5	1.49	-5.0
LDV	6.15	12.0	1.53	+0.5
Hot-wire	11.80	35.5	1.28	-5.0
LDV	11.80	20.5	1.35	-1.0

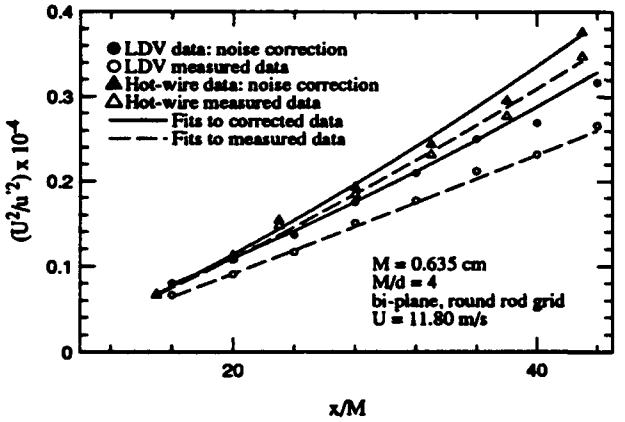

Figure 6. Decay curves for U = 6.15 m/s.

These results are similar to those compiled by Gad-el-Hak and Corrsin summarising 40 years of research in grid generated turbulence. The exponent in the decay relations tended to be in the higher range of the spectrum of measurements made in grid-generated turbulence, but it is doubtful that any noise corrections were applied in the past. These corrected curves would indicate that grid-generated turbulence is even more disparate from homogeneous isotropic turbulence than what has been suggested before.

Figure 7 compares the integral length scale estimates made from all of the corrected autocorrelation measurements. These estimates were made by integrating the discrete Eulerian autocorrelation function up to the point at which it crossed the time axis. The justification for this approach is discussed by Compte-Bellot and Corrsin (1971). The integral length scale tends to be a geometric property of the flow and has been reported to be independent of mesh Reynolds number for this flow. The best fit to the data is:

$$\Lambda_f = 0.11(\frac{x}{M} - 3.0)^{.40} \qquad (10)$$

some 15 % greater than the fit given by Corrsin to a number of previous experiments concerning 25.4 mm meshes. It is unclear whether the low Reynolds numbers in the current experiments were responsible for the deviation.

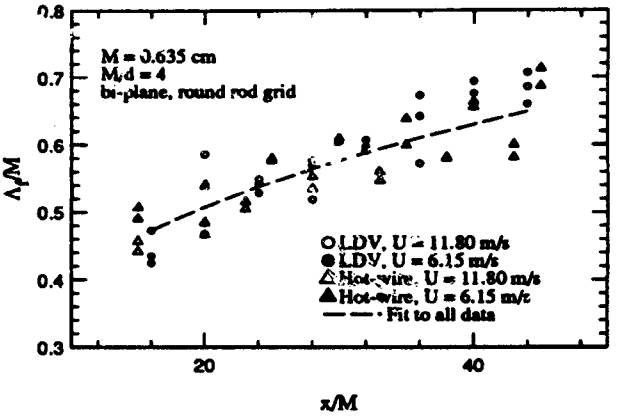

Figure 7. Integral Scale Comparison.

Microscales were estimated from the corrected discrete autocorrelation functions by the fitting of a parabola to the first three discrete estimates of the autocorrelation function. Figure 8 attempts to illustrate the effect of making microscale estimates on correlations without sufficient resolution. If it is assumed that the solid curve, fitted to the first four slots in this case, represents the correct microscale estimate, then one may note that had the sampling rate been lower, lag-products further removed from $t = 0$ would have been used to fit a parabola to the discrete autocorrelation function. The solid line is then the estimate generated by 50 kHz sampling. The dashed line corresponds to 16.7 kHz and the dotted line to 10 kHz sampling. Of course, the important point is that the sampling rate must be on the order of the smallest scales in the flow. Thus, one must always be aware of the Kolmogorov scales in the flow of interest.

Figures 9 and 10 compare the hot-wire microscale estimates to the LDV estimates. Note that the agreement

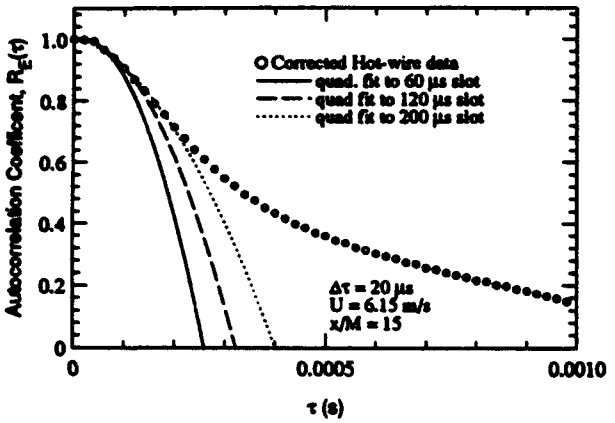

Figure 8. Resolution effects on microscale estimate.

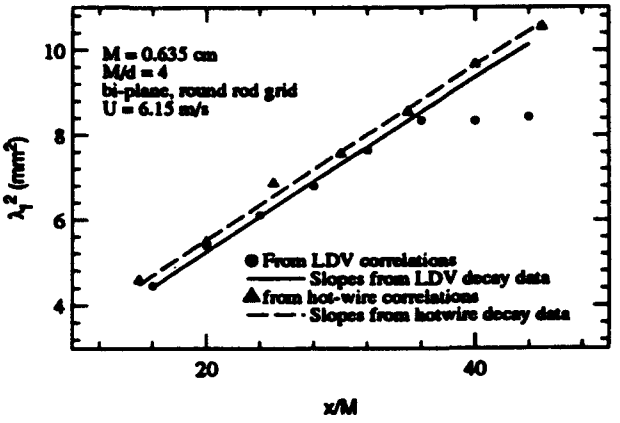

Figure 10. Microscale comparison, U=6.15m/s.

for λ_f itself is actually quite good – well within the experimental uncertainty – as the graphs are showing λ_f^2 which greatly magnifies any discrepancy. More importantly, the estimates are consistent with the variation predicted by the decay laws as measured by each instrument. Note that the estimates for $\overline{U}$ = 6.15 m/s show less scatter than those made at $\overline{U}$ = 11.80 m/s, illustrating the resolution difficulty as the Kolmogorov frequencies increase. This hints at the major problem with autocorrelation measurements in general. Although the length scales remain relatively constant as velocity increases, the time scales drop very quickly owing to the relation between length and time scales given by Taylor's hypothesis. Making spatial measurements is a much more promising way to attack the problem, but requires much more equipment and as yet still unacquired experience.

It might be mentioned in passing that spatial correlation estimates are affected by the same noise problem discussed here. The result in the case of spatial correlations is not a spike near zero separation but rather a failure of the correlation to reach unity at zero separation.

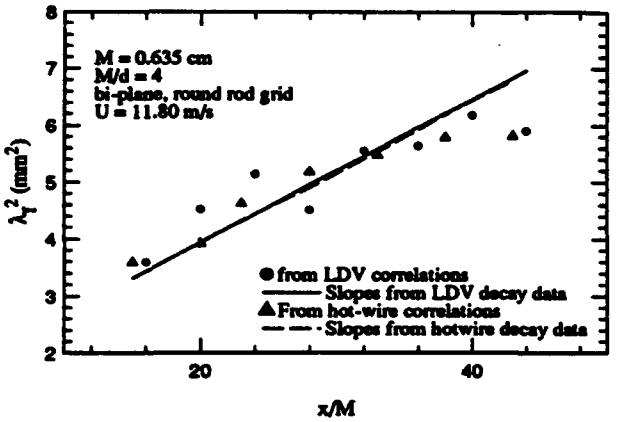

Figure 9. Microscale comparison, U=11.80m/s.

It is also interesting to note the consistent microscales derived from the controlled-processor LDV measurements at $\overline{U}$ = 6.15 m/s. It can be seen in Figure 10 that the agreement is excellent until $\frac{s}{M}$ = 40, at which point the estimates decrease markedly. This phenomenon is actually due to a bias induced from attempting to sample in equal intervals at a frequency too close to the single measurement per burst (SM/B) mean data rate. Recall that equal time measurements were attempted at 16.7 kHs while the continuous data rate was about 110 kHs. Thus the continuous data rate was about 7 times the controlled sampling rate which may be sufficient Gould *et al.* (1989) to produce reasonable equal time measurements. The SM/B data rate at this point was only about 25 kHs, however, dropping to 19 kHs at $\frac{s}{M}$ = 44. Evidently this is close enough to 16.7 kHs that some of the equi-time samples had to have come from the same particle. This implies that multiple measurements per burst were made, thus incurring the type of bias explained above. The bias that caused the results in Figure 9 is barely perceptible to the eye as seen by the 60 μs curves in Figure 11. Though the biased curvature is hardly to be recognised, it has a significant impact on microscale estimates where even slight changes in autocorrelation function curvature make a huge difference. This is why accurate microscale estimates are extraordinarily difficult to make.

To better illustrate the point of sampling too quickly when using a controlled processor, new measurements were made at 25 kHs (*i.e.* slot width = $\frac{1}{40}$ kHs) when the SM/B data rate was approximately 19 kHs. In this case the bias induced in the autocorrelation near t = 0 is readily perceived.

5. CONCLUSIONS

It has been shown that spiking in autocorrelation measurements obtained using LDV is a prevalent phenomena that may be caused by biases induced by continuous sampling (if zero-lag products are not included in the autocorrelation) but more often by the squaring of uncorrelated noise in the zero-lag correlation estimate (variance of the velocity fluctuations). The spiking caused by a continuous processor sampling bias may be overcome to some extent in the post-processing stage by filtering the data to remove the multiply sampled particle measurements if necessary,

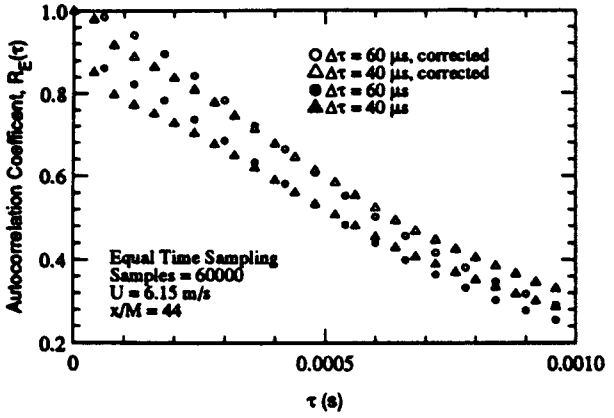

Figure 11. MRD bias in controlled sampling.

but it is recommended that processors be set in the single measurement per burst mode during any autocorrelation measurements.

Spiking caused by squaring of uncorrelated noise is unavoidable at low turbulence intensities, but every attempt should be made to reduce this effect as it is an indication of the signal to noise ratio of the system. As noise is a function data rate, a compromise must be struct between noise and resolution of the autocorrelation function. Often, however, lower noise with a slightly lower data rate allows for better resolution as the slot size chosen in the slotting technique may then be even less than that determined by the mean data rate due to the Poisson arrival statistics. In general it is better to achieve high data rate through higher laser power rather than greater photomultiplier gain and sacrificing data rate in order to count more fringes is a good trade-off at least up to 32 fringes.

Spiking effects that remain even after adjustment of system controls may be removed by backfitting a parabola from the second and third slots and renormalising against the new $t = 0$ autoproduct. This assumes that the slot size has been chosen sufficiently large so as to have stable correlation estimates in the slots near $t = 0$. This backfitting procedure corrects the variance measurement for noise effects and thus gives the correct turbulence intenties in the flow. Grid-generated turbulence results indicate that this procedure allows the LDV to make microscale estimates with precision equal to that of the hot-wire. Both instruments must, of course, sample quickly enough to resolve the smallest scales of the flow in order to obtain accurated microscale estimates.

REFERENCES

Absil, L. H. J., (1990), "Time and Spatial Correlation Measurements in the Turbulent Wake of a Circular Cylinder Using LDA," *Applied Sci. Res.*, 47, pp. 247-271.

Barnett, D. O. and Giel, T. V., (1976), "Application of a Two-component Bragg-diffracted Laser Velocimeter to Turbulence Measurements in a Subsonic Jet," AEDC TR-76-36.

Batchelor, G. K., (1953), *The Theory of Homogeneous Turbulence*, Cambridge University Press.

Benak, M., Sturm, M. Tropea, C. Nobach, H. Fuchs, W. and Mueller, E., (1993), "Correlation Estimators for Two-point Laser Doppler Anemometry," *SPIE vol. 2052: Laser Anemometry Advs. and Appls.*, pp.613-621.

Compte-Bellot, G. and Corrsin, S., (1971), "Simple Eulerian Time Correlation of Full and Narrow-band Velocity Signals in Grid-generated, 'Isotropic' Turbulence," *J. Fluid Mech.*, 48, pp. 273-337.

Edwards, R. V., ed., (1987), "Report of the Special Panel on Statistical Particle Bias Problems in Laser Anemometry," *J. Fluids Eng.*, 109, pp. 89-93.

Gad-el-Hak, M., and Corrsin, S., (1974) "Measurements of the Nearly Isotropic Turbulence Behind a Uniform Jet Grid," *J. Fluid Mech.*, 62, pp. 115-143.

Gould, R. D., Stevenson, W. H. and Thompson, H. D., (1989), "A Parametric Study of Statistical Velocity Bias," *AIAA Journal*, 27, pp. 1140-1142.

Gould. R. D., and Benedict, L. H., (1992), "A Comparison of Spatial Correlation and Autocorrelation Measurements in an Axisymmetric Sudden Expansion Flow Using LDV," *The 13th Sym. on Turb.*, Rolla, Missouri, Sept. 21-23.

Hinze, J. O., (1975), *Turbulence*, McGraw-Hill.

Lau, J. C., Morris, P. J. and Fisher, M. J., (1979), "Turbulence Measurements in Subsonic and Supersonic Jets Using a Laser Velocimeter," *J. Fluid Mech.*, 93, pp. 1-27.

Lau, J. C., (1980), " Laser Velocimeter Correlation Measurements in Subsonic and Supersonic Jets," *J. Sound and Vib.*, 70, pp. 85-101.

Lau, J. C., Whiffen, M. C., Fisher, M. J., and Smith, D. M., (1981) "A Note on Turbulence Measurements with a Laser Velocimenter," *J. Fluid Mech.*, 102, pp. 353-366.

Liu B. Y. H. and Lee, K. W., (1975), "An Aerosol Generator of High Stability," *Amer. Indus. Hygiene Assoc. J.*, 12, pp. 861-865.

Mayo, W. T., Shay, M. T. and Ritter, S., (1974), "The Development of New Digital Data Processing Techniques for Turbulence Measurements with Laser Velocimetry," AEDC-TR-74-53.

Meyers, J. F., (1988), "LDV Data Acquisition and Real Time Processing using a Microcomputer," *Proc. of the 4th Int'l Sym. on Appl. of Laser Anem. to Fluid Mech.*, Lisbon, Port., p. 7.20.

Scott, P. F., (1974), "Random Sampling Theory and its Application to Laser Velocimeter Turbulence Spectral Measurements," Report No. 74CRD216, Tech. Info. Series, General Electric Co., Corporate Res. and Devel.

Smith D. M., and Meadows, D. M., (1974), "Power Spectra from Random-Time Samples for Turbulence Measurements with a Laser Velocimeter," *Proc. II Inter. Workshop on Laser Velocimetry*, ed. H. D. Thompson and W. H. Stevenson, Purdue University, W. Lafayette, Indiana.

Wang, J. C. F., (1975), "Laser Velocimeter Turbulence Spectra Measurments," *Proc. Minnesota Sym on Laser Anem., Oct. 22-24, 1975, Univ. of Minn.*, pp. 538-567.

Session 26.
Particle ImageVelocimetry

MULTIPLE LIGHT SHEET PARTICLE HOLOGRAPHY FOR 3-D FLOW VELOCIMETRY

H. Hinrichs and K.D. Hinsch

FB 8 - Physik, Carl von Ossietzky University
Pf 25 03, D-26111 Oldenburg, Germany

1. INTRODUCTION

In recent years, the problems tackled by experimentalists and theoreticians in fluid dynamics have grown considerably. Sophisticated flow facilities like large size or high speed wind tunnels are the basis for ambitious experiments, and powerful computers allow modelling of very complex flow fields. Interest has turned to nonstationary flows, their spatial structures and their development in time. An ultimate aim is to measure and understand the evolution of turbulence.

The metrological tools for the experimental study of flow fields have also seen an impressive improvement. Optical probing of the flow through tracer particles has been preferred because it allows noncontact remote measurements with high spatial resolution. It relies, however, on the presence of small particles in the flow and assumes, that the particle motion faithfully resembles the fluid motion. In gaseous flows this requires very small particles and sets limits to the largest velocity gradients acceptable.

Fluid velocity, the characteristic parameter of the flow, is a three-dimensional quantity and many flow configurations of interest are of three-dimensional nature. Especially the structural character of a flow, a topic of current interest, is only revealed by its spatial features. When the flows are very voluminous or measuring time is expensive, the effort or the cost to scan the flow with a single point probe are enormous and may be even prohibitive. Even more, when the flows are nonstationary there is no time to move a single point probe through the flow field.

In view of these problems, much recent effort has been dedicated to the development of flow velocimetry in several dimensions. Particle image velocimetry (PIV) is presently the most successful technique for quantitative whole-field flow velocimetry (Hinsch (1993a)). It relies on the double exposure high-speed recording of tracer particles and provides the simultaneous registration of the in-plane velocity components within a plane from the flow volume. The field of observation is selected by the placement of the illuminating light sheet. Usually the particle pair separation is evaluated by processing small interrogation areas. Photographic and video techniques contend for the recording, digital and optical methods for the processing.

Strictly speaking, PIV is not a whole-field technique because velocity is measured at locations in a single plane only and without the depth component. The study of complex and nonstationary flows calls for extensions in all dimensions. Two basic approaches are pursued presently:

- Conventional imaging with more than one camera from different directions. This includes stereoscopic recording of a light sheet as well as video imaging of a large field with several cameras. Depth of focus is a limiting factor in these methods.
- Holographic recording of a deep volume. This solves the focus problem and allows almost unlimited depth of field. Thus, for true three-dimensional studies holography is the method of choice. The reconstructed particle fields can be processed by conventional techniques, stereoscopically, for example.

Holographic records cannot be evaluated by the reliable interrogation schemes developed for PIV. Often, costly three-dimensional particle tracking must be employed. We have therefore developed a concept that preserves favourable properties of ordinary PIV while offering the extension into the third dimension. Yet, the method is restricted in its application to moderately three-dimensional flows because the flow is still sampled by light sheets. For a deep-volume study the system features are:

- The light sheet is retained to establish the region of investigation.
- The deep volume is covered by a hologram of several light sheets at proper spacings in depth.
- Optimum use is made of the illuminating light by

multiple pass through the volume.
- Crosstalk between light sheets can be avoided by coherence adjustments in the holographic recording.
- Light sheets are evaluated one by one by the well-known methods of interrogating a PIV transparency.

2. HOLOGRAPHIC VELOCIMETRY OF PARTICLE FIELDS

2.1. The Principle of Holographic Particle Recording

Holography is the only method for true imaging of three-dimensional space. All particles of interest in the flow are illuminated with a properly taylored laser light wave. In a commonly employed configuration (Fig. 1), the complex light field scattered by the particles is stored by superposing a reference wave from the same laser source and recording the interference pattern on a photographic plate. Due to the oblique angle between reference wave and object light this is called off-axis holography. The coherence length of the laser must be adequate to guarantee interference over all path length differences encountered. The developed pattern (the hologram) is used to reconstruct an image of the object. For this purpose the hologram is illuminated with the original reference wave that reconstructs a virtual image of the particle field. When looking or photographing through the hologram the particle configuration can be seen as it was during the recording of the hologram.

A very useful feature of holography is that also a real image of an object can be obtained without the need for a lens system. For this purpose, the hologram must be illuminated with the complex conjugate of the reference wave. For a divergent spherical reference wave this is a convergent wave from the opposite direction. In this case the hologram produces backward travelling object waves that form a real image of the light sheet. With a CCD-array, for example, a plane anywhere through the field could be examined for particles. If aberrating media like windows or low quality lenses have distorted the object wave on its way to the holographic recording plate, these distortions can be compensated during the backward path of the conjugate wave provided the distorting media are still in the old position.

It should be mentioned that holographic particle imaging in the off-axis configuration provides a solution of the ambiguity problem in double pulse particle velocimetry. When operated with a separate reference beam for each of the pulses the first and second image have been distinguished by Coupland (1987) for removing the directional ambiguity that is inherent in simple double pulse recordings. Hussain (1993) and Adrian (1993) have used a dual pulsed Nd:YAG laser system, for example, to supply suitable pulses that are aligned to travel identical object illumination paths but different reference paths. Upon reconstruction, first and second exposure can be viewed separately.

Off-axis holography is easily disturbed by vibrational noise, requires good coherence, and relies on an accurate reproduction of the reference wave for reconstruction. For small objects like the flow tracing particles, the so-called in-line arrangement is much simpler and provides better stability (Meng (1993)). In this case there is no extra reference wave, because the tiny particles leave enough of the illuminating plane wave light undisturbed so that it can serve as reference light. In-line holography relaxes many of the restrictions mentioned for off-axis holography and its application in particle studies has a long history (see, for example, Thompson (1989) and Vikram (1990)).

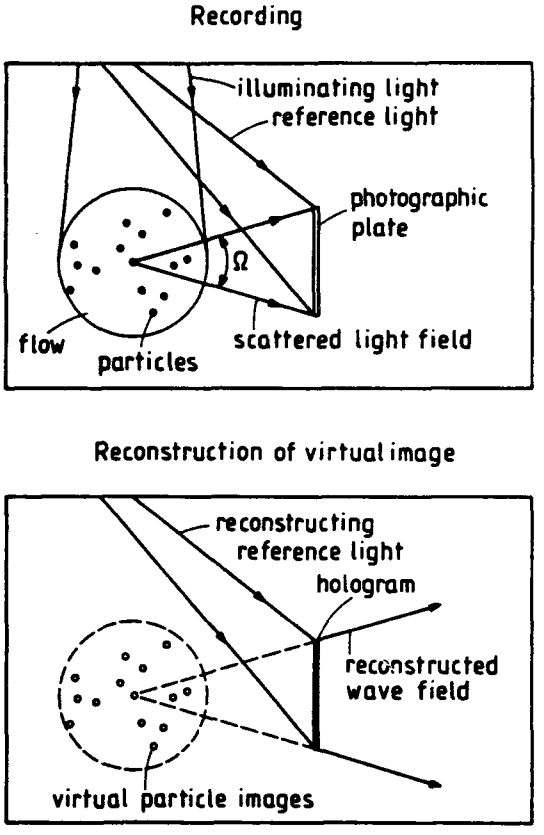

Fig. 1: Holography of a deep flow volume

2.2. Resolution in Holographic Particle Recording

Particle velocimetry calls for small and high quality particle images. Basically, the resolution in optical imaging is limited by diffraction and is

determined by the angular spread Ω of the light that contributes to image formation. Omitting nonessential numerical factors, we obtain for the transversal resolution length (λ being the wavelength of light)

$$d_t \approx \lambda / \Omega \qquad (1)$$

and for the longitudinal resolution length

$$d_l \approx \lambda / \Omega^2 \qquad (2)$$

When a particle is smaller in size than the resolution length it will not be resolved in the image, when it is larger its geometrical image has to be convolved with a point spread function whose width is given by the resolution length.

Generally, in holography the angular spread is limited by the size of the holographic plate and its distance from the particle. This assumes that the particle scatters evenly over the range occupied by the plate. For the commonly used particle sizes (diameter d_p), this is the case for a large angle between illumination and observation direction (as for the 90^0 viewing in PIV). In the in-line arrangement, however, the pronounced contribution from forward scattered light is essential. The intensity in this angular region exceeds the average intensity in other directions by several orders of magnitude. It is concentrated in the central lobe of the diffraction pattern of the particle which is given approximately by $\Omega = \lambda / d_p$. Thus

$$d_t \approx d_p \qquad (3)$$

$$d_l \approx d_p^2 / \lambda \qquad (4)$$

In many practical cases where d_p is considerably larger than λ longitudinal focusing will be much lower than transverse focusing.

Various proposals have been made to improve the resolution in in-line holography: an auxiliary illumination beam has been introduced by Royer (1977) to enhance the scattered object light or two traditional in-line setups at right angles have been combined by Hussain (1993) or Bernal (1993). In another approach multibeam illumination was introduced by Hussain (1993) to increase the aperture by recording several scattered fields, each of extent Ω, on the same hologram. Thus highly effective forward scattering is combined with good axial focusing by a large aperture. Such setups, however, get rather complicated so that a great advantage of in-line holography is sacrificed. These considerations and the beneficial features mentioned earlier place a large bonus on off-axis holography for particle velocimetry. Despite the disadvantage that the overall intensity of the scattered light is much lower for sidewise observation we have therefore made off-axis holography our method of choice.

2.3. Noise in Holographic Particle Recording

The application of holographic particle velocimetry to a volume of large depth introduces a new problem. When the positions or displacements of a pair of particles must be evaluated from a reconstructed image (real or virtual) the light from additional particle images produces a disturbing noise background. This is especially pronounced in in-line holography, where light from both the virtual and real image overlaps and in addition is disturbed by the unused portion of the reconstructing wave. Off-axis holography deserves another credit in this respect, as the various wave components propagate in different directions. The contributions from out-of-focus particles, however, cannot be eliminated when a deep volume is illuminated as a whole. Here, the light sheet concept of PIV is superior, because only the particles of interest are illuminated.

For a simple evaluation of an ordinary deep-volume holographic recording the virtual image of the particle field can be photographed by focusing on different planes in depth, one after the other. When the planes are oriented parallel to the dominant flow direction these records provide the basis for interrogation as in PIV. In this case, what is the degradation due to the many out-of-focus particles?

We have carried out an analysis that is based on a numerical simulation of the image plane superposition of more or less focused images from particles that are distributed within a volume of given depth. A single plane is well in focus, the rest of the volume is sampled in depth by a series of other planes at equal 1mm intervals. All particles are assumed to scatter the same energy that is spread evenly over a disk-shaped image. Within the depth of focus, the size of the image is given by the diffraction limit (16 µm in the present case, set by the F-number of 8 of the imaging optics), outside by the appropriate geometric growth determined by the 4^0 cone of light limited by the aperture. Particle positions are placed at random, the average number per 1 mm^2 interrogation area of 1 mm depth equals 15. This has been found by Keane (1990) to be a proper choice for reliable evaluation. Particle pair separation in the focus plane was chosen to be 160 µm, the minimum value for good performance. For each out-of-focus plane magnitude and direction of the displacement was varied randomly up to a maximum displacement of 500 µm.

This represents a flow situation of practical interest where the velocity changes accordingly within the volume under investigation.

It must be mentioned that in the photography of particles from a holographically reconstructed double exposure image field, the contributions from first and second exposure particles add up coherently. This differs from a directly obtained double exposure record, where they are superimposed one after the other and thus are summed incoherently. In sheet oriented PIV with low particle density this difference is of no importance because hardly any particle images overlap. In our case, however, the out-of-focus images of considerable size offer many possibilities for interference. Thus, in our simulation we attributed a random phase to each particle image. The constant phase approximation within a particle image is justified in the present geometry because the cone of light is restricted to less than the first Fresnel zone.

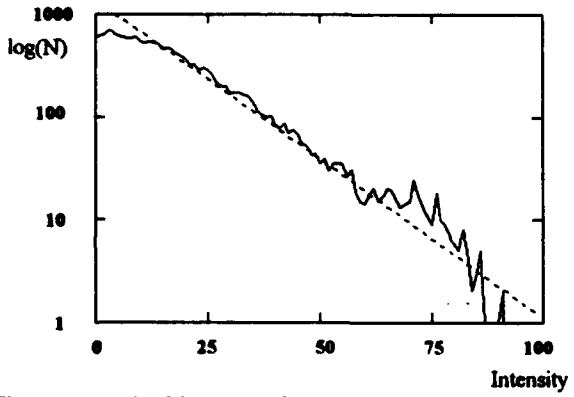

Fig. 2: Intensity histogram for 60 mm volume

The image intensity calculated from this model environment was processed like a common PIV record. We calculated the power spectrum by a Fourier transformation, applied a zero order blocking filter and obtained the autocorrelation function from a second Fourier transformation. Finally, a search for the highest peak was to yield the particle displacement in the plane in focus. The value thus obtained was compared with the input displacement. An experiment was rated successful when both the values agreed.

With growing depth of the volume the image plane intensity showed an increasing amount of noise that deteriorated the in-focus images and spoiled the corresponding double structure. The intensity distribution gradually assumed speckle character which was proven by calculating the probability density function of the intensity. For a 60 mm deep volume Fig. 2 demonstrates the negative exponential dependence.

Accordingly, the autocorrelation peaks for the in-focus displacement gradually were buried in noise.

Light sheet of 1mm thickness:

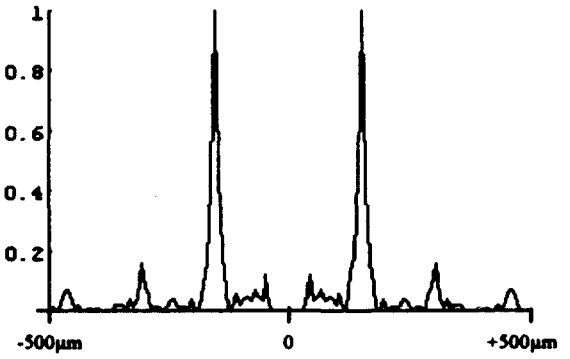

Volume of 10 mm depth:

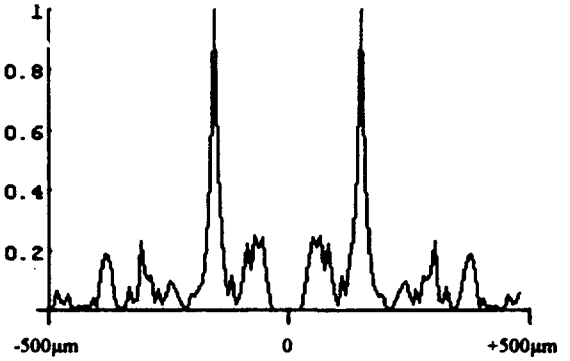

Fig. 3: Scans through autocorrelation functions (center is blocked)

This development is shown by Fig. 3 where we have plotted scans through the autocorrelation function along the direction of the displacement. A single plane particle field is compared with a volume of one centimeter depth (10 layers of model particles). The shown examples are from the outcomes that could be evaluated correctly.

depth [mm]	failed evaluations (of 100)	confidence interval [%]
1	4	[0,7]
10	14	[7,20]
20	56	[45,66]
40	72	[63,80]
80	96	[95,100]

Table 1: Results of simulation

The results of the experiments are summarized in Table 1. 100 realizations were calculated for each depth of volume and the number of erroneous evaluations determined. Furthermore, the 95% confidence interval

THIS PAGE IS MISSING IN ORIGINAL DOCUMENT

26.2.5 and 26.2.6

mm downstream from the cylinder was observed. Holograms were made on Agfa Gevaert HOLOTEST 10E75 plates.

Virtual images of the double exposure particle fields were reconstructed from the hologram. To avoid distortions by a wavelength change, ruby laser pulses were also used for reconstruction, not changing the optical setup. Particle images were photographed with an 85-mm lens at F-number 4 and magnification 0.33. Identical magnification in both light sheets was guaranteed by translating the camera for optimum focus without changing its setting. For further processing, positive contact transparencies were made of the original photographs. Quantitative velocity data were obtained by automatic processing of the transparencies in a combination of Young's fringe generation and digital computation of the autocorrelation function. In the final plot the mean velocity is subtracted to emphasize the structures in the flow.

Velocity vector plots of both the light sheets are shown in Fig. 6. The cylinder is positioned 55 mm upstream to the right and halfway up the frame. The vortex street is evident in both the planes. A clearly visible spatial shift in the periodic structure is evidence of the oblique vortex shedding. It amounts to about 9 mm which yields an angle of about 13°

3. CONCLUSIONS

Our analysis has shown that moderately three-dimensional flows can be sampled successfully by the holographic recording of a set of light sheets. First of all this method makes best use of the available light when a sheet is redirected through the flow repeatedly. Furthermore, a study of signal-to-noise conditions has shown that this is superior to the extraction of a single plane from a deep-volume holographic recording. We have also analyzed the noise produced by out-of-focus particles in the multiple light sheet concept and estimated the improvement that can be gained if individual light sheets can be reconstructed separately from the holographic record. For densely sampled volumes the reliability of the evaluation can thus be raised by our light sheet holography with controlled coherence. Since this requires more effort in the optical setup, such an estimate can guide in system decisions.

REFERENCES

Adrian, R.J. et al. (1993), An HPIV system for turbulence research, in: Holographic Particle Image Velocimetry, E.P. Rood, ed., ASME FED 148, 21.

Bernal, L.P. and Scherer, J. (1993), HPIV measurements in vortical flows, in: Holographic Particle Image Velocimetry, E.P. Rood, ed., ASME FED 148, 43.

Coupland, J.M. et al. (1987), Particle image velocimetry: Theory of directional ambiguity removal using holographic image separation, Appl. Opt. 26, 1576.

Hinsch, K.D. et al. (1993), Holographic and stereoscopic advances in 3-D PIV, in: Holographic Particle Image Velocimetry, E.P. Rood, ed., ASME FED 148, 33.

Hinsch, K.D. (1993a), Particle Image Velocimetry, in: Speckle Metrology, R.S. Sirohi, ed., Marcel Dekker, New York.

Hussain, F. et al. (1993), Holographic particle velocimetry: prospects and limitations, in: Holographic Particle Image Velocimetry, E.P. Rood, ed., ASME FED 148, 1.

Keane, R.D. and Adrian, R.J. (1990), Optimization of particle image velocimeters. Part I. Double pulsed systems, Meas. Sci. Technol. 1, 1202.

Meng, H. et al. (1993), Intrinsic speckle noise in in-line particle holography, J. Opt. Soc. Am. A 10, 2046.

Royer, H. (1977), Holographic velocimetry of submicron particles, Opt. Commun. 20, 73.

Thompson, B.J. (1989), Holographic methods for particle size and velocity measurement - recent advances, in: Holographic Optics II: Principles and Applications, G.M. Morris, ed., Proc. SPIE 1136, 308.

Vikram, C.S. (1990), "Holographic Particle Diagnostics," SPIE Milestone Series, Bellingham.

AN IN-LINE STEREOSCOPIC, COLOUR PIV SYSTEM FOR 3-COMPONENT VELOCITY MEASUREMENTS WITH AMBIGUITY RESOLUTION.

I Grant , S Fu, X Pan, X Wang and A Aroussi*,
Fluid Loading and Instrumentation Centre,
Heriot-Watt University , Edinburgh, UK EH14 4AS.
***Department of Mechanical Engineering,**
Nottingham University.

ABSTRACT.

The paper reviews developments in 3-component sheet and volume velocimetry. An in-line stereo viewing system for PIV is presented and demonstrated in hydraulic and aerodynamic experiments. The colour coding is used to determine directionality.

INTRODUCTION.

There is currently great interest in three component pulsed laser sheet velocimeter (PLV) systems. The authors have previously published studies where both holographic and stereoscopic principles have been demonstrated to be possible scenarios for such a system (Grant et al (1991)). The experimental difficulties and analysis complexity has so far hindered the general acceptance of any universal scheme for three component measurements.

The present paper reviews these methods and presents an approach using two in-line cameras to provide an improved stereoscopic viewing system. The geometry of the technique is discussed and developed into a form which was used for investigating a three dimensional flow. Mathematical transformations are summarised which allow the two images to be reconciled and the data reliably assembled into a three dimensional image.

The visual fusion of the two images is described and the procedure shown to follow a hierarchical scheme. This used spatial cross correlation of corresponding regions in the two views to obtain a coarse alignment. This allowed both the distribution and the order of occurrence of the particle images to be taken into account. Following the coarse matching, where position and destination were considered, individual particle image groups were matched in the two views and the appropriate velocities obtained.

The arrangement has higher resolution away from the optical axis. This feature can be used in reconciling the two views since the limiting case along the optical axis gives overlapping images thus establishing a reference direction or point in each view.

In order to demonstrate the use of the technique for velocity measurement, two experimental studies were conducted.

The first experiment was conducted in a wind tunnel where the mean flow passed through a lights sheet inclined to the flow. This provided a standard through sheet velocity which could be used for method validation.

The second experiment was in a water tank in which vortex motion had been generated by stirring along the vertical main axis. The orientation of the light sheet was vertical so that substantial through-sheet flow was present. In order to measure the through sheet velocity the sheet was thickened. The possibility of directional ambiguity was eliminated by using a colour coded illumination scheme. The flashes and the two camera shutters were synchronised and controlled by a PC. The cameras used colour transparency film.

1. REVIEW

The significant advances in two component Particle Image Velocimetry (PIV) made in the last decade (Grant (1994)) have recently encouraged interest in three component velocimetry where a thickened illumination sheet allows the measurement of the out-of-plane component. The established two component PIV technique suffers from and inherent parallax error which gives an apparent in-plane motion due to through-plane motion at points away from the optical axis of viewing (Laurenco (1986)). The three component development studies may be conveniently classified into holographic and stereoscopic viewing methodologies.

The accurate calibration of the relationship between object and images in stereogrammetry is still the subject of general discussion. Murai (1980) and Kent and Eaton (1982) examined the effect of camera position and lens distortion on the object-image relationship. The efficient application of stereogrammetry methods to PIV, the subject of this paper, was first considered more than a decade ago (see for example Utami et al (1984), Chang et al (1984).

Adamczyk and Rimai (1988) used electronic mixing of the output of two video cameras to store the two views on a single frame. Sinha (1988) demonstrated the relative inaccuracy of the out-of-plane measurements compared with the in-plane measurements. More recent development studies in the application of the method are reported by Grant et al (1991) who used a single camera, split screen arrangement and compared the performance of in-line holography. Trigui et al (1992) considered the digital interpretation of the digital images obtained in three component velocimetry studies.

Other recent variants for three component measurement

include the work of Thompson (1989) who demonstrated the great potential of holography for simultaneous particle size and motion measurement. Cenedese and Paglialunga (1988) used parallel light sheets of different colour to obtain a colour coding from which a depth co-ordinate could be obtained. Willert and Gharib (1992) used a single camera and utilised the degree of defocusing as a means of obtaining depth. They resolved the ambiguity relative to the focal plane using an aperture coding method.

Key problems in stereogrammetry considered by the aforementioned authors have been loss of accuracy in the third (out-of-plane) component, accurate specification of camera and object position and unambiguous registration of the two views. The registration of the two views refers to the unambiguous matching of the two stereo images, usually using feature points as a key. Classical stereogrammetry studies have mostly considered solid objects where reference features, such as edges or apexes, are easily located. In PIV the particle images are frequently considered as being randomly distributed in space in a Poisson fashion.

Investigations which used image groups as registration features rather than individual particle images have been reported. This approach, essentially one of image segmentation and cross correlation, though meeting with some success is computationally intense and does not resolve one of the basic limitations of lateral viewing stereogrammetry, namely loss of resolution in the out-of-plane component (Figure 1).

The procedure adopted in this study was image capture from two in-line cameras, in one of two possible configurations, followed by identification of corresponding regions in the two views where registration features could be identified.

The precise matching of equivalent particle images in the two views is necessary, but not sufficient, to establish the three velocity components. The velocities can only be determined when the relative positions of the cameras and the laser sheet are known. In the present experiments *in situ* calibration was achieved by placing a standard optical calibration grid in the laser sheet and recording its images on the two cameras at one depth positions.

2. THE IN-LINE STEREOSCOPIC PIV SYSTEM GEOMETRY.

Two possible configurations are discussed for the in-line imaging system. These are (i) with the cameras on the same side of the flow and (ii) with the cameras on opposite sides of the flow.

2.1 The Camera Imaging System.

The image formation is discussed here using Gaussian lens formulae. The use of the Gaussian model allowed an accurate description of the image formation process (Figure 2). A single lens was used to represent each camera imaging system with O being the lens centre. O was taken as the origin of a world co-ordinate system with the Z axis co-incident with the lens principal optical axis and X'-O-Y' representing the image plane of the camera. On this plane, the image of the object point P(X, Y, Z) is found on the inverted image at p (x', y'). For simplicity in the geometrical argument we use the pseudo image plane X_a-O_a-Y_a which, as seen from the figure, is placed at the same distance as the image plane from the camera on the opposite side of the lens. The pseudo image plane has an erect image (non-inverted) of the same dimensions as the equivalent image on the camera back focal plane. In the following discussion the "image plane" refers to X_a-O_a-Y_a.

The focal length of the camera lens is f, the image distance (to the pseudo image plane) is $I_a = OO_a$ and the distance from the lens centre to the object point is Z. The Gaussian lens formulae gives

$$\frac{1}{f} = \frac{1}{I_a} + \frac{1}{Z}$$

$$m = \frac{I_a}{Z} = \frac{I_a - f}{I_a} = \frac{f}{Z - f} \qquad \cdots\cdots\cdots(1)$$

and

$$x = mX, \qquad y = mY$$

or r=mR, in a cylindrical co-ordinate system, where R is the radial co-ordinate of the object point and r is the radial co-ordinate of the image point (Figure 2). So

$$r = \sqrt{x^2 + y^2} \quad \textit{and} \quad R = \sqrt{X^2 + Y^2}$$

with m being the magnification between the image plane and the object plane.

2.2 The Geometry of the In-Line Stereo System, Both Cameras on Same Side of Flow.

The experimental realisation of this concept is discussed below in the description of the wind tunnel tests and used a beam splitter to avoid view obstruction between the two cameras.

Figure 3 shows the geometry of the in-line, stereo, viewing optics arranged so that both cameras are on the same side of the region of flow (sheet) to be observed. The camera centres are located at F_a and F_b, on the optical axis. F_a and F_b are separated by distance d. The centres of the two pseudo image planes at O_A and O_B are taken as the centres of two plane Cartesian co-ordinate systems. The object or real-world co-ordinate system is cylindrical with the origin at F_a and the Z-axis co-incident with common optical axis of the two cameras. The relationships between the real-world point P(R, α, Z) and its images on the two pseudo-image planes are

$$\begin{cases} \dfrac{r_a}{I_a} = \dfrac{R}{Z + d} \\ \dfrac{r_b}{I_b} = \dfrac{R}{Z} \\ \alpha_1 = \alpha_2 = \alpha \end{cases} \qquad \cdots\cdots\cdots(2)$$

where I_a=F_a· O_a and I_b=F_b· O_b with I_a and I_b being the image distances from the respective virtual image planes to the corresponding cameras. Equations (2) show that for this configuration the nearer camera, camera A, always has the smaller magnification. The images on the two planes and the

object point always fall on the same azimuthal angle.

Rearranging the equations (2) gives the important result

$$Z = \frac{r_a \cdot l_b}{r_b \cdot l_a - r_a \cdot l_b} \cdot d \qquad \cdots\cdots(3)$$

and

$$R = \frac{r_a}{l_a} \cdot (Z + d) \quad or \quad R = \frac{r_b}{l_b} \cdot Z \qquad \cdots\cdots(4)$$

This shows that the magnification changes with object distance from the appropriate image plane.

2.3 The Geometry of the In-Line Stereo System, Cameras on Different Sides of Flow.

Figure 4 shows the geometry of the in-line, stereo, viewing optics arranged so that the two cameras are on the either side of the flow sheet to be observed with their principal optic axis co-incident with each other and the normal to the light sheet. The experimental realisation of this concept is discussed below in the description of the water tank tests.

Referring to Figure 4 the cameras are placed on either side of the light sheet . The plane equidistant from the two cameras, XOY, is termed the reference plane. The object point in this light sheet, P(R, α, Z) is observed at (r_a, a_a) and (r_b, a_b) on the image planes of the two cameras respectively. The relationship between the co-ordinates in the world (reference) plane and the local co-ordinates in the two observational planes are given by

$$\begin{cases} \dfrac{r_a}{l_a} = \dfrac{R}{L+Z} \\ \dfrac{r_b}{l_b} = \dfrac{R}{L-Z} \\ \alpha_a = \alpha_b = \alpha \end{cases} \qquad \cdots\cdots(5)$$

where $2 \cdot L = F_A F_B$ and

$$Z = \frac{r_b \cdot l_a - r_a \cdot l_b}{r_a \cdot l_b + r_b \cdot l_a} \cdot L \qquad \cdots\cdots(6)$$

In an idea case the image distances and object distances would be the same with $l_a = l_b$. In this case there is no simple constant relationship between the magnifications of the two cameras.

2.4 Calibration of the System.

As seen above, in equations (3) and (4), the image distance and the displacement between the two cameras are required in order to interpret any two stereo views of flow seed particle position. In order to obtain these parameters a standard optical calibration grid was placed at the centre of the light sheet and recorded by the two cameras. The magnification of the two images of the grid is governed by equation (1). Consequently.

$$L_a = \frac{f(1+m_a)}{m_a}, \quad l_a = f \cdot (1+m_a)$$

$$L_b = \frac{f(1+m_b)}{m_b}, \quad l_b = f \cdot (1+m_b)$$

where L_a is the distance from the centre of lens a to the object, L_b is the distance from the centre of lens b to the object and d = L_a - L_b.

Once the calibration has been completed the magnification of the two cameras can be obtained and from this , knowing the focal length of the cameras the distances I and L are obtained. The position and focus of the cameras remains fixed, the flow is started and images captured without disturbing the optics. The three dimensional object space is covered by the depth of field of the cameras.

3. CORRESPONDENCE MATCHING.

As indicated in the introduction, the matching of features between the two stereo images is an essential feature in stereogrammetry. In the present case a hierarchical methodology was used. Firstly the image groups on the individual planes were matched using the statistical PTV approach of Grant and Liu (1989).

The next stage was the correspondence matching between image groups on the two planes. An image group was selected *on one of the planes, A say, then the radial co-ordinate of the* image group, r_a, was measured. The corresponding radius in plane B is then r_b where

$$r_b - r_a = R\left\{\frac{l_b}{Z} - \frac{l_a}{Z+d}\right\} = \frac{r_a}{l_a} \cdot \left\{l_b \cdot (1 + \frac{d}{Z}) - l_a\right\} \quad \cdots(7)$$

In order for this relationship to be used it is necessary to know the depth co-ordinate of the object particle. Since depth co-ordinate is unknown it is only possible to define the extreme values of r_b which define, quantitatively, the radial window search limits on plane A within which the corresponding image will be found. The limits are determined by considering the extremes cases where the object particle was at either edge of the light sheet, thickness 2h.

This gave the limiting values of Z as $Z_{max} = L_b + h$ and $Z_{min} = L_b - h$. Substituting them in equation 7 gives the radial limits of r_b for the search window.

In the case where the observation points are on either side of the illuminated plane

$$r_b - r_a = R\left\{\frac{l_b}{L-Z} - \frac{l_a}{L+Z}\right\} = \frac{r_a}{l_a} \cdot \left\{l_b \cdot \frac{L+Z}{L-Z} - l_a\right\} \quad \cdots(8)$$

gives the relationship between the radial distances on the two planes. The limiting cases for depth parameter, Z, in this case are

$Z_{max} = L_a - L + h$ and $Z_{min} = L_a - L - h$. Substituting them in equation 8 gives the limits of r_b-r_a for the search window.

The angular limits for the search window were chosen, after some empirical iteration, to be

$$\pm\frac{\theta}{2} \quad where \quad \theta = \frac{\Theta}{\ln r_2}$$

The use of the ln function ensured that the search angle increased quickly at small r values to a stable value at large R.

Any ambiguities in pairing which occurred at this coarse matching were resolved by choosing the candidate pairs on the second plane which were nearest to the original pair.

4. EXPERIMENTAL DESCRIPTION.

4.1 The Wind Tunnel Experiment.

The tests were conducted in the Fluid Loading and Instrumentation Centre closed return wind tunnel at Heriot- Watt University. The authors are involved in aerodynamic studies of wind turbine and helicopter rotors where there is an interest both in wake dynamics and in blade vortex interaction. For a detailed description of the experiments see Horner et al (1993) Grant et al (1993).

A Yag laser was located on the wind tunnel roof with the beam being projected down into the working section. Sheet forming optics were used to diverge the beam to a thickness of approximately 10mm.

The cameras were mounted together on a frame on the same side laser sheet. A beam splitter was mounted on the frame to allow the cameras to be placed with their axis orthogonal to each other to avoid interference effects . A HeNe laser was used to define the optical axis of the cameras and allow accurate alignment. Figure 5 is a sketch of the top view of the experimental arrangement.

In order to provide a standard flow whose properties were known the laser beam was arranged so that it was vertical and at 45° to the mean flow. The axis of the camera observation system remained at right angles to the laser sheet. This has the effect of introducing a steady cross sheet flow of known magnitude.

Seeding particles were introduced to the tunnel downstream of the working section , causing no disturbance to the flow measurement volume. This was a clear advantage of a recirculating tunnel. After some use the tunnel accumulated enough seeding to seed the flow automatically. Seeding particles of polycrystalline form, with a volume average of about 30 microns, were used. These particles were found to have high scattering efficiencies.

Figure 6 shows examples of the images from the two viewpoints (cameras) superimposed prior to processing. When the data from the two views is collected for analysis the composite image, when correctly aligned, takes on a radial appearance. This is because, with the cameras on the same side of the experiment, the images points and the corresponding object point always have the same azimuthal angle.

4.2 The Water Tank Experiment.

In this case the two cameras were fixed on opposite sides of a glass sided tank, as shown in Figure 7. The experiment was concerned with local swirling flow measurements in the presence of temperature gradients with applications in energy processes.

In order to eliminate directional ambiguity two white-light, flash guns were synchronised and covered with red and green filters respectively. The slow speeds involved in this experiment, meant that the pulse duration of the flash guns was short enough to obtain a clear image. The images were recorded on colour slide film for analysis. The coloured negatives were examined under white light illumination with preferential red filtering in order to provide an input to the monochrome image processing system which would still carry time signature information. The effect of the filtering was to produce different intensities and sizes in the image partners. At this stage preliminary partner grouping was achieved using methods developed by the author elsewhere Grant and Liu (1990).

A typical stereo image segment pair is shown in Figure 8.

5. THREE DIMENSIONAL DISPLAY.

It is possible to display the three dimensional velocity vectors in a perspective or in an isometric view. The isometric view, when projected onto the surfaces of a notional reference cube containing the data, gave an accurate (measurable) presentation of the velocity components in pairs. The perspective views gave an impression of the three dimensional appearance of the flow.

By animating the perspective views, the image may be cyclically oscillated or rocked through an angle of, say, 90^0, giving a clear three dimension impression. This is because the oscillation provides stereo cues to the observer. This type of cuing is an action unconsciously performed when gauging depth information in the real world. Simulating this action in the graphic display is correspondingly effective and informative in the interpretation of data in the present case.

Examples of wind tunnel data inside a reference cube and presented in a perspective view are seen in Figure 9. Figure 10 shows the data viewed isometrically along the normals to the three cube faces, effectively giving planar projections of the data along the three co-ordinate axis. Figures 11 and 12 give the same data displays for the water tank data.

6. DISCUSSION AND CONCLUSIONS.

A stereoscopic viewing system for three dimensional particle image velocimetry studies has been described. The system uses an in-line viewing configuration which makes the calibration and correspondence matching, implicit and important in strereogrammetry, more reliable and straightforward. The camera set-up procedure, using a low powered laser beam, allows the position of the film planes of the two cameras to be optimised prior to the commencement of the experiment. Calibration of the cameras takes place, *in situ* , using an optical grid in the observation plane. The transformation equations are demonstrated in the present paper to show that the accuracy of the in-depth component measurement increases with distance from the (co-incident) principal optical axis of the cameras.

The method is illustrated by its application to wind tunnel and water tank tests. In all cases where transparent walls are

used to contain the flow, the further advantage of viewing at normal incidence is implicit in the present method.

REFERENCES.

Adamczyd, A and Rimai, L : 1988, 2-dimensional particle tracking velocimetry: technique and image processing algorithms. Exp Fluids. 6: 373-80. *

Cenedese, A and Paglialunga, A: 1988, A new technique for the determination of the third velocity component with PIV, Experiments in Fluids 8, 228-230. *

Chang, T P, Wilcox, N A and Patterson, G: 1984,Application of image processing to the analysis of three-dimensional flow fields. Opt Eng 23(3) : 283-87. *

Grant I (Editor): May 1994, Selected Papers in PIV, SPIE Milestone Volume on Particle Image Velocimetry.

Grant I, Smith G H, Infield D G, Zhao Y , Fu S, Owens E , Reinbold P : 1993, Laboratory and field experiences in the application of particle image velocimetry to wind turbines; Paper 2005-46, Proc Optical Diagnostics in Fluid and Thermal Flow, SPIE Tech Conf 2005, San Diego.

Grant, I and Liu, A: 1989, Method for the Efficient Incoherent Analysis of Particle Image Velocimetry Images", Applied Optics, 28, 10. *

Grant I and Liu, A : 1990, Directional ambiguity resolution in particle image velocimetry by pulse tagging, Experiments in Fluids 10, 71-76. *

Grant, I, Zhao, Y, Tan, Yand Stewart, J N: 1991 Three component flow mapping: experiments in Stereoscopic PIV and holographic velocimetry", Fourth International Conf on Laser Anemometry, Advances and Applications, Cleveland, Ohio, 5 - 9. *

Horner M, Stewart J N, Galbraith R A McD, Grant, I , Coton F N, Smith G H: 1993, Preliminary results from a particle image velocimetry study of blade-vortex interaction, Proc 19th European Rotorcraft Forum and 11th EHA, Como, Italy, September 14-16.

Kent, J C and Eaton, A R: 1982, Stereo photography of neutral density He-filled bubbles for 3-D fluid motion studies in an engine cylinder. Appl Optics. 21(5) : 904-12. *

Laurenco, L M and Wiffen, M C:1986, Laser speckle methods in fluid dynamics applications. In Laser anemometry in fluid mechanics-II. Editors R Adrian et al, pp 51-68. Lisbon. publishers Ladoan-IST, Lisbon.

Murai, S, Nakamura, H and Suzaki, Y: 1980, Analytical orientation for non-metric camera in the application to terrestrial photogrammetry. Int Arch Photogramm 23: 516-25. *

Sinha, S K: 1988Improving the accuracy and resolution of particle image or laser speckle velocimetry. Exp Fluids 6: 67-68. *

Thompson, B J: 1989, Holographic methods for particle size and velocity measurement-recent advances, Proc SPIE, 1136, 308-326. *

Trigui, N, Guezennec, Y and Brodkey, R: 1992, Algorithms for fully automatic, three-dimensional particle image velocimetry. Experiments in Fluids. *

Utami, T and Ueno, T : 1984, Visualisation and picture processing of turbulent flow. Exp Fluids. 2: 25-32. *

Willert, C E and Gharib, M: 1992, Three-dimensional particle imaging with a single camera. Experiments in Fluids 12, 353-358 . *

Those publications marked with a '*' are reprinted in "Selected Papers in PIV",, SPIE Milestone Volume on Particle Image Velocimetry, Editor I Grant, 1994..

FIGURES.

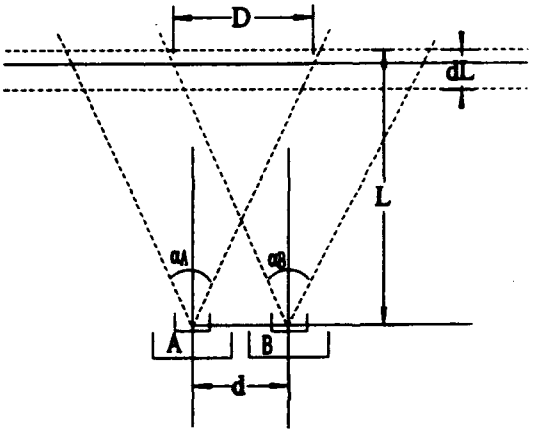

Figure 1. The Optical Arrangement for Parallel Lateral Stereogrammmetry

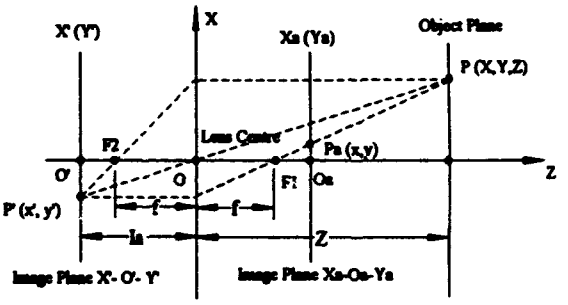

Figure 2. The Gaussian Representation of an Imaging System

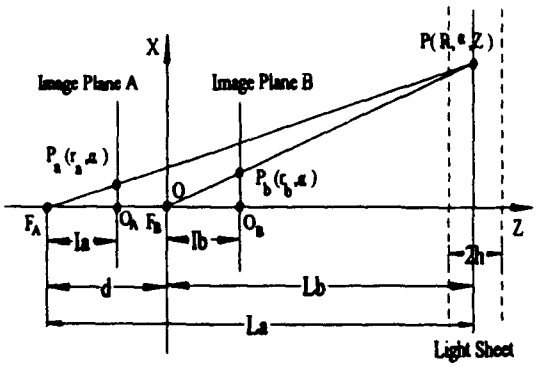

Figure 3. The Geometry of the In-Line Stereoscopic Viewing System, Cameras on the Same Side of the Flow

Figure 6. Flow Images obtained from the Stereo Viewing System Shown in Figure 5 (Wind Tunnel)

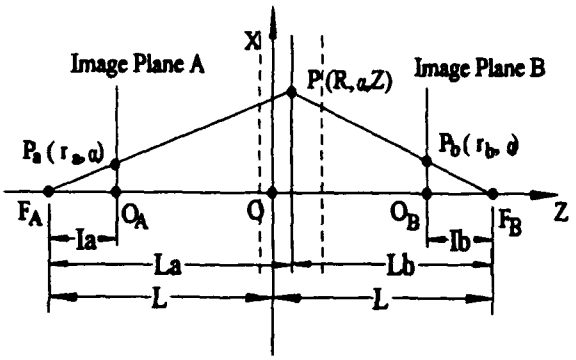

Figure 4. The Geometry of the In-Line Stereoscopic Viewing System, Cameras on Different Sides of the Flow

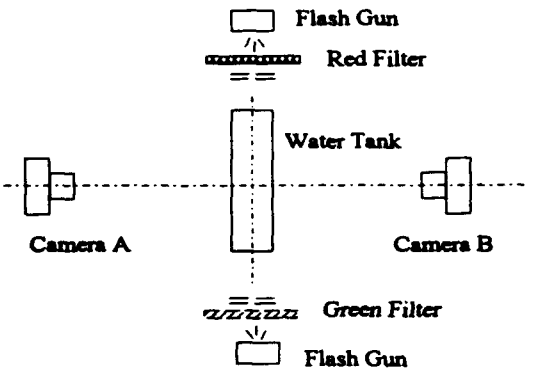

Figure 7. A Plan View of the Water Tank Experimental Arrangement Showing the Cameras on Different Sides of the Flow

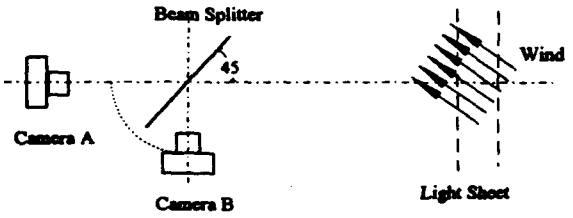

Figure 5. A Plan View of the Wind Tunnel Experimental Arrangement Showing the Cameras on the Same Side of the Flow

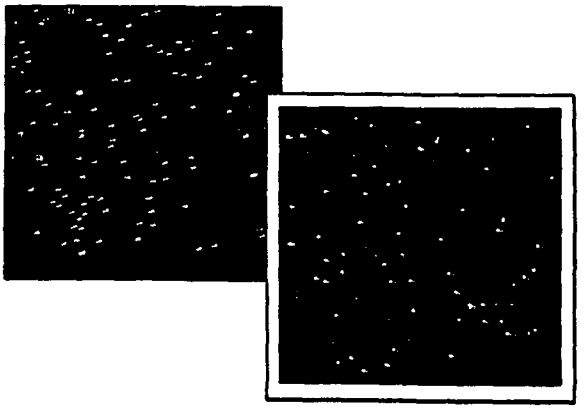

Figure 8. The Flow Images Obtained from the Stereo Viewing System Shown in Figure 7 (Hydraulic Tank)

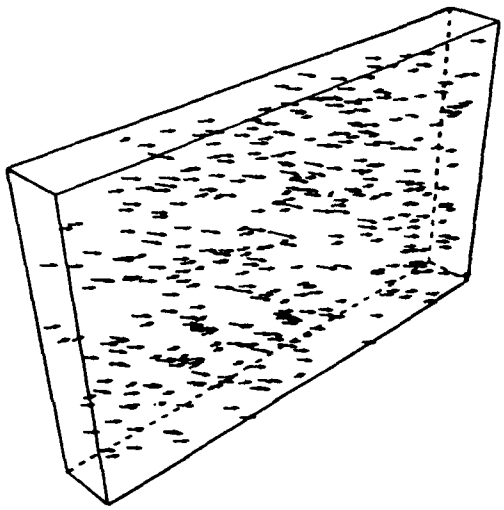

(a). α=–30°, β=45°, D=300.0mm

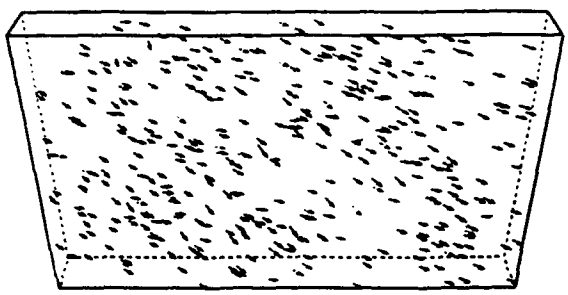

(b). α=–30°, β=90°, D=300.0mm

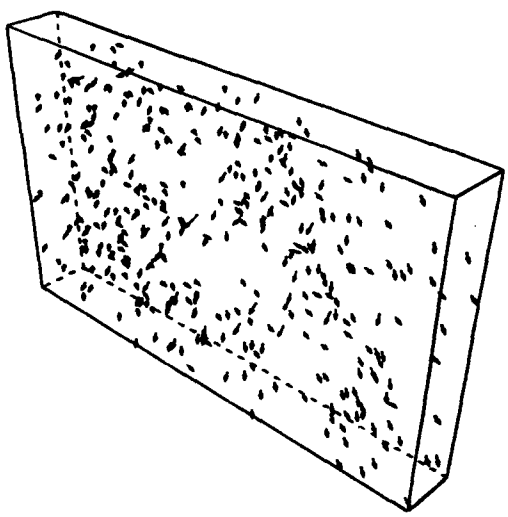

(c). α=–30°, β=135°, D=300.0mm

Figure 9. Three Perspective Projections Showing the Wind Tunnel Data Inside of the Reference Cube. α is theView Pitch Angle, β is the Yaw Angle, D is the Eye Distance from the View Plane.

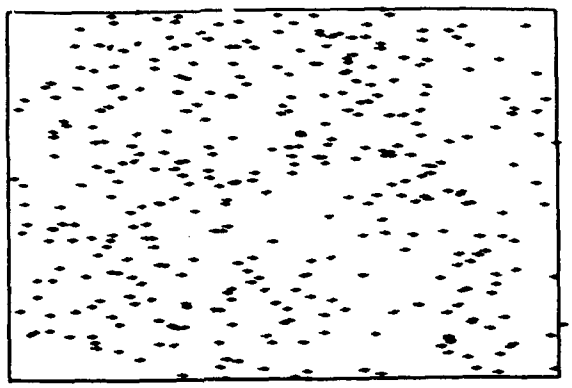

(a). α=0°, β=90°, D=300.0mm (-Z)

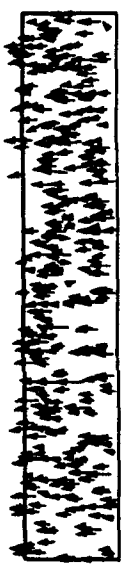

(b). α=0°, β=180°, D=300.0mm (-X)

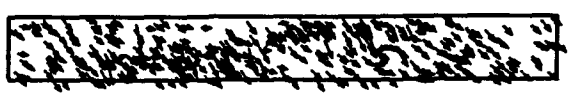

(c). α=90°, β=90°, D=300.0mm (-Y)

Figure 10. Three Planar Projections of the Wind Tunnel Data onto the sides of the Reference Cube. The Data Range:
X:-212.3 to 215.1mm Vx:-1000.0 to 844.7mm/s
Y:-132.6 to 159.1mm Vy:-1957.9 to 2896.6mm/s
Z:-25.7 to 24.2mm Vz:-2676.9 to 20694.1mm/s

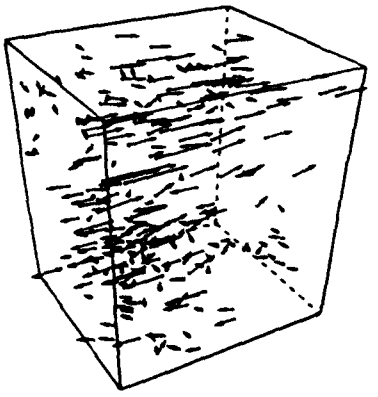

(a). α=−30°, β=150°, D=300.0mm

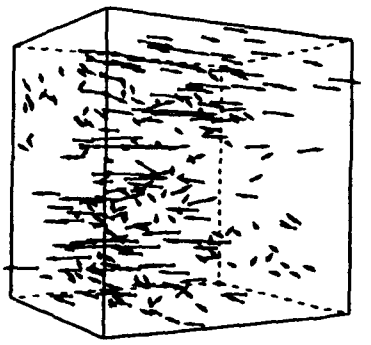

(b). α= 0°, β=150°, D=300.0mm

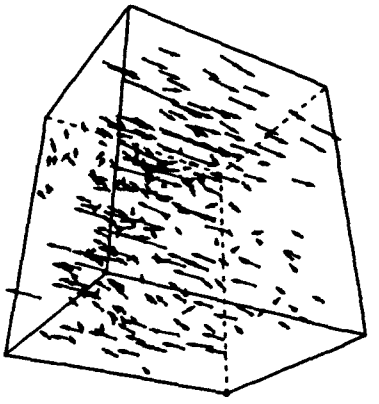

(c). α= 30°, β=150°, D=300.0mm

Figure 11. Three Perspective Projections Showing the Water Tank Data Inside of the Reference Cube. α is theView Pitch Angle, β is the Yaw Angle, D is the Eye Distance from the View Plane (300mm).

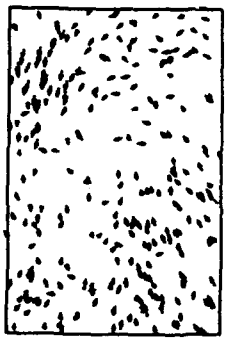

(a). α=0°, β=90°, D=300.0mm (-Z)

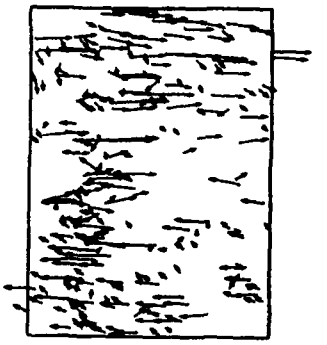

(b). α=0°, β=180°, D=300.0mm (-X)

(c). α=90°, β=90°, D=300.0mm (-Y)

Figure 12. Three Planar Projections of the Water Tank Data onto the sides of the Reference Cube. The Data Range:
X:-26.8 to 30.1mm Vx:-626.2 to 498.1mm/s
Y:-46.0 to 42.1mm Vy:-1019.9 to 1085.9m/s
Z:-39.3 to 27.2mm Vz:-7803.0 to 4587.3mm/s

ON THE ACCURACY AND RELIABILITY OF PIV MEASUREMENTS

Anders Høst-Madsen and Denise R McCluskey

Dantec Measurement Technology A/S
Tonsbakken 16-18, 2740 Skovlunde, Denmark.

ABSTRACT

An analysis of noise in PIV systems was undertaken and it was found that invalid vectors, termed outliers, bias the measured estimate of the velocity towards zero, artificially increase the rms turbulence value and interfere with the experimenter's perception of the flow fields behaviour. By adapting robust statistics so that specific features of both fluid dynamics and the PIV measurement technique were accounted for, three automatic data validation procedures were developed. A measure to assess the performance of the validation methods was suggested. The validation methods were then tested by inputting a simulated vector set containing 25% randomly distributed outliers. It was found the validation methods were feasible to implement and that even with as many as 25% outliers in a vector map it is possible to extract the original vector field with almost no deviation. Thus, it should be possible to obtain reliable measurements under non-ideal conditions and thereby extend the applicability of the PIV measurement technique.

1 INTRODUCTION

This paper will discuss the influence of noise on PIV data sets with a view to developing automatic data validation methods.

The accuracy of PIV data, as with data obtained by any other measurement technique, is critically affected by noise. Therefore, an analysis of the noise found in PIV measurement systems is necessary to ensure optimal performance of the technique. There has been little discussion on data validation of PIV data itself, with only a few papers from Willert & Gharib (1991), Raffel et al (1992) and Moraitis (1991). Instead, the main approach, as illustrated in the series of papers by Keane & Adrian (1992), has been to indirectly ensure data quality by satisfying a number of criteria which encompass all aspects of the measurement technique, that is seeding density, illumination, recording and analysis parameters, as well as properties of the particular flow field under investigation.

However, even if such criteria are satisfied, there is still a need for validation of the PIV data set because there is a finite probability that some PIV velocity vectors will be erroneous and even a single erroneous vector can severely bias the experimental data set. Historically, the main assessment of individual vector reliability has been done on a human intervention basis where the human operator produces a display of the vector map on a screen and intuitively considers whether individual vectors fall outwith expected norms. Vectors which are deemed 'erroneous' are manually removed from the data set. This approach is far from ideal since it produces an indeterminable bias to the experimental data.

One reason for the predominance of manual PIV data validation is that historically researchers have captured only a few frames of each flow field. The low data rate has been partly due to the fact that PIV records have been captured photographically: the time taken to process the film has a significant knock on effect on experimental time particularly when fine-tuning the data acquisition process. Furthermore, when the data acquisition process has finally been idealised, data is captured on only 1 or 2 rolls of film since it typically takes several hours to analyse a single frame. That is, the total number of analysed vectors has been limited by the previously available technology.

With FlowMap from Dantec Measurement Technology A/S evaluating several thousand vectors per second, such technological constraints will no longer exist and so large data sets will be produced. When millions of PIV velocity vectors are evaluated, it is not feasible to validate vectors manually and so criteria for automatic data validation algorithms are required.

Automatic data validation methods would also be of use where flow fields are produced in large scale facilities where experimental time is at a premium. Here, there may be insufficient time to satisfy all the seeding, illumination, recording and analysis system constraints. Thus, researchers

will require as much information as possible from PIV data sets obtained under non-ideal conditions. Here, a reliable means of determining whether individual velocity vectors are reliable would be invaluable.

Furthermore, as the PIV technique becomes even more popular, inevitably there will be instances where researchers will want to stretch the capabilities of the method since many interesting flow fields are inherently complex in their nature. A look at the history of LDA provides numerous illustrations of pushing measurement system capabilities, with full-scale pulverised coal burner measurements being one example. This example is a useful parallel because this application has generated much discussion in the LDA literature with regard to signal processing and validation. In the case of PIV, since the particles are naturally occurring in this flow field and uniform distribution cannot be ensured, indeed particle concentration is often of interest, it is unlikely that idealised PIV measurement procedures can be satisfied throughout the flow field. Therefore, if PIV is to be successfully applied to the study of such flows, mechanisms for automatic data validation should be deployed.

Hence, this paper will discuss PIV noise analysis and suggest approaches for automatic data validation. An important consideration in the identification of spurious vectors, is the direction as well as the magnitude of a velocity vector. That is, either auto-correlation with directional resolution or cross-correlation analysis should be used where the direction of the flow field is uncertain. Either option is readily implemented with FlowMap technology where the experimenter has the choice of using a novel CCD camera with built-in directional resolution or special cameras for cross-correlation analysis.

When comparing auto-correlation and cross-correlation analysis methods from a data validation view point, the robustness of the cross-correlation method makes it the preferred option for determining PIV velocity vectors. Cross-correlation is more robust because it requires fewer seeding particles per interrogation region and has a much larger dynamic range than auto-correlation analysis. Furthermore, unlike auto-correlation, cross-correlation inherently produces vectors with a known direction as well as magnitude. That is, for a given experimental circumstance, there is a greater probability of obtaining a true velocity vector rather than spurious noise when deploying cross-correlation analysis.

While the merits of the cross-correlation analysis method have been discussed in the past, the principal reason for its inclusion in this particular paper is practical: with FlowMap technology, cross-correlation PIV analysis is now feasible for both low and high speed flows.

Note that the terminology of signal processing theory is incorporated in this paper. In particular, invalid vectors will be termed outliers: as will become apparent in the discussion, invalid vectors are normally found in regions of the correlation plane which are far from the position of the true signal peak. That is in outlying regions of the correlation plane. Hence, the term outlier.

2 PIV ACCURACY

The basis of the PIV analysis method is that a multiple exposure of a seeded flow field is recorded, either onto the same frame or successive frames, and the correlation function of small interrogation regions is evaluated. The maximum peak in the correlation plane is at the location of the movement between the two recordings (when disregarding the self-correlation peak in autocorrelation analysis)

$$\left\{\tau \middle| R(\tau) = \max_{t} R(t)\right\} = \{v \cdot \Delta t\}$$

Therefore, by determining the location of the highest peak in the correlation plane the velocity vector is found. However, noise in PIV data and PIV measurement systems produces many noise peaks in the correlation function. In some cases, this noise may affect the accuracy with which the velocity vector is known. A further possibility is that the height of one of the noise peaks may be larger than the height of the actual velocity peak. Unfortunately, this case produces an invalid measurement, termed an outlier.

2.1 Problems of outliers

Outliers interfere with the assessment of the flow field in both a qualitative and quantitative manner. Qualitatively, outliers obscure the visual information in the PIV vector map and this can be illustrated by comparing Figure 1, which is a vector map which includes outliers, and Figure 2 which is the same data set with the outliers removed.

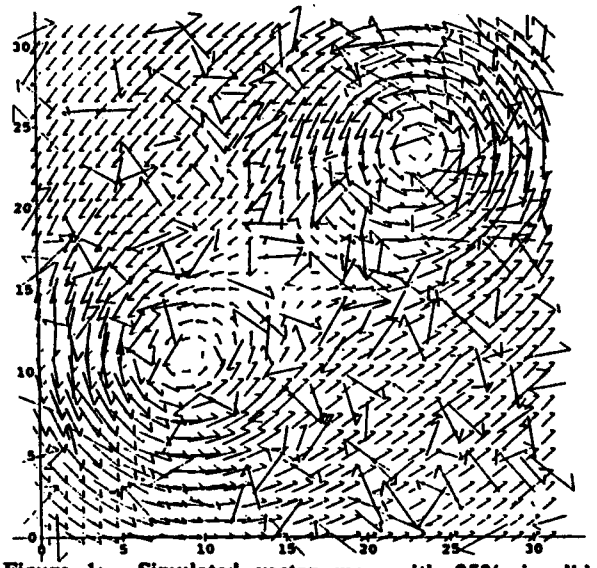

Figure 1: Simulated vector map with 25% invalid vectors.

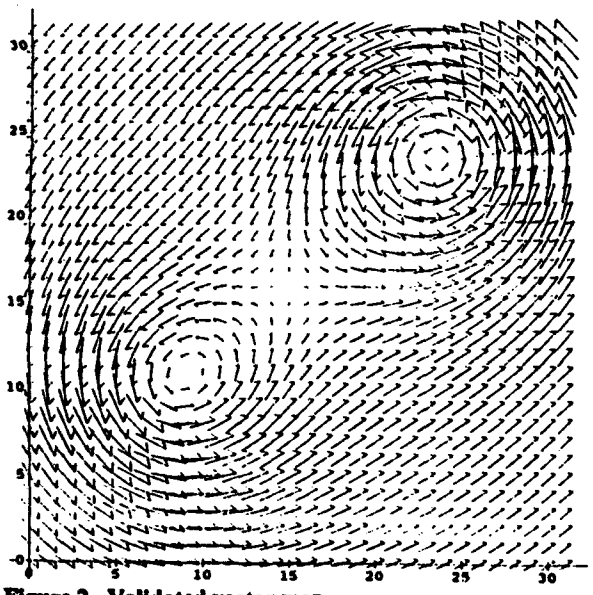

Figure 2. Validated vector map.
This shows the vector map shown in Figure 1 where the outliers have been removed and appropriate substitutions made.

Quantitatively, outliers have a significant effect on the mean and rms velocity statistics. This is illustrated in Figure 3 which shows measured average velocity, where the data set includes outliers, versus the true velocity. For a given seeding density, as the true velocity increases, the measured average velocity decreases. That is, outliers bias the average velocity measurement towards zero and the larger the actual velocity, the greater the bias. The extent of the bias is also influenced by the average number of seeding particles per interrogation region: when there are 12 particles the bias is not significant. Reducing the number of seeding particles per interrogation region increases the bias in the measured velocity. This result is partly explained by Figure 4 which shows the probability of detecting an outlier versus the ratio of velocity to interrogation length. For a given seeding density, as the ratio of velocity to interrogation area length increases, the probability of detecting an outlier becomes greater. In the same figure, it is also clear that the probability of detecting an outlier is dependent on seeding density: the larger the number of particles in the interrogation region, the less likelihood of detecting an outlier.

Thus, the general effect of outliers on statistical quantities, whether these are evaluated as a spatial average over a single PIV recording or as a temporal average over a number of PIV recordings, is to

- bias the measurement of the mean velocity to a value which is lower than the true mean
- produce rms velocities (turbulence intensities) which are greater than the true values

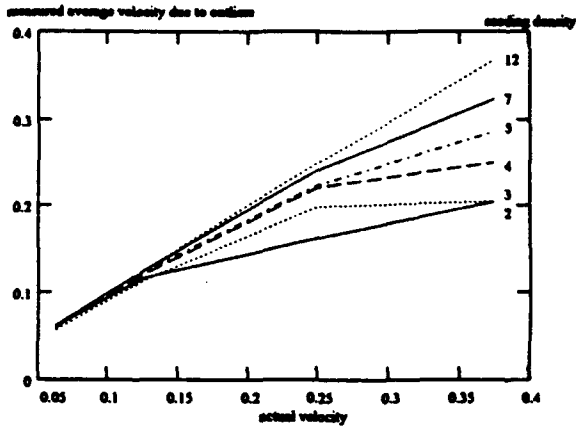

Figure 3. Biasing of velocity measurement due to outliers.
For a given seeding density and invalid vectors (outliers) bias the measured velocity value towards zero. The greater the relative ratio of velocity:length of interrogation region, the greater the bias. The lower the seeding density, the greater the bias. Cross correlation analysis of PIV interrogation area on 32 x 32 pixels. Constant velocity. 300 realizations

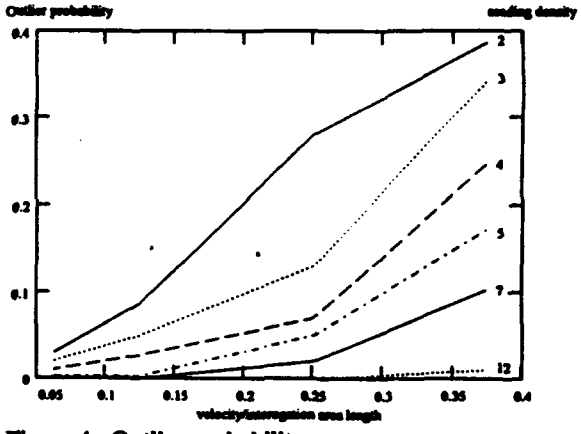

Figure 4: Outlier probability.
The probability of making an invalid measurement due to noise in the correlation plane is examined as a function of the ratio of velocity:length of interrogation region. The greater the ratio, the more likely an invalid measurement is made. This probability is also dependent upon the seeding density: the lower the seeding density, then the greater the probability of obtaining an invalid measurement. Cross correlation analysis of PIV interrogation area on 32 x 32 pixels. Constant velocity. 300 realizations

2.2 Modelling Noise in PIV Systems

In order to quantitatively assess the effects of the above noise on PIV measurements and develop strategies to remove such noise, an analysis of noise in PIV systems is required.

Conceptual Model

Consider the model of the 'noise flow' in a PIV system shown in Figure 5. Here a number of input noise sources are processed through a PIV evaluation system and this results in output noise. This output noise can be classified and has a diverse range of characteristics.

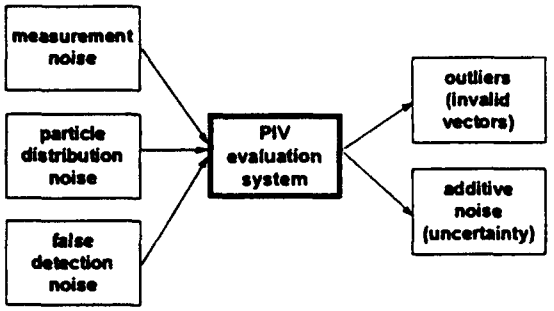

Figure 5. Modelling noise in PIV systems.

An actual source of input noise is that found in the PIV recording. When the PIV recording is evaluated, this noise will give an uncertainty in the velocity estimates. This uncertainty is termed the output noise. The magnitude of the input noise will depend on the particular experimental situation and the laser, camera and other equipment that is used. However, it is possible to qualitatively identify and analyse the sources of noise independently of the specific experiment. Similarly, while the magnitude of the output noise will depend on the specific method of PIV evaluation used, it is possible to categorise the output noise independently of this.

Thus, a PIV system can be optimised by firstly considering input noise and the sensitivity of the PIV evaluation system to it. Subsequently, steps can be taken to minimise the effects of noise on the complete system. However, in this paper the purpose of identifying noise sources and evaluating the effects of such noise on PIV systems is to address the problem of data validation.

A number of input noise sources can be identified and characterised as follows

- *Particle distribution noise* is due to the random distribution of signal particles in the fluid which is being measured. This is inherent in the PIV method.
- *Measurement noise* is caused by optical and electronic noise in the equipment used for recording the PIV images. An example is electronic noise in CCD recorders and the quantisation noise of the chip. Generally, it can be assumed that this noise is Gaussian white or coloured noise. In real life this noise can have other distributions, but the Gaussian white noise assumption usually leads to rather robust estimation.
- *False detection noise* arises when sources of light totally irrelevant to the flow interfere with the measurement. This noise can come from reflected or scattered laser light, dust in the optical system or malfunctioning pixels in the CCD chip. Since this noise depends on the specific measurement situation, no analysis of its distribution or characteristics can be made.

When the aforementioned noise sources are processed by the PIV system, it will result in uncertainty in the velocity estimates. This noise uncertainty can be divided into two distinct categories.

- *Additive noise*: This manifests itself as uncertainty in the location of the exact position of the velocity peak in correlation plane. It arises from the cumulative effects of particle distribution noise, measurement noise and, to a lesser extent, false detection noise. In some cases, it may be reasonable to assume that this is additive Gaussian noise. However, the noise may be dependent upon the measured velocity[1] and so in many situations it could be non-white and non-uniform. This uncertainty also affects the velocity value of neighbourhood interrogation areas if the interrogation areas are overlapping. Furthermore, due to non-uniformity of particle distribution and illumination, this noise uncertainty is location dependent. In spite of these reservations, a Gaussian white-noise assumption gives a reasonable signal characterisation.
- *Outliers*: Noise produces many peaks in the correlation function and in some cases the height of one of the noise peaks may become greater than the height of the peak corresponding to the velocity. This results in an invalid measurement. The form of this outlier noise is distinctly non-additive and, as discussed later in this paper, its distribution is far from Gaussian.

The problem of additive noise is relatively well behaved. Standard methods of signal processing exist for dealing with this problem, even for non-uniform and non-white signals. The fact that, in contrast to most signal processing problems, PIV measurements are multidimensional in several ways, does not pose serious complications. The problems of outliers is less straight-forward and methods of automatically identifying and removing these from the data set will be the main subject of this paper.

[1] E.g. because of dependency the correlation peak height on the velocity.

Mathematical analysis of noise in PIV

In order to develop methods for automatic removal of outliers from the PIV data set, it is necessary to analyse the effect of noise on the calculation of correlation functions. For simplicity of notation, the analysis is one dimensional.

Consider the case where the PIV data has been captured on successive image frames, $v(t)$ and $w(t)$, and so the correlation function is

$$R(\tau) = v(t)w(t-\tau)$$

If the noise can be identified in each frame, the noise-corrupted versions of $v(t)$ and $w(t)$ are $v(t)+n_v(t)$ and $w(t)+n_w(t)$ respectively. If these are captured in a finite interval [-T,T], then the correlation is

$$R'(\tau) = \int_{-T+|\tau|/2}^{T-|\tau|/2} \left(v(t+\frac{\tau}{2}) + n_v(t+\frac{\tau}{2}) \right) \left(w(t-\frac{\tau}{2}) + n_w(t-\frac{\tau}{2}) \right) dt$$

$$= \int_{-T+|\tau|/2}^{T-|\tau|/2} v(t+\frac{\tau}{2}) w(t-\frac{\tau}{2}) dt$$

$$+ \int_{-T+|\tau|/2}^{T-|\tau|/2} v(t+\frac{\tau}{2}) n_w(t-\frac{\tau}{2}) + w(t-\frac{\tau}{2}) n_v(t+\frac{\tau}{2}) + n_v(t+\frac{\tau}{2}) n_w(t-\frac{\tau}{2}) dt$$

$$\approx \left(1-\frac{|\tau|}{2T}\right) R(\tau) + N(\tau)$$

where $N(\tau)$ represents the noise terms. Assuming that the signal and noise are uncorrelated and that the two noise sources $n_v(t)$ and $n_w(t)$ are independent and white, then

$$E\{N(\tau)\} = 0$$

$$E\{N(\tau)^2\} = \left(1-\frac{|\tau|}{2T}\right) E\{N(0)^2\}$$

From this result it can be concluded that

- The height of true correlation peaks will decrease as $(1-|\tau|/2T)$ with increasing velocity magnitude (represented by $|\tau|$). This is a triangular distribution.
- The height of noise peaks will decrease as $\sqrt{1-|\tau|/2T}$. This is a square root distribution.

Thus, the probability of detecting an outlier instead of the true signal increases with increasing velocity. This probability will exacerbate the biasing of the average velocities towards zero.

Characteristics of noise in the correlation plane

The easiest noise to analyse is the measurement noise. This case exactly corresponds to the above general case, in it will thus give an outlier distribution that is symmetric around zero and has the above square-root distribution.

The false detection noise on the other hand is very difficult to analyse since it is caused by specific conditions in the concrete experiment. Let us suppose that any false velocity is equally probable. In this case, the outlier distribution will be symmetric around zero and have the above triangular distribution.

Outlier distribution for particle distribution noise

The outlier distribution due to particle distribution noise is difficult to analyse, yet it can as the only noise source be analysed to good accuracy, since we have a very realistic statistical model of the noise. This further underlines the fundamental nature of this noise.

Since the noise sources can be reasonably assumed to be independent of the velocity, it would seem plausible to assume that the invalid vector value arising from the false correlation peak is uncorrelated with the true velocity. From this assumption, it would be possible to have the following simple model of outlier distribution in velocity vector maps. There is a probability, p, that the measured correlation peak corresponds to the true velocity vector. Otherwise, the measured correlation peak is an outlier and this can be at any location within range with equal probability.

However, the analysis in Section 2.1 shows that the probability of detecting an outlier from a PIV recording is dependent on the velocity of the fluid and the seeding density. Furthermore, computer simulations of PIV data sets show that noise peaks in the correlation plane, and hence outliers, are *not* symmetric around zero. This is illustrated in Figure 6 which shows a plan view of the correlation plane. The true velocity signal is located near the bottom left hand region of the image and the noise peaks towards the top right hand region. This distribution of noise peaks within the correlation plane will further bias the velocity towards zero if outliers are not removed from the data set. Thus, outliers will not be uniformly distributed over the PIV vector map, but concentrate in areas of high velocity and low seeding rate. This feature of outlier noise can be termed ***negative velocity bias***.

The authors consider the finding that the distribution of noise peaks in the correlation plane, and hence outliers, are *not* symmetric around zero is new information in PIV noise analysis. Therefore, a theoretical explanation of this phenomenon has been undertaken. However, due to space limitations, this will be presented in a future paper.

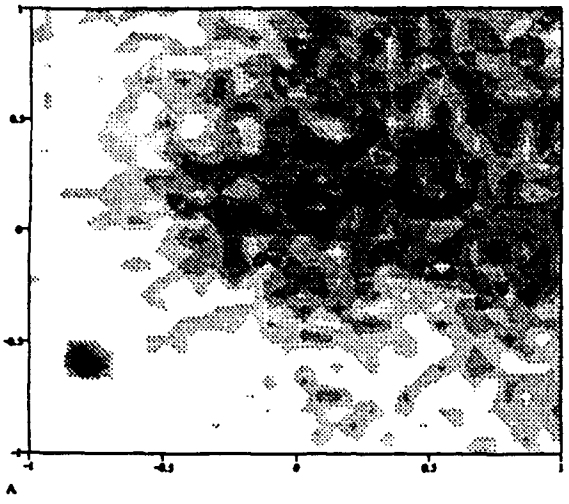

Figure 6. Distribution of outliers in the correlation plane. The true velocity peak is in the bottom left hand region of the correlation plane whereas the noise peaks, which produce outliers, are distributed towards the top right hand region. Cross correlation analysis of PIV interrogation area on 32 x 32 pixels. Constant velocity, on average 5 particles in the interrogation area. 10000 realizations.

2.3 Validity of data validation

Although data sets may contain invalid measurements, it is important to consider whether it is reasonable for experimenters to perform *data validation and question* whether it is justifiable to deem certain measurements to be 'false'. It should be noted that experimenters have a certain *a priori* knowledge of the flow field. This knowledge may be the upper and lower limits of the velocity vectors or that the vectors are gradually (spatially) varying. Automatic data validation is a formalisation of this knowledge in a model and is justifiable if the effects of the model can be tested.

2.4 Evaluation of data validation methods

Before developing methods for validation, it is therefore important that a measure the performance of an evaluation method can be obtained. A natural measure is the proportion of outliers the method correctly invalidates *and* the proportion of correct vectors the method wrongly invalidates. However, this method of evaluation has some problems:

- It does not give us a single number to rank methods. Some methods will be very good at finding the outliers, but may at the same time invalidate many correct vectors, while other methods will perform oppositely.
- It does not take into consideration one of the most important functions of data validation, namely the removal of outliers which strongly diverge from the data set.
- Normally, a method of validation will also define a substitution for those vectors which are invalidated. Even if a methods invalidates many correct vectors, this will not be a problem as long as the substitution is very close to the correct vector.

A measure that takes into consideration all of these effects is the following

$$\frac{\sqrt{\frac{1}{N}\Sigma\left|\mathbf{v}_i-\mathbf{v}_i^{\text{true}}\right|^2}}{\sqrt{\frac{1}{N}\Sigma\left|\mathbf{v}_i^{\text{true}}-\overline{\mathbf{v}^{\text{true}}}\right|^2}} \qquad (1)$$

Here $\mathbf{v}_i$ are the measured vectors (before or after validation) and $\mathbf{v}_i^{\text{true}}$ are the actual vectors. The summation and the averaging is over the PIV measurement field. The measure determines the difference between the non-validated or validated & substituted vector field and the actual vector field. This difference has been normed so that it is reasonably comparable for different vector fields. The norming is so that it more or less measures the artificial turbulence intensity due to outliers relative to the true (spatial) turbulence intensity. This quantity typically is a few percent before validation and a few tenths of a percent after validation.

It is recognised by the authors that this measure is not ideal since it can only be used on simulated measurements or measurements of known flow fields. However, this is a general problem which is encountered in the assessment of most measurement techniques.

3 OUTLIER REMOVAL

Now that a model of outliers and a measure of the performance of validation methods has been established, it is reasonable to proceed with devising methods which will automatically remove outliers from PIV vectors sets. This removal of outliers will be called *validation*.

3.1 Robust statistics

Although there has only been a limited amount of work on data validation in PIV, in statistics outlier removal, which is known as robust statistics, has received much interest during the last two decades. Some recent references include Barroso & Moura (1992), Mirza & Boyer (1993), Atkinson & Mulira (1993), Hardie & Boncelet (1993), Zhong et al (1992) and Veldhuis (1988). While it is possible to get inspiration from these other fields, PIV measurements have some unique characteristics which make it difficult to directly apply the methods. Particular differences are detailed as follows.

1. In PIV the measurements are vectors, not scalars.
2. In signal processing, it is often assumed that the data is a realisation of a stationary process of which the autocorrelation function is known. In PIV, there

is a limited 2D field, with the boundaries playing an important role, and the autocorrelation is not known.

3. In flow measurements, in contrast with image analysis, the values generally change gradually (except in a few cases like boundary layers).
4. In PIV analysis, it is feasible to incorporate knowledge of the fluid dynamics into an analysis of the measurement validity.

In spite of these reservations, the idea of robustness could also be applied to PIV measurements.

Robust statistics is applied when the probability density of the stochastic variables are not known in detail. Robust statistics should give a roughly correct answer for a wide class of probability densities. The above analysis of outlier distribution means that the distribution trends are known although the exact distribution is not.

3.2 Deterministic Model

Two possible approaches to formulating data validation models are deterministic or probabilistic. This paper will consider a deterministic model since this is the most straightforward approach. In this deterministic model there is a (vector) function $\mathbf{f}_\varphi$ of n variables (φ) giving a set of velocity vectors at the PIV measurement locations. Of the n input variables, the parameters of the model, some can be given in advance while others have to be fitted so that the model matches the measurements.

An example of this approach is of a flow field which is constant throughout the PIV measurement area. A model of this flow would then be a function whose input parameters are the direction and magnitude of the flow. The output would be an array of vectors each with this direction and magnitude. If **M** is a PIV measurement (an ordered set of vectors), to satisfy the model φ must be found so that

$$\mathbf{M} - \mathbf{f}_\varphi = 0$$

To allow for (additive) noise in the measurements and a model that does not fit totally, this constraint can be weakened to

$$\left\| \mathbf{M} - \mathbf{f}_\varphi \right\| \leq \varepsilon$$

where $\|\cdot\|$ is some suitable norm (distance function). The model can be formulated as a set of equations that have to be satisfied. If **M** is a PIV measurement, then it has to satisfy the equations

$$\left| \mathbf{g}_\varphi(\mathbf{M}) \right| \leq \varepsilon$$

which allows for a certain deviation.

The number of parameters are called the degrees of freedom of the model. The fewer degrees of freedom the model has then more strict the model is in the removal of outliers. However, the fewer degrees of freedom in the model then the more it will bias the measurements. This bias will be severe if an inappropriate model is applied to measurement validation since it will produce data which fits the model rather than assessing whether the data represents the flow field. That is, the model would be self-fulfilling. Therefore, it is important to achieve a balance when using deterministic models and so choose models with an appropriate number of degrees of freedom. The advantage of the model approach in validation is that the model is explicit and so we can predict what bias the validation will produce in the measurements.

Identifying outliers in the deterministic model

After having chosen a suitable model, the next stage of data validation is to find vectors which are deemed outliers. That is, to find the undetermined parameters of the model so that the 'best possible' fit to a given set of measurements is obtained. A usual way to do this is to use Least Squares (LS) fitting. However, LS fitting presupposes a Gaussian distribution of the errors which is an inappropriate description of outliers. As pointed out in the literature on robust statistics, LS fitting may behave very badly in the presence of outliers. LS fitting is the Maximum Likelihood (ML) estimation (see Papoulis (1991)) for Gaussian errors. In PIV this also seems to be a reasonable method of fitting the undetermined parameters of the model to the measured vector map.

Assuming that the distribution of outliers is such that there is a probability p that a vector is correct. Otherwise, the measured vector is an outlier, which may assume any value independently of the correct vector, with a probability $(1 - p)$. The distribution of the outliers may not be uniform, but the exact distribution will not be important. This approach can be extended so that each measured vector $\mathbf{M}_i$ has an individual probability that it is correct. This probability could be obtained from say the peak heights in the correlation plane. Denoting that the probability that $\mathbf{M}_i$ is correct as $p_i p$, then the probability that it is wrong as $-p_i p$. For a given set of parameters φ, it is then possible to partition the measured vectors **M** into two sets: set **C** comprises correct vectors and the other set is outliers **O** = **M** - **C**. Thus, denoting the model as $\mathbf{g}_\varphi$, **C** must satisfy

$$\left| \mathbf{g}_\varphi(\mathbf{C}) \right| \leq \varepsilon \qquad (1)$$

The likelihood function (as discussed in Papoulis (1991)) for the given partition and the given set of parameters is now

$$L(\mathbf{M};\mathbf{C},\varphi) = \prod_{\mathbf{v}_i \in \mathbf{C}} p_i p \prod_{\mathbf{v}_i \notin \mathbf{O}} (1 - p_i p)$$

Maximum Likelihood estimation is the maximisation of this function with respect to **C** and φ. For general p_i this maximum is complicated to find, but assuming that every vector has the same probability of being correct produces a simpler expression

$$L(\mathbf{M};\mathbf{C},\varphi) = p^{|\mathbf{C}|}(1-p)^{|\mathbf{M}|-|\mathbf{C}|}$$

where $|\mathbf{C}|$ is the number of vectors in **C**. Assuming that $p >$ 0.5 (that is, a measurement is more likely to be correct than wrong) then the maximum of this function is when $|\mathbf{C}|$ is maximum. Note that this maximum is independent of the value of p. If p_i is different for different i this statement is not true. This ML principle can be formulated as

the model should be fitted so that the fewest numbers of vectors are invalidated

Is this a feasible approach?

Although this is a simple principle, it is impossible to do directly in practice. This is because it is a discrete optimisation problem, and in general it is impossible to solve these exactly in a reasonable time. Methods which give an approximate solution to the problem will be discussed in the section 3.3.

Notice that the model fitting breaks down if more than half of the vectors are wrong. In that case the ML principle tells us that we should invalidate all vectors. It is a general feature that outlier removal only works if less than half the measurements are outliers (see Rousseau & Leroy (1987) chapter 4, theorem 7).

3.3 The model / filtering approach

Although discrete optimisation problems are generally impossible to solve exactly, methods of approximate solution do exist. A particular method is simulated annealing (see e.g. Press (1992)) and aspects of this approach will be adapted to PIV vector validation. This approach can be termed the filtering model.

A filter is a function f: $M \rightarrow M$, which given a set of input measurements produces a modified set of measurements. A measurement **M** satisfies the filtering model with filter f if **M** is invariant under f,

$$f(\mathbf{M}) = \mathbf{M}$$

the condition in equation (2) is in this case

$$\|f(\mathbf{M}) - \mathbf{M}\| \leq \varepsilon$$

It has been found that the only reasonable norm to use is the max norm, thus

$$\max_i \|f(\mathbf{M})_i - \mathbf{M}_i\| \leq \varepsilon \qquad (3)$$

where i runs over the set of vectors in the measurement **M**. Suppose that the filter f has a certain convergence property

$$f^{(n+1)}(\mathbf{M}) - f^{(n)}(\mathbf{M}) \rightarrow \mathbf{0} \quad \text{for} \quad n \rightarrow \infty \qquad (4)$$

for all **M**. That is, when starting with any measurement and applying the filter over and over again, the result will converge towards a measurement invariant under f. With this property it is possible to implement a simple validation approach:

Apply the filter to the measured data. Those vectors which deviate too much from their filtered value are labelled as outliers.

This simple method has to be refined to work reasonably. The outliers will affect the filtered measurements also at positions where there are no outliers. Thus many vectors, which are not outliers, will be labelled as outliers. A method to overcome this is by *repeated filtering* (see also Moraitis (1991)) whereby

1. the filter is applied to the measured data
2. those vectors which deviate too much from their filtered value are labelled as outliers and substituted by their filtered value
3. the filter is reapplied to the new set of measurement which contains the substitutions

This loop is repeated a certain number of times. In order for this approach to work optimally one further refinement has to be made. The outlier may cause large deviations between the filtered and the non-filtered measurement also at positions where there are no outliers, especially in the neighbourhood of the outliers. The vectors at these positions will be labelled as outliers and will stay as such throughout the following iterations, even when the true outliers are detected. This is well-known from simulated annealing: if the temperature is lowered too fast (quenching) the system is frozen in a state which does not have minimal energy. By adapting and testing a simulated annealing approach, a method of overcoming this problem has been developed.

In this approach, some random vectors initially labelled 'outliers' subsequently change their state to non-outliers. Although this has some positive effect, it is minimal. A better way is to let ε in equation (3) decrease in value after each iteration. This is has been termed an annealing sequence. In this way, the strongly deviating outliers, which may otherwise cause non-outliers to deviate from their filtered value, are removed during the first iteration. During the next iteration ε is decreased, so that more outliers are found, and so on. With this refinement, the method of filtered validation can be described in exact terms as follows

Let $\mathbf{M}^0$ be the original measurement, and let $\varepsilon_j, j = 1..N$ be an annealing sequence. For each j let

$$\mathbf{M}_i^j = \begin{cases} \mathbf{M}_i^0 & \left\|\mathbf{M}_i^0 - f(\mathbf{M}^{j-1})_i\right\| \le \varepsilon_j \\ f(\mathbf{M}^{j-1})_i & \text{otherwise} \end{cases}$$

The result is $\mathbf{M}^N$, where outliers have been substituted. If $\left\|\mathbf{M}_i^N - \mathbf{M}_i^0\right\| > \varepsilon_N$ then vector i was an outlier.

To use the above method, a suitable annealing sequence $\varepsilon_j, j = 1..N$ has to be found. The ε's have to adapt to the measurement, otherwise one has to experiment with the ε's for each new measurement. If there is a very large outlier in the measurement, this large outlier will also cause other good vectors to deviate strongly from their filtered value. Thus, the ε's must depend on the largest deviation and it was found that it was conveniently to chose

$$\varepsilon_j = \alpha_j \max_i \left\|\mathbf{M}_i^0 - f(\mathbf{M}^{j-1})_i\right\|$$

where α_j is the *acceptance factor*.

To use the model, one thus has to find the number of steps, N, the (final) acceptance factor α_N and a suitable sequence $\alpha_j, j = 1..N-1$ decreasing to α_N. This will be discussed further in Section 5.

Developing Suitable Filters

The next issue to address is which filters to use? Both non-linear and linear filters could be used. Although in general non-linear filters can be superior, linear filters were developed. The reason for this choice is that those measurements satisfying the model, the invariant set of the filters, can be described very easily. Furthermore, it is straight forward to find the convergence properties of the filters. This is a very important feature of a validation method, as mentioned in section 2.4 since this makes it possible to describe and predict the bias of the methods. The filters which will be discussed can be written as a convolution

$$f(\mathbf{M}) = \mathbf{f} \otimes \mathbf{M}$$

(The issue of the boundary conditions shall be discussed below.) Thus, in the Fourier plane the filter is a multiplication

$$f(\mathbf{M})\hat{} = \hat{\mathbf{f}} \cdot \hat{\mathbf{M}}$$

- The invariant set of f are those $\mathbf{M}$ satisfying $\mathrm{supp}(\hat{\mathbf{M}}) \subset \hat{\mathbf{f}}^{-1}(\{1\})$, i.e. those measurement whose Fourier transforms is only non-zero where $\hat{\mathbf{f}}$ is equal to 1.
- The filter f satisfies the convergence condition in equation (4) if and only if $\left|\hat{\mathbf{f}}\right| \le 1$ everywhere.

Three different filters were investigated.

1. Moving average. Here the filtered vector is given by an average of the vectors in a certain neighbourhood. The invariant subset is the constant vector fields.
2. Linear interpolation. The filtered vector is given by fitting the vectors in a neighbourhood to a plane by Least Squares fitting. It is easily proven that this filter can also be expressed on the form given in equation (2), and that the invariant subset are the plane vector fields.
3. Ideal low pass filtering. The filter is given by letting $\hat{\mathbf{f}}(x) = 1$ on some neighbourhood of 0, and zero elsewhere. In two dimensions, not only the band limit, but also the shape of a filter must be determined. We have found that it is reasonable to let the filter be circular symmetric, due to the symmetry of turbulence. The invariant subset are of course those vector field, which are ideal low-pass.

Boundary conditions pose a special problem in the filtering approach. If the flow is viscous, it will converge towards zero on boundaries, and the boundary problem can be solved by setting the flow field to zero outside the boundaries. If the flow can be considered (almost) non-viscous this cannot be used. Furthermore, the boundaries of the PIV data set do not typically correspond to the boundaries of the flow and so setting the flow to zero outside the data set boundaries will give wrong results. A more realistic condition to impose is that the flow extends in a 'continuous' manner across the boundary of the PIV recording, and use this to extrapolate within the measured flow field. How this should be done depends on the specific filter. For moving average filtration and linear filtration it is quite straightforward, but for ideal low pass filtering more advanced solutions have to be found.

It is well-known that a function cannot have bounded support in both the space and frequency domain. Thus, if the bounded domain of a PIV measurement is extended by setting it to zero outside the boundaries, the result will not be low pass. Thus, intelligent boundaries have to be set. The Papoulis-Gerchberg algorithm (see Marks (1991) section 7.3) was adapted to this purpose. Here, the initial step is to pad the PIV measurements by a certain number of zeros and then follow the algorithm in figure 7.23 in Marks (1991), with the modification that in step (5) an additional substitution is made. This will not work so well in practice, since PGA ideally assumes continuous sampling, it does converge very

slowly and it does not converge in the L^2-sense: specifically it does not converge on the boundaries, contrary to what was wanted (Gibb's phenomena). To improve on this, the bandwidth of the filter was allowed to expand from iteration to iteration, initially with a very sharp filter and expanding to the chosen bandwidth.

4 TESTING THE VALIDATION METHODS

The validation algorithms were tested on a number of simulated pictures an example of which is shown in Figure 1. Typically, a random selection of 25% of the vectors were designated outliers. This provided a reasonable method of evaluating the performance of the validation methods although it was not a realistic distribution of outliers.

Figure 2 shows the picture after validation with low pass filtering. Table 1 gives a summary of results of this and the other validation methods. All the data is for 6 iterations and a logarithmic quenching sequence, except the last entry in the table, where a constant acceptance factor was used. It is seen that an appropriate choice of quenching sequence is essential for reasonable performance. Also, when using a slowly decreasing quenching sequence, the choice of acceptance factor is non-critical. If a too low a value of acceptance factor is chosen, many valid vectors will be designed outliers. However, since the value of the substituted vector is so close to the original, this is not a serious problem. The validation will just work as a low pass filter on the data, which should not prose problems provided that an appropriate selection of filter is made in the first instance.

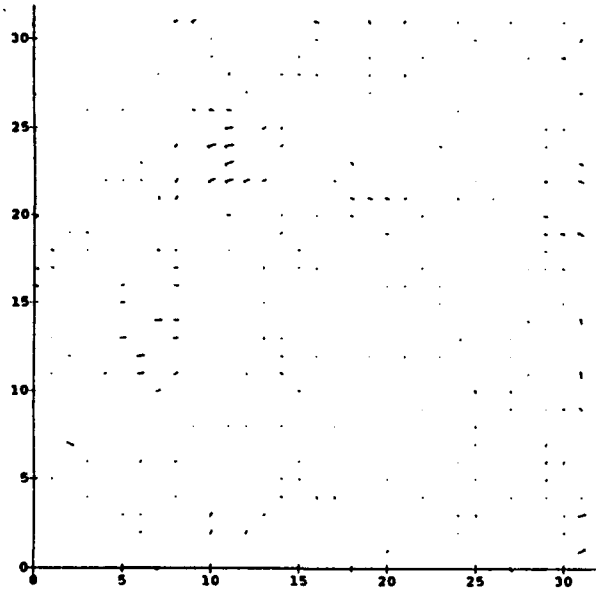

Figure 7: Effect of data validation.

This vector map shows the difference in vector values between the raw data set shown in Figure 1 and the validated data shown in Figure 2. Both these figures are in Section 2.

Table 1: Performance of different filter models.

Filter	measure	Correctly invalidated	Incorrectly invalidated
Low Pass	$.3 \cdot 10^{-4}$	259/261	0
Moving avg.	$.4 \cdot 10^{-4}$	259/261	0
Linear	$.1 \cdot 10^{-3}$	256/261	21
Moving avg[2] .	$6.1 \cdot 10^{-4}$	257/261	12

In all cases the measure given by equation 1 before validation was $6.4 \cdot 10^{-3}$.

5 DISCUSSION & CONCLUSIONS

A review of the PIV literature showed that only a handful of papers had discussed the issue of automatic PIV data validation. Since there is a finite probability that even with ideal data acquisition and analysis procedures invalid vectors will be produced, validation methods are required. Validation methods should be automatic for reasons of practicability and experimental rigour. The practical aspects are that with FlowMap evaluating several thousand vectors per second, it is no longer feasible to examine data sets manually. Experimental rigour is compromised by manual data validation since it produces an indeterminable bias to the measurement process. Further important considerations are that if researchers wish to adopt the PIV technique in situations where data acquisition takes place with non-ideal conditions, then there should be validation methods to ensure that they can reliably distinguish the real data from the noise. This will also be useful if experimenters which to extend the application of the PIV technique to measure complex flow fields.

The analysis of noise in the correlation plane, which was generated by noise from both PIV data and measurement systems, highlighted two problem areas. The first is noise induced uncertainty in the location of the velocity peak and the second problem is detecting a spurious noise peak instead of the peak associated with the velocity. The later occurrence is perhaps the more serious as it produces an invalid vector which was termed an outlier. Analysis of the characteristics of outliers showed that they bias the measured estimate of the velocity towards zero, artificially increase the rms turbulence value and interfere with the experimenter's perception of the flow fields behaviour. Even a single outlier can significantly affect the measurement process.

By adapting robust statistics so that specific features of both fluid dynamics and the PIV measurement technique were

2 with constant acceptance factor.

accounted for, it was possible to develop automatic data validation procedures which were feasible to implement. Three validation methods, flow pass filter, moving average filer and linear filter were proposed. In order to assess the performance of these methods, a measure was suggested. This was used in a controlled test of the validation methods where a simulated vector map was altered so that it contained 25% randomly distributed outliers. It was found that even with as many as 25% outliers in the vector map it was possible to extract the original vector field with almost no deviation. Thus, it should be possible to extend the applicability of the PIV measurement technique to more complex flow fields.

REFERENCES

Atkinson, A.C. and Mulira, H.-M.: The stalactite plot for the detection of multivariate outliers, Statistics and Computing, vol 3, pp 27-35, 1993.

Barroso, V.A.N. and Moura, J.M.F.: An ML algorithm for outliers detection and source localization, IEEE ICASSP 1992.

Hardie, R.C. and Boncelet, C.G.: LUM filters: a class of rank-order-based filters for smoothing and sharpening, IEEE Transactions on Signal Processing, vol 41, no 3, March 1993.

Keane, R.D. and Adrian, R.J.: Theory of cross-correlation analysis of PIV images, Applied Scientific Research, vol 49, pp 191-215, 1992

Marks, R.J. II: Introduction to Shannon sampling and interpolation theory, Springer-Verlag 1991.

Mirza, M.J. and Boyer, K.L.: Performance evaluation of a class of M-estimators for surface parameter and estimation in noisy range data, IEEE Transaction on Robotics and Automation, vol 9, no 1, February, 1993.

Moraitis, C.S.: Flowfield Data Validation, Confidential Report to Dantec Measurement Technology, 1991.

Papoulis, A.: Probability, Random Variables, and Stochastic Processes, Third Edition, McGraw Hill 1991.

Raffel, M., Leitl, D. and Kompenhans, J.: Data validation for particle image velocimetry, 6th Int Symp on Applications of laser techniques to fluid mechanics, Lisbon, Portugal, 1992.

Rousseau, P.J. and Leroy, A.M.: Robust Regression and Outlier Detection, John Wiley & Sons, 1987.

Veldhuis, R.N.J.: Adaptive Restoration of Unknown Samples in Discrete Time Signals and Digital Images, Thesis, Katholieke Universiteit te Nijmegen, 1988.

Willert, C.E. and Gharib. M.: Digital particle image velocimetry, Experiments in Fluids, vol 10, pp181-193, 1991.

Press, H. et al.: Numerical recipes in C, Cambridge University Press, 1992.

Zhong, J., Weng, J. and Huang, T.S.: Robust and physically-constrained interpolation of fluid flow fields, IEEE ICASSP 1992.

NEAR FIELD STRUCTURE OF A SUPERSONIC JET: "ON-LINE" PIV STUDY

A. Krothapalli, D. P. Wishart and L. M. Lourenco
Department of Mechanical Engineering
Florida A&M university and Florida State University
Tallahassee, FL 32316, USA

ABSTRACT

Results of an experimental investigation to determine the velocity field of an axisymmetric supersonic jet using the "on-line" Particle Image Velocimetry are presented. Particular emphasis is placed on the description of a shock cell structure comprising of shocks, expansion fans, and three dimensional shear layers. Comparison of the PIV data with those obtained from pressure and schlieren flow visualization show good agreement. An interesting phenomenon of internal shear layers within the jet are identified.

1. INTRODUCTION

As part of an ongoing program to study the structure of supersonic jets, issuing from different nozzle configurations and exit conditions, a systematic investigation has been carried out on a jet issuing from an axisymmetric nozzle. This program was intiated by the renewed interest in the development of exhauast nozzle configurations for stealth aircraft and high speed civil transport. The focus of this paper is to provide, through PIV data, a better understanding of the shock-cell structure that is associated with imperfectly expanded supersonic jets.

The near field structure of a supersonic jet is mainly determined by the nozzle exit pressure ratio (exit pressure / ambient pressure) and area ratio (exit area/throat area). An ideally expanded jet is the one where the exit plane pressure is equal to ambient pressure, commonly referred to as the design condition. When the pressure in the exit plane is greater or less than the ambient pressure, the jet is referred to as under or over expanded respectively. To minimize thrust losses, exhuast nozzles are generally designed to perform at the ideally expanded condition. However, under many circumstances the nozzle is operated away from the design condition resulting in the generation of a quasi-periodic cell structure containing shocks and expansion fans, referred to as shock-cells. The flow field within these shock cells is yet to be fully understood. This is primarly due to limited measurements within the shock cell structure. In order to characterize the flow field in a supersonic jet, it is necessary to obtain measurements of at least two fundamental variables such as density and velocity. Whole field density measurements have been made with success using interferometeric (Ladenburg and Bershader (1956)) and more recently Moiré-Schlieren methods (Tabei et.al. (1991)). In this paper, we describe a novel Particle Image Velocimetry technique to obtain instantaneous two-dimensional velocity field with in a selected plane of the jet.

On-line Particle Image Velocimetry

A fully digital and operator interactive PIV system developed by Lourenco (1990) was used in this experiment. This instrument uses a high resolution CCD area sensors, replacing the conventional photographic recording and processing step, and state of the art microcomputer hardware and software. Unlike earlier digital approaches, it is capable of recording flows within a wide range of velocities, from a few millimeters per second to several hundreds of meters per second) while retaining the spatial resolution of a conventional 35mm film. The basis for the evaluation of the displacement of particle images is the auto-correlation method (see Lourenco et.al, (1994) for details). This system was designated as "On-line" PIV.

The main components of this fully integrated PIV are the laser source, with associated sheet forming optics, the high resolution video sensor, the microcomuter and image acquisition and processing hardware. A video camera (KODAK 1.4 Megaplus) with a CCD array containing 1320(H) x 1035(V) active pixels was used to acquire the multiply exposed images. The pixels are 6.8 μm square and have a center to center spacing of 6.8 μm. The spatial resolving power of this sensor array is equivalent to 74 line pairs per mm. The camera features a built-in 8 bit anolog to digital converter that produces a digital video output signal containing 256 gray levels. A customized digital interaface and frame buffer board in the host computer receive and store the digital frame data from the camera. For short exposure times, the maximum frame rate is about 6.9 frames/sec. Using a calibration experiment, Lourenco et.al (1994) have demonstrated that

the velocity measurement error is bounded and of the order of ± 1-2% full scale. Using this technique in combination with a velocity bias method, velocity measurements in regions of high shear can be made with good accuracy (Lourenco and Krothapalli (1994)).

2. APPARATUS, INSTRUMENTATION AND PROCEDURES

A blowdown heated jet facility was used for the experiment. This facility consists of a high pressure (2000 psig) reservoir with a capacity of 10 m^3 that is charged using a high displacement reciprocating air compressor. The desired stagnation pressure and temperature for the jet is obtained by passing the high pressure air through a series of control valves and electrical resistive heaters (power = 450kW). Microprocessor based closed loop controllers were used to maintain the stagnation pressure and temperature to within ±1% of the set values. For the detailed description of this facility reference can be made to Wishart (1994).

A convergent-divergent nozzle with a design Mach number of 2 was used. The nozzle exit diameter D, was 2.94 cm. The jet issued into an ambient medium. Stagnation pressure was varied to obtain underexpanded and overexpanded conditions. A converging axisymmetic nozzle with the same throat area (4.45 cm^2) as the Mach 2 nozzle was used to generate a highly underexpanded jet . For all the experiments considered here, the stagnation temperature was about 288 K. The exit Reynolds number based on fully isentropic conditions was about 3 x 10^6.

A standard schlieren technique was used to visualize the jet. The duration of the light flash was about 2.5 μsec. The image was captured on to a high resolution (2048 x 2048 pixels) Video camera (KODAK 4.2 Megaplus).

In applications of PIV to the measurement of high speed flows, the selection and implementation of the proper seeding strategy is a major factor contributing to successful measurements (Lourenco and Krothapalli (1994)). The jet was seeded with 0.8 μm Al_2O_3 particles. They are introduced through an agitated fluidized bed with low mass flow and velocity so as to allow only small particles to enter the flow. The suspended particles are then passed through a cyclone particle separator to remove any remaining large particles. The details of the seeding apparatus were given by Ross et.al. (1994). The ambient air was seeded with smoke generated by a Rosco 1500 Fog/Smoke generator. The generator produces particles in the range of 0.5 to 1.5 μm.

The laser sheet was created by using a Lumonics double pulse (pulse width =20 nsec) Ruby laser operating at 1 Hz. The width of the light sheet was about 15cm. The thickness of the sheet was about 1mm. The time between pulses was set at 1 μsec. To capture the velocity of the entrained fluid from the ambient medium and the details of the shear layers, a velocity bias was applied using a high speed (6000rpm) spinning mirror (Wishart (1994)).

Double pulse images were acquired using a 1.4 MB (1340x1035) Kodak digital Video camera in conjunction with FFD MkIII "On-line" PIV system. The images were processed on a rectangular grid (50x60). Using a i486, 66 MHz, based computer with an i860 accelerator board, velocity vectors were computed at a rate of 30 vectors/sec. A schematic arrangement of the apparatus is shown in figure 1.

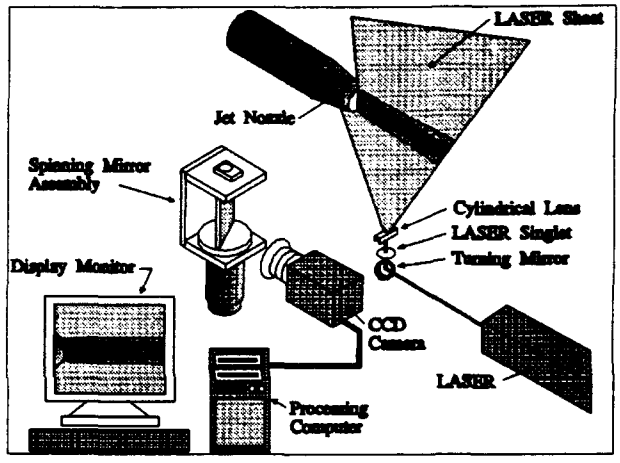

Figure 1. Schematic arrangement of the setup.

3. RESULTS AND DISCUSSION

Figure 2 shows typical schlieren pictures of the near field of the jet, issuing from the convergent-divergent nozzle, operating at three different pressure ratios (stagnation pressure, p_o/ ambient pressure, p_a). Photographs cover the region from the nozzle exit to three diameters downstream. The knife edge is oriented normal to the jet axis to accent the shock cell structure. Figure 2a corresponds to the case where the nozzle is operating close to the design condition with a very weak wave system. When the nozzle is operating away from the design condition, compression (overexpanded jet) and expansion fans (underexpanded jet) occur at the nozzle exit as shown in figures 2b and 2c respectively.

For highly underexpanded jets, strong shocks are formed within the first few diameters of the nozzle exit. Figure 3 shows an example of a highly underexpanded jet issuing from a convergent nozzle. The nozzle pressure

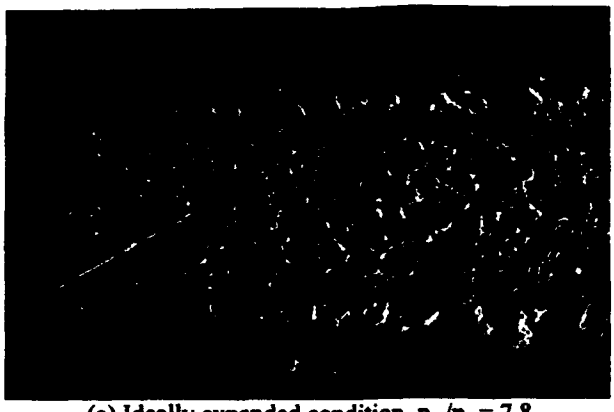

(a) Ideally expanded condition. $p_o / p_a = 7.8$

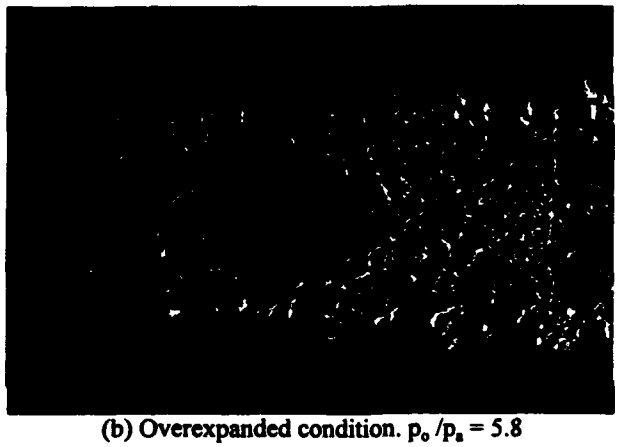

(b) Overexpanded condition. $p_o / p_a = 5.8$

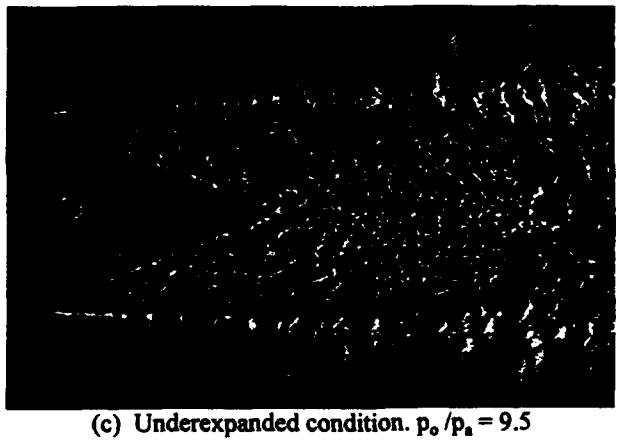

(c) Underexpanded condition. $p_o / p_a = 9.5$

Figure 2. Schlieren pictures of supersonic jet.

ratio correspond to that of an isentropically expanded Mach 2 jet. The resulting static pressure ratio (nozzle exit pressure/ambient pressure) is 4. The dominating feature of this flow field is the normal shock at the center portion of the jet terminated by a triple shock structure. The normal shock is commonly referred to as Mach disk. The distance between the nozzle exit and the Mach disk is a function of the nozzle pressure ratio. In figure 3, this distance was measured to be about 1.78 D in agreement with previous measurements (Landenburg et.al. (1949) and Tabei et.al (1991)).

A typical double exposure digital image of an ideally expanded jet, corresponding to figure 1, is shown in figure 4. Different seeding method used in the ambient (smoke) and the jet fluids (Al_2O_3) appear in the picture as a descriminator between the two distinct fluid regions. Seeding introduced in this fashion along with the velocity

Figure 3. Schlieren image of highly underexpanded jet. $p_o / p_a = 7.8$

bias makes it possible to obtain the data within the shear layers. From this and a number of similar pictures, the large structures observed in the shear layers appear to be incoherent and three dimensional. Such an observation has also been made by Clemens and Mungal (1992) in two dimensional shear layers under similar conditions.

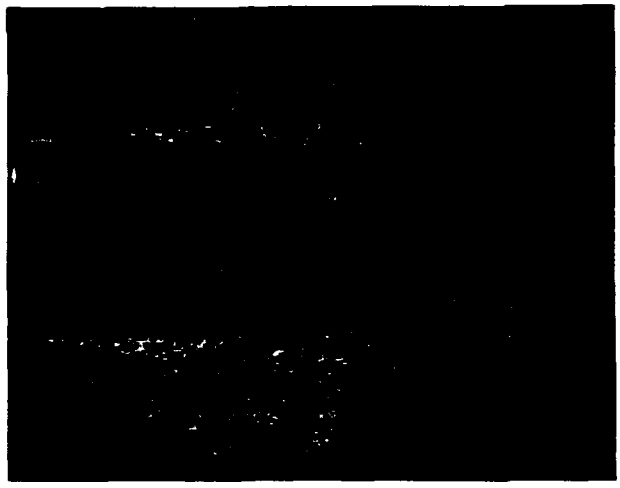

Figure 4. Double exposure digital image of an ideally expanded jet corresponding to figure 2a.

An illustration of the usefulness of double exposure images as flow visualization pictures is clearly seen in figure 5. This picture corresponds to the schlieren picture shown in figure 3. The variations in the particle concentration observed in the picture can be qualitatively related to the density of the fluid. For example, a distinct boundary in particle concentraton is noticed at the location of the Mach disk. In the subsonic region immediatly after the shock, a noticeable increase in the particle concentration is observed suggesting a relatively large value for the density as compared to that ahead of the shock. The slip-line shear layer inside the jet, that originate from the triple point, is also clearly seen. Because of their relative low convective Mach number ($M_c \approx 0.3$; where $M_c = (U_1 - U_2)/(a_1+a_2)$; U, a represent mean velocity and speed of sound respectively, and subscripts 1 and 2 designate the high and low speed sides of the shear layer) large coherent structures are observed. Due to the relatively high underexpanded condition of the jet, outer shear layers follow a concave curvature. Such shear layers generally promote the growth of streamwise structures as noticed by Krothapalli et.al (1991). As a result they become three dimensional.

Figure 5. Double expososure image of highly underexpanded jet corresponding to figure 3.

The double exposure images were processed using a cartesian grid (x, y; where x denotes the ordinate along the axis aligned with the centerline of the jet with its origin at the nozzle exit) of 50x60 corresponding to a physical space of 1.73x1.15 mm. Mean velocity fields corresponding to figure 2 are shown in figure 6 as uniformly scaled velocity vectors. These were computed using 12 instantaneous velocity fields. The mean velocity variation within shock cell structures is captured with

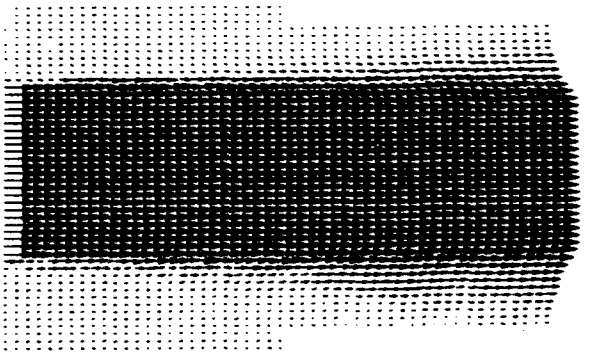

(a) Ideally expanded condition.

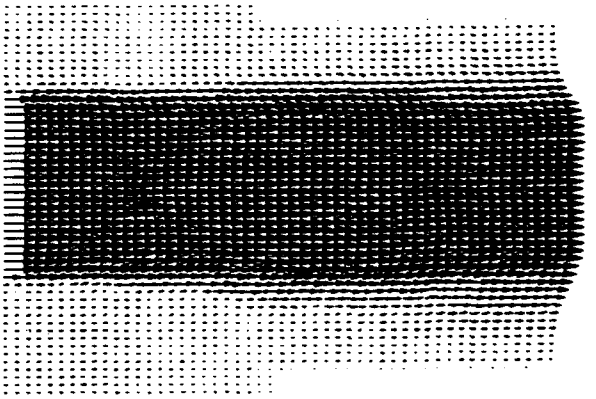

(b) Overexpanded condition.

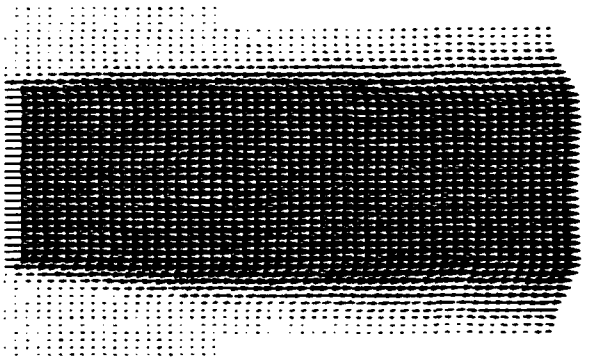

(c) Underexpanded condition.

Figure 6. Mean velocity vector fields for supersonic jets corresponding to schlieren images in figure 2.

fidelity as shown in the figure. A better representation of the shock cell structure is shown in figure 7. The corresponding out-of-plane component of vorticity was obtained as shown in figure 8. In addition to the outer shear layers, the inner slip-line shear layers were also captured. It is of interest to note that the vorticity strength of the slip-line shear layer is comparable to that of the

outer shear layer. For example, the maximum normalized value of vorticity ($\Omega_z D/U_e$) in the outer shear layer is found to be about 15, while for the slip-line shear layer it is about 11.

To asses the accuracy of the PIV data, a comparison is made with the centerline velocity data obtained using pitot and static pressure measurements in an underexpanded jet. Figure 9 shows such a comparison for the jet operating at conditions corresponding to those in figure 7. The velocity data is normalized with the exit velocity obtained from the pressure data, which agrees with the theoretical value. The PIV data at the nozzle exit is suspect due to light reflection from the nozzle surface which dominate the scattering from the particles. The agreement of the PIV data with that derived from pressure measurements is good upto the shock location. Due to the particle lag the PIV data after the shock differs from the fluid velocity. The solid line represents a model taking into account of particle dynamics (Ross et.al (1994).

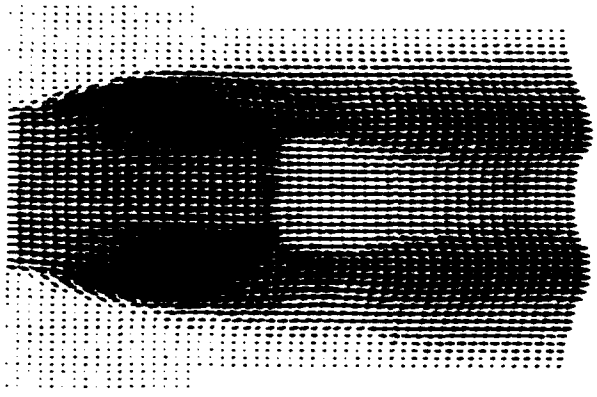

Figure 7. Mean velocity field for highly underexpanded flow condition corresponding to figure 3.

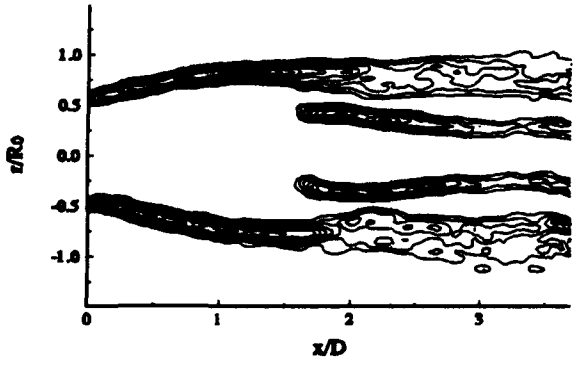

Figure 8. Mean vorticity field for highly underexpanded jet. Outer most contour value = 2 ; increment = 0.9.

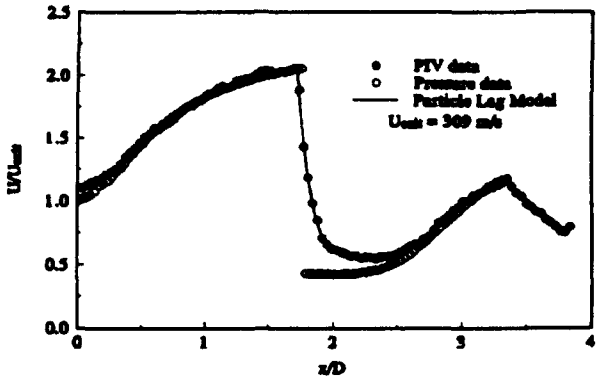

Figure 9. Variation of the normalized centerline velocity of an highly underexpanded jet. $p_o/p_a = 7.8$

4. CONCLUSIONS

Application of the "on-line" PIV, to supersonic jets is demonstrated by the measurement of the shock cell structure in overexpanded and underexpanded axisymmetric jets. By using different seeding material for the ambient medium and the jet fluid in combination with an appropriate velocity bias technique, details of the complex velocity field is obtained with fidelity. These include flows with three-dimensional shear layers, shocks and expansion fans. In particular, for the underexpanded jet, the internal shear layer associated with the slip stream is identified. The particle dynamics model proposed by Ross et.al (1994) was found to accurately estimate the effects of particle lag in the PIV data.

ACKNOWLEDGMENTS

This work was initiated with the support of General Electric Aircraft Engines at Evendale with Dr Chowdary Bobba as the technical monitor. It is currently supported by NASA Hq. under the Grant number NAG - W2930. We like to thank Mr. James King and Mr. Chris Ross for providing us with the pressure and particle dynamics data.

REFERENCES

Clemens, N.T., and Mungal, M.G., "Two- and Three-Dimensional Effects in the Supersonic Mixing Layer", AIAA Journal, Vol. 30, No. 4, 1992, pp 973-981.

Krothapalli, A., Buzyna, G., and Lourenco, L., "Streamwise Vortices in an Underexpanded Jet", Physics of Fluids A, Vol. 3, No. 8, 1991, pp 1848-1851.

Ladenburg, R., and Bershader, D., " Interferometry", in Physical Measurements in Gas Dynamics and Combustion, High Speed Aerodynamics and Jet Propulsion, Vol. IX, 1954, pp 47-75.

Ladenburg, R., Van Voorhis, C.C., and Winckler, J., "Interferometric Studies of Faster than Sound Phenomena. PartII. Analysis of Supersonic Air Jets", Physical Review, Vol. 76, No. 5., 1949, pp 662-677.

Lourenco, L.M., "On-line Particle Image Velocimetry", Bulletin of the American Physical Society, vol. 35, No. 10, 1990, pp 2237.

Lourenco, L.M., Gogineni, S.P., and LaSalle, R.T., "On-line PIV: An Integrated Approach", Applied Optics, Vol. 33, No.13, 1994, pp 2465-2470.

Lourenco, L.M., and Krothapalli, A., "Application of PIV in High-Speed Wind Tunnel Testing (Invited)", 32nd Aerospace Sciences Meeting, AIAA Paper No. 94-0084, January 1994.

Lourenco, L.M., and Krothapalli, A., "On the Accuracy of Velocity and Vorticity Measurements with PIV", Submitted to Experiments in Fluids, May 1994.

Ross, C., Lourenco. L.M., and Krothapalli, A., "Particle Image Velocimetry Measurements in a Shock-Containing Supersonic Flow", 32nd Aerospace Sciences Meeting, AIAA paper No.94-0047, January 1994.

Tabei, K., Shirai, H., and Takakusagi, F., "Density Measurements of Underexpanded Free Jets of Air from Circular and Square Nozzles by Means of Moire-Schlieren Method", JSME International Journal, Series II, Vol 35, No. 2, 1992, pp 212- 217.

Wishart, D.P., "Structure of Heated Supersonic Axisymmetric Jets" Ph.D Dissertation, Florida State University, September 1994.

PRECISION WHOLE-FIELD VELOCITY MEASUREMENTS WITH FREQUENCY-SCANNED FILTERED RAYLEIGH SCATTERING

Richard B. Miles, Joseph N. Forkey, Noah Finkelstein, and Walter R. Lempert

Department of Mechanical & Aerospace Engineering
PRINCETON UNIVERSITY
Princeton, New Jersey 08544 U.S.A.

ABSTRACT

Precision measurements of velocity, temperature, and density with Filtered Rayleigh Scattering require that the filter characteristics be accurately known and that the geometrical factors be properly modeled. Failure to account for these effects in low F number optical systems will lead to large errors in both the velocity and temperature measurements. The best signal-to-noise is achieved with a sharp cut-off blocking filter whose width exceeds the linewidth of the Rayleigh light scattered by the air. The signal-to-noise can be further enhanced by operating in the ultraviolet region of the spectrum where large enhancements in the scattering cross section and better optical filters are available.

1. INTRODUCTION

Filtered Rayleigh Scattering is a diagnostic tool which has been recently developed for imaging high-speed flow fields [Miles and Lempert (1990)]. The approach relies on the utilization of a narrow linewidth laser source which illuminates the flow and an atomic or molecular blocking filter which is placed in front of a camera which observes the scattered light. The filter has a very sharp cut-off (from 10% transmission to 90% transmission in a few hundred MHz) and an attenuation of many orders of magnitude on line center. Filtered Rayleigh Scattering has two major applications. The first is the observation of weak scattering by blocking strong background light which is only a few hundred MHz away. The second is the spectral characterization of the scattered light.

Both of these features have been demonstrated in recent laboratory experiments. The blocking capability of the filter can be used to remove light scattered from windows and walls in order to permit the observation of weak Rayleigh scattering from the flow field itself. For example, a series of two-dimensional cross-sectional slices of the flow field within a Mach 3 inlet duct were imaged using this technique, leading to a volumetric picture of the crossing shock and boundary layer structure [Forkey, et. al. (1994)]. Without the background suppression feature, the light scattered from the air would have been obscured by the light scattered from windows and walls. In this experiment, the flow cross sections were observed from downstream through a mirror placed in the flow on a sting, and the resulting Doppler effect provided enough frequency shift to achieve strong background suppression. This feature has also been used to observe compressible mixing layers [Elliot, et. al. (1992)].

The ability of the filter to resolve the spectral character of the light scattered from a flow was demonstrated in a Mach 5 free jet, which was illuminated at 45° by a laser sheet [Miles, et. al. (1992)]. As the laser was frequency tuned, the light scattered from the Mach 5 jet was swept in frequency through the absorption band of the filter. In this case, the light that was scattered was not only shifted in frequency due to the Doppler effect, but it was broadened by thermal motion of the air molecules. By observing the Rayleigh scattering from air at a particular location in the flow field as the laser frequency was swept, the flow velocity, temperature, and relative density were determined. Other researchers have also addressed this aspect of Filtered Rayleigh Scattering, exploring the velocity profile of mixing layers [Elliott, et. al. (1994)] and examining the potential of Filtered Rayleigh Scattering for measurement of mass flow [Winter and Shirley (1993)].

The utility of the Filtered Rayleigh Scattering technique for the measurement of velocity, temperature, and density, relies on the accuracy with which these measurements can be made. That accuracy depends on numerous factors. The fundamental noise process is shot noise associated with the number of photoelectrons collected from each resolvable image element. To reach this limit, however, many other things must be precisely known. These include precise tracking of the laser frequency, a precise characterization of the cell transmission, and a precise understanding of the errors introduced by the collection optics. Two paradigms will be used in this discussion. The first is the iodine molecular vapor filter used in conjunction with a frequency-doubled Nd:YAG laser, and the second is the mercury atomic vapor filter used in conjunction with a frequency-tripled titanium-sapphire laser. All the Filtered Rayleigh scattering experiments, to date, have been done using the first paradigm, the iodine molecular vapor filter. For future measurements, however, the mercury vapor filter shows great promise. Preliminary mercury filter characterizations scans will be shown together with a discussion of the potential impact of the mercury vapor/Titanium:Sapphire system.

2. IODINE FILTER

The operation of the iodine molecular filter relies on specific absorption lines associated with the B-X electronic band of iodine. These transitions have been studied before, and current literature exists which delineates line positions

and extinction coefficients [Gersternkorn and Luc; Tellinghuisen (1982); Glaser (1985)]. In addition, the line broadening can be modeled assuming a combination of thermal and collisional processes. While the accuracy of the literature values is good, it is not sufficient for precision measurements. For example, relative line positions must be known to an accuracy of a few MHz, the line broadening parameter must be verified to the same accuracy, and the absorption coefficients must be known to within a few percent. These are all important since the measurement of the velocity has an error of approximately 1 m/sec if the line position is off by 1 MHz (or 1 part in 10^8), and the measurement of the temperature is critically dependent on the knowledge of the slope of the filter cut-off, which, in turn, is a function of the broadening parameter and the extinction coefficient. Generally, the iodine molecular absorption cell is operated at high enough iodine density so that the absorption line is optically thick. In that case, the maximum slope of the cut-off scales as the square root of the log of the product of the line center extinction coefficient, α_0, times the path length, l, divided by the thermal linewidth, Δf:

$$\frac{d\left(I/I_0\right)}{df} = \frac{0.74}{\Delta f}\sqrt{ln\left(\alpha_0 l\right)} \qquad (1)$$

In order to achieve sharp cut-off, the thermal linewidth must be narrow (i.e., the temperature low, and the mass of the molecule high), and the extinction must be large (i.e., high vapor pressure or long path length). The accuracy of the measurement improves with a sharp cut-off filter. This suggests that a heavy gas vapor with a high vapor pressure such as iodine or mercury, is desirable. It also suggests that the cell operate at the highest possible extinction coefficient. As a practical matter, this is limited by the out-of band absorption, normally associated with very weak absorption phenomena. In the iodine cell, for example, there is a background continuum absorption due to the C-X transition in iodine. This continuum absorption leads to a maximum contrast before the off-line center transmission begins to drop significantly. In iodine, this maximum contrast is approximately 5 orders of magnitude.

A series of experiments have been conducted in order to establish with precision the location of the absorption lines, the behavior of those lines as a function of cell temperature and iodine partial pressure, the maximum extinction, and the effect of weak background absorption. These experiments used a pair of continuous wave Nd:YAG lasers. The first of these was frequency-doubled, modulated, and locked to a nearby optically thin iodine absorption line. A portion of the infrared beam from this reference laser was passed into an optical fiber and onto a detector. The second laser was frequency-doubled and passed through the iodine cell to be characterized. A portion of the infrared light from this laser was combined with the first laser in the optical fiber and passed onto the detector. The beat frequency between the two lasers was measured using a high frequency counter which was accurate to better than 1 MHz. As the second laser was swept in frequency, the transmission of the iodine cell was recorded while the frequency of the second laser was precisely monitored. These transmission versus frequency measurements were repeated for various different iodine cell vapor pressures, leading to optically thick absorption profiles measured with an accuracy better than 1 MHz.

A model of the iodine absorption profile was initially constructed using literature values for line positions and extinction coefficients, and the classical expression for thermal broadening. This model was then corrected using the accurately measured line positions, so that it gave a precise match with the experimental data taken over the operating range of interest. Figure 1 shows the measurement of the iodine absorption spectrum and the corrected model fit to that measurement. Note the correction has been made for the optically thick line of interest, the residual error is still apparent on other lines shown. Once this model has been developed and validated, it can be used as a tool to deconvolve from the experimental data the lineshape, position, and strength of the scattering from the particular observed element in air.

In the case where the scattering light level is low, fast (i.e., low F number) optics are desirable in order to collect the most light possible. In this case, additional corrections must be made to the data to account for the subtended angle of collection optics. These corrections must take into account two important phenomena. The first is that the Doppler shift associated with light collected through one portion of the optics is slightly different from that associated with light collected through another portion of the optics. This occurs because the Doppler shift observed is related not only to the angle of the incident laser beam, but also to the angle at which the scattering molecule is observed. The second major correction that needs to be applied is due to the varying path lengths of the light rays as they pass through the iodine cell. In the case of an optically thick transition, these varying path lengths do not introduce a significant change in the data, but should be taken into account for the highest precision measurements.

For example, the cell response to an idealized Mach 5 jet (velocity of 721 m/sec, static temperature of 50 K, and static pressure of 40 torr) illuminated at 45°, and with scattered light collected normal to the jet (see Fig. 2), is shown in Figs. 3 and 4 for collection optics with a lens diameter of 1/5 of the distance from the lens to the jet (Fig. 3), and with a lens diameter equal to the distance from the lens to the jet (Fig. 4). Each figure shows three curves. The dark curve corresponds to the response of the system neglecting the geometric factors and neglecting broadening of the light scattered from the air (i.e., assuming a temperature of 0°K or a mass of ∞). This curve just gives the filter response. The dotted line shows the system response to the point in the center of the field-of-view and includes the geometric factors associated with light collection. The dashed curve incorporates the thermal broadening of the air and represents the modeled response of the filter and optical collection system to the 50 K air in the Mach 5 flow. The curves all cross at the same point since the broadening in all cases is symmetric. This crossing point is used to determine the velocity of the flow. It is evident that the $d_o/D = 1$ collection optics lead to an effective broadening of the filter cut-off, which would, in the absence of proper modeling, be misinterpreted as a higher temperature of the gas flow. These geometrical factors are different for different points in the image due to vignetting and the associated scattering angles of the light collected. For example, Fig. 5 shows the effect on the observed element at the farthest edge of the field-of-view.

This figure corresponds to Fig. 4 $\left(\text{i.e., } {}^{d_o}/_{D} = 1\right)$, but note that the frequency is offset somewhat (about 350 MHz) because the element observed is seen from a different angle, so it gives a significantly different apparent velocity. This shift is still apparent with a ${}^{d_o}/_{D} = 5$ collection geometry (Fig. 6), but is significantly smaller (about 70 MHz). Nevertheless, failure to account for this shift will lead to a significant error (approximately 50 m/sec or 7%) in the velocity measurement of the Mach 5 jet.

In addition to the fundamental filter/collector image transfer characteristics, one must also add the laser linewidth to fully model the image transfer function. Once this modeling is complete, then the data associated with any point in the image can be deconvolved so that the frequency shift and line profile associated with the scattering at that point can be determined. A fit to that data then yields the temperature, velocity, and density at that particular point in the flow field. For example, the data for the Mach 5 jet is shown in Fig. 7 together with the fit. Here direct (unshifted) background scattering of the laser is also present and included in the fit. The data is noisy, largely because of jet fluctuations rather than shot noise. Even with this large amount of noise, the fit gave the velocity and density with an accuracy of 4%, and temperature with an accuracy of 8%.

Once the transfer function of the laser filter and collection optics is determined, the limitations of the measurement accuracy are, primarily, signal-to-noise associated with each resolvable element in the image and the experimental factors, such as the precise measurement of the laser incidence angle, the measurement of the scattering element, and the locking stability of the high power laser. This locking stability error arises due to the fact that a pulsed frequency-doubled YAG laser is used for the actual measurement, and that laser is locked to an injection laser which is slowly tuned and precisely monitored. The output of the high power laser is assumed to be at the same frequency as the injection laser. With currently available commercial high power lasers, the ability to track the injection laser is related to the speed of the scan. If the scan is too rapid, the higher power laser cannot track, and the injection locking becomes intermittent. With designs currently under development, the high power laser will track the injection laser on a pulse-by-pulse basis, so intermittent locking will not be present. There may, however, be some residual frequency pulling that has yet to be examined.

In the absence of experimental factors, the fundamental limitation is the shot noise associated with the number of photoelectrons collected from each resolved element. For example, assuming: a laser with an energy, E_L of 100 mJ at 0.532 micron (frequency-doubled Nd:YAG laser); expanded with a height, H, of 2 cm, and a thickness, δ, of 50μ; air at standard temperature and pressure $\left(\frac{N}{V} = 2.69 \times 10^{19}\ /cc\right)$ with a differential Rayleigh cross section, ${}^{\partial\sigma}/_{\partial\Omega}$, of $6 \times 10^{-28} cm^2\ /sr$; a resolved volume element, V, of 50μ x 50μ x 50μ; a collection system consisting an F5 lens, imaging a 2 x 2 cm cross-sectional area of the flow onto a 1 cm^2 CCD device with 25 x 25μ elements (a magnification factor, m, of 0.5); and an additional 10% loss due to optical transmission $(\eta = 90\%)$, the predicted number of photons present at the detector per resolution element (Eq. 2) is 160 for each pulse of the laser.

$$F = \left(\frac{E_L}{\hbar w}\frac{1}{H \bullet \delta}\right)\left(\frac{N}{V}\right)\left(\frac{\partial\sigma}{\partial\Omega}\right)(V)$$
$$(\eta)\left[\frac{\pi}{4F^2}\left(\frac{1}{1+{}^{1}/_{m}}\right)^2\right] \qquad (2)$$

With a 40% quantum efficiency detector (e.g., a high efficiency CCD), this corresponds to 64 photoelectrons collected. The shot noise is equal to the square root of the number of photoelectrons, so with a single shot, the density can only be measured to one part in eight, or 12.5%. To achieve a density measurement of better than 1%, at least 10,000 photons per resolution element must be accumulated. This corresponds to approximately 160 laser pulses, or 16 sec at 10 pulses/sec. For more accurate single pulse measurements, faster collection optics are required. For example, an F=1 lens will collect 25 times as many photons, leading to an accuracy of approximately 2.5% for the measurement of density in a single shot.

The measurement of velocity and temperature requires either that the laser be scanned, that the scattering volume be observed through filters from several different angles, that laser illumination be incident from several angles, or that filters with slightly different cut-off frequencies be used. The most straight-forward approach is to scan the laser frequency. Of course this leads to an average velocity and temperature at each point. The velocity and temperature are then found by fitting the curve, as discussed previously. The velocity is determined from the laser frequency at which the filter attenuates the signal, and the temperature is determined by the rate at which the signal is attenuated as the laser is swept in frequency. The accuracy of both these measurements depends on the quality of the fit. By tuning the laser far enough so that the scattered light has a frequency such that it is fully transmitted through the molecular filter at the beginning of the scan, and again is fully transmitted at the end of the scan, then the velocity can be determined quite accurately from the symmetry of the attenuation profile. In this case, the accuracy of the velocity measurement is similar to that of the density. The temperature measurement, on the other hand, requires that the slope of the curve be fitted. This means that the data associated with low transmissivity is important. This data corresponds to a reduced number of photons collected, and, consequently, a higher shot noise. For this reason, the temperature measurement is intrinsically less precise than velocity or density.

An estimation of the filter performance can be made by recognizing that an ideal notch blocking filter can be visualized as a low pass step filter with a cut-off frequency, f_{-c}, plus a high pass step filter with a cut-off frequency of f_{+c}. The signal passing through the low pass filter can be expressed as the integral of the scattering frequency profile R(f) up to the cut-off frequency.:

$$S_{-} = \int_{-\infty}^{f_{-c}} R\left(f - \frac{v}{\lambda} - f_L\right) df \qquad (3)$$

where the argument $f - \frac{\nu}{\lambda} - f_L$ includes the Doppler shift associated with the flow velocity and the frequency, f_L, of the illuminating laser. The signal passing through the high pass filter is the integral beginning with the upper cut-off frequency and continuing to infinity:

$$S_* = \int_{f_{+c}}^{\infty} R\left(f - \frac{\nu}{\lambda} - f_L\right) df \qquad (4)$$

The overall signal recorded is just the sum of these. As the laser frequency, f_L, is scanned, the signal is swept through the filter profile, and the light collected represents a convolution of the filter characteristic with the signal. For example, if the scattered signal, R(f), has a Gaussian profile, 10% of the light will be attenuated when the lower frequency cut-off, f_{-c}, is $\sqrt{2} \times \Delta f$ above the peak scattering frequency. As the laser is swept, 50% attenuation will occur when the filter cut-off is exactly at the peak frequency, and 90% will occur when the scattering peak frequency is $\sqrt{2} \times \Delta f$ above the lower cut-off. There will be very little light transmitted until the upper cut-off is reached, and then the signal returns to full strength following the same curve. In order to achieve the maximum contrast, the filter width should be much greater than the linewidth of the scattered light. If, for example, the filter width is just equal to the Gaussian scattering linewidth, Δf, then even at the minimum, the filter transmission will still be 16%, since some light will be transmitted corresponding to those portions of the scattering falling above the upper cut-off and below the lower cut-off. For molecular blocking filters much narrower than that, the temperature becomes difficult to measure because the contrast between full transmission and maximum attenuation is reduced. The iodine filter has a linewidth of approximately 1.8 GHz, which matches well the 1.1 GHz Gaussian linewidth of light scattered from room temperature air.

3. MERCURY VAPOR FILTER

An attractive approach to reducing the noise is to move into the ultraviolet portion of the spectrum. The Rayleigh scattering cross section scales as the fourth power of the frequency times the square of the polarizability. In the ultraviolet portion of the spectrum the frequency is approximately a factor of two higher, and the polarizability is increased by 10% or so. Many different materials can be used for optical filters in the ultraviolet, but a very attractive candidate is mercury vapor. Mercury absorbs strongly at 0.2537 microns, and also has the desirable characteristics of high mass and high vapor pressure. The fact that it is an atomic vapor leads to a very simple absorption spectrum consisting of nine spectral lines which come from the six different isotopes of mercury (196, 198, 200, 201, 202, and 204), and associated hyperfine splitting. This region of the spectrum is accessible using frequency-tripled Titanium:Sapphire lasers, or frequency-tripled Alexandrite lasers. An example of an experimental scan of a 5 cm long mercury cell with a side-arm temperature of 23°C is shown in Fig. 8. A close-up of the Hg_{202} transition is shown in Fig. 9, along with the thermally and collisionally broadened model. The maximum transmission of 70% is a consequence of window reflectivity and does not correspond to background absorption in the mercury vapor. The predicted contrast of this filter is 31 orders of magnitude.

An experiment set-up with the same collection optics as described in the previous section, and, again, using a single 100 mJ laser pulse expanded to 2 cm sheet, gives 1.55×10^3 photons collected onto a 25 micron x 25 micron detector array. Using a thinned CCD device, 40% collection efficiency can be achieved, leading to more than 600 photoelectrons collected per pulse. This corresponds to approximately 10 times the number of photoelectrons collected at 0.532 microns in association with the iodine filter. This increased count reduces the shot noise significantly. For example, with this collection geometry the shot noise decreases from approximately 12% to 4% per laser shot. Decreasing the F number to an F1 system increases the number of photons collected per resolution element to 15,000, which leads to a shot noise of less than 1% per pulse. The 2.76 GHz bandwidth of the filter matches well the approximately 2 GHz width which is characteristic of the Rayleigh scattered light at this wavelength.

The mercury filter/Titanium:Sapphire laser system will lead to much higher accuracy in the measurements of density, temperature, and velocity, than would be possible for the iodine filter/frequency-doubled Nd:YAG laser configuration. Several other features of the ultraviolet approach are worth mentioning. One is that the on-line center extinction can be much greater than for iodine vapor, due to the absence of background absorption bands in mercury, so that light scattered from boundary layers close to surfaces can be directly observed. In addition, in the ultraviolet, background scattering from windows and walls is reduced due to the low reflectivity of metallic surfaces at this wavelength. This leads to an additional enhancement in the practical signal-to-noise limit of the experiment.

4. CONCLUSIONS

Filtered Rayleigh Scattering promises to be a highly accurate measurement tool for air flows. In order to achieve high accuracy, the cell must be properly characterized to take into account the filter transmission and collection geometry. Once these have been properly accounted for, the measurement of velocity, temperature, and density is limited primarily by the shot noise associated with photon detection. This shot noise can be reduced by using fast collection optics and high efficiency detectors. Due to the fact that Rayleigh scattering does not saturate, signal levels may also be increased by using higher power laser sources. A particularly attractive approach to reducing the noise level is to move into the ultraviolet portion of the spectrum and take advantage of large enhancement in the scattering cross section. In this case, a mercury atomic vapor filter is used and there is a significant reduction in shot noise.

4. ACKNOWLEDGMENTS

This work was conducted under the support of the Air Force Office of Scientific Research, NASA-Langley, NASA-

Lewis, and Small Business Innovative Research Programs under M.L. Energia, Inc. and Schwartz Electro-Optics, Inc.

5. REFERENCES

Elliott, G.S.; Samimy, M.; and Arnette, S.A. (1992) A study of compressible mixing layers using Filtered Rayleigh Scattering, AIAA-92-0175.

Elliott, G.S.; Samimy, M.; and Arnette, S.A. (1994 Details of a molecular filter based velocimetry technique, AIAA-94-0490.

Forkey, J.N.; Lempert, W.R.; Bogdonoff, S.M.; Miles, R.B.; and Russell, G. (1994) Volumetric imaging of supersonic boundary layers using filtered Rayleigh Scattering background suppression. AIAA 94-0491, 32nd Aerospace Sciences Meeting & Exhibit, Reno, Nevada.

Gersternkorn, S. and Luc, P., Atlas du Spectre d'Absorption de la Molecule d'Iode, (Editions du CNRS).

Glaser, M. (1985) Identification of hyperfine structure components of the iodine molecule at 640 nm wavelength, Opt. Comm., Vol. 54 (No. 6), p. 335.

Miles, R.B. and Lempert, W.R. (1990) Two-dimensional measurement of density, velocity, and temperature of turbulent air flows from UV Rayleigh scattering, Appl. Phys. B, Vol. B51, p.1.

Miles, R.B.; Forkey, J.N.; and Lempert, W.R. (1992) Filtered Rayleigh scattering measurements in supersonic/hypersonic facilities. AIAA-92-3894, 17th Aerospace Ground Testing Conference, Nashville, TN.

Tellinghuisen, J. (1982) Transition strengths in the visible-infrared absorption spectrum of I_2, J. Chem. Phys., Vol. 76 (10), p. 4736.

Winter, M. and Shirley, J.A. (1993) Air mass flux measurement system using Doppler shifted Filtered Rayleigh Scattering,AIAA-93-0513.

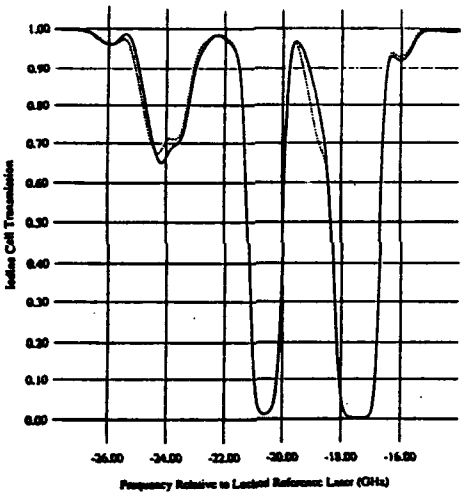

Figure 1. Plots show comparison between I_2 cell data (solid line) and theoretical model of iodine absorption (dotted line). Data is renormalized to 100% transmission away from absorption lines, since background absorption and absorption due to windows is not included in the model.

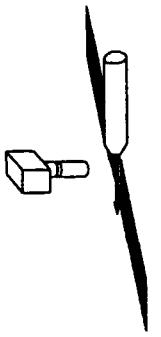

Figure 2. Experimental geometry for Mach 5 jet calculations and measurements. The laser is incident at 45° to the downward directed jet. Flow conditions: Mach 5 with T_O=300 K, P_O=400 psi (velocity: 721 m/s; static temperature: 50 K; static pressure: 40 torr).

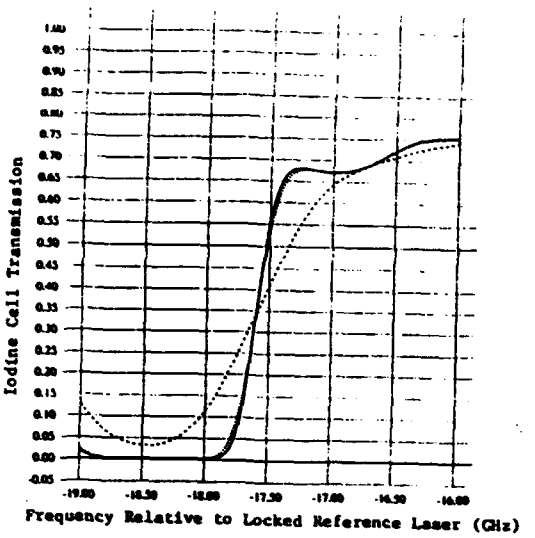

Figure 3. Response of the I_2 filter to the Mach 5 flow with a collection lens placed 5 times its diameter from the sample volume. The solid curve is the ideal response assuming no frequency broadening of the scattered light, the dotted curve is the same with geometrical collection factors added in, and the dashed curve is the predicted response including broadening, geometry, and the filter profile.

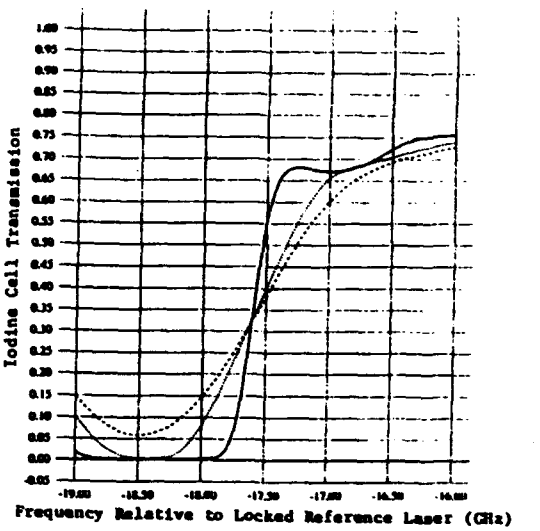

Figure 4. Response of the I_2 filter to a Mach 5 flow with the collection lens placed a distance equal to its diameter from the observed sample volume. Curves are as identified on Fig. 3.

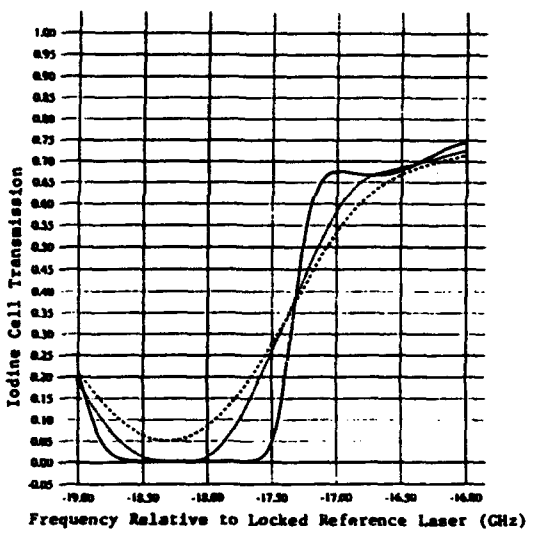

Figure 5. Response of the I_2 filter to the sample volume element at the edge of the field-of-view for the same collection geometry as in Fig. 4. Note that the apparent response of the filter has been shifted by approximately 350 MHz.

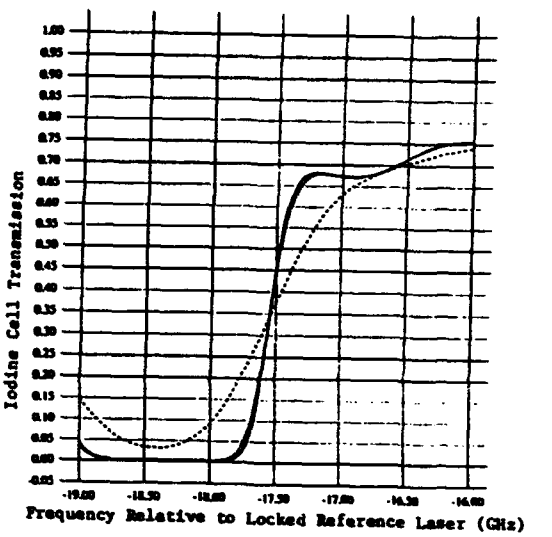

Figure 6. Response of the I_2 filter to a sample volume element at the edge of the field-of-view for the same collection geometry as in Fig. 3. Note that the frequency offset seen in Fig. 5 is reduced, but is still present and must be taken into account.

Session 27.
Two Phase Flow I

LASER SHADOWGRAPHY OF THE BREAKUP OF A LIQUID SHEET DOWNSTREAM OF A MODEL PREFILMING AIRBLAST ATOMISER

M. Adzic[1], I.S. Carvalho and M.V. Heitor

Technical University of Lisbon
Instituto Superior Técnico
Department of Mechanical Engineering
Av. Rovisco Pais
1096 Lisboa Codex, PORTUGAL

ABSTRACT

The break-up of an annular liquid film in the presence of co-flowing air streams is analysed, making use of laser shadowgraphy and a high speed video camera. The experiments were conducted in turbulent flows for a liquid mass flow rate of 10.8 g/s, three primary (i.e., inner) air velocities (20 - 90 m/s), two secondary (i.e., outer) air velocities (20 - 40 m/s), and two liquid film thicknesses (0.2 - 0.7 mm). The results include the analysis of the film structure at break-up and of the distance and time of break-up and are compared with an analytical model, suggesting that the deterioration of the liquid film close to the atomising edge exhibits a periodic behaviour and is mainly dependent on the primary air velocity. Film thickness strongly affects the time and length scales of the break-up process for the velocity range under study.

1. INTRODUCTION

Airblast atomisers have many advantages over pressure atomisers, especially in their application to gas turbine engines (Simmons, 1980; Rizk et al., 1987) of high pressure ratio. They require lower fuel pressures and produce a finer spray. Moreover, because the airblast atomisation process ensures thorough mixing of the air and fuel, the resulting combustion process is characterised by very low soot formation and a blue flame of low luminosity, resulting in relatively cool liner walls and a minimum of exhaust smoke. A further advantage of the airblast atomiser is that it provides a sensibly constant fuel distribution over the entire range of fuel flows. Also important, is that the temperature distribution of the gases, which is determining to turbine blade life at high pressures, may be adequately predicted from temperature surveys carried out at lower and more convenient levels of pressure.

Despite the extensive research on pre-filming airblast atomisation over the last three decades (Rizkalla and Lefebvre, 1975; Rizk and Lefebvre, 1980; Sattelmayer and Wittig, 1986; Aigner and Wittig, 1988; Jasuja, 1990), the basic mechanisms leading to the atomisation need further clarification as a number of determining parameters, which influence the droplet size distribution and have not in general been investigated separately. While increasing air/liquid velocity has been shown to produce smaller droplets, the mechanism for break-up is not yet clearly established, as recently discussed by Engelbert et al. (1994). However, a common analysis has been based on the following processes: i) the shear induced in the liquid/air interface causes waves (dilational and sinusoidal) formed on the surface of the liquid sheet, and ii) the waves grow and separate from the liquid sheet in the form of ligaments and/or liquid clusters, which subsequently fragment into droplets.

Because the geometry of an airblast atomiser is somewhat complex, a planar liquid sheet has been used in most of the experiments (Sattelmayer and Wittig, 1986; Beck et al., 1991; Stapper et al., 1992; Call et al., 1993). Most sheet disintegration research (Arai and Hashimoto, 1985; Sattelmeyer and Wittig, 1986) has since been performed on simplified nozzles similar to those of Rizk and Lefebvre (1980). Previous research has been mainly aimed at studying how the final droplet size distribution is affected by air and liquid properties and geometry of the nozzle (Rizk and Lefebvre, 1980; El-Shanawany and Lefebvre, 1980; Shaw and Jasuja, 1987), as also reviewed by Lefebvre (1989). The analysis has been considerably extended by Engelbert et al. (1994) through the combination of high-speed photography and phase-Doppler velocimetry but, again, the results are limited to the breakup of a simple liquid jet surrounded by a coaxial flow of air.

This paper considers the breakup of an annular liquid sheet surrounded by inner and outer coaxial air streams, in a nozzle configuration which resembles those used in practical combustors. The main concern of the study is

[1] visiting researcher, on leave from the University of Belgrade

the detailed analysis of the near exit zone of a prefilming airblast atomiser. Laser Doppler measurements were carried out to characterise the mean and turbulent air velocity field in the absence of the liquid film. Then, laser shadowgraphy and high speed video were used to analyze the characteristics of the liquid film, and the results used to determine the time and length scales of the break-up process. The next section describes the flow configuration and the experimental techniques used throughout the work. Section 3 presents and discusses the results and the main findings are summarized in the last section.

2. EXPERIMENTAL METHOD

2.1. *The Model Prefilming Airblast Atomiser*

Figure 1 shows a schematic diagram of the airblast atomiser used throughout the work, which consists of three coaxial cones, as follows: i) an inner cone with a 5° angle and an exit radius of R_i = 2.5 mm; ii) an intermediate cone for water flow, which may provide an annular water film with a thickness in the range of 0.2 to 0.7 mm; and iii) a 70 mm long external cone with an angle of 35° and an exit radius of R_O = 20 mm. Air can be fed through the inner and outer cones separately and the results presented here are concerned with single and coaxial jets without swirl for inner air velocities, U_i, up to 89.2 m/s and velocities of the outer air stream, U_O, of 20 and 40 m/s. Table 1 summarizes the flow conditions used. Tests were also carried out with coaxial swirling jets and the results have shown that for the reduced inner atomising air velocities reported here, the influence of swirling the outer air flow is small, when compared with the influence of the inner air velocity. Details of this phenomena are reported elsewhere. The experiments with the liquid sheet were obtained for a constant mass flow rate of 10.8 g/s, and for a liquid film thickness of 0.2 or 0.7 mm.

2.2. *The Experimental Techniques*

The velocity field for the air flow downstream of the model atomiser was measured by a dual-beam forward-scatter laser-Doppler velocimeter, which comprised an argon-ion laser operated at 514.5 nm and with sensitivity to the flow direction provided by light frequency shifting from acoustic-optic modulation (double Bragg cells). The half-angle between the beams was 4.62° and the calculated dimensions of the measuring volume at the e^{-2} intensity locations were 1.676 and 0.135 mm. The transfer function in the absence of frequency shift is 3.194 MHz $m^{-1}s$. Forward scattered light was collected by a 150 mm focal length lens and focused into the pinhole aperture (300 mm) of a photo multiplier with a magnification of 1. The output of the photo multiplier was band-pass filtered and the resulting signal processed by a frequency counter operated in the single-measurement-per-burst mode with a fixed number of cycles validated in the time domain. The validated data were transferred to a computer, where the time-average moments of velocity were evaluated.

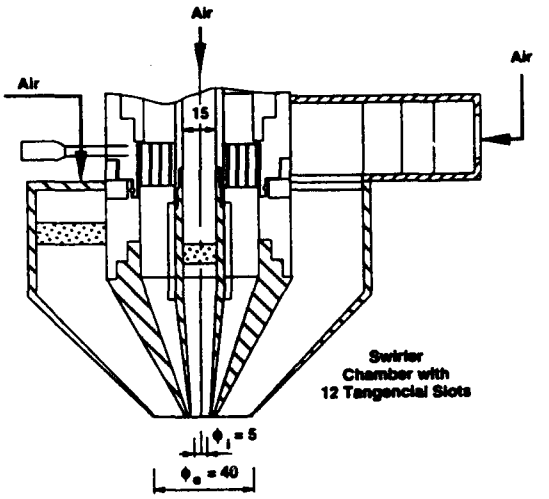

Figure 1. Schematic diagram of flow configuration

Table 1. Flow conditions

RUN	A (single jet)	B (coaxial jets)
U_i (m/s)	20; 40; 89.2	20; 40; 89.2
U_O (m/s)	0	20; 40
$Re_i \times 10^{-3}$	6.6 to 28.7	6.6 to 28.7
$Re_O \times 10^{-3}$	-----	46.4 to 92.9
Liquid sheet thickness, t (mm)	0.2; 0.7	0.2; 0.7
$Re_\ell = \frac{\rho_\ell U_\ell t}{\mu_\ell}$	731; 667	731; 667

For the results presented and discussed in the following section, the origin of the axial axis, x, and of the transverse y and z co-ordinates is taken at the centre of the inner jet exit. The nozzle was fixed and located

vertically directed downwards. The complete LDV system was mounted on a three dimensional traversing unit, allowing the positioning of the laser-velocimeter control-volume within ±0.1 mm. The inner and outer air flows and the ambient air were seeded with atomised liquid paraffin, with rates of particles in proportion to the air flow rate in each one.

The analysis of the two-phase flow downstream of the nozzle was performed, making use of two visualisation techniques, as follows. First, laser shadowgraphy was achieved by using a conventional optical configuration in order to produce a cylinder of parallel light that crossed the flow and project an image on a screen. A 52 mm camera was used to register the flow images in 100 ASA films with an exposure time of 0.125 ms. Second, a high speed CCD camera with a minimum exposure time of 10 nanoseconds and 8 bits resolution was used together with image processing of the results, in order to enable the recognition of certain geometrical characteristics of the sprays analysed as well as a closer insight on the liquid film disintegration process.

The main limitation of the shadowgraphy consisted on the averaging nature of the method, as well as on the minimum time exposure (0.125 ms) required in the present flow. For the image digitisation technique, a narrow focusing plane was used, which increases the noise level at high electronic gains and brings difficulties in penetrating the "haze" associated with high air velocities. In both methods the possibility of a statistical analysis of the collected data is obviously a time consuming approach, and is a severe limitation of the techniques when quantitative information is a primary goal. This is the case of the analysis of the breakup lengths, which have been determined from a larger number of images. The results exhibited a standard deviation up to 25%, so that the vales reported below may be associated with a statistical uncertainty of less than 20%.

3. RESULTS AND DISCUSSION

The analysis of the flows considered in this paper makes use of flow visualisation results, mean velocity vectors and contours of turbulent velocity characteristics. The main objective is to improve knowledge of the atomisation of liquid fuels in practical combustors by having a closer insight into the break-up mechanism of annular liquid films.

Figure 2 shows results of mean and turbulent characteristics for the air flows associated with Runs A (single jet: U_i=20 m/s) and B (coaxial jets: U_i=U_O=20 m/s) in the absence of the liquid film downstream of the atomiser (for details see Barata et al., 1992). The aim is to quantify the turbulent structure of the air flow into which the atomisation process occurs. This is because, although the disintegration of a liquid sheet into ligaments and drops depends on the thickness and velocity characteristics of the liquid sheet, it is particularly influenced by the velocity, density and mass flow rate of the atomising air, as well as by the way atomising air impinges on the liquid sheet. Of great importance is the kinetic energy and turbulence properties of the air streams surrounding the liquid flow in the vicinity of the nozzle in order to achieve optimum interaction between the liquid sheet and the atomising air.

The air flow patterns downstream of the nozzle are readily identified in Figure 2, by the projections of the velocity vectors on the vertical plane passing on the axis of the nozzle. Run A is formed by the discharge of fluid through a circular contraction nozzle of exit diameter D_i into a quiescent ambient environment. In the immediate vicinity of the nozzle exit the discharge of high velocity fluid causes a thin and cylindrical shear layer to be formed about the perimeter of the core. The shear layer is observed to undergo transition and widen with the downstream distance and, eventually, engulfs the potential core at approximately x/D_i= 5, with the turbulent kinetic energy reaching its maximum value along the centreline and at x/D_i=12. The jet turbulent velocity shows evidence of self-preservation after approximately 24 diameters downstream of the nozzle exit.

For Run B, the initial flow close to the nozzle exit consists of two potential cores separated by an annular mixing region surrounded by an external shear zone. The width of each core decreases with downstream distance, with the individuality being lost at approximately x/D_i = 20. The distribution of turbulent energy exhibits two maxima, namely close to the nozzle between the two air jets and along the outer shear layer, in a considerably different way from that found for Run A.

We now turn to the analysis of the process of liquid atomisation downstream of the nozzle used throughout this work, when a liquid sheet is introduced into the air flows analysed above. Figures 3 and 4 show sample results obtained for Run A with laser shadowgraphy and high-speed video, respectively, while Figure 5 shows results for Run B. The figures quantify the effect of the air velocity and film thickness on the atomisation process and are important to improve understanding of liquid breakup in airblast atomisers.

At very low velocities of the inner air flow a bubble is formed due to pressure differences between the inner and the outer flows. The pressure from the surrounding flow plus the surface tension forces are balanced by the pressure inside the bubble, which is due to the kinetic energy of the inner flow.

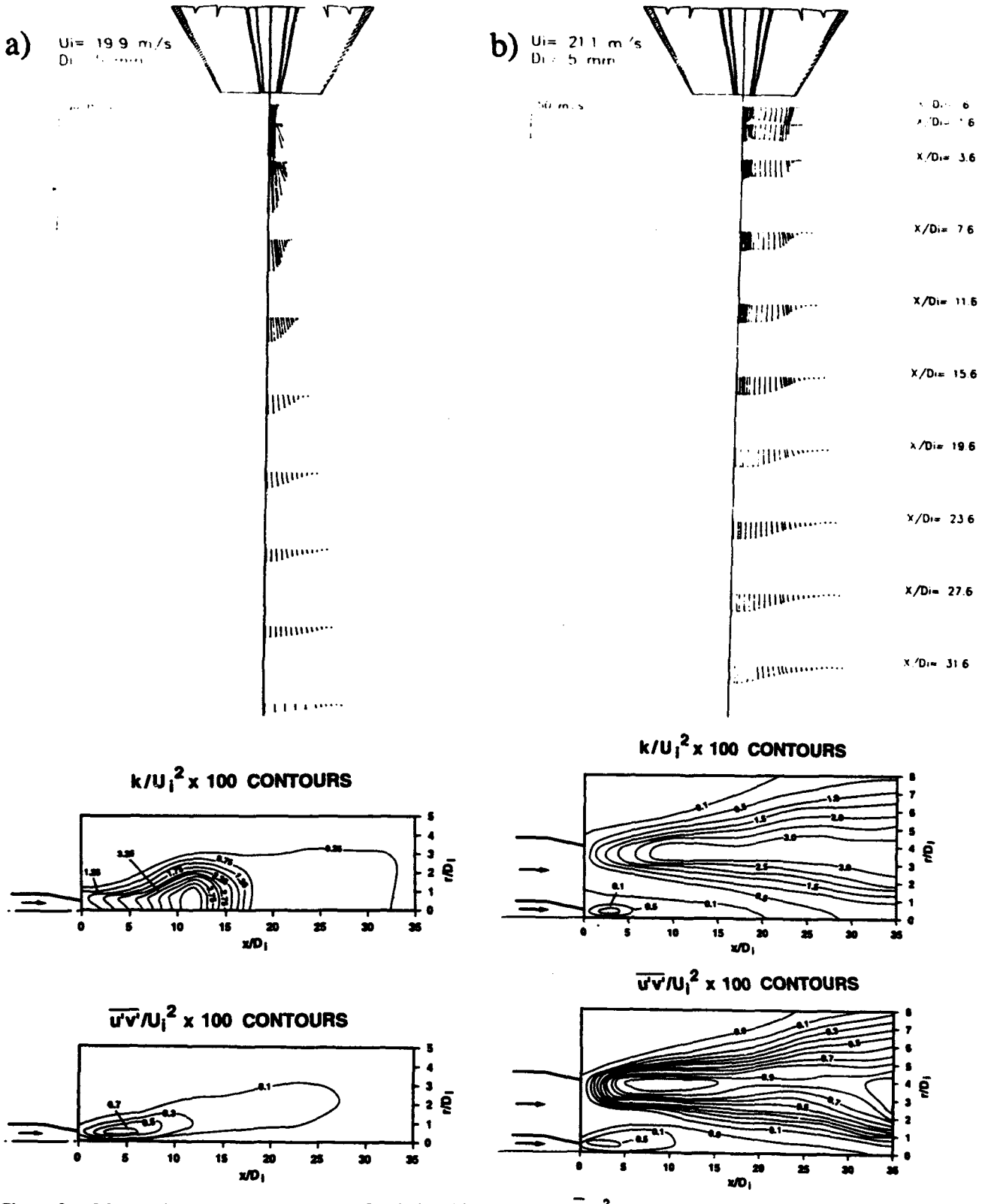

Figure 2. Mean velocity vectors, contours of turbulent kinetic energy, $\overline{k}/U_i^2 \times 100$ and of Reynolds shear stresses, $\overline{u'v'} / U_i^2 \times 100$ for the air flows of Run A and Run B
a) Run A, $Re_i = 6600$; b) Run B, $Re_i = 6600$; $Re_o = 46400$

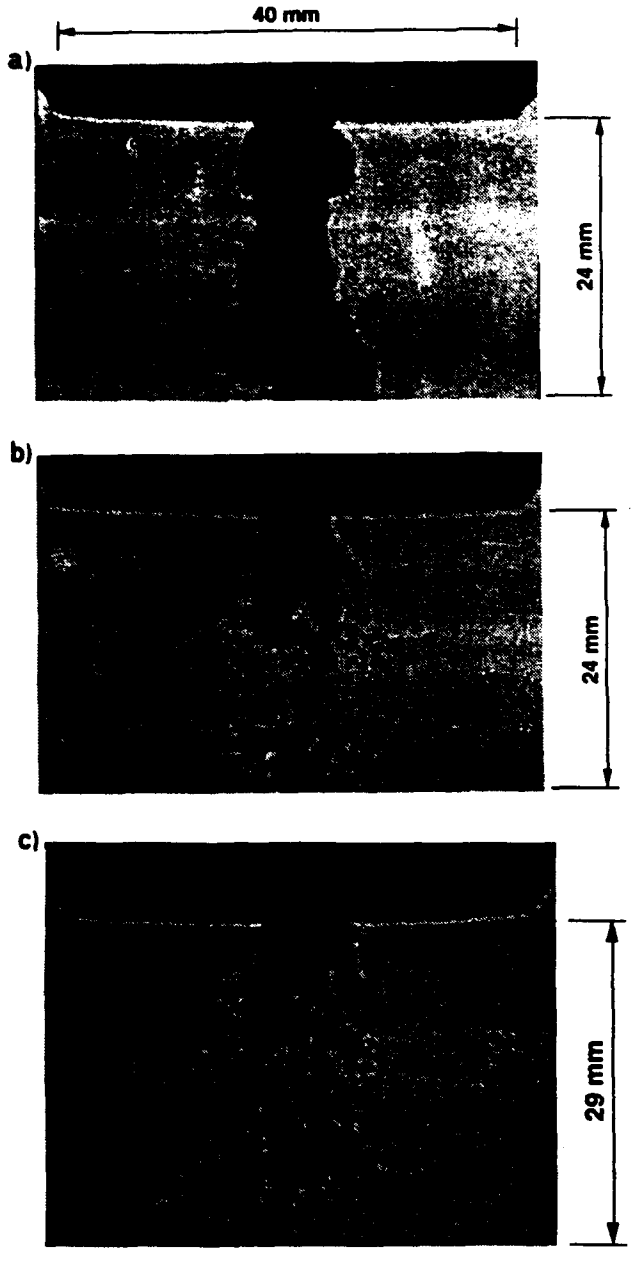

Figure 3. Laser Shadowgraphy of the liquid sheet in the near exit zone of the atomiser for Run A (t = 0.7 mm)
a) U_i=20m/s; b) U_i=40m/s; c) U_i=89.2m/s

The total pressure inside the bubble increases with the inner air velocity and, eventually, becomes higher than the total pressure of the outer flow plus surface tension forces and the bubble will burst at its bottom. If U_i keeps increasing, the bubble is not formed and the liquid film becomes unstable, giving rise to the formation of ligaments which will break into droplets. The formation of these ligaments is induced by natural instabilities of the liquid film and by friction forces between the inner air flow and the co-flowing liquid film. The higher the inner air velocity will be, the shorter the break-up length, and smaller ligaments are formed, which consequently will lead to the formation of smaller drops and, therefore, to a better atomisation. Then, the break-up process described above can be analysed by considering that the sheet is destabilised by aerodynamic forces and the instability is damped by surface tension.

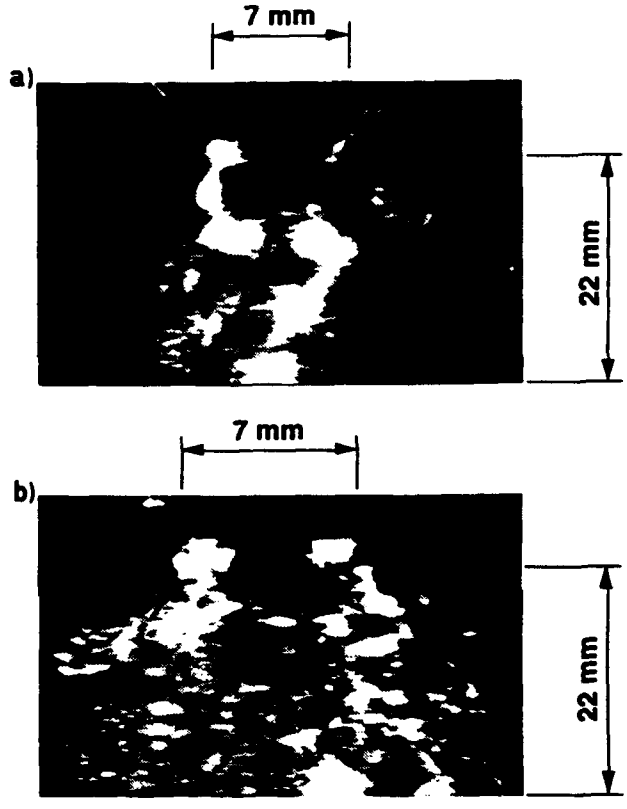

Figure 4. High speed video visualisation of the liquid sheet for Run A (U_j = 20 m/s)
a) t = 0.2 mm, b) t = 0.7 mm

The patterns discussed in the previous paragraphs are readily analysed in the schematic diagram of Figure 6. At the lowest gas/liquid velocity, (a), the break-up follows from dilational distortion of the liquid sheet, in agreement with the theories of Rayleigh. An increase of the relative velocity, (b), leads to movement of the "break-point" closer to the nozzle, shorter fundamental wavelength and hence smaller drops. At even higher velocities, (c), the first order instability (Azzopardi et al., 1989) is observed. Further increase of the liquid sheet velocity, results in stripping of ligaments from the sheet surface and for velocities higher than 100 m/s the liquid appears to promptly atomise at the nozzle. The results are independent of the outer air velocity in the range $0 < U_o$ (m/s) < 20 and this is a remarkable finding of the results presented here.

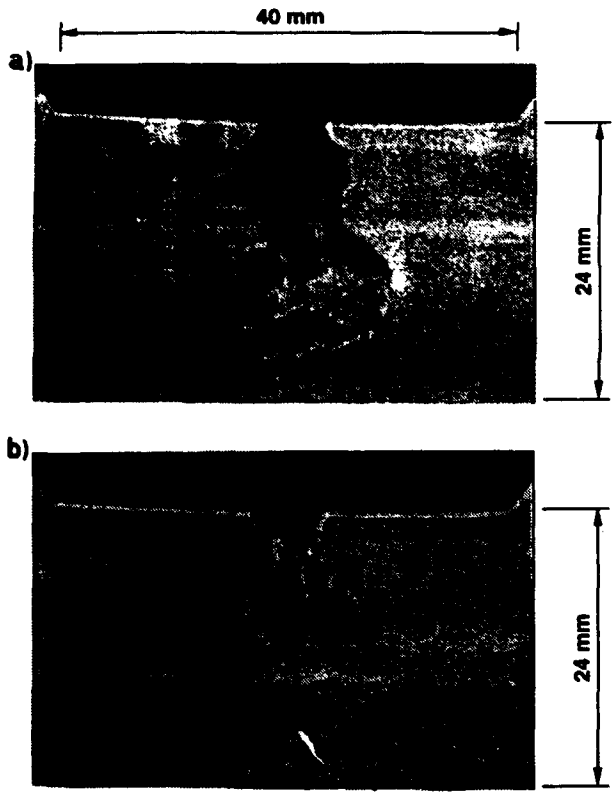

Figure 5. Laser Shadowgraphy of the liquid s[illegible] in the near exit zone of the atomiser for Run B (t = 0.7 mm)
a) $U_i=U_O=20$m/s; b) $U_i=20;U_o=40$m/s

The effect of the atomising air velocity on the break-up length and time for single and coaxial jets for the two liquid film thicknesses used throughout the work is shown in Figures 7 and 8, respectively. The results quantify the length from the nozzle tip to the point at which the liquid film fragments and show that as the primary air velocity increases, the break-up lengths, for both single and coaxial jets, decreases due to reduced aerodynamic shear forces acting on the liquid film. The break-up length is also dependent on the liquid velocity, as can be observed by comparing the results for the two different initial film thicknesses (0.2 and 0.7 mm), with higher liquid velocities leading to longer break-up lengths.

The figures mentioned above include results (for t = 0.7 mm) obtained with shadowgraphy and with the high speed camera, and show that the former are always higher than the latter, due to the time exposure limitation as noted above. The measured results are surrounded by two curves, which represent the error range considered.

In order to quantify the interaction time between liquid and air streams, a break-up time was calculated by dividing the break-up length by the liquid velocity at the nozzle tip, and the results are plotted in Figures 7b) and 8b). The break-up length and time increase by decreasing air velocities and a substantial deterioration in the spray quality is obtained for reduced air velocities. It was observed that the threshold value of air velocity below which atomisation is of poor quality, is around U_i = 40 m/s and further reduction in velocity results in lack of atomisation. For an easier comparison, the results are ploted together for both single and coaxial jet in Figure 9.

Figures 7 and 8 show also a comparison of the experimental results described before with the analytical model of Dombrowski and Johns (1963), which considers a liquid sheet thinning in time and moving in the streamline direction through a stationary gas. The model predicts (at least, qualitatively) the experimental results, for high inner air flow velocities but, otherwise, overestimates the present results, due to the prevailing "bubble" form that usually precedes the break-up of the liquid sheet into ligaments.

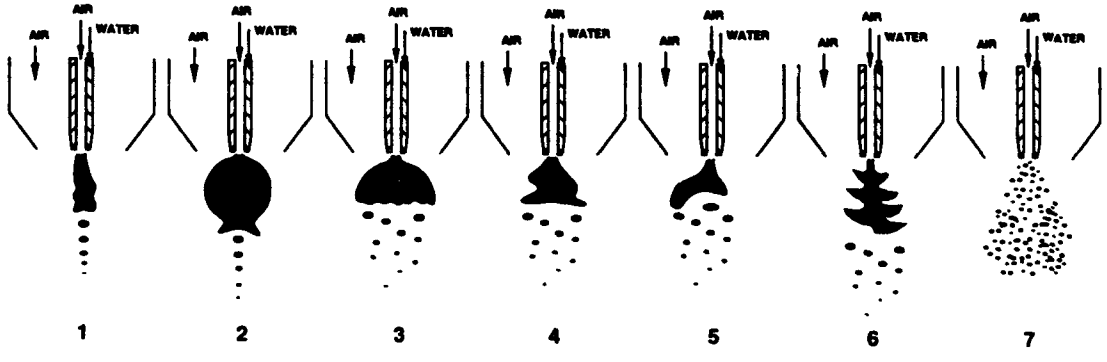

Figure 6. Schematic diagrams of the breakup of the liquid sheet as a function of the inner air jet velocity (U_i) for outer jet velocities in the range $0 < U_o < 20$ m/s. U_i increases from diagram (1) to (6), respectively from 0 to 90 m/s. Diagram 7 corresponds to prompt atomization for $U_i > 100$ m/s

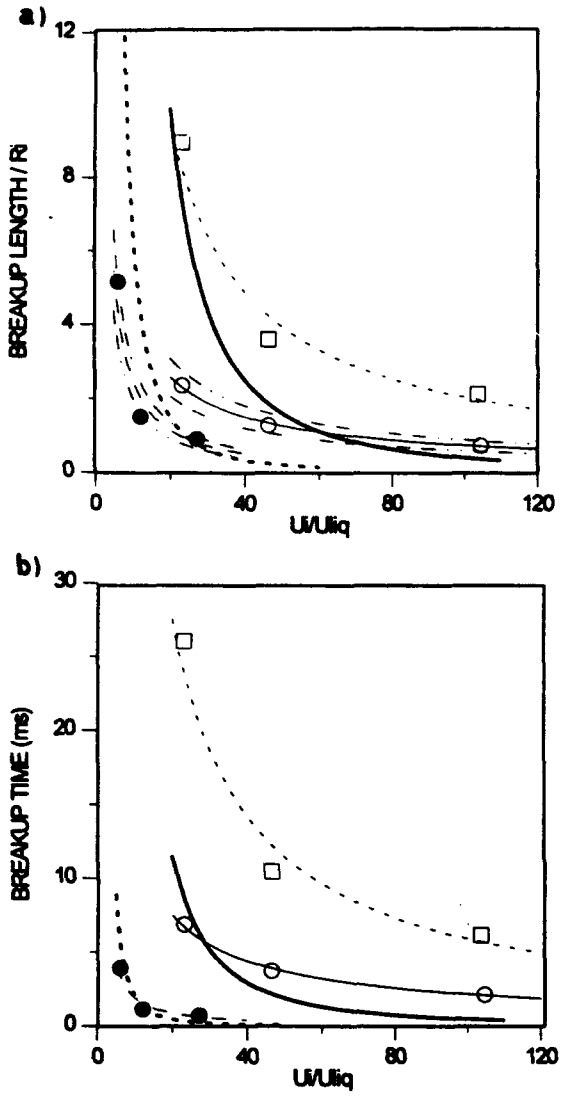

Figure 7. Effect of the atomisation air velocity and liquid film thickness on break-up length and time scales for single jets (Run A)

Key:

O; t=0.7mm; —— best fit

●; t=0.2mm; —— best fit

□; t=0.7mm; - - - - best fit (shadowgraphy)

—— t=0.7mm
- - - t=0.2mm
} Dombrowski's model

--- ·---·--- error range ± 20%

a) Film break-up length

b) Film break-up time

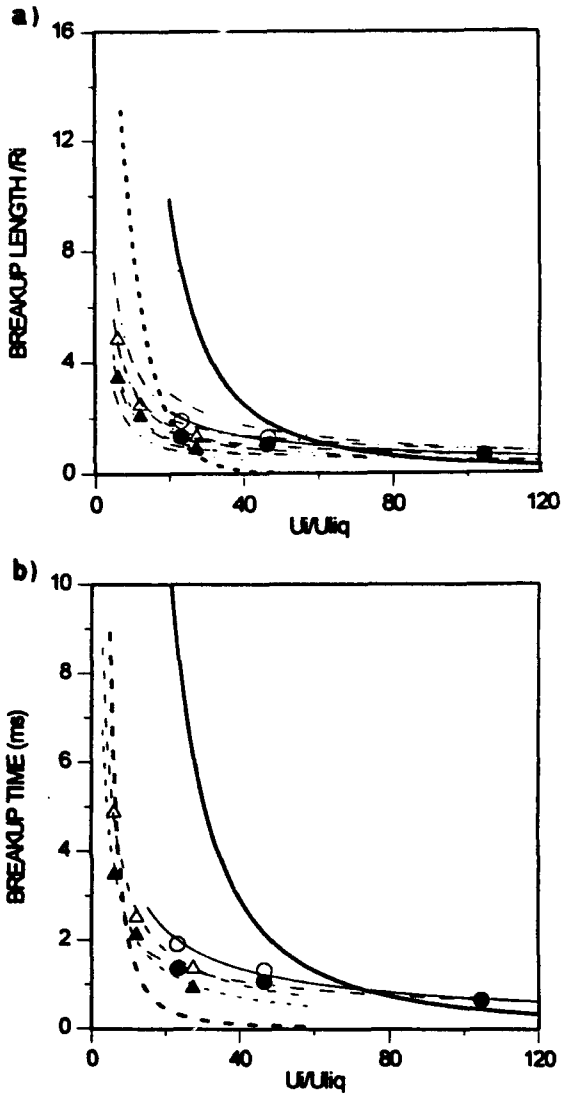

Figure 8. Effect of the atomisation air velocity and liquid film thickness on break-up length and time scales for coaxial jets (Run B)

Key:

O; t=0.7mm; U_o=20m/s

●; t=0.7mm; U_o=40m/s

Δ; t=0.2mm; U_o=20m/s

▲; t=0.2mm; U_o=40m/s

—— t=0.7mm
- - - t=0.2mm
} Dombrowski's model

--- ·---·--- error range ± 30%

a) Film break-up length

b) Film break-up time

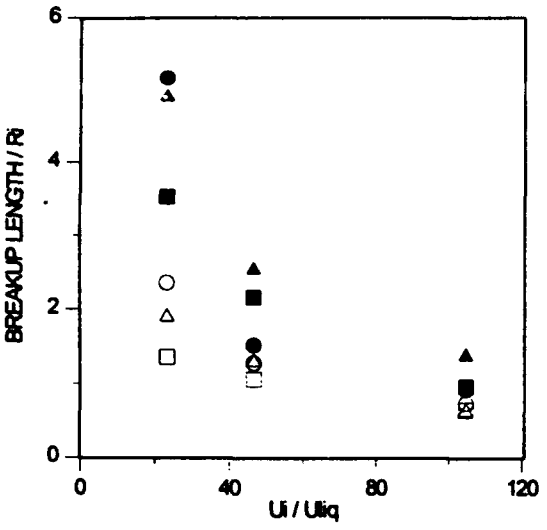

Figure 9. Effect of the atomisation air velocity and liquid film thickness on break-up length and time scales for Run A and Run B

t=0.7: O U_0=0; Δ U_0=20m/s; □ U_0=40m/s
t=0.2: ● U_0=0; ▲ U_0=20m/s; ■ U_0=40m/s

Figures 10 and 11 quantify the influence of the air/liquid mass ratio on the breakup process, which is a variable usualy reported in the modelling of airblast atomisation (e.g. El-Shanawany and Lefebvre, 1980). Since this type of atomisation relies upon the airstream momentum for the liquid disintegration, the air/liquid mass ratio influences the spray quality. This is because the deficiency of air results in failure to overcome the viscous/surface tension forces that are resisting to liquid disintegration. Finally, it is important to establish the performance of the present airblast nozzle in terms of those tested previously and reported in the literature and Figure 12 accomplishes this by comparing the present results with those obtained by Stapper et al. (1992) in a planar configuration and with those of Lavergne et al. (1993) in a nozzle similar to that used throughout this work. The reference parameter in the comparison is the velocity of the liquid film at the nozzle tip: Stapper et al. (1992) used a film thickness of 0.508 mm, corresponding to U_{liq}= 1 m/s for coaxial flows with U_i=U_0 (range: 20 - 60 m/s), while Lavergne et al. (1993) used either a liquid film thickness of 0.400 or 0.700 mm, corresponding to U_{liq}= 0.95 m/s for a constant value of U_i=10 m/s, varying U_0 from 30 to 62 m/s.

The agreement found is particularly good for a film thickness of 0.7 mm, and suggests the likely dependence of the process on the film characteristics, apart from the observed dependence upon the primari air flow rate.

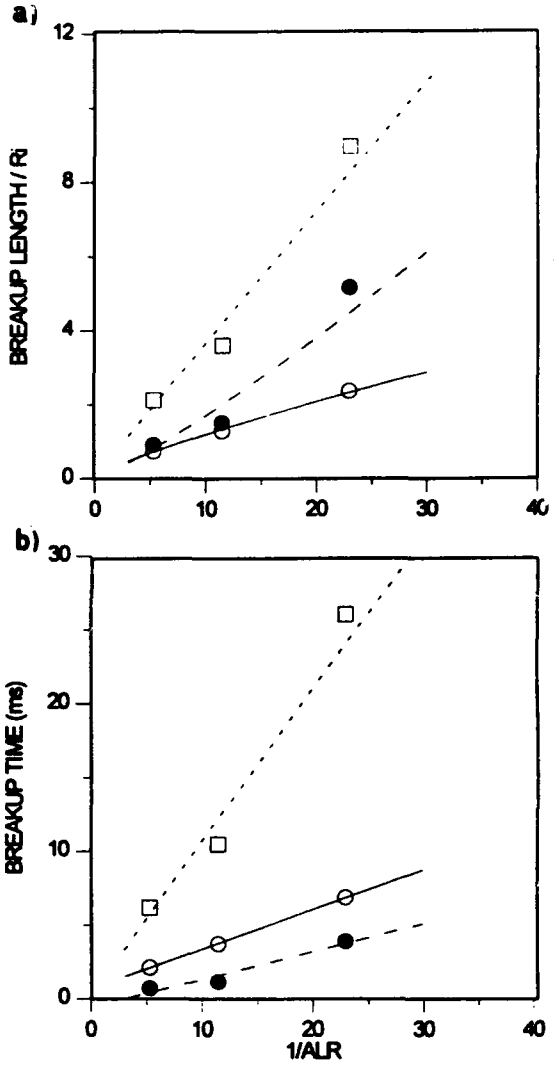

Figure 10. Effect of the atomisation air velocity and liquid film thickness on break-up length and time scales for Run A, as a function of the air/liquid mass ratio, ALR

O; t=0.7mm; —— best fit
●; t=0.2mm; —— best fit
□; t=0.7mm; - - - - best fit (shadowgraphy)

a) Film break-up length
b) Film break-up time

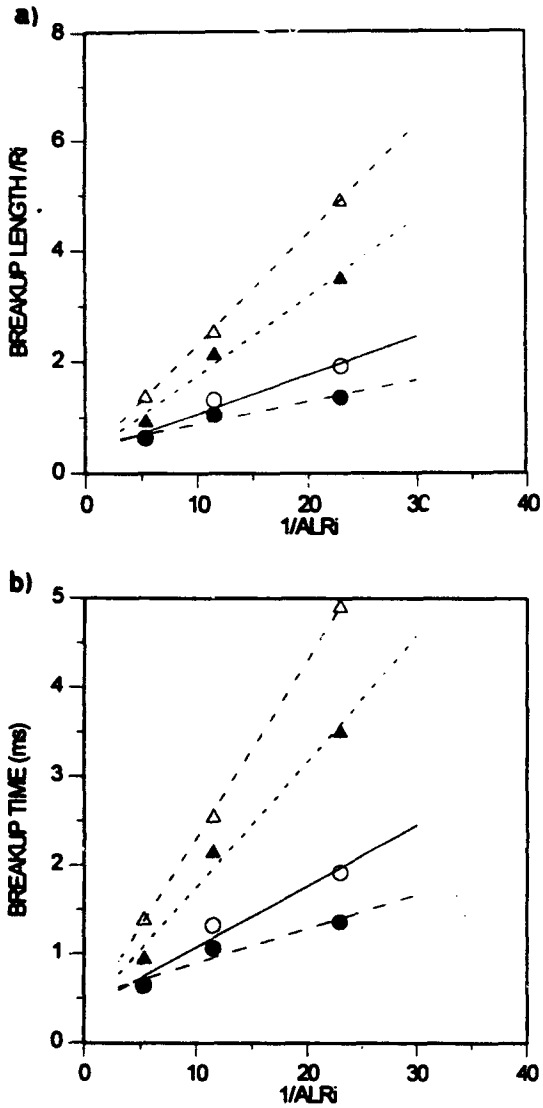

Figure 11. Influence of the air/liquid ratio on the break-up length and time scales for Run B, as a function of the inner air/liquid mass ratio, ALR_i

O; t=0.7mm; U_o=20m/s

●; t=0.7mm; U_o=40m/s

Δ; t=0.2mm; U_o=20m/s

▲; t=0.2mm; U_o=40m/s

a) Film break-up length

b) Film break-up time

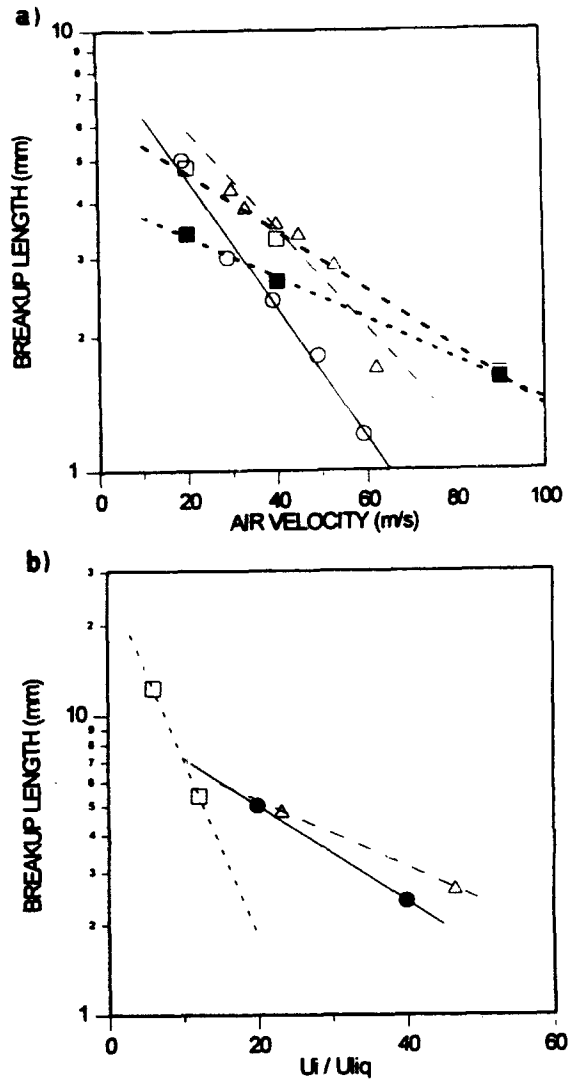

Figure 12. Effect of the atomisation air velocity on break-up length for coaxial jets (Run B)

a) Comparison with Stapper et al. (1992) and Lavergne et al (1993) for a wide range of flow conditions (t=0.7)

□ U_o=20m/s O Stapper et al. (1992)

■ U_o=40m/s Δ Lavergne et al. (1993)

b) Comparison with Stapper et al. (1992) for U_i=U_o=20 m/s and U_i=U_o=40 m/s

□ t=0.2 mm

Δ t=0.7 mm

} $U_i = U_o$

● Stapper et al. (1992)

4. CONCLUSIONS

Laser-Doppler measurements of mean and turbulent velocity characteristics are reported for the air flow downstream of a model airblast prefilming atomiser, along with near-nozzle visualisation of the liquid film break-up making use of both shadowgraphy and a high speed video camera. The flows analysed correspond to single and coaxial turbulent jets downstream of a conical nozzle and include the analysis of the break-up of an annular liquid film in a field of co-flowing shearing air.

It was observed that both instabilities and disintegration of the liquid film are induced by the dynamic pressure and shear layer between the inner and outer air streams. The results support the "wavy bubble" mechanism of the liquid film disintegration. When the inner air velocity is small, the bubble at the atomiser's exit becomes unstable and bursts into poor quality atomisation. At higher air velocities the amplitudes of the liquid film instabilities sharply grow leading to pronounced shorter break-up lengths and, consequently, better atomisation quality. The outer air flow appeared to be less effective on the break-up mechanism, with the corresponding length and time scales being primarily dependent on the inner air flow rate.

ACKNOWLEDGEMENTS

The present nozzle was built in the laboratory of Prof. M. Ledoux, University of Rouen, and adapted at the workshop of the Applied Thermodynamics Section of IST. The many discussions with staff of SNECMA, TURBOMECA and CERT are gratefully appreciated. Financial support has been provided by the BRITE/EURAM Programme of the European Commission. Thanks are also due to Messrs. Jorge Coelho and Carlos Carvalho for helping in the preparation of this paper.

REFERENCES

Aigner, M. and Wittig, S. (1988). Swirl and Counter Swirl Effects in Prefilming Airblast Atomisers. J. Eng. for Gas Turbines and Power, **110**, pp. 105-110.

Arai, T. and Hashimoto, H. (1985). Behaviour of Gas-Liquid Interface on a Liquid Film Jet. Bulltein of JMSE, **28** (245), paper No. 245-21.

Azzopardi, B.J., Teixeira, J.C.F. and Jepson, D.M. (1989). Drop Sizes and Velocities in Vertical Annular Two-Phase Flow. International Conference on Mechanics of Two-Phase Flows, June 12-15, Taipei, Taiwan.

Barata, J.M.M., Carvalho, I.S. and Heitor, M.V. (1992). Laser-Doppler Analysis of the Air Flow Downstream of a Model Prefilming Spray Injection. Proc. 6th Intl. Symp. on Appl. of Laser Techniques to Fluid Mechanics, Lisbon, July 20-23.

Beck, J.E., Lefebvre, A.H. and Koblish, T.R. (1991). Airblast Atomisation at Conditions of Low Air Velocity. J. Propulsion, 7(2), pp. 207-212.

Call, C. J., Lozano, A. and Dopazo, C. (1993). An Investigation of the Breakup of Thin Liquid Sheets. Joint Meeting of the Italian and Spanish Sections of The Combustion Institute, June 28 - July 1, Stresa, Italy.

Dombrowski, N. and Johns, W.R. (1963). The Aerodynamic Instability and Desintegration of Viscous Liquid Sheets. Chem. Engng. Sci., **18**, pp.203-214.

El-Shanawany, M.S. and Lefebvre, A.H. (1980). Airblast Atomization: Effect of Linear Scale on Mean Drop Size. J. Energy, 4(4), pp.184-189.

Engelbert, C., Hardalupas, Y. and Whitelaw, J.H. (1994). Breakup Phenomena in Coaxial Airblast Atomisers. Imperial College of Sci. Tech. Medicine, Mech. Engng. Dept., Internal Report No. TF/94/18.

Jasuja, A.K. (1990). Stucture of an Airblast Atomised Spray. ILASS-EUROPE, 6th Annual Conference on Liquid Atomisation and Spray Systems, July 4-6, Pisa, Italy.

Lavergne, G., Trichet, P., Hebrard, P. and Biscos, Y. (1993). Liquid Sheet Disintegration and Atomisation Process on a Simplified Airblast Atomiser. J. Engng. Power Gas Turbines, **115**, pp.461-466.

Lefebvre, A.H. (1989). Atomization and Sprays. Hemisphere Publishing Corporation.

Rizk, N.K. and Lefebvre, A.H. (1980). The Influence of Liquid Film Thickness on Airblast Atomization. Trans. ASME, J. Engng. Power, **102**, pp.706-710.

Rizk, N.K., Mostafa, A.A. and Mongia, H.C. (1987). Modeling of Gas Turbine Fuel Nozzles. Atomisation and Spray Technology, 3,pp.241-260.

Rizkalla, A.A. and Lefebvre, A.H. (1975). Influence of Liquid Properties on Airblast Atomiser Spray Characteristics. Trans. ASME, J. Engng. Power, April, pp.173-179.

Sattelmayer, T. and Wittig, S. (1986). Internal Flow Effects in Prefilming Airblast Atomisers: Mechanisms of Atomisation and Droplet Spectra. Trans. ASME, J. Engng. Gas Turbines Power, **108**, pp.465-472.

Shaw, S.G. and Jasuja, A.K. (1987). Effect of Injector Geometry Variables Upon the Spray Performance of a Plain-Jet Airblast Atomizer. Atomisation and Spray Tech., 3, pp.107-121.

Simmons, H.C. (1980). The Prediction of Sauter Mean Diameter for Gas Turbine Fuel Nozzles of Different Types. Trans. ASME, J. Engng. Power, **102**, pp.646-652.

Stapper, B.E., Sowa, W.A. and Samuelsen, G.S. (1992). An Experimental Study of the Effects of Liquid Properties on the Breakup of Two-Dimensional Liquid Sheet. J. Engn. Gas Turbines Power, **114**, pp. 39-45.

MEASUREMENT OF VELOCITY PROFILES IN A FALLING LIQUID FILM IN COUNTERCURRENT ANNULAR FLOW

W. Pun, C. Lorencez, M. Kawaji, G. Karimi, F. Kaminaga[1], H. Akimoto[2] and Y. Sudo[2]

Dept. of Chem. Eng. & Applied Chemistry, Univ. of Toronto, Toronto, Ontario M5S 1A4, Canada

1. Dept. of Mech. Eng. Ibaraki Univ., Ibaraki, Japan

2. Japan Atomic Energy Research Institute, Ibaraki, Japan

ABSTRACT

A laser-induced photochromic dye activation technique was used to determine the flow structure in a thin, falling liquid film with a countercurrent gas flow in order to investigate the physical mechanisms responsible for flooding in a vertical tube. Instantaneous velocity profile data obtained indicate occurrence of no flow reversal inside the liquid film, even at the onset of flooding conditions. Direct measurements of the wall shear stress also indicate that presently used correlations based on average fluid velocities can significantly underpredict the data.

NOMENCLATURE

D	= pipe diameter [m]
g	= acceleration due to gravity [m/s^2]
j	= superficial velocity [m/s]
j^*	= dimensionless velocity
Q	= volumetric flow rate [m^3/s]
Re	= Reynolds Number
u	= axial velocity [m/s]
u^+	= dimensionless axial velocity (= u/u^*)
u^*	= wall friction velocity [m/s]
y	= distance from wall (radial) [m]
y^+	= dimensionless distance from wall (= $\rho u^* y/\mu$)

Subscripts

F	= Film
G	= Gas
L	= Liquid
w	= wall

Greek Letters

δ	= liquid film thickness [m]
μ	= dynamic viscosity [kg/m·s]
ρ	= density [kg/m^3]
τ	= shear stress [N/m^2]

1. INTRODUCTION

Understanding of countercurrent flow limitation (CCFL) phenomena is important in the safety analysis of nuclear reactors, particularly during a hypothetical loss-of-coolant accident (LOCA), however, the physical mechanisms responsible for the onset of flooding have not been fully understood despite over thirty years of research. Most of the previous experimental studies have focused on the measurement of liquid film thickness and surface wave characteristics. On the analytical side, one-dimensional mass and momentum balances have been mostly used to predict the flooding data. However, conclusions drawn from different studies about the role of surface waves or the wall and interfacial shear stresses on the flooding phenomena are often in disagreement or even contradictory.

Hewitt and Wallis (1963) predicted that the gas-liquid interfacial shear is insufficient to cause liquid flow reversal and that flooding would occur due to the growth of large surface waves. Two-fluid model predictions, however, require artificially large interfacial friction factors to correctly predict the flooding gas velocities (Abe et al., 1991).

Zabaras and Dukler (1988) and Binge et al. (1989) observed that the surface waves on the liquid film propagate in the downwards direction but they are never large enough in amplitude to bridge the tube. Govan et al. (1991), on the other hand, claimed that flooding is caused by the upward propagation of a wave and the accumulation of other waves falling onto the initial one.

Better understanding of the flooding mechanisms require more detailed knowledge of the flow structure in the wavy liquid film falling through a vertical tube with a countercurrent flow of gas. The gas flow would impose a significant interfacial shear stress on the liquid film in the upward direction and may have a large influence on the flow structure of the liquid film. To determine the continuously changing velocity profiles in such thin, wavy films requires a novel measurement technique, since conventional velocity measurement techniques such as LDV and HWA methods can not be expected to yield truly useful information.

To this end, the laser-induced photochromic dye activation technique (PDA) has been used to obtain the axial velocity profiles across the liquid film, with an aim to provide new insights into the physical mechanisms responsible for the

initiation of flooding in countercurrent annular flow. The PDA technique is a non-intrusive flow visualization technique based on the UV laser activation of a photochromic dye dissolved in a transparent liquid, and has recently been successfully applied by Kawaji et al. (1993) to the study of flow structures in various two-phase flow regimes.

For a falling liquid film without any gas flow, Ho and Hummel (1970) first applied this technique to measure the time-averaged velocity profiles and proposed the following non-dimensional correlation.

$$y^+ = u^+ + 0.111(e^{0.281u^+} - 1) \qquad (1)$$

Their measurements were made in a falling kerosene film with a surface active agent added to suppress interfacial waves and the correlation was proposed for $y^+ < 30$ and $Re_F = \rho u\delta / \mu \approx 1000$.

2. EXPERIMENTAL FACILITY

A schematic of the test loop used to conduct vertical, countercurrent annular flow experiments is shown in Fig. 1. The test section consisted of a 2.39 m-long Pyrex tube, with an inner diameter of 50.8 mm and a 3.8 mm wall thickness. The working fluids were Shell-Sol 715 (deodorized kerosene) and air. The kerosene was circulated by a pump through a set of flow meters to the upper plenum and flowed down the test section into the lower plenum. Compressed air obtained from the building air supply was injected into the test section through a stainless steel tube, which penetrated through the lower plenum and entered into the bellmouth of the test section as shown in Fig. 1.

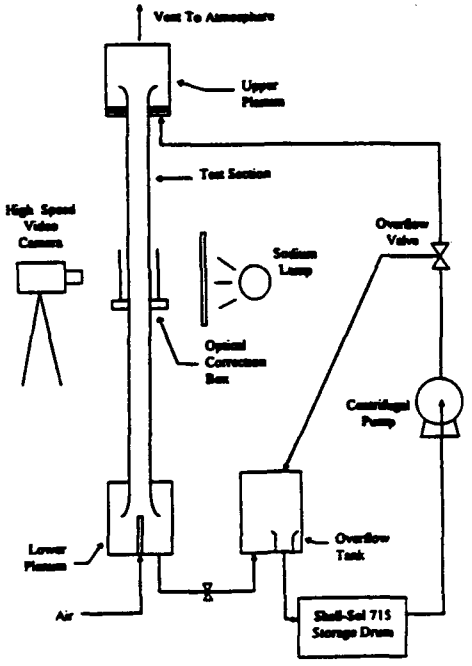

Fig. 1 Countercurrent Annular Flow Loop

A photochromic dye, 1',3',3'-trimethyldoline-6-nitrobenzospiropyran (or TNSB) was dissolved in dilute concentration in kerosene. Pulses of UV light from an EXCIMER laser (Lumonics Model TE-860-4) were focused using a five-lens array with a focal length of 250 mm, into the test section as shown in Fig.2, to create five thin traces in the liquid film. The motions of the traces were recorded by a high-speed video camera (Photron Model HSV-11B), which has a CCD camera with 256x256 pixel resolution, at a speed of 744 frames per second with an electronic shutter speed of 1/10,000 second. The laser was fired at 50 Hz and the trace images were analyzed using a microcomputer-based image analysis system.

To minimize optical distortion of the images captured by the video camera due to the use of a cylindrical tube, an optical correction box was installed around the tube as in Fig. 2. The linearity of the actual and observed distances from the inner wall surface was confirmed by conducting calibration work insitu.

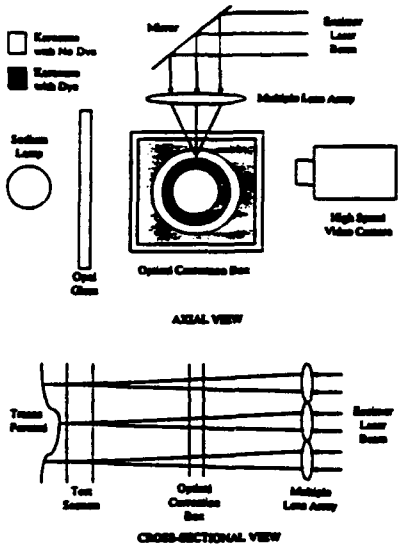

Fig. 2 Optical Arrangement

3. RESULTS AND DISCUSSION

In this study, three different cases, as shown in Table 1, were examined, where the liquid and gas superficial velocities, j_L and j_G, and non-dimensional velocities, $\sqrt{j_L^*}$ and $\sqrt{j_G^*}$, are shown. The present flooding experiments are characterized by the Wallis' flooding curve given by, $\sqrt{j_G^*} + m\sqrt{j_L^*} = C$ with the constants m and C equal to 0.70 and 0.68, respectively, as shown in Fig. 3. The runs in Table 1 are also indicated in Fig. 3.

Table 1 Experimental Conditions

Run	j_L [m/s]	j_G [m/s]	$\sqrt{j_L^*}$	$\sqrt{j_G^*}$
1	0.063	4.06	0.30	0.46
2	0.0025	7.00	0.059	0.63
3	0.0025	3.05	0.059	0.41

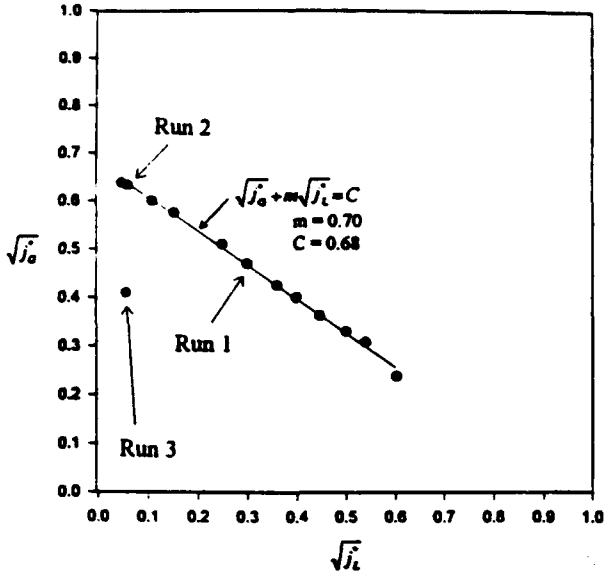

Fig. 3 Flooding Curve

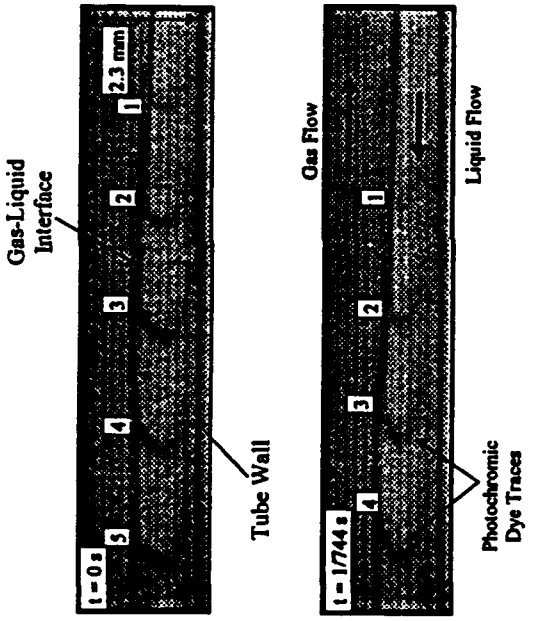

Fig. 4 Motion of Traces in Run 1 (Frames 388 and 389)

3.1 Flow Reversal

An important question concerning the onset of flooding is whether or not flow reversal occurs in the liquid film especially near the gas-liquid interface. The photochromic dye traces formed in the film indicated that flow reversal does not occur even when large surface waves are present and the interfacial shear due to the gas flow reaches its maximum value at the onset of flooding. This is clearly shown in Fig. 4, where the traces in the liquid film observed in two consecutive frames in Run 1 are moving downward everywhere. In all the traces observed in every run, the trace never moved upward to indicate flow reversal (upward flow) in any part of the liquid film.

The instantaneous velocity profiles were obtained from the trace motion in consecutive frames as shown in Figs. 5 through 7 for Runs 1 through 3, respectively. The instantaneous velocity profiles also indicate that although the interfacial drag causes retardation of the film flow near the interface, the downward velocities are still substantially large and far from reaching zero or positive velocities. Of course, a higher gas flow rate causes more significant retardation of the liquid film near the interface as clearly evident from a comparison of Runs 2 and 3. But, even the maximum interfacial shear stresses reached at the flooding gas velocities are not sufficient to cause flow reversal and upward flow in the liquid film.

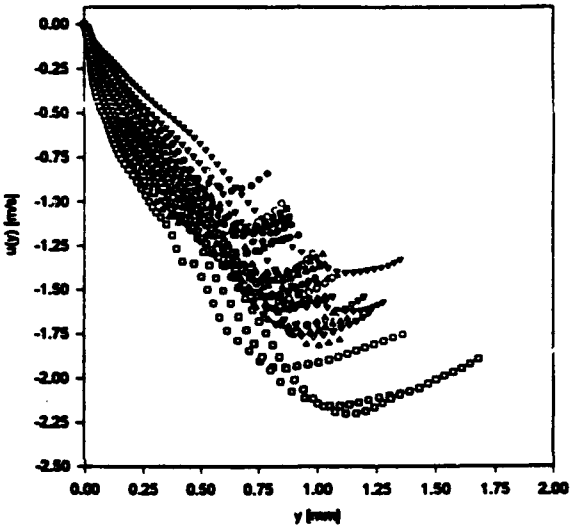

Fig. 5 Instantaneous Velocity Profiles of Run 1 just before the onset of flooding

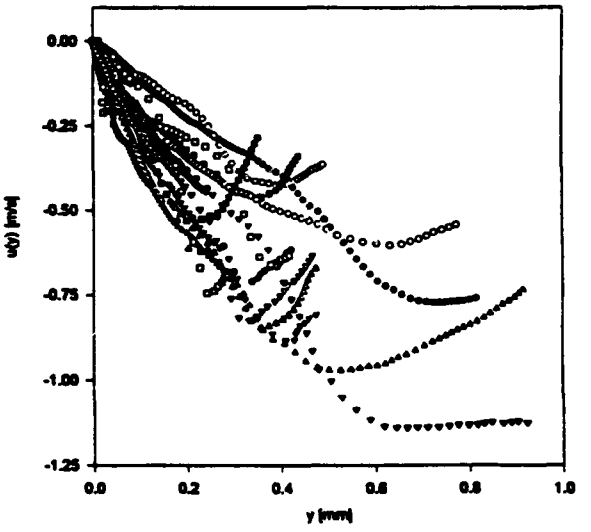

Fig. 6 Instantaneous Velocity Profiles of Run 2 just before the onset of flooding

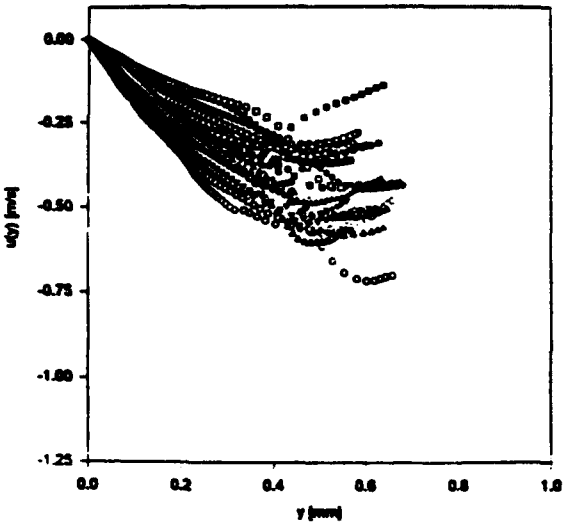

Fig. 7 Instantaneous Velocity Profiles of Run 3 well before the onset of flooding

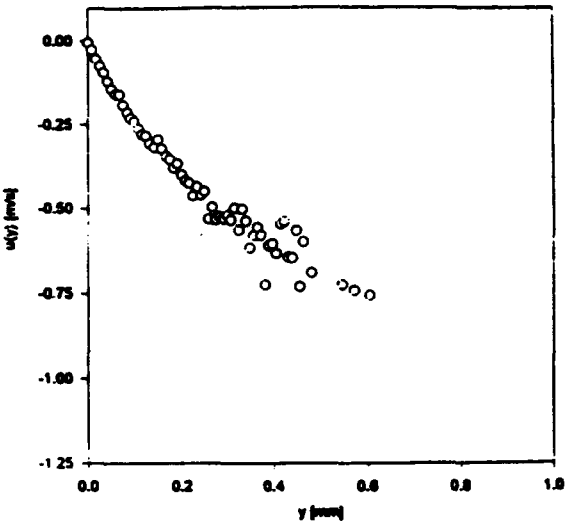

Fig. 9 Average Velocity Profile for Run 2 just before the onset of flooding

3.2 Wall Shear Stress

From the instantaneous velocity profiles, the average axial velocity profiles can be evaluated as shown in Figs. 8 through 10 for Runs 1 through 3, respectively. Using the average axial velocity profiles, the wall shear stresses can be readily obtained from the product of the velocity gradient at the wall and the

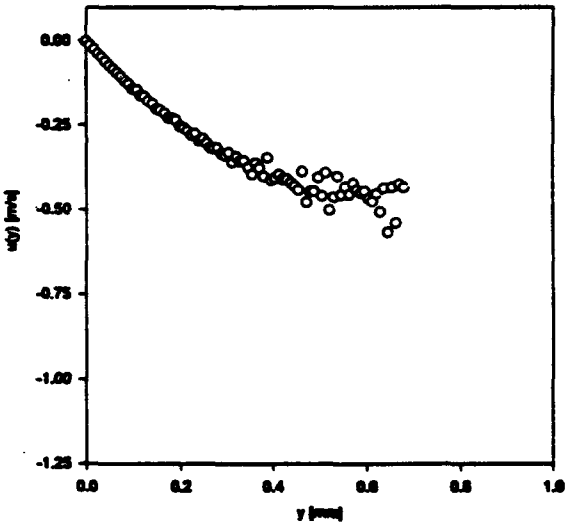

Fig. 10 Average Velocity Profile for Run 3 well before the onset of flooding

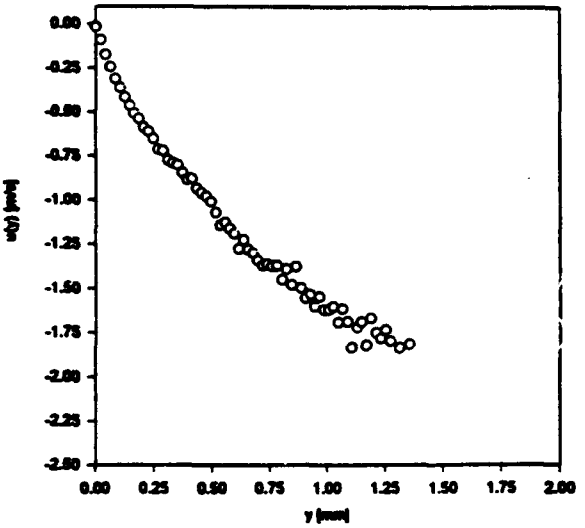

Fig. 8 Average Velocity Profile for Run 1 just before the onset of flooding

dynamic viscosity of liquid. The measured values of wall shear stress can be compared with those predicted by one-dimensional models such as the Bharathan and Wallis' (1983) correlation. Here, we have used Wallis' (1969) correlation for the liquid film thickness, δ, to obtain the void fraction, α.

$$\frac{\delta}{D} = 0.063 j_L^{*2/3} \qquad (2)$$

$$\alpha = \left(1 - \frac{2\delta}{D}\right)^2 \qquad (3)$$

Using the estimated void fraction, Bharathan and Wallis (1983) proposed evaluating the wall shear stress using the following equation.

$$\tau_w = \frac{f_w}{2} \cdot \frac{\rho_L j_L^2}{(1-\alpha)^2} \qquad (4)$$

For the wall friction factor, Bharathan and Wallis (1983) recommended using a constant value of $f_w = 0.005$, but different values can also be used based on single-phase friction factors, $f_w = 16/Re_F$, for laminar film, and $f_w = 0.079/Re_F^{-1/4}$ for turbulent film. Here, a constant value of $f_w = 0.005$ was used.

A comparison of the measured and predicted wall shear stresses is shown in Table 2. The experimental data obtained in this work clearly suggest that the prediction method based on average liquid velocity and single-phase friction factor significantly underestimates the data, as previously pointed out by Abe et al. (1991). The underprediction may be due to inaccuracy in estimating the void fraction (or the film thickness), Eqs. (2) and (3), but it clearly points out the need to improve the overall prediction method.

Table 2 Comparison of Experimental and Theoretical Wall Shear Stresses

Run	Experimental τ_w (N/m^2)	Theoretical τ_w (N/m^2)	$\frac{\tau_{w_{exp}}}{\tau_{w_{theory}}}$
1	5.0	3.00	1.7
2	3.3	1.27	2.6
3	2.0	1.27	1.5

Another interesting result is that the measured wall shear stress is actually higher when the gas flow rate is closer to flooding (Run 2) than when the gas flow rate is approximately half the flooding gas flow rate (Run 3). A possible explanation to account for this is the presence of more and larger waves at the onset of flooding. These waves are formed due to the faster countercurrent gas flow, which tends to retard the liquid film velocity near the interface. However, the same wave action which decelerates the liquid film at the interface, could accelerate the liquid near the wall, if the liquid film thickness remains little changed and constant mass flow rate is maintained. Vortices created by the wave action at the interface may also tend to partially cause the liquid acceleration near the wall, and the liquid film deceleration at the interface. These effects should also be clarified in the future.

3.3 Non-Dimensional Velocity Profiles

The average velocity profiles were non-dimensionalized with wall friction velocities calculated from the experimentally evaluated wall shear stresses. A comparison with the law of the wall for single-phase turbulent flow and Eq. 1 proposed by Ho and Hummel (1970) for a freely falling liquid film without any upward flow of gas are shown in Figs. 11 through 13 for Runs 1 through 3, respectively. In all cases, a reasonable agreement was obtained in the laminar sub-layer region, suggesting that this region is unaffected by the countercurrent gas flow. In the buffer zone ($5 < y^+ < 30$), a slightly lower velocity is observed for the liquid film than predicted by the law of the wall. Due to the extremely thin films which occur in countercurrent annular flows, Runs 2 and 3 contained no data extending into the turbulent core region ($y^+ > 30$). However, at a higher liquid flow rate such as in Run 1, the film thicknesses did reach the turbulent core region (Fig. 11), and the experimental data yielded velocities considerably higher than the values suggested by the law of the wall.

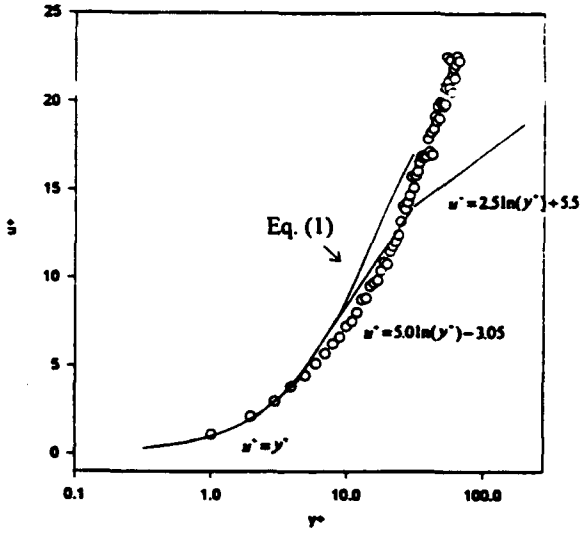

Fig. 11 Non-Dimensional Velocity Profile for Run 1 just before the onset of flooding

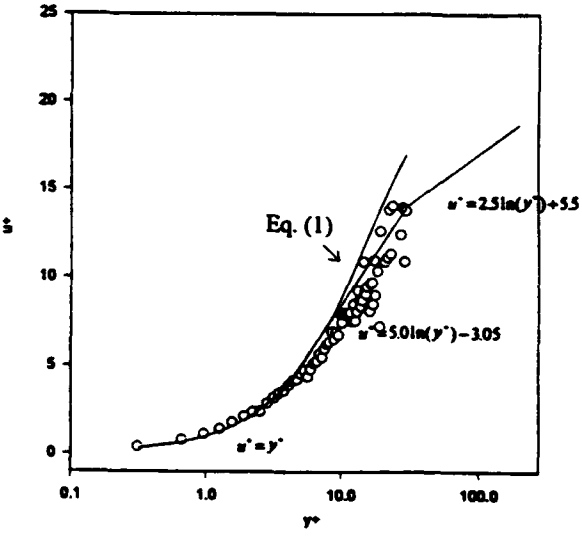

Fig. 12 Non-Dimensional Velocity Profile for Run 2 just before the onset of flooding

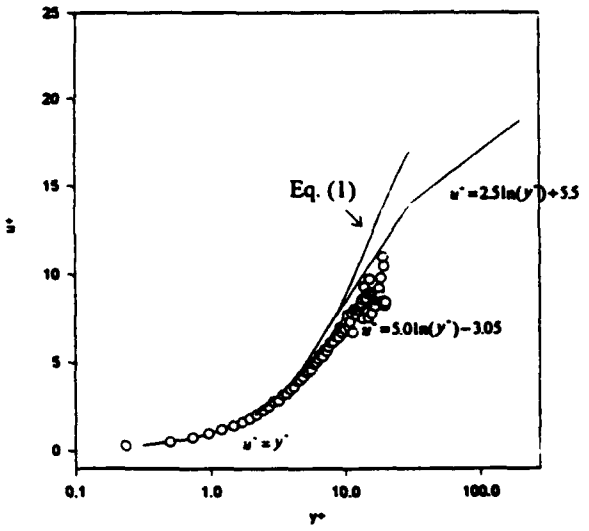

Fig. 13 Non-Dimensional Velocity Profile for Run 3 well before the onset of flooding

A comparison with the correlation for a falling liquid film with no gas flow given by Ho and Hummel (1970) provided a good indication of the consistency of the present results. Over the range for which their correlation was valid ($y^+ < 30$ for $Re_F \approx 1000$), the present data always indicated lower velocities near the interface. This is reasonable, since the countercurrent gas flow would tend to retard the liquid film near the interface.

4. CONCLUSIONS

The photochromic dye activation technique has been used to study the flow structure of a liquid film in vertical, countercurrent annular two-phase flow. The velocity profiles obtained indicated that the interfacial shear imposed by the countercurrent gas flow does cause some retardation of the film velocity near the interface, however, the interfacial drag was never sufficient to cause flow reversal in any part of the liquid film even at the onset of flooding. This means that the flow reversal in the liquid film is not responsible for the onset of flooding. The experimentally determined wall shear stresses were significantly underpredicted by an existing predictive method based on the average liquid velocity, even at conditions near the onset of flooding.

REFERENCES

Abe, Y., Akimoto, H., and Murao, Y., "Estimation of Shear Stress in Counter-Current Annular Flow", *J. of Nuclear Science and Technology*, Vol. 28, No. 3, March 1991, pp. 208-217.

Bharathan D., and Wallis, G.B., "Air-Water Countercurrent Annular Flow", *Int. J. of Multiphase Flow*, Vol. 9, No. 4, 1983, pp. 349-366.

Binge, M., Delhaye, J.M., and Nakach, R., "The Flooding Transition: An Experimental Appraisal of the Chaotic Aspect of Liquid Film Flow Before the Flooding Point", Proceedings from Heat Transfer - Philadelphia, 1989, pp. 274-279.

Govan, A.H., Hewitt, G.F., Richter, H.J., and Scott, A., "Flooding and Churn Flow in Vertical Pipes", *Int. J. of Multiphase Flow*, Vol. 17, No. 1, 1991, pp. 27-44.

Ho, F.C.K., and Hummel, R.L., "Average Velocity Distributions within Falling Liquid Films", *Chem. Eng. Sci.*, 1970, Vol. 25, pp. 1225-1237.

Kawaji, M., Ahmad, W., DeJesus, J.M., Sutharshan, B., Lorencez, C., and Ohja, M., "Flow Visualization of Two-Phase Flows Using Photochromic Dye Activation Method", *Nuclear Engineering and Design*, Vol. 141, Nos. 1&2, 1993, pp. 343-355.

Zabaras, G.J., and Dukler, A.E., "Countercurrent Gas-Liquid Annular Flow, Including the Flooding State", *AIChe Journal*, Vol. 34, No. 3, March 1988, pp. 389-396.

ANNULAR TWO PHASE FLOW SAUTER MEAN DIAMETER MEASUREMENTS - COMPARISON WITH EMPIRICAL PREDICTIONS

C J Bates and M R Ayob

Division of Mechanical Engineering & Energy Studies
School of Engineering
University of Wales College of Cardiff
P O Box 925, Cardiff CF2 1YF, UK

ABSTRACT

Experimental Sauter mean diameter (d32) measurements, based upon a hydrodynamic development length of 228 and a tube diameter of 32 mm, are compared with four empirical correlations which have been developed to predict d32 for vertical upward annular two-phase flows. Two gas flowrates and a range of liquid flowrates have been considered, each empirical correlation underpredicts d32 at the higher gas flowrate of 82.21 kg/m²s. At the lower gas flowrate (25.14 kg/m²s) serious overprediction is evident from one correlation and underprediction, to varying degrees, from the other relationships considered.

1. INTRODUCTION

Vertically upward annular two phase flow is characterised by the existence of a thin wavy liquid film on the pipe wall with an inner core of the flow which comprises the gas and the entrained droplets. The droplets exist as a result of entrainment and various break-up mechanisms. Experimental observation has shown that the growth of waves on the wall film and subsequent liquid entrainment are caused by the high gas velocity. Bates and Sheriff (1922) have reviewed the experimental techniques used to establish the range of droplet size and the variations reported over the past three decades.

Two dimensional Phase Doppler Anemometry (PDA) techniques have been used, based upon optical components which provided a probe volume on the green line with a length of 9.56 mm and a diameter of 302 micron. Coupled with a scattering angle of 70 degrees this provides a droplet sizing range up to 776 microns, as well as axial and radial velocities of 72 m/s and ±26 m/s respectively. This droplet sizing range is far in excess of the 224 micron figure previously discussed by Bates and Sheriff (1992). To achieve this range advantage has been taken of the minimum aperture setting available, via the common translation mechanism, which is operated by a micrometer screw at the rear of the Dantec receiving optics. For the current measurements off axis forward scatter at 70 degree has been considered, to take advantage of the dominance of first order refraction and the reduced influence of both reflection and higher orders of refraction. Some ambiguity has been experienced when annular two-phase flow measurements have been compared, on the same flow facility, using both 30 and 70 degree scatter, Bates and Ayob (1994).

Experimental data bases have been assembled by a number of researchers taking advantage of diffraction based light scattering instrumentation. Empirical correlations have subsequently been developed based mainly upon the physical parameters of the annular two-phase flow. Azzopardi (1985) proposed that

$$\frac{d_{32}}{\lambda_T} = \frac{15.4}{(We')^{0.58}} + 3.5\frac{G_{LE}}{\rho_L U_G} \qquad (1)$$

for those flowrates where the drop size increases with liquid flowrate, suffixes L and G represent the liquid and gas respectively, λ_T denotes the Taylor wavelength ($\lambda_T = \sqrt{\sigma/\rho_L g}$), σ is the liquid's surface tension, g represents gravitational acceleration and ρ the density. The first term describes the effect of the gas phase, where We' denotes the Weber number based on the Taylor Wavelength, ($We' = \rho_L U_G^2 \lambda_T / \sigma$, U_G is the superficial gas velocity), whilst the second term accounts for the liquid concentration, G_{LE} is the entrained liquid mass flux.

Azzopardi *et al* (1980) had previously proposed a different relationship:

$$\frac{d_{32}}{D_T} = 1.91\frac{Re^{0.1}}{We^{0.6}}\left(\frac{\rho_G}{\rho_L}\right)^{0.6} + 0.4\,\frac{G_{LE}}{\rho_L U_G} \qquad (2)$$

specifically for situations where the liquid was introduced through a porous wall, here We is the Weber number based on the tube diameter $We = \rho_G U_G^2 D_T / \sigma$ and Re is the conventional Reynolds number ($Re = U_G D_T / \nu_G$, in which ν is the kinematic viscosity). The form of this relationship was developed from turbulent droplet break-up and coalescence analysis, the tube diameter (D_T) is also a variable. The droplet break-up term contains the observed effect of gas velocity within the Reynolds and Weber numbers, while the concentration term accounts for the small increases in drop size as the liquid mass flux is increased.

Gibbons (1985) investigated the use of equations (1) and (2) for his experimental data and subsequently proposed that:

$$d_{32} = 370\lambda_T \frac{1}{(We)^{0.65}} \left(\frac{\rho_G}{\rho_L}\right)^{0.4} \left(\frac{\mu_G}{\mu_L}\right)^{0.05} + \frac{0.4 D_T G_{LE}}{\rho_L U_G} \quad (3)$$

The weak effect of viscosity has been incorporated by the introduction of $(\mu_G / \mu_L)^{0.05}$, which relates the gas viscosity to that of the water in order to account for a small increase of droplet diameter with increasing liquid viscosity. The exponent of the Taylor wavelength based Weber number has been increased to 0.65 to take into consideration the effect of gas velocity on droplet diameter.

Ambrosini *et al* (1991) proposed another empirical correlation

$$\frac{d_{32}}{m} = X_1 \left(\frac{\sigma}{\rho_G f_i U_G^2 m}\right)^{0.5} \left(\frac{\rho_G}{\rho_L}\right)^{X_2} \times \exp\left(X_3 \frac{G_{LE}}{\rho_L U_G} \frac{D_T}{d_{32}} + \frac{X_4}{We}\right) \quad (4)$$

Here f_i is the interfacial friction factor representing the roughness of the gas/liquid interface and m is the wall film thickness. Both f_i and m were determined using correlations based upon published experimental data. Optimised values of the constants X1 (22.0), X2 (0.83), X3 (0.6) and X4 (99.0), as shown in the brackets, were determined to fit two experimental data banks. One of the latter being the Harwell Laboratory data bank, which has been accumulated over a period of at least two decades.

Teixeira (1988) reviewed the performance of other correlations, advantage has been taken of his observations to focus only on these four correlations since in general they showed the best overall performance. The current measurements update those on a restricted sizing range reported by Bates *et al* (1994).

2. EXPERIMENTAL FLOW FACILITY/DATA ACQUISITION

The experimental facility was ostensibly the same as that previously used by Bates and Sheriff (1992), as shown in Figure 1(a). Compressed air was supplied to the flowline which was 7.3 m long, between the inlet and outlet sinter sections. Water was injected into the rig via the lower porous sinter section, the air then transports the liquid upwards and an annular wall film is formed. The wall film was removed just prior to the optical measurement section, the water supplied to the lower sinter was continuously monitored, together with that extracted at the upper level. The difference between the two readings provides the entrained liquid mass flux (G_{LE}). PDA measurements were obtained at the optical head immediately after the upper sinter section. The optical head, as shown in Figure 1(b), was designed to provide access to

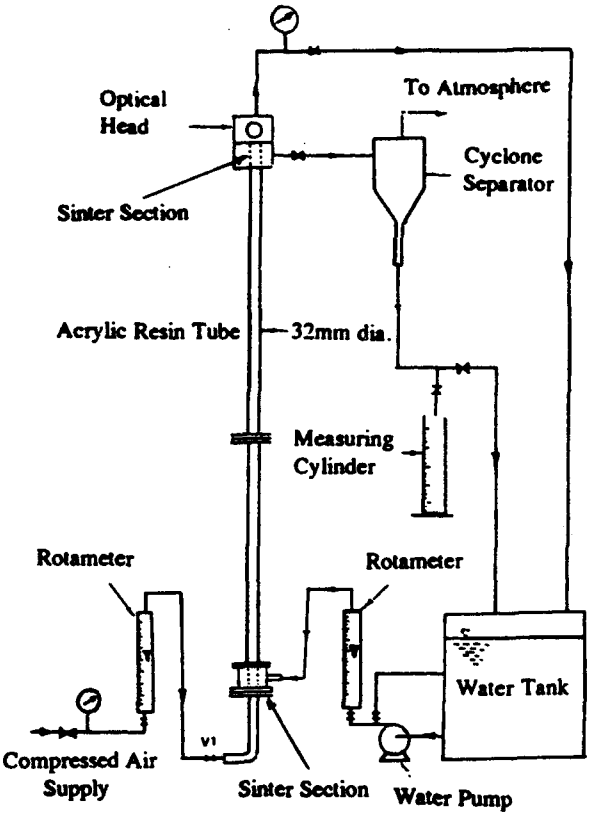

Figure 1(a) Experimental Rig

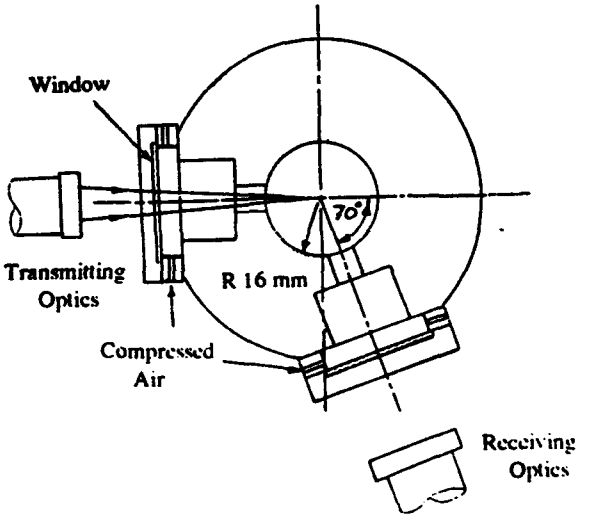

Figure 1(b) A Plan View of The Optical Head

the flow via a 50 mm diameter optical window 3 mm thick. The scattered light was collected at 70°, via an identical optical window, air purges were provided to prevent droplet deposition upon either window. The pressure at the point of measurement was maintained at 1.6 bar (absolute), other

experimental vertically upward annular two-phase flow measurements at or near this pressure within 32 mm diameter flow lines are shown in Table 1. The table also shows the hydrodynamic development

Table 1 Summary of Previous Work on Droplet Size-Velocity in Vertical Annular Air-Water Two-Phase Flow

Reference	L/D	U_G (m/s)	U_L (mm/s)	Size (μm)	Technique
Whalley *et al* (1977)	156	23-29	2-18	40-450	Photography
Azzopardi *et al* (1978)	125	23-42	16-95	11-1128	Diffraction
Gibbons (1985)	160	20-80	10-20	20-200	Visibility
Hadded (1986)	31.25	25-35	13-42	20-210	Visibility
Teixeira (1988)	125	15-75	16-125	11-1128 30-120 30-650	Diffraction Visibility PDA
Tayali (1989)	31.25	14-25	10-30	75-1500	Large Particle Monitor
Sheriff (1993)	135-228	12-43	10-65	5.5-224	PDA
Current	228	13-50	10-92	19-776	PDA

length (L), together with the range of superficial gas (U_G) and liquid (U_L) velocities and the technique employed to determine droplet sizes and the sizing range.

The table shows that the current measurements provide both a hydrodynamic development length and a sizing range capability which compares favourably with the previous investigations.

Data collection on the centreline was based upon a two-dimensional orthogonal optical configuration, from a 300 mW Argon-ion air cooled laser, with the green line being used to provide the droplet's vertical velocity and the diameter, whilst the blue line provided the radial velocity. The four photomultiplier output signals were processed via a Dantec co-variance processor, in the SIZEWARE software package all the validation functions were enabled with a maximum phase error of 20° and a spherical deviation of 20%. The sample size was based upon either a maximum of up to 30000 validated points or an elapsed time duration of 180 seconds, depending upon which occurred first.

3. EXPERIMENTAL MEASUREMENTS

Droplet count histograms are presented in Figure 2(a) and (b) for air mass fluxes of 25.14 kg/m²s and 82.21 kg/m²s and two liquid mass fluxes. At the lower gas flow rate the normalised histograms virtually overlay one another, although as the data rates show greater entrainment is evident with the higher liquid mass flux. At the higher gas flowrate Figure 2(b) shows small variations in the histograms with increasing liquid mass flux. The histograms confirm the existence of more droplets in the 100-200 μm range at the higher liquid mass flux (41.90 kg/m²s) compared with the lower mass flux (18.96 kg/m²s). The data associated with each respective histogram shows that a greater percentage of spherical droplets satisfying the validation criteria with the lower liquid mass flux 95.8% and 98% for the lower and higher air mass fluxes respectively. These figures compare with values of 89% and 93.4% for the greater liquid mass flux and the corresponding air fluxes.

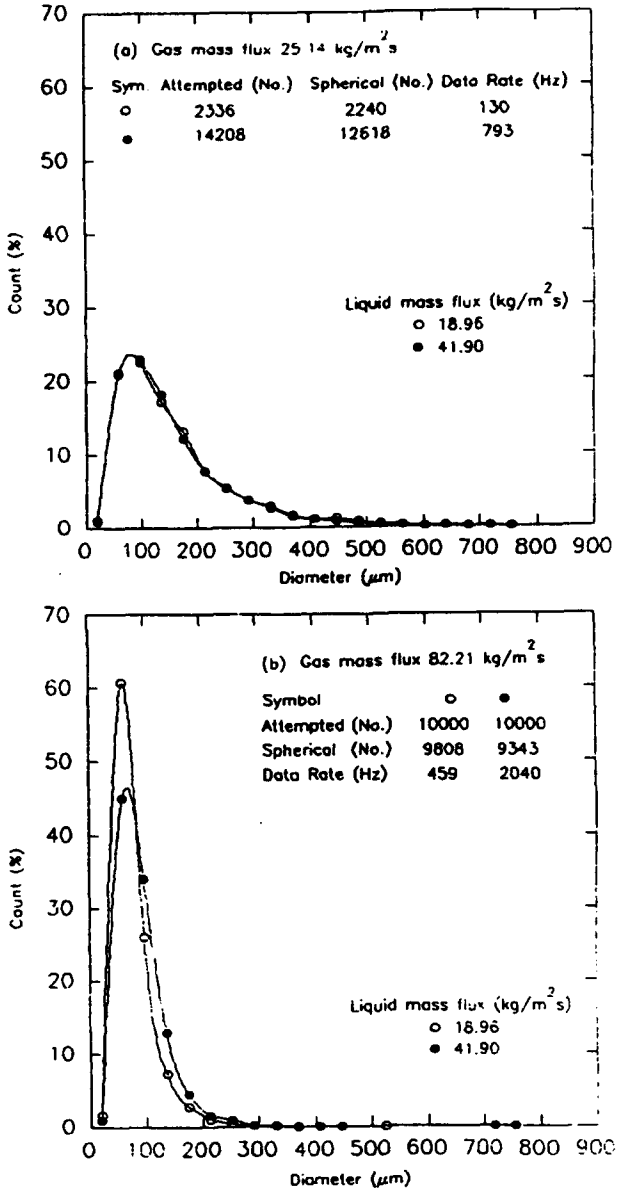

Figure 2 Histogram of Drop Mean Diameter At Constant Gas Mass Flux

The variation of number mean (d10) and Sauter mean (d32) diameters for liquid mass fluxes of 18.96 kg/m²s and 41.90 kg/m²s and the range of air mass fluxes investigated (25.14-82.21 kg/m²s) are shown in Figure 3. The results show a general and almost exponential decay of both d10 and d32

with increasing air mass flux, converging to values of 80 μm and 140 μm respectively at the highest gas mass flux.

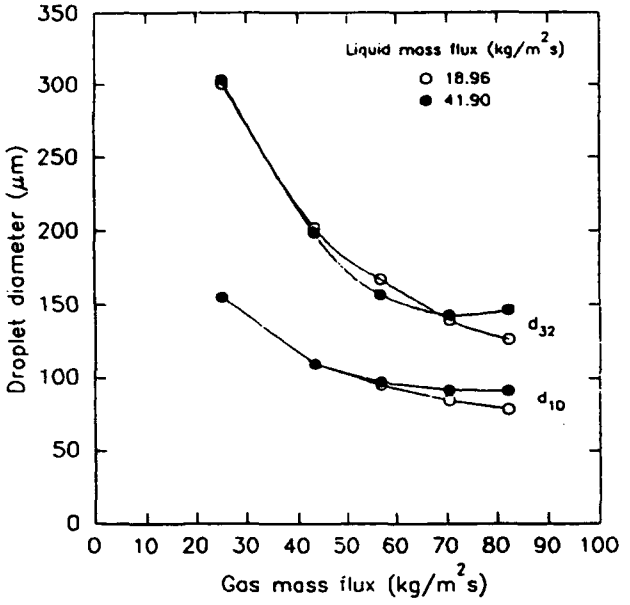

Figure 3 Variation of Number Mean (d10) and Sauter Mean (d32) Diameter With Gas Mass Flux

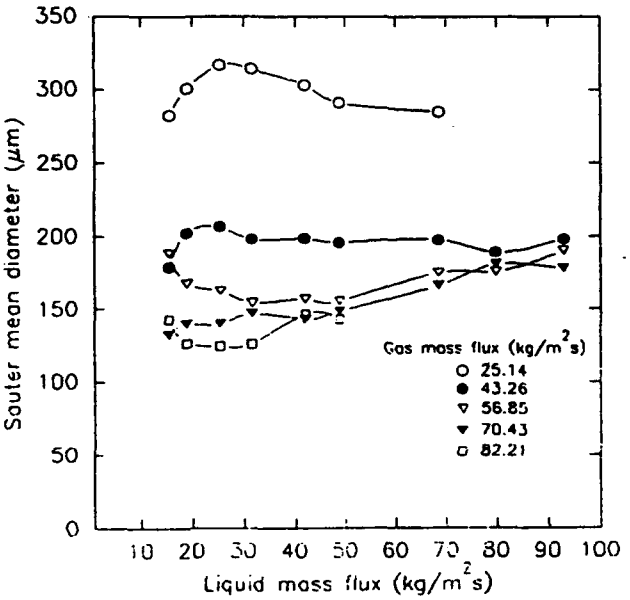

Figure 4 Variation of Sauter Mean Diameter (d32) With Liquid Mass Flux

Variation of d32 with increasing liquid mass flux, for the range of gas mass fluxes considered is shown in Figure 4, the trend is such that the diameter increases slowly with increasing liquid mass flux and decreases with increasing gas mass flux, although only small differences are evident at the higher gas flowrates.

Droplet velocity versus diameter correlations are presented in Figure 5 for the maximum (82.21 kg/m²s) and minimum (25.14 kg/m²s) gas flowrates and liquid mass fluxes of 18.96 kg/m²s and 41.90 kg/m²s respectively. At the lower gas flowrate droplets are shown to exist over virtually the whole sizing range, for each of the liquid flowrates considered. The profiles show little variation in the decay characteristics with variation in the liquid mass flux. At the high air mass flux, Figure 5 shows significant

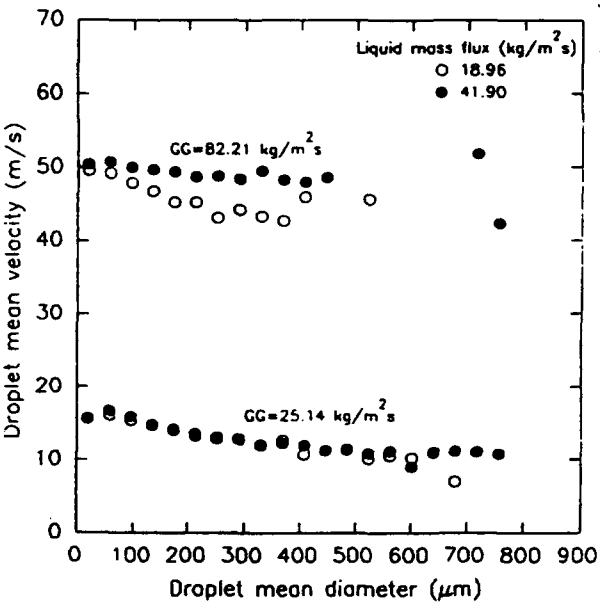

Figure 5 Droplet Mean Velocity-Diameter Correlation

differences with varying liquid flux, few if any large droplets are observed greater than 450-500 μm particularly at the lower liquid mass flux. The occasional large droplets maybe travelling at a velocity greater than that of the average value of the more numerous smaller droplets. Much less droplet slip, compared with the superficial gas velocity, is evident with the higher liquid mass flux correlation.

4. DISCUSSION

The current experimental variations of d32, together with those of Sheriff (1993), and the correlation achieved with equations 1-4 are shown in Figures 6(a) and (b) for gas mass fluxes of 82.21 and 25.14 kg/m²s respectively and the liquid mass flux range investigated. The current measurements show much higher d32 values, typically 300 μm, for the lower air mass flux compared with the 120 μm results of Sheriff. This reflects the truncated sizing range of 224 μm which he investigated. The histograms in Figure 2(a) show that a large number of droplets greater than 224 μm are present in the flow. Better agreement is evident at the higher gas mass flux, since as Figure 2(b) shows the vast majority of the droplets are less than 200 μm.

As is evident from Fig 6(a) each empirical correlation shows some degree of underprediction, the most serious discrepancies being evident from Gibbons empirical

relationship (equation 3). The current measurements show that d32 reaches a minimum value of 120 μm at a liquid mass flux of approixmately 25 kg/m²s and increases thereafter.

The results, in Figure 6(b), for the lower gas mass flux show that serious overprediction of d32 is shown by the relationship of Ambrosini et al. The best correlation with the experimental data is achieved by Azzorpardi's empirical

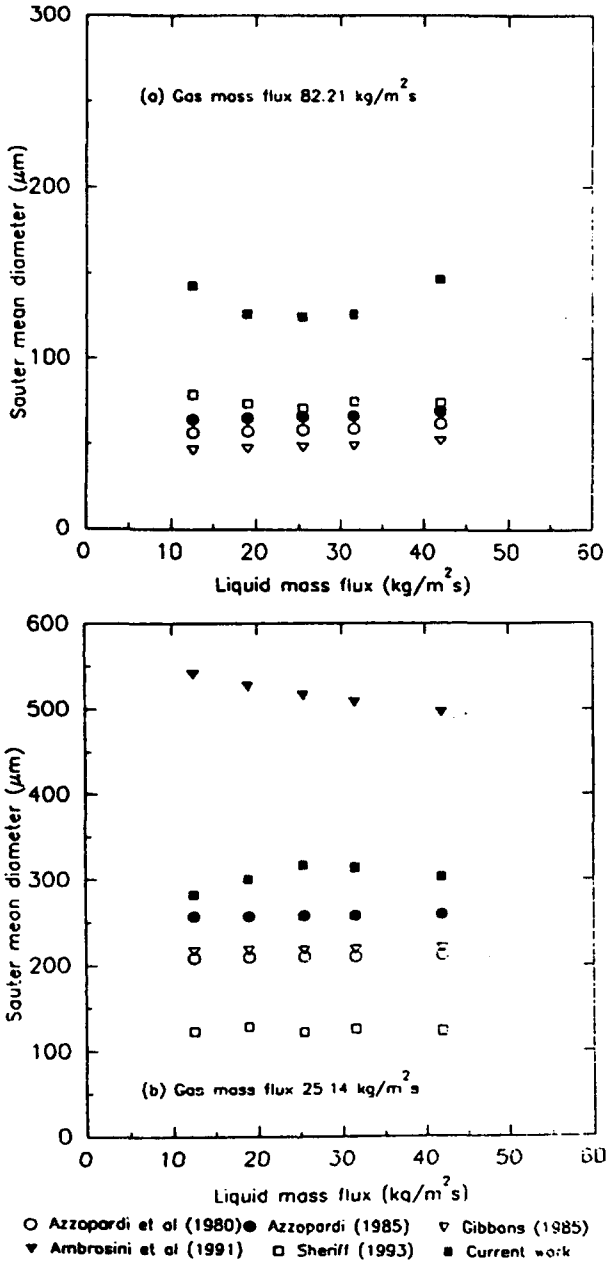

Figure 6 Comparison of Experimental And Empirical Prediction of Sauter Mean Diameter With Liquid Flow Rate

relationship (equation 1), whilst the other two relationship underpredict the variation of d32 with liquid mass flux. Each of the flow correlations takes into account the effect of liquid flow rate. The fact that the current measurements provide d32 values greater than those reported by other researchers reflects, as shown in Table 1, the range of droplets which could be observed by each measurement technique. The current sizing range capability compares favourably with the other investigators shown in Table 1. Since the empirical correlations reflect the experimental sizing range, upon which they are based, it is not surprising that significant differences are observed. Not surprisingly the signal processing capability of the equipment used in the current investigation greatly exceeds that used for all previous studies, apart from that of Sheriff (1993).

The current measurements based on a hydrodynamic development length of 228 provides a greater opportunity for the flow to become established and fully developed. However the d32 measurements in Figure 3 do not provide conclusive evidence that the flow is fully developed. The reduction in d32 with increasing gas mass flux may be represented, for the data in Figure 3 by $d32 = k(G_G)^{-0.73}$, where G_G is the gas mass flux.

At the higher gas flowrates the results, shown in Figure 4, confirm Azzopardi's observation of his data that d32 at first decreases with increasing liquid flux and then increases. The droplet velocity versus diameter correlations show that at the lower gas flowrate the results are independent of the water flowrate, whereas at the higher gas flowrate the correlations show appreciable variations. The droplet axial velocity could be expected to increase, at the higher liquid mass flux, because of the reduction in the void fraction and the much greater droplet entrainment which occurs at the higher gas flowrate. This increase in droplet mean velocity is observed in Figure 4 at the higher gas flowrate over the whole range of droplets measured.

5. CONCLUSIONS

The current measurements show a strong influence of gas mass flux on droplet size and that the Sauter mean diameter (d32) is dependent on the gas mass flux to the power of -0.73. The measured values of d10 and d32 are only weakly dependent on the liquid mass flux. Of the four empirical correlations considered, each underpredicts d32 at the highest gas mass flux. At the lower gas mass flux reasonable correlation is achieved by equations 2 and 3 and in particular with the correlation proposed by Azzopardi (equation 1).

REFERENCES

Ambrosini, W, Andreussi, P and Azzopardi, B J, 1991, A Physically Based Correlation for Drop Size in Annular Flow, Int J Multiphase Flow, Vol 17, 497-507.

Azzopardi, B J, Freeman, G and King, D J, 1980, Drop Sizes in Annular Two-Phase Flow, UKAEA Report AERE R-9634, Harwell, UK.

Azzopardi, B J, Drop Sizes in Annular Two-Phase Flow, 1985, Exp Fluids, Vol 3, 53-59.

Azzopardi, B J, Freeman, G and Whalley, P B, 1978, Drop sizes in Annular Two-Phase Flow, UKAEA Report AERE-R9074 Harwell, UK.

Bates, C J and Sherriff, J M, 1992, High Data Rate Measurements of Droplet Dynamics in a Vertical Gas-Liquid Annular Flow, Flow Meas Instrum, Vol 3, No 4, 247-256.

Bates, C J and Ayob, R, 1994, Annular Two Phase Flow Measurements using Phase Doppler Anemometry with Scattering Angles of 30° and 70°, Flow Meas Instrum, in press.

Bates, C J, Sheriff, J M and Teixeira, J C F, 1994, Phase Doppler Anemometry Measurements and Comparison with Empirical Annular Two Phase Flow Predictions, Int J Multiphase Flow in press.

Gibbons, D B, 1985, Drop Formation in Annular Two-Phase Flow, PhD Thesis, University of Birmingham, UK.

Hadded, O, 1986, A Packaged Laser Instrument for Drop Size and Velocity Measurements in Two-Phase Flow, PhD Thesis, University of Wales, UK.

Sheriff, J M, 1993, Laser Doppler Measurements of Droplet Size and Velocity in a Vertical Upward Gas-Liquid Annular Two-Phase Flow, PhD Thesis, University of Wales, UK.

Tayali, N E, 1989, Particle Sizing using Laser Doppler Anemometry Technique, PhD Thesis, University of Wales, UK.

Teixeira, J C F, 1988, Turbulence in Annular Two-Phase Flow, PhD Thesis, University of Birmingham, UK.

Whalley, P B, Azzopardi, B J, Pshyk, L and Hewitt, G F, 1977, Axial View Photography of Waves in Annular Two-Phase Flow, UKAEA Report AERE-R8787, Harwell, UK.

VELOCITY AND PARTICLE SIZE MEASUREMENT IN A TWO-PHASE FLASHING JET

R. Balachandar, S. R. Mulpuru and M. H. Ungurian

Atomic Energy of Canada Ltd.,
Containment Analysis Branch, Whiteshell Laboratories
Pinawa, Manitoba, Canada, R0E 1L0

ABSTRACT

Pressure vessels and pipe networks containing high enthalpy liquids under pressure are a common occurrence in the nuclear industry. The failure of a vessel or pipe in the form of a small hole, results in the formation of a two-phase jet containing a mixture of water droplets and steam. These droplets are generated by flash boiling and aerodynamic fragmentation. There is the possibility of the presence of the fission products suspended or dissolved in the high enthalpy fluid and the droplets formed can thus act as carriers of activity. Experimental data on size and velocity distribution of the droplets are required to support safety and licensing calculations on the transport of fission products in the containment. Furthermore, a good understanding of the droplet release mechanisms is necessary in order to specify the source terms for subsequent dispersion calculations. Efforts are currently underway at AECL Research, Whiteshell laboratories, to obtain the size and velocity of water droplets in flashing jets generated using various nozzle geometries and reservoir test conditions. To this end, a phase Doppler anemometer is used to obtain the necessary information. This paper deals with the presentation of results obtained using a custom made nozzle having a diameter of 0.061 cm and a throat length of 0.61 cm (L/D = 10). Typical results obtained at a test pressure of 4 MPa and a temperature of 230°C are presented. Efforts are made to obtain the representative diameter to characterize droplet size in flashing jets. Attempts are also made to obtain the proper scaling variables that can be used to characterize a flashing jet.

1. INTRODUCTION

During a postulated accident condition involving a break in the primary heat transport system, the high-enthalpy water can discharge into the containment in the form of a flashing jet. The effluent jet consists of a two-phase mixture of steam and small water droplets generated by flash boiling atomization and aerodynamic fragmentation. The presence of the fission products in the high enthalpy fluid is quite plausible and consequently the water droplets formed can act as carriers of activity. Experimental data on size and velocity distribution of the droplets are required to support safety and licensing calculations on the transport of fission products in the containment.

There has been a widespread interest in the study of the mechanics of flashing. Flash boiling atomization has applications in fuel-injection devices used to improve engine performance. Aerosols generated from spray cans by flashing have wide household utilization as insecticides, deodorants, etc. Studies have been conducted to understand the physics of the flashing process [Appleton, P. R., 1984; Jones, Jr., O. C., 1980; Koestel, A., et al. 1980; Lienhard et al.,1970; Oza, R. D., 1984; Sher, E. and Elata, C. 1977]. Attempts have also been made to measure droplet sizes in heated water jets [Anderson, R. C., et al. 1984; Bates, C. J., et al. 1986; Reitz, R. D., 1990].

Many of the earlier drop size measurements reported, involved the use of photography or some form of light-scattering techniques. In the present study, a phase Doppler anemometer (Dantec Inc.) is used to obtain experimental data on the size and velocity of water droplets formed in flashing jets. With the advent of the phase Doppler anemometer (PDA) some of the difficulties encountered in the earlier measurements have been effectively overcome [Bachalo, W. D. and Houser, M. J., 1986; Durst, F., 1982; Tayali, N. E. and Bates, C. J., 1990]. It should be noted that the light intensity of the transmitting beams and the sensitivity of the photodetectors have a distinct influence on the particle size measurement. These factors have been discussed in a recent paper [Balachandar et al. 1994]. This study will focus on the measurement of water droplet velocity and size, as the effluent jet progresses into the containment. The tests are conducted at a pressure of 4 MPa and a

temperature of 230°C. Radial distributions of the mean velocity and particle size are presented at two axial stations.

2. EXPERIMENTAL SET-UP

Figure 1a shows a schematic of the experimental set-up used in the present study. The water is heated to the required temperature by means of a heating source inside the vessel. The vessel is pressurised by adding nitrogen gas from the top. After the test conditions are attained, the pipe connecting the pressure vessel to the nozzle arrangement is also heated to the required value. The boiler and the piping system are well insulated to minimize heat losses. The nozzle assembly [Inset, Figure 1b] consists of a straight section 150 mm long and 4.83 mm in diameter. This is followed by a sudden contraction leading to a throat section 0.61 mm in diameter and 6.1 mm long (L/D = 10). As the hot water is depressurized through the nozzle, a flashing jet is formed at the tip of the nozzle. For the pressure and temperature chosen in the present study, visual observations indicate that the flashing jet is characterised by the formation of a nearly hemispherical expansion followed by a linear spreading.

At any point in the flow field of a flashing jet, the particle size and the velocity in the axial direction are simultaneously measured using the phase Doppler anemometer (PDA). The present system uses a variable power, water cooled, Argon-Ion laser having a wave length of 514.5 nm. A fiber optic probe fitted with a lens of focal length 400 mm forms the transmitting optics. The receiving optics is fitted with a convex lens having a focal length of 600 mm. A system of three photomultiplier (PM) tubes with built in pre-amplifiers is fitted on the receiving optics to obtain and validate the phase information contained in the Doppler signals. The transmitting and receiving optics were mounted on independent traversing arrangements. These traversing arrangements were computer controlled and allowed a simultaneous movement of both the transmitting and the receiving optics.

The PDA system was calibrated for the measurement of both size and velocity using standard procedures. The velocity measurements were validated by conducting measurements in known flow fields such as the potential core of an air jet. The size measurements were validated by conducting measurements in an air jet seeded with monodisperse soda lime glass beads of known sizes. A remark regarding size measurement in flashing jets using the PDA is in order. In a related study [Balachandar et al. 1994], it was found that the water droplets were fairly polydisperse in nature and their size ranged from about 1 to 100 μm. It was also realized that at a given location in the flashing jet, the count - size distributions obtained were quite different at various intensities of the transmitting laser beam. Based on a series of systematic tests, it was found that intensity of the transmitting beams coupled with the sensitivity of the photodetectors have a distinct influence on the size measurement. It was found that smaller particles (< 10 μm) do not scatter sufficient light when the intensity of the transmitting beams is low and hence are not recognised by the PM tubes. Similarly, when the high voltage gain of the PM tubes is low, the smaller particles are once again not visible. A proper combination of these two factors was found necessary in order to conduct size measurements with a higher accuracy and in the minimum possible measurement time. For the measuring environment present in a flashing jet, it has been established that the high voltage gain of the PM tube should be set at 1000 V and the intensity of the transmitting laser beam should be set at 2.5 W [Balachandar et al. 1994]. This ensured the measurement of very small particles and the acceptance rate of the data acquired was close to 100%. The signal-to-noise ratio was set at 0 dB and following the analysis presented in a previous study [Balachandar et al. 1994], the sample size (N) was set at 3000.

Figure 1b shows a simple schematic of the flashing jet and the coordinate system adopted. Measurements were conducted along the radial direction (Y axis) at two axial stations (Z = 48.8 and 146.4 cm; Z/D = 800 and 2400). The nozzle assembly was mounted on a traversing mechanism to facilitate the movement of the jet axially (Z - direction). The vertical direction (Y) measurements were achieved by simultaneously moving the transmitting and receiving optics. The variables of interest include the mean velocity, the count mean diameter, the Sauter mean diameter, count median diameter and the volume median diameter.

3. RESULTS

3.1 Radial distribution of mean velocity:

Preliminary tests indicated that the velocity distributions were symmetrical about the jet axis. Consequently, the measurements were mainly conducted on one side of the jet and the range of measurements were limited to $-20 < Y\ (cm) < +5$. Figure 2a shows the radial distribution of the mean velocity at two axial locations measured along the Y - axis. In this figure, a value of Y = +15 indicates the top portion of the jet, where as Y = -15 indicates the lower part of the jet. The velocity distributions denote an increase in the spreading of the jet as the distance from the nozzle increases. Using distributions such as in Figure 2a, the half width (δ) of the jet [the radial location where the velocity is

one half of the centre-line velocity] was evaluated. Figure 2b shows the variation of δ with increasing distance from the nozzle. The jet appears to spread linearly and furthermore, the rate of growth of the jet resembles that obtained in a two-phase plane jet [Goldschmidt, 1966]. Figure 3 shows the variation of the mean velocity along the radius of the jet at the two axial stations using U_{cl} and δ as the normalizing velocity and length scale respectively. Here U_{cl} is the value of the velocity along the axis at any given station. The data collapse on to a single curve indicating that the mean velocity profiles are similar. For qualitative comparison purposes, a typical velocity distribution obtained in a single phase flow [Hetsroni et al. 1971] is also shown in Figure 3. Compared to previous measurements in free jets, it should be borne in mind that the present measurements are conducted at much larger distances from the nozzle.

Figure 4a shows the probability density distributions of velocity at various radial locations for Z/D = 800. The distributions are fairly similar at two symmetrical locations (Y/δ = +1 and -1) on either side of the jet. The distributions appear to closely follow a Gaussian curve. A sensitive test of the closeness of fit with a Gaussian curve is provided by the flatness factor $F = \{\Sigma_i(U_i - U_{mean})^4/s^4N\}$ of the distribution. Here, U_i is the velocity of the ith particle in the axial direction, U_{mean} is the mean velocity and s is the standard deviation of the velocity set under consideration. The theoretical value of F for a normal distribution is 3.0. Figure 4b shows the radial distribution of F at the two axial stations. In the present study, at Z/D = 800, the experimental values of F ranged from 2.8 to 3.3 in the core region of the jet ($-1.0 < Y/\delta < 1.0$). This resembles the values obtained in single phase jets [Hetsroni, 1971]. One also notes from Figure 4b that at radial locations beyond the half-width of the jet, the F values increase with increasing distance from the jet axis. A similar observation was noted by Wygnanski et al. [1969] in single phase free jets. A measure of the relative skewness ($S = \{\Sigma_i(U_i - U_{mean})^3/s^3N\}$ of the jet is indicated in Figure 4c. The theoretical value of S for a normal curve is zero. Figures 4b and 4c indicate that the deviations of the probability density distributions from a Gaussian curve are considerable towards the outer edges of the jet and these deviations are fairly similar at the two axial stations considered. The variation of both S and F, from normal conditions could be attributed to the fairly high droplet concentrations at the various measuring locations in a flashing jet. Furthermore, it should be borne in mind that the particles are polydisperse in nature travelling with various velocities. For obvious reasons, the larger particles cannot be expected to faithfully follow the general flow and some of them can be visually seen to be dropping off beyond Z/D = 1000. The behaviour of the higher order moments indicate a general tendency to maintain self preservation as one progresses axially along the jet. Figure 5a shows the radial distribution of longitudinal turbulent intensities measured along the Y - axis. The distribution resembles the ones obtained in single phase flows [Hetsroni 1971, Wygnanski 1969]. Figure 5b shows the same set of data replotted in a normalized fashion using U_{cl} and δ as the normalizing scales. There is a larger amount of scatter in the data at Z/D = 2400. One should bear in mind that the two stations being compared to determine the self preserving nature of the flow are quite far from each other. The near coincidence of the dimensionless turbulent intensity profiles (lower order moments) reveal once again the inherent similarity of turbulent free jets.

3.2 Radial distribution of particle size:

Figure 6a shows the variation of the mean diameter along the radius at the two axial stations. At a section closer to the nozzle, the droplets are larger along the middle portions of the jet. A similar observation was noted by Reitz (1990). Using two different illumination techniques, Reitz (1990) was able to observe that the jet consists of two regions; a core region and a surrounding fine spray region. Reitz (1990) further speculated that the main jet had several sub jets whose breakup constituted the smaller particles in the outer edges while longer wave length breakup (hence larger particles) contributed to the core region. This is reflected in the present measurements. However, in Figure 6a, one notes that the larger particles are found to occur below the axis of the jet and the size distributions are clearly asymmetric. At any axial station, the mean diameters are generally larger along the lower half of the jet (Y < 0). One would speculate that this is a consequence of gravitational settling and hence the asymmetry. However, it is interesting to note that along the jet axis, the value of the mean diameter decreases with increasing distance from the nozzle. As indicated earlier, during visual observations, the particles could be seen physically dropping off after about Z/D = 1000. Figure 6b shows the radial variation of the Sauter mean diameter ($= \Sigma d_i^3/\Sigma d_i^2$) at the two axial stations. Here, d_i is the diameter of any given particle and the maximum value of i = 3000. At Z/D = 800, the distribution resembles that obtained for the mean diameter. At Z/D = 2400, the particle size increases drastically with increasing distance from the jet axis along the bottom half of the jet.

The use of the mean diameter does not in reality reflect the proper nature of the size distribution. It should be borne in mind that the particles crossing the measuring volume at a given measurement location are highly polydisperse. Consequently, it is necessary to

study the entire size distribution and obtain more representative diameters such as the count median diameter (CMD) and the volume median diameter (VMD). Figure 7a shows the variation of cumulative count - size distribution along the radius of the jet at an axial station Z/D = 800. One can note that at a location Y/d = 1.0 (top portion of the jet), the range of particles measured varies from about 1 to 60 μm. At this location, about 50% of the particles measured are below 6.5 μm while 90% of the particles are below 20 μm. The procedure for obtaining the CMD is also indicated in Figure 7a. Using such sketches, the CMD is evaluated and Figure 7b shows the radial variation of CMD at Z/D = 800. Figure 7b indicates that the variation of CMD is very similar to the variation of mean diameter. No additional information can be obtained by studying the radial variation of the CMD alone at a given axial station.

Figure 8a shows the variation of the volume median diameter along the radius at both the axial stations. As one proceeds from the top to the bottom of the jet, one perceives an increase in VMD along the radius. The radial variation of VMD at Z/D = 800 is quite different from the variation of the mean diameter or the CMD. Indications of gravitational settling can be clearly inferred from Figure 8a. Furthermore, along the jet axis, unlike the variation of the mean diameter, the VMD increases with increasing distance from the nozzle. Figure 8b shows the variation of the relative span factor $\{\Delta = (D_{90\%} - D_{10\%})/D_{50\%}\}$ along the radius. Here, $D_{90\%}$, $D_{50\%}$ and $D_{10\%}$ refer to the 90th, 50th and 10th percentile of the cumulative volume respectively. The relative span factor provides a direct indication of the range of the droplet sizes relative to the VMD. At Z/D = 800, the values of Δ decrease towards the jet axis, indicating that particles tend to be of more uniform distribution towards the core of the jet. At Z/D = 2400, there is considerable scatter in the data and the Δ values tend to decrease towards the outer edges of the jet.

In order to obtain a better understanding of the characteristics of size distribution, several plots of the cumulative counts / volume distribution were evaluated. Figure 9a shows a set of data evaluated at Z/D = 800 while Figures 9b and 9c show similar sets obtained at Z/D = 2400. In addition to the mean diameter, VMD and CMD, these sketches also show the dispersion $s = (D_{16\%}/D_{84\%})^{0.5}$ in terms of both counts and volume. For a location along the axis of the jet, one notes from Figure 9a that of the 3000 particles measured at a given location, 1500 particles (d < 16 μm) contribute to about 10% of the total volume. At the same time, about 50% of the total volume is contributed by particles accounting for less than 7.5% of the total counts (d > 30 mm). The scenario changes as one proceeds axially along the jet to Z/D = 2400 (Figure 9b). In this situation, with the particles arranged in ascending order of size, the first 1500 of the total number of particles contribute to about 1% of the total volume while 50% of the total volume is contributed by the last 1% of the number of particles. As one progresses to a location in the lower half of the jet (Figure 9c), the number of particles contributing to more than 50% of the total volume decreases further. A vast majority of the particles are very small (eg., 85% of the particles are less than 25 μm in Figure 9c) while the range is quite wide (varying from 1 to 70 μm). A very small percentage (1%) make a much larger contribution to the total volume. In this respect, the CMD is a good indicator of the smaller particles in the jet while the VMD is a better measure of the larger particles. Data on both CMD and VMD are required for modelling transport of water droplets in reactor containments, where aerosol mechanisms such as thermophoresis can affect primarily the smaller particles while gravity will influence mainly the larger particles.

4. OBSERVATIONS

The following observations can be drawn from the present set of results:

1. Visual observations indicate that for the given nozzle configuration and experimental conditions (Pressure = 4 MPa, Temperature = 230°C), the flashing jet initially expands in a near hemispherical fashion followed by a linear spreading.
2. The axial velocity measurements indicate that the velocity decreases with increasing distance from the nozzle. The radial distribution of the mean velocity exhibits a typical Gaussian distribution and this behaviour is similar to that noticed in single phase flows. Furthermore, the half-width of the jet indicates that the jet grows fairly linearly beyond the hemispherical expansion. The half-width of the jet appears to be the proper normalizing variable.
3. The values of the mean diameter and count median diameter along the jet axis, decrease with increasing distance from the nozzle, while, the VMD increases with increasing distance from the nozzle. At any point along the jet axis, there appears to be a greater dispersion in the size range as one proceeds from the mouth of the nozzle. The radial distribution of particle size clearly indicate that particles are highly polydisperse. Representative diameters like the count median, volume median and Sauter mean are collectively required to give a better description of the size distribution and provide the necessary data for modelling of droplet transport in reactor containments. The influence of gravitational settling along the vertical downward direction is clearly noticed in the size distribution.

ACKNOWLEDGEMENTS

This work is funded by the CANDU Owners Group (COG) consisting of AECL Research, Ontario Hydro, New Brunswick Power and Hydro Quebec.

REFERENCES

Appleton, P. R., 1984, A study of axi-symmetric two-phase flashing jets, Safety and Reliability Directorate, U. K. Atomic Energy Authority, SRD R 303.

Anderson, R. C., Erdman, C. A. and Reynolds, A. B., 1984, Droplet size distribution from bulk flashing, Nuclear Science and Engineering, 88, pp. 495 - 512.

Bachalo, W. D. and Houser, M.J., 1986, An instrument for two-component velocity and particle size measurement, Third Intl. Symp. on Applications of Laser Anemometry to Fluid Mechanics, Lisbon, Portugal, Paper # 18.3, pp. 1-6.

Balachandar, R., Mulpuru, S. and Ungurian, M. H., 1994, A note on particle size measurements in two phase flows, Symp. on experimental and computational aspects of validation of multiphase CFD codes, ASME, Lake Tahoe, June 18 - 23.

Bates, C. J., Hadded, O. and Yeoman, M. L., 1986, High pressure steam/water jet measurements using a portable particle sizing laser Doppler system, AIAA - ASME 4th Fluid Mechanics, Plasma Dynamics and Lasers Conference, pp. 59 - 64.

Durst, F., 1982, Review - Combined measurements of particles velocities, size distributions and concentrations, J. Fluids Engineering, Vol. 104, pp. 284 - 296.

Goldschmidt, V. and Eskinazi, S., 1966, Two-phase turbulent flow in a plane jet, J. of Applied Mechanics, Trans. ASME, December, pp. 735 - 747.

Hetsroni, G and Sokolov, M., 1971, Distribution of mass, velocity and intensity of turbulence in a two-phase turbulent jet, J. Applied Mechanics, June, pp. 315 - 327.

Jones, Jr., O. C., 1980, Flashing inception in flowing liquids, J. Heat Transfer, Vol. 102, pp. 439-444.

Koestel, A., Gido, R. G. and Lamkin, D. E., 1980, Drop-size estimates for a Loss-of-Coolant-Accident, NUREG/CR-1607, Los Alamos Scientific Laboratory.

Lienhard, J. H. and Day, J. B., 1970, The breakup of superheated liquid jets, J. Basic Engineering, ASME, Vol. 88, pp. 512 - 522.

Oza, R. D., 1984, On the mechanism of flashing injection of initially subcooled fuels, J. Fluids Engr., Vol. 106, pp. 105 - 109.

Reitz, R. D., 1990, A photographic study of flash-boiling atomization, Aerosol Science and Technology, Elsevier Sci. Publ. Co., 12, pp. 561 - 569.

Sher, E. and Elata, C., 1977, Spray formation from pressure cans by flashing, Ind. Eng. Chem., Process Des. Dev., Vol. 16, No. 2, pp. 237 - 242.

Tayali, N. E. and Bates, C. J., 1990, Particles sizing techniques in multiphase flows: A review, Flow, Meas. Instrum., Vol. 1, pp. 77 - 105.

NOMENCLATURE

CMD	Count median diameter (μm)
D	Diameter of the nozzle
$D_{n\%}$	nth percentile of cumulative volume or count
d	Mean diameter (Count mean, μm)
d_i	Diameter of ith particle
L	Throat length of the nozzle
N	Sample size
R	Radial location (cm)
s	Velocity standard deviation
U	Mean velocity in the axial direction (m/s)
U_i	Particle velocity in the axial direction (m/s)
U_{cl}	Mean velocity along the axis of the jet (m/s)
VMD	Volume median diameter (μm)
X	Coordinate perpendicular to the jet axis along the horizontal
Y	Coordinate perpendicular to the jet axis along the vertical
Z	Coordinate along the jet axis
σ	$(D_{16\%}/D_{84\%})^{0.5}$
δ	Half width of the jet (Radial location where U = $U_{cl}/2$)

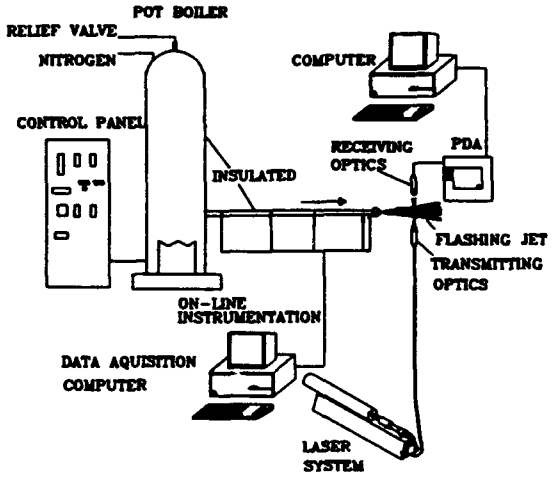

Figure 1a: Schematic of experimental set-up

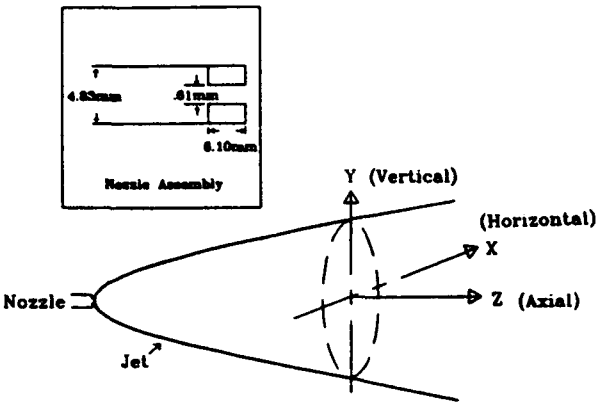

Figure 1b: Schematic of flashing jet

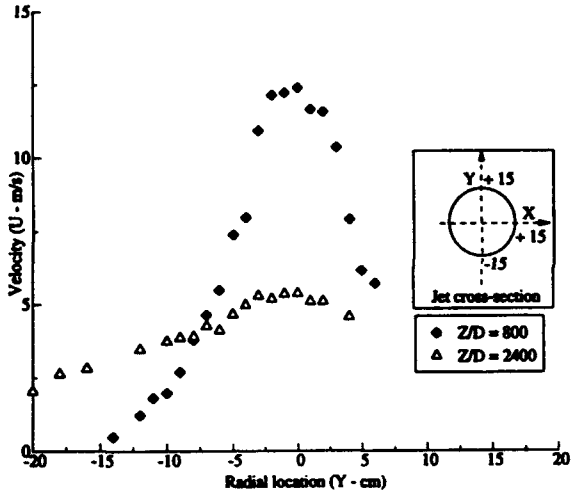

Figure 2a: Radial distribution of mean velocity

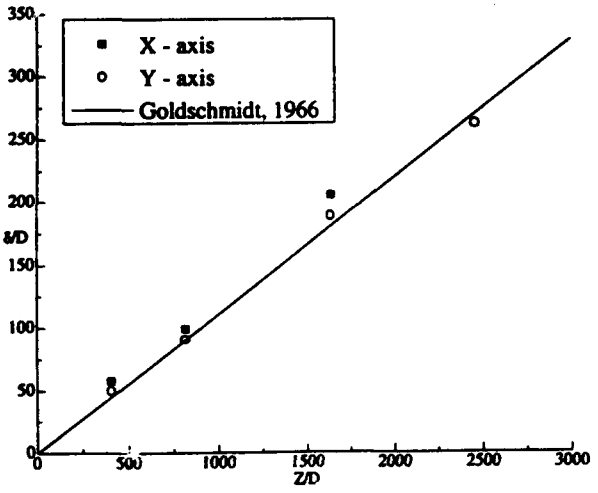

Figure 2b: Axial variation of jet half-width

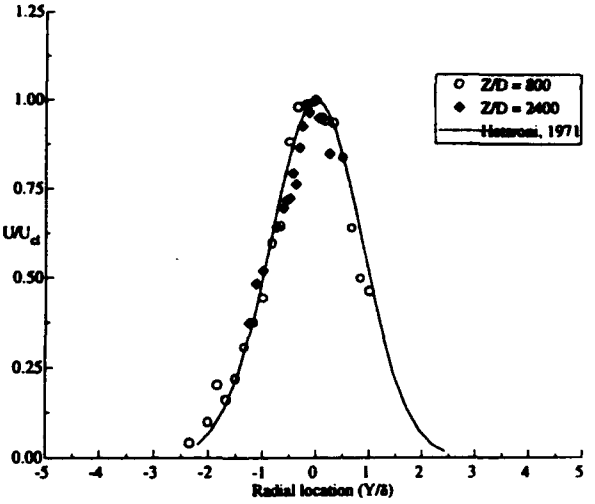

Figure 3: Radial distribution of normalized velocity

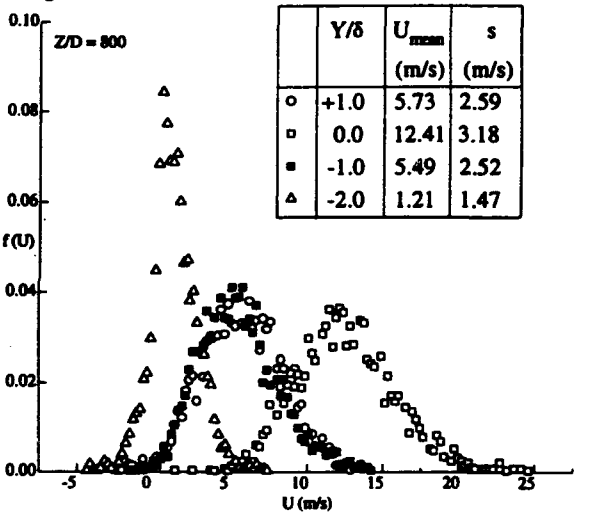

	Y/δ	U_{mean} (m/s)	s (m/s)
○	+1.0	5.73	2.59
□	0.0	12.41	3.18
■	-1.0	5.49	2.52
△	-2.0	1.21	1.47

Figure 4a: Probability density distributions of velocity

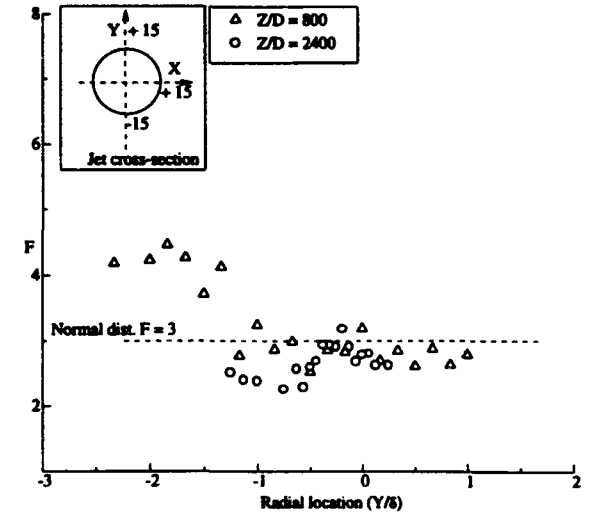

Figure 4b: Radial distribution of Flatness factor

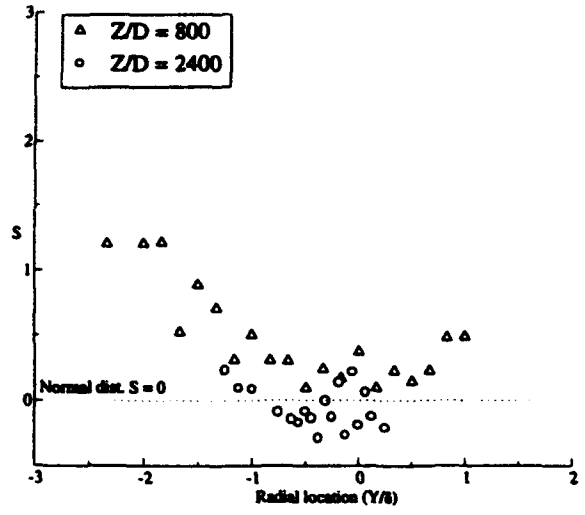

Figure 4c: Radial distribution of skewness

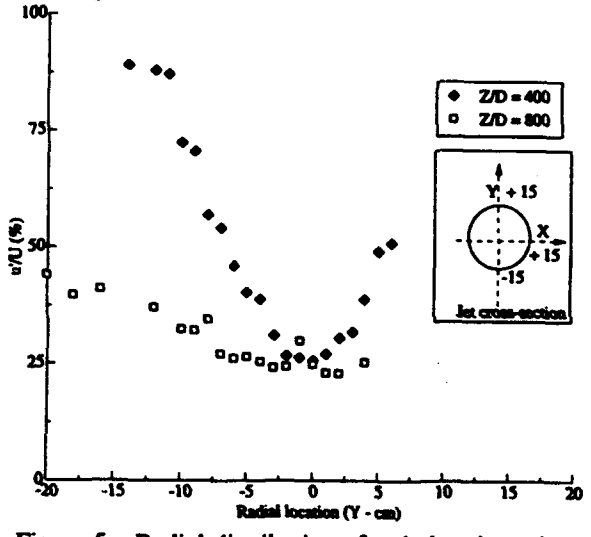

Figure 5a: Radial distribution of turbulent intensity

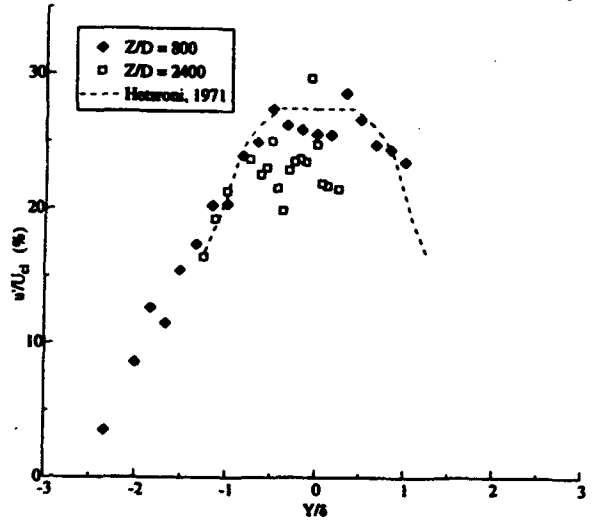

Figure 5b: Radial distribution of normalized turbulent intensity

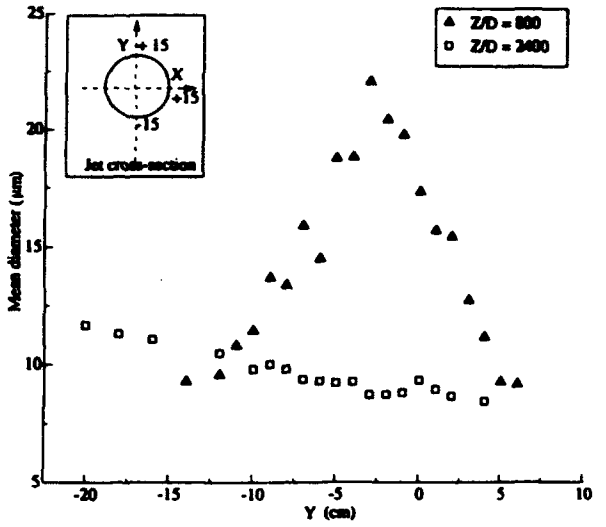

Figure 6a: Radial distribution of mean diameter

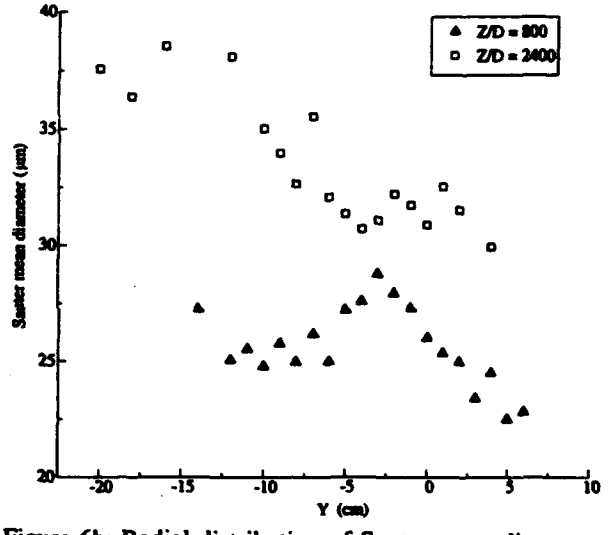

Figure 6b: Radial distribution of Sauter mean diameter

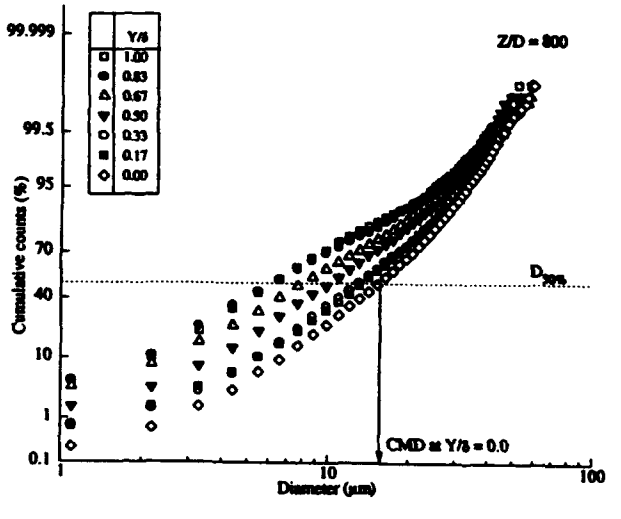

Figure nulative count size distribution at Z/D = 800.

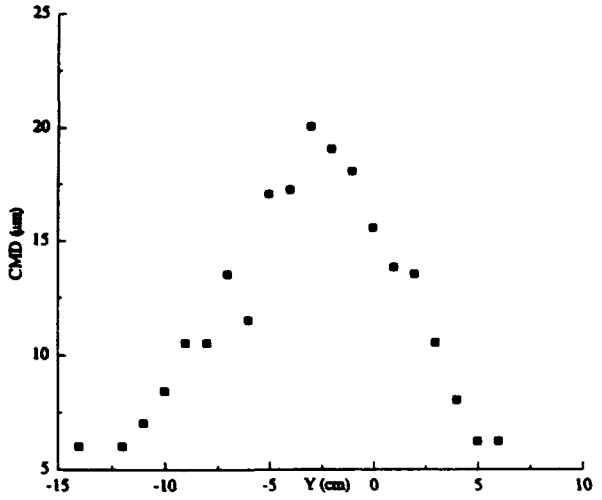

Figure 7b: Radial variation of Count median diameter

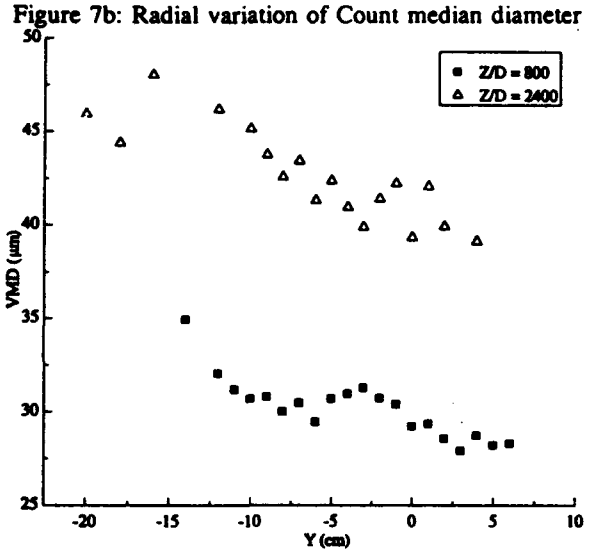

Figure 8a: Radial variation of volume median diameter

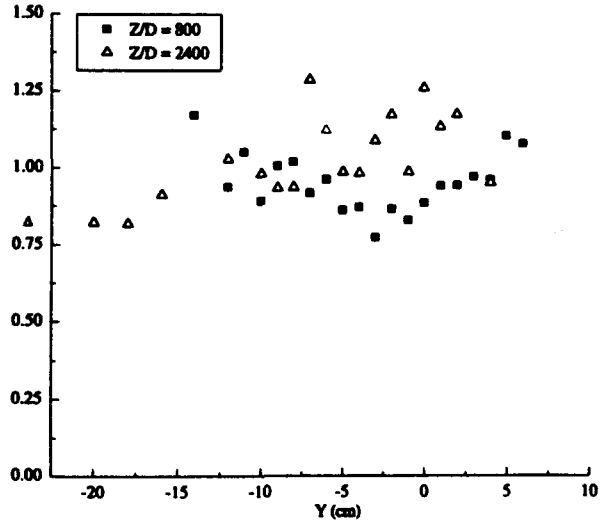

Figure 8b: Radial variation of relative span factor

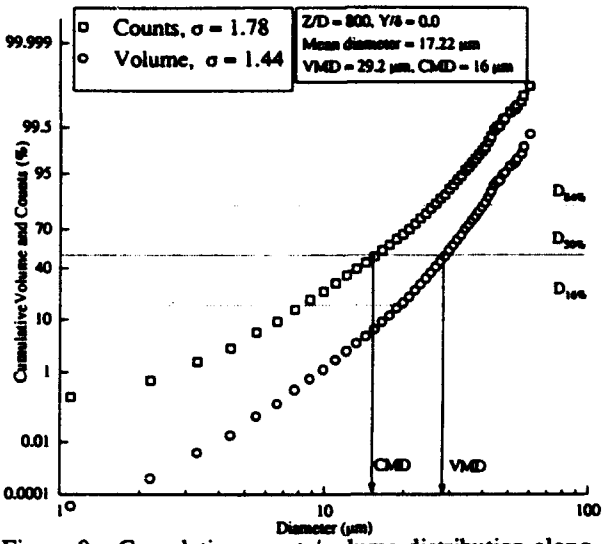

Figure 9a: Cumulative counts/volume distribution along the axis at Z/D=800.

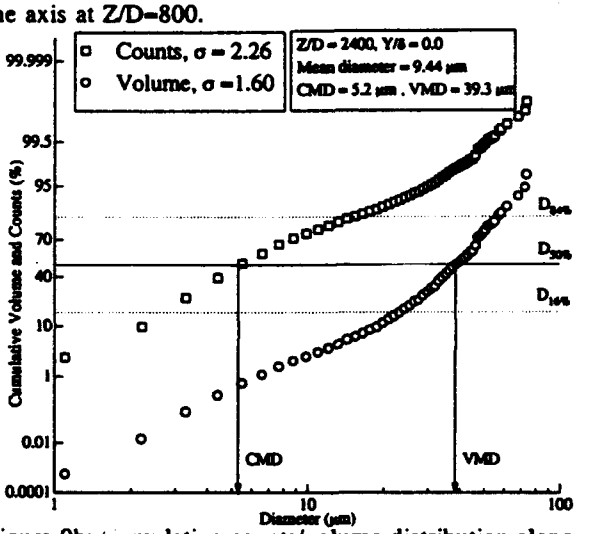

Figure 9b: Cumulative counts/volume distribution along the axis at Z/D=2400

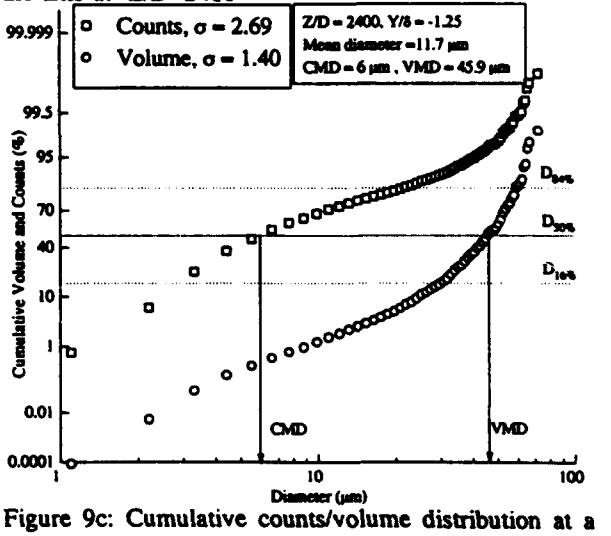

Figure 9c: Cumulative counts/volume distribution at a lateral location at Z/D=2400

Session 28.
Bend Flows

The Experimental Study on the Characteristics of Turbulent Polymer Solution Flow in a 180 Degree Square Sectioned Bend

Feng Tong
Shanghai Institute of Applied Mathematics and Mechanics
Shanghai University of Technology
China

Sun Houjung
Beijing Institute of Civil Engineerig and Architecture
Beijing
China

ABSTRACT

The comparative experimental study has been performed in the dilute polyacrilamide solution (PAM,300 w.ppm) and the relevant pure water flow in a 180° square sectioned duct at the same volumetric flow rate. The results of the velocity measurements by means of laser Doppler anemometry shows the existence of a stronger radial flow while the dilute polyacrilamide solution streams through the curved duct. The results of pressure and velocity measurements shows the consistency that the stronger radial flow is caused by the lager difference of the radial pressure between the inner and the outer wall of the curved duct, and, therefore, it may cause more pressure loss in the curved duct than the relevant pure water flow.

NOMENCLATURE

- V_s tangential component of velocity
- V_r radial component of velocity
- Q volumetric flow rate
- A cross-sectional area of square duct
- V_b volumetric mean velocity, $V_b=Q/A$
- a width of square cross-section of duct
- r^* non-dimensional co-ordinate in radial direction, $r^*=(r-r_i)/a$, where r_i is the radius of the inner wall of the curved duct
- θ co-ordinate in tangential direction
- z^* non-dimensional co-ordinate in spanwise direction
- y^* non-dimensional co-ordinate in vertical direction in straight section, $y^*=y/a$
- X_H non-dimensional co-ordinate in horizontal direction in straight section, $X_H=x/(a/2)$
- h pressure head
- g acceleration due to gravity
- w.ppm weight concentration, 1 w.ppm=$1/10^6$

1. INTRODUCTION

The investigations on drag reduction in turbulent flow by polymer additives, also known as "Toms effect", see Toms (1948), and the other relevant researches have been carrying out for decades. However, a drag increase was observed by Barness & Walters (1969) when the dilute polymer solution streams through curved pipes. This phenomenon recognised as a paradoxical behaviour to the well-known fact of drag reduction includes two aspects as follows: (1) drag reduction occurs in the laminar flow, while the dilute polymer solution passes through curved pipe, which normally causes drag increment in straight pipe flow; (2) drag increment occurs in the relevant turbulent flow, which normally causes the drag reduction in straight pipe flow. Ranade and Ulbrecht (1983) measured the laminar flow by means of laser Doppler velocimetry and attributed the drag reduction to the weaker secondary flow in the core region of pipe due to the elastico-viscosity of fluids [3].

To find out the explanation about this peculiar phenomenon, a range of measurements including the velocity measurement with laser Doppler velocimetry have been completed on the dilute polyacrilamide(PAM,300 w.ppm) solution flow in a 180 degree square sectioned bend. The comparative water flow measurements were also performed at the same Reynolds number (5.64×10^4).

2. EXPERIMENTAL APPARATUS

2.1. Polymer solution flow rig

Geometrically, the flow rig and test system for the present study was as identical as the one described by Feng Tong et al (1990), see

Fig.2.1.(a). However, for the purpose of polymer solution study, some special designs and measures have been made to prevent the mechanical degradation of the polymer solutions, which includes replacing the common centrifugal pump by a low shear pump and setting up the temperature and sample monitoring devices. During the lasting Laser Doppler Anemometry measurements, the flow rig was operated in the so-called one-pass way by injecting the higher concentration polyacrilamide solution stored in a pressurised container though the stainless steel nozzles around the upstream pipe section, see Fig.2.1.(a), into the pure water. To ensure the polymer solution to be well mixed with the water, a series preliminary tests and the monitoring sampling tests have been performed from time to time during the test. A fluctuation of the solution concentration has been found within 5% of the mean value range.

The bend section with the cross-section of 30x30 mm and the mean curvature radius of 150mm was manufactured as a mixture of perplex-glass construction, see Fig.2.1.(b), which enables elimination of the noises caused by the scratched transparent walls hence enhanced the validation rate of optic-electric signal collection for the present laser Doppler anomometry.

2.2. Laser Doppler Anomometery

A one-component laser Doppler velocimetry system (PDLDV-100, Beijing Institute of Photographic Machinery) including a 10 mW He-Ne laser source was used for the velocity measurement. The laser Doppler anemometer was established in the forward-scatter alignment. The incident angle of the laser beam is 7.1°. By means of rotating the principal axis of optical probe volume , the time-averaged tangential and radial components of velocity as well as the relevant mean Reynolds stress components are possibly obtained at the same spatial point in the flow region, as deducted by Melling & Whitelaw (1976). An on-line data acquisition system which consists of a counter (JPS-2, Beijing Institute of Universal Technology) and a personal computer was applied for data collection and analysis. The laser Doppler anemometer was mounted on a three-dimensional mechanism to reach the measuring positions in the flow region.

2.3. Pressure and rheological measurements

The pressure measurement was performed using an inclined manometer. A number of pressure taping holes were established along both the inner and the outer wall of the curved bend in order to acquire the detailed information about the static pressure distribution.

According to the non-Newtonian property of the polyacrilamide solution, the low shear rate rotating viscometer (Low-Shear 30, Contraves Industrial Products Ltd, West Germany) and the gun rheometer (Deimos Ltd, Britain) were chosen to cope with the determination of the rheological coefficients of the polyacrilamide solution. The details has been given in the further section.

The strict measures such as temperature control and sample detection were undertaken through the test to ensure the consistency of the experimental conditions.

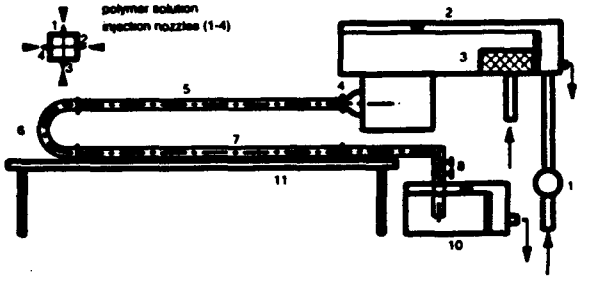

(a) Polymer solution flow rig

1.low shear pump 2.upper overflow tank 3.honeycomb 4.bell-mouth section
5.upstream section(2.1m) 6.180 degree bend 7.downstream section(2.4m)
8.control valve set 9.lower steady-head tank

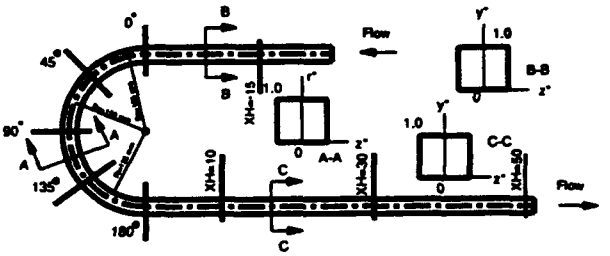

(b)Coordinate system and measurement station

Figure 2.1. Polymer Solution Flow Rig and Coordinate system

3. EXPERIMENTAL RESULTS

3.1. Results of pressure measurement

As above mentioned, the pressure measurements were carried out along the whole length of the straight and curved section for the pure water and the polyacrilamide solution flow. Comparing to the pure water flow with almost the same volumetric flow rate (Q=1.692 l/s), the

polyacrilamide solution with the weight specific concentration of 300 w.ppm gained the drag reduction rate of 40% along both the upstream and the further downstream section. This observation conforms the drag reduction effect in the turbulent flow through the straight pipe. However, by means of the definition of the pressure loss suggested by Ito (1959,1960), the pressure loss has calculated for both the pure water and the polyacrilamide solution flow through the curved bend. The results turned out that the pressure loss for the polyarilamide is greater than the relevant pure water one by 17.6%, as shown in Fig.3.1.(a).

Figure 3.1.(b) illustrates the local details of the non-dimensional pressure distribution along the curved bend. By matching the non-dimensional value of pressure head ($2gh/v_{b2}$) at station (θ=20°) on the convex wall together, the radial pressure difference between the inner and the outer wall can be clearly specified. For the polyacrilamide solution flow, the radial pressure differences at all stations in the curved bend are more or less greater the one of the pure water, especially the maximum one at station (θ=160°) is greater than the relevant value of pure water flow by 13%, etc. Considering the secondary flow in curved ducts is significantly driven by the radial pressure difference, see Humphrey et al (1977,1981), this deviation of the radial pressure difference may impact some influence on the
flow in curved bend. The details will be discussed in the further section.

3.2. Results of rheological measurements

In the present investigation, a commercially available polyacrilamide powder was chosen as the drag reduction agent. This product supplied by Shanghai Factory of Polylamide has been used by previous investigators for the purpose of drag reduction research, see Zhao et al (1979).

The rheological measurements were performed after the polyacrilamide powders had well resolved into the water solvent. The results revealed the polyacrilamide solution is bound to be classified as a power-law typed fluid, as shown as in figure 3, and has the shear-thinning property within a certain range of shear rate ($4 < \gamma < 100\ s^{-1}$). However, as the shear rate increases further, the solution converts to a Newtonian fluid again but with a reduced constant viscosity.

According to the theory of rheology (Chu,1988), for the dilute water-polymer solution, the relationship between shear viscosity μ and shear rate γ can be described in the universal form of Cole law in both the low and high shear rate region as below

$$\mu=\mu_{\infty}+(\mu-\mu_{\infty})(1+(\lambda\gamma)^{n})^{-1} \qquad (1)$$

where λ is the maximum relax time which can be used as a factor to estimate the visco-elastic property of the polymer solution. For the polyacrilamide solution used in this study, the formula has been deducted based on the test data as follows

$$\mu=1.85+9.72(1+(0.013\gamma)^{0.99})^{-1} \qquad (2)$$

where the unit of μ and γ are mPasec and sec^{-1}, respectively.

Based on the tests, the conclusion can be drawn that the polyacrilamide solution used in the present study is a shear thinning visco-elastic fluid.

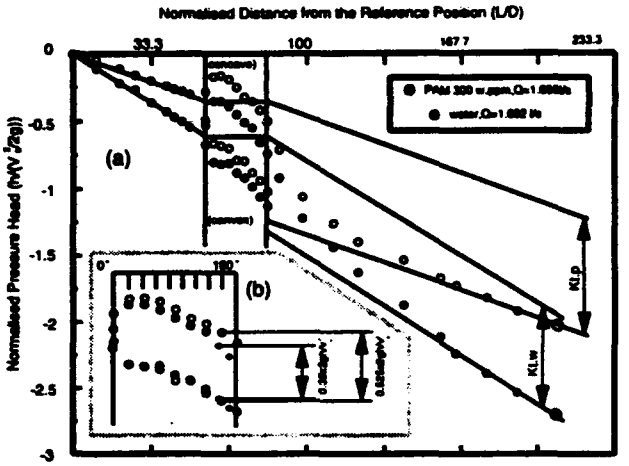

Figure 3.1.(a)&(b) Pressure Distribution along the Duct

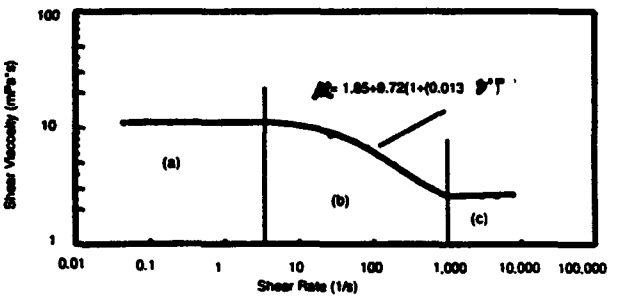

Figure 3.2. Shear Viscosity vs Shear Rate (PAM solution 300 w.ppm)

3.3. Results of velocity measurements

According to the symmetry of the geometric configuration of the duct, velocity measurements were merely performed within the right-hand half of the duct cross-section at the following stations: X_H=-15, θ =0°, 45°, 90°, 135°, 180°, X_H=30 and X_H=50. As well known, the flow in curved duct and even in square sectioned duct prevails the apparent three-dimensional characteristics. A great amount of attention has given by the present authors to this complex behaviour. Therefore, the velocity measurement results are demonstrated in two parts as bellow.

(i) tangential components of velocity

The development of tangential or main component of velocity has been shown in figure 4. At the entry of the 180 degree bend, the velocity profile of polyacrilamide solution flow seems more pointed than the one of water flow over the whole region of duct, see the profiles of the tangential components of velocity (V_s/V_b) at the station of X_H=-15. However, at the station of (θ=45°), the inner part of velocity profile of polyacrilamide solution flow is relatively plumper, after the station of (θ=90°), the outer part has been more pointed than the one of water flow. This implies that, in polyacrilamide solution flow, there exists a stronger radial mass and momentum transfer from the inner to the outer side of the curved duct.

(ii) radial components of velocity

The development of the radial components of velocity as shown in figure 5 supports the above mentioned facts with the details of the development of radial flow along the curved duct. Again, at the entry of the curved duct, the radial flow of polyacrilamide solution is slightly weaker than the one of water flow. At the station of (θ =45°), an obvious stronger radial flow has been found in the polyacrilamide solution flow, which results in the more apparent shift of its tangential velocity profile from the inner side to the outer side, so called "over shooting", which occurs in the section between the station of (θ=45°) and the station of θ=90°. After the station of (θ=45°), the radial flow of polyarilamide solution keeps exceeding the one of water flow even in the core region of the duct and then keeps this trend along the rest of the duct sections. In the entire curved section, a stronger radial flow at the most measurement stations has been observed in the polyacrilamide solution flow.

The results of velocity measurements indicates the consistency with the results of the pressure measurement, as the driven force of the secondary circulation in the curved duct is attributed to the pressure difference between the inner and the outer wall of the duct.

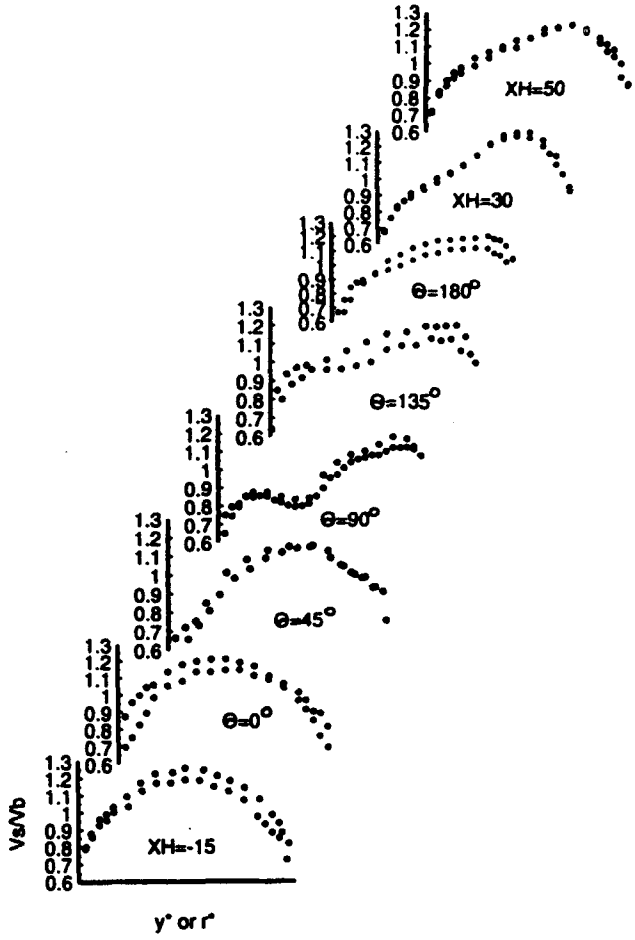

(a) Velocity profiles (Vs) at z*=0.00

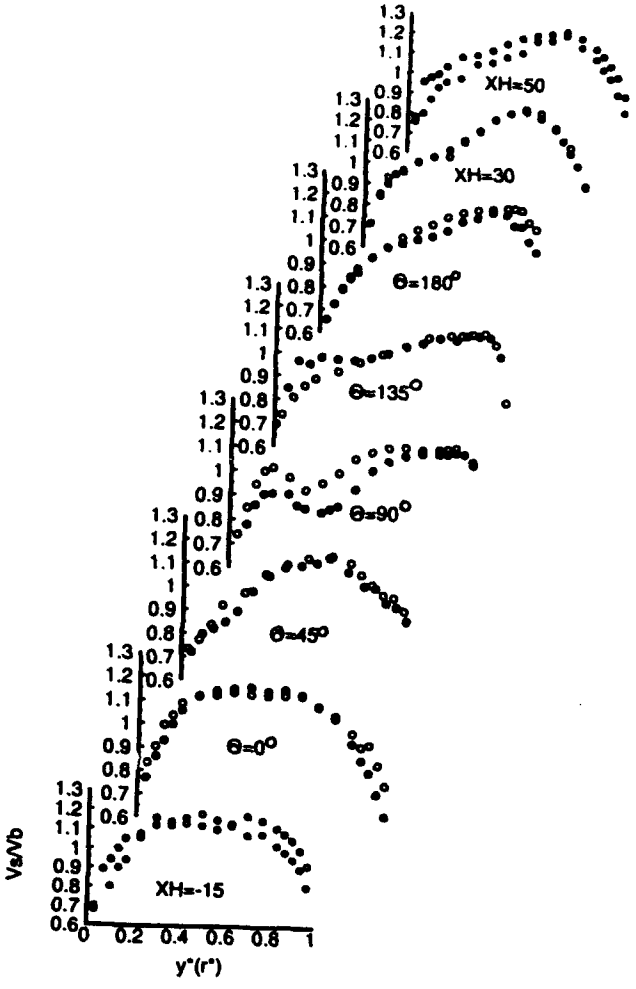

(b) Velocity profiles (Vs) at z*=0.40

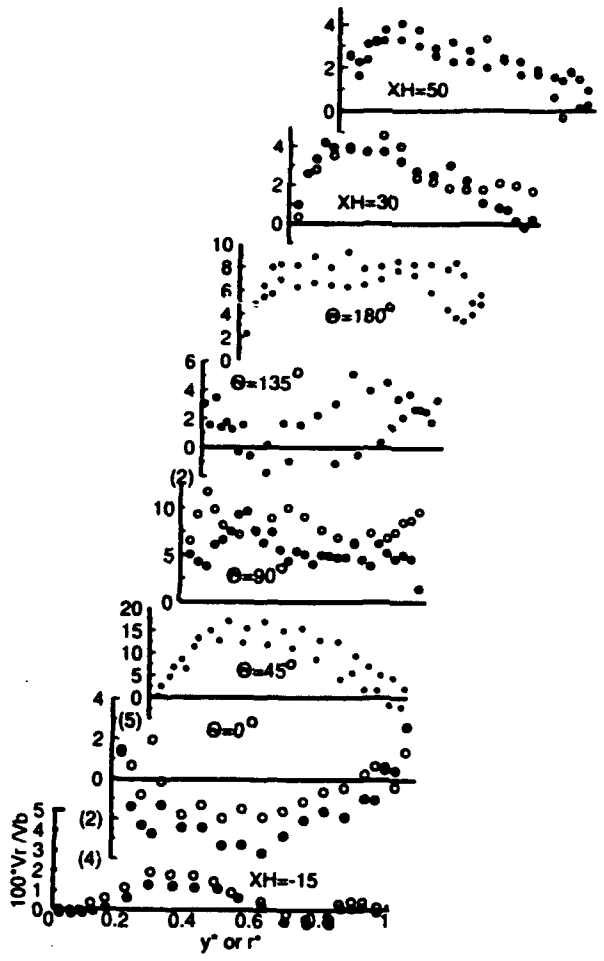

(a) Velocity profiles (Vr) at z*=0.00

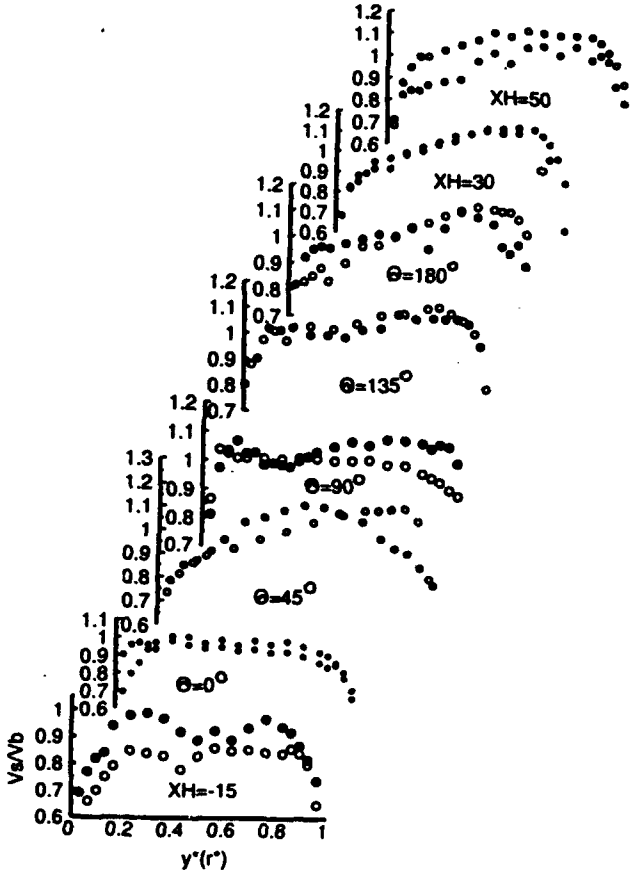

(c) Velocity profiles (Vs) at z*=0.80

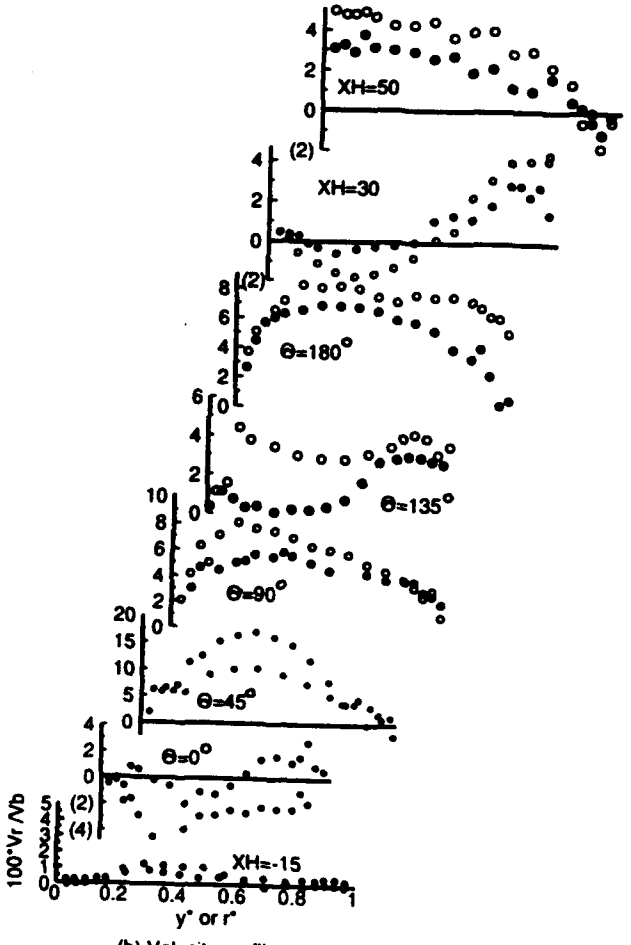

(b) Velocity profiles (Vr) at z*=0.40

Figure 4.1. Comparison of Tangential Velocity Components

28.1.5.

○ PAM solution ● water

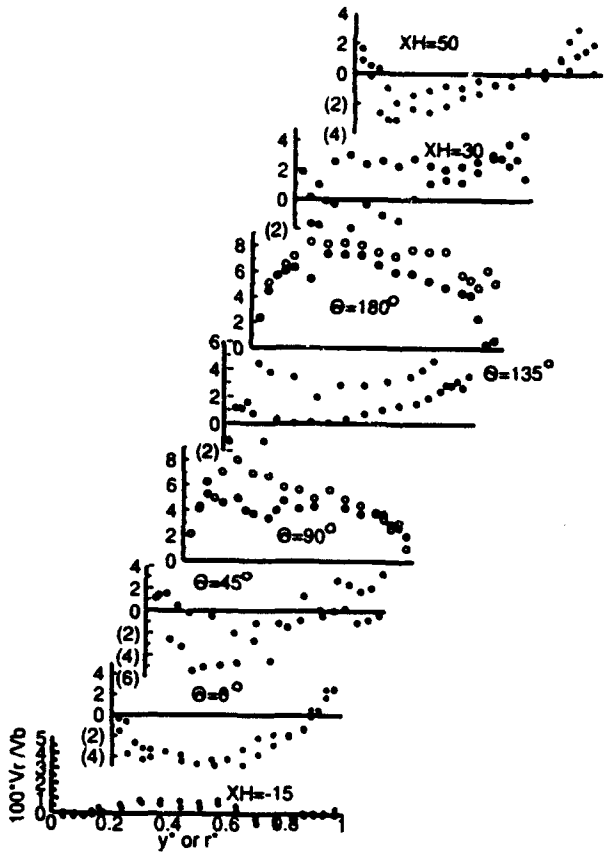

(c) Velocity profiles (Vr) at z*=0.80

Figure 4.2. Comparison of Radial Velocity Components

○ PAM solution ● water

4. CONCLUSIONS

A range of detailed measurements have been performed on the polyacrilamide solution (300 w.ppm) and the relevant water flow at the same Reynolds number of 5.64×10^4.

The tangential and radial components of velocity of the dilute polymer solution flow have been obtained and compared with the ones of water flow. The stronger radial flow in the curved duct suggests the existence of the more intensive mass and momentum exchange in the polymer solution flow.

According to the elastico-viscosity of the fluid, the stronger secondary flow in the polyacrilamide solution flow may cause more pressure loss in the curved duct.

REFERENCES

Toms,B.A.(1948) Proc.1st Int.Rheol.Congr. (Holland)

Barness,H.A. & Walters,K.(1969) Proc.Roy.Sci.London. A314, pp.85-109

Ranade,V.R. & Ulbrecht,J.J.(1983) Chem.Eng.Commun. Vol.20, pp.253-72

Feng Tong, Sun Houjung & Qian Weichang (1990) Study on Characteristics of Turbulent Flow in a 180 Degree Square Sectioned Bend, Proc.5th International Symposium on Applications of Laser Techniques to Fluid Mechanics, Lisbon, Portugal

Melling,A. & Whitelaw,J.H (1976) J.Fluid Mech. Vol.78

Ito,H.(1959) J.Basic Engn.Trans.ASME. June. pp.123-34

Ito,H.(1960) J.Basic Engn.Trans.ASME. March. pp.131-43

Humphrey,J.A.C., Taylor,A.M.K. & Whitelaw,J.H.(1977)J.Fluid Mech. vol.83, pp.509-27

Humphrey,J.A.C., Whitelaw,J.H. & Lee,G.J.(1981) J.Fluid Mech. vol.103, pp.443-63

Zhao,X., Zhong,S., Shen,C. & Xiu,G.(1979) Proc. 2nd National Conference on Fluid Mechanics, pp.258-61, Nanjing,China

Chu,Z.(1988) Polymer Structual Rheology, Sichuan Press of Education (Chinese edition)

FLOW STRUCTURE IN MEANDERING COMPOUND CHANNEL FOR OVERBANK

K. Shiono*, Y. Muto**, H. Imamoto** and T. Ishigaki**

* Department of Civil Engineering, Loughborough University of Technology, UK
** DPRI, Kyoto University, Japan

ABSTRACT

Measurements of secondary flow are very difficult in a laboratory scale since the magnitude of secondary flows are sometimes very small compared with the streamwise velocity. In recent years a laser doppler anemometer system has been improved rapidly and made it possible to measure accurate velocity components in a laboratory scale. Measurements of secondary flow and the Reynolds stresses have been taken place in a meandering compound channel for an overbank flow condition using a two component laser doppler anemometer system with a small probe head. Fluctuations of the streamwise, lateral and vertical components of velocity were measured by placing the head above water surface and submerging the probe head in water. The structure of the secondary flow and the Reynolds stresses along the meandering channel for the overbank flow conditions was obtained. Results show development of the secondary flow and locations of intensive Reynolds stresses along the meandering channel.

1. INTRODUCTION

Rivers often have a straight flood plain bank with a straight main channel and a meandering flood plain bank with a meandering main channel in order to discharge water on to flood plains at a time of high discharge. The prediction of water level at such high discharge is vitally important for flood alleviation schemes. The relationship between the water level and discharge is influenced by the structure of secondary flow and turbulence. A study of flow in a straight channel with straight flood plain banks has been undertaken recently by Knight and Shiono(1990) and Shiono and Knight (1991) . They have measured secondary flows and turbulence in a relatively large physical model, namely the Science Engineering Research Council Flood Channel Facility (SERC-FCF), using a two component laser doppler anemometer system with a small probe head. The results showed that the flow resistance was greatly influenced by the secondary flow even the straight channel.

Meandering flood plain banks are commonly constructed along a meandering channel and the structure of secondary flow and turbulence is not well known along a meandering compound channel for an overbank flow condition. The recent study for a meandering channel was undertaken by Willettes and Hardwich (1993). They illustrated the secondary flow structure using a dye tracing technique and flow current meters. However the magnitude of the secondary flow and the Reynolds stresses were not measured. It is important to know the magnitudes of the secondary flow and turbulence levels in order to improve the relationship between the flow resistance and discharge for the overbank flow conditions.

This paper describes the measurement techniques and some results of the secondary flow and turbulence in a meandering compound channel.

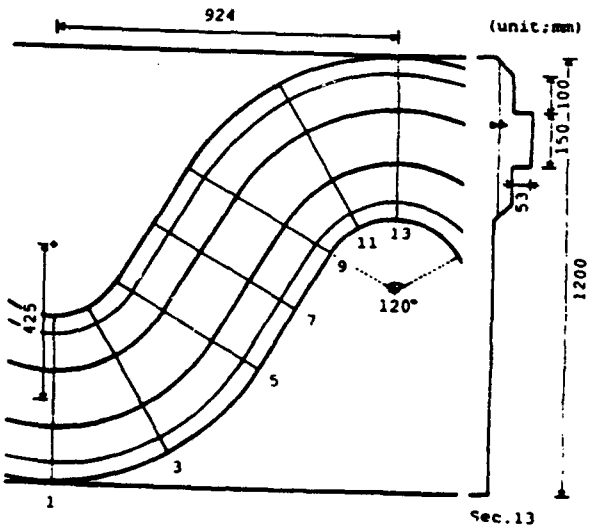

Figure 1 Configuration of meandering channel.

2. EXPERIMENTAL APPARATUS

Five meanders were constructed in a flume of 1.2 m wide, 350 mm deep and 9.2 m long. A valley bed slope was set as 1/1000 and the dimensions of one meander were as follows : bed width 150 mm, flood plain height 53 mm and bed radius 425 mm with a vertical main channel wall, cross-over length 380 mm, meander wave length 924 mm and a cross-over angle of 60 degree. Flood plain banks were

constructed parallel along the meandering channel with a flood plain width of 100 mm and a flood plain bank slope of 1:1 (see Fig. 1). In the five multiple meanders, a half meander wave length of the 4th meander section was used as a test section and was divided into 13 cross sections of which the turbulent measurements were undertaken at the 7 cross sections.

The turbulent measurements were undertaken using a 2-component LDA system with a computer controlled automatic traverser system. A TSI 2-component LDA system was operated in a back scatter mode with 10 m long fibre optic cable connecting the laser and signal processing system to a 15 mm diameter submergible measurement probe head. Data was collected for 60 seconds or 120 seconds depending on the location of measurement with an average data rate of 100 Hz. Silver powder of mean diameter size of 50μm was used as a seeding agent. The vertical and longitudinal components of velocity were measured by submerging the probe head mounted on a cylindrical tube of a 20 mm diameter with a 45 degree angle mirror. The lateral and longitudinal components of velocity were measured by setting the probe head above the water surface (see Fig.2).

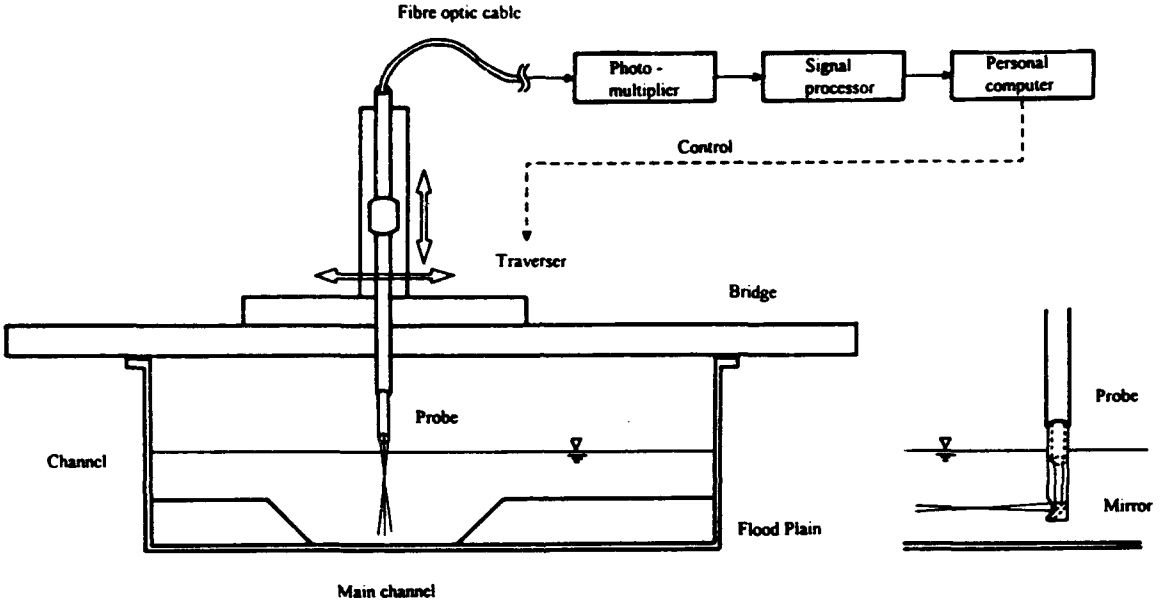

Figure 2 Diagram of setting instruments.

3. MEAN FLOW CHARACTERISTICS

The depth of water varies from a bankfull level to an overbank level. For the overbank case a represented notation of water depth is expressed as a relative depth , Dr=(H-h)/H, where H and h are water depth at the main channel and the flood plain height respectively. There have been a number of studies on meandering channels for inbank flow conditions (e.g. Ikeda and Parker (1989)). However turbulence measurements have not been undertaken since an instrument was not available to measure the secondary flow and turbulence in a meandering channel.

The mean flow structure in the meandering channel for the bankfull flow condition is briefly described as follows : The depth mean velocity distribution along the meandering channel for the bankfull condition, Dr=0.0, is shown in Fig. 3. The maximum velocity appears to be located near the left hand side of the main channel, and the velocity decreases transversely at the bend apex (section 1 in Fig. 3). As flow goes downstream, the position of the maximum velocity follows the shortest length of the water course, which is different from that of curved natural rivers (normally faster flow in the right hand side of the main channel). Change of high momentum flow towards the concave bank side is not completed before that bank becomes the convex one, owing to the fixed flat bed which prevents developing the secondary flow due to the bend.

For the overbank conditions, It can be seen from Figs. 4 that the water on the left flood plain at the bend apex tends to flow into the main channel with some angle. This is created by the inertia of flow parallel along the cross-over on the right flood plain. There can be observed a horizontal circulation on the left flood plain just after the bend apex. This circulation creates a stagnation area in which deposits sediment or traps pollutant.

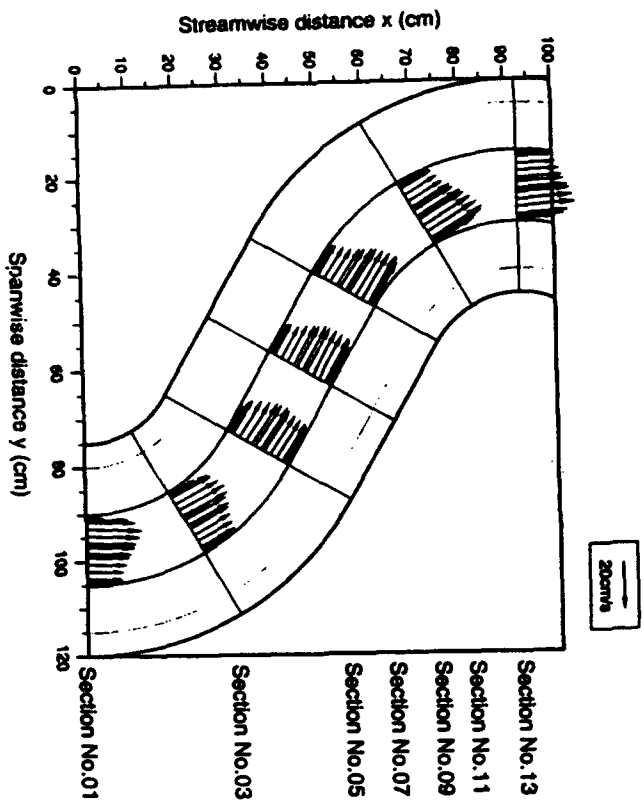

Figure 3 Depth average velocity for Dr=0.0 (bankfull).

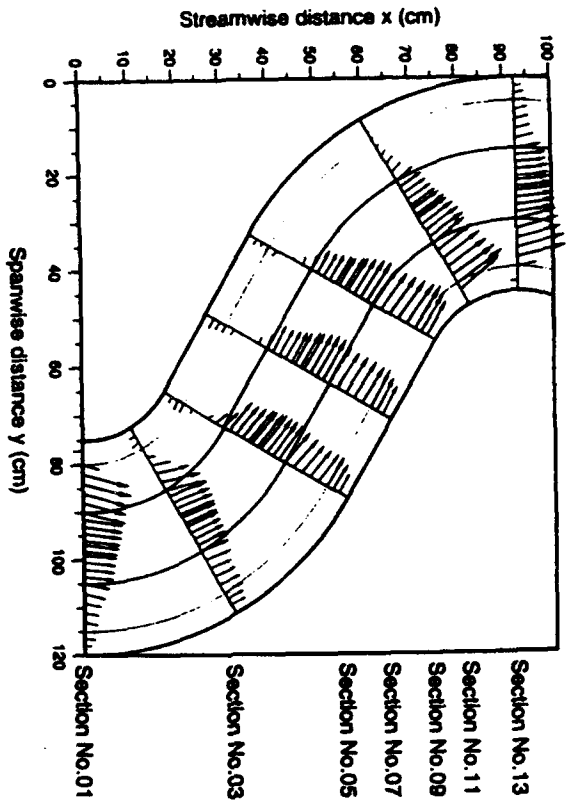

Figure 4 Depth average velocity for Dr=0.5 (overbank).

4. STRUCTURE OF SECONDARY FLOW

The measurements of the secondary flow in the meandering channel for bankfull and overbank flow conditions were undertaken by a two component LDA system. The secondary flows were expressed as a vector form in Figs.5 and 6 for the bankfull, Dr=0.0, Dr=0.15 and Dr=0.5. It can be seen from Fig. 5 that the clockwise circulation of secondary flow at section 1 occurs stronger at the left bank side rather than at the right bank side for the bankfull flow case. There exists anti-clockwise circulation on the right bank side. This circulation remains along the meandering channel which may prevent to development of circulation due to the centrifugal effect of the bend. The structure of the secondary flow in the model differs from that of natural rivers.

For the overbank conditions, the secondary flow cells at section 1 in Fig. 6 separate into three parts : two parts are in a clockwise direction below the bankfull level in the main channel. An anti-clockwise cell occupies above the bankfull level. The clockwise cell near the left bank below the bankfull level can be generated by the flood plain flow rolling over the main channel flow. The clockwise cell near the right hand bank can be due to the cross flow deflecting to the right hand main channel wall. A clockwise circulation forms above the bankfull level between sections 9 and 11 in the main channel, which remains up to the next section 3 as an anti-clockwise circulation. This cell is against the flood flow entering into the main channel and then creates a plunge flow at the meeting place. There is clearly indicating the main channel flow at sections 3, 5 and 7 overflowing onto the left flood plain. The flood plain flow enters into the main channel at section 9 for Dr=0.15. For the deeper case, Dr=0.5, these phenomena are pushed further downstream.

5. STRUCTURE OF REYNOLDS STRESSES

The Reynolds stresses were calculated from a cross product of turbulent fluctuations using the raw data, and the Reynolds stresses normalised by the shear velocity $u_*^2 = \rho g R S_0$ at section 1, where ρ = density of water, g = gravitational acceleration , R = Hydraulic radius and S_0 = bed slope, were plotted on Figs. 7, 8 and 9. For the bankfull condition, the value of $-\overline{uw}/u_*^2$ seems to vary

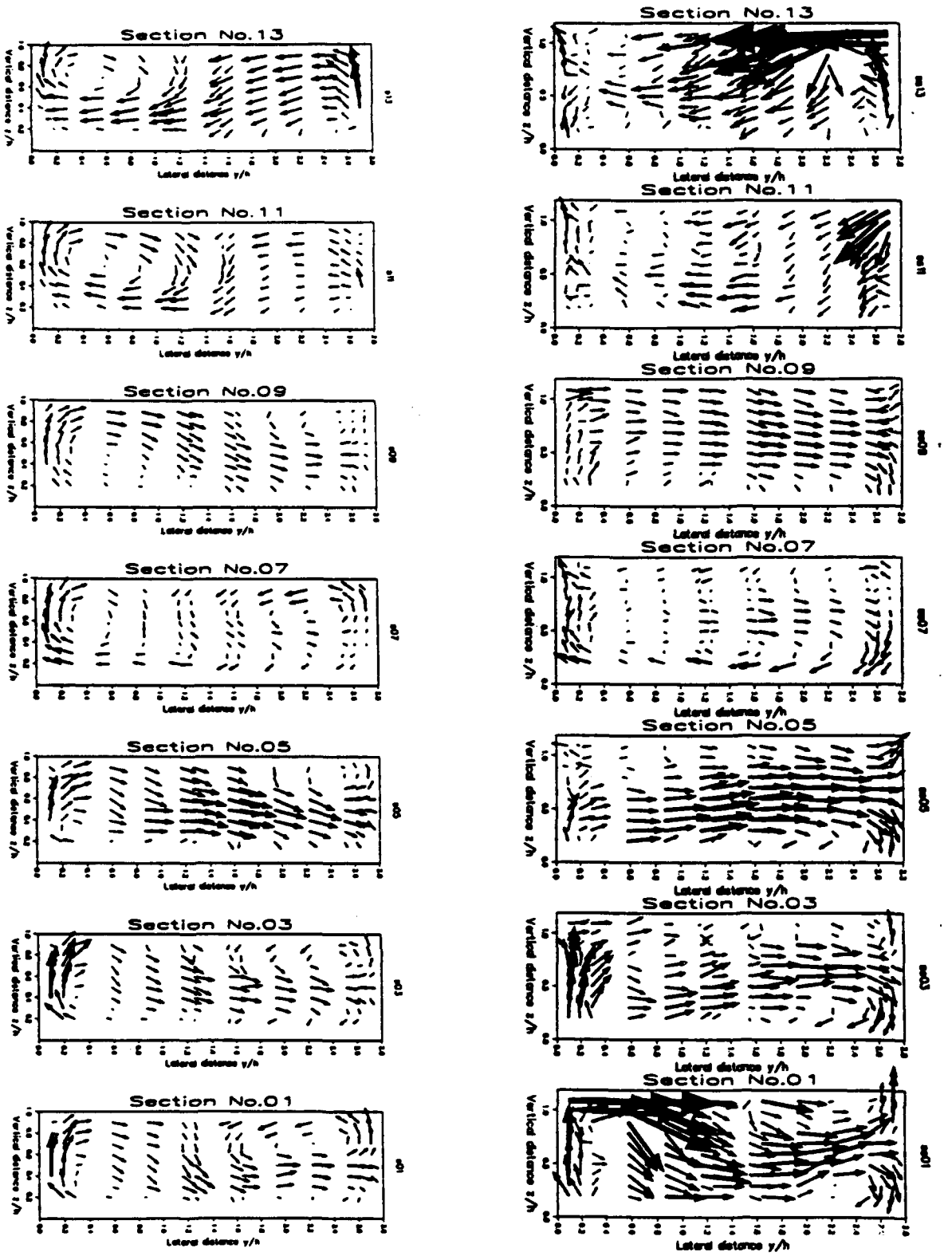

Figure 5 Structure of secondary flows along meandering channel for Dr=0.0 and 0.15.

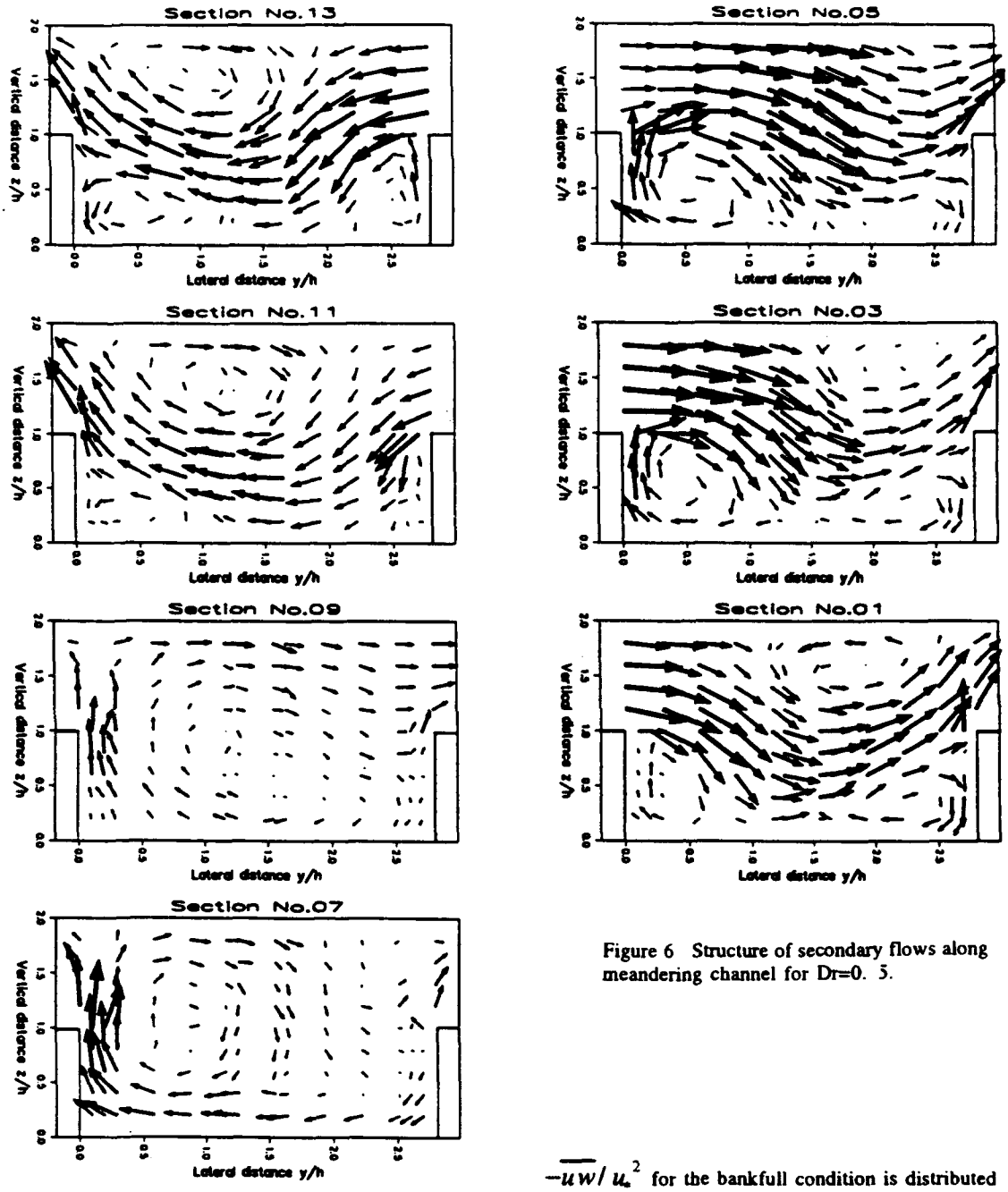

Figure 6 Structure of secondary flows along meandering channel for Dr=0. 5.

linearly from the bed to the position of the maximum velocity, about 1/3 of water depth, in which the bed generated turbulence is dominant. The bed shear stress obtained from the Preston tube was compared with that obtained using logarithmic velocity profiles near the bed . These were good agreement. For the overbank conditions, the distribution of the shear stress near the bed has similar trend as the bankfull condition. The negative value of $-\overline{uw}/u_*^2$ for the bankfull condition is distributed above the zero of $-\overline{uw}/u_*^2$ and the maximum magnitude is the same order as the positive maximum value in some cross sections but most cases are smaller. These areas are strongly connected to the secondary circulation areas. For the overbank condition, Dr=0.15, at section 3 the negative magnitude of $-\overline{uw}/u_*^2$ is two times bigger than the bed shear stress near the bankfull level although the velocity gradient is relatively small compared with that near the bed. This phenomenon is also observed at Dr=0.5.

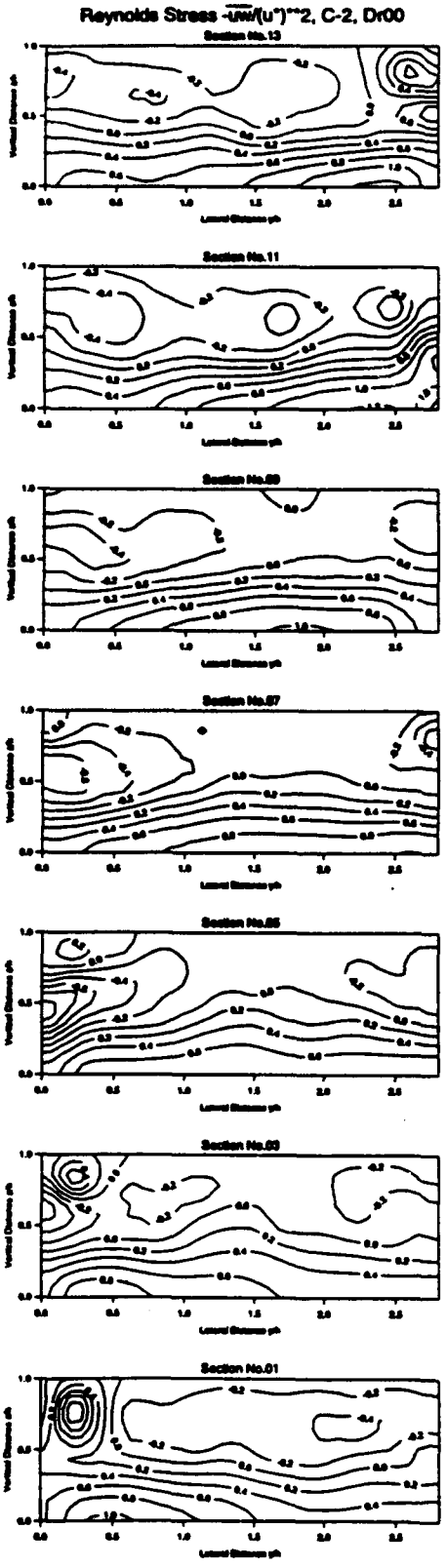

Figure 7 The Reynolds stress, $-\overline{uw}/u_*^2$, along meandering channel for Dr=0.0.

The large value of $-\overline{uv}/u_*^2$ for the bankfull condition occurs near water surface along the meandering channel. For the overbank conditions, there have consistently large values at the place where the large values of $-\overline{uw}/u_*^2$ exist although the value of $\partial U/\partial y$ is relatively small compared with that near the main channel wall. There is an existence ofhigh turbulence level along the left side of the edge of the main channel. This region is the boundary between the horizontal circulation on the left flood plain and the main channel flow. It is noted that the zero value is not corresponding to the region of $\partial U/\partial y = 0$ and shifted slightly to the left side of the region. The reason why this happened is not known.

6. CONCLUSIONS

Measurements of secondary flow and Reynolds stresses in a meandering compound channel were undertaken using a 2-component laser doppler anemometer system. The measurements of the lateral and vertical components of velocity were carried out successfully by placing the small probe head above water surface and by submerging the head in water respectively. The structure of the secondary flow and the Reynolds stresses were obtained. Development of the secondary flow along the meandering compound channel for overbank flow conditions was observed and the region of intensive turbulence was identified.

ACKNOWLEDGMENTS

The authors gratefully acknowledge the financial support of the Science & Engineering Research Council (SERC) : Grant No : Gr /H 14655 and GR /F91193. The authors would like to thank to Professor RA Falconer in the Department of Civil Engineering, University of Bradford, UK for his support.

REFERENCES

1. Ikeda, and Parker,G (1989), River meandering, American Geophysical Union, Water Resources Monograph, No.12.

2. Knight, DW and Shiono, K (1990), Turbulence measurements in a shear layer region of a compound channel, J. Hyd. Res., Vol. 28, No. 2, pp.175-194.

3. Shiono, K and Knight, DW (1991), Turbulent open channel flows with variable depth across the channel, JFM, Vol., 222, pp.617-646.

4. Willetts and Hardwich (1993), Stage dependency for overbank flow in meandering channels, Proc. Inst. Civ. Engrs. Wat., Mari. and Energy, 101, March, pp.45-54.

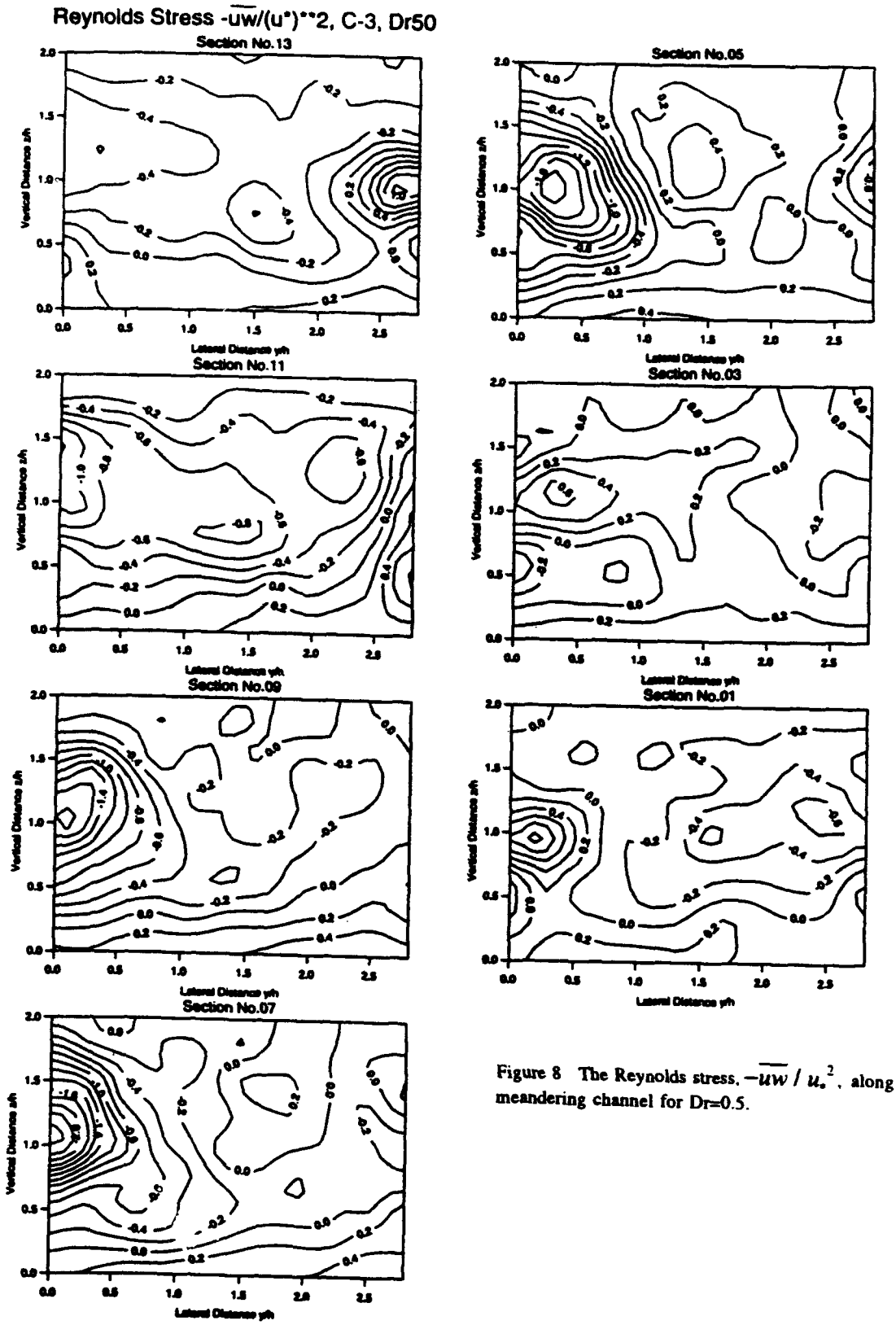

Figure 8 The Reynolds stress, $-\overline{uw} / u_*^2$, along meandering channel for Dr=0.5.

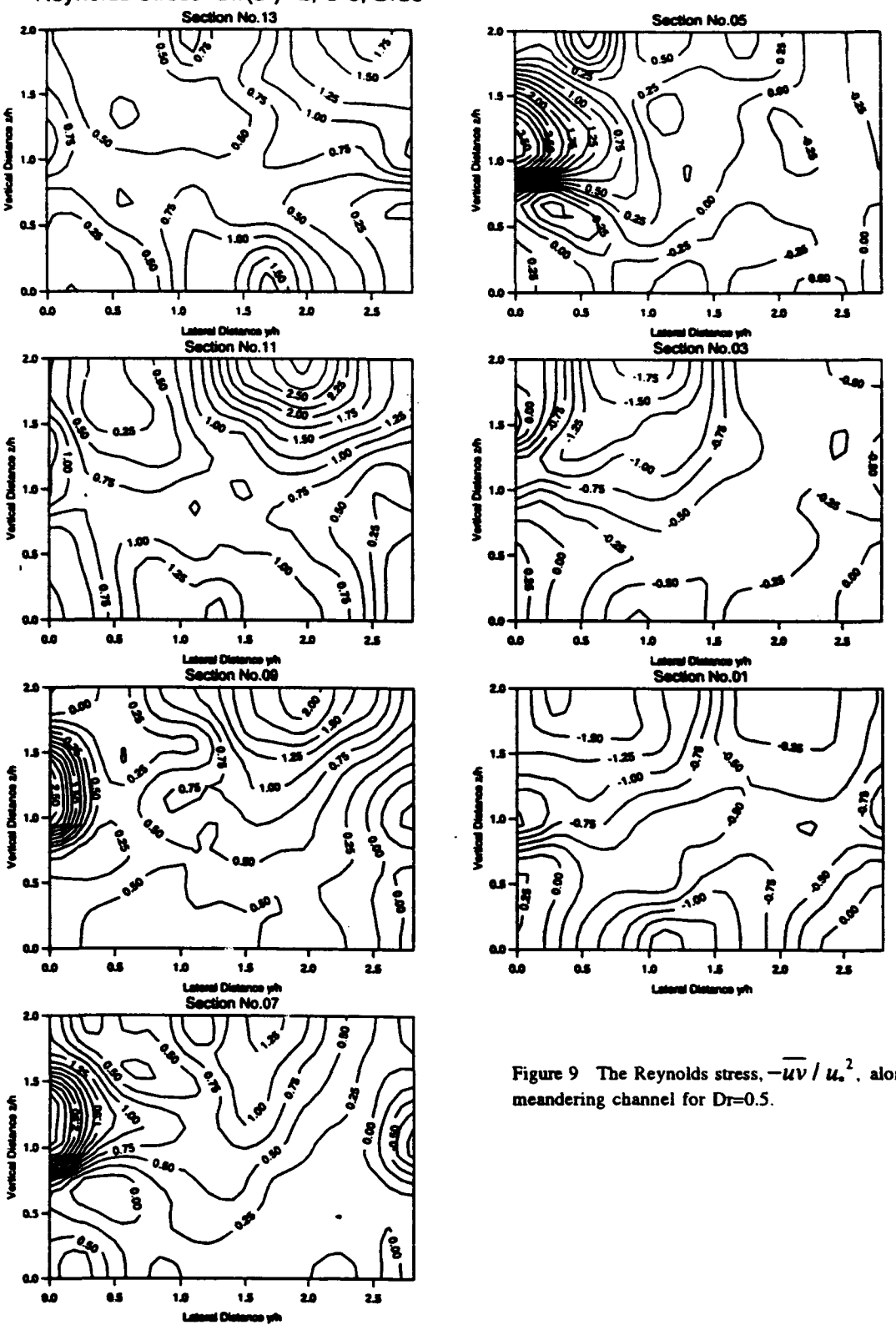

Figure 9 The Reynolds stress, $-\overline{uv} / u_*^2$, along meandering channel for Dr=0.5.

Velocity Measurements in a Rotating U-Bend Using a Stationary Fibre Optic LDA Probe

by

S C Cheah, H Iacovides, D C Jackson, H Ji and B E Launder

Mechanical Engineering Department, UMIST, Manchester, UK

ABSTRACT

This paper describes the use of LDA in the investigation of turbulent flow through a U-bend that rotates in orthogonal mode. A stationary 2-channel fibre optic probe is employed to collect instantaneous flow measurements from the rotating test section. The flow Reynolds number is 100,000, and the U-bend curvature ratio is 0.65. Three cases have been examined: flow through a stationary U-bend, flow through a U-bend rotating positively (the trailing side coinciding with the bend outer side) at a rotation number (Ro = $\Omega D/U_m$) of +0.2, and rotation at a rotation number of -0.2. The resulting measurements produce a detailed mapping of the mean and fluctuating flow fields, from which the effects of strong curvature and rotation on the flow development can be understood.

1 INTRODUCTION

Flow development within rotating U-bends of strong curvature is of great interest to gas-turbine designers because of its relevance to blade cooling. In modern gas-turbines, serpentine passages traverse the inside of the blade. In an attempt to predict the heat transfer within these passages numerical procedures have been developed (Bo et al 1991, Bo et al 1994), but it is essential to ensure that these solvers are able to produce reliable results so as to avoid potentially costly mistakes at the design stage. Numerical modellers therefore need to know how together rotation, strong curvature and secondary flow influence the development of the mean and the turbulent fluid motion in a three dimensional flow.

Most studies of blade cooling flows have so far been solely concerned with heat-transfer measurements (Guidez 1988, Wagner et al 1989). Moreover, because in previous investigations, experimental models had to be of a relatively small size, most of the available data on rotating passage flows, involve only averaged values. The present work produces detailed flow-field data, by developing an experimental apparatus that is able to provide LDA mappings of the mean and the fluctuating motions in a U-bend of square cross-section that rotates orthogonally around an axis parallel to the axis of curvature. The main objective is to produce flow measurements suitable for CFD code validation, over a range of Reynolds and rotational numbers that are typical of engine operating conditions. The paper describes the experimental apparatus, the instrumentation and the data processing system that enable the collection of rotating flow data from a stationary probe and presents a representative selection of the resulting measurements. A fuller presentation of the experimental data is simultaneously reported in Cheah et al (1994).

2 EXPERIMENTAL APPARATUS

In order to be able to resolve the flow field in sufficient detail, a reasonably large scale rig was necessary. As a result, rotational speeds could be kept at modest levels thus avoiding problems due to mechanical stresses. To reproduce engine conditions at modest rotational speeds, water was chosen as the working fluid because of its low kinematic viscosity. The test rig consists of a motor-driven turntable mounted in a 1.22 m diameter water tank. A U-bend of 50mm square cross-section and of curvature ratio Rc/D = 0.65, shown in Figures 1(a) and 1(b), is mounted on the turntable with the curvature axis of the duct parallel to the axis of rotation. Flow is fed to the duct

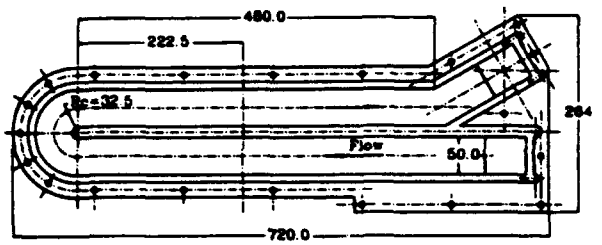

(a) Plan view

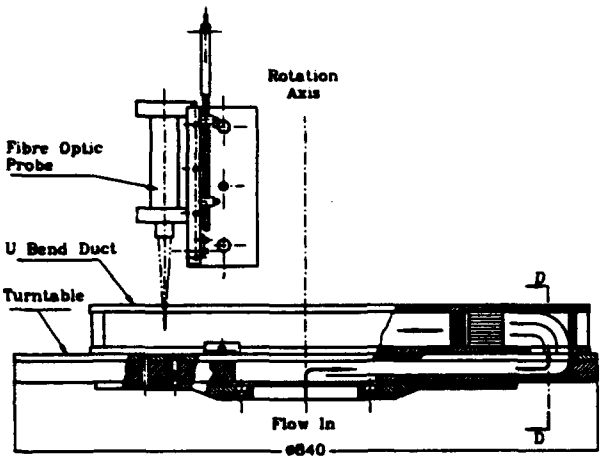

(b) Side view

Figure 1 Experimental Apparatus

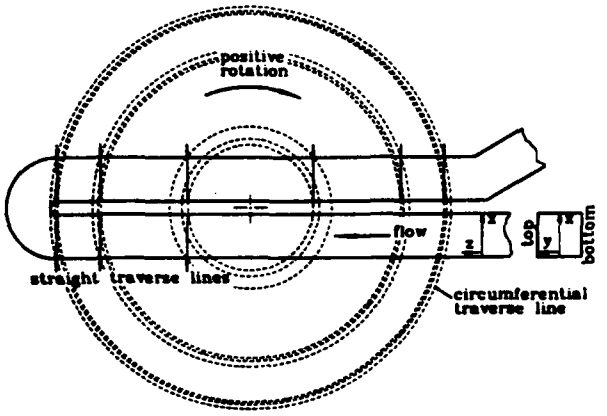

Figure 2 Circumferential traverse lines

through a passage that is built into the rotating turntable, as shown in Figure 1(b); the outflow is into the open water tank. The test section is made of 10mm thick perspex for optical access. The rotor turntable can be driven at any speed up to 250 rpm in either direction. The water volumetric flow rate is monitored with an orifice-plate arrangement. At the entrance to the test section, a combination of fine wire meshes and a honeycomb section ensure that at a station five diameters upstream of the bend the flow is uniform and symmetric.

2.1 DATA ACQUISITION

The LDA system employed was a TSI two-channel, four-beam, fibre-optic probe system with frequency shifting on both the blue and green channels. A 4-watt Argon-ion laser was used to power the system and two counter processors(TSI 1980B) were used for signal validation. Subsequent data processing was done through a Zech data acquisition card on an Opus PC.

Flow measurements within the rotating U bend were made with a two channel 10 m long fibre-optic cable and probe. The probe was clamped into a stationary X-Y-Z traversing unit mounted directly above the U-bend. With this arrangement measurements could be made with the probe set at a fixed radius (with the bend rotating) or the probe could be traversed to collect data for flow in a stationary bend. In the case of the rotating U-bend the data were collected as the duct swept past the stationary laser beams, as shown diagrammatically in Figure 2, with the laser beams entering the working section of the U-bend through the top wall. The height of the measuring volume above the bottom wall was determined by establishing the intersection of the laser beams on the bottom wall as the reference point and then monitoring the height by which the probe was raised. As the probe is raised by 1 mm in air the measuring volume is raised by 1.33 mm. in water. The radial position of the probe measuring volume was determined from the radial location of the traversing unit. The laser measuring volume within the U-bend passage has a diameter of approximately 91 μm and a length of 1.8 mm these being average dimensions for the two colours. The angular position of the bend was recorded with each measurement.

For the stationary case the traversing unit was

aligned with a radial line drawn from the axis of rotation to the bend axis, shown as line O-O2 in Fig 2. Traverses were made across the straight passages with the probe measuring the streamwise and transverse velocities within the passages. When radial traverses were made within the bend the orientation of the probe relative to the traversing unit remained unchanged. Use of this method ensured that the laser probe remained undisturbed. Mean and rms quantities were determined from at least 2000 instantaneous velocity measurements at each measuring point along the traverse line.

The two orthogonal velocity measurements were obtained with the blue (488E-9m) and green (514.5E-9m) channels with a coincidence time window set at 20 μs for signal validation. The laser signals were filtered between high- and low-pass filters. Comparison between the periodic time averaged over 5 cycles to that averaged over 8 cycles was set so that only signals having periodic times differing by less than 1% were validated. Each validated measurement, according to its circumferential location, was stored in a corresponding angular segment bin in the form of a summed value. Each angular segment bin contained the accumulated sums of the measured instantaneous values of velocity and all velocity moments up to third order i.e. $\widetilde{U_1}$, $\widetilde{U_2}$, $\widetilde{U_1^2}$, $\widetilde{U_2^2}$, $\widetilde{U_1U_2}$, $\widetilde{U_1^3}$, $\widetilde{U_2^3}$, $\widetilde{U_1U_2^2}$ and $\widetilde{U_1^2U_2}$ together with the number of data points accumulated in that particular bin. For every 1000 data records collected, the acquisition program performed a statistical calculation based on all the collected data and calculated the mean velocity components, Reynolds stresses and triple correlations. This method ensured that storage requirements were held within finite bounds. The number of measurements recorded along each traversing circle during the rotating flow traverses was between 60000 and 100000, which meant that several hundred measurements were accumulated in each bin.

Seeding requirements were determined during an earlier study, using the same basic rig, of flow in a rotor-stator cavity, Cheah et al (1992). It was found that the natural seeding material within the closed-loop water circuit produced a too low data acquisition rate. Normal hard particle seeding in the circuit was considered to be inappropriate as this could have caused damage to the large diameter seals that had been used in the construction of the turntable. The introduction of cornflour caused a dramatic improvement in the signal-to-noise ratio. The specific gravity of cornflour is about 1.3 and the measured diameters of the particles were in the range of 15-25 μm. Only small amounts were added so as to ensure as far as possible that there was only one particle in the measuring volume at any time. A more detailed account of the comparisons between the seeded and unseeded measurements can be found in Cheah et al (1992) and Ji (1994).

The angular location of the rotating U-bend was obtained from a half-degree incremental encoder attached to the motor drive shaft. The motor drive shaft was connected to the turntable drive shaft by a toothed belt drive with a speed reduction of 4 to 1. With this arrangement and without any backlash in the drive, it was possible to measure the position of the U-bend to one eighth of a degree. With a pulse doubler in the LDA data acquisition interface, it was thus possible to achieve an angular resolution of 1/16 of a degree. The 5760 incremental pulses per revolution of the U bend are referenced to a reset pulse that comes from an optical switch attached to the turntable. The angular position at any time is thus determined by the pulse counter reading that is fed into the 24-bit shaft-angle input on the data acquisition system.

The rotational speed of the turntable was monitored using a counter fed with 360 pulses per motor shaft revolution from the incremental encoder. As this shaft rotated at four times the speed of the U-bend turntable this represented 1440 pulses per turntable revolution. As most of the current tests were run at 76 RPM, this translated to a turntable speed of 1824 counts per second.

As the measurements were taken over a period of several hours it was essential that the rotational speed of the rig was maintained constant. The Ward Leonard drive system employed is an open loop system but, with the aid of an electronic speed control system that utilises the pulses from the incremental encoder, it was possible to maintain a constant rotational speed for the duration of the tests.

2.2 DATA PROCESSING

The velocities measured as the U bend sweeps past the measuring volume are the absolute velocities for a stationary frame of reference, collected along circular arcs. It is therefore

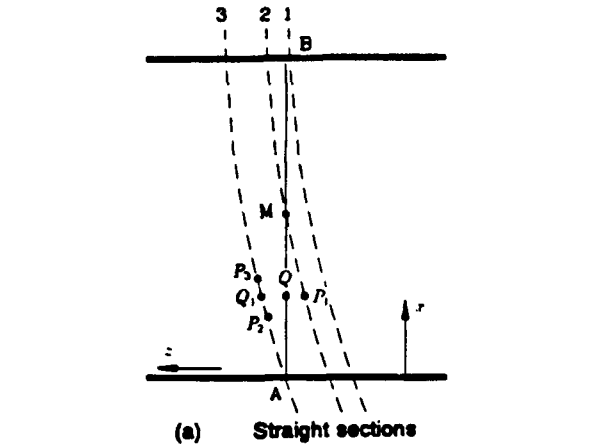

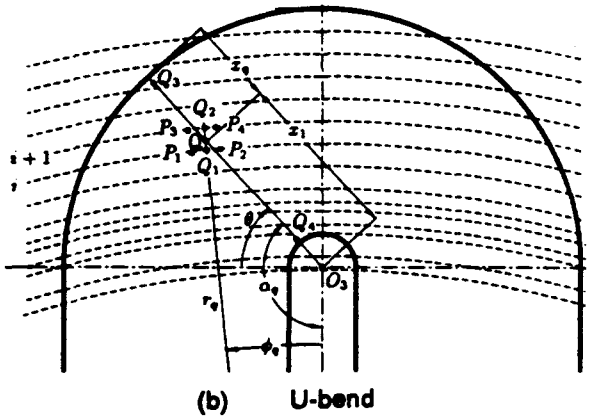

Figure 3 Interpolated data lines

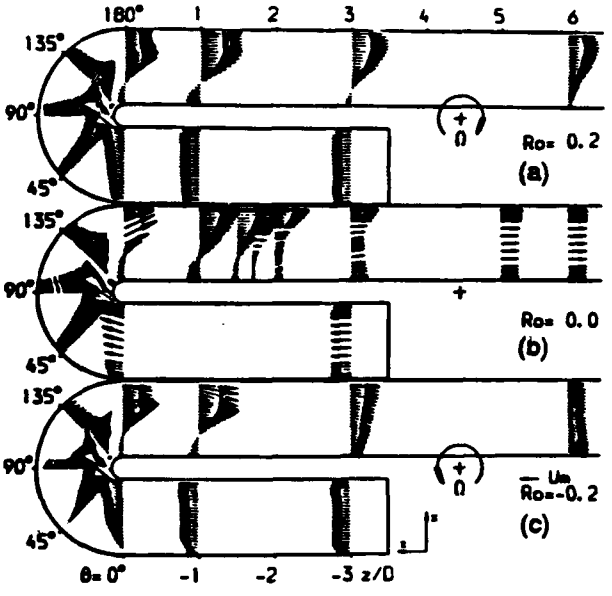

Figure 4 Measured velocity vector field along the symmetry plane

necessary to transform the measurements into a form that is easier to understand. The resulting transformations produced a set of velocities for a rotating frame of reference, resolved along the axial and the cross-duct directions and along straight traverse lines across the duct.

In order to apply these transformations two distinct regions of the rotating duct needed to be considered: the two straight sections and the bend itself. The probe collects measurements for two velocity components along the radial and circumferential directions relative to the axis of rotation. In order to transform these measurements to a rotating frame of reference, the local turntable velocity is subtracted from the measured fluid circumferential velocity. Then, at each angular location, the flow quantities that are initially measured along the circumferential and radial locations, are resolved along the axial and cross-duct directions.

Of course, it is convenient to record the data over planes normal to the duct axis. For each selected plane velocity data are therefore successively recorded along three closely spaced circular trajectories that span the plane in question (AB in Fig 3a). The locations of these data records are denoted as points P_n in Fig 3a. Bi-linear interpolation, either between arcs 2 and 3 to the line segment AM or between arcs 1 and 2 for the segment MB establish the relevant data values at points such as Q along AB.

In the U-bend region data interpolation was made onto straight lines passing through the centre of the bend in the same way that traverses were made in the stationary duct. The interpolation method employed is similar to that adopted in the straight sections. In this region the four adjacent bins on the two nearest arcs containing data were used for three linear interpolations as shown in Fig 3b. Interpolations were made at 15-degree intervals around the bend. Each straight line had 49 interpolated points spaced at 1 mm intervals along the line. The 14 arcs on which data had been taken in the bend, provided more than 2500 bins of data points in the bend region from which the interpolated data were derived.

With data being stored at 1/8 degree intervals for the rotating cases, the length of the storage bins varied as the probe was set at different radii. At the

smallest radius the width of the bin was 0.157 mm and at the largest 0.6 mm. Due to the difference in storage bin size, along traverse arcs of smaller radii there were more bins containing flow data, but with fewer data points stored in each bin. Within the straight sections, data from adjacent bins were therefore combined to obtain the ensemble average. The total circumferential length of the combined data bins did not however exceed 0.8 mm.

The overall estimated uncertainties for the non-dimensionalised mean velocities in the streamwise and cross-duct directions U_z and U_x respectively, and of the corresponding turbulence quantities are:

$$U_z \leq 0.02U_m \quad ; \quad \sqrt{\overline{u_z^2}} \, , \sqrt{\overline{u_x^2}} \leq 0.02\, U_m$$

$$U_x \leq 0.03U_m \quad ; \quad \overline{u_z^2} \, , \overline{u_x^2} \leq 0.09U_m^2$$

In arriving at the above figures the following effects were considered: the uncertainty of the rotor speed, phase uncertainty of the doppler signal, uncertainty of wavelength and beam angle, velocity gradient broadening, velocity bias and flow rate uncertainty associated with the orifice plate.

3 RESULTS

Measurements have been obtained along the symmetry plane (y/D = 0) and also along a plane near the top wall ($2y/D$ = 0.75), where y is the vertical distance from the symmetry plane. A number of cross duct traverses have been produced covering a region from 3 hydraulic diameters (D) upstream of the bend entry to 8D downstream. The three cases investigated, Ro = -0.2, 0.0, 0.2, were all at a flow Reynolds number (Re = U_mD/ν) of 100,000. A positive rotation direction, as shown in Figure 1, is defined as one in which the duct trailing (pressure) side coincides with the outer side of the U-bend. Due to space limitations only symmetry plane measurements are presented here. A more detailed account is provided in Cheah et al (1994).

The mean velocity measurements along the symmetry plane are presented in the vector plots of Figure 4. The stationary U-bend results indicate that at the bend entry there is a strong flow

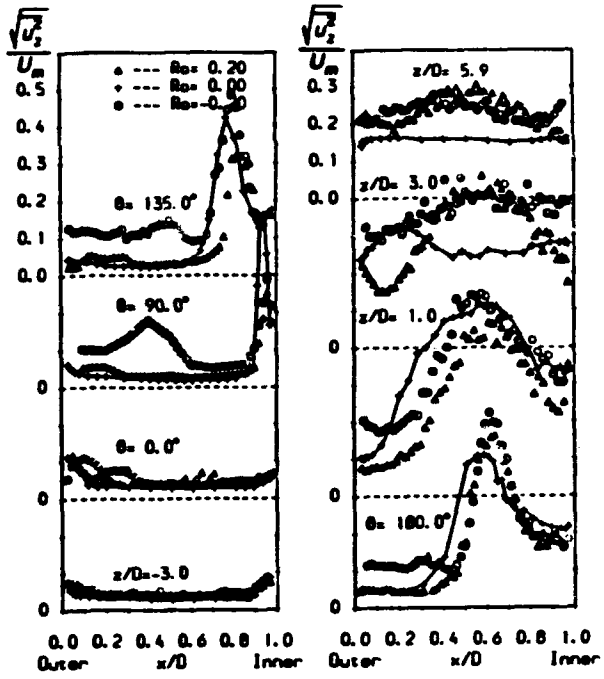

(a) Streamwise component

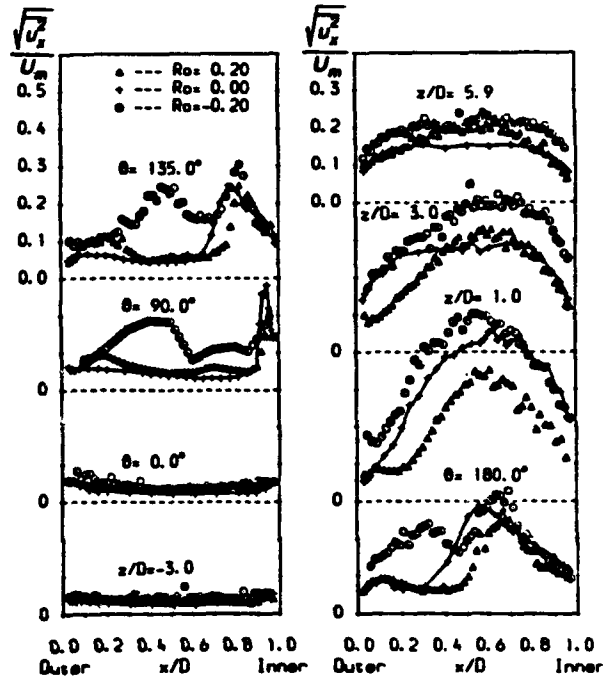

(b) Cross-duct component

Figure 5 Normal stresses along symmetry plane

acceleration along the inner wall, while along the outer wall, the flow is strongly decelerated. Within the bend, a separation bubble is formed along the inner wall near the 90° location. Reattachment occurs at 1.7D from the bend exit (for the stationary case). Positive rotation (Ro = 0.2) mainly affects the downstream flow. The Coriolis induced secondary motion opposes the return of the high momentum fluid to the inner side of the duct, almost doubling the length of the separation bubble. Further downstream, the flow approaches fully developed flow conditions for a rotating straight duct. The high momentum fluid accumulates along the trailing side of the (rotating) duct, which for positive rotation, coincides with the U-bend outer wall. Under negative rotation, the Coriolis-induced secondary motion transports the low momentum fluid to the outer side of the duct. As a result, a small region of flow reversal develops along the outer wall at the bend entry. In the downstream region, the Coriolis-induced secondary motion begins to move the fluid across the duct towards the inner side causing reattachment to occur at around 2D downstream of the exit. After reattachment, the cross-duct movement transports the fast moving fluid to the duct inner side.

Profiles of the normal turbulent stresses along the streamwise and cross-duct directions are shown in Figures 5(a) and 5(b) respectively. In general, turbulence levels are found to be low in regions where the flow accelerates and high in regions of flow deceleration and separation. In the presence of negative rotation, turbulence levels are consequently higher than those for flow through a

stationary U-bend whereas positive rotation is found to have the opposite effect.

The distribution of the turbulent shear stress component $u_z u_x$ within the cross-duct plane is shown through the profiles of Figure 6. Since most of the significant shear stress variation occurs downstream of the bend, only the downstream profiles are shown. Within the first three downstream diameters, turbulence shear stress levels rise significantly. The shear stress distribution is also affected by rotation. Negative rotation increases shear stress levels while positive rotation has the opposite effect.

Finally Figure 7 presents the distribution of triple moment components in the downstream region; again in this region the triple-moment correlations have substantially higher levels than upstream. These four triple moments reach their highest levels at 1D downstream of the U-bend. The triple moments are also affected by the sense of rotation, negative rotation leading to higher values than positive rotation with the stationary results lying in between. Negative gradients of the triple moments imply a local diffusive gain of fluctuating energy. In the downstream region, the regions close to the inner and outer walls are consequently gaining energy at the expense of the highly turbulent fluid in the core.

4 CONCLUSIONS

In this paper we have shown that, with a suitable data monitoring and processing system, it is possible to collect accurate LDA measurements for internal flows through rotating ducts, using a stationary fibre-optic probe. This method has generated detailed mappings of the mean and fluctuating flow fields in rotating U-bends of strong curvature. The results reveal that within the U-bend the flow is dominated by the strong streamwise pressure gradients. At the U-bend exit these gradients cause flow separation along the duct inner wall, which starts at about the 90° location, and strong flow acceleration along the outer side. Regions of flow acceleration are also found to be regions of relatively low turbulence and in regions of flow separation turbulence levels are considerably higher. The triple-moment measurements indicate that in the exit region there is significant transport of turbulence from the core region to the near-wall regions through turbulence mixing.

Orthogonal rotation at a rotational number of 0.2 is found to have significant effects on the flow development. Positive rotation increases the length of the separation bubble downstream of the bend and generally suppresses turbulence within the bend and in the downstream region. Negative rotation causes flow separation along the outer wall at the U-bend entry and also increases the overall turbulence levels.

ACKNOWLEDGEMENTS

The research has been supported by the SERC through Grant GR/F89039. Outstanding technical assistance has been provided by Mr J Hosker and

Mr D Cooper. The camera-ready mats have been prepared by Mr Michael Newman with appreciated care. Authors' names are listed alphabetically.

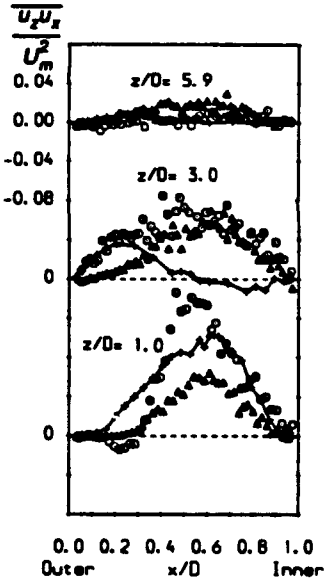

Figure 6 Distribution of shear stress $u_z u_x$ along symmetry plane

5 REFERENCES

1 Bo T, Iacovides H and Launder B E, "Convective discretization schemes for the turbulence transport equations in flow predictions through sharp U-bends", To appear Int J Num Meth in Heat & Fluid Flow, 1994

2 Bo T, Iacovides H and Launder B E, "The prediction of convective heat transfer in rotating square ducts", 8th Symp on Turbulent Shear Flows, Munich, Germany, 1991.

3 Cheah S C, Iacovides H, Jackson D C, Ji H and Launder B E, "LDA measurements of an enclosed rotor-stator disc flow", Symp on LDA in Reciprocating, Reacting or Rotating Flows, Swansea, 1992.

4 Cheah S C, Iacovides H, Jackson D C, Ji H and Launder B E, "LDA Investigation of the flow development through rotating U-ducts", ASME Paper 94-57-226 Int Gas-Turbine Congress, The Hague, 1994

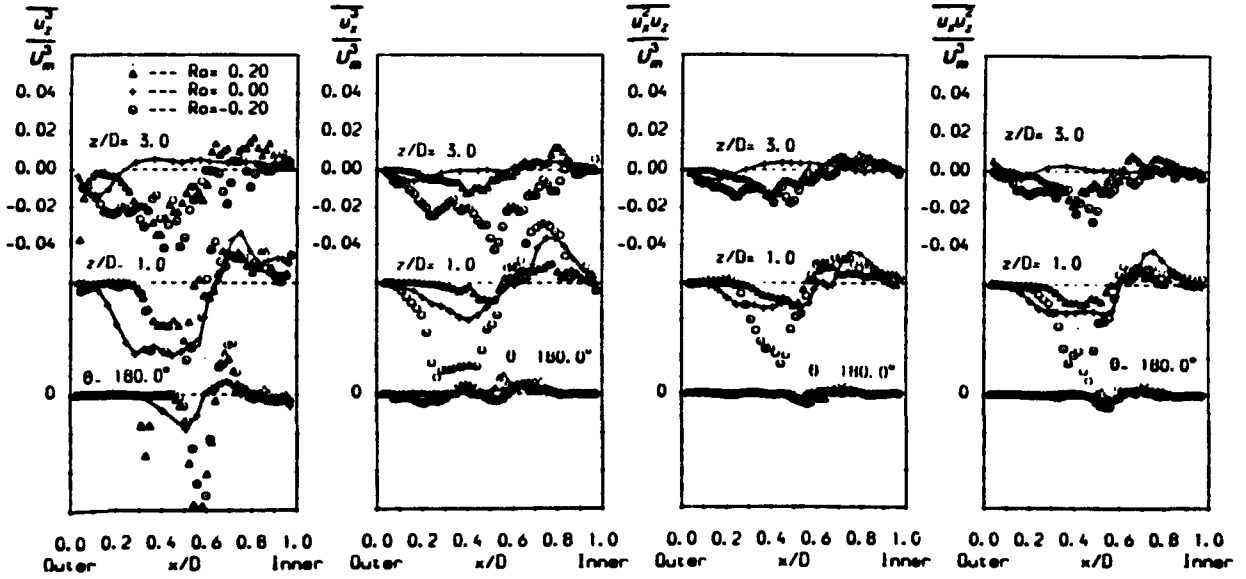

Figure 7 Distribution of triple moment components along symmetry plane

5 Ji H, "An Experimental investigation of two rotating turbulent shear flows with gas-turbine applications", PhD Thesis, Faculty of Technology, University of Manchester, 1994.

6 Guidez J, "Study of convective heat transfer in rotating coolant channel", ASME Paper 88-GT-33, Int Gas-Turbine Congress, Amsterdam, 1988.

7 Wagner J H, Johnson B V and Hajek T J, "Heat Transfer in rotating passages with smooth walls and radial outward flow", ASME paper 89-GT-272, Int Gas Turbine Congress, Toronto, 1989.

3-DIMENSIONAL LASER DOPPLER MEASUREMENTS IN A CURVED FLUME

Robert Booij and Jan Tukker

Faculty of Civil Engineering, Delft University of Technology,
P.O. Box 5048, 2600 GA Delft, The Netherlands

SUMMARY

Measurements of the three Reynolds shear stresses in a fully developed flow in a mildly curved flume were executed using a 3-dimensional laser-Doppler velocimeter. The assumption of equal eddy viscosity coefficients for the different Reynolds shear stresses, depending only on the main flow, which is often used for such a mildly curved flow appears not to be justified. The results of the measurements confirm results of previous much simpler 2-dimensional measurements, which were however unreliable because of the required beam configurations. Moreover the 3-D measurements can be used to obtain higher order correlations of the three velocity components that can be used to evaluate results of advanced turbulence models.

1. INTRODUCTION

The curvature of the flow in river bends gives rise to flow components perpendicular to the main flow direction, the so-called secondary flow. This secondary flow has important consequences for the morphology of alluvial beds in river bends. Near the bottom the flow, and therewith the sediment transport, is directed towards the inside bank of the river bend. As a result the outer side of the river bend is eroded and undermining of the outside bank can occur (Bendegom, 1947; Odgaard, 1981).

A thorough knowledge of the secondary flow is essential for predictions about the morphology of alluvial river bends. Computed intensities and vertical distributions of the secondary flow depend strongly on the modelling of the Reynolds shear stresses, in particular the shear stress that accounts for the vertical exchange of secondary flow momentum. Generally gradient type momentum transport and isotropic eddy viscosity are assumed (Leschiner and Rodi, 1979).

To examine the correctness of the assumptions and, if not, to improve the turbulence modelling measurements of mean velocities and turbulence quantities were executed in a mildly curved flume in the Laboratory for Fluid Mechanics of the Delft University of Technology, the LFM flume, see fig. 1. (The measures of the flume are: radius of curvature, $R = 4.10$ m; width, $W = .50$ m and the water depth, $h \approx .05$ m) The cross-section of the flume is rectangular and bottom and sidewalls are transparent to allow velocity measurements by means of a laser-Doppler velocimeter (LDV).

Previous measurements showed that in the second part (>90°) of the bend the flow varied only slightly along the flume. Consequently the flow in the cross-section at 135°, where the measurements were executed can be considered fully adapted to the flume curvature. In this part of the flume the main flow can be defined as the flow component in the direction of the flume axis and the secondary flow as the flow components perpendicular to the flume axis. Of the secondary flow components the horizontal one is the most important.

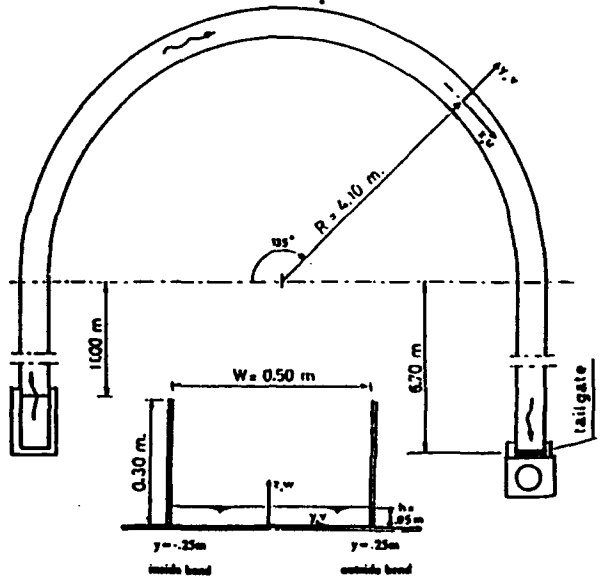

Fig. 1. The L.F.M. flume: layout and cross-section.

2. THE EXPERIMENTAL PROCEDURE

In the ss-section at 135° the instantaneous (local) velocity co nts u, v and w in longitudinal direction, x, in trans irection, y, and in vertical direction, z, respectively, were measured (see fig. 1). The positive vertical co-ordinate is taken upward with z = 0 at the bottom of the flume and the positive transverse co-ordinate is taken outward with y = 0 at the flume axis. The instantaneous velocities (u, v, w) were decomposed into the time-averaged velocities ($\bar{u}$, $\bar{v}$, $\bar{w}$) and the turbulent velocity components (u', v', w'), e.g.

$$u = \bar{u} + u' \qquad (1)$$

Cross-correlations of the turbulent v ity components yield the three Reynolds shear stre

$$\tau_{xz} = \rho \overline{u'w'}, \quad \tau_{xy} = \rho \overline{u'v'} \text{ and } \quad \tau_{yz} = \rho \overline{v'w'} \qquad (2)$$

and auto-correlations the three turbulence energies components $\overline{(u')^2}$, $\overline{(v')^2}$, $\overline{(w')^2}$.

Several years ago measurements with a 2-dimensional reference beam mode LDV with a 10 mW He-Ne laser were executed. A 2-dimensional LDV allows the simultaneous measurement of only 2 velocity components, from which only one shear stress can be obtained. To measure the three shear stresses several beam configurations, all with a vertical optical axis, were used. The conventional spatial beam arrangement of fig. 2a yielded simultaneous measurements of the velocity components u and v and therewith the shear stress τ_{xy}.

The LDV arrangement of fig. 2b with the beams in the cross-section plane allowed the simultaneous measurement of v and w and consequently the shear stress τ_{yz}. (The same information with a spatial beam configuration would have required the almost impossible setup with the optical axis in the flume direction.) The same arrangement rotated over 90° about the vertical yielded u, w and τ_{xz}. A drawback of this plane configuration is the small angle between the two measured velocity components. As a consequence the errors in the measured values for w and for the shear stresses τ_{yz} and τ_{xz} are relatively large. Moreover it is impossible to obtain higher order correlations of the three velocity components. The results of the 2-dimensional measurements were reported in Booij (1985).

This paper describes the first results obtained by means of a 3-dimensional LDV. The measurements were executed with a DANTEC 3-colour fibre optics system with a 4 Watt Coherent Ar-ion laser and DANTEC BSA

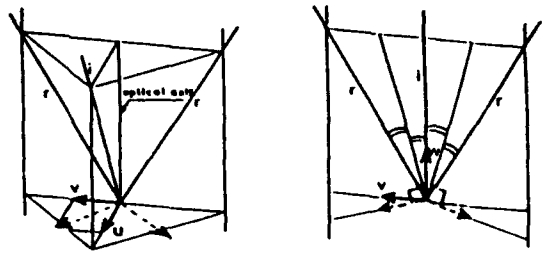

a) spatial configuration b) plane configuration

Fig. 2. 2-Dimensional LDV; laser beam configurations. (i and r are the illuminating and reference beams respectively, ---> are the measured velocity components)

processors. The optical system used was a combination of a 2-dimensional probe and a 1-dimensional probe, see fig. 3. The velocity components measured with the 2-D probe (directions 2 and 1 in fig. 3) are the velocity component in transverse direction v and a combination of velocity components u and w. Combination of the last one with the velocity component (direction 3 in fig. 3) measured with the 1-D probe yields u and w. The relatively large angle (60°) between direction 1 and 3 allows a precise determination of w with this beam configuration. Identity of the measured particles is assured by requiring arrival time coincidence.

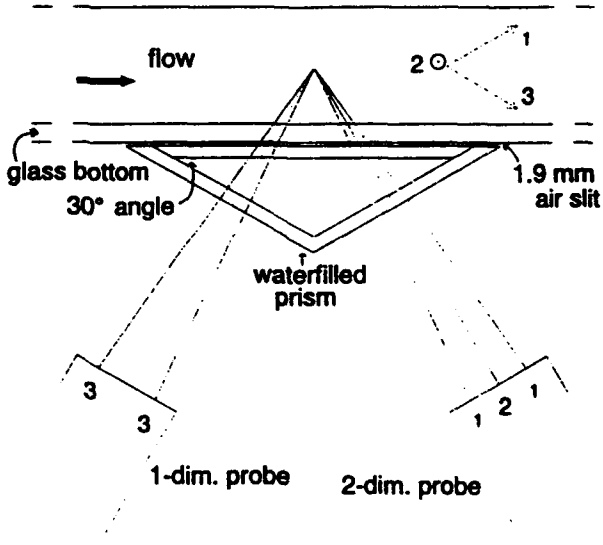

Fig. 3. The 3-Dimensional LDV beam configuration.

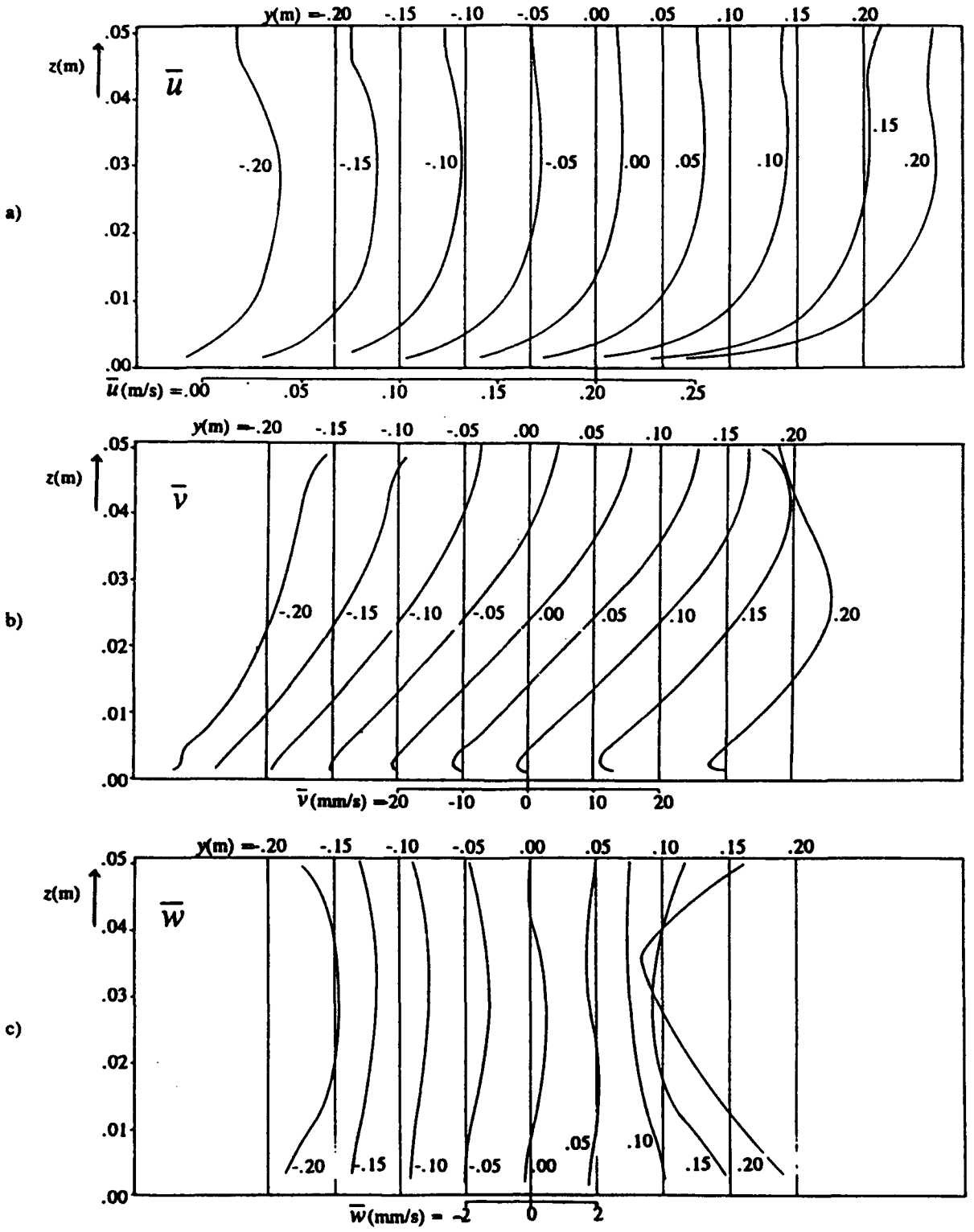

Fig. 4. Vertical profiles of the time-averaged velocity components at different places in the cross-section. (The velocity scale for $y = 0$ m is given at the bottom. The velocity scales for the other verticals are displaced, see top of each plot. The vertical lines indicate the characteristic velocity, e.g. $u = .2$ m/s.)

To simplify aligning of the many laser beams a water-filled prism, with sides perpendicular to the optical axes of the two probes, was attached under the measuring cross-section, see fig. 3. The refraction by the glass-plates forming the bottom of the flume and the top of the prism, which were at an angle to the optical axis, complicated the creation of overlapping measuring volumes for the different beam pairs. This refraction effect of the glass plates could be effectively compensated for by a small air-filled slit between them. The measuring system can be traversed in y- and z-direction and the two probes independently in the x-direction. This combination of 4 movements is required to be able to execute measurements over the cross-section without having to align the beams between measurements. A small measuring volume of the order of .1 mm in all three directions was realized.

The use of semi-automatic measuring procedures allowed measurements of 6 minutes each over a fine grid (up to 37 measuring points at each of 21 depths) to be executed within two months. The plots in this report are composed from the smoothed results of these measurements. The individual measurements are not reproduced here for clarity of the plots.

3. TIME-AVERAGED VELOCITIES

Vertical profiles of the measured time-averaged velocities at different places in the cross-section are plotted in fig. 4. Fig. 4a shows an increase of the depth averaged main flow velocity $\bar{u}$ towards the outside bend. This is caused by convection of the main flow by the secondary flow.

The transverse velocity $\bar{v}$ in fig. 4b and the vertical velocity $\bar{w}$ in fig. 4c show the usual secondary flow cell, rotating clockwise. Near the water surface the flow is directed towards the outside flume wall and near the bottom towards the inside wall. The secondary cell is closed by a downward flow along the outer wall and an

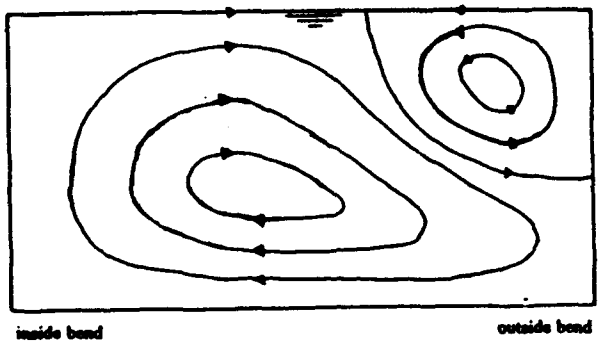

Fig. 5. Sketch of a two cell system of secondary flow.

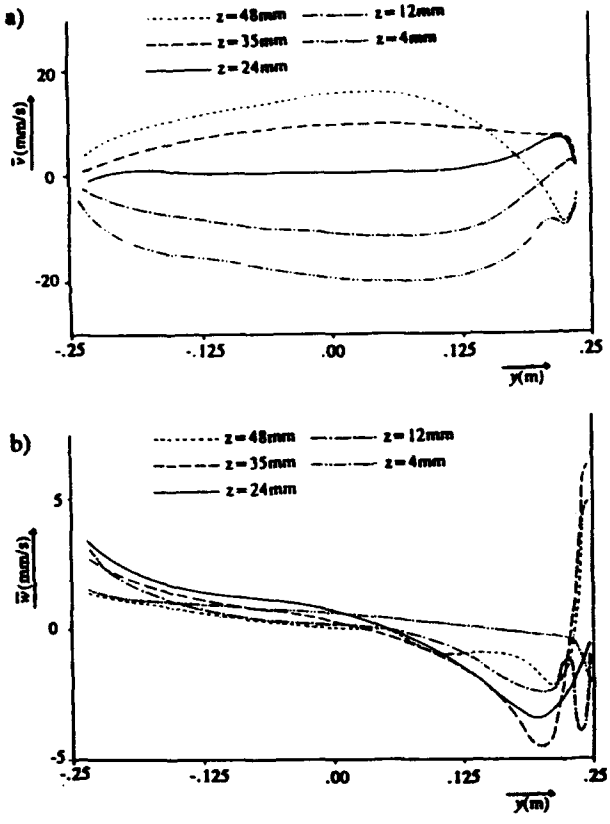

Fig. 6. Horizontal profiles of secondary flow velocity components at different depths.

upward flow along the inner wall. The vertical velocity in the flume centre is almost zero. An additional small counter-rotating second cell near the upper outside flume wall can be distinguished (Vriend (1981a), see the sketch in fig. 5). This second cell stems from an instability of the flow along a concave wall (Vriend, 1981b).

The presence of a two cell system is more obvious in fig. 6, where a few horizontal velocity profiles of the measured secondary flow components at different depths are plotted. The distribution of the secondary flow velocity components in the lower outside bend corner appears to indicate the existence of a small secondary cell in this region. This kind of secondary flow cell, which is also found in straight flumes is caused by an anisotropy of the turbulence.

The main secondary flow cell has two marked effects on the distribution of the main flow. The convection of the main flow by the secondary flow distorts the nearly logarithmic velocity profiles of the main flow in free surface flow, as slower moving water from the inside bend is convected towards the outside bend in the upper

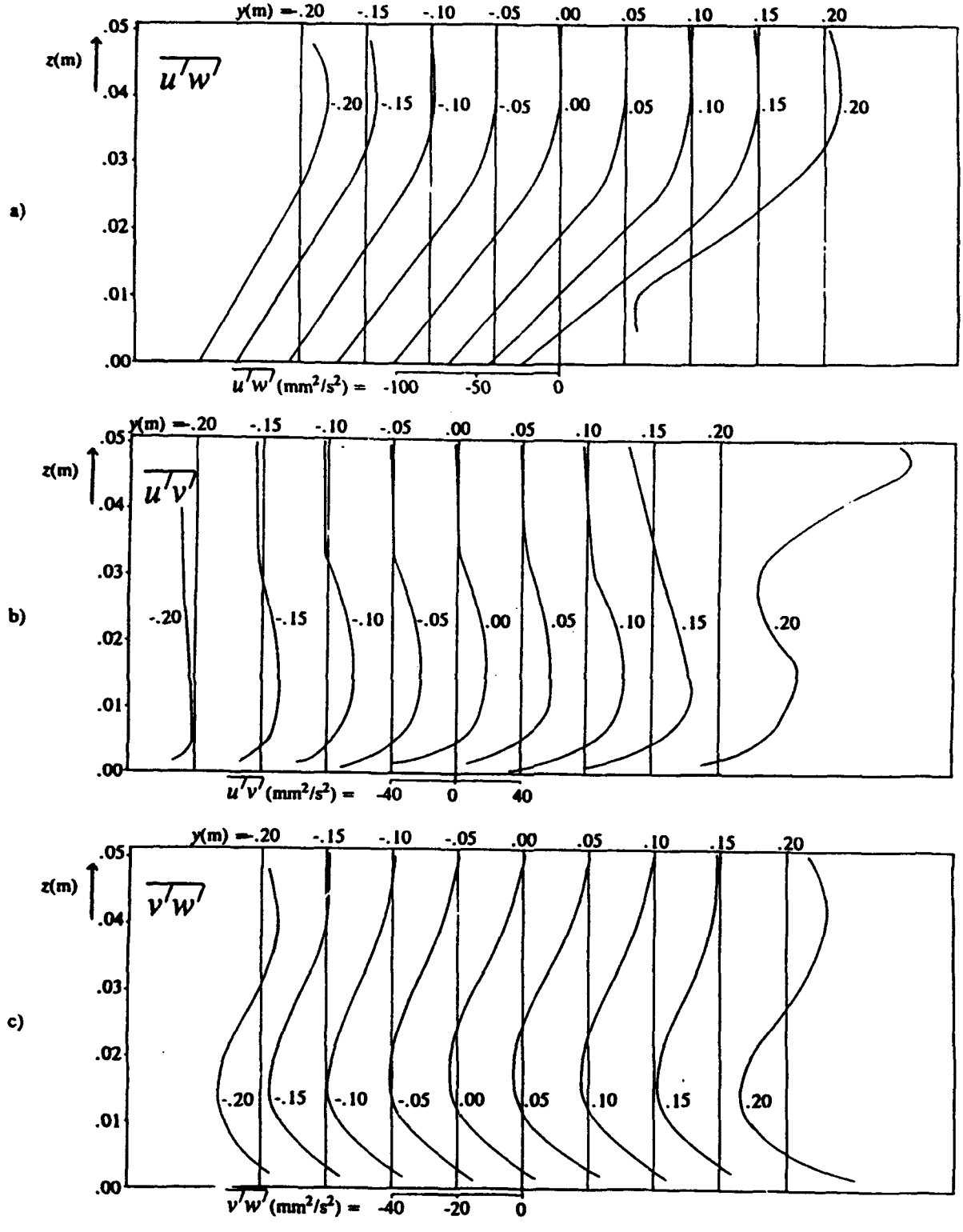

Fig. 7. Vertical profiles of the shear stresses at different places in the cross-section. (The scale for $y = 0$ m is given at the bottom. The scales for the other verticals are displaced, see the top of each plot. The vertical lines indicate the characteristic shear stress value.)

part of the flow. As a result the maximum value of the main flow velocity $\bar{u}$ in the centre of the flume is reached well below the water surface. Moreover the local depth-averaged main flow velocity increases towards the outside wall.

Attention should be paid to the difference of the scales for the different velocity components in fig. 4. The scale of $\bar{v}$ is about 10% of the scale of $\bar{u}$ and the scale of $\bar{w}$ is of the order of 1% of that of $\bar{u}$, which is of importance for the relative errors in the secondary flow velocity components and in particular for the accuracy in the determination of the vertical velocity.

4. SHEAR STRESSES AND EDDY VISCOSITIES

The vertical profiles of the different Reynolds shear stresses obtained from the cross-correlations of the measured turbulent velocity components at different places in the cross-section are plotted in fig. 7. These shear stresses provide for the transport of main flow momentum and secondary flow momentum in combination with the convective transport. Assuming gradient-type momentum transports in the various directions, eddy viscosity coefficients ν_{xz}, etc, for those transports can be derived, using

$$\frac{\tau_{xz}}{\rho} = \overline{u'w'} = -\nu_{xz}\left(\frac{\partial\bar{u}}{\partial z} + \frac{\partial\bar{w}}{\partial x}\right) \simeq -\nu_{xz}\frac{\partial\bar{u}}{\partial z} \qquad (3)$$

$$\frac{\tau_{xy}}{\rho} = \overline{u'v'} = -\nu_{xy}\left(\frac{\partial\bar{u}}{\partial y} + \frac{\partial\bar{v}}{\partial x}\right) \simeq -\nu_{xy}\left(\frac{\partial\bar{u}}{\partial v} - \frac{\bar{u}}{R}\right) \qquad (4)$$

$$\frac{\tau_{yz}}{\rho} = \overline{v'w'} = -\nu_{yz}\left(\frac{\partial\bar{v}}{\partial z} + \frac{\partial\bar{w}}{\partial y}\right) \simeq -\nu_{yz}\frac{\partial\bar{v}}{\partial z} \qquad (5)$$

Here the approximations

$$\frac{\partial\bar{w}}{\partial x} \simeq 0\ ;\quad \frac{\partial\bar{v}}{\partial x} \simeq -\frac{\bar{u}}{R} \quad \text{and} \quad \frac{\partial\bar{w}}{\partial y} \simeq 0 \qquad (6)$$

are used. The assumptions for the velocity-derivatives $\partial\bar{w}/\partial x$ and $\partial\bar{v}/\partial x$ can be made as the flow varies very slowly in the longitudinal direction in this part of the flume. $\partial\bar{w}/\partial y$ is negligible except near the sidewalls. Vertical profiles of the three introduced eddy viscosities in the center of the flume are plotted in fig. 8. Apparently the three eddy viscosities are far from equal and the assumption of an isotropic eddy viscosity in analytical or numerical flow models is not justified for this kind of flows. The singular behaviour of the eddy viscosities at points with a zero velocity gradient is of minor importance as the shear stresses are generally small too there.

The shear stress τ_{xz} transports main flow momentum in vertical direction. The measured τ_{xz} profile deviates significantly from the linear profile found in a wide straight open channel. In the central part of the flume the shear stress almost vanishes in the upper part of the flow. The corresponding eddy viscosity ν_{xz}, obtained from the measured shear stress and the vertical gradient of the main flow using equation (3) is also very small in this region (appreciably smaller than the theoretical value around half depth). To understand this behaviour of τ_{xz} and ν_{xz} it is useful to consider the distribution of the shear stress τ_{xy}.

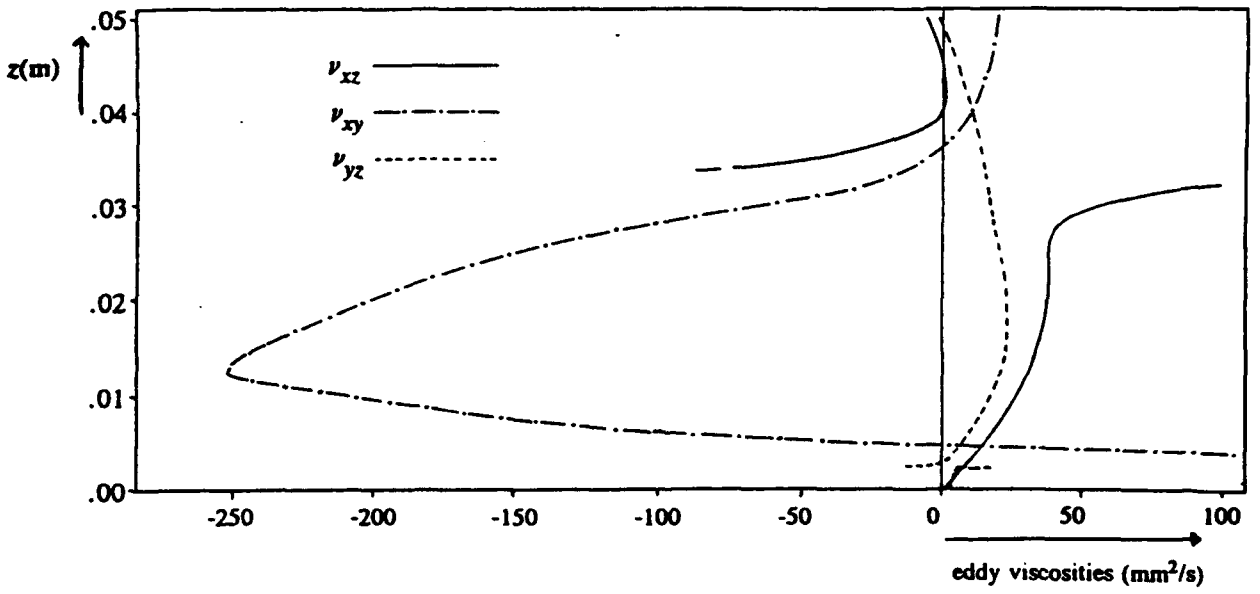

Fig. 8. Vertical distribution of the three eddy viscosities in the center of the flume.

The shear stress τ_{xy} transports main flow momentum across the flume. In a large central part of the flow the transport appears to be in the wrong direction, corresponding to a negative eddy viscosity (see fig. 8). An explanation can be found taking a closer look at the turbulence structure.

In boundary layer flow and in open channel flow an important aspect of turbulence is the movement of coherent parcels of water from the bottom in upward direction. These coherent parcels and to a lesser extent the compensating fluid moving in downward direction provide the largest contribution to the stress τ_{xz} (Brodkey, 1974). The upwards moving parcels arriving at a higher level have a positive value of w, and a relatively low value of u and v, implying a positive w' and negative u' and v'. Downward moving parcels have analogously negative w' and positive u' and v'. Both kind of parcels give a negative contribution to $\overline{u'w'}$ and a positive contribution to $\overline{u'v'}$. The positive value of $\overline{u'v'}$ measured has evidently nothing to do with a gradient of $\bar{u}$ across the flume, but stems from the mechanism described above.

The low value of τ_{yz} near the surface seems to indicate that the upward movement of coherent parcels which is important over the whole depth in a straight flume is hindered in curved flow, especially in the upper part. This is confirmed by the distribution of the turbulence energy per unit of mass, k, see fig. 9, where

$$k = \frac{1}{2}\left(\overline{(u')^2} + \overline{(v')^2} + \overline{(w')^2}\right) \qquad (7)$$

In fig. 9 the measured turbulence energy in the centre of the cross-section is plotted and compared to the

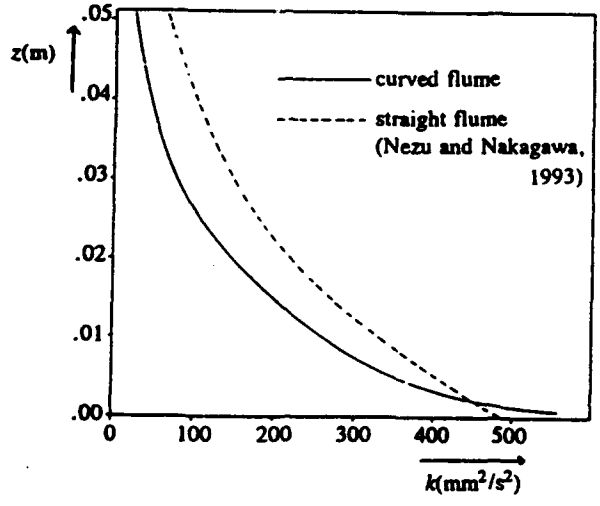

Fig. 9. Comparison between turbulence energy in curved flow and in straight flow.

corresponding turbulence energy in a straight flume. The damping of the turbulence in the central part of the curved flow increases with the distance to the bottom.

The hindrance of the vertical movement of the fluid parcels in the upper part of the curved flow is presumably caused by the typical main flow profile induced by the convection of the main flow by the secondary flow. Then the rate of damping depends on the aspect ratio h/B, as the convection by secondary flow in relatively wide channels is less important compared to the influence of the bed shear stress. This damping of the vertical movement of the parcels coming from the bottom region reduces also the values of τ_{xz} and ν_{xz} measured in the upper part of the flow compared to a straight flume.

The shear stress τ_{yz} transports secondary flow momentum in vertical direction. The measured negative values of $\overline{v'w'}$ agree with the positive w' and negative v' for upward moving and the negative w' and positive v' for downward moving parcels. The upward moving parcels are created around $y^+ = yu_*/\nu = 30$ (Brodkey et all., 1974) or at about 1 mm from the bottom. This is near the depth where the negative secondary velocity is largest. A positive shear stress τ_{yz} that is expected below this depth is found in these measurements (see fig. 7), where in the previous 2-dimensional measurements near the bottom the noise prevented this.

The eddy viscosity ν_{yz} is smaller then the eddy viscosity of the main flow ν_{xz}. This can be understood, when it is considered that the shear stresses do not only depend on local conditions, but also on the properties transported by the parcels created in the bottom regions. This smaller eddy viscosity leads to higher secondary velocities than predicted with estimates based on the assumption of equal eddy viscosities and explains the deviations often found between measurements and theories.

5. CONCLUSIONS

- By carefully designing the optical arrangement a 3-D LDV configuration can be used to do semi-automatic simultaneous measurements of various turbulence moments e.g. the three Reynolds shear stresses in a flume.
- Descriptions of the flow in curved channels using gradient-type momentum transport concepts are of limited use.
- Use of equal eddy viscosities for the various momentum transports in curved channel flow is not justified.

REFERENCES

Bendegom, L. Van, 1947, Some considerations on river

morphology and river improvement, De Ingenieur, vol.59-4, pp. B1-11, in Dutch. English translation: Nat. Res. Council of Canada, Tech. Transl., 1054, 1963.

Booij, R., 1985, Eddy viscosity in channel bends, Proc. int. symp. on refined flow modelling and turbulence measurements, Iowa, E21.

Brodkey, R.S. et all., 1974, Some Properties of Truncated Turbulence Signals in Bounded Shear Flows, J.Fluid Mech., 63, 209.

Nezu, I and H. Nakagawa, 1993, Turbulence in open-channel flows, IAHR Monograph, Balkema, Rotterdam.

Odgaard, A.J., 1981, Transverse bed slope in alluvial channel bends, J.Hydr.Div., ASCE, vol.107 (HY12), pp. 1677-1694.

Leschiner, M.A. and Rodi, W. 1979, Calculation of strongly curved open channel flow, J.Hydr.Div., ASCE, vol.105 (HY10), pp. 1297-1314.

Vriend, H.J. De 1981a, Velocity redistribution in curved rectangular channels, J.Fluid Mech., vol.107, pp. 423-439.

Vriend, H.J. De 1981b, Steady flow in shallow channel bends, Communications on Hydraulics, 81-3, Dept. of Civil Engrg., Delft Univ. of Technology.

Session 29.
Scalar Measurements II

A REAL-TIME FREE-SURFACE ELEVATION MAPPING TECHNIQUE

D. Dabiri, X. Zhang, M. Gharib

California Institute of Technology

ABSTRACT

Recently, there has been an increased interest in the interaction of vortices and turbulence with free surfaces. A central issue in understanding the free surface turbulence is to relate the surface elevation to the near surface flow field. In that respect, the lack of a global surface mapping technique which could reveal the temporal evolution of the surface elevation has prevented the progress of viable research. Thus it is the purpose of this work to present a new technique integrating optics, colorimetry, digital image processing, to measure the 3-D surface elevation for a time-evolving flow.

BACKGROUND

It is highly undesirable to use a probe which extends through the water surface to study surface structures due to the fact that the probe interacts with the free-surface. It is therefore highly desirable to use optical methods since these techniques do not interfere with the free-surface. As suggested by Cox, it is convenient to measure the water-surface slope instead of the free surface elevation, since the higher frequency waves have lower amplitudes while they maintain higher slopes. Therefore, Cox (1958) measured the surface slope by the refraction of light through a free-surface. A light source of spatially linearly-varying intensity was placed at the bottom of a water tunnel, and a telescope imaged one point on the water surface into a photocell. Therefore, the brightness of the light seen by the photocell was proportioned to one component of the slope of the free-surface. This technique is referred to as the "refraction mode" since the observed light rays are refracted through the surface. Likewise, one can perform the experiment by illuminating the surface of the water from air and observing the reflections. This technique is referred to as the "reflective mode" since the observed light rays are reflected from the surface. Using a photo diode array and a laser as a single point light source, Long and Huang (1976) were able to measure both components of the surface slope at one point. Further work done by Keller and Gotwols (1983), Jahne and Wards (1989), and Jahne and Riemer (1990), progressed the technique to allow for two slope component measurements, one slope at a time. Zhang and Cox (1992) extended this work by allowing the measurement of two slope components simultaneously, throughout a two-dimensional spatial domain. Since the technique is photographically-based, it allowed data acquisition at only one point in time. In this paper, we report on the development of a real-time version of this technique that facilitates studies of time evolving flows.

MEASUREMENT TECHNIQUE

By combining the technique developed by Zhang and Cox with a video recording system, and with digital image processing, we have produced a technique capable of measuring surface slopes in a two-dimensional spatial domain for time-evolving flows. Figure 1 shows the set-up for this technique. A 2-D diffused white light source is covered with a color palette. Therefore, color is now a function of position on the light source. The color palette used to cover the light source is shown in figure 2. A large lens is placed at exactly one focal length away from the colored light source. This will then create a system of parallel color beams. Each set of colors will be parallel, but in different directions with respect to other colors. As can be seen from figure 1, green, which emanates from near the center of the light source, turns into a parallel set of beams which are near-parallel to the axis of the lens. However, blue, which emanates from the edge of the light source, is transformed into a parallel set of beams which are parallel, yet at an angle to the axis of the lens. This system of parallel beams are used to illuminate the free surface. A 3-chip RGB color camera is located far away to observe the color reflections of the free-surface. By placing the camera as far away as we can, we make the beams entering the camera as parallel as we can. It is important to realize that 1) each of the different colors incident on the free surface at different angles, will be reflected only from a certain angle from the free surface toward the camera, and 2) the reflections must all be almost parallel, regardless of their color in the direction to the camera. Figure 3 shows a close-up of the color reflection from the surface. With these two points in mind, it becomes clear that this technique color-codes the different slopes of the free-surface.

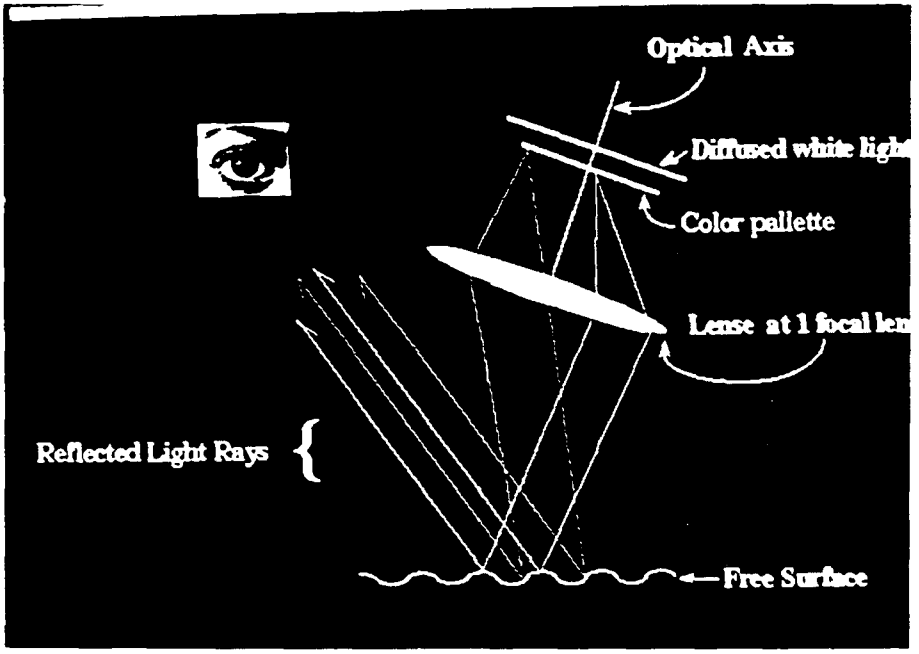

Fig. 1 This picture demonstrates the principle of the measurement technique. A diffused white light source illuminates a color palette (see Fig. 2). A lens, located at its focal plane from the color palette, transforms the merging color-coded light into a multiple system of parallel colored beams. This system of beams, after being reflected from the free-surface, is captured by a camera located far away. It is important to note that each color will reflect from a particular slope of the free-surface. Thus, the basis of the technique lies in the fact that different slopes of the free-surface are coded with different colors, through the setup of the color palette and lens.

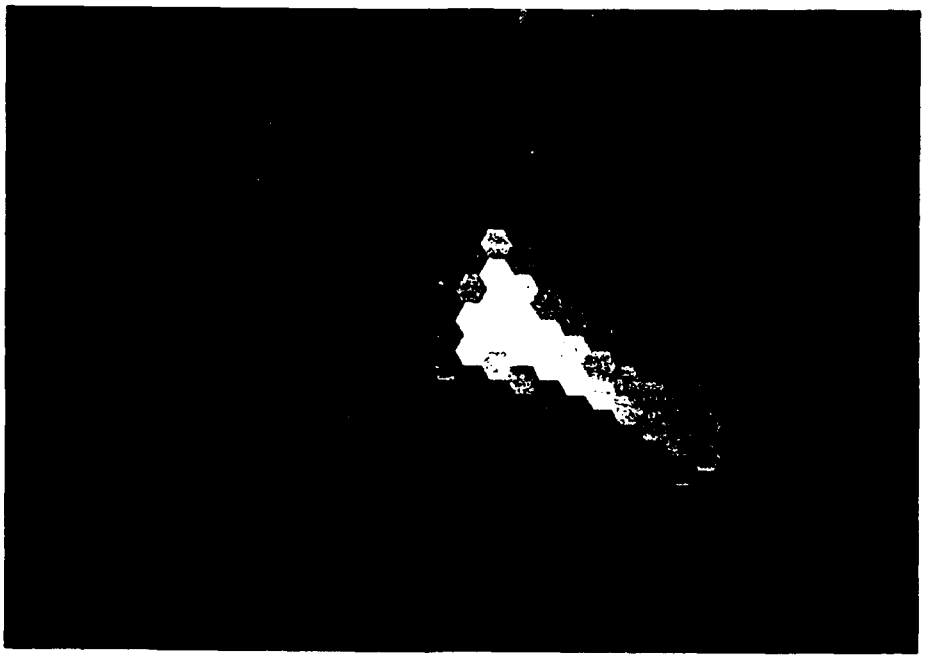

Fig. 2 This is the color palette used for color-coding the free-surface slopes. The color palette can be varied to resolve various scales of the free-surface slopes

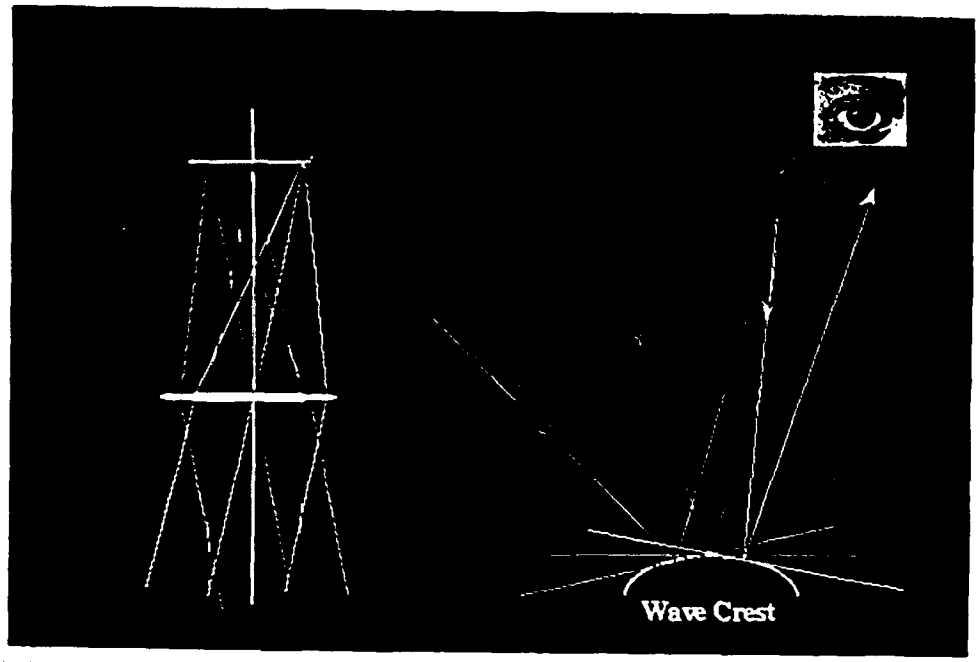

Fig. 3 This is a close-up of the color reflection from the surface. Note how the different colors incident from different angles will reflect away into the same direction depending on where they hit the free-surface.

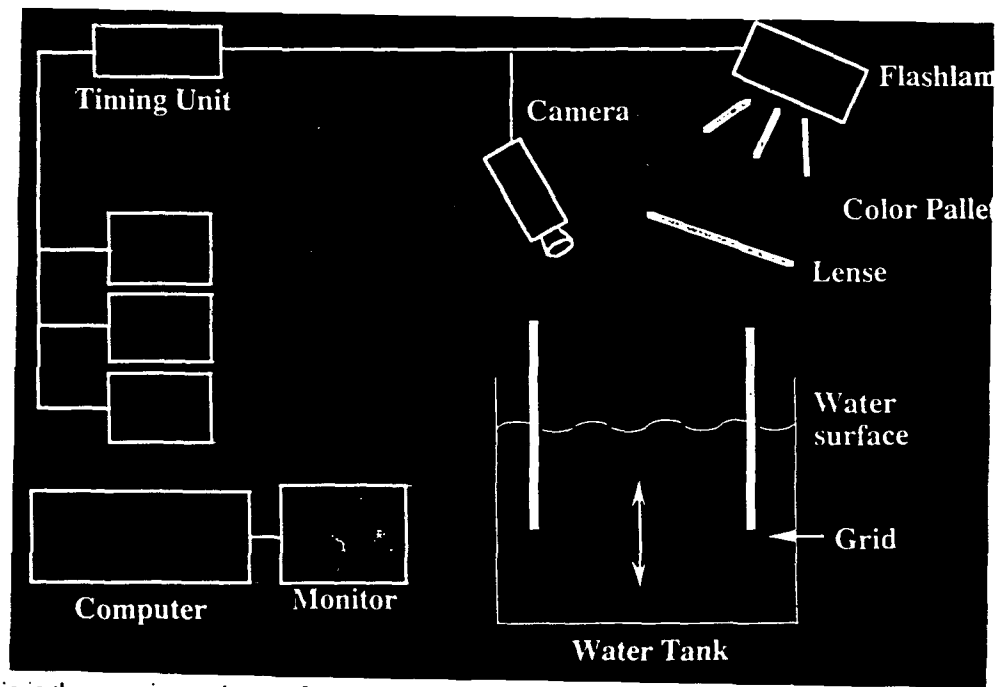

Fig. 4 This is the experimental setup for measuring the free-surface deformations due to near surface turbulence. The color palette and lens are chosen and setup to respond to surface slopes from -4 to 4 degrees. A three-chip color video camera captures the surface deformations. The images are then recorded onto three laser disk recorders for capturing time-evolving flows. Each laser disk recorder records one of the three color signals (red, green, and blue) of the camera, thereby increasing the bandwidth of the acquired data. Finally, the images are analyzed individually with the color frame grabber residing on the computer.

Fig. 5 A picture of the free-surface captured by a RGB color video camera. The surface is deformed by the turbulence generated within the volume of the fluid. The images covers an area of 22 cm by 15 cm. Again, it is necessary to emphasize that this picture and picture 6 are real, and are not pseudo-colored.

Fig. 6 A picture of the free-surface captured by a RGB color video camera. All specifications are identical to those given for picture 5 except that this picture was acquired 1 second after picture 5. Also, circular color patterns similar to the color pattern shown is picture 2 are seen showing the evolution of the cortex connections with the free-surface as compared with picture 5.

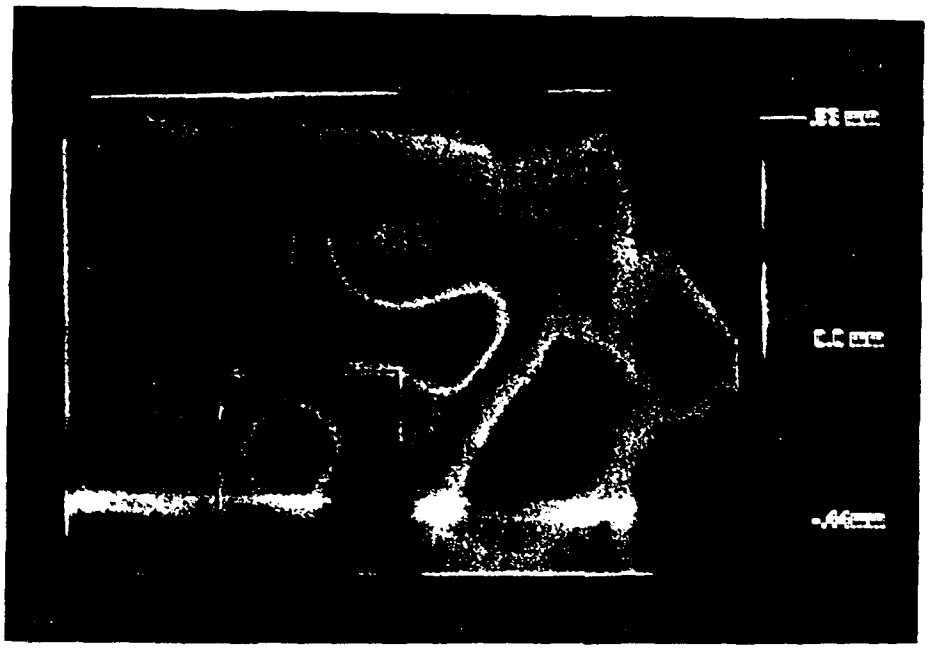

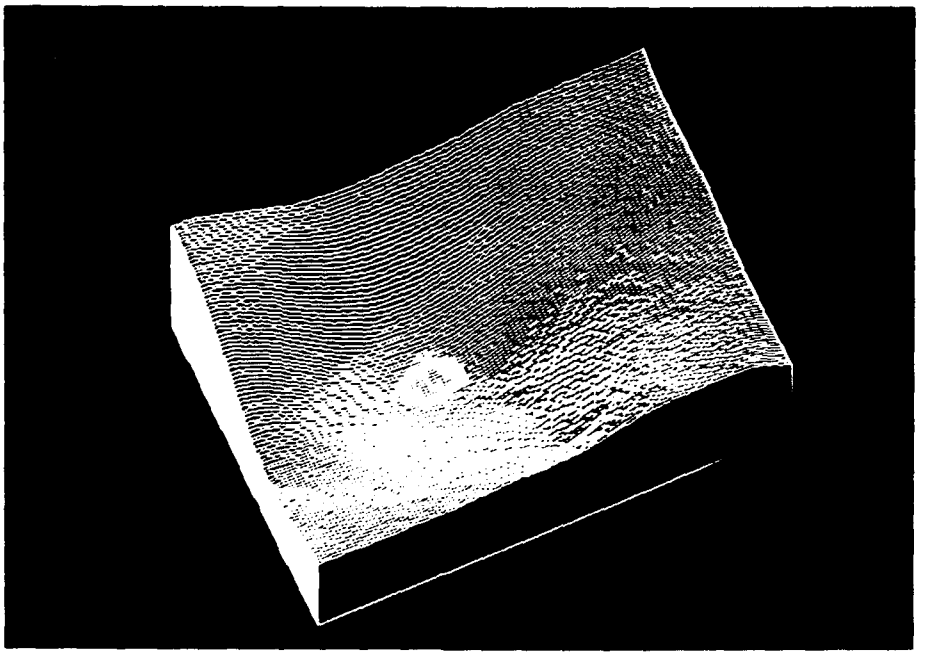

Fig. 9 The three-dimensional surface plot of the vortex reconnection to the free-surface. This plot shows vortex 1 in the boxed area of picture 5, showing the surface elevation in detail.

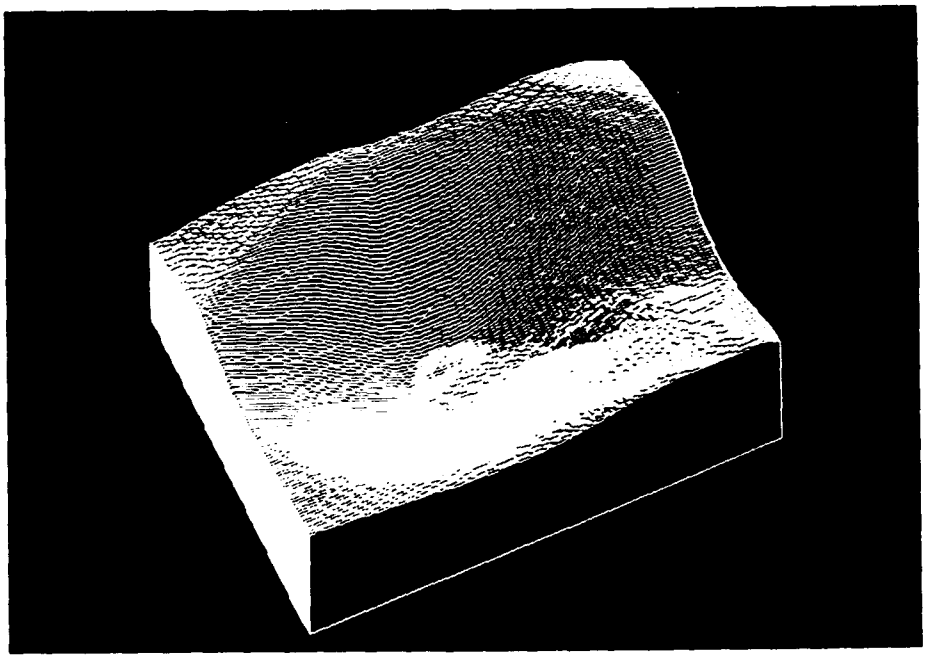

Fig. 10 The three-dimensional surface plot of the vortex reconnection to the free-surface. This plot shows vortex 1 in the boxed area of picture 6 showing the surface elevation in detail, after 1 second.

ANALYSIS

The images are acquired in the RGB domain However, analysis of the data in the RGB color domain is quite difficult. Therefore, analysis is done in the HSI color-domain (Zhang, 1993; Dabiri and Gharib, 1992). Through the use of a calibration image, colors are translated into slopes of the free surface. The reconstruction of the surface elevation is done in Fourier space. Let the Fourier series expansions of the surface elevation and its gradients be $F(k_x, k_y)$, $F_x(k_x, k_y)$, and $F_y(k_x, k_y)$ respectively, where k_x and k_y are the two orthogonal wave number components. Then, the following relations hold:

$$f^T(x, y) \square F(k_x, k_y)$$
$$f_x{}^T(x, y) \square ik_x F(k_x, k_y) = F_x(k_x, k_y)$$
$$f_y{}^T(x, y) \square ik_y F(k_x, k_y) = F_y(k_x, k_y)$$

where the double-headed arrow represents a Fourier series transformation and superscript T denotes the periodically extend function. By multiplyin$_{\text{L}}$ factors ik_x and ik_y to $F_x(k_x, k_y)$ and $F_y(k_x, k_y)$ separately, we find

$$F_x(k_x, k_y) \cdot (-ik_x) + F_y(k_x, k_y) \cdot (-ik_y) = (k_x^2 + k_y^2) F(k_x, k_y)$$
$$= k^2 F(k_x, k_y)$$

or

$$f^T(x, y) \square F(k_x, k_y) = \frac{F_x(k_x, k_y) \cdot (-ik_x) + F_y(k_x, k_y) \cdot (-ik_y)}{k^2}$$

The last expression generates the elevation of the water surface from the transforms of the slope components.

APPLICATION TO EXPERIMENT

This technique is applied to study the interaction of turbulence with the free-surface. Figure 4 shows the set-up for the experiment in which this technique is used. A turbulence-generating grid is dropped through a tank filled with still water. The parallel color-generating equipment is set up to illuminate the free-surface of the water tank. The color palette and lens are chosen and set up to respond to surface slopes from -4 to 4 degrees. A 3-chip color camera located far away observes the color reflections from the free surface. The images are recorded into 3 laser disk recorders, one for each of the 3 color signals--red, green and blue--thereby increasing the bandwidth of the data signal. The acquisition is done in real-time, thereby allowing for analysis of time-evolving flows. After acquisition, a P.C. based color-image-processing system is used to analyze the data in order to extract the surface elevations. This study could have been done using the refractive mode, where the parallel-color generating equipment would be placed underwater, and refractions would be observed. However, since the angle of refraction is less than the angle of reflection for a given angle of incidence, the reflection mode is more sensitive to the surface deformations than the refraction mode. Figures 5 and 6 show two sequential raw images acquired with a 0.1 second time interval. It is important to realize that these images are true color images and are not pseudo-colored. The images cover an area of 22 cm by 15 cm. Figures 7 and 8 show the surface elevations calculated from the measured slopes extracted from pictures 5 and 6, respectively. Note the evolution of the vortices on the free-surface. Vortex 1 has remained stationary while its relative depression has decreased. Vortices 3 and 4 (in figure 7), within 0.1 seconds, have begun to merge into a larger vortex (labeled vortex 3 in figure 8) with a relatively lower depression. Figures 9 and 10 show the 3-D surface plot of vortex 1 shown in figures 7 and 8.

In conclusion, we have presented a technique capable of measuring the elevation of the free-surface in real time. We have also demonstrated its capabilities by applying the technique to study the interaction of turbulence with the free-surface.

ACKNOWLEDGMENT

This work was sponsored by
(ONR-URI) NØØØ14-92-J-1610

REFERENCES

1. Cox, C. S., (1958), Measurement of Slopes of High-Frequency Wind Waves, J. Marine Res., vol. 16, no. 9, 199-225.

Dabiri, D. and Gharib, M. (1991), Digital Particle Image Thermometry: The Method and Implementation, Exp. In Fluids, vol., 11, 77-96.

Jahne, B. and Waas, S., (1989), Optical Measuring Technique for Small Scale Water Surface Waves, Advanced Optical Instrumentation for Remote Sensing of the Earth's Surface from Space, SPIE Proceeding 1129, International Congress on Optical Science and Engineering, Paris, 24-28 April 1989, 147-152.

Jahne, B. and Riemer, K. S. (1990), Two-Dimensional Wave Number Spectra of Small-Scale Water Surface Waves, J. Geophys. Res., vol. 95, no. c7, 11531-11546.

Keller, W. and Gotwols, B. L., (1983), Two-Dimensional Optical Measurement of Wave Slope, Appl. Opt., vol. 22, 3476-3478.

Long, S. R., and Huang, N. E., (1976), On the Variation and Growth of Wave-Slope Spectra in the Capillary-Gravity Range with Increasing Wind, J. Fluid Mech., vol. 77, part 2, 209-228.

Zhang, X. (1993) A Study of Capillary-Gravity Wind Waves: Their Structures, Distributions, and Energy Balances. Ph.D. Dissertation, University of California, San Diego

Zhang, X. and Cox, C. S., Measuring the Two-Dimensional Structure of a Wavy Water Surface optically: A Surface Gradient Detector. Submitted to Exp. In Fluids

AN OPTICAL METHOD FOR DETERMINING THE GEOMETRIC CHARACTERISTICS OF LIQUID FILMS FLOWING AROUND A HORIZONTAL TUBE

P. Speck, M. Khan, P. Desevaux and P.K. Panday

Institut de Génie Energétique, Université de Franche-Comté
Parc Technologique, 90000 Belfort, France

ABSTRACT

In this paper, an optical method is presented for determining the geometric characteristics (film thickness, equation of the external contour) of liquid films flowing around a horizontal tube. Two techniques are used as a function of the studied area. One of them allows the visualization of the film section under the tube, and the other one permits the punctual measurement of the film thickness around the upper half circumference of the tube. Both methods use Laser-Induced Fluorescence (L.I.F.) and Image Processing techniques.

1. INTRODUCTION

Knowledge of the geometric characteristics of the liquid film flowing around horizontal tubes is of great interest to study the mass and heat transfer in many modern industrial equipments as radiators or condensers. Concerning the condensation around horizontal tubes, these characteristics, especially the film thickness, are calculated analytically by many simplified models [Nusselt (1916), Shekriladze (1977), Rose (1984)]. These models, which assume the film to be laminar and continuous, give correct results for the calculation of the global heat transfer coefficients. Shklover & Semenov (1981) and Pritchard (1986) have studied experimentally the discontinuous nature of the condensate flowing in drop form and in more or less stable columns. Usually, the characteristics of liquid films flowing on flat plates are obtained experimentally by measuring the variation of the electrical conduction through the fluid [Lyu & Mudavar (1991)] or by surface contact devices. These measuring techniques are difficult to apply in the case of non-flat walls. Optical techniques have also been developed for determining the characteristics of a liquid film in a nonintrusive manner. In this way, techniques applying Laser-Induced Fluorescence have been used recently to measure the thickness of a liquid film in movement [Driscoll et al. (1992)], and to visualize the whole section of a liquid film flowing between two rotating cylinders [Decré & Buchlin (1994)] or in narrow grooves [Khan et al. (1993)]. The latter method is extended here to the investigation of liquid films flowing around a cylindrical horizontal tube. The condensate film is produced artificially. The high difference in the film thickness between the upper and lower parts of the tube imposes the use of two distinct optical techniques.

2. EXPERIMENTAL SETUP

2.1 Flow System

The liquid film is artificially produced by the flow system shown in figure 1.

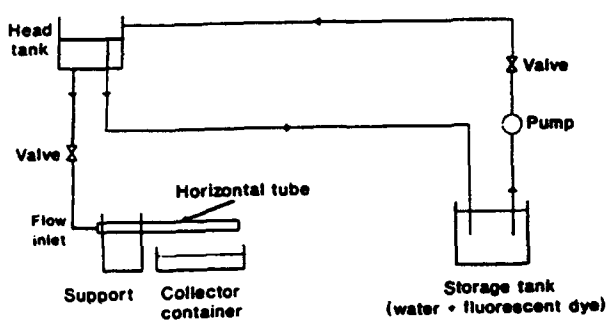

Fig. 1: Schematic representation of the flow system

A horizontal tube (Φ_{ext} = 18 mm, Φ_{int} = 16 mm) is fed by water seeded with fluorescent dye (fluorescein or rhodamine B) in a weak proportion (concentration of about 50 mg / liter), which does not significantly change the physical properties of the water. This mixture flows out from inside to outside of the tube through a set of holes (1 mm diameter) perforated along a line at the upper surface of the tube and spaced 3 mm apart. A pump ensures the circulation of the mixture from the storage tank to the head tank maintained at a constant level. The mixture flows by gravity from this tank to the inlet of the test tube. Flow regulation is achieved by means of a valve mounted in the circuit. The mass flow rate is measured by weighing the fluid collected in the collector container.

This study is facilitated by mounting this tube on a sliding support, which can be translated to change the studied section during the investigation of the liquid film along the tube. It may be noted that we use an unpolished copper tube in order to facilitate the establishment of the liquid film.

2.2 Optical Device and Image Acquisition System

The film thickness is found to vary strongly around the tube circumference from top to bottom of the tube. Consequently, we distinguish between the two studied zones which are indicated in figure 2. These zones require for investigation the use of two different techniques.

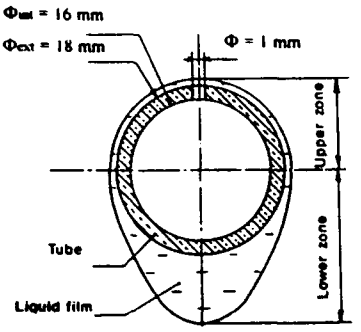

Fig. 2: Tube section

Optical devices required in both techniques are schematized in figure 3. Regarding the lower part of the tube, the visualization of the whole section of the film is possible. This visualization is obtained by integrating Laser sheet methods [Prenel et al. (1988)] and Laser-Induced Fluorescence techniques. The optical device utilized allows the generation of a vertical light sheet which illuminates a cross section of the film flowing around the tube. The light beam issues from a continuous wave argon laser operating in the blue line (λ = 488 nm, P = 150 mW). The laser beam is directed perpendicularly to the tube axis with the aid of mirrors. A spherical telescope focuses the beam at the surface of the tube. A cylindrical lens spreads this beam, forming a thin laser sheet of a thickness of about 0.3 mm. The intersection of this light sheet with the water flow doped with fluorescein produces a fluorescent light section. This section is observed through a video camera microscope (magnification × 20, effective pixels 579 × 583). The presence of the liquid film along the lower part of the tube between the studied section and the camera prevents the front viewing of this section. As a consequence, the camera makes an angle θ (which does not exceed 15°) with respect to the tube axis. Furthermore, as only fluorescence light must be received, a stop-band filter (λ = 488 nm) is placed in front of the camera to remove the incident light. The obtained images are then digitized and processed by an image processing software (PCSCOPE).

This visualization technique is not applicable for investigating the flow around the upper half circumference of the tube, where the liquid film is extremely thin. The observation of such a film requires a great magnification of the image which is incompatible with the visualization of the whole section of the film. Consequently, a local measurement technique, also based on the L.I.F. principle, is used to measure the liquid film thickness in this zone. Figure 3 also presents the optical device utilized in this case.

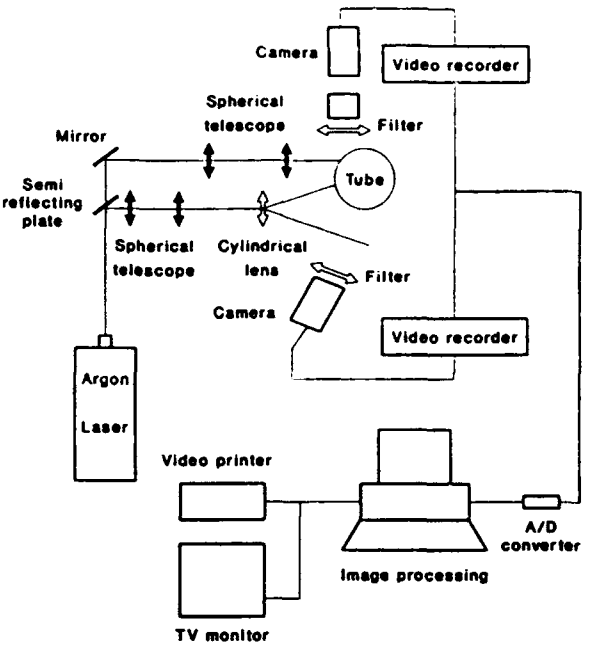

Fig. 3: Visualization and image acquisition system

A spherical telescope ensures the focalisation of the laser beam at the tube surface. At this surface, the focused beam diameter is about 0.2 mm. The portion of liquid crossed by the laser beam is observed from the top by using an assembly of a video camera microscope and a photographic objective with great magnification. This observation is carried out through a stop-band filter (λ = 488 nm), and the obtained image is digitized and then analysed by the image processing software.

During the utilization of both techniques, special care is taken into account in locating the camera in order to realize correct centring of the visualized zone.

3. INVESTIGATION PROCEDURE

3.1 Investigation of the Liquid Film in the Lower Part of the Tube

The visualization of the film section obtained show a distortion of the optical image due to the three-dimensional effects and to the film concavity, which acts as an optical diopter and thus makes the light rays deviate by refraction. However, the representation of the front external contour is not deformed, and the back external contour is deduced from symmetry. On the other hand, the dissymmetry which appears in the images of the film section comes from the

tilting angle θ of the camera. This deformation is taken into account at the time of mathematical reconstitution of the contour.

The series of pictures presented in figure 4 illustrates the main processes applied to the original image to draw out information concerning the liquid film geometry.

a: Thresholded original image

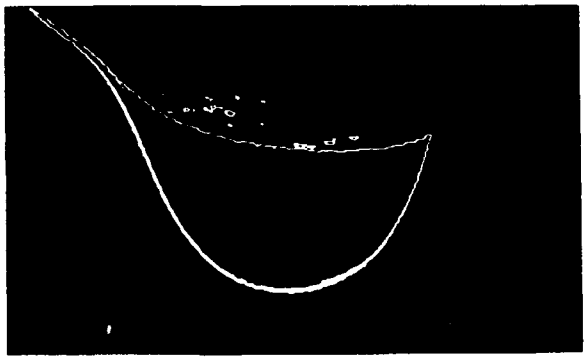

b: Image after applying a gradient operator

c: Final image after skeletonizing

Fig. 4 a-c: Image processing procedure

In a first step, the original image is digitized and an appropriate thresholding of the gray levels is applied to remove the background noise and to obtain a clear image (figure 4a). An edge detection is then achieved by applying a gradient operator. This operator extracts the edges of the lines as well as providing a thin gray-level strip (figure 4b). This picture is then converted to a binary image in order to obtain a binary boundary and to extract the contour of the film. Finally a typical image of the film obtained after skeletonizing is shown in figure 4c. To obtain quantitive information about the liquid film geometry, calibration is required to give the relationship between the distances measured in pixels and millimeters. This calibration is obtained by recording a reference object located at the laser light section. It is then possible to determine for several values of the abscissa x, the distances $h(x)$ from the contour to a chosen reference line (here the horizontal tangent to the bottom of the tube, as shown in figure 5).

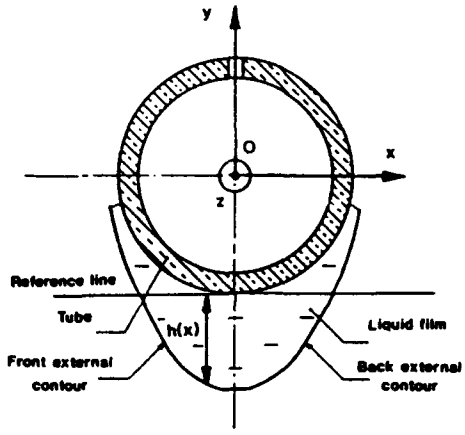

Fig. 5: Reference system

Knowing a sufficient number of points, a mathematical computation software (MATHEMATICA) allows reconstitution of the contour curve (figure 6) and deduction of its mathematical equation.

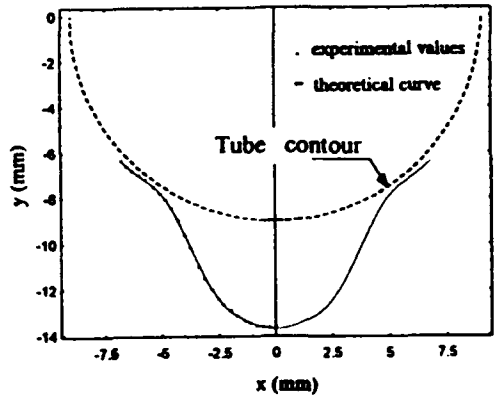

Fig. 6: Reconstitution of the external contour of the film

The calculation procedure takes into consideration the tilting angle θ of the camera and gives the correct representation of the external contour of the film section under the tube.

As an example, the contour shown in figures 4 and 6 can be assimilated, in the (O,x,y) coordinate system (with O taken at the tube axis), to a curve of the following polynomial equation.

$$y(x) = \Sigma a_i x^i$$

where:

$a_0 = -13.7359$	$a_1 = 0$
$a_2 = 0.264833$	$a_3 = 0$
$a_4 = -0.116082$	$a_5 = 0.0806921$
$a_6 = -0.0194694$	$a_7 = -0.00170891$
$a_8 = 0$	$a_9 = 4.95046\ 10^{-6}$

This technique is proved to be adapted for following the temporal evolution of the liquid film in the lower part of the tube. Figure 7 presents a series of pictures showing the formation of a drop under this tube.

t = 0.32 s

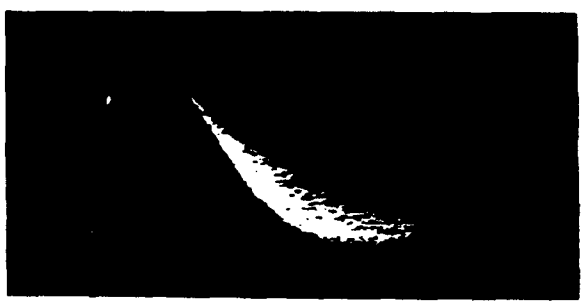

t = 0.52 s

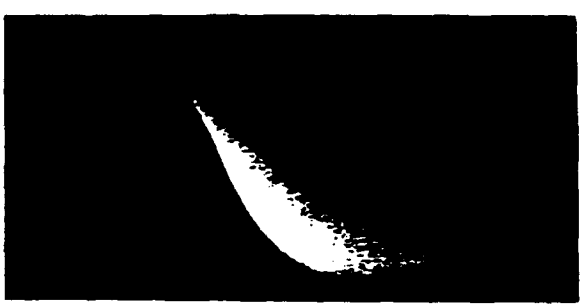

t = 0.76 s

Fig. 7: Temporal evolution of the liquid film

The time origin t = 0 is taken when the previous drop separates from the tube. Figure 8 regroups the mathematical reconstitutions related to these pictures. Two inflection points may be observed on the contour curve corresponding to the time t = 0.76 s. These inflection points correspond to a striction of the liquid film which appears in the region where the drop separates from the tube.

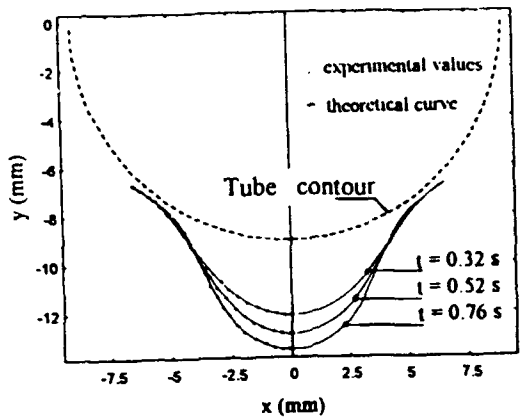

Fig.8: Reconstitutions of the film contour at t = 0.32 s, 0.52 s and 0.76 s

3.2 Measurement of the Film Thickness in the Upper Part of the Tube

The film thickness around the upper half circumference of the tube is determined by a local measurement technique. The use of this technique is justified by the fact that the film thickness can be considered constant in this region [Nicol & Dempsey (1982)]. For convenience, the measurements are carried out in the horizontal median plane of the tube, as shown in figure 9.

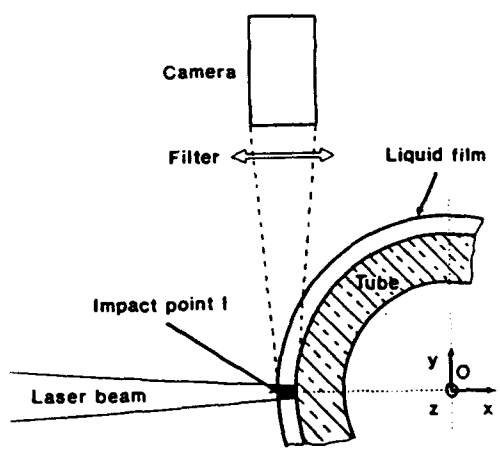

Fig. 9: Measurement of the film thickness in the upper part of the tube

The portion of the liquid film crossed by the laser beam appears as a bright spot (figure 10).

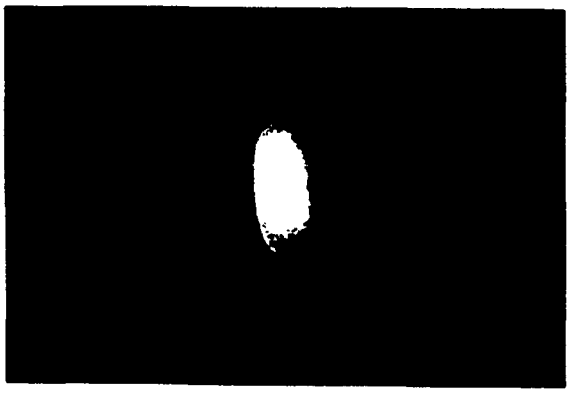

Fig. 10: Visualization of the liquid film thickness in the upper zone of the tube

The film thickness cannot be obtained by direct measurement of the spot length. Indeed, the film curvature deviates the light rays by refraction and causes a distortion of the optical image. The impact point I of the laser beam at the external surface of the film is the only one observed without distortion. The film thickness is hence obtained by measuring the distance from this point and to the dry tube surface filmed in the absence of liquid film. Measurements are performed with PCSCOPE software and also require a calibration to give the relationship between the distances measured in pixels and millimeters.

This technique appears to be relatively sensitive as illustrated in figure 11. This figure presents three bright spots related to three different flow conditions, and shows an increase in film thickness which goes up from about 180 µm to 330 µm.

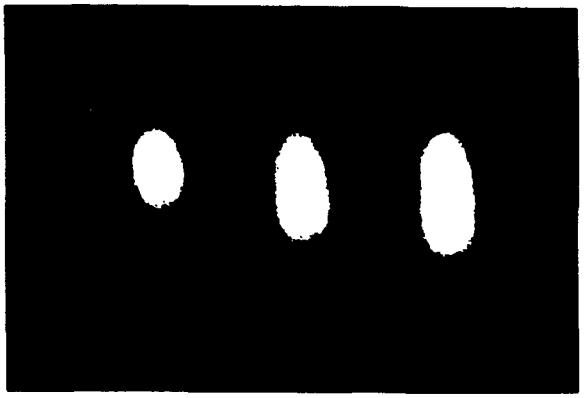

Fig. 11: Evolution of the liquid film thickness as a function of the flow conditions

It may be noted that measurements of the film thickness must be achieved rapidly to avoid local superheating of the liquid film due to the focused laser beam.

4 CONCLUSION

The investigation method reported in this article allows us to study and to characterize the geometric form of liquid films flowing around a horizontal tube. This method integrates visualization of a film section under the tube and punctual measurement of the film thickness around the upper half circumference of this tube.

In the two cases, we combine the principle of the Laser-Induced Fluorescence (L.I.F.) with the image processing techniques to extract the mathematical equation of the external contour of the film and to measure the film thickness.

It is difficult to estimate the accuracy of this investigation technique, because of the many parameters in this procedure. However, the accuracy here is related directly to the magnification of the objective of the camera used and depends strongly on the measurement of the tilting angle of the camera.

The application of this optical method gives the possibility to follow the evolution of the film geometry for different flow conditions. By combining this technique with a rapid video acquisition system, the study of the separation of the drop from the tube, and the observation of the drop behavior during its fall are possible. We are now working to extend this method to investigate the liquid film generated by condensation. It may lead to a better understanding of the tearing mechanism of droplets in tubular condensers.

REFERENCES

Decré, M. & Buchlin, J.M. 1994, An Extra-thin Light Sheet Technique Used to Investigate Meniscus Shapes by Laser Induced Fluorescence, Exp. in Fluids, vol. 16, pp. 339-341.

Driscoll, D.I., Schmitt, R.L. & Stevenson, W.H. 1992, Thin Flowing Liquid Film Thickness Measurement by Laser Induced Fluorescence, J. Fluids Eng., vol. 114, pp. 107-112.

Khan, M., Desevaux, P., Panday, P. & Prenel, J.P. 1993, An Optical Method For Determining The Meniscus Characteristics of Liquid Films Flowing in a Groove, Journal of Flow Visualisation and Image Processing, vol 1, no. 3, pp. 171-179.

Lyu, T.H. & Mudavar, I. 1991, Simultaneous Measurements of Thickness and Temperature Profile in a Wavy Liquid Film Falling Freely on a Heating Wall, Exp. Heat Transfer, vol. 4, pp. 217-223.

Nicol, A.A., & Dempsey, M.J., 1982, Condensation of Wet Steam on a Horizontal Tube With Additional Droplet Deposition, Int. J. Multiphase Flow, vol. 8, no. 3, pp. 207-216.

Nusselt, W. 1916, Die Oberflachen Kondensation des Wasserdampfes. Z.V.D.I., no. 60, pp. 541-546, pp. 569-575.

Prenel, J P , Porcar, R & Hostache, G 1988, Evolution Récente des Visualisations d'Ecoulements par Nappes de Lumière Laser , Rev Gén Thermique, no 317, pp 308-312

Pritchard, W G 1986, Instability and Chaotic Behaviour in a Free-Surface Flow, J of Fluid Mech., vol 165, pp 1-60

Rose, J W 1984, Int. J. Heat Mass Transf., no 27, pp. 39-47.
Shekriladze, I G 1977, Analysis of Laminar Film Condensation from a Moving Vapor. Inzh. Fiz. Zh., vol. 32, no.2, pp. 221-225

Shklover, G G. & Semenov, V.P 1981, The Flow Mode of Condensate in a Multirow Horizontal Tube Bundle, Heat Transfer, Soviet Research, vol. 13, no. 3, pp 127-133

APPLICATION OF LASER INDUCED FLUORESCENCE FOR MEASURING THE THICKNESS OF LIQUID FILMS ON TRANSPARENT WALLS

Jean-François LE COZ, Claudio CATALANO and Thierry BARITAUD

Institut Français du Pétrole
Rueil-Malmaison, France

ABSTRACT

A non-intrusive method is developed to quantify the thickness of liquid fuel layers that cover the intake pipe walls in port-injected spark-ignition engines. The technique is based on laser-induced fluorescence, which has been adapted for local measurements through transparent walls.

The fuel studied is a mixture of iso-octane and a fluorescent tracer. The tracer concentration in the liquid film may vary because of different evaporation rates of the two components. The selection of suitable tracers in the ketone family is based on liquid-vapor equilibriums.

The optical set-up uses a single optical fibre for transmission of both laser excitation and fluorescence. The technique is calibrated on a precise liquid wedge. An application is realised on a transparent pipe, with stationary air flow and pulsed low-pressure injection. The technique has proven to be able to show the essential phenomena. The impact of the spray, the deposition of a large quantity of fuel and the displacement of liquid waves are quantified and followed with time.

INTRODUCTION

This work is justified by the need of a characterisation of the injection of gasoline in the intake pipe of a port-injected spark-ignited engine. In port-injected engines, injectors are located very close to the intake valves in order to allow a fast response under transient conditions; the time available to obtain an homogeneous mixture of gasoline with air is extremely short. Once the droplets are generated by the injection, evaporation and convection may not prevent some of the droplets from impacting the wall. The largest droplets have particularly a small drag coefficient compared with their inertia and go directly to the walls. As they transport a large proportion of the injected quantity, a continuous liquid film is formed. The primary atomisation can be practically erased by the film formation which acts as a buffer between the injector and the valve seat. This film flows towards the valve seat, where secondary atomisation occurs [1]. This secondary atomisation is poor, so that probably large liquid drops reach the walls of the combustion chamber [2]. The amount of liquid accumulated on the walls finally influences the mixture preparation inside the combustion chamber. The subsequent mixture quality determines the unburned hydrocarbons emissions (from liquid fuel stocked in piston crevices), especially under cold conditions, and also the combustion stability through the fuel distribution in the combustion chamber. In conclusion, there is a need for a better understanding of the processes going on inside the intake manifold of port-injected engines. In particular, the development of the liquid film and its evolution towards the intake valve is an important matter.

We will examine the different methods used for measuring the thickness of liquid films. Then the technique based on laser-induced fluorescence will be described. The choice of the fluorescent tracer will be explained in detail. The calibration is realised on a liquid wedge, and an application on a transparent tube with pulsed injection will demonstrate the efficiency of the technique.

LIQUID FILM DIAGNOSTIC DEVELOPMENT

Choice of measuring technique

A rather common method employed for two-phase flows uses the difference in conductivity between the liquid and the gaseous phase. Conductivity probes mounted in a wall sense the resistance of the fluid and, hence, the thickness. This method is not suited for liquids with weak conductivity, as hydrocarbons [3]. In the case of pure water, which has also a weak conductivity, a capacitance method is applicable [4]. Unfortunately, the dielectric constant of an hydrocarbon is much lower than that of water : 1.94 for iso-octane, 78.54 for water. Therefore, the capacitance method would be more difficult to apply to gasoline films.

Optical methods look more adapted to the measurement of liquid films. Absorption through the film have already been used to determine the thickness of methanol films [5]. This solution needs optical access on both sides of the film. Fluorescence has been used essentially for measuring the thickness of oil films [6, 7, 8, 9, 10, 11] or the concentration of chemical solutions (e.g. [12]). With the use of laser sources and optical fibres flush mounted in opaque walls, the probe is practically non-intrusive. For transparent walls, the optical system can be very simple and easily movable for scanning large zones. Only one optical access is needed. This is the reason why we decided to build such a system.

Theory of fluorescence

A volume of matter illuminated can absorb a part of the incident light. The molecules from this matter are brought to an excited level. When they return to their original energy level, they can emit light with the same wavelength, that is elastic diffusion, or with a different wavelength, almost always longer, that is inelastic diffusion. Among inelastic diffusions, we find fluorescence, in which there is a passage through an intermediate energy level. The properties of the fluorescent light are : omnidirectional, incoherent, and very often broad band emission. The release process leading to fluorescence requires a time of the order of 10^{-8} seconds. The intensity of fluorescence is described by the equation : $F = \Phi I_0(1-e^{-\varepsilon bc})$ where Φ is the quantum efficiency, I_0 the intensity of the incident radiation, ε the molar absorptivity, b the path length in the liquid film and c the molar

concentration. For small thicknesses, absorption is not very intense and the equation can be fitted by a linear function : $F = \Phi I_0 \varepsilon b c$ For these conditions, the fluorescent intensity is simply proportional to the thickness of the measured volume, to the concentration of the fluorescent compound, and to the excitation intensity.

Optical configuration

A fibre optic laser induced fluorescence technique is developed, similar to a previous one used at I.F.P. to determine the thickness of oil films [13]. In theory, the fluid can be fluorescent itself, or a fluorescent tracer can be added to provide a controlled fluorescence. The optical arrangement is suited for transparent walls (see Figure 1).

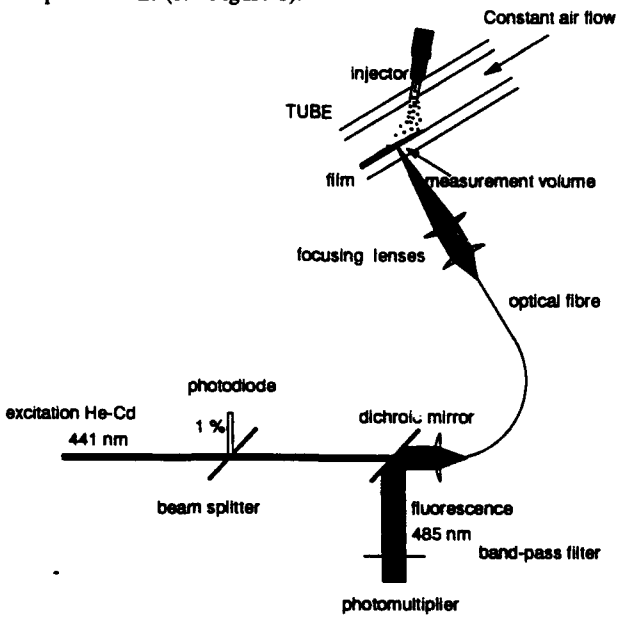

Figure 1 : Optical set-up for laser-induced fluorescence using optical fibres

Excitation is done by a continuous laser He-Cd whose wavelength (441 nm) is suited for the fluorescent tracer that will be selected. The laser light is carried by an optical fibre and focussed on the inner surface of a transparent wall. The reception of the fluorescence light -located around 485 nm- is performed in the reverse optical path. A dichroic mirror separates the fluorescence from the excitation and directs it towards selective optical filters and a photomultiplier. The excitation intensity is monitored by a photodiode that receives about 1% of the incident light reflected by a beamsplitter.

Several filters are used for extracting the useful fluorescence : first a band-pass filter (λ=485 nm, $\Delta\lambda$=20 nm) centred about the maximum in the fluorescence spectrum of the selected tracer; second a long-pass filter (λ>455 nm) for attenuating the light at the excitation wavelength, coming from reflections in the interfaces : beam splitter, transparent wall; third, a short-pass filter (λ<500 nm) for excluding phosphorescence from the tracer and possible fluorescence from optical components and the material of the wall.

Signal Processing

The film thickness can be calculated from the fluorescence and the excitation intensity. The following equation is used if absorption is not strong :

$$b = \frac{F}{I_0(\varepsilon\Phi)c}$$

The requirements are the following. The background light which is different from controlled fluorescence by the tracer needs to be subtracted precisely. A precise calibration is needed, in order to determine the correspondence between the thickness and the fluorescence efficiency for a given tracer concentration : $(\varepsilon\Phi)c$. It must be verified that absorption of the excitation light across the film does not introduce a non-linear behaviour. Finally, the tracer concentration must be constant in the liquid film.

CHOICE OF A FLUORESCENT TRACER

Requirements

The evaporation process gives a very restricting condition for our application : the compounds responsible for fluorescence need to have a constant concentration in the film under evaporation. This is equivalent to say that their concentrations are the same in the liquid phase and in the vapour phase with respect to the total concentration of fuel; in other words, that they follow correctly the evaporation of fuel.

Gasoline does exhibit fluorescence when exposed to blue light. But very different "efficiencies" are found between all the components. Factors of the order of one thousand or greater can be easily found between the main components : paraffins, olefins and aromatics. The latter are the most fluorescent. Moreover, according to an analysis performed at I.F.P., fluorescence is generated mostly by one molecule, naphthalene, which is not representative of the mean feature of gasoline, because its boiling point is located at 217 °C,. This temperature is quite higher than the 50% evaporated point of ordinary 95 octane number gasoline, which is close to 109°C. A chemical analysis of gasoline has shown a molar concentration of 0.3% of naphthalene [4]. Furthermore, the composition of gasoline is not certified. In conclusion, only traces (of the order of 0.1%) can provide the largest contribution to the overall fluorescence.

For these reasons, we preferred to use a well-defined component that is not fluorescent at all, and to add a fluorescent tracer. This way we can at least quantify our accuracy : the equilibrium between the film and the vapour phase could theoretically be determined exactly. We chose iso-octane as fuel, because it is a common reference fuel with high purity and easy supply. This fuel is fluorescence free.

Ketones are widely used in studies observing mixing processes in gaseous turbulent jets [15] or fuel distribution inside the cylinder of spark-ignition engines [16, 17, 18]. Their use in engine studies is justified by a boiling point which is relatively close to that of iso-octane [19], or close to the 50% point of the distillation curve of normal gasoline. In all these applications they are used in the vapour phase. The use of aromatics compounds, as laser dyes, used in oil films or in diesel sprays is excluded because of their very high boiling points. By comparison, ketones have a fluorescence yield that is approximately 1000 times lower than aromatics compounds.

The fluorescence from ketones comes from their C=O carbonyl bond [20]. Mono-ketones have one isolated carbonyl bond. Their absorption is maximum near 270 nm, and changes slightly with the molecule. The fluorescence spectrum ranges

from 330 nm to 630 nm with a maximum near 430 nm. Tests realised in our laboratory showed a maximum fluorescence of 3-pentanone with an excitation around 300 nm. Fluorescence is divided by 2 with excitation at 275 nm or 330 nm, and divided by 25 with an excitation at 350 nm.

α-Diketones, as biacetyl, are molecules with two neighbouring carbonyl bonds. The conjugaison of the two bonds shifts markedly the absorption band to 440 nm, in the visible range. This allows the use of numerous materials for the walls. For our concern, plexiglas is commonly used in transparent models of pipes or cylinder heads. It does not allow transmission of UV light. This is why α-diketones are interesting. Moreover, continuous lasers near 440 nm are much more affordable than those near 300 nm.

One could classify the ketones by their boiling point and choose that with the boiling point closest to iso-octane. This would simply insure that iso-octane and the ketone have similar pressure vapour curves versus temperature. When mixed however, the two compounds do not behave as if they were separated. Repulsive molecular interactions disturb their respective equilibrium with the vapour phase. The most visible effect is the formation of a lower azeotrope. This phenomenon can be seen as an expulsion of the minority compound from the liquid to the vapour phase by the majority compound. On principle, the tracer concentrations used are low. So, the tracer vapour pressure with a tracer/iso-octane liquid mixture is higher than with the pure liquid tracer. The practical consequence is a higher evaporation rate of the tracer than expected according to its pressure curve. The tracer whose evaporation follows iso-octane needs to have a higher boiling point than iso-octane. This results in a lower vapour pressure and tends to compensate for the repulsive forces exerted by iso-octane. A list of possible tracers is given in Table 1 with their boiling points.

molecule	boiling point (°C)	type
iso-octane	99	alcane
3-pentanone	102	mono-ketone
4-methyl 2-pentanone	117	"
2-hexanone	127	"
2,3 butanedione	88	α-diketone
2,3 pentanedione	108	"
2,3 hexanedione	130	"

Table 1 : List of possible tracers

Liquid vapour equilibriums

The liquid/vapour phase equilibrium was completely calculated for 3-pentanone/iso-octane mixtures. The boiling point of 3-pentanone is 103°C, that of iso-octane 99°C. The following result is obtained : at low concentrations the molar fraction of 3-pentanone in the vapour phase is twice that in the liquid phase (Figure 2). This is observed for concentrations of 3-pentanone lower than 5% and for temperatures between 298K and 375K. Certainly 3-pentanone concentration will rapidly decrease in a liquid film under evaporation.

In the following discussion, we will call discrimination coefficient the ratio between the concentration of ketone in the vapour phase and that in the liquid phase, relatively to the concentrations of iso-octane in each phase. If this coefficient is larger than 1, the tracer concentration decreases in the liquid phase during evaporation. If it is lower than 1, the tracer concentration increases in the liquid phase. Figure 3 illustrates the discriminated evaporation.

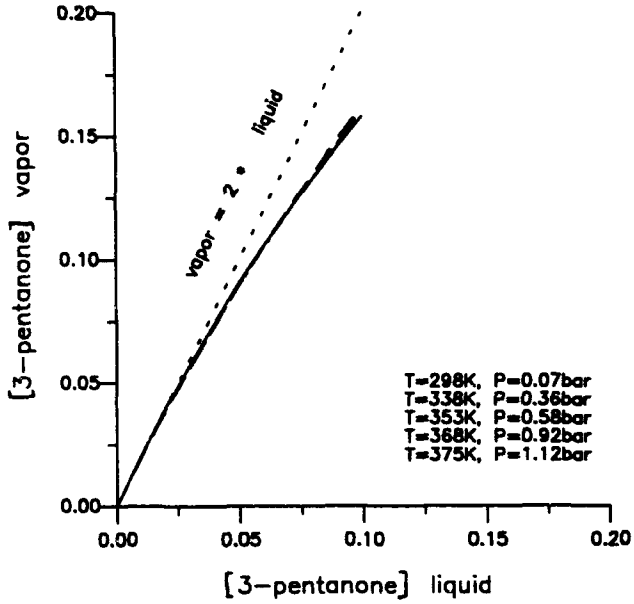

Figure 2 : Liquid/vapour equilibrium iso-octane + 3-pentanone

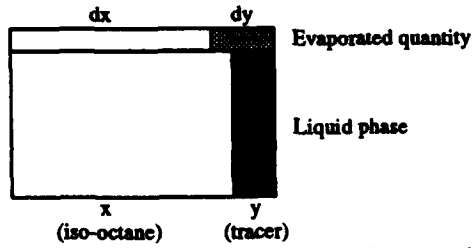

Figure 3 : Definition of discriminated evaporation

$\frac{dy}{dx} = \alpha \frac{y}{x}$, where x stands for iso-octane and y for the tracer.

α is called the discrimination coefficient between the two phases. Assuming that this coefficient is constant, as practically observed with 3-pentanone, one can integrate the equation versus x, the iso-octane quantity, and obtain the evolution of the tracer concentration versus the remaining liquid fraction :

$$\frac{y}{x} = \left[\frac{x}{x_0}\right]^{(\alpha-1)} \left[\frac{y_0}{x_0}\right]$$

We will determine the values of the discrimination coefficient for the most suitable tracers whose coefficients are probably close to unity.

Calculations of the liquid/vapour equilibrium are possible only for mono-ketones. Interaction between the carbonyl bonds in α-diketones cannot be included in the chemical models at this time. We have seen that pentanone is a too light compound for tracing the evaporation of iso-octane. Thus, we made calculations with two hexanones : 2-hexanone and 4-methyl 2-pentanone. Figure 4 shows the equilibriums for iso-octane + 5% ketone mixtures. It is observed that the ideal behaviour is approached by 2-hexanone. One can notice that the concentration in the vapour phase changes rapidly with the boiling point.

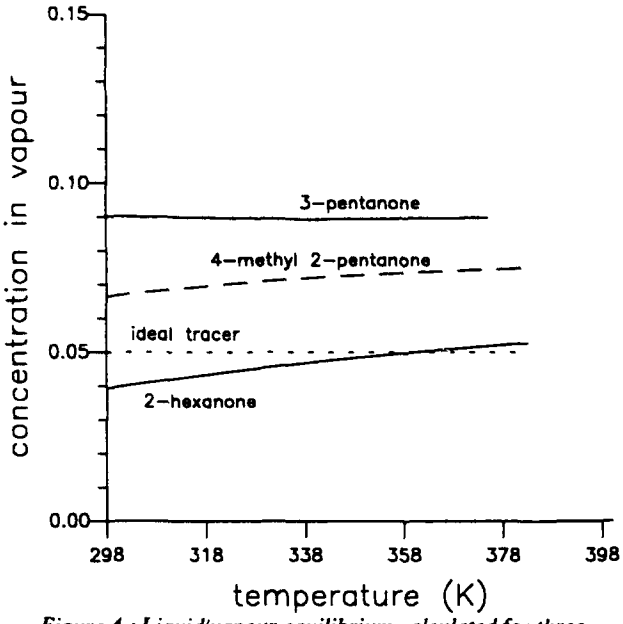

Figure 4 : Liquid/vapour equilibrium calculated for three tracers, mixtures iso-octane + 5% ketone

Experiments have been conducted to validate the calculations with mono-ketones and to provide data with one α-diketone, 2,3 hexanedione, which was guessed to be a satisfactory tracer. A continuous air flow is introduced in a bubbler containing a mixture of iso-octane with 5% ketone. Some samples are taken for analysis as evaporation goes along. Then, from the initial concentration, the remaining quantity and the new concentration, the discrimination coefficient is determined. The final results at 20°C are presented in Table 2.

The accuracy is about 0.05 for both calculated and experimental values. The agreement between calculations and experiments is satisfactory. The difference between hexanone and hexanedione is not important. The best tracer at this moment is 2,3 hexanedione for an application in the visible range with iso-octane. No perfect matching of a tracer can be achieved.

tracer	calculated α	measured α
3-pentanone	1.8	2.19
2-hexanone	0.8	0.8
2,3 hexanedione	not available	0.75

Table 2 : Discrimination coefficients, 20°C, mixtures iso-octane + 5% ketone

Error Analysis

An error analysis is now possible, based on the discrimination coefficients. If the tracer concentration decreases in the evaporating liquid film, the situation worsens as the liquid quantity decreases. Figure 5 shows that the tracer concentration diverges progressively from the original one as evaporation goes along.

Let us consider again the fluorescence technique. If it is assumed that the concentration is constant, an error is introduced in the determination of the liquid amount, or the equivalent film thickness. The absolute error on the liquid amount is :

$$\left\{1-\left[\frac{x}{x_0}\right]^{(\alpha-1)}\right\}\bullet x$$

This error is proportional to the amount of liquid x. If we divide this error by the initial liquid amount, we obtain the following relative error :

$$\left\{1-\left[\frac{x}{x_0}\right]^{(\alpha-1)}\right\}\bullet\frac{x}{x_0}.$$

Figure 6 shows that the relative normalised error passes by a minimum during evaporation. Discrimination coefficients of 0.8 and 1.2 lead to estimated maximum errors about 7 % of the initial liquid amount. A discrimination coefficient of 2. gives a unacceptable error of 25% of the initial liquid amount. From this error analysis we can conclude that 2-hexanone and 2,3 hexanedione follow correctly the evaporation of iso-octane.

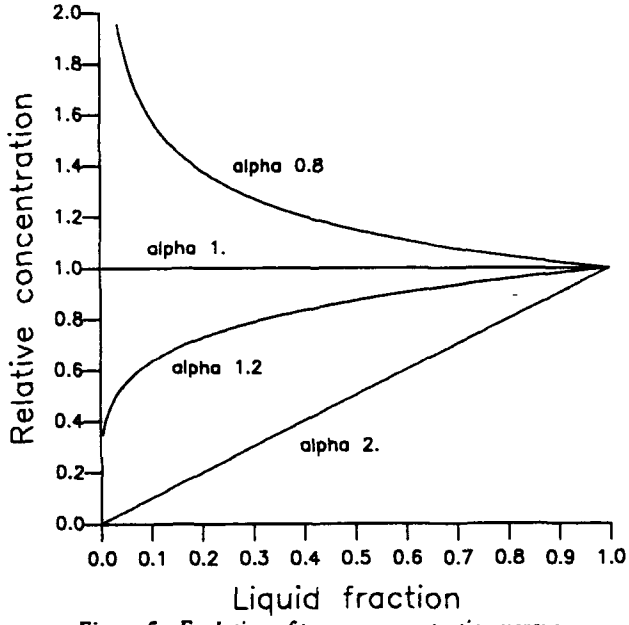

Figure 5 : Evolution of tracer concentration versus discrimination coefficient

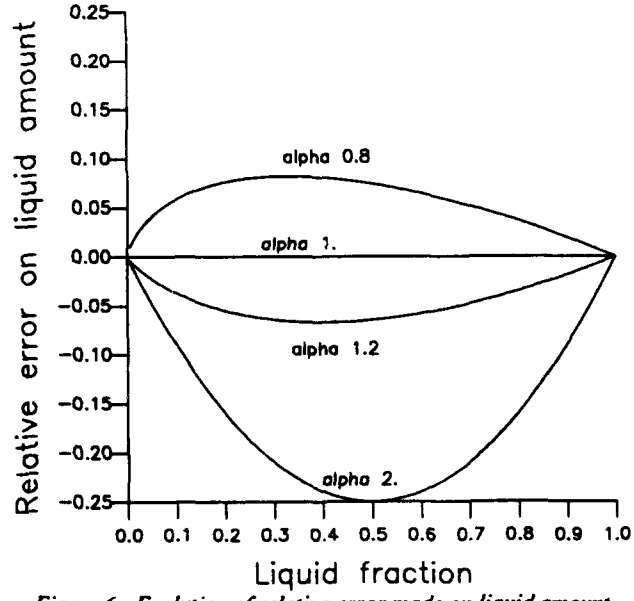

Figure 6 : Evolution of relative error made on liquid amount when assuming constant tracer concentration

CALIBRATION

Calibration set-up

To calibrate the technique, it is important to create very precise thicknesses of the order of those found in common situations. We use a wedge illustrated in Figure 7 that is formed by two superposed flat quartz plates separated by a scheme on one side. The flatness and the roughness of the surfaces are thus controlled. The thickness varies linearly from 0 to 500 microns from one side to the other. The displacement of the measurement volume along the horizontal plane is done by a motion controller unit whose accuracy is about 1 µm.

The influence of temperature on fluorescence was not investigated in this work. It could be introduced as a factor changing the gain of the calibration curve.

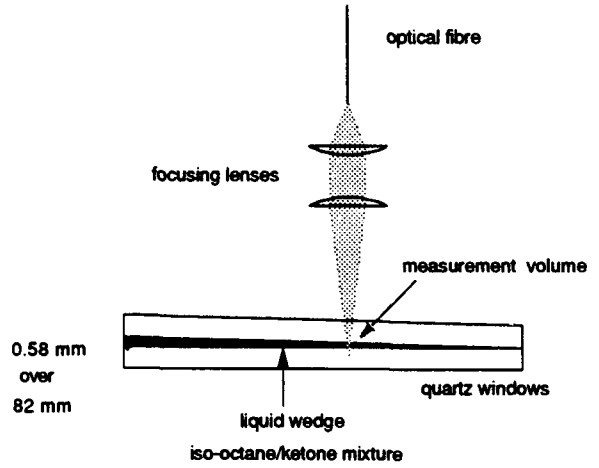

Figure 7 : Calibration wedge

Calibration procedure

Measurements are done at locations corresponding to increasing thicknesses with a step of 20 microns, from 20 to 540 microns. The acquisition lasts for 1 second without excitation and 1 second with excitation. The mean level before excitation is an offset reference for the two signals. Then, the maximum in the photomultiplier signal is only kept, and divided by the excitation intensity. The following expression summarises the data processing :

$$s_{signal} = \frac{\max(signal_2) - \overline{signal_1}}{\overline{laser_2} - \overline{laser_1}}$$

'signal' represents the P.M. signal, 'laser' the laser intensity signal. Index 1 indicates the first part of the record, without excitation, that is the offset. Index 2 indicates the second part with excitation. Despite the filters, background light is always present, probably additional fluorescence from optical components made of glass, and excitation light reflected on the optical interfaces. A test is done with pure iso-octane, which allows quantification of the background solely.

$$s_{background} = \frac{background_2 - \overline{background_1}}{\overline{laser_2} - \overline{laser_1}}$$

The final normalised useful fluorescence is the normalised fluorescence signal corrected by the normalised background :

$$s_{fluorescence} = s_{signal} - s_{background}$$

After a complete path on the quartz window and after processing, the data are plotted in a graph versus film thickness.

Calibration results

Three tracers were tested : 2,3 butanedione (also called biacetyl), 2,3 pentanedione, and 2,3 hexanedione. Calibrations with 1%, 2% and 4% butanedione are shown in Figure 8. The graph shows a good linearity of the fluorescence intensity with respect to the film thickness. The fluorescence increases with the tracer concentration, as expected, but with 4% butanedione, a stronger absorption of the laser light does not allow to use a linear curve fitting. A second order fit is more accurate in this case. Such a fit could also be used for increasing the accuracy of thicknesses smaller than 300 microns for every concentration. From this variation of concentration, the correct concentration of butanedione is 2%, for the [0-300 microns] thickness range.

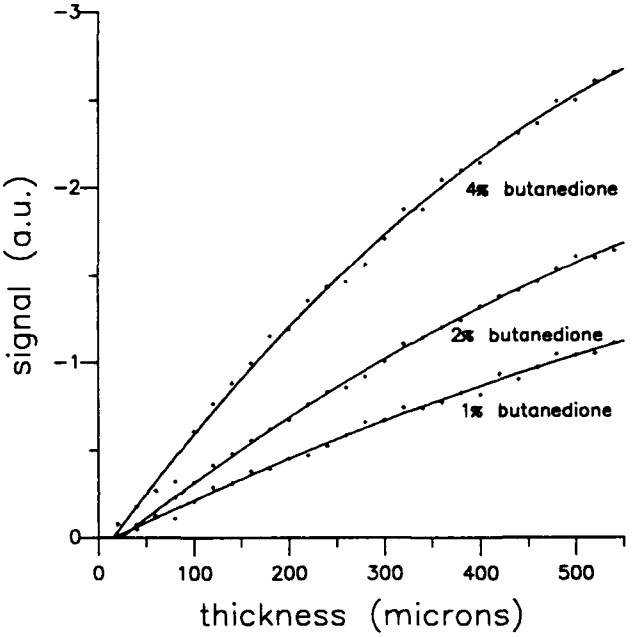

Figure 8 : Calibrations with mixtures isooctane + 1%, 2% and 4% butanedione

The same tests were done with two other tracers : 2,3 pentanedione and 2,3 hexanedione. Figure 9 shows the calibrations obtained with these tracers, with concentrations of 2% and 4%. With both tracers, a concentration of 2% gives a lower fluorescence intensity than with butanedione. A concentration of 4% is required in order to get sufficient intensities. A lower absorption is obtained, thus the correct operating concentration of pentanedione and hexanedione is 4%.

We verified that either quartz or plexiglas can be used in a model of intake pipe or cylinder head. Using an upper window made of plexiglas instead of quartz in the calibration wedge does not modify the fluorescence signal significantly. Figure 10 shows calibrations made with the same mixture iso-octane + 4% hexanedione with a quartz and a plexiglas window. No additional background is added by using plexiglas. The results are encouraging and show the possibility of using plexiglas instead of quartz.

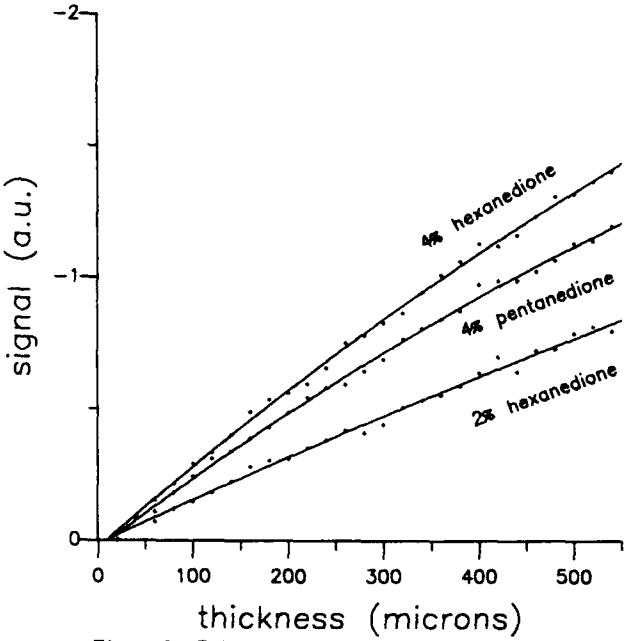

Figure 9 : Calibrations with mixtures isooctane + 4% pentanedione, 2 and 4% hexanedione

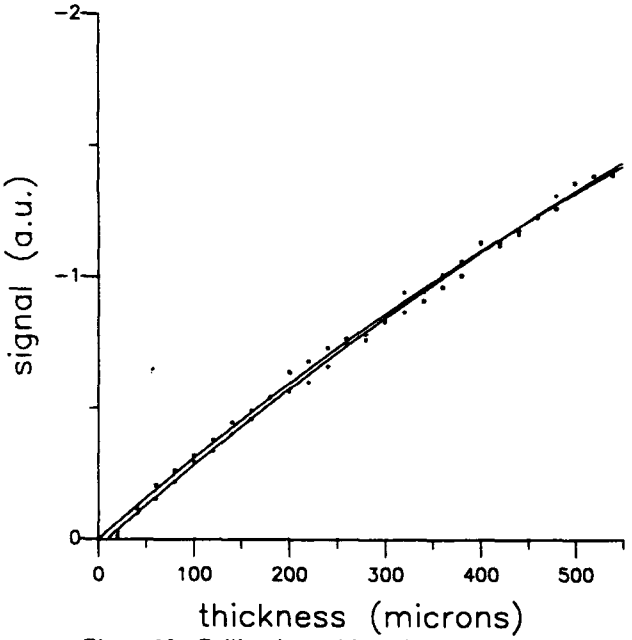

Figure 10 : Calibrations with a mixture isooctane + 4% hexanedione with a plexiglas wall and with a quartz wall

APPLICATION TO A MODEL INTAKE MANIFOLD

Description

The goal is to test the measurement technique in a situation similar to the intake pipe of an engine under cold conditions. The test pipe is cylindrical and made of quartz. Its inner diameter is 36 mm. It is inclined 30 degrees with respect to the horizontal. A constant air flow is introduced in the pipe at atmospheric pressure. A standard injector BOSCH EV 1.3 A is fixed to it, directing the spray with an angle of 45 degrees with respect to the tube axis. Injection is pulsed as in a port-injected engine. The fuel is supplied at 3 bars. The monitoring system controls the injection duration and frequency. A PC synchronisation board generates coding signals and injection control pulses as a shaft encoder would do. This allows to simulate engine conditions.

Operating condition

One condition is tested to assess the performance of the measuring technique. The air flow rate, the injection frequency and the injected quantity are representative of the simulated engine condition reported in Table 3.

displ. volume	441 cm^3
engine speed	1200 rpm = 10 Hz
vol. efficiency	0.8
fuel/air eq. ratio	1
injection duration	94 CAD = 13 ms
injected quantity per shot	43 mm^3
air flow rate (0°C, 10^5 Pa)	0.211 m^3/min

Table 3 : Simulated engine condition

Experimental procedure

The measuring probe attached to the optical fibre is simply moved from the calibration wedge to the pipe. We observed that background light changes with time for these unstationary measurements. Probably feedback occurs between reflections and liquid film because we have an open film. Thus, a correction is necessary for each measurement location versus crank-angle degree (CAD). For this purpose, each test is repeated a second time with pure iso-octane, which allows quantification of the background solely. The acquisition and processing procedures are the same as those used for the calibration except that the signal and the background are functions of CAD. The fluorescence signal is obtained by normalising by the laser power and by subtracting the normalised background. This signal is transformed to a thickness signal by inverting the equation determined by the calibration.

Comparison between three tracers

First, the three tracers were compared at one location, 250 mm downstream from the impact zone of the spray. At this point, the liquid film is almost stabilised; there is a strong liquid stream on the lower side wall of the tube. Before forming this stream, evaporation has certainly affected the liquid film. The ensemble mean film thicknesses are shown in Figure 11. It is clear that 2,3 butanedione gives a wrong information. Its concentration has certainly decreased by more than 30% along the liquid stream. With 2,3 pentanedione, the situation is not yet acceptable. A change of 10% in concentration can be inferred when comparing with 2,3 hexanedione. The latter tracer is supposed to give the most precise estimation of the real film thickness.

Scan of the tube

A mixture iso-octane + 4% hexanedione is used for scanning the tube in the region where the spray impinges the wall. Figure 12 displays the measurement locations; the axial step is 15 mm, the radial step is 10 degrees. A translation and a rotation stages allow displacement of the probe throughout the entire pipe.

Some curves are reported at locations lying on the intersection line between a vertical plane and the bottom of the tube (on the side opposite to the injector). We present ensemble mean cycles calculated over 100 injection cycles in Figure 13. In the upstream region, the impact of the spray is clearly shown. A

delay between the onset of injection and the increase of the film thickness is visible. The injection duration is also detectable in location 3. The film thickness gradually increases downstream. The arrival of the spray on the pipe wall clearly generates a peak which is transformed into a wave in location 6. This wave is moving downstream under the influence of air flow and gravity. The film velocity can be determined from the time delay of the wave peak between two locations. The wave is not yet damped at a distance of 100 mm from the impact zone.

A map of the total mean film thickness is shown in Figure 14. The x-axis is a symmetry line. The film is spread on a large area in the impact zone. This area becomes narrower and the thickness increases when the liquid is flowing down. A strong stream is finally formed in the bottom of the tube, with a thickness of 250 microns.

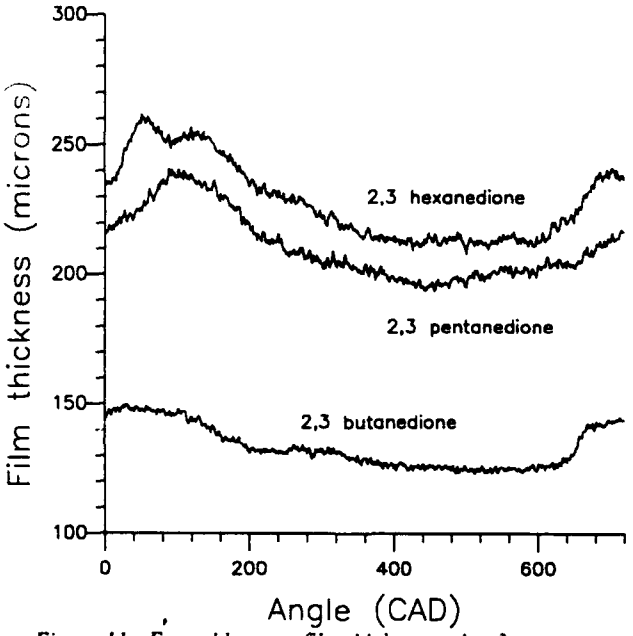

Figure 11 : Ensemble mean film thickness using 3 tracers : butanedione, pentanedione and hexanedione, location 250 mm downstream the injector

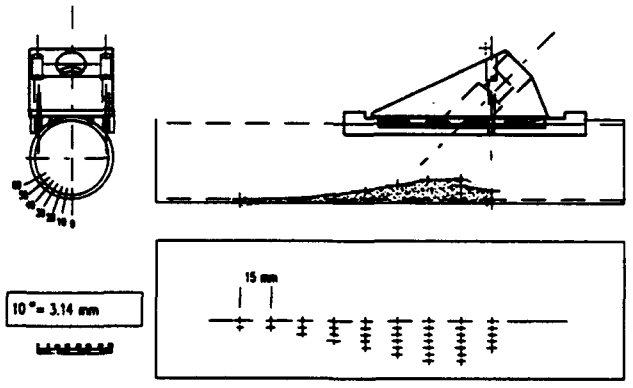

Figure 12: Test pipe with measurement locations

CONCLUSIONS

Evaporation of liquid films inside intake pipes of gasoline engines makes the measurement of their thickness by laser-induced fluorescence difficult. The fluorescent tracer used has to be matched to the fuel studied, here iso-octane, in order that its concentration in the liquid film keeps the most constant possible. The best tracers found in the ketone family are 2-hexanone and 2,3 hexanedione. The latter was selected because it is excitable in the visible range.

Excitation light at 441 nm is carried by an optical fibre and focussed on the inner surface of a transparent wall. Collection of fluorescence light around 485 nm is performed in the reverse optical path. A dichroic mirror separates the fluorescence from the excitation and directs it towards optical filters and a photomultiplier. The excitation intensity is monitored by a photodiode.

The fluorescence is calibrated on a precise liquid wedge which makes the thickness vary from 0 to 500 microns. The working tracer concentration is 4% by mass, which showed sufficient fluorescence yield and weak absorption by the liquid, i.e. linear response with film thickness up to 300 microns.

An application of the technique is realised on a model intake pipe : a stationary air flow inside an inclined straight pipe, and pulsed low-pressure injection. Three tracers with different boiling points are tested. It is confirmed that matching the liquid-vapor equilibrium of the tracer to iso-octane is of great importance, even under cold conditions. The technique has proven to be able to show very interesting phenomena. The impact of the spray, the deposition of a large quantity of fuel and the displacement of liquid waves are typically quantified and followed with time. The technique accommodates to plexiglas models.

ACKNOWLEDGEMENTS

The authors would like to acknowledge the technical support provided by V. Ricordeau and P. Lessart, and the calculations of liquid/vapour thermodynamic equilibriums by J. Vidal. This work was partially supported by the Commission of the European Communities within the frame of the Joule II Programme, Contract JOU2-CT92-0162, by the Swedish National Board for Industrial and Technical Development NUTEK, by the Austrian Government, and by the Joint Research Committee of European automobile manufacturers (Fiat, Peugeot SA, Renault, Rover, Volkswagen and Volvo) within the IDEA EFFECT Programme.

REFERENCES

[1] H.P. Lenz, Mixture Formation in Spark-Ignition Engines, SAE Publications

[2] M.J. Miller, C.J.E. Nightingale, P.A. Williams, "Measurement of Spark-ignition Engine Mixture Preparation and Assessment of its Effects on Engine Performance", IMechE 1991, C433/022

[3] I. Sherrington, E.H. Smith, "Experimental Methods for Measuring the Oil-film Thickness between the Piston-rings and Cylinder-wall of Internal Combustion Engines", Tribology International, Vol. 18, No. 6, Dec. 1985

[4] R.K. Sun, W.F. Kolbe, B. Leskovar and B. Turko, "Measurement of Thickness of Thin Water Film in Two-phase Flow by Capacitance Method", IEEE Transactions on Nuclear Science, Vol. NS-29, No. 1, Feb. 1982

[5] V. H. Muller, H. Bellmann, J. Himmelsbach, A. Elsasser, W. Samenfink, and M. Hallmann, "Gemischaufbereitung und Wandfilmverhalten in Saugrohren von Ottomotoren", MTZ No. 3 and No. 4, March and April 1994

[6] A.E. Smart, R.A.J. Ford, "Measurement of Thin Liquid Films by a Fluorescence Technique", Wear No. 29, pp 41-47, 1974
[7] R.A.J. Ford, C.A. Foord, "Laser-based Fluorescence Technique for Measuring Thin Liquid Films", Wear No. 51n pp 289-297, 1978
[8] L.L. Ting, "Development of a Laser Fluorescence Technique for Measuring Piston Ring Oil Film Thickness", Journal of Lubrication Technology, Vol. 102, pp 165-171, Apr. 1980
[9] D.P. Hoult, J.P. Lux, V.W. Wong, S.A. Billian, "Calibration of Laser Fluorescence Measurements of Lubricant Film Thickness in Engines", SAE 881587
[10] B.T. Shaw II, D.P. Hoult, V.W. Wong, "Development of Engine Lubricant Film Thickness Diagnostics Using Fiber Optics and Laser Fluorescence", SAE 920651
[11] D.E. Richardson, G.L. Borman, "Using Fiber Optics and Laser Fluorescence for Measuring Thin Oil Films with Application to Engines", SAE 912388
[12] D.A. Walker, "A Fluorescence Technique for Measurement of Concentration in Mixing Liquids", J. Phys. E: Sci. Instrum. 20 (1987) pp 217-224
[13] J. Trapy, "Mesure des épaisseurs de films liquides au moyen de la fluorescence induite par laser", I.F.P. report 38687, 1991
[14] E. Robert, personal communication, Institut Français du Pétrole
[15] A. Lozano, B. Yip, R.K. Hanson, "Acetone : a Tracer for Concentration Measurements in Gaseous Flows by Planar Laser-induced Fluorescence", Exp.in Fluids Vol. 13, pp 369-376 , 1992
[16] T.A. Baritaud, T.A. Heinze, "Gasoline Distribution Measurements with PLIF in a S.I. Engine", SAE 922355, 1992
[17] T.A. Heinze, T.A. Baritaud, "Development of Laser Induced Fluorescence Method to Visualise Gas Distribution in a S.I. Engine", 6th International Symposium on Applications of Laser Technology to Fluid Mechanics, Lisbon, July 20-23 1992
[18] W. Lawrenz, J. Kohler, F. Meier, W. Stolz, R. Wirth, W.H. Bloss, R.R. Maly, E. Wagner, M. Zahn, "Quantitative 2D LIF Measurements of Air/fuel Ratios During the Intake Stroke in a Transparent SI Engine", SAE 922320
[19] H. Neij, B. Johannsson, M. Aldén, "Development and Demonstration of 2D-LIF for Studies of Mixture Preparation in SI Engines", 25th Symp. (Int.) on Combustion, Irvine, July 31st-August 5th 1994
[20] C.N.R. Rao, Ultra-Violet and Visible Spectroscopy, Butterworths, London 1967

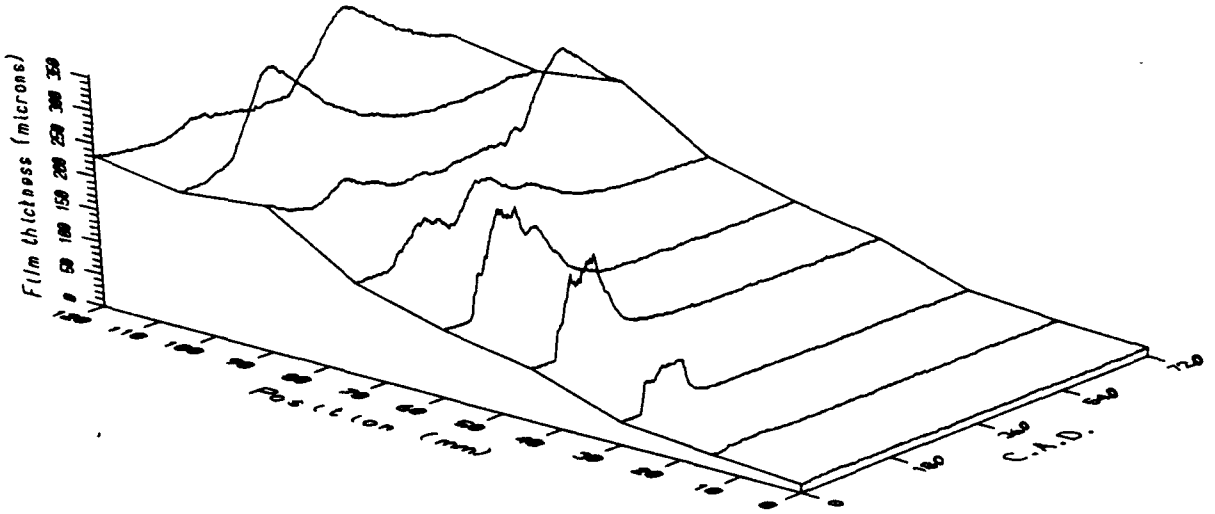

Figure 13 : Evolutions of the ensemble mean film thickness along the bottom of the tube

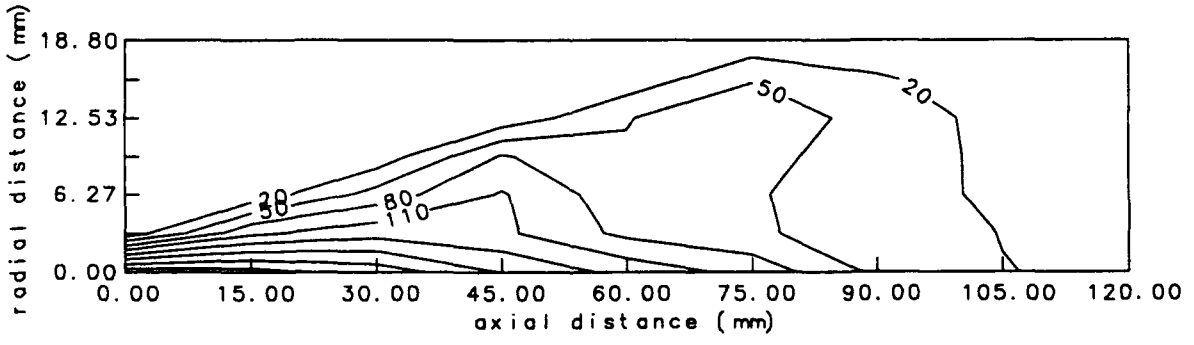

Figure 14 : Map of the total mean film thickness in the investigated area (unit : microns)

A LIF TECHNIQUE FOR THE MEASUREMENT OF CONCENTRATION PROFILES IN THE AQUEOUS MASS BOUNDARY LAYER

Thomas Münsterer

Institute for Environmental Physics, University of Heidelberg
Im Neuenheimer Feld 366, D-69120 Heidelberg, Germany
Phone: (49) 06221-56-3403, email: tmuen@dali.uphys.uni-heidelberg.de

Bernd Jähne

Scripps Institution of Oceanography, PORD
La Jolla, CA 92093-0230, USA
and
Interdisciplinary Center for Scientific Computing
Im Neuenheimer Feld 368, D-69120 Heidelberg, Germany

ABSTRACT

A laser-induced fluorescence (LIF) technique has been developed to measure vertical concentration profiles of dissolved gases in the aqueous mass boundary layer at a wavy interface. An optical wave follower is used to track the surface with a CCD camera.

One dimensional time series of vertical concentration profiles with a temporal and spatial resolution of 2 ms and 30 μm, respectively have been measured at the circular wind/wave facility at the Institute for Environmental Physics, University of Heidelberg at low and medium wind speeds ranging from 2.4 to 4.6 m/s. The boundary layer shows substantial variations in thickness. The time series also reveal large eddies sweeping parts of the boundary layer down into the bulk. From these time series, mean vertical profiles are computed. The mean boundary layer thickness and the transfer velocity are determined.

1 INTRODUCTION

Despite of significant experimental and theoretical efforts the mechanisms controlling the transfer processes across a gas/liquid interface are only superficially understood. It is still state-of-the-art to use various disturbed equilibrium methods to determine mean flux densities across the interface. Unfortunately these techniques cannot give much insight into the mechanisms. For example, Jähne (1989) showed that it is impossible to distinguish large-scale eddy (surface renewal) models from multi-stage eddy diffusivity models with these techniques even if the Schmidt number dependency is measured by multitracer experiments.

This paper describes a laser-induced fluorescence technique which measures vertical concentration profiles within the aqueous mass boundary layer with a very high spatial and temporal resolution. The fundamentals of the technique used here have already been described in earlier papers by Jähne (1991) and Jähne (1993). Here experimental results of the one-dimensional technique are presented.

2 THE AQUEOUS MASS BOUNDARY LAYER

The transfer of moderately soluble and slowly reacting gases is controlled by a thin aqueous mass boundary layer. This layer is in the order of 20 – 200 μm thick, roughly one order of magnitude less than the viscous sublayer. Mass transport through this layer is described as an interplay between molecular and turbulent processes. Boundary layer models usually describe the turbulent transport part either by a turbulent diffusion coefficient (K model) caused by small eddies (Coantic (1986)) or by statistical renewals of the surface layer by large eddies (SR model) (e.g. Münnich and Flothmann (1975)). Without any assumption about the transport mechanism one can define the transfer velocity, k, and the characteristic vertical length scale (*boundary layer thickness*) z_*. The transfer velocity is given as the ratio of the flux density, j, and the concentration difference between the very surface and some suitable reference depth:

$$k = \frac{j}{\Delta C}. \tag{1}$$

The boundary layer thickness z_* is given as the depth at the intersection of the tangent to the concentration profile at the water surface and the reference concentration level. The steepness of this tangent at the water surface can be directly related to the flux density across the water surface. At the very surface the influence of turbulent transport has to vanish. This assumption is independent of any model, especially it is also valid for surface renewal models. This is simply caused by the fact that a diffusive flux scales with the distance squared. For short distances it overcomes the influence of any turbulent transport, and so also of surface renewal when averaged over time (Jähne (1993)). With this property we can apply Fick´s first law for diffusion:

$$z_* = \frac{\Delta C}{\frac{\partial C}{\partial z}|_{z=0}} = \frac{D\Delta C}{j} = \frac{D}{k}. \tag{2}$$

Measurements of the mean concentration profiles within the aqueous mass boundary layer give a direct measurement of the boundary layer thickness and according to eq. 1 the transfer velocity. The relation of boundary layer thicknesses of different tracers measured under the same conditions is since given by Jähne (1985):

$$\frac{z_{*1}}{z_{*2}} = \left(\frac{D_1}{D2}\right)^{1-n}, \tag{3}$$

where the indices 1 and 2 denote the different tracers and n is the relevant Schmidt number exponent. Jähne (1989) showed that in contrast to mass-balance based measurements of the transfer velocity, vertical profile measurements can distinguish different conceptual models, since they result in different concentration profiles (see figure 7). Also statistical fluctuations on short time scales predicted by several models, e.g. by McCready *et. al.* (1986), could be detected by investigating time series of measurements within the aqueous mass boundary layer.

3 CONCENTRATION MEASUREMENTS WITHIN THE AQUEOUS MASS BOUNDARY LAYER

High-resolution concentration profile measurements at the water surface require non-contact optical techniques. So far, exclusively laser-induced fluorescence (LIF) techniques have been used. While Wolff *et. al.* (1991) measured oxygen profiles via the quenching of fluorescence by oxygen, the technique used here effectively replaces the flux of the gas across the boundary layer by the flux of a fluorescent pH indicator. This has the advantage of a significantly better signal to noise ratio compared to the oxygen quenching technique.

Using such a system requires that the fluorescent light is directly proportional to the concentration of the tracer transported through the aqueous mass boundary layer. The simplest chemical system that can meet this requirement is a buffer solution containing both forms of a fluorescent pH indicator, denoted here as HR and R^-, in equal concentrations. The following equilibrium holds:

$$\frac{[H^+]\,[R^-]}{[HR]} = K_i, \qquad (4)$$

where K_i is the equilibrium constant of the fluorescent indicator. Therefore equal concentrations of HR and R^- are given for a pH value equal to the pK_i value. The transfer process is initiated by injecting traces of an alkaline or acid gas, e.g. NH_3 or HCl, into the air space of a wind/wave flume. The gas is quickly transported to the air/water interface, where it promptly dissociates. Using data from Yam *et. al.* (1988) calculations show that within the first 0.5 μm 99% of the HCl gas gets dissociated. So at the very water surface the R^- gets instantaneously protonated into HR. This process constitutes a sink for R^- and a source for HR resulting in a concentration difference across the aqueous mass boundary layer (see figure 1). Using eq. 1 the flux densities are therefore given by

$$j_w = k_w\,\Delta[HR] = -k_w\,\Delta[R^-] = j_a = k_a[HCl] \qquad (5)$$

The H^+ concentration adjusts in such a way that the chemical equilibrium is maintained everywhere, but since HR and R^- are much more abounded than H^+ (at least two orders of magnitude) no significant concentration changes in the bulk occur for HR and R^- due to this reaction. The essential fact is that no significant chemical reactions occur while the ions and molecules are transported across the boundary layer. In conclusion, HR and R^- behave in the bulk just like an inert gas tracer except for a different molecular diffusion constant. The R^- concentrations are obtained

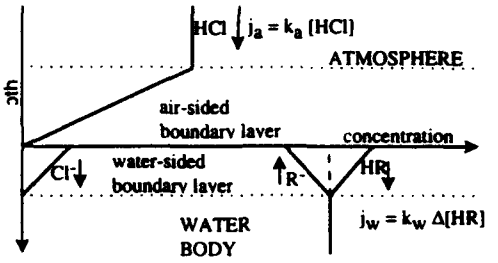

Fig. 1: *Schematic representation of the vertical concentration profiles at the air-water interface, when HCl is absorbed by a buffer solution.*

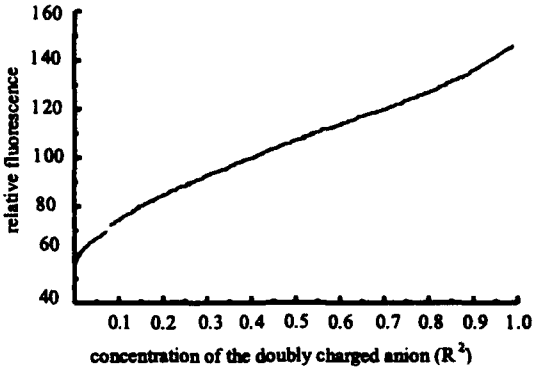

Fig. 2: *Intensity of fluorescent light versus concentration of the doubly charged fluorescein anion.*

by measuring the intensity of the fluorescent light.

For the fluorescent indicator fluorescein used here the intensity of the fluorescent light is proportional to the concentration of the doubly charged anion over a wide range of intensities. Since fluorescein is used at its second pK value all the conclusions made above hold if HR and R^- are replaced by HR^- and R^{2-} respectively. Assuming a 10^{-5} M fluorescein solution, the maximum usable change in concentration of the doubly charged anion would be 3×10^{-6} mol/l to stay within the linear region of 2. This concentration change is brought about by less than 0.2 ppm HCl in the air space.

4 1D-MEASUREMENTS

Measurements were performed in the circular wind/wave facility at Heidelberg University. This facility consists of a 30 cm wide and 70 cm high gas-tight annular channel with an outer diameter of 4 m. Wind was generated by a rotating paddle-ring driven by 24 small DC motors. The channel is filled up to a height of 25 cm; so the water and air volumes are 0.88 and 1.6 m^3, respectively.

fluorescein was added to the deionized water (conductivity $< 1\,\mu$S) to form a 2×10^{-5} M solution which was titrated to its buffer point at pH 7 (equal concentrations of HR and R^-, see eq. 4). At the beginning of each experiment about 2.5 - 3.5 Ncm^3 of HCl were injected into the air space resulting in an initial concentration of about 2 ppm. Fluorescence was excited by a 20 mW argon ion laser at 488 nm focussed on the water surface with a cross section of about

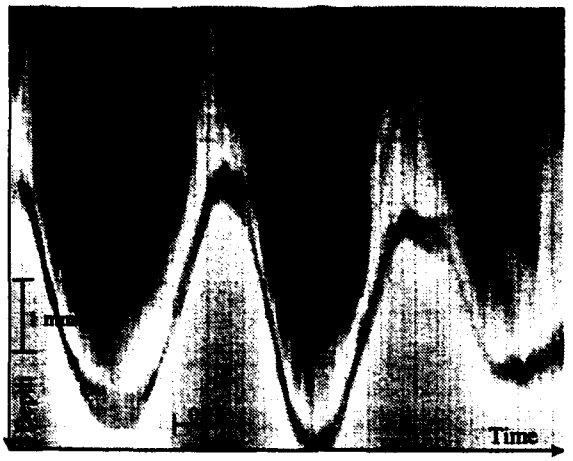

Fig. 3: *Space-time-image at a wind speed of 2.4 m/s. The sequence shown here is about 0.8 s long. The image height is about 6 mm*

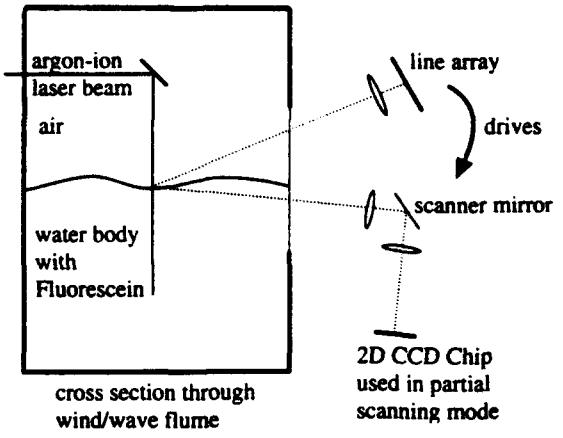

Fig. 4: *Sketch of the one-dimensional experimental setup with optical wave follower and imaging CCD-camera.*

$0.05\,mm^2$.

Figure 5 shows a 0.8 s long part of a space-time-image at 2.4 m/s wind speed. The aqueous mass boundary layer can be seen as a wavy dark line in the image. Above this layer a distorted mirror image at the wavy water surface can be seen. It is obvious that even at low wind speeds the boundary layer tends to be carried out of the field of vision by the waves.

Therefore an optical wave follower was used in the optical path of the CCD-camera (figure 4) to track the water surface with an accuracy better than 1 mm. The use of an optical wave follower is inevitable to keep the moving water surface within the range of vision of the imaging sensor at medium wind speeds. A separate line array camera was used to detect the water surface. The amplitude signal from this camera was processed in real time to drive a scanner mirror in the optical path of the CCD-camera. With this mechanism waves with a peak to peak amplitude up to 3.5 cm could be followed. More details of the experimental setup are described by Münsterer (1993). The CCD-camera (Pulnix TM-640) took images of a 0.3 mm (horizontal) x 6.6 mm (vertical) sector at a rate of 600 frames per second.

These image sectors were averaged over the horizontal width of 0.3 mm in order to integrate the fluorescence intensity over the whole width of the laser beam. The resulting columns were stacked to form so called space-time-images. One of those space-time-images consists of 8000 single concentration measurements performed in 13.3 s.

5 RESULTS AND CONCLUSIONS

Figure 5 shows a 0.8 s long part of a space-time-image at the wind speed of 2.4 m/s as in figure 3. As can be clearly seen the wave follower is capable of keeping the boundary layer well within the field of vision. This was possible up to a wind speed of 4.6 m/s. After this the optical distortions become untolerably large. It should be noted that the position of the boundary layer in the image does not reflect the wave height but rather a function of response time of the wave follower.

Figure 6 shows the same sequence already transferred into a z-coordinate system relative to the mov-

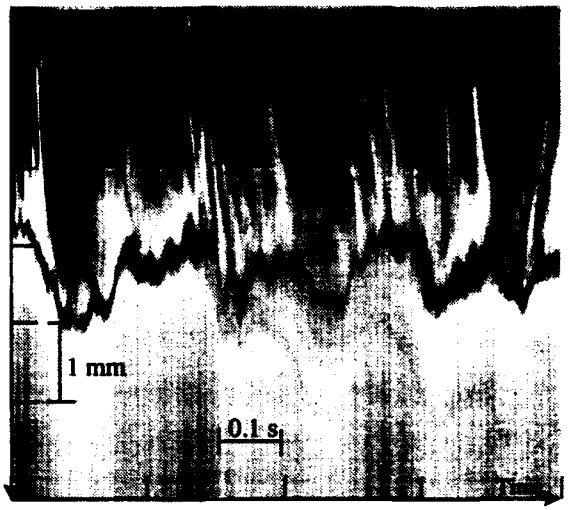

Fig. 5: *Unprocessed space-time-image with the use of an optical wave follower.*

ing water surface using digital image processing techniques. This is necessary for any further processing step. For details of the image processing see Münsterer (1993). The aqueous boundary layer is visible as the thin dark layer at the top of the image. With this technique certain characteristics can be seen more clearly. The boundary layer thickness shows strong fluctuations in time. Variations in thickness at least up to a factor of five can be detected. Such fluctuations were also reported by Wolff (1991) although not as time series with a comparable time resolution. In this sequence at about 0.3 s part of the boundary layer is swept into the bulk. Such an effect was detected in all sequences at all wind speeds ranging from 2.4 to 4.6 m/s. Obviously these effects can only be detected in time series with a high temporal resolution and a good signal to noise ratio.

Averaging over such an image results in a mean boundary layer profile. Figure 7 shows such a profile

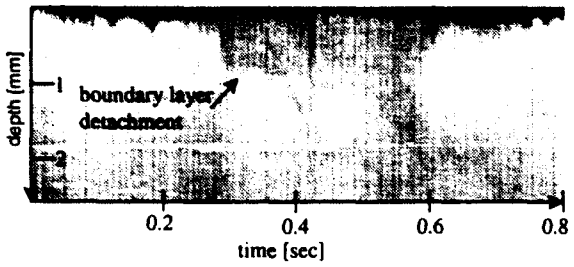

Fig. 6: *Space-time-image in the frame of reference of the moving water surface.*

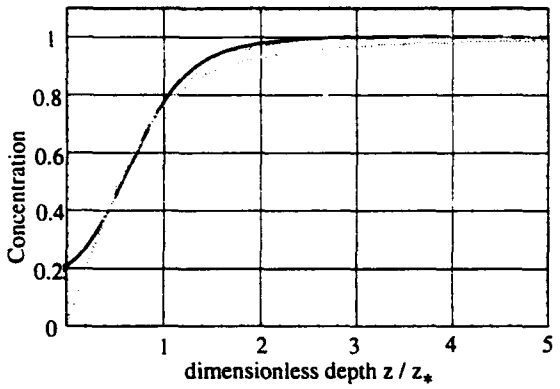

Fig. 7: *Comparison of a measured mean concentration profile (black solid line) at 2.4 m/s with the theoretical predictions of the SR-model (grey dashed line) and the K-model (grey dotted line).*

together with the theoretical profiles for the K and SR-model using a Schmidt number exponent of 2/3. The measured profile seems to agree better with the mean concentration profile predicted by the SR-model. The deviation of the measured profile from the predicted linear profile right at the water surface is caused by the still limited resolution of our optical system of about 30 μm.

The experiments were performed together with classical oxygen mass balance measurements. Figure 8 shows a comparison of the results. The diffusion coefficients in eq. 3 were taken as 2.4×10^{-5} cm^2/s for oxygen (St.-Denis and Fell (1971)) and 3.67×10^{-6} cm^2/s for fluorescein (Hodges and LaMer (1948)). The mean boundary layer thickness is systematically measured too high. This deviation is obviously caused by the limited resolution and/or difficulties in detecting the water surface with image processing techniques. Therefore further improvements in the system's resolution are required.

6 OUTLOOK

Currently experiments using a two dimensional light sheet instead of the focussed laser beam are under way. The 20 mW argon ion laser was replaced by a 1 W laser at the same wavelength. An improved optical system using a digital camera with frame rates of 200 frames per second is used. The optical wave

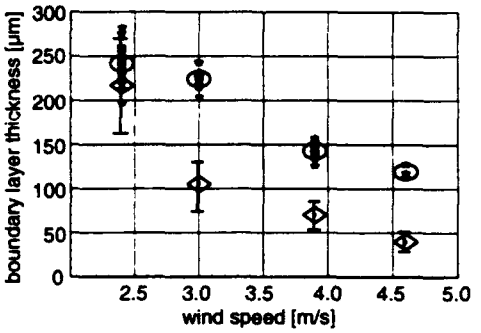

Fig. 8: *Measured boundary layer thicknesses for different wind speeds. Stars denote single measurements averaged over 13.3 s, ovals stand for the average over all these single measurements for one wind speed and diamonds show the result of the parallel oxygen invasion measurements.*

follower was changed from a scanner mirror to mounting the complete optical system to a belt driven linear positioning table.

ACKNOWLEDGEMENTS

Financial support of this research by the National Science Foundation (Grant OCE9217002) is gratefully acknowledged.

REFERENCES

Campbell J.A. and Hanratty T.J. 1983, Mechanism of turbulent mass transfer at a solid boundary, AIChE Journal vol. 29, no. 2, pp. 221-229

Coantic, M. 1986, A model of gas transfer across air-water interfaces with capillary waves, J. Geophys. Res., vol. 91, pp. 3925 - 3943

Hodges, K.C. and LaMer, V.K., 1948, Solvent effects of the Quenching of the fluorescence of Uranin and Aniline, Am. Soc., vol. 70, pp. 724

Jähne, B. 1985, Transfer processes across the free water surface, Habilitationsschrift, Faculty of Physics and Astronomy, University of Heidelberg

Jähne, B., Libner, P., Fischer, R., Billen, T. and Plate, E.J. 1989, Investigating the transfer process across the free aqueous viscous boundary layer by the controlled flux method, Tellus vol. 41B, pp. 177–195

Jähne, B. 1991, From mean fluxes to a detailed experimental investigation of the gas transfer process, Air-Water Transfer, selected papers from the 2nd Int. Symposium on Gas Transfer at Water Surfaces, Minneapolis, Minnesota, September 1990, eds. S.C. Wilhelms and J.S. Gulliver, ASCE, pp. 582–592

Jähne, B. 1993, Imaging of gas transfer across gas/liquid interfaces, Imaging in Transport Processes, eds. S. Sideman and K. Hijikata, Begell House Publishers, New York, pp. 247–256.

McCready, M.J., Vassiliados, E. and Hanratty, T.J. 1986, Computer simulations of turbulent mass transfer

at a mobile interface, AIChE, vol. 32, no. 7, pp. 1108–1115

Münnich K.O. and Flothmann D. 1975, Gas exchange in relation to other air-sea interaction phenomena, SCOR Workshop on 'Air/Sea Interaction Phenomena', Miami, Dec. 8-12

Münsterer, T. 1993, Messung von Konzentrationsprofilen gelöster Gase in der wasserseitigen Grenzschicht, Diploma thesis, Institute for Environmental Physics, University of Heidelberg, Germany

St.-Denis, C.E. and Fell, C.J.D., 1971, Diffusivity of oxygen in water, Can. J. Chem. Eng., vol. 49, pp. 885

Wolff, L.M., Liu Z.-C. and Hanratty T.J. 1991, A fluorescence technique to measure concentration gradients near an interface, Air-Water Transfer, selected papers from the 2nd Int. Symposium on Gas Transfer at Water Surfaces, Minneapolis, Minnesota, September 1990, eds. S.C. Wilhelms and J.S. Gulliver, ASCE, pp. 210–218

Wolff L.M. 1991, The Study of Gas Absorption at a Wavy Air-Water Interface, Ph.D. thesis, University of Illinois at Urbana-Champaign

Yam, R., Nachliel, E. and Gutman, E. 1988, Time resolved proton-protein interaction. Methodology and kinetic analysis, J. Am. Chem. Soc., vol. 110, pp. 2636–2640

Session 30.
Open Forum

OPEN FORUM

The *Open Forum* is aimed to present recent research on laser techniques for flow measurements and results of significance to fluid mechanics. Reference to the theory and practice of laser methods will be made where it facilitates new improved fluid mechanical investigations by laser methods including laser-doppler anemometry, particle sizing and other methods for the measurement of velocity and scalars such as particle image velocimetry and laser induced fluorescence.

All the participants are welcome to submit a contribution for the Open Forum based on work prepared during the last months. **Prof. F. Durst** will coordinate the Forum and should be contacted by those interested in particpating. **The program of the Forum will be announced in the morning of Wednesday, July 13, 1994.**

Session 31.
Two Phase Flow II

BEHAVIOUR OF A FLOW CONTAINING SPRAY PARTICLES IN THE SURROUNDING OF A BLUFF-BODY

Kobe University of Mercantile Marine
Department of Marine Engineering Systems
1-1, 5-Chome Fuke-Minamimachi
Higashinada-ku, Kobe 658, Japan
Osani NISHIDA
Hirotsugu FUJITA
Wataru HARANO

Seika Corporation (K.K.)
20-3, 1-Chome Nishi-Shinjuku
Shinjuku-ku, Tokyo 160, Japan
Katsuhiko FUKUZATO

ABSTRACT

Particle-laden flows are of practical interest due to widespread commercial applications. Industrial and food processors involve handling of solid particles of various sizes and shapes. While solid particle-laden flows are important in environmental and pollution engineering, liquid particle-laden flows are important for combustion engineers. The behaviour of flows containing liquid particles, or droplets, in the surroundings of a bluff-body are of considerable practical interest because the size and velocity of the particles play an important role in relation to the stability and combustion length of turbulent spray flames. In this study, a Phase Doppler Analyzer and Laser Sheet Photography System are applied simultaneously in a complementary fashion to characterize the spray particle flow in the regions surrounding the bluff-body. A cone-shaped bluff-body was placed axially down steam from the spray nozzle, with the "point" of the cone towards the nozzle. The results showed that the mean diameter lied between 4.0 and 50 microns in all locations. The particle size became smaller approaching the sides of the bluff-body as well as in the wake region. Conversely, larger diameters were measures further out from the sides of the bluff-body. Higher number densities were measured in regions of smaller diameters. A recirculation zone, containing negative velocities, was formed in the wake region of the bluff-body. The mechanism of bluff-body spray flame stabilization has been investigated from the various measured results.

1. INTRODUCTION

In industrial nozzles typically used for high-load combustors, the exit velocities are sufficiently high for the flow to be turbulent at the nozzle exit. In a typical case, the fuel exists from an annular nozzle and with a bluff-body placed axially downstream of the nozzle, a region of reverse-flow forms in the wake region of the bluff-body. The reverse-flow is instrumental to flame stabilization.

Considerable understanding of the role of bluff-bodies achieved by measurements of aerodynamic flow patterns (1), (2), (3). However, in order to get a more detailed understanding of the role of bluff-bodies in the combustion of high-sped spray flows, it may be necessary to investigate the distribution of size, number density, and velocity of spray particles in regions surrounding the bluff-body (4), (5), (6).

2. EXPERIMENTAL APPARATUS AND PROCEDURE

In this study, a cone-type of bluff-body is fixed in the jet at 23 mm downstream from the nozzle exit. The experimental fuel is fed through a nozzle of 0.5 mm inner diameter. The nozzle pressure was selected to be either 20 kPa or 50 kPa.

Figure 1 shows a block diagram of the experimental apparatus, which consists of a compressor, experimental fuel (water), air supply system, and the injector nozzle. Figure 2 shows a schematic diagram of the nozzle. The two fluids are fed through the nozzle, as shown in the figure. The flow rates were 2.8 cc/min at 20 kPa nozzle pressure and 4.7 cc/min at 50 kPa. A schematic diagram showing the measuring points (x), the bluff-body outline, along with selected streamlines are all shown in Fig 3. The coordinates L_c and R in the figure represent the axial distance from the nozzle tip and the radial distance from the spray axis, respectively.

In this work, a Phase Doppler Particle Analyzer (PDPA) and Laser Sheet Photography (LSP) systems are used to analyze the spray. Detailed profiles of spray droplets are measured with the PDA together with the overall visualization of the spray flow from the photographs. The physical arrangement of the PDPA is shown schematically in Figs 4 (a) and (b). The PDPA, an Aerometrics model DSA 3000, is set up for 2 axis (L_c and R in the figure) velocity measurements and is equipped with fiber-optic transmitter and collector units. The half-angle of beam intersection, Θ, was set to 1.3177 degrees and the receiver was arranged to collect the scattered light at an angle ϕ = 50.0 degrees from the transmitter axis. The receiver contained three "detector" fibers (DF_1, DF_2, DF_3) for gathering the fringe phase and spacing information. These spacings were set to 10.07 mm for DF_1 to DF_2 and 30.21 mm for DF_1 to DF_3. The probe volume was 2.9×10^{-4} cc.

The Laser Sheet Photography (LSP) system was used to image the light scattered by the spray. A 70 degree scattering angle was chosen and the light was formed into a sheet measuring 50 mm by 0.5 mm. The 488 nm line of a 2 W Argon ion laser was used in this system. The camera shutter speed ranged from 1/15 to 1/500 s. In order to carry ut localized studies near the bluff-body, the injector nozzle and bluff-body were attached to a three-dimensional traverser, while the PDPA and LSP were fixed in the laboratory frame. To improve the accuracy of the experiments, the entire apparatus was enclosed in a darkened "booth" during data acquisition.

3. RESULTS AND DISCUSSION

For brevity the results here will concentrate on the data at 4.7 cc/min, i.e. 50 kPa nozzle pressure. Photographs of scattered light at 1/125 s for a plane perpendicular to the spray axis are shown in Fig 5 (a) with the bluff body and Fig. (b) without the bluff-body. The flow-rate was 4.7 cc/min (50 kPa). As shown in Fig 5 (a) the adverse pressure gradient downstream of the bluff body is strong enough to cause separation of the boundary layer. A recirculating vortex of particles is formed in the wake region of the bluff-body. The size of the recirculation eddy is about 27 mm (axially) x 16 mm (half-base of the cone).

Particle size and velocity histograms at the end of the wake region (L_c = 65 mm, R = 18 nm) are shown in Fig 6. This measurement point is within the boundary layer of the recirculation zone and jet flow stream, and thus we see both positive and negative velocities. The Sauter Mean Diameter, (SMD or D_{32}) at this point was about 13 μm. Summarized in Fig 6 are "Attempts", "Validations", "Corrected Count", and "Run Time". Attempts refer to the total number of Doppler bursts, and hence, potential velocity-diameter data points, "seen" by the detectors. Validations refer to the number of valid velocity-diameter data points actually accepted by the PDPA software. Data are rejected for various reasons, including out-of-range values, non-spherical droplets, conflicting phase data, etc. Although the actual probe volume is fixed, the effective probe volume depends on the size of the particle passing through it. Since larger particles scatter from a larger region in space than smaller ones and the instrument can only accept single particles in the probe volume at any one time, the data must be corrected for this bias, particularly for the smaller diameter particles (7). Hence, a corrected count is obtained. The run time refers to the time interval during which the data was obtained.

Spatial distribution (maps) plots for the regions surrounding the bluff-body are shown in Figs 7 to 12. These plots show the following data: the Sauter Mean Diameter D_{32}, Arithmetic Mean Diameter D_A (both in μm), Number Density (Particles cc/s cm^2), Mean Velocity (U, in m/s), and RMS or "fluctuating" velocity (U', in m/s).

Several trends can be observed from Figs 7 to 10. The SMD lies within the limits of 8 to 49 μm, while the arithmetic mean diameter lies between 4 and 41μm. The particle sizes become significantly smaller nearer the side surface regions and near the rearward parts of the bluff-body, but significantly larger further out from the sides of the bluff-body. The number density lies within the range 10^2 to 10^5 particles/cc, and is higher in regions of smaller diameters but only slightly lower further out from the sides of the bluff-body. The volume flux, which refers only to the volume of particles, varied from 10^{-5} to 10^{-2} cc/s cm^2. Larger values were found at the upper of the bluff-body where the sizes were not large, but the number densities were large.

Looking at Figures 11 and 12 the following observations can be made. The mean velocity U ranged from - 0.7 m/s to about 16 m/s and was negative for all the measuring points in the wake region. The RMS velocity was from 2 to 7 m/s in the upstream of the bluff-body, but only 0.3 to 0.5 m/s in the wake region.

Correlation plots of particle size -vs- velocity at four [R_c, L_c] points [9 mm, 35 mm], [15 mm, 35mm], [15 mm, 55 mm], [15 mm, 60 mm] are shown in Figs 13 to 16. The location of Figs 13 and 14 are typical points for the regions away from influence of the bluff-body. The particle sizes near the bluff-body are comparatively small, but their velocity range is quite wide. For the two locations in the wake region at the rear of the bluff-body, shown in Figs 15 and 16, the diameters are quite similar - ranging from 2 to 20 μm. The velocities at Lc = 55

mm, which is near the bluff-body, are seen to be all negative values, but at Lc = 60 mm both positive and negative velocities appear. The size and strength of the recirculation eddy decays rapidly to free jet proportions near this point.

CONCLUSIONS

Local size and velocity measurements were obtained in regions surrounding a bluff-body to better understand its effect on practical combustion systems. The following conclusions are drawn from this study:

1. The Sauter and arithmetic mean diameters lie within the limits of 8 to 49 μm and 4 to 41 μm, respectively. The particle sizes are smalier nearer to the sides and in the wake of the bluff-body, but the number density is higher in both regions.

2. The volume flux of particles is slightly higher near the side surface regions of the bluff-body, but significantly lower in the wake.

3. The particle velocity is highest upstream of the bluff-body and lower along the sides. A recirculating zone is established in the wake of the bluff-body.

4. The size of the recirculation eddy, estimated from the velocity profiles of the particles, is equivalent to the longitudinal sectional area of the bluff-body.

ACKNOWLEDGMENTS

The work was supported in part by the Great Budget (1992) of the Japan Ministry of Education, Science and Culture. The authors wish to thank the Research Laboratory for Petroleum Products at the Mitsubishi Oil Company for their support of this study.

REFERENCES

Hosokawa, S., Minato, T., Ikeda, Y., and Nakajima, T., Proc of the 30th Symposium on Combustion, Dec. 1992, pp. 43-45, [in Japan].

Lee, C.E., and Onuma, Y., Transactions of the JSME-B, Vol., 57, No. 544, Dec. 1992, pp. 276-281.

Haniu, H., Sakamoto, H., and Dogan, Y., Transactions of the JSME-B, Vol. 59, No. 567, Nov. 1993, pp. 276-281.

Kurihara, N., Ikeda, Y., Yamamoto, T., and Nakajima, T., Proc. of the 29th Symposium on Combustion, Dec. 1991, pp. 196-198, [in Japan].

Nishida, O., Fujita, H., Harano, W., Okamoto, N., and Harano, N., Journal of the JSME, Vol. 28, No. 7, July 1993, pp. 443-452.

Nishida, O., Fujita, H., Harano, W., Hatano, N., and Okawa, H.,Proc. of the JSME, Vol. 52, Oct. 1993, pp. 71-74.

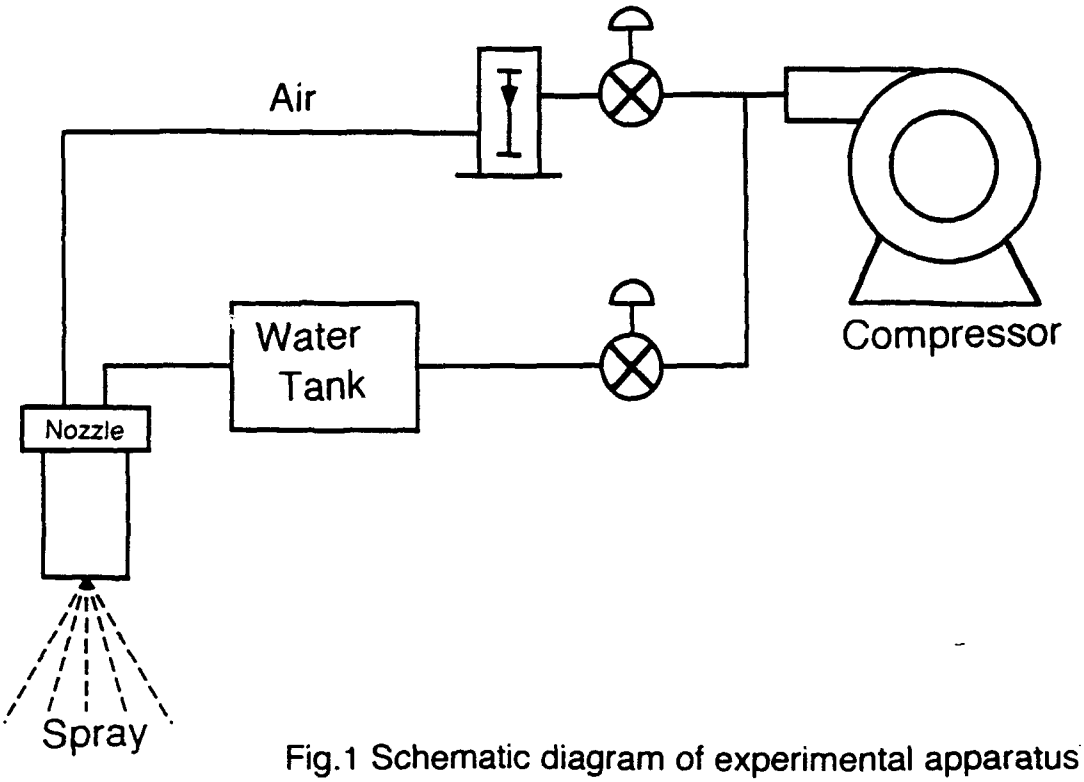

Fig.1 Schematic diagram of experimental apparatus

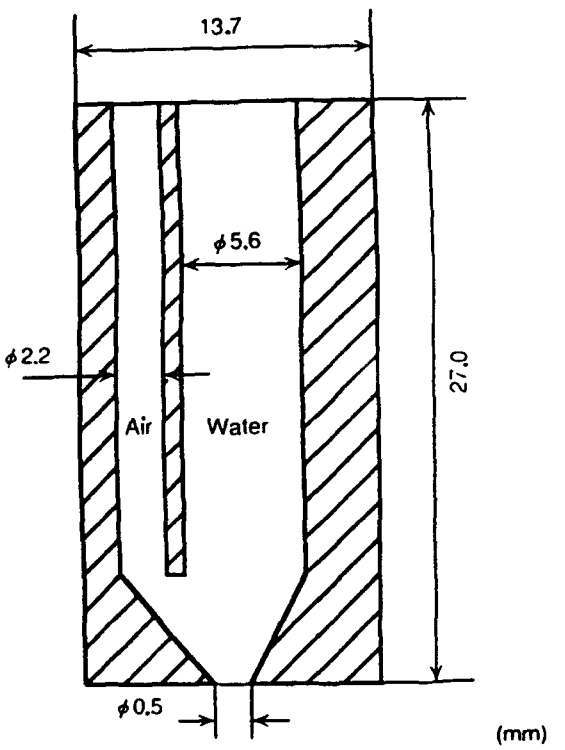

Fig.2 Detailed design of the nozzle (non · Pintle type) . Dimensions in millimetres

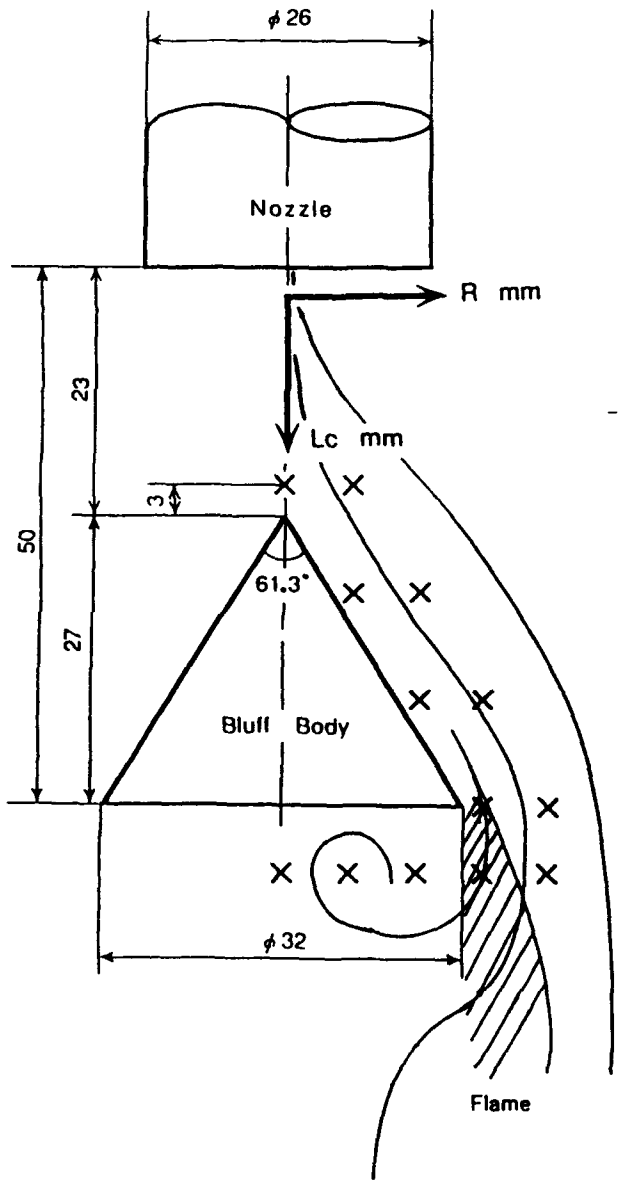

Fig.3 Detailed design of the nozzle and position of the bluff body

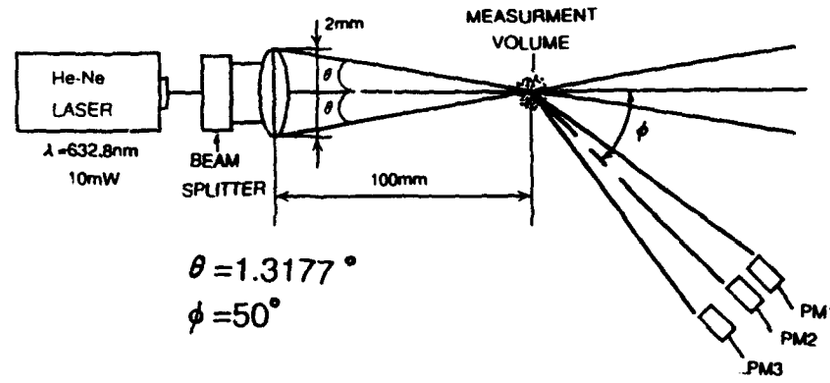

(a)

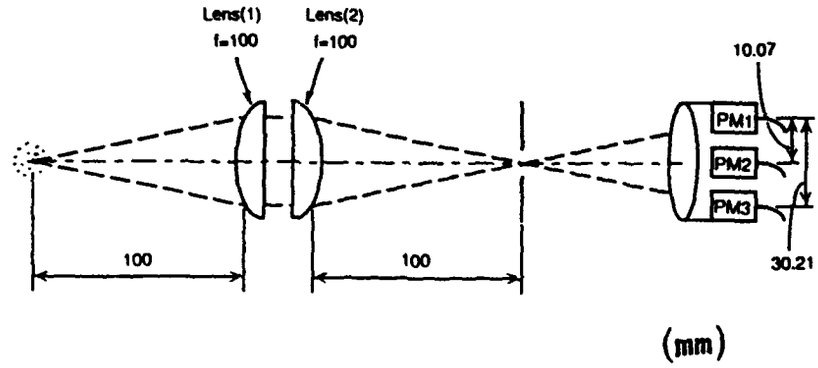

(b)

Fig.4 Schematic of the optical system for LDV and Droplet siger (PDPA)

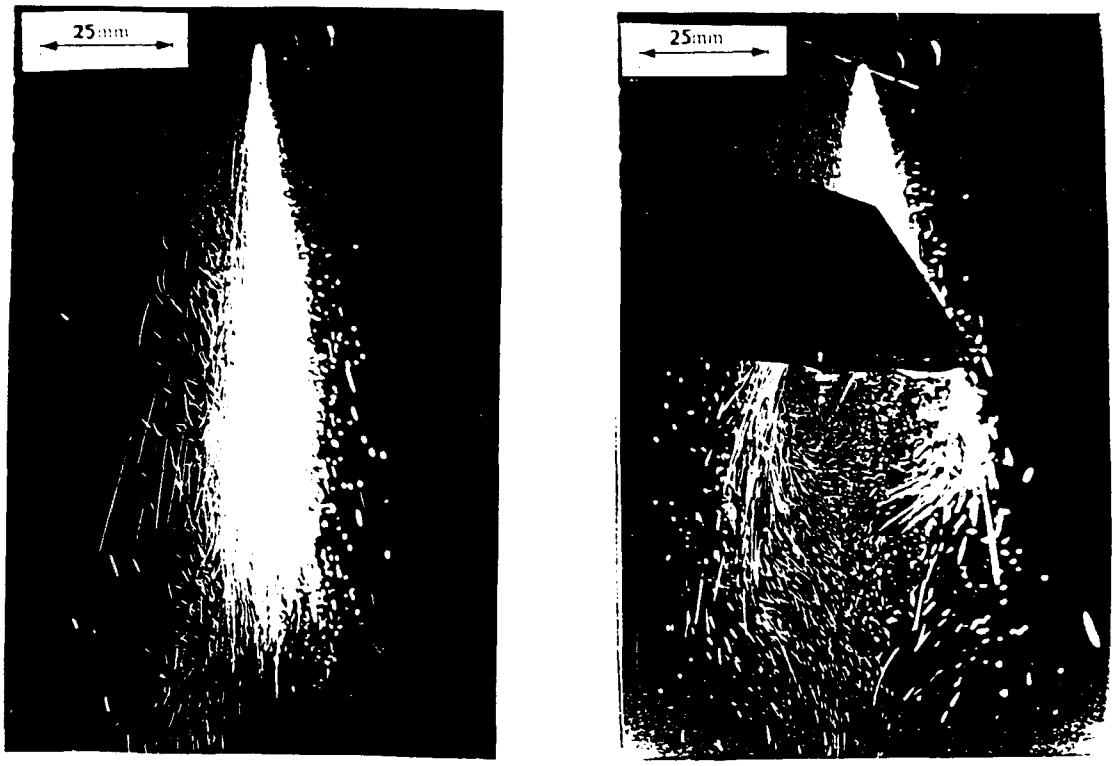

(a) Without bluff-body (b) Withbluff-body

Figs.5 Photographs of spray flow system

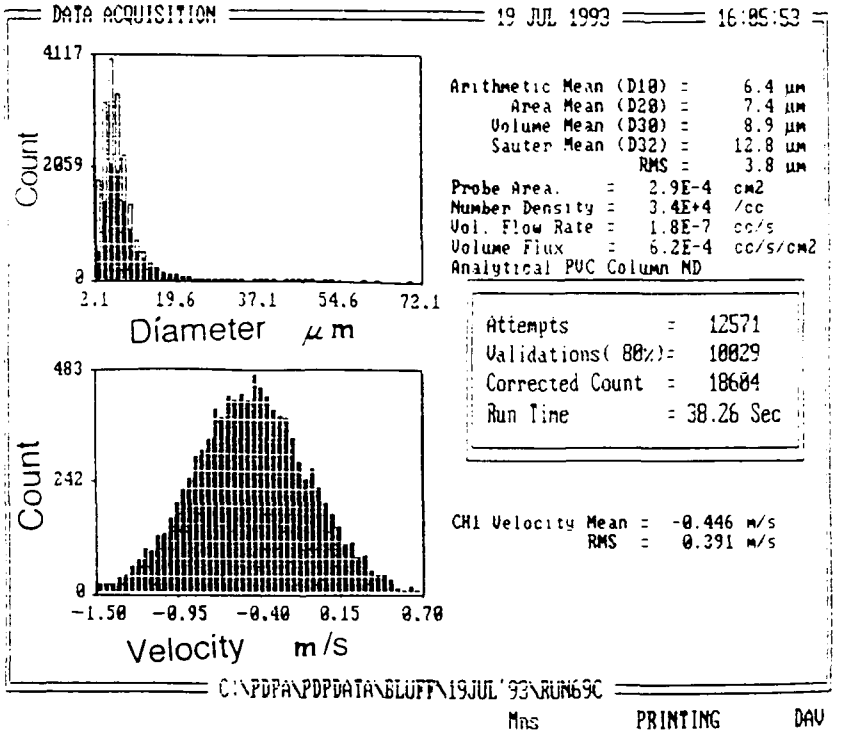

Fig.6 Velocity and size data histogram

(Measurement point: Lc=65mm, R=18mm)

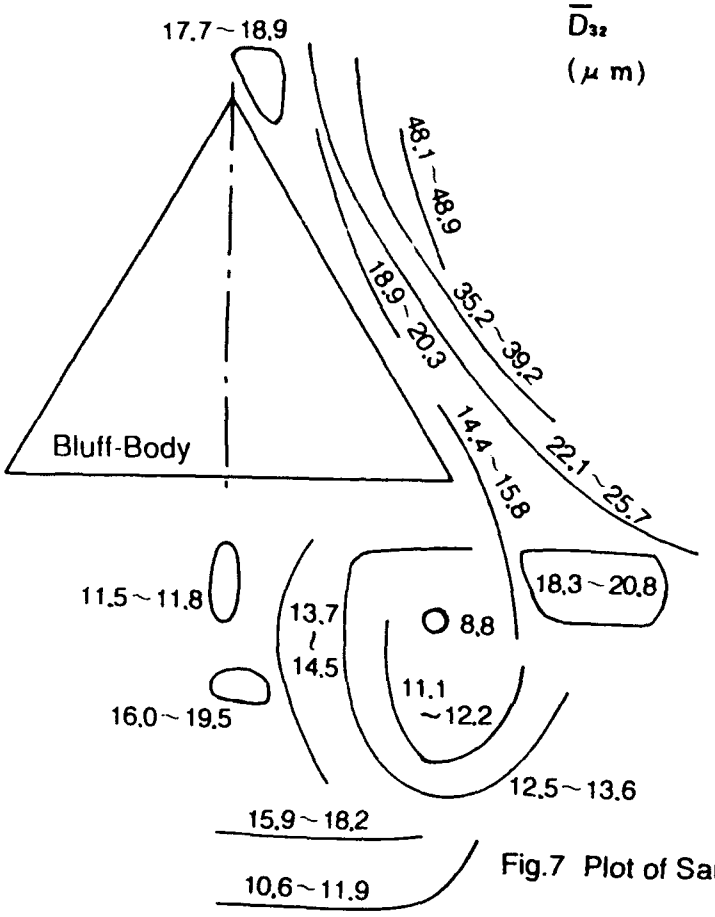

Fig.7 Plot of Sauter mean diameter ($\overline{D}_{32}$)

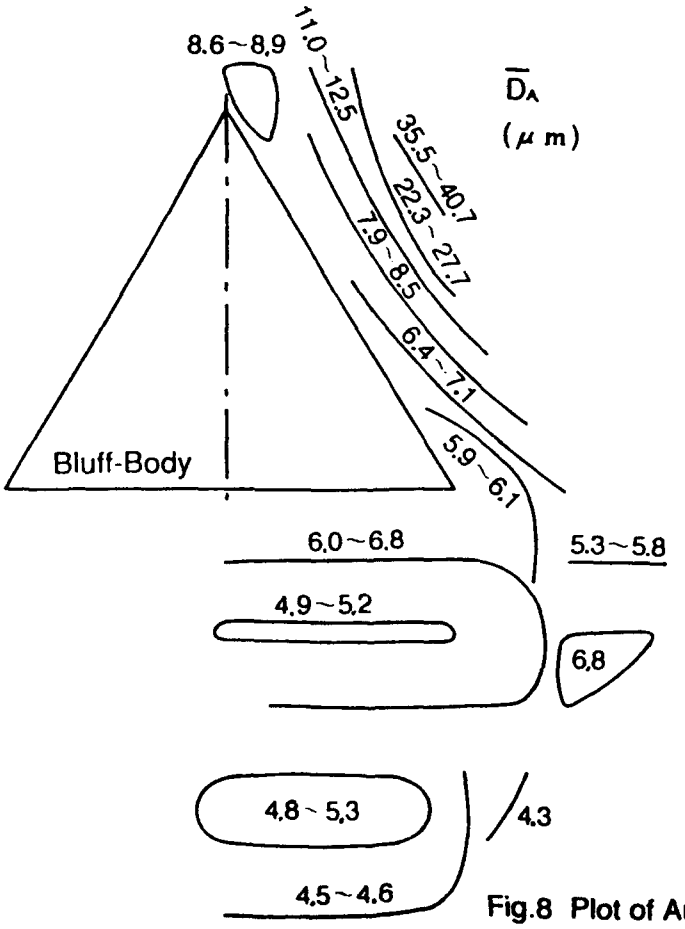

Fig.8 Plot of Arithmetic mean diameter ($\overline{D}_A$)

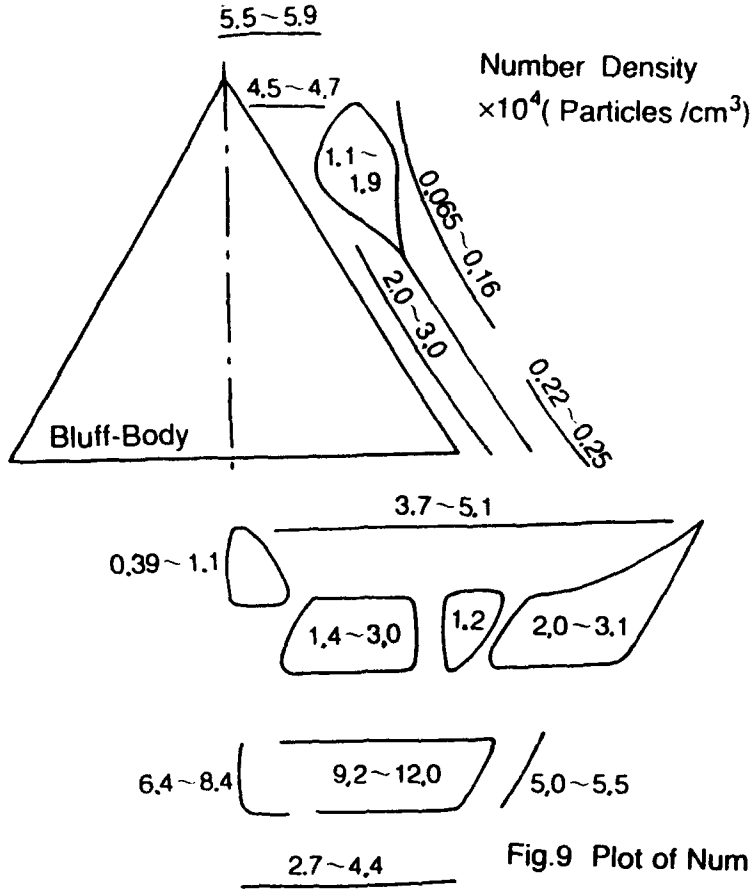

Fig.9 Plot of Number density

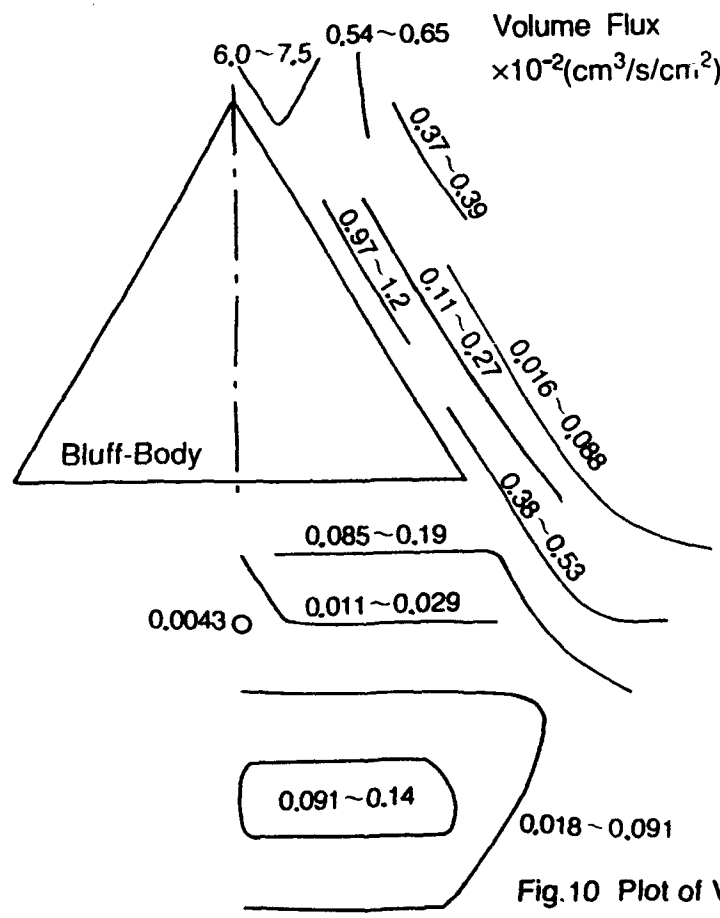

Fig.10 Plot of Volume flux

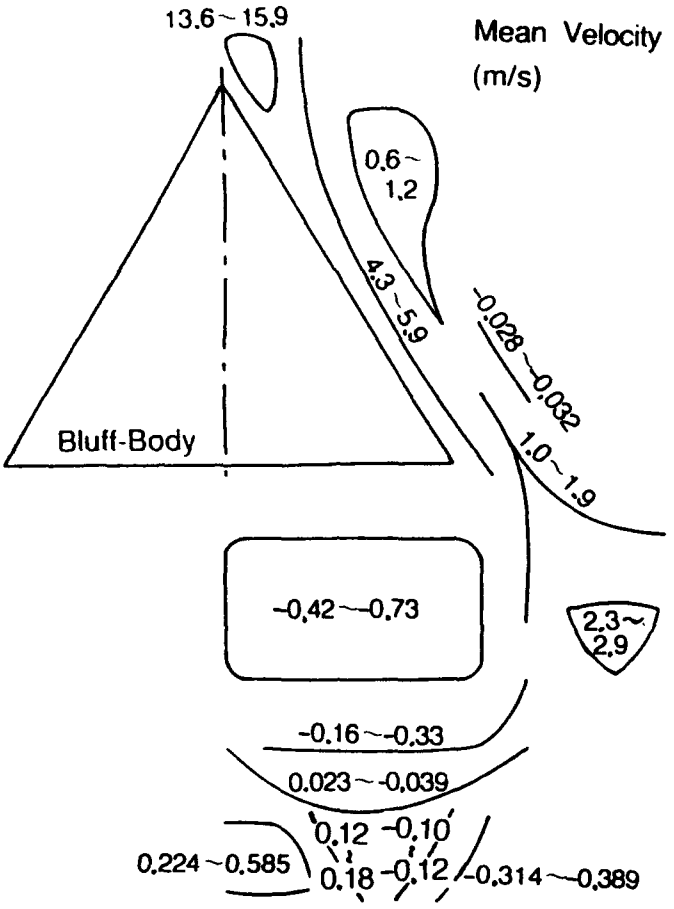

Fig.11 Plot of Mean velocity

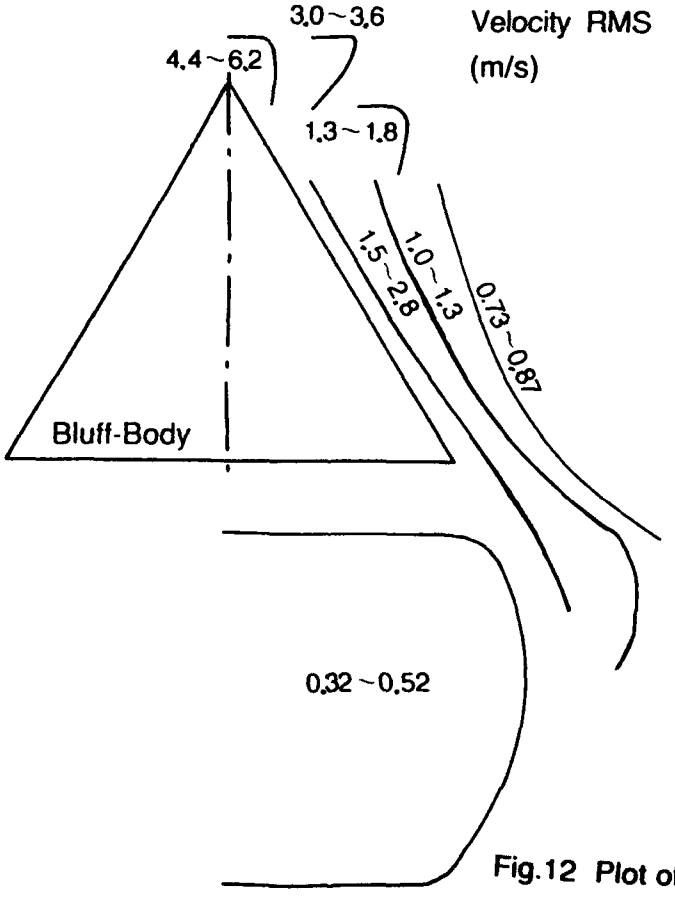

Fig.12 Plot of Fluctuating velocity

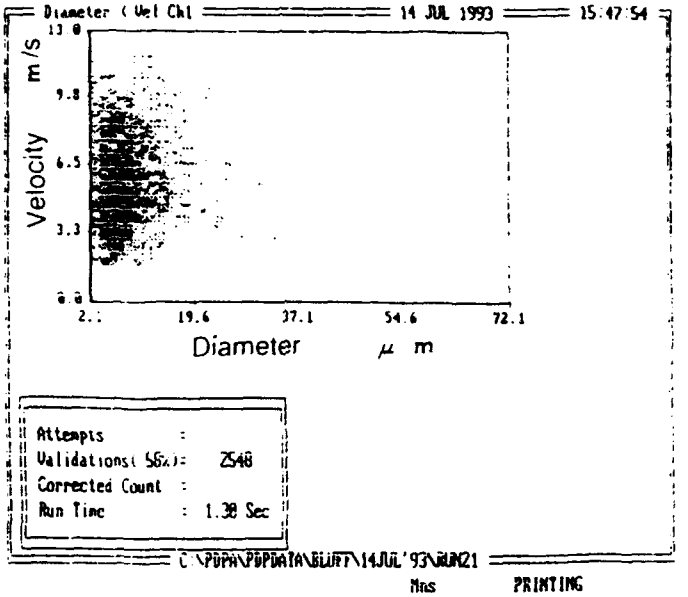

Fig 13 Size-Velocity Correlation
(Measurement point Lc=35mm . R=9mm)

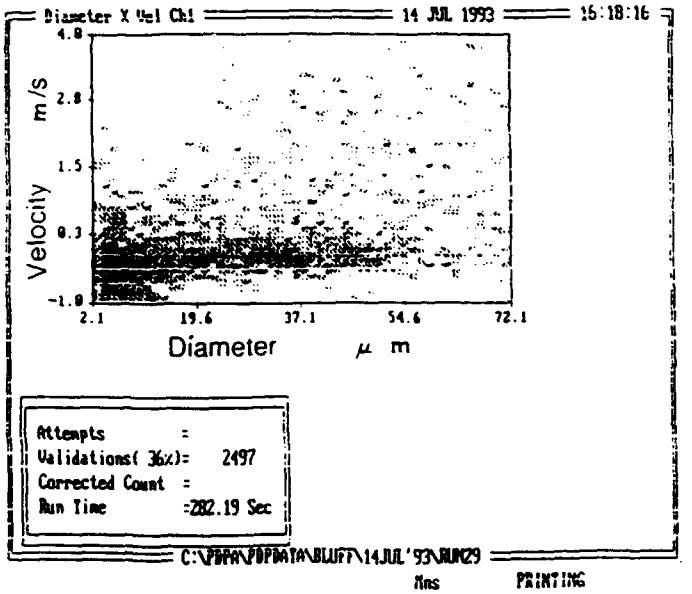

Fig.14 Size-Velocity Correlation
(Measurement point Lc=35mm . R=15mm)

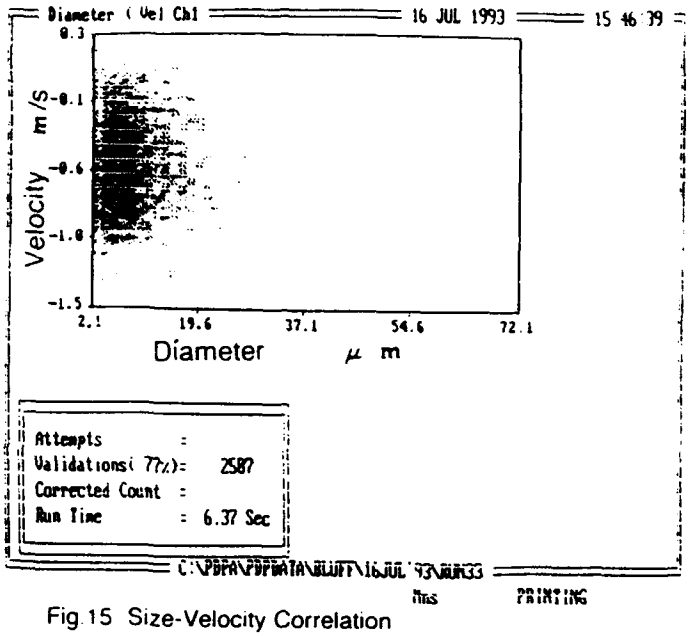

Fig.15 Size-Velocity Correlation
(Measurement point: Lc=55mm , R=15mm)

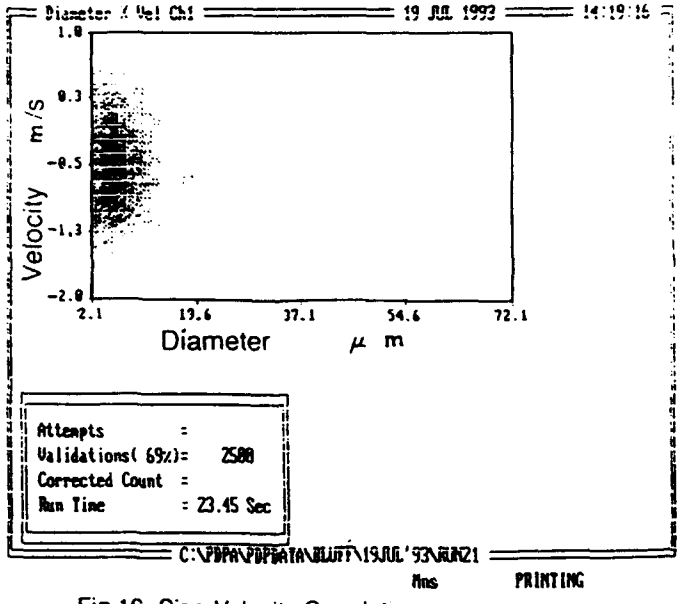

Fig.16 Size-Velocity Correlation
(Measurement point: Lc=60mm , R=15mm)

EXPERIMENTAL STUDY OF MULTIPLE INTERACTING SPRAYS BY PHASE DOPPLER ANEMOMETRY

Masahiro HIGUCHI, Tsuyoshi SHIRAKAWA, Hiroshi MORIKITA, Koichi HISHIDA and Masanobu MAEDA

Department of Mechanical Engineering, Keio University
3-14-1 Hiyoshi Kohoku-ku, Yokohama, 223 JAPAN

ABSTRACT

Measurements of droplet size and velocity in multiple impinging sprays were carried out by phase Doppler anemometer(PDA) in order to achieve a passive control of local size distribution of the droplets. A FFT based signal processor featured by a digital signal processor(DSP) with specific functions of the software triggering was employed in order to achieve improvement the accuracy in droplet mass flux measurement at a lower signal-to-noise ratio(SNR).

The resultant validation rate of acquiring Doppler burst signal was increased up to 31% compared with the fixed trigger..., due to the 'burst center triggering' by software and/or by optical triggering with dual coaxial measuring volumes

Measurements in interaction region of four hollow-cone sprays revealed that the area of uniform droplet size was observed in circle region whose area was 1% of spreading flow area where 20% of the total mass was concentrated. In the uniform size region, the variation of the average diameter through the region did not exceed 9 %, which were normalized by average value in uniform size region respectively.

1. INTRODUCTION

The flow field accomplished with multiple impinging sprays has been expected to shape an uniform spatial droplet size distribution, and to contribute to many industrial processes such as spray cooling, spray painting, spray dryer, etc.

The studies of interaction flow field within dual air jets have been widely conducted by D.R.Miller & E.W.Comings(1960), and E.Tanaka(1970)(1974). Y.F.Liu(1990) and C.S.Wang(1993) reported the existence of the reverse flow in the interaction region, and the self-preservation of mean velocity, velocity fluctuations, and Reynolds shear stress.

Two spray interaction with electrically charged droplets was examined by S.R.Snarski & P.F.Dunn (1991) using PDA. This study attempted not to analyze interaction flow field itself, but to evaluate the effects of charge force and of the distance between two sprays.

In the present study, the signal processor was optimized to enable the signals of smaller particle to extract from total system noises. The employed signal processor working on FFT, developed by author's group (K.Kobashi et al. 1988, 1990, 1992), was consisted of digital signal processor and transient memories. The burst center triggering function realized to increase in validation rate for relatively low SNR Doppler burst signal compared with the fixed triggering. To evaluate the flow of multiple interacting sprays, the function of trigger was investigated. The result indicates that this function enables us to analyze the interaction flow structure.

Estimating mass flux, size distribution in higher accuracy, both the dual coaxial measuring volume and measuring volume with a specific estimating method were employed: the former can eliminate the sizing errors by trajectory ambiguity, the latter was estimated by calibration based upon Gaussian profile of beam intensity. Consequently, the accuracy of mass flux of a single spray examined varying both the measuring distance from spray and provided pressure. Two and four sprays impinging currents were investigated in the present study in order to characterize the flow of the interaction region of multiple sprays,

2. OPTICAL APPARATUS AND SIGNAL PROCESSING

2.1 Optical Arrangement

Figure 1 schematically illustrates the measuring system of the two-components PDA optical system and signal processor. A 2.0W Argon-ion laser with multi-line operation was employed as a light source, and green and blue beams were selected by a beam-splitter. For each color, double Bragg cells were mounted on the system so as to produce differential frequency, and the beams were transmitted through optical fiber probes. The differential frequency was occasionally optimized with the flow condition, and was adjusted from 2 to 10MHz. Optical configuration and constants were set as listed in Table 1

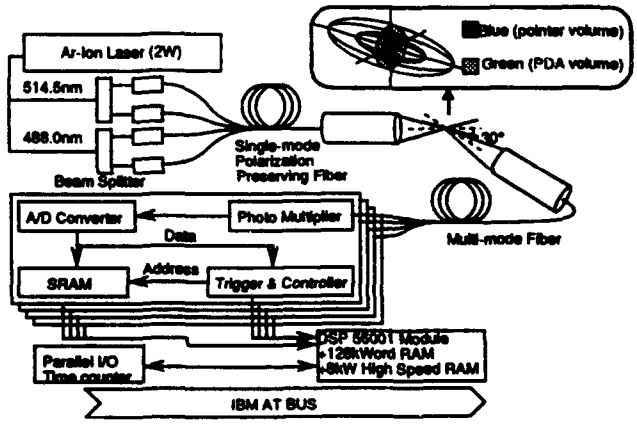

Fig. 1 Schematic of the measuring system

Table 1. Optical parameter set up Table

(a) Transmitting optics

Parameter	Unit
Wave length of laser λ	488.0nm(Blue) 514.5nm(Green)
Power of laser	2.0 W
Beam interaction 2θ	4.96°
Shift frequency	2 MHz(Blue) 5 MHz(Green)
Size of measuring volume	$125\times125\times3000\ \mu m^3$ (Blue) $250\times250\times5800\ \mu m^3$ (Green)
Fringe spacing δ	5.943μm(Blue) 5.766μm(Green)
Focal length	300mm

(b) Receiving optics

Parameter	Unit
Off axis angle	30°
Focal length of collimating lens	300mm
Slit size	200μm
Detector angle	2.076°, 4.753°
Phase factor	1.377 degree/μm 3.152degree/μm
Rectangular aperture	$3\times20\ mm^2$

In order to reduce sizing error due to the trajectory ambiguity, two green and blue beams were aligned into different size coaxial measuring volumes; for elimination of trajectory ambiguity and increasing SNR as described in the next section. The size of measuring volume of green beam, which was used for sizing droplets was set at about 8 times larger than that of blue beam. Measuring volumes were $250\times250\times5800\ \mu m^3$ and $125\times125\times3000\ \mu m^3$ for green and blue beams respectively.

Receiving optics assembled by four channel fibers, that is, three of them for PDA with green measuring volume and one for lateral velocity measurement with blue measuring volume, were set at near forward position with an off axis angle of 30 degree. Displacement of three apertures for PDA are also listed in Table 1. The collected lights were converted to electric signals by photomultipliers (Hamamatsu, R1447) and transferred to a signal processor.

2.2 Signal Processor

LDA signal processing has always encountered the difficulty of discrimination of Doppler burst signal from electronic and optical noises. Various noise sources prevent the signal processor from acquiring low SNR signals, especially in measurements of dense smaller particles.

The FFT based signal processor usually provides more accurate information than the other type of those for LDV in an insufficient noise environment. In the present study, a transient memory system which was designed by the authors group (Kobashi et al. 1988, 1990, 1992) was employed to accomplish measurements under the low SNR conditions.

The signal processor consisted of high speed A/D converter, a transient memory and a Digital Signal Processor (DSP, Motorola 56001RC27) as shown in Figure 1. The flash A/D converters can convert the signals up to 40MHz sampling rate with 8bit resolution, and transient memories had 2Mbyte storage for each channel, which corresponds to 0.2sec storage at 10MHz sampling rate, with which the performance are enough for the measurement of the present study.

The trigger and memory controllers had two operational modes for each channel, to enable us to optimize the specifications under various conditions as described in the reference (Kobashi et al. 1992). The trigger controller provided pre-triggering and post-triggering functions: the pre-triggering is for storage of whole signals, so it was operated storing whole signals, with the pre-triggering mode in all the measurements described as in next section.

The memory controller has two different type operations, so called sequential process mode(real time mode) and continuous storage mode. The sequential process mode uses small amount of memory which is required to obtain frequency information, and the DSP starts processing signals from the point which every trigger event occurs; The continuous storage mode is to store signals up to full memory size and processing is proceeded at once. The remarkable advantage of the continuous storage mode is that the signals can be captured and processed even when the amplitude of signals was lower than the fixed trigger level or was comparable to the environmental noise.

Since the FFT based processor had an ability to accept signals with relatively low SNR, the bias error on size distribution caused by the fact that the signal amplitude depends on the droplet size, could considerably be improved. The procedure for FFT was done by software run on the DSP and host computer, so the processing algorithm was optimized without changing hardware.

2.3 Signal Processing

Figure 2 indicates the timing chart of sequential process mode and continuous storage mode. In the sequential process mode, the signals were stored in a short memory and processed by FFT sequentially. FFT calculations are carried out from the point of trigger event occurrence which correspond to the beginning of signals (FFT.p (1) and FFT.p (3) in Figure 2(a))with lower SNR than the center of those. This operation results in data loss by processing the part with low signal quality. Moreover, the signals (signal(2) and signal(4) in Figure 2(a))which exist within the processing duration time of triggered signal (FFT.t(1), FFT.t(3) in Figure 2), were neglected. Since the number of signals existing within the processing duration time was affected by the maximum processing capable rate and number density of particles, the data loss by processing time was not considered in section 3.

In the continuous storage mode, as the transient memory continuously acquires the signals up to full memory size without any processing such as detection of signals, the trigger loss cannot be found in principle.

As for the algorithm of signal detection, the processing of all parts of storage memory data needs a plenty of FFT calculations although one needs not to adjust the trigger level. In order to reduce the number of FFT calculations to that of Doppler signals, the center triggering whose trigger level is comparable with noise level but less than fixed trigger level, was employed. When signal was triggered, the center part of signal which can be selected by searching the peak of signal, is processed by FFT (Figure 2(c)). Thus, the continuous storage mode which can be conducted only by the signal processor with the transient memory, can be a reliable signal detection method using the center-triggering function which helps effectively to detect all signals.

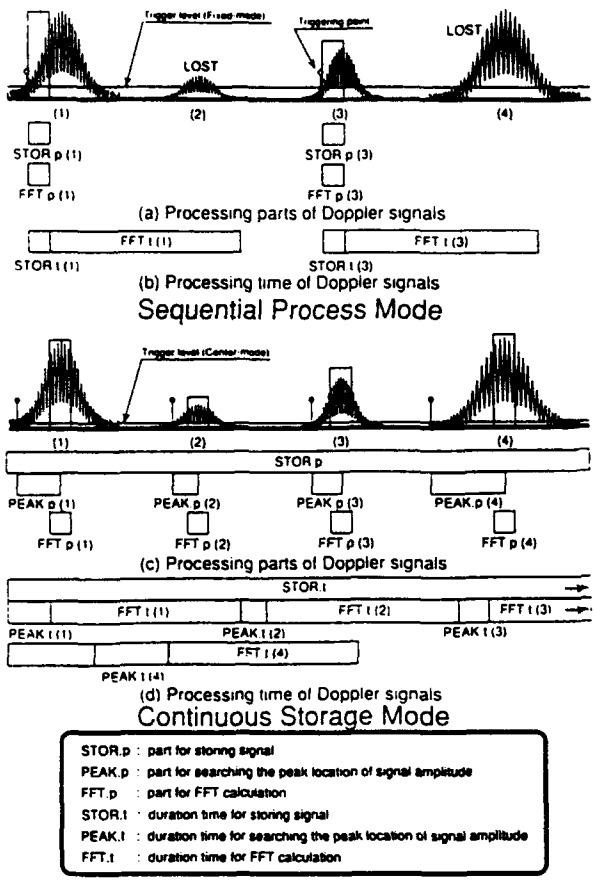

Fig. 2 Difference between sequential process and continuous storage mode

3. SPECIFIC FUNCTIONS FOR ACCURATE DETERMINATION OF SIZE

3.1 Contributions of the Continuous Storage Mode to Validation Rate and the Effect of Trigger Level

Sequential operation of the memory can be an effective method to measure large particles with high SNR, however, it neglects the signals in dense spray because of two major reasons: since the total processing time of DSP including a duration time for data transfer is longer than the sampling time, the data acquisition must be inhibited while the every processing is completed; if the signal amplitude is comparable or smaller than the trigger level the trigger event never occurs. A typical A/D converter c[illegible]nvert with 8bit resolution; so the droplets in the small [illegible]ze range could be neglected to cause distortion into resultant size distribution lacking small particles. If the analog circuit at front-end of the A/D converter was designed by linear amplifiers, 8bit resolution approximately corresponds to 10times difference in particle size range; therefore, the trigger level should be set as low as possible, while, the trigger level is usually set at certain level in order to avoid mis-triggering by the noise which cause the number of neglecting particles.

To evaluate the improvement derived by the continuous storage mode, a series of digitized data, which was obtained from a single spray and stored in the hard-disk, was used. Figure 3 compares the size distribution obtained with the continuous storage to those of the sequential process mode with various trigger levels. The validation to judge whether sampling data can be Doppler burst signal, or not, was carried out by the following procedure:

1) The summation of the peak spectrum and two spectrum around the peak frequency should be more than 5 times of the second peak spectrum
2) Each velocity among three receive channels for PDA should be coincident.
3) The ratios of phases obtain between channels must be the same ratio of geometrical configuration of the observing point.

Both probability density and accumulated probability density were defined as eq.2 and were normalized by 30000 data which were the maximum data number inferred with the burst center triggering described in the next subsection. The trigger level denotes the normalized amplitude by half of the maximum dynamic-range of the 8bit A/D converter(eq.1), and the maximum level of the signals corresponding to the amplitude of about 80μm particles in the configuration. It should be noted that all results were from the same signals which were in the external storage of the host computer.

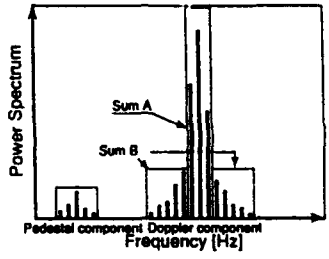

$$SNR = 10\log[SumA / SumB]$$

Fig. 3 Schematic of SNR definition

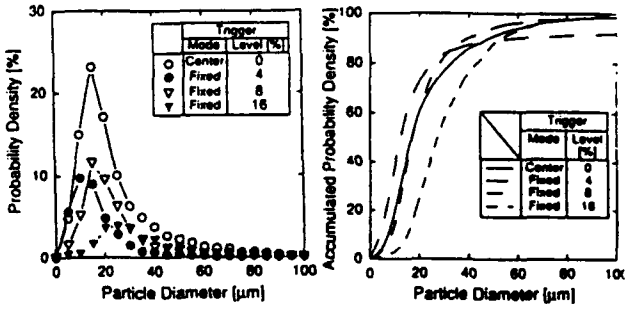

(a) (b)

((a) is based on the number of data in the continuous storage mode)

Fig. 4 Effect of lowering fixed trigger level

$$TL[\%] = \frac{Trg\ Amp - Ofst\ Amp}{FR} \times 100 \qquad (1)$$

$$PD(d_i)[\%] = \frac{N_{fix}(d_i)}{N_{cen}(d_i)} \times 100$$

$$APD(d_i)[\%] = \frac{\sum_{j=0}^{i} N(d_i)}{Total\_N} \times 100 \qquad (2)$$

As Figure 4(a) and (b) show the shapes of probability density, and those of accumulated probability density, respectively as a parameter of the trigger level. Size distributions as shown in Figure 3(a) are normalized by the number of data in the continuous storage mode. It is obvious that the continuous storage mode has an advantage in terms of the validation rate. In principle, lower trigger level would result in higher validation rate over the size range, however, the probability density(Figure 3(a)) of 20μm size triggered at 8% is higher than that triggered at 4%. On the other hand, the accumulate probability density's(Figure 3(b)) show that the signals detected by the trigger level 4% relatively include the particles smaller than 30μm compared with the result of the trigger level 8%; this is likely to be caused by the difference of the SNR which is at a part of FFT processing. Since the trigger level of 4% corresponds to the signal amplitude of 10μm size, most of the particles with 10μm size was triggered at the center of the signals which correspond to maximum SNR, as shown in Figure 5-c, although the signals larger than 10μm size whose proper trigger level is 8%(Level A) in Figure 5-b, were processed at the beginning part which corresponded to lower SNR with triggering at 4%(Level B) as shown in Figure 5-a. Thus, as for SNR of FFT processing part, the results showed a difference by employed technique. To eliminate this effect and increase the validation rate, the center, that is, the most clear part, of the signal was to be selected for processing the signal of individual particle.

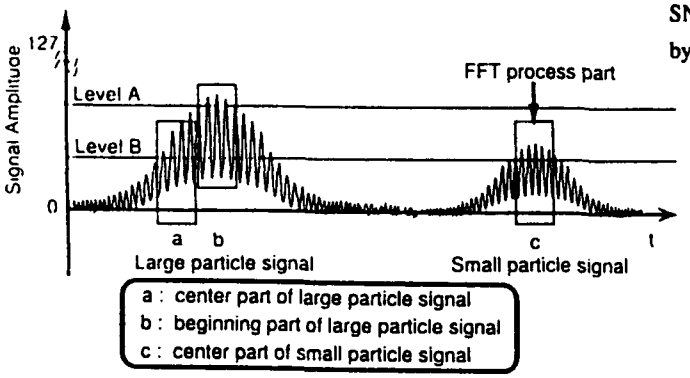

Fig. 5 Schematic of difference of the processed location by the center and the fixed triggering

3.2 Burst Center Triggering

Burst center triggering is a function to obtain the maximum SNR in a Doppler burst signal, by searching the maximum amplitude of the signal. Since this function can be accomplished by only the continuous storage mode, because the center of the signal must be stored. It is a typical application aids to a fast transient memory system with the DSP.

Demonstrating the effect of the function, the same source signals in the memory was processed with and without the function. Figure 6 compares the size distribution with the trigger level at 5.5% which is the proper trigger level so that the validation rate with the fixed triggering can become maximum. It is noted that the result of the continuous storage mode was accompanied with a triggering to compare with them properly.

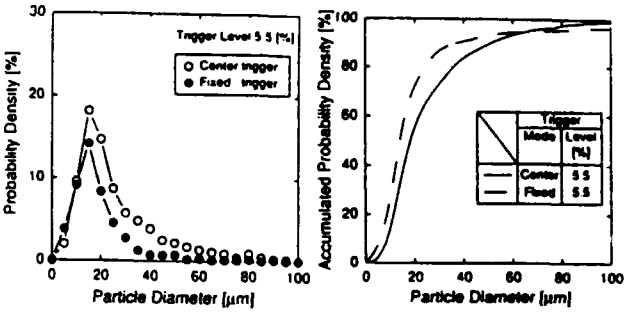

(a) (b)

Fig. 6 Comparison between the center and the fixed triggering ((a) is based on the number of data in the continuous storage mode)

As compared with the size distribution with the fixed triggering(Figure 6(a)), the total number of the validated data by the center triggering was raised up to 31% and the effect was especially remarkable in the small size range. The improvement is important because a spray atomizer often derives Rosin-Rammla distribution; hence the data rejection in the small size particles causes bias error on the probability density.

Figure 7 shows the validation ratio as a function of SNRcen varying the trigger level. The calculation method of SNR (SNR_{cen}, and SNR_{fix}) and validation rate was defined by the following Eq. 3 and Figure 3 respectively:

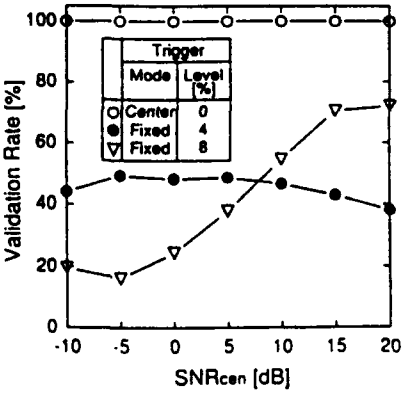

Fig. 7 Validation rate by different trigger levels (based on the number of data in the continuous storage mode)

$$VR(SNR_{cen}) = \frac{N(SNR_{fix})}{N(SNR_{cen})} \times 100 \qquad (3)$$

With a lower trigger level, large particles (SNR_{cen}<10dB) were triggered at the beginning of their

signals, consequently the data dropped and the validation ratio remains around 50%. On the contrary, smaller particles were neglected by higher fixed trigger level. The burst center triggering function satisfies for the large and small particles and effectively removed bias in the validation by the trigger level.

Figure 8 illustrates the contour of the correlation between SNR_{cen} and SNR_{fix} with and without the center-triggering at the same condition as Figure 6. The value of contour was normalized by total number of data. Left side of the diagonal line denotes data of which the SNR was improved by the function. The maximum value in the map located at the point where the SNR_{cen} was 10dB with the center-triggering of 10dB, whereas the SNR_{fix} without the center triggering was 2dB, thus the improvement of the SNR in the sampled signals was 8dB. This result confirms that noise was reduced effectively in the sampled signals, and hence, the function contributed to increase the validation ratio.

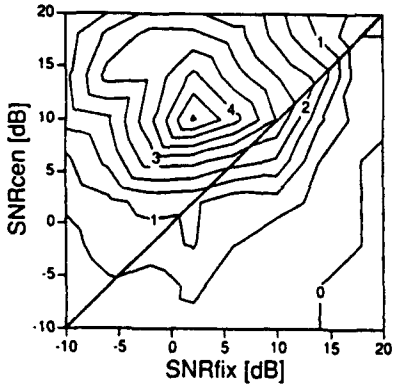

Fig. 8 SNR improvement in sampled signals by the center triggering(Trigger level 5.5%)

3.3 Coaxial Measuring Volumes by Two Color Four Beams

Coaxial measuring volumes are provided to eliminate trajectory ambiguity on sizing and to realize the higher validation rate. Since the duration time of the signals from small measuring volume by blue beams is short compared to that from large measuring volume by green beams, the center of the sizing signal is processed by triggering the signal of blue beams. Figure 9 shows the improvements by the coaxial measuring volumes indicating the validation ratio of the size information as a function of SNR_{cen} of the signal. The keys by closed circle and open triangle correspond to those of triggered by blue beams and green beams respectively, which were normalized by the maximum particle number obtained by the continuous storage mode. The result of validation rate was low compared with typical condition, because the particle flow was dense enough to make optical noise. It should be noted that both beam intensities were set to give the same signal levels. The number of accepted particles differed about 1.5 times by the existence of the blue measuring volume, and caused no bias respecting to SNR. The role of the coaxial measuring volume function was substantially similar to the center triggering function on the software, because the center of the sizing signal was processed optically. In the case that a signal processor does not have any storage, such as a counter system, one can eliminate the error by coaxial dual measuring volumes optically.

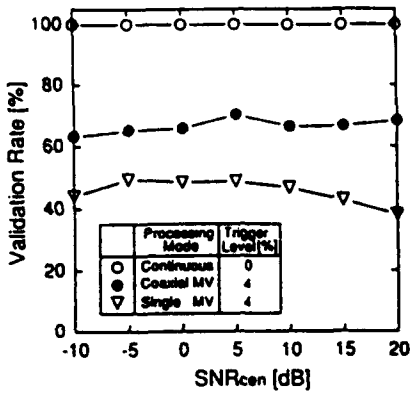

Fig. 9 Comparison of the validation rates between the coaxial and the single measuring volume (based on the number of data in the continuous storage mode)

4. Experimental Result

In the present study, the size and two-component velocities of droplets in the interaction within multiple sprays were measured to achieve passive control of the local size distribution of droplets. Combinations with two and four spray nozzles were examined.

Figure 10 shows a geometric arrangement of the two spray nozzles and coordinates system. The solid lines indicate outer edges of the two hollow-cone sprays which contain most of the droplets after the atomization.

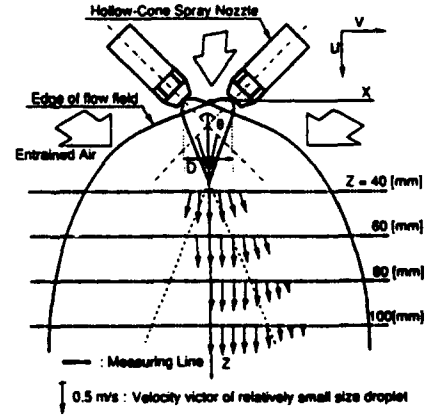

Fig. 10 Schematic of two spray arrangement

Experiments were carried out with various inclined angles of 15, 30 and 45degrees and distance between two sprays of 20, 25 and 30mm. The spray nozzles were aligned with suitable distance between two sprays to avoid interaction before the atomization completed. For all the measurement, sprays were driven with 1.263×10^{-3} kg/sec in flow-rate and 588kPa in pressure recommended configuration by the manufacturer(Delavan, Type A, Hollow cone).

Applying the continuous storage mode, mass flux were measured by calibrating the measuring volume. A

measurement of mass flux, and particle concentration by PDA is unavoidable from the problem of calibrating measuring volume, which depends on particle size due to Gaussian profile of laser beam intensity.

The measuring volume calibration by Doppler burst length(M. Saffman(1987)) needs the restriction that the mass flux can be defined only in the case of flow field with one direction. The accuracy of the mass flux was sensitive for the trigger level and SNR.

On the contrary, M. Sommerfeld(1992) suggested the method by Doppler burst amplitude which was independent of direction of flow direction. The method had great advantage not to be influenced by the parameters of signal amplitude(laser power, electric gain, optical configuration, and particle concentration) in spite of the estimation by signal amplitude.

Y.Hardulpas represented in the measurement of the particle concentration near the stagnation point where the mean velocity of particle was very low, the method by the burst residence time of particle was superior to that based on particle mean velocity.

For determination of mass flux, the following method by scattering power estimation was used, because no reverse flow was involved and the mass flux is defined as follows;

$$Massflux = \rho \sum_{i=0}^{n} [(V(di) \times N(di))/(A(di) \times Ts)] \qquad (4)$$

where ρ is density of droplet, $V(d_i)$ and $N(d_i)$ is the volume and the number of droplets in size class "i", where the class includes diameters between di and di+5 [μm], and T_S is the sampling time. $A(d_i)$, the effective cross-sectional area of the measuring volume of the anemometer normal to the flow, is described as

$$A(d_i) = 2r_{max} \times z \qquad (5)$$

where z is the length of image of the image of spatial filter. r_{max} is, as yet known, the maximum displacement from the center of the measurement volume and derived as follows. Laser beam intensity profile is Gaussian profile, and is written as.

$$I(r) = I_{max} \times exp(-2r^2 / w^2) \qquad (6)$$

where w is the beam waist of laser, r is distance from the center of the beam. Due to Mie Theory, in the range of droplet size we discuss, the intensity of scattered light is proportional to the square of droplet size as follows.

$$I_{max} = C_1 \times d^2 \qquad (7)$$

then eq. (6) and eq. (7) gives

$$r_{max} = C_2 \times (ln(I_{max} / I_{min}))^{1/2} \qquad (8)$$

I_{max} and I_{min} are the maximum and minimum intensity scattered by particles . C_1 and C_2 are the constants respecting the intensity of scattering particle which is influenced by the optical and electrical gain.

On the accuracy of mass flux using above estimation, the mass flow rate obtained by two dimensional integration of mass flux agreed with the total mass balance to about 8%, varying the measuring distance from a single spray and provided pressure.

Figure 11 shows the profile of Sauter mean diameter with two sprays at Z=40, 60, 80, 100mm with a inclined angle and distance between two sprays of 45degree and 20mm, respectively.

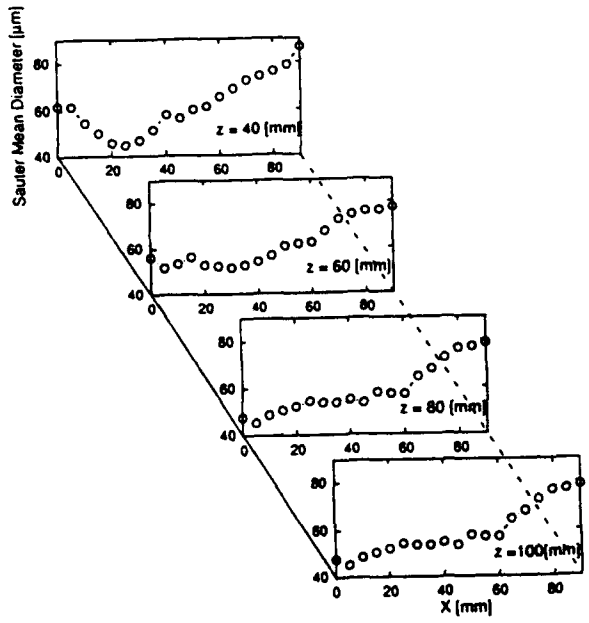

Fig. 11 Profile of Sauter mean diameter distribution

The profile of size distributions were modified by the existence of the second spray flow, and was obviously flatten at the center core of the flow, and the similar distributions were observed at the positions Z. The size distributions corresponding to each plot in Figure 11 are also shown in Figure 12 (a), (b), (c) and (d), respectively. (a) and (c) are center of the region which has similar profiles in their size Probability density, and (b) and (d) are outside of it.

The lateral velocity profile of the air phase was also measured so as to compare with that of particles of each size classes. Figure 13 shows lateral velocity profiles of air(a), 20μm particles(b:fine), 50μm particles(c:middle) and 70μm(d:coarse), respectively. Tracer particles of which the diameter was approximately up to 8μm, were selected by a supersonic humidifier. Discrimination of the tracers were achieved with size information inferred by PDA.

The result of the air phase velocity denoted that air induced by particle motion was driven in vertical direction at the center of the geometry.

The particles of 20μm had already smaller lateral velocity component even at upper location Z=40mm, and seem to follow the air flow, and the particles of 70μm(coarse) almost penetrated through the interaction region. Particles in both size ranges hardly fall in the interaction region. On the contrary, particles of 50μm(middle) moderately followed the air flow, and were likely concentrated into the center core region.

For practical application of similar size droplets concentrated below the interaction region, mass flow rate should also be constant over the cross sectional area. Figure 14

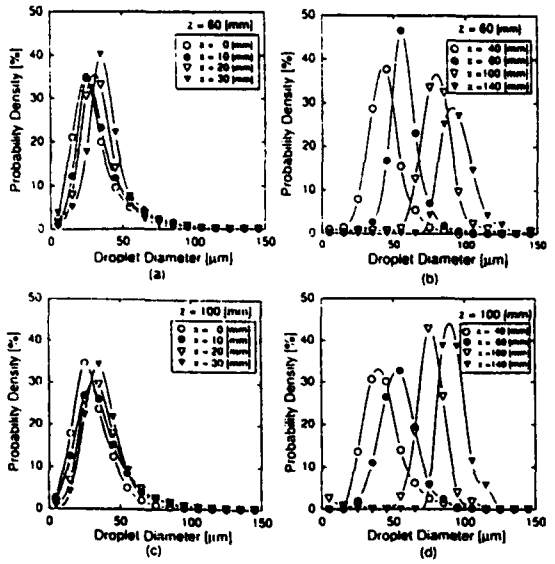

Fig. 12 Droplet size distribution

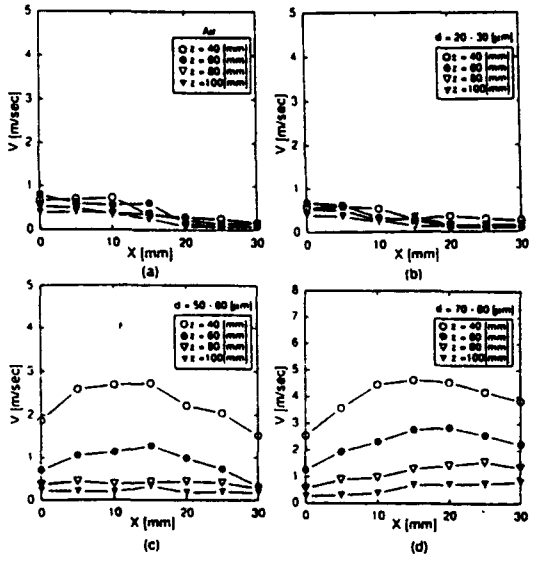

Fig. 13 Mean v-velocity profile

shows mass flux profile of total size class evaluated by eq.4. Variation of the mass flux which was inside of X=15mm at Z=60, 80, 100mm cannot exceed 13% normalized by the average mass flux in the region which average diameter was flatten, and showed flat profile.

In case of two sprays, most of the entrained air flowed from the outside of flow configuration to the core along X coordinate due to two spray arrangement. The region of uniform size distribution which was influenced by the flow direction of entrained air, resulted in one dimensional.

Since the force of entrained air flow by the two sprays forms the uniform size region which was occupied at high flow rate, it is expected that the enhancement of entrained

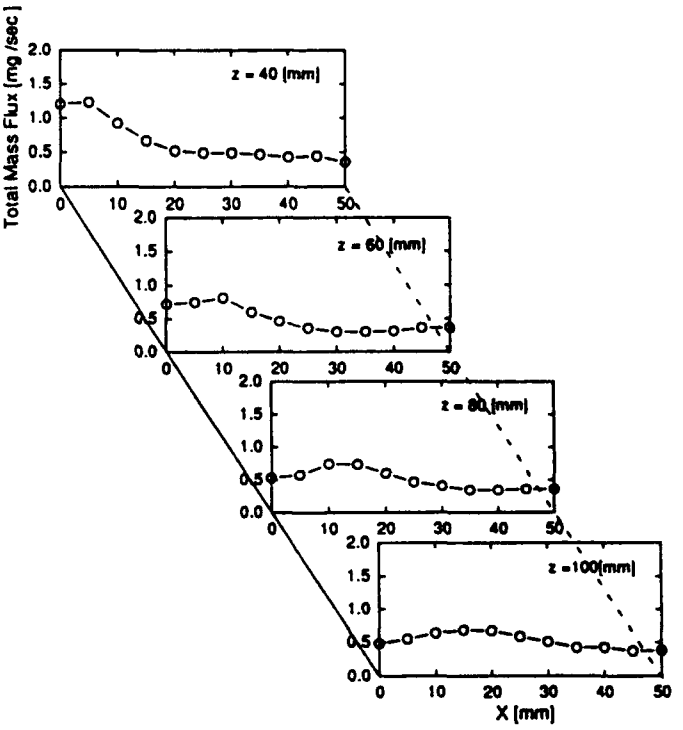

Fig. 14 Profile of total mass flux spatial distribution

force by employing four sprays can contribute not only to realize uniform size region certainly, but also to form two dimensional region. From these points of view, the examination of size distribution in the downstream of four spray, was beneficial attempt for sprays application.

The flow field by four spray nozzles was formed with symmetrical geometry as show in Figure 15. Figure 16 indicates that Sauter mean diameter cannot exceed 9% which this uniformity of Sauter mean diameter was enhanced compared with two sprays from the center of flow field to X=15mm at Z=100mm. The result also showed that in 1%(circle region with 15mm radius) of spreading area, 20% of total mass was concentrated since the enhancement of entrained force made most of droplets follow the air flow.

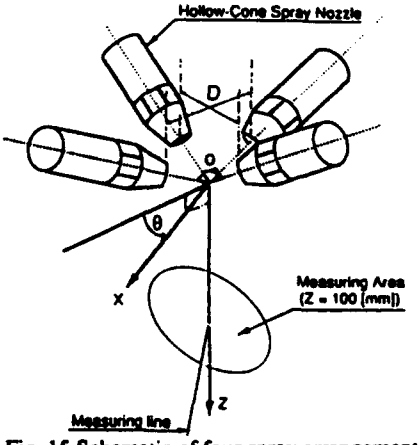

Fig. 15 Schematic of four spray arrangement

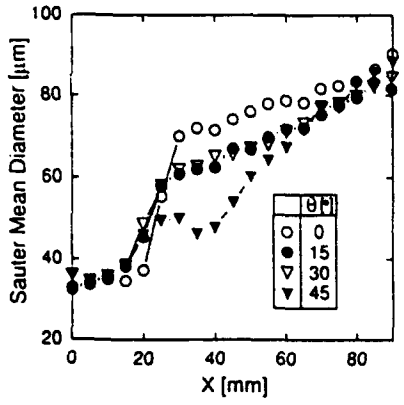

Fig. 16 Profile of Sauter mean diameter

6. CONCLUSION

Size distribution and two dimensional velocities of the multiple interaction sprays has been measured by PDA, and the effective processing method was demonstrated. Results are summarized as follows:

1) Both the burst center triggering function and coaxial dual measuring volumes formed by two dimensional LDA improved the validation rate for sizing information up to 31% in the present configuration compared with the method of the fixed triggering. The burst center triggering function remarkably improved resultant size distribution of spray droplets, because size of droplets concentrated in relatively smaller size range.
2) Triggering with low trigger level without center triggering could reduce the validation rate. Signals from larger particles were processed in the beginning of the signal, therefore, worse quality, that is, the part with lower SNR of the signal was extracted by lower trigger level, compared with higher trigger level. The burst center triggering eliminated the error with reasonable processing time.
3) The region of uniform size distributions was clearly observed in downstream of the multiple interaction sprays. Variation of Sauter mean diameter with four sprays was 9% in all over the circle region which corresponds to 1% of spreading area at Z=100mm. The total mass flux of the region was 20% of that supplied into the sprays.
4) The results of the velocity denoted that the modification of the local size distribution was caused by variation of the inertia of the droplets and drag forces, and the interaction was induced by the air entrained by the droplets themselves. This implies that passive control of local size of droplets can be available without auxiliary driving of the air.

7. ACKNOWLEDGMENT

I greatfully acknowledge helpful discussions with Mr.T.Maeda on several points in this paper.

NORMENCLATURE

APD :	Accumulated probability density
di :	Size class of droplet diameters whose interval is 5 [mm]
FR :	Full scale range of A/D convrter(7bit)
Nfix(di) :	Number of droplets with di size detected by fixed triggering
Ncen(di) :	Number of droplets with di size detected by center triggering
N(di) :	Numbr of droplets with di size
N(SNR) :	Number of signals with the same SNR
Ofst Amp :	Offset value of signal amplitude(128)
PD:	Probability density
SNRcen :	Signal-to-noise ratio of signal part selected by center triggering
SNRfix :	Signal-to-noise ratio of signal part selected by fixed triggering
SumA :	Summation of power of three spectrums around the spectrum which has the peak valueo
SumB :	Summation of power of spectrums except SumA
TL :	Trigger level
Total_N :	Total number of droplets detected by continuous storage mode
Trg Amp :	Absolute value of trigger in A/D converter
VR :	Validation rate

8. REFERENCE

Bachalo, W. D., Rudoff, R. C. and Brena de la Rosa, A., "Mass Flux Measurements of a High Number Density Spray System Using the Phase Doppler Particle Analyzer", AIAA 26th Aerospace Sciences Meeting Jan. 11-14, 1988/ Reno, Nevada, AIAA-88-0236.

Durst, F.and Ruck, B., "Effective particle size range in laser-Doppler anemometry", Exp. in Fluids, 5,1987,pp. 305-314.

Fitzpatrick, J. A., Lambert, B. and Murray, D. B., "Measurements in the Separation region of a gas-particle cross flow", Exp. in Fluids, 12, 1992, pp. 329-341.

Hishida, K., Kobashi, K. and Maeda, M., "Application of Laser/Phase Doppler Anemometer to Dispersed Two-Phase Jet Flow", Part. Part. Syst. Charact., 7(1990), pp.. 152-159.

Hardalupas, Y. and Taylor, A. M. K. P., "On the measurement of concentration near a stagnation point", Exp.in Fluids, 8, 1989, pp. 113-118.

Hardalupas, Y., Taylor, A. M. K. P. and Whitelaw, J. H., "Fringe Count Limitations on the Accuracy of Velocity and Mass Flux in Two-Phase Flows", Proc. 5th Int. Symp, Applications of Laser Anemometry to Fluid Mechanics, Lisbon, Portugal, 1990, July 9-12.

Ikeda, Y., Kurihara, N.and Nakajima,T., "Burst Detection of LDV by Correlation Method", ASME, Laser Anemometry 1991, vol. 2.

Kobashi, K., Hishida, K. and Maeda, M., "Multi-Purpose High Speed Signal Processor for LDA/PDA Using DSP Array", Presented at the Third. International Conference, Laser Anemometry Advances and Applicxations, Seasea, Wales, 1989.

Maeda, M., Sanai, N., Kobashi, K.and Hishida, K., "Measurement of Spray Mist Flow by a Compact Fiber LDV and Doppler-Shift Detector wuth a Fast DSP", Proc. 4th. Int. Symp. Applications of Laser Anemometry to Fluid Mechanics, Lisbon-Portugal, 1988.

Miller, D. R. ; Comings, E. W. ,"Force momentum fields in a dual-jet flow", J. Fluid Mech. 7, pp. 237-256.

Paine, A. J., "Error Estimates in the Sampling from Particle Size Distributions", Part. Part. Syst. Charact., 10, 1993, pp. 26-32.

Qiu, H. H. and Sommerfeld, M., "A reliable method for determining the measurement volume size and particle mass fluxes using phase-Doppler anemometry", Exp.in Fluids, 13, 1992, pp. 393-404.

Saffman, M., "Automatic calibration of LDA measurement volume size", Applied Optics, vol. 26, No.13, 1 July 1987, pp. 2592-2597.

Snarski, S. R. and Dunn, P. F., "Experiments characterizing the interaction between two sprays of electrically charged liquid droplets", Exp. in Fluids, 11, 1991, pp. 268-278.

Tanaka, E ,"The interference of two-dimentional parallel jets", Bulletin, JSME. 13, 1970, pp. 272-280.

Tanaka, E., "The interference of two-dimentional parallel jets", Bulletin, JSME.17,1974, pp. 920-927.

Wang, C. S., Lin, Y. F. and Gheu, M. J., "Measurements of turbulent inclined plane dual jets", Exp. in Fluids, 16, 1993, pp. 27-35.

LDA MEASUREMENTS OF TURBULENT AIR-SOLID SUSPENSION FLOW IN A 90° BEND OF SQUARE CROSS-SECTION

B. Hlwatika, Y.D. Tridimas and N.H. Woolley

School of Engineering and Technology Management
Liverpool John Moores University, Byrom Street, Liverpool, L3 3AF, UK

ABSTRACT

A turbulent air-solid suspension flow in a 90° bend of square cross-section was investigated using a two-channel Laser Doppler Anemometer. The bend had a radius ratio of 4.0 and a cross-sectional area of 50mm×50mm. The flow Reynolds number was 2.8×10^4. Glass ballotini particles with a mean diameter of 485μm were used with a loading ratio of 1.32. The results showed that the most significant effect of the solids on the air flow occurred midway around the bend where local solids concentration was at its highest.

NOMENCLATURE

D_H	hydraulic diameter, non-dimensionalising length scale
k	$=(u^*)^2+(v^*)^2+(w^*)^2$, (proportional to turbulence kinetic energy)
N	particle number rate
R_c	radius of curvature of the bend
Re	Reynolds number
S	correlation of the fluctuating velocity components ($=\overline{uv}/U_B$)
U_B	fluid bulk mean velocity
U, V, W	mean velocity components in the streamwise, radial and spanwise directions respectively
U^*, V^*, W^*	dimensionless velocity components
u, v	fluctuating velocity components in the x, y coordinate directions
u^*, v^*, w^*	dimensionless streamwise, radial and spanwise turbulent intensities ($u^*=\sqrt{\overline{u^2}}/U_B$, $u^*=\sqrt{\overline{v^2}}/U_B$, $w^*=\sqrt{\overline{w^2}}/U_B$)
x, y, z	streamwise, radial and spanwise coordinate directions
x^*, y^*, z^*	dimensionless coordinate directions -0.5(inside wall)$\le y^* \le 0.5$(outside wall)
θ	angular position around the bend

1. INTRODUCTION

Two-phase suspension flows are found in many industrial situations including power plants and pneumatic conveying lines. The erosion damage sustained by nozzles or turbine blades is caused by solid particles or liquid droplets. Erosion, the extent of which is governed by the wall material, particle velocity and angle of impingement, can be very severe in curved ducts used in pneumatic conveying lines. The ability to predict particle trajectories requires detailed and reliable experimental data.

Fluid flow in curved ducts has been investigated by Humphrey et al (1981) and Chang et al (1983); it is similar to that found between blade passages of turbines but its two-phase character has received limited attention. The availability of laser-based non-intrusive techniques makes it possible to advance knowledge of two-phase flows. Durst and Zaré (1976) demonstrated the possibility of obtaining the velocity of large particles in two-phase flow. Zisselmar and Molerus (1979) studied turbulent air-solid suspension flow in a pipe using LDA. They found that the presence of the particles (with 53μm mean diameter and concentration of up to 5.6% by volume) in the turbulent stream led to an increase in the intensity of turbulence near the wall and a dampening in the core of the pipe. Tridimas (1981) carried out LDA experiments in air-solid suspension pipe flows. He found that the velocity profiles of the two-phases crossed close to the wall and that there was a decrease or increase in the air turbulence depending on particle shape, size, concentration and flow Reynolds number. Yianneskis and Whitelaw (1984) varied the concentration of 270μm mean diameter particles between 0.5% and 1.0% by mass with Re=42,500 in a pipe using water as the carrier fluid. There were no noticeable differences between both the velocity profiles and turbulence intensities of the loaded and unloaded water flows.

LDA measurements of turbulent air-solid suspension flow in a 90° bend of square cross-section were reported

by Kliafas (1984). The air velocities were obtained without particles being present in the flow. Comparison of the particle and air flow velocity profiles showed that they crossed near the wall. A 90° pipe bend was used by Al-Rafai (1990) and Parry (1991). They investigated the effect of different curvature and particle loading ratios. Tanaka et al (1989) studied the distribution of particle velocity and concentration using different air-solid flow regimes ranging from dispersed to sliding bed flow. The velocity distributions in the sliding bed flow were non-uniform and had large gradients while the distributions in the dispersed phase were uniform across the section. Profiles of the concentrations showed severe distortion in the bend owing to the centrifugal force. Rashidi et al (1990) varied the particle size, particle density, loading and flow Reynolds number and found that large (1100μm) particles caused an increase in the number of particle-wall ejections, leading to an increase in the measured turbulence intensities and Reynolds stresses. Smaller (120μm) particles gave rise to a decrease in the number of wall ejections, causing a decrease in measured turbulence intensities and Reynolds shear stresses.

Previous studies of two-phase suspension motion in curved ducts have mostly used pipe flow which is restrictive when using two-channel laser Doppler anemometry because of the curved walls. The present work attempts to provide quantitative information on the mean velocity distribution of both phases, the turbulent kinetic energy and shear stresses of the air and the solids concentration. Results reported here are limited to the symmetry plane of a square section bend. Spherical particles with a mean diameter of 485μm were used. The solids mass loading ratio and flow Reynolds number were 1.32 and 2.8×10^4, respectively. Measurements were made using a two channel laser Doppler anemometer.

2. EXPERIMENTAL DETAILS

2.1 Flow Rig

Figures 1 and 2 show a schematic diagram of the flow rig and the test bend, respectively. The square duct was made of transparent perspex to allow optical access. A vertical leading tangent of 66 hydraulic diameters was provided in order to achieve fully developed air flow at entry to the bend. A rigid steel platform was used to gain access to the test bend and to manually operate the traversing gear on which the probe-head was mounted. An orifice flow meter and a micromanometer was used to monitor the air flow. The solid particles were gravity fed into the flow down a flexible tube through an orifice and a venturi. A cyclone separator located at exit from the bend allowed separation and recycling of the particles.

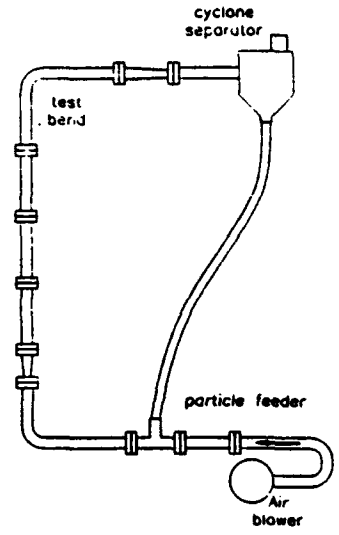

Figure 1. Schematic diagram of the flow rig

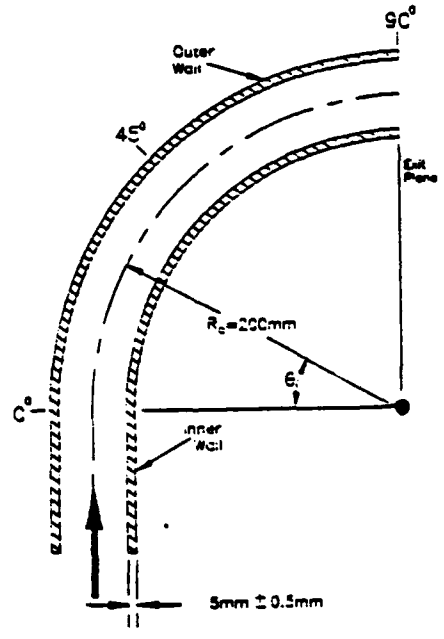

Figure 2. Test bend

2.2 The LDA Optics

A DANTEC two-channel optical system operating in the backscatter mode was used. It incorporated a 500mW Argon-ion laser, colour separator, Bragg cell, polarization preserving single mode optical fibres and an optical probe head with focal length 160mm. Table 1 gives details of the LDA system.

PARAMETER	DIMENSIONS
Focal length of imaging lens	160mm
Beam separation distance	38mm
1) λ=488nm	
Fringe spacing	2.068μm
Probe volume diameter at $1/e^2$	0.0765mm
Probe volume length	0.649mm
2) λ=514.5nm	
Fringe spacing	2.182μm
Probe volume diameter at $1/e^2$	0.081mm
Probe volume length	0.684mm

Table 1. LDA system parameters

2.3 Instrumentation and Signal Processing

The scattered light collected by the probe head was delivered to two photomultipliers. The resulting signals were processed using DANTEC burst spectrum analysers (BSAs). System layout is shown in Figure 3.

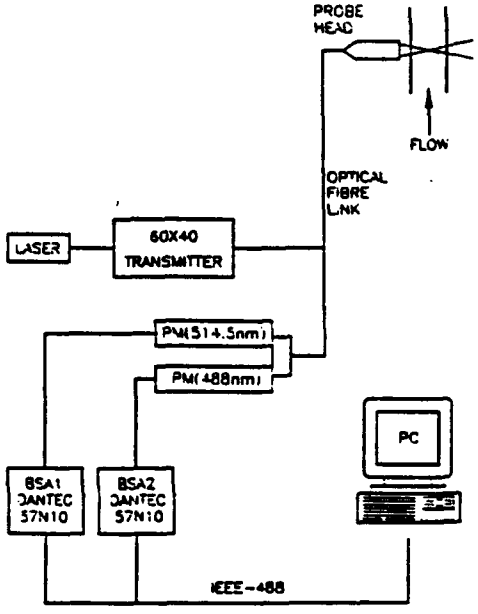

Figure 3. Layout of the LDA system

Measurements of air flow in the presence of solids present many experimental difficulties including the low signal-to-noise ratio which can lead to excessively low data rates. Discrimination against large particle signals is based on a combination of a pedestal threshold level and visibility parameter. A further function which allows attenuation of the Doppler burst pedestal, when combined with the visibility level, makes it possible to discriminate against small particles, thus minimising cross-talk between phases.

2.4 Experimental Procedure

Stable conditions were achieved by running the rig for about one hour prior to taking measurements. Positioning of the probe volume was achieved by means of a manual traversing mechanism made of a combination of translation stages whose accuracy was within ±0.01mm. Estimates of probe positioning uncertainty are given in Table 2 .

COORDINATE	UNCERTAINTY
x	±2mm
y	±0.5mm
z	±0.5mm
θ	±3°

Table 2. Maximum probe volume positioning uncertainty

All measurements were made on the symmetry plane with typically 17 points in a profile. At each point the mean flow and turbulence characteristics were obtained from populations consisting of 2000 to 4000 signal bursts. The air was seeded with incense smoke and data rates up to 1kHz were achieved. Longer data acquisition times were required close to the walls to compensate for the reduced signal-to-noise ratio.

2.5 Measurement Uncertainty

The flow investigated consists of a large axial component and much smaller secondary flows. Misalignment in the orientation of the beams can give large errors, particularly in the case of the secondary flow components, e.g. a 1° misalignment can give an error of the same order as the secondary component. Residence time weighting, Buchave(1979) was used to correct the measurement bias. Measurement of transverse velocity components with large standard deviations and small means required the collection of a relatively large number of signal bursts in order to reduce errors in flow statistics. In two-phase flow measurements, the two main sources of uncertainty are low signal-to-noise ratio, particularly close

to the wall, and cross-talk between the phases. Table 3 contains details of the estimated uncertainties. Velocity gradient and other broadening effects have not been taken into account in the uncertainty estimates.

QUANTITY	UNCERTAINTY(%)		
	Air Only	Air with solids	Solids
k	±6	±6	-
U_B	±4	-	-
U	±2	±2	±3
V	±5	±5	±4
W	±5	±5	±4
u^*	±2	±2	-
v^*	±4	±8	-
w^*	±4	±8	-
uv	±4.5	±8	-
N	-	-	±19

Table 3. Estimates of maximum measurement uncertainty

3. RESULTS AND DISCUSSION

3.1 Mean Velocities

Figure 4 shows non-dimensionalised mean velocity profiles along the symmetry plane of the bend at locations ten hydraulic diameters upstream of the bend ($-10D_H$) and 0°, 45°, 75°, and 90° around the bend. Each graph shows profiles of air alone, air in the presence of solids, and solids. The experiments were designed to keep the air flow rate constant, with or without solids present. The mean velocity profiles at $-10D_H$ and 0° for air reveal similar features, reflecting little effect of the presence of solids on the air flow. The flatness of the solids profiles is evident at these locations. At 45° there is a marked difference between the air profiles. Whilst the air alone still exhibits symmetry, the effect of the solids concentration on the air mean velocity results in significantly lower velocities towards the outside of the bend. The solids velocities remain fairly constant. From this point to the exit of the bend at 90°, the two air profiles gradually become similar. There appears little evidence in the solids profiles that the bend is having any influence, the same basically flat profile being maintained.

3.2 Turbulent Shear Stresses

The $\overline{uv}$ correlation, which gives a measure of the magnitude of one component of turbulent shear stress, is shown in Figure 5. These appear to have the same magnitude and to be unaffected by the presence of solids at $-10D_H$ and 0°. Small differences appear as the wall is approached, with the addition of the solids seemingly causing a reduction in the magnitude of $\overline{uv}$. At 45° the addition of the solids appears to produce a marked reduction in the magnitude of $\overline{uv}$ towards the outside of the bend in the region where the mean velocity profiles are significantly affected. In the region near the inside wall and in the core of the duct the $\overline{uv}$ correlation values are remarkably similar in magnitude. At 75° and 90°, similar trends of $\overline{uv}$ are shown across the section with the larger values occurring near the outside wall.

3.3 Turbulent Kinetic Energy

Symmetry plane k profiles, obtained by measuring and summing the dimensionless mean square values of the three velocity components, are shown in Figure 6. The results for the air with solids at $-10D_H$ upstream and at 0° display similar profiles. At 45° similar profiles of k indicate generally little effect on turbulent energy levels. Towards the outside wall, there appears a small reduction in the levels of k. This is seen to be caused by reduced turbulence energy production caused by a reduction in shear stress rather than the mean velocity gradient which appears relatively unaffected by the presence of solids. It is clear that between 0° and 45°, levels of k at the outside of the bend have increased accompanied by a decrease at the inside wall. Between 45° and 75°, the turbulent kinetic energy at the inner wall shows a significant increase, equally with or without solids, whilst values at the outer wall are maintained. Levels of k at the walls diminish between 75° and 90° for the air only case. This reduction is not evident in the presence of solids. By comparing the individual mean square values of the three velocity components which make up k, it is clear that the addition of solids did not alter the isotropic nature of the turbulence in the core of the duct.

3. 4 Particle Number Rates

The particle number rates presented in Figure 7 are indicative of the local solids concentrations. Reasonable uniformity of solids distribution is apparent at 0° and 90°. The general reduction of level at 90° is indicating an increase of concentration towards the side walls. The major feature of these results is the high level of solids concentration towards the outside of the bend at 45° and a lack of solids towards the inner wall.

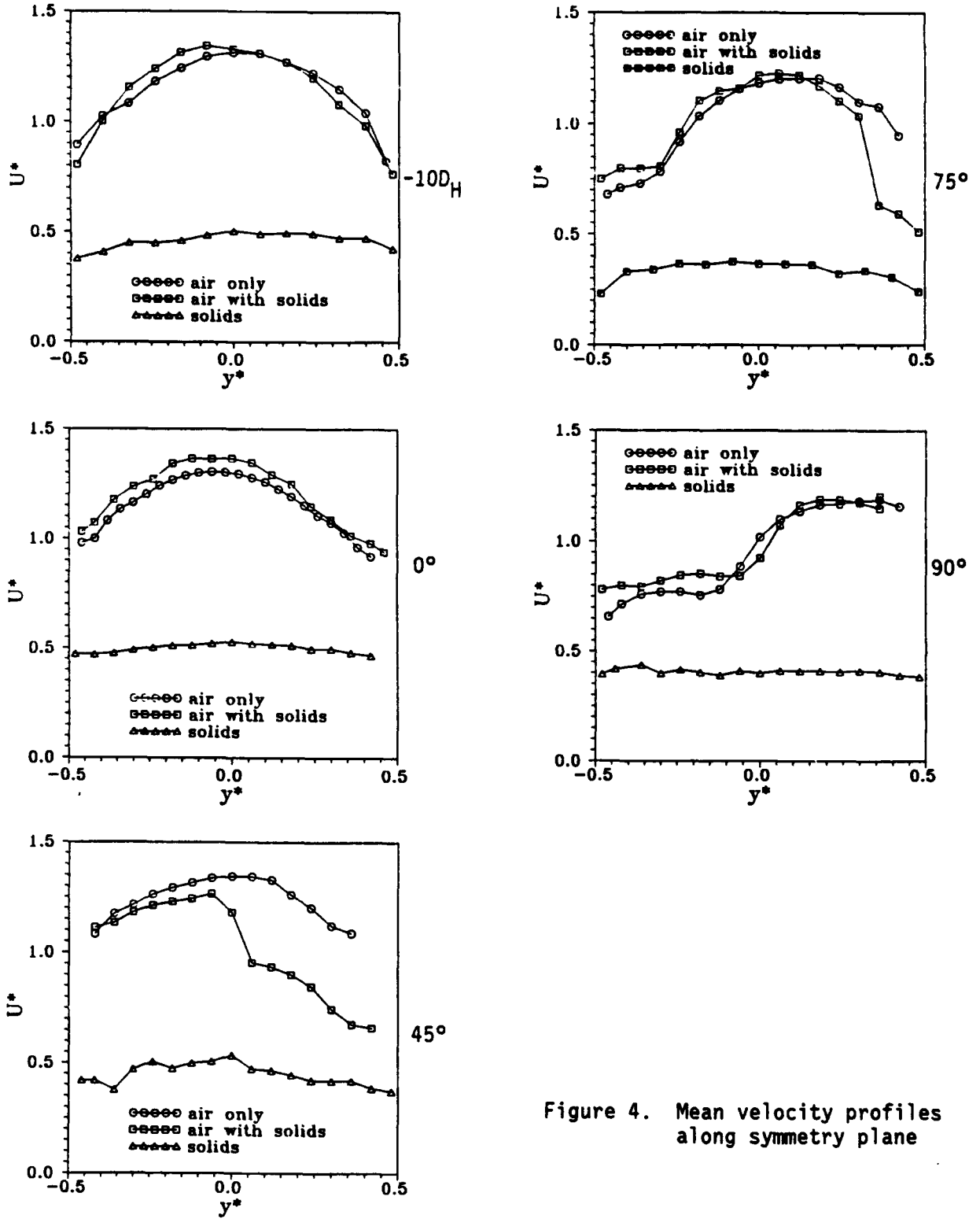

Figure 4. Mean velocity profiles along symmetry plane

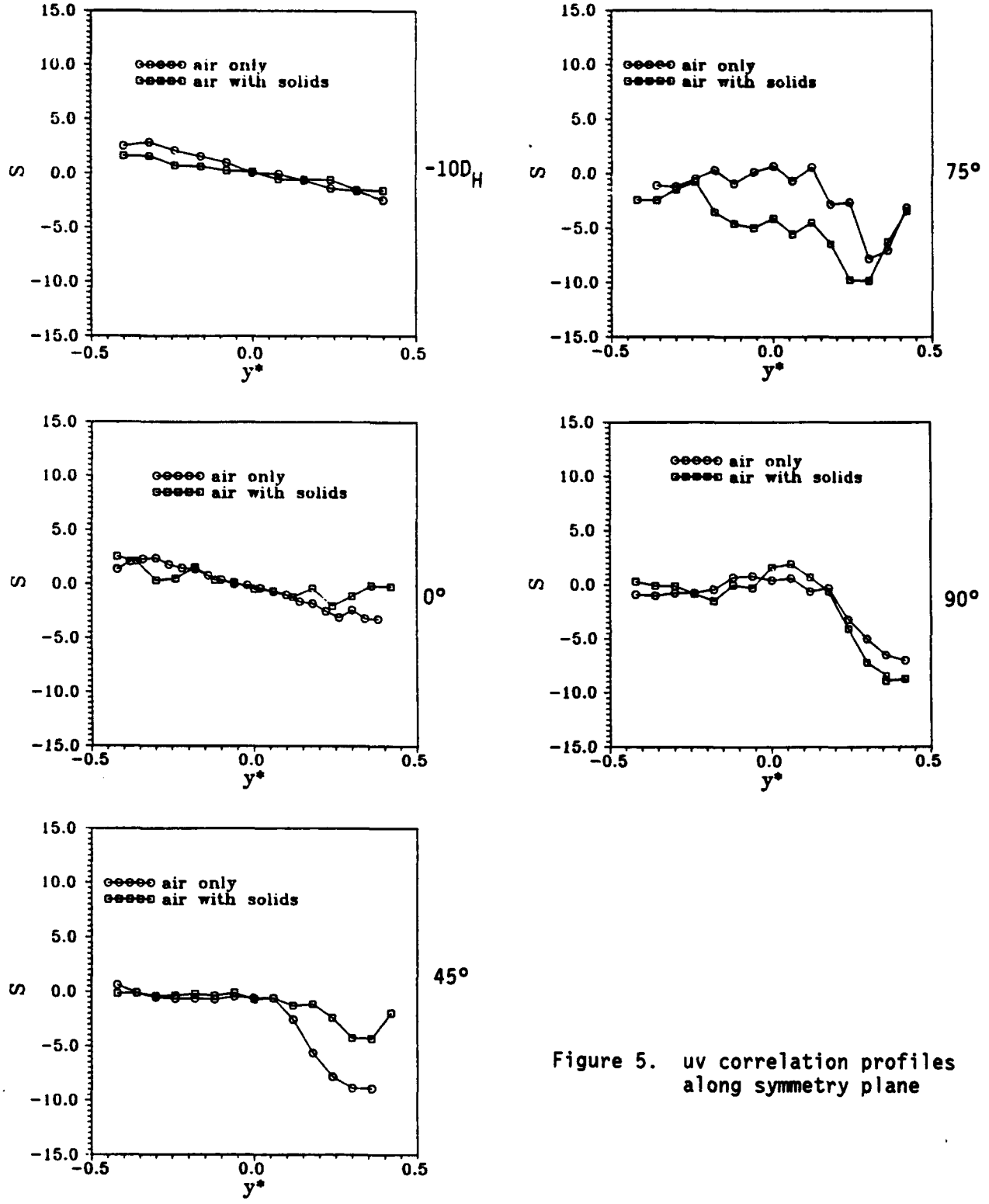

Figure 5. uv correlation profiles along symmetry plane

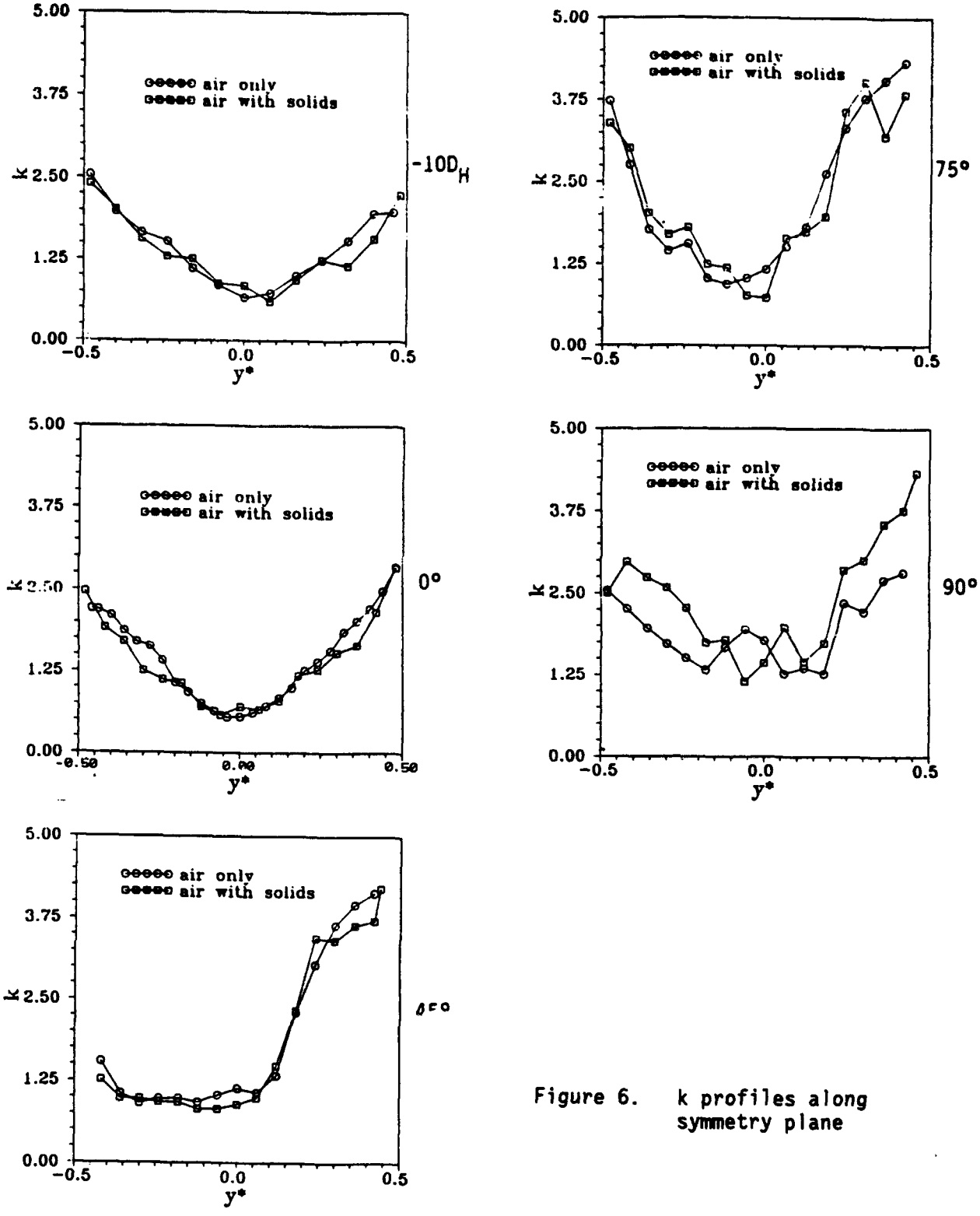

Figure 6. k profiles along symmetry plane

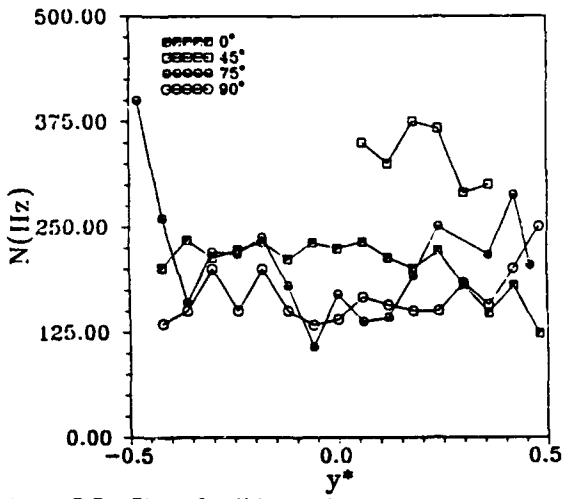

Figure 7. Profiles of solids number rates

4. CONCLUSIONS

1. In the straight section of the duct, the air mean axial velocity, turbulent kinetic energy and the measured component of turbulent shear stress are unaffected by the presence of solids.
2. The major effect of the presence of solids on the air flow was observed at 45° around the bend, a region which coincides with locally high solids concentration. The addition of solids resulted in a significant reduction of the air mean velocity and turbulent shear stress and a smaller reduction of turbulent kinetic energy.
3. Measurement of turbulent parameters in a two-phase bend flow has been carried out successfully using LDA.

REFERENCES

Al-Rafai, W. N. 1990, A Study of Turbulent Gas-Solid Suspension Flows in Pipe Bends using Laser Doppler Anemometry and Computational Fluid Dynamics, Ph.D. thesis, Liverpool Polytechnic.

Buchave, P. 1979, The Measurement of Turbulence with the Laser Doppler Anemometer - Errors and Correction Methods, Ph.D. thesis, State University of New York at Buffalo, Buffalo, NY.

Chang, S.M., Humphrey, J.AC., & Modavi, A. 1983, Turbulent Flow in a Duct with Strong Curvature and Downstream Tangent of Square Cross-Section, PCH PhysicoChemical Hydrodynamics, vol. 4, no. 3, pp. 243-260.

Durst, F. & Zaré, M. 1975, Laser Doppler Measurements in Two-Phase Flow, Proceedings of LDA Symposium Copenhagen

Humphrey, J.A.C., Whitelaw, J.H. & Yee, G. 1981, Turbulent Flow in a Duct with Strong Curvature, J. Fluid Mech., vol. 103, pp.443-463.

Kliafas, Y. 1983, Two-Phase Turbulent Flow Measurements in a 90° Bend using Laser Doppler Anemometry. Ph.D. thesis, Lawrence Berkeley Laboratory Report - 17244.

Parry, A.J. 1991, A Study of Turbulent Gas-Solid Flows in Pipe Bends, Ph.D. thesis, Liverpool Polytechnic.

Rashidi, M., Hetsroni, G. & Banerjee, S. 1990, Particle Turbulence Interaction in a Boundary Layer, Int. J. Multiphase Flow, vol. 16, no. 6, pp. 935 - 949.

Tanaka, T., Ishibashi, H., Tsuji, Y. & Morikawa, Y. 1989, Air-Solid Two-Phase Flow through a Bend (2nd Report: Particle Velocity, Concentration, and Effect on the Downstream), Trans. Japan Soc. Mech. Engineers, Part B, vol. 55, no. 518, pp. 2951 - 2956.

Tridimas, Y.D. 1981, Development and Application of Laser Doppler Anemometer Instrumentation for the Study of Gas-Solid Suspension Flows, Ph.D. thesis, Liverpool Polytechnic.

Yianneskis, M. & Whitelaw, J.H. 1984, Velocity Characteristics of Pipe and Jet Flows with High Particle Concentration, Proceedings Symp. on Liquid-Solid Flow and Erosive Wear in Industrial Equipment, New Orleans.

Zisselmar, R. & Molerus, O. 1979, Investigation of Solid-Liquid Pipe Flow with regard to Turbulence Modification, The Chemical Engineering Journal, 18, pp. 233 - 239.

PNEUMATIC PARTICLE CONVEYANCE IN PIPE BEND: SIMULTANEOUS TWO-PHASE PIV MEASUREMENTS OF THE SLIP VELOCITY BETWEEN THE AIR AND THE PARTICLE-PHASES

M L Jakobsen[1], D R McCluskey[1], W J Easson[1], D H Glass[2] and C A Greated[3]

[1] Department of Mechanical Engineering
[2] Department of Chemical Engineering
[3]Department of Physics and Astronomy

The University of Edinburgh, King's Buildings, Mayfield Road, Edinburgh, EH9 3JL, UK

1. INTRODUCTION

Pneumatic conveyance of solid particles is of interest in many industrial processes and has direct applications in most industrial powder handling. Important examples include coal combustion and food processing. However, it is a complex phenomenon with a technology, which at present is mostly based on empirical methods. The practical interest in understanding pneumatic particle conveyance is to be able to optimise the efficiency of a pipeline system to transport a given type of powder under given conditions. A minimum air flow is preferable to minimise both the energy input to the system and erosion particularly at pipeline bends. However, these constraints must not lead to sedimentation of powder and risks of blockage of the pipeline. One possible mechanism of particle deposition is the formation of ropes when the air and the solid phase segregate in upstream bends. Investigations using the Particle Image Velocimetry technique (PIV) (Adrian (1991)) for simultaneous velocity measurements of the air- and the particle-phases can provide more detailed experimental information to aid understanding of pneumatic conveyance and validation of numerical models of this phenomenon. In this case the formation of ropes in a vertical-to-horizontal 90° bend will be studied.

2. ROPING IN PIPE BEND

When a two-phase flow enters a bend and changes direction, segregation of the phases will occur if the acceleration of the flow becomes comparable with or exceeds the possible acceleration of the solids due to drag by the gas phase. If this is the case the solids will tend to continue along their original course and at some point collide with the outer wall of the bend. The curvature of the outer wall will focus the solid-phase by a combination of sliding and single/multiple collisions and finally form a more or less dense rope-shaped structure of solids, travelling along the outer bend wall. In the present situation, where the bend is 90 degrees with a vertical inlet and an outlet into a horizontal ducting, the rope will emerge from the bend along the top wall of the pipe. In the ducting gravity will disperse the rope, and the solids will then either be picked up by the gas flow again or fall to the bottom ducting, where they will form a new rope and eventually decelerate and deposit (McCluskey (1989)).

The rope will have a very high solid concentration and the kinematic behaviour of the solids will therefore be strongly influenced by particle-wake interaction and mutual collisions. Thus by mutually "sheltering" each other, the rope formation takes a consistent nature, which generally makes it difficult to re-disperse the rope. In a rope formation the particles will be in direct or indirect contact with the wall all the time. Thus high wall friction and reduced effective drag coefficients characterise the rope phenomenon. Besides these points the difficulties of splitting the rope up equally when bifurcating the pipeline adds to a general interest in understanding the generation and behaviour of roping.

3. TWO-PHASE PIV MEASUREMENTS

This extended PIV technique is unique in the way that it will obtain measurements from both the air-phase and the particle-phase simultaneously and hence enable a study of the interaction between the phases. The particle-phase consists of particles with a mean diameter in the range of 50-200μm. Under the given conditions their inertia will introduce considerable slip velocities, which are easy to measure. The velocity measurements of the air-phase is obtained by seeding it with particles so small (1-2μm) that they can follow the given air flow within the measurement accuracy (better than 1%). Thus by photographic means, the air-phase information can be distinguished from the particle-phase information. The acquired PIV image is then digitised and by means of image processing, the air-phase seeding and the particle-phase are separated. A combination of both image size and intensity are used to identify the two types of particle images. The separated PIV records are then analysed independently using conventional PIV techniques. Thus, the instantaneous spatial velocity map of each phase, and hence the slip velocity, can be determined. Figure 1 demonstrates a separation of the two phases on a PIV image acquired from a set-up of a particle-laden jet issuing into a concurrent air stream (McCluskey (1994)).

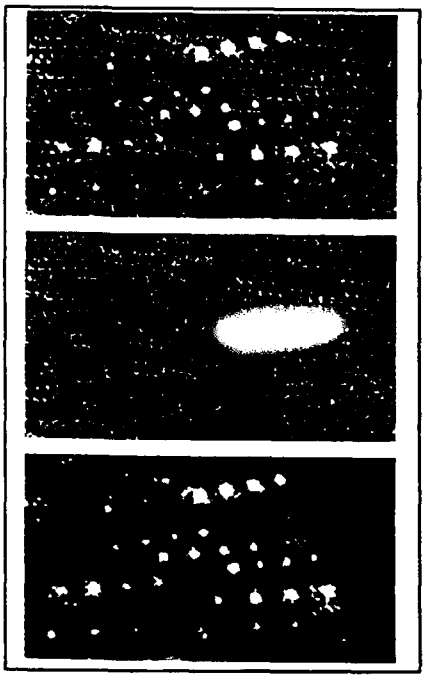

Fig. 1 Separation of air- and particle-phase in two-phase PIV images. From the top: a) The raw PIV image. b) The air-phase only after the particles have been identified and erased. c) The particle-phase only after subtracting the air-phase image from the raw PIV image.

4. EXPERIMENTAL SET-UP

The rig for the experiments on pneumatic conveyance is shown in figure 2. A fan generates the air flow and directs it through a small wind tunnel with grids and meshes to form a laminar flow. The air seeding (corn oil droplets) is introduced at the first stage of the wind tunnel. The last stage of the wind tunnel forms a contraction section to interface the pipeline. The pipeline is made of glass and has a inner diameter of 26mm. The particle phase (glass spheres) is introduced to the flow via a dust hopper at the vertical stage of the pipeline. Both phases then enter the test section, which consists of a 90 degree bend with a bend radius of 82.5 mm. After the bend follows a 2m long horizontal ducting before a cyclone separator and the outlet.

The fan can give a pure air flow velocity in the pipeline of up to 25m/s, and can roughly be adjusted with the help of a pitotstatic sensor in a range down to near zero velocity. The corn oil droplets have a diameter of 1-2μm, a mass density of 850kg/m^3 and are generated by an aerosol generator driven by compressed nitrogen. The glass spheres have a mean diameter of 75μm (94% above 44μm/3% above 115μm) and as solid spheres they have a mass density of 2500kg/m^3. They can, with the current dust hopper, be seeded at a rate of 1.2g/s.

A double Q-switched Nd-YAG laser delivers two short light pulses (6-7ns of duration) of 0.1J each at a wavelength of 532nm and with a pulse separation in time of 50μs. A lens arrangement and a parabolic mirror then collimate the laser beam into a thin light sheet. The sheet is less than 1mm thick and intersects the pipe bend in the plane of mirror symmetry - coming from above the test section. The camera is focused on the plane of the light sheet and is set up to acquire double exposed PIV images with a magnification of 0.25. Below a pulse separation of 40μs the pulse energy decreases quickly. Thus, restrict to using maximum pulse energy, the minimum size of the interrogation area possible for analysing the PIV image appeared to be 3mm in the image plane.

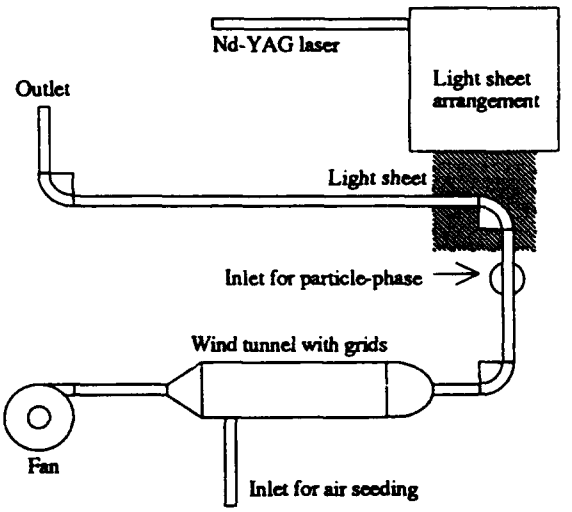

Fig. 2 Experimental set-up for PIV on pneumatic conveyance in a pipe bend.

5. EXPERIMENTS

The figures 3, 4 and 5 show the PIV images and corresponding velocity maps using an air flow velocity of approximately 15m/s and having a solid-air weight-ratio of 0, 4% and 7% respectively. Note that all the figures and corresponding velocity maps of the bend are rotated clockwise 90 degrees relative to the true orientation of the bend.

Figure 3.a shows the entire pipe bend and highlights the main problem of the present experimental configuration - reflections of the light sheet. The lines along the horizontal part of the pipe are reflections of diffracted light, emerging from the areas where the light sheet is transmitted through the pipe wall. The reflections only make PIV measurements possible in a very narrow area of the horizontal part of the pipe. Thus this paper will only consider the initial part of the pipe bend as illustrated by the corresponding "subtracted" velocity map of the air-phase in figure 3.b. A tangential velocity of a constant absolute value has been subtracted from the velocities in the map to illustrate the flow structures in more detail. Of special interest is a small region near the inner bend (just after the inlet) indicated by a relative broad boundary region with low air velocity. Further, a tendency of the velocities to have a radial component directed towards the

outer bend (even near the boundary at the inner bend) illustrates the secondary flow in the bend (Hawthorne (1951)).

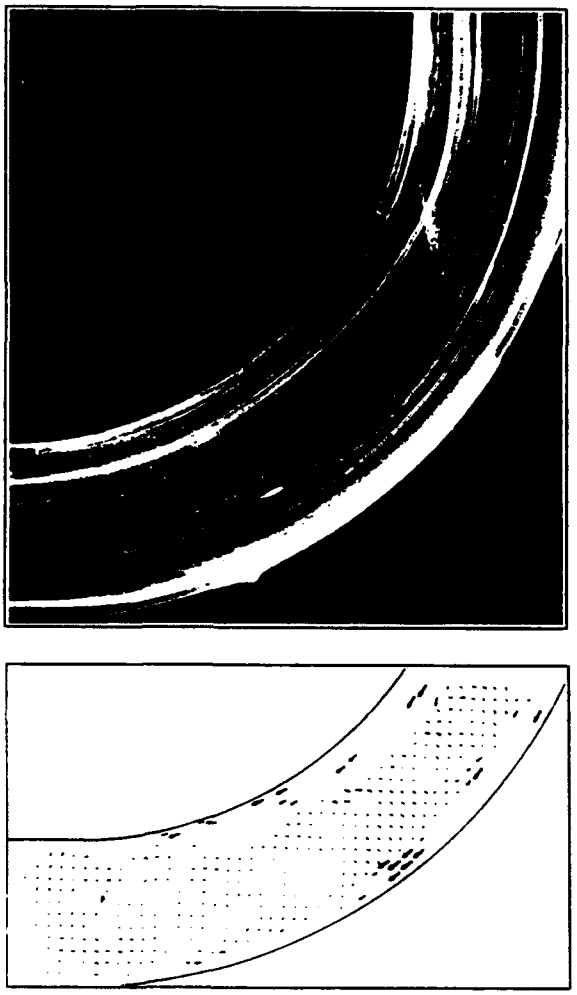

Fig. 3: Air flow with a solid/air ratio of 0%. From the top: a) A PIV image of entire pipe bend. b) The corresponding "subtracted" velocity map of the air-phase, acquired near the bend inlet.

Figure 4.a shows the particle-phase entering the bend almost uniformly distributed over the cross section of pipe. Particles colliding with the outer bend are redirected either by single or multiple elastic collisions or by sliding along the wall. The "subtracted" velocity map of the air-phase (figure 4.b) loses data near the inner bend (in the upper right part of the illustrated bend) due to additional reflections from the particles. Near the outer bend, data becomes more unstructured due to travelling single particles, whose wakes can not be resolved with the given experimental conditions. In general, the effective air velocity within this particle-wake area is reduced.

The velocity map of the particle-phase (figure 4.c) represents the particle velocities under the assumption that it is the average velocity within the interrogation area. With a low solid-air ratio the assumption of considering the particle-phase as a continuum is not appropriate. Multiple value measurements are possible due to the individual paths the particles in a given interrogation area might have taken. Particles which have collided once or only a few times with the wall have mostly conserved their inlet velocity. Particles which have collided many times and/or slid along the wall have lost considerable kinetic energy (as is the case for mutual collisions in the dense area, where the rope is formed) and are also likely to have gained spin.

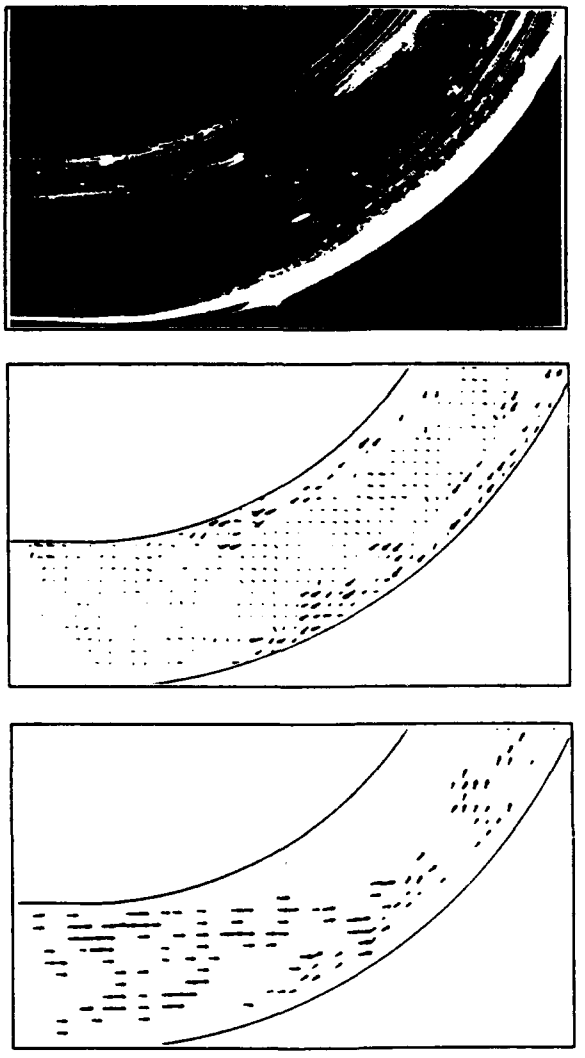

Fig. 4: Air-particle flow with a solid/air ratio of 4%. From the top: a) A PIV image of pipe bend. b) The corresponding "subtracted" velocity map of the air-phase. c) The velocity map of the particle-phase.

In figure 5.a the flow structure of the particle-phase becomes clearer. The relative high density of particle images (near the right corner of the image) indicates the area where the particle-phase is focused by collisions with the pipe wall. Most of the particles pass this region with significant velocity components perpendicular to the measurement plane. Thus, any early state of the rope will be scattered out of the measurement plane temporarily and leave the plane immediately upstream of the focus almost empty of particles. However, the curvature of the pipe bend will recapture the particles further upstream and finally form a stable rope, emerging from the bend along the pipe top wall.

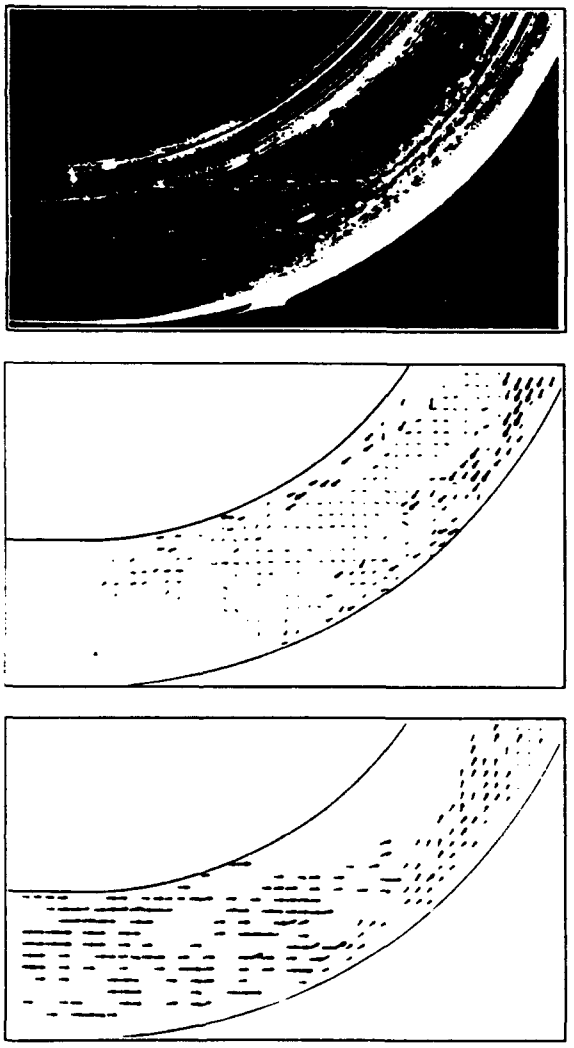

Fig. 5: Air-particle flow with a solid/air ratio of 7%. From the top: a) A PIV image of pipe bend. b) The corresponding "subtracted" velocity map of the air-phase. c) The velocity map of the particle-phase.

The influence of the particle-phase on the air-phase (figure 5.b) becomes more pronounced by increasing the solid-air ratio. The air flow appears to be split into two regions after the focus of the particle-phase: A region near the rope within which particle wakes are reducing the effective air velocity and a region of the "undisturbed" air flow with almost no particles but high air velocity. When increasing the solid/air ratio the first region expands in size and as the second region reduces, the air velocity of the "undisturbed" air flow increases due to continuity of the flow. At the same time, as figure 5.c illustrates, the PIV measurements of the particle-phase becomes more consistent. The measurements shown in these figures have not been corrected for aberrations due to using the pipe wall as a window for the PIV measurements.

6. FUTURE WORK

In figure 5 a considerably cross-talk between the two phases appears near the inlet of the pipe. This illustrates a problem of separating the phases when using algorithms based on global thresholds of e.g. intensity. Near the inlet of the bend the intensity of the light sheet is reduced partly due to significant reflections at the pipe wall, when the angle of incidence increases, and partly due to obstruction of the light sheet by a dense particle-phase (the area of focus) just above the inlet. Further it appears that the light sheet illuminates an increasing number of unfocused particles when the solid-air ratio is increased. This indicates that the forward scattering cone of the particles near the outer bend disperses a considerable amount of light away from the light sheet and additionally, by giving a misty background, the scattering effects complicates the global phase-separation algorithms directly. A future, more efficient algorithm for separating the two phases must therefore involve local setting of its parameters.

Also, from the point of view of analysing the PIV image, a new experimental configuration would be able to overcome some of the problems of the present rig. By letting the light sheet diverge from a point near the centre of the pipe bend, losses due to reflections at the pipe wall can be minimised, obstruction of the light by the particle-phase at high solid-air ratios will be avoided and scattering from the particle-phase will be reduced due to being backwards scattering instead of forward scattering.

Finally, involving a second and similar Nd-YAG laser, the pulse separation can be reduced by a factor of two thus enabling more detailed measurements in the pipe.

7. CONCLUSION

The work presented here is preliminary work on a project to investigate the pneumatic conveyance in pipeline bends and develop the PIV technique for this purpose. The first two-phase PIV measurements acquired on roping in a pipe bend have been shown and discussed in the view of improving the experiments for more detailed measurements. The results illustrate a clear influence from the particle-phase on the air-

phase when increasing the solid/air ratio. The air flow separates into a region of low effective air velocity near the forming rope and a region of high air velocity and a very poor solid density. The present experiments have only enabled measurements in the vertical part of the bend. However, future improvements on the experimental set-up will give measurements within the entire pipe bend, with less cross-talk between the phases and a higher spatial resolution.

ACKNOWLEDGEMENTS

The assistance of Tuffy, P. for photographic work and Hind, A.K. and Gray, C. for computational work. The work is funded by a research grant from Science and Engineering Research Council

REFERENCES

Adrian, R.J. 1991, Particle-imaging techniques for experimental fluid mechanics, Annu. Rev. Fluid Mech., vol. 23, pp 261-304.

McCluskey, D.R., Easson, W.J., Greated, C.A. & Glass, D.H. 1989, The use of particle image velocimetry to study roping in pneumatic conveyance, Particle & Particle Systems Characterisation, vol. 6, pp 129-132.

McCluskey, D.R., Hind, A.K., Rix, S.J.L., Jakobsen, M.L., Christy, J.R.E., Easson, W.J., Glass, D.H. & Greated, C.A. 1994, Development and application of a simultaneous two phase PIV system for the analysis of air-particle flow fields, Proc. IMechE Conference on Optical methods and data processing in heat and fluid flow, London, pp 99-109.

Hawthorne, W.R. 1951, Secondary circulation in fluid flow, Proc. Roy. Soc. A, vol. 206, pp 374-387.

MEASUREMENT OF PSEUDO-TURBULENCE IN BUBBLY FLOWS BY PHASE DOPPLER ANEMOMETRY

CARTELLIER A.

Laboratoire des Écoulements Géophysiques et Industriels
CNRS - UJF - INPG, Grenoble, France

ABSTRACT

Bubble-induced turbulence, or pseudo-turbulence, appears in two-phase flow modelling as a Reynolds stress tensor. The knowledge of this closure law is needed to predict the behaviour of bubbly flows in various engineering processes. Since Poiseuille bubbly flows offer an opportunity to directly characterise this tensor, experiments have been done at low Reynolds number of the liquid phase, and with spherical and quasi-monodispersed bubbles. This paper provides transverse profiles of the axial mean velocities and fluctuations for liquid and gas phases measured by PDA. Adaptations of the PDA system to get access to these variables are reported. Experimental data are checked against global flow rates, and the relative velocity is shown to agree with existing results. The importance of pseudo-turbulence in Poiseuille bubbly flows is confirmed, and the need for new modelling proposals of this tensor is demonstrated.

1. INTRODUCTION

Pseudo-turbulence stands for the agitation induced on the continuous phase by the presence of a dispersed phase. This concept, first introduced by Buyevich (1971), formally appears in two-phase flow modelling as a Reynolds stress tensor : it is one of the closure laws needed in the liquid momentum balance equation.

Pseudo-turbulence is of importance in engineering processes such as bubble columns, gas-liquid contactors, electrolysis cells, aerators, etc..., for which the shear-induced turbulence of the continuous phase is weak or absent. It could also be of importance for dispersed gas-liquid flows in ducts at high liquid Reynolds numbers, as it has been early shown by Sato and Sekoguchi (1975) and by Serizawa et al. (1975).

However, attempts to model the pseudo-turbulence are scarce. Nigmatulin (1979) derived a stress tensor for a uniform cloud of clean spherical bubbles at high particulate Reynolds number. Assuming that each bubble induces a potential disturbance of the liquid flow field, he obtained :

$$\overline{\overline{v_L v_L}}^X = \alpha \left[C_{T1} \left(\overline{v_G}^X - \overline{v_L}^X \right)^2 I + C_{T2} \left(\overline{v_G}^X - \overline{v_L}^X \right) \cdot \left(\overline{v_G}^X - \overline{v_L}^X \right) \right] \qquad (1)$$

where the coefficients C_{T1} and C_{T2} are of order unity. Similar formulas have been proposed by Biesheuvel and Van Wijngaarden (1984), Lance (1986), Arnold et al. (1990). However, eq.(1) does not take into account the influence of wakes (especially for contaminated interfaces), that of collective effects (inducing distorted trajectories), without speaking about the interactions between the shear-induced turbulence and the dispersed phase. To deal with such a complexity, recent trends in modelling introduce a specific treatment for the agitation induced by bubbles (Lance and Lopez de Bertodano (1992), Bel Fdhila and Simonin (1992)).

Few investigations have been devoted to the experimental characterisation of pseudo-turbulence. In a turbulent continuous flow field, it is indeed difficult to separate its contribution from that of the shear-induced turbulence. The common practice, which seems valid at low void fraction, is to assume that these two contributions can be superposed. Thus, the pseudo-turbulence is obtained as the difference between the Reynolds stress measured in two-phase flow conditions and that measured in one-phase flow at the same liquid flow rate.

To directly quantify pseudo-turbulence, we started an experimental investigation of bubbly flows at low Reynolds number of the continuous phase (Cartellier (1986)). Indeed, while the laminar / turbulent transition is not reached, the measured Reynolds stress reduces exactly to pseudo-turbulence. Beside, providing that both mean phasic velocities are accessible, and that the void fraction α is known, the validity of the eq.(1) can be checked.

Such "laminar" bubbly flows have been scarcely studied. Sato et al. (1981) investigated a single laminar condition, probably with ellipsoidal bubbles. More detailed results are available for cylindrical ducts and for controlled bubble size distributions, from Valukina et al. (1979), Nakoryakov et al. (1987), Kashinsky et al. (1993). These authors use the electrochemical method to get the liquid velocity and the void fraction ; the gas velocity was not measured.

Our own investigations are concerned with a plane Poiseuille flow disturbed by spherical and quasi-monodispersed bubbles. Some experimental results have been presented by Cartellier et al. (1993, 1994). The purpose of the present paper is to detail how the Phase Doppler Anemometry (PDA) technique has been used for local liquid and gas velocities measurements, and to underline the difficulties encountered with it. Examples of phasic velocity profiles will be given, and pseudo-turbulence measurements will be discussed.

2. EXPERIMENTAL FACILITY

The experimental facility is described in Cartellier et al. (1993) ; only key features are given hereafter. The test section (Fig.1) consists of a vertical (L=500mm x e=60mm) rectangular duct of height 4.5m. The liquid is a mixture of water and glucose syrup : its kinematic viscosity ν_L is about 30 $10^{-6}m^2/s$, its density is ρ_L = 1220 kg/m^3, and the surface tension with air is 0.059 N/m. Air is injected at the bottom, through 686 capillaries of internal diameter 90µm. The bubbles are all spherical. Their average diameter d (=2a) evolves slightly with gas and liquid flow rates in the range [1.15, 1.74]mm. For given flow rates, the deviation of size distributions is less than 20% of the average diameter, thus their diameter is always within the interval [0.95, 2.4]mm.

These co-current upward bubbly flows are characterised by six dimensionless variables :

* a channel aspect ratio which is fixed (k = L/e = 8.3),
* a dimensionless bubble radius ε = a/e, which is almost constant for these experiments ; it evolves from 0.0098 to 0.0145,
* a particulate Reynolds number $Rep = \rho_L G (2a)^3 / \mu_L^2$ built with the absolute value of the axial pressure gradient G, and which varies between 1 and 5,
* a measure of the contamination of interfaces $\kappa = \zeta / \mu_L$, where ζ denotes the retardation coefficient. ζ has been qualified : it leads to κ = 6.27, that means that interfaces are heavily contaminated,
* a volumetric gas flow rate ratio $\beta = Q_G/(Q_G+Q_L)$,
* a Poiseuille number $P = Q_L \mu_L / (\rho_L g L e^3)$ (or a liquid Reynolds number $Re_L = \rho_L Q_L / (2 L \mu_L)$), where $\mu_L = \rho_L \nu_L$, g is gravity, Q_L and Q_G are respectively the liquid and gas flow rates. For this study, P (or Re_L) and β are the actual control parameters.

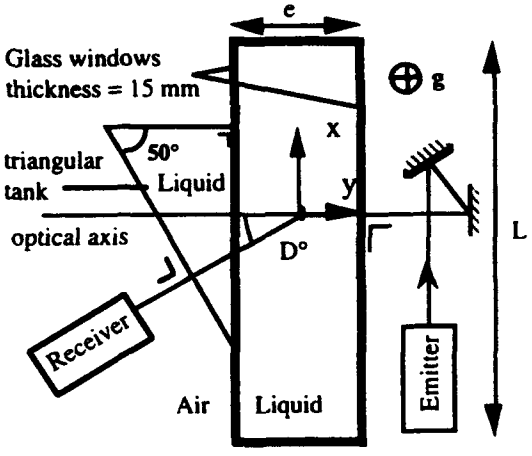

Fig. 1 Test section and optical set-up.

3. PDA IN BUBBLY FLOWS

It has been recognised early, probably first by Davies (1973), that large bubbles interacting with a laser Doppler anemometer (LDA), could deliver exploitable bursts. Large means here a bubble of the order or greater than the probe volume. Since that time, various problems have been studied ; let us recall briefly some of these.

The frequency/velocity relationship for large particles was discussed by Durst and Zaré (1975), and by Cartellier and Achard (1985). The latter authors have also detailed the nature of the velocity which is measured. It is indeed important to relate measured quantities with concepts introduced in modelling, and this question is by no means trivial in fluid/fluid two-phase flows.

LDA in bubbly flows was mainly used for continuous phase measurements so that efforts were dedicated to the elimination of the data issuing from the dispersed phase (Marié (1980), Theofanous and Sullivan (1982)). Some attempts have been also done to measure the dispersed phase velocity with LDA (Mahalingam et al. (1976), Ohba and Yuhara (1979)). To discriminate between phases, various procedures have been proposed based on waveform analysis or on the relative velocity. None of these is fully satisfactory. Thus, the advent of PDA allowing simultaneous measurements of size and velocity has provided a priori a reliable mean for the

discrimination between phases. Simulations of the response of large spherical bubbles have given some confidence on size measurements (Saffman et al. (1984), Borner and Zhan (1988), Brena de la Rosa et al. (1989), Cartellier (1992)). Defects of PDA such as trajectory ambiguity start to be analysed in detail (Gréhan et al. 1994), and alternate solutions are now proposed (Vassallo et al. (1993)). However, while PDA has been extensively used for mist flows, its application in bubbly flows involving large bubbles is still not so common, partly because bubble shapes are usually highly distorted, hindering thus accurate size measurements.

The bubbly flow investigated here is well suited for PDA since (i) bubbles remain spherical (which is a necessary condition for accurate size estimates) (ii) their size distribution is narrow, and (iii) the size of tracers is kept below 30µm thanks to mechanical filtering. Although few bigger tracers are expected to be also present (rust from pumps), the size distribution, composed of two well separated peaks, is almost ideal. Yet, the next sections will show that practice is not straightforward.

3.1 The PDA system

All the results given hereafter have been obtained with a PDA from Aerometrics (transmitter model XMT-1200-4S, receiver RCV-2200). The signal processing is a counter (software version 4.27F). Incident beams are perpendicular to the thick glasses which form the largest side of the channel. The deviation D is relative to the fluid medium. The actual deviation in air is larger due to the refractive index of the fluid which is about 1.47. To correct for this effect, a triangular tank, filled with the liquid used in the test section, is placed along the glasses. It allows the light scattered by bubbles at D=40° to cross the liquid/air interface at normal incidence. Thus, the projected fringe width as seen by the detector could be corrected by simple formula.

3.2 Simultaneous measurements

A first difficulty consists in the choice of an adequate optical configuration. For our apparatus, phase/diameter relationships for bubbles are available for receivers located in the plane of fringes, and for D=40° or 60° in the reflection mode. Only D=40° is possible here due to the high refractive index of the liquid. Since the fringe spacing δ defines the accessible size range, the sizes of bubbles lead to choose δ as large as 100µm (collimating lens 160mm, frontal lens 1m, track 1). With the existing software, simultaneous measurements imply that the same phase / diameter relationship is applied to both phases. Since the nature of tracers was not known (water is naturally seeded), the relation used for bubbles is probably not valid for tracers. However, this is expected to have a weak influence on velocity measurements. Indeed, since tracers are smaller than the fringe spacing, their phase cannot be miscalculated as corresponding to a bubble. Thus, cross talk error is avoided even though the diameter of tracers is not well measured.

Another difficulty is related with the large difference of amplitude between bursts delivered by tracers and bursts delivered by bubbles. Indeed, it is difficult to adjust the PM voltage and the trigger level to obtain comparable validation rates for both phases. This problem becomes more and more crucial as the void fraction increases since the background noise induced by multiple scattering on bubbles increases in proportion. Beside, to ensure an acceptable accuracy during the digitalisation of bursts, the size range dynamic is restricted to a factor of about 36. If diameters up to 3mm are to be detected, the minimum detectable size is about 80µm. Inversely, if tracers are to be seen, it is not possible to include large bubbles in the same acquisition. Clearly, simultaneous measurements of phasic velocities with this system are impossible in our conditions ; only the gas phase is well detected with this optical configuration.

3.3 Separate measurements with a single optical set-up

To detect the tracers with the previous optical configuration, we have tried to eliminate the information relative to bubbles. In this prospect, one can think to exploit a difference between reflection and refraction modes : these modes deliver projected fringes with opposite sense of rotation on the detector. To check the feasibility of this procedure, it was first necessary to test the ability of the system to detect the sense of rotation of the projected fringes. This was done in a simple experiment where a stream of monodispersed bubbles is generated by a single capillary tube. A change from reflection to refraction mode did not bring any difference on the recorded histograms. The processing is thus unable to detect the sense of rotation of fringes, so the validation of bursts delivered by bubbles cannot be hindered. Another solution is needed to get access to the liquid phase.

3.4 Separate measurements

Simultaneous measurements being not possible with this system, we choose to optimise the optical configuration according to the phase to be detected.

For the gas phase, the optical set-up described in §3.1 is used. The gas velocity is obtained by considering only the sub-set of data corresponding to diameters above 950µm. The results are almost insensitive to this

procedure because very few data are below this size. Due to the existence of noise, the sensitivity of the measurements to the threshold level has been checked. The axial mean gas velocities are almost insensitive to this parameter over a reasonable range. The fluctuation, overestimated at low threshold, reaches a well defined plateau for higher values, as it can be seen in Fig.2. Notice also that, to improve the accuracy, validation criteria were strengthened. This choice, combined with the low void fraction investigated, lead to validation rates below 1Hz.

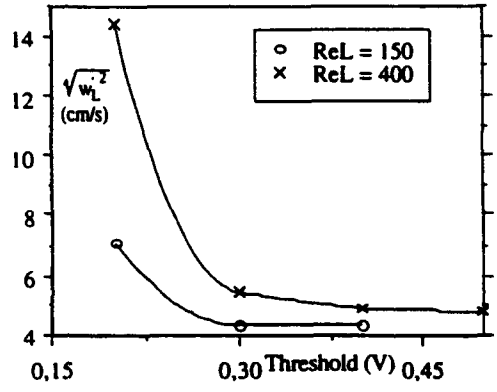

Fig.2 : Threshold effect on gas velocity fluctuations.

For the liquid phase, it is necessary to increase the amplitude of bursts delivered by tracers above the level of the noise induced by surrounding bubbles. This is done by positioning the receiver at a lower deviation, namely 15° (the triangular tank is not used). Since the discrimination cannot be ensured by size measurements, we used an alternative procedure based on visibility. The idea, previously exploited for LDA (Cartellier (1987)), is to match the projected fringe spacing to the detector sensitive area to increase the visibility of bursts emitted by tracers. In the same time, the projected fringe spacing from bubbles δ' becomes quite small (it evolves as 1/a). Providing that δ' is much less than the detector aperture, the visibility of the corresponding bursts strongly decreases leading to their rejection by the validation criteria. This procedure was adjusted by using raw signals, as shown in Fig 3 a and b. It is also probable that for such a deviation, the bubble bursts are composed of reflected and refracted rays : the combination of modes leading to distorted modulations, this effect reinforces the elimination of bubble signals.

An additional criteria is imposed on the burst amplitude. A typical size / amplitude plot is given in Fig.4. In that optical configuration, the detectable size range is restricted to 60µm : thus the bubbles can be seen

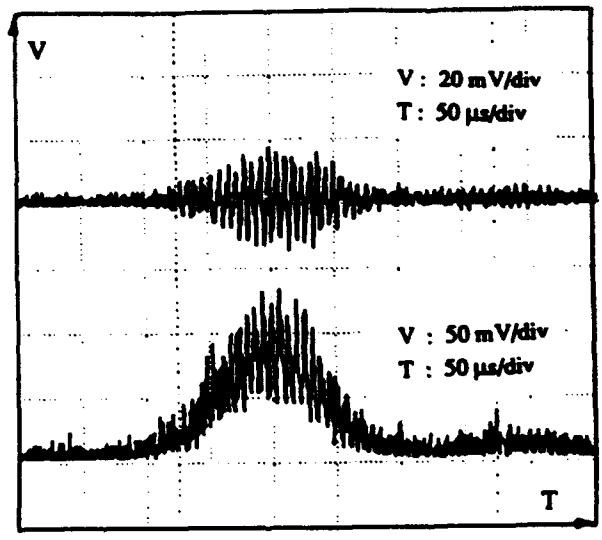

Fig.3 - a : Tracer burst for D=15°.

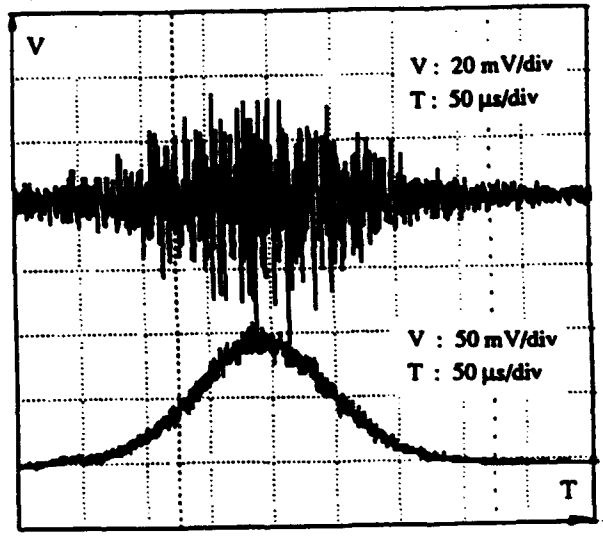

Fig.3 - b : Bubble burst at D=15°.

as small particles due to the periodicity of the phase / diameter relationship. However, very few data correspond to a high amplitude, that means that very few bubbles are actually detected and validated : this supports the proposed procedure. The existence of low amplitude data even above 30µm could be explained by the mode chosen i.e. reflection 30 which does not give the correct phase / diameter relationship for tracers (D=15°, the nature of tracers is unknown). Thus, to avoid as far as possible cross talk error, the validation is restricted to the data enclosed in the triangle ABC depicted in Fig.4.

Clearly, this somewhat qualitative procedure needs to be confirmed and quantifie. It should be considered as a practical tentative whose efficiency will be checked by the coherence measurements.

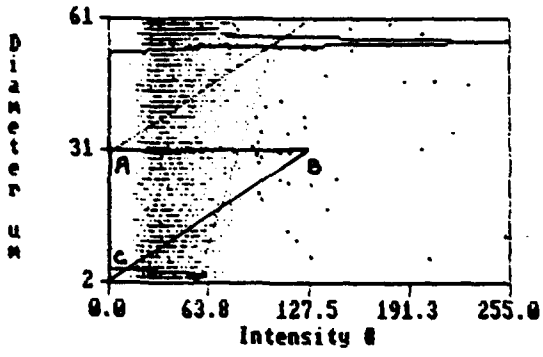

Fig.4 : Size/amplitude plot for D=15°.

3.5 Additional difficulties

During the experiments on bubble streams, the validity of size measurements at D=40° has been tested. Most recorded size histograms have a marked narrow peak. The agreement with the size obtained from photographs is about 10%. Starting with a given regular stream of bubbles, the injector was slightly moved, inducing a shift of the bubbles trajectories parallel to the plane of fringes : the size histogram thus obtained exhibits two well defined peaks (Fig.5) : the modified trajectory leads here to an underestimation of the size.

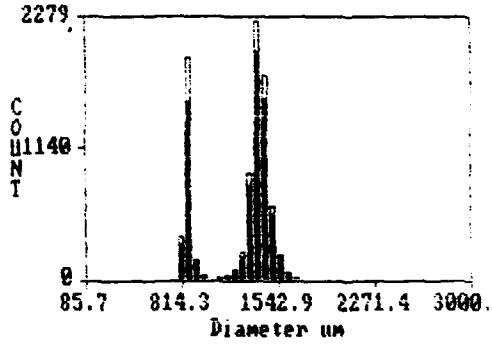

Fig.5 : Double peak size histogram due to trajectory influence.

In the test section, an opposite tendency was sometimes observed since some size histograms contains both true diameters (around 2.2mm) and overestimated diameters up to 3.4mm. This trend agrees with the simulations of Grehan et al. (1994). The reasons for the presence or absence of this defect are not clear. Possibly, for some flow conditions, strong interactions between bubbles lead to huge variations of trajectories while, at low void fraction, the deviations from vertical trajectories are less pronounced, and the corresponding histograms do not exhibit such overestimated sizes such as that shown in Fig.6.

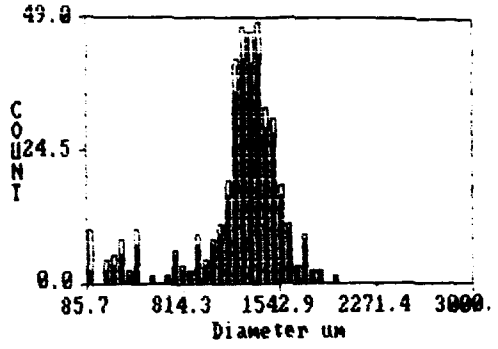

Fig.6 : Bubble size histogram recorded with PDA.

Another technical problem was encountered. Indeed, the velocities to be measured are quite low (0 to 50cm/s), inducing low Doppler frequencies especially during gas measurements for which the fringe spacing is large. The electronic filters of our system being unable to process these frequencies, a frequency shift has to be used in all cases. This shift, obtained by the rotation of the gratings, cannot be less than 2m/s because the rotation is unstable below approximately 200 rpm. As a result, the frequency shift is much higher than the frequency range of bursts, and it induces a loss of accuracy on velocity measurements, and probably a high artificial turbulence which is hard to quantify. For the liquid phase, the situation is better because of the lower fringe spacing used (δ = 2.7μm). The artificial turbulence, checked in Poiseuille flow, has been found to be about 3% : this value, although not excellent, is low enough to allow representative measurements of pseudo-turbulence in two-phase conditions.

4. MEAN VELOCITIES AND VOID FRACTION

Experimental results given hereafter have been obtained 3 meters above the injector. Typical transverse (y direction) liquid velocity profiles obtained in the median plane (x=0) are shown in Fig.7 for β=2.5%. For Re_L =160, the global liquid flow rate deduced from these data (combined with the liquid fraction distribution) agrees within 4% with global measurements. For other Re_L, the flow is not exactly two-dimensional (Cartellier et al. (1993)) and the comparison exhibits defects up to 10%.

The deviation from the parabolic solution of Poiseuille flow is pronounced especially near walls.

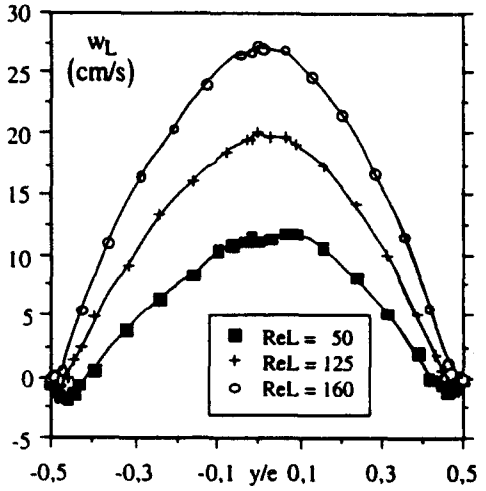

Fig.7 : Axial liquid velocity profile for $\beta = 2.5\%$.

When the liquid Reynolds number increases, a secondary motion appears in the vicinity of walls where the liquid flows downward. This behaviour has also been observed in bubble columns.

Fig 8 gives all the local variables for fixed flow rates. Although these measurements have been done over different days, i.e. with slightly different liquid viscosities, the gas velocity follows closely the liquid profile. Also, the relative velocity is in agreement with available data (Cartellier et al. (1993)) except at the center of the channel and near walls. The former error is attributed to the bad convergence of the average velocities : indeed, by doubling the number of data, a relative velocity of 2.2 cm/s was obtained, a value which is close to the expected one (i.e. 2.8cm/s). For the wall region, it must be noticed that no correction has been introduced for the localisation of the actual probe volume for bubbles. Indeed, the largest dimension of this volume is directed along y, and it is quite huge (few centimetres) for the optical set-up used for bubbles. Thus, it is difficult in practice to precisely control the locii of measurements. This uncertainty is probably larger than the probe volume correction which is of the order of the bubble size. Beside, bubbles never stick on the wall, and are not much deformed in the vicinity of the wall. Thus, it is senseless to try to get gas measurements at distances to the wall less than a bubble radius. For Re_L=300 and β=2%, the average bubble diameter is 1.46mm. Thus gas measurements were stopped at 0.7mm from the wall ; beyond this point, no validation occurs.

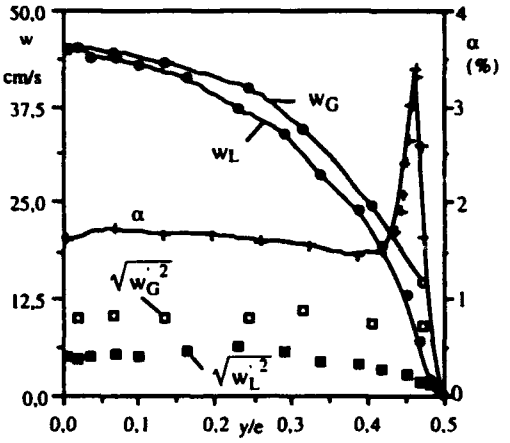

Fig.8 : Profiles of local variables for Re_L=300, β =2%.

The agreement between global flow rates and those obtained by the integration of transverse profiles (weighted by the void fraction) are 7% for the liquid phase and 1.5% for the gas phase. This gives some confidence in the proposed discrimination technique.

5. PSEUDO-TURBULENCE

Only the axial velocity fluctuations have been measured. Fig.8 illustrates the high values recorded for this term : in the center of the channel where the void fraction is less than 2%, the gas fluctuations are about 10%, and the liquid fluctuations are about 6%. Similar magnitudes are reported by Kashinsky et al. (1993). Other profiles of the liquid fluctuations, given in Fig.9, show comparable values of the liquid agitation for various Re_L.

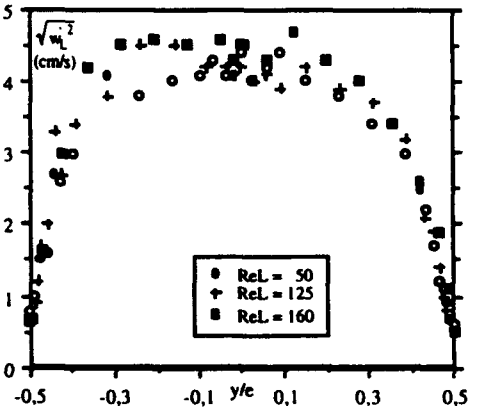

Fig.9 : Liquid axial velocity fluctuations for $\beta = 2.5\%$.

To analyse the modifications of the liquid fluctuations versus the control parameters, additional measurements have been done at the center of the duct, in a region where the void fraction is nearly uniform. The evolution of the relative fluctuation with Re_L at fixed values of β is given in Fig.10. Gas fluctuations are clearly larger than those of the liquid phase, despite the uncertainty due the artificial turbulence (see.§3.5). From Fig.11, the fluctuations are shown to increase with β, with a sharp increase at low gas content. Notice that PDA results are in good agreement with the data obtained with conical hot film probes (indicated as HFP).

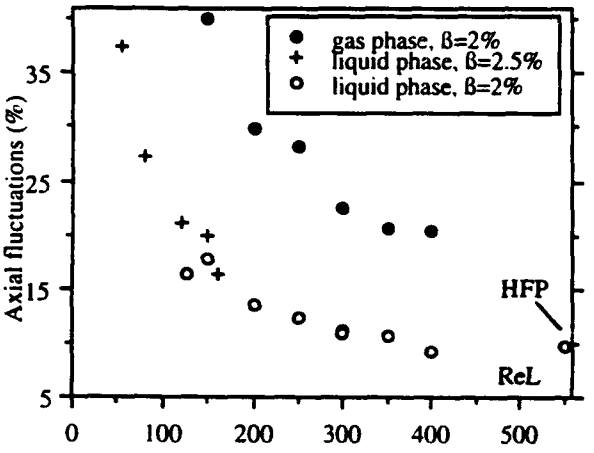

Fig.10 : Axial fluctuations for both phases for β =2%.

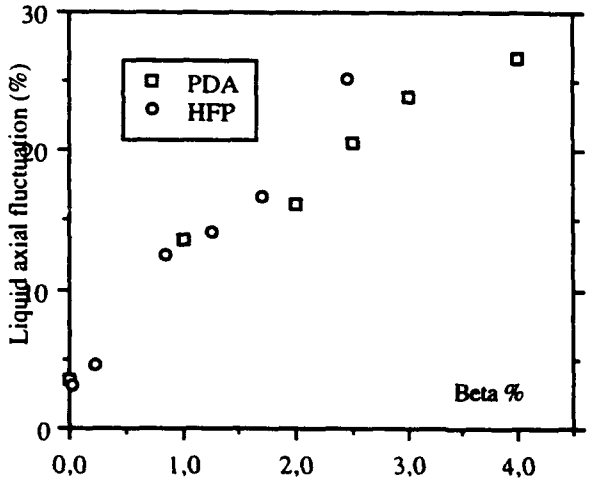

Fig.11 : Liquid axial fluctuations for Re_L = 125.

Finally, eq.(1) has been checked using measured variables. Since the fluctuations are of the magnitude of the relative velocity, the coefficient C_{Ti} are not of order one but are far greater. In fact, these experimental conditions deviate from the hypothesis of the model since the particulate Reynolds number is rather low. Thus, the flow disturbances are mainly due to the distorted trajectories observed in our conditions. Such complex trajectories are induced by strong interactions between bubbles, interactions which are promoted here by the high viscosity of the continuous phase. Thus, new closure laws traducing such effects are needed.

6. CONCLUSION

PDA has been applied to an almost ideal bubbly flow composed of spherical bubbles with a narrow size distribution and tracers of much smaller size. Simultaneous measurements have been shown to be impossible with our PDA. An alternate solution has been proposed, which gives access to mean and fluctuating components of both phasic velocities. The experimental profiles have been cross-checked with available results, demonstrating the correctness of the measuring technique. However, improvements are necessary to ensure (i) a better discrimination between phases, (ii) an accurate localisation of the measurements, and (iii) a reliable detection of the continuous phase. It is hoped that detailed simulations of PDA will provide some solution to these problems.

A first quantification of pseudo-turbulence in Poiseuille bubbly flow has shown that the theoretical proposal is in default when strong interactions between bubbles occur. Thus there is a crucial need for modelling pseudo-turbulence by including such effects. Future experimental studies will be dedicated to quantify the transverse fluctuations (along y) and some extra diagonal terms among which the zy component which is expected to play a major role in the dynamics of Poiseuille bubbly flows.

ACKNOWLEDGMENTS

Part of this work was accomplished under a grant of CNRS and GREDIC.

REFERENCES

Arnold, G., Drew, D. & Lahey, R. 1990, An assessment of multiphase flow models using the second law of thermodynamics, Int. J. Multiphase Flow, vol.16, pp.481-494.

Bel Fdhila, R. & Simonin, O. 1992, Modélisation des écoulements turbulents à bulles application à un élargissement brusque en conduite verticale, Note

Technique, HE 44/92.08, EdF.
Biesheuvel, R. & van Wijngaarden, L. 1984, Two-phase flow equations for a dilute dispersion of gas bubbles in liquid, J. Fluid Mech., vol 148, pp.301-318.
Borner, T. & Zhan, L. 1988, LDV-signal-analysis for particle velocity and size detection using geometrical optics, in Optical particle sizing : theory and practice, ed. G. Gouesbet & G. Gréhan, pp.177-192, Plenum Press, New York and London.
Brena de la Rosa, A., Sankar, S., Weber, B., Wang, G. & Bachalo, W. 1989, A theoretical and experimental study of the characterization of bubbles using light scattering interferometry, Proc. FED - Int. Symp. on Cavitation Inception, ed. W. Morgan & B. Parkin,vol.89,pp.63-72.
Buyevich, Yu. 1971, Statistical hydrodynamics of dispersed systems I, J. Fluid Mech., vol. 49,pp.489-507.
Cartellier, A. 1986, Contribution à l'étude des écoulements à bulles : cas des écoulements laminaires plans, Thèse INP, Grenoble.
Cartellier, A. 1987, LDA signals in dispersed flows : discrimination and noise, Proc. 2nd Int. Conf. Laser Anemometry - Advances and Applications, Strathclyde, pp.443-452.
Cartellier, A. 1992, Local velocity and size measurements of particles in dense suspensions : theory and design of endoscopic grating velocimeter-granulometers, Applied Optics, vol.31,pp.3493-3505
Cartellier, A. & Achard, J.L. 1985, Limitations of the classical LDA formula for velocity measurements for large particles in two-phase suspension flows, Phys. Chem. Hydrodynamics, vol.6,pp.463-481.
Cartellier, A., Moechti, T. & Achard, J.L. 1993, Plane Poiseuille bubbly flows : void fraction and wall shear stress, Experimental Heat Transfer, Fluid Mechanics and Thermodynamics, ed. Kelleher M. et al., vol.2, pp.1402-1409, Elsevier.
Cartellier, A., Moechti, T. & Achard, J.L. 1994, Local variables in plane Poiseuille bubbly flows, 7th Workshop on two-phase flow predictions, Erlangen, Ercoftac/IAHR.
Davies, W. 1973, Velocity measurements in bubbly two-phase flows using laser doppler anemometry - I, Technical note 184, University of Toronto.
Durst, F. & Zaré, M. 1975, Laser Doppler measurements in two-phase flows, Proc. LDA Symp., Copenhagen.
Gréhan, G., Onofri, F., Girasole, T., Gouesbet, G., Durst, F. & Tropea, C. 1994, Measurement of bubble by phase doppler technique and trajectory ambiguity, Proc. 7th Int. Symp. on Applications of Laser Techniques to Fluid Mech., Lisbon.
Kashinsky, O., Timkin, L. & Cartellier, A. 1993, Experimental study of "laminar" bubbly flows in a vertical pipe, Exp. in Fluids, vol.15,pp.308-314.
Lance, M. 1986, Étude de la turbulence dans les écoulements diphasiques dispersés, Doctorat d'Etat, Lyon.
Lance, M. & Lopez de Bertodano, M. 1992, Phase distribution phenomena and wall effects in bubbly two-phase flows, Third Int. Worshop on Two-phase Flow turbulence, Imperial College, London.
Mahalingam, R., Limaye, R. & Brink, J. 1976, Velocity measurements in two-phase bubble-flow regime with laser doppler anemometry, AIChE J., vol.22, pp.1152-1155.
Marié, J.L. 1980, Contribution au développement de la LDA en écoulements dispersé, Thèse D.I., ECL, Lyon.
Nakoryakov, V., Kashinsky, O., Kozmenko, B. & Gorelik, R. 1987, Investigation of upward bubbly flow at low liquid phase velocities, Soviet J. Appl. Physics, vol.1,pp.13-18.
Nigmatulin, R. 1979, Spatial averaging in the mechanics of heterogeneous and dispersed systems, Int. J. Multiphase Flow, vol.5, pp.353-385.
Ohba, K. & Yuhara, T. 1979, Velocity measurements of both phases in two-phase flow using laser doppler velocimeter, Proc. IMEKO Symp. on Flow Measurement and Control in Industry, Tokyo, pp.191-186.
Saffman, M., Buchhave, P. & Tanger, H. 1984, Simultaneous measurement of size, concentration and velocity of spherical particles by a laser Doppler method, Proc. 2nd Int. Symp. on Applications of Laser Anemometry to Fluid Mechanics, Lisbon, paper 8.1.
Sato, Y. & Sekoguchi, K. 1975, Liquid velocity distribution in two-phase bubble flow, Int. J. Multiphase Flow, vol.2, pp.79-95.
Sato, Y., Sadatomi, M. & Sekoguchi K. 1981, Momentum and heat transfer in two-phase bubble flow -I & II, Int. J. Multiphase Flow, vol.7, pp.167-190.
Serizawa, A., Kataoka, I. & Michiyoshi I. 1975, Turbulence structure of air-water bubbly flow - II Local properties, Int. J. Multiphase Flow, vol.2, pp.235-246.
Theofanous, T. & Sullivan, J. 1982, Turbulence in two phase dispersed flows, J. Fluid Mech., vol.116, pp.343-362.
Valukina, N., Kozmenko, B. & Kashinsky, O. 1979, Characterisation of a flow of monodispersed gas-liquid mixture in a vertical tube, translated from Inzhenerno-Fizicheskij Zhurnal, vol.36,pp.695-699.
Vassallo, P., Trabold, T., Moore, W. & Kirouac, G. 1993, Measurement of velocities in gas-liquid two-phase flow using laser Doppler velocimeter, Exp. in Fluids, vol.15,pp.227-230.

Session 32.
Holog. Interf. & Tomography

Mass Transfer Measurement by Holographic Interferometry for a Turbulent Jet Impinging on a Flat Surface at Moderate Reynolds Numbers

J J Nebrensky and N Macleod

Department of Chemical Engineering, University of Edinburgh

Edinburgh, Scotland EH9 3JL

ABSTRACT

The swollen polymer method is an established technique for the measurement of both local and averaged mass transfer coefficients, but in the past attempts to determine local transfer coefficients by using this method in conjunction with live fringe holographic interferometry have been hampered by spurious fringe movements. By using a prism to gain optical access to the polymer surface from behind it is possible to eliminate these movements and get quantitative measurements of the local transfer coefficient solely from the observation of live fringes. As an illustration of this technique, measurements are reported of the convective mass transfer coefficients due to a free jet impinging on a flat surface from a distance of 2.1 tube diameters at Reynolds numbers of 8100 to 18700.

1. INTRODUCTION

The swollen polymer method is an established technique for making mass transfer measurements which has several advantages over the conceptually similar napthalene sublimation technique. A test surface is coated with a layer of silicone rubber which is then swollen to equilibrium with an appropriate solvent. Evaporation of the solvent causes the polymer layer to shrink and it can be shown that, for an initial period of time (the "constant rate period"), the local rate of recession is directly proportional to the local mass-transfer coefficient (Macleod & Todd 1973). The use of live-fringe holographic interferometry to measure surface recession can provide both qualitative and quantitative results in real time over the whole field of view.

Previous users of this technique (Larez, 1982; Gholizadeh, 1992) have observed spurious fringe movements, mainly of two distinct kinds known as "woozing" and "wavering", which make it difficult to determine fringe order accurately at a given point. Woozing involves the concerted motion of all visible fringes, and is attributable to refractive index variation in the path of the reference beam. Wavering is localised motion, say only of part of one fringe, which is caused by refractive index fluctuations in the fluid near the test object.

These refractive index changes in the fluid are due to composition variations: different fluid regions may contain different amounts of the solvent. Near the swollen polymer surface large concentration gradients may be present, which will produce the wavering effect in an analogous process to the everyday phenomenon of heat shimmer. The large scale movement of fluid away from the mass-transferring surface will also tend to carry solvent vapour into the relatively narrow unexpanded beams, causing the woozing effect. Wavering and woozing could also be due to thermal effects in certain situations, such as where the jet is at a different temperature to the surroundings.

By incorporating a right-angle prism into the coated substrate (Fig. 1), it is possible to make holograms of the transparent polymer coating from behind by using the phenomenon of total internal reflection; thus keeping the light paths away from solvent laden fluid (Harper and Macleod, 1978). Problems arising from a progressive loss of fringe contrast have been reported with this total internal reflection technique in the past, but were not encountered in this work.

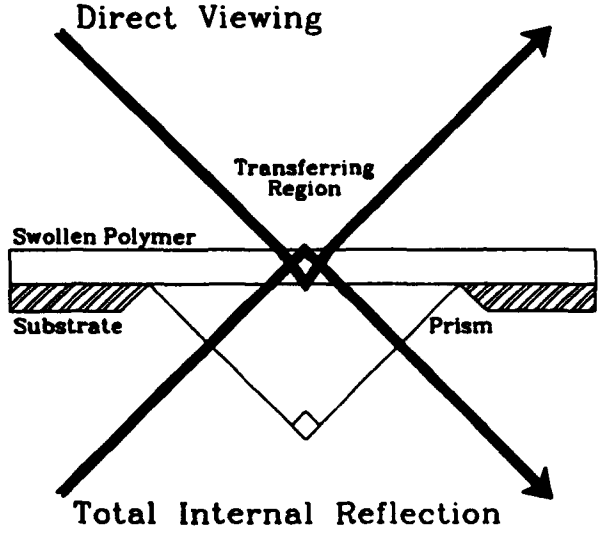

Figure 1: Diagram showing that direct view illumination of the test plate passes through the solvent-laden fluid, whereas the total internal reflection method avoids this.

As mass transfer proceeds, alternate light and dark interference fringes form when the receding surface is viewed through a hologram of its original state. The fringes will be seen to move away from areas of high mass-transfer towards areas of low mass-transfer. For a flat test surface the fringes will represent contour lines of equal mass transfer coefficient. Local maxima in the mass-transfer coefficient show up as sources of fringes and local minima show up as areas where fringes converge and vanish. The local mass transfer rate at a given point can be found simply from counting the number of fringes passing that point during a known time, while the distribution is clearly apparent from the overall fringe pattern.

After use the test plate can easily be restored simply by re-soaking in a bath of solvent for a couple of hours. Use of different solvents allows a wide choice of transfer rate to suit different conditions and allows investigation of the effects of Schmidt number variation.

2. THEORY

During the constant rate period the volumes of the solvent and the polymer are taken to be strictly additive, i.e. if a region of the swollen polymer surface of area δA recedes a distance h due to the evaporation of solvent over a time t, then the volume of liquid solvent lost can be taken to be $h\,\delta A$. The mass of solvent lost must then be $h\,\rho_s\,\delta A$, where ρ_s is the density of the liquid solvent, and so it can be seen that the mass flux per unit area $\dot{m}$ will be given by:

$$\dot{m} = \rho_s h/t \qquad (1)$$

The surface recession h is measured by holographic interferometry as follows: if one bright fringe passes across the point of interest, then the optical path through that point has been altered by the surface recession by one wavelength λ. It is convenient to relate the surface recession with the path length change by using a geometrical constant C, whose value will depend on the refractive index of the swollen polymer and the angle at which the light is reflected from the surface, such that

$$h = N\lambda/C \qquad (2)$$

and so

$$\dot{m} = \rho_s \lambda/C\ N/t \qquad (3)$$

where N is the number of bright fringes that pass over a point during a time t.

The mass flux per unit area is proportional to the concentration driving force, so we have

$$\dot{m} = \beta M_s (c_w - c_b) \qquad (4)$$

where β is the mass transfer coefficient, M_s the molar mass of the swelling agent and c_w and c_b are the molar concentrations of the agent at the polymer surface and in the bulk of the fluid respectively. The latter can be taken to be zero. During the constant rate period the swelling agent in the polymer will be in equilibrium with that just outside, and so c_w can be obtained from the vapour pressure of the solvent P_s by using the Ideal Gas Equation to get:

$$c_w = P_s / RT \qquad (5)$$

Substituting (5) into (4) then gives

$$\dot{m} = \beta M_s P_s /RT \qquad (6)$$

Re-arranging and substituting (3) in thus gives:

$$\beta = 1000\,(\lambda\, RT/CP_s M_s)\, N/t \qquad (7)$$

where all quantities are in common metric units. The factor of one thousand is due to the fact that M_s is usually expressed in grams per mole, rather than kilograms/mole.

The above analysis is valid for both the direct viewing and total internal reflection methods as the only difference will be in the value of C used. For the total internal reflection work the value of C was 1.89, whereas for a typical direct view case C is around unity.

The mass transfer coefficient β may be non-dimensionalised as the Sherwood number Sh:

$$Sh = \beta L / D \qquad (8)$$

where L is a typical length for the system and D the diffusion coefficient of the swelling agent in the fluid.

3. EXPERIMENTAL METHOD

The test surface was made by setting a glass right-angle prism 64 by 64 by 91 mm with its hypotenuse flush with the surface of an Aluminium sheet 200 by 200 mm (Fig. 2), and applying a uniform layer of GE RTV 615 transparent silicone rubber about 1mm thick over the entire front face. The rubber was then left to cure at room temperature for 24 hours, forming a smooth front surface as it set. The cured polymer was initially swollen by putting the plate face down in a tray of Ethyl Salicylate for a day.

The removable test plate was supported in a kinematic mount on an air-cushioned optical table. Holograms were made using a Newport HC300 thermoplastic holographic camera with an HC500 controller. Illumination was provided by a polarised 25mW Helium-Neon laser. The object and reference beams were separated using a variable ratio beam splitter and both were spatially filtered by microscope objectives and pinholes. A ground glass plate was placed in the object beam just before and as close as possible to the prism to reduce glare. The HC500 controller automates hologram production after the initial setting up, and the holograms are ready to view approximately 15s after exposure.

The plate was then subjected to a normal free jet of compressed air from a plain circular nozzle 7 mm in diameter 15mm from the plate, with Reynolds numbers ranging from 8100 to 18700 based on the tube diameter. The air was taken from the building's compressed air supply, with the flow rate measured by a rotameter.

As the mass transfer progressed the developing fringe pattern was recorded with a video camera on to VHS videotape, for later analysis.

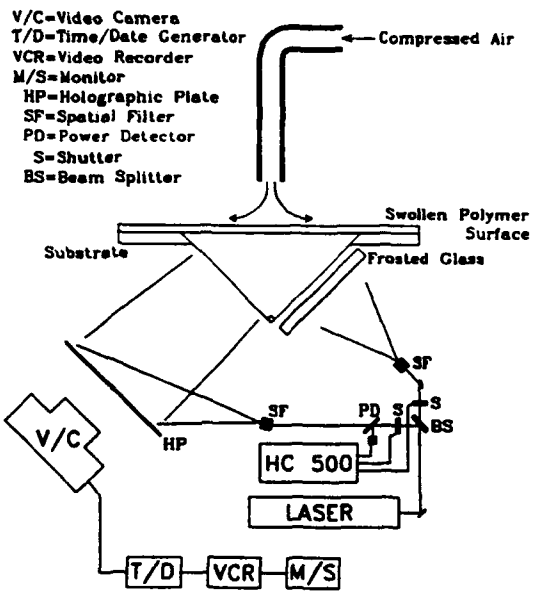

Figure 2: Experimental layout.

4. RESULTS

Figure 3 shows part of a series of photographs of live fringes developing at a Reynolds number of about 16 000. They appear elliptical as they are being viewed at an angle (Fig. 2). Line A indicates the stagnation point, where two successive dark fringes can be seen to form and spread outward.

Fringes can also be seen to form and move out from the area marked by line C (dark fringes forming in frames 2 and 5). This indicates a secondary maximum in transfer coefficient, separated from the central maximum by a local minimum at line B, where fringes can be seen to merge (light fringes in frames 1 and 3).

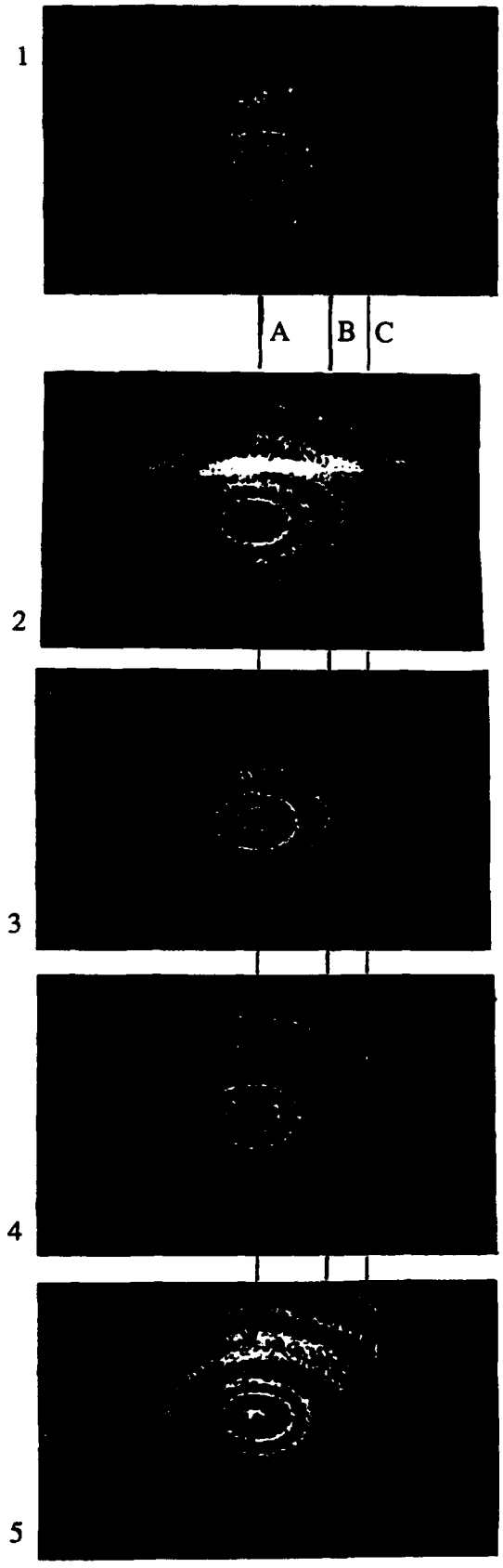

Figure 3: Part of a series of photographs of live fringes developing at a Reynolds number of about 16 000, with the stagnation point A and secondary minimum B and maximum C of mass transfer indicated.

As the flow rate is increased the difference between the secondary maximum and minimum becomes greater, whereas at lower flow rates they merge into a plateau. Figure 4 shows the results from several runs at different Reynolds numbers, as well as normalised local Nusselt numbers obtained for a jet with a Reynolds number of 23300 by Baughn et al (1991) using a liquid crystal technique.

It can be seen that the methods agree on the location of the secondary maximum and minimum, but the liquid crystal results tend to be significantly lower than the mass-transfer ones. This is probably because Baughn et al were looking at a constant heat flux case rather than the constant wall temperature one modelled here, and may also be due to inaccuracies in the values of the diffusion coefficient and vapour pressure of Ethyl Salicylate used in the derivation of the results.

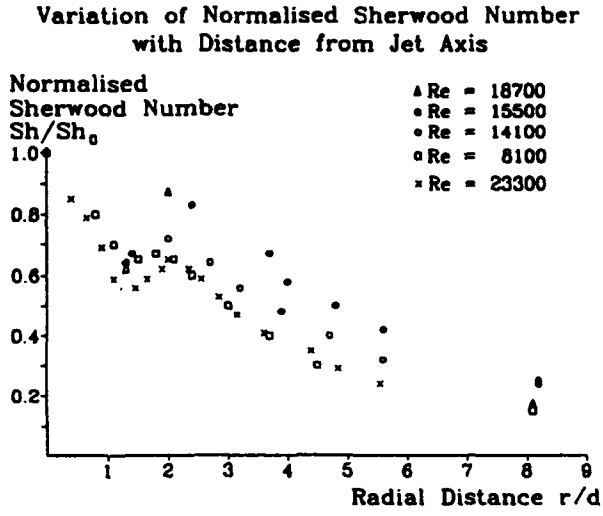

Figure 4: Graph of normalised local Sherwood number (based on nozzle diameter d) against radial distance from jet axis for Reynolds numbers of 8100, 14100, 15600 and 18700, also showing normalised Nusselt numbers obtained by Baughn et al (1991) at a Reynolds number of 23300.

5. CONCLUSION

The total internal reflection method for the holographic interferometry of swollen polymers allows the light paths to be kept separate from the experimental fluid. This eliminates woozing and wavering to such a degree that quantitative measurements can be obtained solely from observation of live fringes.

Keeping the optical paths and fluid separated allows the use of non-transparent or inhomogeneous fluids. It should also be possible to use other optical techniques, such as LDA or PIV, to make simultaneous measurements of the bulk fluid flow in front of the plate without any interference between the two systems.

At present work is in progress to extend the technique to situations involving natural or mixed convection, by identifying suitable solvent and polymer combinations.

Acknowledgement: This work was supported by an SERC CASE award in association with AEA Technology, Windscale, Cumbria.

REFERENCES

Baughn, J.W, Hechanova, A.E. and Yan, X. 1991. Experimental Study of Entrainment Effects on the Heat Transfer from a Flat Surface to a Heated Circular Impinging Jet. ASME Journal of Heat Transfer vol.113 pp 1023-1025.

Gholizadeh, N. 1992. Interferometric Measurement of Local Mass Transfer Rates to an Impinging Jet by Non-Photographic Holography. PhD Thesis, University of Edinburgh, UK.

Harper, A.J and Macleod, N. 1978. Hot Spots in Heat Transfer. Physics Bulletin January 1978 p.13.

Larez, A L. 1982. The Measurement of Convective Mass Transfer Coefficients by Holographic Interferometry. PhD Thesis, University of Edinburgh, UK.

Macleod, N and Todd, R.B. 1973. Experimental Determination of Wall-Fluid Mass-Transfer Coefficients using Plasticised Polymer Surface Coatings. Int. Journal of Heat and Mass Transfer vol. 16 pp 485-504.

TOMOGRAPHIC HIGH-SPEED DIGITAL HOLOGRAPHIC INTERFEROMETRY MEASUREMENTS IN FREE-JET FLOWS

Brenda H. Timmerman
Department of Aerospace Engineering
Delft University of Technology
Laboratory for High Speed Aerodynamics
P.O. Box 5058, 2600 GB Delft, The Netherlands

David W. Watt
Department of Mechanical Engineering
The University of New Hampshire
Kingsbury Hall
Durham, NH 03824, USA

1 ABSTRACT

A dual-reference beam, plane-wave illumination, holographic interferometry set-up has been developed which can operate in a rapid double-pulse mode and which provides multiple simultaneous views of a compressible flow field. It is intended for the quantitative study of the density distribution in a 3-D (turbulent) flow field as well as for the study of density changes that take place in a compressible turbulent flow in very short time intervals (1 - 800 μsec). Preliminary results were obtained for compressible free-jet flows.

2 INTRODUCTION

Holographic phase-stepping interferometry is a flow visualisation method which is non-intrusive and can give quantitative results concerning the density distribution in a compressible flow field.

Since no probes have to be put into the flow and no seeding particles are needed it is a truly non-intrusive technique which produces whole-field measurements at one instant of time.

Using this technique the phase delay of a light beam going through the flow field is measured. This phase delay is caused by an inhomogeneous distribution of the refractive index (density) and is proportional to a line integral of the density along the light path through the flow field. Therefore, once the phase delay is known, the average density in the flow field can be determined directly.

A two-reference beam, plane wave, holographic interferometer set-up has been used which can be placed over a flow field, e.g. generated in a wind tunnel (Lanen *et al.*). The flows are recorded on a holographic plate with a pulsed ruby laser. Also, the set-up can be used to capture two flow situations separately at very small time intervals (1-800 μsec) using the laser in double-pulse mode. By phase-stepping the resulting interferograms, rapid density fluctuations in the flow can be determined quantitatively, which will provide some insight regarding the time-scales involved in turbulent motion.

However, as these measurements represent data integrated along the width of the flow field (i.e. projection data) the local density (fluctuations) in a 3-D flow field cannot be determined from a single projection. Also, the observed density changes in the double pulsed recordings are the result of the sum of all changes over the width of a 3-D flow. As the transient phenomena captured in the double-pulsed experiments are essentially three-dimensional, the integration effect has to be overcome. Therefore the existing system has been modified so that multiple projections can be obtained at different angles simultaneously, making tomographic reconstruction of the flow field possible.

The accuracy of tomographic reconstructions depends on the field being imaged, on the imaging geometry, and on the computational reconstruction method. Therefore, simulations were performed for the present configuration in order to get an impression of the results that may be expected. The calibration is based on a model image of a turbulent flow generated using a fractal sum of pulses method.

Preliminary experimental results using this system were obtained for a compressible jet flow emitted from a 3 mm diameter tube at subsonic and supersonic conditions. Although this narrow flow field produces only a weak signal, tomographic reconstructions were made and give insight into the three-dimensional flow field.

3 DIGITAL HOLOGRAPHIC INTERFEROMETRY

When a light beam traverses a field with an inhomogeneous refractive index it is retarded locally, so that the phase of the beam leaving the flow field is changed according to the refractive indices it has met.

For weak refraction, the phase delay is proportional to a projection of the refractive index field (Vest 1979):

$$\Delta\phi = \frac{2\pi}{\lambda}\int[n(x(s),y(s),z(s)) - n_0]ds \qquad (1)$$

where λ is the wavelength of the probe beam, n is the refractive index distribution, n_0 is the background refractive index field, $\Delta\phi$ is the phase difference between a beam passing the flow field and one which only passes the background field and s is the light path through the field.

Once the refractive index is found the density is calculated from the Gladstone-Dale relation: $n - 1 = K\rho$, where K is the Gladstone-Dale constant (about $0.225{\cdot}10^{-3}$ m^3/kg for air) and ρ is the density (Merzkirch 1987).

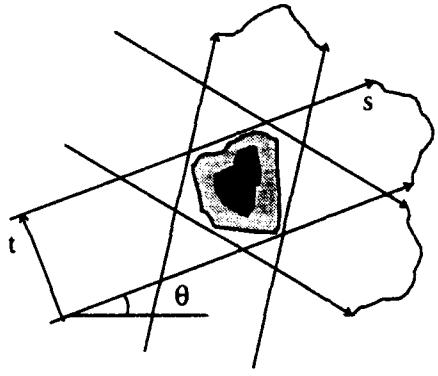

Figure 1: Projection imaging geometry

To determine the phase delay caused by a flow field, the probe beam is combined with a second, coherent light beam. The interference pattern created by these two beams is described by:

$$I(x,y) = I_{bias}(x,y) + I_{mod}(x,y)\cos\Delta\phi(x,y) \quad (2)$$

where x, y are the projection plane coordinates, I_{bias} is the background intensity, I_{mod} is the modulation intensity (contrast) and $\Delta\phi$ is the phase difference between the interfering beams.

Using phase-stepping the phase difference can be determined on an interval $[0,2\pi >$ for each pixel in the projection plane. Phase-unwrapping is used to remove all 2π ambiguities so that the continuous phase map is obtained.

Since the interferograms are produced from projections of the density in the flow field this density can only be determined directly for 2-D flows (where the refractive index is constant along each light ray) or for a truly axi-symmetric flow (Abel inversion).

In general, however, and especially for the turbulent structures the set-up is designed for, the density distribution will not be 2-D or axi-symmetric. Interpretation of the results is further troubled by the fact that several structures may be involved which may be moving with different velocities (time-scales).

Therefore, to make the study of 3-D flows possible and specifically to facilitate the interpretation of the double-pulsed results a tomographic system has been built.

4 TOMOGRAPHY

Tomographic techniques are most familiar from medical uses, however they are applied more and more to other fields as well (e.g. fluid dynamics, plasma physics and seismic sciences).

The purpose of optical tomography is to obtain 3-D measurements of a scalar quantity from a set of projections like those obtained in compressible flow interferometry. There, the phase delay that is extracted from interferograms is proportional to a line integral of the density. When projections are obtained from several viewing angles the integrals may be inverted to obtain the original scalar density distribution.

Using tomographic reconstruction a cross-sectional image ($\tau o \mu o \varsigma$ = slice) of a source function, $f(x,y)$, is obtained from its projections. These projections are described by the Radon transform $R(t,\theta)$:

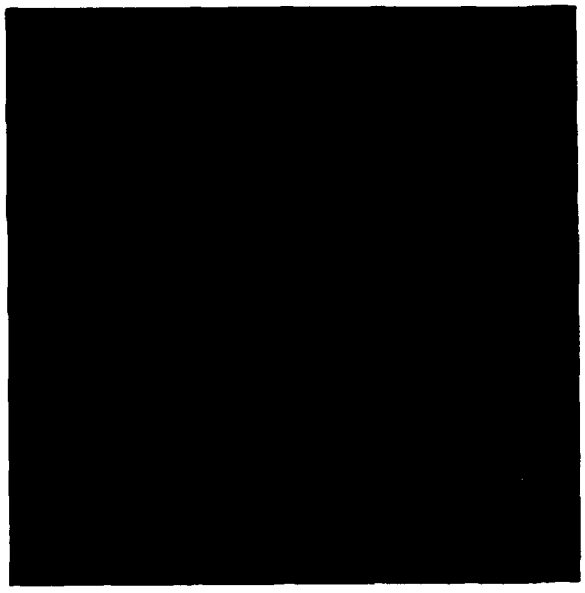

Figure 2: Test field for simulations

$$R(t,\theta) = \int f(x,y)\delta(x - s\cos\theta + t\sin\theta, y - s\cos\theta + t\sin\theta)ds \quad (3)$$

which in the case of interferometry represents the modified phase of a light beam. Here t is the transverse coordinate, θ is the viewing angle and s is the coordinate along the ray path (see Fig. 1). By inverting this equation the refractive index distribution and hence the density can be found.

For continuously sampled data, R can be inverted directly to obtain the source function. However, for data sampled discretely in a limited number of views, the results will be contaminated by reconstruction artifacts.

In general there are two methods for reconstructing a 3-D image from its projections: analytical inversion (e.g. Daens 1989) and iterative algebraic methods (e.g. ART, SIRT, MART) (Gilbert 1972, Herman and Lent 1976, Medoff 1987). The most common analytical inversion method makes use of the mathematical relation between the projections and the Fourier transform of the source function (Rosenfeld and Kak 1982). To determine the reconstruction the convolution of the projections and a suitable high-pass filter are calculated. The reconstruction is then determined by projecting the convolutions back onto the field. The advantage of the Fourier methods over the iterative methods is that they are much faster because of the use of Fast Fourier transforms. However these methods require a large number of uniformly spaced projections for accurate reconstructions, which is often not feasible in practical applications.

Iterative methods divide the field into a large number of elements which are assumed to have a constant value. Then an algebraic set of equations is deter-

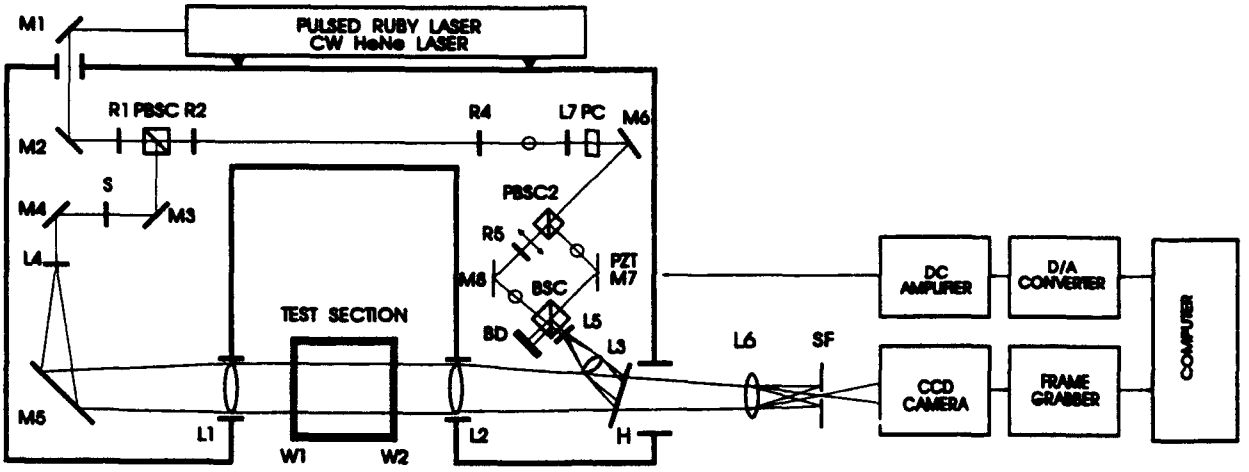

Figure 3: Rapid-switching digital holographic interferometer set-up. M_i: mirror, L_i: lens, BSC: beamsplitter cube, $PBSC_i$: polarizing beamsplitter cube, PC: Pockels cell, H: holographic plate, R_i: retardation plates, PZT: piezo-electric transducer, BD: beam dump, S: shutter

mined from the integrals over these elements and the projection values. The reconstruction is determined by solving this set of equations.

The iterative methods are well-suited for using *a priori* knowledge and for cases where the angle of sight is limited. A disadvantage of the iterative methods is that, although they need fewer projections than the Fourier methods, the matrix used in solving the equations becomes very large, making the computation time consuming. As computational speed has increased, this issue has diminished in importance.

Unsteady fluid dynamics problems require that all tomographic data must be obtained at a single instant in time so that all views have to be recorded simultaneously. Also, the number of views has to be minimized in order to minimize the size and cost of the data acquisition system and to minimize the time needed to reduce the experimental data. Furthermore, the range of available viewing angles is often restricted (e.g. because of wind tunnel walls). Therefore, algebraic techniques seem to be suited best for fluid dynamics studies and here only the algebraic (iterative) techniques have been considered. The algebraic algorithm used here (Constrained Conjugate Gradient Algebraic Reconstruction) is an iterative method (Watt and Conery 1993). An image estimate is initialized and updated based on mismatch between the projection data and the projections of the estimate.

The optical and image acquisition system for tomography becomes very complex and an additional computational reconstruction step is required. Also, the accuracy of the reconstruction not only depends on the quality of the original projections, but also on the computational reconstruction method, the complexity of the field to be studied and the imaging geometry (spread of the viewing angles). Therefore it is necessary to calibrate a tomographic system numerically, using accurate models for the test object, the view configuration, misalignment and noise.

The test object (representing a turbulent flow field) is generated by a modified version of the fractal sum of pulses method (Lovejoy and Mandelbrot, 1985). The image (on a grid of 75 x 75 pixels) has a fine-grained structure that is similar to that expected in a turbulent scalar field (see Fig. 2).

Previous studies using this test field (Watt and Conery 1993) have shown that, as may be expected, with an increasing number of views the minimum level of the image residual error (the reconstruction error) decreases while the image detail of the reconstruction increases. Although the reliability of the reconstruction improves with of the number of views, important features of the field were found to be already revealed in images reconstructed from as few as 6 views.

The configuration of the views is important as well. It was found that limited angle reconstructions are distinctly inferior to a reconstruction spanning a full 180 degrees. However, when views are limited, reconstructions from two bands at 90 degrees to each other are better than those obtained from configurations with the same viewing range, but limited to one band.

Misalignment is another important issue in tomographic reconstructions. Here, two types of misalignment are considered: lateral misalignment and angular misalignment.

Lateral misalignment is the difference between the actual and the assumed radial position of the projection measurement and angular misalignment is the difference between the actual and the assumed view angle.

Since the detectors in a CCD chip are linked rigidly, each projection in a view will have the same lateral and angular misalignment.

Angular misalignment of 1 degree in all projections results in a somewhat blurred image, obscuring a number of important features while lateral misalignment of one pixel produces severe line artifacts across the image.

When both misalignments are present the image is extremely corrupted. However, lateral misalignment seems much more critical for the quality of the recon-

struction than angular misalignment.

For the simulations noise was modelled as Gaussian noise because random noise is usually the dominant error source. The standard deviation is expressed as some fraction of the maximum projection value. When that fraction exceeds 1% the quality of the image was found to be severely degraded.

The largest errors in reconstructing the test image are concentrated in the off-centre region, where the steepest gradients occur.

Essential flow features may be seen in as few as 6 views, but finer-scale resolution requires many more views. Capturing dissipation-scale behaviour seems remote however.

5 SET-UP

The holographic interferometer set-up is shown in Fig. 3. A ruby pulsed laser (pulse length either 0.5 msec or 30 nsec) is used to create a plane wave which passes through the flow field (object beam) and two reference beams. A flow situation is captured by storing the object beam on a holographic plate using one of the reference beams while the other one is blocked by a mechanical shutter. This way, two flow situations can be recorded and separately reconstructed (Lanen *et al.* 1992).

In the post-processing stage, the object beam is blocked, while both reference beams are used. The holographic plate is illuminated with a continuous wave HeNe laser and four plane-wave, phase-stepped interferograms are generated, which are digitally stored and processed (512 x 512 pixels). Using these four interferograms the difference in phase, $\Delta\phi$, between the two flow situations is calculated. In the reconstruction stage the CCD-camera is focused at the symmetry plane of the flow, as for axi-symmetric flows this has been shown to minimise refraction errors.

When two flow situations are stored on one holographic plate and made to interfere at a later time the difference in phase (density) between the two flow situations is found. This can be used to compare two stationary flow fields (to remove wind tunnel wall effects and to only measure the disturbance caused by a model placed in the flow) or to determine the difference between two unstationary flow fields.

Studying rapid density changes in a turbulent flow requires a very small time interval between the recording of two flow situations. However, to get quantitative data for phase differences (from differential interferograms) the two situations need to be recorded by separate reference beams. This is achieved using the double-pulse facility of the ruby laser, which can give two 30 nsec pulses with an interval adjustable between 1 and 800 μsec. A Pockels cell is used for rapid switching between the reference paths to enable phase-stepping of the resulting interferogram (Timmerman 1993).

The time scale for turbulent structures is expected to be in the microsecond range as well, so that density differences on a scale from 1-800 μsec should give useful information on the turbulent effects.

As explained earlier, the phase map obtained in one direction contains information about the flow field density projected ('averaged') over the light path

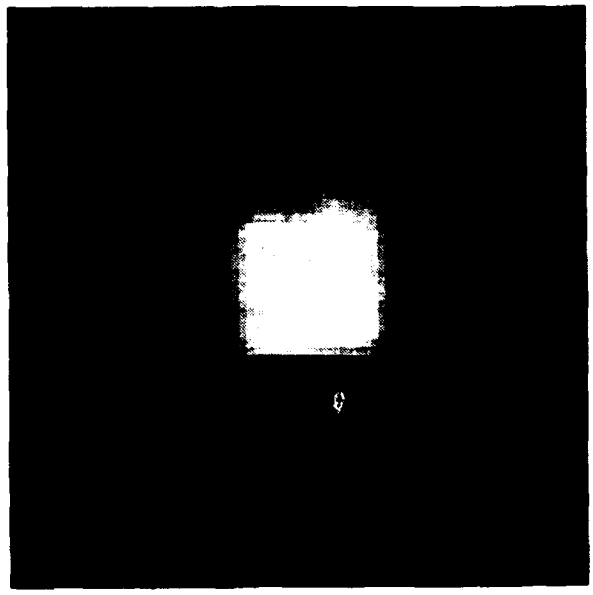

Figure 4: Simulated reconstruction of source image from projections at -12, 0, 12, 78, 90 and 102 degrees. Rms residual error: 0.17

through the flow. For turbulent flows, which are essentially 3-D in nature, therefore, a tomographic method is needed to obtain the local density distribution. Therefore, the system was modified so that multiple projections can be recorded simultaneously on the holographic plate.

In the present set-up, the number of views is limited to six. To achieve this the object beam which leaves the collimating lens L_1 is split into two beams at 90 degrees to each other, which are each sent through a diffraction grating. Each of these two gratings (which are mounted at 90° to one another) produces three high intensity beams so that a total of six beams pass through the test field at angles of -12, 0, 12, 78, 90 and 102 degrees. The field of view is about 15 x 30 mm^2.

After going through the flow field the six, plane-wave beams are collected with an elaborate system of mirrors making them all parallel to each other before passing through a converging lens (L_2) which directs the beams to the holographic plate. There they are stored in such a way that they do not overlap, while they are still all completely covered by both reference beams.

This way, all views can be separately imaged by the CCD camera, which, because all views are made parallel before being directed onto the holographic plate, does not need to be rotated to image each view correctly. Since each object beam has a different path length between lenses L_1 and L_2, however, the camera does have to be focused on a different plane for each view (so that it is focused at the centre plane of the flow for all views).

The reference paths have been lengthened somewhat so that their optical path length differs no more than 10 cm from all object paths (which are equal in

Figure 5: Sinogram for the subsonic case, filtered with a two-dimensional low-pass filter. Viewing order from left to right: -12, 102, 0, 90, 78 and 12 degrees

Figure 6: Sinogram for the supersonic case

length to within 20 cm of each other) to ensure good interference.

The phase maps that are calculated for each viewing direction using phase-stepping are then used for tomographic reconstruction of the recorded field.

For this tomographic reconstruction all views have to be aligned properly, and their magnification has to be determined as well, so that the correct (projected) pixels are compared. For this, some markers are needed which can be seen in each view. In this case, a needle was placed close to the nozzle exit, so that its point could serve as a reference point. Also, the nozzle itself was used to determine the magnification and tilt for each projection.

Simulations using the fractal sum of pulses method indicate that for the geometry used here, the general flow features may be determined, though small scale structures will not be resolved (see Fig. 4).

6 RESULTS

The preliminary system with six views has been tested on the jet flow leaving a cylindrical tube at both subsonic and supersonic conditions. The tube was about 20 cm long and the supply pressure was measured at about 2 m from the tube, making exact characterisation of the flow difficult. However, the Reynolds number can be estimated as greater than 10^5 for both cases.

The phase maps of the six projections were used for each case to generate a sinogram, which is the collection of the projections from the six viewing directions at a given axial location y. The individual phase images were unwrapped, and corrected for tilt and magnification variation to obtain the projection measurements at 101 points in each of 101 planes centred in the nozzle. Fig. 5 and Fig. 6 show the sinograms of all 101 of these planes. After the sinogram was constructed, reconstruction of each plane was made using the Constrained Conjugate Gradient Algebraic Reconstruction Technique. Prior to reconstruction, the sinogram projections were filtered on a row by row basis.

Fig. 7 and 8 show the reconstruction for the subsonic and the supersonic case, respectively. Here the results are shown as cross-sectional slices of the jet. The left top image is the slice at the most upstream position, the one underneath it the second slice, continuing column per column until the bottom left one. Fig. 9 and 10 show the same results, however now the slices are taken parallel to the jet axis, instead of orthogonal to it.

The cross-sectional and axial slice images show rather different features of the flow fields. In the subsonic case, the cross-sectional image shows that the jet is undergoing alternating compression and decompression. However, the axial slices indicate that the jet possess a helical structure and that the regions of low density are not aligned along the jet axis. The supersonic jet on the other hand shows a regular aligned series of compression and decompression region that are aligned along the jet axis.

There were several complications with these experiments. First the signal-noise-ratio was less than 10-1, which in itself generates significant image artifacts. Second, the orientation of the interferometric images caused the routine to interpolate data from outside the camera field of view. This produced nonsensical results at the borders of some images. Finally, as our simulations showed, this was not the optimal geometry, but rather a preliminary study.

7 SUMMARY CONCLUSIONS

A tomographic holographic interferometry system has been developed with which 6 views can be recorded simultaneously on a holographic plate. The application of optical tomography in fluid mechanics makes it possible to obtain spatially resolved measurements of density non-intrusively.

However, it is difficult to determine the accuracy of the tomographic reconstructions. For this reason, simulations have been performed to calibrate the experimental set-up.

From these simulations it was concluded that though the distribution of the views is not optimal,

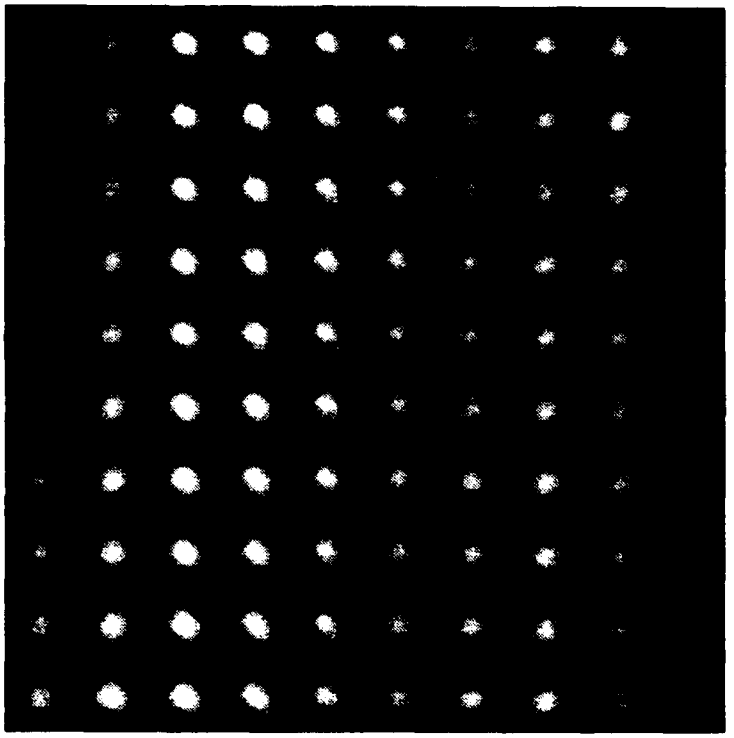

Figure 7: Cross-sectional reconstructions from filtered projections for the subsonic case. Black: atmospheric density, white: 0.39 kg/m^3 above atmospheric density. Volume: 5 x 5 x 5 mm^3

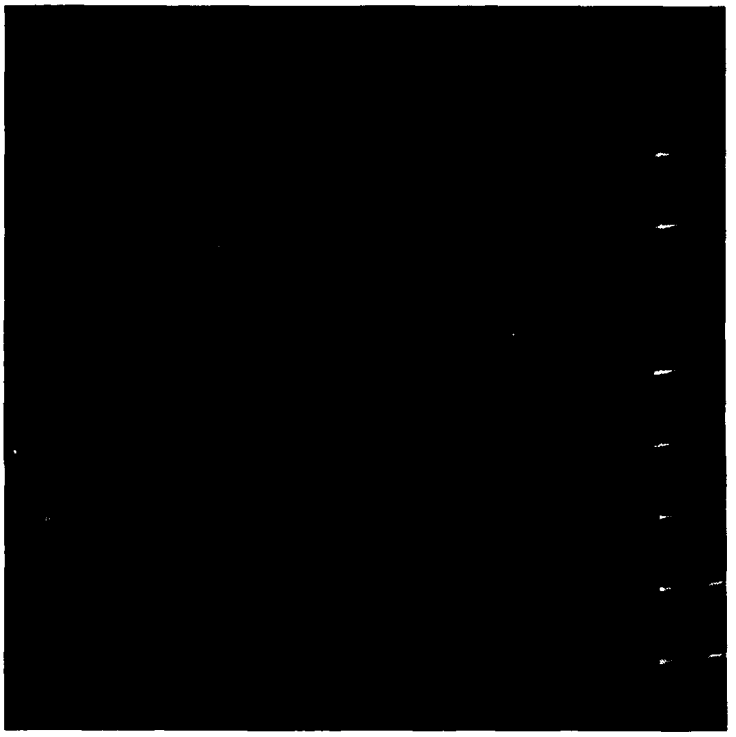

Figure 8: Cross-sectional reconstructions for the supersonic case. Black: atmospheric density, white: 0.676 kg/m^3 above atmospheric density

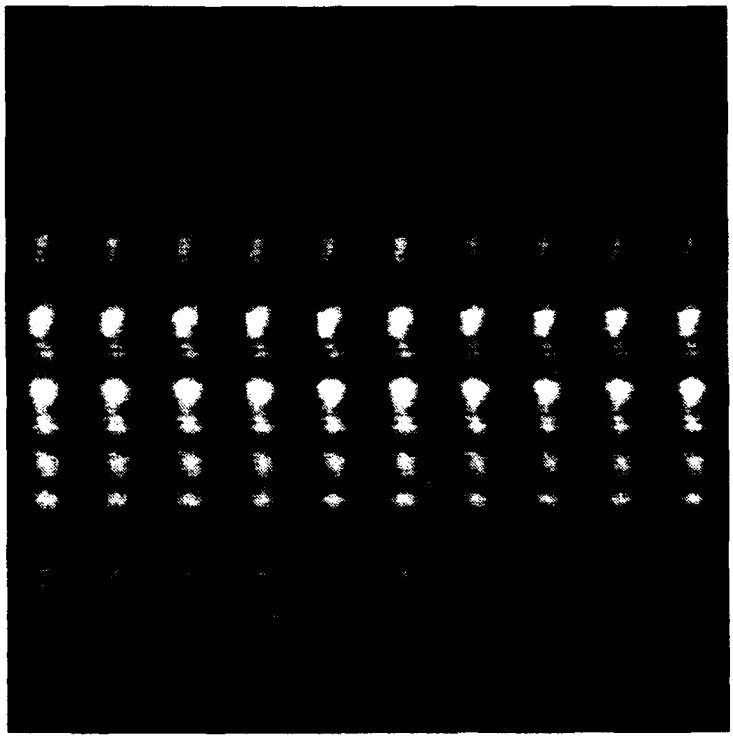

Figure 9: Axial reconstructions for the subsonic case

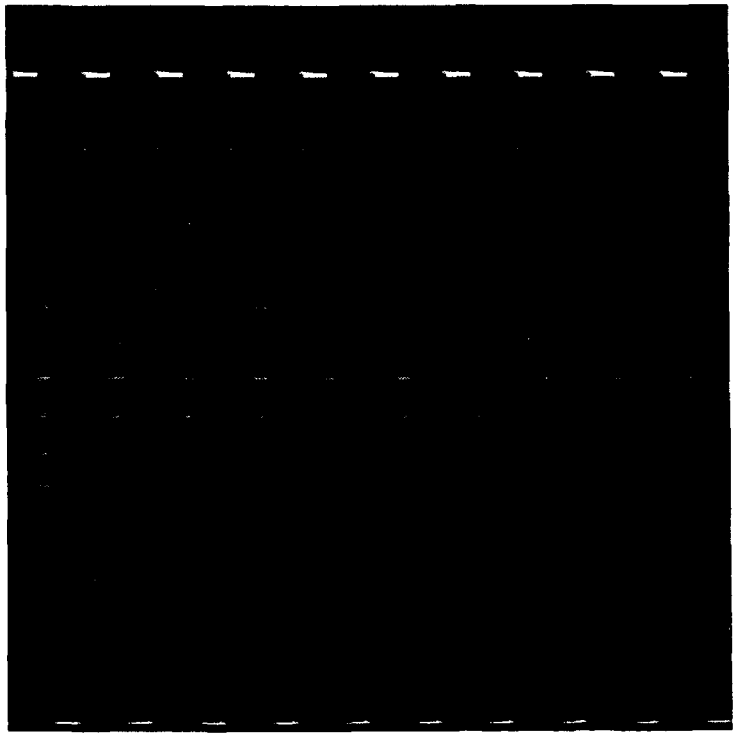

Figure 10: Axial reconstructions for the supersonic case

the general shape of the test field could be reconstructed reasonably well. The finer details, however, cannot be adequately resolved, but some insight should be gained into the magnitude and the dominating spatial scales of the density variations. These simulations also allowed the analysis of alternative designs, and facilitated the design of a new tomographic geometry.

Results have been obtained for a compressible jet flow at subsonic and supersonic conditions.

The combination of this tomographic system with the rapid-switching double pulse facility of the DHI set-up will facilitate locating 3-D density structures in turbulent flows as well as determining the 3-D instantaneous flow structure.

Also, insight can be gained regarding time-scales involved in compressible turbulent motion.

8 ACKNOWLEDGEMENT

David Watt's participation on this project was supported in part by NSF Grant #ECS-8910350 and by the NATO Collaborative Research Grants Programme.

9 REFERENCES

Daens, S.R. 1983, *The Radon transform and some of its applications*, Wiley and Sons, NY.

Gilbert, P. 1972, Iterative methods for the three-dimensional reconstruction of an object from projections, *J. Theoretical Biology*, vol. 36, pp. 105-107.

Herman, G.T. & Lent, A. 1976, Iterative reconstruction algorithm, *Computational Biology and Medicine*, pp. 272-294.

Lanen, T.A.W.M., Bakker, P.G. & Bryanston-Cross, P.J. 1992, Digital holographic interferometry in high-speed flow research, *Exp. Fluids*, vol. 13 , pp. 56-62.

Lovejoy, A. & Mandelbrot, B. 1985, Fractal properties of rain and a fractal model, *Tellus*, vol. 38, pp. 209-323.

Medoff, B.P. 1987, Image reconstruction from limited data: theory and application in computerized tomography, in *Image Recovery: Theory and Application*, ed. Stark, H., Academic Press.

Merzkirch, W. 1987, *Flow Visualization*, 2nd ed., Academic Press.

Rosenfeld, A. & Kak, A.C. 1982, Chap. 8: Reconstruction, in *Digital picture processing*, 2nd edition, vol. 1, Academic Press, NY.

Timmerman, B.H. 1993, Development of a high-speed digital holographic interferometry system for study of rapid density fluctuations in compressible flow, *Proc. ICIASF '93, 20-23 September 1993, Saint-Louis, France.*

Vest, C.M. 1979, *Holographic Interferometry*, Academic Press.

Watt, D.W. & Conery, D.G. 1993, Computational aspects of optical tomography for fluid mechanics and combustion, *Proc. Third Symposium on Experimental and Numerical Flow Visualization at the ASME Winter Annual Meeting, Dec 3-5 1993, New Orleans, La., USA.*

THREE COMPONENT VELOCITY MEASUREMENTS IN A CONVECTIVE FLOW BY HOLOGRAPHIC INTERFEROMETRY

N. Andrés, M. P. Arroyo and M. Quintanilla

University of Zaragoza. Faculty of Sciences, Dpto. Fisica Aplicada.

Ciudad Universitaria, 50009-Zaragoza, Spain.

ABSTRACT

A holographic interferometry technique has been used to obtain the three components of the velocity in some planes of a Rayleigh-Bénard convection flow where small tracers are suspended.

With our recording system the analysis of one interferogram gives information about the component perpendicular, but to determine the velocity, the analysis of several interferograms with different sensitivity vectors from the same hologram are required.

Some results have been compared with those obtained from velocimetry and show a good agreement.

The interferometry can be used itself to determine the three components and in some cases as a complemtent tecnique of the velocimetry for a complete study of the flow.

1. INTRODUCTION

The continuous development of laser-based diagnostic techniques offers considerable potential for advanced research on fluid dynamics because of their non-intrusive nature. In order to study fluid motion it is essential to obtain information from an extended region of the flow. Holographic interferometry is a laser-based thecnique which provides this information about the velocity field of the flow. Up to nowonly one component measurements have been reported. Ueda, Kagawa, Yamada, Yamaguchi & Harada (1982).

The purpose of this work is to show the feasibility of the holographic interferometry to simultaneously measure the three components of the velocity field in a whole plane.

The analysis of several interferogramas with different sensitivity vectors, obtained from the same hologram by varying the viewing direction, allows us to obtain the three components of the velocity.

2. OPTICAL ARRANGEMENT

In the optical configuration used in these experiments (Fig. 1) the beam from an Argon ion laser is shaped into a sheet of light which illuminates the flow under study. The light scattered by the small tracers suspended in the fluid is recorded on the holographic plate with a mean angle of 20º with the illumination direction. A double exposure of the illuminated plane is taken using a collimated reference beam.

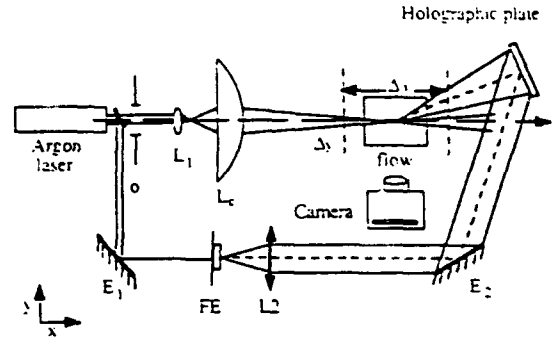

Figure 1. Holographic recording system

3. RECONSTRUCTION OF THE IMAGE

The holographic plate is illuminated with an unexpanded collimated laser beam to produce the real image, which is taken with a CCD camera and stored in a IBM PC-compatible computer for measuring the corresponding fringe patterns.

Several interferograms with different sensitivity vectors are obtained from the same hologram by changing the coordenate of the illumination point. That produces changes in the mean observation direction of the image, wich affects the light distribution on the image taken by the camera. To record all viewing directions with enough intensity a holographic lens which acts as a directional field lens is placed in the image plane. Andrés N. Arroyo M.P., Quintanilla, M., 1992.

4. VELOCITY MEASUREMENTS

The determination of the velocity is made by comparing the order of the interference fringe at the same position in the plane of the fluid in several

interferograms.

In some cases, the geometry described above allows us to determine from the analysis of only one interferogram the component perpendicular to the illuminated plane, V_y, if it is not negligible Ueda, Kagawa, Yamada, Yamaguchi & Harada (1982).

The automatic analysis of the interferograms looks for the maxima and minima of the intensity to get the skeleton. Due to the noise it is recommended to filter the image previously to reduce the effect of speckle. To assign an interference fringe order to intermediate points between maxima and minima positions the dependence of the intensity with the phase cosine has been used.

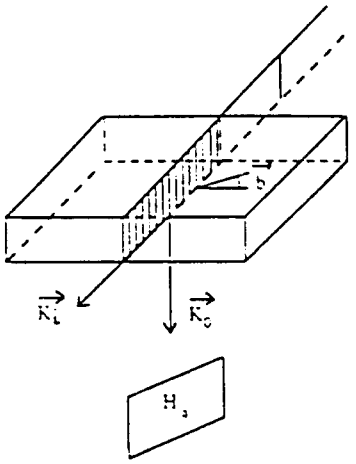

Figure 2: Optical arrangement for measuring flow velocity by holographic interferometry.

In the figure, k_i is the illumination vector, in the propagation direction of the sheetlike incident light, k_o the observation vector and v the velocity in the flow. In the reconstructed image observed in the direccion denoted by k_o the bright interference fringes appear at the position where

$$v\,K\,T=m\,\lambda \qquad (1)$$

where λ is the wavelenght in the fluid, m the interference order and T the time interval between expositions and the the sensitivity vector, K, is defined as

$$K=k_o-k_i \qquad (2)$$

The direction of the propagation vectors are different in both media due to the refraction index change, and the same happens to the wavelenght. It is noticeable that all the parameters are considered in the fluid.

With the geometry described above, the accuracy decrease with the hologram-object distance. The accuracy is higher for V_z and for the component perpendicular to the plane, and quite small for the component parallel to the illumination vector, D. Nobis, C.M. Vest (1978).

5. RESULTS IN A BIDIMENSIONAL FLOW

The technique described here has been applied to a Rayleigh-Benard convective flow in a cell with dimensions L_x=25mm, L_y=25mm and L_z=12.3mm. The cell is filled with silicone oil where 1.1μm latex particles have been suspended.

The present experiments have been done for Rayleigh numbers about Ra=6.5 Ra_c (Ra_c=1707) giving velocities up to 0.28 mm/s. Double exposure holograms have been recorded from several YZ and XZ planes. At the same time photographs of those planes were taken to analyse the flow by particle image velocimetry.

The convective flow at Ra= 6.5 Ra_c is anticipated to be a 2-D roll structure perpendicular to one side of the cell, with V_y being much smaller than V_x and V_z, Arroyo, Yonte, Quintanilla, Savirón (1988)

The P.I.V. analysis of the XZ planes allows us to determine V_x and V_z, the two components in the plane. By holographic interferometry only V_z is determined with accuracy because the contribution to the fringe pattern due to the others components are negligible, V_y because is very small and V_x because is parallel to the illumination direction. In some cases, from the analysis of only one interferogram, chosen with the smallest Z contribution to the fringes, the Y component can be determined.

The reconstructed image has a different fringe pattern depending on the position of the reconstruction beam. When the Z coordinate change the fringe pattern have a different forme, (fig. 3.a,b). The X coordinate change give a slightly change in the fringe number, too small to determined V_x with accuracy, (fig. 3.c,d).

In the plane y=3 mm, V_z and V_y have been measured with a 7% relative accuracy (fig.4). The maxima velocities are V_y=80 μm/s and V_z=240 μm/s, being V_y around three or four times smaller than V_z. In the central planes the maximum velocity is V_z=280μm/s, twenty times bigger than V_y, then only V_z is determined.

In both cases, the results show a good agreement with those obtained from particle image velocimetry.

The analysis of YZ planes by particle image velocimetry give information about the Vy and Vz components in this case. The importance of the component perpendicular to the plane in that cases decrease the number of points measured and the accuracy of the technique.

In the interferograms from these planes the components of the velocity have a different contribution depending on the plane. In general V_x and V_z can be determined with a good accuracy. The results for V_x and V_z in the plane x=3 mm from three interferograms are shown in fig. 5. The maxima velocities are Vx=70 μm/s and Vz=140 μm/s The accuracy is around 8%.

In the central plane hologram only V_z has an important contribution to the fringe pattern. Thus only two interferograms are required to determine this component. The maximum velocity determined is Vz=240μm/s. From the interferogram with the smallest Z contribution V_x can be estimated, (fig. 6). It is noticeable that is twenty times smaller than V_z.

In the plane x=6 mm only V_x contribute to the fringe pattern. In all these planes, the V_y, quite small and

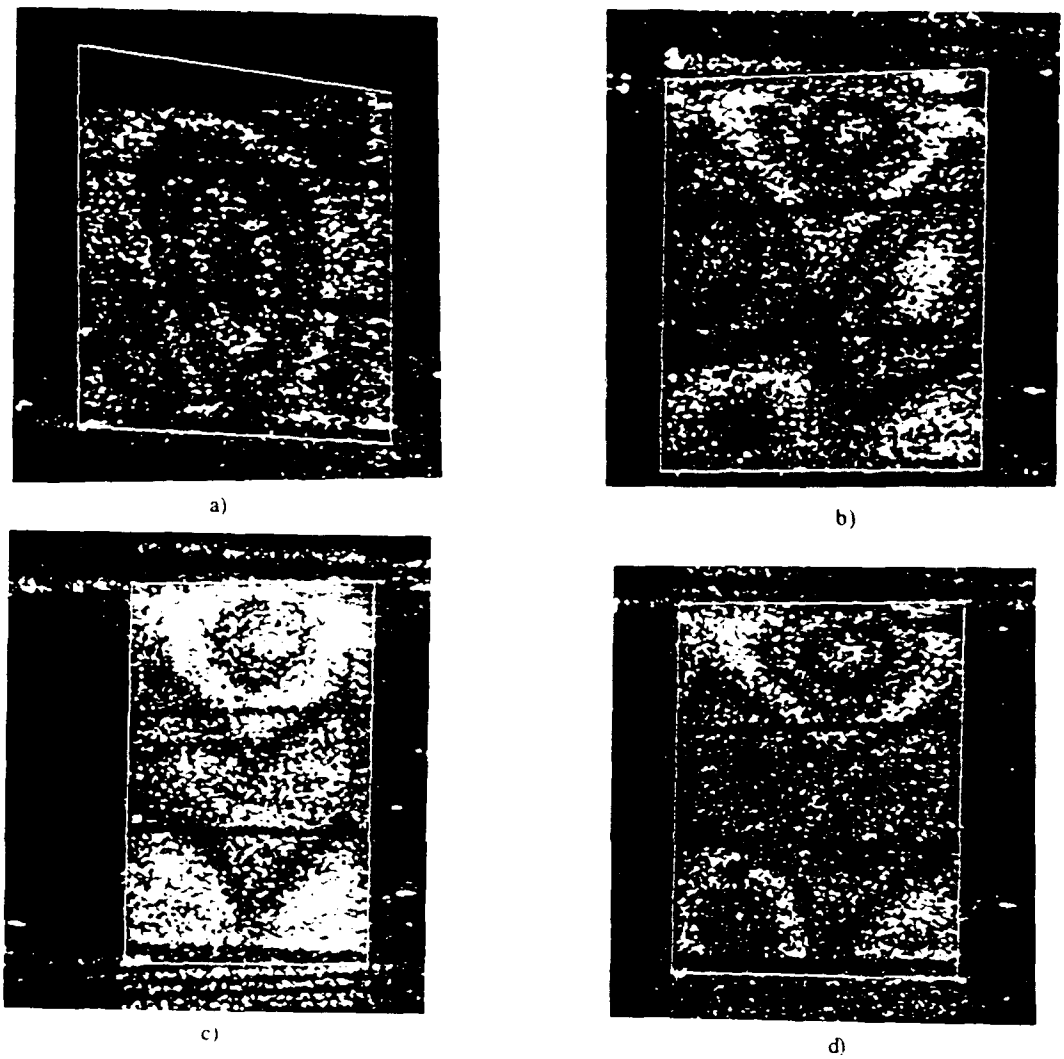

Figure 3. Reconstructed image of the y=3mm plane at Ra=6.5 Rac for differents positions of the reconstruction beam. a) y b) X-position change, c) y d) Z-position change

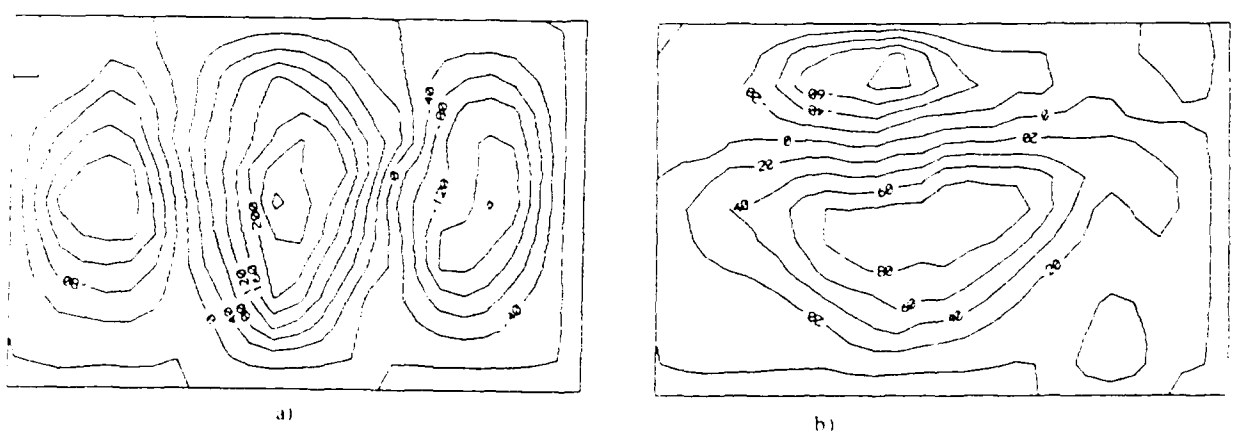

Figure 4. Velocity measurements at Y=3mm for a Ra= 6.5 Ra_c a) V_z, b) V_y

parallel to the illumination direction, has a negligible contribution.

6. RESULTS IN A TRIDIMENSIONAL FLOW

The present experiments have been done for Rayleigh numbers about Ra=30 Ra_c giving velocities up to 1.1 mm/s. Particle image photographs and double exposure holograms have been recorded for several YZ and XZ planes.

The analysis of the XZ planes by particle image velocimetry allows us to determine V_x and V_z. The holographic interferometry analysis determines with a good accuracy V_z and Vy. The X contribution to the fringe pattern is negligible because is parallel to the illumination direction and the contribution is small with our geometry.

In figure 7 some interferograms of the plane y=3 mm are shown. The fringe patterns change its forme when Z position of the reconstrucion beam change, and only the number of them with the X posision change. From the analysis of these interferograms V_z and V_y are obtained with a good accuracy, (fig. 8). The maxima velocities determined are V_z=450 µm/s and V_x=140 µm/s and the accuracy is around the 7%.

7. CONCLUSIONS

The holographic interferometry technique with the geometry described in this work allows to determine Vz and the component perpendicular to the illuminated plane, in some cases Vx and in other Vy. The component parallel to the illumination direction has a very small contribution to the fringe pattern.

Both components can be determined using phase differences with a good accuracy. In some cases, if the component perpendicular is small from the analysis of only one interferogram is possible to estimate it.

This technique is useful for a complete study of the flow with particle image velocimetry simultaneously

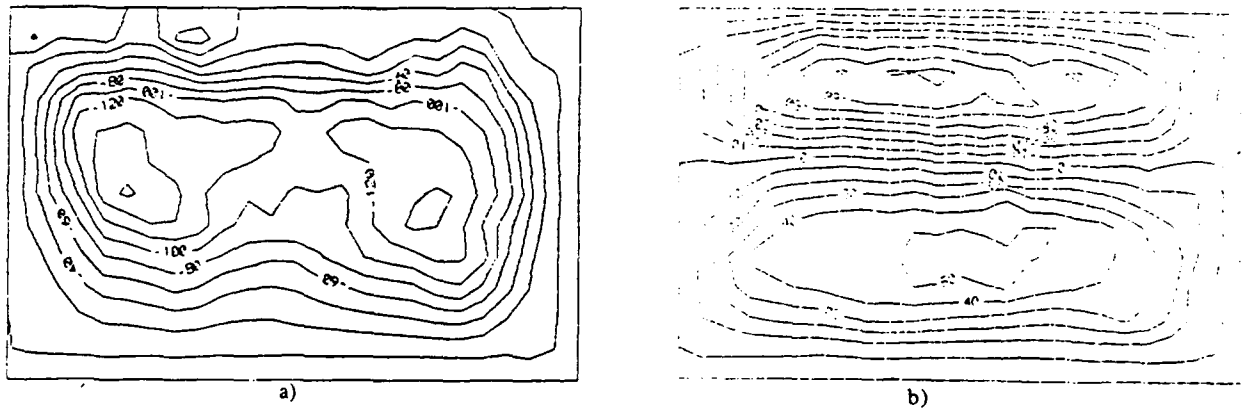

a) b)

Figure 5. Isovelocity distribution in the plane x=3 mm. a) V_z b) V_x

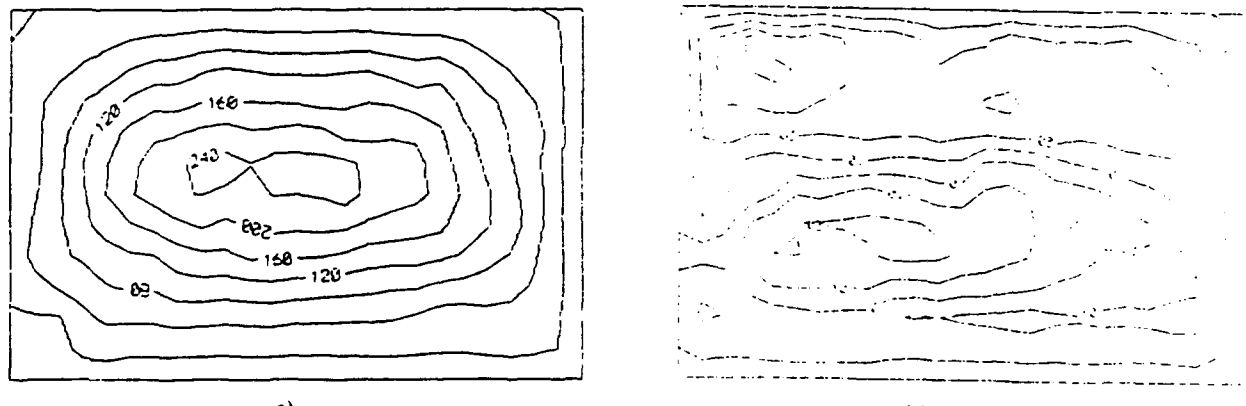

a) b)

Figure 6. Isovelocity distribution in the plane x=12.5 plane. a) V_z b) V_x

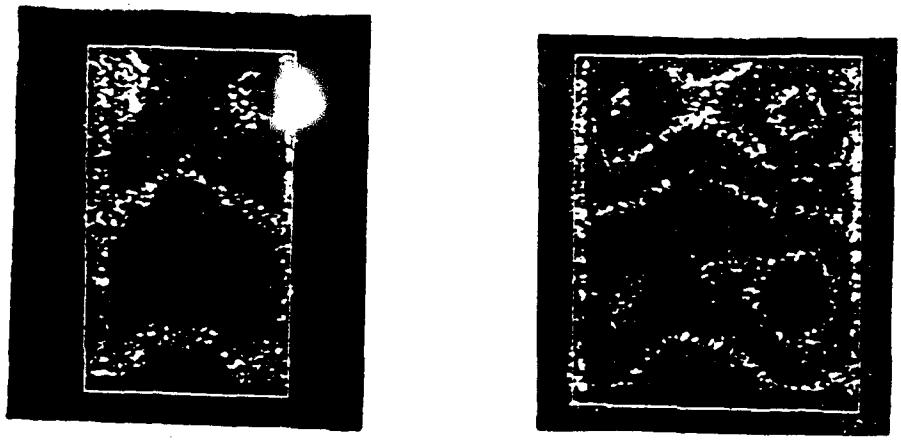

a) b)

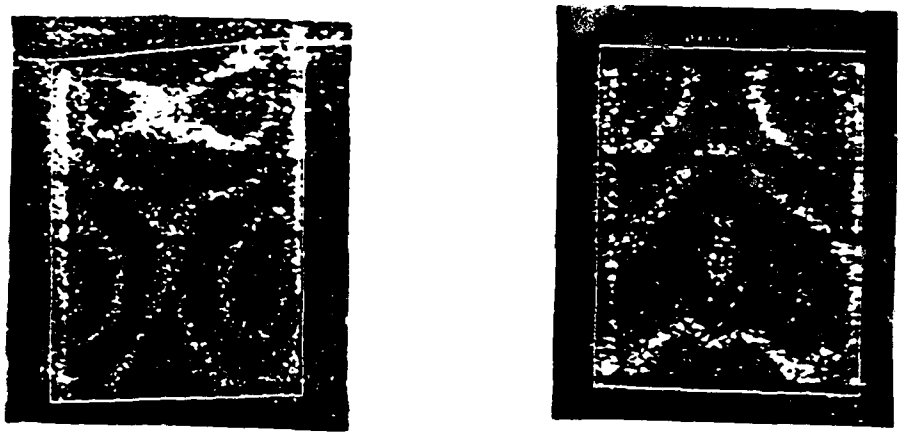

c) d)

Figure 7. Interferograms of the y=3mm plane at Ra=30 Rac for differents positons of the reconstructed beam. a) y b) X-position change. c) y d) Z position change.

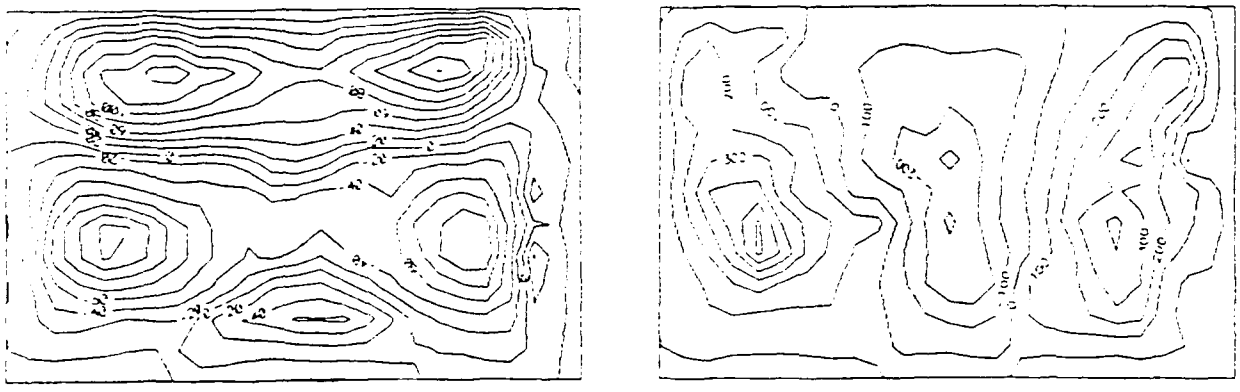

a) b)

Figure 8. Velocity measurements in the x=3 mm plane. a) V_y, b) V_z.

REFERENCES

(Book)
Vest M. (1979) Holographic Interferometry.

(Journal article)
Arroyo M.P.,Yonte T.,Quintanilla M. ,Saviron J.M. 1988, Velocity measurements in convective flows by particle image velocimetry using a low power laser. Opt. Engng. 27,641-649.

(Journal article)
Nobis D., Vest C.M.,1978, Statistical analysis of errors in holographic interferometry. Applied Optics vol 17, n 14, 2198-2204.

(Journal article)
Ueda M., Kagawa K.,Yamada K.,Yamaguchi, C.and Harada C. 1982. Flow visualization of Bénard convection using holographic interferometry. Appl. Opt. 21 n. 18, 3269-3272.

(Journal article)
Ueda M., Miyasaka K., Okuno S. (1989) Three dimensional flow visualization system by holographic interferometry. Optical and Quantum electronics 21, 409-414.

(Syposium proceedings)
Andrés N., Arroyo M.P., Quintanilla M. (1992) Velocity measurements in fluid by holographic interferometry. Sixth international Symposium on applications of laser techniques to fluid mechanics.

MEASUREMENTS OF GAS FLOW VELOCITY AND TEMPERATURE USING LASER PHOTOTHERMAL EFFECT WITH A DIFFERENTIAL INTERFEROMETER

Noboru Nakatani, Takanori Oshio
Ashiya University
13-22, Rokurokuso-cho, Ashiya, Hyogo 659, Japan
Toshiya Sakabe
Nara National College of Technology
22, Yata-machi, Yamato-kooriyama, Nara 639-11, Japan

ABSTRACT

This paper describes measurements of flow velocity and temperature using photothermal effect. We developed a differetial interferometer for detecting small phase variation caused by photothermal effect. The operating point is set on the maximum inclination of fringe intensity curve by the use of a piezomechanical translator. This system uses two focal points for time-of-flight method. Using jet of nitrogen gas mixed with ethylene gas, it is confirmed that this method is a useful tool to measure flow velocity and temperature.

1. INTRODUCTION

The laser Doppler velocimeter (LDV), which has some advantages such as non-perturbing quality, capability of remote operation and high spatial resolution, has been well developed to measure flow velocity. However, the LDV [Durst, Melling and Whitelaw (1981)] needs to seed scattering particles in flow. Recently, to be freed from this problem, velocimeters using photothermal effect have been investigated [Nie, Hane and Gupta (1986)] . In this study we investigated on measurements of flow velocity and temperature using photothermal effect. The nonintrusive methods of temperature measurement in a flame that have been proposed and demonstrated (CARS [Attal, Mueller-Dethlefs, Debarrc and Taran (1982)] or LIF [Daily (1977)]) rely on a measurement of Boltzman dsitribution among rotational sublevels of the molecules. Therefore, one must assume that the thermal equilibrium exists, which is not always found to be the case. These techniques have further following problems; Signal intensity obtained by CARS is very weak because of using non-linear effect. LIF is suffered from quenching effect. Photoacoustic deflection spectroscopy free from these problems was proposed by Rose, Salamo and Gupta (1984) to measure gas temperature. Propagation velocity of a photoacoustic pulse (sound) produced by the heating and the thermal expansion of the pump laser-irradiated region is detected by deflection of probe beams. The fast change in refractive index of gas caused by the sound is about a tenth of that caused by a photothermal effect. We needed to increase detection sensitivity for obtaining reliable data. The fiber heterodyne interferometer which we developed in the previous studies [Nakatani et al. (1989), (1991)] can not be used for this purpose because of low response. In this study, in order to increase the sensitivity and to detect the fast change in refractive index of gas, we developed a differential interferometer. A laser beam passed through a Wollaston prism is divided to two beams, and the beams are foucused for time-of-flight method. The operating point is set on the maximum inclination of fringe intensity curve by the use of a piezomechanical translator. A TEA CO_2 laser of short pulse width is used as a pump beam to produce photoacoustic sound. The difference in phase between the two focal points is measured to measure photoacoustic sound-velocity for gas temperaure measurement and velocity of puff of photothermal phase variation for flow velocity. Using jet of nitrogen gas mixed with ethylene gas, it is confirmed that this method is a useful technique to measure flow temperature and velocity.

2. A DIFFERENTIAL INTERFEROMETER

A laser beam is passed through a Wollaston

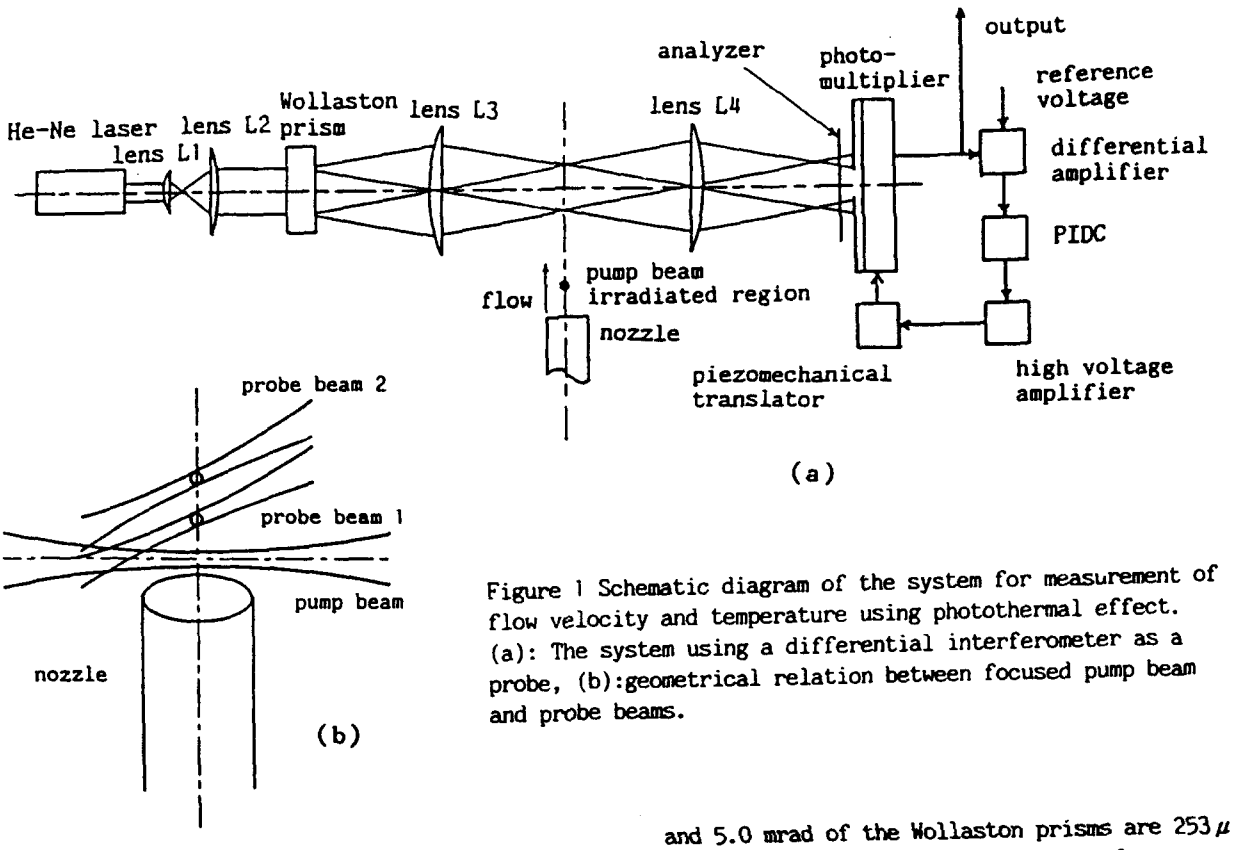

Figure 1 Schematic diagram of the system for measurement of flow velocity and temperature using photothermal effect. (a): The system using a differential interferometer as a probe, (b):geometrical relation between focused pump beam and probe beams.

prism for dividing two beams and obtaining two focal points of time-of-flight method. The operating point is set on the maximum inclination of fringe intensity curve by the use of a piezomechanical translator for increasing sensitivity of a interferometer. The experimental set up is shown in Figure 1. A He-Ne laser of wavelength 632 nm, power 5 mW and beam diameter 1 mm was used as the light source. The laser beam is expanded to 10 mm diameter by lenses L_1 and L_2 for making focal points small. The expanded two beams are passed through a Wollaston prism of 2.5 mrad or 5 mrad in dividing angle for dividing two beams. The laser beams are focused on two points with a spherical lens L3 (focal length F_3 = 200 mm). The distance between the two focal points is 0.5 mm and 1 mm for the dividing angle 2.5 mrad and 5 mrad, respectively. The phases of their beams are varied by passage of puff of phase variation by photothermal effect. The beams are collimated with a spherical lens L4 (focal length 200 mm), and are superimposed at the beams cross region. The two beams of orthogonal electric vectors are interferenced through an analyzer. The periods of the interference fringes for dividing angle 2.5 mrad and 5.0 mrad of the Wollaston prisms are 253 μm and 127 μm, respectively. The interference light is received with a photomultilier through a rectangular slit of 1 mm x 15 μm for increasing visibility. The difference between the phases of the beam for upstream focal point and the beam for downstream focal point changes the intensity of interference fringe. As the two beams are close to each other, the phase variation of the two focal points is detected mainly, and the interferometer is very stable. The operating point of the interferometer is set on the maximum inclination of fringe intensity curve by the use of a piezomechanical translator. The ouput signal of the photomultiplier is divided, one signal inputs into a digital storaged oscilloscope, the other signal inputs into a differential amplifier. The differential amplifier and PIDC controler are used as the electric circuits for controling the slit of the photomultiplier and setting the slit on maximum inclination of the fringe intensity curve.

3. MEASUREMENT OF FLOW TEMPERATURE

The medium absorbs the optical energy from the CO_2 pulse laser and if the pressure is suf-

ficiently high (i.e., if the quenching rates are sufficiently fast), most of this energy quickly appears in the rotational-translational modes of the medium. In a medium at atmospheric pressure, this condition is easily satisfied, and only a negligible fraction of the energy appears as fluorescence. The CO_2 pulse laser irradiated region thus gets slightly heated, leading to a localized heating of the gas, and giving rise to a pressure increase. This acoustic pulse travels outward, causing a change in the refractive index of the medium. The velocity of an acoustic wave which is propagating through a flame is depending on the temperature of the flame. The relation between the temperature and the acoustic wave-propagation velocity is given as

$$T = (M/\gamma(T)R) \cdot V_s^2, \qquad (1)$$

where M is average molecular weight of the gases in the flame, R is the universal gas constant, V_s is the sound velocity, and $\gamma(T)$ is the temperature-dependent average specific heat ratio at constant volume in the flame.

The solution of Eq. (1) for temperature T requires that M and $\gamma(T)$ are known. In a premixed ethylene-air flame in the experimental conditions of the future study, the main gases component is N_2 with the major components being CO_2 and H_2O. An adiabatic flame code can be used to yield the gaseous composition of the flame as a function of temperature from which M and $\gamma(T)$ can be calculated and used to extract a temperature from a sound-velocity measurement. In the most accurate case, this is the approach of choice. However, to a first approximation the composition can be assumed to be constant with temperature; and by simply rationing the velocity measured by ambient conditions to that in the flame, a temperature can be determined by

$$T_f/T_a = (V_{sf}/V_{sa})^2. \qquad (2)$$

If the gas velocity is small compared to the velocity of sound, Eq. (2) can be simply written as

$$T_f/T_a = (\Delta t_a/\Delta t_f)^2, \qquad (3)$$

where Δt_a and Δt_f are the measured times required for the acoustic pulse to travel between the two probe beams with and without the flame. Eq. (3) is found to give only a small underestimate of the correct T value (in flame conditions) compared with Eq.(1) which uses the appropriate M and $\gamma(T)$ values as well as takes into account the gas velocities of flame. In general, this will not be the case in a turbulent diffusion flame where M can vary greatly, and thus, Eq. (1) must be employed. The basic experiment is to measure the velocity of an acoustic pulse as it travels through the gas flow as shown in Figure 1 (b). Nitrogen gas mixed with ethylene gas of volume ratio 0.10 was used as a fluid. The nozzle of 4.8 mm in diameter is used. The TEA CO_2 pulse laser is focused into flow by a lens of ZnSe and focal distance 50 mm to produce acoustic pulse. The diameter of the focused beam is 0.05 mm. The focal point of the TEA CO_2 pulse laser is 3 mm downstream the exit of the nozzle. The pulse laser was made by ourselves, is 20 mJ in the maximum energy and is about 50 ns in the pulse half-width. The arrival of the acoustic pulse travel at a beam was measured with the differential interferometer. Two focusing probe beams separated by d = 0.5 mm or 1 mm were used to observe the sound velocity. The probe beam 1 was arranged 3.15 mm downstream the foacal point of the pump beam for detecting acoustic pulse without influence of photothermal puff produced by the pump beam. The operating point of the interferometer is set using signal whose high frequency fluctuation above 100 Hz is blocked by electronic filtering. Thus, the setting is free from interference of the acosutic pulse. The typical oscilloscope traces of acoustic signals in d = 1.00 mm and 0.50 mm are shown in Figures 2 and 3. The flow rate is 1.5 l/min.

The analytical models for obtaining velocities from those traces are shown in Figures 4 and 5. Figure (a) shows the relation between the moving puff of phase variation caused by photothermal effect and the probe beams. Figure (b) shows the traces of detection signal. The Gaussian distribution of the phase variation is simplified by triangular shape. In the analytical model of Figure 3 the width of the puff is larger than the distance between two probe beams and the half width of the puff is smaller than the distance. In the analytical model of Figure 4 the width of the puff is smaller than the distance between the two probe beams. In step a the edge of the puff of the phase variation reaches the edge of the probe beam 1, and the detection signal begins to decrease. In step b the phase-variation peak of the puff reaches to the intensity peak of the probe beam 1, and the detection signal shows minus peak. In step c the edge of

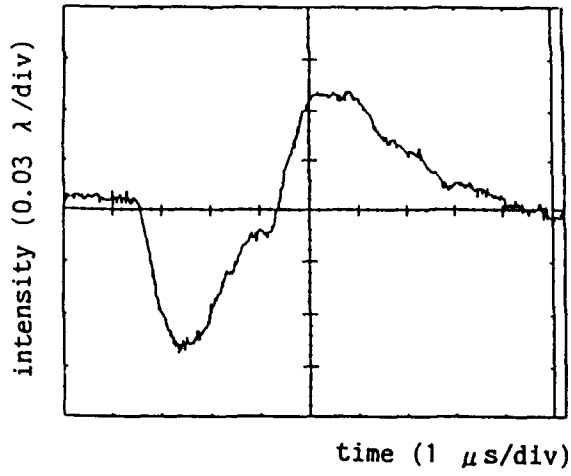

Figure 2 Typical oscilloscope trace of photoacoustic signal for temperature measurement. The distance between the probe beams is 1 mm.

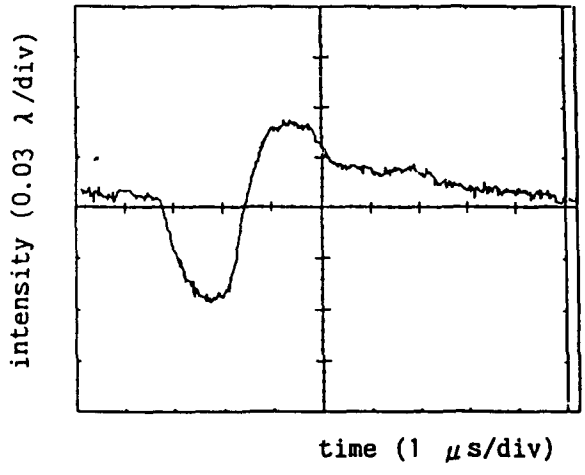

Figure 3 Typical oscilloscope trace of photoacoustic signal. The distance between the probe beams is 0.5 mm.

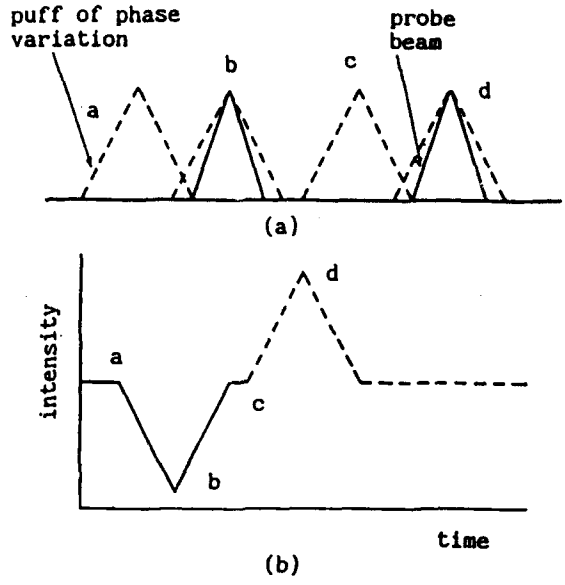

Figure 4 Analytical model of observed photoacoustic and photothermal signals. The width of puff of phase variation is smaller than the distance between the two probe beams. (a): Relation between puff of the phase variation and probe beams, (b): observed signal.

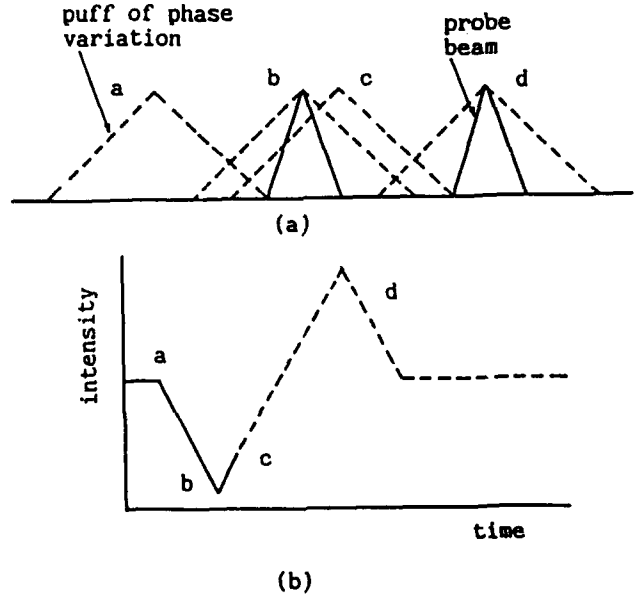

Figure 5 Analytical model of observed photoacoustic and photothermal signals. The width of puff of phase variation is larger than the distance between the two probe beams and the half width of the puff is smaller than the distance. (a): Relation between puff of phase variation and probe beams, (b): observed signal.

the puff reaches to the edge of the probe beam 2, and the detection signal increase rapidly. In step d the phase-variation peak of the puff reaches to the intensity peak of the probe beam 2, and the detection signal shows plus peak. Considering from these model, it is concluded that time interval between a and c of trace of detection signal or time interval between b and d is for transit time of the puff between the two probe beams.

As the peaks of Figures 2 and 3 have gentle slope, we used the time interval between a and c. The transit times obtained from those figures are 1.43 μs and 2.85 μs. Using these transit times and the distances between the probe beams 0.50 and 1.00 mm, velocity 350.5 m/s is calculated. Considering flow velocity 2.7 m/s obtained by flow rate, the acoustic sound velocity is 347.8 m/s. T = 294 K is obtained by Eq. (2) using this sound velocity, M = 28.02, and γ = 1.402. This value is almost equal to room temperature 293 K. From these experimental results, we could confirm the reliability of this method.

4. MEASUREMENT of FOW VELOCITY

The CO_2-laser irradiated region thus gets slightly heated, leading to changes in the refractive idex in the region. The movement of puff of this phase variation is detected by the interferometer. The time-of-flight method is used to measure flow velocity.

Using laminar jet of nitrogen gas mixed with ethylene gas of volume ratio 0.10, it is confirmed that this velocimeter is a useful tool to measure flow velocity. The nozzle of 4.8 mm in diameter is used. The flow velocity is calculated by measured flow rate. The experimental conditions are same as those predescribed in temperature measurement of section 3. Typical oscilloscope traces of the measured phase varia-

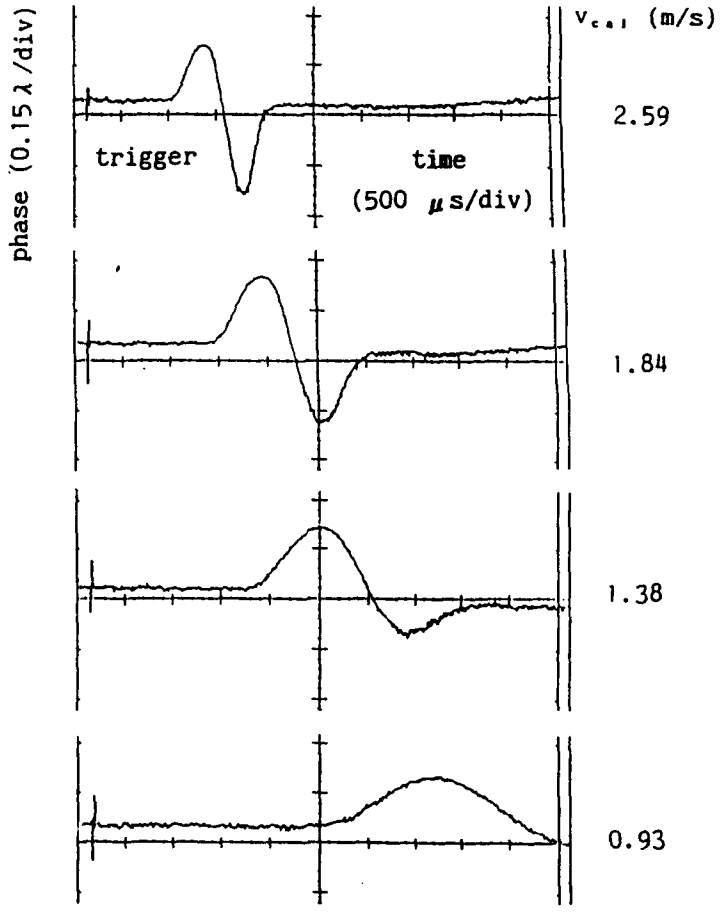

Figure 6 Typical oscilloscope traces of photothermal signals for measurement of flow velocities. The probe beam 1 was arranged 3.15 mm downstream the focal point of the pump beam. The distance between the probe beams is 1 mm.

Nakatani, N., Oshio, T., Kataoka, T. and Kishida, K. 1991, Simultaneous Measurements of Flow Velocity and Concentration with a Photothermal Velocimeter Using an Optical Fiber Heterodyne Interferometer. Laser Anemometry Advances and Applications vol. 1, ASME, New York, 83.

Nie, Y. X., Hane, K. and Gupta, R. 1986 Measurements of Very Low Gas Flow Velocities by Photothermal Deflection Spectroscopy. Appl. Opt. 25, 3247.

Rose, A, Salamo, G. J. and Gupta, R. 1984 Photoacoustic Deflection Spectroscopy: a New Specie-Specific Method for Combustion Diagnostics. Appl. Opt. 23, 781.

Session 33.
Engines I

SIMULTANEOUS TWO-COMPONENT VELOCITY AND DROPSIZE MEASUREMENTS IN A COMBUSTING DIESEL FUEL SPRAY

G. Pitcher and G. Wigley

AVL List, Graz and FMCS, Kumberg, Austria

ABSTRACT

The application of a two-component PDA system to characterise the spatial and temporal development of a Diesel fuel spray injected into the quiescent combustion chamber of a single-cylinder research Diesel engine is reported. Details of the two- component PDA transmitter system are given to emphasise the accurate alignment necessary to guarantee confocal measurement volumes and therefore coincident signals from single droplets.

Data are presented for the mean axial and radial velocity components, dropsize and sample number as profiles in both space and time to allow precise comparisons and evaluation of the spray characteristics. An animation of the spray data has been made to visualise the dynamic planar flow field structure in terms of the time varying droplet trajectories, velocities and sizes.

1. INTRODUCTION

In an earlier work published by Pitcher and Wigley (1992) a 1-component PDA system was applied to study the break-up and atomization of a Diesel fuel spray injected into the quiescent combustion chamber of a single cylinder research Diesel engine. This complementary work describes here the use of a 2-component PDA system to characterise the radial growth of the fuel spray as it penetrates downstream and the entrainment processes that it generates. This represents the most comprehensive Diesel spray study to date but also involved a significant increase in the complexity of the measurement task.

The PDA technique is a single particle counting technique so the measurement of the 2- orthogonal velocity components must come from the same droplet. This is unlike the practice in LDA where small coincidence times between the signals can be acceptable. The necessity for 2 confocal orthogonal measurement volumes forces a high alignment precision and accuracy on the coaxial orthogonal beam pairs used to form the two measurement volumes. Furthermore, the PDA signal processor demands coincident signals from each velocity channel since the burst detector, which enables the processing electronics, is only triggered from one channel.

The first part of this paper details the extensions that were carried out to the original PDA system to enable it to measure 2 orthogonal components of the droplet velocity and the dropsize simultaneously.

A fine spatial grid of PDA measurements in a spray can generate vast amounts of data and here with the highly transient nature of the Diesel spray a severe problem for data evaluation and presentation is posed. While axial and radial profiles of the time varying mean quantities can be presented in a precise manner it is very difficult to build up a mental picture of what is happening in the spray , not only locally but globally. An attempt has therefore been made at a planar visualisation of the spray data to obtain an animation of the spatial distribution of the mean droplet trajectories, velocities, dropsizes and their population distributions.

The second part of this paper concentrates on an analysis of the spray data, based upon the liquid jet break-up model, Ruiz and Chigier (1985), and uses both mean data profile comparisons and the animation as tools to identify the major events taking place in the transient, combusting Diesel fuel spray.

2. INSTRUMENTATION

The basic 1- component PDA transmission system was described in detail by Pitcher and Wigley (1991). In 2-component form it is shown in the schematic of Figure 1. It consists of a Dantec 55X29 Bragg cell for both frequency shifting, 40 MHz, and beam splitting, 50/50, and 2 separate 1-component beam expander optical systems mounted in parallel with precision steering of 1 planar beam pair. Of particular interest is the beam splitting and wavelength separation method. The Coherent Innova 90/5 laser was operated in the all-lines mode with 1.75 Watts total output power. This ensured TEM00 mode structure on both the 488 and 514.5 nm wavelengths and the absence of thermal focusing of the laser beam by the Bragg cell. The Bragg cell was orientated so that the zero and first order diffracted beams were in the horizontal plane and that the Bragg angle was satisfied The RF power to the Bragg cell was reduced to provide equal intensities in the zero and first order diffracted beams. A pair of fused silica Pellin Broca prisms were used for wavelength separation with the dispersed beams exiting in the vertical plane. The combination of the Bragg cell

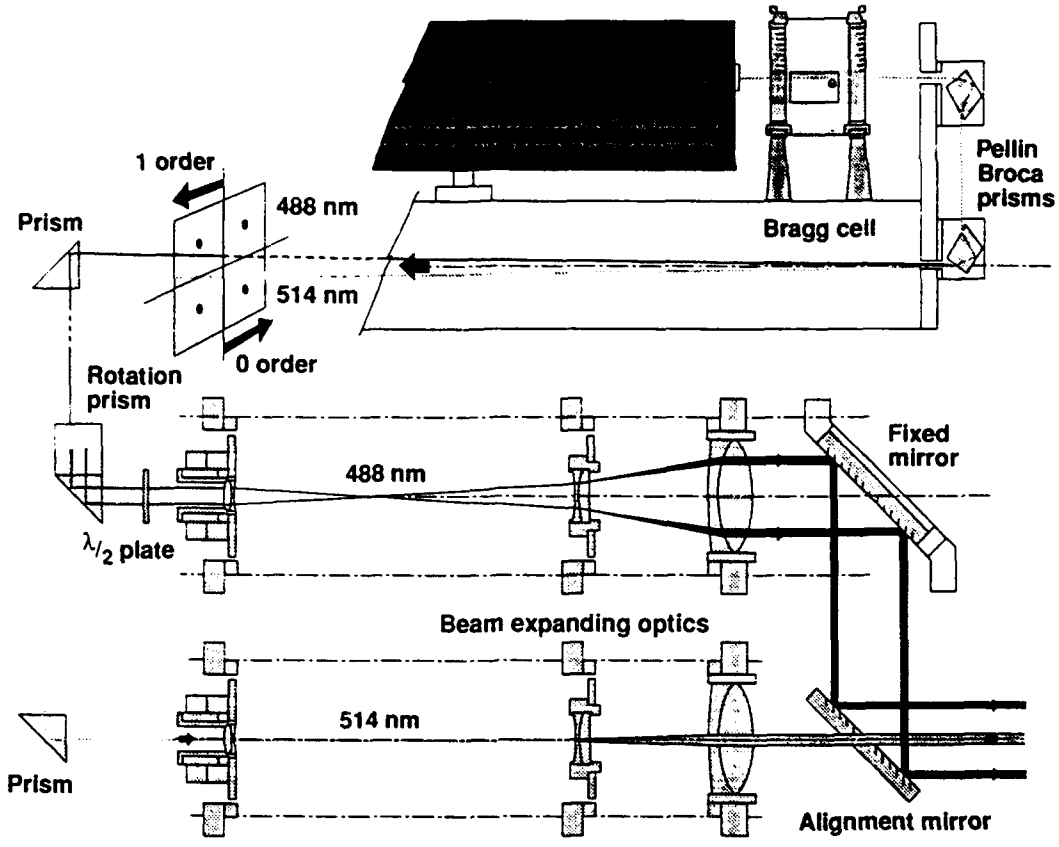

Fig. 1 Two component transmission optics

diffraction and the prism pair dispersion produced the near square symmetrical laser beam pattern, as shown in Figure 1. with the diffracted beam pairs at 488 and 514.5 nm lying in horizontal planes, one above the other.

The optical geometry of the prisms that direct each beam pair to their beam expanding optical systems is only shown in principle in the 2-dimensional schematic of Figure 1. One pair of beams enters directly its beam expander, here the 514.5 nm wavelength pair, while the 488 nm wavelength pair must have their plane rotated through 90 degrees . This plane rotation was performed by two prisms with their hypotenuse faces at 90 degrees to each other. As this method also rotates the plane of polarization of each beam, a lambda/2 plate placed at the entrance to the 488 nm beam expander restores the polarization parallel to the plane of the fringe patterns.

The separation of each beam pair entering and exiting the beam expanders were 13.2 and 50.0 mm respectively, i.e. an expansion ratio of 3.8 which also applied to the individual output beam diameters. To bring the orthogonal 488 nm beam pair to a common optical axis with the 514.5 nm beam pair a mirror periscope was used which consisted of a fixed circular mirror and a slim rectangular alignment mirror. To ensure that the 488 and 514.5 nm beam pairs were co-axial and parallel, they were checked over a throw of more than 30 metres. Corrections to the former were made by translation of the alignment mirror along the optical axis and/or tilt and twist of this mirror about the optical axis. Adjustments for parallelism required a precision translation of the negative lens in the individual beam expanders.

While this produced a high degree of alignment accuracy a final check for confocal measurement volumes was made, in situ, after projecting them through the optical access window and onto the vertical axis of the cylindrical combustion chamber. This involved the complete optical system with the receiver, a Dantec 57X10, positioned to collect the light scattered through the other window in the cylinder head located to produce a 70 degree scattering angle. The fuel injector was removed from the cylinder head and replaced by an artist's airbrush to produce a spray of alcohol droplets directed down through the confocal measurement volumes. The 2-component version of the 57X10 receiver has 4 photomultipliers, 3 for the 514.5 nm optics for the measurement of the vertical velocity component and dropsize and 1 for the 488 nm optics for the measurement of the horizontal velocity component, the output from which were also balanced during this alignment check.

The signals from each photomultiplier were monitored on a Tektronix 2430A digitising oscilloscope. The digitising rate was too low (100 MHz) for faithful reconstruction of the Doppler signals (~50 MHz) but adequate when the oscilloscope was operated in *envelope mode* for recording

and comparing the envelopes of the Doppler signals. Equalisation of the 4 signal envelope peaks was then adjusted by the high voltage supply levels to the photomultipliers and the coincidence of the 488 nm signal with any of the 514.5 nm signals was easily adjusted by corrections to first, the alignment mirror and secondly, to the focus, if the signal peak could be improved upon. With such attention to detail the data and validation rates were readily maximised and for 2-component velocity and dropsize measurements on the airbrush spray inside the engine combustion chamber the validation rate would exceed 95%.

The single cylinder research Diesel engine and its operation have been described in detail by Pitcher and Wigley (1992), but for completeness a short description is given here. The combustion chamber is a vertical cylinder of 50 mm diameter and height inside the cylinder head which is accessed by 2 vertical plane circular windows angled to produce the required 70 degree light scattering geometry. The fuel injector is mounted in the top of the combustion chamber and produces one fuel spray directed vertically down the axis of the combustion chamber. The combustion chamber is pumped by the piston of a 3-litre single cylinder 2-stroke Diesel engine to produce, at the time of injection, a near quiescent but turbulent compressed air charge of peak pressure 56 Bar and temperature 900 K when the engine was motored at 500 RPM. A Bosch 4 in-line Diesel injector pump with only one active pumping element was driven directly by the engine crankshaft and supplied fuel to a Bosch DSLA Diesel injector drilled to produce a sac type single hole nozzle of diameter and length 0.2 and 1.0 mm respectively. The nozzle flow control needle opened at a fuel line pressure of 220 Bar, peak injection pressure reached 386 Bar , 0.39 ms after the needle opening, and 8.9 mm^3 of fuel were injected during the injection period of 1.66 ms. The fuel line pressure at the injector was measured with a piezo-electric quartz transducer and digitised to be displayed with the velocity/dropsize data animation.

The alignment of the measurement volume and the measurement grid within the spray followed the same procedure as in the earlier study. The spray axis was identified by the intense light scatter coming from a thin column within the spray. The radial measurement positions were in 0.1 mm increments for the axial locations of z = 5 and 10 mm and 0.2 mm increments for z = 15, 20 and 25 mm downstream relative to the nozzle. It was noted that the spray trajectory was not truly vertical between z = 0 and 15 mm.

At each measurement position 15,000 validated samples were recorded. This required between 300 and 1200 injections depending on the degree of atomization of the fuel and the local air/fuel void fraction. Each sample consisted of the axial and radial velocity components, the dropsize and the droplet arrival time relative to a trigger occurring shortly before each injection. To ensure that all the data collected was attributable to the injected fuel droplets the burst detector in the Dantec PDA Covariance processor was activated for a period of 4 ms after the trigger. In processing, the velocity and dropsize data were averaged over consecutive 40 μs time bins to allow the mean time histories of the 2-velocity components, dropsize and sample number to be plotted. A minimum of 10 samples was required in any bin.

3. RESULTS AND DISCUSSION

As discussed earlier, Pitcher and Wigley (1992), a ligament of liquid fuel moving through the measurement volume was identified by a zero or minimum in the time history of the sample distribution plots on or close to the spray axis respectively. They were most easily observed between z = 5 and 10 mm below the nozzle and were associated with a peak in the mean axial velocity time history in the immediate shear layer. A similar behaviour was also observed here but only 3 ligaments were found rather than the 5 observed in the previous study. The only differences between the nozzles and their operation were those associated with normal machining tolerances and surface finish, a slightly shorter fuel injection period, 1.66 ms instead of 2.00 ms, and therefore a lower peak pressure, 386 Bar instead of 425 Bar. Once again the effect of a ligament moving through the measurement volume produced a peak in the axial mean velocity in the immediate shear layer but, furthermore, a peak in the radial mean velocity was also observed indicating droplets being entrained in towards the ligament.

A typical example of this behaviour is shown in Figure 2 for the measurement location z = 10 mm and r = 0.3 mm. The axial (U) velocity component is the upper profile and is presented as positive, down from the nozzle while the radial (V) velocity component is positive for droplets moving radially out from the spray axis. The histogram represents the sample number contained in each 40 μs time bin, normalised to the peak containing 2000 samples. In the following discussion the analysis presented has been based on all the data obtained and cannot necessarily be derived uniquely from that presented in Figure 2.

The fuel on the tip of the spray was poorly atomized, h only a few droplets appear at 0.6 ms and were followed by a ligament of fuel of approximately 0.3 mm radius and lasting 80 μs. The few droplets on the spray tip are moving down and radially out from the spray axis with the same velocity, only 7 m/s. Droplets sheared directly from the following ligament have a much higher axial velocity but show a negative radial velocity component, i.e. droplets immediately behind the spray tip are entrained into the spray.

The second ligament is more substantial, it appears shortly after 1 ms and persists until 1.3 ms. This is followed by a slow growth in sample number until 1.60 ms after which the sample number increases, to a peak at 1.83 ms, with the break-up of this ligament tail and/or the arrival of a portion of the spray that is atomized. At this stage the mean axial velocity profile has a minimum, dropping down to 16 m/s, while the entrainment velocity has been steadily decreasing with the radial velocity profile showing a value of -4 m/s.

The third ligament approaches the measurement volume shortly before 2.00 ms and lasts until 2.25 ms. It is followed by the highest sample number counts recorded, i.e. the highest degree of atomization of the fuel at this specific location. The injection of this ligament occurs just before the needle closes at 2.14 ms. The axial and radial velocity profiles have maximum and minimum values respectively during the passage of the ligament. In the well atomized portion of the spray behind the ligament, after 2.5 ms, the radial velocity component is virtually zero with the axial velocity decreasing as the momentum of the residual spray is dissipated.

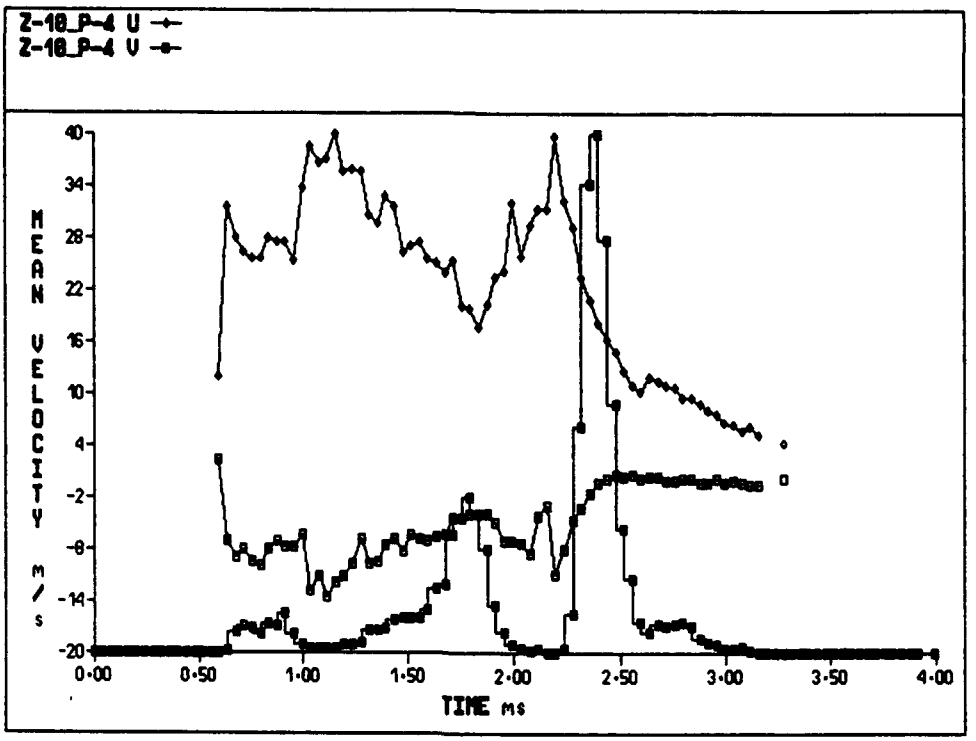

Fig. 2 Axial and radial velocity components with sample distribution

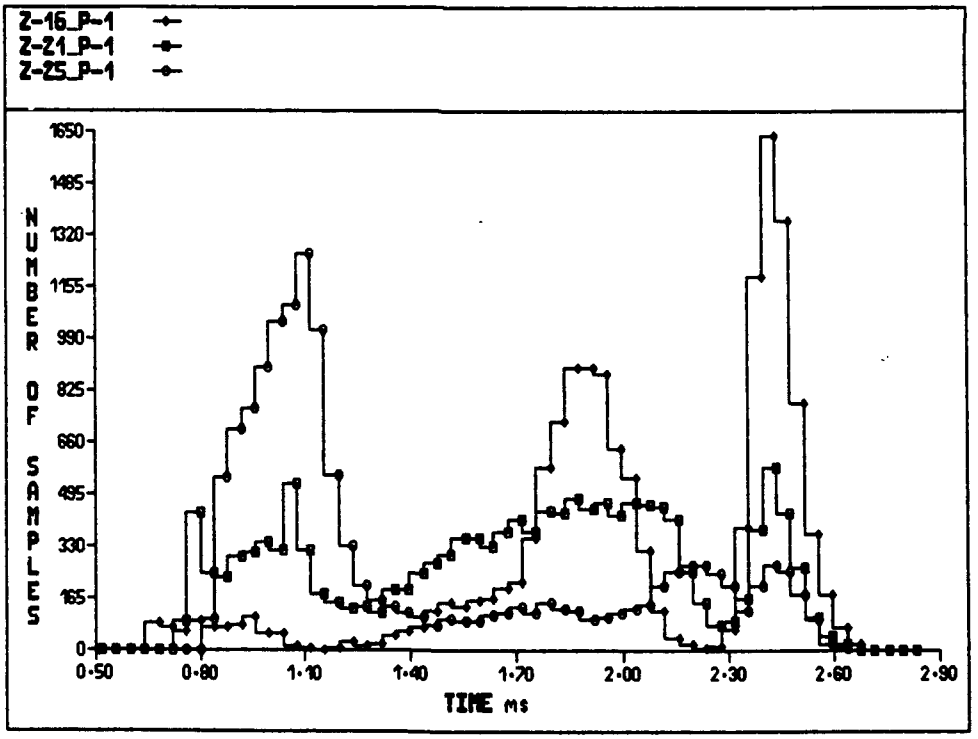

Fig. 3 Sample distribution plots for different axial locations

To indicate how these ligaments propagate downstream and finally break-up, plots of the sample number distributions are shown in Figure 3 for the spray axis, r = 0 mm, at the axial locations of z = 16, 21 and 25 mm. The time of flight of the spray tip between the three axial locations is 80 μs, giving a mean tip penetration velocity of initially 62.5 m/s and decreasing to 50 m/s. The sample number distributions at z = 16 and 21 mm are similar with the two main ligaments clearly present, at 1.10 ms and 2.20 ms for the first location and with a short delay for the time of flight for the second location. However, at this second location non-zero sample numbers indicate that the ligaments are not always present i.e. spatial instabilities and/or break-up occurs. This partly explains the large changes observed in the sample number distribution recorded for the third location, z = 25 mm. A high degree of atomization now occurs in and behind the spray tip with the peak sample number found at 1.1 ms which is followed by a steep decline in numbers and a levelling off after 1.40 ms.

There are several processes which determine the sample number distribution between z = 16 and 25 mm. The growing instabilities, break-up and atomization of the ligaments responsible for the downstream droplet generation and vaporisation, ignition and combustion accounting for droplet consumption. The dominant mode for droplet production is considered to be shear acting on the surface of the high speed ligaments. However, the shear force associated with these high pressure transient sprays varies in both space and time. The fuel injection pressure varies during the injection period and the resistance to the fuel flow decreases downstream from the nozzle as the upstream droplets transfer their momentum to the surrounding air. All of these effects contribute to determining the droplet size. Figure 4 shows how the dropsize time history varies between z = 10, 16, 20, 21 and 25 mm for a fixed radial position in the spray of r = 0.4 mm. The family of dropsize profiles follow a curve similar to a shallow parabola with an initial decrease in the dropsize, until after 1.1 ms, which is followed by an increase, after 1.22 ms, but with each profile having a different rate of rise. The times of 1.1 and 1.22 ms are significant, the first coincides with the fuel line pressure being a maximum at the nozzle while the latter is the time at which combustion is detected at z = 25 mm. The droplets on the spray tip at every axial location, other than z = 10 mm, have the same arithmetic mean diameter, D_{10} , of 3.5 μm. All the dropsizes decrease after the spray tip but the smallest, down to 2 μm, are to be found between z = 10 and 16 mm. The dropsize profiles at z = 20, 21 and 25 mm exhibit an increase in time but also an additional increase with increasing distance downstream from the nozzle. However, it is not that larger droplets are being produced in increasing numbers, as is the case close to the nozzle, but that the small dropsize classes, less than 1 μm, are being depleted from the dropsize distribution.

Variation in the dropsize profile as a function of radial position in the spray also has a certain dependence on the axial location. Between z = 5 and 15 mm the dropsize decreases quite steeply across the core and shear regions of the spray to a near uniform value in the spray periphery. At z = 16, 20 and 21 mm there is also a decrease in the dropsize from the spray axis out into the shear layer to r = 0.6 mm but then an increase, at r = 0.8 mm, before the dropsize profiles again decrease with increasing radial location in the spray

This radial variation in the dropsize profiles is shown in Figure 5 at the axial location of z = 21 mm. The high dropsize values in the shear layer are at r = 0.8 mm, position 5 in the plots. One point of note is that the time history of radial velocity component for r = 0.8 mm is the first to show predominately positive values. These droplets are much less affected by entrainment which has a greater influence on the smallest dropsize classes. An analysis of the raw data revealed that fewer small droplets were recorded but that also the validation rate had a significantly lower value here than at neighbouring radial positions. The explanation to this behaviour lies in the final break-up and atomization of the unstable ligaments whose swept cross-sectional area is greater than that of the initial axial ligaments. Effective droplet generation is still to be found at the location of greatest shear

While this mean velocity, dropsize and sample presented in a precise manner it is difficult to visualise happening in the spray, not only locally but globally, animation of the spray data has been made to visualise the planar droplet flow field structure. Four frames of this are presented to highlight some of the events taking place. Each flow field frame shows a geometric representation of the injector injecting in the horizontal direction. The spatial distribution of the data at any specific time shows the local mean droplet velocity and trajectory represented by a vector and the dropsize as a circle centred on the vector. The relevant time and scales are given above in the title bar, the vector arrow head also scales according to the vector length. The title bar also contains the colour or grey scale code for each vector which is based on the data sample count in each 40 μs time bin and only represents the recorded droplet density distribution. The fuel line pressure diagram is also included in the flow field frame. Needle lift occurs at 220 Bar (0.46 ms), peak pressure is 386 Bar (1.02 ms) and the needle closes at 136 Bar (2.12 ms). To reduce confusion with overlying vectors the radial distances have been expanded relative to the axial distances downstream from the nozzle.

The first frame, in Figure 6, is at 0.78 ms and the fuel line pressure has reached 294 Bar. It shows that the spray tip has reached the 21 mm axial measurement plane and that only those droplets in the downstream peripheral regions of the spray, r > 1.4 mm at z = 16 mm and r > 0.8 mm at z = 20 and 21 mm, have any appreciable outward radial trajectories. Elsewhere, behind the spray tip and particularly in the measurement planes z = 5, 10 and 15 mm the droplets exhibit a considerable degree of entrainment back into the spray. It is important to note that the absolute vertical and horizontal velocity components were measured and not those parallel and normal to the local spray axis trajectory.

The variation in the vector lengths in the different axial measurement planes indicates the complex interactions of the fuel ligament in the spray tip and the transfer of momentum from the droplets to the initially quiescent airflow. The ligament is responsible for the spray tip penetration and droplet generation with high instantaneous velocities, at z = 15 and 16 mm, while the high drag on the droplets cause rapid deceleration, high momentum transfer rates and low terminal droplet velocities at z = 5 and 10 mm.

The spatial variation in dropsize shows the largest found are at z =5 mm and close to the spray axis at z = 15

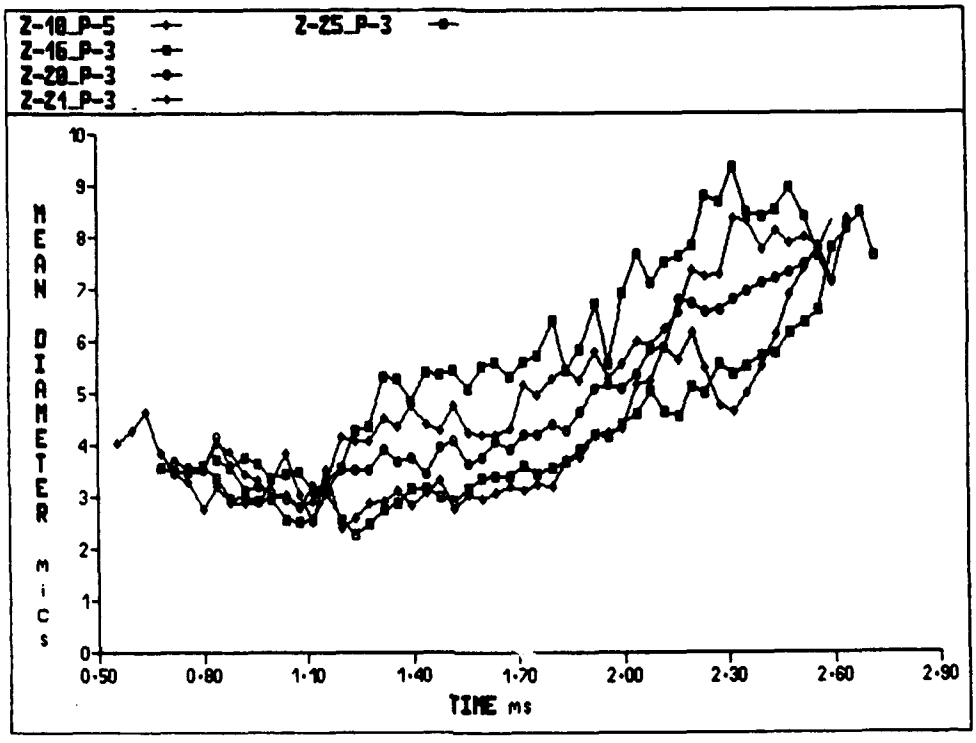

Fig. 4 Mean dropsize plots for different axial locations

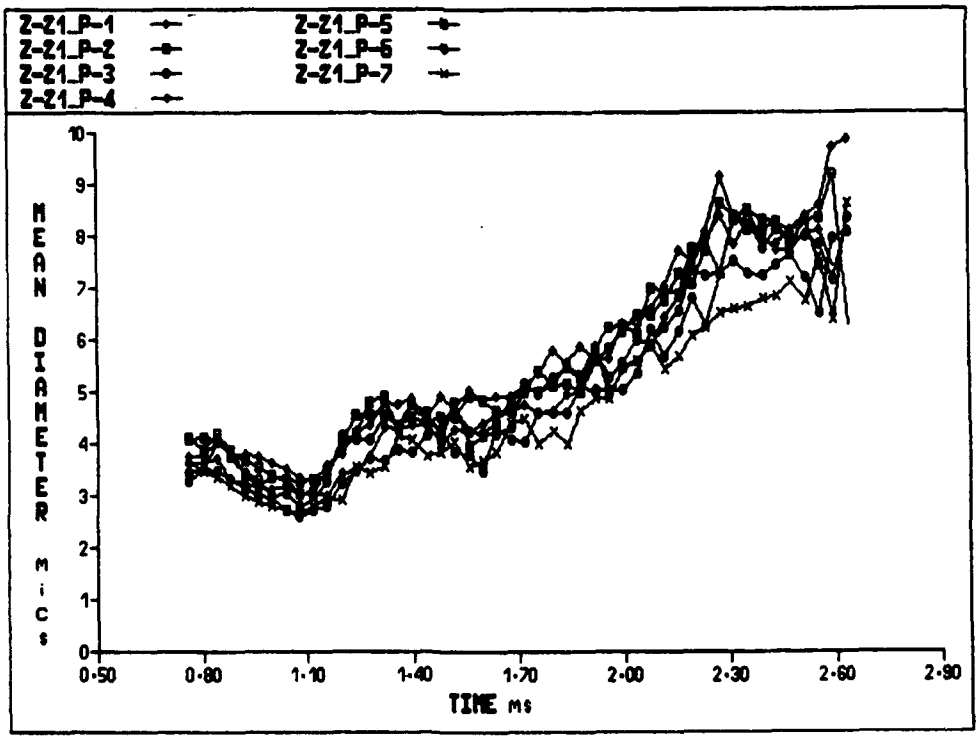

Fig. 5 Mean dropsize plots for different radial locations

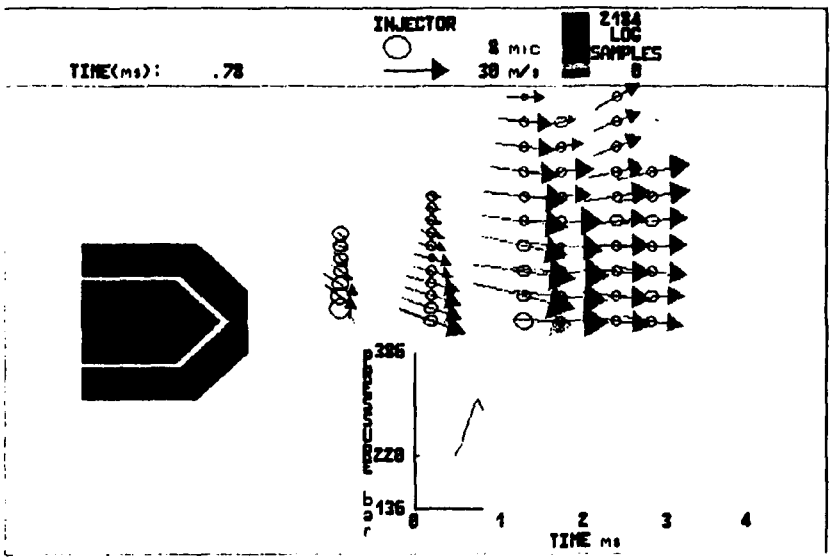

Fig. 6 Velocity vector and dropsize field at 0.78ms

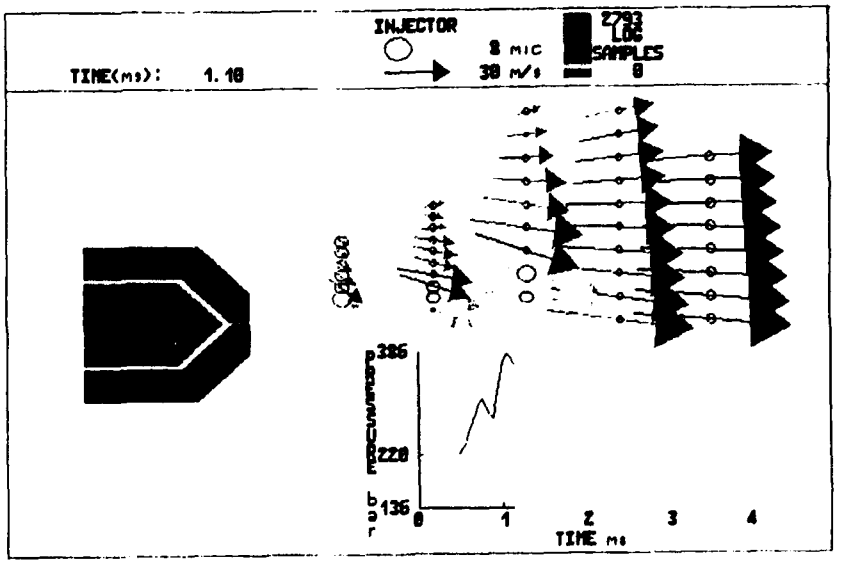

Fig. 7 Velocity vector and dropsize field at 1.1ms

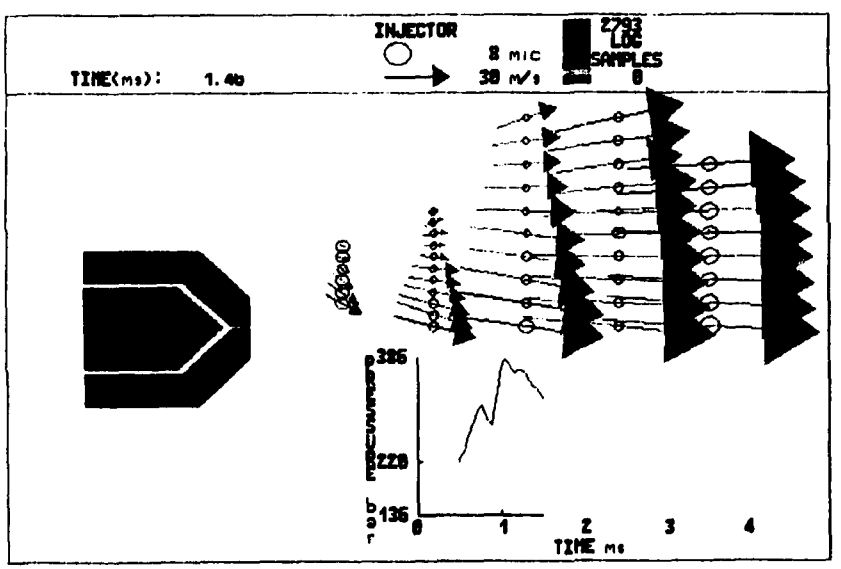

Fig. 8 Velocity vector and dropsize field at 1.46ms

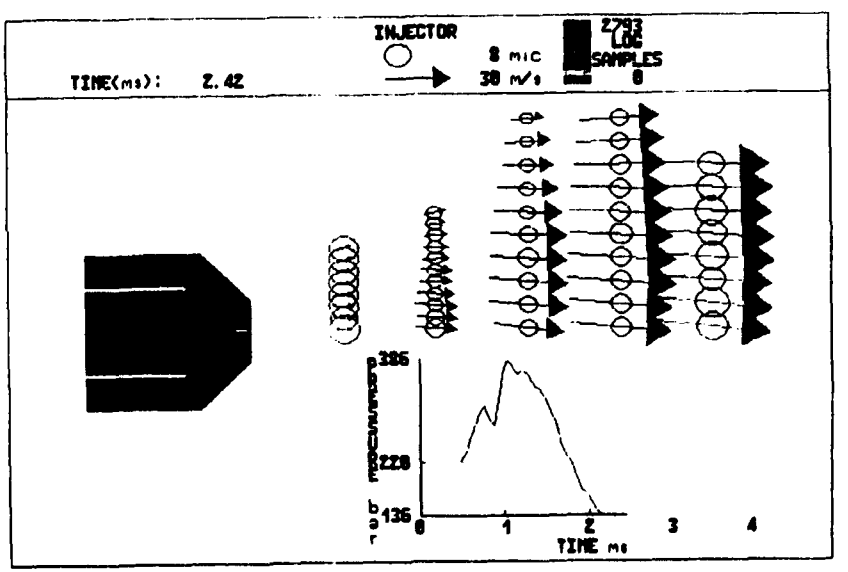

Fig. 9 Velocity vector and dropsize field at 2.42ms

mm. The smallest droplets are found at z = 10 mm and in general the dropsize decreases with increasing radial location. The highest recorded droplet sample counts are on the spray periphery at the axial locations z = 15, 16 and 20 mm.

The second frame, in Figure 7, at 1.1 ms shows how the droplet flow field structure has developed up to the estimated time at which peak pressure at the nozzle is reached, the line pressure indicates 368 Bar. This time coincides with the smallest dropsizes being measured throughout the spray. The flow structure on the spray axis is dominated by the second fuel ligament passing through the locations z = 5, 10 and 15 mm. It appears to produce few, but comparatively large droplets with high velocities and entrainment in the neighbouring radial measurement locations. Away from the spray axis the droplet velocities show a systematic increase with distance downstream from the nozzle with the droplets in the spray tip, i.e. at z = 25 mm, having the highest velocities, up to 70 m/s, and a near linear but weak velocity gradient in the radial direction. The sample density distribution across the spray at z = 25 mm is quite uniform out to r = 1.2 mm and higher than anywhere else in the spray. The dropsizes are generally smaller in this frame than in the previous one and, excluding those on the spray axis, have a narrow distribution of sizes. The largest droplets are to be found at z = 5 mm, up to 5 μm, followed by those at z = 25 mm at 3.5 μm.

The third frame in Figure 8, at 1.46 ms and fuel line pressure of 324 Bar, shows the droplet flow field structure at the time when the droplet velocities at z = 25 mm have reached their maximum values of approximately 99 m/s. The fuel ligament of the previous frame is coming to an end, its presence can only be found at z = 5 mm at r = 0 and 0.1 mm but low sample counts are still to be found on the spray axis even down to z = 15 mm. Entrainment of the droplets back into the spray is still high in this region and extends out to approximately 0.5rmax where also the highest droplet sample counts are to be found. At z = 20 and 25 mm the droplet sample count and axial velocity across the spray is quite uniform out to r = 1.0 mm. At greater radial positions the droplet sample count decreases, the radial outflow increases and the axial velocity component decreases. The droplet sizes have all increased compared with the previous frame but the increase at z = 20 and 25 mm is higher since combustion started at 1.26 ms at z = 25 mm. The smallest droplets are still to be found at z = 10 and 15 mm with a decreasing size profile as the radius increases.

Apart from the third ligament appearing at 1.9 ms the velocity field slowly relaxes as the fuel line pressure decreases. The needle closes at 2.12 ms, with a fuel line pressure of 136 Bar, which causes this ligament to break-up close to the nozzle by 2.30 ms. This produces the highest recorded droplet sample counts to be observed on the spray axis. The flow field structure in Figure 9 at 2.42 ms indicates that the highest droplet sample counts are found between z = 5, 10 and 15 mm for r less than 0.2, 0.4 and 0.4 mm respectively. These high sample counts do not penetrate down to z = 20 mm, where a uniform distribution is found across the spray, while at z = 25 mm the sample count is a minimum on the spray axis.

Without more fuel being injected the spray moves under its own momentum and generates a radial out flow to be observed at z = 5 and 10 mm although the velocities are small. They are less than 10 and 15 m/s respectively with the former being obscured by the large scale of the dropsize data. The velocity profile across the spray at z = 20 and 25 mm is virtually a plug flow but with a slight radial in-flow on the spray axis. Assuming that the flow field structure is fully developed this would mean that the spray axis itself was inclined to the vertical and if not due to the mechanical alignment of the nozzle then it was due to the in-cylinder air motion and/or combustion.

The dropsize distribution now shows large increases in the dropsize at all locations but particularly at z = 5, 20 and 25 mm. Not only are large droplets produced close to the nozzle after the needle closes but evaporation and combustion are depleting the lower dropsize classes elsewhere. After this time the dropsize steadily increases while the axial velocities decrease until, at 2.70 ms, droplets are no longer found at z = 20 and 25 mm. Droplets can still be found between z = 5 and 15 mm as late as 3.3 ms but with velocities of only a few m/s and with dropsizes of up to 20 μm or more

4. CONCLUSIONS

Simultaneous two component velocity and dropsize measurements have been performed in the near nozzle region of a Diesel injector in a firing engine, using Phase Doppler Anemometry. The results support the presence of a central single phase core of liquid, from which droplets are formed in the shear layer between the core and the gas. The measurement of the radial component of velocity has allowed the entrainment of droplets back into the spray to be identified. The central core is not contiguous during the entire injection period, but is composed of several well defined and coherent ligament structures.

ACKNOWLEDGEMENTS

The authors are pleased to acknowledge the encouragement and support for this work given by AVL-List GmbH and Dantec Measurement Technology A/S, and the sponsorship of the German Forschungsvereinigung Verbrennungskraftmaschinen (FVV).

REFERENCES

Pitcher, G. & Wigley, G. 1992, A Study of the Breakup and Atomization of a Combusting Diesel Fuel Spray by Phase Doppler Anemometry, Proc.Sixth Int. Sym. on Applications of Laser Techniques to Fluid Mechanics, Lisbon, pp. 25.1.1-25.1.7.

Pitcher, G. & Wigley, G. 1991, The Design and Application of a Two Component LDA System to Study Engine Flows, Proc. Laser Anemometry Advances and Applications, Cleveland, vol. 1, pp. 179-189.

Ruis, F. & Chigier, N. 1985, The Mechanics of High Speed Atomization, Proc. Int. Conf. on Liquid Atomization and Spray Systems, London.

CORRELATION BETWEEN THE CHARACTERISTICS OF AN IDI DIESEL SPRAY MEASURED WITH PDA AND INSTANTANEOUS CONDITIONS IN THE NOZZLE

J.M. Desantes, J. Arrègle and J.V. Pastor

CMT. Dpto. Máquinas y Motores Térmicos
Universidad Politécnica de Valencia, Spain.

ABSTRACT

Characteristics and physical phenomena inherent to an IDI Diesel spray (pintle injector) vary considerably during the injection process and depend mainly on instantaneous conditions upstream the injector.

Velocity and diameter distributions of fuel droplets have been obtained for a given spray at various distances downstream the injector. Images of the spray at each instant were also taken in order to obtain the evolution of macroscopical characteristics of the jet such as tip penetration and angle of the spray.

A description of the experimental facilities used to study atmospheric IDI Diesel sprays is presented. The paper concludes with a correlation made between the behaviour of the spray and the instantaneous characteristics in the nozzle.

1. INTRODUCTION

Characteristics of the fuel spray injected inside the cylinder of a Diesel engine, is one of the main factors affecting the combustion process and, so the engine efficiency and pollutant emissions.

The need of obtaining "cleaner" engines nowadays, makes necessary to improve the knowledge of phenomena of spray atomisation.

Many researchers have focused their efforts towards the study and characterization of Diesel injection, some of them studying the spray directly inside real fired engines (Quoc & Brun (1993), Ahmadi-Befrui et al. (1991) and Wigley (1990)). The complexity and difficulties inherent to this kind of experiments has lead to the development of many physical models more or less close to real engines in order to make this study easier. Such models go from the Rapid Compression Machine (Takahashi et al. (1991)) to the injection in atmospheric conditions. The main advantages of this kind of simplified models are the accessibility to observe and measure in the jet, and the close control of many experimental parameters.

The aim of research works on Diesel injection is often to determine characteristic variables of the spray. The more available ones are the geometrical characteristics, as spray tip penetration and spray angle. Many works have been based on observation by means of standard photography (Sánchez et al. (1992) and Arcoumanis et al. (1989)), CCD camera (Ahmadi-Befrui et al.(1991)) and high–speed cinematography (Reitz & Braco (1979) and Takahashi et al. (1991)) in order to obtain geometrical characteristics as a function of test conditions.

A very important variable to characterize the atomisation process of the liquid stream sprayed by a nozzle is the break-up length. It has been determined by measuring the electrical conductivity inside the spray (Hiroyasu & Arai (1990) and Chehroudi et al. (1985)).

Counting of droplets collected in liquid or solid surfaces, was first used to measure the final diameter of fuel droplets (Hiroyasu & Arai (1990)). More recently, optical techniques have permitted to determine droplet diameters distributions in any given point of the jet.

An important step taken towards the comprehension of the liquid stream atomisation (primary atomisation) phenomena, the break-up of the largest unstable droplets into smaller ones (secondary atomisation) and the coalescence, has been the development and application of PDA to the study of Diesel sprays. The simultaneous determination of the velocity and diameter of the droplets in any point of the jet has made possible to follow the evolution of spray structure, and to observe directly

the result of the different atomisation processes.

As a consequence of the general and relevant results obtained from these studies, a series of empirical expressions describing the relationships between characteristics of DI Diesel sprays and injection parameters, in particular, diameter of the orifice, relation between fuel and air densities and injection pressure.

It must be noted that, apart from some exceptions (Zhang & Shi (1990), Arcoumanis et al. (1989) ...), most results are referred to DI plain orifice injectors.

IDI systems (pintle nozzle) sprays are different from DI systems for several reasons. Besides the fact that injection pressures are significantly lower, the shape of the orifice of the injector is a ring, generally non symmetrical, whose section and geometry are controlled by the position of the pintle. Because of this, the hydrodynamic characteristics of the fluid at the exit of the injector are very different of those of the direct injection and vary considerably along the injection process as a function of the pintle lift. Figure 1 shows that conditions peculiar to direct injection are placed inside the "atomization" jet breakup regime defined by Reitz (Lefebvre (1989)). Conversely, in the case of a pintle injector,

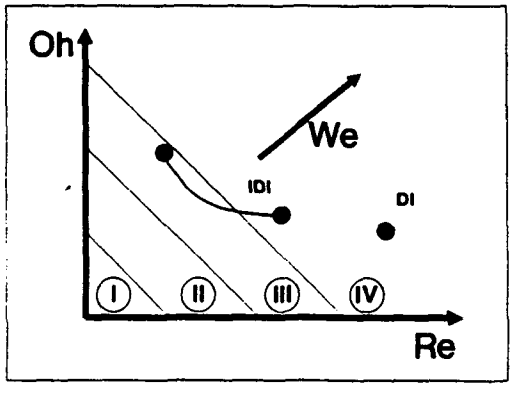

Figure 1: Jet breakup regimes. I: Raleigh breakup, II: First wind induced breakup, III: Second wind induced breakup, IV: Atomization breakup

conditions in the nozzle vary along the injection period and can go from the "atomisation" jet breakup regime to the "second wind induced" jet breakup regime. Thus, great differences in the spray behaviour when changing from one regime to another are expected.

Results obtained with DI systems can not be always extrapolated to IDI sprays because of aforementioned reasons.

2. OBJECTIVES OF THE WORK

The object of this paper is to characterize free sprays injected by a pintle injector under atmospheric conditions and to establish the relations between the behaviour of the spray and the instantaneous geometric and hydrodynamic conditions upstream the nozzle.

With this purpose different injection parameters are measured in order to obtain the instantaneous conditions in the injector hole. On the other hand, PDA and shadowgraph techniques are employed to characterize the spray behaviour. Tests have been performed varying injection conditions and geometric characteristics of the injector, in order to cover the whole range of injection conditions peculiar to IDI Diesel engines.

In this paper, experimental facilities used for the study of sprays under atmospheric conditions are described and an example of the results obtained is given.

3. EXPERIMENTAL FACILITIES

As a consequence of their variability, geometrical and hydrodynamic conditions in the nozzle play a very important role in the spray behaviour. Thus it is very interesting to determine them in detail. A previous characterization of the injector allows to determine the effective section of the nozzle and the hydraulic equivalent diameter as a function of pintle lift. During PDA measurements and shadowgraphy, a signal corresponding to this pintle lift is provided by an inductive transducer. From this signal, it is possible to analyze the dynamics of all moving pieces and thus, to determine the pressure strengths acting against them. By means of this method (Payri et al. (1993)), different parameters are obtained: instantaneous pressure upstream the nozzle, injection rate and instantaneous characteristics at the injector exit, such as effective section, hydraulic equivalent diameter, flow conditions ...

The experimental setups for PDA measurements and spray imaging are shown in figures 2 and 3.

The emitting optics of the PDA system includes a 4W water cooled Ar^+ Laser source operated at 400mW, a 40 Mhz Bragg cell as frequency shifter and a TSI 15mm laser probe linked by 10m length fibre optics. A lens with a focal length of 100mm was placed after the probe in order to increase the range of velocities allowed by the system. Collecting

Laser wavelength	514.5 nm
Number of fringes	29
Fringe spacing	8.708μm
Effective scattering angle	68°
Receiving lens focal length	310 mm
Polarization orientation	0° parallel
Phase factor U1-2	3.09 deg/μm
Phase factor U1-3	1.55 deg/μm

Table 1: PDA configuration

optics and electronics are those of a standard Dantec 1-component system. PDA configuration used is summarized in table 1.

PDA measurements were performed without temporal gating. The 1 x cycle signal given by the injection pump bench was used as a trigger for the PDA system. In order to use the injection line of standard engines keeping all injection parameters controlled, the injector was fixed in horizontal position and no movement was allowed. The PDA optics were mounted vertically on a X-Y-Z table what permits measuring at any point of the jet. Spray was injected into the atmosphere. The aspiration system was designed to collect most of injected fuel, generating an air stream weak enough not to disturb the jet.

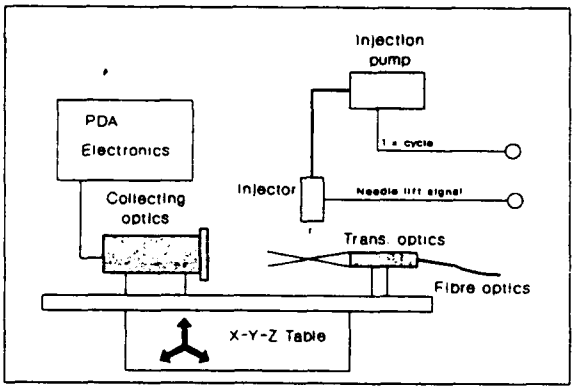

Figure 2: Test facility for injection rate and PDA measurements.

Measurements were performed at 18 points and 5000 samples were validated for each one. Axial symmetry of the jet was assumed. Thus 10 points were located on the axis of the jet (Z = 5, 10, 15, 20, 30, 50, 100, 150, 200, and 250mm from the injector), and the other 8 points were placed out of the axis (r = 2, 4, and 8mm for Z = 20, and r = 2, 4, 8, 12, 16mm for Z=100mm). These point were chosen to sweep a zone equivalent to that of the real free length of the spray in engine conditions.

To take photographs of the spray, a Nikon 601-M camera with a 60mm Macro objective and ISO 100/21 standard film was used. Obturation of the camera was manually operated. As illumination device, a Metz CT-45 flash with fixed duration of 70 μs was placed behind the jet. A white metacrilate plate and a rough glass were used as diffusors, in order to obtain homogeneous illumination in a rectangular area of at least 300x150mm.

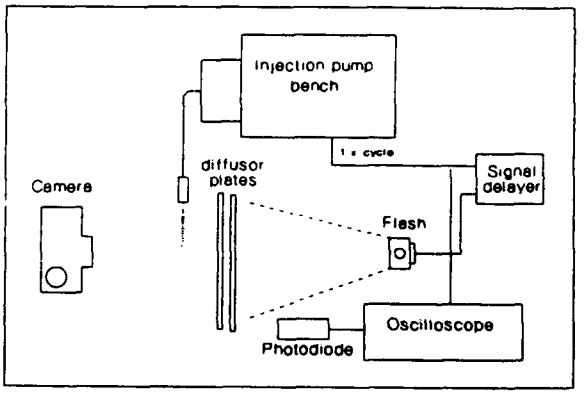

Figure 3: Test facility for spray imaging.

A TTL reset signal coming from the injection pump bench, electronically delayed at a previously defined time with respect to the injection beginning, was used as trigger signal for the flash. The system allows to obtain only one photography each time, but taken at a prefixed delay with respect to the injection beginning. So, images were taken at instants separated 20μs, along the whole injection duration. Global macroscopic characteristics such as the angle of the jet and the spray tip penetration have been obtained with a simple processing. Although quantitative information of microscopical parameters such as density distribution of the jet would need a shorter exposure time, this system has proved to be a useful tool to compare sprays coming from different injectors or from the same injector under different injection conditions, as well as to guide PDA measurements.

4. DISCUSSION OF RESULTS

Experimental results shown in this paper are a typical example of IDI spray corresponding to a full

load injection with a pump speed of 1250 rpm. As said before, the main characteristic of this kind of injection is the variation of effective section. In figure 4, two zones with different behaviour can be noted. Up to a pintle lift of 0.4mm approx., section increases slowly to create a pilot injection. Since 0.4mm, opening is quicker and appears a discontinuity in flow conditions. As a consequence of this behaviour, Weber Number, which describes opposite strengths with influence on liquid core atomisation, presents three rather different zones.

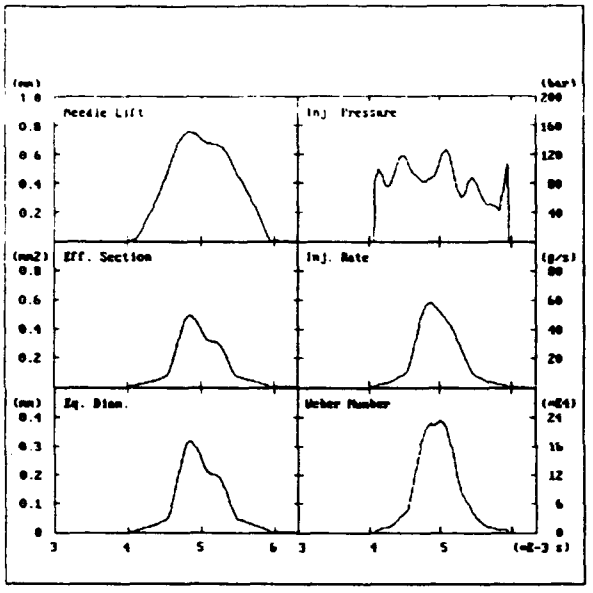

Figure 4: Injection parameters.

Figure 5 shows results provided directly by PDA. The first plot represents the velocities of 5000 droplets measured at 5mm from the nozzle, on the axis of the jet. Each velocity sample has been plotted by a dot, whereas the continuous line shows the phase averaged value of Sauter Mean Diameter. Injection takes place 3.5ms after the beginning of the pump cycle.

Great variations of the droplet velocities can be observed during the injection duration (2ms). Three different zones appear, corresponding exactly to those of Weber Number previously commented. For We around 20 000, very low velocities between 20 and 50 m/s are obtained. In the central zone of the injection, for We > 100 000, velocities are much higher, reaching 130m/s. The low velocities measured at the beginning and at the end of the injection are partially due to the fact that the first droplets injected find a static air and thus are quickly braked; on the other hand, the last 0.5ms of injection correspond to relatively low pressures. However, the main cause of this effect is the modification of exit conditions.

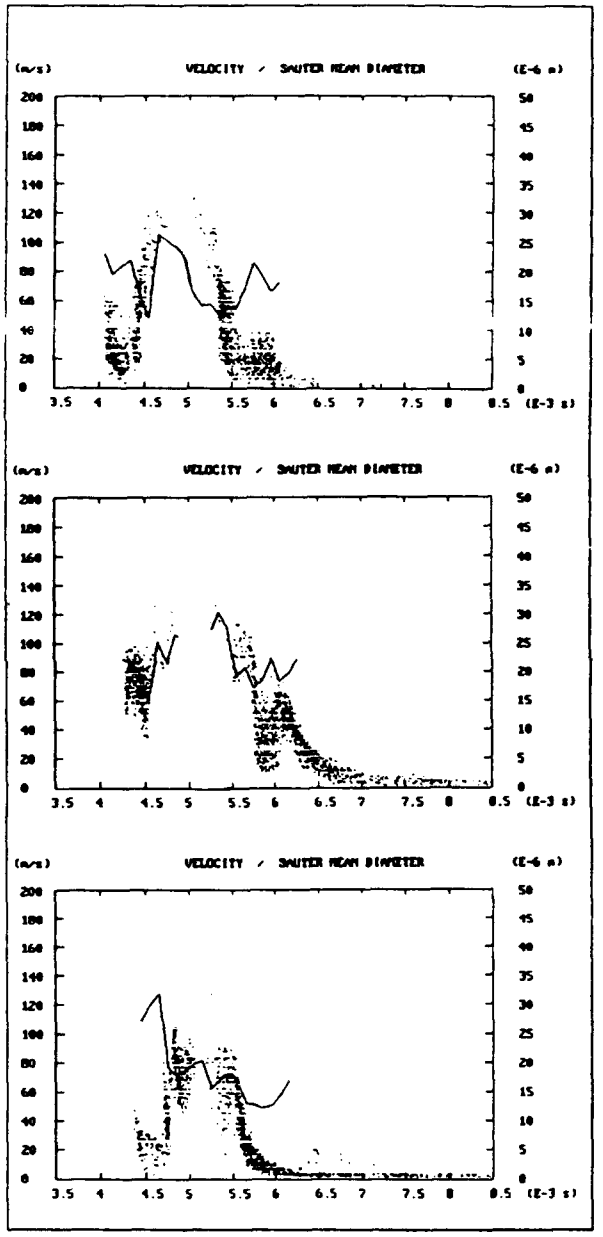

Figure 5: PDA results. (a) Z=5mm, r=0; (b) Z=20mm, r=0 ; (c) Z=20, r=2mm.

In agreement with Hiroyasu & Arai (1990), an increase in Weber number implies a better atomisation of the spray and a decrease of the quantity Breakup length/Φ_{eq}. However, due to the great variation of

Φ_{eq} along the IDI injection process, the increase of Weber number implies, in our case, an increase of the breakup length. For We < 50 000 atomisation is already complete at a short distance from the injector and the existing droplets are quickly braked. Conversely, for larger We the liquid core is more important. Fuel maintains a velocity close to the exit theoretical velocity until a larger distance from the injector.

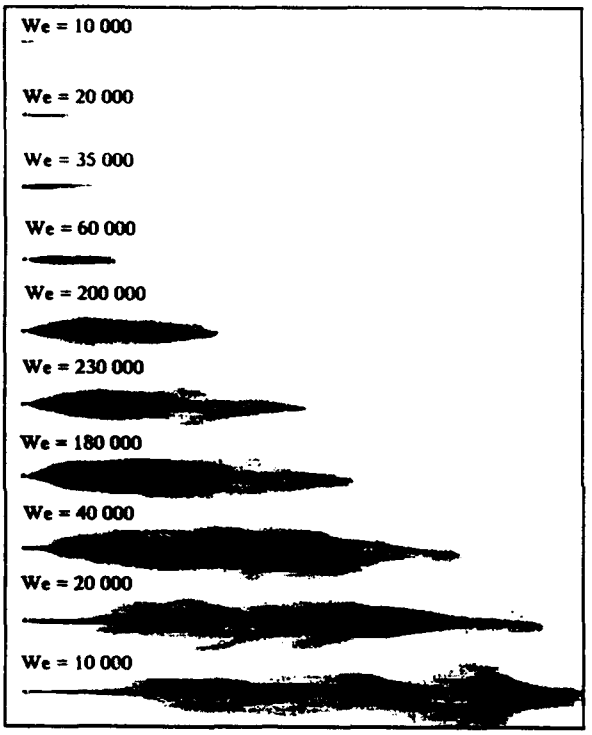

Figure 6: Evolution of the spray. Photographs are taken at intervals of 20μs. Instantaneous Weber number is indicated above each photograph.

This discontinuity in the injected fuel braking process explains the apparent acceleration of the spray tip observed in figure 7 as a hard change in the slope of the tip penetration curve starting on 4.0ms. The presence of the liquid core can be observed in the graphs of PDA results (figure 5(a) and (b)) as a zone with very few data at the centre of the injection.

PDA measurements out of the axis of the jet as well as shadowgraphs' results (figure 7) also evidence the dependence of the spray angle on Φ_{eq} and Weber Number. For low We, injection conditions are placed inside (or on the border of) the "second wind induced" breakup regime, which corresponds to a low spray angle. Conversely, for large values of We, we are closer to typical conditions of direct injection, and spray angles are larger.

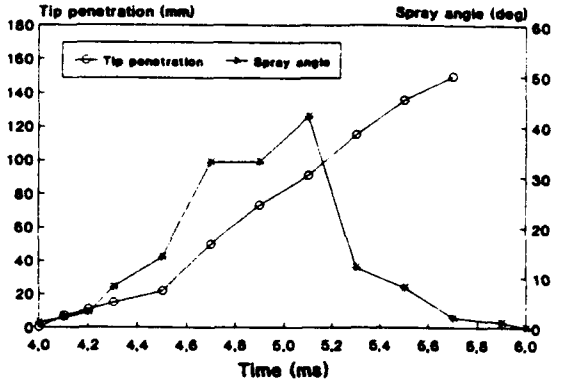

Figure 7: Spray angle and tip penetration.

It must be noted that, due to the variable behaviour of the jet, its structure is not uniform and "fuel packets" injected at every instant are overlapped by the next injected ones making difficult to analyze directly PDA results at large distances from the nozzle. A method for processing results provided by PDA which will allow to follow the trajectories of the fuel packets at any instant and thus analyzing better the relationships between instantaneous injection conditions and behaviour of the spray is being developed at CMT.

5. CONCLUSIONS

In this paper, facilities put into operation for the study of IDI Diesel sprays, have been presented through an example. Simultaneous measurement of hydrodynamic instantaneous characteristics at the nozzle and of droplets' velocities and diameters by means of PDA, as well as shadow photography permit to obtain information for a better understanding of phenomena which take place in this kind of sprays.

First studies have evidenced that spray characteristics vary considerably along the injection process, and their behaviour depends directly on instantaneous Weber number.

Due to these important variations in the atomisation process, the spray development is not homogeneous and the rapid droplets catch up with the slow ones, increasing the difficulty to draw conclusions from PDA measurements. Nowadays a method

to follow the evolution of "fuel packets" injected at every instant is being developed. The method will allow determining the relationship between the exit conditions and the atomisation process and spray development.

ACKNOWLEDGMENTS

The authors would like to thank PSA-Peugeot-Citröen for collaborating in the fulfilment of this work.

NOMENCLATURE

Z, r	coordinates of measurement points
Φ_{eq}	Hydraulic equivalent diameter
v_i	initial velocity of the spray
ν	kinematic viscosity (2.25 E-6 m^2/s)
ρ_a	air density (1.3 Kg/m^3)
ρ_l	fuel density (820 Kg/m^3)
σ	Surface tension (0.024 Kg/s^2)
Re	Reynolds Number ($Re = \frac{V_i \Phi_{eq}}{\nu}$)
We	Weber Number ($We = \frac{\rho_l V_i^2 \Phi_{eq}}{\sigma}$)
Oh	Ohnesorge Number ($Oh = \frac{\nu \sqrt{\rho_l}}{\sqrt{\sigma}\sqrt{\Phi_{eq}}}$)

REFERENCES

Ahmadi-Befrui, B., Wiesler, B. & Winklhofer, E. 1991, The Propagation of Fuel Sprays in a Research Diesel Engine - A Joint Numerical and Experimental Analysis. SAE paper 910181.

Arcoumanis, C., et al. 1989, Transient Characteristics of Single-Hole Diesel Sprays. SAE paper 890314

Behrouz, C. 1990, Preliminary Drop Size and Velocity Measurements in a Dense Diesel-Type Spray. SAE Paper 901673.

Chehroudi, B. et al. 1985, On the Intact Core of Fuel-Cone Sprays SAE paper 850126.

Hardalupas, Y., Taylor, A.M.K.P. & Whitelaw. J.H. 1992, Characteristics of the Spray from a Diesel Injector. Int. J. Multiphase Flow, Vol. 18, No. 2, pp 159-179.

Hiroyasu. H. & Arai, M. 1990, Structures of Fuel Sprays in Diesel Engines. SAE paper 900475.

Koo, J.Y. & Martin, J.K 1990, Droplet Sizes and Velocities in a Transient Diesel Fuel Spray. SAE paper 900397

Lefebvre, A.H., 1989, Atomization and Sprays, Hemisphere Publishing Corporation, New York.

Payri, F., Desantes, J.M. & Arrègle, J. 1993, Determination du Taux d'Introduction sur Moteur Diesel à Injection Indirecte. ENTROPIE No. 174/175, pp.61-68.

Quoc. H.X., & Brun. M. 1993, Analyse Expérimentale du Jet de Gazole dans un Moteur Diesel a Injection Directe par la Méthode des Phases Doppler. Proc. Congres International SIA: Moteurs Diesel: Actualité-Potentialité, Lyon pp 71-77, No. 93054.

Reitz, R.D. & Bracco, F.B. 1979, On the Dependence of Spray Angle and Other Spray Parameters on Nozzle Design and Operating Conditions. SAE paper 790494.

Reitz, R.D. & Bracco, F.B. 1982, Mechanism of Atomization of a Liquid Jet. Phys. Fluids, vol. 25, No. 10, pp. 1730-1742.

Sánchez, M. et al. 1992, Installation pour l'Etude des Jets Biphasiques avec un Système PDA et Techniques Photographiques. Proc. Congres International SIA: Le groupe motopropulseur: développements et perspectives, Valencia pp 140-145. No. 92004.

Takahashi, H. et al. 1991, Characteristics of Diesel Spray with Unsteady and Higher Injection Pressure Using a Rapid Compression Machine. SAE paper 910226.

Wigley, G. 1990. Phase Doppler Anemometry for the Study of Droplet Dynamics in Automotive Fuel Sprays. AVL-LIST GmbH, Graz - Austria.

Zhang, Y.S. & Shi, S.X. 1990, Experimental and Numerical Study of Diesel Fuel Spray from Pintle Nozzles. Proc. Int. Sym. COMODIA 90, pp.287-292.

MANIFOLD INJECTION AND THE ORIGIN OF DROPLETS AT THE EXIT OF AN INLET VALVE

M.Posylkin, A.M.K.P.Taylor and J.H.Whitelaw

Imperial College of Science, Technology and Medicine
Mechanical Engineering Department
Exibition Road, London SW7 2BX, U.K.

ABSTRACT

Distributions of droplet size, axial velocity and liquid flux have been measured downstream of a model inlet valve with a phase-Doppler velocimeter. The valve had a diameter of 40mm, a 45° bevelled edge and was arranged at the exit of a straight tube of inside diameter 34mm with the lifts of 2, 4 and 6mm. Suction was applied by a variable speed electric fan to simulate the intake stroke of a cylinder of 400cc displacement at 1200 RPM, with an air flow rate for the 4mm valve lift of $0.99m^3$/min, corresponding to the bulk velocity of 38m/s in the valve gap. Gasoline was supplied either by a commercial injector located 70mm from the valve or by its introduction on the surfaces of the valve and port.

The injection of fuel with an open valve led to Sauter mean diameters between 80 and 100μm, lower than the 130μm appropriate to the free unconfined spray. With 2mm valve lift, the spray emerged between angles of 10° to 70° to the horizontal axis and with larger valve lifts it emerged with narrow angle close to that of the valve head surface immediately upstream of the valve bevel, that is 25°. The introduction of fuel as a liquid streams led to a Sauter mean diameter of 240μm with the maximum flux emerging from the edges of the valve and seat bevels, at angles of 50° and 40° to the horizontal axis, respectively.

1. INTRODUCTION

Port injection of fuel can lead to mixture control, fuel economy and low emissions particularly when combined with a three way catalyst in a spark-ignition engine. Electronic control offers an added advantage in setting of the injection timing for individual cylinders and Quader (1982) has demonstrated that axial stratification, which can be beneficial with lean mixtures, can be achieved by injecting fuel into the inlet port before the end of the intake stroke with the inlet valve open.

The droplet sizes produced by a pintle injector, see for example Hardalupas, Taylor and Whitelaw (1990) and Dementhon (1992), correspond to Sauter mean diameter of about 130μm and, for injection with an open valve, Miller and Nightingale (1990) quote 10μm as the largest droplet diameter which is able to follow the gaseous phase in the inlet port and therefore able to avoid impingement on the solid surfaces of the valve and the port. Thus, most droplets impinge on solid surfaces and the consequences depend on the orientation and location of the injector. The liquid may re-atomize, for example by impingement, or remain as liquid on the surfaces to be removed ultimately by evaporation or by the air flow.

Extensive research has been carried out to study the effect of the interaction between sprays and solid surfaces. Photographic methods were used with single droplets, for example by Stow and Hadfield (1981) and Chandra and Avedesian (1991), and have shown that the droplet impinging on a solid surface may spread, rebound or form smaller droplets according to the droplet size, velocity, surface roughness and temperature. However, the results were limited to droplets of approximately 1mm diameter and should be extrapolated with care to the substantially smaller droplets of the impinging spray produced by a gasoline injector. Hardalupas, Okamoto, Taylor and Whitelaw (1992) used phase-Doppler velocimetry to examine the consequences of a spray impinging on a inclined disk, without co-flowing air, and showed that resulting Sauter mean diameters were smaller than in the free spray upstream of the disk but up to 180μm close to the downstream edge, possibly due to impingement on the surface covered with liquid film from previous injections. Similarly, impingement on a rod led to secondary atomization and a reduction of Sauter mean diameter immediately upstream of the rod and to a liquid film with most of the liquid content of the spray in the form of a stream downstream of the rod. Measurements of the droplet sizes downstream of the inlet valve in a steady and unsteady flow simulation of the isothermal manifold of a spark ignition engine, for example Miller and Nightingale (1990) and Dementhon (1992), have shown diameters in excess of 200μm which are larger than those of the incident spray and probably due to the formation of liquid film. Formation of surface liquid was also conjectured from measurements of the droplet sizes in a firing engine and with injection with the inlet valve closed, Vannobel, Robart, Dementhon and Whitelaw (1994) and Posylkin, Taylor,

Vannobel and Whitelaw (1994), which have shown large effects of the residence time of the fuel on the surface of the valve from which there must be evaporation, though not immediately after the start-up when the inlet valve is still cold.

Due to the complexity of induction phenomena it is difficult to distinguish between the consequences of a spray impinging on a solid surface and of the removal of liquid from a solid surface by co-flowing air. Thus, the purpose of the present work was to measure size, velocity and flux characteristics at the exit from an inlet valve of a spray produced by injection of fuel with an inlet valve open and to compare the results with these for subsequent experiments in which liquid fuel was allowed to flow down the valve stem and down the pipe wall to be subsequently removed by air flow, as with injection during a cold start with the inlet valve closed.

The following section describes the experimental arrangement and instrumentation. The results are presented in the third section and the paper ends with a summary of the more important findings.

2. EXPERIMENTAL ARRANGEMENT

The steady flow arrangement used to investigate the nature of droplets in the valve curtain area is shown in figure 1, together with co-ordinate system, and with an injector directing a fuel spray towards a valve. Air was drawn through a flow contraction, with area ratio of 16, mounted on the top of the inlet pipe which was 400mm long, with inner and outer diameters of 34 and 40mm. The valve was located on the axis of the inlet pipe to within ±0.5mm by a spacer arrangement with a valve stem of 4mm diameter and 410mm long. The axial location was controlled and measured by a micrometer arrangement to within ±0.05mm. The bulk of the micrometer arrangement was located in the contraction and so did not disturb the flow within the inlet pipe. The valve diameter was 40mm at the bottom face and 34mm diameter at the upper face, with a 45° bevelled edge which corresponded to a similar bevelled edge on the exit of the inlet pipe. The valve arrangement was mounted vertically on the lid of a closed cylindrical chamber of 220mm inside diameter and identical to that described by Hardalupas et al (1990). A variable speed electric fan was connected to the bottom of the chamber to induce an air flow through the inlet pipe and the volumetric flow rate of the air was monitored by a rotameter.

Unleaded gasoline of density 765 kg/m^3 and viscosity 0.515 cSt at 25°C was drawn from a tank by an electric fuel pump and supplied through a diaphragm pressure regulator, which maintained a nominally constant pressure of 3 bar gauge, to either a commercial injector or, through a control valve and rotameter, to the upper valve surface or the port wall. The fuel injector was located 70mm from the valve and at 24° to the vertical axis of the pipe, so that the axis of symmetry of the injector was directed to the centre of the valve. Fuel was supplied to the surface of the valve through six radial 1mm holes located 3mm above the upper surface of the valve which had a hollow stem, and to the port wall from a pipe of 5mm diameter located 400mm above the valve from which it was allowed to spread freely over the circumference of the wall.

Two 90mm diameter glass windows provided optical access to the chamber and permitted collection of the scattered light at an angle of 30° to the axis of the transmission optics of the phase-Doppler anemometer. The optical characteristics of the anemometer are summarized in Table 1 and the electronic signal was processed by a counter triggered by a TTL pulse train of 1ms duration from the delayed gate output of an oscilloscope and synchronized with the injection pulse from the driving electronics of the injector. Size-discriminated measurements of the velocity vectors were achieved by rotation of the plane of the beams about the axis of the transmitting optics as described by Hardalupas and Liu (1992).

The accuracy of sizing was unaffected by the presence of non-spherical droplets because their velocities resulted in Weber numbers less than unity for a typical measured Sauter mean diameter of 100μm, which is far below the critical breakup value of around 12. The measurements were based on about 5000 samples at each point, resulting in statistical uncertainties of less than ±3% in the mean, ±10% in the rms of the velocity signal and ±2% in the cumulative size distribution based on the number of droplets (Tate, 1982). The liquid flux measurements are presented in arbitrary units since the uncertainty in the individual measurements is difficult to quantify and may be more than 30% in some regions of the flow.

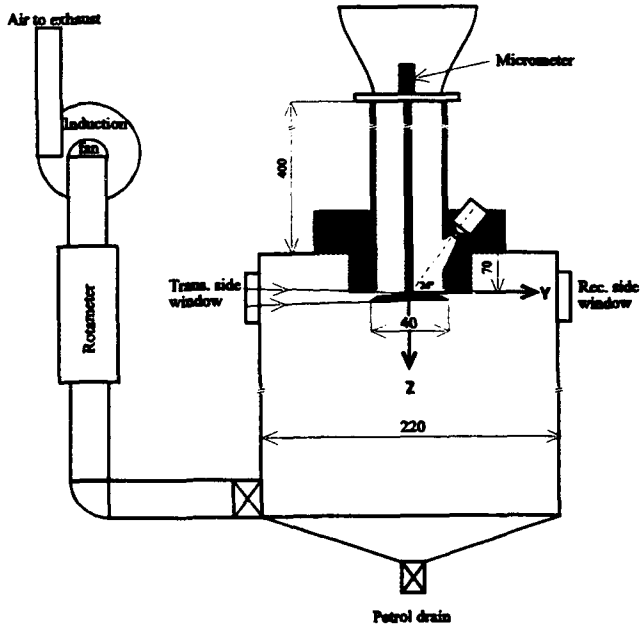

Figure 1: The experimental arrangement

TABLE 1: Characteristics of the Phase-Doppler Velocimeter

*Transmitting Optics**

300 mW (nominal) Ar^+ laser wavelength	514.5 nm
operated at	100 mW
Beam diameter, at e^{-2} intensity	1.25 mm
Focal length of lenses:	
imaging lens from laser to grating	80 (100) mm
collimating lens after grating	200 mm
imaging lens to form measuring volume	600 mm
Number of lines on radial diffraction grating	16384 (8192)
Shift frequency (nominal) due to rotation of grating	3 MHz (1.5)
Short-term stability of shift frequency (r.m.s.)	0.3 %
Beam separation	34 (17) mm
Measured half-angle of intersection	1.62° (0.88°)
Calculated dimensions of beam intersection volume at $1/e^2$ intensity	4.44 (8.8) mm 0.125 (0.156) mm 0.125 (0.156) mm
Fringe spacing	9.106 (16.69) μm
Calculated number of fringes within $1/e^2$ intensity	14 (9.4)
Frequency to velocity conversion factor	0.109 (0.0599) MHz/ms^{-1}

Receiving Optics

Location of collection optics from forward scatter	30 degrees
Focal length of collimating lens in receiving optics	600 mm
Apertures at collimating lens:	
dimension of rectangular apertures	45 x 6 mm
separation between apertures 1 and 2	25 mm
separation between apertures 1 and 3	50 mm
Focal length of imaging lens in receiving optics	300 mm
Width of spatial filter before the photomultipliers	100 μm
Magnification of receiving optics	2
hence effective length of measuring volume	400 μm
Phase angle-to-diameter conversion factor for channel 1 and 3	0.51 (1.02) μm/degree

3. RESULTS AND DISCUSSION

The results are presented in two sub-sections which describe size, velocity and liquid flux characteristics of droplets in the valve curtain area as a result of injection with an open valve and those produced by fuel introduced entirely as a liquid stream on either the upper surface of the valve or on the port wall. The axial distributions of droplet characteristics as a result of injection with an open valve are presented for valve lifts of 2, 4 and 6mm and with air flow rates of 0.56m^3/min, 0.99m^3/min and 1.2m^3/min, respectively. Additional results are then presented for a valve lift of 4mm which was required to avoid impingement of emerging droplets on the bevelled edge of the port, with a steady suction pressure of 2kPa gauge in the cylindrical chamber which resulted in co-flowing air flow rate of 0.99m^3/min and bulk velocities of 18.2m/s in the inlet pipe and 38m/s in the valve gap. This flow rate was about four times higher than the time averaged air flow rate into a single cylinder of 400cc displacement operating at 1200 RPM and was chosen because induction occurs during one of the four strokes. The injection duration was kept constant at 7ms, unless otherwise stated, with a corresponding charge of 25mm^3/injection and an injection frequency of 10 Hz, which resulted in a fuel flow rate of 15cc/min, and also corresponded to a speed of 1200 RPM in a four stroke engine. For the experiments with introduction of steady fuel streams, the flow rate should be larger than 15cc/min to simulate the high instantaneous flow rate experienced by a solid surface during the impingement and therefore, since the 7ms injection duration corresponds to about one third of the duration of the intake stroke at 1200 RPM, the fuel flow rate was varied in the range of 12 - 42cc/min.

The results are presented as ensemble averages over the injection cycle and with time measured from the beginning of injection. The velocity results have been normalized by the bulk air velocity in the valve gap, that is U_o = 43.7, 38 and 31m/s for the valve lifts of 2, 4 and 6mm, respectively, and the diameter of the valve, D = 40mm, was used to normalize the radial and axial distances from the valve exit. Measurements were made at a radial distance of Y = 24mm from the valve exit which was chosen to allow at least 0.5ms between detachment of droplet from the valve and arrival at the measuring volume to ensure spherical droplets, Naber and Farrell (1993), and to remain close enough to the valve exit to preserve temporal information. The measurement locations were between Z = 1mm and 30mm below the exit, where droplets emerged as a result of injection or introduction of liquid stream on valve or port surfaces, and corresponded to 0.025 < Z/D < 0.75 at Y/D = 1.1. Velocity measurements are presented for four ranges of droplet diameters, namely 24 to 30μm, 56 to 62μm, 120 to 126μm and 141 to 153μm, which are referred to as the 27, 59, 123 and 147μm droplet-size ranges. The 27μm range was representative of droplets subject to secondary atomization and able to follow the gaseous velocity most closely, the 59μm and 123μm ranges were representative of the most probable diameter and of the sizes carrying more than 50% of the liquid flux when the fuel was injected with the valve open, and the 147μm size range was typical of the most probable diameter when films were removed by air.

3.1 Spray Injected with theValve Open

Figure 2(a-c) shows time averaged spatial distributions of arithmetic and Sauter mean diameters, mean axial velocities of most probable size class and liquid flux for valve lifts of 2, 4

* Values in brackets show the modified setting used to increase the measurable range of a PDA instrument during the experiments with liquid streams.

and 6mm, with the velocities of the co-flowing air, measured in absence of fuel, shown by vectors. For the valve lift of 2mm, the liquid flux had a flat distribution and emerged in the range $0.05 < Z/D < 0.75$, that is in an arc between 10° to 70° to the horizontal axis, and a Sauter mean diameter of around 100μm compared with that of 130μm in the free unconfined spray. With increase in the valve lift to 4 and 6mm, the axial distribution of flux exhibited maxima at $Z/D = 0.075$ and 0.125 respectively, which suggests that most of the droplets emerged from the region close to that of the valve head immediately upstream of the valve bevel. Size-discriminated measurements of the axial and radial velocity components at the locations of flux maxima confirmed that the velocity vectors in the Y-Z plane were at about 25° to the horizontal axis, compared with about 35° for the co-flowing air, and did not depend on the droplet size. The Sauter mean diameters were some 20% smaller than with the 2mm valve lift, at about 80μm. The axial velocity of the most probable size class, that is 57μm, at the location of flux maxima, was about 10m/s and the magnitude of velocity vector of about 23m/s considering the trajectory of droplets. Reduction of the air flow rate, and consequently the bulk air velocity in the valve gap, by a factor of two did not affect the spatial distribution of liquid flux although there was an increase of 10% in Sauter mean diameter.

Figure 3 shows the effect of injection duration on arithmetic and Sauter mean diameters of emerging droplets, averaged over the injection cycle, with the valve lift of 4mm and at $Z/D = 0.075$, corresponding to the location of flux peak of figure 2(b). The Sauter mean diameter increased monotonically from 75 to 100μm as the duration of injection increased from 3 to 11ms and the larger difference between arithmetic and Sauter mean diameters with increased injection duration suggests that the relative number of large droplets increased.

Figure 4 shows the temporal development of Sauter mean diameter, axial velocities of three size ranges and fluxes at the same vertical location as in figure 3 and for injection durations of 4, 7 and 10ms. The Sauter mean diameter increased monotonically with the time elapsed from the beginning of injection, with the largest droplets emerging at the end of the injection cycle and their size increasing with injection duration. The axial velocities of the large droplets were found to be lower than those of the small droplets and independent of injection duration. This temporal development of Sauter mean diameters and size-velocity relationship is opposite to that measured in the free unconfined spray by Hardalupas et al (1990) and Posylkin et al (1993). The temporal development of the liquid flux shows that the peak has been displaced towards trailing edge of the spray, as compared with 1ms delay after the spray tip arrival in the free unconfined spray of Posylkin et al (1993).

The differences between characteristics of the spray at the exit of an inlet valve and these of the free unconfined spray are likely to follow from the impingement of incident spray on the solid surfaces. It is worth noting that, to avoid impingement on the valve, a droplet must acquire a radial component of velocity

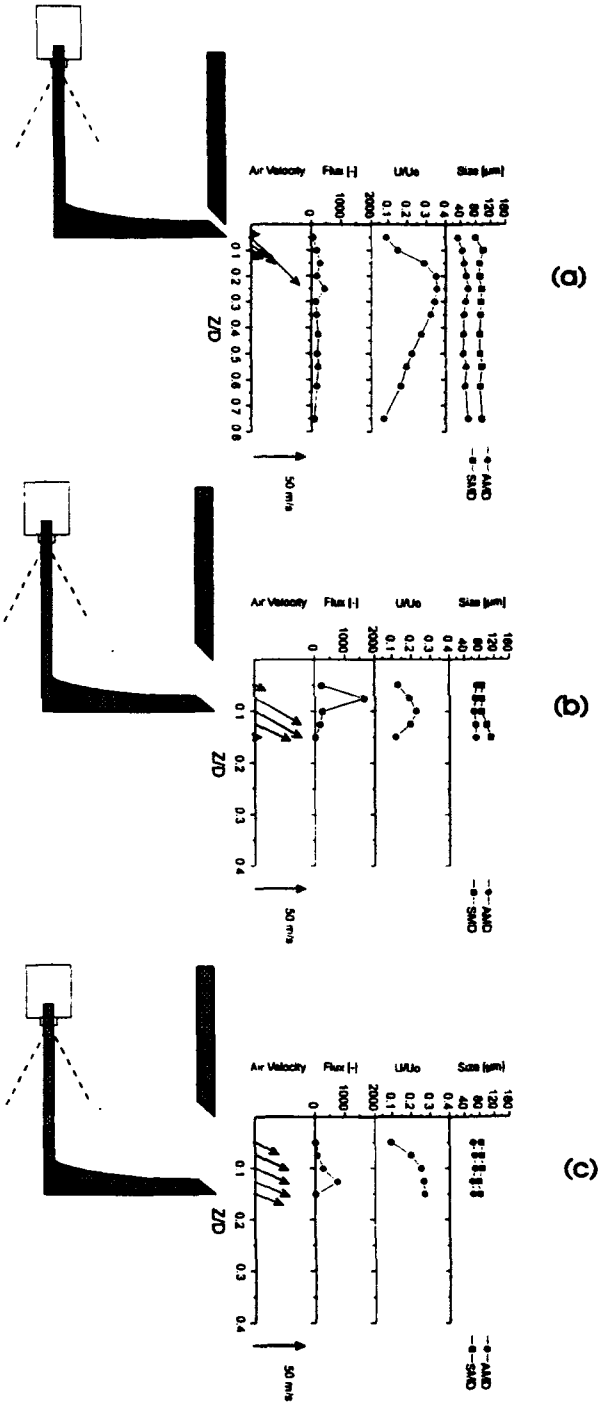

Figure 2: Spray injected with valve open: Axial distribution of mean diameters, axial velocity of 57μm size class, flux and air velocity vectors for valve lifts of (a) 2mm (b) 4mm and (c) 6mm. $Y/D = 1.1$

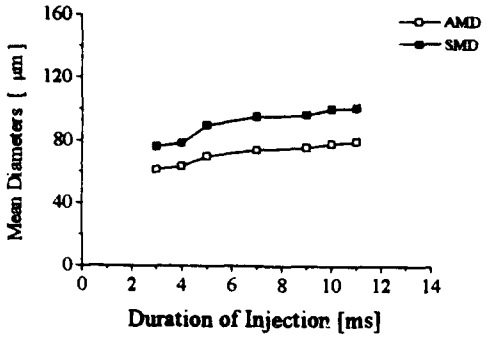

Figure 3: Spray injected with valve open: Effect of injection duration on mean diameters of droplets downstream of the inlet valve. Valve lift = 4mm; Y/D = 1.1; Z/D = 0.075. Diameters averaged over injection cycle.

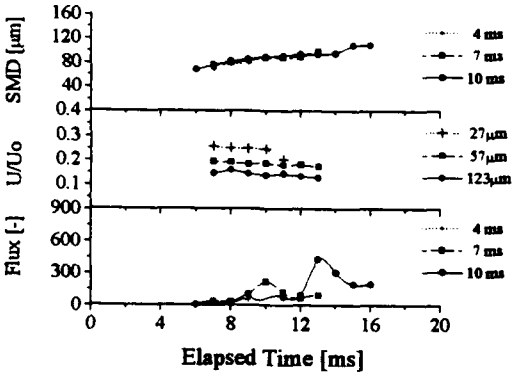

Figure 4: Spray injected with valve open: Temporal development of Sauter mean diameter, axial velocities of 27, 57 and 123μm size classes and liquid flux for injection durations of 4, 7 and 10ms. Valve lift = 4mm; Y/D = 1.1; Z/D = 0.075

from the air in the valve gap and, hence, the time of flight from the injector to the valve, t_f , must be large compared to the Stokes response time, $\tau = r_l d_l^2 / 18\mu_a$, where r_l and d_l are the density and diameter of the liquid droplet and μ_a is the viscosity of air. Thus the Stokes number $S_t = t_f / \tau$ should be of the order of 10, Ingham et al. (1990), and a typical value of t_f is about 3ms for the present experimental arrangement, so that droplets larger than 20μm are incapable of satisfying the Stokes criterion. This suggests that more than 90% of injected into the port flux will impinge on surfaces. The increase in size of the droplets emerging from the valve with time elapsed from beginning of injection could occur due to coagulation as more droplets are accelerated towards a narrow gap, probably with some formation of a liquid film. It is unlikely, however, that a continuous and stable liquid film could cover the valve head since the maximum film thickness would be less than 20μm assuming that all injected fuel remained on the valve. Secondary atomization by splashing would result in an even thinner estimate of film thickness, as argued in Appendix A, and would be unstable. The droplets, produced as a result of impingement, would be removed by the co-flowing air to explain the temporal development of the emerging spray, figure 4, where small droplets appeared first. With increase in injection duration and time elapsed from the start of injection, impingement of droplets could occur on already wetted surfaces and to contribute to an increase of the mean diameters, as indicated by figures 3 and 4, respectively. It is not possible to deduce from the above results the relative contribution of the drag applied by the co-flowing air on films, as with injection against a closed valve, and the following sub-section considers this by introducing the fuel entirely as a liquid streams on the surface of the valve and port walls.

3.2 Fuel Introduced on the Valve and Port Surfaces

Figure 5 shows the effect of fuel flow rate when introduced as a steady liquid stream on the head of the valve on Sauter mean diameter, axial velocities and liquid flux of droplets, and the spatial distribution of these parameters will be discussed in relation to figure 6. The three volumetric flow rates of fuel were 12, 27 and 42cc/min and corresponded to those introduced by injection with durations of 5, 10 and 15ms. Increase in the volumetric fuel flow rate caused the integrated flux profiles to increase in proportion with the amount of fuel supplied but hardly affected either the axial velocities and Sauter mean diameters of the droplets. A three-fold increase in the fuel flow rate resulted in an increase of less than 5% in the Sauter mean diameter, far below than that predicted by the relation suggested by Rizk and Lefebvre (1980) for pre-filming air blast atomizers. Variation in the fuel flow rate introduced on the port wall resulted in similar independence of the sizes of droplets downstream of the valve.

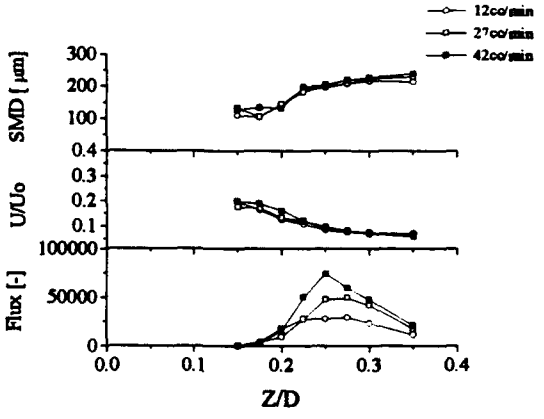

Figure 5: Steady liquid stream on the valve head: Effect of the fuel flow rate on Sauter mean diameter, axial velocity of 147μm size class and liquid flux. Valve lift = 4mm; Y/D = 1.1

Figure 6 shows a composite of spatial distributions of droplet characteristics measured with liquid streams introduced on the valve head and the wall surface at different times. The volumetric flow rate of the fuel was 15cc/min and similar to that of injected fuel with a duration of 7ms and frequency of 10Hz, so that results can be compared with these of figure 2(b). The distributions of flux showed that most of the spray emerged from the lower edges of the valve and seat bevels, with the attached arrows indicating the flux maxima which were located at Z/D = 0.25 and Z/D = 0.05, and at angles of 50° and 40° to the horizontal axis, respectively. More than 90% of the liquid flux emerged as droplets with Sauter mean diameters larger than 200μm, increasing to about 240μm at locations of flux maxima. The axial velocities at these location were less than 4m/s which, considering the trajectory of droplets, led to the magnitude of velocity vector of about 6m/s or 15% of that of the bulk velocity of the air in the valve gap. The remained fraction of the flux emerged in the region around Z/D = 0.15 as smaller droplets with higher velocities, possibly due to the stripping of the liquid upstream of the bevels.

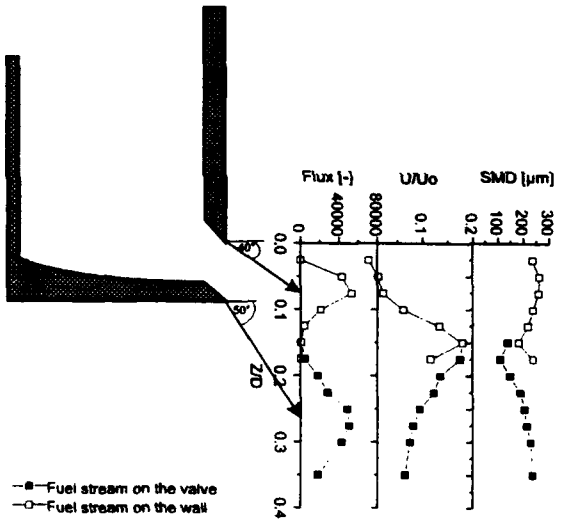

Figure 6: Steady liquid stream on the valve head and port wall: Axial distribution of Sauter mean diameter, axial velocity of 147μm size class and flux.
Valve lift = 4mm; Y/D = 1.1; Fuel flow rate = 15cc/min

The above results suggest that more than 90% of fuel was in the form of droplets with Sauter mean diameters above 200μm which were swept to the edges of the valve or seat bevels before emerging at the angles of these surfaces and with velocities which were comparatively low since the interface occurred at the intersection of liquid and air boundary layers. Thus, injection with the inlet valve closed is likely to imply that the initial characteristics of the spray are unimportant for the droplets at the exit of an inlet valve.

4. CONCLUSIONS

The following is a summary of the most important findings:

1. Injection with the inlet valve open implied reduction of the Sauter mean diameter of the spray from 130μm to around 90μm in the valve curtain. With valve lifts larger than 2mm, most of the droplets emerged from the region close to the surface of the valve head at an angle of about 25° to the horizontal axis and for the 2mm lift they emerged between angles of 10° and 70°. The magnitude of velocity vector of emerging droplets was around 20m/s and effect of the flow rate of air on their trajectory and size was small.

2. Injection with the inlet valve open led to mean diameters which increased with time from the beginning of injection, and larger droplets emerged at the end of the injection cycle. Increase in the duration of injection from 3 to 11ms led to increase in the Sauter mean diameter, averaged over the injection cycle, from 75 to 100μm.

3. The introduction of the fuel as liquid streams on the valve and port surfaces resulted in about 90% of the flux emerging from edges of the valve and seat bevels at angles of 50° and 40° to the horizontal axis, respectively. The Sauter mean diameters at locations of flux maxima were around 240μm, almost independent of the fuel flow rate, with magnitude of velocity vector of about 6m/s. These results are likely to imply that initial characteristics of the spray are unimportant for the droplets at the exit of an inlet valve with injection with the inlet valve closed.

APPENDIX A: Estimate of surface film thickness due to the impact of a single droplet.

An estimate of the effect of impingement by the single droplet on the valve head on the thickness of developing liquid film can be obtained from the energy balance before and after the impingement and assuming first that no splashing has occurred and that the evaporation during the period of droplet's shape transformation is negligible.

Before the impact kinetic and surface energy of the droplet are given by:

(1) $$E_{k_1} = \frac{1}{2}\rho_l U^2 \left(\frac{\pi}{6} d_1^3\right)$$

(2) $$E_{s_1} = \pi d_1^2 \sigma$$

where σ is the surface tension of the liquid drop. After the impingement, kinetic energy was expended to transform the droplet into a disc of diameter D and with surface energy (Chandra and Avedisian, 1991)

(3) $$E_{s_1} = \left(\frac{1}{4}\pi D^2\right)\sigma(1-\cos\Theta)$$

where Θ, defined in figure A1, is the angle between the solid surface and the tangent line to the disk front and is dependent on the solid surface temperature, with $\Theta \approx 30°$ for the surface at ambient temperature according to experimental results of Chandra and Avedisian (1991).

The work lost in deforming the liquid against the viscous forces can be estimated by assuming that the flow of expanding liquid is one dimensional, the volume of the drop is equal to the volume of the liquid once it has flattened out into the shape of disc and the time over which the expansion takes place to be equal to the time needed for the droplet of height h to go from its maximum value of d_1 to zero at velocity U. Based on the above assumptions it can be shown that the work lost, W, is:

(4) $$W = \frac{3}{8}\frac{\pi\mu U D^4}{d_1^2}$$

From energy conservation $E_{k_1} + E_{s_1} = W + E_{s_2}$ the expression for diameter of the flattened disc D yields:

(5) $$\frac{3}{8}\frac{\mu U}{d_1^2}D^4 + \frac{\sigma(1-\cos\phi)}{4}D^2 - d_1^2\left(\frac{1}{12}\rho U^2 d_1 + \sigma\right) = 0$$

and the thickness of the liquid disc t_d therefore can be obtained from:

(6) $$t_d \approx \frac{2}{3}\frac{D^3}{d_1^2}$$

For the droplets produced by a pintle injector, with a Sauter mean diameter of about 100μm and impinging on the valve surface with velocities between 20m/s and 10m/s, (Hardalupas et al. 1990), the thickness of the developing disc shaped film is estimated to be 4μm and 6μm respectively, based on the analysis described above. It is unlikely that such a thickness could be sustained in practice due to the instabilities developed in the shear flow at both liquid-solid and liquid-air interfaces and the film is expected to be unstable and to break-up under the contracting action of the surface tension.

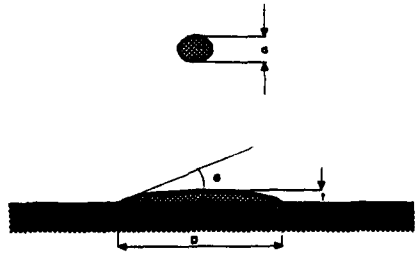

Figure A1: Impingement of a single droplet on solid surface

5. REFERENCES

Chandra, S., Avedisian, C.T. (1991) On the collision of a droplet with a solid surface. Proc. R. Soc. Lond. A432, 13-41.

Dementhon, J.B. (1992) L'injection essence dans un moteur a etincelle: mesures granulometriques par la methode des phases Doppler et phenomnes de pulverisation. These presentee a la Faculte des Sciences de l'Universite de Rouen, Rouen, France.

Hardalupas, Y. and Liu, C.H. (1992) Size-Discriminated Velocity Cross-Correlation Measured by a Single Channel Phase-Doppler Velocimeter. In Laser Anemometry in Fluid Mechanics 6, 145-165. (Editors: R.J.Adrian, D.F.G.Durao, F.Durst, M.Heitor, M.Maeda and J.H.Whitelaw). Springer Verlag.

Hardalupas, Y., Taylor, A.M.K.P., Whitelaw, J.H. (1990) Unsteady Sprays by a Pintle Injector. JSME International Journal, Series II, 33, 2, 177-185.

Hardalupas, Y., Okamoto, S., Taylor, A.M.K.P. and Whitelaw, J.H. (1993) Application of phase-Doppler anemometer to a spray impinging on a disk. In Laser Anemometry in Fluid Mechanics 6, 490-506. (Editors: R.J.Adrian, D.F.G.Durao, F.Durst, M.Heitor, M.Maeda and J.H.Whitelaw), Springer Verlag.

Ingham, D.B., Hildyard, L.T., and Hildyard, M.L (1990) On Critical Stokes' Number for Particle Transport in Potential and Viscous Flows near Bluff Bodies. J. Aerosol Sci., 21, 935-946.

Kadota, T., Mizutani, S., Wu, C.Y., and Hoshino, M. (1990a) Fuel Droplet Size Measurement in the Combustion Chamber of a Motored SI Engine via Laser Mie Scattering. SAE paper 900477.

Miller, M.J. and Nightingale,C.J.E. (1990) Measurement of the charges in mixture preparation that occur during flow past the inlet valve of an SI engine. IMechE Int'l conference on Automotive Power Systems, Chester, paper C394/004

Naber, J.D., Farrell, P.V. (1993) Hydrodynamics of droplet impingement on heated surface. SAE paper 930919.

Posylkin, M., Taylor, A.M.K.P. and Whitelaw, J.H. (1993) Size and velocity characteristics of fuel droplets in the valve curtain area of a straight, steady-flow inlet manifold. Imperial College, Thermofluids Section, Mechanical Engineering Department Report no. TF/93/05.

Posylkin, M., Taylor, A.M.K.P., Vannobel, F. and Whitelaw, J.H. (1994) Fuel droplets inside firing spark ignition engine. Paper submitted for presentation at the 1994 Fuels and Lubricants Meeting of SAE.

Quader, A.A., (1982) The Axially-Stratified-Charge Engine. SAE paper 820131

Rizk, N.K., Lefebvre, A.H. (1980) Influence of liquid film

thickness on airblast atomization. Trans. ASME J. Eng. Power, 102, 706-710.

Stow, C.D., Hadfield, M.G. (1981) An experimental investigation of fluid flow resulting from the impact of a water drop with an unyielding dry surface. Proc. R. Soc. Lond. A373, 419-441.

Tate, R.W. (1982) Some Problems Associated with the Accurate Representation of Droplet Size Distributions. In Proc. of 2nd Int'l Conf. on Liquid Atomisation and Spray Systems (ICLASS), Wisconsin, USA.

Vannobel, F., Robart, D., Dementhon, J.B. and Whitelaw, J.H. (1994) Velocity and size distributions in the cylinder of a two-valve production SI engine. To be published in the Proceedings of COMODIA

ASPECTS OF LEAN-BURN COMBUSTION AND IMPLICATIONS FOR SPARK-IGNITION ENGINES

C. Arcoumanis, D. Hull, J. H. Whitelaw and H .M. Xu

Department of Mechanical Engineering
Imperial College of Science, Technology and Medicine
London, England

ABSTRACT

Experiments have been carried out in a single-cylinder spark-ignition engine and a constant-volume combustion chamber to investigate various aspects of lean-burn combustion. The engine was fuelled with gaseous propane at equivalence ratios of 0.7 to 0.9 and operated at 1000 rpm with two in-cylinder flow conditions, namely quiescent and with swirl generated by a shrouded valve, whereas the constant-volume chamber employed a secondary injection system which added a small amount of rich mixture in the vicinity of the spark plug, with the remainder of the lean mixture premixed with overall equivalence ratios of 0.72, 0.39 and 0.34. The engine results showed an improvement on the cyclic combustion variations in the presence of swirl but with limitations imposed by very lean mixtures and a small effect from the premixedness of the injected fuel, while those obtained in the constant-volume chamber demonstrated that 100% ignitability could be achieved even at equivalence ratios as low as 0.39 by the local injection towards the spark plug of a small quantity of rich mixture.

1. INTRODUCTION

The recent trend towards manifold fuel injection and its arrangement so as to provide stratification of the air-fuel mixture has been documented in several references including those of Quader (1982), Horie et al (1992), and Kiyota et al (1992). It involves injection of liquid fuel over a crank-angle interval of around 90 degrees, in either a sequential or parallel mode. There remains considerable uncertainty about the preferred timing not least because measurements of the concentration of fuel within the cylinder at the time of ignition remain small in number and of uncertain accuracy. More information is available of the immediate consequences of port injection as a result of experiments such as those performed by Posylkin, Taylor and Whitelaw (1994) and Vannobel, Robart, Dementhon and Whitelaw (1994) which show that the characteristics of the spray matter little except where injection takes place towards an open inlet valve. In this case, and provided the spray is characterised by a small Sauter mean diameter, late injection with a fully open valve may be preferable in achieving charge stratification by avoiding contact of the spray with the surfaces of the port and cylinder head. On the other hand, injection against a closed valve is preferred in many production engines and it is evident from the experiments conducted so far that injection well before intake valve opening will enhance fuel evaporation with a number and size of droplets which reduce as a function of the time spent within the port and on hot solid surfaces from which they can more easily evaporate. Injection towards a closed valve just before valve opening will result in a proportion of the spray taking the form of wall liquid films which will be stripped by the slower moving air stream close to the wall as the valve opens, with consequent large and low-velocity droplets making up most of the liquid content.

The results and deductions summarised in the previous paragraph provide an incomplete picture of the way in which the fuel enters the cylinder as a consequence of manifold injection and a pessimistic view, at least in the short term, of the possibility of relating this information directly to the distribution of the fuel at the time of ignition. The experiments presented in this paper make two related contributions to understanding the consequences of fuel injection and do so specifically in the context of lean mixtures. The first part of the investigation was conducted in a single-cylinder engine with injection of gaseous fuel at equivalence ratios of 0.7 to 0.9 and two in-cylinder flow conditions, namely quiescent and shroud-generated swirl. The second part was carried out in a constant-volume chamber in which a small proportion of the total fuel/air mixture was injected towards the spark plug with the remainder of the mixture premixed with overall equivalence ratios of 0.72, 0.39 and 0.34. The engine results showed an improvement on the cyclic combustion variations in the presence of swirl but with limitations imposed by very lean mixtures and a small effect from the premixedness of injected fuel. Those obtained in the constant-volume chamber demonstrated that 100% ignitability can be achieved with an overall equivalence ratio of 0.39 and local mixture stratification; obviously, this represents a remote target for port-injected spark-ignition engines but every effort should be made to optimise fuel injection, local flow conditions and ignition in order to extend the present air/fuel ratio limit of 25 in production engines even further.

2. ENGINE, CONSTANT-VOLUME CHAMBER AND INSTRUMENTATION

The single-cylinder engine, Fig. 1, has been described previously by Vafidis, Whitelaw and Xu (1992), Whitelaw and Xu (1993) and Whitelaw and Xu (1994) and has the characteristics shown on Table 1. It was designed and constructed by Centro Richerche Fiat with provision for optical access through the piston and through two windows located in the cylinder liner.

Gaseous propane was supplied to the engine at equivalence ratios of 0.7-0.9, defined in terms of the fuel and air charged during each cycle in either of the two ways, i.e., port injection or premixed. In the first case, a specially designed injector was located at a position typical of port-injection engines, and commenced injection at 30° CA after TDC of induction. In the second case, propane was supplied at the entry of an extended manifold of 0.6 m length at a steady flow rate, the manifold was baffled and contained wirewool which helped to achieve premixed fuel and air with small turbulent scales.

The engine was operated at part load with volumetric efficiency (ηv) of 0.72, in skip firing mode which comprised five firing cycles followed by ten motored cycles in order to ensure the integrity of the engine optical components, and the water temperature was controlled at 323°K for the same reason. Whitelaw and Xu (1993) showed that with the above mixture preparation system the first 'firing' cycle tended to be a misfire and the second a fast-burning cycle caused by the residual unburned fuel from the first cycle so that the results discussed here are those from cycles 3, 4 and 5, which are believed to be representative of the combustion process in continuous firing cycles.

Table 1 Operating characteristics of the Fiat research engine

Bore	79.5	mm
Stroke	86.0	mm
Connecting rod length	145.0	mm
Clearance height	7.6	mm
Compression ratio	10	
Inlet valve opens	5°	BTDC
Inlet valve closes	225°	ATDC
Exhaust valve opens	225°	BTDC
Exhaust valve closes	5°	ATDC
Engine speed	1000	rpm
Mean piston speed	2.87	m/s
Volumetric efficiency	0.72	
Fuel injection starts	30	°ATDC
Ignition	315-320	°CA (MBT)
Nominal Equivalence ratio	0.7-0.9	

The flow generated by the cylinder head was first characterised in a steady flow rig with a shrouded intake valve selected to alter the intake flow pattern. The velocity and turbulence levels in the vicinity of the spark plug at the time of ignition during engine operation were quantified by laser Doppler velocimetry with light scattered from 0.56 μm diameter zirconium dioxide particles introduced into the inlet manifold.

The steady flow tests showed that the inlet flow in the cylinder was symmetrical about the diameter of the intake valve centre (Whitelaw and Xu, 1993c) in the case of the conventional non-shrouded intake valve, with almost zero swirl (Table 2, case CV) and a weak tumble motion which originated from the off-center intake valve position, with a tumble vortex

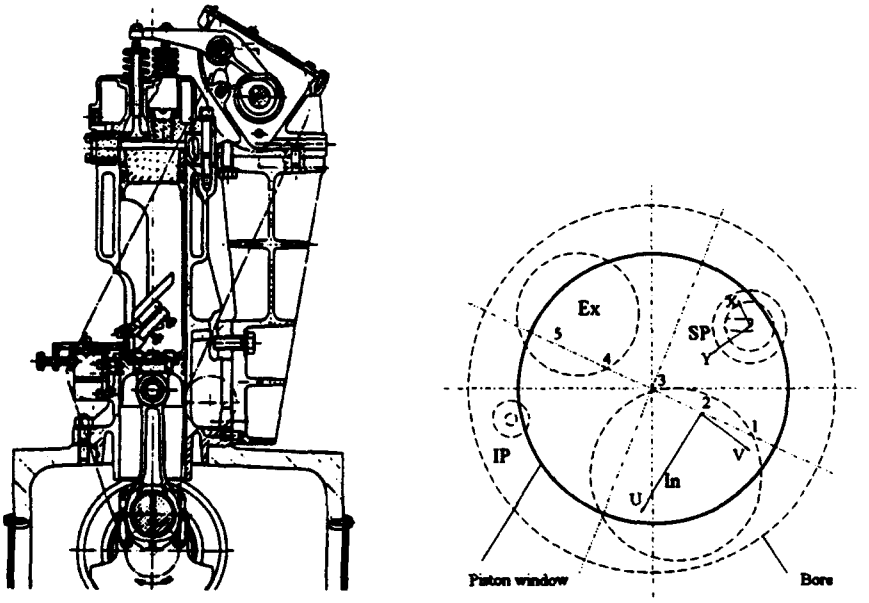

Figure 1 The single cylinder research engine and a bottom view of the combustion chamber.

Table 2 Characteristics of in-cylinder flow

Intake Valve	CV	SV-V
Conf.	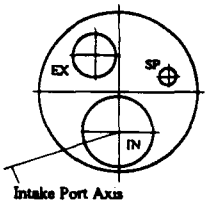	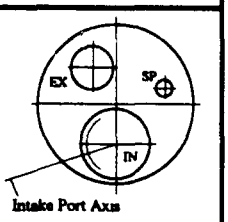
RS	≈0	2.1
TVRo	0.58	0.83
Mean* Velocity	0.35-0.4 Vp	1.4-2.1 Vp
Rms* Velocity	0.70-0.75 Vp	0.90-1.0 Vp

* measured at the location of the spark plug gap, 310-330°CA

ratio TVRo (Arcoumanis et al, 1990) of 0.6. With the shrouded intake valve, a swirl ratio of 2.1 was generated by aligning the shroud bisecting line perpendicular to the cylinder diameter through the intake valve centre and the tumble motion was also enhanced (Table 2, case SV-S). The swirl inclination angle was calculated to be approximately 20 deg, compared with the 30-45 deg found to be most beneficial in the four-valve pent-roofed Toyota lean burn engine (Furuno et al, 1992).

Velocity measurements obtained at the location of the spark plug gap in the motored engine, supported the results of the steady flow tests and are summarised briefly in Table 2, which indicates that flow field in the cylinder at the time of ignition with the non-shrouded valve (case CV) was nearly quiescent with turbulence levels of 0.7-0.75 Vp. For the shrouded valve (case SV-S), the convection velocity in the vicinity of the spark plug was 1.4-2.1 Vp, or 4-6 m/s, which is close to the 3-5 m/s recommended by Pischinger and Heywood (1991). The turbulence intensity, represented by the spatially-averaged rms velocities, was 0.9-1.0 Vp, i.e., about 30 % higher than that with the non-shrouded valve.

The constant-volume chamber is that previously described by Arcoumanis and Bae (1992) and by Arcoumanis, Hull and Whitelaw (1994) and is shown in Fig. 2 together with the mechanical device which allowed the injection of a small quantity of a mixture of propane and air with slightly rich concentration into the chamber. The volume of the vessel is 59 cm^3 and is equipped with two ports for the introduction of the mixture, a port for the spark plug and windows which allow observation of the flame kernel and its propagation. The consequences of gas motion, caused by the tangential entry of the mixture and the time allowed for the flow to transcend to quiescent state, were quantified by Arcoumanis and Bae (1992). Here a mixture of propane and air with an equivalence ratio of 1.1 and a volume of 10 cm^3 was injected through one of the ports towards the spark plug at times corresponding to those of Arcoumanis and Bae (1992) and with the duration of injection as a variable. The mixture was ignited with a conventional spark plug of 1.6 ms duration and 15 mJ energy output (NGK BPR5ES) using a commercial automotive ignition system.

The present investigation focuses on ultra lean air-fuel ratios between 22 and 54, corresponding to equivalence ratios from those of the engine 0.7-0.9 down to 0.29, where this is defined in terms of the total quantity of fuel and air, that is the content of the initially quiescent mixture plus that of the rich 'local' jet. Results are presented in terms of ignitability, time to burn as deduced from the pressure signal, and mass fraction burned and are complemented by photographs of the propagation of the flame front which were obtained with a single-shot shadowgraphy system.

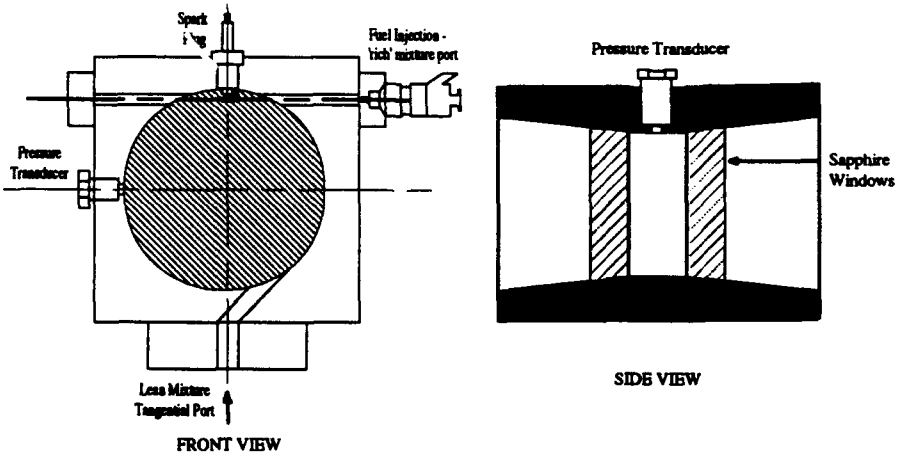

Figure 2 Diagram of the constant-volume combustion chamber.

3. RESULTS AND DISCUSSION

Fig. 3 shows typical pressure traces in the Fiat engine for mixtures of equivalence ratio 0.9 and 0.7, with each represented by 15 cycles. Compared with the case of ϕ=0.9, the burning rate with the leaner mixture was slower with the maximum pressure reduced by approximately 35%. Cyclic variations appear to be more evident at the later stages of the combustion process for the leaner mixture, in support of the suggestion of Stone et al (1992) that the indicated mean effective pressure (IMEP) should be included in the evaluation of the cyclic variability, as shown in Fig. 4. With the leaner equivalence ratio, the spread of the peak pressure decreases with its mean magnitude, and the relative deviation increases rapidly, Fig. 4a. The equivalence ratio at which the relative peak pressure spread reaches 10% is about 0.8 and 0.75 for the no swirl case and swirl case, respectively. IMEP, which defines the indicated work per cycle, has a direct relationship with engine torque and vehicle driveability problems usually result when COV_{imep} exceeds about 10% (Heywood, 1988). Fig. 4b shows that the cyclic variability of IMEP deteriorates rapidly for lean mixtures especially for equivalence ratios lower than 0.8 and reaches 10% at an equivalence ratio of about 0.73 without swirl and 0.68 with swirl. Therefore, IMEP seems to provide complementary information about the lean limit to that of the peak cylinder pressure.

It is well known that the influence of mixture preparation on combustion is more important for lean mixtures (Peters and Quader, 1978), but the extent of its effect seems to vary from one engine to another. The cyclic variations measured with the homogenous premixed mixture in the extended manifold, Fig.5, are little different from those with port fuel injection,

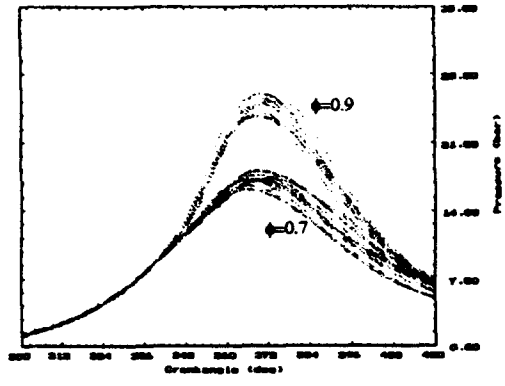

Figure 3 Typical in-cylinder pressure traces of lean combustion with equivalence ratio of 0.9 and 0.7 (n=1000 rpm, ηv=0.72, no-swirl).

especially in the presence of shroud-generated swirl. This is because the cyclic variability in the Fiat engine seems to be dominated by other factors such as the velocity fluctuations and residual gas dilution.

It is evident from the above results that an improvement in the combustion of lean mixtures for this engine can be achieved by introducing swirl but not beyond an equivalence ratio of 0.68, corresponding to an air-fuel ratio of 23. With gaseous fuel there is also very little possibility of achieving charge stratification at the time of ignition even if it were known that stratification is necessary to improve operation with very lean mixtures. With liquid fuel and port injection, attempts have been made, to achieve stratification as for example by Quader (1982), Vannobel et al (1994) and Posylkin et al (1994)

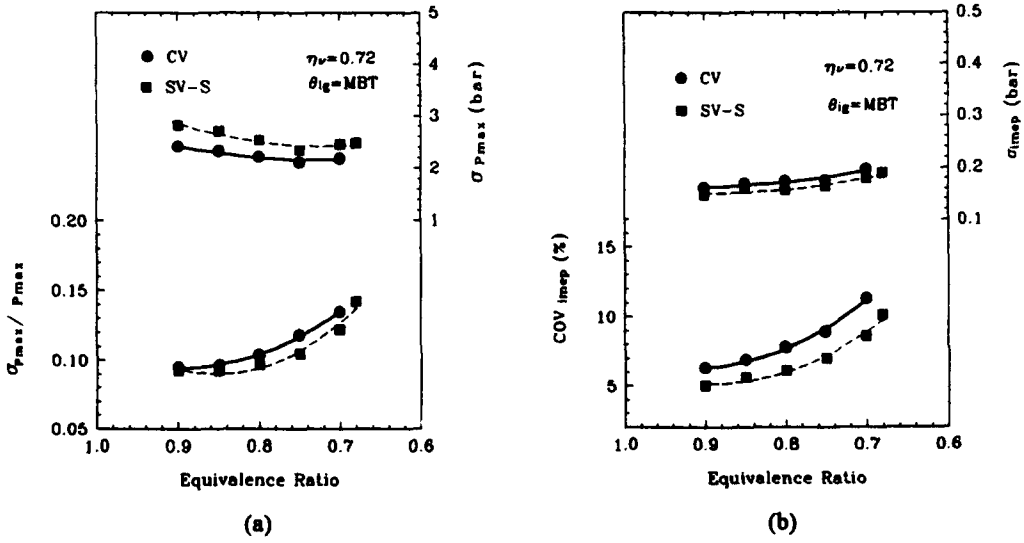

Figure 4 The cyclic variations of peak pressure (a) and IMEP (b) of the engine as a function of mixture equivalence ratio, with the conditions of no swirl and swirl (n=1000 rpm, ηv=0.72).

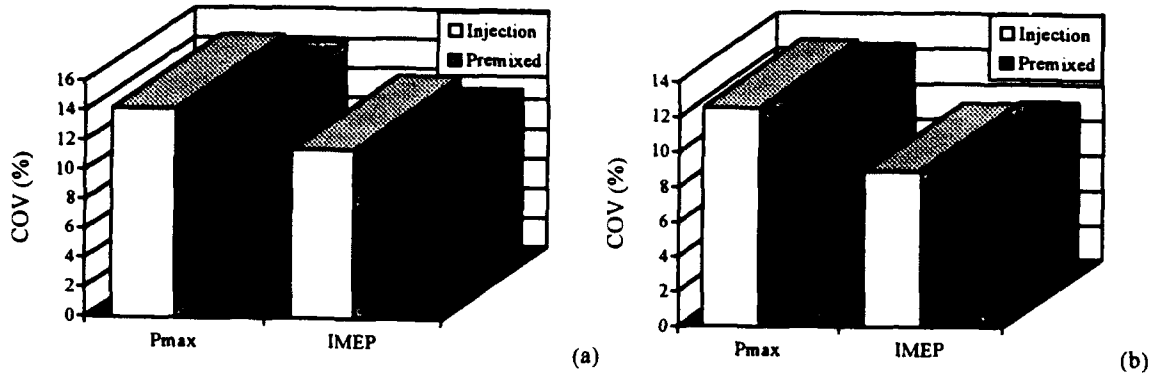

Figure 5 Consequence of mixture preparation as cyclic variations (n=1000 rpm, ηv=0.72, ϕ=0.7).

to distribute vaporised fuel, small droplets and large droplets by taking advantage of large scale motions such as swirl and tumble, even if the degree of stratification of the vaporised fuel at the time of ignition is a matter for conjecture. For gaseous fuels, the stratification of the charge, if there is any, is mainly presented as heterogeneous rich mixture pockets resulting from incomplete premixedness due to the physical properties of the gas (Zhao et al, 1994), and the subsequent influence on combustion is relatively small. An alternative approach is to maintain a homogeneous lean charge as in the present engine experiment and to add a small quantity of a richer mixture close to the spark plug at the time of ignition.

This alternative approach of direct fuel injection locally towards the spark gap has been examined by Arcoumanis, Hull and Whitelaw (1994) in the constant-volume chamber and it has been shown that 100% ignitability can be achieved with an overall equivalence of 0.39 when 15 % of the fuel is injected as a mixture of equivalence ratio 1.1 over a period of 110 ms in the vicinity of the spark plug and with the remainder of the fuel/air mixture at an equivalence ratio of 0.25. Fig. 6 shows the variation of gas pressure with time for four overall equivalence ratios and in one case without local injection of the small quantity of rich mixture. It is evident that the ignitability falls off rapidly below an equivalence ratio of 0.39 although this value may be further reduced by more careful optimisation of the rich mixture injection. Also, the maximum pressure is considerably enhanced by the rich charge even at an equivalence ratio of 0.72 and it can be conjectured that this is due to an improvement in the stability of the flame kernel and in the consistency of its growth.

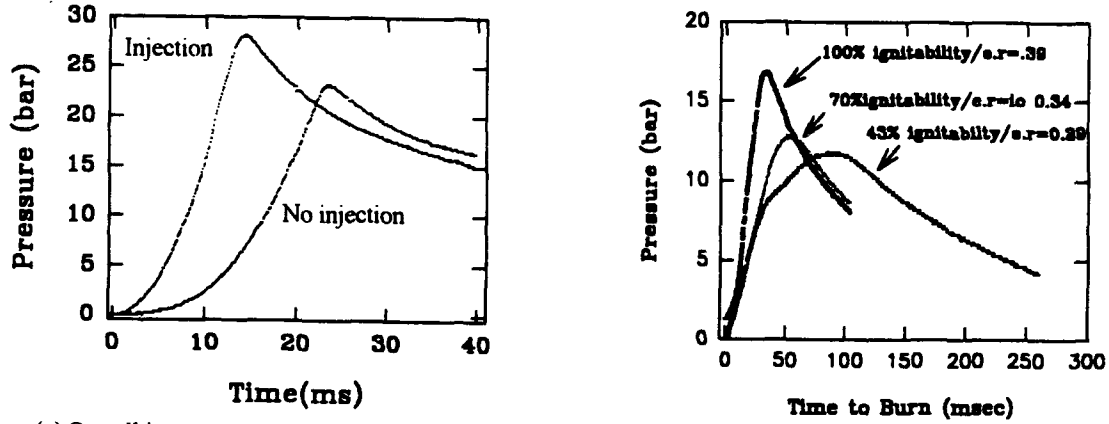

(a) Overall improvement at Φ_o=0.72
(Injection: 180° orient, 1mm port, u_m=8m/s, T=120°C, P_i=6bar, injection in direction of bulk flow, w=1mm, 10cc injected. No injection: 0° orient, u_m=22m/s, T=120°C, w=1mm, P_i=6bar)

(b) Improvement in Lean Limit
(T=120°C, w=1mm, P_i=6bar, 180° orient)

Figure 6 Pressure traces from the combustion chamber with and without local stratification of the charge.

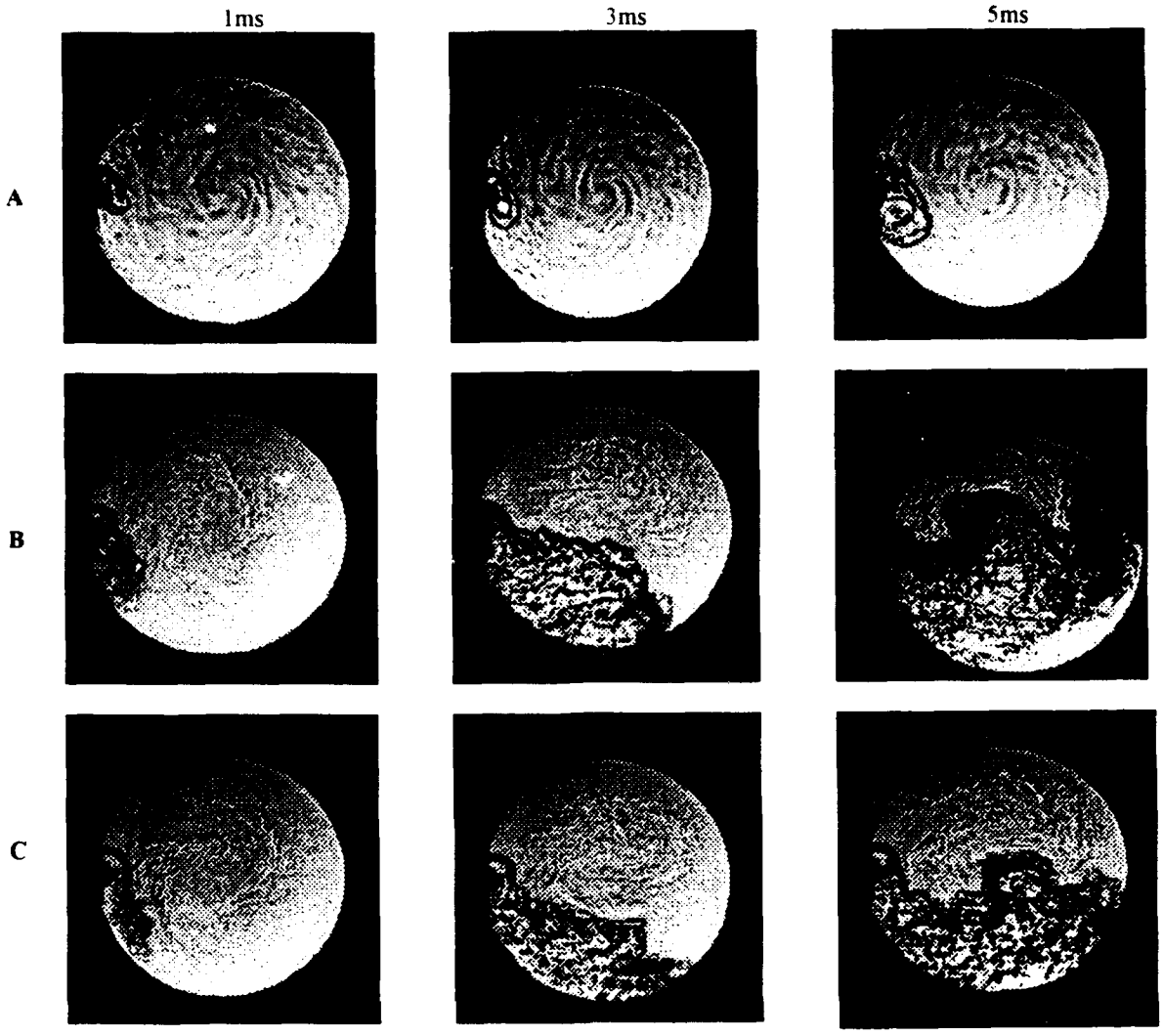

Figure 7 Shadowgraphs of flame kernel growth in the constant volume chamber. (a) ϕ=0.72, no additional injection; (b) ϕ=0.72, with local injection; (c) ϕ=0.39, with injection

The photographs of Fig. 7 confirm the conjecture of the previous paragraph in that the growth of the flame kernel in the case of local rich mixture injection is greatly enhanced during the initial stage of combustion and produces a more convoluted flame front in the two cases presented, corresponding to overall equivalence ratios of 0.72 and 0.39.

CONCLUDING REMARKS

Experiments in a single-cylinder spark-ignition engine with gaseous port fuel injection and in a constant-volume chamber with secondary direct mixture injection towards the spark plug revealed the following:

1. The high convection velocity and fluctuation intensity in the engine with shroud-generated swirl resulted in fast burning rates which sustained less cyclic variations of combustion with the COV_{imep} reduced by approximately 30%. The lean burn limit at which the COVimep reached 10% was extended from an equivalence ratio of about 0.73 without swirl to 0.68 with swirl.

2. With gaseous port fuel injection, the influence of fuel preparation on the combustion cyclic variability was small and the effect of stratification not evident, which prevented further extension of the lean burn limit by means of intake-generated swirl.

3. The experiments performed in the constant-volume combustion chamber showed the clear advantages of the local injection near the spark plug of a small quantity of slightly rich mixture into a mixture of very low overall equivalence ratio. The lean limit has been extended to 0.39 with 100% ignitability

and even greater improvements seem possible with further optimisation of the position of the rich mixture relative to the electrode orientation and of injection duration relative to the spark timing and ignition energy distribution.

ACKNOWLEDGEMENT

The authors are pleased to acknowledge the financial support from the Science and Engineering Research Council under Grant GR/H44943 and from the US Department of Energy under Grant DE-FG04-91/ER 75332. They would also like to thank Dr. Vafidis of Fiat Research Centre for his contribution to the development of the engine experimental facilities and Dr. Witze of the Sandia National Labs for arranging the loan of the constant volume chamber to Imperial College.

REFERENCES

ARCOUMANIS, C., AND BAE, C-S. (1992), "Correlation Between Spark Ignition Characteristics and Flame Development in a Constant-Volume Chamber," SAE paper 920413.

ARCOUMANIS, C., BAE, C-S., WHITELAW, J.H. AND XU, H.M. (1994), "Imaging of Lean Premixed Flames in Spark Ignition Engines, " Paper to be presented at the 1994 SAE Fuel and Lubricants Meeting, Baltimore, October, 1994.

ARCOUMANIS, C., HULL, D. R. AND WHITELAW, J. H. (1994), "An Approach to Charge Stratification in Lean-Burn, Spark-Ignition Engines, " Paper to be presented at the 1994 SAE Fuel and Lubricants Meeting, Baltimore, October, 1994.

ARCOUMANIS, C., HU, Z., VAFIDIS, C., AND WHITELAW, J.H. (1990), "Tumbling Motion: A Mechanism for Turbulence Enhancement in SI Engines." SAE paper 900060.

ENOTIADIS, A., LINGENS, A., VAFIDIS, C. WHITELAW, J.H. AND XU, H.M. (1992), "Mixture Turbulence Characteristics During Flame Propagation in a Spark Ignition Engine," Proc. SIA/STA Int. Symp. "The Powertrain: Development and Future," Valencia..

FURUNO, S., IGUCHI, S., OISHI, K. AND INOUE, T. (1990), "The Effects of the 'Inclination Angle of Swirl Axis' on Turbulence Characteristics in a 4-Valve Lean-Burn Engine with SCV," SAE paper 902139.

HEYWOOD, J. B. (1988), "Internal Combustion Engine Fundamentals," McGraw-Hill, ISBN 007-100499-8.

HORIE, K., NISHKIZAWA, K. (1992), "Development of a High Fuel Economy and High Performence 4-Valve Lean Burn Engine," Proc. Conf. on Combustion in Engines, Technology and Enviroment, IMechE, C448/014.

HU, Z., LINGENS, A., VAFIDIS, C., WHITELAW, J.H. AND XU, H.M. (1992), "A Study of Mixture Turbulence During Flame Propagation in a SI Engine Using Conditionally-Sampled Laser Velocimetry," Proc. 3rd Int. Conf. on Innovation and Reliability in Automotive Design and Testing, Florence.

INOUE, T., MATSISHITA, S., NAKANISHI, K AND OKANO, H. (1993), "Toyota Lean Combustion System-The Third Generation System, " SAE paper 930873.

PETERS, B. D., AND QUADER, A. A. (1978), "'Wetting' the Appetite of Saprk Ignition Engines for Lean Combustion, " SAE paper 780234.

PISCHIGER, S. AND HEYWOOD, J. B. (1990),. "How Heat Losses to the Spark Plug Electrodes Affect Flame Kernel Development in an SI-Engine," SAE paper 900021.

POSYLKIN, M, TAYLOR, A. M. K. P. AND WHITELAW, J. H. (1994), "Size and Velocity Characteristics of Fuel Droplets in the Valve-Curtain Area of a Straight, Steady-Flow Inlet Manifold, " to be Presented at the 7th Int. Symp. on the Applications of Laser Techniques to Fluid Mechanics, Lisbon.

QUADER, A. A. (1982), "The Axially-Stratified-Charge Engine, " SAE paper 820131.

STONE, C. R., BROWN, A. G. AND BECKWITH, P. (1992)," A Turbulent Combustion Model Used to Give Insights into Cycle-by-Cycle Variations in Spark Ignition Engine Combustion," Proc. of Conf. on Combustion in Engines, IMechE, C448/013.

VAFIDIS, C., WHITELAW, J. H. AND XU, H. M. (1992), "Conditional and Frequency Analysis of LDV Signals from a Gas-Fuelled Engine, " Proc. 6th International Symposium on the Applications of Laser Techniques to Fluid Mechanics, Lisbon.

VANNOBEL, F, ROBART, D, DEMENTHON, J-B AND WHITELAW, J. H. (1994), "Velocity and Drop-Size Distributions in a Two-Valve Production Firing Engine, " to be presented at COMODIA.

WHITELAW, J.H. AND XU, H.M. (1993a), "An Experiment Study of Gas Velocity, Flame Propagation and Pressure in a Spark Ignition Engine," SAE Paper 932702.

WHITELAW, J.H. AND XU, H.M. (1993b), "Data Processing Techniques for Turbulence Analysis in SI Engines," Report TF/93/4, Dept. of Mech. Eng., Imperial College.

WHITELAW, J.H. AND XU, H.M. (1993c), "Steady Flow Characteristics of a FIAT Engine Cylinder Head with Conventional and Shrouded Intake Valves," Report TF/93/21, Dept. of Mech. Eng., Imperial College.

WHITELAW, J.H. AND XU, H.M. (1994a), "Flame and Turbulence Interaction in a Four Stroke SI Engine, " *Unsteady Combusting Flows*, NATO ASI Series, edited by Culick, F. E. C., Heitor, M. and Whitelaw, J. H., Published by Kluwer.

WHITELAW, J.H. AND XU, H.M. (1994b), "Effects of Valve-Shrouding on the Flow and Combustion in a Optical SI Engine,"Report TF/94/15, Dept. of Mech. Eng., Imperial College.

XU, H. M. (1994), "Turbulence and Cyclic Combustion Variations in a Lean-Burn Spark-Ignition Engine," PhD Thesis, Imperial College, in Preparation.

ZHAO, F. Q., TAKETOMI, M., NISHIDA, K. AND HIROYASU, H. (1994), "PLIF Measurements of the Cyclic Variation of Mixture Concentration in a SI Engine, " SAE paper 940988.

COMPARISON OF IN-CYLINDER SCAVENGING FLOWS IN A TWO-STROKE CYCLE ENGINE UNDER MOTORED AND FIRED CONDITIONS

P.C. Miles, R.M. Green, and P.O. Witze

Combustion Research Facility
Sandia National Laboratories
Livermore, CA 94551-0969 USA

ABSTRACT

The in-cylinder flow field of a loop-scavenged, two-stroke engine has been characterized using laser Doppler velocimetry. The radial component of gas velocity was measured along the axis of the cylinder for both motored and fired operation. Measurements were obtained under conditions simulating both crankcase and external blower driven scavenging. Mean profiles of the radial velocity show marked differences in the global flow structure between motored and fired operation for both scavenging methods. These differences persist throughout the scavenging process and survive compression of the fresh charge. Root mean square (rms) velocity fluctuations near TDC were also determined, and significant differences between motored and fired operation are observed. The rms fluctuations are found to correlate well with the mean shear during compression.

1. INTRODUCTION

The experimental investigation of the in-cylinder flow field in an internal combustion engine is often performed under motored conditions for a variety of reasons. Early studies employing hot-wire anemometry to measure the fluid velocity were obviously restricted to motored operation due to the inability of the probe to survive the harsh combustion environment. Similarly, engine simulation rigs used for research purposes are often not designed to withstand fired operation. Because of significant experimental advantages, studies under motored conditions continue to be made despite the use of optical diagnostic methods in engines capable of fired operation. Principally, concern over the survival of the windows which allow optical access into the cylinder motivates this tendency to avoid fired operation. Under fired conditions, peak in-cylinder pressures and temperatures are considerably higher than under motored conditions, and the mechanical and thermal stress induced on the windows is correspondingly higher. In addition, the windows tend to foul more rapidly with combustion, necessitating their frequent removal for cleaning. Finally, for most optical velocimetry techniques, it is necessary to introduce seed particles into the flow in order to obtain the measurement. If measurements are desired throughout the engine cycle, these particles must survive the combustion process. This requirement precludes the use of many non-abrasive or low-density particles, such as oil droplets or latex spheres. The commonly used refractory particles present additional concerns—notably the difficulty of dispersing dry powders, the corrosive by-products associated with chemical methods of generating particles, and increased engine wear due to abrasion.

Although obtaining velocity measurements in a motored engine is considerably easier than obtaining the corresponding fired measurements, it is not clear that the motored data provide an accurate representation of the flow field under firing conditions. Studies comparing motored and fired data in a four-stroke cycle engine have observed large differences in both mean velocities (e.g., Baritaud et al. (1986)) and turbulent intensities (e.g., Witze et al. (1989)) between motored and fired operation. Because engine performance in two-stroke cycle engines is strongly influenced by the scavenging process, accurate knowledge of the mean flow during scavenging is, arguably, of greater importance than knowledge of the mean flow field in a four-stroke engine. There are several factors that may be expected to cause differences in the mean scavenging flow field between motored and fired operation. Perhaps of greatest importance is the difference in fluid properties of the fresh mixture and the residual gas in the combustion chamber. Under fired operation, the jets of fresh charge issuing from the intake ports typically have a density 60% higher than the residual gas (Blair, 1990). Similarly, the viscosity of the residual gas is over twice that of the fresh charge. With motored operation, the 'residual' gas may actually be cooler than the fresh charge due to heat transfer during the compression and expansion portions of the cycle. Concomitantly, the fresh charge is characterized by a lower density and higher viscosity than the residual gas. Clearly, conditions for the dynamical similarity of the motored and fired flow fields are not satisfied. In addition, pressure waves in the exhaust and intake manifold are known to affect the scavenging flows. Under fired conditions, both the magnitude and phasing of these pressure waves can differ from motored conditions; consequently, the scavenging flow fields may differ as well.

Experimental studies comparing motored and fired flow velocities in the intake and exhaust passages of a Schnürle (loop) scavenged, two-stroke engine have been performed by Ikeda et al. (1991) and Ohira et al. (1993). These studies report large differences in both the magnitude and phasing of the peaks in velocity. Obokata et al. (1987,1988) have measured mean velocities and turbulence intensities inside the clearance volume of a modified Schnürle-scavenged motorcycle engine. Mean velocities were found to be strongly dependent on whether or not the engine was fired, although turbulence intensities and characteristic time scales near the time of ignition were not found to vary significantly between motored and fired operation. None of these previous studies reported measurements of the

flow field in the volume swept by the piston, which largely determines the effectiveness of the scavenging process.

In this paper we report in-cylinder velocity measurements obtained in the controlled environment of a single-cylinder, Schnürle-scavenged research engine. The intent of this work is to identify large-scale, global differences in the scavenging flow fields associated with motored and fired operation. Measurements are reported for simulations of both blower and crankcase scavenging to illustrate the relative sensitivity of each scavenging method to the mode of operation. Because turbulence levels at the time of ignition can significantly affect combustion performance, and because the generation of turbulence is determined by the mean shear, we also examine differences in rms velocity fluctuations during the compression process for both modes of operation.

2. EXPERIMENTAL DESCRIPTION

2.1 Engine

The engine used in this study is a modified Cooperative Lubrication Research (CLR) engine, in which the head was removed and replaced by an extended cylinder assembly (Fig. 1) containing a liner with intake and exhaust port openings. An extended piston was mounted to the top of the CLR piston. The intake transfer passages and port geometries were designed to impart a Schnürle-loop directional characteristic to the flow as it enters the cylinder through the scavenge ports. The cylinder head supported a window located above a pancake shaped combustion chamber of the same diameter as the cylinder bore. To reduce the maximum flame-travel distance across the combustion chamber, the spark plug was mounted in the center of the piston crown. An AVL Model QC42D-E piezo-electric pressure transducer was mounted in the head to monitor the in-cylinder pressure, and the crankshaft was instrumented with a shaft encoder with 0.5 crank angle degree (CAD) resolution. The important geometric characteristics of the engine are summarized in Table 1.

The engine operating conditions used in this study are summarized in Table 2. To achieve realistic scavenging conditions while reducing the thermal loading of the window, we adopted a "burst-fired" ignition strategy, wherein the engine was fired on 13 consecutive cycles followed by 27 consecutive cycles of motored operation. The first cycles of the fired burst exhibited transients in the mean peak cylinder pressure and in the crank-angle of peak pressure. By the tenth cycle, however, the statistics of peak pressure and the crank angle of peak pressure had converged to relatively constant levels, indicating that quasi-steady conditions of fired operation had been reached. Velocity measurements were therefore obtained from the scavenging portions of cycles 9-13, for a total of 5 representative fired cycles per burst. Measurements of twenty such bursts were obtained for a total of 100 engine cycles. The motored velocity measurements were also obtained over approximately 100 engine cycles.

The engine configuration described above was used for both the crankcase and blower scavenging methods. To simulate blower scavenging, fresh mixture was supplied through a critical orifice to large-diameter supply lines which served as a high-volume plenum. Pressure fluctuations due to wave dynamic effects were damped by elbows and a honeycomb section in the supply lines; the pressure at the intake ports was thus maintained at a reasonably constant level throughout the time that the intake ports were open. To simulate crankcase scavenging, the orifice

Table 1 Engine Characteristics

Type:	Single cylinder, two stroke w/ piston-controlled porting
Bore:	94.4 mm
Stroke:	95.3 mm
Clearance Height:	9.5 mm
Comp. Ratio (Geom.):	11.0
Comp. Ratio (Eff.):	6.0
Intake Port Opens:	120 CAD
Intake Port Closes:	240 CAD
Exhaust Port Opens:	90 CAD
Exhaust Port Closes:	270 CAD

Table 2 Engine Operating Conditions

Engine speed:	800 RPM
Fuel :	Propane (homogeneous charge)
Equivalence Ratio:	1.0
Delivery ratio:	0.3 - 0.85 (variable)
Firing strategy:	Burst fired
Firing sequence:	13 cycles fired 27 cycles motored
Ignition timing (1st fired cycle):	7.5 BTC
Ignition timing (other cycles):	22.5 BTC

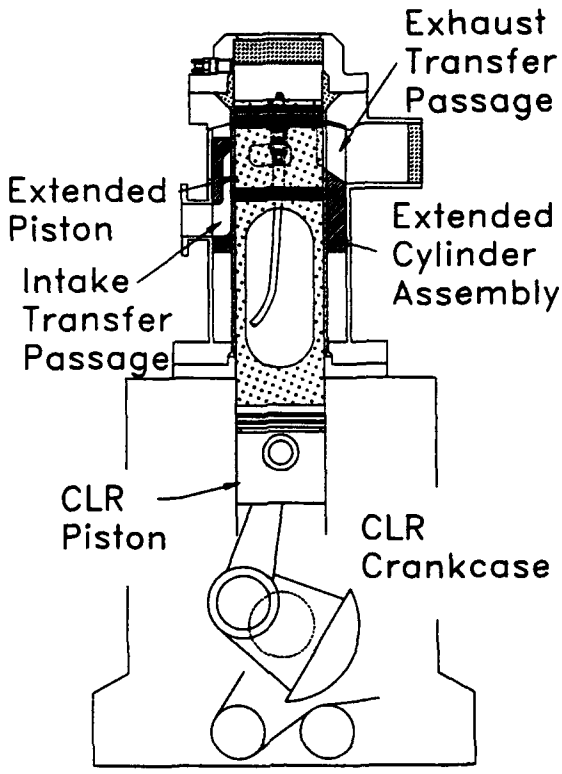

Figure 1 Two-stroke optical research engine.

metering the flow into the plenum was removed, and a second orifice inserted between the plenum and the intake manifold (Fig. 2). In this case, the flow into the manifold caused an increase in the pressure at the ports while the intake ports were closed. Upon opening of the intake ports, the gas in the manifold was rapidly discharged into the cylinder, simulating the initial blowdown period of a crankcase scavenged engine. For the remaining portion of the scavenging process, the mass flow rate through the intake ports was low due to the restriction of the orifice. The volume of the intake manifold was tailored to obtain an intake port pressure history typical of crankcase scavenging. Additional details of the engine, its operation, and the simulation of blower and crankcase scavenging are described by Miles et al. (1994).

2.2 Laser Doppler Velocimetry (LDV)

Measurements of the in-cylinder radial velocity component were obtained with a custom-built fiber-optic LDV probe. In the configuration used in this work, a 310 mm focal length transmitting lens focused the beams to measured waist diameters of 52 μm at the LDV probe volume. Such tightly focused waists were required in order to obtain sufficient signal levels with the backscatter collection geometry employed. The beam spacing in the probe head was 50.0 mm, giving a fringe spacing of 3.21 μm with the green line (514.5 nm) of an Argon ion laser. A differential frequency shift of 10 MHz was used, and the Doppler signals were band-pass filtered between 2 and 50 MHz for a measurement bandwidth of -25 to 130 m/s. The filtered signals were processed with a counter type processor (TSI 1990C), which was operated in a single-measurement-per-burst mode and set to count the time for 8 fringes with a 1% validation criterion. Velocity data and simultaneous crank angle readings were transferred to a laboratory computer using a DOSTEK 1400A interface.

Measurements of the radial component of velocity were obtained along the cylinder centerline at 12 axial locations spaced 8.0 mm apart. The uppermost measurement location was 4.0 mm below the inner surface of the window, and the lowest location was approximately 13 mm above the piston crown at bottom center. The axial coordinate z identifying these locations has its origin at the inner surface of the window. The measured radial component of velocity lies in the plane of symmetry defined by the cylinder port geometry; this plane is shown by the dashed line in Fig. 2. Velocities in this plane are identified as positive when the flow is towards the exhaust port. The velocity/crank-angle pairs obtained were sorted by crank angle into bins 2 CAD wide for computation of the velocity statistics. Results are reported only for those data obtained when the distance from the probe volume to the ground electrode of the spark plug exceeded 3.6 mm or, equivalently, 7.0 mm from the piston crown. Due to noise associated with light scattered from these surfaces, the data obtained closer to the piston are not considered to be reliable.

LDV seed particles were generated from the high-temperature thermal decomposition of titanium tetra-isopropoxide (TTIP), using an apparatus similar to that described by Okuyama et al. (1986). Although we have not yet characterized the output of the seeder, we were able to obtain large, relatively stable quantities of TiO_2 with, judging from the LDV signal, a reasonably narrow size distribution. As seen in Fig. 3, the seeder is a simple device wherein nitrogen gas is passed over a heated pool of liquid TTIP in a closed evaporator, such that the gas leaving the evaporator is saturated with TTIP vapor. The mixture then passes through a high temperature reactor where the decomposition reaction takes place. It is important to ensure that the reactor temperature remains high enough and the mixture residence time long enough to react the greater part of the TTIP vapor. Otherwise, condensation downstream tends to cause flow blockage. This seeder has several important advantages: 1) the TiO_2 particles are well

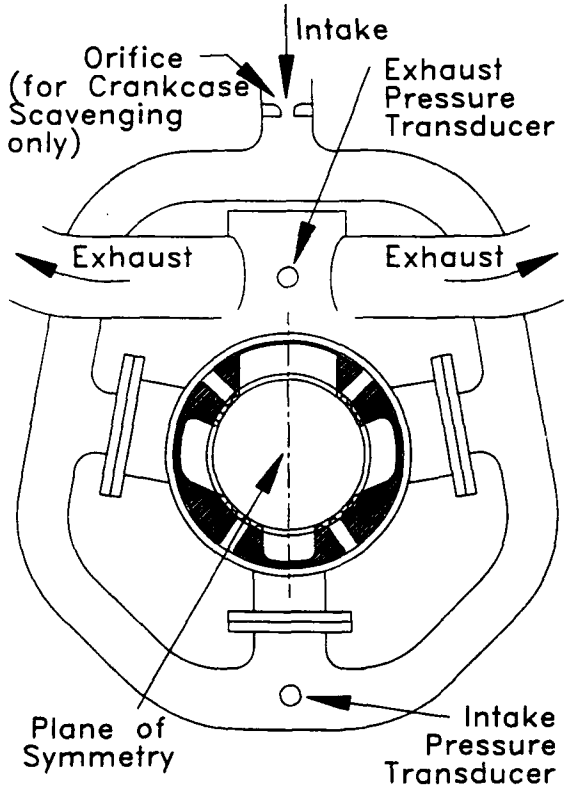

Figure 2 Plan view of the port layout and manifolding.

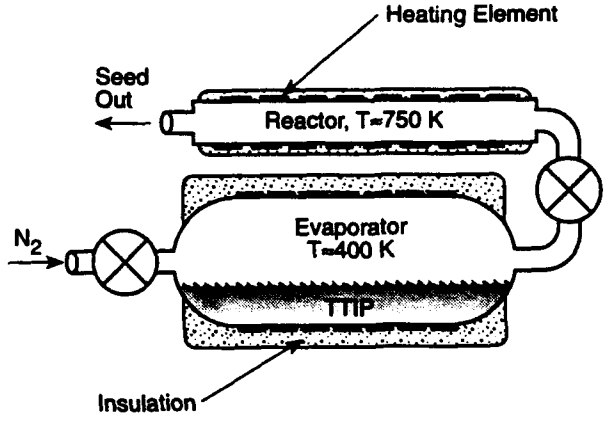

Figure 3 LDV seed particle generator

dispersed and further agglomeration can be minimized by the addition of diluents downstream of the seeder; 2) particle size appears to be controllable via TTIP vapor concentration and/or residence time in the reactor; 3) chemical by-products of the decomposition reaction are relatively innocuous—H_2O and C_3H_6; 4) the seeder can operate at extremely low flow rates; 5) the seeder can be designed to dispense seed into high pressure systems; and 6) by substituting the appropriate metal alkoxide feedstock it may also be possible to produce suitable Al_2O_3 and SiO_2 particles. At present, the major disadvantage appears to be plugging of the tubing between the evaporator and the reactor after a few hours of operation. We are encouraged by our experiences with this type of seeder and believe that it warrants further development.

3. RESULTS AND DISCUSSION

A comparison of the mean radial velocity profiles under motored and fired conditions is presented for both crankcase and blower scavenging, for a single delivery ratio of 0.6. For organizational purposes, the cycle is divided into periods which are discussed separately: cylinder blowdown, 90–120 CAD; early scavenging, 120–150 CAD; mid-scavenging, 150–210 CAD; late scavenging, 210-270 CAD; and compression, 270-360 CAD.

3.1 Mean Velocity Profiles – Crankcase Scavenging

The crankcase scavenged radial velocity profiles during blowdown at selected crank angles are shown in Fig. 4. The profiles are quite different throughout the blowdown period, as might be expected. Early in the blowdown period, at 100 CAD, the fired velocity profiles show a strong, positive flow toward the exhaust port. As the blowdown period progresses, the positive flow rapidly reverses and a negative radial velocity is established along much of the cylinder centerline. This negative velocity is likely caused by a backflow from the exhaust manifold into the cylinder due to the cylinder volume expansion associated with piston motion, and persists until the intake ports open (IPO) and the scavenging process begins. In contrast, the motored profile shows a pronounced in-flow at 100 CAD, again due to a backflow from the exhaust manifold. These negative velocities, however, are much larger than those seen at later crank-angles for fired operation. Later in the blowdown process, negative velocities persist in the central and upper portion of the cylinder, but a positive flow is established near the piston top. By 110 CAD a tumble vortex, rotating counter-clockwise from the point of view of Fig. 4, appears to have been established in the lower portion of the cylinder. This apparent tumble motion changes little until IPO.

During the early portion of the scavenging process (Fig. 5), the fired mean velocity profiles rapidly become positive in the upper portion of the cylinder, such that the flow is characterized by a dominant tumble vortex rotating clockwise (130 CAD). The velocities near the top of the cylinder continue to increase, and the center of the tumble motion moves toward the piston top, until a positive radial flow has been established along the entire centerline. By 140 CAD, this positive flow profile is of nearly uniform magnitude. The motored profiles, however, continue to display a counter-clockwise rotation near the bottom of the cylinder, and establishment of strong, positive radial velocities near the top of the cylinder is delayed until approximately 130 CAD. From this point, radial velocities in the central portion of the cylinder gradually become positive, and

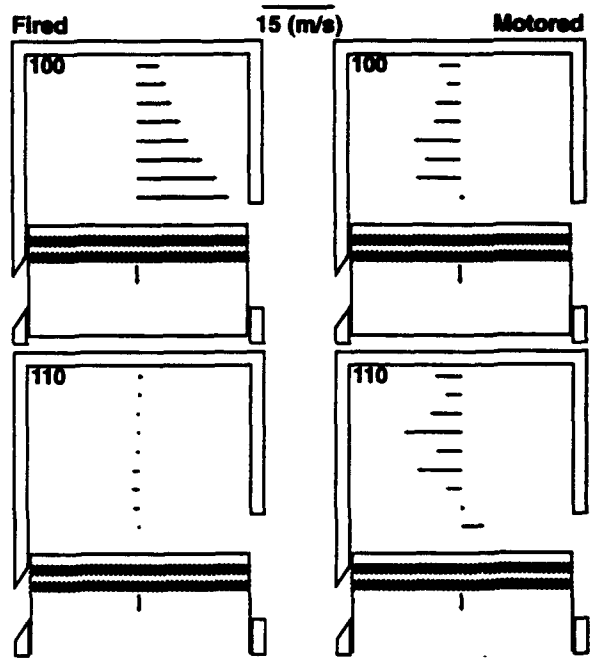

Figure 4 Mean radial velocity profiles measured during cylinder blowdown for crankcase scavenged operation.

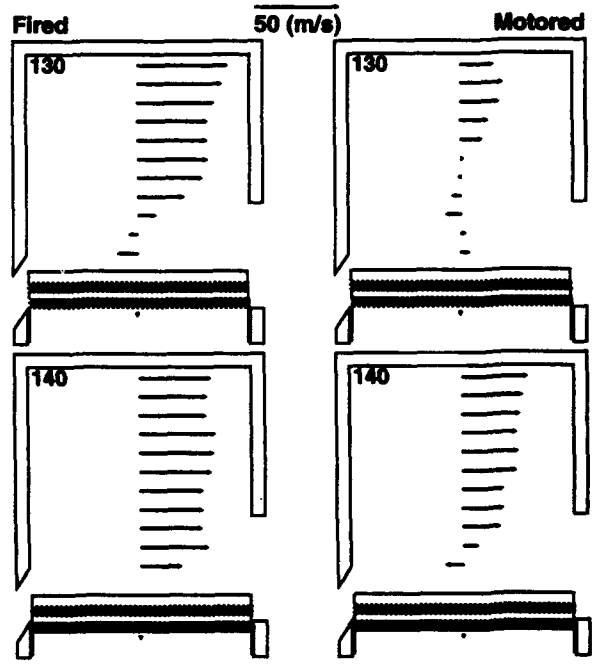

Figure 5 Mean radial velocity profiles measured during early scavenging for crankcase scavenged operation.

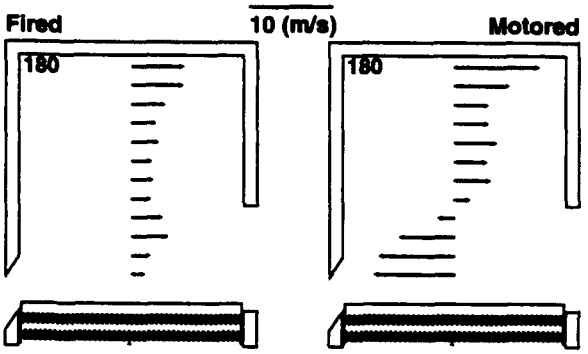

Figure 6 Mean radial velocity profiles measured during mid-scavenging for crankcase scavenged operation.

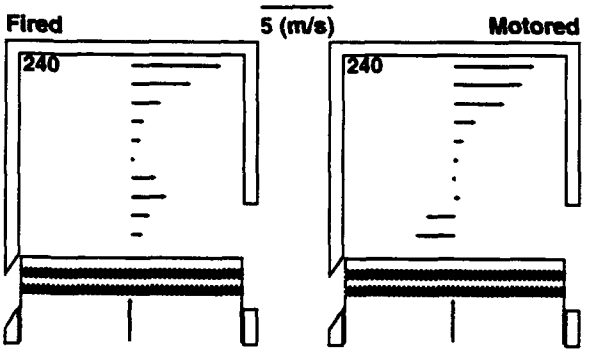

Figure 7 Mean radial velocity profiles measured during late scavenging for crankcase scavenged operation.

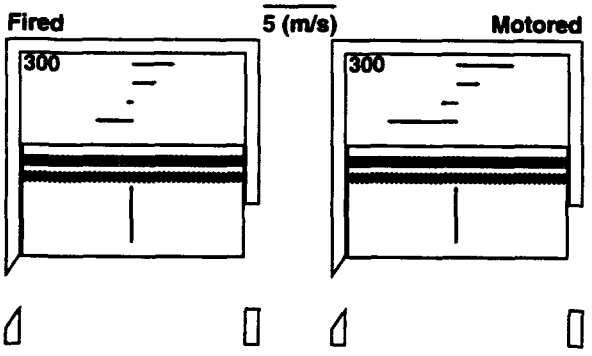

Figure 8 Mean radial velocity profiles measured during compression for crankcase scavenged operation.

the positive velocities low in the cylinder diminish. By 140 CAD, only the lowest axial location exhibits a negative radial velocity.

Throughout the middle portion of the scavenging period (Fig. 6) the differences between the fired and motored profiles persist. For fired operation the radial velocities decrease rapidly, and by 180 CAD (bottom center) the profile is still uniformly positive, although with much lower velocities. Thereafter, the flow becomes more complex, with diminishing velocities in all but the upper regions of the cylinder. For motored operation, the clockwise tumble motion seen low in the cylinder does not change initially, but then moves upward as indicated in the profile shown for 180 CAD. Beyond 180 CAD, the tumble motion is generally centered in the cylinder and changes little thereafter.

During the latter portion of the scavenging process (Fig. 7), the fired velocity profiles can not be simply characterized, but do become uniformly positive and remain so until just before exhaust port closure. As seen in the profile shown at 240 CAD, the velocity profiles during this period exhibit a maximum near the top of the cylinder, and a secondary maximum near the piston top which may be indicative of a piston driven flow out the exhaust port. In contrast, the motored profiles during this period continue to be characterized by a dominant clockwise tumble motion which remains roughly centered in the volume.

Finally, during compression (Fig. 8) both the fired and motored flow fields are well characterized by a dominant clockwise tumble vortex. However, the mean velocity gradients in the axial direction are everywhere greater for the motored profiles.

3.2 Mean Velocity Profiles – Blower Scavenging

The blower scavenged radial velocity profiles during blowdown are shown in Fig. 9. For fired operation, the profiles

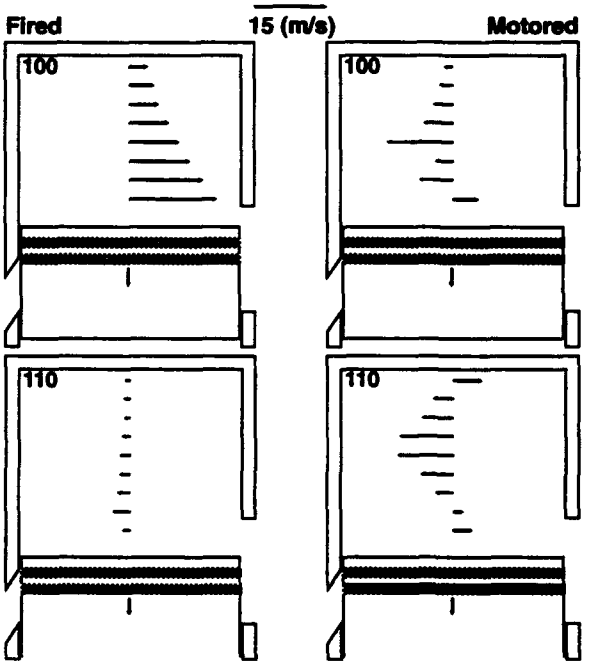

Figure 9 Mean radial velocity profiles measured during cylinder blowdown for blower scavenged operation.

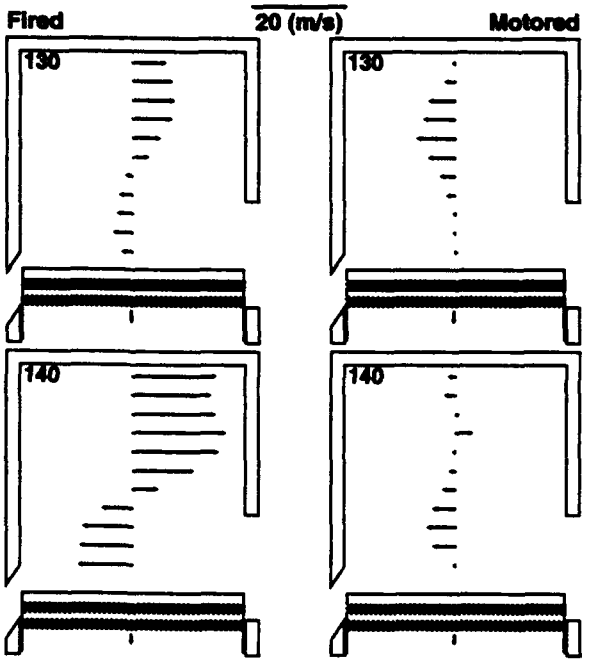

Figure 10 Mean radial velocity profiles measured during early scavenging for blower scavenged operation.

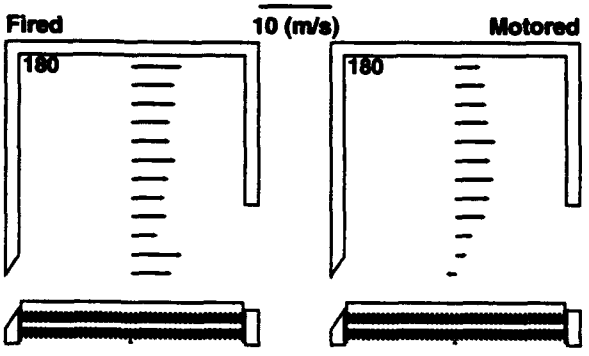

Figure 11 Mean radial velocity profiles measured during mid-scavenging for blower scavenged operation.

are quite similar to those observed with crankcase scavenging, although larger negative velocities are observed prior to intake port opening. Under motored operation, the earlier discussion of the crankcase scavenged profiles applies, although a surprising difference is observed near the top of the cylinder where positive radial velocities are seen throughout the latter half of the blowdown period under blower scavenged operation.

In the early scavenging period, the radial profiles for fired and motored operation remain different (Fig. 10), and are quite distinct from the corresponding crankcase scavenged profiles (Fig. 5). The fired profile is characterized by a well-defined tumble vortex that continues to build strength throughout this

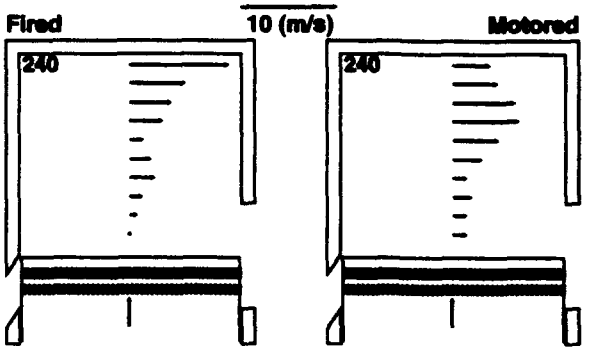

Figure 12 Mean radial velocity profiles measured during late scavenging for blower scavenged operation.

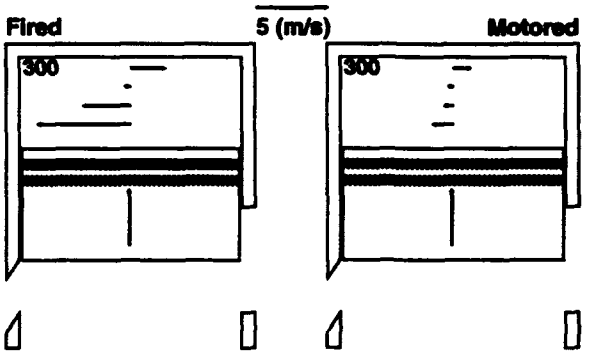

Figure 13 Mean radial velocity profiles measured during compression for blower scavenged operation.

period. In contrast, the motored profile changes little during this period, and strong positive velocities are not observed at any location on the cylinder centerline.

By 180 CAD the fired and motored profiles are somewhat comparable. The tumble motion characterizing the fired profile is no longer apparent (Fig. 11), and a positive radial velocity is observed at all axial locations throughout the remainder of the mid-scavenging period. For motored operation, the profile is also generally positive by bottom center, and remains so for the remainder of this period. During the late scavenging period (Fig. 12), the fired and motored profiles both exhibit a radial velocity maxima in the upper region of the cylinder, although the profiles differ in detail. Such a rough, qualitative similarity holds until exhaust port closure.

It is clear, however, that despite the rough similarity seen in the centerline profiles during the late scavenging process, the over-all flow fields must have been dramatically different to give rise to the compression profiles shown in Fig. 13. Under fired operation, the profile is clearly dominated by a tumble vortex and characterized by high shear. In contrast, the motored profile appears far less linear and is characterized by velocities of considerably lesser magnitude than the corresponding fired velocities.

3.3 RMS Velocity Fluctuations

Rms fluctuations in velocity during compression, from 270 CAD to 330 CAD, are shown in Fig. 14 for the upper three measurement locations under crankcase scavenging conditions. Despite the larger axial gradients in the radial velocity component seen in Fig. 8, the rms fluctuations observed during this period are similar for motored and fired operation at these locations. Under blower scavenged conditions (Fig. 15), however, the effect of the large mean shear observed for fired operation (Fig. 13) is manifested in the observed fluctuating velocities at all of the measurement locations shown.

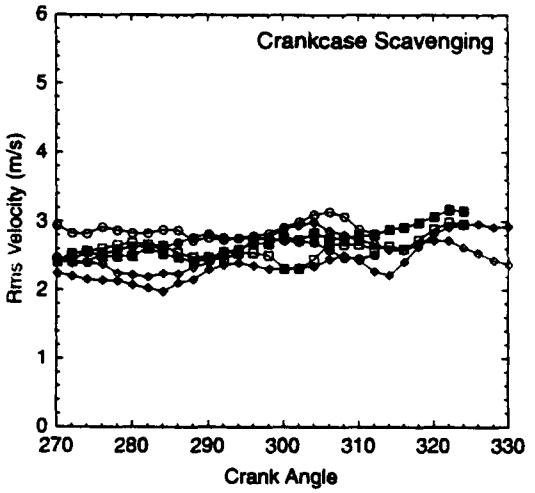

Figure 14 Rms fluctuating velocities for crankcase scavenging. The filled symbols indicate data obtained under motored conditions. —◆— z=4.0 mm; —■— z=12.0 mm; —●— z=20.0 mm.

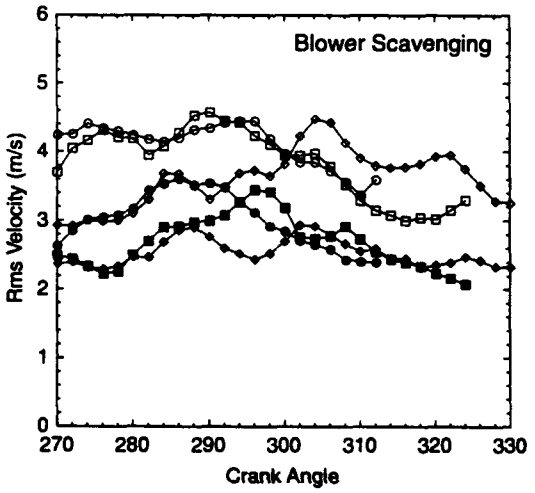

Figure 15 Rms fluctuating velocities for blower scavenging. The filled symbols indicate data obtained under motored conditions. —◆— z=4.0 mm; —■— z=12.0 mm; —●— z=20.0 mm.

4 SUMMARY AND CONCLUSIONS

Measurements of the radial component of velocity along the cylinder centerline in a two-stroke engine have been obtained for simulations of blower and crankcase scavenging under motored and fired operation. Mean profiles of the radial component of velocity are reported at selected crank angles, and rms velocity fluctuations during the compression process are also presented.

Significant differences in the mean velocity profiles for motored and fired conditions indicate that the general nature of the in-cylinder flow is changed dramatically. These differences are observed for both blower and crankcase driven scavenging, and persist throughout the compression process. Rms velocity fluctuations near top center are also affected, and are found to correlate reasonably well with the mean shear observed during the compression stroke.

In general, we conclude that the scavenging flow field for motored operation is not representative of the flow field in a fired engine. Realistic measurements of the in-cylinder scavenging flow field of two-stroke engines can only be assured by running the engine in a steady or quasi-steady fired mode.

Finally, we caution against forming universal conclusions about the relative differences in the motored and fired flow fields under blower and crankcase driven scavenging, based solely on the limited data presented here. For example, in contrast to the similar rms velocity fluctuations shown in Fig. 14, we observe significant differences in the motored and fired rms velocities during the compression stroke for crankcase scavenging at other delivery ratios.

ACKNOWLEDGMENTS

The authors particularly wish to acknowledge E.G. Groff, T.D. Fansler, and W.R. Matthes of the General Motors NAO R&D Center for the design of the porting and transfer passages employed in this work and for many helpful and illuminating discussions. Duane Sunnarborg has provided assistance with all mechanical aspects of this work. This work was performed at the Combustion Research Facility of the Sandia National Laboratories, and was funded by the U.S. Department of Energy, Office of Advanced Industrial Concepts.

REFERENCES

Baritaud, T., Trapy, J. & Monreal, J. 1986 Effects of Swirl and Combustion on the Fluid Motion in a S.I. Engine, Proceedings of the Third International Symposium on Applications of Laser Anemometry to Fluid Mechanics, Lisbon, Paper 7.3.

Blair, G.P. 1990 The Basic Design of Two-Stroke Engines, SAE, Warrendale, PA.

Ikeda, Y., Hikosaka, M., Nakajima, T. & Ohira, T. 1991 Scavenging Flow Measurements in a Fired Two-Stroke Engine by Fiber LDV, SAE Paper 910670.

Miles, P.C., Green, R.M. & Witze, P.O. 1994 In-cylinder Gas Velocity Measurements Comparing Crankcase and Blower Scavenging in a Fired Two-Stroke Cycle Engine, SAE Paper 940401.

Obokata, T., Hanada, N. & Kurabayashi, T. 1987 Velocity and Turbulence Measurements in a Combustion Chamber of S.I. Engine under Motored and Firing Operations by L.D.A. with Fiber-optic Pick-up, SAE Paper 870166.

Obokata, T., Hanada, N. & Kurabayashi, T. 1988 Laser Doppler Anemometer Measurement of Gas Flow in the Wedge-Type Combustion Chamber of a Two-Cycle Spark Ignition Engine, in Combustion in Engines - Technology and Applications, Institution of Mechanical Engineers, Mechanical Engineering Publications Ltd., p.213-223.

Ohira, T., Ikeda, Y., Takahashi, T., Ito, T. & Nakajima, T. 1993 Exhaust Gas Flow Behavior in a Two-Stroke Engine, SAE Paper 930502.

Okuyama, L., Kousaka, Y., Tohge, N., Yamamoto, S., Wu, J.J., Flagan, R.C. & Seinfeld, J.H. 1986 Production of Ultrafine Metal Oxide Aerosol Particles by Thermal Decomposition of Metal Alkoxide Vapors, AIChE J., vol. 32, no. 12, p.2010-2019.

Witze, P.O., Hall, M.J. & Bennet, M.J. 1989 Are Gas Velocities in a Motored Piston Engine Representative of the Pre-ignition Fluid Motion in a Fired Engine?, Exp. In Fluids, vol. 8, p.103–107.

Session 34.
Two Phase Flow III

PARTICLE FLOW DIAGNOSIS IN POWDER INJECTION LASER ALLOYING PROCESS

C. Herschkorn*, J. Lascu**, P. Gougat**, D. Kechemair*, R. Prud'homme**

*Laboratoire d'Application des Lasers de Puissance, Unité mixte ETCA-CNRS
16 bis, av. Prieur de la Côte d'Or, 94114 Arcueil Cedex, France

**Laboratoire d'Aérothermique du CNRS
4ter route des Gardes, 92190 Meudon, France

1. Introduction

The development of laser cladding and alloying techniques is of great importance in many industrial fields, particularly in the aeronautical industry which makes a great use of aluminium alloys, as that process allows the improvement of the surface properties of materials like resistance to wear, corrosion and oxidation. The reasons of this interest lie in the high quenching rate, the good fusion bonding and the localized heating which reduce the thermal distorsions and the size of the heat affected zone.
The process may be performed by either preplacing the powder on the substrate or blowing the powder into the laser-generated molten pool. It can also be done by applying the clad material as a wire sheet or plasma spraycoat or electroplate coat. The blown powder process is preferable to the preplaced powder technique, in so far as the shape of the clad and the level of dilution are easier to control [1].

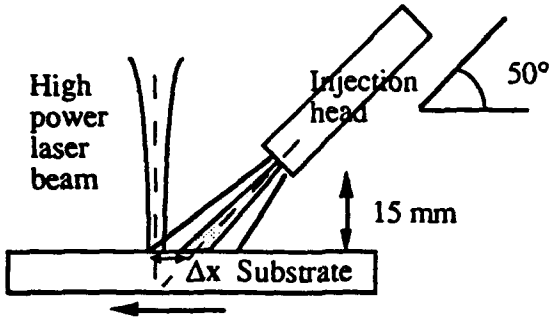

Fig 1 : The laser cladding set-up

As shown on figure 1, the alloyed layer is created by injecting powder into the laser melted surface with an angle θ around 50° defined from horizontal. The CO_2 source is a 22 kW U.T.I.L laser. The incident beam is homogenized through a kaleidoscope device which permits delivery of an energy distribution in the transverse direction of about a few 10^4 W/cm^2 on a typically 4 x 10mm^2 surface (figure 2)[1].

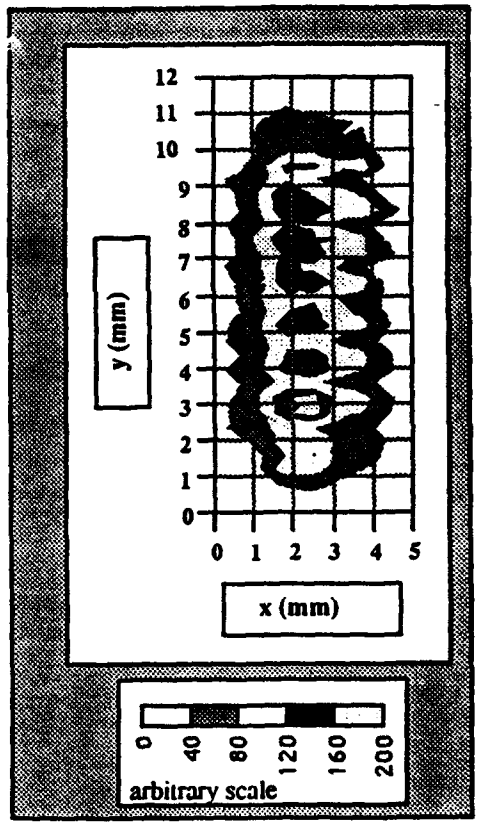

Fig 2 : Laser beam analysis in the interaction zone

High power laser beam analysis is performed by an appropriate device which is mainly constituted by a rotating hollow cylinder with 40 µm diameter holes regularly spaced in screw. During laser irradiation, each hole takes a part of the incident laser beam which is focused on pyro-electric detectors (λ = 10,6 µm).

Considering hole location and rotative speed of the cylinder (50 cm in diameter), the whole intensity distribution in the interaction area is achieved by this well-tried apparatus [2, 3]. This original optical device allows effective shaping of the 22 kW laser beam with a symmetric distribution of power density.

The CO_2 laser sources usually devoted to laser surface treatment range from 2 to 5 kW which lead to surface transformation of narrow tracks placed side by side to generate extended treatments in width.

In our experiments, laser powers of up to 16 kW have been used in the Al/Ni surface alloy formation on aluminium substrate leading to 10 mm large alloyed tracks in one step.

In order to provide homogeneous powder delivery in the interaction zone, an injection head with rectangular geometry had been chosen.
Several phenomena governing the alloyed layer formation depend on transport of the powdery material in the carrier gas : powder interaction time, laser material coupling, surface alloy composition...
It appears that no melting occurs without powder, wheras a molten pool is generated on the ground surface when powder is injected showing that powder particles enhance the global absorption of laser energy.

Due to the great influence of powder in the laser material interaction , different experimental set-up described below have been developped aiming at particle and gas flow study in the zone of interest to take a step forward in the blown powder process control.
The powder injection head consists in a 10 mm large slit nozzle, whose thickness e can be varied continuously from 1 to 4 mm. This geometry has been chosen to ensure the maximum particle entrapment into the laser melted surface. The nozzle presents two additional slits delivering argon gas to protect the substrate from oxidation. The powder injection head is fed with Al50/Ni50 premixed alloy particles, 0.06 mm in average diameter, carried by argon gas. The particle jet is produced in a Plasma Technik feeder, presenting wheels with grooves in which the powder falls. The powder mass flow rate is determined by the rotation speed of the wheel and the dimension of the grooves.

Two non intrusive techniques are implemented in order to investigate the two-phase flow jet: Laser doppler anemometry of the gas flow issuing the injection head and Particle Image Visualization of the powder jet.

2. Laser Doppler Anemometry of the gas flow jets

In order to characterize the flow velocity field in the interaction zone, experimental measurements of both mean and rms values of the axial component of gas velocity in abscence of metallic powders are carried out.

2.1. Experimental set-up

Velocity measurements are performed using a one-component Laser Doppler Anemometer operating in the backward scatter mode as schematically illustrated on figure 3.
A 2 W argon laser supplies the light source. The laser beams (λ = 0.514 µm) issued from the beam splitter are focused by a 193 mm focal length lens to form a probe volume with a diameter of 90 µm and a length of 701 µm. The fringe spacings are 2 µm.
The main jet (carrier gas) and the shielding gas jets are separately seeded with sub-micronic oil-droplets which have been both able to follow the gas flow and to backscatter light from measurement volume.
As there is no influence of gravity, the nozzle-plate system is rotated for convenience. The plate represents the substrate in the impinged region during laser surface treatments defining a 50°angle with the jet axis.

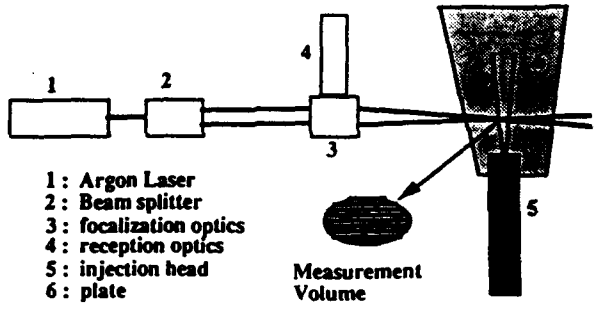

Fig 3 : Scheme of the set-up

Taking z = 0 at the nozzle exit, mean velocity measurements are obtained from 5.6 mm to 18 mm in the jet axis (4 mm from the plate) (figure 4) .

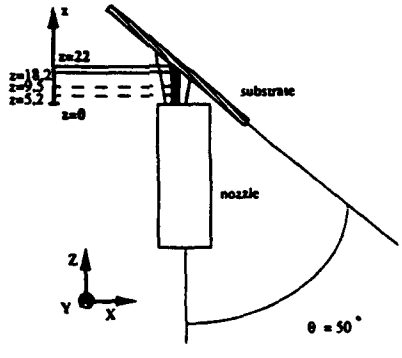

Fig 4 : L.D.A measurement locations

Reproducing experimental flow conditions, gaz flow rates values from 2.5 to 8.5 l/min are supplied in a Plasma Technik feeder to produce the main jet when 40 l/min are distributed in secondary jets.

2.2. Results

At first, gas flow rate effects on mean velocity are achieved in the main jet alone. An homogeneous mean gas velocity is observed along y axis as expected.
Following x axis, symmetric velocity profiles are observed as shown on figure 5 (z = 5.2 mm) ; this free jet region exists up to 10mm above the nozzle exit. Axial mean velocity increases with flow rate at a fixed nozzle geometry.

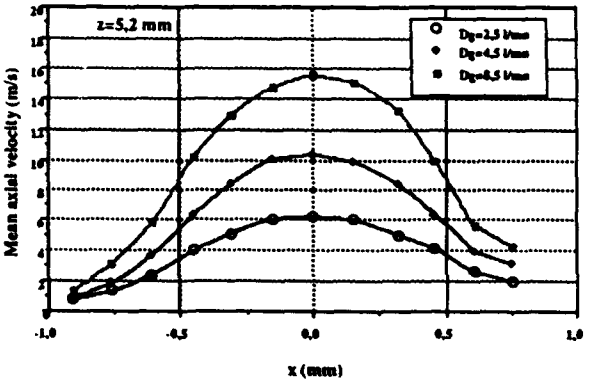

Fig 5 : Influence of the gas flow rate (free jet region) (e = 1)

At the location z = 18 mm, mean axial velocity profiles are no longer symmetric due to plate-flow interaction, as shown on figure 6. Jet impingement leads to higher decay of mean axial velocity and smoothed velocity profiles above exit nozzle at a gas flow rate of 8,5 l/min.

The secondary flow mean axial velocity profiles are described by means of two different seeding procedures. Oil droplets are first injected in the main jet (carrier gas). Because of particles diffusion, LDA measurements may be performed over a wider zone than the main jet region and allow shielding gas flow field measurements. In a second step, when both main and secondary jets are seeded, it appears that the same velocity field is depicted at the z = 10 mm cross section. This accounts for the gas jet mixing (figure 7).

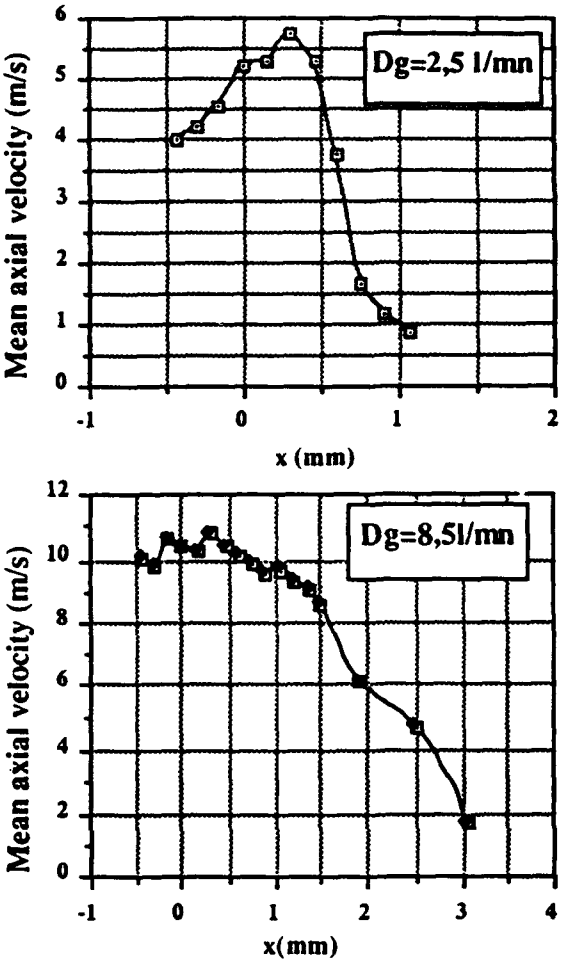

Fig 6 : Mean gas velocity profiles (z = 18mm ; e = 1mm)

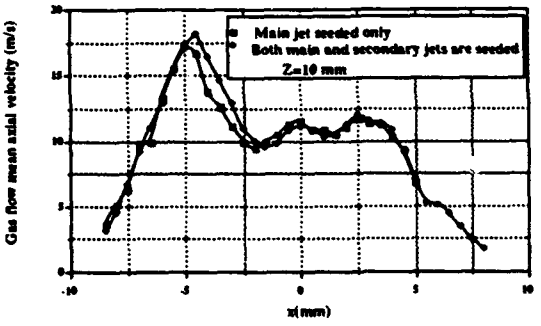

Fig 7 : Flow velocity measurements

Thus, in our experimental conditions, LDA measurements yield that secondary jets may have a great influence on the carrier gas jet. Nevertheless, respective gas flow rates (main and secondary jets) insure effective confinement of the central jet.

3. Particle Image Visualization

In order to investigate particle flow, a particle image visualization method based on trajectories recognition is applied to metallic powder carried by argon gas.

3.1. Experimental procedure

The particle velocity is obtained by means of the set-up presented on figure 8. An argon laser sheet illuminates cyclically the plane containing the particle trajectories. The time base is given by an acousto-optic modulator (10 kHz). The frames, corresponding to a 2.6 mmx 2 mm window, are recorded by means of a CCD camera on a micro computer hard disk.

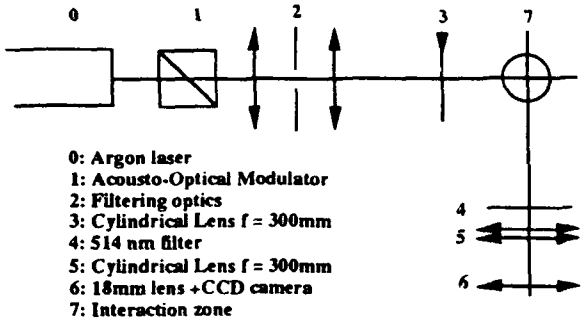

Fig 8 : Experimental set-up

3.2. Particle velocimetry

Image processing makes possible to identify automatically the trajectories and to calculate the average velocity along each trajectory. Strong trajectory rejection criterions have been introduced in order to prevent errors of identification. Trajectory recognition algorythm is based on imposed residual light beetween two luminous intensity maxima (see figure 9) .

A sequence of 15 frames may be automatically acquiered and treated (trajectory recognition and distance measurement on validate ones). A hundred particle mean velocity measurement is achieved within the interaction zone.

Fig 9 : Trajectory recognition and powder velocity measurements

As a result, particle mean velocity corresponding to specific aerodynamic conditions which have been used during thermal treatment (rectangular nozzle with e = 1 mm and gas flow rate varying from 2.5 to 8.5 l/mn) is identified (see figure 10).

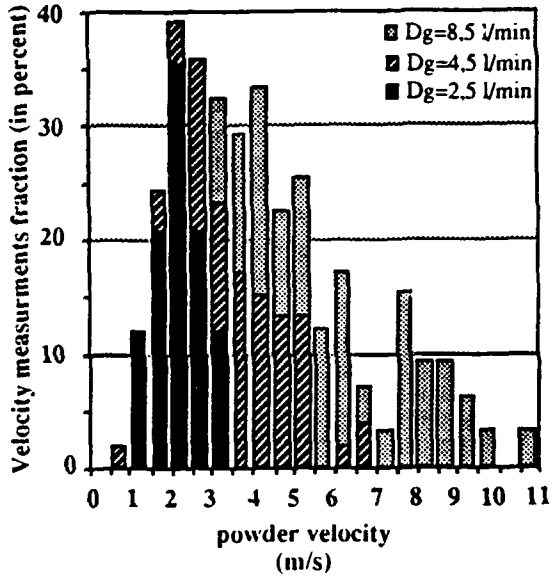

Fig 10 : Particle velocity increase with carrier gas flow rate

The main limitation of the method is due to low solid phase volume fraction needed to achieve trajectories recognition (nearly 10^{-3}) .

3.3. Density distribution in the particle jet

The determination of density distributions of the particles uses the same apparatus (see figure 8) but requires the argon laser sheet to be perpendicular to the particle jet axis. The laser sheet irradiates continuously a 50 µm cross section. Each metallic powder particle passing through laser beam scatters an amount of light to CCD camera. The luminance in each point of the image is then supposed to be proportional to the local particle density.

The two-phase flow jet is weakly diverging. The subsequent lowering of density distribution may be described qualitatively at a given location in the jet axis.

The entrapment rate depends on the area of the molten pool with respect to the particle jet impingement, as particles falling outside the pool are lost. Powder distribution in the near substrate region is of great importance in order to optimize this characteristic, as shown on figure11.

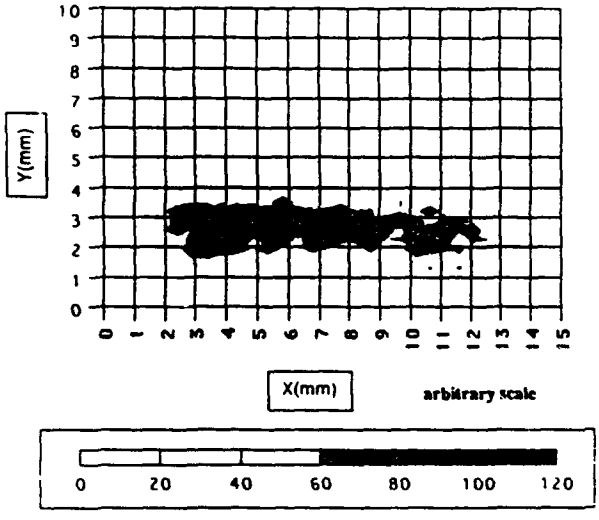

Fig 11 : Particle flow cross section near the substrate (particle density distribution)

The maximum particle entrapment rate is around 65%. The best results have been obtained with an injection angle of 50° (defined from horizontal) and a distance Δx (horizontal) to the molten pool around 15 mm from the nozzle exit. As the entrapment rate varies from 32% to 65% for 1.5 mm change in Δx, this distance has to be defined very accurately (see figure 12).

A low particle velocity is preferable in order to minimize ricochet losses from the molten pool. The laser power is absorbed partly by the particles cloud and partly at the clad/substrate interaction zone. As a result, powder entrapment rate around 65% was obtained by means of both laser beam and particle flow shapings (homogeneous in one direction).

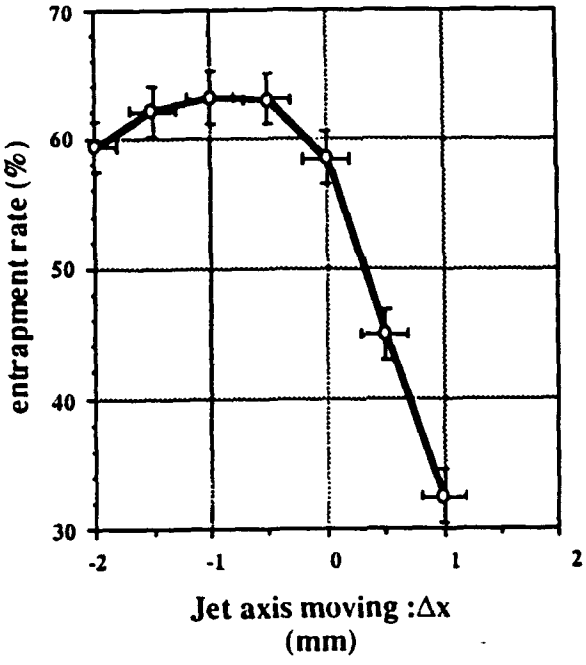

Fig 12 : Effect of jet axis translation with respect to high power interaction zone

4. Conclusions

LDA measurements have been achieved in order to investigate gas flow jets mean axial velocity during high power laser surface treatments.

A flexible processing image device allows us to qualify our slit nozzle in term of particle velocity and powder density distribution.

AKNOWLEDGMENTS

The participation of Mr L. Sabatier to the experiments and the technical aid concerning image processing developments of Mr F. Coste are greatly acknowledged.

REFERENCES

[1] Steen W.M. 1986. "Laser Surface Cladding" Laser surface treatment of metals, Nato ASI Series.

[2] Myamoto I. 1990." Novel Shaping Optics of CO_2 Laser Beams : LSV Optics". Proceedings of ECO 3, The Hagues.

[3] Chablat J., Paradis J.L., Gerbet D. 1985. "Analyseur d'intensité laser infra-rouge de haute puissance", Opto 85, Paris.

MICROPROJECTILE VELOCITIES IN A GAS DRIVEN LAUNCHER

A.L. Duval, N.W. Page and K. Bremhorst

Department of Mechanical Engineering
The University of Queensland,
Brisbane QLD 4072, Australia

ABSTRACT

Microprojectile methods of genetic engineering sometimes employ a macroprojectile which launches the microprojectiles when it hits a stopping plate. A study has been made of the relationship between the velocities of the macroprojectile and the microprojectiles it launches. Macroprojectile velocities were measured using a novel laser beam cutting method and the microprojectile velocities measured directly using a laser Doppler anemometer. Particles of tungsten, titanium dioxide and silicon carbide were investigated as microprojectiles. The microprojectile velocity has been found to depend not only on the macroprojectile velocity but also on the microprojectile size and material, the bond strength with the macroprojectile and the gas flow that develops ahead of the macroprojectile. On average, the microprojectile launch velocity was similar to the macroprojectile velocity. However, some tungsten particles had velocities 2 or 3 times this value. Experimental evidence suggests that these higher velocities were caused by early break-away of this heavier particle material from the macroprojectile followed by further acceleration by aerodynamic drag arising from the gas flow ahead of the macroprojectile.

1. INTRODUCTION

There is currently considerable interest in the use of microprojectile techniques to introduce new genetic material into living cells (see for example Sanford et al (1987), Klein et al (1992). A gas driven microprojectile acceleration device suitable for this purpose has been developed at The University of Queensland (Nabulsi et al, 1994). This device uses a light-weight macroprojectile to which microprojectiles are attached to the downstream side, these microprojectiles having previously been coated in the new genetic material. In operation, a shock wave is used to accelerate the macroprojectile to high velocity. The macroprojectile then strikes a stopping plate. The inertia of the microprojectiles is sufficient for them to break away from the macroprojectile and fly off into the target section of the device. There, the microprojectiles penetrate through the wall of target cells carrying new genetic material into the cell interior. A recent review of this method of genetic engineering is given in Klein et al (1992).

For genetic engineering purposes the microprojectile impact velocity on the cell wall is of the greatest importance - the microprojectile must have sufficient velocity to penetrate cell walls but without destroying them. Other studies have been made of the terminal ballistics phase in which the microprojectile strikes the target cells (Kwong 1993). This paper is primarily concerned with the launch phase of the microprojectiles. Of interest in a microprojectile launcher of this type is the relationship between the macroprojectile and microprojectile velocities. The macroprojectile velocity is the one directly controlled by the shock tube driver. While clearly related, the microprojectile velocity at impact on the cell wall also depends on the interaction between the microprojectile and the gas flows caused by the macroprojectile motion. An understanding of microprojectile separation from the macroprojectile and its subsequent drag history in the macroprojectile generated flows is necessary for process optimisation.

2. APPARATUS

A schematic of the microprojectile accelerator is shown in Figure 1. The macroprojectile consisted of a membrane placed across the end of a shock-tube driver consisting of a reservior and driven tube, with a stopping plate on the downstream side of the macroprojectile separating it from the target chamber. Full details are given in Nabulsi et al (1994). In the version used for genetic engineering experiments, the stopping plate consisted of a regular array of small holes, with an open area of 60%. This led to the minimum blockage possible consistent with the stopping plate having sufficient strength to support the load of the impacting macroprojectile. It was important to maximize the flow area to minimize gas pressure buildup between the macroprojectile and the stopping plate which would have had the effect of decelerating the macroprojectile before it reached the stopping plate. The small size of the holes in the stopping plate prevented the macroprojectile from bursting and having driver gas contaminate the target section.

In operation, the shock tube reservoir was pressurized and the primary diaphragm separating the shock tube reservoir

from the driven tube ruptured so that a pressure wave was generated in the driven tube. This pressure wave struck the thin membrane macroprojectile accelerating it towards the stopping plate. Microprojectiles coated in new genetic material had previously been dispersed on the stopping plate side of the macroprojectile. The motion of the macroprojectile was arrested when it struck the porous stopping plate. In practice, the macroprojectile would begin to decelerate before striking the stopping plate because of the pressure developed in the gas being compressed by its movement towards the stopping plate. The velocity of the microprojectiles reaching the target chamber would depend on when they detached from the macroprojectile and what subsequent aerodynamic drag they were subjected to. Once in the target chamber they would continue on to the target cells penetrating through the cell walls carrying the new genetic material into the cell. For successful genetic transformation, a large number of cells must express the new genetic material and survive the trauma of the impact event.

For the present study, a simplified experimental model of the stopping plate was used in which flow through a single orifice was considered. This avoided the complication of complex interaction of multiple jet flows produced by the original stopping plate. A diameter of 20 mm for this nozzle gave a good compromise between maintaining flow area and preventing the macroprojectile from bursting. Nabulsi et al (1994) have discussed a variety of geometric configurations possible for this basic microprojectile accelerator in which the length of the shock-tube driver and initial geometry of the macroprojectile were varied. For the study described here, a combination of a long driven tube and an initially flat macroprojectile was used.

2.1 Macroprojectile Velocity Transducer

The velocity transducer is based on the principle of the cutting of a single beam of light by the macroprojectile. This single beam device is extremely compact providing a "near point" measurement of the macroprojectile velocity very close to the end of its motion. This design is particularly suited to the tight geometric constraints and the unsteady nature of the velocity measured in the present study.

The velocity transducer consists of a light emitting diode which directs a parallel beam normal to the motion of the macroprojectile onto a photodetector. As the light beam is cut, the voltage output from the photodetector reduces. This voltage reduction is linear with beam blockage over the centre 0.8 mm of the 3 mm diameter beam. The device was calibrated using a depth micrometer to block varying fractions of the light beam. Only two different depth micrometer positions were required for a calibration. The two voltages corresponding to the two known positions of the calibrating micrometer were recorded on the same oscilloscope as the time varying signal output from the transducer when the beam was cut by the macroprojectile. The average velocity of the macroprojectile between the calibration points could then be calculated.

The light source chosen was a Radio Spares 1 mW optical output power laser diode module with a built on focussing lens. A recessed pressure tapping in the stopping plate was used to measure static pressure in the nozzle with a PCB model 11A26 piezo-electric pressure transducer. Details of the design and testing of this transducer are given elsewhere (Nabulsi et al, 1994), Duval 1993).

2.2. Laser Doppler Anemometer

The laser Doppler anemometer was used to measure particle velocities of 3 different microprojectiles, details of which are shown in Table 1. Particle diameters were measured with a Malvern Mastersizer. Prior to particle size measurement, ultrasonics were used to disperse the powders in water with the aid of the additive Calgon.

The laser used was a Spectra Physics Model 165-08 argon ion laser operated at a wavelength of 514.5 nm and maximum power output of 1.7 W. The diameter of the beam at the $1/e^2$ level is 1.23 mm. No frequency shifting was required as the microprojectile velocity direction was known. The photomultiplier signal was processed by a TSI Model 1990 counter type signal processor to give particle velocities from burst frequencies. The monitor output from the processor, which is a voltage inversely proportional to the particle velocity, is the signal which was recorded.

A schematic of the microprojectile accelerator with the positioning of the LDA beams is shown in Figure 1. Tektronix type 2211 (20 MHz) oscilloscopes were used for recording the macroprojectile velocity transducer signal, the static pressure in the nozzle, the output from the LDA signal processor (microprojectile velocity information) and the incident shock pressure.

3. RESULTS

Preliminary experiments were performed under the same conditions shown as Series 1 in Table 2. The LDA measurements were performed in a diametral plane of the axisymmetric window with the measuring volume in the center of the nozzle. In these shots the measured macroprojectile velocity was significantly lower than those of the microprojectiles (approximately one third). This velocity differential was attributed to interaction of the microprojectiles with the gas flow developed through the stopping plate as a result of gas compression between the macroprojectile and the stopping plate. This mechanism is discussed further below in Section 4, but to minimise these effects, a second series of experiments was conducted with different flow parameters. If the macroprojectile velocity and initial fill pressures are low enough, the static pressure buildup in the nozzle would be significantly reduced, Series 2 settings in Table 2. With these settings the peak static pressure in the nozzle throat was measured to be 9.3 kPa. Assuming isentropic expansion from the space ahead of the macroprojectile, this static pressure corresponds to a stagnation pressure of only 17.6 kPa. Under these conditions a typical experimentally measured pressure behind the reflected shock driving the macroprojectile was 60 kPa.

LDA measurements were also undertaken using Series 2 conditions. A typical result of LDA velocity and macroprojectile velocity signals is shown in Figure 2. It is seen that the monitor output signal is highly discontinuous with only a few changes in voltage per shot. Each step in voltage corresponds to a particle of different velocity passing through the measuring volume. Only a few particles per shot produce velocity data points. The first of these is used to characterize the microprojectile response. It is assumed that this particle left the diaphragm first (had the lowest bond strength and so should have the highest velocity) and traveled to the LDA measuring volume along the shortest path length.

Four different experimental configurations were used. The first two used the same tungsten microprojectiles at two different measurement stations, one 5 mm downstream from the nozzle exit and the second 20 mm downstream from the nozzle exit. The other two configurations measured microprojectile velocities at a fixed location (5 mm downstream from the nozzle exit) but used two different microprojectile materials, titanium dioxide and silicon carbide.

Results for different particle systems are compared in Figure 3 (a)-(d). Error bars incorporating the inaccuracies of the measuring apparatus are also shown. The velocity ratio is the ratio of the microprojectile velocity based on the first pulse captured on the LDA and the macroprojectile velocity. If Δt is the time delay between the macroprojectile velocity measurement and the corresponding microprojectile velocity measurement as a consequence of the spatial separation between the two measurement points, V_{ma} the macroprojectile velocity and D is the axial separation of the macroprojectile measurement position and the LDA measuring volume then the normalised time $\overline{\Delta t}$ is,

$$\overline{\Delta t} = V_{ma}\,\Delta t/D \qquad (1)$$

Not included in the error analysis are sources of scatter such as the stretching of the macroprojectile through the nozzle hole, the non-constant motion of the particles and the variable size of the particles being measured. The curvature of the macroprojectile coupled with the irregular shape of the particles may cause them to move in non-rectilinear trajectories. Since the particles are of variable size the drag for each will be slightly different and this may also cause some scatter.

4. ANALYSIS AND DISCUSSION

An important feature of the motion of microprojectiles is the aerodynamic drag between them and the gas flow through the stopping plate. A drag coefficient correlation formula for small spheres has been given by Henderson (1976). The flow regimes covered include continuum, slip, transition and free molecular flow at Mach numbers up to 6 and Reynolds numbers up to the laminar-turbulent transition. The effect on the drag of a temperature difference between the sphere and the gas is also incorporated. Since in this case a convergent nozzle is used, the maximum possible Mach number for the gas is 1. The microprojectiles will be moving in the same direction as the gas and so the slip velocity between the particles and the gas will be such that the Mach number based on this slip velocity will also be less than 1. Hence only Henderson's subsonic drag correlation need be used here. This gives the drag coefficient C_d in terms of the Reynolds number (*Re* based on sphere diameter, on ΔV - the slip velocity between the gas and sphere and on the freestream density and viscosity), the Mach number (M based on ΔV), the molecular speed ratio (equal to $M\sqrt{\gamma}/2$, where γ is the ratio of specific heats), the temperature of the sphere (T_w assumed to be isothermal) and the temperature of the gas in the freestream (T). In the present case T_w is assumed to be equal to T.

Using this equation an analysis of the effect of the drag on the microprojectiles can be performed. The flow conditions in the nozzle are complicated due to unsteady flow, however, some details are clear from velocity and pressure data. There is a pressure buildup with the pressure staying constant for a short time (indicating choking of the nozzle) then the pressure drops again approximately returning to its original value as the rarefaction wave caused by the macroprojectile hitting the stopping plate reaches the pressure transducer section. Since the period of higher pressure lasts only a short time (approximately 50 μs) compared with the time delay between the velocity transducer and LDA signals (approximately 0.35ms) by the time the particles were entering the LDA measuring volume, they would be passing through gas affected by the rarefaction arising from the macroprojectile stopping at the stopping plate. Thus, the gas pressure and temperature would have been close to the initial fill conditions, and the relative velocity would, therefore, be the particle launch velocity or macroprojectile velocity. These conditions were used in the subsequent analysis. From the definition of drag coefficient and using the equivalent volume sphere approximation, the particle acceleration is

$$\alpha = \frac{d}{dx}\left(\tfrac{1}{2}V_p^2\right) = 0.75\,C_d\,\frac{\rho_{gas}}{\rho_{part}}(\Delta V)^2/d \qquad (2)$$

where x is the coordinate in the streamwise direction, V_p is the velocity of the particle, ρ_{gas} is the gas density, ρ_{part} the microprojectile density and d its diameter. Equation (2) must be integrated numerically using a Runge-Kutta method because C_d is obtained from Henderson's drag equation which is also a function of ΔV. This gives the particle velocity as a function of travel distance. Three different initial particle velocities were considered - 50 m s^{-1}, 100 m s^{-1} and 150 m s^{-1} (as these were close to the microprojectile launch velocity or terminal macroprojectile velocity) moving into a gas at rest. The reason for the gas being assumed to be at rest is as stated above - after the nozzle choking the pressure returns close to its original value and hence the gas velocities are assumed to be low when this happens. The results are presented in Figure 4.

Clearly, over the distance being considered (nominally 46.5 mm - the distance between the macroprojectile velocity measurement and the LDA measuring volume), the drag has only a small effect in reducing the tungsten particle velocity, that is, its response to the gas is quite small and a constant velocity assumption would be a good approximation. The other powders are affected more by the drag under these

conditions; that is their velocity is lower than that of the tungsten or closer to that of the gas for any given distance under the conditions considered. However, with the exception of the SiC initially at 50 m s^{-1}, none of these powders is brought close to rest (the gas velocity) over the distance considered.

The following results are apparent from the data of Figure 3:

1. the tungsten particles are mostly moving at velocities similar to that of the macroprojectile, however, there are some particles which are moving faster than the macroprojectile, indeed some are moving about twice as fast as the macroprojectile
2. higher velocity particles appear at an earlier time, especially for the tungsten
3. there is no obvious difference in tungsten velocity at the two measurement locations
4. the silicon carbide and titanium dioxide particles are moving more slowly than the tungsten particles.

Clearly the different particle systems gave different velocity outcomes. There are two possible mechanisms that could explain these differences - one relating to different strengths of attachment of the microprojectiles to the macroprojectile, and one relating to different interaction of the microprojectiles with the gas flow set up ahead of the macroprojectile. These will now be considered in turn.

Anomalously high velocities were not observed with any of the titanium dioxide or silicon carbide particles. These particles are smaller and lighter than the tungsten particles. Furthermore, unlike the tungsten particles, they are electrically non-conducting thus possibly leading to an electrostatic charge which bonded them more securely to the macroprojectile surface. This higher bond strength coupled with their lower mass would have meant that they were more tenaciously held to the macroprojectile under both deceleration and gas entrainment effects. This could explain why higher velocities than the macroprojectile were not observed with these particles.

Alternatively, all results can be understood in terms of the interaction between the macroprojectile motion and the gas flow this causes through the stopping plate. Particles that stayed attached to the macroprojectile until the sudden deceleration caused by it hitting the stopping plate would be released into gas affected by the rarefaction wave arising from the same macroprojectile deceleration. This rarefaction wave would travel at the local speed of sound relative to the gas - much faster than the particle velocities under study. Once launched, the velocity history of these particles would depend on aerodynamic drag effects caused by the slip velocity. The generally higher velocities of the tungsten particles compared with the other particles is consistent with this mechanism in that aerodynamic drag retardation is less significant in their case, Figure 4.

Another result that could be explained in terms of the aerodynamic drag effects was the observation that some of the tungsten particles were measured to be moving faster than the macroprojectile, in fact in some cases at about twice the velocity of the macroprojectile. It was observed that these measurements generally occurred at an earlier time. One possible mechanism that might explain these particles with anomalously high velocities would be aerodynamic drag effects in the stopping plate flow. Drag effects have been considered previously in terms of retardation of the particles downstream of the stopping plate. These effects were analyzed on the basis of particles moving through quiescent gas. In this case the slip velocity would have been of the order of the microprojectile velocity. If gas was compressed ahead of the macroprojectile, this gas would expand through the nozzle in the stopping plate possibly reaching high velocity. Any particle dislodged from the macroprojectile prior to it hitting the stopping plate would be entrained into this gas flow and accelerated by the drag force dependent on the slip velocity, in this case with the gas velocity larger than the particle velocity.

To investigate this possible mechanism, a gas flow analysis was performed. Assuming isentropic flow for a choked (M = 1) nozzle, the stagnation pressure leading to the static pressure recorded on the transducer (9.3 kPa) is 17.61 kPa. Further assuming that ahead of the moving macroprojectile there was isentropic compression from the initial fill pressure, the stagnation temperature for the choked nozzle flow would have been 830 K leading to a static temperature in the throat of 691 K. This leads to a speed of sound (and hence gas velocity since M = 1 at the throat) of 527 m s^{-1}. The response of the tungsten particles to this gas flow can be found using the same computer program as for the results of Figure 4. Results for three different tungsten particle sizes - 1 μm, 5 μm and 12 μm (the mean size) initially at rest are shown in Figure 5.

Clearly the response of the particles to the gas flow is a very strong function of diameter which could explain some of the faster tungsten velocities. The higher velocities could correspond to smaller particles which left the macroprojectile early and were entrained into the gas flow. This agrees with the results of the graphs in Figure 3 where the faster moving tungsten particles are measured at an earlier time. This tungsten particle velocity being faster than that of the macroprojectile also agrees with other results - Klein et al (1992) measured a microprojectile velocity of 1350 m s^{-1} at a point 1.97 cm below the stopping plate for a macroprojectile velocity of 750 m s^{-1} in a gunpowder driven biolistic device. They associated this higher velocity of the microprojectiles with the extrusion of the macroprojectile through the small orifice in the stopping plate thus further accelerating the microprojectiles. They did not make it clear whether this was a drag effect due to the velocity of the gas in this orifice acting like a nozzle accelerating the microprojectiles or if it was some other effect.

The arrival of the microprojectiles at an earlier time than expected is consistent with early particle release and entrainment in the gas stream prior to the macroprojectile reaching the stopping plate. However, for the purposes of determining the depth of penetration of the microprojectile and the amount of damage to the cell it is not really relevant since it is the velocity of the particle and not its time of arrival which determines this. From the LDA velocity measurements performed here it is clear that any attempt to calculate damage to cells and depth of penetration of microprojectiles in cells

under the same launch conditions must take account of the fact that the microprojectiles may be moving at twice the velocity of the macroprojectile. This is important because the macroprojectile velocity measurement is easier to perform and is likely to be recorded for each shot.

The mean velocity ratio for the tungsten particles at the two measurement locations (5 mm and 20 mm downstream from the nozzle exit) is 1.09 and 1.05 respectively. These values show that for the conditions used in this study, assuming that the microprojectiles have the same velocity as the terminal velocity of the macroprojectile is a good approximation which would be useful data for gun design.

5. CONCLUSIONS

On average, under the conditions considered, the velocity of the tungsten microprojectiles was the same as the terminal macroprojectile velocity. This is an important result for microprojectile accelerator design. Some of the tungsten particles were measured to be moving faster than the macroprojectile at velocities 2 or 3 times its value. Furthermore, these fast particles arrived sooner at the velocity measuring location. Both these results could be explained by the fact that the smaller tungsten particles in the distribution could be entrained in the gas and accelerated by aerodynamic drag to higher velocities than the macroprojectile. These faster tungsten particle velocities agree with data published by Klein et al (1992) for a gunpowder driven biolistic device.

The anomalously high particle velocities were not observed with either the titanium dioxide or silicon carbide particles. These were smaller, less dense and non-conducting and may have been more tenaciously attached to the microprojectile surface thus inhibiting entrainment in the gas stream prior to the macroprojectile striking the stopping plate.

If this anomalously high tungsten particle velocity is indeed due to entrainment in the gas then this principle could be exploited in a shock driven macroprojectile particle inflow gun (Finer et al, 1992) in which the tungsten would not be bonded to the macroprojectile but injected into the gas in front of it. The high temperature of the gas between the macroprojectile and the stopping plate means that it could achieve a higher speed of sound and hence a higher velocity than systems expanding room temperature gas alone. This velocity could be further increased by using a convergent-divergent nozzle for the gas rather than just a convergent nozzle. Hence a much faster gas-driven microprojectile velocity launcher may be able to be developed.

Table 1: Microprojectiles

Material	Diameter		Density	Source
	Mean (μm)	SD (μm)	(kg/m^3)	
Tungsten	11.98	12.20	19250	Sylvania M20
Titanium dioxide	5.61	3.97	4100	TSI Model 10082
Silicon carbide	2.32	2.12	3200	TSI Model 10081

6. ACKNOWLEDGMENTS

The authors would like to thank Mr. R. Gammie for assistance with design of the apparatus, Mr. B. Allsop for assistance with the design of the macroprojectile velocity transducer, and Mr. S. Nabulsi and Ms. Y. Seabrook for helpful discussions on the use of microprojectile guns. Financial assistance by the Australian Research Council is also gratefully acknowledged.

REFERENCES

Duval, A.L. 1993, The launch of microprojectiles from a high speed shock driven macroprojectile. M.Eng.Sc. Thesis, The University of Queensland, Brisbane, Queensland.

Finer, J.J., Vain, P., Jones, M.W. and McMullen, M.D. 1992, Development of the particle inflow gun for DNA delivery to plant cells. Plant Cell Reports, vol.11, pp.323-28.

Henderson, C.B. 1976, Drag coefficients of spheres in continuum and rarefied flows. AIAA Journal, Vol.14(6), pp.707-708.

Klein, T.M., Arentzen, R., Lewis, P.A. and Fitzpatrick-McElligot, S. 1992, Transformation of microbes, plants and animals by particle bombardment. Biotechnology, Vol.10, pp.286-291.

Kwong, P.K-Y. 1993, Terminal ballistics of microprojectiles on organic targets. M.Eng.Sc. Thesis, The University of Queensland, Brisbane, Queensland.

Meyer, R.F. 1958, The impact of a shock wave on a movable wall. J of Fluid Mechanics, Vol.3, pp.309-323.

Nabulsi, S.M., Page, N.W., Duval, A.L., Seabrook, Y.S. and Scott, K.J. 1994, A gas driven gene gun for microprojectile methods of genetic engineering. Measurement Science and Technology, Vol.5, pp.267-274.

Sanford, J.C, Klein, T.M., Wolf, E.D. and Allen, N. 1987, Delivery of substances into cells and tissues using a particle bombardment process. Particulate Science and Technology, Vol.5, pp.27-37.

Table 2: Initial Settings

	Series 1	Series 2
Shock tube diaphragm		
thickness (μm)	50	12
bursting pressure (kPa)	220	variable
Macroprojectile thickness (μm)	50	50
Gas upstream of macroprojectile	air	air
initial pressure (kPa abs.)	5	0.5
Gas downstream of macroprojectile	air	He
initial pressure (kPa abs.)	5	0.5

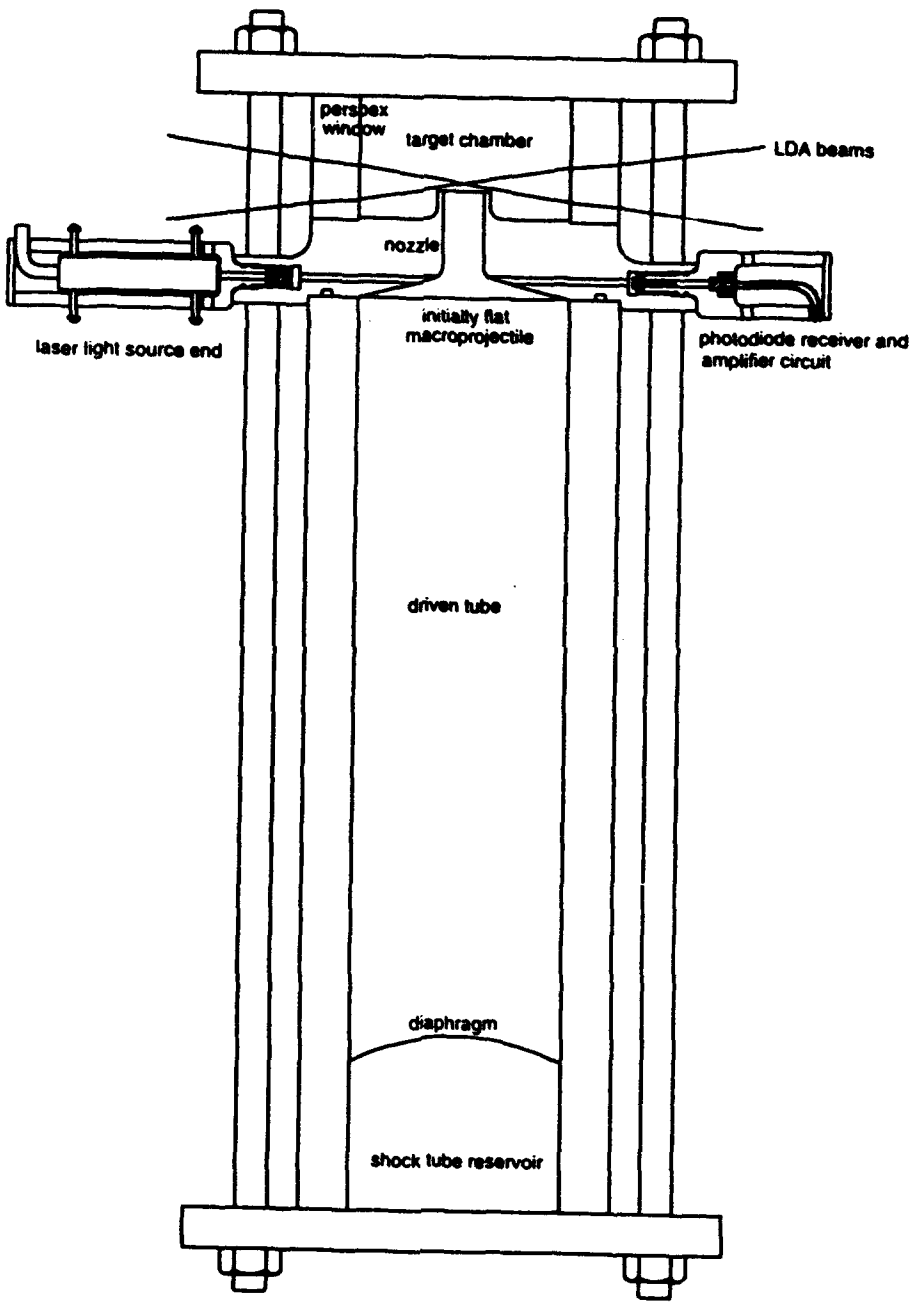

Figure 1: Apparatus Layout

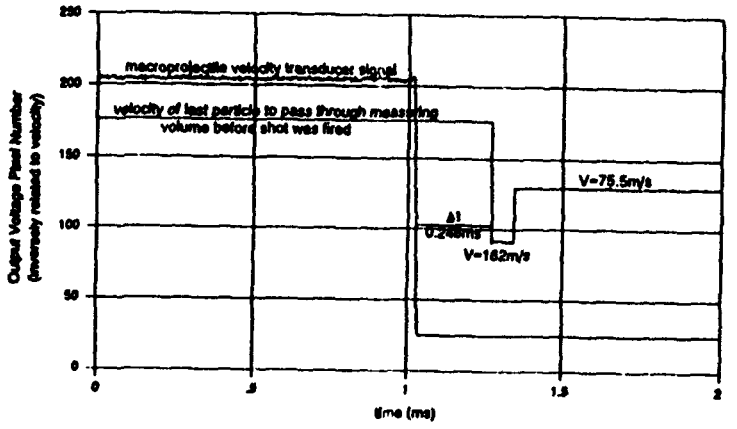

Figure 2: A Sample Result of LDA Velocity Information and Macroprojectile Velocity Transducer Signal Recorded on the Same Oscilloscope

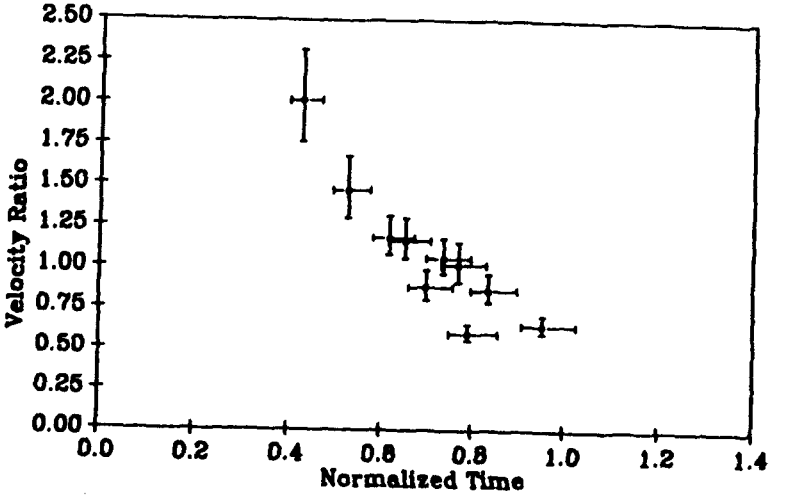

Figure 3: Velocity - Time Results: (a) 5 mm from nozzle exit (Tungsten particles);

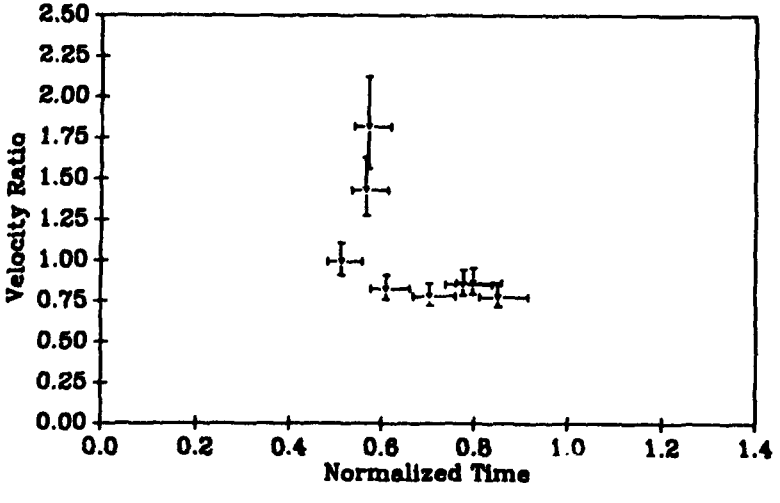

(b) 20 mm from nozzle exit (Tungsten particles)

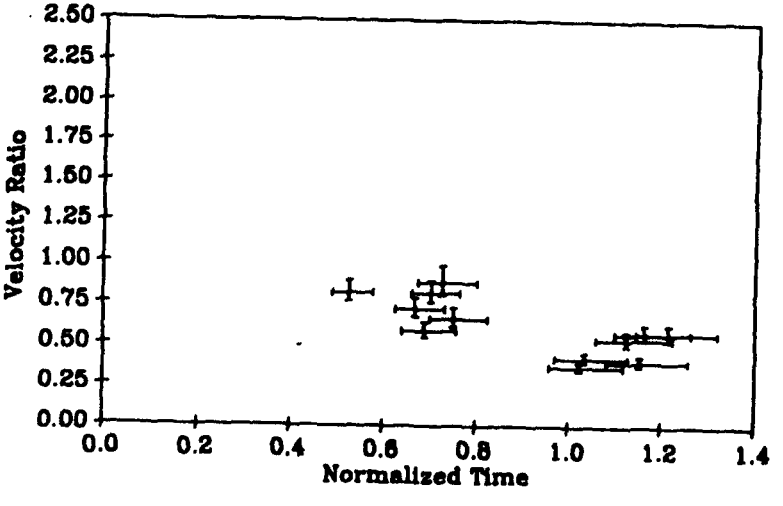

(c) 5 mm from nozzle exit (Titanium dioxide particles)

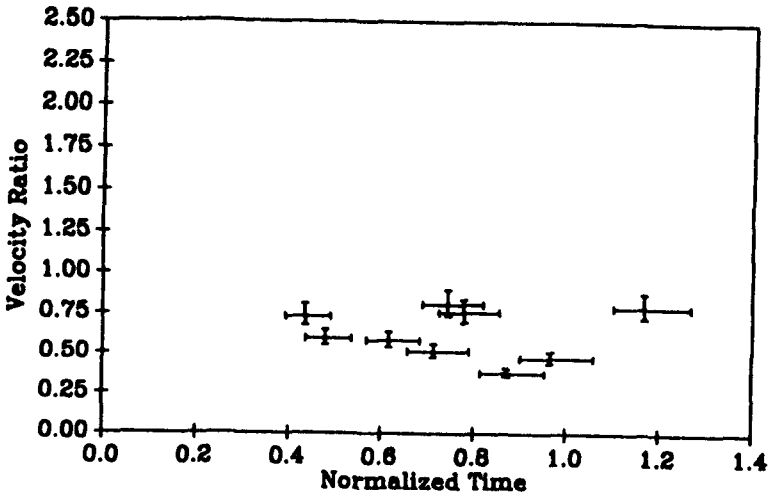

Figure 3: Velocity - Time Results (Cont):
(d) 5 mm from nozzle exit (Silicon carbide particles)

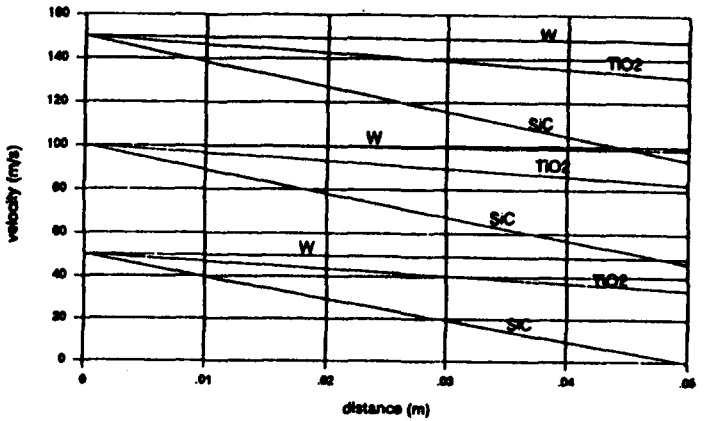

Figure 4: Velocity versus distance for the three different powders moving into quiescent gas for different starting velocities. Average particle sizes are: W - 12.00 μm, TiO_2 - 5.61 μm, SiC - 2.32 μm

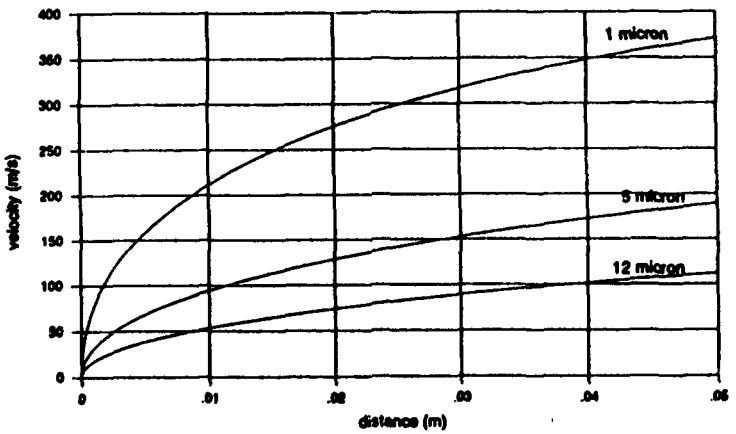

Figure 5: Response of Various Diameter Tungsten Particles to the Nozzle Flow

LASER HOLOGRAPHIC STUDIES ON DEFORMATION AND FRAGMENTATION OF DROPLETS IN THEIR OWN VAPOUR

G. Zerf and K. Hornung

Universität der Bundeswehr München
D-85577 Neubiberg / Germany

ABSTRACT

An experimental study of the motion and deformation of small water droplets in a shock tube is reported. In-line double pulse holography has been used to monitor the deformation and displacement of water droplets for particle diameters in the range of 17 to 220 μm. The studies were performed in a shock tube filled with 26 mbar water vapour at room temperature. Droplets were introduced perpendicular to the flow axis by means of a vibrating orifice aerosol generator and were then exposed to a weak shock (Ma=1.2-2.0). The displacement data are fitted by means of the equation of motion, yielding droplet velocities, accelerations, and drag coefficients. Deformation and fragmentation modes are presented for Weber numbers between 3.6 and 39.2 as well as Reynolds numbers between 69.72 and 317.04. The formation of jet-instabilities in the range of Weber numbers, around We=25, is observed.

1. INTRODUCTION

Mixtures of vapour and droplets like in sprays, clouds or in fogs form two phase systems of great technological and meteorological importance. Their nonequilibrium behaviour depends on the motion and interior thermodynamic state. Mass exchange (condensation and evaporation) is considered and investigated in several studies (B. Schmitt 1988). In general, when a drop with surface tension σ is exposed to an external flow, such as the flow behind a shock wave and if a critical value of the Weber number $We = \rho u^2 D_p/\sigma$ is reached, the drop ceases to vibrate and undertakes an irreversible and continues deformation until the particle finally breaks up. It should be noticed that, instead of the Weber number, the effects of acceleration on drop fragmentation are sometimes considered in terms of the Bond number. But, since both parameters are approximately expressed through the drag coefficient $Bo = 3/8 c_d We$, it becomes a matter of convenience which one is used in theoretical description. Break up occurs, when the applied aerodynamic pressure forces exceed the restoring forces due to surface tension. A critical Weber number We_c is associated to this limiting case and is discussed in the literature (Simpkins 1971). Within the present study, the droplets are immersed in their own vapour with no additional carrier gas. The question is whether the deformation and fragmentation changes its characteristics by the presence of strong condensation and evaporation.

Generally the break up of droplets is caused by forces of various character like the surface tension, windforces and shearing forces but in most cases it is not known which force causes which breack up mode. Basically we can assume that the process of break up depends on three causes: *i*) internal motions within the droplets, *ii*) external fluid motion around the droplets and *iii*) the properties of the interface. Like the case of droplet oscillation the different modes of particle break up were also discussed in several studies (Reinecke and Waldman 1975 and Hässler 1970). There are some data reported on break up of droplets in pure water vapour (Hässler 1970 and 1972). Schneider (1981 and 1982) found out, that when a droplet moves through its own vapour at saturation conditions, the drag of the droplet is influenced by phase transitions at the droplet surface. The aim of this investigation is to contribute new experimental information on deformation, fragmentation and drag behaviour for the droplet-in-vapour situation.

2. EXPERIMENTAL APPARATUS

The basic components of the experimental setup are a horizontal shock tube, a droplet generator and a double pulse ruby laser. The reconstruction system of the holograms uses a three-dimensional micropositioning device and an image processing system. These components are briefly described in the following.

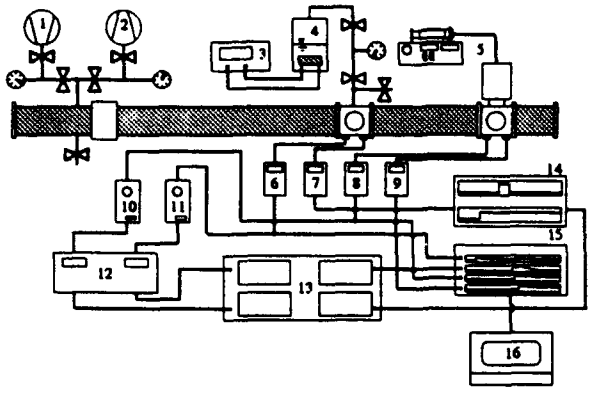

Figure 1: Experimental setup (1 compressor, 2 vacuum pump, 3 control of temperature, 4 destilled water vessel, 5 droplet generator, 6-9 charge amplifiers, 10-11 differential amplifiers, 12 trigger unit, 13 pulse laser control unit, 14-15 oscilloscopes, 16 PC)

2.1 Shock Tube

Figure 1 is a schematic diagram of the tube and the experimental arrangement. The tube has a length of 1043 cm and is made of stainless steel with a wall thickness of 1.2 cm and a circular crossection with an internal diameter of 10 cm. In all our experiments we used air as driver gas resulting in Mach numbers from 1.1 to Ma=2.0 for driver pressures between 100 mbar and 6 bar respectively. To produce shock waves of a controlled strength we used diaphragms made of commercially available cellophane having a thickness of 0.1 mm. In the case of small driver pressure around 100 mbar it was necessary to scratch slightly the cellophane film in order to create a controlled crack behaviour. To fill the test section with water vapour, the dump tank was separated from the test section by a thin 0.08mm cellophane film which would break up after shock passage. After evacuating the test section, vapour of 26 mbar at a room temperature of 22°C is filled, which means saturation conditions. The upper piezoelectric pressure transducer is used to trigger the pockels-cell of a ruby laser with a pulse duration of 20 ns. The flash lights are triggered independently about 1 ms before by an additional upstream piezo probe. The Mach number is determined directly by two piezo transducers located at the observation window. To avoid condensation at the surface of the piezo transducer (Luger 1990) after shock passage and in order to get good signals we placed a 0.2 mm silicone film over the probes.

2.2 Droplet Generator

The droplets are produced by a vibrating orifice aerosol generator (model TSI 3450). The vibration is provided by a bimorph transducer and the fluid flow of the liquid can be regulated separately. The wavelength λ of the disturbance represents the spacing between any two consecutive droplets. In Mulholland, Srivastava and Wendt (1988) it is shown that this spacing influences the value of the drag coefficient, but in our case this influence could be neglected as compared to the drag increase caused by droplet deformation. Destilled water was used to produce the uniformly sized droplets. Careful filtering of the water was necessary to remove suspended impurities which might obstruct the small pinhole apertures. A list of the theoretically possible droplet sizes is shown in the following table

orifice $[\mu m]$	$D_{p,min}[\mu m]$	$D_{p,max}[\mu m]$
10	17.380	21.898
20	34.760	43.795
35	60.830	76.642
50	86.901	109.488
100	173.801	218.976

It is not recommended to produce droplets with a size between the listed intervals because the droplet generator would not work stable and give nonuniform particles. The production of very small droplets required much effort. The pinhole had to be purified often and sometimes the whole apparatus had to be cleaned by using isopropanol. Droplets were introduced perpendicular to the flow axis into the shock tube. They were then exposed to the shock wave.

2.3 Holographic Camera and Reconstruction

Double pulse in line holography has been used to monitor the deformation and movement of water droplets. A ruby laser with a maximum pulse performance of 1J (TEM_{oo}-mode) and a pulse duration of 20 ns served as holographic camera. The wavelength of 694 nm has the advantage of being near the wavelength of the helium neon laser (λ = 633 nm) chosen for the reconstruction, because the main requirement for high resolution reconstruction is wavelength ratio as near to unity as possible to avoid chromatic aberrations. After several experiments we found that the optimal pulse energy is about 0.5 mJ. This was achieved by using several gray filters of different filter capacity placed after the exit of the laser beam. With a combination of a convex and a concave lenses the beam is expanded and parallelized. To obtain optimum hologram quality, special windows for the test section of

the shock tube were used. Background light was reduced by a red filter as well as by a shutter placed in front of the holographic plate. No additional optics between the droplets and the plate were used. All magnifications were done in the reconstruction unit since this leads (Rath, Wiegand, Winandy 1988) to better contrast results. The holograms were recorded on Agfa-Geveart 8E75 HD holographic plates and then developed with Refinal developer as amplitude holograms. The evaluation of the developed holograms is done with a three dimensional micropositioning device connected with an image processing system. The droplet shapes were examinated on a monitor in the undeformed (first laser pulse) as well in the deformed state (second laser pulse). The arrangement for the reconstruction is given in figure 2. A helium neon laser

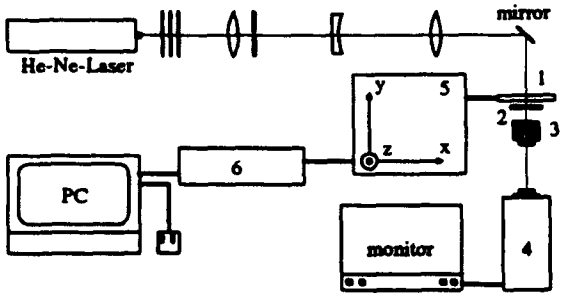

Figure 2: Reconstruction arrangement (1 hologram plate, 2 aperture, 3 objective, 4 videocamera, 5 micropositioning device, 6 control of the stepping motor)

is used as light source. The beam is spatially filtered. After passing the pinhole the beam is parallelized by using a combination of a concave and convex lenses. The light then passes the hologram plate and provides a real image behind and a virtual image of the droplets in front of the plate. The three dimensional micropositioning device allowed to move the hologram plate so that the real image is projected by means of an objective onto the target of a videocamera. The resulting image which is enlarged 200 times (depending on the distance of the objective and the videocamera) then allows the examination of the particle shapes. Even in in-line holography there are speckle-like distortions which have a not negligible intensity level. By means of a small aperture between the hologram plate and the objective it was possible to reduce these speckles. With the three dimensional micropositioning device it is possible to focus every droplet falling in the shock tube and store the spatial position they had at the moment of the laser pulses. The droplets do not maintain their depth coordinate (in laser beam direction) during their falling and acceleration. This was the main reason why we choose in line holography for visualising the particles instead of direct photography. Filters which were positioned before the pinhole served to optimize the contrast and brightness of the holograms.

3. CHARACTERISTICS OF THE SHOCK TUBE FLOW

The intepretation of our optical displacement data in terms of drag coefficient first requires a quantitative knowledge of the post-shock flow, especially its time dependence. In an ideal shock tube the distance between shock front and contact surfaces increases with distance from the diaphragm. In the real shock tube, however the wall boundary layer acts as a mass sink. This causes an acceleration of the contact surface and a deceleration of the shock front thus reducing the distance l below the ideal value. The separation will attain a limiting maximum value l_m. At this limiting condition the shock and contact front move with the same velocity. In the literature (Mirels 1966) a laminar and a turbulent boundary layer is treated. When a shock wave propagates through the nearly saturated vapour the passage of the front causes condensation at the wall of the shock tube. A thin liquid film is formed which acts like the wall boundary layer as a sink. This effect was investigated by Luger (1990). The theoretical description is analogous to the one by Mirels (1966). Let us consider a moving frame of reference in the limiting case moving with the velocity u_s of the shock front. By this way we can eliminate the time from all equations and instead of a transient problem we obtain a stationary description. In this shock stationary coordinate system the wall moves with the velocity u_s which equals the shock velocity in the laboratory system. The Mach number of the flow immediately behind the shock front is given by the equation (Mirels 1966)

$$M_{2s} = \sqrt{\frac{(\gamma-1)\,M_s^2+2}{2\gamma M_s^2-(\gamma-1)}} \qquad (1)$$

where M_s is the Mach number of the shock wave propagation. The advantage of the moving frame of reference is that the Mach number in the post shock region is expressed by the parameter l/l_m,

$$M_2 = \left[1-\left(\frac{l}{l_m}\right)^n\right] M_{2s}\left[\frac{2+(\gamma-1)\,M_2^2}{2+(\gamma-1)\,M_{2s}^2}\right]^{\frac{\gamma+1}{2(\gamma-1)}} \qquad (2)$$

where the parameter n is 1/2 for the laminar and 4/5 for the turbulent wall boundary layer. Luger (1990) found that $n = 1/2$ describes well the case of conden-

sation. He also showed, that the conventional boundary layer effects are negligible in comparison with the effects due to wall condensation. With a coordinate transformation $t = l/u_s$, it is possible to obtain the time dependence from the distance parameter l. This means, that in the laboratory frame of reference the gas will accelerate until it reaches the velocity of the shock front. In figure 3 a fit of the velocity behind the shock wave to the LDA data obtained from Luger (1990) is shown. Obviously the particle velocity ex-

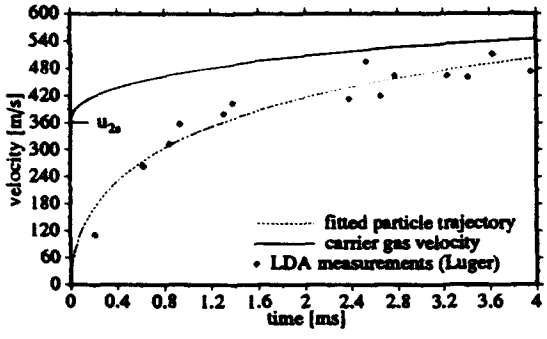

Figure 3: Post shock velocity fitted to LDA data, $M_s = 1.61$, $D_p = 20.3\mu m$

ceeds the velocity u_{2s} immediately behind the shock front. We establish a simple phenomenological description for the limiting case, which is quasi-stationary in the moving frame, but nonstationary in the reality. In figure 4 data of l_m dependig on the Mach number are shown for the wall condensation case. The turbulent

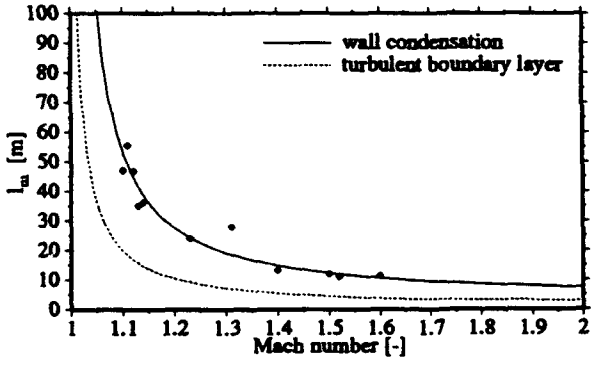

Figure 4: Limiting case parameter l_m in dependence on the Mach number

boundary layer case is plotted just for comparison, but turbulence can be excluded at our low Mach numbers.

In figure 5 resulting density, pressure and temperature profiles are listed. These variables of state are import-

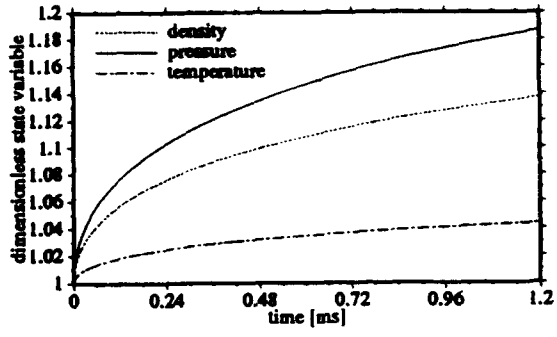

Figure 5: Dimensionless variables of state versus time in the post shock region, $M_s = 1.61$

ant for the calculation of the local Reynolds- and Weber numbers.

4. DRAG MEASUREMENTS

Many studies have been dedicated in the past to the drag coefficient of spheres in a fluid flow. In more recent work of Temkin, Kim (1980) and Luger (1990) on droplets the Weber number is kept low to exclude deformation effects. Temkin and Kim show that the forces on a sphere do not depend on the Reynolds number alone but the drag coefficient depends also on the relative acceleration between fluid and sphere. In an other study of Mulholland, Srivastava and Wendt (1988) the influence of droplet spacing on the drag coefficient is determined. In our investigation we assume that all these dependences are negligible when the Weber number is high enough. Our experiments were performend in an interval $3.6 \leq We \leq 39.2$. Temkin and Kim (1980) assumed $We = 0.15$ as the limiting value below which deformation is no longer significant. Although the test conditions of Reinecke and Waldman (1975) were different some similarities in the results were observed. In Reinecke and Waldman the experiments were performend in air with higher pressures and stronger shock wave velocities. As shown in figure 6 a plot of dimensionless displacement X and dimensionless time T has the same character in our case. X and T are defined as follows (Reinecke and Waldman)

$$X = \frac{x_p}{D_p} \qquad T = \frac{t u_{2s}}{D_p}\sqrt{\frac{\rho_{2s}}{\rho_l}} \qquad (3)$$

with x_p being the displacement, D_p the diameter and ρ_l the density of the particle. The density ρ_{2s} and

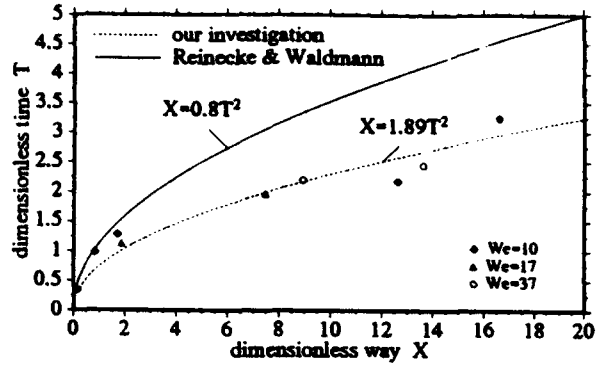

Figure 6: Dimensionless displacement data of the droplets

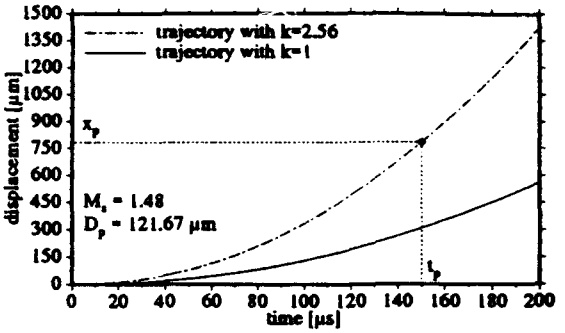

Figure 7: Particle trajectories for one experiment with various drag-coefficients

velocity u_{2s} describe the state just behind the shock front. The data of our investigation are lower than in the literature and this may be caused by deformation. The curve was fitted by least square method. Another possibility to get the x-t diagram of one particle is to solve the equation of motion of one droplet

$$m_p \frac{d\bar{u}_p}{dt} = \bar{F} \tag{4}$$

Here is m_p the mass of the droplet $m_p = (\pi/6)D_p^3\rho_l$, $\bar{u}_p$ the absolute velocity vector and $\bar{F}$ the vector of external forces (gravitation and wind force) which act on the particle. Since in our experiments the droplets and the surrounding fluid are in motion, it is convinient to use the relative velocity between fluid and particle. We obtain for the horizontal vector component the following equation of motion

$$\frac{du_p}{dt} = c_d \frac{3}{4}\frac{\rho_2}{\rho_l D_p}|\bar{u} - \bar{u}_p|(u - u_p) \tag{5}$$

$$\frac{dx_p}{dt} = u_p \tag{6}$$

We can see that the right hand side of this differential equation depends on the state in the post shock region characterized by the parameter l_m. To solve this equation of motion we assume a drag coefficient proportional to the standard drag. The standard drag coefficient is given by

$$c_{ds} = \frac{24}{Re}\left(1 + \frac{1}{6}Re^{\frac{2}{3}}\right) \tag{7}$$

where $Re = |\bar{u} - \bar{u}_p| D_p\rho_2/\eta$. As shown in figure 7 we fitted the parameter k of $c_d = kc_{ds}$ to the measured x_p-t_p point of our experiment. In our calculation we used within the relative velocity $|\bar{u} - \bar{u}_p|$ also a contribution resulting from the vertical exit velocity from the vibrating orifice

$$u_r = |\bar{u} - \bar{u}_p| = \sqrt{v_p^2 + (u_2 - u_p)^2} \tag{8}$$

$$v_p = \frac{2}{3}\frac{fD_p^3}{D_s^2} \tag{9}$$

where f is frequency of the vibrating orifice and D_s is the orifice diameter. Experiments show that the pressure of 26 mbar in the shock tube before shock passage didn't decelerate appreciably the vertical velocity of the particle. Figure 8 shows the dependence of the factor k on the Weber number. Like Luger (1990) we

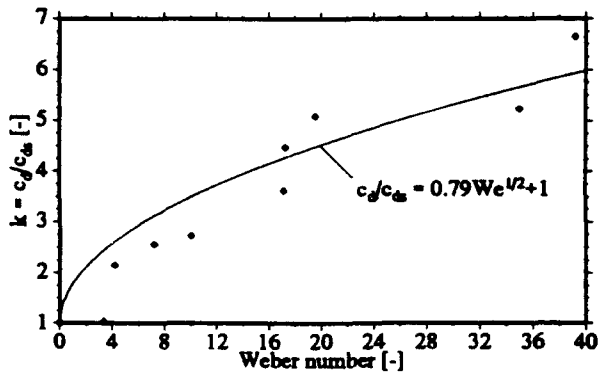

Figure 8: Dependence of the drag coefficient on the initial Weber number immediately behind the shock front

observed an increase of the drag coefficient with the Weber number. Figure 9 shows the Weber number and the Reynolds number during the shock passage. The relaxation zone of the post shock region is calculated

at any time. With the actual particle velocities the relative velocity can be calculated.

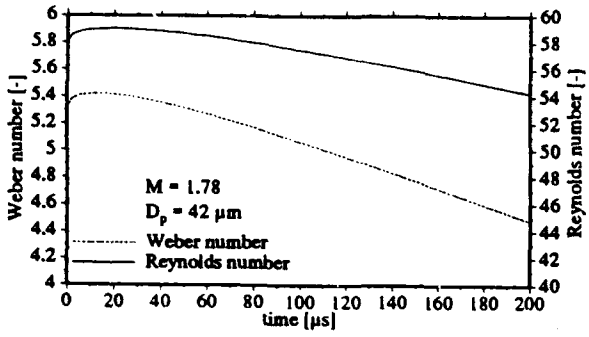

Figure 9: Reynolds- and Weber numbers in the post shock region

5. FRAGMENTATION AND DEFORMATION SHAPES

For our investigation we use water droplets which are surrounded with nearly saturated vapour. After shock passage however, the fluid is not in phase equilibrium. In our case the external fluid motion as well as the interface are affected by the presence of condensation of water vapour onto the droplets surface. This may be the cause why we found a different

Figure 10: Vibration of a $139\mu m$ drop at $We = 10.8$ and $57.2\mu s$ after shock passage. With double exposure technique the undeformed (left) as well as the deformed shape (right) are available. The shock wave travels from left to right.

deformation behaviour (Reinecke and Waldman 1975) as compared to water drops in air. The results of our studies cover a relatively wide range of Weber numbers ($3.6 \leq We \leq 39.2$) from the deformation threshold up to fragmentation. For the critical Weber number we found larger values as compared to other studies (Reinecke and Waldman 1990, Simpkins 1971, Hanson 1963). Figure 10 shows that even at a Weber number of 10.8 an oscillation without break up of the drop could be observed. The undeformed particle is also available by the double exposure technique used for these studies. For intermediate Weber numbers similar break up mechanisms as in Hässler (1970), Andersen (1965), Patel (1981) and Engel (1958) could be observed, although our droplets are much smaller in size. Figure

Figure 11: The bag break up of a $120\mu m$ drop begins $86.6\mu s$ after shock passage at $We = 15$

11, 12 and 13 show the classical bag break up which in our case occurs at Weber numbers around 15. This is slightly less then described in Reinecke and Waldman (1975), where the water drops are immersed in air and the bag break up is estimated for Weber numbers around 20. At higher Weber numbers ($We \approx 35$)

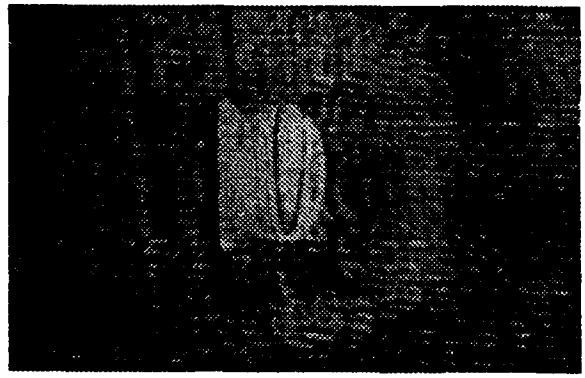

Figure 12: Bag break up of a $120\mu m$ drop at $95.4\mu s$ after shock passage at $We = 15$

complex movement of the whole droplet could be observed which is different from what one knows from the parachute-like shapes of droplets in air. The formation of long and fine whiskers from local surface

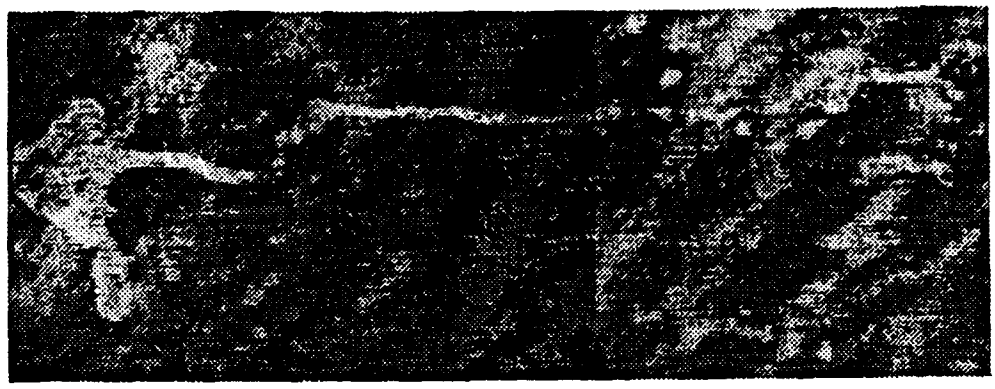

Figure 14: Formation of jet-instabilities on the surface of a 231.6μm water droplet at $We = 39.2$ and 161.2μs after shock passage

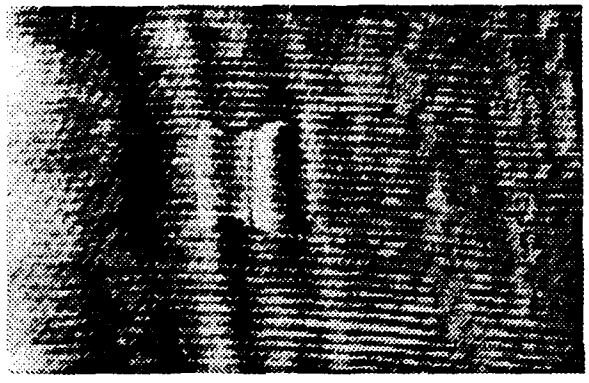

Figure 13: Bag break up of a 120μm drop at 104.2μs after shock passage at $We = 15$

Figure 15: Spiral forming jet-instability of a 115.8μm droplet at $We = 32.4$ and 148μs after shock passage

instabilities is very characteristic for this range of Weber numbers. These whiskers then break up into very small individual droplets. This means that we have found a kind of stripping mode, i.e. break up into droplets, which are very much smaller than the host droplet, but already at small Weber numbers (the classical stripping mode typically is at Weber numbers of 1000 as described in Reinecke and Waldman 1975). Figure 14 shows an example for this situation. In figure 15 the whisker forms a kind of spiral which means that the flow around the droplet is very complex. The double-exposure technique furthermore allowed to monitor the displacement of the droplets. This gives information on the total effective drag force in the case of strongly deformed droplets (see figure 8). Such information should be of relevance to many technical droplet-in-vapour flows. As could be expected the corresponding drag coefficient drastically differs from the standard drag curve.

6. CONCLUDING REMARKS

Our investigation shows that small water drops when accelerated by their own vapour show in some respect a different behaviour than do droplets in air. A fragmentation mode with spiral form jet-instabilities could be observed. It may be assumed that these jets are caused by complex interface motions in the presence of mass-exchange at thermodynamic states far from phase equilibrium. For lower Weber numbers we observed the same bag type break up as described in the literature for droplets in air. The deformation of droplets in their own vapour is also accompanied by an drastic increase of the drag coefficient.

ACKNOLEDGMENT

The authors are especially indebted to Peter Luger for the LDA data of the particle velocities he made available as well as to Stefan Dworak and Thorsten Wiegel for their enthousiastic cooparation.

REFERENCES

W.H. Andersen and H.E. Wolfe (1965), Aerodynamic breakup of liquid drops, Proccedings of the 5th Int. shock tube Symp., pp. 1145-1169

O.G. Engel (1958), Fragmentation of waterdrops in the zone behind an air shock, J. of Research of the National Bureau of Standards, Vol. 60, No.3, pp. 245-280

G. Hässler (1970), Break-up of large water drops under the influence of aerodynamic forces in a steady stream of steam at subsonic velocities, Proc. of the third Int. Conf. on Rain Erosion and related phenomena, Hampshire England

G. Hässler (1972), Untersuchungen zur Zerstörung von Wassertropfen durch aerodynamische Kräfte, Forsch. Ing.-Wes, Nr.6, pp. 183-192

A.R. Hanson, E.G. Domich and H.S. Adams (1963), Shock tube investigation of the breakup of drops by air blasts, The Physics of fluids, Vol. 6, pp. 1070-1080

P. Luger (1990), Experimentelle Untersuchungen zu Stoßwellen in einkomponetigen Zweiphasengemischen, PhD-Thesis, Universität der Bundeswehr

H. Mirels (1966), Flow nonuniformity in shock tubes operating at maximum test times, The physics of fluids, Vol. 9, Number 10, pp. 1907-1912

J.A. Mulholland, R.K. Srivastava, J.O.L. Wendt (1988), Influence of droplet spacing on drag coefficient in nonevaporating, monodisperse streams, AIAA Journal, Vol. 26, No. 10, pp. 1231-1237

P.D. Patel and T.G. Theofanous (1981), Hydrodynamic fragmentation of drops, J. Fluid Mech., Vol.103, pp. 207-223

K. Rath, H. Wiegand, A. Winandy (1988), Holographische Bestimmungen von Tröpfchenverteilungen, DFLR-Mitt. 88-05

W.G. Reinecke and G.D. Waldman (1975), Shock layer shattering of cloud drops in reentry flight, Aerospace Sciences Meeting, Pasadena Calif.

W. Schneider (1981), Drag of droplets moving through their own vapour, Part I, Continuum Flow, PCH Physico Chemical Hydrodynamics Vol. 2, No. 2/3, pp. 135-141

W. Schneider (1982), Drag of droplets moving through their own vapour, Part II, Free molecule flow, PCH Physico Chemical Hydrodynamics Vol. 3, No. 2, pp. 119-126

B. Schmitt-v. Schubert (1988), Kühlung eines Gases durch Tröpfchen- Verdampfung, Ingenieur-Archiv Vol. 58, pp. 205-214

P.G. Simpkins (1971), Non-linear response of deforming drops, Nature physical science, Vol. 233, pp. 31-33

S. Temkin and S.S. Kim (1980), Droplet motion induced by weak shock waves, J. Fluid Mech., vol 96, part1, pp 133-157

SINGLE PARTICLE OPERATIONS BY LDA-ASSISTED ELECTRODYNAMIC THERMOGRAVIMETRY

M. D'Amore(*), G. Donsi(*), P. Giordano(*), G. Raso(^)

* Dipartimento di Ingegneria Chimica e Alimentare,
Università di Salerno, Italy
^ Istituto Ricerche sulla Combustione,CNR - Dipartimento di Ingegneria Chimica,
Università di Napoli, Italy

keywords: laser-doppler anemometry, single particle, electrodynamic balance

ABSRACT

Absolute measurements in unit operations on single submilliliter particles are made possible by the application of Laser-Doppler anemometry to an electrodynamic balance. The flow field of the gas inside the hyperboloidal chamber of the balance is characterized. Cigarette smoke is used as a tracer. Gas velocity profiles are measured in the temperature range 293-620 K. A direct utilization of the results for measuring the absolute aerodynamic drag force exerted on a 48 μm spherical glass particle by a gas at any given velocity is shown.

1. INTRODUCTION AND PURPOSE

In the study of the treatment of solids or drops in conventional apparatuses some parameters are difficult to be properly taken into account. This specially occurs when analysing results from unit operations on populations of particles where heat and mass transfer interactions may hinder the interpretation of experimental data collected. For instance, in gas and vapour adsorption on solids, evolution of heat on sorption and cooling on desorption could result in a time-dipendent drift of sorption equilibria (Gregg and Sing, 1982)

The use of the electrodynamic balance as a tool for the analysis of momentum and mass transfer phenomena between gas and particles or drops has recently come up to the attention, as the balance is able to hold, by means of electric fields, a single particle suspended in space (Davis and Ray, 1980; Spijut et al., 1985, 1986, Cohen et al., 1987; Sageev Grader et al., 1987; Davis et al., 1987). By continuous determination of gas flow-rate and weight and size of the levitated particle, direct measurements of mass fluxes and evaluation of momentum and mass transfer coefficients are possible. As a simple application, the study of the drag force exerted on solid particles by a gas may be simply performed at any condition, since the particle can be indefinitely kept levitated inside the chamber. Measurements of drag forces in hot gas streams from chemical reactors or of mass transfer coefficients in the spray-drying of food are typical fields where new insights could be expected .

However, the peculiar configuration of the measuring cell does not allow for a prediction nor a simple evaluation of the local gas velocities. Moreover, no intrusive measurement techniques can be used, as they would influence the gas velocity profiles with respect to the tipical size of the suspended particles (less than 200 μm). As a matter of fact, indirect calibrations by standard solids have been used in the past works to estimate a cell constant somehow related to the gas velocities (Davis et al., 1987; d'Amore et al., 1988)

The laser-doppler anemometry in the special arrangement here adopted appears to be a valuable way to overcome the experimental difficulties and to characterize the flow field in the chamber, at the different operating conditions. This work aims at demonstrating that application of LDA to the electrodynamic balance leads to an unique experimental apparatus for studying heat, mass and momentum transfer mechanisms between particles and fluids.

2. EXPERIMENTAL

2.1 Apparatus

A schematic view of the whole experimental apparatus is shown in Fig. 1.

The electrodynamic chamber (Wuerker et al., 1959; Davis and Ray, 1980; Philip, 1981; Spijut, 1985) consists of three electrodes in an hyperboloidal configuration. The chamber creates a dynamic electric field capable of suspending a single, charged particle. The AC or ring electrode (6) provides lateral stability to the particle through an imposed AC field oscillating sinusoidally ±2000 volts at 100 Hz. The DC top and

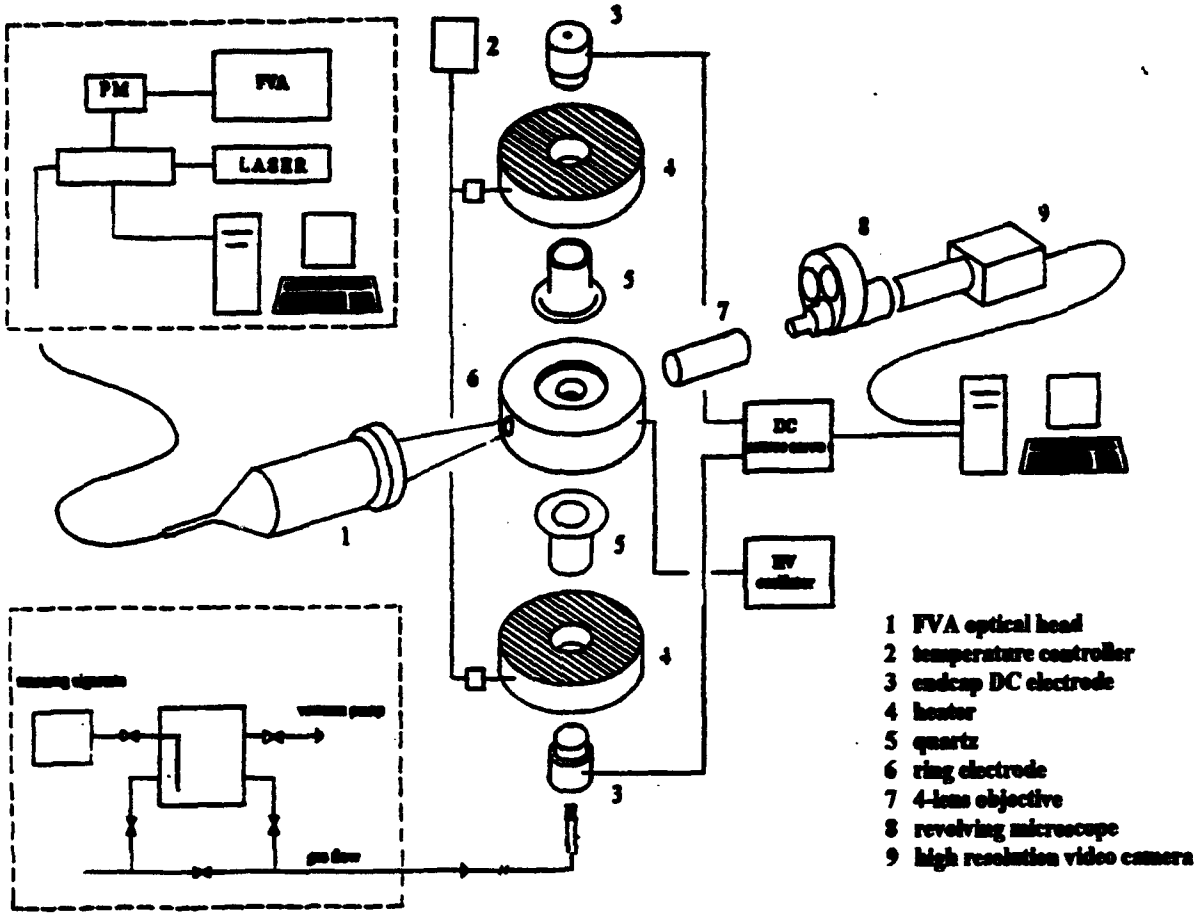

Fig. 1 - The experimental apparatus

bottom electrode (3) provide vertical stability by balancing the gravitational force, thus stably suspending the charged particle at the chamber center. The characteristic lenght of the balance used in this work is 4 mm, that means that the distance between the two DC electrodes is 8 mm and the internal diameter of the ring electrode is $8\sqrt{2}$mm (d'Amore et al., 1988). A section of the hyperboloidal chamber is reported in Fig. 2. Three couples of DC electrodes have been used in this work, having 5, 2.5 and 1.5 mm holes, respectively, drilled through for the gas flow path. A specially designed microscope (8), a videocamera (9) and an image processing system allow for sizing and position controlling of the levitated particle. The four-lenses objecive (7) provides a high magnification together with a great focal lenght (0.110 m), so as to have no lenses inserted in the ring electrode. The image of the suspended particle captured by the high resolution videocamera (9) is sent to a digitizer. A developed software for image analysis follows position, motion and size of the particle, and keeps center by a PID controller acting on the DC supply. Mass flow controllers, and special electrical heaters (4) coupled by a temperature controller (2) make possible to operate the balance in controlled atmosphera.

An Ar-ion laser (Coherent, Innova 90, 4W nominal power) coupled to an optical and electronic group (Dantec, Flow Velocity Analyser) is used for the laser-doppler anemometry (Fig. 1, Block 1). The measuring volume is obtained by intersection of two frequency-shifted laser beams, adducted to the electrodynamic balance center through a 2.5 mm hole drilled in the ring electrode. The beams are generated by an integrated optical units and brought to the apparatus by optical fibers (1). The scattered signal is acquired by the same device and then computer-processed through a dedicated software.

Cigarette smoke is used as a tracer. The smoke is generated by a smoking machine (Fig.1, Block 2)

consisting in a flask connected to a vacuum pump on one side and a cigarette holder on the other side. After the pump has evacuated the flask, the cigarette is connected and "smoked". Two-way electrovalves then change the path of the gas flowing to the balance, letting is pass through the flask. The smoke produced is conveyed to the measuring cell, and its tracing effect is satisfactory.

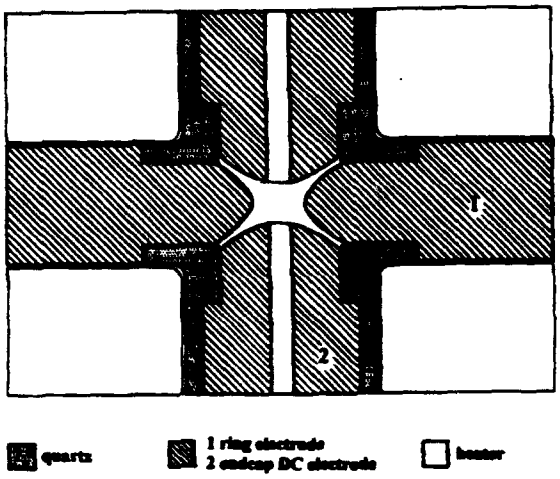

Fig. 2 - Section of the electrodynamic balance

2.2 Techniques

In the drag force runs, a particle is injected into the balance by a syringe. Particle charging by tribo or frictional electrification occurs naturally. Changes in the gas flow rate tend to move the particle from the chamber center, where electrical and gravity force are in equilibrium. The particle is brought back to the center by changing the DC voltage, i.e. the electrical force exerted on it. The new balancing voltage is then recorded and furtherly processed to obtain the aerodynamic drag force as a function of the gas flow rate.

After the smoke has been produced, a controlled gas flow rate is passed through the flask and then is adducted to the balance, for laser-doppler anemometry. A long calibrated tube ensures the fully development of the gas flow before the entrance in the hyperboloidal chamber. By means of microslides, the laser beams entering the chamber are aligned so as to have their intersection running on the horizontal simmetry plane of the hyperboloidal chamber. In a typical run the 650 μm measuring volume generated by the beams is brought twice back and forth along the chamber diameter. Measurement points are spaced 0.5 mm from each other. Gas velocity profiles along the chamber diameter have been measured at gas flow rate of 4.65, 9.30, 13.95, 18.60 cm^3/s and at gas temperature of 293, 400, 460 and 620 K for the three DC electrode couples indicated above. At each operating condition, measurements of the centerline gas velocity as a function of the gas flow rate, in the range 0-37.20 cm^3/s have been also performed.

3. RESULTS AND DISCUSSIONS

3.1 Aerodynamic drag force

A force balance on a particle in equilibrium in the chamber in absence of gas flow gives:

$$mg = qE \qquad (1)$$

where mg is the gravity force, q the charge on the particle, E the electric field strenght in a vertical upward direction. The electric field in the vertical direction in an electrodynamic balance is

$$E = CV_1/z_0 \qquad (2)$$

where V_1 is the DC voltage across the vertical electrodes required to balance the levitated particle, C the chamber constant, and z_0 the characteristic lenght of the chamber. In presence of a gas flow from downward direction, the force balance modifies as follows:

$$mg = F_d + qCV_2/z_0 \qquad (3)$$

where F_d is the aerodynamic drag force acting in vertical direction, and V_2 is the new balancing voltage. By combining eqs. (1), (2) and (3) it is obtained :

$$\frac{F_d}{mg} = \frac{V_2 - V_1}{V_1} \qquad (4)$$

if the Reynolds number is far less than 1, Stokes's law holds, and the drag force can be expressed as

$$F_d = 3\pi d\mu v, \qquad (5)$$

where μ is the gas viscosity, d the particle diameter and v is the gas velocity .

From equations above, one would expect a linear relationship between the quantity F_d/mg, i.e. the fractional virtual weight reduction of the particle, and the gas velocity, i.e the gas flow rate for a given section. However, results reported in Fig. 3 for a 48 um spherical glass particle show a relati far from being linear.

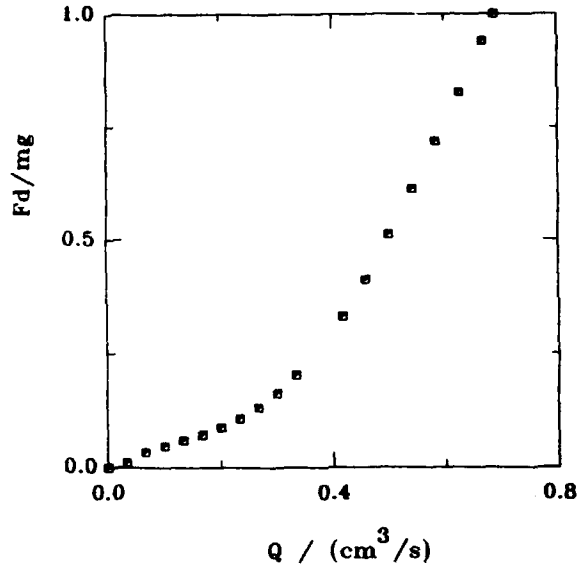

Fig. 3- Normalized aerodynamic drag force as a function of the gas fow rate.
Particle diameter = 48 μm.
Temperature run = 300 K

3.1 Laser doppler anemometry

Figure 4 reports the gas velocity profiles along a chamber diameter measured by laser-doppler anemometry at four different gas flow rates. The hole in the DC electrodes is 5mm. Before any analysis, a mass balance has been done on the gas flow to check the reliability of the gas velocity values measured. If v(r) is the gas velocity at a given chamber radius r, and R is the chamber radius, then:

$$Q_c = \int_0^R v(r) r dr \qquad (6)$$

where Q_c is the gas flow rate calculated by means of the laser doppler anemometry results. The difference beteween the calculated values, and the measured gas flow rates fed to the chamber have been found in the order of 2-3 %.

Curvature of the profiles at the axis of the balance, where particles are suspended, is such that the profile can be considered flat with respect to the particle size. The inflection points shown by the curves indicate that a simple laminar flow assumption does not apply in this case, in spite of the very low Reynolds numbers. Moreover, the strong decrease of the gas velocity near the ring electrode walls suggests that a gas recirculation could occur at higher flow rates. This would mean a more than linear increase of the centerline gas velocity for an increasing flow rate.

Figure 5 reports the gas velocity profile obtained with a DC electrode couple with a 2.5 mm hole, at a gas flow rate of 13.95 cm^3/s.

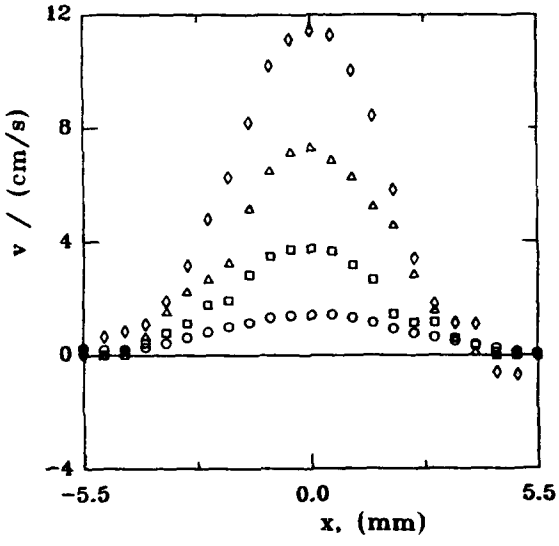

Fig. 4 - Gas velocity profiles at various flow rates
Hole diameter in the DC electrode: 5mm
○ Q = 4.65 cm^3/s; □ = 9.30
Δ = 13.95 ◊ = 18.60

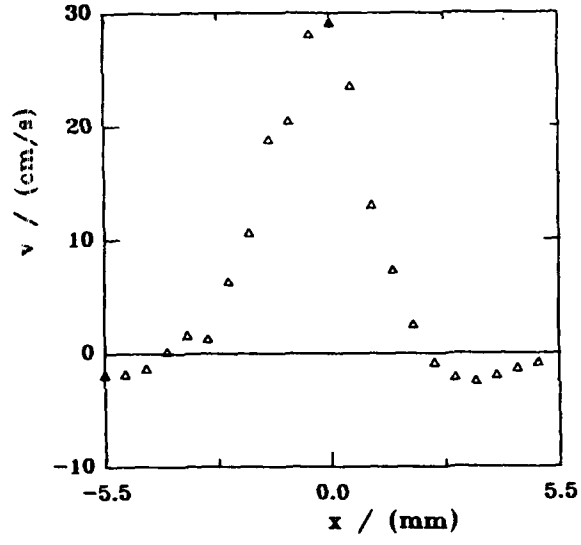

Fig. 5 - Gas velocity profile at flow rate Q = 13.95 cm^3/s
Hole diameter in the DC electrode: 2.5mm

As the gas outlet section at the bottom DC electrode is 4-times smaller than the one of the previous runs (Fig. 4), the gas enter the chamber at a higher velocity. The gas recirculation above mentioned is now more evident. It has to be pointed out the greater significance of the mass balance verification by eq. (6), since the tremendous increase in the downward flow rate. Note that the greater the radius, the higher is the section available for the gas flow. A trivial approach to the fluid dynamics inside the hyperboloidal chamber could be to figure it out as a boundary-layer flow in a channel with small angle of divergence (Schlichting, 1979). The condition for the avoidance of back flow at the wall in a divergent tube of radius R(z) was found to be $dR/dz < 12/R_e$, where R_e is the Reynolds number referred to the mean velocity of flow through the channel an to its diameter. The condition above is verified for the runs in Fig. 4, whereas it does not hold for the run reported in Fig. 5. As a matter of fact the figure does show a fully developed back flow .

Figure 6 shows the gas velocity profiles measured in hot conditions, being the temperature profiles along the vertical axis of the whole balance very flat.

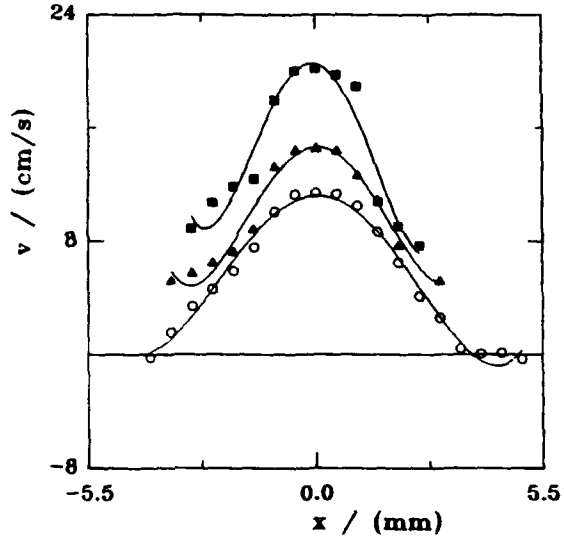

Fig. 6 - Gas velocity profiles at various temperatures
Gas flow rate Q = 18.60 cm^3/s; Hole diameter in the DC electrode: 5mm
O T = 300 K; Δ = 390 K; ■ = 620 K

The centerline velocity increases more than expected, suggesting that back flow at the chamber walls may play a major role under those experimental conditions.

The centerline velocities measured in cold conditions with a 5 mm hole in the DC electrode are reported as a function of the gas flow rate in Fig. 7. The non linear relationship shown in the curve confirms the indications above that a distortion in the velocity profiles holds when flow rate increases .

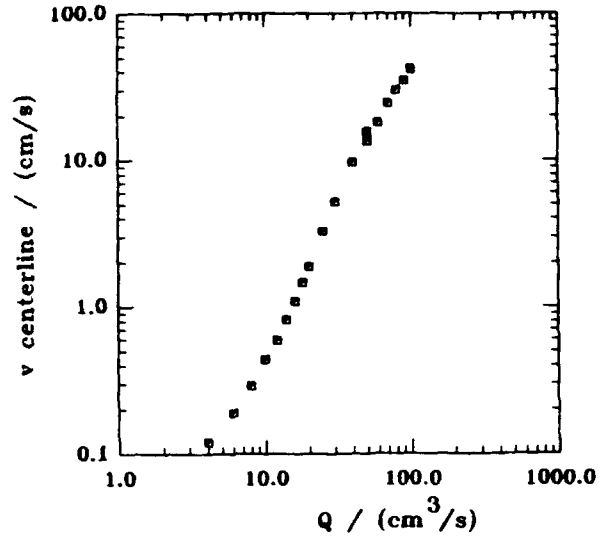

Fig. 7 Centerline gas velocity as a function of gas flow rate
. Hole diameter in the DC electrode = 5 mm
Temperature run = 300 K

Nevertheless, the knowledge of the gas velocity profiles inside the chamber allows to get rid of any complication of the fluid dynamics. A proof is in Fig. 8,

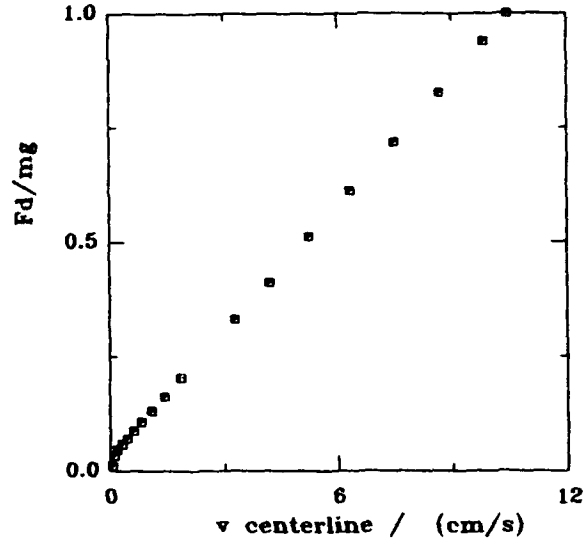

Fig. 8 - Normalized aerodynamic drag force as a function of the centerline gas velocity.
Particle diameter = 48 μm.

where the drag foce results, already reported in in Fig. 3, are now analysed in terms of the true absolute gas velocity at the chamber centerline. It can be seen that a linear relationship holds, as expected. Note that each point in the plot is representative of an experimental measurement at a given gas velocity.

4. CONCLUSIONS

The electrodynamic balance has already been used in the study of the unit operations in chemical engineering, for its special feature of being a sort of microreactor for single particle operations. However, a greater chance is offered by its coupling to the laser-doppler anemometry, as it may be now possible to gather absolute data for many parameters of interest in the unit operations on solid and liquid particles. The study of drag force on differently shaped particles, either at extremely low Reynolds number or far beyond the terminal velocity, where relationships found in literature suggest corrections to the drag coefficient (Clift et al, 1978), and in cold and hot conditions , and the analysis of the dependence of momentum and mass transfer coefficients on local velocity for different particle sizes are some of the promising applications of this LDA-assisted electrodynamic balance.

AKNOWLEDGMENTS

Authors are indebted to the Mr. G. Visconti for his help in designing and building up the special heating system. One of he Authors (M. d'A.) is grateful to dr. G. Caliano for his assistance in the final part of the work.

REFERENCES

Wuerker, R.F., Shelton, H. & Langmuir, R.V., 1959 J. Appl. Phys. 30,342

Schlichting H., 1979, Boundary Layer Theory, pp. 108-109, McGraw Hill, New York

Clift R., Grace, J.R. & Weber, M.E., 1979, Bubbles, Drops and Particles, Academic Press, New York

Davis, E.J. & Ray, A.K., 1980, Single Aerosol Particle Size and Mass Measurements Using an Electrodynamic Balance, J. Colloid Interface Sci., 75, pp. 566-575

Philip, M.A., 1981, M.S. Thesis, Mass. Inst. of Technology, Cambridge, Ma.

Gregg S.J. & Sing K.S.W., 1982, Adsorption Surface Area and Porosity, Academic Press, London

Spjut,R.E., Sarofim, A.F., & Longwell, J.P., 1985, Laser Heating and Particle Temperature Measurement in an Electrodynamic Balance, Langmuir, 1, pp.355-360

Spjut,R.E., Bar-Ziv, E., Sarofim, A.F., & Longwell, J.P., 1986, Electrodynamic Thrmogravimetric Analyser, Rev. Sci. Instrum., 57, 1604-1610

Davis J.E., Zhang, S.H., Fulton, J.H. & Perissamy R., 1987, Measurement of the Aerodynamic Drag Force on Single Aerosol Particles, Aerosol Sci and Techn., 6, pp. 273-287

Sageev Grader G., Arnold S., Flagan R.C. & Seinfeld J.H., 1987,Fourier Transform Infrared Spectroscopy of a Single Aerosol Particle , J. Chem. Phys., 86, pp. 5897-5903

Cohen, M.D., Flagan, R.C. & Seinfeld, J.H., 1987, Studies of Concentrated Electrolyte Solutions Using the Electrodynamic Balance, J. Phys. Chem., 17, pp 4565-4590

D'Amore, M., Dudek, D., Sarofim, A.F., & Longwell, J.P., 1988, Apparent Particle Density of a Fine Particle, Powder Techn., 56, 129-134

PHASE-DOPPLER ANEMOMETRY (PDA) A NEW TOOL FOR MONITORING THERMAL SPRAYING

R. Zeller, J. Domnick*, E. Schubert, H. W. Bergmann, F. Durst*

ATZ-EVUS, Rinostr.1, D-92249 Vilseck

* Lehrstuhl für Strömungsmechanik
Universität Erlangen-Nürnberg, Cauerstr.4, D-91058Erlangen

ABSTRACT

Thermal spraying is an expanding technology with growing markets. Especially the variety of plasma spraying techniques offers a number of possibilities for new and advanced applications. The spraying of sophisticated materials, the demand for generating coating structures or substrate/coating combinations with novel properties and the improvement of the spraying efficiency require a more detailed understanding of the physical and chemical reactions inside the plasma, in order to achieve an appropriate process control. The present paper demonstrates that phase-Doppler anemometry (PDA) is applicable as a powerful tool for process diagnostics in plasma spraying. Yielding simultaneous measurements of particle size and velocity at discrete locations, the PDA-technique generates new possibilities to characterize and further improve the spraying process.

1. INTRODUCTION

Thermal Spraying is a multitask coating process in modern surface technology. Plasma spraying, initially developed for the aerospace industry, is one of the youngest but also most universal thermal spray processes *(Busse, 1988)*. The heat source for the processing of materials with high melting points (oxide ceramics, carbides, borides, nitrides, silicides) is a plasma jet, exceeding temperatures between 6000 K and 20 000 K. However, also low melting materials could be sprayed with this technique achieving high deposition rates *(Lugscheider et al. 1991)*. The plasma gun consists mainly of two electrodes. A rod shaped tungsten cathode is located inside a coaxial copper ring anode. A high frequency ignition forms an arc between the electrodes. By excitation, dissociation and ionization of the fluidizing gas between the electrodes a 4-5 cm long plasma free jet is generated, exiting the nozzle at very high velocities. Applicable gases are Nitrogen, Argon, Helium and Hydrogen, and also mixtures of two or more of these gases. The gun parts are water cooled to sustain the high operation temperatures and to avoid melting of the electrodes. Particles are injected into the plasma jet, heated up, accelerated towards the substrate and finally deposited forming a functional layer *(Herman, 1988)*. Many experimental efforts have been made to characterize the spraying process in order to achieve a better understanding of the governing parameters. However, due to the extreme conditions inside the plasma jet (temperature approx. 10 000 K, gas velocity between 300-600 m/s) only a few techniques are applicable. Temperature measurements with spectroscopy or enthalpy probes are common techniques *(Pfender & Spores, 1987)*, yielding an overall impression of the temperature distribution. For locally resolved measurements of the velocity field, laser-Doppler anemometry (LDA) has been used recently *(Mayr et al. 1993, Fouchais et al. 1992)*. Based on experimental results many attempts have been made to simulate the spraying process *(Pfender & Chyou 1989)*. Nevertheless, at the current state these models cannot deliver a detailed description of the process because of too many simplifications necessary for modelling *(Joshi 1992)*. On the other hand great efforts have been made to save expensive powders forming functional layers by an adequate process control. Up to this point all control mechanism are based on the same principle, keeping the machine setting constant and assuming that there is no change in the spray process or in the layer quality. Certainly, this is not satisfactory, but due to the complexity of the interacting parameters no successful on-line control is available at the moment. The use of the PDA-technique may be a big step towards an improvement of this situation.

2. TEST RIG

The plasma spray facility used in this investigation consisted of a METCO 9MB watercooled air plasma

spray gun facility with power supply and control unit for the mixing of the plasma gases. The spray gun and a 4-axis ISEL traversing system were mounted in a sound proof chamber. The powder feeder was a METCO 4 MP type. Typical machine operation parameters are given in table 1.

Parameter	Argon	Hydrogen	Current
Range	30-80 l/min	1-10 l/min	300-500 A
Parameter	Voltage	Powder feed rate	Carrier gas
Range	56-80 V	5-50 g/min	1-10 l/min

Table 1: Range of variable gun settings

3. EXPERIMENTAL SET-UP

In order to obtain a rough idea of the flow field downstream the nozzle exit, thermal imaging for different spray conditions was performed. Using an infrared thermo-camera (Hörotron Infravision 500), positioned perpendicular to the spray cone at a distance of 1 m, the interesting regions of the particle stream were visualised. The position of the camera was arranged in such a way that the tip of the flame operating without powder was just at the edge of the monitor. This arrangement was necessary because the core of the plume was too bright for the selected filter combination. The camera was operated in a temperature window from 1273 K - 2273 K. The intensity reduction was achieved by using specific grey filters. This setting was appropriate for most of the powders, since only a few ceramic powders have melting points exceeding a temperature of 2273 K. Preliminary measurements of the particle velocities were made using an INVENT DFLDA laser-diode based fibre optics system, operating at 6 MHz shift frequency. The backscatter transmitting probe was equipped with a 250 mm focal length lens, yielding a probe volume with a diameter of 200 µm and a length of approx. 2 mm. For the PDA measurements, this transmitting system was completed with an INVENT PDE 2 detector receiving unit. The receiver focal length was 310 mm. Since the investigated metal particles are highly absorbing, PDA measurements could be made with scattered light based on reflection. A scattering angle of 55° was chosen, yielding a reasonable scattering intensity at the particle sizes investigated. Through this arrangement, a final size range of 3 - 160 µm was achieved. The obtained Doppler signals were filtered by an INVENT PDE filterbank and further evaluated with a QSP PDA 100 FFT processing system, yielding a frequency bandwidth of 50 MHz. Fig. 1 gives a schematic illustration of the experimental set-up in combination with the plasma spray gun. The measurement location of the LDA and the PDA was moved by traversing the gun, leaving the optical arrangement fixed. The investigated powders were a CuSn 6 bronze and a CrNi-powder. A typical SEM image of the bronze powder with a size range of 0-63 µm in solidified state is given in fig.2. Clearly, the overall shape of the particles appears to be spherical, nevertheless some slight ellipsoids may also be recognized. The surface has a certain roughness, which might disappear when the particles are molten. Also, the collectives of small and large droplets could be destroyed inside the plasma flame. As mentioned above, scattered light from reflection was used for the PDA measurements without any noticeable problems. The mean vaidation rate in the measurements was more than 90 %.

4. PRELIMINARY INVESTIGATIONS

Fig. 3 shows an example of images taken by the thermo camera for 4 different sets of spraying parameter. The picture mainly visualizes the temperature field generated by the heated and accelerated particles, thereby indicating also regions with high and low particle number density. Without going too much into details, it should be noted that the particle stream splits into two separate jets beginning at approximately 100 mm downstream the plasma gun. According to Pfender (1987) this is a region with highly turbulent gas flow, influencing heavily the final properties of the layer. The observation of separate jets is also confirmed by first LDA measurement. Fig. 4 exhibits the isotachs at 120 mm downstream the nozzle exit. In this diagram two distinct regions of high velocities can be detected. At these positions the mean velocity reaches maximum values around 145 m/s. Near the spray edge, a strong negative velocity gradient exiss, however, mean velocities at the outermost measurement points are still around 75 m/s. It should be noted, that the LDA measurements basically reflect the velocity of the particles, which might differ strongly from the gas velocity. Also, some size/velocity correlations were obtained in the PDA measurements. The results of the LDA measurements were used to identify interesting areas for the PDA measurements.

5. RESULTS

The PDA measurements were performed at the following operating conditions:

Gas flow rate	Ar 50 l/min	H_2 7 l/min
Powder feed rate	30 g/min	
Voltage	60 V	
Current	450 A	

Table 2: Settings of the plasma gun during the measurements

The measurements were made at an axial distance of 150 mm from the spray gun, which corresponds to the standard working distance between plasma gun and substrate. Therefore, the results indicate the properties of the particles when reaching the target. In order to limit the powder and process gas consumption and also to reduce the heating of the optical system, the measurement time was limited to 10 s at each point. Therefore, the number of samples taken varied between approximately 50 and 2500 according to the local number density of the particles. In a first set of measurements, two different particle fractions of the bronze powder, i.e. size distributions from 0-63 µm and 63-160 µm, were compared. The result of this comparison, which was made at an axial distance of 150 mm and 10 mm below the nominal centerline of the spray cone, is shown in fig. 5. Clearly, two distinct number weighted size distributions can be recognized with peak values around 25 and 125 µm. The obtained widths of the distributions compare very well with the nominal size ranges with only a few samples laying outside. From this result, it can be concluded that the PDA delivers the size of the bronze particles inside the plasma jet to a high degree of reliability. In fig. 6 the measured number distributions for the powder fraction from 63-160 µm are shown for different y-positions at an axial distance of 150 mm. These measurements were taken at x = 0.0 mm, i.e. on the vertical line of symmetry. It is evident that the percentage of large particles at the right hand side of the size distribution is increasing with decreasing y-position, i.e. below the centerline of the spray. This can be explained by gravity effects, which influence the trajectories of the different particle sizes. The separation of the particle size classes is also indicated by the mean values given in table 3.

y (mm)	d_{10} (µm)	d_{30} (µm)	u_{mean} (m/s)
0	97.7	113.0	37.3
-5	105.6	117.4	49.6
-10	120.1	123.7	74.5
-15	118.3	121.4	70.8

Table 3: Mean values at x = 0.0 mm, powder 63-160 µm

The velocities at these locations are relatively low, which is due to an asymmetric shape of the spray cone, as will be discussed later. In fig. 7, the mean velocities are given as a function of the particle sizes, indicating a strong positive correlation between size and velocity. Obviously, 150 mm downstream the spray gun the gas flow has already decelerated with the smaller particles being able to follow this axial velocity gradient. On the other hand larger particles still keep their initial velocity. This behaviour will strongly influence the residence time of different particle sizes inside the plasma flame and, hence, the properties of the particles in terms of temperature and state when reaching the substrate. To examine a region of high mean velocities obtained in the LDA measurements, a grid of 25 measurement points was arranged at 150 mm axial distance. These points were distributed in one quarter of the spray cone below the horizontal line of symmetry, i.e. at negative y-coordinates. The measurements were made with bronze particles of a 0-63 µm size fraction. The result in terms of validated samples in 10 s is given in fig. 8. The maximum number of samples, and hence, the maximum particle number flux is obtained almost in the center of this region, strongly decreasing along x and along y. The maximum measured particle arrival rate with the PDA is approximately 200 1/s, which is in the order of the nominal arrival rate of 700 1/s, estimated from the powder feed rate, the volume mean diameter and the probe volume cross section, assuming a homogeneous number flux. The corresponding distribution of the arithmetic mean diameter d_{10} is shown in fig. 9. Basically, the mean diameter is increasing towards the vertical line of symmetry, reaching its maximum 15 mm below the centerline of the spray cone. Maximum arithmetic mean diameters are around 45 µm. The distribution of the volume mean diameter, which is not shown here, has a very similar shape. Surprisingly, the region of the highest number flux is not correlated with

any specific particle sizes. This is also true for the axial mean velocity exhibited in fig. 10. Here, a smoothly decreasing mean velocity can be obtained moving along the x-axis. Furthermore, the mean velocity is almost constant along the y-axis. This is in contrast to the results shown in fig. 7; however, it should be noted that the size ranges of the particles are completely different. In general, the measurements indicate a strong asymmetry of the spray cone. Most likely, this is the result of an asymmetric particle feeding system. Since the particles are injected into a region with extremely high mean velocities and velocity gradients, the formation of the spray is heavily sensitive to any disturbances in that region. It should be mentioned again, that the duration of the experiments and their spatial resolution had to be chosen as a compromise between the practical value of the results and the consumption of expensive plasma gases and powder.

6. SUMMARY AND OUTLOOK

The obtained results, although still having a preliminary character, strongly indicate the feasibility of using phase-Doppler anemometry as an appropriate measuring technique for the investigation of plasma sprays. Some major characteristics of the spray, i.e. a vertical separation of particles of different sizes due to gravity or the presence of positive size/velocity correlations have already been identified. One problem that was recognized during the measurements is the strong spatial variation of the particle number density. Low particle number density regions could lead to either long measurement durations with expensive gas and powder consumption or to significant reductions of the number of samples taken and, hence, to reductions of the statistical reliability. Also, it should be noted that the measurements presented herein were made with initially spherical metallic powders. If non-spherical particles are used, which do not melt completely inside the plasma flame, erroneous size measurement would occur. Further problems may appear, if particles of ceramic materials are used. Here, the optical properties necessary for the layout of a phase-Doppler system, i.e. the complex refractive index, have to be determined with great care. If measurements with reflected light are not feasible, the refractive index at the process temperatures of the particles has to be measured. Nevertheless, the use of the PDA-technique in plasma sprays could yield an improved understanding of the plasma spray process through detailed investigations of the gas-particle interactions inside the plasma flame. In the future, this knowledge might be used for the development of more sophisticated and more accurate simulation models. Futhermore, small and robust PDA-systems might become a tool for an on-line control of the spraying process, rather than just keeping the spray gun settings constant during operation.

REFERENCES

Busse, K.H.,(1988), Thermisches Spritzen Moderne Oberflächentechnik, Oberfläche, vol.9, pp 30-39

Lugscheider,E., Eschnauer, H., Müller,U., Weber, T., (1991), Quo Vadis, Thermal Spray Technology, Powder Metallurgy International, vol.25, no.1, pp18-20

Herman, H. , (1988), Plasma Sprayed Coatings, Scientific American, no.9, pp.78-81

Pfender, E., Spores R., (1987), Flow Structure of a turbulent Thermal Plasma Jet, Surface and Coating Technology, Vol.37, pp.251-270

Mayr, W., Landes, K., Reusch, A., (1993), Untersuchungen des Partikelverhaltens im Spritzstrahl mittels Laser-Doppler-Anemometrie, Proc. Thermal Spray Conference TS93 Aachen, pp.143-147

Fauchais, P., Coudert,J.F., Vardelle, M., Denoirjean, A., (1992), Diagnostics of Thermal Spraying Plasma Jets, Journal of Thermal Spray Technology, vol.1, pp.117-127

Chyou, Y.P., Pfender, E., (1989), Modeling of Plasma Jets with Superimposed Vortex Flow, Plasma Chemistry and Plasma Processing, vol. 9,no. 2, pp. 291-328

Joshi S.V., (1992), A Prediction Model to Assist Plasma and HVOF Spraying, Materials Letters, vol. 14, pp. 31-36

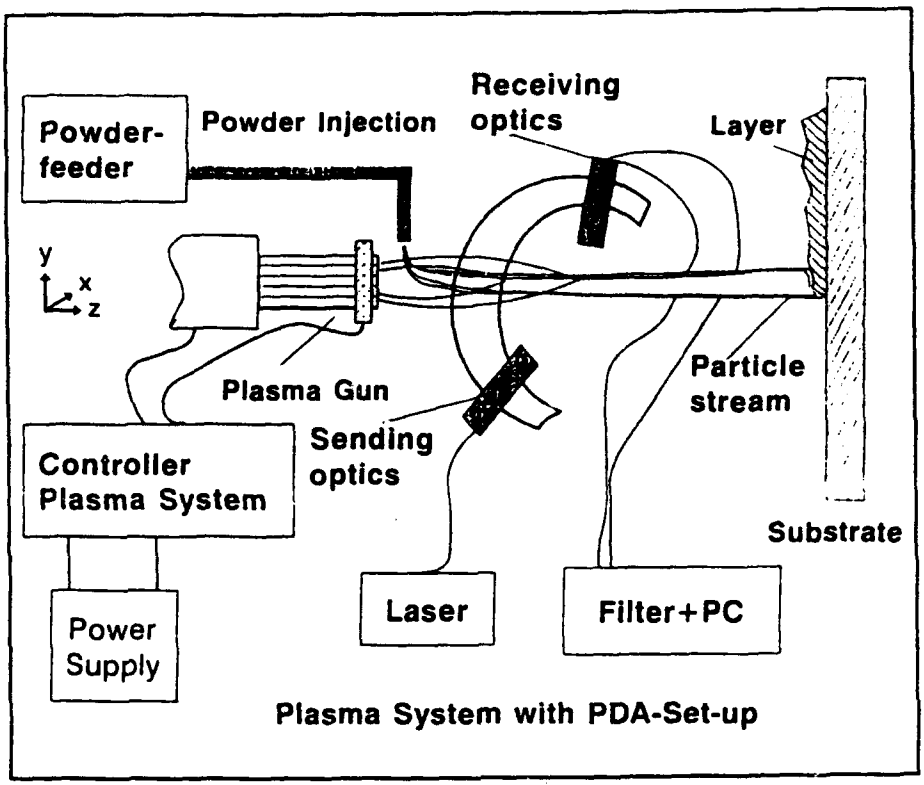

Fig.1: Schematic of the experimental set-up

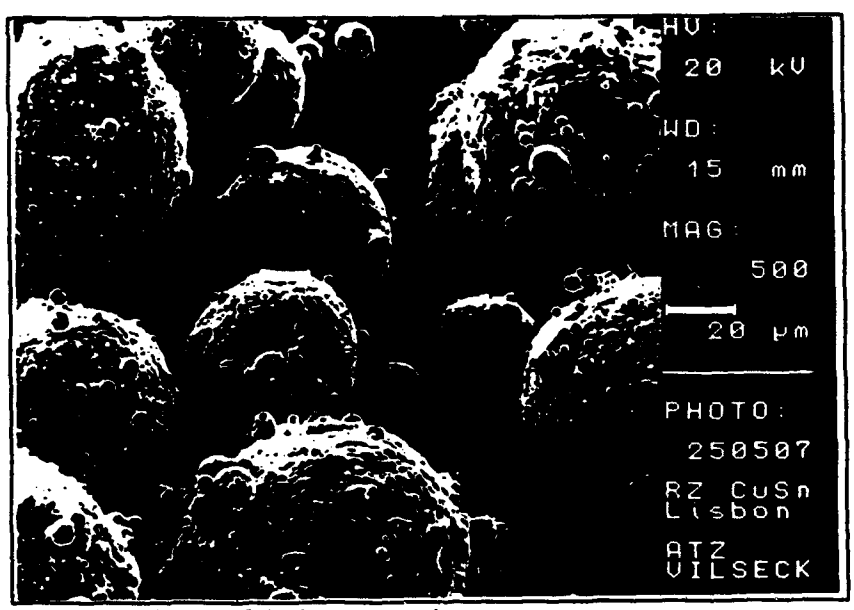

Fig. 2: SEM-image of the bronze powder

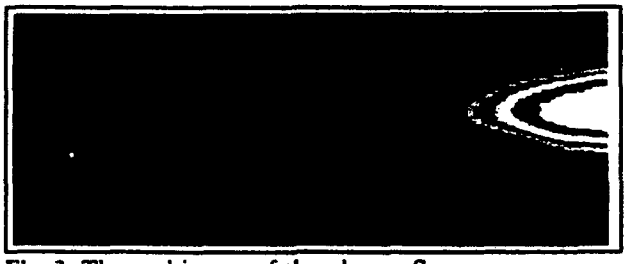

Fig. 3: Thermal image of the plasma flame

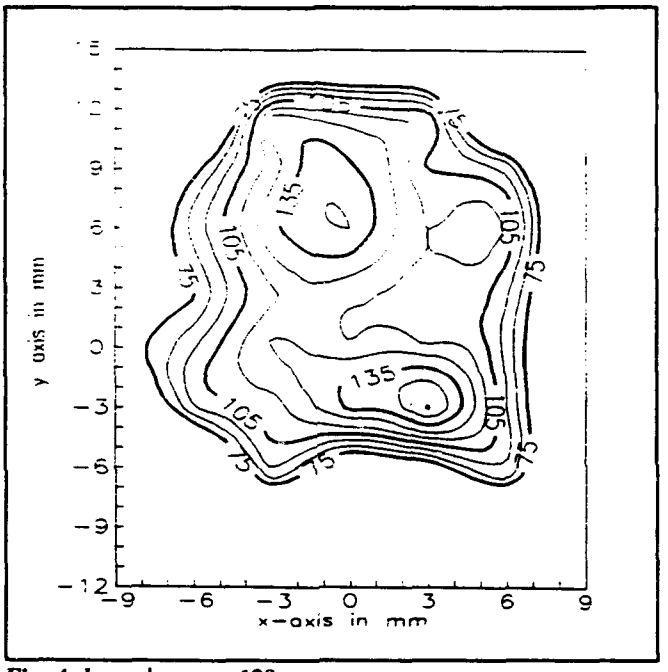

Fig. 4: Isotachs at $z = 120$ mm

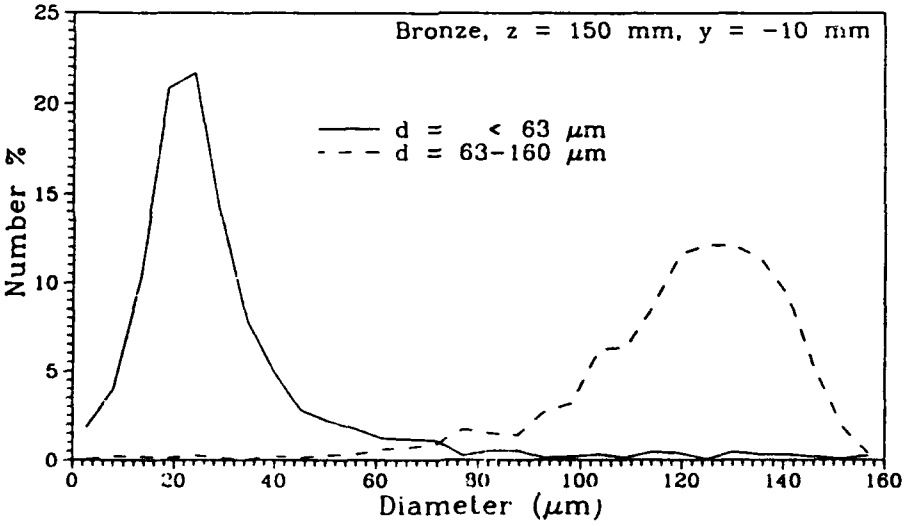

Fig. 5: Comparison of measured size distributions of two different powders

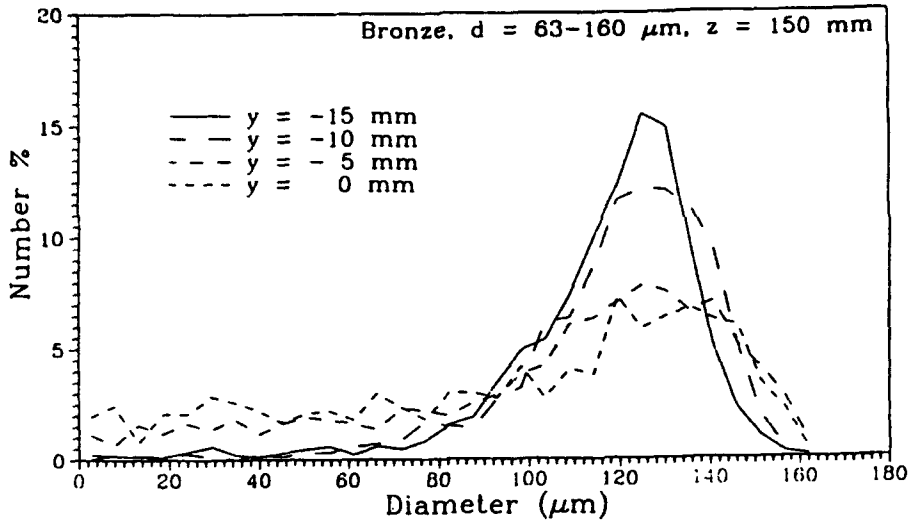

Fig. 6: Size distributions at different vertical positions at z = 150 mm

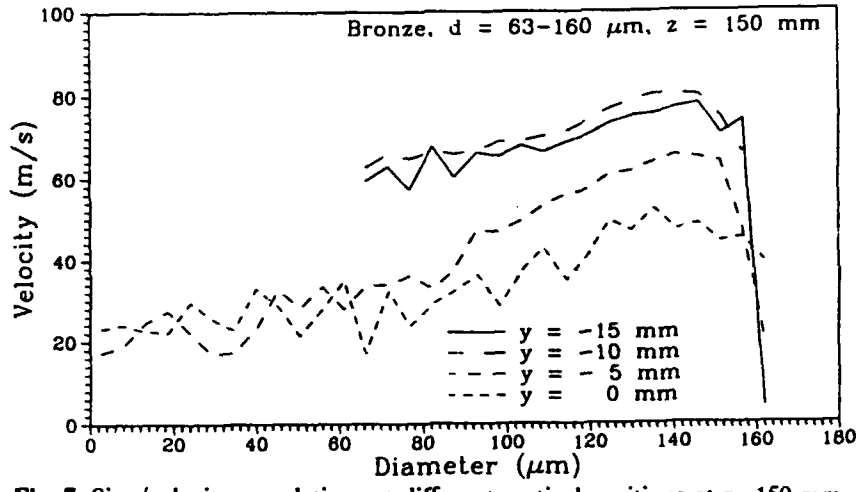

Fig. 7: Size/velocity correlations at different vertical positions at z = 150 mm

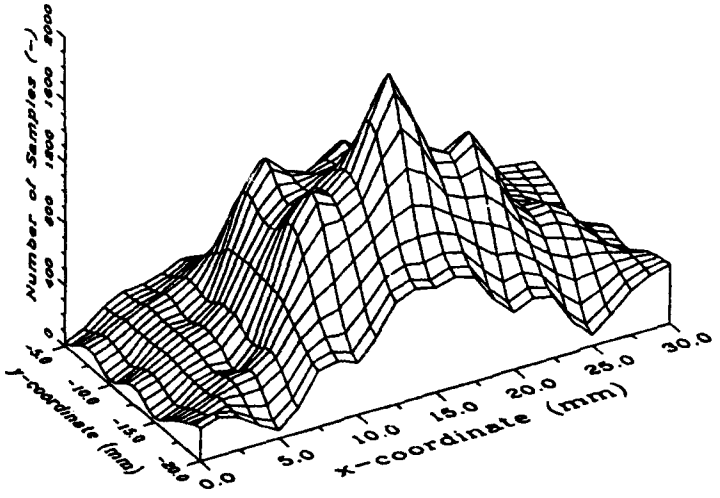

Fig. 8: Distribution of the number of samples at z = 150 mm (d = 0-63 μm)

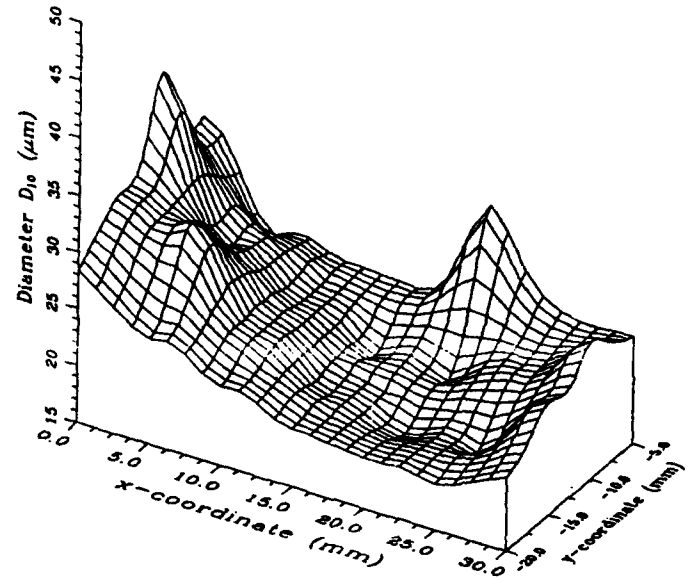

Fig. 9: Distribution of the arithmetic mean diameter at z = 150 mm (d = 0-63 µm)

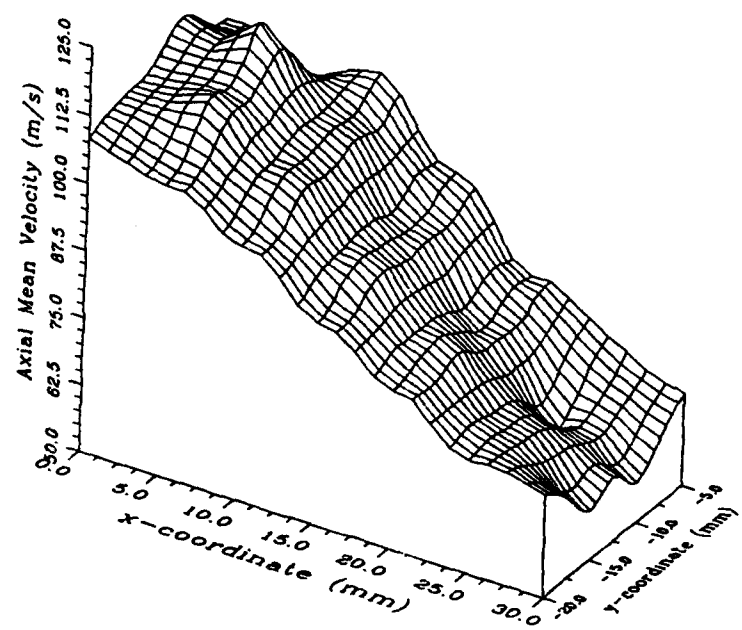

Fig. 10: Distribution of the axial mean velocity at z = 150 mm (d = 0-63 µm)

Session 35.
PIV & PTV Signal Processing

A Fast Data Acquisition System for Digital PIV

application to fully-developed and transitional turbulent pipe flow

J. Westerweel, A.A. Draad, J.G.Th. van der Hoeven & J. van Oord

Laboratory for Aero & Hydrodynamics
Delft University of Technology
Rotterdamseweg 145, 2628 AL Delft, the Netherlands

Abstract

A new and unique image acquisition system was built for measurements with digital particle image velocimetry (DPIV) in turbulent flows. The system can record sequences of 1016×1000-pixel images at a rate of 10 images per second with a total real-time storage capacity of 256 MB. The system is used in two experiments: (1) the measurement of fully-developed turbulent flow, and (2) the measurement of the transition from laminar to turbulent flow. The results for the fully developed flow are compared with those from a direct numerical simulation and with those from a conventional PIV measurement. We conclude from these data that the level of accuracy for DPIV is comparable to that of conventional PIV, while the image analysis in DPIV is completed in a fraction of the time needed in conventional PIV.

1 Introduction

One of the most challenging applications of particle image velocimetry (PIV) is the measurement of turbulence. For example, the measurement in a turbulent channel flow or pipe flow may require an image size large enough to include the flow from wall to wall with a resolution that is sufficient to resolve the small-scale motions. In addition the measurement error needs to be small enough in order to measure the small velocity fluctuations near the centerline and close to the boundary. And finally, as was pointed out by Westerweel *et al.* (1991), the investigation of turbulent flows with PIV will require the analysis of large numbers of images, e.g. to determine the flow statistics or to investigate the dynamics of coherent flow structures from image sequences.

Conventionally, PIV images are recorded on photographic film, and the negatives are then analyzed by computing the spatial correlation in small interrogation images — of typically 256×256 pixels — with a yield between 1,000 and 10,000 interrogations per negative. This approach is inherently slow, and therefore unsuited to deal with the large amount of images anticipated for measurements in turbulent flows.

An alternative approach — referred to as *digital* particle image velocimetry (DPIV) — was suggested simultaneously by Willert & Gharib (1991) and by Westerweel *et al.* (1991): they proposed to recorde the images directly with a CCD camera, and to interrogate the images digitally in small 32×32-pixel sub-images. Hence, DPIV effectively avoids any overhead for the processing of photographic film and the mechanical translation of the negative along the interrogation optics. In addition, the reduction of the number of pixels in the computation of the spatial correlation from 256×256 to 32×32 pixels reduces the total analysis time of a single image from 1-2 hours to less than 30 seconds.

One may expect that the reduction from 256×256 to 32×32 pixels affects the accuracy. This is true when the centroid of the displacement-correlation peak is determined with the conventional center-of-mass estimator (Prasad *et al.* 1992). However, Willert & Gharib (1991) found that the estimation error at low pixel resolution can be reduced considerably by using a Gaussian peak-fit estimator. Recently, Westerweel (1993a,1993b) demonstrated that the estimates for the spatial correlation are correlated over an area proportional to the particle-image diameter. This implies that the information content of the estimated displacement-correlation peak does not improve above a resolution of 32×32 pixels. Thus, the analysis with only 32×32 pixels yields by principle the same accuracy as with 256×256 pixels.[1] Therefore, it should be possible for DPIV to reach the same level of accuracy as conventional PIV.

So far, DPIV has mainly been applied to low-speed flows for which the standard NTSC/PAL video format provides adequate spatial and temporal resolution (see e.g. Westerweel *et al.* 1991; Willert & Gharib 1991). With this type of equipment one can only take DPIV measurements of turbulence in a relatively small area of the flow (Van der Hoeven *et al.* 1992). To carry out DPIV measurements that include a substantial area of the flow we need to use high-resolution CCD cameras that also have high frame rates; this requires a fast image acquisition system with a high bandwidth. In order to accommodate a large number of images it should also be equipped with a large real-time storage capacity. It was decided to design and to build an image acquisition system for DPIV — based on existing specialized hardware — for the purpose of turbulence measurements. A description of this system is given in Section 2.

[1] Provided that we use an optimally efficient estimator for the given pixel resolution.

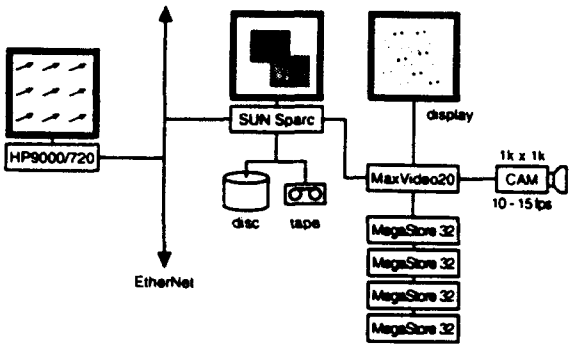

Figure 1: Schematic diagram of the image acquisition system.

To illustrate the capabilities of this new and unique system we present in this paper the results of two pilot experiments: (1) the measurement of fully-developed turbulent pipe flow, and (2) the measurement of the transition from laminar pipe flow to turbulent pipe flow. Both experiments were carried out in the same water flow facility. A description of this facility and of the relevant experimental parameters will be given in Section 3; the results are discussed in Section 4.

The measurement of fully-developed turbulent flow matches the flow conditions in an extensive study of turbulent pipe flow by Eggels *et al.* (1994) that included both numerical simulations and experiments. We will compare our present results with two contributions to this joint study: the direct numerical simulation (DNS) by Eggels *et al.* (1993) and the PIV measurements by Westerweel *et al.* (1993). In addition to these data we will also compare our results with those by Tahitu (1994), who carried out measurements with laser-Doppler anemometry (LDA) in the same flow facility and at the same flow condition as our DPIV measurements.

2 The image acquisition system

The image acquisition system is equipped with two cameras. For the measurements presented in this paper we used one camera; the second camera is intended to be used in future applications. For example, a two-camera system can be used for stereoscopic or two-color imaging. A schematic of the system is shown in Figure 1.

The heart of the image acquisition system is a pair of two MaxVideo-20 (DataCube) pipeline processors. Each processor is equipped with four MegaStore-32 memory boards, which yields a total real-time storage capacity of 256 MB. The pipeline processors are capable of digitizing, recording and processing images at a data rate of 26 MHz with 8-bit resolution. (For comparison: the bandwidth of standard NTSC-video is 8 MHz.)

Each processor board connects to a CCD camera (Texas Instruments). The CCD array consists of 1000×1016 square pixels, with a 100% fill ratio. The maximum frame rate of the cameras is 15 Hz. However, under full external control (i.e. for the timing of the exposure and for image read-out) the frame rate reduces to 10 Hz. The frame timing and pixel clock for image read-out are supplied by the MaxVideo-20 boards. The cameras are equipped with electro-optical shutters, which again are controlled by the MaxVideo-20 boards. These shutters avoid any exposure of the CCD during image read-out.

The system is controlled by a VME/UNIX workstation (Sun-sparc). A large storage disk (1 GB) and digital tape unit are used to store and to backup the image data, so that the system can be operated as a 'stand-alone' machine. An ethernet connection gives access to other machines, which makes it possible to access other software (e.g., for image processing and data visualization) or peripherals, or to use a high-performance workstation for the data reduction.

Images can be recorded at any frame rate up to 10 Hz. The two cameras can be operated simultaneously, or with a given time delay. It is also possible to acquire an image at the response of an external trigger signal, or to record a whole sequence of images started by an external trigger ('conditional start'). The system can also acquire images continually, and then be stopped by an external trigger ('conditional stop'). This particular feature was used in the measurement of the transition from laminar to turbulent pipe flow, reported later in this paper.

3 Experiments

In this section we discuss the pipe flow facility. For the fully-developed turbulent flow we matched our flow conditions to those of the PIV measurement by Westerweel *et al.* (1993). In Table 1 we compare the relevant experimental parameters for the PIV and DPIV measurements. These parameters will be discussed in greater detail below.

3.1 flow facility

For the measurements we used a closed-loop water facility. A detailed description of this facility is given by Tahitu (1994). The main flow line is a smooth pipe with an inner diameter of 40.2 mm and a total length of 8.65 m. The return line has the same length and diameter. The wa-

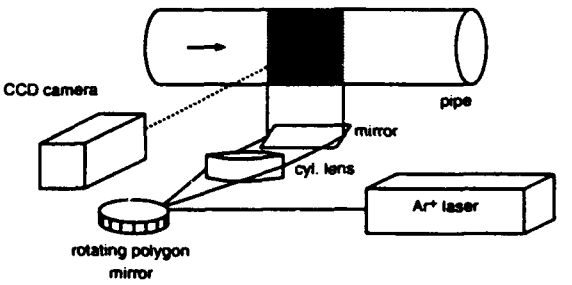

Figure 2: Optical configuration for the digital PIV measurements in a pipe.

Table 1: The experimental conditions for the photographic PIV measurement (PIV) by Westerweel *et al.* (1993) and for the digital PIV measurement (DPIV).

		PIV	DPIV
Pipe:			
diameter (D)	(mm)	127	40.2
length	(m)	17	8.65
Flow:			
fluid		air	water
kin. viscosity	(mm^2/s)	15.22	0.998
velocity (U_b)	(mm/s)	627	130
Re		5,277	5,251
Seeding:			
type		oil droplets	Optimage
size	(μm)	1 - 2	30 ± 10
number dens.	(mm^{-3})	40	6.1
Illumination:			
source		2× YAG	Ar^+
beam type		expanded	scanning
thickness	(mm)	0.4	0.5
energy/power		120 mJ	5 W
time delay	(ms)	0.30000	2.685
no. of exposures		2	8
Recording:			
type		photograph	electronic
magnification		0.70	0.30
viewing area	(mm^2)	150×130	40.0×40.7
Interrogation:			
area	(mm^2)	1.4×1.4	1.3×1.3
image dens. (N_I)		20.1	23.1
time[a]	(s)	1,010	12
Data set:			
vectors/image		8,500	3,721
no. of images		33	100

[a]interrogation time per 1,000 vectors

ter temperature in the facility is maintained at a constant value of 20.3°C.

The two experiments required different flow conditions at the pipe inlet. For the first experiment we want a fully-developed pipe flow. We therefore bypassed the settling chamber, and connected the inlet of the main flow line directly to the pump. The disturbances in the flow caused by the pump are sufficient to establish a turbulent flow state. In the second experiment (i.e. transitional flow) the fluid passes a settling chamber and enters the pipe through a smooth funnel. Now the flow remains laminar over the full length of the pipe at a Reynolds number of 5,600 (based on the pipe diameter and the bulk velocity), until dynamic instabilities cause the flow to become turbulent.

The measurements are carried out in a test section located at a distance of 6.5 m from the pipe inlet. This distance is more than 160 times the pipe diameter, so that for the first experiment we may indeed expect here a fully-developed turbulent flow (Schlichting 1979). The test section consists of a square, water-filled box that encloses a section of the pipe. Inside this box the normal pipe wall has been replaced by a thin sheet with a thickness of 0.01 mm. The box and thin wall reduce optical aberrations that result from refraction of light by the curved pipe wall, and allows us to measure the velocity close to the pipe wall.

Westerweel *et al.* (1993) stressed the importance of an independent and accurate measurement of the friction velocity in order to normalize the experimental data correctly. In these measurements the friction velocity was determined from the measured pressure drop between two taps located at 4.40 m and 8.60 m from the inlet. The friction velocity is found from the pressure drop by (Schlichting 1979):

$$u_* = \sqrt{\frac{\Delta P D}{4 \rho L}} \qquad (1)$$

where ΔP is the pressure drop over a length L, ρ the density of the fluid, and D the diameter of the pipe. The pressure difference was determined with a relative measurement error of 0.8%, and through Eq. (1 we found: u_*=9.081±0.004 mm/s.

3.2 seeding

The flow has been seeded with small tracer particles that have a nominal diameter of 30 μm (Optimage). These particles are almost neutrally buoyant in water. Sufficient time was allowed to ensure that the particles are distributed evenly over the entire flow volume before we carry out the measurements. These particular tracer particles are rather large, and in order to keep the volume fraction of the seeding below 10^{-4}, while at the same time maintaining an adequate image density, we decided to record multiple-exposure images (Keane & Adrian 1991). We will return to this point in Section 3.4.

3.3 light sheet

The optical configuration for the light sheet is shown in Figure 2. The beam of a 5 Watt argon-ion laser is guided through an optical fiber, and is deflected by a rotating 36-faceted polygon mirror. A cylindrical lens converts the angular motion of the reflected beam into a parallel motion. A 45°-mirror directs the beam through the test section. The plane of the light sheet coincides with the centerline of the pipe. A small inverted telescope at the fiber exit contracts the beam so that the width of the light sheet in the test section is 0.5 mm.

3.4 image recording

The time delay between two consecutive passages of the scanning beam is set to 2.685 ms. Each image is exposed 8 times, which makes the total exposure time equal to 18.8 ms. The Kolmogorov time scale τ ($=\eta^2/\nu$, with $\eta u_*/\nu$=1.6; Eggels *et al.* 1994) for this flow is equal to 31 ms. Since the total exposure time is less than τ we may assume that the flow field during the exposure is essentially frozen.

An image of the particles in the light sheet is formed on the CCD array with a 50 mm focal length lens with a numerical aperture of f/D=4. The optical axis of the lens is perpendicular to the plane of the light sheet. The image magnification is 0.30, so that the view area of the camera

is one pipe diameter in both the axial direction and the radial direction with respect to the pipe.

In the first experiment (i.e. fully-developed turbulent pipe flow) we deliberately used a low frame rate of 1 Hz. The integral time scale for the turbulent pipe flow is estimated at 0.3 s ($=D/U_b$; see Tab. 1); so that we may assume that consecutive images are statistically independent. For the measurement of the transitional flow we used the maximum frame rate (i.e. 10 Hz), which enables us to resolve the event in a sequence of images. For this measurement we used the system in 'conditional stop' mode. In both experiments we recorded a sequence of 100 frames, which occupy about 100 MB of storage each.

3.5 data reduction

Each image is interrogated in 32×32-pixels sub-images at intervals of 16 pixels (i.e. a 50% overlap). The size of an interrogation sub-image corresponds to a measurement volume of (1.3×1.3×0.5=) 0.85 mm^3 in the flow. The displacement of the tracer particles between two exposures at the centerline of the pipe is about 12 pixel units (px), which is almost 40% of the width of the interrogation image. The image density (i.e. the average number of particle image pairs) is equal to 23.1.

The interrogation is done symmetric with respect to the location of the centerline on the images; this makes it possible to combine the flow statistics from the upper and lower sections of the images directly.

Reliable measurements of the displacement are obtained down to 14 px from the pipe wall — which corresponds to a distance of only 0.57 mm (or 5.2 viscous wall units). The centroid of the interrogation region closest to the pipe wall is located 1.16 mm from the wall (10.6 viscous wall units).

Each image yields a data set of 61 rows of 61 vectors each. The image sequences are processed on a HP9000/720 workstation, which completes the analysis of one image (i.e. 3,721 interrogations) in less than 30 seconds. Compare this with an analysis time of 2.5 *hours* (see Table 1 that was required for the interrogation of a single PIV photograph (Westerweel *et al.* 1993).

Each data set is subjected to a data-validation procedure to remove erroneous measurements of the displacement. (Erroneous measurements occur naturally as a result of insufficient particle-image pairs in certain interrogation sub-images.) We use the median-filtering method described by Westerweel (1994) to identify displacement vectors that deviate unphysically from adjacent vectors: all vectors that deviate more that 2.5 px from their local median value have been discarded from the data set. The average fraction of detected spurious vectors is 2.8%, with the lowest and highest fractions being equal to of 1.2% and 5.7% respectively. The discarded vectors are replaced by the local-average of the (accepted) adjacent displacement vectors.

Figure 3 shows a typical result of the instantaneous fluctuating velocity measured in the fully developed turbulent pipe flow. The top and bottom axes in Fig. 3 coincide with the pipe wall. To visualize the small fluctuations in displacement we scaled the arrows in this figure by a factor of 15. In fact, most of the arrows showed here actually correspond to fluctuations of the displacement of less than 0.5 px. This demonstrates the ability of DPIV to resolve displacements at sub-pixel level. Also note the turbulent flow structures close to the upper and lower walls. Figure 4 shows two examples of grey-scale maps of the out-of-plane component of the vorticity (ω_z). One may recognize coher-

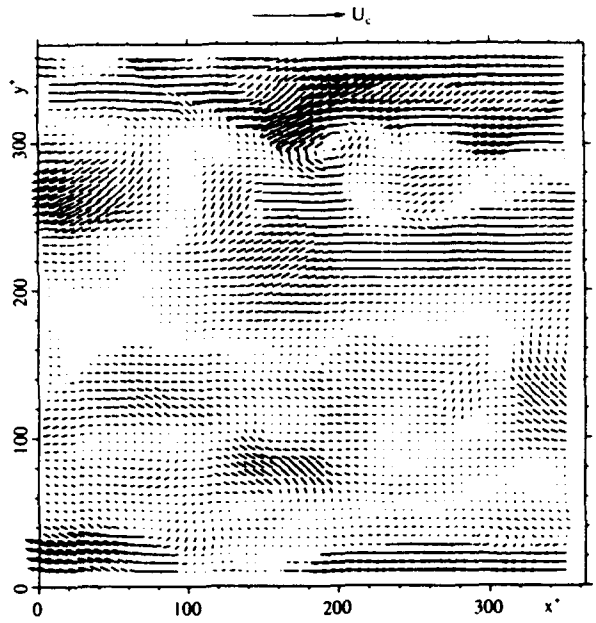

Figure 3: A vector map of the measured instantaneous fluctuating velocity. The vector at the top represents the mean velocity at the centerline.

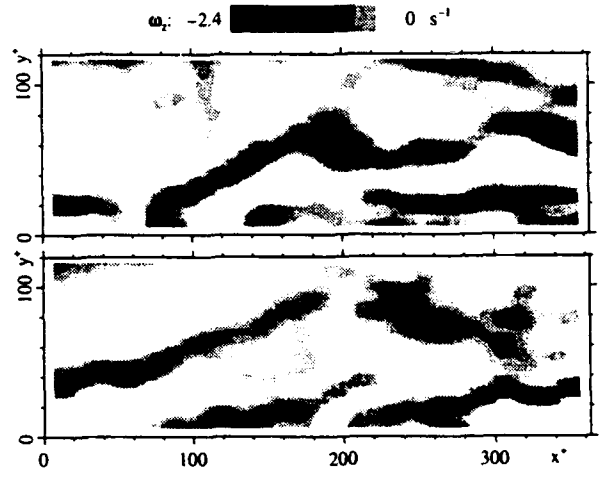

Figure 4: Grey scale maps of negative vorticity in s^{-1} perpendicular to the image plane. The flow is from left to right. The pipe wall is located at $y^+=0$.

Table 2: The flow conditions for the DNS (Eggels *et al.* 1994) and for the measurements with PIV (Westerweel *et al.* 1993) and DPIV.

		DNS	PIV	DPIV
Re		5,300	5,277	5,251
Re_*		360.0	366.3	365.9
U_b	(mm/s)	—	626.6	130.4
U_c	(mm/s)	—	842.9	174.5
U_c/U_b		1.312	1.345	1.338
u_*	(mm/s)	—	43.5	9.081
U_b/u_*		14.72	14.40	14.35
U_c/u_*		19.31	19.38	19.21
c_f		0.00932	0.00964	0.00943
ν/u_*	(mm)	—	0.3467	0.1099
$\frac{1}{2}D^+$		180.0	183.2	181.6
Δr^+		1.88	4.12	5.81
Δx^+		7.03	4.12	5.81
Δz^+		8.84[a]	1.15	4.55

[a]Tangential resolution at the pipe wall.

ent structures that closely resemble the 'shear-layer' and 'vortex' structures that were observed in the PIV data set (ref. Westerweel *et al.* 1993). In this paper we will not further examine these structures; instead we concentrate on the comparison of the measured flow statistics. These results are discussed in the next section.

4 Results

In this section we present the results from the measurement of the fully-developed turbulent pipe flow and of the transitional pipe flow. We will use u and v to denote the velocity components in the axial (x) and radial (r) directions respectively. The velocity statistics will usually be normalized by the friction velocity (u_*) and plotted as a function of the dimensionless distance from the centerline (viz. r/D). The axes for vector maps show the dimensions expressed in wall units; in these cases the y-coordinate denotes the distance from the (lower) pipe wall.

4.1 Fully-developed turbulent flow

Table 2 summarizes the conditions of the DPIV measurements of the fully-developed turbulent flow, together with the flow conditions of the DNS and of the PIV measurements. Note the close correspondence of the flow conditions for the three data sets; the only real difference is reflected in the spatial resolution (viz., Δr^+, Δx^+ and Δz^+). Let us compare the resolution of three data sets against Grötzbach's criterion, i.e.:

$$\Delta < \pi\eta \quad \text{with} \quad \Delta = (\Delta r \Delta x \Delta z)^{1/3} \qquad (2)$$

(Grötzbach 1983; Eggels *et al.* 1994) where η is the Kolmogorov length scale. For the DNS, PIV and DPIV data sets we find $\Delta^+ = 4.9$, 2.7 and 5.4 respectively. The Kolmogorov length scale for this flow is estimated at $\eta^+ = 1.6$ (Eggels *et al.* 1994), so that $\pi\eta^+ = 5.0$. The DNS and the PIV data sets satisfy Grötzbach's criterion, whereas the DPIV data set exceeds the criterion by less than 10%. This

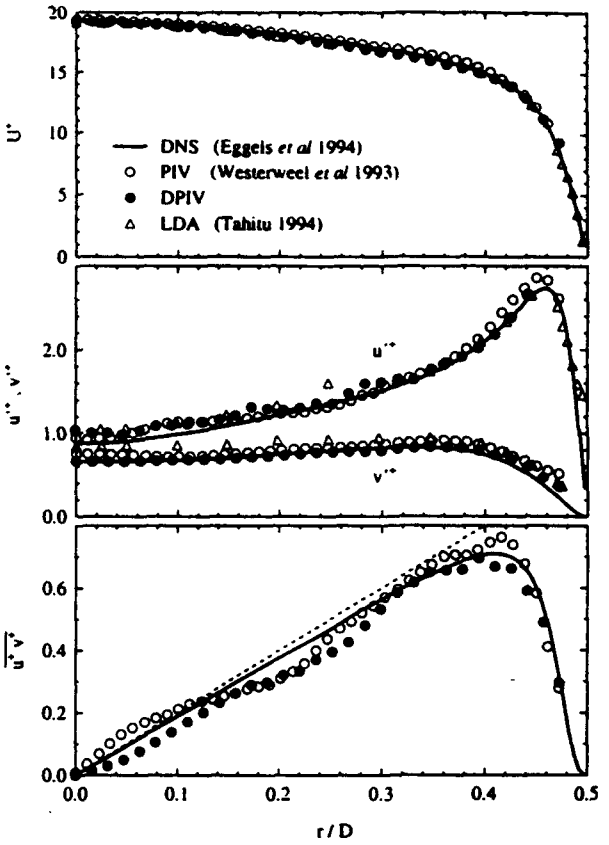

Figure 5: The mean axial velocity, the axial and radial RMS fluctuating velocities, and Reynolds stress, normalized by friction velocity, as function of the dimensionless distance from the centerline.

amount is so small that even though the criterion is not met in a strict sense, we still view our data set as to have fully resolved all flow scales for $y^+ > 10$ (i.e. outside the viscous sub-layer).

The flow statistics of fully-developed turbulent pipe flow are homogeneous along the axial direction, and symmetric with respect to the centerline. We determined the flow statistics from the measured data by averaging the data along rows over all frames, and then combining the results from opposite sides of the centerline. In Figure 5 we have plotted the results for the mean axial velocity (U), for the axial and radial root-mean-square (RMS) fluctuating velocities (u' and v' respectively), and for the Reynolds stress ($\overline{uv}$). We also plotted the corresponding results from the DNS and from the PIV and LDA measurements.

The data in Fig. 5 show that the differences between the DNS, PIV, DPIV and LDA results are very small. We therefore plotted in Figure 6 the residuals for the experimental data with respect to the DNS data.

For the mean axial velocity the PIV data are mostly larger than the DNS result, whereas the DPIV data are

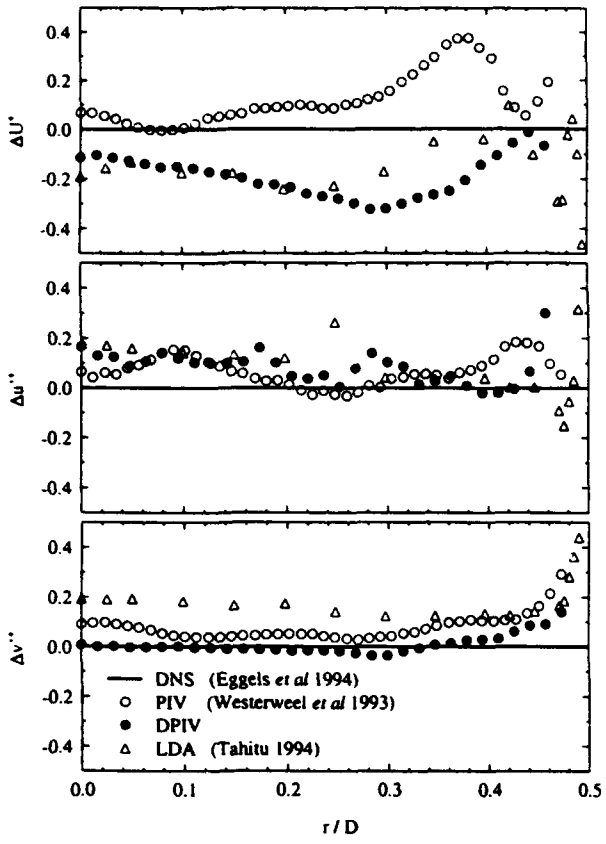

Figure 6: The residuals for the mean axial velocity (ΔU^+) and of the axial ($\Delta u'^+$) and radial ($\Delta v'^+$) RMS fluctuating velocities with respect to the corresponding DNS results for the PIV, DPIV and LDA measurements. The residuals are normalized by the friction velocity, and are plotted as a function of the dimensionless distance from the centerline.

mostly smaller. Note that the results from the LDA measurement (taken in the same facility and at the same flow condition as the DPIV measurement) coincide with the DPIV results. This indicates that the systematic deviations of the DPIV from the DNS cannot be attributed to non-ideal behavior of the tracer particles, or to the difference between the number of exposures in the PIV and DPIV measurements. We therefore conclude that the systematic deviations are not the result of differences between PIV and DPIV, but should be attributed to the fact that the measurements were carried out in different flow facilities.

The differences between the PIV and DPIV results for the residuals of u'^+ and v'^+ are negligible taking into account the random scatter of the data. If the random errors (i.e., noise) in the DPIV data were substantially larger than those in the PIV data, we would expect that the results for u'^+ and v'^+ from the DPIV measurement are biased with respect to results from the PIV measurement. The corresponding residual profiles in Fig. 6 show that this is not the case, which supports the conclusion by Westerweel (1993a,1993b) that DPIV can yield velocity data with the same level of accuracy as PIV.

Note how $\Delta u'^+$ for the LDA and DPIV data exhibit the same systematical deviations over a considerable range in r/D; again a clue that the differences we may observe between the PIV and DPIV results reflect differences in the flow rather than differences in accuracy. On the other hand, there is a considerable bias in the residual profiles of v'^+ for the LDA data with respect to the DPIV data. We believe that this is a result of cross-talk between the $u+v$ and $u-v$ signals in the LDA measurement (see Tahitu 1994).

We would like to emphasize here on which level of detail we evaluated the DPIV data in Fig. 6: a difference of 0.2^+ in these residual profiles corresponds to a displacement of 0.12 px in the digital images. Note how small the fluctuations are with respect to the equivalent size of a pixel.

We also determined the skewness and kurtosis factors (denoted by S and K respectively), which are shown in Figure 7 together with the corresponding results for the DNS and PIV data sets. The skewness and kurtosis factors are directly related to the third and fourth order statistics, and are generally considered to be more sensative to noise than first and second order statistics.

The skewness factors of both u and v for the PIV and DPIV data coincide over a considerable range in r/D. Note the similarity of the skewness factors for the two experimental data sets: they both deviate from the DNS data in the same manner. We emphasize that this is only a small

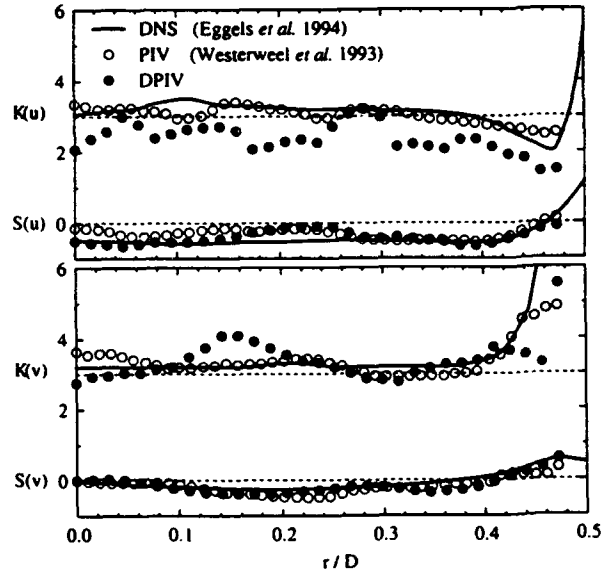

Figure 7: The skewness (S) and kurtosis (K) factors for the axial (top) and radial (bottom) velocities, as a function of the dimensionless distance from the pipe wall. The dashed lines represent the skewness and kurtosis for a normal random process.

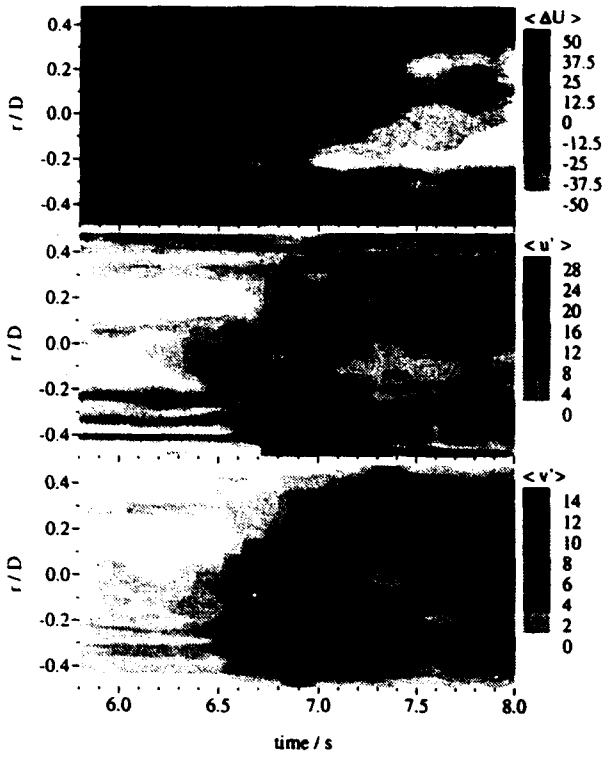

Figure 8: Grey scale maps of the combined spatially filtered profiles for the image taken at 0.1 s intervals. The top graph represents the residual mean axial velocity with respect to the velocity in the laminar flow state; the middle and bottom graphs represent the result for the axial and radial RMS fluctuating velocities respectively. The scale of the contour levels is in mm/s.

difference, but it might indicate an aspect of the flow that is not correctly reproduced by the DNS.

The differences in accuracy level between the PIV and DPIV data sets are more prominently visible in the results for the kurtosis. Although there still may be a fair agreement of the DPIV data with respect to the DNS and PIV data for $K(v)$, there is an obvious bias of the DPIV data for $K(u)$ with respect to the DNS and PIV data. It should however be mentioned that the identification of spurious vectors in the PIV data was done interactively, whereas the identification of spurious vectors in the DPIV data was done automatically; the automated procedure may have left a small fraction of spurious data undetected. Besides, this procedure is based on second-order statistics only, which may also have contributed to the bias. It is therefore likely that the bias is a result of minor shortcomings of the detection procedure, and that an improvement of this procedure may compensate for the bias.

4.2 transitional flow

In the measurement of the transitional flow the camera frame rate was set to 10 Hz. The acquisition was done in the 'conditional-stop' mode: this means that images are acquired continuously until an external trigger signal is generated. In this measurement the acquisition was stopped when a natural transition from the laminar to the turbulent flow state had occurred. We found that the transition passed the view area of the camera between 5.8 and 8.0 seconds after the acquisition of the first frame in the sequence.

To visualize results we determined the mean axial velocity and RMS axial and radial fluctuating velocities in the axial direction for each individual frame. This can be viewed as applying a moving-average filter to the instantaneous flow field, i.e.:

$$\left.\begin{aligned} \langle U(r)\rangle_i &= \int_L u_i(r,x)\,\mathrm{d}x \\ \langle u'(r)\rangle_i^2 &= \int_L [u_i(r,x) - \langle U(r)\rangle_i]^2\,\mathrm{d}x \end{aligned}\right\} \quad (3)$$

(and *vice versa* for v) where the index i denotes the frame number, $u_i(r,x)$ the instantaneous velocity field, and L is the integration length along the axial direction (viz., x). For the DPIV data the (maximum) integration length is determined by the size of the images in the axial direction, which is here equal to one pipe diameter. By combining the filtered-velocity profiles we obtain two-dimensional scalar data sets that reveal the changes in the flow across the pipe as a function of time. Figure 8 shows the results for $\langle \Delta U\rangle$, $\langle u'\rangle$ and $\langle v'\rangle$, with: $\langle \Delta U\rangle = \langle U\rangle - U_{\mathrm{lam}}$, where U_{lam} is the mean axial velocity profile in the laminar flow state (i.e. for frames with index i <56). The transition first appears near the centerline at t=6.2 s. Fluid near the centerline decelerates, while fluid near the pipe wall accelerates. By t=7.1 s the transition has reached the upper and lower sections of the pipe wall, but the mean velocity continues to develop until t=8.0 s.

Flow structures that move with the speed of the mean bulk velocity (see Table 1) will take about 0.3 s to travel across the field of view, and we may therefore capture these structures in three consecutive frames. Figure 9 shows sections of three vector maps of the instantaneous fluctuating velocity of the turbulent flow state taken at intervals of 0.1 s. Note a fairly large structure which deforms and apparently grows in size, while it passes a smaller structure that travels at a lower speed close to the pipe wall.

5 Conclusions

From the results presented in the previous section we conclude that our new image acquisition system complies with the requirements for (D)PIV measurements in turbulent flows:

- the image resolution is adequate to resolve both the large-scale and the small-scale structure of the flow;
- the measurement error is sufficiently small to obtain accurate results for the statistics (of order four or less) of the fluctuating velocity;
- the frame rate is high enough to capture the motion and temporal evolution of large-scale coherent flow structures.

For the first time a detailed comparison has been made between PIV and DPIV measurements in a non-trivial, unsteady flow. From the results we conclude that DPIV can provide data at the same level of accuracy and resolution as the conventional PIV method. The required computational effort for the interrogation of the DPIV images is only a fraction of that for the conventional PIV method. We would like to emphasize the fact that the DPIV measurements were carried out in a water flow does *not* imply that DPIV is restricted to water flows: it only requires a proper scaling of the parameters listed in Tab. 1 to facilitate DPIV measurements in an air flow.

The transitional flow data demonstrate the potential of the acquisition system with respect to the measurement of time-resolved image sequences. At this point the temporal resolution of the acquisition system is still modest (i.e. 10 Hz per channel). However, an upgrade is scheduled for the near future in which the system will be equipped with two new cameras that have a frame rate of 33 Hz each. This will allow a more detailed study of the dynamics and temporal evolution of coherent flow structures.

So far, we have not utilized the capabilities provided by the use of both cameras. In the future we intend to carry out measurements in which we will use the system for stereoscopic and two-color imaging.

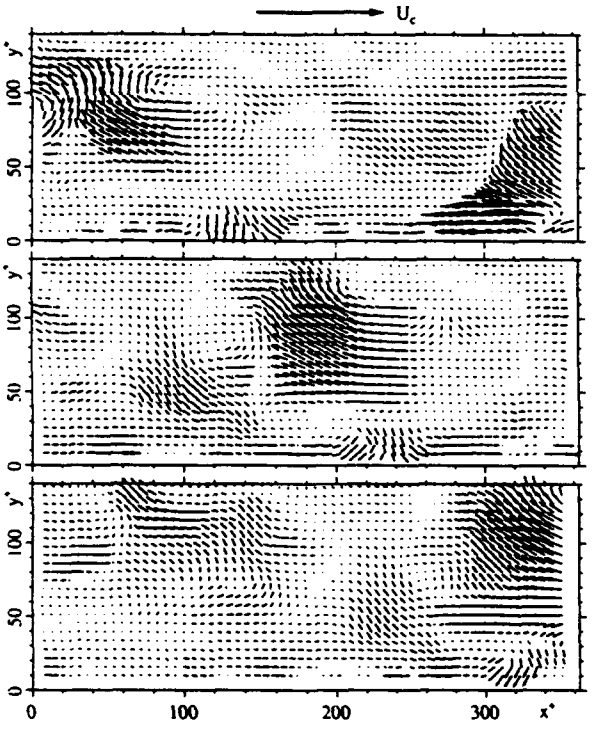

Figure 9: A sequence of three vector maps of the fluctuating instantaneous velocity in a turbulent pipe flow, taken at intervals of 0.1 s. The top arrow represents the mean axial velocity at the centerline. The pipe wall is located at $y^+ = 0$.

References

Eggels, J.G.M., Westerweel, J. & Nieuwstadt, F.T.M. 1993 Direct numerical simulation of turbulent pipe flow. *Appl. Sci. Res.* **51**, 319-324.

Eggels, J.G.M., Unger, F., Weiss, M.H., Westerweel, J., Adrian, R.J., Friedrich, R. & Nieuwstadt, F.T.M. 1994 Fully developed turbulent pipe flow: a comparison between direct numerical simulation and experiment. *J. Fluid Mech.* **268**, 175-209.

Van der Hoeven, J.G.Th., Westerweel, J., Nieuwstadt, F.T.M. & Adrian, R.J. 1992 Application of digital particle image velocimetry to a turbulent pipe flow. In: *Proc. of IUTAM Symp. "Eddy Structure in Free Turbulent Shear Flows"* (Poitiers) Oct. 12-14. Kluwer Academic, Dordrecht.

Grötzbach, G. 1983 Spatial resolution requirements for direct numerical simulation of the Rayleigh-Bénard convection *J. Comp. Phys.* **49**, 241-264.

Keane, R.D. & Adrian, R.J. 1991 Optimization of particle image velocimeters. Part II: Multiple-pulsed systems. *Meas. Sci. Technol.* **2**, 963-974.

Prasad, A.K., Adrian, R.J., Landreth, C.C. & Offutt, P.W. 1992 Effect of resolution on the speed and accuracy of particle image velocimetry interrogation. *Exp. Fluids* **13**, 105-116.

Schlichting, H. 1979 *Boundary-Layer Theory* 7th Ed. McGraw-Hill, New York.

Tahitu, G.J.R. 1994 The possibilities for laser-Doppler velocimetry in a turbulent pipe flow. *Report MEAH-117* (Delft University of Technology). M.Sc.-thesis (in Dutch).

Westerweel, J., Flōr, J.B. & Nieuwstadt, F.T.M. 1991 Measurement of dynamics of coherent flow structures using particle image velocimetry. In *Applications of Laser Techniques in Fluid Mechanics* (eds. R.J. Adrian *et al.*) Springer, Berlin. pp. 476-499.

Westerweel, J. 1993a *Digital Particle Image Velocimetry — Theory and Application.* Delft University Press, Delft.

Westerweel, J. 1993b Analysis of PIV interrogation with low pixel resolution. *Proc. SPIE-2005 "Optical Diagnostics in Fluid and Thermal Flow"* July 14-16, San Diego.

Westerweel, J., Adrian, R.J., Eggels, J.G.M. & Nieuwstadt, F.T.M. 1993 Measurements with particle image velocimetry of fully developed turbulent pipe flow at low Reynolds number. In: *Applications of Laser Techniques in Fluid Mechanics* (eds. R.J. Adrian *et al.*). Springer-Verlag, Berlin. pp. 285-307.

Westerweel, J. 1994 Efficient detection of spurious vectors in particle image velocimetry data sets. *Exp. Fluids* **16**, 236-247.

Willert, C.E. & Gharib, M. 1991 Digital particle image velocimetry. *Exp. Fluids* **10**, 181-193.

A COMPACT AND SIMPLE ALL OPTICAL EVALUATION METHOD FOR PIV RECORDINGS

Andreas Vogt, Frank Reichel[1], and Jürgen Kompenhans

Institut für Strömungsmechanik
Deutsche Forschungsanstalt für Luft- und Raumfahrt (DLR)
Bunsenstraße 10, D-37073 Göttingen, Germany

[1])Jenoptik Technologie GmbH
Carl-Zeiss-Straße 1, D-07739 Jena, Germany

ABSTRACT

The Particle Image Velocimetry (PIV) is a technique which is utilized for measuring complete velocity vector fields in a few microseconds time. However, a lot of time is required during the evaluation. E. g., if employing the autocorrelation technique it is necessary to calculate a few thousand auto-correlation functions (ACFs) for each PIV recording. In this paper an evaluation system for photographical PIV recordings will be described, which allows the determination of the ACFs of small sub areas of the recording completely analog optically. An optically addressable liquid crystal spatial light modulator was utilized to store the Young's fringes pattern appearing in the frequency plane at the output of a first optical Fourier processor and to provide them as the input for a second optical Fourier processor. Our analog optical autocorrelator offers a high processing speed and simultaneously a high resolution in the autocorrelation plane. The realized set up is compact and very easy to handle.

1. INTRODUCTION

Today Particle Image Velocimetry (PIV) is a quite well known measuring technique in fluid mechanical research. Although complete and satisfyingly performing systems are already commercially available the development is still going on since PIV is still a relatively new method.

Some of the working PIV systems utilize CCD cameras and video technique for the recording of the PIV images and then perform a completely digital evaluation. However, for fluid mechanical problems with increased requirements concerning the space-bandwidth product (i. e. high resolution and a large observation field) the conventional photographic technique is still superior to the digitally working video systems. Photographic film (24 × 36 mm² format) can have a resolution of more than 100 line pairs per mm (lp/mm), whereas CCD chips with e. g. 2048 × 2048 pixels and 25 × 25 mm² sensor size achieve only 40 lp/mm. Because a huge amount of information contained in one PIV exposure has to be processed during the evaluation, systems utilizing the conventional photographic recording have a second major advantage. It is possible to perform a great part of the evaluation of the exposures analog optically so that the computation time can be reduced significantly. Furthermore, with digital systems there still exists the problem of writing the recorded data (4 MByte/recording for the above example) onto a recording device in a reasonable time and to supply the storing capacity for up to several hundred images during a measuring campaign.

For the evaluation of the PIV exposures a few thousand two-dimensional ACFs per exposure have to be computed. For each of these functions the local maximum indicating the mean particle displacement in a small subregion of the original image has to be found [1], [2]. The computation of the ACF, which is done indirectly by computing two two-dimensional Fourier transforms in most cases, and the peak detection in the autocorrelation plane are the critical procedures for the PIV evaluation with respect to time. The desired ACF can be determined digitally or, with relatively simple setups, optically. There have been quite a few suggestions how to realize such optical based techniques [3], [4], [5]. Although the digitally and optically working systems for the time consuming evaluation of the PIV recordings increased their processing speed considerably in the last years, a faster determination of each ACF is still desirable and the ultimate aim remains the evaluation in real time. Therefore the competition between the digitally and optically working techniques has not stopped yet. Digitally based systems increase their processing speed every few months by utilizing new and more powerful hardware components whereas on the optics side new optical components are developed and employed. Because in principle the optical systems can yield the ACF in real time (the determination of the involved Fourier transforms is carried out with the speed of light) the work in this field still continues.

As mentioned above two two-dimensional Fourier transforms have to be determined to get the desired ACF [1]. The input to the first optical Fourier processor is achieved by simply illuminating a small so called 'interrogation area' of the photographic negative of the PIV exposure with a laser light beam. The major problem for the existing optical systems is how to get the output data of the first optical Fourier processor, the so called Young's fringes, into the second one. In principle the output of the first processor can be recorded with a video camera and subsequently be fed to a liquid crystal spatial light modulator (LC-SLM) [4], [5]. Another possibility is to write the fringe pattern optically to an appropriate light modulator. Optical set ups with electronically adressable liquid crystal light modulators are easy to handle and allow frame rates (data input) about 100 Hz, but due to the finite size of their pixels (currently about 60 × 76 µm²) their spatial resolution is limited.

Furthermore the input data to these devices, the fringes, have to be digitized before they are fed into this kind of light modulator. The optically adressable $Bi_{12}SiO_{20}$ (BSO) spatial light modulators on the other hand have a higher spatial resolution but at the same time they require some effort for operation (high voltage, flash lamps for erasing the data, etc.).

The optically working evaluation system presented here combines the advantages of the above mentioned techniques by simultaneously avoiding their disadvantages. Our system utilizes an optically adressed liquid crystal spatial light modulator capable of frame rates in the order of the video frequency and with a high spatial resolution of 40 lp/mm (in the frequency domain). The device is extremely easy to handle (operating voltage ca. 5 V a. c., frequency 10 - 1000 Hz) so that the entire optical setup itself is also quite simple and compact.

2. EXPERIMENTAL SET UP

2.1. Optical part of the evaluation system

Up to now two systems for the evaluation of photographical PIV recordings by means of the optically addressable SLM (type 300 p/01 of *Jenoptik Technologie*) are realized. The one built at DLR makes use of already available hardware components belonging to an existing analog-optical / digital evaluation system which involves the employment of a workstation for the peak detection and post processing of the data. The second one which was developed at *Jenoptik Technologie* is a PC based system. The optical set up for both systems is the same in principle. Figure 1 shows the optical part of the evaluation system as it was realized at DLR.

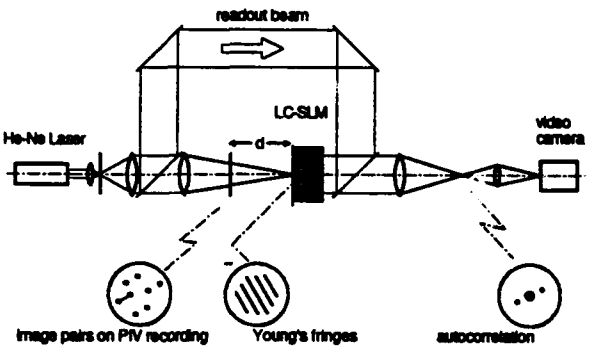

Figure 1: All optical autocorrelator for the evaluation of photographical PIV recordings

On the left hand side of Figure 1 there is the light source, a He-Ne laser, with a subsequent spatial filter which removes the imperfections of the original laser beam. The spatial filter therefore helps to provide a low signal to noise ratio as well in the frequency plane as in the autocorrelation plane. Behind the spatial filter the beam is splitted. The rays passing the beam splitter (the write beam) are focused by the subsequent Fourier lens onto the light modulator. The PIV recording which is to be analyzed is placed between Fourier lens and Fourier plane, i. e. in the converging part of the beam [10]. (This arrangement allows an adjustable interrogation spot size on the PIV recording.) This way the Young's fringes pattern (i. e. the two dimensional spectrum) corresponding to the particle image displacement inside the present interrogation spot is imaged onto the light sensitive layer of the light modulator.

The readout beam is reflected onto the back plane of the SLM by means of two mirrors and a second beam splitter. This beam impinges onto the right hand side of the SLM and is phase modulated by the device according to the Young's fringes pattern. (The working principle of the optically addressable spatial light modulator is explained in detail below.) Due to a mirror inside the SLM the readout beam is reflected back again. The part of the now modulated readout beam passing the beam splitter is then also Fourier transformed by another Fourier lens thus yielding the two dimensional spectrum of the Young's fringes pattern, i. e. the autocorrelation of the greyvalue distribution inside the interrogation spot. The ACF is recorded by a video camera.

2.1.1. Optically addressable LC spatial light modulator

The optically adressed LC-SLM (see also [6], [7], [8]) is a sandwich system consisting of a photoconductor, a liquid crystal layer, a dielectric mirror, alignment layers, and transparent electrodes on glass substrates (figure 2). The alternating voltage applied to the transparent electrodes is divided according to the impedance of the different layers. As light impinges onto the photoconductive material, the conductivity of the latter increases so that the correspondingly increasing voltage drop across the liquid crystal results in a variation of the orientation of the molecules. This SLM may therefore be used to transform two-dimensional intensity distributions into suitable distributions of refractive index on the output side, if the selection and control of suitable photoconductors does not produce any noticeable lateral charge balancing.

In the SLMs Plasma-CVD-deposited a-Si:H on indium-tin-oxide (ITO) -coated glass substrates is used as a photoconductive layer. To reflect the light, a multilayer dielectric mirror is produced between a-Si:H and LC by electron-beam evaporation of TiO_2 and SiO_2. With planar, untwisted alignment a nematic LC is a uniaxial birefringent medium. Alignment is achieved by a polyimide layer.

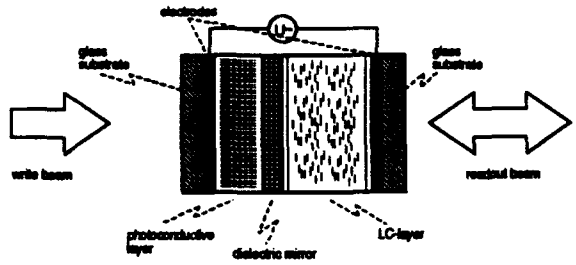

Figure 2: Principle of the optically adressable liquid crystal light modulator

Due to the birefringent properties of the molecules light passing the liquid crystal is phase modulated according to the pattern of the more or less tilted molecules. The write beam with the input pattern incidents from the left onto the device whereas the readout beam falls onto the device from the right hand side. The readout beam passes the liquid crystal and is reflected by the dielectric mirror so that it passes the crystal twice. Leaving the device the readout beam is thus phase modulated corresponding to the input pattern.

The scope of possible SLM applications in Fourier processors is determined, among other things, by the absolute and spectral sensitivity of the LC-SLM [9]. Figure 3 shows the illumination dependence of the phase shift $\Delta\varphi$ of the readout light with different drive frequencies. For this measurement the readout wavelength is given by $\lambda_{ro} = 551$ nm and the write wavelength by $\lambda_{w} = 633$ nm. The direction of polarization of the readout light is parallel to n_e, the extraordinary refractive index. At a drive frequency of $\omega = 100$ Hz and an effective voltage of $U_{eff} = 3{,}25$ V an illumination intensity of $I_w \approx 10\ \mu W/cm^2$ is required to generate a phase shift of $\Delta\varphi = \pi$. The higher the selected drive frequency, the higher the illumination intensity must be chosen ($I_w \sim \omega$). The stabilisation of the phase shift on the readout side is guaranteed by controlling the SLM drive frequency. The maximum spectral sensitivity for typical a-Si:H layer thicknesses of about 3 µm ranges between 600 and 630 nm.

In another test rectangular gratings were projected onto the a-Si:H-layer with a line-to-space ratio of 1:1 to determine the resolution of the device. From the intensity of the zeroth order of diffraction I_0, the diffraction efficiency η can be determined as a function of the spatial frequency ε of the grating. Figure 4 shows the dependence measured for a LC layer thickness $d_{LC} = 6$ µm. A diffraction efficiency of max. $\eta = 100$ % is obtained for rectangular phase profiles with a line-to-space ratio of 1:1 and a phase deviation of $\Delta\varphi = \pi$. The drop in diffraction efficiency with increasing spatial frequency is due to the change in phase form caused by a spread of the field distribution in the LC and a lateral charge balance in the a-Si:H or the mirror system, respectively. With the usual LC thicknesses of $d_{LC} = 6$ µm, the resolution limit is around 35 - 40 lp/mm.

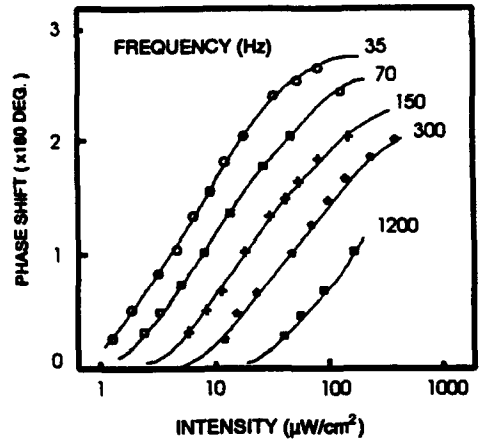

Figure 3: Dependence of phase shift on write light intensity for different drive frequencies

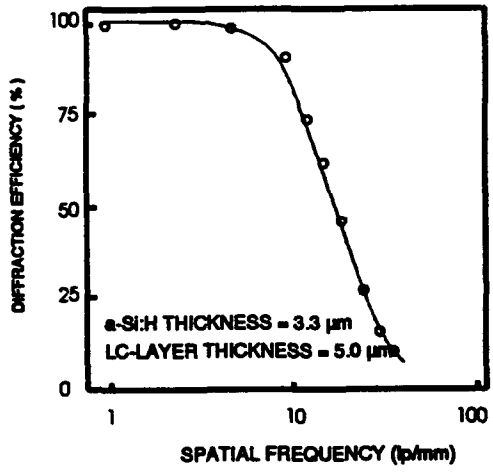

Figure 4: Modulation transfer function of the LC-SLM

The dynamic behaviour of the LC-SLM, i.e. the optical response to the illumination pulses, is determined by the speed of the voltage change between the a-Si:H and LC-layers as well as by the dynamics of the LC molecule distribution of the LC-layer. Figure 5 shows an oscillogram with the switching behaviour of the SLM. The illumination pulse was attained with a mechanical shutter, the exposure intensity I_w giving a phase difference of the readout light of $\Delta\varphi = \pi$.

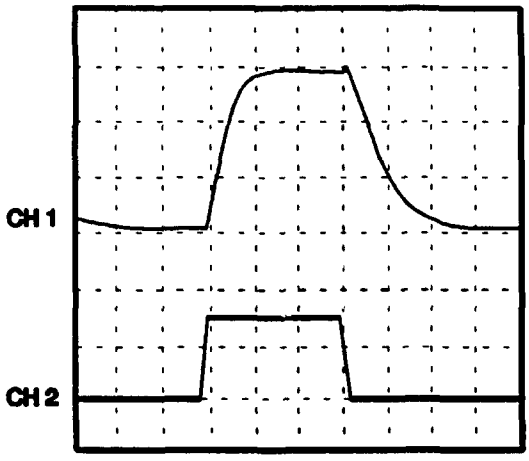

Figure 5: Time response of the LC-SLM (CH1: output light response; CH2: write light, horizontal scale 20 ms div^{-1})

2.2. Digital part of the evaluation system

After the ACF is recorded the coordinates of the peaks in the autocorrelation plane representing the particle image displacement are still to be determined. This is done digitally. The ACF is therefore transferred to the memory of a computer by means of a frame grabber. In our case a workstation (SUN sparc station 10/41), or a 486-PC resp., are utilized for this purpose.

With no a priori knowledge about the position of the correlation peaks the whole autocorrelation plane has to be searched for these peaks. The algorithm implemented on the workstation clips the greyvalue distribution of the ACF at an automatically calculated threshold and connected parts of the ACF with greyvalues bigger than the threshold are labeled. In a second step the centre of these labelled areas is determined considering the grevalues of the individual pixels and their location. A curve fit of the peaks with e. g. a two dimensional Gaussian function is also implemented. This whole algorithm is quite time consuming. Whereas the determination of the ACF itself can nearly be done with video frequency in our system the grabbing of the ACF and the peak determination are now the limiting operations with respect to speed: the workstation based evaluation system with the above described algorithm for the peak detection therefore still requires 1 second for evaluating one interrogation spot. An adaptive (with respect to size and location) region of interest would significantly reduce this time. This has not been implemented up to now, as the DLR PIV system is rather aimed at high quality (high spatial reslution, small fluctuations, no loss of data) than at high speed evaluation. The evaluation system based on the workstation is working fully automatically.

The PC based system of *Jenoptik Technologie* comprises an IBM compatible 486-PC equipped with slots for a x-y stage controller, the SLM controller and the frame grabber. The CCD camera is a Sony XC-77 CE (756 × 581 pixels), working on 2/3" interline-transfer-module basis. The x-y stage can be operated with a maximum speed of 52400 steps /second (minimum step size 1 µm). An alternating (square-wave) voltage programmable in amplitude and frequency is generated by the SLM controller and this a.c. voltage is selected according to the PIV film contrast. Using this system components in combination with a plain peak detection algorithm in an interactively defined region of interest a processing speed of 165 ms per velocity vector can be achieved. Therefore an evaluation of a PIV recording consisting of approx. 3500 interrogation spots as e. g. in Figure 9, 10 or 12 lasts less than 10 minutes. It is expected that this speed can even be increased by a factor of two applying a local-bus PC.

3. TEST OF THE NEW EVALUATION SYSTEM

Some basic tests were performed before the first PIV recordings were analyzed by the all optical autocorrelator. First of all the linearity of the system was checked. For this purpose we utilized some 'artificial' PIV exposures, so called specklegrams. The utilized specklegrams were achieved with a double exposure of a speckle pattern before and after this pattern was shifted by a certain amount. Therefore they show a noise pattern of constant displacement over the whole image. The displacement of the different specklegrams is determined by means of a microscope and by eye.

The evaluation of specklegrams with three different displacements (152 µm, 217 µm, and 406 µm resp.) revealed the expected linear relationship between the displacement on the analyzed images and the location of the correlation peaks in the ACF plane.

To determine the scale in the ACF plane further tests were performed by evaluating three different specklegrams at different positions with respect to the distance between PIV recording and SLM in the optical set up [5]. With these tests the also linear dependency between the scale in the ACF plane and the distance d between the recording and the corresponding first Fourier plane (see figure 1) was checked and proved. The recordings with the nominal displacement of 151 µm and 406 µm were evaluated at two different distances d and the recording with the nominal displacement of 217 µm at three different distances.

These measurements were simultaneously utilized to calibrate the whole evaluation system, i. e. the optical and the digital part of the system as a whole. This is necessary because the result of the peak determination is related to the pixel grid of the frame grabber that recorded the ACF. Thus for calculating the displacement on the analyzed PIV recording a relation between these pixel coordinates and the original displacement with the unit 'meter' has to be established.

Figure 6 shows the results in form of the determined calibration factor. The expected linear relationship between displacement on the recordings and the distance d on the one hand, and the displacements given by the peaks in the ACF plane on the other hand is obvious. The standard deviation error bars are considerably smaller ($\approx 10^{-2}$ µm/pixel) than the symbols utilized for the measurement points and therefore not plotted in this figure.

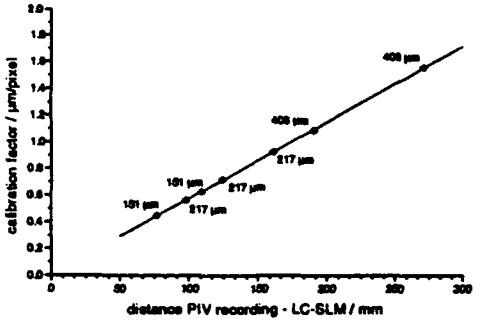

Figure 6: Linearity and calibration curve of the all optical autocorrelator (see text for details)

4. COMPARISON WITH OTHER EVALUATION SYSTEMS

To compare the performance of the new all optical evaluation system with a conventional analog-optical / digital system as described by Höcker [11] and with the analog-optical / analog-optical system presented by Vogt and Kompenhans in [5] three different PIV recordings of the kind described in the previous chapter were analyzed with the different systems. The computer programs utilized for the processing of the ACFs were the same in all three cases.

The displacements of the three analyzed patterns were determined by eye under a microscope and were found to be 151 µm, 217 µm and 433 µm. A displacement of 200 µm between the image pairs on a PIV negative is a value which is typical for the DLR-PIV system. The measurement of the displacements by eye might not be the best way to proceed, but for the purpose of comparing the evaluation systems the constancy of the displacement is the only important feature, not the displacement value itself. The fact that the displacement is constant all over the recording is guaranteed by the way the specklegrams were created.

Each of the images was evaluated at 400 different interrogation spots whithin an area in the centre of the recordings. The results are given in the tables 1, 2 and 3. The first column indicates the measured shift on the recording, the second the result of the evaluations, the third the standard deviation of the determined displacement and the fourth the standard deviation in relation to the absolute value of the determined shift.

The last columns of the tables indicate that the new all optical evaluation method yields the smallest *relative* error for the determined displacements. This is mainly due to the fact that the optics of the evaluation system allow an individual and continuous adjusting of the distance of the correlation peaks with respect to the center in the ACF plane. Such an adaption can not be carried out with fully digitally working systems. The possibility to adapt the scaling within the evaluation system also explains that after a rearrangement of the optical set up a larger displacement in the specklegrams can yield a smaller value for the corresponding displacement in the ACF plane.

Table 1: Analog-optical / digital evaluation

Δs_{ref} / µm	$\bar{r}$ / Pixel	$\bar{\sigma}_r$ / Pixel	$\bar{\sigma}_r / \bar{r}$
151	44,55	0,0192	$4{,}31 \cdot 10^{-4}$
217	40,74	0,0138	$3{,}39 \cdot 10^{-4}$
433	34,18	0,0110	$3{,}22 \cdot 10^{-4}$

Table 2: Analog-optical / analog-optical evaluation with electronically addressable LCD-SLM

Δs_{ref} / µm	$\bar{r}$ / Pixel	$\bar{\sigma}_r$ / Pixel	$\bar{\sigma}_r / \bar{r}$
151	198,85	0,0609	$3{,}06 \cdot 10^{-4}$
217	196,56	0,0422	$2{,}15 \cdot 10^{-4}$
433	168,78	0,0375	$2{,}22 \cdot 10^{-4}$

Table 3: Analog-optical / analog-optical evaluation with optically addressable LC-SLM

Δs_{ref} / µm	$\bar{r}$ / Pixel	$\bar{\sigma}_r$ / Pixel	$\bar{\sigma}_r / \bar{r}$
151	339,70	0,082	$2{,}41 \cdot 10^{-4}$
217	314,59	0,044	$1{,}40 \cdot 10^{-4}$
433	380,22	0,044	$1{,}16 \cdot 10^{-4}$

In another more qualitative comparison the system utilizing the electronically addressable SLM and the optically addressable SLM were compared with PIV recordings of a turbulent flow field. These recordings were made 1.3 m downstream of a regular grid with a rod diameter of 1.5 mm and a mesh size of 19.0 mm. This grid produced an additional turbulence of 0.46 % (measured with a hot wire anemometer) in a laminar wind tunnel flow. The figures 7 and 8 show the results of this comparison in a small sector of the recorded flow field. (Figure 9 shows the result of the whole evaluation.) From these figures the enhanced resolution of the new all optical autocorrelator becomes evident.

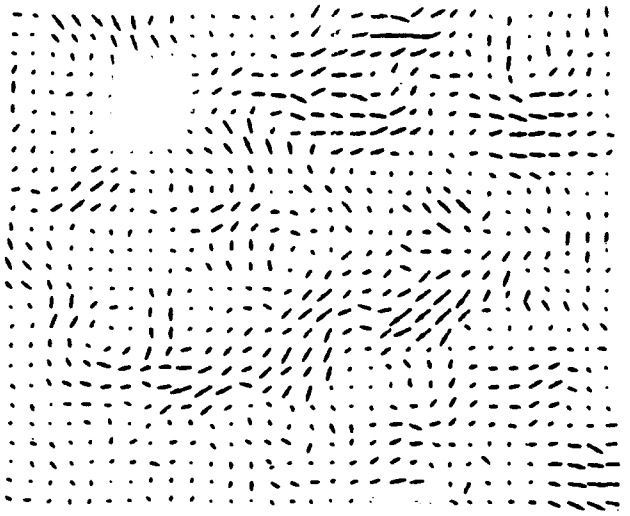

Figure 7: Sector of a flow field behind a grid determined with an evaluation system utilizing an electrically addressable SLM

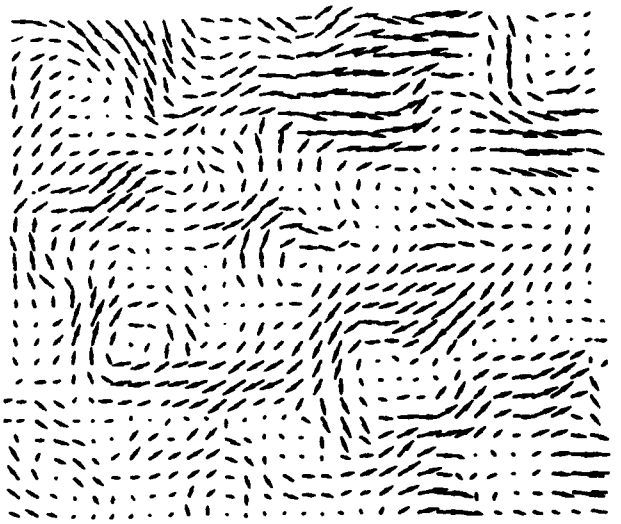

Figure 8: Same sector as in figure 7, but now evaluated with an evaluation system utilizing the optically addressable SLM

5. EXAMPLES OF DIFFERENT APPLICATIONS

The new evaluation system was utilized to evaluate PIV recordings of different measurement campaigns performed at DLR Göttingen. The following figures show the results of a flow field behind a grid, behind a circular cylinder in cross flow, above a NACA 0012 airfoil, and the flow field behind a car model. It is emphasized that the displayed results are raw data, i. e. they are not filtered or smoothed.

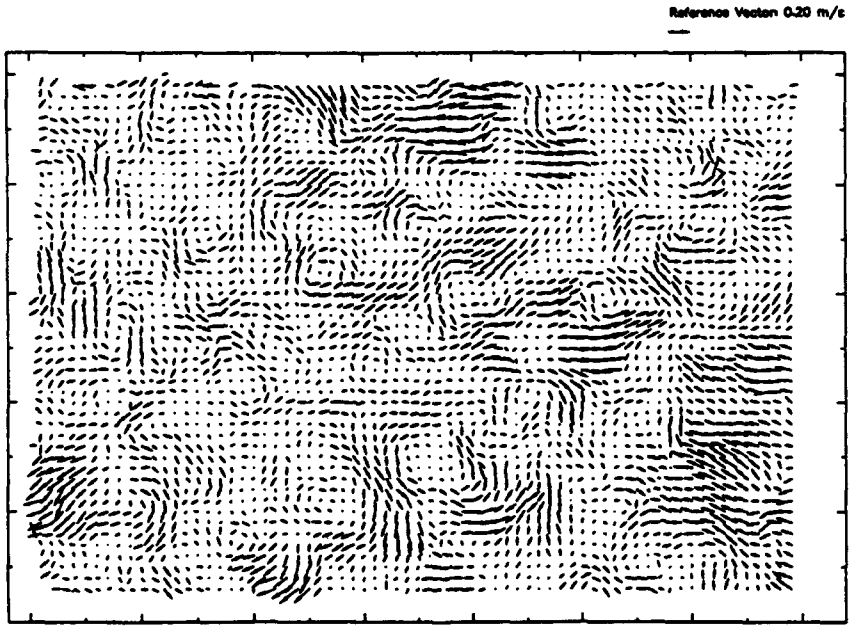

Figure 9: Turbulent flow field behind a grid, U_∞ = 10 m/s, mean flow velocity subtracted. Turbulence level 0.46%, size of observation field 10 x 15 cm², (peak detection and post processing with the workstation based system of DLR)

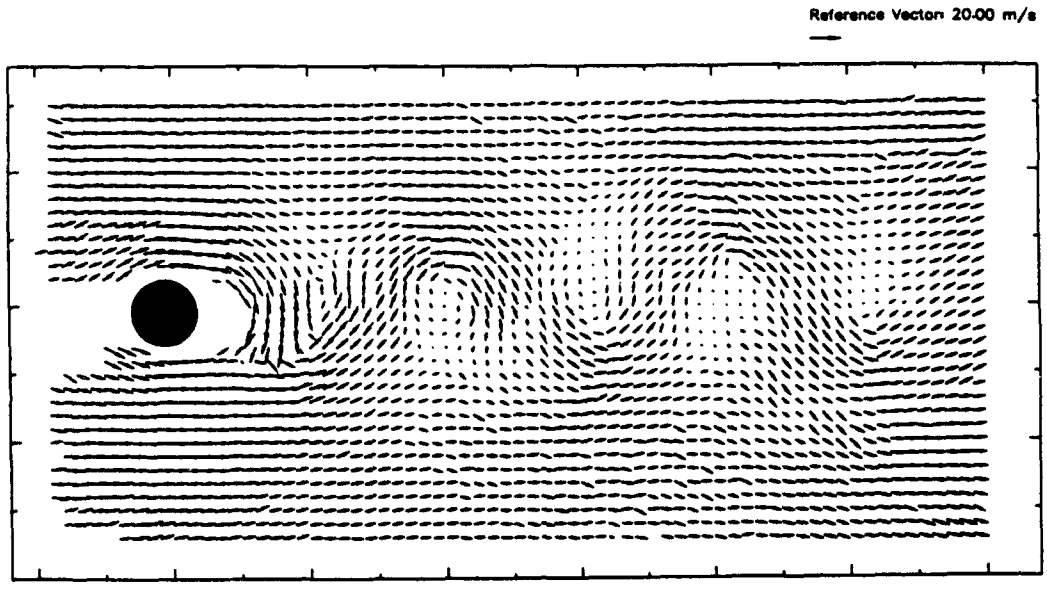

Figure 10: Wake behind a circular cylinder in cross flow; Re = 20000, U_{∞} = 15 m/s, u_{ref} = 8.7 m/s subtracted, diameter of cylinder 2 cm, (peak detection and post processing with the workstation based system of DLR)

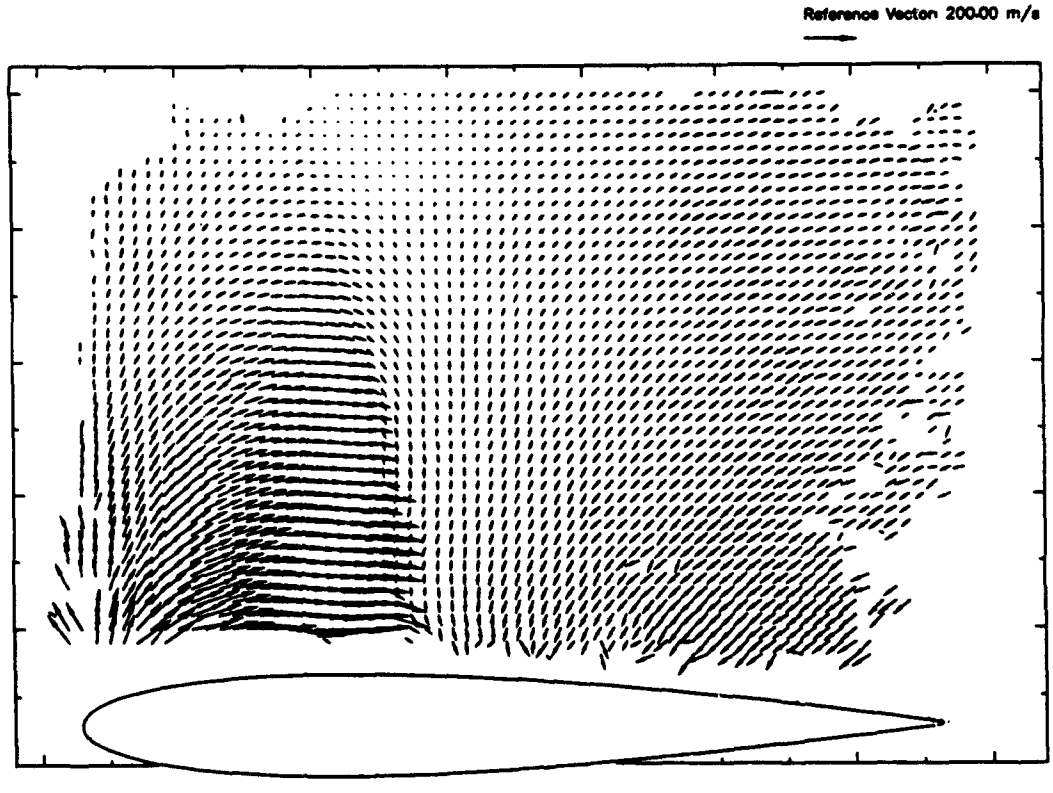

Figure 11: Flow field above a NACA0012 airfoil (from [6]), Ma = 0.75, angle of attack: 5°, u_{ref} = 311 m/s subtracted, chord length of airfoil = 20 cm, (peak detection and post processing with the workstation based system of DLR)

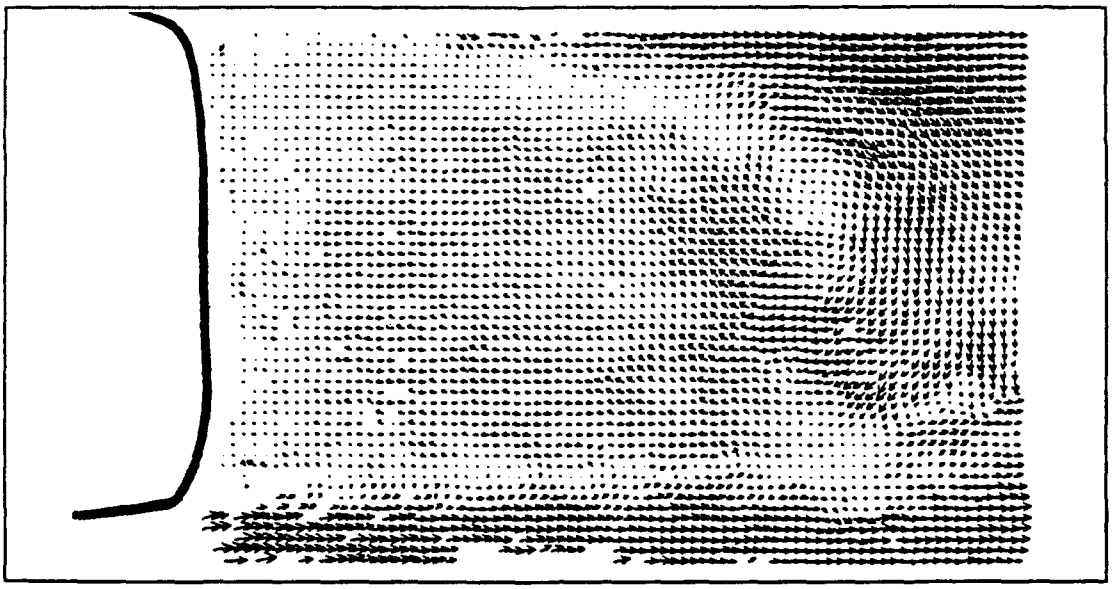

Figure 12: Flow field behind a car model (from [9]). U_∞ = 50 m/s, u_{ref} = 38 m/s subtracted, size of observation field 20 × 31 cm², (peak detection and post processing with the PC based system of Jenoptik, evaluation time ≈ 10 min)

7. CONCLUSION

The results presented in this paper show that the all optical autocorrelator with the optically addressable spatial light modulator is a very suitable tool for the evaluation of photographical PIV recordings. The first major advantage of the system is the short time which is necessary to determine the ACF. Due to the fact that the ACF can be determined almost with video frequency the need for faster but nevertheless exact and general peak searching algorithms in the ACF plane now becomes increasingly important. The second advantage of our set up is the enhanced displacement and therefore velocity resolution (see figure 7 and 8), which allows to detect even small velocity fluctuations and very weakly pronounced structures in the flow.

REFERENCES

[1] Keane, R. D., Adrian, R. J., "Optimization of Particle Image Velocimeters", L.I.A., Vol 68, ICALEO (1989), pp. 141 - 160

[2] Prasad, A. K., Adrian, R. J., Landreth, C. C., Offutt, P. W. "Effect of resolution on the speed and accuracy of particle image velocimetry interrogation", Experiments in Fluids, 13, (1992), pp. 105 - 116

[3] Lee, J., Farrel, P. V., "Particle Image Velocimetry measurements of IC engine valve flows", pp. 25.4.1, Conference Proceedings of the Sixth International Symposium on Application of Laser Techniques to Fluid Mechanics, July 20th - 23rd, 1992, Lisbon

[4] Morck, T., Andersen, P. E., Westergaard, C. H., "Processing speed of photorefractive optical correlators in PIV-processing", pp. 27.2.1., Conference Proceedings of the Sixth International Symposium on Application of Laser Techniques to Fluid Mechanics, July 20th - 23rd, 1992, Lisbon

[5] Vogt, A., Raffel, M., Kompenhans, J., "A comparison of optical and digital evaluation of photographic PIV recordings"; pp. 27.4.1., Conference Proceedings of the Sixth International Symposium on Application of Laser Techniques to Fluid Mechanics, July 20th - 23rd, 1992, Lisbon

[6] Efron, U., Grinberg, J., Braatz, P. O., Little, M. J., Reif, P. G., Schwartz, R. N., "The silicon liquid-crystal light valve", J. Appl. Phys. 57 (1985), pp. 1356 - 1368

[7] Ashley, P. R., Davis, J. H., "Amorphous Silicon Photoconductor in a Liquid Crystal Spatial Light Modulator", Appl. Opt. 26 (1987), pp. 241 - 246

[8] Gabor, A. M., Landreth, B., Moddel, G., "Integrating mode for an optically addressed spatial light modulator", Appl. Opt. 37 (1993), pp. 3064 - 3067

[9] Reichel, F., Löffler, W. "Optical space frequency analysis for real-time pattern recognition", J. of Optoelectronics, 1994 (in press).

[10] Goodman, J. W., "Introduction to Fourier Optics", Mc Graw Hill, 1986

[11] Höcker, R., Kompenhans, J., "Some technical improvements of Particle Image Velocimetry with regard to its application in wind tunnels", Proceedings of the International Congress on Instrumentation in Aerospace Simulation Facilities- ICIASF '89, Sept. 18 - 21, 1989, pp. 545-554

[12] Raffel, M., Kompenhans, J., "PIV mesurements of unsteady transonic flow fields above a NACA 0012 airfoil", Proceedings of the 5th International Conference on Laser Anemometry - Advances and Applications, Veldhoven, The Netherlands, 23rd - 27th August 1993, SPIE Proceedings Volume 1987, pp. 527 - 534

[13] Vogt, A., Raffel, M., Kompenhans, J., Hack, A., "Particle Image Velocimetry für instationäre Strömungen in großen Windkanälen", Tagungsband Lasermethoden in der Strömungsmeßtechnik, 2. Fachtagung 1993, 14. - 16.9.93, PTB Braunschweig, pp. 33.1-33.3

A new paradigm for Particle Tracking Velocimetry, based on graph-theory and pulsed neural network

Dominique DEROU - Laurent HERAULT
LETI - (CEA-Technologies Avancées)
DSYS / SCSI - CENG-17 rue des Martyrs
38054 - Grenoble Cedex 9 - France

1 Introduction

The Particle Tracking Velocimetry (PTV) technique works by recording, at different instances in time, positions of small tracers particles following a fluid flow and illuminated by a sheet, or pseudo sheet, of light. It aims to recognize each particle trajectory, constituted of n different spots and thus determine each particle velocity vector. In the present paper, we devise a new method, taking into account a global consistency of the trajectories to be extracted, in terms of visual perception and physical properties. It is based on **a graph-theoretic formulation of the particle tracking problem** and the use of **an original neural network, called pulsed neural network.**

1.1 Background

Particle tracking is one of the simplest and most powerful methods of quantitative visualization. It is among the few capable of providing instantaneous maps of magnitude, over extended areas, such as velocity or vorticity. Some reviews on particle tracking velocimetry (PTV) describe the principles and applications of many types of PTV ([Adr91], [Hes88], [Agu87], [Adr86], [Buc92]), which are applicable from slow to supersonic flows. Various methods have been developped for PTV, using classical image processing techniques : estimation of the particle's mean displacement during two images and search of the new position of the particle on the following image thanks to the estimated velocity [Nis89], minimization of an objective function [Cha85], point-by-point matching by statistical analysis of displacement vectors [Has91], [Gra89]. It appears that those current methods present several drawbacks :

- the algorithms use image processing techniques like correlation or search-tree, which imply a high sensitivity to noise and a low speed of computation,
- they provide degraded results. As a consequence, a post-processing step is necessary to suppress errors.

Obviously, improvements can be obtained by using more sophisticated image processing techniques, so as to use, for instance, the information present in the original image, with a higher efficiency. Several papers express some feature grouping problem as combinatorial optimization problems and try to minimize a global cost function including local constraints ([Par89], [Sha88], [Moh92], [Den89], [Pet91], [Gyu91], [Yui91]). A major drawback is that all these methods need to be parameterized. Moreover, their computational time is so great that they are only applied to small size problems.

1.2 A new formulation for the particle tracking velocimetry problem

Our algorithm consists of two distinct processing stages :

1. Creation of potential features extracted from the original image, thanks to metric constraints imposed by the image acquisition process, and determination of a matrix representing mutual consistency between potential features, by use of perceptual grouping notions and physical properties of the studied phenomena.
2. Extraction of a set of features satisfying each constraint in terms of global consistency, through a global constraints satisfaction problem and a pulsed neural algorithm.

First and foremost, some points identified as particle spots are extracted from the original numerical image. The corresponding points list will be used to generate a certain number of potential features. Each feature represents a potential particle trajectory. Generation of such potential features (or trajectories) uses some *a*

priori knowledge related to the experimental acquisition process (namely : number of points making up a trajectory, points layout, fluid maximal speed). At this stage, numerous errors can exist. Our aim is to obtain a solution without these errors. Our method makes use of perceptual grouping notions and physical properties of the fluid, like viscosity, speed, Reynolds number, so as to define consistency coefficients between each pair of potential trajectories.

The particle tracking problem can be formulated as a global constraints satisfaction problem. One defines a graph, in which vertices are potential features, and each edge between two vertices is weighted by a binary incompatibility coefficient between the corresponding features. Incompatibility coefficients between features are defined thanks to perceptual considerations and physical incompatibilities on the image. The incompatibility graph points out which particle trajectories are mutually incompatible. It provides hard constraints on the features subset to be selected. Another coefficient, called consistency coefficient, is defined between any two features, through physical properties on fluid. A function of all the potential trajectories measures the global consistency of any subset of potential features labelled as particles. Such a function is called global consistency function. The problem is then to select the subset of potential features which maximizes this global consistency function, while satisfying all hard incompatibility constraints. In a word, the solution must be the best independent set of the incompatibility graph, maximizing the global consistency function. Therefore, the particle tracking problem is a global constraints satisfaction problem.

We will devise a neural method to solve this global constraints satisfaction problem, using a new family of neural network : the pulsed neural network.

2 Pulsed neural network

2.1 Formulation of the global constraints satisfaction problem

Let us define a graph $C = (V, E)$, with a vertices set $V = \{0, 1, \ldots, N\}$ and an edge set $E = \{ij \mid (i,j) \in < 1, N >^2, i \neq j\}$. The adjacency matrix of C, $A_C = (c_{ij})_{(i,j)\in<1,N>^2}$, is a binary matrix and represents compatibility ($c_{ij} = 1$) or incompatibility ($c_{ij} = 0$) between features i and j. Let $\bar{C}$ be the incompatibility graph, corresponding to C, such that its adjacency matrix is $A_{\bar{C}} = (\bar{c}_{ij})_{(i,j)\in<1,N>^2}$, with $\bar{c}_{ij} = 1 - c_{ij}$.

Let $Q = (q_{ij})_{(i,j)\in<1,N>^2}$ be a consistency matrix, which measures a real consistency value between features i and j. We define $\vec{p} = (p_1, \ldots, p_N)$ a vector in which $p_i = 1$ if i is retained in the final solution and $p_i = 0$ otherwise. Given these definitions, we define a quality function $E(\vec{p}) = \sum_{i=1}^{N} \sum_{j=1}^{N} q_{ij} \cdot p_i \cdot p_j$.

From a mathematical point of view, the global constraints satisfaction problem that we need to solve is :

$$\text{finding } \vec{p} \text{ maximizing } E(\vec{p}) = \sum_{i=1}^{N} \sum_{j=1}^{N} q_{ij} \cdot p_i \cdot p_j$$
$$\text{while satisfying : } \begin{cases} \forall i,\ p_i \in \{0,1\} \\ \forall i, j,\ p_i = p_j = 1 \Longrightarrow \bar{c}_{ij} = 0 \end{cases} \quad (1)$$

or, in other words : finding $\vec{p}$ such that $\{p_i \mid p_i = 1\}$ is an independent subset of $\bar{C}$ and such that $\vec{p}$ maximizes $E(\vec{p})$.

2.2 The pulsed neural network model

The mathematical model of an artificial neural network is composed of two principal components : neurons and synaptic weights T_{ij} between neurons. T_{ij} represents the synaptic connection strength between neurons i and j. Each artificial neuron has an input u_i, called potential, and an output p_i. The gain function $p_i = f(u_i)$ used is a step function, named Mc Culloch-Pitts neuron model :

$$\begin{cases} p_i = 1 \text{ if } u_i > 0 \\ p_i = 0 \text{ if } u_i < 0 \end{cases}$$

The vector $\vec{p} = (p_i, \ldots, p_N)$ represents the state of the neural network. Our artificial neural network consists of recursive neurons which are auto-connected ($T_{ii} \neq 0$) and potentially fully inter-connected with symmetric weights ($T_{ij} = T_{ji}$). The potential temporal evolution is given by :

$$u_i(t+1) = F(p_1(t), \ldots, p_{i-1}(t), p_i(t), p_{i+1}(t), \ldots, p_N(t))$$

Such a network is a variant of the Hopfield model ([Hop82]).

A neuron is ascribed to each vertex of the incompatibility graph $\bar{C}$. A neuron belonging to the final solution will have its output equal to 1 in the final state vector. A neuron with an output equal to 0 will not belong to the final solution. Initially, all ouputs are set equal to 0 and all inputs are randomly generated with negative values. So as to speed up convergence time, the potential u_i are bounded. Due to the small enough bounding interval, every potential variation induces a state shift of the value p_i.

The evolution equation is defined so that to maximize the quality function $E(\vec{p})$, while satisfying all hard constraints. The problem is to find an independent set of the incompatibility graph $\bar{C}$ that maximizes the quality function $E(\vec{p} = \sum_{i=1}^{N} \sum_{j=1}^{N} q_{ij} \cdot p_i \cdot p_j)$. For

this reason, an updated neuron must have a transformation that increases the quality function. A neuron, whose state is inactivated ($p_i = 0$) just before its updating, must be shifted to $p_i = 1$ only if its new state contributes towards quality function increase. Furthermore, so as to obtain an independent subset of the incompatibility graph, we impose that, if an inactivated neuron i is updated to $p_i = 1$, then all the activated neurons j incompatible with it (such that $\bar{c}_{ij} = 1$ and $p_j = 1$) will be unfired. Indeed, if a neuron is updated to 1, it infers that this neuron is regarded as belonging to the final solution. In order to obtain an independent set for the solution, all neurons activated and incompatible with this neuron must be disactivated.

Consider that neuron i, such that $p_i = 0$, is updated. It will be shifted to 1, and the activated neurons incompatible with it will be shifted to 0, if these transformations induce an increase of the quality function :

Before the transformations : $p_i(t) = 0$

After the transformations :
$\begin{cases} p_i(t+1) = 1 \\ \forall j \text{ such that } p_j(t) = 1 \text{ and } c_{ij} = 1,\ p_j(t+1) = 0 \end{cases}$

Now we determine the expression of the quality function variation, when these neurons state transformations are performed :

$$\begin{aligned} \Delta E_i(t+1) &= -2 \sum_{\{s|\bar{c}_{is}=1\}} \sum_{j\neq s\ ,\ j\neq i} q_{js}.p_j(t).p_s(t) \\ &\quad +2 \sum_{j\neq s\ ,\ j\neq i} q_{ij}.p_j(t) - \sum_{\{s|\bar{c}_{is}=1\}} p_s(t) + 1 \end{aligned}$$

The equation evolution will use this relation. The evolution equation is :

$$\begin{cases} \Delta u_i(t+1) &= (1-p_i(t)).max(0, \Delta E_i(t+1)) \\ &\quad -p_i(t).\delta(\Delta\vec{u},t).k(\vec{p},i) \\ \forall j \neq i\ ,\ \Delta u_j(t+1) &= -\bar{c}_{ij}.(1-p_i(t)). \\ &\quad max(0, \Delta E_i(t+1)) \end{cases}$$

The functions used in the previous relation are defined by :

- $\delta(\Delta\vec{u},t)$: pulsation function defined by :

$$\delta(\Delta\vec{u},t) \rightarrow \begin{cases} 1 & \text{if } t \ mod\ N = 0 \text{ and} \\ & t > 0 \text{ and } \forall i,\ \Delta u_i(t) = 0 \\ 0 & \text{otherwise} \end{cases}$$

- $k(\vec{p},i)$: several possibilities can be used for this inhibitory function. Its purpose is to inhibit some activated neurons, in an attempt to test another solution. Two possibilities are :
  - Random selection of X activated neurons ($p_i(t) = 1$), which are disactivated at time $t+1$ ($k(\vec{p},i) = \infty$ and so $p_i(t+1) = 0$)
  - Determination of the mean degree of the incompatibility graph $\bar{C}$. Disactivation of all nodes whose degree is higher than this mean degree. Thus, the inhibitory function intends to inhibit all nodes which display an "*a priori* bad" degree.

The dynamic system evolution devised consists, in the first term, in updating neurons whose output is equal to 0. An inactivated neuron will be activated if its state shift increases the quality function. Since, at the same time, all activated neurons incompatible with the updated neuron are shifted to 0, hard constraints are imperatively guaranteed. The use of the first term would be sufficient to provide a solution satisfying all hard constraints, i.e. an independent set. This network converges towards a solution satisfying all constraints in a limited computational time. At convergence, for all neurons i, $\Delta u_i = 0$. At this time, the network has reached a local "maximum".

Notwithstanding, the problem is to find a near optimal solution, that we define as maximizing the quality function $E(\vec{p})$. The network must have the ability to find several solutions all satisfying the constraints, in order to choose the one with highest quality function value. The network must be able to leave a local "maximum" and converge towards a new solution. The pulsation function and the inhibitory function (second term of the evolution equation) will enable the network to converge to a new feasible solution. Initially the pulsation function $\delta(\Delta\vec{u},t)$ is set equal to 0, until each neuron potential variation Δu_i becomes null. Then $\delta(\Delta\vec{u},t)$ is activated to 1 during one complete updating of the N neurons. During this pulsation phase, the network modifies completely its vector state. The second term of the equation comes in. The idea is to inhibit some of the activated neurons. Previously, we present two possibilities for the inhibitory function. After the pulsation, $\delta(\Delta\vec{u},t)$ is set to 0 again. The network, conducted by the first term of the evolution equation, can converge once again to another feasible solution.

The network can be viewed as a network composed of Potts model neurons. A Potts model is a generalization of the two-state Ising model to an arbitrary number of discrete states [Fis91]. In our case, a Potts neuron, i.e. a vector, corresponds to each variable p_i. This vector has a components number equal to the degree of vertex i in the incompatibility graph $\bar{C}$ plus one. Since the running mode chosen is an asynchronous by bloc mode, at each step of the iterative process, all components of Potts neuron i are simultaneously updated.

3 A combinatorial optimization formulation for the particle tracking problem

3.1 Extraction of potential features

The basic information that our particle tracking algorithm needs is a set of potential features extracted from the original image. In a first module, our analysis starts with a classical point detection process. It involves the recognition of each spot constituting a virtual particle trajectory, by applying computation of local histograms, determination of thresholds thanks to histograms, thresholding of the original image, connexity analysis, and computation of the centroïd of each particle spot.

The second module receives as input a list of points and their respective attributes (here, the grey level). Its purpose is to determine a list of potential features. It uses *a priori* knowledge (metric constraints) coming from the experimental process. This knowledge can be expressed by : "a potential feature is constituted of n distinct and consecutive spots, laying on a parameterized curve and verifying some metric relations". For instance, in our fluid mechanics application, features are composed of three spots, aligned in a fixed length ratio. The method uses a local search tree for each point. This tree is defined by the possible matches between this point and the others. It can be pruned by using local constraints corresponding to the *a priori* above-mentionned knowledge. By this way, a list of potential features satisfying the experimental conditions is obtained. The potential trajectories identified are directed ; we obtain vectors. Obviously, local constraints can lead to select completely erroneous features. What follows seeks to detect and suppress those erroneous trajectories. From an original image (Fig. 1), the extracted points are presented on Fig. 2. Fig. 3 depicts all potential trajectories created after the processing stage.

3.2 Notion of consistency and incompatibility between features

Many authors have emphasized the capacity of the human visual system to complete some components of an image, in order to get features, edges, regions, by using local spatial constraints and satisfying a global consistency in the image, like in the illusory contours examples. We intend to use this observation in order to detect and suppress some of the features, which are radically inconsistent with the flow motion. Furthermore, some physical properties of the observed phenomena can be used (like fluid viscosity).

We define consistency and incompatibility coefficients between any two features. The consistency coefficient is the higher as feature pair is consistent with the fluid motion in its local environment. The binary incompatibility coefficient will indicate the strict incompatibility between features. Our goal is to extract and quantify, in both coefficients, the features ability to induce a continuity feeling beyond their physical limits.

3.2.1 The consistency coefficient

Let i and j be two potential features. We want that the interaction between these features satisfies the perceptual knowledge on the flow. If the pair of features (i, j) contributes to the perception of the global movement, the coefficient c_{ij} must be high. Otherwise their interaction must be low. This coefficient is a consistency measure. We use some Gestallt principles so as to express the components of a consistency coefficient (our underlying goal is to keep the interpretaion as simple as possible in a Gestallt sense).

Similarity : similar elements are grouped together.
Neighbouring particles have about the same speed. In fluid mechanics, this observation is the higher as the fluid viscosity is great. The similarity coefficient $c_{ij}^{similarity}$ constrains particles i and j to have a similar speed. We devise the following expression :

$$\forall j \in V(i),\ c_{ij}^{similarity} = 1 - \frac{\Gamma(\Theta_i, \Theta_j)}{\pi/2}$$

with :

Θ_i and Θ_j : orientation of features i and j,
$V(i)$: neighbourhood of feature i,

$$\Gamma(b,a) = \begin{cases} |\, a-b \,| & \text{if } |\, a-b \,| \leq \frac{\pi}{2} \\ |\, a-b-\pi \,| & \text{if } \frac{\pi}{2} < a-b \leq \pi \\ |\, a-b+\pi \,| & \text{if } -\pi \leq a-b < -\frac{\pi}{2} \end{cases}$$

The similarity coefficient quantifies the direction similarity of two particles. Its value belongs to $[0, 1]$. The coefficient will be null for perpendicular trajectories, equal to 1 if the trajectories are collinear, and will linearly vary according to the angular difference of the particle orientations.

Proximity : elements that are close together tend to be grouped together.
Only a neighbourhood of each feature must be taken into account. Otherwise, particle influence over another particle decays with distance. The proximity coefficient has to take into account the proportionality between the influence the coefficient must have and

the distance between features. The proximity coefficient must vanish smoothly as the two features are farther from each other. We choose, as in [Her93] :

$$c_{ij}^{proximity} = \exp - \frac{d_{ij}^2}{2.\sigma_d^2}$$

where d_{ij} is the distance between the features i and j, and σ_d is a fraction of the standard deviation of all the distances over the image.

Formulation of the consistency coefficient :
We define the consistency coefficient as a combination of the coefficients just defined :

$$q_{ij} = \lambda_1 . c_{ij}^{similarity} + \lambda_2 . c_{ij}^{proximity}$$

This sum gives a weighted measure of the consistency of features pair. Parameters λ_1 and λ_2 are related to the physical properties of the fluid. The more two features have high consistency, the more salient they are. Consistency coefficients form a consistency matrix $Q = (q_{ij})_{(i,j)\in<1,N>^2}$, with $q_{ij} \in [0,1]$.

3.2.2 The incompatibility coefficient

The incompatibility coefficient establishes hard constraints between potential features. Indeed, incompatibilities can exist between some features. Two strict conditions induce incompatibility :

- **Sense** : two neighbouring features cannot have opposite senses.
- **Common point** : two features cannot share a common spot.

Sense :
The sense coefficient imposes that particles i and j must have strictly the same sense. This coefficient is calculated by :

$$\bar{c}_{ij}^{sense} = D(i,j)$$

where: $D(i,j) = \begin{cases} 0 & \text{if } \vec{i}.\vec{j} \geq 0 \\ 1 & \text{if } \vec{i}.\vec{j} < 0 \end{cases}$

Common point :
Two features cannot share a common spot.

$$\bar{c}_{ij}^{common\ point} = \begin{cases} 1 & \text{if i and j share a common point} \\ 0 & \text{otherwise} \end{cases}$$

Formulation of the incompatibility coefficient :
We define the incompatibiliy coefficient as the maximum of the sense coefficient and the common point coefficient. Thus, the incompatibility coefficient will belong to $\{0,1\}$ and will be equal to 0 only if both hard constraints are satisfied :

$$\bar{c}_{ij} = \max\left(\bar{c}_{ij}^{sense}, \bar{c}_{ij}^{common\ point}\right)$$

Incompatibility coefficients form an incompatibility matrix $\bar{C} = (\bar{c}_{ij})_{(i,j)\in<1,N>^2}$, with $\bar{c}_{ij} \in \{0,1\}$.

3.3 A combinatorial optimization statement

A consistency matrix and an incompatibility matrix have been generated. At this stage, we intend to select the most consistent features, satisfying hard constraints. The solution of the particle tracking problem is consequently a subset of the potential trajectories, in which all "erroneous trajectories" have been detected and suppressed. Those "erroneous trajectories" are features which display a low consistency with their local environment or which do not satisfy the constraints inherent in the problem. For this reason, the problem can be expressed as finding a subset of potential features maximizing a quality function representing the global consistency of the image, and satisfying all hard constraints. If $\vec{p} = (p_1, \ldots, p_N)$ is a vector in which $p_i = 1$ if the trajectory i is a good one, representing a real particle, or $p_i = 0$ if it is an erroneous one, the problem can be expressed by (1). This global constraints satisfaction problem is solved by our previously described pulsed neural network.

4 Experimental results

The algorithm described in the previous section has been applied to many series of fluid mechanics images. The experimentation that has provided these images was carried in a wave tank. A uniform intensity incoherent white light source was used. A mechanical chopper has enabled to pulse the continuous light to obtain stroboscopic illumination. The fluid has previously been sowed with tracer particles, which scatter light into a numerical photographic system. A trajectory is made up of three consecutive and aligned spots. The directional ambiguity is overcome by using particles tagging pulse : the duration between the two first pulses is twice the duration between the two following pulses.

Figs. 1, 2 and 3 show successive processing results. Fig. 4 presents the final result, obtained after neural network processing. Experiments were performed on a standard SUN SPARC 10 workstation. As inhibitory term, we have chosen to randomly pulse 15 neurons. The results are calculated with 30 pulsation phases.

The algorithm we propose is quite rapid : the processing has needed about 3 minutes on a SUN SPARC 10 workstation. Besides, it is far quicker than all classical velocimetry methods. The result proposed in Figs. 4 testifies to the great visual quality of the algorithm. Regardless of the image tested, the algorithm recognizes most of the particles seeded in the fluid. A statistical description of the recognized particles has showed that, among all particles recognized, about 97% were right particles. The quality of the results provided by our algorithm is undoubted. However, we must observe that some particles have not been recognized, more particularly in vortex center. The main reason is that particles speed is so slow in vortex center that corresponding positions spots are superimposed and cannot be identified as individual spots.

It is very difficult to quantify the performance of a particle tracking algorithm on real images. The experiment presented here is therefore qualitative. A quantitative comparison has to be done with numerical simulations provided by finite-elements based methods. Such comparisons are currently being done. Thanks to them it will be possible to quantify the performance and limitations of our algorithm.

5 Conclusion

In this paper, we have proposed a new paradigm for the feature grouping problem, with special emphasis on the problem of particle tracking.

First and foremost, we suggested a mathematical encoding of the problem, which takes into account metric constraints specific to the problem, perceptual properties of the image and physics properties of the studied phenomena. Second, we proposed a new statement of the particle tracking problem as a global constraints satisfaction problem. This new formulation has the advantage to take into account :

- available informations on the physical nature of the experiment and of the studied phenomena,
- perceptual informations on the original numerical image.

Endly, in order to solve this combinatorial optimization problem, we devised an original neural network, named pulsed neural network. The advantages of this new neural network are :

- The pulsed neural network needs no coefficient. Accordingly it has a completely black-box behaviour for the user.
- When the network has converged, the solution found is guaranteed to be a feasible solution, satisfying all constraints.
- The network regularly puts forward a feasible solution. It is possible to impose a computational time limit.
- The iterations number necessary to converge is much smaller than most of other methods.

It is clear from the real experimental results proposed that our algorithm provides very good solution. Nevertheless realistic simulations must be investigated in order to quantify the performances and limitations of our algorithm. In the future, we plan to continue to try to improve our method so as to be able to treat any type of fluid flows (laminar, vortex). We also plan to devise and implement a regularization procedure, based on computer vision and phenomena physics properties, in order to obtain velocity and vorticity maps of the flow. Finally we intend to extend the approach advocated in this paper to other vision problems.

6 Acknowledgements

The authors would like to thank J.M. Dinten for many valuable discussions, as J.J. Niez (CEA-CESTA) and P. Puget. They are grateful to Y. Dolias (CEA-DRN), who provided them with fluid mechanics images, and G. Cognet (CEA-DRN) for helpful conversations on fluid mechanics theory.

References

[Adr86] R.J. Adrian. Multi-point optical measurements of simultaneous vectors in unsteady flow–A review. *Int. J. Heat Fluid Flow*, 23:261–304, 1986.

[Adr91] R.J. Adrian. Particle-imaging techniques for experimental fluid mechanics. *Annual Review of Fluid Mechanics*, 23:261–304, 1991.

[Agu87] J.C. Agui and J. Jimenez. On the performance of particle tracking. *Journal of Fluid Mechanics*, 185:447–468, 1987.

[Buc92] P. Buchhave. Particle image velocimetry–Status and trends. *Experimental Thermal and Fluid Science*, 5:586–604, 1992.

[Cha85] T.P.K. Chang, A.T. Watson and G.B. Tatterson. Image processing of tracer particle motions as applied to mixing and turbulent flow–I.The technique. *Chemical Engineering Science*, 40(2):269–275, 1985.

[Den89] B. Denby and S.L. Linn. Status of hep net research in the usa. *Computer Physics Communications*, 57:297–300, 1989.

[Fis91] K.H. Fisher and J.A. Hertz. *Spin glasses*. Cambridge University Press, 1991. ed. D. Edwards.

[Gra89] I. Grant and A. Liu. Method for the efficient incoherent analysis of particle image velocimetry images. *Applied Optics*, 28(10):1745–1748, 1989.

[Gyu91] M. Gyulassi and M. Harlander. Elastic tracking and neural network algorithms for complex pattern recognition. *Computer Physics Communications*, 66:31–46, 1991.

[Has91] Y.A. Hassan and R.E. Canaan. Full-field bubbly flow velocity measurements using a multiframe particle tracking technique. *Experiments in Fluids*, 12:49–60, 1991.

[Her93] L. Herault and R. Horaud. Figure-ground discrimination: a combinatorial optimization approach. *IEEE Transactions on Pattern Analysis and Machine Intelligence*, 15(9), 1993.

[Hes88] L. Hesselink. Digital image processing in flow visualization. *Annual Review of Fluid Mechanics*, 20:421–485, 1988.

[Hop82] J. Hopfield. Neural networks and physical systens with emergent collective computationnal abilities. *Proc. of National Academy of Science of USA*, 79:2554–2558, 1982.

[Moh92] R. Mohan and R. Nevatia. Perceptual organization for scene segmentation and description. *IEEE Transactions on Pattern Analysis and Machine Intelligence*, 14(6):616–635, 1992.

[Nis89] K. Nishino, N. Kasagi, M. Hirata. Tree-dimensional particle tracking velocimetry based on automated digital image processing. *Transactions of the ASME*, 11:384–391, December 1989.

[Par89] P. Parent and S.W. Zucker. Trace inference, curvature consistency and curve detection. *IEEE Transactions on Pattern Analysis and Machine Intelligence*, 11(8):823–839, 1989.

[Pet91] C. Peterson and T.Rognvaldsson. An introduction to artificial neural networks. lectures given at the 1991 CERN School of Computing, Ystad, Sweden, July 1991.

[Sha88] A. Sha'ashua. Structural saliency: the detection of globally salient structures using a locally connected network. Master's thesis, dept. of Applied Math., Weizmann Institute of Science, Rehovot, Israel, 1988.

[Yui91] A.L. Yuille, K. Honda and C. Peterson. Particle tracking by deformable templates. In *Proc. Int. Joint Conference on Neural Networks, Seattle, WA*, volume 1, pages 7–12, 1991.

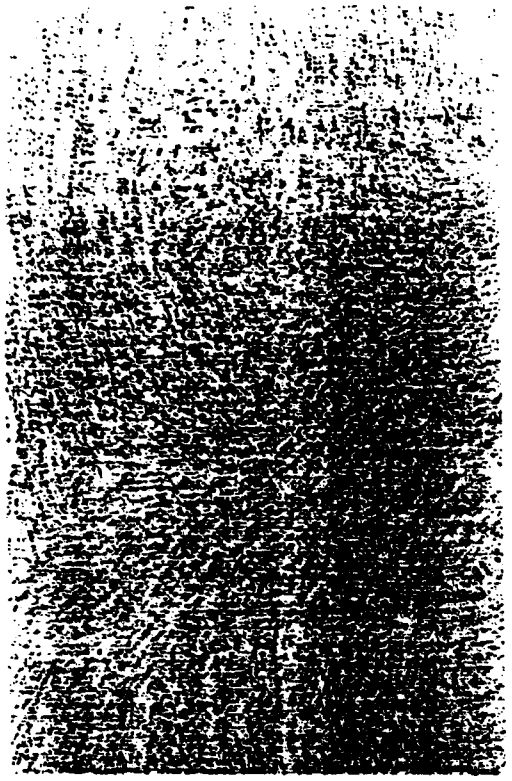

Figure 1: A particle tracking image of 1500*900 pixels.

Figure 2: Set of points extracted. 11844 spots have been extracted from the original image.

Figure 3: Potential trajectories extracted after pre-processing. 3808 potential features have been created.

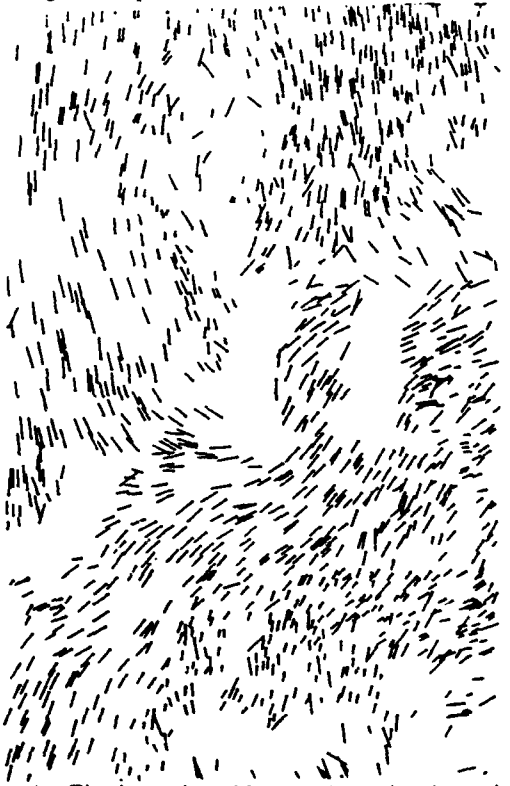

Figure 4: Final result. 1341 trajectories have been recognized.

THE APPLICATION OF THE NEURAL NETWORK TECHNIQUE TO THE ANALYSIS OF PARTICLE TRACKING (PIV) IMAGES OBTAINED IN FLOWS WITH A DIRECTIONAL AMBIGUITY.

I Grant , X Pan and A Aroussi*,
Fluid Loading and Instrumentation Centre,
Heriot-Watt University, Edinburgh, UK
* Department of Mechanical Engineering,
University of Nottingham.

SUMMARY.

The development and use of a multi layer, neural network in the analysis of low image density PIV images using the particle tracking methodology is described. The images carry a time signature, or 'tag', in order that the flow direction may be determined unambiguously by the net.

The application of the net is demonstrated through the analysis of flow images obtained from both simulations and experimental data. The first category of data allowed an assessment of the performance of the net to be made.

1. INTRODUCTION.

An important branch of computer science which has seen rapid development in the last two decades is the neural network method. The inherent parallelism of the method has meant that it has acted as the inspiration for hardware an software developments revolutionising complex task analysis. An area where it has found particular success is in pattern recognition and motion tracking. This makes it a particularly attractive technique for the analysis of PIV images obtained in the particle tracking mode.

Previously published work by the authors (Grant and Pan (1993), (1994))and others (Cenedese (1992)) has demonstrated that the neural method offers significantly improved performance in matching multiple image of flow following particles over earlier methods based on statistical windowing procedures .

The present paper describes an improved, four layer neural net. The net could analyse 'tagged' images where the direction of the flow was determined a pulse coding strategy (Grant and Liu (1990)). The first layer acted as an input buffer, the second layer acted as an code interpreter to determine direction. The third layer acted as a filter, or selection module, where an assessment of the accumulating memory of the flow was used to provide broad band filtering. The fourth layer acted as narrow band filter constructed from a knowledge of the local flow conditions or those in the immediate vicinity.

The four layer net was applied to two types of data image. The first were synthetic, produced by a Monte Carlo simulation of various flow types. Unidirectional flows with various levels of turbulence were considered. Flows with variable mean flow direction were also examined. The image density was treated as an independent variable to establish its effect on the reliability of the method. The success ration, sr, of this neural net was compared with that of the three layer net which lacked the directional discriminating layer.

The neural method is also applied to experimental data obtained in hydraulic studies involving vortex shedding and cavity flows. In each case estimates of the performance of the neural network were made and compared with that of an earlier net model.

2. THE NEURAL NETWORK MODEL.

In summary, the mathematical view of the brain considers it to be composed of processing elements, or neurons. Each neuron receives input signals from other neurons to which it is linked. The tranmission efficiency of the interconnecting link is treated as a multiplicative weight. The decision as to whether the neuron will generate an output signal is determined by an output operator or switch function. The switch function may be one of various types, such as binary, sigmoid or threshold linear. In this paper a binary output operator was used.

The multi-layer, neural net model used here acts as a competitive, adaptive filter which performs well in feature recognition tasks typical of PTV or PIDV. The model has developed from previous work by the authors in statistical windowing methods (Grant and Liu (1989), (1990)), parallel processing (Grant et al (1987)) and two and three layer neural networks (Grant and Pan (1993), (1994)). The present paper further develops the neural methodology by evolving a four layer adaptive net which can distinguish direction in flow images having a time signature.

3. THE COMPETITIVE, ADAPTIVE, NEURAL NETWORK FOR PTV IMAGE ANALYSIS.

3.1 Pre-Processing.

In common with procedures in general use the experimental images were pre-processed prior to image recognition and matching. The methods used were edge detection and image centroid centering. The edge detection algorithm was based on a Laplacian operator.

3.2 The Neural Network.

which generated a random distribution of *virtual* seed particle images into the synthetic flow. The seeds were then displaced, by the appropriate amount as calculated from the prescribed local flow conditions, to their new positions. Different sizes were assigned to the first and second images. The synthetic images all had 10% shot noise (unpaired particle images) added to them prior to processing.

The global images were then processed using the four layer net. In every case 100 images were generated to represent each flow condition and the processing ensemble averaged the appropriate parameters. A success ratio (sr) was calculated in each case by measuring the number of successful pairings as established by the software and the actual number of image pairs inserted on the synthetic image. The variation of the sr was compared in each case with the sr of the three layer neural net described in Grant and Pan (1994).

The image density was treated as an independent variable and the success ratio dependence on this parameter measured. The *image density parameter* was defined, following Adrian and Yao (1984), as $\frac{C \cdot \pi \cdot d_{max}^2}{4}$ where C is the mean number of particles per unit volume and d_{max} is the maximum possible displacement of the particle.

4.1 Flow with Superimposed Turbulence.

The conditions of virtual flow speed and (apparent) image capture magnification were adjusted to give a mean displacement between image centres of 10 pixels. The turbulence intensity components in the two orthogonal, in plane, directions were obtained from a uniform random distribution and added to the mean displacement vector.

Figure 2a shows typical flow simulation images generated for this case. The sr as a function of the turbulence intensity is seen in 2b while 2c shows the sr plotted against image density. A range of image types were examined covering low to high image density and a range of turbulence levels. The resulting sr values were also plotted as a surface and are shown in the isometric view Figure 2d.

The sr obtained from the three layer net described in Grant and Pan (1994) is also plotted in Figures 2b and 2c. The new four layer net is seen to perform more efficiently. This is because, as noted above, the additional constraint of size variation in image pair selection reduces the chances of erroneous pairing.

Figure 3a shows examples of the digital images generated in a flow with a systematic direction change. The sr as a function of the angular range is shown in 3b while the variation with image density is seen in Figure 3c. In this latter case the mean flow has a 40% angular change in direction over the global image. 10% noise and 10% turbulence have been introduced to the images in this case. Figure 3d shows an isometric projection of the sr surface as a function of the angular change and the image density. In this instance the new network performs significantly more efficiently than the three layer model, particularly at high image density and angular range.

Figure 4a shows the flow image produces when the direction is able to rotate though 360^{O} in the course of the global image. The success ratio is then plotted as a function of elliptical ratio and image density in Figures 4b and 4c respectively. The sr surface is plotted in Figure 4d. The larger angular gradients make the increased efficiency of the four layer network evident at all seeding densities.

4.2 The Interconnecting Weight Surfaces.

In each case the appropriate final interconnecting weights can be visualised as surfaces. The surfaces representing the weights between the second and third layers are plotted (Figures 2e, 3e and 4e) while typical (local) interconnecting surfaces between the third and fourth layers are also shown (Figures 2f, 3f and 4f).

The surfaces connecting the lower planes have shapes which are characteristics of the global flow. The surface 2e has a flat topped plateau shape. The size and curvature of the plateau is characteristic of the level of the flow turbulence. Surface 3e has a meniscus shape whose angular extent is determined by the range of angles in the input sets and whose upper area is, as in Figure 2e, determined by the turbulence present in the flow. 4e has a large upper plane of a multifaceted, disk like nature. This has been produced by a range of input sets. The large uniform surfaces indicates that this lower filter will not be an effective filter unless aided by a more discriminatory upper weight surface.

The interconnecting weights surfaces representing the connections between the third and fourth layers (Figures 2f, 3f and 4f) are seen to have higher surface gradients indicating a more discriminatory filtering style.

4.4 Experimental Flows.

The validation procedures using simulated flows have shown the neural net method to be particularly effective in analysing coded PTV images obtained in flows with systematic direction change. This corresponds to the conditions encountered in many experimental studies. Two examples are presented here which provide quite different images both containing global systematic changes in direction.

The first example is the flow behind a circular cylinder in a cross flow. This well known vortex wake has been the subject of many studies by the author and others. The beauty of the imagery obtained in wake visualisation is matched by the complexity of the flow and has proved an attractive area of research since the last century. In the present case the images were obtained in a hydraulic flow seeded with crystalline seeding particles The result of applying the net filter to this image is seen in Figure 5.

The flow can be seen to be similar to the digitally simulated turbulent flow with systematic change in direction. In the present case the image density was found to be 1.01. 612 pairs were correctly matched and 25 erroneously matched. The success ration was thus 95.9%. The errors principally occurred at the image identification stage where binarisation drop out occurred on weaker images. Previous statistical analysis procedures used on this type of image had shown erroneous pairing and drop-out at significantly higher levels.

The second example considered was obtained in a study of cavity flows. This type of flow is important in civil engineering applications, where moisture ingress in the gaps between facade elements is a serious problem in long term integrity. There are also numerous offshore applications where the geometry is important. One particular area of work by the author has been diver comfort and safety in work habitats of this type of geometry.

The first layer is the input layer where a segment of the total image entered the network. Each segment had a valid particle image as its origin. The dimensions of the segment were $2d_{mm}$ where d_{mm} was the maximum displacement between partner images expected. The images were processed so that spatially adjacent images were consecutively processed. This was an important consideration since it allowed the memory of the flow conditions to be updated in a systematic and meaningful fashion.

The images were 'tagged' using the principal image coding method where the image size was varied by altering the brightness of the laser flash in a temporal fashion. Alternatively, if an electronically shuttered camera is used with continuous illumination, the duration of the shutter open-time may be used in the coding (Grant and Wang (1994)). That is, the largest image comes first in any image group.

Each neuron in the second layer, whose purpose was to determine direction , had two inputs, X_0 and X_i, where X_0 was the input from the origin (neuron) of the current input layer sub-image, and X_i was the input from the equivalent neuron on the input layer. The interconnecting weights between the input layer and this first layer are set to 1 or -1 depending on the time signature convention adopted. Since the flow in the present case was from the largest image to the smallest image, the weights were set to $W_0 = 1$ and $W_i = -1$.

The inputs, X_0 and X_i, were set equal to the image areas. The output of the second, or directional layer, was determined by a switch function which compared the inputs from the origin particle image. The switch function was defined at the origin by

$$Y = f(X_0 \cdot W_0 + X_i \cdot W_i) = f(X_0 - X_i) = \begin{cases} 1 \text{ if } X_0 \succ X_i \\ 0 \text{ if } X_0 \le X_i \end{cases}$$

Consequently, all candidate images whose particle size was smaller than the origin were accepted. These ensured that the final output from the network not only gave a matching pair, but also eliminated inconsistent directional grouping or ambiguity.

The network, through the method of operation of its constituent layers, implicitly made allowance for local variations in intensity or size which may occur in a real experiment as a result variations in fluid characteristics, seeding particle characteristic or laser beam profile.

The third layer was the same size as the second layer. On initialisation the interconnecting weights between the second and third layers, $[W_{mn}]$, were set to low values. The network was then subjected to supervised learning where a training set was presented to the input layer and the corresponding output compared with the training set. The differences were used to adjust the interconnecting weights during training.

When processing, the pattern to be analysed was passed to the neurons on the third layer after scalar multiplication with the appropriate interconnecting weights. The neuron, on this competitive layer, with the maximum output level was identified as the 'key' neuron.

Updating of weights occurred if a successful outcome was generated on the fourth level of the net (see below). In this case the 'key' neuron (on the third layer) had its weight adjusted to unity, while the surrounding weights were adjusted according to their distance, d_{mnij} from the active neuron. The weights were adjusted according to the rules

$$\left.\begin{aligned} d_{mnij} &= \sqrt{(m-i)^2 + (n-j)^2} \\ U_{mn(new)} &= \frac{d_{max} - d_{mnij}}{d_{max}} \end{aligned}\right\} \qquad (1)$$

At initialisation the discrimination switch functions, f_1 and f_2, which regulate the outputs of the third and fourth layers respectively, were given threshold values between 0 and 1 and thenceforth acted as discriminators. When the signal presented at the output of either layer was less than the threshold no output took place. When the signal was greater than the threshold, unit output took place. High threshold levels between the second and third layer lead a more discrimination but restricted the learning of new patterns.

The particle matching proceeded according to $S_{mn} = f_1(W_{mn} \bullet R_{mn})$ where the R and S matrices were the input and output of the third layer respectively and $T_{ij} = f_2(\max(U_{mn} \bullet S_{mn}))$ where T was the output of the fourth (competitive) layer. The competition selected only the maximum component of the $U \cdot S$ matrix for output and only if it exceeded the preset threshold.

If $[T] = [0]$ then no matching had occurred and the next image entered the input layer. If a non-zero component of the T matrix was obtained then the neural net adjusted its weights between the second layer and the third layer according to (1).

The interconnecting weights between the third and fourth layer were adjusted according to

$$\left.\begin{aligned} U_{mn}(new) &= (1-\alpha) \times U_{mn}(old) + \alpha \times \frac{d_{max} - d_{mnij}}{d_{max}} \\ U_{mn}(new) &= \frac{U_{mn}(new)}{\max(U_{mn}(new))} \end{aligned}\right\} \qquad (2)$$

Self learning then took place as the image analysis proceeded. The weights , U, represented the local flow distribution with the highest value corresponding to the local flow vector. α was a memory efficiency parameter which determined the rate at which the short term memory degraded and the stability and the rate at which the network learned. The net could tolerate α values between 0.05 and 0.95 and was chosen, empirically, as 0.3 in the present case. The broad filter shape which evolved between the second and third layers provided stability for the network, while that between the third and top layers provided a more discriminating filter.

4. APPLICATION OF THE FOUR LAYER NETWORK.

The neural network was applied to two categories of PIV image. The first type was produced by numerical simulation, the second by hydrodynamic studies of vortex shedding and cavity flows.

Three flow types were investigated by numerical simulation, a uniform flow with superimposed two-dimensional turbulence, a flow with systematic direction change with superimposed turbulence and an ellipsoidal rotational flow where the mean direction varied through 360^0. The ratio of the major and minor axis was an independent variable in this latter case.

The numerical simulation consisted of Monte Carlo approach

The experiments were conducted in a 7 m, re-circulating hydraulic flume. An 18 watt, CW, Argon Ion laser had its beam mechanically interrupted by a spinning disk configured to give tagged images. The light was introduced into the transparent base of the tank and shaped into a sheet (for further experimental details see Aroussi and Grant (1992) and Aroussi et al (1992).

The result of applying the net filter to this type of image is seen in Figure 6. The flow can be seen to be similar to the digitally simulated elliptically rotational flow. In the present case the image density was found to be 0.89. 283 pairs were correctly matched with 28 being erroneous matched. The success ration was thus 90%. As in the vortex shedding case the errors principally occurred at the image identification stage where binarisation drop out occurred on weaker images. Statistical analysis procedures used on this type of image had shown significantly higher levels of erroneous pairings with the technique failing to cope with the systematic direction changes. The ability of the present method to adapt to systematic changes in direction proved important in this case.

5. DISCUSSION AND CONCLUSIONS.

The study has considered a four layer neural network as a means of processing time-signature coded particle tracking images obtained in low image density PIV studies. Digital flow simulations have been used as a means of calibrating the net with turbulent and rotational flows being considered. High success ratios have been found in all cases even where systematic changes in flow direction were present and significant improvements in overall image grouping success rates obtained compared with uncoded images in similar conditions.

The operation of the net on experimental data has been demonstrated using PIV images obtained hydrodynamic studies of vortex shedding from a circular cylinder and a recirculating cavity flow. The success ratios obtained in these cases were shown to be consistent with those obtained in the calibration studies. In all cases the sr was found to be improved on that obtained with a three layer net.

6. REFERENCES.

Adrian R and Yao C-S: 1984, Development of pulsed laser velocimetry (PLV) for measurement of turbulent flow, Proc Symp Turbul, ed X Reed, G Paterson, J Zakin. pp 115-29. Lisbon: Ladoan-Inst Super Tec. 541 pp. *Also in* "Selected Papers on PIV"; SPIE Milestone Volume MS99, Editor Ian Grant, May 1994.

Aroussi A, Grant I: 1992, Confined Multiple Eddy Systems" Int Conf on Computational Methods in Engineering, Singapore, Nov 1992.republished in Computational Methods in Engineering, Vol 1, pp 547-552, World Scientific Pub Co.

Aroussi, A, Yan, Y-Y, Grant, I: 1992, Experimental verification of numerical simulation of turbulent flow past enclosures in offshore structures. Optics and lasers in Engineering 16 , 391-409.

Cenedese A, Paglialunga, Romano G P, and Terlizzi M: 1992, Neural net for trajectories recognition in a flow, Paper 27.1, Int Symp on Laser Anemometry, Lisbon.

Grant I and Liu A : 1989, Method for the efficient incoherent analysis of Particle Image Velocimetry images, Applied Optics, 28, 10. Also in "Selected Papers on PIV"; SPIE Milestone Volume MS99, Editor Ian Grant, May 1994.

Grant I and Liu A: 1990, Directional ambiguity resolution in particle image velocimetry by pulse tagging, Experiments in Fluids, 10, pp 71-76. Also in" Selected Papers on PIV"; SPIE Milestone Volume MS99, Editor Ian Grant, May 1994.

Grant I, Owens E H, Smith, G H: 1987, Parallel (DAP) and serial computer methods for image processing in pulsed laser velocimetry, Proc 4th Int Symp on Optical and Optoelectronic Applied Science and Engineering, Hague, the Netherlands.

Grant I , Pan X : 1993, The neural network method applied to particle image velocimetry, Paper 2005-43, Proc Optical Diagnostics in Fluid and Thermal Flow, SPIE Tech Conf 2005, San Diego.

Grant I and Pan, X : 1994, An investigation of the performance of a multilayer, neural network applied to the analysis of PIV images. Submitted to Experiments in Fluids 1994.

Grant I and Wang X: 1994, Directionally unambiguous, digital particle image velocimetry studies using an image intensifier camera, submitted to Experiments in Fluids, 1994.

FIGURES.

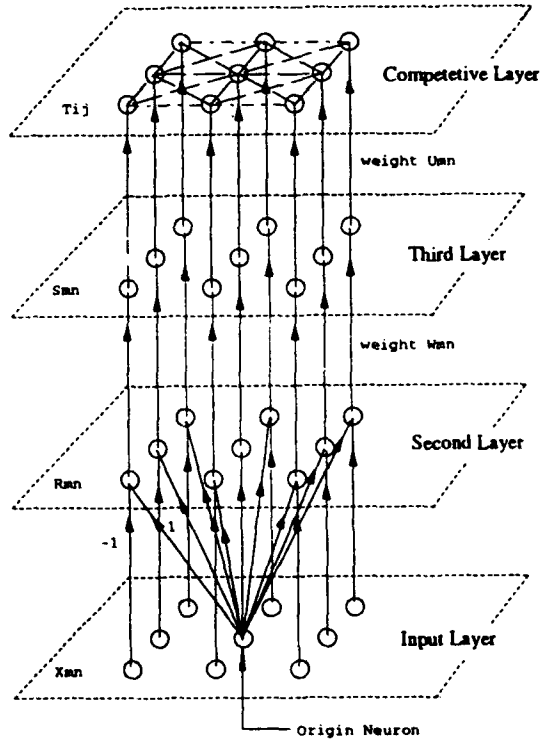

Figure 1. The Four Layer Neural Network.

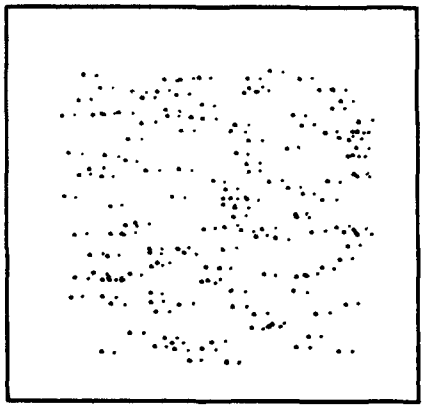

Figure 2a. A Typical Digital Simulation of the Turbulent Flow

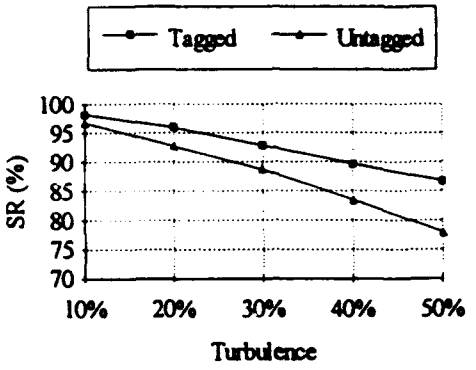

Figure 2b. The Success Ratio (SR) as a Function of Turbulence Intensity

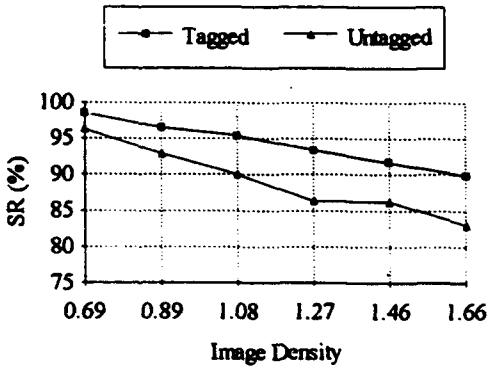

Figure 2c. The Success Ratio (SR) as a Function of Image Density

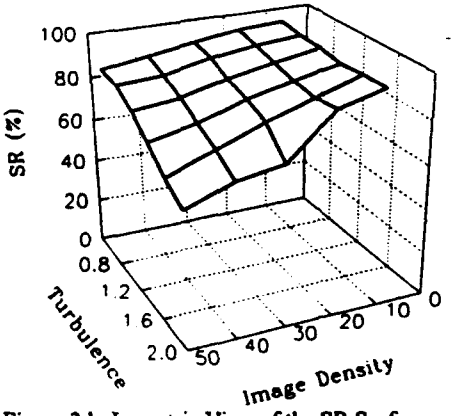

Figure 2d. Isometric View of the SR Surface

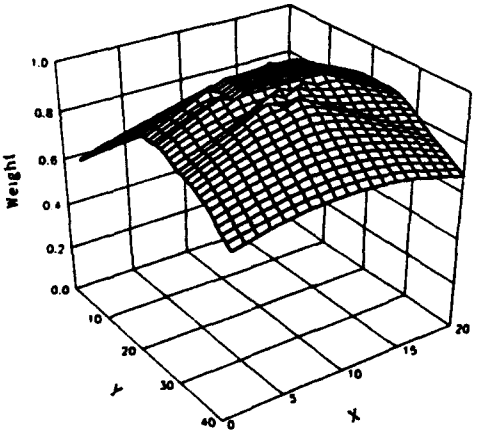

Figure 2e. The Final Interconnecting Weight Surface Between the Second Layer and the Third Layer

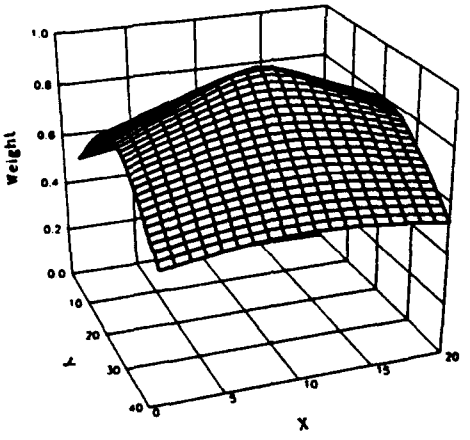

Figure 2f. A Typical Interconnecting Weight Surface Between the Third Layer and the Fourth Layer

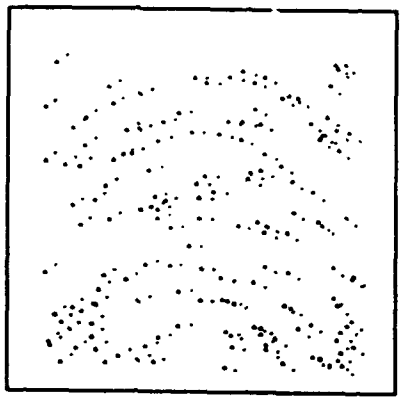

Figure 3a. Typical Turbulent Flow Simulation with a Systematic Direction Change

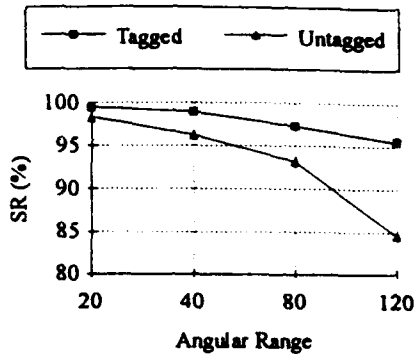

Figure 3b. The Success Ratio (SR) as a Function of the Angular Range

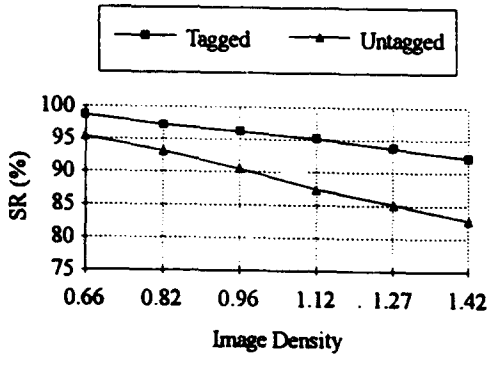

Figure 3c. The Success Ratio (SR) as a Function of Image Density

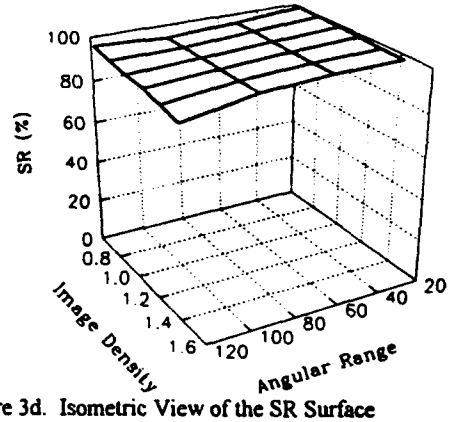

Figure 3d. Isometric View of the SR Surface

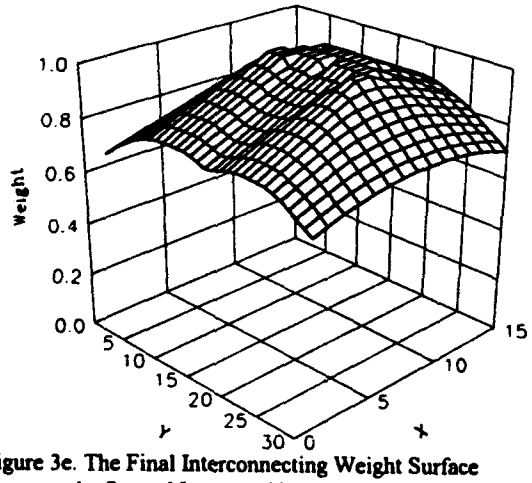

Figure 3e. The Final Interconnecting Weight Surface Between the Second Layer and Third Layer for the Systematic Direction Change Case

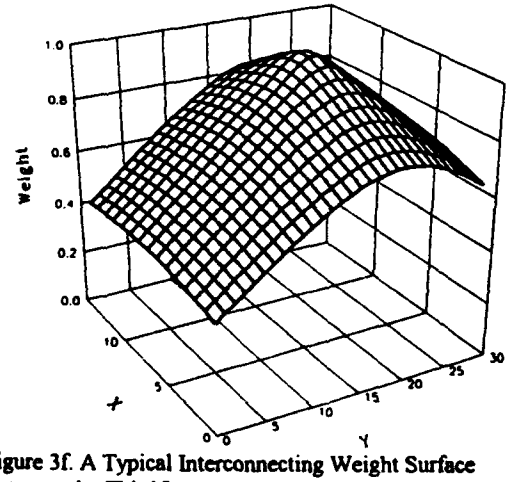

Figure 3f. A Typical Interconnecting Weight Surface Between the Third Layer and top Layer for the Systematic Direction Change Case

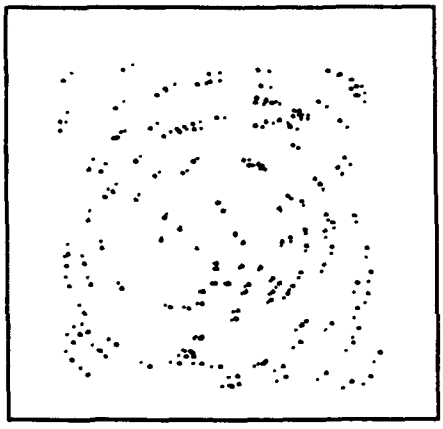

Figure 4a. An Example of a Digital Simulation of a Rotating Flow

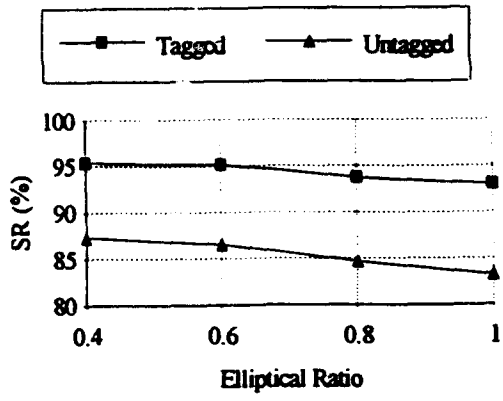

Figure 4b. The Success Ratio (SR) as a Function of the Elliptical Ratio

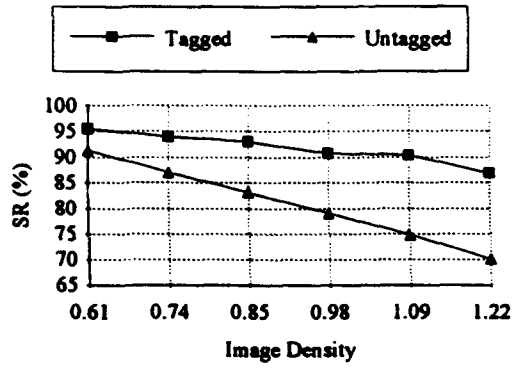

Figure 4c. The Success Ratio (SR) as a Function of Image Density

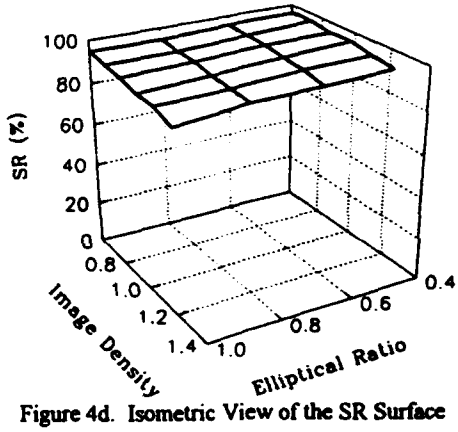

Figure 4d. Isometric View of the SR Surface

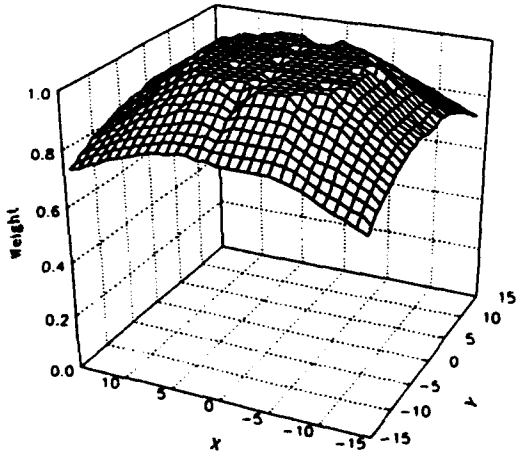

Figure 4e. The Final Interconnecting Weight Surface Between the Second Layer and the Third Layer for the Rotating FLow Case

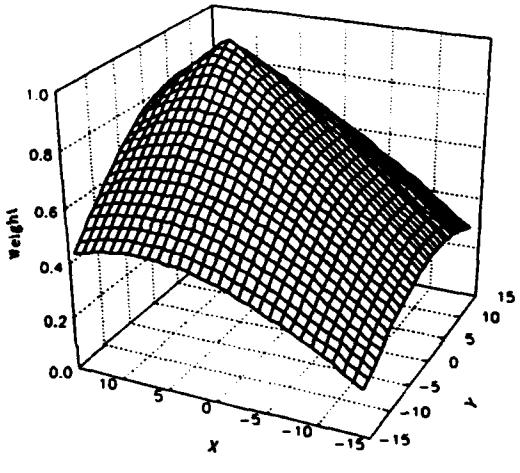

Figure 4f. A Typical Interconnecting Weight Surface Between the Third Layer and Top Layer for the Rotating Flow Case

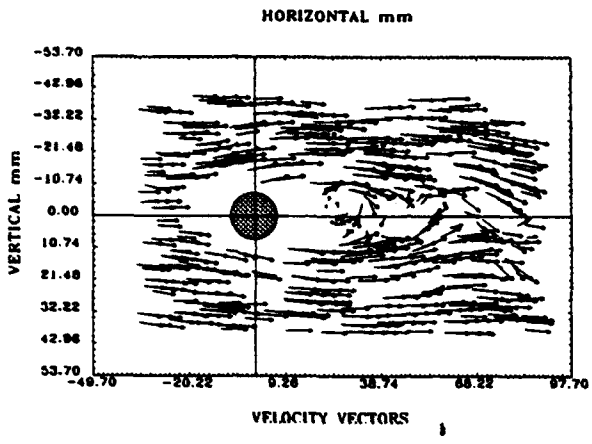

Figure 5. The Matched Tagged Image Pairs Obtained from the Vortex Shedding Image using the Neural Net Method

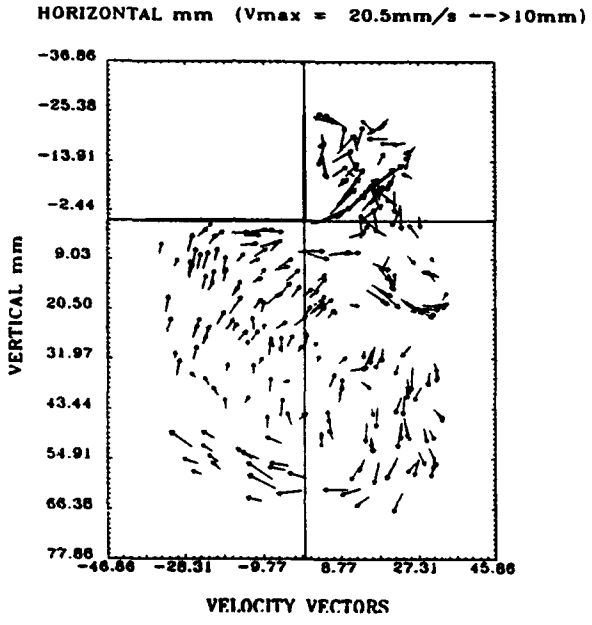

Figure 6. The Matched Tagged Image Pairs Obtained from the Cavity Flow Image using the Neural Net Method

ERROR ANALYSIS FOR PIV RECORDING UTILIZING IMAGE SHIFTING

Markus Raffel and Jürgen Kompenhans

Institut für Strömungsmechanik
Deutsche Forschungsanstalt für Luft- und Raumfahrt (DLR)
Bunsenstraße 10, D-37073 Göttingen, Germany

ABSTRACT

The development of high-performance image shifting systems has led to an increased potential for applying particle image velocimetry (PIV) to the widest variety of flows. More and more frequently, the instantaneous velocity vector fields measured with PIV are compared with the results of numerical calculations. However, it is very important for a meaningful comparison to have as much information as possible about the errors, which are inevitably involved in every experimental investigation. Several papers have been presented in the last years illuminating the different aspects of the accuracy of the PIV technique as a whole or for the evalution system only. In the following article the main error sources which depend on the recording parameters, especially if utilizing image shifting, will be discussed. A number of experimental and theoretical simulations were made to show the main influence of the parameters qualitatively and quantitatively.

INTRODUCTION

Due to recent advantages on the PIV recording side, especially due to the development of different image shifting devices for low and also for high speed flows the PIV technique becomes more and more suitable for a wide range of applications. This is also true for complicated flows which have to be investigated in the frame of industrial research in wind tunnels. This results from the fact that the image shifting technique, originally developed to resolve the directional ambiguity (Adrian 1986), moreover provides the opportunity to influence other parameters important to the PIV technique and, thus, to adapt the method to a wide range of different flows. For instance, a parallel adaptation of pulse separation and image shift is necessary to obtain high quality data of velocity vector fields even in highly three dimensional flows (e.g. above rotorblades), in flows with strong velocity gradients (with shocks embedded in the flow field) and in flows with small scale turbulence structures (with a degree of turbulence of about 0.5%).

This situation requires a discussion of different aspects of the accuracy of the technique. It will be attempted to answer the following questions:

1. How does the choice of pulse separation and image shift influence the evaluation noise?
2. It is known that a larger out-of-plane velocity component can be tolerated while simultaneously maintaining the same signal-to-noise ratio, if an additional velocity bias is applied. How does this influence the accuracy of the velocity measurement qualitatively and quantitatively?
3. How does the application of a rotating mirror for image shifting influence the velocity vector map?

THE CHOICE OF IMAGE SHIFT AND PULSE SEPARATION

The following considerations arise from an evaluation method that is based on the autocorrelation technique. According to Keane & Adrian (1990), this evaluation technique requires an optimum displacement of the particle images X_{opt} and an optimum dynamics ΔX_{opt} of the particle image displacement to be evaluated. For purpose of simplicity, the flow velocities and the resulting lengths are presented as scalars below.

The following criteria apply for the selection of the shift velocity U_{shift} and the pulse separation T:

In order to discriminate reverse flow regions, it is required that the smallest particle image displacement is greater than the smallest displacement which is still evaluable. Even if zero flow velocities are present, image shifting has to be applied in order to avoid overlap of the particle images.

$$(U_{min} + U_{shift}) \cdot M \cdot T > X_{opt} - \frac{\Delta X_{opt}}{2}.$$

Where M is the image-object magnification.

Furthermore, image shifting can be used for adapting the given dynamics of the flow velocity in the observation field to the limited dynamics as determined by the evaluation method by adapting the pulse separation T at the recording:

$$T = \frac{\Delta X_{opt}}{(U_{max} - U_{min}) \cdot M}.$$

and the shift velocity U_{shift} at the recording:

$$U_{shift} = \frac{X_{opt}}{M \cdot T} - U_m .$$

where

$$U_m = \frac{(U_{max} + U_{min})}{2}.$$

The selection of the shift velocity influences the dynamics of the recording of the entire observation field as well as the variance of the velocity contained within each individual interrogation spot. A reduction in the fluctuation makes it possible to favourably influence peak detection in the autocorrelation plane (Keane & Adrian 1990), even if shocks are embedded in the flow field (Raffel 1993).

The out-of-plane component is also subject to tight constraints depending on the magnification, light sheet thickness and the depth of focus. The most important advantage of an image shifting system is the possibility to limit the relative extent of the out-of-plane component to, e.g. less than 30% of the component within the plane, if using an additional in-plane component. Since the following applies,

$$(U_m + U_{shift}) \cdot M \cdot T = X_{opt},$$

the required pulse separation T is reduced if proceeding in this way. This means that less particles leave the light sheet plane between the two exposures. In combination with a reduction in velocity fluctuation within the interrogation spots, this leads to an improved signal-to-noise ratio at the evaluation.

As has been explained, an additional, virtual flow component (image shift) has still to be superimposed on the flow velocity for a number of different reasons, although this effects the attainable accuracy of the velocity measurement. This is due to the fact that the choice of shift velocity U_{shift} also effects the choice of pulse separation T. The pulse separation itself influences the effect of the error of the evaluation method on the velocity measurement. According to Adrian (1991), this error ΔX_{eval} is independent of the mean particle image distance X within an interrogation spot. Calculating the error contained in the velocity measurement due to the evaluation noise ΔX_{eval} yields:

$$\Delta U_{eval} = \frac{\Delta X_{eval}}{M \cdot T}.$$

The velocity error ΔU_{eval} thus increases with decreasing pulse separation T. Applying negative shift velocities, i.e. by shifting the observation area towards the mean flow direction and appropriately increasing the pulse separation, this correlation can be used to investigate flows with very low degrees of turbulence (Fischer et al. 1993, Kompenhans et al. 1993). In the case of positive shift velocity and a reduced pulse separation, however, this fact leads to a growing influence of the evaluation noise. This disadvantage must be weighed against the improved evaluability as possible by means of image shifting, e.g. in strongly three-dimensional flows.

There is a another source of inaccuracy if measuring three-dimensional flows. This inaccuracy results from the fact that the projection of the 3D velocity vector of the flow field into the 2D plane of recording is not a parallel projection, as it is mostly assumed for simplification, but a perspective projection. The influence of this error has already been reported in the literature (e.g. Lourenço 1988). Now this effect becomes of considerable importance through the possibility of measuring strongly three-dimensional flows by image shifting. A systematic error arises, especially at the edge of the observation field, if the out-of-plane component and its value, which might be obtained e.g. by stereoscopic methods, are not considered.

THE INFLUENCE OF THE PERSPECTIVE PROJECTION IN CASE OF A 3D FLOW

The following discussion is based on the assumption of a flow with a strong out-of-plane component. In order to describe the influence of the perspective projection qualitatively and quantitatively an example shall be given:

A potential vortex is assumed, similar to vortices occuring in natural flows (hurricane) and flows in technical devices (cyclone). In the case of an isoenergetic flow the Bernoulli-equation yields for the velocity components C_y and C_z:

$$\sqrt{C_y^2 + C_z^2} = \frac{C_1 \cdot R_1}{R}.$$

where C_1 is the absolute flow velocity, and R_1 the radius of a point outside the vortex core.

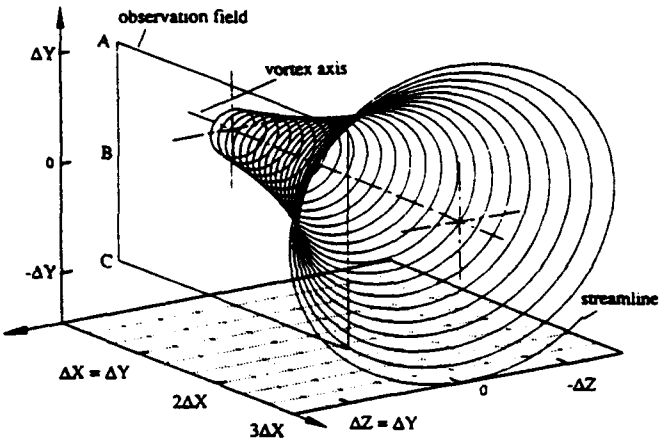

Fig. 1: 3-D representation of the coordinate system, the observation field and a streamline ($\alpha_0 < \pi/4$ for better representation)

The X-axis of the observed plane of the flow is parallel to the vortex axis, and is located outside the vortex core as illustrated in Figure 1. The Y and Z components can be calculated according to the formula given above, while the X-component of the velocity is assumed to have a value of 20% of the other velocity components in point B. This leads to the

following equations for the velocity components as functions of the XYZ-coordinates:

$$C_x = +C_1 \cdot \frac{1}{\sqrt{2}} \cdot 0.2$$

$$C_y = -C_1 \cdot \cos(arctg(\frac{Y}{\Delta Y}) + \alpha_0) \cdot \frac{\Delta Y}{\sqrt{\Delta Y^2 + Y^2}}$$

$$C_z = +C_1 \cdot \sin(arctg(\frac{Y}{\Delta Y}) + \alpha_0) \cdot \frac{\Delta Y}{\sqrt{\Delta Y^2 + Y^2}}$$

In the case of the following numerical simulation of the PIV recording process $\alpha_0 = \pi/4$ is assumed, so that $C_y = 0$ at point A and $C_z = 0$ at point C. Using the classical PIV method, only the X- and Y-components within the light sheet plane can be determined (see Fig. 2).

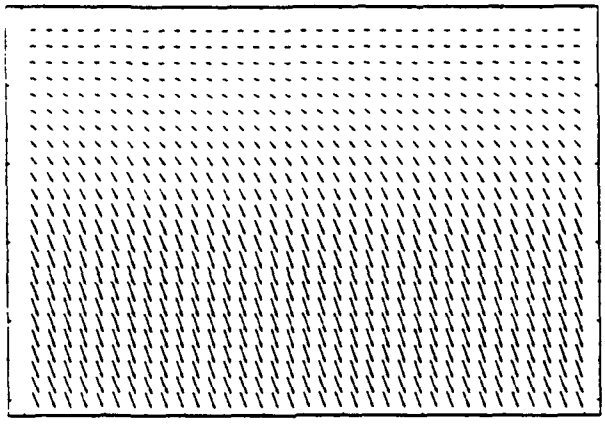

Fig. 2: Illustration of the X- and Y-components of the velocity vectors of a simulated potential vortex within the observation field shown in Fig 1.

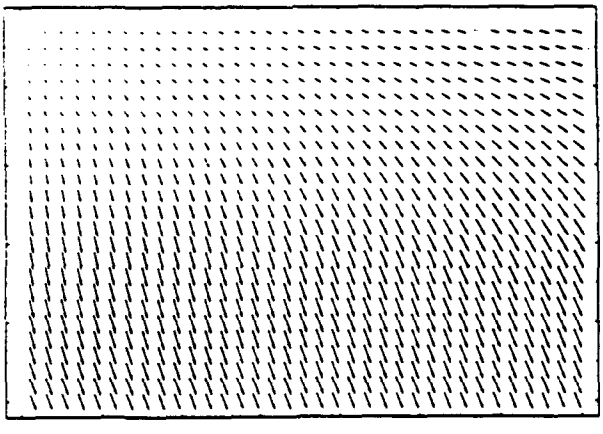

Fig. 3: Illustration of two components of the velocity vectors after "PIV recording" (M = 1/4, 35mm film, f = 60mm) calculated by means of perspective transformation from the same velocity vector field as presented in Fig. 2.

It is possible to calculate the values that would have been obtained by a PIV measurement from the 3D velocity vectors in the X-Y-plane, by means of linear algebra utilizing the algorithms for transformation as presented by Raffel (1993). It is necessary to employ a presentation in a homogeneous, four-dimensional vector-space because the projection under consideration is a non-linear transformation (Gonzalez & Wintz 1987). Figure 3 shows the same velocity vectors a PIV recording of the flow field discussed above would show. The calculation is based on the following parameters: magnification M = 1/4, film size 35 x 24 mm^2, focal length of the object lens f = 60mm. These parameters are realistic values for PIV recording for aerodynamic applications in wind tunnels.

The difference between the real X-Y data and the calculated "PIV recording" data is up to 16.6% of the mean flow velocity in this case of idealized conditions. In order to achieve accurate data, this deviation is clearly to be assessed as a considerable error, but its systematic influence does not hamper the interpretation of the instantaneous flow field when looking for structures as it would be the case for random errors. In order to illustrate this statement, an error of the same size but with random angular distribution was superimposed on the real velocity data (see Fig. 4).

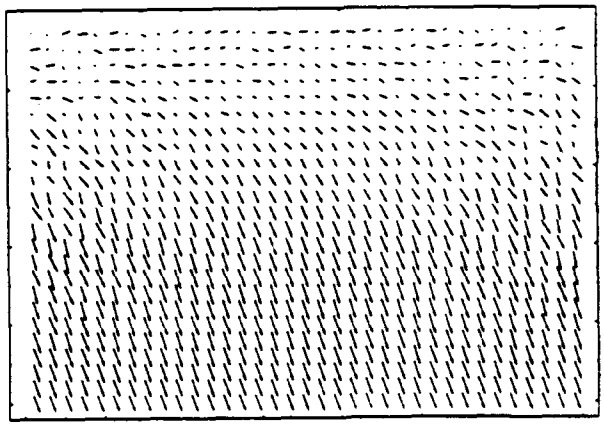

Fig. 4: Illustration of two components of the velocity vectors via a "PIV recording" with a random error of the same order as contained in the "PIV recording" shown in Fig. 3.

The only way to avoid the error due to the perspective projection of the velocity vectors for a highly three-dimensional flow is to measure all three components of the velocity vector, for example by means of stereoscopic techniques.

SYSTEMATICAL SHIFT ERRORS

Another source of errors is the way the virtual image of a particle is shifted by an image shifting system. This displacement and the resulting shift of the particle images do not represent the desired case of a uniform shift for all points of the observed field. This problem appears in the case of an image shifting system utilizing a rotating mirror and also if using a birefringent crystal and differently polarized light as reported by Reuss et al. (1993). If this fact is not taken into account properly, errors will result of a magnitude which can not be neglected.

As an example the displacement of the particle images as generated by a rotating mirror determined theoretically and experimentally will be shown. The displacement of the particle images on the film is mainly influenced by the 3D motion of the virtual image of the light sheet plane. This 3D motion generates, together with the perspective projection of the imaging lens, errors, if only a constant shift over the entire observation field is assumed. In contrast to the case of a unknown out-of plane flow component as discussed in the previous chapter, in this case the influence of the third component can be calculated and the error due to this component can be eliminated.

In our experiment the images of particles in air at rest have been illuminated by two laser pulses and recorded via a high speed rotating mirrror utilizing a f=100 mm object lens. The PIV recordings, showing two images of each particle at rest due to the artificial image shift by means of the rotating mirror, have been evaluated in the usual way (abtocorrelation technique).

First the displacement of the images of the tracer particles has been determined theoretically. The calculation of the geometric relations, the perspective projection and the rotation of the mirror yield the following equations for the shift of the tracer images ΔX and ΔY in the film plane (details see Raffel 1993):

$$\Delta X_{(X,Y)} = \frac{X - M \cdot (S_o - S_m) \cdot 2\omega_m T}{(X + (S_l - S_m) \cdot M) \cdot 2\omega_m T \cdot f^{-1} \cdot (1+M)^{-1} + 1} - X$$

$$\Delta Y_{(X,Y)} = \frac{Y}{(X + (S_l - S_m) \cdot M) \cdot 2\omega_m T \cdot f^{-1} \cdot (1+M)^{-1} + 1} - Y$$

f	focal length
M	image-object magnification
$(S_o\text{-}S_m)$	distance mirror axis to observation field (Z-direction in Fig. 1)
$(S_l\text{-}S_m)$	distance mirror axis to optical axis of the lens (X-direction in Fig. 1)
T	pulse separation
ω_m	mirror speed in rad/s

In many cases the distance mirror axis to optical axis of the lens $(S_l\text{-}S_m)$ can be adjusted to zero. The mirror axis is assumed to be parallel to the Y-axis of the coordinate system shown in Fig. 1.

Figure 5 shows the calculated difference between the local shift (ΔX, ΔY) of the images of the particles caused by the rotating mirror and the shift in the center of the observation field X_{shift} as caused by the rotating mirror. The image displacement was 194 µm in the center of the PIV recording. This displacement increases up to 200 µm at the edges of the image.

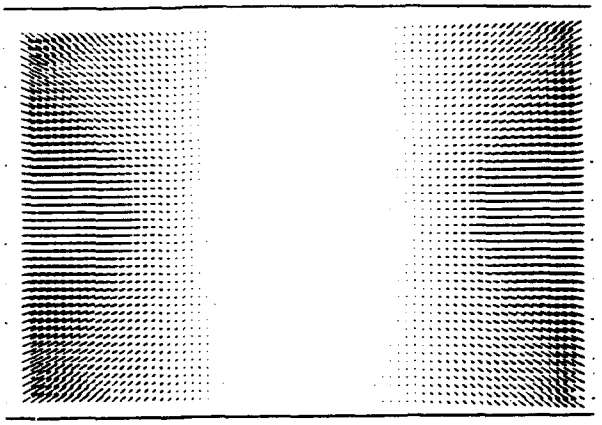

Fig. 5: Map of the calculated tracer image shift ($\Delta X\text{-}X_{shift}$, ΔY) on the film. Magnification M = 1:4, time between two the pulses T = 20 µs, distance of the rotating mirror axis from the lightsheet R = 512 mm, mirror speed ω_m = 62,8 rad/s, focal length f = 100 mm.

The displacement of the images of the particles has also been determined experimentally employing the same parameters as for the theoretical calculation. Fig. 6 again displays the difference between the local shift (ΔX, ΔY) of the images of the particles caused by the rotating mirror and the shift in the center of the observation field X_{shift} as caused by the rotating mirror, scaled in the same way as in Fig. 5. An excellent agreement between the theoretical and experimental results can be seen when comparing Figures 5 and 6. The deviations of the experimental values from the calculated values lie within the resolution of our PIV-evaluation system and do not display any systematic errors. Therefore, we can assume that the rotating mirror-camera system has been modeled correctly.

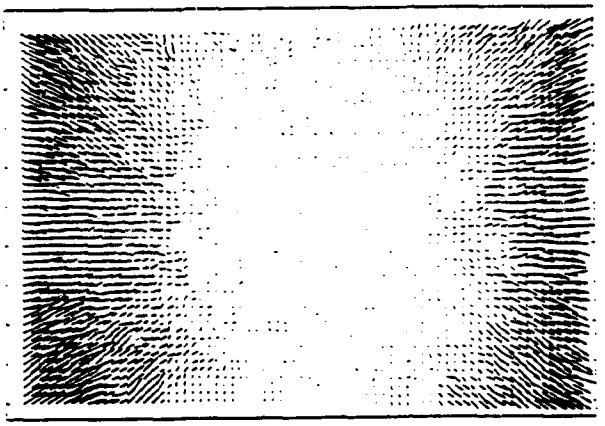

Fig. 6: Map of the experimentally determined tracer image shift ($\Delta X\text{-}X_{shift}$, ΔY) on the film. Magnification M = 1:4, time between two the pulses T = 20 µs, distance of the rotating mirror axis from the lightsheet plane R = 512 mm, mirror speed ω_m = 62,8 rad/s, focal length f = 100 mm.

The conventional practice of assuming that the value for the tracer image shift is constant over the whole image as described in literature e.g. (Adrian 1986).

$$\left|X_{shift}\right| = 2\,M\,\omega_m(S_o - S_m)T$$

leads to systematic errors of 2% to 3% of the mean tracer image shift at the edges of the observation field. Due to the reasons stated above, a virtual shift greater than the mean flow velocity has often to be chosen for practical applications. This may result in errors of up to 10% of the mean flow velocity. Utilizing the exact equations as given above one obtains the tracer image shift depending on the length scales of the experimental set up and the imaging process. They depend on the observation distance, the focal length of the lens and the position of the mirror axis. This means that, for a given imaging configuration, the virtual, locally varying tracer image shift has to be determined theoretically only once for each experimental configuration in order to remove the systematic error from the measurements.

SUMMARY

In PIV measurements the separation between the two pulses for illumination can be selected in a wide range independently from the value of the mean flow velocity, if employing the image shifting technique. A long pulse separation considerably decreases the influence of the evaluation noise on the velocity measurement. A short pulse separation decreases the evaluation noise itself due to an increased number of paired particle images and a smaller variance of the velocity within each interrogation spot, if utilizing image shifting. Thus, the maximum attainable accuracy of the measurements results from the chosen compromise between an enhanced resolution due to a long pulse separation and a noise reduction due to a short pulse separation.

A systematic error at the edges of the observation field becomes of considerable importance through the possibility of measuring strongly three-dimensional flows by means of image shifting. For the observation of flows with a strong out-of-plane component, the third flow component should also be measured in order to reduce the error of both in-plane components, e.g. by utilizing stereoscopic methods. It has been shown that measuring only the in-plane components could lead to an error of more then 15% of the mean flow velocity.

In order to take into account the influence of a rotating mirror system on the exact determination of the velocity vectors, the virtual, locally varying image shift has to be determined for each experimental configuration.

REFERENCES

Adrian, R.J.: Image shifting technique to resolve directional ambiguity in double-pulsed velocimetry. Appl. Optics 25, pp. 3855-3858, 1986.

Adrian, R.J.: Particle-imaging techniques for experimental fluid mechanics. Annu. Rev. Fluid Mech., pp. 261-304, 1991.

Fischer, M.; Raffel, M.; Vogt, A.; Kompenhans, J.: Combined PIV and visualization experiments on instabilities in a flat plate boundary layer with zero pressure gradient. Int. Symposium on 'Optical diagnostics in fluid and thermal flows' SPIE Proceedings Vol. 2005, pp. 448-456, 1993.

Gonzalez, C.R.; Wintz, P.: Digital image processing. Addison-Wesley Publishing Company Massachusetts, 1987.

Keane, R.D.; Adrian, R.J.: Optimization of particle image velocimeters. Part I: Double pulsed systems. Meas. Sci. Technol. 1, pp. 1202-1215, 1990.

Kompenhans, J.; Raffel, M.; Vogt, A.; Fischer, M.: Aerodynamic investigations in low and high speed wind tunnels by means of Particle Image Velocimetry. Proc. of 15th ICIASF, St. Louis, France, 20 - 23 September 1993, paper 46.

Lourenço, L.M.: Some comments on particle image displacement velocimetry. Lecture Series 1988-06, von Karman Institute for Fluid Dynamics, 1988.

Raffel, M.: PIV-Messungen instationärer Geschwindigkeitsfelder an einem schwingenden Rotorprofil. DLR FB 93-50, 1993.

Reuss, D.L.: Two-dimensional particle-image velocimetry with electrooptical image shifting in an internal combustion engine. Int. Symposium on 'Optical diagnostics in fluid and thermal flows' SPIE Proceedings Vol. 2005, pp. 413-424, 1993.

THE IMPORTANCE OF IMAGE SHIFTING TO THE APPLICABILITY OF THE PIV TECHNIQUE FOR AERODYNAMIC INVESTIGATIONS

Jürgen Kompenhans and Markus Raffel

Institut für Strömungsmechanik
Deutsche Forschungsanstalt für Luft- und Raumfahrt (DLR)
Bunsenstraße 10, D-37073 Göttingen, Germany

ABSTRACT

Image shifting is primarily known as a method for eliminating the ambiguity of the direction (i.e. sign) of the velocity vector when recording the images of the tracer particles at Particle Image Velocimetry. However, there exist further capabilities of the image shifting technique, which - in general - increase the applicability of the PIV method for measuring complex flow fields. These capabilities are discussed and the efficiency of image shifting by means of the DLR high speed rotating mirror system is demonstrated by referring to the results of different wind tunnel measurements.

1. INTRODUCTION

Employing the Particle Image Velocimetry (PIV) in its 'classical' form, the information about magnitude and direction of an instantaneous velocity vector is determined from the displacement of the images of tracer particles, illuminated in a plane of light within the flow by two laser pulses of the same wavelength and of the same (short) pulse length, which are delayed by a time interval τ of a few microseconds (Adrian 1991). The images of the particles due to the first and second exposure are both stored on the same PIV recording. The velocity vectors are determined by subdividing the PIV recording into interrogation spots and employing well described statistical evaluation techniques such as histogram-analysis, analysis of Young's fringes or autocorrelation method. These methods are widely used as they are easy to implement when developing a fast and reliable fully automatic working evaluation system. However, one main drawback is involved with these 'classical' evaluation techniques. It is obvious from the description of the recording process as given above, that the sign of the direction of the motion of the particles within each interrogation spot cannot be determined with these recording and evaluation techniques since there is no way to decide which image is due to the first and which is due to the second exposure of a particle. Although, for many applications the sign of the velocity vector can be derived from a priori knowledge of the flow, in reverse flows, for example in areas of detached flow and in wakes behind models, steps have to be taken to determine the sign of the displacement and hence the velocity vector correctly.

In principle the cross correlation technique instead of autocorrelation methods can be employed for ambiguity removal. However, for this purpose it must be possible to store the images of the tracer particles due to the first and due to the second exposure on two separate recordings (two illuminations - two recordings). The temporal sequence of the recordings is known. Thus, it is no problem to decide which image was first and which was second. The cross correlation technique has been realized in connection with the development of Digital Video PIV by Willert and Gharib (1991). In the case of video PIV two subseqent video frames are utilized to store the images of the particles at two subsequent illuminations. For video as well as for high speed photographic recording there remains the problem that there exists a minimum time which is necessary to change between two subsequent recordings (video frame rate, transport speed of film). This means that at the present state of the development of PIV the cross correlation technique for ambiguity removal is restricted to applications in low speed flows.

However, the great interest in PIV measurements in many different fields of research requires a flexible technique for ambiguity removal which can be applied to a variety of experimental situations. Especially for aerodynamic investigations it is very important to be able to apply this technique at high speed flows, i.e. with short time intervals of a few microseconds between both exposures. Such a method is the image shifting technique as described by Adrian (1986), Landreth *et al* (1988a), and Gauthier and Riethmuller (1988), which enforces a constant additional displacement on the image of all tracer particles at the time of their second illumination. Only minor modifications of the evaluation technique either by means of the Young's fringes or the autocorrelation method are required when applying the image shifting method for recording at PIV.

2. IMAGE SHIFTING

At present the most widely used experimental technique for image shifting is to utilize a rotating mirror system. The observation area in the flow is imaged onto the recording area in the camera via a rotating mirror. The magnitude of the additional displacement of the images of the tracer particles depends on the number of revolutions of the mirror per time, the distance between light sheet plane and mirror, the magnification of the imaging system and the time delay between the two illuminations, see Landreth *et al* (1988a). Experimental set-ups employing rotating mirrors as realized by different authors show

good experimental results, e.g. at the investigation of dynamic flow detachment (wake with reverse flows) above profiles Lourenço (1986). The application of rotating mirror systems on turbulent and convective flows made also evident the important influence of this method on the attainable resolution of the PIV technique (Landreth *et al* 1988a, Grant *et al* 1989).

In order to achieve very high shift velocities electro-optical methods employing differently polarized light for illumination have been proposed and applied by Landreth & Adrian (1988b), Lourenço (1993) and Molezzi & Dutton (1993). The constant shift of the particle images is obtained e.g. by means of birefringent crystals of appropriate thickness. Reuss (1993) describes problems of this method as e.g 'depolarization effects'. The following discussion on the application of image shifting is independent of the fact which technique is employed to achieve the additional displacement of the images of the particles.

Due to our experience we see most practical advantages at aerodynamic investigations if applying a rotating mirror system for image shifting. A high speed rotating mirror system as described by Raffel (1993b) has been developed at DLR in order to be able to carry out measurements even in transonic flows. The frequency of rotation ranges from 1 Hz to 100 Hz, thus covering a range of shift velocities from 5 m/s to 500 m/s (at a ratio of reduction of 1:4 between observation plane in the flow to the recording plane). This system has been successfully applied to different aerodynamic investigations in wind tunnels. A detailed analysis of the errors involved with image shifting by means of a rotating mirror has also been given by Raffel (1993b).

During evaluation the PIV recording is interrogated in small sub areas. The diameter of the interrogation spot is typ. 0.7 mm in our evaluation set-up. Due to our experience best results concerning resolution, accuracy and number of valid data is obtained if the displacement of the tracer particles, measured on the recording area (photographic plate) is 150 µm $\leq d_{opt} \leq$ 250 µm. This agrees with the results of the simulation of the PIV recording and evaluation process by Keane & Adrian (1990). The number of particle images within the interrogation spot should be $N \geq 15$ due to these simulations. In the following four typical experimental situations appearing at investigations of flow fields in wind tunnels shall be explained.

2.1 Elimination of the ambiguity of direction

Fig. 1 explains the well known way to remove the ambiguity of direction by means of image shifting in the case of flow reversal. By adding an additional shift to the flow-induced displacement of the images of the tracer particles one retains the same imaging conditions for complex flows as are valid for flows without reverse-flow areas. However, by selecting the additional shift in such a way that it is always greater than the maximum value of the reverse-flow component, it is guaranteed that the tracer images of the second exposure are always located in "positive" direction with respect to the location of the first exposure (see Fig. 1). For eliminating the ambiguity of direction it does not matter in which direction within the observation plane the shift takes place, if the maximum of the corresponding reverse-flow component is interpreted accordingly.

Thus, an unambiguity of the sign of the velocity vector is established. The value and correct sign of the velocity vectors d_1 and d_2 will be obtained by subtracting the "artificial" contribution X_{shift} at the evaluation of the PIV recording.

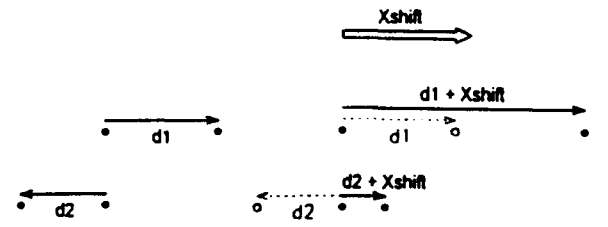

without image shifting with image shifting

Fig. 1. Elimination of the ambiguity of direction of the velocity vector.

Fig. 2 shows the instantaneous flow field above a pitching NACA 0012 airfoil at an angle of incidence of $\alpha = 24°\uparrow$ in upstroke motion at a mean flow velocity of $U_\infty = 28$ m/s (Kompenhans *et al* 1994). A strong vortex with reversal of flow direction can be seen above the airfoil (the so-called 'dynamic stall' vortex).

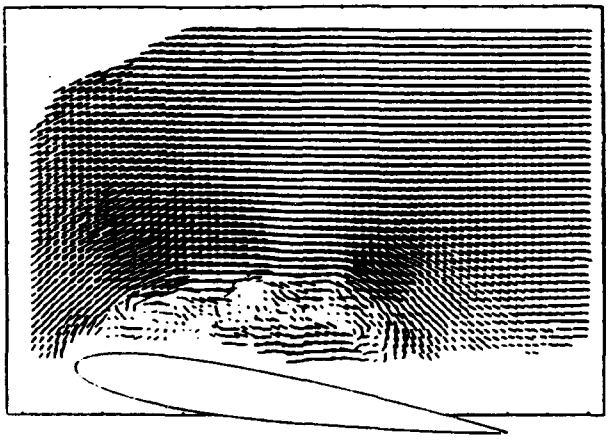

Fig. 2. Instantaneous flow field above NACA 0012 airfoil at $\alpha = 24°\uparrow$ in upstroke motion and $U_\infty = 28$ m/s; $U_{shift} = 128$ m/s.

Table 1 lists the parameters of the experiment and explains how the application of image shifting (i.s.) eliminates the ambiguity of direction. The magnification M at imaging from the flow onto a 35 mm film and typical values for the number N of particles per interrogation spot within this recording are also given.

M = 1:7.9 N ≈ 30

	U_{min} [m/s]	U_{max} [m/s]	τ [µs]	U_{shift} [m/s]	d_{shift} [µm]	d_{min} [µm]	d_{max} [µm]
without i.s.	-28	+50	56	0	0	-198	+354
with i.s.			12	128	194	+152	+270

Table 1. Parameters at recording of instantaneous flow field shown in Fig. 2.

As already mentioned, the technique of image shifting furthermore provides the opportunity to influence other important parameters during recording as well and, therefore, helps to employ the PIV method for investigations in a wide range of different flows.

2.2 Measurement of highly three-dimensional flows

At 'classical' PIV the light, which is scattered by particles illuminated two times within a light sheet, is recorded. This feature of the PIV method limits its application in highly three-dimensional flow-regimes. The restriction is caused by the fact that particles moving perpendicular to the light sheet will leave the light sheet in between the two illuminations and thus will not yield data when evaluating the PIV recording but will only add noise. This problem gets even more severe for measurements in gaseous media, where very small particles are required in order to follow the flow faithfully. Small particles scatter little light, which results in a small effective depth of focus at recording. In our experiments the depth of focus is of the order of the thickness of the light sheet, i.e. ≈ 0.5 mm. Experience shows that the depth of the light sheet or the depth of focus cannot be increased considerably by changing the experimental set-up.

The simulation carried out by Keane & Adrian 1990 showed that the conventional PIV technique is only applicable to flows in which the out-of-plane velocity component amounts to less than 30% of the in-plane components.

The only practical way to reduce the number of particles leaving the light sheet plane is to decrease the time between the light pulses considerably (see Fig. 3). In the same way the diplacement of the images of the tracer particles will be reduced. However, the optimal distance between two particle images d_{opt} required for the evaluation by means of the autocorrelation technique can be re-established by applying image shifting (see Fig. 4). Since the number of dual-particle images is increased considerably by this method, the number of valid data can be increased significantly. Therefore, a much greater third component of the flow velocity is tolerable at the same signal-to-noise ratio.

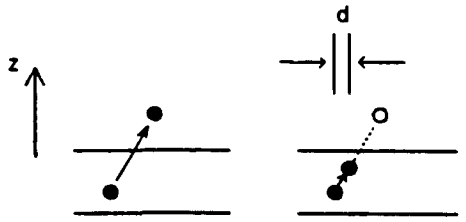

Fig. 3. Effect of reducing the time between two pulses (figure is not to scale).

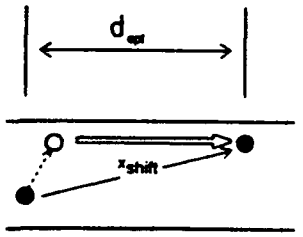

Fig. 4. Re-establishing the optimal distance between pulses.

As an example for measurements in a highly three-dimensional flow field the result of test measurements on a helicopter rotor (NACA 23012) at U_∞ = 33 m/s and a rotation of f = 47 Hz, which results in a blade tip velocity of -280 m/s, is shown in Fig. 5. A shift velocity of U_{shift} = 540 m/s has been applied at these tests in order to avoid data drop-out by out-of-plane motion. Fig. 5 shows that in this test the shift velocity was too large in order to resolve the vortical structures in the flow adequately. Table 2 gives the parameters of this experiment.

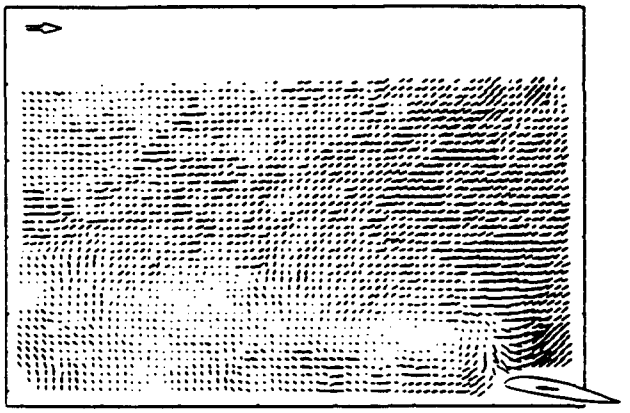

Fig. 5. Instantaneous flow field above helicopter rotor (NACA 23012) at U_∞ = 33 m/s and a frequency of rotation of f = 47 Hz (blade tip velocity -280 m/s); U_{shift} = 540 m/s.

M = 1:6.5 N ≈ 10 ... 20

	U_{min} [m/s]	U_{max} [m/s]	τ [µs]	U_{shift} [m/s]	d_{shift} [µm]	d_{min} [µm]	d_{max} [µm]
without i.s.	-280	+50	5	0	0	-215	+38
with i.s.			3	540	249	+120	+272

Table 2. Parameters at recording of instantaneous flow field shown in Fig. 5.

It has to be kept in mind, that the resolution of the velocity measurement is decreased by reducing the time between the light pulses. This has to be balanced against the improved signal-to-noise ratio. The maximum attainable accuracy of the method results from the chosen compromise between resolution and signal-to-noise ratio. Additionally, it has to be mentioned that allowing a significant velocity component perpendicular to the light sheet plane leads to an error due to this component. This error is known from the literature and arises from the fact that the camera lens reproduces the tracer particles by perspective projection and not by parallel projection (details see e.g. Raffel & Kompenhans, 1994).

2.3 Reduction of the variance within an interrogation spot

Even if high velocity gradients are present the signal-to-noise ratio is increased by additionally shifting the tracer images between the two illuminations.

At the autocorrelation technique the displacement vector is determined by averaging over all displacements between image pairs within one interrogation spot. Therefore it has to be

assumed that the flow velocity does not change magnitude and direction within the interrogation spot. If this assumption is no longer valid, it becomes difficult to determine the location of the signal peak in the autocorrelation plane accurately. This means, that for successfull detection of the displacement vector, the variance of the particle image displacement within the interrogation spot has also to be limited (Keane & Adrian, 1990). The variance of the displacement within the interrogation spot can be reduced by application of image shifting, i.e. by decreasing the delay between the two pulses for illumination and adding an additional shift in the same direction. Less data drop-out is to be expected by this means.

The same argument as for a local interrogation spot holds for the whole PIV recording. As explained above, there exists an optimal range of particle displacements of 150 µm ≤ d_{opt} ≤ 250 µm for evaluation. The upper and lower limit of the displacement of the tracer particles in the flow, which is determined by the flow to be investigated, can be adapted to the optimal range of displacement on the recording medium by applying the image shifting technique.

Strong velocity gradients are present within shocks embedded in transonic flows. Fig. 6 shows such an instantaneous flow field - again above a NACA 0012 airfoil, now at Ma_∞ = 0.75 (Raffel & Kompenhans 1993a). By subtracting the speed of sound from all velocity vectors the supersonic flow regime and the shock are clearly detectable. Due to the application of image shifting no data drop-out is found even in interrogation spots containing the flow field in front and behind the shock (flow velocities from U = 200 m/s to 520 ms).

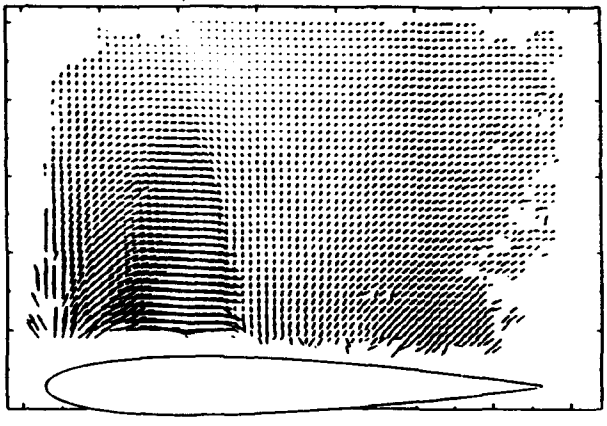

Fig. 6. Instantaneous flow field above NACA 0012 airfoil at α = 5 ° and Ma_∞ = 0.75; U_{shift} = 174 m/s.

The parameters at recording are presented in Table 3.

M = 1:6.7 N ≈ 10 ... 20

	U_{min} [m/s]	U_{max} [m/s]	τ [µs]	U_{shift} [m/s]	d_{shift} [µm]	d_{min} [µm]	d_{max} [µm]
without i.s.	200	520	5	0	0	149	388
with i.s.			3	174	78	167	311

Table 3. Parameters at recording of instantaneous flow field shown in Fig. 6.

2.4 Improving the resolution

In flows with only a small velocity component perpendicular to the main flow direction and with only small fluctuations in the main flow direction, an increase in resolution can be achieved by choosing longer time delays between the illumination pulses and image shifting 'against' the main flow direction. This situation is explained in Fig. 7.

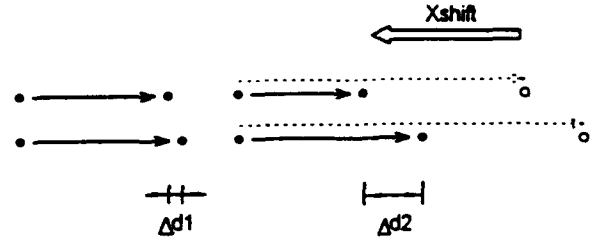

without image shifting with image shifting

Fig. 7. Effect of increasing the resolution by increasing the pulse delay and shifting 'against' the main flow direction.

By increasing the resolution it is now possible to obtain meaningful PIV results even in flows with a degree of turbulence of Tu ≈ 0.5%. Fig. 8. shows the instantaneous flow field behind a grid (Kompenhans *et al* 1993). The degree of turbulence, as measured by means of a hot wire, was Tu = 0.46 %. The small turbulent structures present in the flow field can be clearly detected. This was possible by means of 'negative' image shifting with U_{shift} = -5.8 m/s. The parameters of the measurement are given in Table 4.

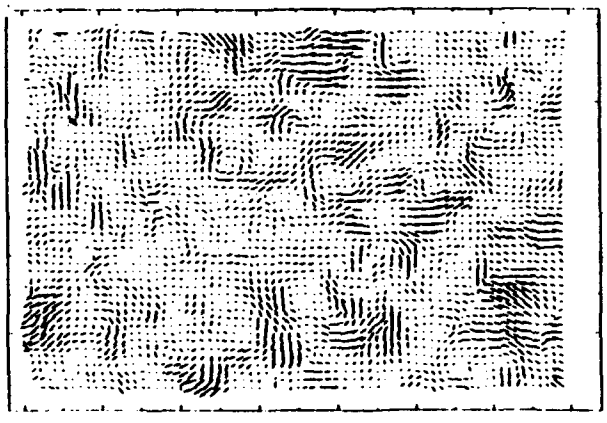

Fig. 8. Instantaneous flow field of the fluctuating velocity component behind a grid at U = 10 m/s and Tu = 0.46%; U_{shift} = -5.8 m/s.

M=1:4.7 N ≈ 10 ... 13

	U_{min} [m/s]	U_{max} [m/s]	τ [µs]	U_{shift} [m/s]	d_{shift} [µm]	d_{min} [µm]	d_{max} [µm]
without i.s.	9.9	10.1	80	0	0	198	202
with i.s.			225	-5.8	-278	196	206

Table 4. Parameters at recording of instantaneous flow field shown in Fig. 8.

If applying image shifting in this way a compromise between an improvement of the resolution of the velocity measurement and a reduction of spatial resolution (due to a larger effective interrogation spot) has to be found.

DISCUSSION

At present a higher spatial resolution is obtained at PIV if employing photographic recording instead of digital video recording, even for 35 mm photographic material. Though CCD sensors with greater pixel numbers are continuously under development and brought into the market, it will last some time till video recording is possible with the same spatial resolution as with 60 mm or 120 mm film format. Another problem, which remains with video PIV, is to store the huge amount of data, which will be captured during a measuring campaign in a wind tunnel within reasonable time digitally instead in an analog form on film. This means that for PIV applications, where high resolution concerning velocity and space is required, the photographic technique must be utilized. One main disadvantage of the photographic technique is - amongst others - that - at present - it is not possible to record the images of the tracer particles on two different photographic plates, at least, if for aerodynamic investigations pulse separations of the order of microseconds are required. That means that the problem of ambiguity removal has to be solved for photographic PIV in a reliable and flexible way by image shifting. Additionally, the application of image shifting helps to be able to perform PIV measurements in strongly three-dimensional flows and in flows with strong velocity gradients. By 'negative' image shifting the resolution of the velocity measurement can be increased. Our experience has shown that all these applications of image shifting can best be done by means of a rotating mirror system.

If employing the 'two illuminations - one recording' method, there is another possibility to increase the flexibility of the PIV system for applications in different types of flows, i.e. by first digitizing the PIV recording and then utilizing the cross correlation technique for two sub areas of the recording (Keane & Adrian 1992) instead of autocorrelation. The size of the two interrogation windows and their displacement can be adapted during evaluation. This technique can cover the problems of not having chosen the optimal distance between tracer particles at recording still during evaluation, but it cannot remove the ambiguity of direction of the velocity vectors or handle situations with image displacements of the order of the diameter of the particles. Furthermore, if considering high resolution measurements, the autocorrelation technique by means of an all-optical set-up yields the best resolution of small velocity fluctuations as shown by Vogt *et al*, 1994.

CONCLUSION

In this paper the advantages and the problems at the application of image shifting have been discussed. Summarizing one can say, that when designing an experimental set-up for PIV, one first should decide on the priority of goals: high spatial and/or temporal resolution of the flow field to be investigated, necessary resolution of velocity fluctuations, time interval in which the measurements have to be carried out, how to store the PIV recordings etc.. After having done this an appropriate system for recording can be selected. However, it must be kept in mind, that not every requirement can be fulfilled due to technical limits e.g. in laser power, pulse repetition etc.. The selection of the recording system also influences the method for ambiguity removal, which can be utilized and, hence, the evaluation technique to be used. At the present stage of the development of the PIV technique the application of the image shifting technique (by means of a rotating mirror) seems to be the method best suited for ambiguity removal and flexible adaptation to the flow field in order to meet the requirements, which have to be fulfilled to obtain high quality data at investigations of flow fields in aerodynamics.

REFERENCES

Adrian, R.J. 1986, Image shifting technique to resolve directional ambiguity in double-pulsed velocimetry, Appl. Optics, vol. 25, pp. 3855-3858.

Adrian, R.J. 1991, Particle-Imaging techniques for Experimental Fluid Mechanics, Ann. Rev. Fluid Mech, vol. 23, pp. 261-304.

Gauthier, V. & Riethmuller, M.L. 1988, Application of PIDV to complex flows: Resolution of the directional ambiguity, Lecture Series v. Karman Inst. Fluid. Dyn. 1988-06, March 21 - 25, 1988.

Grant, I., Smith, G.H., Lui, A., Owens, E.H. & Yan, Y.-Y. 1989, Measuring Turbulence in Reversing Flows by Particle Image Velocimeter, ICALEO '89, L.I.A. Proc. 68, pp. 92-100.

Keane, R.D. & Adrian, R.J. 1990, Optimization of particle image velocimeters. Part I: Double pulsed systems, Meas. Sci. Technol., vol. 1, pp. 1202-1215.

Keane, R.D. & Adrian, R.J. 1992, Theory of cross-correlation analysis of PIV images, Appl. Sci. Res., vol. 49, pp. 191-215.

Kompenhans, J., Raffel, M., Vogt, A. & Fischer, M. 1993, Aerodynamic investigations in low and high speed wind tunnels by means of Particle Image Velocimetry, Proceedings 15th ICIASF, 20.-23.9.1993, Saint -Louis, France, pp. 46.1-46.5.

Kompenhans, J., Raffel, M., Wernert P. & Schäfer, H.J., 1994, Instantaneous flow field measurements on pitching airfoils by means of Particle Image Velocimetry, Proc. 'Optical Methods and data processing in heat and fluid flow', April 14 - 15, 1994, London, pp. 117-121.

Landreth, C.C., Adrian, R.J. & Yao, C.S. 1988a, Double pulsed particle image velocimeter with directional resolution for complex flows, Exp. Fluids, vol. 6, pp. 119-128.

Landreth, C.C. & Adrian, R.J. 1988b, Electrooptical image shifting for particle image velocimetry, Appl. Optics, vol. 27, pp. 4216-4220.

Lourenço, L.M., Krothapalli, A., Buchlin, J.M. & Riethmuller M.L. 1986, A non-invasive experimental technique for the measurement of unsteady velocity and vorticity fields, AIAA Journal, vol. 24, pp. 1715-1717.

Lourenço, L.M. 1993, Velocity bias technique for particle image velocimetry measurements of high speed flows, Appl. Optics, vol. 32, pp. 2159-2162.

Molezzi, M.J. & Dutton, J.C. 1993, Application of particle image velocimetry in high-speed separated flows, AIAA Journal, vol. 31, pp. 438-446.

Raffel, M. & Kompenhans, J. 1993a, PIV measurements of unsteady transonic flow fields above a NACA 0012 airfoil, Proc. 5th Int. Conf. 'Laser Anemometry - Advances and Applications', Veldhoven, The Netherlands, August 23 -27, SPIE Proceedings Volume 1978, pp. 527-535.

Raffel, M. 1993b, PIV Messungen instationärer Geschwindigkeitsfelder an einem schwingenden Rotorprofil, DLR Forschungsbericht, DLR-FB 93-50.

Raffel, M. & Kompenhans, J. 1994, Error analysis for PIV recording utilizing image shifting, Proc. 7th Int. Symp. on Applications of Laser Techniques to Fluid Mechanics, Lisbon, Portugal, July 11 - 14, 1994.

Reuss, D.L. 1993, Two-dimensional particle-image velocimetry with electrooptical image shifting in an internal combustion engine, Optical Diagnostics in Fluid and Thermal Flow, S. S. Cha, J. D. Trollinger, (eds.), Proc. SPIE 2005, pp. 413-424.

Vogt, A., Reichel, F. & Kompenhans, J. 1994, A compact and simple all optical evaluation method for PIV recordings, Proc. 7th Int. Symp. on Applications of Laser Techniques to Fluid Mechanics, Lisbon, Portugal, July 11 - 14, 1994.

Willert, C.E. & Gharib, M. 1991, Digital particle image velocimetry, Exp. Fluids, vol. 10, pp. 181 - 193.

HIGH ACCURACY TECHNIQUES APPLIED TO THE EXTRACTION OF ABSOLUTE POSITION ESTIMATES IN A 3DPIV SYSTEM

M. Funes-Gallanzi, P. J. Bryanston-Cross & D.D. Udrea

Optical Engineering Laboratory
Department of Engineering
University of Warwick, U.K.

1. Abstract

The work presented in this paper deals with means of making spatial PIV measurements at high speeds more accurate. The PIV technique is now a well developed technique for fluids research. Further, a move to three dimensional measurement of the velocity field, to bring the accuracy of the estimates up to the standards demanded by aerodynamicists, is the next step in the development of the technique. At high speeds, the seeding density in regions of interest, such as wakes or boundary layers, are not high enough to enable the use of frequency techniques; which in any case cannot capture small scale information.

Essentially, a diffraction limited optical component has been used to provide aberration free particle images. Secondly, the sensitivity of the CCD cameras has been increased with the use of bespoke tuning for laser operation. Thirdly, it has been found that it is possible to record double, with a lower displacement than in the past, particle images using a pulsed laser. Fourthly, the particle data can be automatically analyzed using a software program. Finally, since the data is recorded in stereo, it is possible to obtain instantaneous 3-D particle whole field velocity. This 3D velocity estimate is made accurate to the order of $40\mu m$ with the help of high precision measurements of position in all three dimensions: exploiting the intensity information in the data. Such an intensive amount of processing is only possible due to the large data compression which is possible when using the spatial approach to PIV analysis.

2. Introduction

For many years several groups of people have been researching optical methods for the extraction of three-dimensional flow. Throughout the last decade several techniques have been developed. Laser Doppler Anemometry (LDA) using a continuous wave laser to temporally scan a single spatial point through the flow field is the most commercially exploited technique. At face value the application of LDA seems straightforward. However, as the study of fluid dynamics has evolved, from being able to solve and measure the steady state problem towards the reality of three-dimensional turbulent unsteady flows, the inherent limitations of temporally averaged data have become more apparent. Alternatively, whole field flow visualization methods such as holographic interferometry have failed to deliver a true solution to this problem for two main reasons. Firstly, the complexity of the holographic system has made its application specific to the experimental case in question. Secondly, the complexity of deconvolving an integrated refractive index field adds a further limitation to the general application of the technique.

The more recently evolved Particle Image Velocimetry (PIV) simplifies the acquisition of whole field data to a photographic and/or CCD imaging process, but like LDA, still requires considerable mathematical processing of data. The PIV data to date has, as yet, inherently been of a two-dimensional nature. In order to extract the out-of-plane component various authors have concentrated on the use of triangulation. However, if only triangulation is used, the relative error in the out-of-plane direction is of the order of three times larger than in the x-y direction. This effectively makes the technique of no practical industrial use where three dimensional flow obtains. Furthermore, both the relative and absolute co-ordinate systems remain basically unrelated as the measurements obtained by triangulation are relative between pairs of particles and have no relation to a frame of reference. Moreover, PIV data is notoriously difficult to interpret without a complementary qualitative picture, to set the framework for the more quantitative information provided by PIV. This last topic is covered in a companion paper also presented at this conference.

The experiments described in this paper provides a fundamental shift to 3DPIV and addresses the limitations. With computer automated particle image processing, it is then possible to construct the vectorial distribution of position and velocity of the flow field by a combination of techniques.

3. Experimental systems

Testing was carried out in the ILPC at DRA Pyestock and at the new transonic facility of the Department of Engineering, University of Warwick. The ILPC is a short duration facility designed to allow high quality heat transfer and aerodynamic measurements to be taken for a full-size annular cascade of turbine vanes. The use of this technique for turbomachinery measurements was pioneered by Schultz et al, (1973). The Pyestock facility is described by Brooks et al, (1985).

The Warwick University Transonic Blowdown facility is s transient tunnel surrounded by an Anacote chamber. The initial function of the test cell had been the evaluation of noise levels at the exit of a transonic jet. The facility is described in detail in the companion paper presented at this conference (Funes-Gallanzi, 1994). The seeding required for PIV experiments, is injected into the settling chamber, at a pressure of approximately 8 bar.

Images employing a CCD camera and K2 diffraction limited optics arrangement were recorded; using a frame grabber and related electronics. The particle images shown were then pro-

cessed using a software package developed at the University of Warwick called APWin. APWin performed its processing under Windows on a PC and displayed the resultant velocity field on a SVGA monitor. The results were then downloaded via Ethernet onto the departmental Sun Sparc station 1. A second stage of processing followed, at the end of which a revised velocity vector plot was produced using the Matlab environment.

4. Absolute Position estimation

The application involves 3DPIV experiments at transonic speeds and illustrates a novel high accuracy absolute position estimation technique. A well known and quite difficult problem in conventional PIV is to ensure that the data is being viewed - or at least displayed after suitable rotations/translations - orthogonally to the light-sheet. This problem is exacerbated in 3DPIV and it has been found to be impossible to determine absolute position as accurately as required; under realistic experimental conditions. Therefore, a novel approach is being presented of making an initial estimate of the parameters on-site, and subsequently improve on these, by employing two views of a reference image and a mixture of techniques implemented in the REGISTER software package; developed by the Warwick Optical Engineering group.

It is of crucial importance to find the absolute position of the frame of reference provided by the focal distance. In this way, the relative position (and therefore velocities) of particle pairs can be firstly found relative to this point, and then its absolute position in space can be ascertained.

Error analysis for stereoscopic PIV has been investigated for the geometric parameters as shown by Prasad & Adrian (1993). However, a comprehensive investigation, even for the geometric aspects, including the effects of registration error was not covered. Particle size, which is given by the speed of flow under consideration, influences accuracy in two distinct ways. Firstly, its image size relative to the pixel size determines the maximum spatial resolution. By exploiting grey level information, it is possible to achieve sub-pixel (of the order of 1/10th of a pixel) accuracy with no bias. Secondly, varying particle sizes, electronic noise, image smearing, etc. contribute to a random component. By employing the image intensity approach to PIV, it is possible to discriminate particles according to their size and to deal with electronic noise, thus reducing the impact of random errors on the accuracy of the measurements. Image smearing is sometimes present in DPIV data and not accounted for; when the CCD sensor dimensions are not matched by the image grabber (commonly a 512 by 512 grabber is used while the image is sensed by a 768 by 576 pixels array). The description of how the absolute position of the frame of reference can be accurately described is split into two distinct parts:

The first part involves the calibration of the solid state cameras to suit the dynamic range and ensure that their light response is identical. This is achieved with the help of a Baum chart and USAF 1951 resolution chart. This stage is of crucial importance, if grey level information is to be used in the data analysis stage. Thus, although some authors consider the use of digital cameras in PIV to be merely an extension of the technique, if grey level information is also of interest, more general solid state information and calibration is required. The determining factor is the effective number of grey levels employed (or in other words the contrast). Therefore, to tailor the dynamic range of the cameras to the experimental light conditions yields large improvements in accuracy.

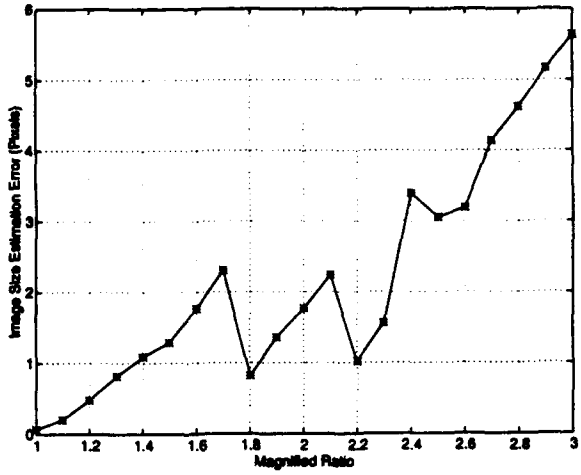

Figure 1

The second part consists of placing an England finder and taking a picture with the stereo PIV arrangement. An England finder is a graticule containing labeled squares of 1mm by 1mm which are each split into four regions and contain the square label in an inner circle. From these images, it is possible to make a first attempt at reconciling all views of the finder; using the measured parameters of location and distances of the cameras to region of interest et cetera. In the ideal case, if no errors were present, these would result, after a transformation to a common viewing point, in identical images being formed from all cameras. However, this is in general not the case. Therefore, various characteristics of the images are used to minimize these errors and produce corrected estimates which can locate the frame of reference with a high degree of accuracy. The chosen common viewing point is given by a plane orthogonal to the light-sheet at the average focal distance of the viewing cameras.

The technique consists of using a non-linear Nelder-Meade approach to estimate errors due to rotation about the x and y-axis, spiral FFTs to estimate rotation of one camera with respect to the other (about the z-axis) and England finder image ratios/labels to estimate translations.

The system was successfully tested at the new Warwick University transonic blowdown facility; using an England finder as the reference image. The translation error, after software correction, in the x and y-direction was limited to no more than 1 pixel for translations of up to 50 pixels. The error for translations in the z-direction is shown in Figure 1. On the other hand, the rotational errors measured in pixels versus degrees are shown in Figures 2 and 3. Figure 3 shows the errors due to rotation about the y-axis (the errors due to rotation about the x-axis being identical) between 0 and 30° using a non-linear Nelder-Meade algorithm, which are shown to be 2.3 pixels at 30°. Lastly,

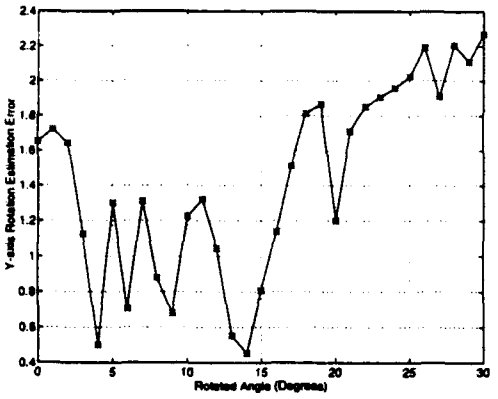

Figure 2

Figure 3 shows the errors, using the spiral FFT technique, between 0 and 43°, with a maximum error of 1 pixel at 43°.

The whole process is involved and time consuming but can be adapted to virtually any set of test conditions. Thus, the price paid for this increase in accuracy in PIV measurements, is a somewhat longer and rigorous setup stage before measurements are actually taken. A new software package to automatically carry out corrections to the initial estimates on the basis of the image information is currently under further development so it can be integrated with the existing PIV software. The main advantage of such an approach is that, particularly in an industrial environment, it is often not possible to make physical measurements with great accuracy; given the facilities and time available. Therefore, a second corrective stage afterwards makes possible highly accurate PIV measurements; even in hostile industrial conditions.

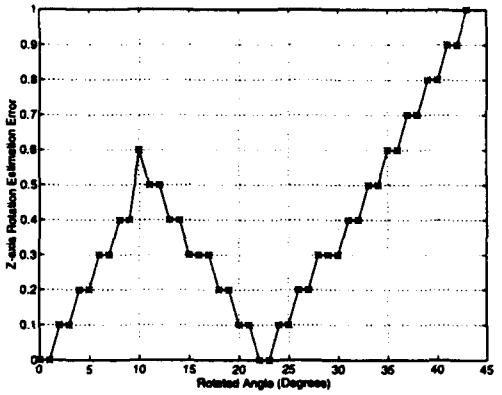

Figure 3

5. PIV image processing using APWin

The objective of image processing is to automatically produce a velocity vector field from the digitized particle field. The digitized particle field analyzed by APWin is a binary image. The images contain several features which need to be separated without ambiguity. These being:

- Images of the paired particles.
- Single unmatched particles.
- Glare from laser light reflection.
- Noise.

The processing must identify the spacing of the paired particles and translate them into velocities. The predominant view to date has been to process the data after a transformation into the frequency domain. The alternate perspective developed in APWin has been to process the information directly in the spatial domain.

APWin is a computer program which is the result of a long period of research directed towards the automatic extraction of particle image data from stored digital images. A direct spatial digital processing method was adopted. This approach was taken after reviewing the work of Goss, 1989. The particle data at transonic speeds tends to be sparse, which makes the processing of individual particles far more attractive than the global processing usually applied to low speed flows. There are several significant advantages of working with a direct image as opposed to the more conventional Fourier domain approaches of Adrian, 1985:

- The frequency technique suffers in comparison to the spatial technique from a high computational overhead. This handicap has been addressed by some authors, for instance Prasad et al (1992), in an attempt to gain speed by lowering the resolution and the accuracy of the measurements.
- The spatial domain allows the use of well developed image processing algorithms.
- The particle image field can be very quickly reduced to a sparse array of data points. Thus, instead of the intensive processing of large digital images, typically of the size of 8 to 20 Mbytes; the data is reduced to a single of 30 to 100 kbytes vector representing the particle field.
- The frequency technique also requires that the out-of-plane motion of the seeding particles should be small compared to the thickness of the illuminating light sheet (large displacement tends to decrease the correlation amplitude as shown by Adrian 1988). The successful interrogation of a 3DPIV picture through the frequency approach, is limited by the constraint that the particles should not move more than 30% of the light sheet thickness between exposures (Keane & Adrian, 1990). The maximum attainable out-of-plane particle displacement being about 1/4 the thickness of the light

sheet (Gauthier et al, 1988). Therefore, the dynamic range of velocities, available with the frequency technique, is drastically reduced compared to the spatial approach.

- By viewing the particle data individually, the user has a direct image of the particle field, whereas the FFT approach presents a more ambiguous global view of the data. That is to say, it is unable to yield small-scale results, as the results obtained are local averages representing the observed velocity field (Adrian, 1988). In some cases, such as wakes and boundary layers, where seeding is notoriously difficult to inject, limited individual particle data can yield useful information.

- In making such a large data reduction it is then possible to apply very intensive processing to evaluate the information.

An automatic spatial analysis strategy has been evolved to deal efficiently with the sparse data fields encountered. Aimed at reducing the effect of ambiguity in particle pairing, and accommodating the changing flow directions, this strategy incorporates the following steps in an iterative fashion until no new pairs are encountered.

- Initial particle pairing.
- Ambiguous pair recognition.
- Setting/updating a velocity and direction range.
- Removal of background flare and noise.
- Final particle sorting.

6. Out-of-plane Velocity Measurement

The use of the stereo approach enables the measurement of the relative velocities within the region of interest illuminated by the light sheet. Two stereoscopic configurations can be used. The angular method has the optical axis of both cameras intersect the illuminated field containing some angle thereby. The translation method has the optical axis of both viewing cameras parallel to each other and perpendicular to the light sheet. According to Gauthier & Reithmuller (1988), the angular displacement method is more accurate. However, the required depth of field is larger than in the translation method. For a given magnification, a large depth of field can only be obtained by increasing the f-number; i.e. decreasing the light sensed by the CCD array. This is also a limitation on the widest practical angle between the cameras. In practical applications such as turbomachinery, the area of interest (boundary layer, wake,etc.) is generally quite small in absolute terms. This fact, coupled with the need for a realistic stand-off distance using diffraction-limited optics, means that only the angular method can be reliably used yielding a meaningful overlapping area.

The 3D approach allows the measurement to be more accurate than previous two-dimensional estimates. To illustrate this concept, consider Figure 4. This shows a typical particle pair X_1 and X_2. O_1, O_2 and O_3 represent three viewing positions with O_1 perpendicular to the light-sheet (referred to as the on-axis view) and with O_2, O_3 symetrically displaced about the centre of the interrogation area (off-axis views). Consequently using simple trigonometry the following relationships can be derived:

$$d = h \cos \varphi$$

$$d_1 = h \cos(\varphi - \theta)$$

$$\frac{d_1}{d} = \frac{\cos(\varphi - \theta)}{\cos\varphi}$$

where d is the magnitude of the normal from X_2 to X_1O_1 (i.e. the shortest distance), h is the shortest distance between the two particles at X_1 and X_2, φ is the angle between X_1X_2 and X_2A, θ is the angle between the two observation points and the perpendicular to the light-sheet. Therefore,

$$x = \frac{d_1 - d.\cos(\theta)}{\sin(\theta)}$$

where x is the magnitude of X_1A; i.e. the required depth parameter.

For calibration purposes, an England finder graticule of 1 Inch by 3 Inches is used as it provides accurate and detailed information; which can be used for absolute position estimation, as previously described, and PIV scaling.

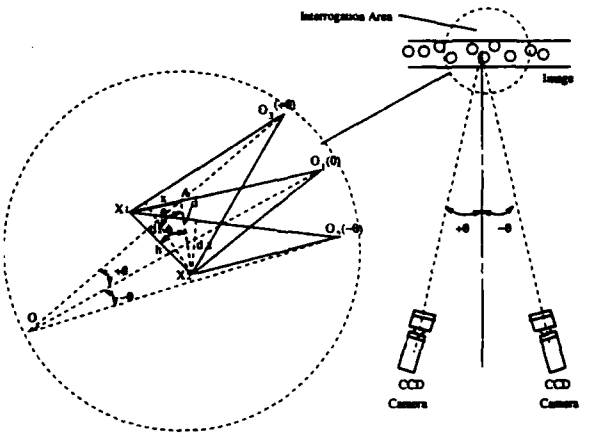

Figure 4 Schematic diagram for 3D velocity estimation

7. Relative Position Estimation

Once initial results were obtained it became clear that, given the high errors in the out-of-plane direction, the stereoscopic approach to PIV would remain inpractical unless a way was found to increase the accuracy in the z-direction.

One way to increase the accuracy in general, is of course to increase the angle subtended by the two cameras. However, this is often not possible in real applications as facilities have to be adapted to, which often were not particularly designed for visualization purposes, the depth of field required increases as the angle increases(leading to less photons falling on the imaging sensor), and are further restricted by the need for simplicity and

Figure 5 PIV image of a field

economy. Furthermore, as the angle increases the absolute spatial errors also increase; thus denying some of the increase in accuracy.

As mentioned earlier, the spatial approach to PIV has as one of its advantages the ability to apply fairly intensive processing to the PIV pairs found; thanks to the large data reduction involved.

Now, a digital image is a spatial, intensity and temporal quantized representation of a real-world scene. The precise representation of position is critical to the successful extraction of velocity data from a PIV image. For a solid state approach to PIV to approach the precision of a photographic image, accurate sub-pixel position estimates are necessary. Without such an approach, the large number of required digital images present currently un-surmountable problems of registration and data volume and throughput.

Studies on the nature of digital images rarely take specific notice of the effects and opportunities offered by intensity quantization. Normally, only spatial quantization is considered; though occasionally the strong effect which the number of bits per pixel has is recognized. A full description of the combined effects of spatial and intensity quantization has been reported (A.M. Bruckstein, 1987 for instance) but in a statistics context and without regard to the geometry or specific image content.

In view of this, an approach is currently being developed based on the concept of position equivalence classes, referred to as "locales", and first developed by D. Havelock (1989). Some independence from image form is attained by considering a general gray scale shape. A natural consequence of the concept is the definition of an optimally precise position estimate given by the centroid of the locale. It can thus be shown that useful dynamic range is far more important than pixel size for obtaining geometric precision when data volume is constrained. Furthermore, it can also be shown that the best way to allocate spatial and intensity resolution for a digitizing scheme subject to data volume constraints is to allow only enough spatial resolution for effective detection and recognition and employ all remaining data capacity to maximize the available intensity resolution.

Typically, if the irradiance is given by:

$$I(r) = \frac{P}{2\pi\sigma^2} e^{\frac{-r^2}{2\sigma^2}}$$

where P is the input power, the beam diameter is given conventionally by $d=4\sigma$, which means that over the interval considered($0 \le r \le 2\sigma$) only 86% of the power is contained. The rest provides stray illumination and leaks through the diffraction limited optics to lower the contrast. Thus, the CCD cameras have to be tuned to the prevailing light conditions to yield the greatest available contrast.

Turning now to the application of this concept to PIV, a fairly realistic representation of the image of a particle (assuming it is spherical) can be provided by a Gaussian form.

$$E(x,y) = A\, e^{\frac{-((x-x_o)^2 + (y-y_o)^2)}{2\sigma^2}}$$

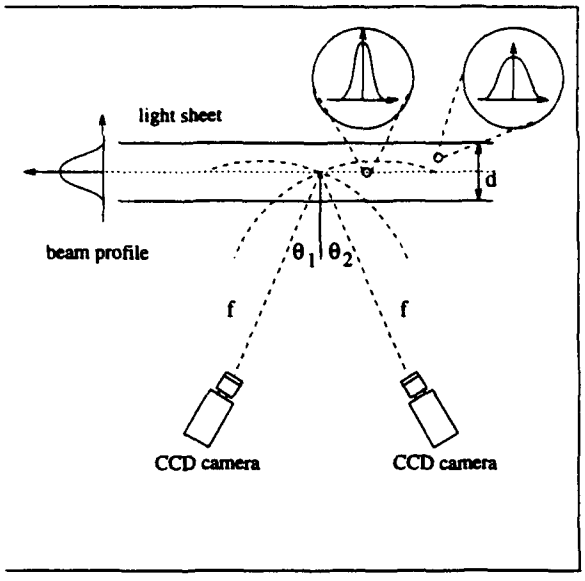

Figure 7 Gaussian form dependence on position

The particle image is located at (x_o,y_o). The Amplitude A and width σ are the only parameters of its circularly symetric shape.

Many algorithms can be found to estimate the position of the centre of this object. For instance, a centroid estimate gives the correct answer in the absence of noise and quantization. In the presence of spatial quantization there appears a skew error which can be accounted for in a unique mapping. In the presence of intensity quantization, as is normal for digital images, there is not a unique but a set of possible object positions. These regions are referred to as locales and their size determines the uncertainty in object position. There is no equivalent situation in non-digital imagery.

With reference to the schematic diagram in Figure 7, it is possible to establish what these two parameters, A and width σ, in turn depend on.

Note that in order to simplify the discussion, the centre of the Nd:YAG sheet and the centre of of focus are made co-incident and the depth of view is made somewhat larger than the width of the light sheet. Thus, the amplitude can be seen to depend on the z-position of the particle and vary according to the change in intensity of the laser over the depth of the region of interest. On the other hand, σ varies approximately linearly according to the z-position in relation to the position of focus. This focal length can be quite accurately calculated for a given objective in the case of the K2 diffraction limited optics. As the particle moves out of focus, so σ will vary. Thus if the ratio of A/σ (referred to as the depth ratio) is considered, it is directly and linearly related to the focal position.

This technique has two major advantages. Firstly, it provides three measures for the z-component. Two from the A/σ ratio from each image in a stereo case, and the third from triangulation. Just as importantly though, it provides a way in which these relative velocity measurements can be related to an absolute frame of reference. The depth ratio will exhibit a maximum where the particle is in line with the focal length of the lens, and will then tail off as a particle moves in front or behind this position. Thus, the system has a symetry about this focal length leading to an ambiguity in the measurement of the depth ratio. In order to account for it, triangulation needs to be used as well. Thus if a particle pair lies in a equidistant positions from this axis, the ratio will be equal but triangulation will show one to lie ahead of the other, thus enabling the data to be unscrambled.

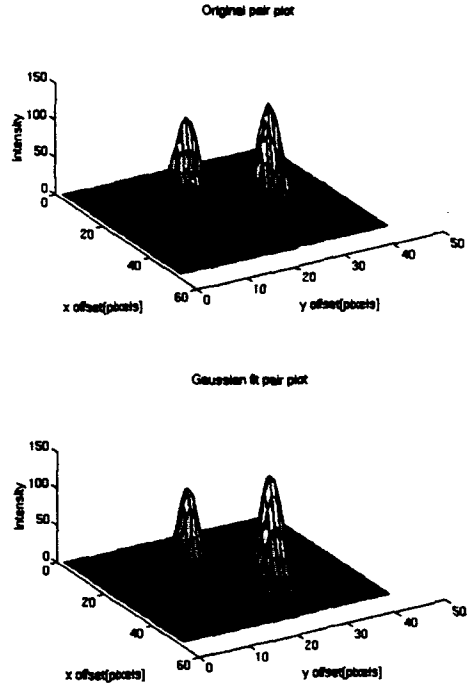

Figure 6 MATLAB plots of a particle pair in grey scale

The system can be calibrated by plotting all the depth ratios and finding the maximum; which is the frame of reference as it is co-incident with the focal length. The relationship between the depth ratio and absolute depth can also be ascertained from this plot by introducing the width of the ligh-sheet and thus deduce the scaling factor. The potential accuracy of this approach has been estimated at 20-30μm in all three directions. This is arrived at by considering an effective grey level dynamic range of 100-150 grey levels, and assumes that all parameters have been estimated by the use of REGISTER as previously discussed.

Preliminary results are shown in Figures 5 and 6. A particle pair was obtained from the data field shown on Figure 5; this is a PIV image of a wake at 1.2 Mach shot at the ILPC transient facility of DRA Pyestock. A pair, highlighted in the image, was

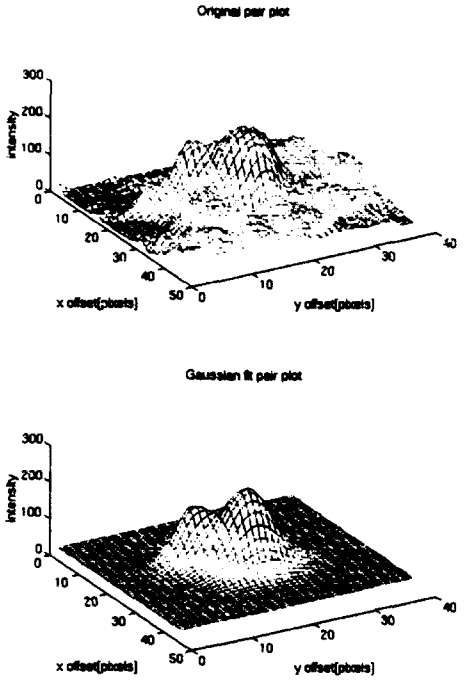

Figure 8 MATLAB plots of overlapping pair in grey scale

plotted to confirm the broad nature of the particle images. The two particle positions were then calculated to sub-pixel accuracy by a combination of data intensity calculations and depth ratio estimates; as shown in Figure 6. This new estimates were in agreement with the previously calculated data. The estimated accuracy was in the order of 40μm; an improvement on previous estimates but not as high as can be expected. The software, currently implemented in MATLAB, makes use of the output from APWin to provide an initial estimate of particle position and pair velocities, which is then improved upon by the abovementioned techniques. Further research is currently under way to fully automate the process, include it in the APWin environment and gain more experience with both the locales approach to sub-pixel estimation and the statistical properties and experimental characteristics of the depth ratio approach previously described.

Two further advantages of this approach are that normally some astigmatism is present in the particle data. This can be removed by applying the techniques described. Secondly, particles which are close together and would normally be erroneously interpreted as one can be recognized and treated correctly, as shown in Figure 8, where such a case is shown. The bounds of the depth ratio are defined by the power profile on the lightsheet, the particle size and shape, and by the prevailing light conditions. Therefore, particle of a different size and/or shape to those representing the seeding can be recognized and treated accordingly. Thus, the presence of stray particles in the flow does not influence the analysis.

The accurate measurement of relative velocity in three dimensions presents some formidable problems. In particular, the whole approach requires the centre of focus to lie within the light sheet. This has proven to be particularly difficult in industrial applications. A relible way to overcome this problem has been to make use of an oscilloscope to focus rather than sight. The locales approach, while more accurate than centroid estimation or Fourier phase estimation, is still under active development. Calibration of the cameras so they are not saturated at the focal length and other calibration requirements mean that although the accuracy is increased, the complexity in performing these experiments also increases.

8. Conclusions

The techniques described deal first of all, with the successful determination of absolute co-ordinate information, in an industrial environment, to an accuracy of +/- 2 pixels for the experiments described. This approach involves a second corrective software-implemented corrective stage, after all parameters have been physically measured.

Secondly, the grey level information was employed to provide an estimate of the three dimensional relative position with an accuracy of 40μm. The relative and absolute position estimates could then be combined.

Three dimensional measurements of the particle pairs were successfully accomplished and so 3D velocities were estimated. The software package APWin was employed to obtain the velocity information. A further program was used to plot and estimate the three dimensional position of the particle pairs found, exploiting not only triangulation but also grey level information. Lastly, the technique was extended to allow for the recognition of close overlapping particle pair data and the removal of astigmatic effects. The development of these techniques, and the measurements obtained, mean that the short term target of achieving 1% accuracy for 3DPIV measurements at high speeds, for complex unsteady flow turbomachinery applications, is now possible.

9. Acknowledgements

The authors gratefully acknowledge the support of DRA Pyestock through Mr. K.S. Chana in funding part of this research.

10References

Goss, L.P. et al, "A novel technique for blade-to-blade velocity measurements in a turbine cascade",AIAA/ASME/SAE/ASEE 25th Joint Propulsion Conference, Monterrey CA July 10-12, 1989.

Adrian, R.J. & Yao, C., "Pulse laser technique application to liquid and gaseous flows and the scattering power of seed materials", Applied Optics, Vol. 24 No1 Jan, 1985.

Adrian R.J., "Statistical properties of particle image velocimetry in fluid Mechanics-III", Ladoan-Instituto Superior Tecnico, Lisbon, pp. 115-129, 1988.

Brooks, A.J. et al," The Isentropic Light Piston Cascade at RAE Pyestock" AGARD-CP-390, 1985.

Malyak, P. H., & Thompson, B. J. 'Particle displacement and velocity measurement using holography', Opt. Eng. 23 (5), 1984, 567-576

Ewan, B. C. R. 'Particle velocity distribution measurement by holography', Appl. Opt. 18 (18), 1979, 3156

Payne, P. R., Carder, K. L., Steward, R. G. 'Image analysis techniques for holograms of dynamic oceanic particles', Appl. Opt., 23 (2), 1984, 204

Hassan, Y., Blanchat, T. 'Flow velocity measurements using digital pulsed laser velocimetry', Opt. Eng., 30 (8), 1991, 1220

Sinha, S. K., Kuhlman, P. S. 'Investigating the use of stereoscopic particle streak velocimetry for estimating the three-dimensional vorticity field', Exp. in Fluids, 12, 1992, 377-384

Weinstein, L. M., Beeler, G. B., Lindemann, A. M. 'High-speed holocinematographic velocimeter for studying turbulent flow control physics', Proc. AIAA Shear Flow Control Conf., paper AIAA-85-0526, Boulder, Col., USA, March 1985

A.M. Bruckstein,"On optimal image digitization", IEEE Trans. Acoustic Speech, Signal Processing, vol. ASSP-35, pp. 553-555, Apr. 1987.

Bryanston-Cross, P.J., Funes-Gallanzi, M., Quan, C. & Judge, T.R.,"Holographic particle Image Velocimetry", Optics & Laser Technology, Vol. 24, No. 5, 1992.

Bryanston-Cross, P.J., Epstien, A. 'The application of submicron particle visualization for PIV (Particle Image Velocimetry) at transonic and supersonic speeds', Prog in Aerospace Sci. 27, 1990, 237

Bryanston-Cross, P.J., Harasgama, S. P., Towers, C. E., Towers, D. P., Judge, T. R., Hopwood, S. T. 'The Application of Particle Image Velocimetry (PIV). In a Short Duration Transonic Annular Turbine Cascade', Submitted to the American Society of Mechanical Engineers, for the 36th ASME International Gas Turbine & Aeroengine Congress, Orlando, Florida, USA, June 3-6 1991

Meynart, R. 'Equal Velocity Fringes in a Raleigh-Bernard Flow by a Speckle method', Appl. Opt., 19, 1980, 1385

H.J. Caufield, (ed.), "Handbook of Optical Holography", Academic Press, New York, 1979.

J.W. Goodman, "Introduction to Fourier Optics", McGraw-Hill, New York, 1968.

E. Hecht, "Optics", Addison-Wesley, 2nd ed., 1987.

M.A. Karim, "Electro-Optical Devices and Systems", PWS-Kent, 1990.

Gauthier V. & Reithmuller M.L., Application of PIDV to complex flows: Measurement of the third component. In VKI-LS 1998-06 "Particle Image Displacement Velocimetry", Von Karman Institute for Fluid Mechanics, Rhode-Saint-Genese (Belgium), 1988.

A.K. Prasad, R.J. Adrian, C.C. Landreth & P.W. Offutt, "Effect of resolution on the speed and accuracy of particle image velocimetry interrogation", Exp. in Fluids, 13, 105-116, 1992.

A.K. Prasad & R.J. Adrian, "Stereoscopic particle image velocimetry applied to liquid flows", Exp. Fluids, 15, 49-60, 1993.

Schultz, D.L. and Jones, T.V.,"Heat transfer measurements in short duration hypersonic facilities"AGARD-AG-165, 1973.

R.D. Keane & R.J. Adrian, "Optimization of particle image velocimeters", Part I: Double pulsed systems, Meas. Sci. Technol. 1, 1202-1215, 1990.

Session 36.
Engines II

SIMULTANEOUS MEASUREMENT OF INLET FLOW AND VALVE MOTION IN INTERNAL COMBUSTION ENGINES BY LASER DOPPLER TECHNIQUES.

N.Paone, C.Santolini, E.P.Tomasini.

Dipartimento di Meccanica, Univ. di Ancona,
60131 Ancona, Italia.

ABSTRACT.

The paper describes the development of a test bench in which a laser Doppler vibrometer and a laser Doppler velocimeter are employed for simultaneous measurement of valve motion and flow velocity in an internal combustion engine head. The test bench and the measurement system and methodology are presented; optical access was obtained inside the cylinder through its transparent walls and inside the intake manifold, by specially designed optical windows. Measurements are taken at different camshaft angular speed, up to a regime in which jumps and bounces of the valve occurr.

1. INTRODUCTION.

At present the experimental study of inlet flow in a combustion engine is not carried on simultaneously to the measurement of valve motion: the two activities are performed independently and correlated to each other by synchronizing the acquisition systems to the camshaft angular position θ via an encoder. If both measurements could be performed simultaneously it would be possible to study in detail even some anomalous behavioirs of the poppet valve, like jumps and bounces at high rpm, and to experimentally observe their effect on the flow field inside the engine. In order to perform such an analysis it has been developed a measurement system based on optical instruments, capable of simultaneous measurement of valve motion and air velocity on motored engine heads.

2. EXPERIMENTAL SET-UP AND MEASUREMENT METHODOLOGY.

A test bench has been developed which allows to drive the camshaft and the valve train of an internal combustion engine at variable speed by an AC electric motor controlled by an inverter. Camshaft is driven by a pulley and belt transmission, similar to that normally employed when the head is installed on a real engine. The engine head of a FIAT 4 cylinder 1.6 l engine is installed on a plexiglass cylinder connected to a settling chamber; inlet flow is generated by a centrifugal compressor connected to the settling chamber and to the cylinder. Flow rate is monitored by a Venturi pipe and it can be adjusted by a by-pass valve at the intake of the compressor. A complete inlet manifold is installed on the engine head, without air filter. Fig. 1 shows a scheme of the test bench.

The measurement system is completely based on optical instruments which employ the Doppler effect on light beams scattered by moving objects; a classical fiber optic two component differential laser Doppler velocimeter is used for flow velocity measurements, while a fiber optic laser Doppler differential vibrometer is used to measure independently the displacement and the velocity of the poppet valve. Crosstalk between the two optical instruments is avoided by employng different wavelength in the laser radiation of each of them. In particular, the laser Doppler vibrometer operates with a 5 mW He-Ne laser source while the laser Doppler velocimeter operates with a 4 W Ar^+ ion laser. Much lower power is needed for a laser Doppler vibrometer compared to a laser Doppler velocimeter for flow velocity measurement; in fact the laser vibrometer operates with light scattered from a solid surface, which is orders of magnitute more intense than light scattered from small tracer particles within a moving flow.

The instruments are synchronized to each other by an encoder on the camshaft which produces 720 or 1440 pulses/rev and a reset pulse at each rotation of the camshaft. Data are acquired digitally; it is therefore possible the simultaneous measurement of valve kinematics and flow velocity. Being all probes non-intrusive, it is possible to monitor valve velocity and valve lift, without disturbing the flow; this constitutes the major advantage of this test bench over classical solutions, where electromagnetic proximity probes are inserted downstream the valve to monitor valve motion, causing flow distorsion.

The test bench is provided with transparent windows for optical access which is necessary for both instruments.

The differential laser Doppler vibrometer shines two parallel beams at two different locations; they are used to measure relative motion and relative velocity between the two illuminated points. The measurement occurrs by eterodyning the two scattered radiations, collected by a backscatter optical system which employs the same monomode fibers used for bringing ligth to the measurement locations. Being the system equipped with a 40 MHz Bragg cell on one of the two beams, the positive or negative frequency shift on the Doppler signal is proportional to positive or negative relative velocity between the two illuminated points; fringe counting can be used to measure independently relative valve displacement. Only components of motion along the optical axis of the instrument can be measured, Selbach et al. (1992). Therefore the instrument can measure valve motion relative to the engine head if one beam is focussed on the valve head and the other is focussed on valve seat; relative motion measurements are important in order to subtract engine head vibration which is always present to some extent in any test

bench and which would add noise to valve motion measurement, therefore decreasing uncertainty as discussed in Paone et al. (1994). The two beams must be aligned parallel to valve stem, in order to measure correctly valve motion. In order to shine the beams on the valve and on the head it is necessary an optical access from the bottom of the engine head; this is accomplished by the construction of a transparent settling chamber, built in perspex. The beam which points on the valve is focussed when the valve is at its half lift position, in order to optimize the response of the instrument when valve motion brings the measurement point out of focus by several millimeters. Reflected light at the surfaces of the perspex window cause noise which disturbs the measurements; the amount of light diffused by these surface to the sensing heads can be significantly decreased if beams are not aligned perpendicular to the perspex surface, which acts as a flat mirror. This solution keeps signal to noise ratio at high level.

Optical access of the laser Doppler velocimeter to the flow around the valve is achieved by the same transparent settling chamber, whose dimensions are established in order to use relatively short focal lenses on the fiber optic probe, so that probe volume dimensions are kept to a maximum size of 0.64 x 0.075 mm. Access from the settling chamber to the cylinder allows measurement of radial and tangential velocity components. In order to measure axial flow velocity component, a transparent cylinder is installed between the settling chamber and the engine head; its internal diameter is 84 mm, as in the real engine. Cylinder is manufactured in perspex, and it is 3 mm thick, therefore refraction correction is not necessary when measurements are taken in the central region of the cylinder, Bicen (1982).

Special attention is devoted to optical access to the inlet manifold whose diameter and whose curvature radius are very small, therefore causing problems due to refraction if thick curved windows are employed. In order to keep the internal shape of the duct unchanged it was decided not to employ flat windows, as it is usually done in most of the literature known to the authors, for example in Arcoumanis et al. (1988). Therefore it was decided to build extremely thin optical windows, made of plastic transparencies, which are glued inside the duct, on which a hole was previously drilled. Optical windows having 10 mm diameter were built by using this technique, and glued at the internal surface of the inlet duct, a pipe whose diameter is 29 mm. Window thickness is 0.1 mm; it causes therefore a step on the inner wall of the duct whose size is much smaller than the boundary layer thickness. The velocity profile should not be altered by such disturbance. The thin window, when glued on the duct wall, reproduces the curved shape of the duct with great accuracy. All these considerations on optical access to the duct allow to conclude that intrusivity of the measurement technique is kept to its minimum.

Inlet flow is seeded by water droplets produced by an atomizer installed in proximity of the air intake, upstream the intake manifold. Mean droplet diameter is in the order of 1 μm, which is sufficiently small for the water droplets to follow flow fluctuations in the kHz range, therefore they are suited for measurements of intake flow with low uncertainty.

3. MEASUREMENTS AND DATA PROCESSING.

3.1 Valve Lift Measurement.

All the measurements reported in this paper are performed while the valve motion is being monitored by the Doppler vibrometer, which is focused on the valve head. Fig.2 shows the plots of valve motion acquired at three different camshaft regimes, n_C=1000+3500+4200 rpm, corresponding to an engine angular speed of 2000+7000+8400 rpm respectively. In what follows all angular speeds will be referred to the camshaft. It is interesting to observe the differences in valve motion put in light by the three plots. While at 1000 rpm the valve motion is fully determined by the cam profile, at higher rpm the valve loses contact with its cam during the deceleration which occurrs during valve lift, then moves according to a ballistic motion under the effect of inertia forces and spring load; this phenomenon is known as valve jump. At 3500 rpm jump is rather small, but it grows up to about 0.3+0.4 mm at 4200 rpm. When the valve returns to its seat, if it is not properly decelerated by the cam, it impacts on valve seat and then rebounces due to elastic effects. It is evident at 4200 rpm, where a bounce of about 0.4 mm can be measured. The height of the bounce is a considerable fraction of maximum valve lift and in this situation the inlet duct is again opened towards the cylinder, contrarily to what the designer of the valve train has prescribed. Such valve behaviour is dangerous in terms of valve resistance and could affect also inlet fluid-dynamics. Resulting effects of valve bounces on the flow will be shown in the next paragraph.

3.2 Measurements Inside the Cylinder.

Measurements of flow velocity have been performed in the cylinder and in the inlet manifold; only few results will be reported in this paper, whose purpose is to focus on measurement methodology. Fig.3 shows an example of results obtained in vicinity of the valve at a camshaft speed n_C=1000rpm, with maximum valve lift h_{max}=8.7mm and a flow rate M=6.5g/s. All figures report scattered data samples, superimposed to averaged velocity and to valve lift. About 25000 radial velocity samples are collected while the valve is moving; radial velocity is plotted versus encoder pulses, i.e. angular position of the camshaft. A large number of samples is acquired when the valve is open, while their number rapidly drops at the closure of the valve, due to the lack of seeding particles. Velocity data can be averaged over selected angular windows; fig.3 shows averaged data superimposed to scattered samples. Data are averaged by using a 1° wide angular window. Data rate is not so high to enable cycle to cycle analysis of the velocity data, therefore averaged velocity profile suffers from uncertainty due to cyclic variations in the flow structure. The amplitude of the angular window employed for averaging the data has to be chosen as compromise between the need of averaging a number of data statistically meaningfull and the necessity to limit its width in order to reduce bias induced by averaging process on non-stationary phenomena. Within a 1° window, over most of the period during which valve is open, about 60 data per 1° are collected, so that statistics can be considered sufficient. Number of collected data drops when valve closes baecause particles do not enter any more into the cylinder and those already inside the cylinder quickly avaporate, therefore the velocity data population is not statistically meaningfull; this causes scatter on avearagd data, which is not due to flow unsteadiness, but is related to poor statistics. Therefore data are meaningfull only in those regions where number of samples is statistically sufficient, while averaged data have large uncertainty elsewhere. Window amplitude $\Delta\theta$ also affects the computation of turbulent velocity fluctuations; if it increases, turbulenee apparently is increased by crank-angle broadening effects in all regions where velocity varies rapidly.

Cycle to cycle variations also artificially increase computed turbulence level. All these problems could be solved if data rate was sufficiently high, i.e. if the flow was heavily seeded. This is not the case in most of these experiments; inside the cylinder in these experiments. The plots of fig. 3 are typical of in-cylinder inlet flow; similar velocity profiles are measured at different locations in the cylinder. They all show a large flow acceleration and deceleration at valve opening and closure; flow acceleration is evident also when valve is fully open, probably due to flow inertia. Of course these data collected in a test bench in absence of a moving piston, may differ from operating engines. Being the measurement point located at about 4 mm from valve seat, flow through that point happens only when valve lift is larger than 4 mm.

When camshaft regime is increased at 3500 rpm, radial velocity at valve exit remains similar as above, as shown in fig.4. At this speed mass flow rate is M=9.5 g/s. Again, data averaged over a 1° angular window are plotted together with valve lift. The presence of valve jump does not affect significantly the flow, but oscillations in air velocity can be observed. Measurements of inlet flow in the duct upstream the valve will show same kind of oscillations, related to water hammer phenomena occurring in the inlet duct at valve closure; dumped oscillations in the inlet duct propagate downstream the valve into the cylinder.

Fig.2 showed large bounces at 4200 rpm; in fig.5 it can be observed the radial velocity measured at the same location as in figs. 3 and 4, superimposed to averaged valocity and to valve lift. Oscillations are evident also at this regime and during valve bounce flow seems to be affected, although due to the little number of data available mean velocity profiles are scattered and affected by large uncertainty. Effects of valve bounces will be more evident inside the manifold.

3.3 Measurements Inside the Inlet Manifold.

Major interest has been devoted to the measurements of flow velocity profiles inside the inlet manifold.

Axial and radial velocity profiles are measured at n_c=1000+3500+4200 rpm rpm along a diameter of the inlet manifold about 80 mm upstream the inlet valve; 11 points per traverse are sampled and 25000 velocity samples per point are collected. Again, only a few results will be reported in this paper.

Fig.6, 7 and 8 show axial velocity measurements at the center of the inlet manifold, plotted versus encoder pulse at the three camshaft regimes as above. Data collected during several camshaft revolutions are superimposed. Average velocity is computed as above on an angular window $\Delta\theta$=1°. About 60 velocity data per 1° are recorded; in this case data are recorded even when valve is closed, because seeding particles remain inside the inlet duct. Valve lift is also plotted.

At all regimes it is possible to observe dumped oscillations which appear at valve closure, typical of resonance in closed ducts. The phenomenon appears highly repeatible, being relatively small the scatter of data from different cycles. Frequency content of dumped oscillations increases at higher rpm; in fact oscillations show different harmonics superimposed to each other and harmonic content is function of engine regime. Amplitude of oscillations is larger at higher rpm, due to the increased inertia of the moving mass of fluid. At higher rpm oscillations do not dump out in the time between two cycles of camshaft, so they disturb flow motion also at valve opening, as visible in figs.7 and 8. Such oscillations where also observed downstream the valve, in figs. 4 and 5.

Furthermore from fig. 8 is is evident that when valve bounces occurr, oscillations in the inlet duct are disturbed by the opening of the valve; it can be observed that the first cycle does not show the negative peak in axial velocity,. Actually the flow enters the cylinder during valve bounce, as shown by a short positive velocity peak.

4. CONCLUDING REMARKS.

The development of a test bench and related non intrusive instrumentation suited for inlet flow studies in internal combustion engines has been presented; the whole measurement system relies on optical instruments, employing Doppler effect to measure flow and valve velocity. Optical access to a motored engine head has been achieved by a transparent cylinder made in perspex and very thin curved windows on the inlet manifold. Simultaneous data acquisition allows to correlate fluid velocity to valve motion, even at high rpm, when valve jumps and bounces occurr, which prove to affect inlet flow. The measurement system appears a valuable tool for investigating inlet fluid dynamics in engines.

5. REFERENCES.

Arcoumanis C., Flamang P.,Whitelaw J.H. 1988 Flow in the inlet manifold of a production Diesel engine, Proc. 4th Int. Symp. on Applic. of Laser Anem. to Fluid Mech., Lisbon, Portugal.

Bicen A. 1982 Refraction correction for LDA measurements in flows with curved optical boundaries, TSI Quarterly, n. 8.

Paone N., Santolini C., Tomasini E.P. 1994 Application of a laser Doppler vibrometer to evaluate engine poppet valve kinematics, Proc. 12th Int. Conf. on Modal Analysis, Honolulu Hawaii.

Selbach H., Lewin A.C., Roth V. 1992 Laser Doppler vibrometer for applications in the automotive industry, Proc. 25th ISATA Conf. Laser Applic. in the Automotive Ind., Firenze, Italia.

6. ACKNOWLEDGMENTS.

Part of the work has been financed by Italian Research Council CNR, under contract no. 91.02497.PF74. V.Ponzio has contributed to the construction of the test bench, while M.Gasparetti to the conduction of the experiments.

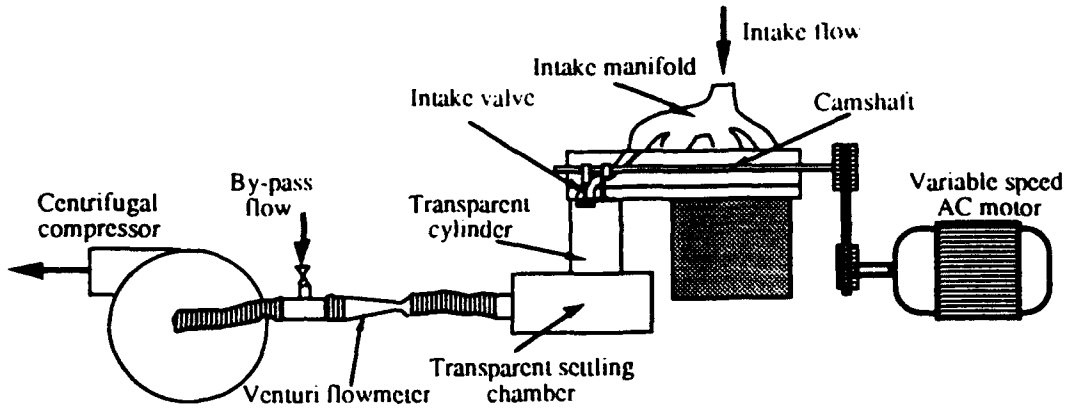

Fig. 1 - Scheme of the test bench.

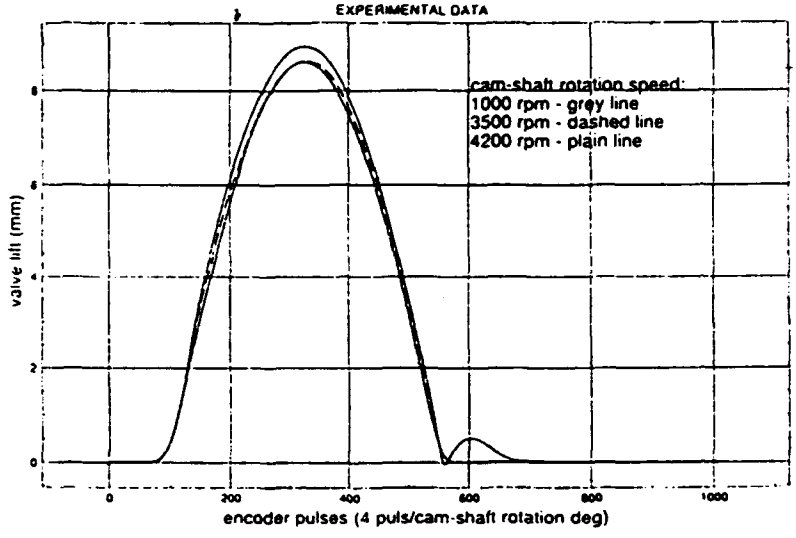

Fig. 2 - Valve lift measurements.

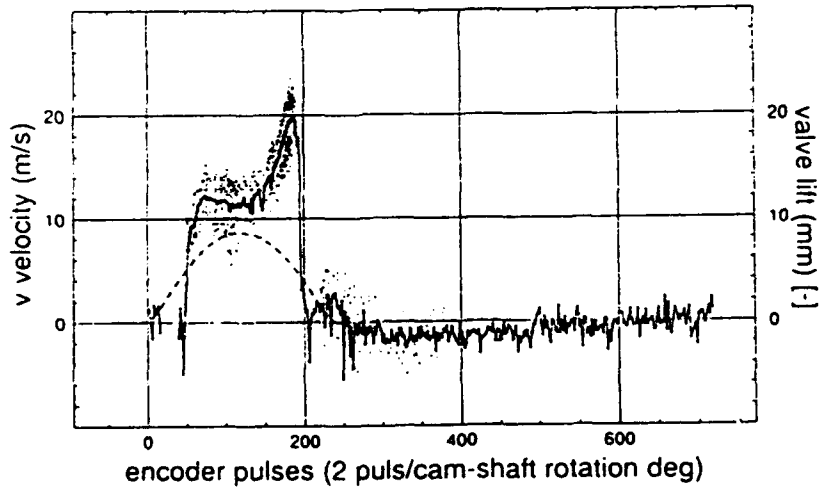

Fig. 3 - Measurement of radial air velocity close to the valve (valve lift, scattered data, averaged data) . (n_C=1000 rpm, M=6.5g/s) 25000 samples.

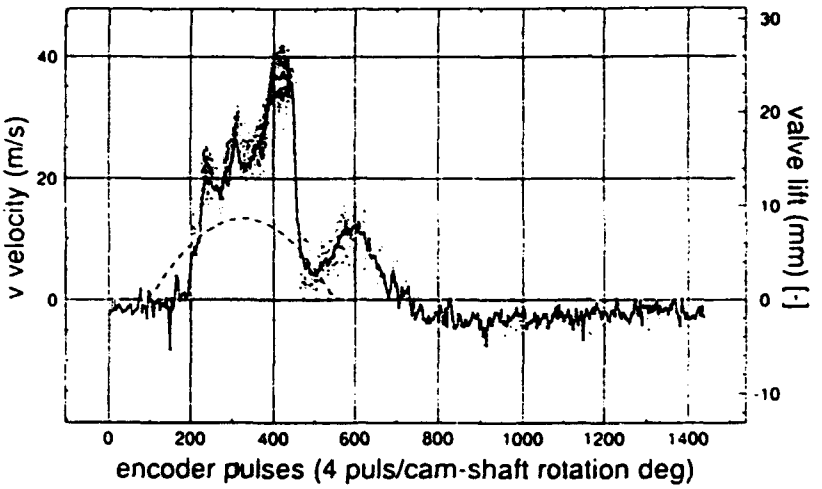

Fig. 4 - Measurement of radial air velocity close to the valve (valve lift, scattered data, averaged data) . (n_C=3500 rpm, M=9.5g/s) 25000 samples.

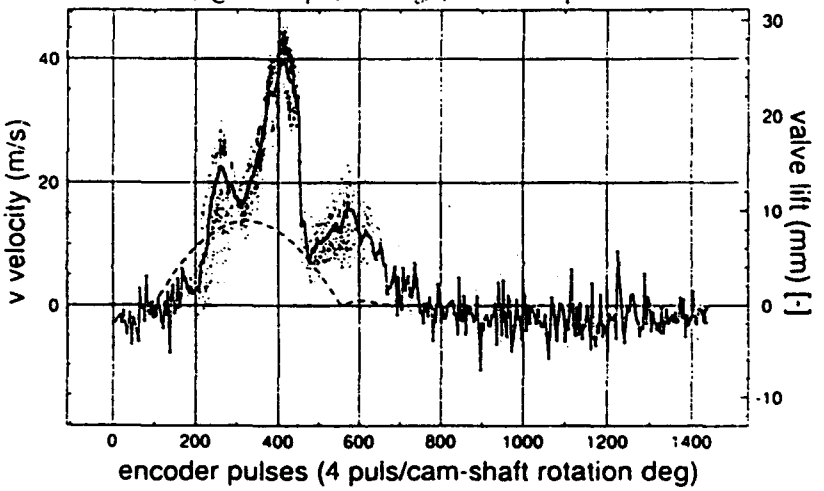

Fig. 5 - Measurement of radial air velocity close to the valve (valve lift, scattered data, averaged data) . (n_C=4200 rpm, M=10 g/s) 25000 samples.

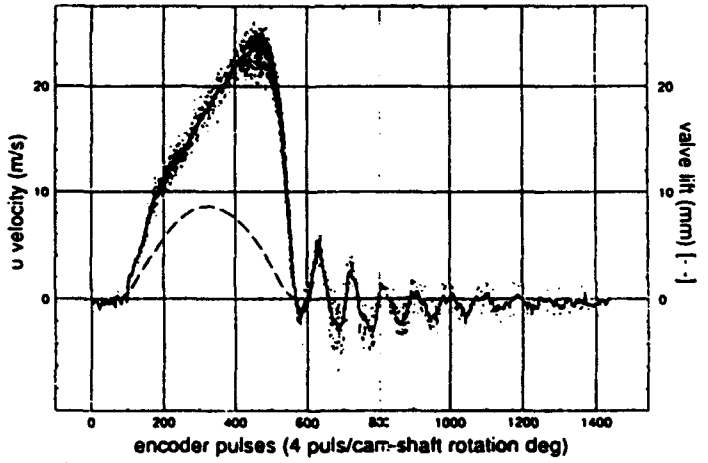

Fig. 6 - Measurement of axial velocity inside the inlet manifold (valve lift, scattered data, averaged data) . (n_C=1000 rpm, M=6.5g/s): 25000 samples.

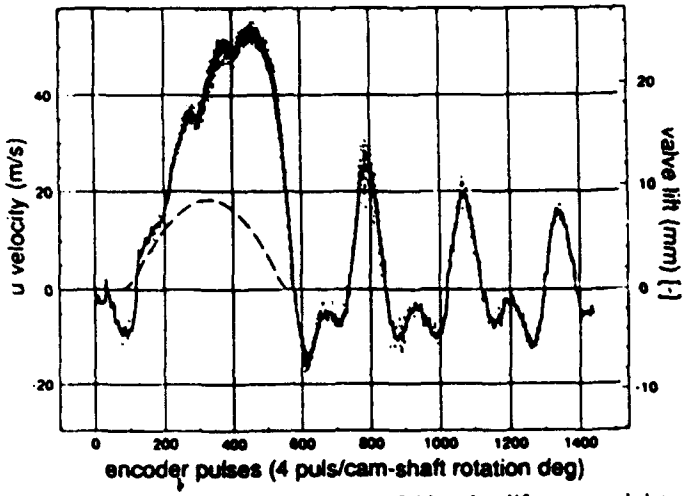

Fig. 7 - Measurement of axial velocity inside the inlet manifold (valve lift, scattered data, averaged data) ; (n_C=3500 rpm, M=9.5g/s) 25000 samples.

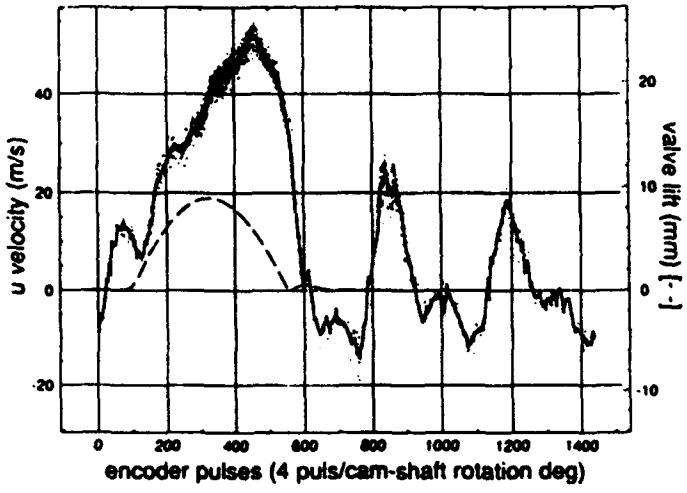

Fig. 8 - Measurement of axial velocity inside the inlet manifold (valve lift, scattered data, averaged data) , (n_C=4200 rpm, M=10 g/s): 25000 samples.

INVESTIGATION OF THE FLOWS THROUGH TWO PRODUCTION CATALYTIC CONVERTERS

D.P.E. Foster†, K.C. Lee†, M. Yianneskis† and G. Ganti*

†Centre for Heat Transfer and Fluid Flow Measurement
School of Physical Sciences and Engineering
King's College London, Strand, London. WC2R 2LS, U.K.

*Ford Motor Company Ltd.
Research and Engineering Centre
Laindon, Basildon, Essex. SS15 6EE, U.K.

ABSTRACT

In this study L.D.A. was used to measure the velocities upstream and downstream of two catalytic converters with different geometries and identical monoliths. The investigation was mainly concerned with the effect of inlet conditions on the flow distribution through the monolith and the determination of any other phenomena important to converter performance. Measurements of the mean and r.m.s. velocity components were made for three flowrates. The results showed that, for the catalytic converters tested, the dominant factors for the flow distribution through the monolith are the effects of flow resistance and manufacturing imperfections within the monolith itself.

1. INTRODUCTION

It is generally accepted that the most important parameters affecting the flow through a catalytic converter are the inlet pipe orientation and curvature, the diffuser geometry and the monolith flow resistance. Ideally, a diffuser should allow efficient expansion of the flow through the transition from the end of the inlet pipe to the beginning of the monolith. In reality, car designers must adhere to space and weight limitations so that the transition has to be short and abrupt. This leads to a poor flow distribution through the monolith causing separate areas of extremes in the usage of catalyst material.

The problems discussed above have led researchers to investigate the nature of the flow in catalytic converters to assess the most influential parameters. The work has been a mixture of analytical, computational and experimental studies.

Lemme and Givens (1974) found through experiment that the flow distribution was improved by; decreasing the ratio of the monolith cross-sectional area to the inlet pipe area, lengthening the distance from the inlet pipe to the monolith inlet face and increasing the monolith flow resistance. Increased resistance, however, has the adverse effect of raising the back pressure on the engine. As expected, the downstream geometry was found to have only a very small effect on the flow distribution through the monolith. A notable point made by the authors was that the flow just before the monolith has a strong radial component as it meets the monolith. This means that measuring the axial velocity profile here does not give a good picture of the flow distribution through the monolith. Therefore their measurements were made downstream of the monolith where the flow is predominantly axial. Howitt and Sekella (1974) experimented with a set of devices placed in the diffuser to help expand the flow evenly across the brick face. These mechanical devices aimed to inhibit the flow to the centre of the monolith and encourage it to pass through the monolith's outer parts. The more balanced exhaust gas flow across the brick face resulted in improved use of the catalyst material, but at the expense of slower converter light-off and increased pressure drop.

Flow-visualization by Wendland and Matthes (1986) revealed the flow structure within the diffuser as being similar to a jet flow surrounded by an uneven toroidal vortex, which formed a recirculation region close to the diffuser walls. Near to the monolith inlet face the flow fanned out as it met the resistance of the monolith.

Pressure loss characteristics of single- and double-monolith catalytic converters were investigated by Wendland *et al* (1991). The converters had previously been used on fired engines. The measurements were executed in room-air, hot-gas and engine-exhaust flows. The data from the three different test conditions correlated well with inlet pipe Reynolds number when the pressure was normalised by the inlet pipe dynamic head. The authors concluded that in the future this will enable inexpensive room-air tests to be used to estimate converter pressure losses for fired engine conditions.

Bella *et al* (1991) used a one-dimensional reacting flow model for the monolith flow in conjunction with a three-dimensional viscous model outside the substrate. The authors found that the flow distortion caused by a 90° bend or an inadequate diffuser upstream of the converter results in non-uniform exploitation of the converter. The insertion of devices, designed to improve the flow distribution in the converter, was also modelled. It was found that such devices improve the flow presentation to the monolith.

Zygourakis (1989) developed a two-dimensional equivalent continuum model for estimating transient performance in a catalytic converter. The model showed that the significance of flow distribution in transient operation is as important as the heat transfer characteristics and chemical kinetics. Clarkson *et al* (1993) reported that their development of a transient three-dimensional model of the converter fluid dynamics, chemical kinetics and heat and mass transfer characteristics produced results which appeared promising.

Lai *et al* (1992) compared computational and experimental results with good agreement. They found that the flow distribution was a function of inlet flow Reynolds number, monolith flow resistance and inlet pipe curvature.

L.D.A. data on the flows through a production catalytic converter are lacking; most importantly measurements downstream of the monolith, where the velocity profile will reveal more about the flow distribution through the monolith than measurements upstream. The present investigation was undertaken to redress the balance by measuring the flows through two production catalytic converters, both upstream and downstream of the monolith.

2. APPARATUS

A steady-state air flow rig was used for the L.D.A. measurements in two production catalytic converters. Two compressed air supplies were used; one leading to a 50 mm diameter pipe that provided the main bulk of the flow for the converter and a second to supply the air for the silicone oil atomiser. The atomiser provided oil droplets with an average diameter of 1-2μm for seeding the flow. Silicone oils of different viscosities were used to achieve acceptable data rates at different measuring locations. The seeded air from the atomiser was then fed into the mainstream flow upstream of an orifice plate. The orifice plate was manufactured according to B.S. 1042 and was attached to a manometer to measure the air mass flowrate through the converter.

The two production converters that were supplied had previously been run under fired engine conditions. As can be seen in figure 1, the converters differed in terms of diffuser geometry, but both had identical double-substrate sections. The substrate consisted of a honeycomb structure with square cells. The cell density was 64cells/cm^2 and the single-substrate length was 70mm. The first converter had a short diffuser of length 50 mm and a half-angle of divergence equal to 54°. The second converter had a much longer diffuser of 120 mm length, giving it a shallower half-angle of divergence equal to 28°. Also, the second converter had the inlet axis at an angle of 8° to the converter centreline.

Some of the measurements were made with a bias plate positioned just before the converter inlet to provide a certain amount of skewness to the flow being presented to the converter. The bias plate consisted of a circular metal plate with holes drilled into it. The holes varied in size across the plate diameter. The L.D.A. results confirmed that this arrangement presented a flow pattern to the monolith similar to that of a sharp 90° entrance bend, see for example Taylor et al (1987).

The flow passed through the bias plate (if in position) and into the monolith via a diffuser. It is the shape of the diffuser and its effect on the flow presented to the monolith that was the main topic of investigation in this study. The converter had windows cut out of it to afford good access for the L.D.A. laser beams. The flow leaving the converter was directed into a sound attenuation box designed to reduce the considerable noise emanating from the compressed air supply.

3. LASER-DOPPLER ANEMOMETER

The L.D.A. optical system was mounted on a single bench placed on a traversing table. This arrangement allowed three degrees of movement for the whole optical set up without the need for realignment. The laser produced light at a wavelength of 632.8 nm and with a power output of 10 mW. The photomultiplier voltage output was fed to a T.S.I. frequency counter interfaced to an Apple II computer for data processing. For a virtually identical L.D.A. system, the overall errors for the mean and r.m.s. velocities have been estimated by Suen (1992) to be of the order 5% and 10% respectively. The principal characteristics of the laser anemometer are listed in Table 1.

Table 1 L. D.A. system parameters

laser wavelength	λ=632.8 nm
control volume half angle	$\theta/2$=5.9°
beam diameter from laser	b_0=0.83 mm
beam diameter at control volume	b=0.194 mm
control volume length	b_x=1.8 mm
control volume width	b_y=0.2 mm
frequency shift	f_s=4.37 MHz
control volume fringe spacing	λ^*=3.08μm

4. TEST PROCEDURE

A detailed diagram of the catalytic converter measuring locations and co-ordinate system is shown in figure 2. This shows a side view of the converter, in the x-z plane. The measuring locations, lines along which measurements were taken, are in the y-direction. In figure 2 they are seen end-on and so appear as points. In a addition to the differences in the distances in between measuring locations, the second converter has its inlet plane at an angle of 8° with respect to the monolith face; this feature can be seen in figure 1.

The procedure for taking measurements was as follows: The L.D.A. bench was positioned so that the control volume was located at measuring location 1. Profiles of the mean and r.m.s. components of velocity, U and u' respectively, were taken for each of three flowrates 55 kg/h, 108 kg/h and 200 kg/h. The L.D.A. bench was then repositioned to the next measuring location and the process repeated until the mean and r.m.s. profiles for all three flowrates had been obtained at all four measuring locations. The positional accuracy was $\pm$ 0.05 mm.

As already mentioned the access for L.D.A. in the first converter was restricted at some measuring locations, which meant that complications arose in obtaining a complete profile along the y-direction. Larger windows could not be inserted in the converter walls without altering significantly the shape of the containing walls. At measuring location 2 in the first catalyst, the measuring volume could only be traversed across half the width of the converter, thus for the unbiased case measurements were taken up to the converter centreline. In the biased case measurements were taken with the bias plate orientated in one direction up to the converter centreline. The bias plate was then rotated through 180° and the measurements taken again. At measuring location 3, restricted access meant that the $\pm$45° measurement technique was employed and the data was resolved to give the mean velocity component.

5. RESULTS

5.1 Measuring Location 1

Figure 3 shows the mean and r.m.s. velocity component profiles across the y-direction at measuring location 1 for the biased and unbiased flow cases.

For convenience, the skewness of the velocity profiles is defined in the following text as a percentage difference between the maximum and minimum mean velocity divided by the maximum mean velocity. The unbiased inlet flow case results are shown in figure 3(a). The insertion of honeycomb sections in the bend has helped to reduce the effects of curvature upstream of measuring location 1. The profiles show a small amount of skewness which increases with mass flowrate from 4% at 55 kg/h to 16% at 200 kg/h. The skewness was attributable to the secondary flow effects of the pipe bend before the measuring location; as the mass flowrate increased the greater effect of the flow in the bends caused more vigorous secondary flow action and thus greater skewness. The r.m.s. velocities remained low for all three flowrates, not exceeding 1.1 m/s. This is partly due to the suppression of turbulence by the honeycombs.

The biased flow profiles, presented in figure 3(b), showed that the insertion of the bias plate resulted in a much greater skewness in the mean velocity profile as intended. The skewness decreased with mass flowrate from 58% at 55 kg/h to 32% at 200 kg/h. The r.m.s. velocity profiles show higher turbulence levels than in the unbiased case and scale with mass flowrate, varying from 1.4 m/s at 55 kg/h, to 2.7 m/s at 108 kg/h and 4.8 m/s at 200 kg/h. The results indicate clearly that the bias plate was generating a considerable amount of turbulence. As the mass flowrate increases, the level of turbulence increases, promoting greater mixing downstream of the bias plate. This effect appears to reduce the skewness generated by the bias plate as the mass flowrate increases. Another noticeable trend was the rising r.m.s. values towards the low momentum side of the pipe. This may be caused partly by the greater turbulence generated by the smaller holes on that side of the bias plate and partly by the steeper mean velocity gradients found on the low velocity side of the pipe.

5.2 Measuring Location 2

Figure 4 shows the unbiased mean and r.m.s. velocity profiles at measuring location 2 for the first converter. The mean velocity profiles are similar to a jet flow, as also observed by flow-visualization in Wendland and Matthes (1986). The jet width is approximately 90-100 mm (the inlet pipe width in the x-y plane for the first converter is 80mm). This clearly indicates that the inlet flow is not expanding to follow the shape of the diffuser, but emerges as a jet. The mean velocity tends to zero very close to the converter wall, suggesting the existence of a weak recirculation in the form of a toroidal vortex. The maximum r.m.s. values scale with mass flowrate and occur at the point where the mean velocity gradient is steepest, as might be expected.

Figure 5 shows the biased flow case. The bulk flow is clearly offset from the centre, as a result of the presence of the bias plate upstream, so that the maximum mean velocity occurs at y = -10 mm. The r.m.s. velocities for 55 kg/h and 108 kg/h are nearly uniform across the diffuser, whereas the 200 kg/h profile shows a "peak-trough-peak" profile typical of jet flow. The peaks indicate regions of shear on either side of the jet centre-line (as with the unbiased case), and at the centre where velocity gradients are small the trough represents a region of lower turbulence intensity.

Figure 6 shows the mean and r.m.s. velocity profiles at measuring location 2 in the second converter for the unbiased case. As with the first converter the profiles show a jet-like flow issuing from the converter inlet, surrounded by a weak recirculation, indicated by the small magnitudes of the mean velocities towards the edge of the jet.

Figure 7 compares the mean velocity profiles of both converters at measuring location 2. A notable feature is that the profiles for the first converter are broader than those for the second converter. According to Lemme and Givens (1974) the main factors affecting the flow expansion into the converter are the inlet width and the distance of the inlet from the monolith face. In the converters tested in this work conditions were most favourable in the first converter which, although it had a shorter distance between the inlet and the monolith face, had a much wider inlet width.

Another feature worthy of note in figure 7 is that the profiles for the second converter are biased towards the positive y-direction. As already mentioned, the second converter had the inlet at an angle to the converter centreline, within the x-y plane, in such a way that it was expected to cause bias in the negative y-direction. It is thought that this opposite bias is possibly caused by manufacturing imperfections in the weld where the inlet flange and converter diffuser are joined. The imperfections may cause the creation of a separation bubble on the negative y-direction side and thus strengthen the recirculation on this side. This would have the effect of redirecting the flow towards the positive y-direction.

Figure 8 shows the biased mean and r.m.s. velocity profiles at location 2 in the second converter. The bias plate was orientated to give a higher flowrate towards the positive y-direction. There are two unexpected features, the biasing of the flow towards the negative y-direction and the lower mean velocities, in comparison with the unbiased case, for all three flowrates. Figure 9 compares the mean velocity profiles for biased and unbiased cases. One reason for the biasing of the flow being in the opposite y-direction to that expected, may be that the turbulence generated by the bias plate may have reduced the size of the separation bubble causing the unexpected biasing in the unbiased case, as seen in figures 6 and 7, and allowing the flow to continue in the direction defined by the converter inlet angle. The unusually low peak mean velocities seen for all three flowrates in the biased case indicates that the flow is more evenly spread across the face of the monolith. This could be as a result of the comparatively higher turbulence levels (generated by the bias plate) reducing the strength of the recirculation zones in the diffuser and allowing greater lateral diffusion of momentum.

5.3 Measuring Location 3

The mean velocity profiles for the first converter at measuring location 3 are shown in figure 10. The profiles for the biased and unbiased flows are clearly very similar. The small differences in the results indicate that the bias of the flow upstream of the brick does not affect the flow downstream to any significant extent. The non-uniformity of the profiles indicates manufacturing imperfections within the monolith passages.

The $\overline{uv}$ shear stresses were also measured in this location. The resulting values were very small indeed, smaller than inherent L.D.A. errors so the results could not be used. These low turbulence stress values are due to the laminarisation of the flow caused by the very small channels in the monolith.

The unbiased mean velocity profiles for the second converter at measuring location 3 are shown in figure 11. As with the first converter, the irregular profile is evidence of local regions of high flow resistance and possible blockaging in the

monolith. This may be caused by loose catalyst material clogging the small brick passages. But, a noticeable feature in figures 10 and 11 is that the velocity peaks and troughs occur in similar positions for both converters. This phenomenon points towards the regions of high flow resistance being caused by manufacturing imperfections in the substrate. It is difficult to mass produce a substrate with perfectly identical individual passages throughout and so the flow resistance is bound to vary across it. This effect seems to be the most important factor in determining the flow distribution through the monolith.

Figure 12 shows the mean and r.m.s. velocity profiles at three different y-z planes, z=-20 mm, z=0 mm and z=20 mm for the flowrate of 108 kg/h and without bias. The erratic nature of, and differences between, all three profiles clearly indicate the effect of high flow resistance inside the monolith and the presence of a highly three-dimensional flow field. As expected the highest velocities are found at z=-20 mm and y=0 mm, the position closest to the outlet pipe. At this point the mean velocity is 3.0 m/s. The r.m.s. velocities are on the whole very low due to the laminarisation effect of the narrow monolith passages.

5.4 Measuring location 4

Figure 13 shows the unbiased mean and r.m.s. velocity profiles for the flow leaving the first converter through the outlet pipe. The velocity components in the axial direction, with respect to the exhaust pipe, were measured. The turbulence suppressing effect of the monolith is still evident at this location where the r.m.s. velocities are consistently low for all mass flowrates, not exceeding 1.5 m/s. The corresponding turbulence intensity (r.m.s. velocity divided by the mean velocity) for all three flowrates is approximately 2.6%. The mean velocity profiles are very uniform, although the measured profiles do not extend to the pipe wall. The profiles are characteristic of the plug-flow found a few diameters down from the entrance to a pipe.

5.5 Pressure measurements

The pressure drop across the two converters was measured by means of static pressure tappings located 45 mm upstream of measuring location 1 and 50 mm upstream of measuring location 4. Figure 14 shows the graph of the pressure drop across the converter versus the mass flowrate for six flowrates, including the three flowrates used in the L.D.A. measurements. The graph shows a relationship between pressure drop and mass flowrate which is more parabolic than linear and nearly identical for both converters. Since the only significant variation between the two converters was the diffuser geometry, it can be assumed that the effect of the diffuser shape had no noticeable effect on the pressure drop across the converter.

6. DISCUSSION

In this section the results presented above are compared with results obtained by other authors. Figure 15 shows a graph of the inlet pipe Reynolds number versus the pressure drop. The data obtained from the first and second converters described in this paper is compared with data from Wendland et al (1991) and Lemme and Givens (1974). Although the catalytic converters employed by Wendland et al (1991) were single-substrate converters, the length of the substrate (152mm) was similar to the overall length of the double-substrate in the converters used in this work. The cell density (64cells/cm^2) was also similar and the converters had been run under fired-engine conditions for 100 hours. As a result the pressure drop for both sets of data follow similar trends. Lemme and Givens employed a single-substrate converter, but its length was 76.2 mm, half that used in the other sets of data. This fact is reflected in figure 15 if we assume that the pressure drop is directly proportional to the substrate length as reported by Lemme and Givens (1974) and Wendland et al (1991).

In figure 16 velocity profiles upstream of the monolith are compared. The abscissa represents the y-position normalised with the inlet pipe diameter. The ordinate is the mean velocity normalised by the bulk velocity for each profile. Excluding the lower Reynolds number result from Lai et al (1992), the profile shapes are surprisingly similar in many respects, given the differences in the geometries of the converters.

To quantify the comparison between the upstream velocity profiles seen above a parameter termed the spread of the flow was used in figure 17. The spread for each profile was obtained by dividing the standard deviation of the mean velocities in each profile by the corresponding bulk velocity. The spread appears to remain within the range 0.45-0.67 for Reynolds numbers between 25,000-100,000. The unexpected profile from Lai et al (1992) presented in figure 17 for Re=25,000 falls short of the other data in figure 18 as would be expected from its flat appearance. The shape can perhaps be explained by the use by Lai et al of a very elongated control volume for the L.D.A., introducing greater scope for errors into the measurements.

7. CONCLUSIONS

In this study L.D.A. was used to measure the velocities in two catalytic converters. The experiments were carried out primarily to establish the effects of inlet conditions on the flow through the monolith. The results were also compared with those from other sources. The following conclusions were drawn:

- The bias plate, inserted upstream of the catalytic converter, achieved the aim of skewing the upstream flow profile in a manner similar to a 90 degree bend. Also, the bias plate was responsible for generating higher turbulence levels upstream of the converter monolith.
- The catalytic converter diffusers were too divergent to effectively diffuse the flow to any degree. A properly designed diffuser would be too long for practical use.
- The ineffectiveness of the diffusers resulted in the flow emerging from the inlet pipe as a free jet surrounded by a weak toroidal vortex. The flow distribution directly prior to the monolith inlet face can be improved by increasing both the inlet pipe diameter and its distance from the monolith inlet face.
- The flow through the monolith had a non-uniform distribution, as witnessed by the flow profiles downstream of the monolith. This is most likely due to manufacturing imperfections in the monolith passages, but may also be caused by loosened catalyst material and exhaust particulates. As a result the catalytic converter operates inefficiently. It appears that in the case of the converters used in this work, the determining factor in the distribution of flow through the monolith is the above mentioned manufacturing imperfections rather than the upstream conditions.

- Strong viscous forces in the narrow monolith passages caused a strong turbulence suppressing effect on the downstream flow.
- Comparisons of the upstream velocity profiles just before the monolith inlet face and the pressure drop across the catalytic converter with data from other sources showed good agreement.

REFERENCES

Bella, G., Rocco, V. & Maggiore, M. 1991, A study of inlet flow distortion effects on automotive catalytic converters, Trans. ASME, J. Engng. Gas Turbines and Power, vol. 113, no. 3, pp. 419-426.

Clarkson, R.J., Benjamin, S.F., Jasper, T.S. & Girgis, N.S. 1993, An integrated computational model for the optimization of monolith catalytic converters, Joint IMechE/SAE Conf. "Vehicle Thermal Management Systems (VTMS)", Columbus, Ohio.

Howitt, J.S. & Sekella, T.C. 1974, Flow effects in monolithic honeycomb automotive catalytic converters, SAE paper 740244, 1974.

Lai, M.C., Lee, T., Kim, J.Y., Cheng, C.Y., Li, P. & Chui, G. 1992, Numerical and experimental characterizations of automotive catalytic converter internal flows, J. Fluids and Structures, Vol. 6, pp 451-470.

Lemme, C.D. & Givens, W.R. 1974, Flow through catalytic converters- an analytical and experimental treatment, SAE paper 740243.

Suen K. 1992, Investigation of Gas Flow in a Motored High Speed Diesel Engine by Laser Doppler Anemometry, Ph.D. Thesis, Mech. Eng. Dept., King's College London.

Taylor, A.M.K.P., Whitelaw, J.H. & Yianneskis, M. 1982, Curved ducts with strong secondary motion: velocity measurements of developing laminar and turbulent flow, J. Fluids Engng., Vol. 104, 1982.

Wendland, D.W. & Matthes, W.R. 1986, Visualization of automotive catalytic converter internal flows, SAE paper 861554.

Wendland, D.W., Sorrell, P.L. & Kreucher, J.E. 1991, Sources of monolith catalytic converter pressure losses, SAE paper 912372.

Zygourakis, K. 1989, Transient operation of monolithic catalytic converters: a two-dimensional reactor model and the effects of radially non-uniform flow distributions Chem. Engng. Sci., Vol. 44, no. 9, pp 2075-2086

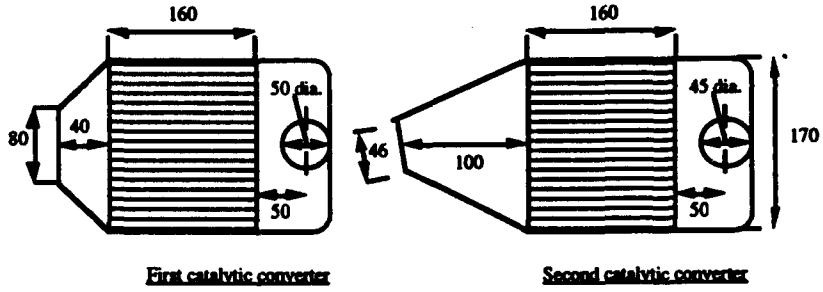

Figure 1 Catalytic converter general arrangement drawings (dimensions in mm).

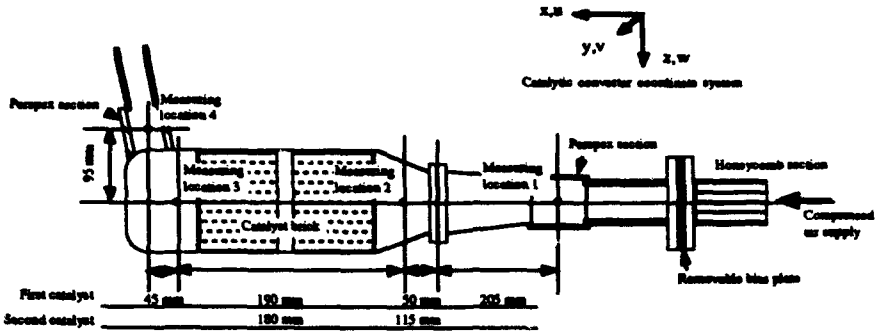

Figure 2 Side view of the catalytic converter and its coordinate system.

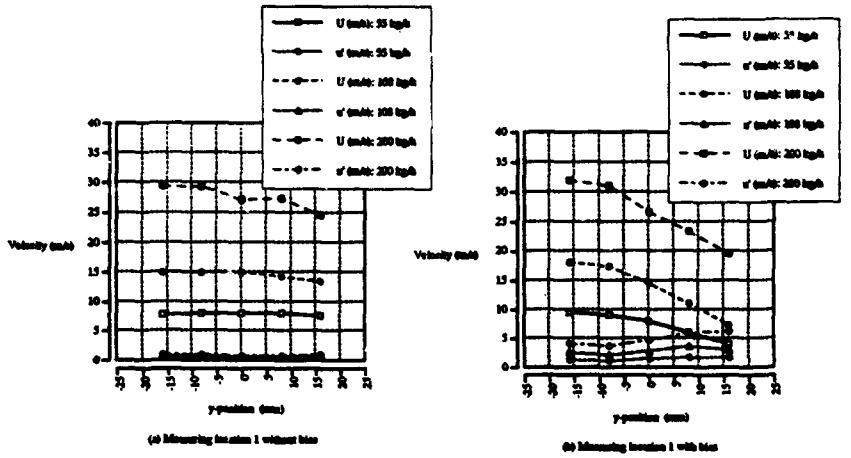

Figure 3 Mean and r.m.s. velocities at measuring location 1

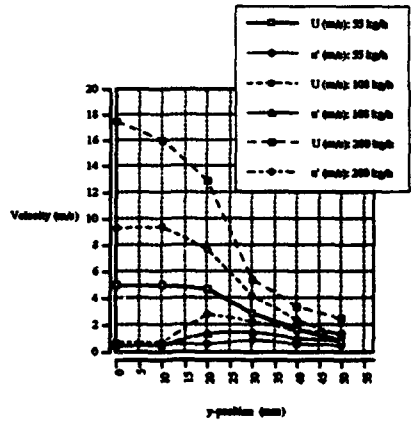

Figure 4 Measuring location 2 (x=-15 mm from the upstream brick face) without bias for the first converter.

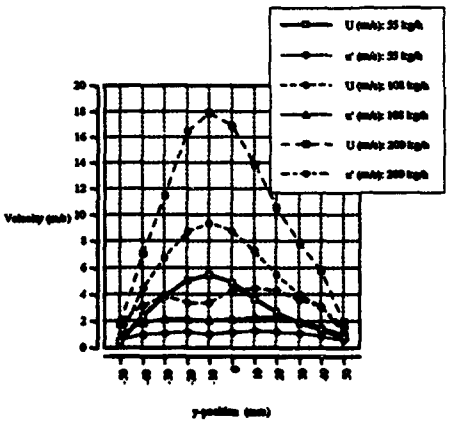

Figure 5 Measuring location 2 (x=-15 mm from the upstream brick face) with bias for the first converter.

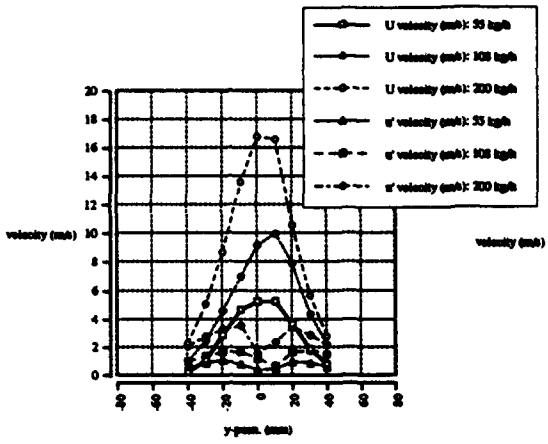

Figure 6 Mean and r.m.s. velocity profile at measuring location 2 (x=-18 mm from upstream brick face) for the second converter. Unbiased case.

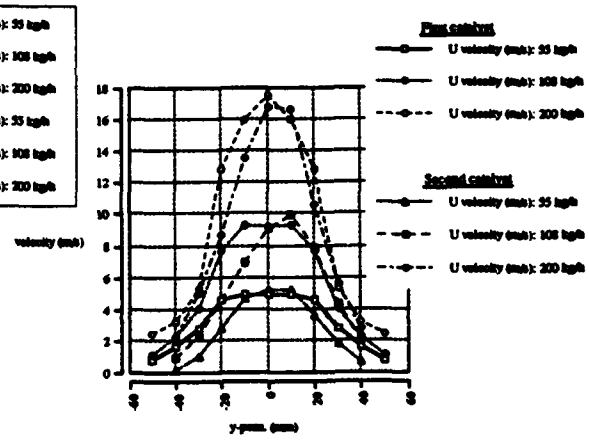

Figure 7 A comparison between the mean velocity profiles for both converters at measuring location 2. Unbiased case.

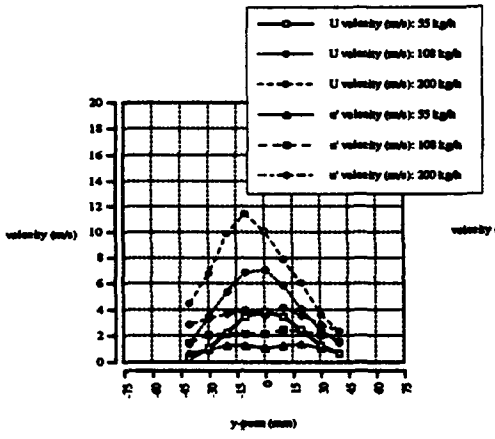

Figure 8 Biased mean and r.m.s. velocity profiles at measuring location 2 (x=-18 mm upstream from brickface) for the second converter.

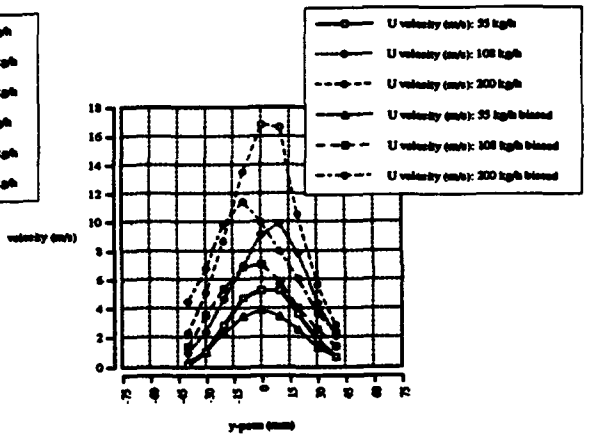

Figure 9 A comparison between biased and unbiased mean velocity profiles at measuring location 2 for the second converter.

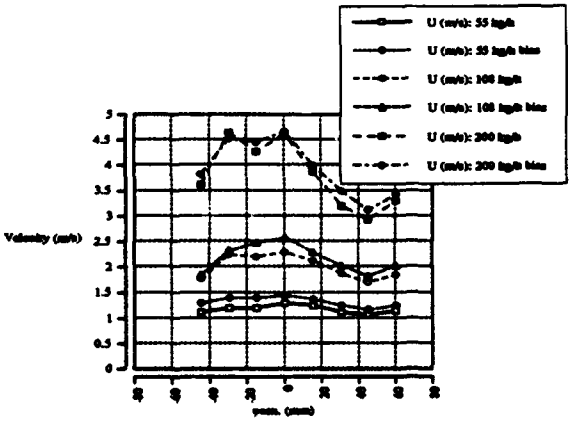

Figure 10 Biased and unbiased mean velocities at measuring location 3 (x=15 mm from downstream brickface) for first converter.

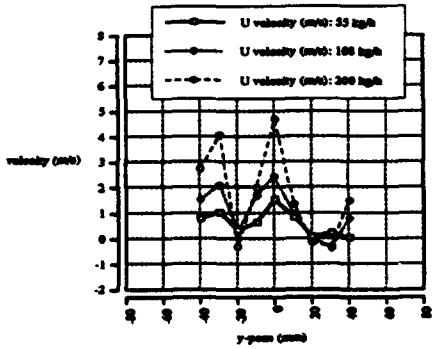

Figure 11 Mean velocity profile at measuring location 3 (x=15 mm from downstream brickface) for the second converter.

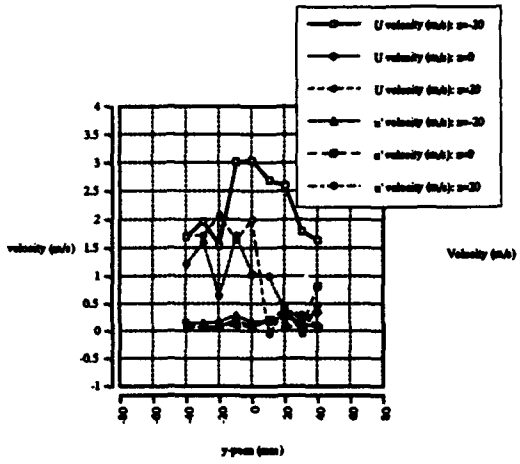

Figure 12 Mean velocity profiles at measuring location 3 in the second converter for z=20 mm, 0 mm and -20 mm. z=-20 mm is the profile closest to the outlet pipe. Unbiased case.

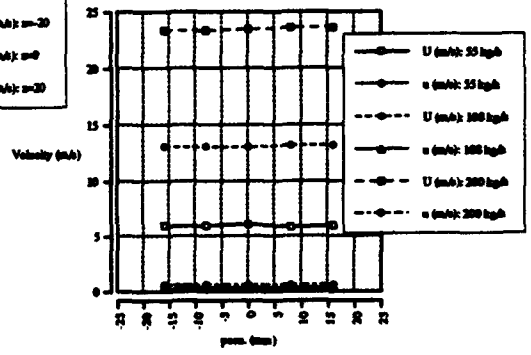

Figure 13 Mean and r.m.s. velocities at measuring location 4 for the unbiased case.

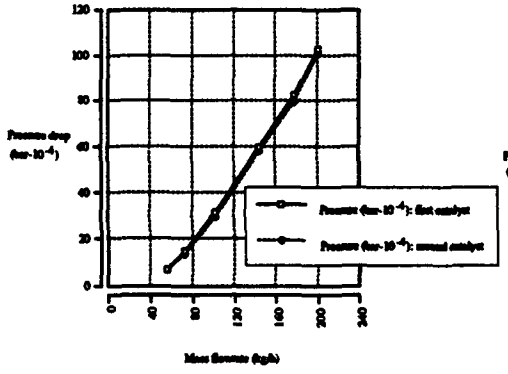

Figure 14 Pressure drop across the converter versus mass flowrate.

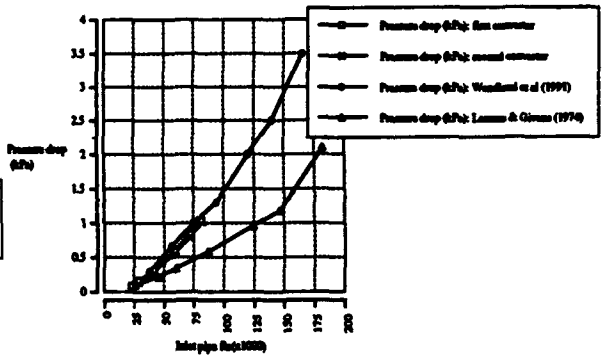

Figure 15 Variation of pressure drop with inlet pipe Reynolds number.

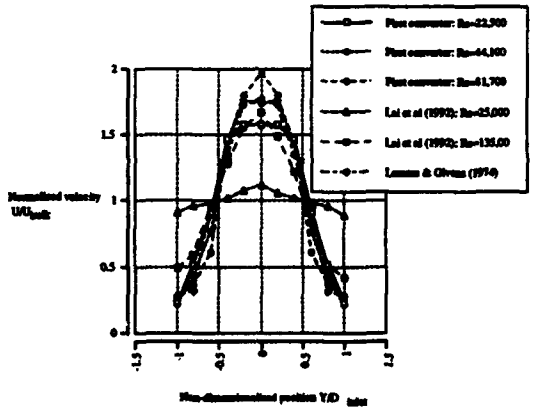

Figure 16 Normalised velocity profiles from various sources compared with the data from this work.

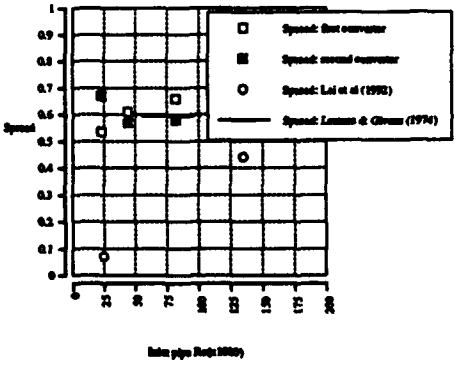

Figure 17 A graph showing the spread (standard deviation divided by mean) of the velocity profiles from figure 16 versus the inlet pipe Reynolds number.

PHASE DOPPLER CHARACTERIZATION OF A DIESEL SPRAY INJECTED INTO A HIGH DENSITY GAS UNDER VAPORIZATION REGIMES

A. Coghe*, G.E. Cossali**

* Politecnico di Milano, Dipartimento di Energetica, - Milano, Italy.
** Università di Bergamo - Bergamo, Italy

ABSTRACT

Phase Doppler measurements of drop size and velocity in an unsteady diesel spray were performed. The spray was injected into a quiescent gas with density ranging from 0.95 to 18 kg/m^3 and temperature ranging from 20°C to 100°C; to simulate high back pressure, a gas with high molecular weight (SF_6) was used to obtain the same density at lower pressure. The effect of fuel vaporisation on spray structure was found to be noticeable despite of the relatively low (100°C) gas temperature. An increase of the mean drop diameter was observed increasing the temperature which may be explained by a selective depletion of the smaller droplets due to evaporation. Cycle resolved measurements allowed to evidence the strong unsteady structure of the main injection period.

1. INTRODUCTION

Diesel sprays injected into a gas at atmospheric pressure and temperature have been studied by many investigators with a widespread range of techniques and injection conditions although the most detailed measurements have been performed under staedy conditions. Those studies have gathered a considerable amount of data about the whole spray structure, penetration, entrainment, droplet velocity and size distributions, etc. A strong limitation of the results is due to the fact that steady injection and atmospheric gas conditions are quite far from the realistic engine ones and that does not allow a straightforward extrapolation of the results mainly because of three reasons: 1) atomisation is due, under atomisation regime, to the aerodynamic interaction between the outcoming liquid jet and the gas, which is infuenced by the gas density and in a diesel engine the air density can be 15-20 times the atmospheric one; 2) droplet size it is also controlled by evaporation which for diesel oil is negligible at atmospheric temperature, but quite strong under engine conditions; 3) unsteday sprays may have a stucture quite different from that of steady ones.

Experimental investigation of diesel sprays under engine conditions were usually performed with the main aim of understanding the combustion process [Sato et al. (1986), Karimi (1988), Arcoumanis et al. (1991), Shundoh et al.(1991), Kobayashi et al. (1992), to name but a few] so that the most of the published works are concentrated on spray combustion characteristics rather than spray fluid mechanics. However, combustion characteristics are influenced by the gas-fuel mixing which is obviously controlled by the spray dynamics, then investigation of the spray dynamics characteristics under vaporisation regime may result useful in understanding and explaining the features of the combustion process [Pitcher and Wigley (1989), (1992)]. The present investigation performed with gas temperature ranging from atmospheric to 100°C and gas density from 0.93 to 18 kg/m^3 is a step toward conditions more realistic than the atmospheric ones but still enough manageable for using the Phase Doppler Technique with good performances. The study is part of an ongoing effort to understand the behaviour of diesel sprays impinging on a wall. The understanding of recent preliminary measurements of the deposited liquid film thickness on a flat wall (Coghe et al. 1993) required a detailed characterization of the spray before impingement under the same conditions and at an axial location equal to the wall-nozzle distance (z=57 mm).

2. EXPERIMENTAL SET-UP

A Bosch single hole injector (0.25 mm nozzle diameter) was mounted on the top of a closed cylindrical chamber (89 mm i.d.,300 mm height). Two glass windows mounted on tubes protruding from the chamber side to minimise window fouling by deposition of fuel droplets, were positioned to allow the use of the PDA in the 70 deg forward scattering, which has been shown to be the configuration which gives the smallest dependence of the size measurement results on the particle refractive index [Pitcher et al. (1990)], as commercial Diesel oil was used as fuel, and its temperature was unknown. The injection system was operated in the single shot mode and over 2000 data were collected for each measurement point over many subsequent injections. The needle lift opening at 20 MPa was triggering the acquisition. The repeatability of the injection pressure curve was tested and found to be more than acceptable; measurements were performed over a 7 ms time window, which was larger than the injection duration (3.4 ms).

The chamber could sustain a pressure not grater than 6-7 bar (the limit was mainly due to the window thickness) and in order to analyse conditions where density should be comparable to that found in Diesel engines, SF_6 (M.W.=146 kg/kmol) was used instead of air to obtain density up to 18 kg/m^3. Gas was heated by an electric heater located on the gas inlet duct and gas temperature measured through a thermocouple positioned inside the chamber at few centimetres from the top and well outside the spray path with 0.5°C accuracy. During the measurements gas temperature decreased, due to heat conduction through the chamber walls, and when the variation was higher then 5°C the

gas was discharged and the chamber flushed with new gas; residual liquid fuel was evacuated through a tap on the chamber bottom by aspirating with a vacuum pump connected to the tap through a cyclone to separate the liquid drops from the gas.
Injection conditions where not varied through all the experiments and are summarised in table 1:

Table 1

Inj.Press. [peak] (MPa)	Inj. Vol. (mm^3)	Inj. Period (ms)	Nozzle Diam. (mm)	Fuel type	Inj. mode
70	32	3.4	0.25	diesel oil	single

Gas density and temperature were changed during the experiments and the following table summarises the conditions:

Table 2

Exp.	ρ (kg/m3)	z (mm)	T (°C)	gas
A	1.18	57	20	air
B	1.07	57	50	air
C	0.93	57	100	air
D	0.93	52	100	air
E	0.93	62	100	air
F	12.0	57	20	SF_6
G	5.93	57	20	air
H	6.00	57	20	SF_6
I	18.00	57	20	SF_6
L	17.4	57	100	SF_6

The Phase Doppler Anemometer (Dantec PDA) comprised a conventional fibre optical LDV transmitting unit, an Argon-ion laser (5 W nominal power), a Bragg cell (40 MHz) based transmitting optics for frequency shifting and directional sensitivity and a 600 mm focal length front lens. A beam expander was mounted on the transmitting optics and the length of the geometrical control volume was about 1 mm and its diameter 0.08 mm ; the effective length was anyway much less than 1 mm due to the 70 deg observation angle. The receiving optics was the 57X10 Dantec unit equipped with three preamplified photomultipliers. The covariance processor of the PDA instrument was capable of 1 μs time resolution in data acquisition. The measurable velocity range, from -25 to 136 m/s (defined by the 36 MHz frequency bandwidth and the transmitting optics configuration), was generally enough for the present investigation except for experiment A (atmospheric conditions). In that case the configuration was modified by eliminating the beam expander to decrease the angle between the beams and the measurable velocity range was almost doubled. However, the choice of the optical configuration was a compromise, to limit the measurable size range to 80μm which resulted the most appropriate in the present case. Drop size was measured together with one velocity component (the axial one) at distances from the nozzle equal to 52, 57 and 62 mm along a radial direction. Despite of the relatively wide optical access, a whole spray diameter could not be effectively spanned, due to high light obscuration when the control volume was positioned on the other side of the spray cone respect to the transmitting optics, and measurements over slightly more than half diameter were collected.

2. RESULTS AND DISCUSSION

The injection conditions (see tab. 1) where not varied during the experiments, whereas gas density and temperature where changed so that gas density ranged between 0.93 to 18 kg/m^3 and gas temperature between 20°C and 100°C. The time resolution of the acquisition system is quite narrow (1 μs) but, in order to better show the spray characteristics, two time windows were chosen to perform a time average (superimposed to the ensemble average produced by overlapping many subsequent injections); the time windows were: T1) from 0.3 ms ASI (After Start of Injection) to 0.9 ms ASI; T2) from 0.9 ms ASI to 2.5 ms ASI. The first time window (T1) is representative of the early injection period whereas the second one (T2) is representative of the main injection period.

As above mentioned, to obtain high gas density conditions without reaching high pressure, SF_6 was used in place of air in some experiments. SF_6 happens to have almost the same viscosity of air ($\mu_{SF6} = 1.53\ 10^{-5}$ kg/m s at 20 °C [Ueda and Kigoshi (1974)]) so that under the same density conditions the drop Reynolds number is the same. However, an experiment at room temperature (20°C) and medium gas density (about 6 kg/m^3) was performed using both gases and the results are compared in fig. 1.

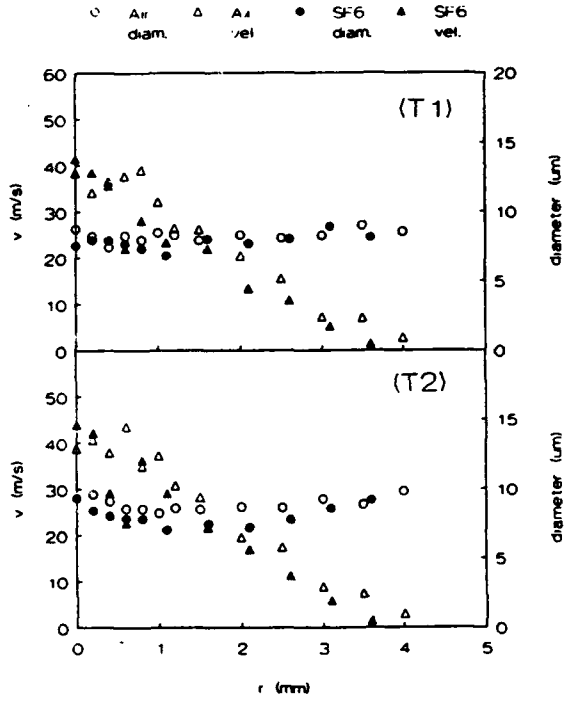

Fig.1 Comparison between drop velocity and diameter for experiments G (air) and H (SF_6).

It can be seen that mean drop velocity and size profiles do not differ appreciably, as well as other statistical parameters (not shown) such as size-velocity cross correlation and velocity and size rms, thus confirming that the use of SF_6 instead of air will not alter the spray dynamic characteristics.

The effect of gas density was analysed by comparing the results of experiments A,G,H,F and I, all performed at room

temperature (about 20°C) to reduce the effects of vaporisation; velocity profiles are shown in figure 2.

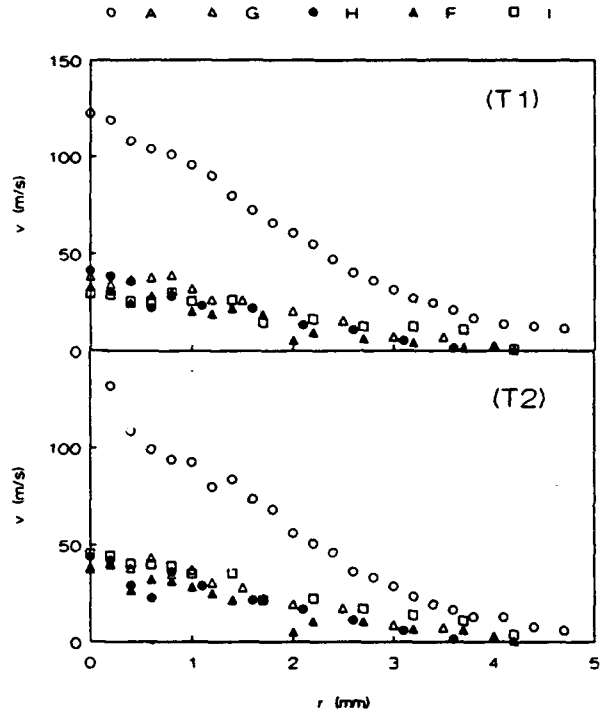

Fig. 2 Mean drop velocity profiles for different values of gas density: A(1.18 kg/m^3), G (5.93kg/m^3), H (6.00 kg/m^3), F (12.0 kg/m^3), I (18.0 kg/m^3)

A macroscopic effect of increasing the gas density is expected to be the increase of the initial spray angle as $\rho^{1/2}$ for steady sprays [Wu et al. (1983)] although discrepancies can be found in the literature regarding the exponent value [Varde et al., 1984]. The profile of case "I" should then have a width four times that of case A. However, the mean drop velocity profiles evaluated over time windows T1 and T2 do not show any evident difference in width. Interpolating the profiles by a pseudo-gaussian curve ($V=V_{cl}\ \exp[-x^2/(ax+b)^2]$ to make allowance for the non gaussian flatness of the profiles [Wu et al. (1984)]) and using a least square method the $r_{0.5}$ width was found to be almost independent on gas density and case I width was lower than 1.3 times case A width.

The same procedure was applied to the velocity profiles (evaluated over the same time windows) of the smallest droplets (D < 5 μm) which are expected to be representative of the entrained gas velocity profiles. Again the variation was much smaller then expected by applying the $\rho^{1/2}$-law. There are a few reasons which may explain the discrepancy: 1) the width of the profiles is not easy to estimate, due to the variability of the velocity measurements so that the estimated widths may be affected by large errors; 2) the spray is unsteady and differences from steady sprays must be expected; 3) the spray width is measured at 228 diameters downstream, thus it is not representative of the initial angle, at this distance from the nozzle the flow may be more similar to that of a particle laden gas jet (and this is more true for high gas density conditions) injected into a gas of approximately the same density and the jet width in this case is not expected to change with gas density.

The entrained air flow under the same conditions of case A (table 2) was measured in a previous experiment [Cossali et al. (1991)] up to 40 mm (160 diameters) from the nozzle. Extrapolation of those results to 228 diameters were compared to the mass flowrate calculated by numerically integrating the interpolated small drop (d<5μm) velocity profiles and were found to be roughly consistent (extrapolated value of previous experiment: 4.7 10^{-3} kg/s (T1) 6.0 10^{-3} kg/s (T2), present experiment after integration: 2.87÷2.93 10^{-3} kg/s (T1 and T2)) thus supporting the statement that the smaller drops are in equilibrium to the air at least at this location (it must be pointed out that the way to measure the entrained mass flow rate by integration over a radial profile is usually affected by large errors due to the weight that the cylindrical symmetry gives to the measurements in the outer region, which usually are affected by the greatest relative errors).

Drop size-velocity correlation coefficient was evaluated for all the experiments and the results plotted in figure 3.

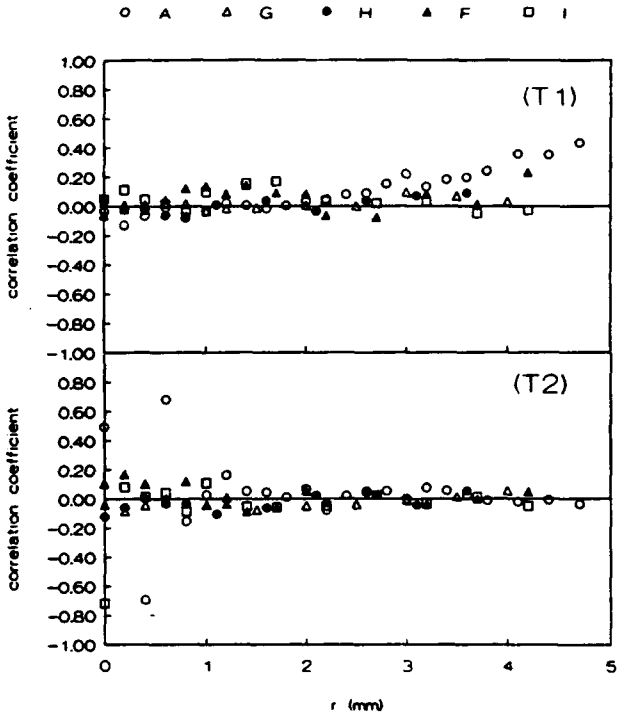

Fig. 3. Size-velocity correlation coefficient: $(\langle Dv\rangle-\langle D\rangle\langle v\rangle)/(\sigma_v\sigma_D)$

The only case which shows a consistent positive cross-correlation is Case A (time window T1) but the magnitude is low. This may lead to the conclusion that drops at this location are generally in equilibrium with the gas for all the experimental conditions with a possible exception of Case A.

The entrained gas mass flow rate is expected to follow the law :

$$m_e = m_o K_e (z/d_o)(\rho_g/\rho_o)^{1/2} \qquad (1)$$

where K_e is the entrainment coefficient and it was found to depend slightly on z for full cone steady [Ruff et al. (1988)] and unsteady [Cossali et al. (1991)] sprays, at least during the main injection period. Entrained mass flowrate can be calculated as:

$$m_e = C_g \rho_g r_{0.5}^2 V_{cl}$$

(where Cg is a constant that depends on the velocity profile $r_{0.5}$ is the half radius, d_0 the nozzle diameter, $m_0=\pi d_0^2/4 \cdot v_0 \rho_0$ is the injected mass flowrate, v_0= is the mean fuel exit velocity, ρ_0 the fuel density). The spray width is expected to depend almost linearly on z but it can also depend on (ρ_g/ρ_0):
$r_{0.5} = F(\rho_g/\rho_0)\, z$ and equ. 1 gives:

$$V_{cl} / vo = (K_e\pi)/(4C_gF^2)(\rho_g/\rho_0)^{1/2}\,(d_o/z) =$$

$$= (K_1\pi)/(4C_gF^2)\, z^{*-1}$$

where $z^*=(z/d_0)(\rho_g/\rho_0)^{1/2}$.
The parameter F is expected to be constant in the far field (i.e. when z is sufficiently high to be in the "incompressible" jet regime), whereas is expected to be proportional to $(\rho_g/\rho_0)^{1/2}$ in the near field [Wu et al. (1983)].

Figure 4 shows the V_{cl}/v_0 ratio for the present measurements (V_{cl} was calculated by interpolation from the measured velocity profile).

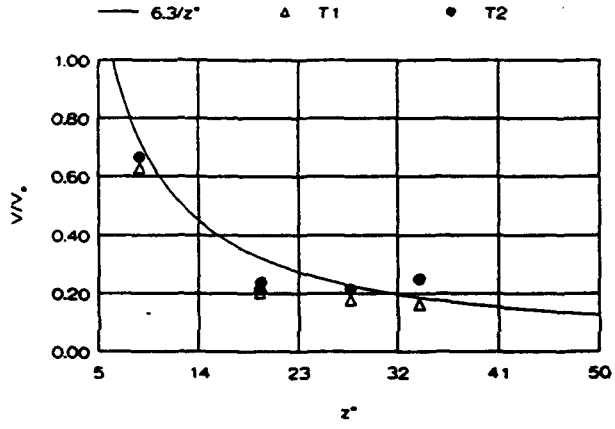

Fig. 4. V_{cl}/v_0 ratio vs nondimensional axial location

The solid line represent the expected value for an incompressible jet [Wu et al. (1984, Chatwani and Bracco (1985), Martinelli et al. (1983)] and the measured values are generally in agreement with it (the data for time window T2 are usually the most affected by the laser beam obscuration), consistently with the hypothesis that the spray behaves as a particle laden gas jet at this location (although the unsteadyness of the present spray may not allow the estrapolation of results obtained on steady sprays or jets).

The mean diameter (fig 5) appears to decrease from experiment A (ρ=1.18 kg/m^3) to experiments G-H (ρ=6 kg/m^3) and again to increase when ρ increases.

Actually, there are two opposite effects of the gas density on the drop mean diameter: an increase of the gas density is expected to improve atomisation but the decrease of the drop velocity increases the probability of coalescence [Kao and Martin (1990)] (droplets are slower and closer each other). This may explain the non monotone behaviour of the mean drop diameter as a function of gas density.

The entrained mass flow rate was estimated for all the gas density conditions by the same method above explained (integration of the interpolating profiles) and the results are shown in tab.3.

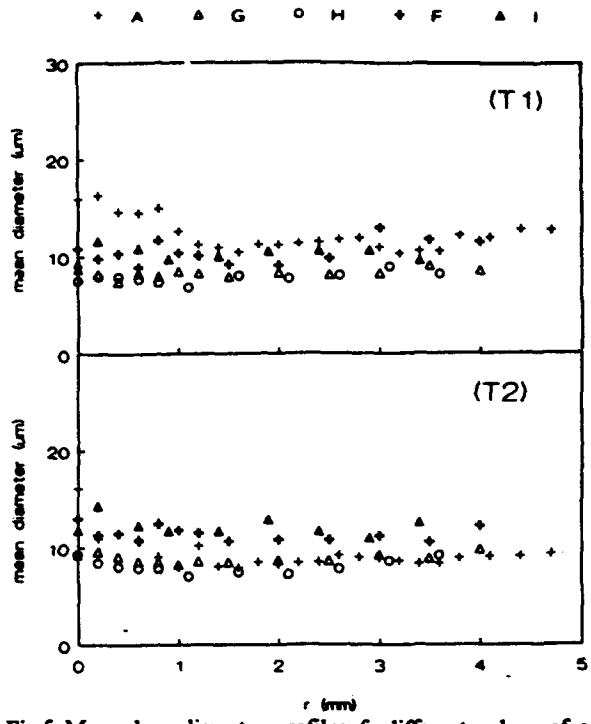

Fig.5 Mean drop diameter profiles fordifferent values of gas density: A(1.18 kg/m^3), G (5.93kg/m^3), H (6.00 kg/m^3), F (12.0 kg/m^3), I (18.0 kg/m^3)

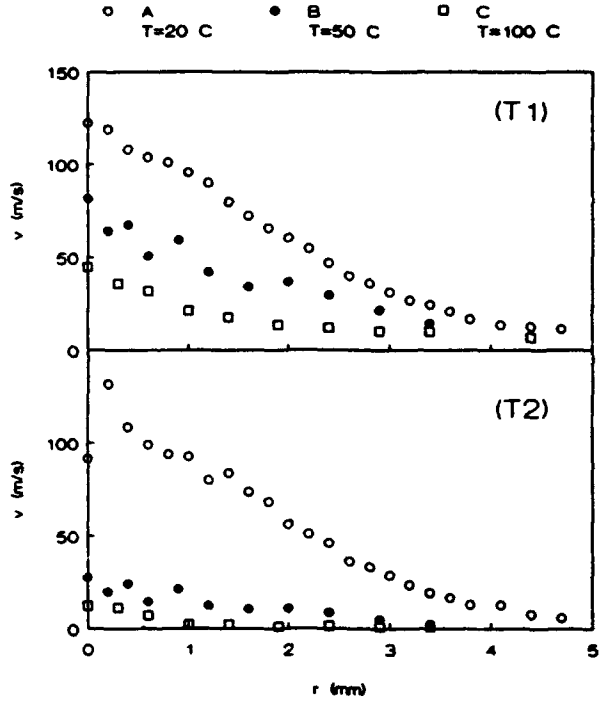

Fig. 6. Velocity profiles for different gas temperaure: A (T=20°C), B (T=50°C), C (T=100°C).

Table 3

Exp.	ρ (kg/m^3)	me (kg/s) (T1)	me (kg/s) (T2)
A	1.18	2.87 10^{-3}	2.93 10^{-3}
G	5.93	2.63 10^{-3}	3.12 10^{-3}
H	6.0	2.69 10^{-3}	3.17 10^{-3}
F	12.0	4.31 10^{-3}	5.4 10^{-3}
I	18.0	13.72 10^{-3}	19.8 10^{-3}

The mass flow rate increases with the gas density, as expected, but the errors that the present method may introduce (due also the variability of the measured data, particularly for time window T2) does not allow to draw quantitative conclusions about the validity of equ (1).

The effect of gas temperature at room gas density can be observed by comparing the results of experiments A,B, and C. Fig. 6 shows the mean velocity profiles, and the most macroscopic effect is the strong reduction of the drop velocity by an increase of only 80°C of the gas temperature.

The influence on the mean mean drop diameter is not clear from figure 7, but a comparison of the mean diameter measured under vaporisation conditions (100°C) at different distances from the injector (experiments D,C, and E, see fig. 8) shows an increase of the mean drop diameter when vaporization take place.

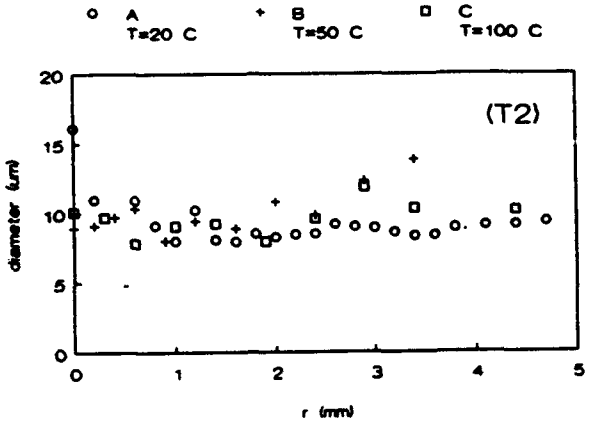

Fig. 7 Mean drop diametre profiles for different gas temperaure: A (T=20°C), B (T=50°C), C (T=100°C).

A likely explanation may rely on the fact that the PDA measures the size of only those droplets having a diameter higher than 1-2 μm and drop vaporisation can be sufficiently described by the law: $d(D^2)/dt = - K$, where K is the evaporation rate (and it was found to depend slightly on the diameter and on the gas-drop relative velocity [Ranz and Marshall (1952), Tokuota et al. (1982)]) and D the drop diameter; the equation can be written as: $d(D)/dt = - K/2D$. Small droplets undertake a larger variation of diameter than the bigger ones during the same time interval and although the total liquid volume must decrease, the average diameter may increase due to the selective depletion of the smaller droplet population and also to the fact that the smaller droplets (D<1μm) contribution to the average is lost. Moreover, the decrease of the drop velocity increases the probability of collision followed by coalescence.

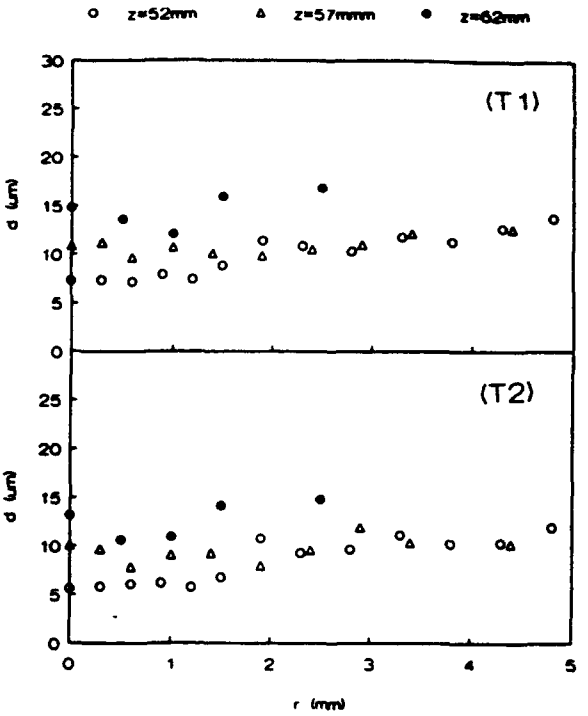

Fig. 8. Mean drop diameter profiles for different distances from the injector

Deceleration of liquid droplets is due to drag produced by a momentum exchange between drops and gas, which for a non evaporating droplet is driven by drop gas relative velocity, drop size and gas viscosity. Air viscosity at 20°C and 100 °C differ for less than 15%. Mean drop size measured at z=57mm has an average observed difference of about 20% with maximum differences of 50% (see fig 7). The above mentioned variations in D and μ may cause an increase of the drop response time ($\tau = D^2\rho_o/18\mu$) of about 30-40% which cannot explain an increase of the drag. The observed variation of the drop velocities can then be caused either by differences in the entrained gas flow field or by a direct effect of vaporisation on drag, or more likely by both. However, the possible variation on the entrained gas flow field can only be due itself to a direct effect of vaporisation, because the gas density variation with temperature is lower then 25% (see table n.2) (and decreases with temperature) and also taking into account the variation of gas density due to the fuel vapour will give a maximum increase of gas density of about 40% (calculated by supposing air saturated with n-dodecane). Entrained gas mass flow rate is expected to depend on the square root of the gas density [Ruff et al. (1988)] so that only a decrease of about 20% of the gas velocity (and thus a likely lesser amount of the drag decrease) can be explained by inertial effects. Thus, the decrease of entrained mass flow rate, which may be deduced by the diminishing of the average velocity of the smaller (D<5μm) droplets (see fig 6), must be due to a direct influence of vaporisation on the drop-gas momentum exchange mechanism (which is responsible of the gas entrainment). From those results it is evident that also the spray width is reduced in Case C (100°C) but only during the main injection period (T2), and the estimated entrainment rate shown in table 4 is also strongly reduced during the main period.

Table 4

Exp.	ρ (kg/m^3)	T (°C)	m_e (kg/s) (T1)	m_e (kg/s) (T2)
A	1.18	20	$2.87\ 10^{-3}$	$2.93\ 10^{-3}$
B	1.07	50	$1.43\ 10^{-3}$	$0.595\ 10^{-3}$
C	0.93	100	$0.314\ 10^{-3}$	$0.023\ 10^{-3}$

Drop and gas momentum decrease appears inconsistent (injected momentum is the same for case A,B and C and it should be equal to the sum of drop and gas momentum if pressure gradients and viscous stresses are neglected [Chatwani and Bracco (1985)]) but no satisfactory explanation was found and further investigations are needed. The same trend was confirmed by comparison of the results from experiments I and L, performed at high gas density and different temperature. Figure 9 shows again a decrease of the drop velocity, as a consequence of an increase of gas temperature, and again an increase of the mean drop diameter (fig. 10), and in this case, due to the relative small reduction of the mean velocity, coalescence should not alone explain the difference.

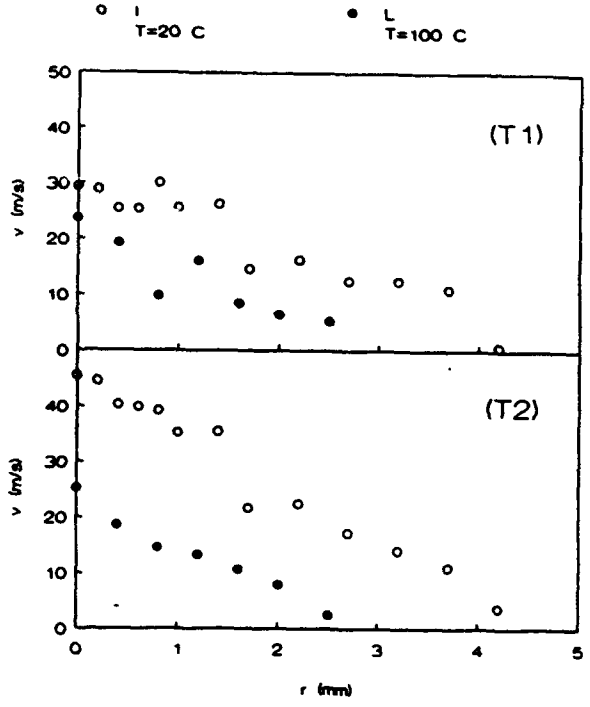

Fig.9. Drop mean velocity profiles for different values of gas temperature (20°C and 100°C) at high gas density.

The effects of such a relatively small change of gas temperature appear too strong and it cannot be excluded that the increased temperature of the injector itself (which was not thermally isolated from the chamber) may have an effect on the injection characteristics (like bubble formation inside the sac prior to the injection).

Another interesting feature of the spray flow is the high unsteadiness also during the main injection period (which is often treated as a quasi-steady regime). Fig 11a) shows a typical drop velocity vs time plot, obtained by overlapping many injections and at a first sight the main injection period appears quasi-steady, although characterised by a strong variability.

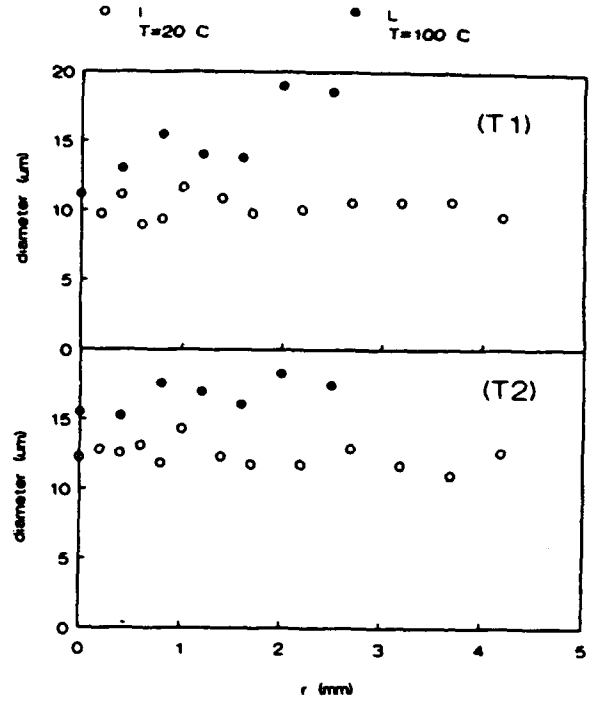

Fig.10. Drop mean diameter profiles for different values of gas temperature (20°C and 100°C) at high gas density.

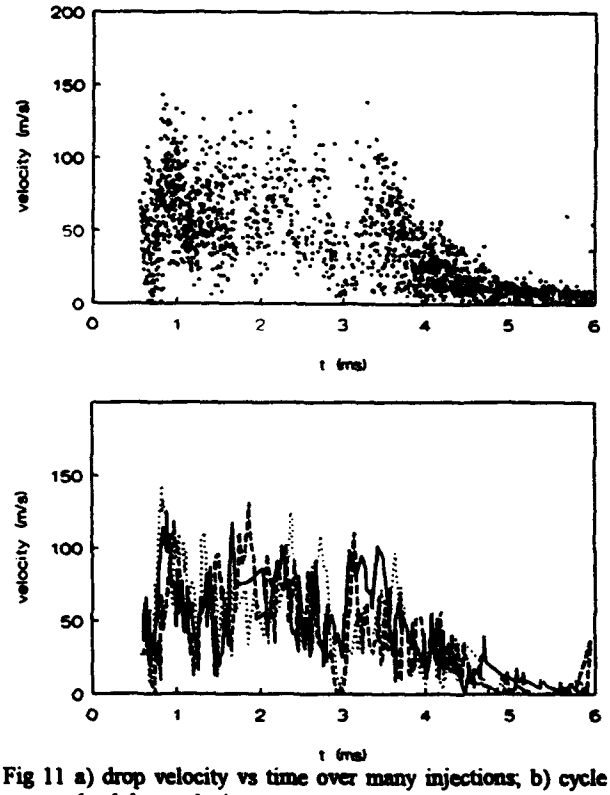

Fig 11 a) drop velocity vs time over many injections; b) cycle resolved drop velocity

But when cycle resolved velocities are considered (fig 11b) the velocity field results as an overlapping of strongly fluctuating velocity histories with no phase correlation. The main injection period appears then characterised not by a sort of quasi-steady flow of drops having a very broad velocity PDF, but rather by a train of "pulses"; a structure which is lost when ensemble average is performed.

A Fourier analysis was performed on each cycle for many experimental conditions and different radial positions but no clear evidence of periodicity was observed. The velocity histories shown in fig.11b) suggest two possibilities: 1) the observed drop pulses are the result of a modulated injection, possibly due to highly fluctuating injection pressure; although the measured injection pressure curve does not show any strong fluctuation, it must be remembered that the pressure is measured at the injector inlet, and the variation of the fuel passage section inside the injector give rise to pressure waves which travel back and forth along the injector, producing strong variation of the pressure at sac position; 2) the spray at this location behaves as a turbulent particle laden gas jet; the second explanation appears to be more consistent with the model which stems also from the results previously presented.

3. CONCLUSIONS

The experimental investigation of a diesel spray injected into quiescent gas at different density and temperature revealed the following:

1) Entrained gas mass flow rate increases with gas density although the accuracy of the way of estimating it does not allow to compare it with the $r^{1/2}$-law.
2) Vaporisation produces a strong decrease of the particle velocity and of the entrained air mass flow rate, particularly during the main injection period.
3) Measured drop mean diameter increases with vaporisation due to the selective depletion of smaller droplets by the D^2 law and the limitation of the measuring range.
4) At the location analysed in the present study (204 to 248 diameters downstream) the spray behaves as an incompressible gas jet, and the main injection period is characterised by a strong fluctuation with no characteristic frequencies.

ACKNOWLEDGEMENTS

The experimental work was performed at CNPM-CNR laboratory in Milan. The authors would like to thank Mr. G. Galbiati for the help given during the experimental work and Mr G. Brunello for his assistance.

REFERENCES

Arcoumanis C., Hadjiapostolou A., Whitelaw J.H.; "Flow and Combustion in a Hydra Direct-Injection Diesel Engine"; SAE paper n. 910177, 1991

Chatwani, A.U., Bracco, F.V.; "Computation of Dense Spray Jets"; ICLASS-85 1985

Coghe,A, Reggiori,A. "Investigation on Spray Ignition and Combustion and Spray wall Interaction" CNPM-Int. Rep. 1993

Cossali,G.E., Coghe,A., Brunello, G.; "LDV Characterization of Air Entrainment in Transient Diesel Sprays"; SAE paper n. 910178 ,1991

Kao, J.Y., Martin, J.K., "Ambient Gas Density Effects on Droplet Diameter and velocity in a Transient Diesel Spray", Int. Symposium. COMODIA-90. 225-230 1990

Karimi E.R.; "High Speed Photography of Fuel Spray and Combustion Events in a Production Diesel Engine and Combustion Bomb"; The small internal combustion engine; IMECHE - 1988.

Kobayashi,S., Sakai,T., Nakahira,T., Komori,M., Tsujimura,K., "Measurements of Flame Temperature Distribution in D.I. Diesel Engine with High Pressure Fuel Injection". SAE paer n. 920692, 1992

Martinelli, L., Reitz, R.D., Bracco F.V., " Comparison of computed and measured dense spray jets" 9th Int. Colloquium on Dyn. of Explosions and Reactive Systems. Poitier. France. 1983

Pitcher G.and Wigley G., ; "Velocity and Dropsize Measurements in Fuel Sprays in a Direct Injection Diesel Engine"; Int. Confeence on:"Mechanics of Two- Phase Flows" Taiwan ,1989.

Pitcher, G., Wigley, G.; "A study of the Breakup and Atomization of a Combusting Diesel Fuel spray by Phase Doppler Anemometry"; 6th Int. Symp. on Laser Tech. Appl. to Fluid Mech. , Lisbon, 1992

Pitcher,G., Wigley, G., Saffman, M.; "Sensitivity of Dropsize Measurements by Phase Doppler Anemometry to Refractive Index Change in combusting Fuel Sprays"; Fifth International Symposium on Appl. of Laser Tech. to Fluid Mech., Lisbon, 1990

Ranz,W.E., Marshall, Jr W.R., "Evaporation from drops" part1 and part2, Chem. Eng. Prog., 48-3, 1952, p.141; and 48-4,1952, p.173

Ruff G.A., Sagar A.D., Faeth G.M. "Structure and Mixing Properties of Pressure-Atomized sprays" AIAA 26th Aerospace Sciences Meeting, Nevada,1988

Sato J., Konishi K., Okada H., Niioka T., "Ignition Process of Fuel Spray into High Pressure High Temperature Atmosphere". Twenty first Symposium (Int.) on Combustion, The Combustion Institute 1986, pp. 693-702.

Shundoh S., Kakegawa T., Tsujimura K., Kobayashi S.; "The Effect of Injection Parameters an Swirl on Diesel Combustion with High Pressure Fuel Injection"; SAE paper n.910489, 1991

Tokuota,N., Kobayashy,T., Sato, G.T.; "The Evaporation of small droplets in a hot Air Stream"; ICLASS-82 13-3, 1982

Ueda,K., Kigoshi,K.; "The viscosity of the gaseous hexafluoirides of Sulfur, Selenium and Tellurium"; J. inorg. nucl. Chem., Vol 36, 989-992., 1974

Varde,K.S., Popa,D.M., Varde,L.K.; "Spray Angle and Atomization in Diesel Sprays"; SAE paper n. 841055, 1984

Wu,K.-J., Coghe,A., Santavicca ,D.A.,Bracco,F.V., "LDV measurements of drop velocities in Diesel Type Sprays", AIAA Journal, Vol. 22,N.9,1984

Wu,K.-J.,Su,C.C., Steinberg, R.L., Santavicca,D.A., Bracco, F.V., ; " Measurement of Spray Angle of Atomizing Jets"; J. of Fluid Engin. ; Transaction of ASME; Vol. 105, Dec, 506-413, 1983

LDV-MEASUREMENTS IN NON-STATIONARY TURBULENCE IN A COMPRESSED JET-FLOW

H.-J. Nuglisch, J. Borée, R. Truquet, G. Charnay

Insitut de Mécanique des Fluides de Toulouse
ENSEEIHT - INPT - URA CNRS 005
Av. du Prof. Camille Soula
31400 TOULOUSE, FRANCE

D. Veynante

Laboratoire EM2C
UPR 288 CNRS et Ecole Centrale Paris
92295 Chatenay Malabry, FRANCE

ABSTRACT

In order to improve the understanding of the behavior of compressed turbulent flow, a compression machine for an axisymmetric jet flow has been build. The flow was analysed by one component LDV.

For the analysis of the non-stationary turbulence within the jet flow, filter techniques and spectral analysis for transient flows have been used.

The results show an increasing jet width during compression due to an enhanced entrainment mechanism. The turbulence intensity seems to be amplified over the complete spectrum.

1. INTRODUCTION

The increasing demand for an increased efficiency of internal combustion engines and for a diminution of the pollutant emissions (LEV and ULEV regulations) results in a growing interest in precise simulation tools for the internal aerodynamics and mixing processes in piston engines. In order to optimize these simulation tools there is still a lack in basic knowledge concerning the unsteady behavior of a turbulent flow field submitted to rapid compression.

A large amount of experimental work has been done to understand the flow inside the cylinders of piston engines. The measurements of mean and fluctuating gas velocities are mainly done with LDV in nearly production like engines, special research engines and compression machines. A review of experimental results concerning the compressed turbulence can be found in Nuglisch (1992).

For three-dimensional simulation of the flow field, classical turbulence models (k-ε) with special extensions for compressed flow are used (Ahmadi-Befrui et al. (1990), Morel and Mansour (1982), Ahmadi-Befrui and Gosman (1989)). However, comparisons between simulation and measurements still show discrepancies due to the incapability of the used turbulence models to predict the behavior of out-of-equilibrium turbulence in highly unsteady flow. There is a strong need to increase basic physical understanding of such flows.

A large amount of knowledge, both theoretical and experimental, is already acquired of the behavior of homogeneous turbulence undergoing rapid compression, see Hunt and Carruthers (1990), Wu et al. (1985), Cambon et al. (1992), Serre and Le Penven (1992), but in real flowfields there is a strong interaction between compression, turbulence and mean flow field. This triangular interaction cannot be simulated by homogeneous turbulence. A rapid compression affects the turbulence generating flow field and the turbulence structure. There will be a mutual interaction between modified mean flow field and turbulence.

Using a flow field having a complexity intermediate between real engine flows and homogeneous turbulence, we investigate at the IMFT in Toulouse the behavior of a free axisymmetrical air jet under rapid compression. For stationary conditions, the jet flow is well documented, thus effects of unsteadiness can be clearly identified.

The regions, where unsteady flow behavior can be expected, are determined by the ratio of the local flow time scale and the compression time scale. This dimensional analysis has been presented and is not repeated here, see Borée (1990) and Nuglisch et al. (1991).

2. EXPERIMENTAL SYSTEM AND DATA REDUCTION

2.1 The experimental device

Figure 1 shows the flow configuration considered for this investigation. We investigate an axisymmetric air jet with an initial nozzle diameter of 2 mm and a Reynolds number of 6500 based on the nozzle diameter. The jet is submitted to a symmetric compression by two pistons.

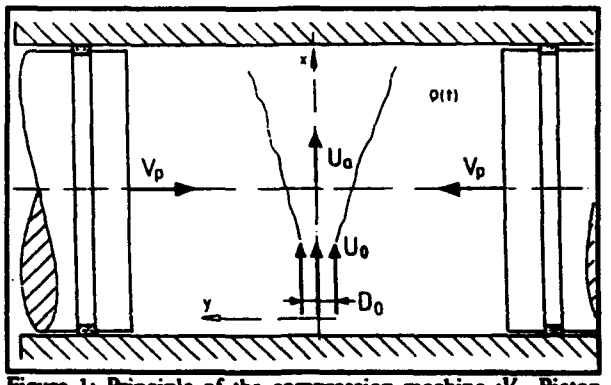

Figure 1: Principle of the compression machine : V_p Piston velocity, D_0 Jet nozzle diameter, U_0 Ejection velocity, U_a Mean velocity on the jet axis

The Reynolds number is maintained constant during the compression by constant mass flow rate using a 0.3 mm diameter sonic nozzle.

After each compression the compression chamber is opened to ambient air to assure repeatable initial conditions. For more details, see Nuglisch (1992).

Velocity measurements were performed using a one component LDV system in forward scatter configuration with Bragg cell. As signal processor a TSI 1980B frequency counter was used. Data were sampled in the free running processor mode using a PC with a DOSTEK 1400 data acquisition card.

2.2 Data reduction schemes

Mean velocities. The mean velocity profiles during compression are obtained by a combination of phase-averaging and time averaging. For each realization a time-interval weighted average is calculated over an interval of ΔT = 10 ms in order to correct for velocity bias and seeding inhomogeneity, then the ensemble average is built over N = 25 or N = 50 compressions. The mean velocity $\overline{U(t_k)}$ at time t_k becomes :

$$\overline{U(t_k)} = \frac{1}{N}\sum_{i=1}^{N} \overline{U_i(t_k)}$$

and the time averaged mean velocity for the time interval

$$k\,\Delta T - \frac{\Delta T}{2} < t_k < k\,\Delta T + \frac{\Delta T}{2}$$

for the i^{th} compression becomes :

$$\overline{U_i(t_k)} = \frac{1}{\Delta T}\sum_{j=M_{i,k-1}}^{M_{i,k}} \Delta t_j \frac{U_i(t_j) + U_i(t_{j+1})}{2}$$

with: $\Delta t_j = t_{j+1} - t_j$, $\Delta T = \Delta T_{i,k} = \sum_{j=M_{i,k-1}}^{M_{i,k}} \Delta t_j$

and $M_{i,k-1}$ and $M_{i,k}$ the first and the last measurement within the k^{th} interval and the i^{th} compression

$1 < k < N_{int}$, N_{int} = number of intervals ΔT in the sample

In order to reduce the cyclic variability, the pressure rise for each compression has been visualized and compared to a reference compression. If the instantaneous pressure in the chamber deviated more than 3% from the reference pressure, the measurements were rejected.

Reconstruction of a periodic signal from the non-uniformly sampled velocity data. After a first analysis of the mean velocities, more sophisticated data-reduction schemes were implemented in order to use more easily algorithms for filtering and spectral analysis of the velocity data:

The raw LDV velocity samples were resampled with constant frequency. Before resampling, the continuous signal was reconstructed from the non-uniform spaced samples by an extension of the Shannon interpolation, see Veynante and Candel (1988) and Clark et al. (1985).

This extension is obtained by a transformation of the time variable:

$f(t) \dashrightarrow h(\tau)$ were τ is uniformly spaced.

Further data reduction is performed based on the resampled signal.

Filter algorithms for the transient velocity signal. Usually, the turbulent velocity signal in unsteady flows is separated in the ensemble mean and a fluctuating component (Reynolds decomposition):

$$U(t) = \overline{U}(t) + u(t)$$

In order to get more detailed information on the evolution of the turbulence during the compression and the physics of non stationary turbulence, the velocity signal is separated in 3 components, the ensemble mean velocity $\overline{U}$ and the high and low frequency fluctuating components u_{HF} and u_{LF}:

$$U(t) = \overline{U}(t) + u_{HF}(t) + u_{LF}(t)$$

with the RMS values :

$$u'_{HF}(t) = \sqrt{\overline{u_{HF}^2}} \quad and \quad u'_{LF}(t) = \sqrt{\overline{u_{LF}^2}}$$

As cut-off frequency f_C for the separation between high and low frequency components, an estimation of the local and instantaneous integral time scale has been chosen. The integral time scale has been estimated using the integral length scale measurements in an axisymmetric jet, reported by Wygnanski and Fiedler (1969). The time scale was estimated using Taylors hypothesis and the convection velocity U_C in function of the mean velocity given by Wygnanski and Fiedler.

Different filter algorithms can be applied. The most simple technique is the filtering by the moving window technique with a step window function. Looking at the transfer function in the frequency domain, it can be seen that no precise cut-off frequency is obtained and a correlation term remains in the equation for the fluctuating components:

$$U(t) = \overline{U}(t) + u(t)$$

$$u'(t) = \left(u'^2_{HF}(t) + u'^2_{LF}(t) + 2\,\overline{u_{HF}u_{LF}}(t) \right)^{1/2}$$

A better separation of the high and low frequency components can be obtained by a FFT transformation, by setting the frequency components above the cut-off frequency to zero and by performing an inverse FFT.

The total fluctuation becomes in this case :

$$u'(t) = \left(u'^2_{HF}(t) + u'^2_{LF}(t) \right)^{1/2}$$

This technique, however, is difficult to apply to transient signals with varying cut-off frequency.

The technique chosen for our application is a moving window technique with a window function of the type sin x/x giving a step transfer function in the frequency domain for an infinite window width. The sensitivity of this filter technique to the window width has been investigated using a steady flow velocity signal. Figure 2 shows the high and low frequency fluctuation intensity as function of the window width. The window width is defined by the amplitude ratio between the local enveloppe $1/x$ and the central peak. For satisfactory results, a minimum window width of 0,05 has been retained.

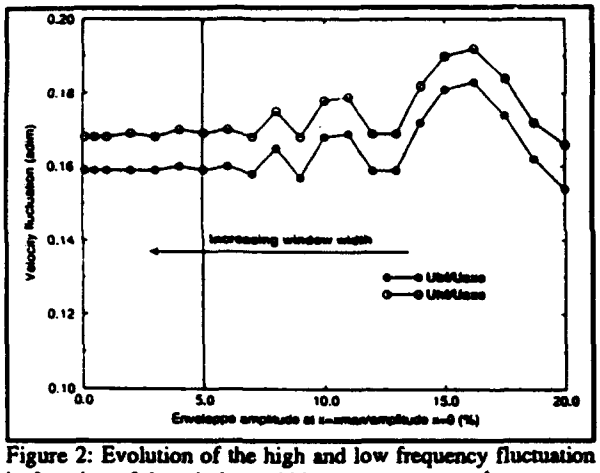

Figure 2: Evolution of the high and low frequency fluctuation in function of the window width

On figure 3 a comparison of this sin x/x window filter with a classical FFT/inverse FFT technique is shown. The result is very good for the whole range of cut-off frequencies.

The figure 4 shows this separation in 3 components for a steady jet at different radial positions in the jet at x/D=40. It can be noticed, that the main part of the turbulent energy is contained in the fluctuations with a typical time scale greater than the local integral scale of the turbulence.

Spectral analysis. Two different spectral analysis methods have been applied to study the time evolution of the spectral energy density.

i – A classical periodogram technic

ii – An auto regressive method (Méthode de Fougère) implemented by D. Veynante (see Veynante and Candel (1988)).

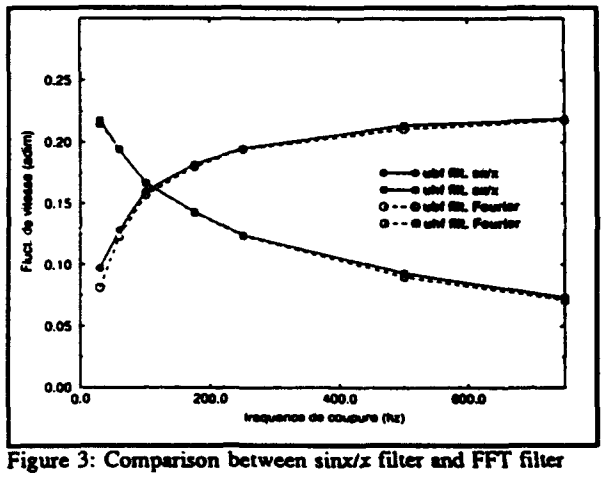

Figure 3: Comparison between sinx/x filter and FFT filter

To obtain a time evolving spectrum, a square window was used. The duration of the window was chosen greater than the jet local time scale in order to resolve the low frequency components. The obtained spectrums were then phase averaged over all the realizations of the compression at the spatial location considered.

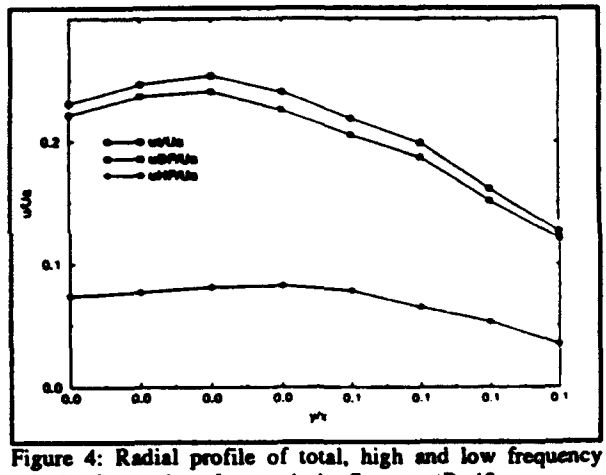

Figure 4: Radial profile of total, high and low frequency velocity fluctuations for steady jet flow at x/D=40

The advantage of the second technique is that the signal, which is only known for a limited time duration, is first modeled for longer time duration by using modern filtering and optimization schemes. The spectral analysis is then performed on the modeled signal and is very adapted to time dependent frequency analysis (Marple (1987)).

3. RESULTS

3.1 Mean velocities

Figure 5 shows the radial velocity profile at x/D=10. The velocity is decreasing proportional to the density rise in the chamber because of the constant mass flow through the sonic aperture in the ejection system.

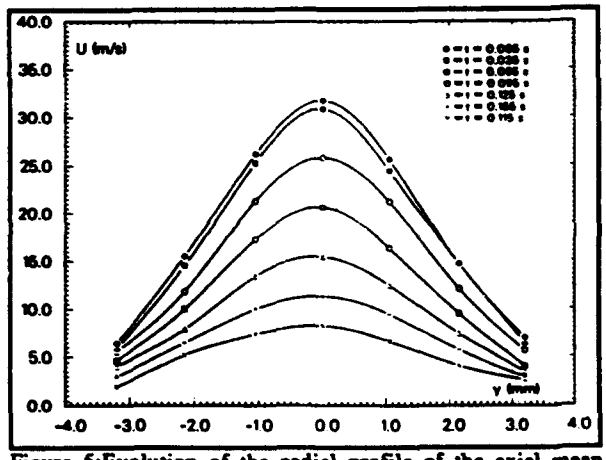

Figure 5: Evolution of the radial profile of the axial mean velocity $U(t)$ at x/D=10 during compression

The non-dimensional velocity profile presented in figure 6 shows only a slight deviation from the profile at the beginning of the compression. This proves that the velocity decrease is quasi stationary as predicted for this axial distance by the dimensional analysis presented in a previous

paper (Nuglisch et al. (1991)). Further downstream an unsteady behavior should be observed due to the strong increase of the characteristic time scale of the mean flow.

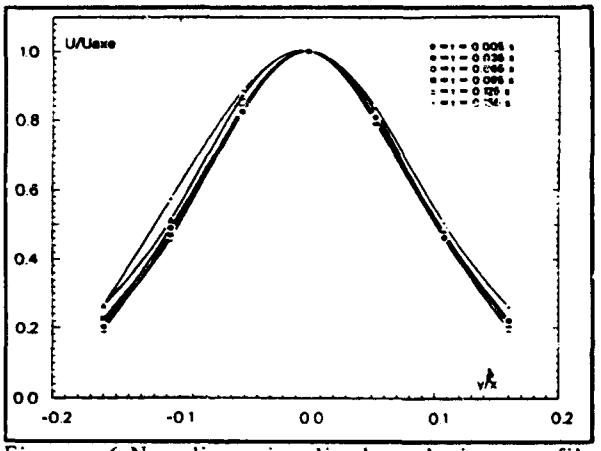

Figure 6:Non-dimensionalised velocity profile U(y,t)/U(y=0,t) at x/D=10

We are now presenting the radial profiles of the mean velocity at x/D=40. The dimensional analysis had shown that this position should clearly show an unsteady behavior of the compressed jet flow (BORÉE (1990)).

The non dimensional mean velocity profile at x/D=40 shows a clear and progressive increase of the jet diameter during the whole compression phase (figure 7).

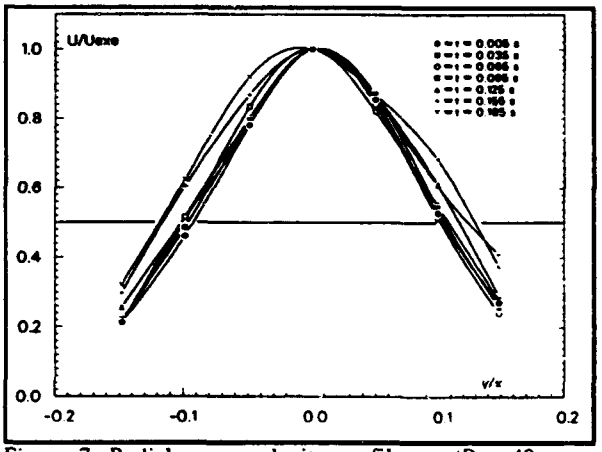

Figure 7: Radial mean velocity profile at x/D = 40, non-dimensional, during compression

On the contrary, a velocity profile measured perpendicular to the compression axis showed a different behavior. The half-velocity diameter of the jet remains constant. This becomes more evident in figure 8, where the half-velocity diameter of the jet as function of the time has been visualized for two perpendicular profiles at x/D=40. It can be seen, that the jet is axisymmetric at the beginning of the compression, but it loses progressively this symmetry because of the increasing jet diameter in the direction aligned with the compression axis. This behavior can be explained considering that the compression axis and the rotating axis of the main large scale structure of the jet are orthogonal for structures in the compression plane (Y plane) and aligned for structures in the Z plane. Analytical computation of the interaction between a given vortex and compression effectively shows that the interaction is maximum when the compression and rotation axis are orthogonal and null when these axis are aligned.

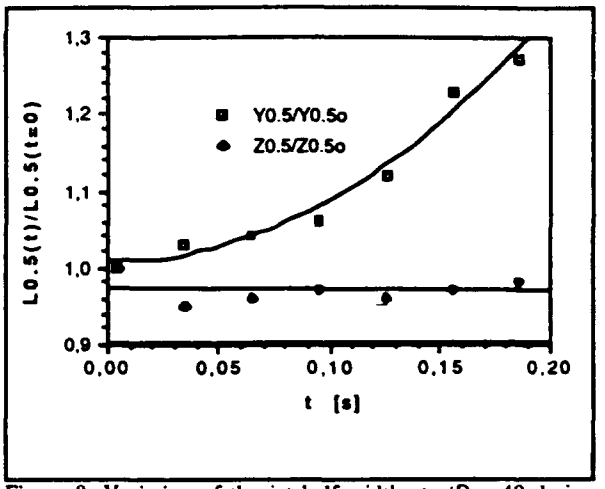

Figure 8: Variation of the jet half-width at x/D = 40 during compression

3.2 Turbulent fluctuations

As shown in figure 5, the mean velocity decreases during the compression due to a constant mass flow at the nozzle exit. At x/D=10 the turbulence intensity shows nearly no modifications during the compression (see figure 9). This is coherent with the hypothesis of quasisteady flow at this location. At x/D=40 the turbulence intensity is increasing strongly (figure 10).

The figure 11 shows the influence of the variable cut-off frequency on the separation of the two fluctuating components during compression.

The results obtained with an variable cut-off frequency equal to the local instantaneous integral time scale of the turbulence, show an increase of the intensity of both, the low and the high frequency components (see figures 12 and 13).

It can be noticed that the intensity of the low frequency fluctuation shows a radial distribution comparable to the radial distribution of the total fluctuation. On the contrary, the high frequency fluctuations are distributed homogeneously over the jet profile during compression.

The result that the high frequency fluctuations were affected nearly as strongly as the low frequency fluctuations by the compression, was a quite astonishing result, but it confirms the theoretical results of Cambon et al. (1992). In order to get more detailed information, a spectral analysis has been performed (figure 14). The velocity spectra confirm the findings presented above. The fluctuation energy density is increasing over the whole spectrum during compression.

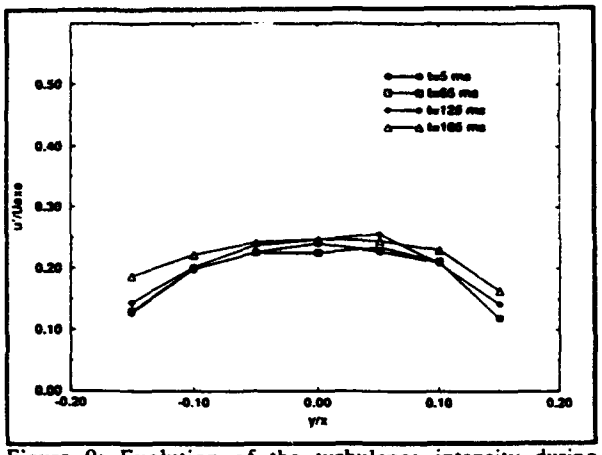

Figure 9: Evolution of the turbulence intensity during compression at x/D = 10

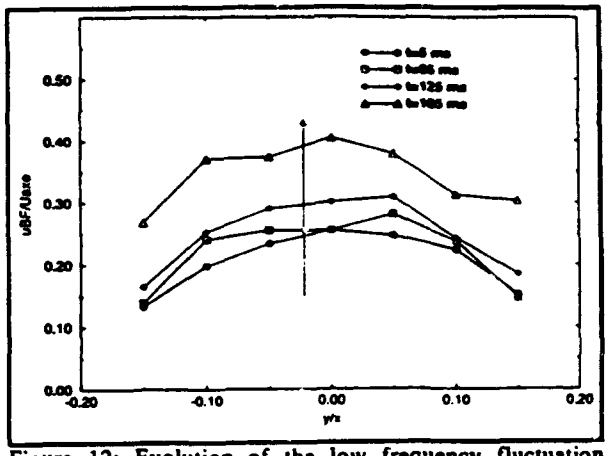

Figure 12: Evolution of the low frequency fluctuation intensity at x/D = 40

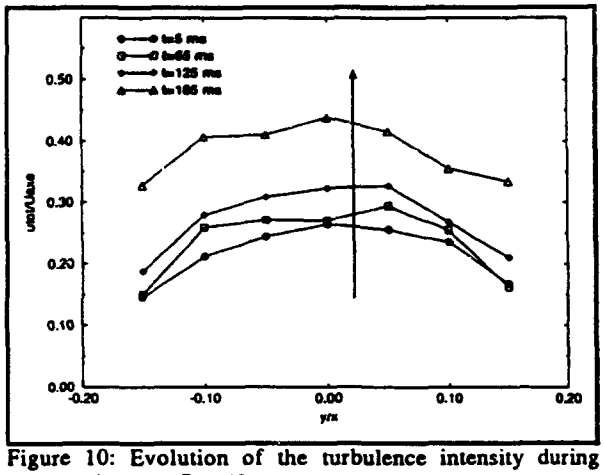

Figure 10: Evolution of the turbulence intensity during compression at x/D = 40

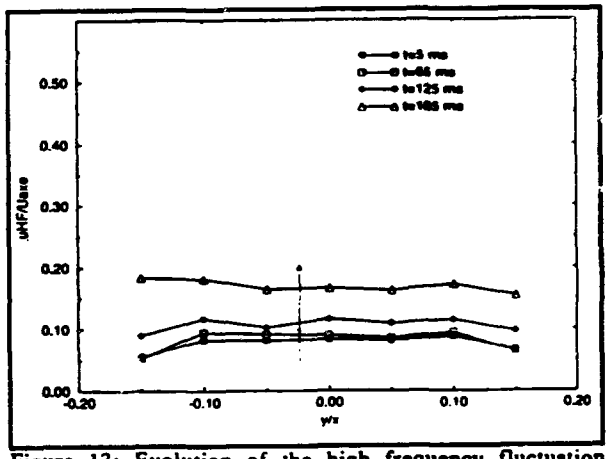

Figure 13: Evolution of the high frequency fluctuation intensity at x/D = 40

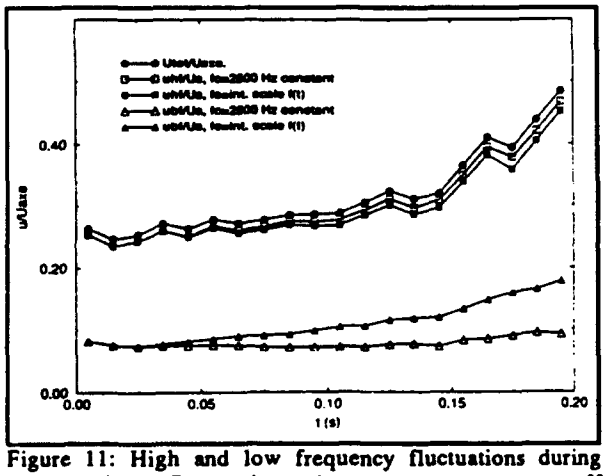

Figure 11: High and low frequency fluctuations during compression. Comparison between constant cut-off frequency and instantaneous integral scale

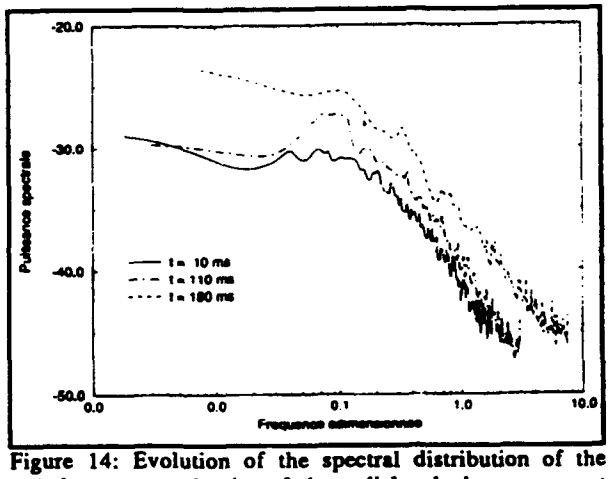

Figure 14: Evolution of the spectral distribution of the turbulent energy density of the radial velocity component during the compression. x/D=40, ensemble mean over 50 realizations.

4. CONCLUSION

We have presented different data reduction methods for unsteady turbulent flow. These techniques allow a more detailed analysis of transient flow by monitoring the evolutions of the mean velocities, the energy of the turbulent fluctuations with scales greater and smaller than the integral scale and at the end the spectral analysis as most detailed tool.

The main result of our investigation is that the jet flow is strongly affected during the compression.

Initially axisymmetric, the jet diameter increases in the direction of the 1-D compression. At x/D=40 this increase is as important as 30% of the initial diameter. This global behavior can be explained by an enhanced entrainment mechanism.

The most important result from these investigations is that the increase of the turbulent energy density during the compression is distributed over the whole turbulence spectrum. This result agrees with results from theoretical work carried out at the Ecole Centrale Lyon.

ACKNOWLEDGEMENTS

The authors are indebted to H. Haminh and his research team for lending the LDV systems and more particularly to M. J. Bonnefont and M. G. Couteau for the technical support.
This work was supported by the CNRS - PIRSEM and the CEE (JOULE) within the research program on "Basic Researches on Combustion Modelling in Piston Engines". M. Nuglisch thanks for financial support of the CEE.

REFERENCES

Ahmadi-Befrui, B. & Gosman, A.D. 1989, Assessment of variants of the k-ε turbulence model for engine flow application, Int. J. for Numerical Methods in Fluides, Vol.9

Ahmadi-Befrui et al. 1990, Simulationsmodel zur Berechnung der Luftbewegung in Zylindern von Verbrennungsmotoren, MTZ vol. 51

Borée, J. 1990, Analyse physique et expérimentale d'un écoulement de jet compressé, Ph.D. thesis, Institut National Polytechnique de Toulouse, France

Cambon, C., Mao, Y. & Jeandel, D. 1992, On the application of time dependent scaling to the modelling of turbulence undergoing compression, Eur. J. Mech., B/Fluids, 11, No. 6

Clark, J.J., Palmer, M.R. & Lawrence, P.D. 1985, A Transformation Method for the Reconstruction of Functions from Nonuniformly Spaced Samples, IEEE Transactions on Acoustics, Specch, and Signal Processing, Vol. ASSP-33, No. 4

Hunt, J.C.R. & Carruthers, D.J. 1990, Rapid distortion theory and the "problems" of turbulence, J. Fluid Mech., Vol. 212

Marple, S.L. 1987, Digital spectral analysis with applications, Prentice – Hall signal processing series

Morel, T. & Mansour, N.N. 1982, Modelling of turbulence in internal combustion engines, SAE-Paper N° 820040

Nuglisch, H.-J. 1992, Etude expérimentale d'un jet axisymétrique compressé. Situation modèle de l'aérodynamique interne des moteurs à pistons, Ph.D. thesis, Institut National Polytechnique de Toulouse, France

Nuglisch, H.-J., Borée, J., Atassi, N. & Charnay, G. 1991, Response of turbulent jet flow to rapid compression 14th International Congress on Instrumentation in Aerospace Simulation Facilities, Rockville, Maryland

Serre, G. & Le Penven, L. 1992, Laser Doppler Measurements of a Grid - Generated Turbulence Undergoing a Volume Reduction6th Int. Symp. on Appl. of Laser Techniques to Fluid Mechanics, Lisbon, Portugal

Veynante, D. & Candel, S.M. 1988, Application of nonlinear spectral analysis and signal reconstruction to laser doppler velocimetry, Experiments in fluids 6, pp. 534 - 540

Wu, C.T., Ferziger, J.H. & Chapman, D.R. 1985, Simulations and modelling of homogeneous compressed turbulence, Report No. TF-21, Stanford University

Wygnanski, I. & Fiedler, H. 1969, Some measurements in the self preserving jet, J. Fluid Mech., Vol. 38

PDA ANALYSIS OF TRANSIENT SPRAY FLOWS INITIATED FROM AIR ASSISTED INJECTOR

Tomio Obokata, Hideaki Tanaka and Tetsuji Koyama
Department of Mechanical Engineering, Gunma University
1-5-1 Tenjin, Kiryu, 376 Japan

and

Toru Mashimo and Kazumitsu Kobayashi
UNISIA JECS Co.
1671-1 Kasukawa, Isesaki, 372 Japan

ABSTRACT

In order to study the characteristics of flow and particle diameters in the unsteady spray from an air assisted fuel injector in the atmospheric condition has been analyzed using a phase Doppler anemometer (PDA). In the experiments, the frequency of injection is 50Hz, the pressures of both fuel and air are changed in three steps. Radial and axial distributions of bulk velocity and Sauter mean diameter of spray particles are obtained. It is found that the profile of mean velocity is close to the normal distribution and the Sauter mean diameter of droplets in the spray is as small as 20 to 30μm. The log-hyperbolic function (LHF3) has also been applied to the spray and the characteristics of the distribution of spray particle sizes are represented clearly by the three parameters of the LHF3.

1. INTRODUCTION

Improving combustion of gasoline engine is one of the important problems for conservation of the global environment and effective use of fossil resources. Various methods of fuel injection system have been proposed since combustion of spark ignition engine is affected by the mixture formation processes depending on the form and characteristics of fuel spray and by the injection timing. Recently, air assisted fuel injector has been used for gasoline engine with lean fuel/air mixture to improve the fuel consumption and NOx emission.

Presently, a phase Doppler anemometer (PDA) has been successfully applied to characterize the fuel sprays for Diesel engine [Hosoya & Obokata (1992, 1993a, 1993b), Obokata & Long (1994), Brunello et al. (1990), Coghe & Cossali (1992), Arcoumanis et al. (1992), Pitcher & Wigley (1992), Özdemir (1992)] and gasoline engine [Kobashi et al. (1990), Vannobel et al. (1992), Obokata et al. (1993)]. So, to study characteristics of flow and particle diameters in the spray initiated from air assisted injector, unsteady fuel spray in the atmospheric condition has been analyzed using the PDA and compared with steady spray and ordinary pintle type fuel spray.

2. EQUIPMENT AND METHOD OF EXPERIMENTS

2.1 Fuel Injection System

Figure 1 shows the outer mixing type air assisted fuel injection nozzle which was mounted on a pintle type fuel injector. The fuel was intermitted by the pintle however the assisted air continuously flowed in the nozzle. The nozzle outlet was 2mm in diameter. In experiments, the frequency of injection was 50Hz, the pressures of fuel were 147, 250 and 588kPa and the pressures of air were 98, 147 and 196kPa. The alternative fuel of Laws (Shell) was used for injection instead of gasoline. Physical properties of Laws are listed in Table 1. Figure 2 shows a schematic diagram of the injection tester used in this experiment.

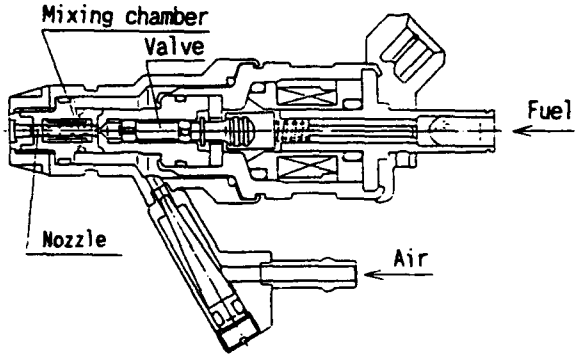

Fig. 1 Cross section of air assisted fuel injector

Table 1 Physical properties of fuel (Laws)

Density	g/cm^3	0.794
Surface tension (20° C)	N/m	2.64×10^{-2}
Kinematic viscosity (20° C)	mm^2/s	1.08
Coefficient of cubical expansion (25° C)	($°C^{-1}$)	8×10^{-4}

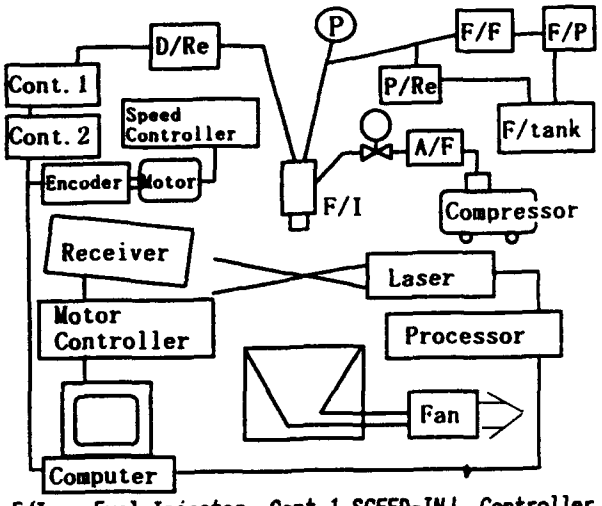

F/I Fuel Injecter Cont.1 SCEED-INJ. Controller
F/F Fuel Filter Cont.2 SCEED-IGN. Controller
F/P Fuel Pump P Pressure Pickup
F/Tank Fuel Tank D/Re Dropping Resistor
P/Re Pressure Resistor A/F Air Filter

Fig. 2 Schematic diagram of experimental apparatus

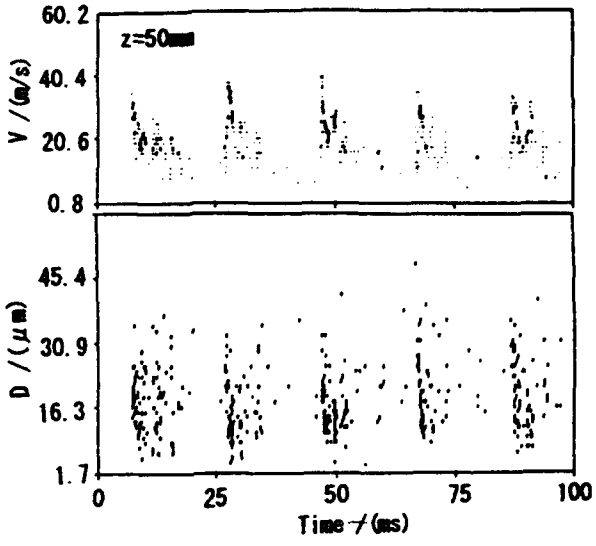

Fig. 3 Time series of droplets size and velocity (Air assisted injector, z=50mm, r=0mm. Pa=147kPa, Pf=250kPa, Δ t=2.5ms, g=5.1mg/stroke)

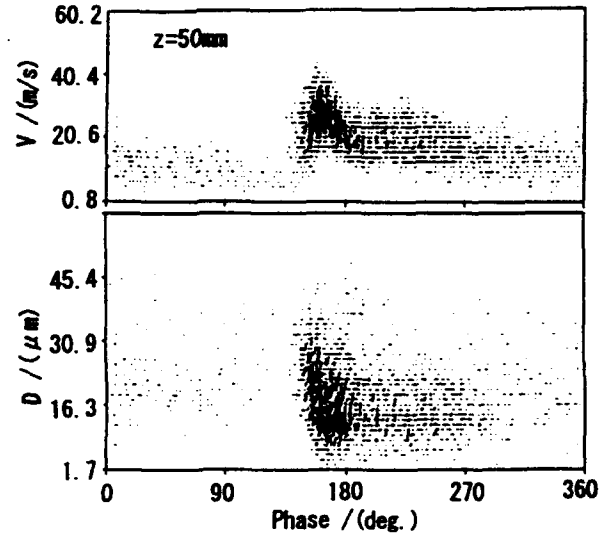

Fig. 4 Phase r tched plot of droplets size and velocity

2.2 Phase Doppler Anemometer

The phase Doppler particle analyzer (PDPA) made by Aerometrics was used to measure the particle diameter and flow velocity of the spray. The diameter of the measuring volume was adjusted to more than five times the maximum particle diameter, to remove measurement errors which would be affected by the Gaussian distribution of intensity of the incident beam [Grehan et al. (1991)]. The diameter of the measuring volume used in this experiment was about 0.7mm and the total intersection angle of incident beams was 5.4° and forward scattering mode was used with the detector inclined by 30° from the axis of the incident beams.

3 RESULTS OF EXPERIMENTS AND DISCUSSION

3.1 Distribution of Particle Diameter and Velocity of the Spray

Time series of droplets diameter and velocity measured at z=50mm on the spray center line (r=0mm) are plotted in Figure 3 where the air pressure Pa=147kPa, the fuel pressure Pf=250kPa, valve opening duration Δt=2.5ms, the amount of fuel g=5.1mg in each injection cycle and the flow rate of the air Q=0.255Nℓ/s. The maximum data rate is about 20kHz at the spray and the mean data rate is 5kHz in this measuring point. We assume that the z-axis is the direction in which the spray advances and that the radius r is perpendicular to the z-axis.

Figure 4 is ensemble plots of velocity and size of particles where the time axis of Figure 3 was converted into the injection phase angle. The ensemble averaged mean velocity (Vm m/s) and the Sauter mean diameter (D_{32} μm) of the spray are shown in Figure 5-a) and -b). The highest Vm and the lowest D_{32} were observed near the front part of main spray cloud.

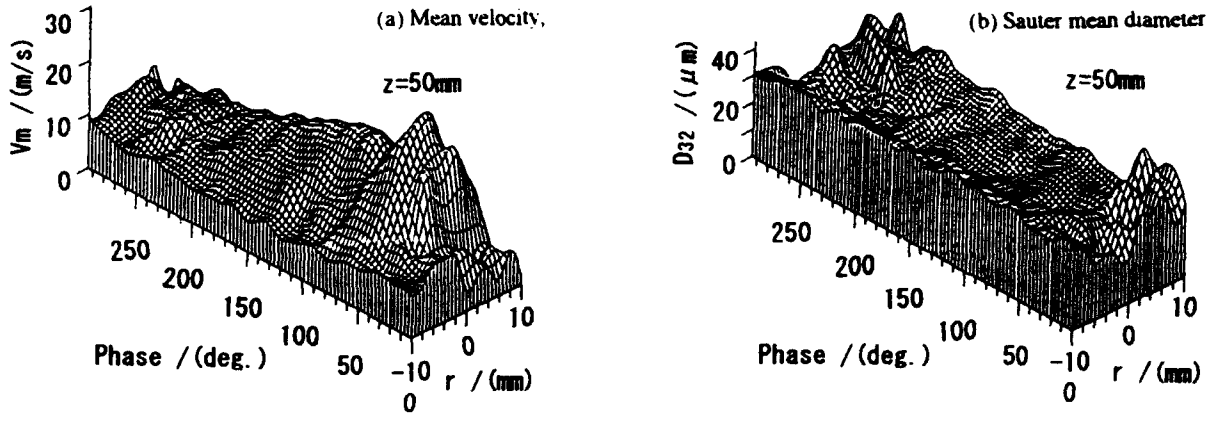

Fig. 5 Three dimensional plot of mean velocity (a) and Sauter Mean diameter (b)

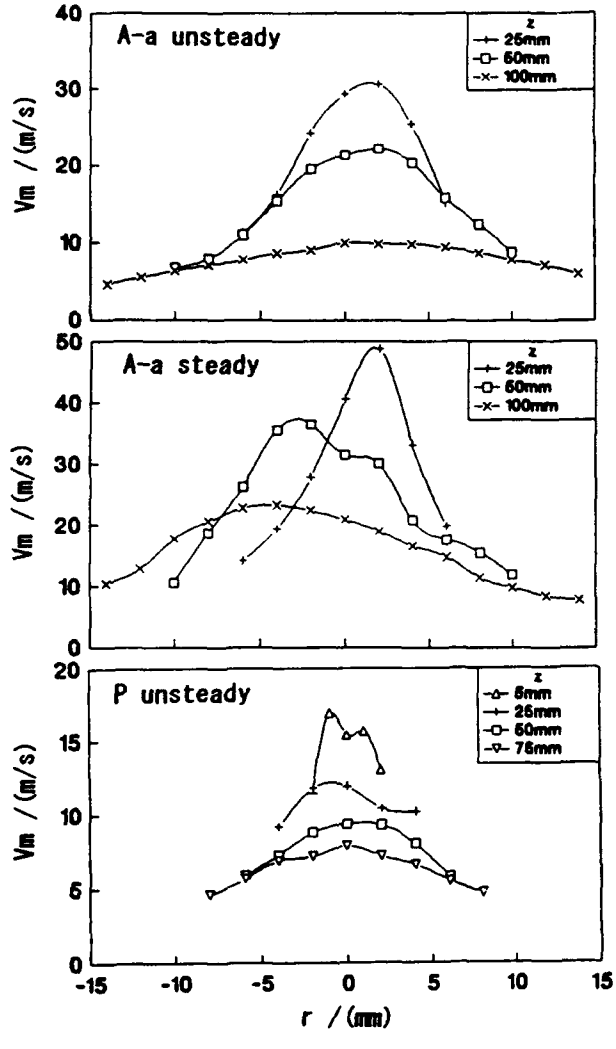

Fig. 6 Radial distributions of the mean velocity

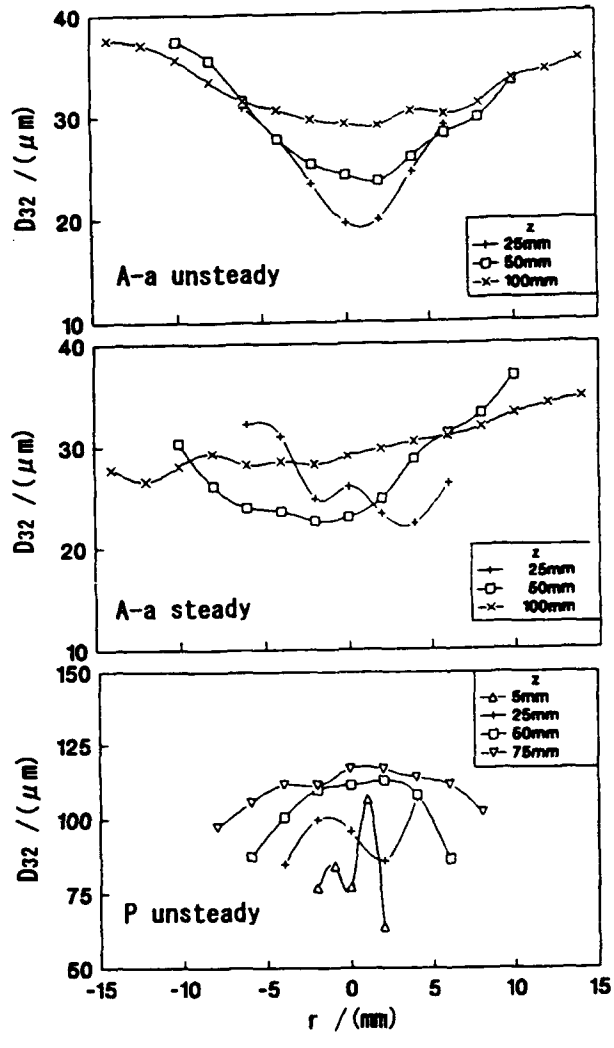

Fig. 7 Radial distribution of the Sauter mean diameter

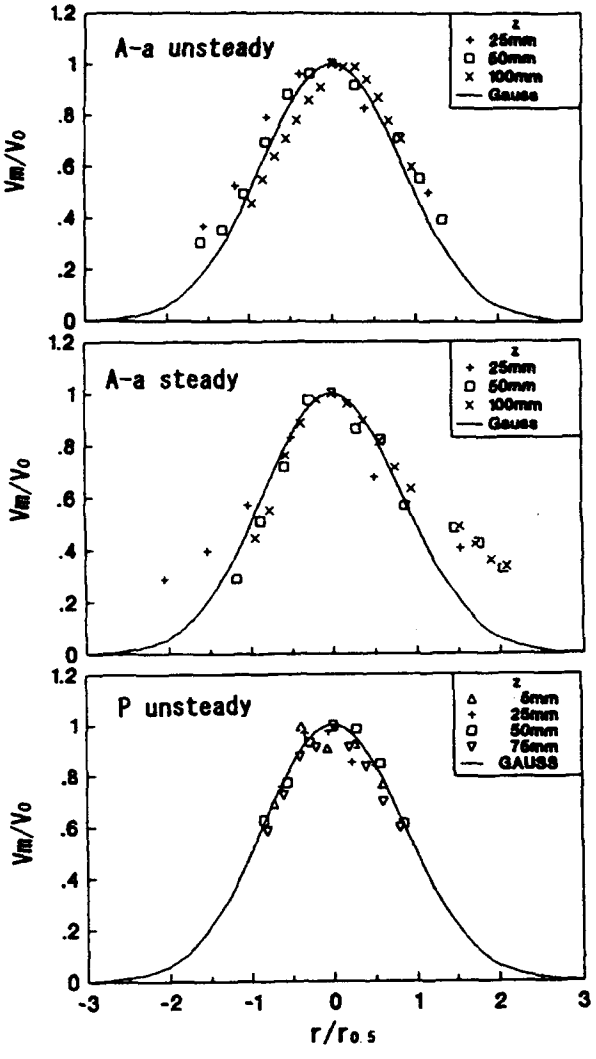

Fig. 8 Dimensionless expression of mean velocity

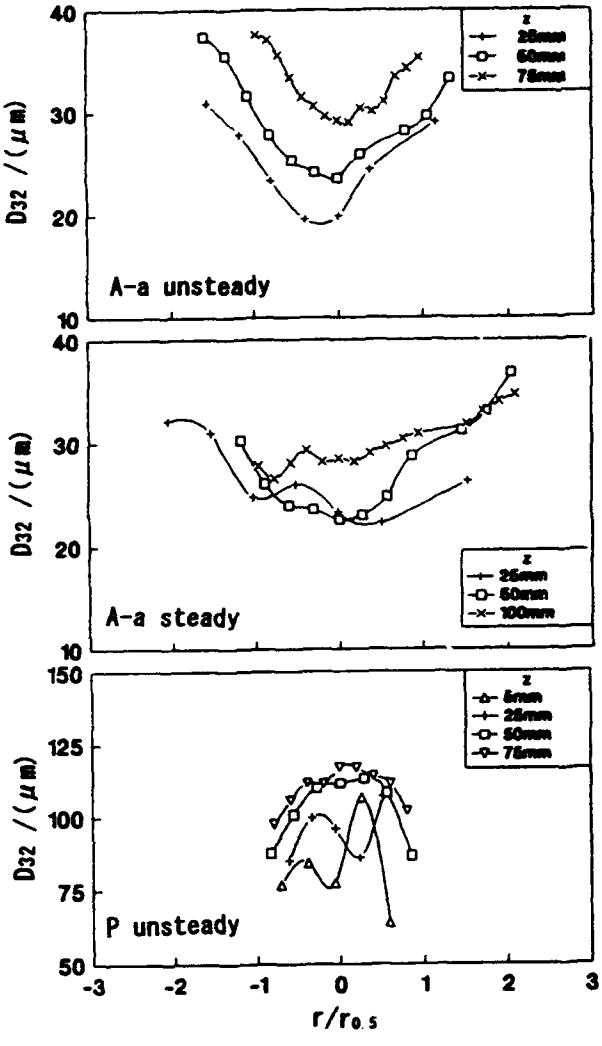

Fig. 9 Radial distribution of Sauter mean diameter

Figures 6 and 7 show the radial distributions of mean velocity and the Sauter mean diameter respectively observed at a few axial positions. Three types of spray flows, the air assisted intermittent spray (A-a unsteady, fuel flow rate g=5.1mg/cycle) or steady spray (A-a steady, g'=1.84g/s) and pintle type intermittent spray (P unsteady, g=6.5mg/cycle), are compared each other. At the intermittent air assisted spray, wider and axisymmetric distributions of Vm and D_{32} are shown. Inverse distribution pattern between Vm and D_{32} are observed here as described in Figure 5, i.e. Vm decreases along axial direction however D_{32} increases. In the steady air assisted spray which was produced by the same injector of unsteady spray injector by valve opening duration $\Delta t=\infty$, spray flow pattern was not stable and the peak of velocity profile was radially shifted along the axial direction. A[illegible]e times bigger particles with the narrower velocity distr[illegible]han the air assisted spray are shown in the spray from th[illegible]ntle type injector.

Figure 8 shows the distributions of mean velocity where the velocity and radius are made dimensionless respectively by the maximum velocity (V_0) at the axis and by the half-value width ($r_{0.5}$) of the velocity distribution curve. From here we find that the three data sets are close to a normal distribution. The fact that velocity measurements at the outskirts of the spray were greater than the normal distribution was attributed to the biasing effect in LDA measurement. Figure 9 shows similar results for the size distributions where only the lateral axis is made dimensionless using $r_{0.5}$ from velocity distribution of Figure 8. The change of non dimensional widths of spray distribution along the axial direction is small in each spray.

Effects of fuel flow rate (g) on the mean velocity and the Sauter mean diameter of spray from air assisted injector are shown in figure 10 and 11. Increased Vm and D_{32} are observed along with increased fuel flow rate and the effect of air pressure (Figure 10) is greater than that of fuel pressure (Figure 11).

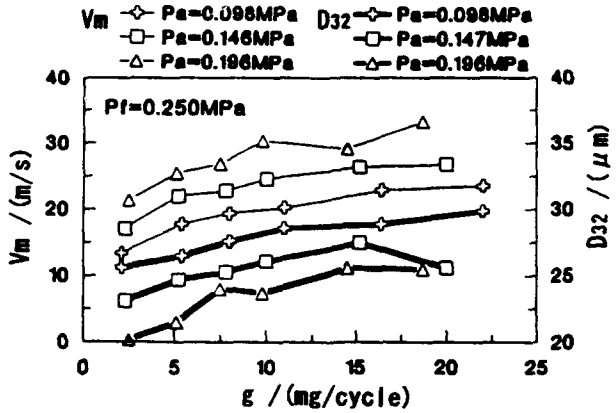

Fig. 10 Effects of injection condition on the spray characteristics (Pf=constant)

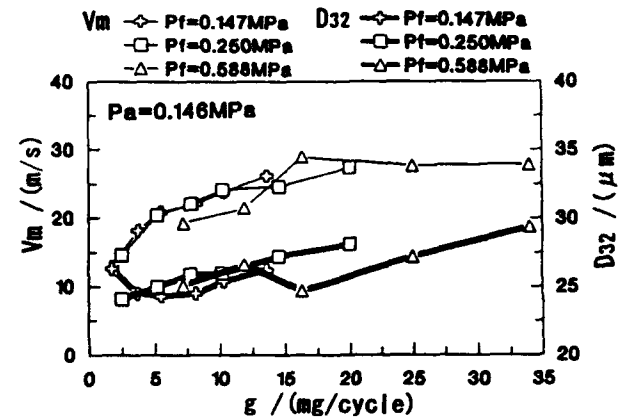

Fig. 11 Effects of injection condition on the spray characteristics (Pa=constant)

3.2 Divided Evaluation of the Spray

It is difficult for PDA measurement to catch all of the spray every time and particles were measured at a rate of about 20kHz of effective data rate. Thus, the data was represented by ensemble averages for varying crank angle. Figure 12 is re-plot of Figure 4 where total number of data was 4000. The authors tried to represent the spray by dividing the spray to the central part (C) which corresponded to the central $t_0\sqrt{3}$ width of the half value duration (t_0) of spray velocity, the fore $t_0\sqrt{3}$ part (F), the rear $2t_0\sqrt{3}$ part (R) and the remained tail part (T). The divisions are shown in Figure 12. Figures 13 A, F through T show the correlation plots of particle size and velocity calculated from the same data as Figure 12. The data S corresponds the same air assist spray in steady state injection and the data P shows the spray from the pintle nozzle. In A, where all the spray data was used, it can be seen that the larger particles have smaller velocities at small size range. This distribution is unusual compared with that of a common steady spray.

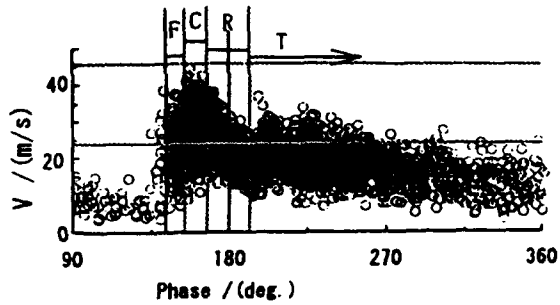

Fig. 12 Division of intermittent spray

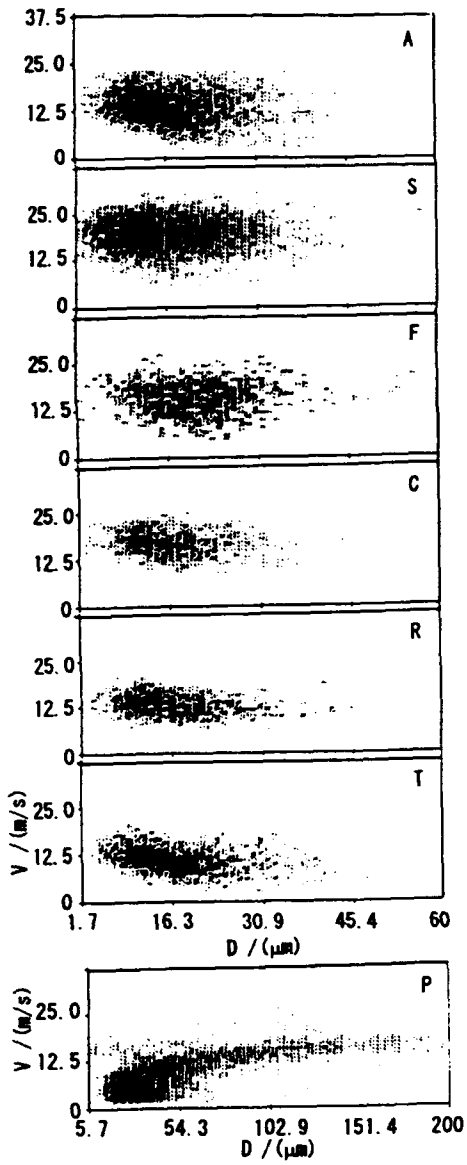

Fig. 13 Correlation between droplets size and velocity

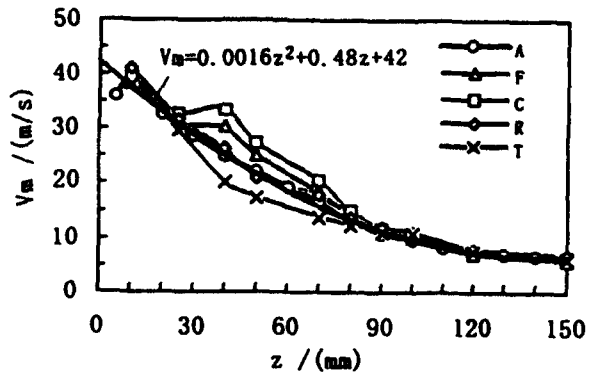

Fig. 14 Axial distribution of the mean velocity

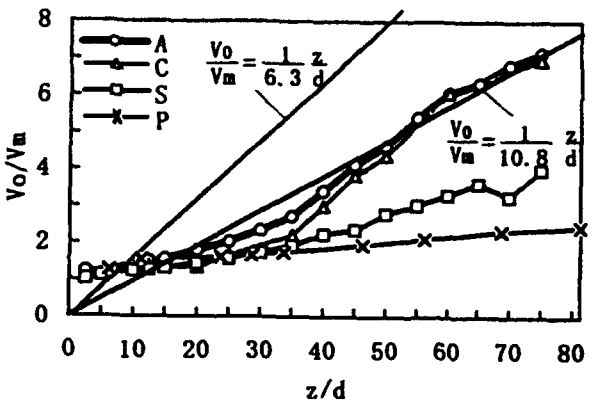

Fig. 15 Decrease of centerline velocity of the spray

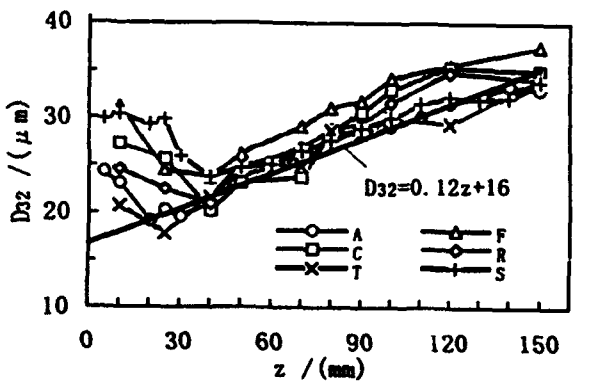

Fig. 16 Axial distribution of the Sauter mean diameter

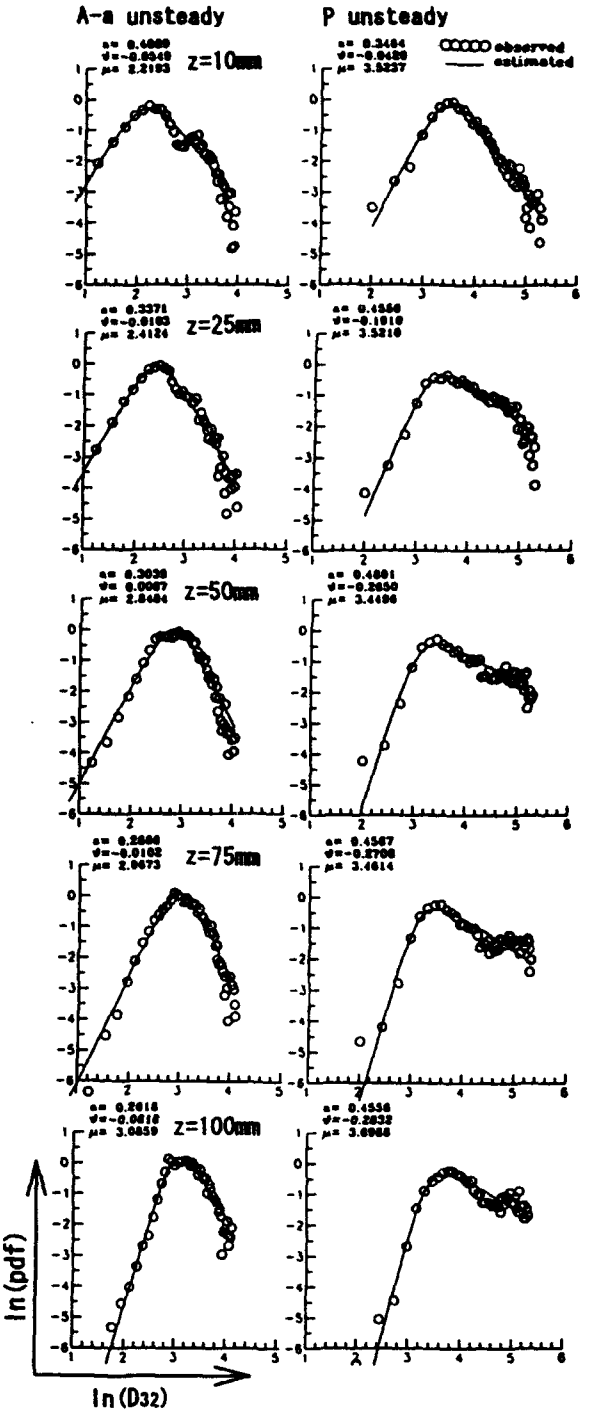

Fig. 17 Distribution of droplet diameters and results of the log-hyperbolic fitting (Air assist nozzle and pintle nozzle)

The individual distribution diagrams reveal that larger particles have higher velocities in average except at the tail part T where the fuel on the mixing chamber wall was blown off by the air and negative correlation would be detected. The unusual correlation of A will be caused by the negative correlation of T.

Figures 14 to 16 show the z axial distribution of the mean velocity (Vm) and the Sauter mean diameter (D_{32}) in each part of spray. The changes in the mean velocity and the Sauter mean diameter of particles for all spray (A) in the axial direction have been approximated by simple formulae and plotted in each figure. In Figure 15, decreasing ratio of axial spray jet velocity is about 1.6 times smaller than that of air jet.

3.3 Evaluation of the Distribution of Particle Sizes with a Log-Hyperbolic Function

The log-hyperbolic function has been reconsidered recently [Xu et al. (1991)] as one of the functions used to represent the distribution of particle sizes. It has been reported that the function provides a good approximation for Diesel sprays [Long et al. (1994)]. This method plots the particle sizes and number density distribution on a diagram of logarithmic scales and are approximated with a hyperbolic curve. It is considered that deviation in the distribution of particle sizes and average particle size can be evaluated from the angle (a) of opening of the hyperbolic curve, inclination (θ) of its axis, and horizontal coordinate (μ) of its peak. Here we apply the three-parameter log-hyperbolic function (LHF3) to the distribution of spray particle diameters measured in varying part of unsteady spray. Figure 17 shows the comparison between measurements (o) of the distribution of all particle diameters (A) along the central axis of unsteady spray with LHF3. Results of LHF3 applied for spray particles from the pintle nozzle are also plotted here. The functional approximation using LHF3 was good in all cases.

Figure 18 shows changes of the parameters, a, θ and μ, of particle size distribution in the axial direction. Large differences, wider distribution, more negative inclination and larger mean diameter are observed in spray flow from pintle nozzle. Thus, characteristics of the distribution of spray particle sizes were represented clearly with the three parameters of LHF3.

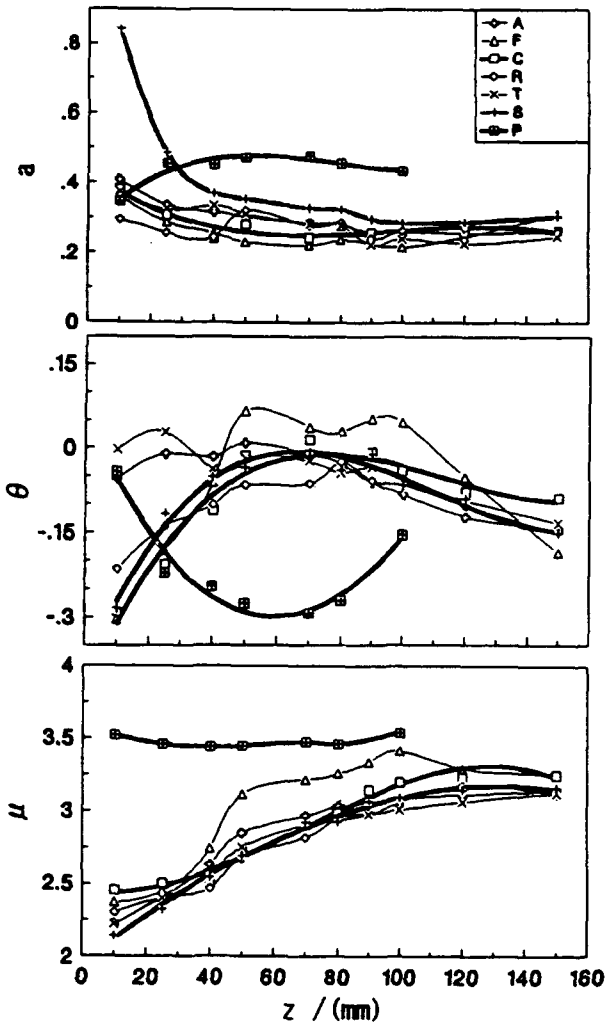

Fig. 18 Change of fitting parameters along the injection direction

4 CONCLUSIONS

1. The ensemble averaged mean velocity (Vm m/s) and the Sauter mean diameter (D_{32} μm) of the air assisted fuel spray are obtained and the highest Vm is 30 to 10m/s and the lowest D_{32} is 20 to 30 μm are observed near the front part of the spray.

2. Dimensionless radial distribution of axial mean velocity of the spray is close to the normal distribution.

3. The changes of Vm and D_{32} for all spray in the axial direction are approximated by simple formulas and decreasing ratio of axial spray jet velocity is about 1.6 times smaller than that of air jet.

4. At the correlation between particle sizes and velocities, individual distribution diagrams reveal that larger particles have higher velocities in average except at the tail part where the fuel on the mixing chamber wall was blown off by the air and negative correlation would be detected. The unusual correlation of all spray will be caused by the negative correlation of tail part.

5. Increased Vm and D_{32} are observed along with increased fuel flow rate and the effects of air pressure is greater than fuel pressure.

6. Evaluating the distribution of particle diameters with a log-hyperbolic function is found effective as it described well the characteristics of particle size of the spray.

ACKNOWLEDGMENTS

The authors appreciate Prof. Durst and his coworkers at University of Erlangen, Germany, for providing the log-hyperbolic function.

REFERENCES

Arcoumanis, C. Paál and Whitelaw, J.H. 1992, Structure of Unsteady Sprays Injected from Pintle-Type Nozzles, Proc. of 6th. Int. Symp. on Appli. of Laser Techniques to Fluid Mech., Lisbon, Paper No. 37.4.

Brunello, G. Coghe, A. Cossali G.E. and Gamma, F. 1990, Characterization of Transient Spray Structure in Cross Flows, Proc. of 5th. Int. Symp. on Appli. of Laser Techniques to Fluid Mech., Lisbon, Paper No. 21.4.

Coghe, A. and Cossali, G. E. 1992, Experimental Analysis of Wall-Spray Structure by Laser Doppler Techniques, Proc. of 6th Int. Symp. on Appli. of Laser Techniques to Fluid Mech., Lisbon, Paper No. 25. 3.

Gréhan, G., Gouesbet, G., Naqwi, A. and Durst, F. 1991, Evaluation of Phase Doppler System using Generalized Lorenz-Mie Theory, Proc. Int. conf. Multiphase Flows. Tsukuba, pp. 291-294

Hosoya, H. and Obokata, T. 1992, LDA Measurements of Spray Flow from a Single Hole Diesel Type Nozzle under Steady Conditions, Proc. of 6th Int. Symp. on Appli. of Laser Techniques to Fluid Mech., Lisbon, Paper No. 37.5.

Hosoya, H. and Obokata, T. 1993a, Effect of Nozzle Configuration on Characteristics of Steady-State Diesel Spray, SAE Paper No. 930593.

Hosoya, H. and Obokata. T. 1993b, LDA Measurment and LHF Analysis of Diesel Type Sprays, Proc. of 3rd. Int. Congress on Optical Particle Sizing, Yokohama, pp. 495-502.

Kobashi, K., Hishida, K and Maeda, M. 1990, Measurement of Fuel Injector Spray Frow of I.C.Engine by FFT Based Phase Doppler Anemometer, Proc. of 5th. Int. Symp. on Appli. of Laser Techniques to Fluid Mech., Lisbon, Paper No. 21. 2.

Long, W.Q., Hosoya, H., Mashimo, T., Kobayashi. K., Obokata, T., Durst, F. and Xu, T.H. 1994, Analytical Functions to Match size Disributions in Diesel-Sprays, Proc. thr 3rd. Int. Symp. on Diagnostics and Modeling of Combustion in Internal Combustion Engines., Yokohama, Papar ID No. J58.

Obokata, T. and Long, W.Q. 1994, LDA/PDA Characterization of Conical Spray for Diesel Engine, Proc. of 6th. Int. Conference on Liquid Atomization and Spray Systems., Rouen, Paper No. IC94/90.

Obokata, T., Takeuchi, H., Mashimo, T., and Kobayashi, K. 1993, PDA Analysis of Transient Spray Flow Initiated from Low Pressure Injector, Preprint of JSME, No.930-63, Vol. D, pp.308-310. (in Japanese)

Özdemir, I. B. 1992, Correlation Between the Size Characteristics of the Wall Jet and the Dynamics of the Unsteady Film Formed after the impingement of an Unsteady Two-Phase Jet, Proc. of 6th Int. Symp. on Appli. of Laser Techniques to Fluid Mech., Lisbon, Paper No. 37.2.

Pitcher, G. and Wigley, G. 1992, A Study of the Breakup and Atomization of a Combusting Diesel Fuel Spray by Phase Doppler Anemomtory, Proc. of 6th. Int. Symp. on Appli. of Laser Techniques to Fluid Mech., Lisbon, Paper No. 25.1.

Vannobel, F., Dementhon J. B., Robart, D. 1992, Phase Doppler Anemometry Measurements on a Gasoline Spray Inside The Inlet Port and Downstream of the Induction Valve: Steady and Unsteady Flow Condititions, Proc. of 6th. Int. Symp. on Appli. of Laser Techniques to Fluid Mech., Lisbon, Paper No. 29.2.

Xu, T.-H., Durst, F. and Tropea, C. 1991, The Three-Parameter Log-Hyperbolic Distribution and its Applications to Particle Sizeing, Proc. Int. Conf. on Liquid Atomization and Spray systems, ICLASS 91, Gaithersburg, Paper No.31, pp. 315-324.

Session 37.
PIV Applications

PIV MEASUREMENTS IN SIMULATED MICROBURSTS

Ellen K. Longmire and Abbas Alahyari

Department of Aerospace Engineering & Mechanics
University of Minnesota, Minneapolis MN 55455 USA

ABSTRACT

In this work, atmospheric microbursts are modeled as volumes of heavier liquid which descend through an ambient environment and impact on a horizontal surface representing the ground. Particle image velocimetry is used to map the evolving velocity and vorticity fields present in the flow. The PIV results show a large primary vortex developing at the head of the downburst fluid. Large downward velocities exist across the fluid inside of the vortex and persist until after the vortex impinges on the bottom surface. After impingement, the vortex intensifies as it expands radially. Very large horizontal velocities are found beneath and upstream of the primary vortex. These velocities and the associated radial gradients correspond to extremely large windshears in atmospheric microbursts. The results generally agree with data from the numerical study of Lundgren, Yao, and Mansour (*JFM*, vol. 239, 1992). The PIV results, however, show maximum horizontal velocities occurring much earlier after vortex impingement than in the numerical study.

1. INTRODUCTION

A microburst (or small-scale downburst) is an intense concentrated downdraft of "heavy" air which occurs in the atmosphere. The relatively heavy air is generated in locations where rain or hail falls from a cloud into dry air and rapid evaporation occurs. The air is cooled, and its density increases. The increased density coupled with drag from any remaining precipitation produces a strong downward velocity in the volume of fluid. As a microburst nears the ground, it rolls up into a large vortex ring which then spreads radially outward and generates large horizontal wind velocities. Aircraft flying through downbursts at low altitudes can experience radical variations in wind velocity ("windshear") which pose extreme hazards.

Since atmospheric downbursts occur intermittently at fairly random locations, it has been difficult to obtain detailed data on their strength and structure. Two field programs, NIMROD near Chicago in 1978 and JAWS near Denver in 1982, performed intensive Doppler radar measurements to document the occurrence of many microbursts of varying size and intensity. (Fujita (1985, 1986)). Numerical studies have included both large eddy simulations (LES) (Proctor (1988, 1989), Droegemeier (1988)) and an inviscid vortex dynamics model (Lundgren *et al.* (1992)). These efforts, which agreed well with available atmospheric data, confirmed the presence of the primary vortex ring and showed secondary vorticity of opposite sign developing along the ground ahead of the primary structure. They also showed that buoyancy-driven convection was the dominant mechanism in microburst propagation.

Experiments on laboratory scale thermals and microbursts include visualizations by Scorer (1957) and Fujita (1986). The only known quantitative experimental data are from Lundgren, Yao, and Mansour (1992), and Yao (1993) where a heavy cylindrical volume of salt water was dropped into a tank of fresh water. The data include propagation velocities of the microburst front and hot film measurements showing very large velocity magnitudes and gradients near the bottom surface corresponding to the downburst passage. Existing quantitative experimental data on downbursts is thus limited, and the current experiments attempt to obtain high-resolution two-dimensional velocity fields in the dynamically evolving flow. In particular, velocity vectors near the ground are desired since, in this region, radar data are noisy and numerical studies rely on boundary layer models.

In the current experiments, the transient slug flow and scaling law of Lundgren *et al.* (1992) is used. The important independent parameters in this flow are the density difference between the downburst and surrounding fluids $\Delta\rho$, the initial height of the downburst above the plate H_0, and the volume of the downburst parcel V. The scaling law absorbs these parameters into length and time scales. The density difference between the two fluids is assumed to be small enough that the Boussinesq approximation holds. A characteristic length R_0 is chosen as the equivalent spherical radius of the volume of heavy fluid, and a characteristic time is chosen as

$$T_0 = \sqrt{\frac{R_0 \rho}{g \Delta \rho}}.$$

The appropriate Reynolds number to characterize the large-scale motion is then

$$Re = \frac{R_0 v_0}{\nu}.$$

where $v_0 = R_0/T_0$. Lundgren *et al.* (1992) found that the lower limit of the burst propagation velocity for Reynolds number invariance was 3000. Therefore, our experiments are designed to exceed this value.

2. FACILITY AND PROCEDURE

The flow facility is depicted in Figure 1. The flow is contained in a large glass tank which provides optical access from the sides and bottom. In order to minimize wall effects, the downburst fluid impinges on a raised circular plate that allows heavier fluid to spill over its edges. The downburst release mechanism consists of an aluminum cylinder and a solenoid which drives a piercing needle. The cylinder has an inside diameter of 63.5 mm and an outside height of 87.0 mm yielding an equivalent spherical radius of 38.8 mm. A thin latex sheet is stretched over the open bottom of the cylinder which is then filled with the heavier downburst fluid. The top of the cylinder contains 50% open area to allow entrainment of ambient fluid as the downburst fluid descends. At the time of release, the piercing needle travels approximately 1 cm and bursts the latex sheet. The needle speed is minimized to reduce disturbances caused by the bursting latex.

In order to achieve Reynolds numbers greater than 3000 with this facility, density differences between the downburst and surrounding fluids of at least 3% are required. The refractive index in the two fluids must be matched very precisely to yield clear photographic images of the seeded flow field. In these experiments, 6% solutions of glycerol in water and potassium phosphate (KH_2PO_4) in water were chosen as the tank and downburst fluids respectively yielding $\Delta\rho$ of 3%. This combination yields excellent PIV results.

The flow field is illuminated by a two-pulse sequence from a pair of frequency-doubled Surelite I Nd:YAG lasers. The lasers are triggered externally during the experiment to achieve variable pulse separation. The beam profiles are converted into thin sheets with spherical and cylindrical lenses of 1 m and 19.0 mm focal length respectively. Figure 2 shows the optical set up. Since reversing flow occurs during the downburst evolution, spatial image shifting between laser pulses is required to resolve directional ambiguity in the PIV photographs. We use a method similar to Adrian (1986) where a rotating mirror is placed between the photographing lens and the laser sheet. The mirror is mounted so that its axis of rotation is vertical, yielding a horizontal shift. In the current experiments, the time between laser pulses is 2 ms, and the shift velocity is 0.56 m/s in real space. A custom circuit couples the timing of the laser pulsing, the rotating mirror, the solenoid, and the camera shutter.

The flow is seeded with TiO_2 particles with a specific gravity of 3.5 and a nominal diameter of 3 μm. A standard 35 mm camera (Nikon N8008s with AF Micro-Nikkor lens) photographs light scattered by the seed particles at a magnification of 0.16. Photographic negatives are interrogated with a high-resolution scanner (Nikon Coolscan) and software from FFD, Inc. The negatives are scanned at 2000 dpi, and 64 x 64 pixel arrays are used for each interrogation zone. The spatial resolution of each vector computed is 5 mm in real space, and the vectors are plotted with a 50% overlap. All vectors shown in the plots result from a computed autocorrelation. Hence, none were interpolated from surrounding interrogation zones.

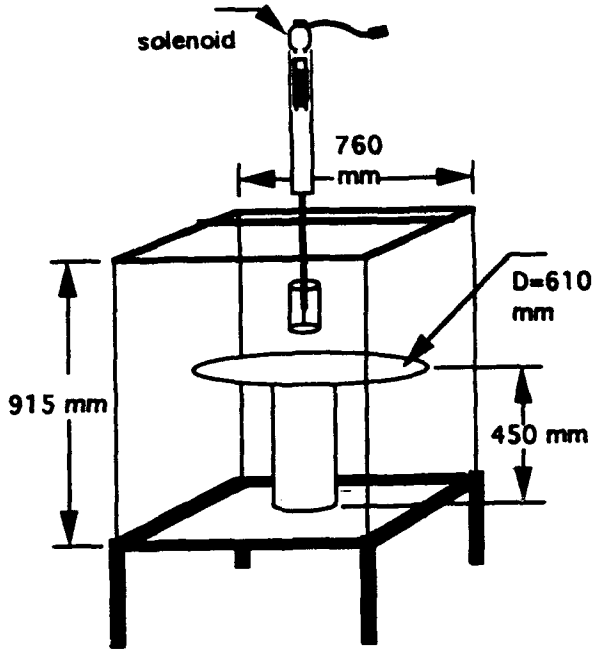

Fig. 1. Microburst Facility

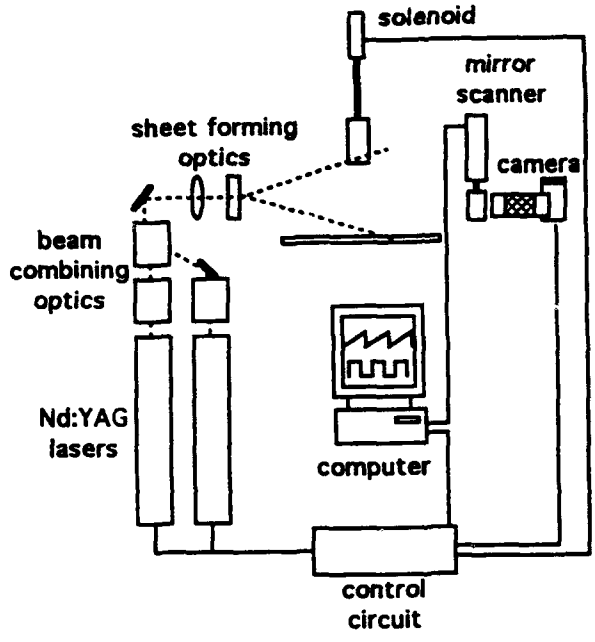

Fig. 2. Schematic of optical set up.

3 RESULTS

Sequences of instantaneous velocity vector and vorticity plots are shown in Figures 3 and 4. The drop height measured from the bottom of the cylinder is H_0/R_0 = 3.81, and the Reynolds number is 3600. The time scale T_0 is 0.36 s, and the velocity scale v_0 is 0.11 m/s. In each plot, the bottom row of vectors corresponds to interrogation regions with lower bounds approximately 0.5 mm above the bottom surface. (Reflections prevent the interrogation regions from extending all the way to the wall). Local vorticity was computed by integrating the line integral of velocity using the 8 points surrounding each position.

The velocity plots show that the flow is reasonably but not completely axisymmetric. The primary vortex at the head of the downburst has rolled up by T/T_0 = 2.75. Beginning at this time a second trailing vortex is also apparent. Thus, unlike in previous numerical studies, the vortex sheet that develops between the downburst and ambient fluid is not smooth and continuous but unstable to large-scale perturbations. As the flow descends, the radius of the primary vortex grows from $0.8R_0$ to over $1R_0$. The vorticity levels in the two structures remain fairly constant (Figures 3c and 4c) until the presence of the plate is felt. Then, the vorticity in the leading vortex intensifies as it expands radially and as trailing fluid continues to sweep past it. Ahead of and beneath the primary vortex, vorticity of opposite sign is observed, although any coherent secondary vortices are small. The primary vortex maintains its height as it expands. Meanwhile, the trailing vortex persists until the last frame, but does not intensify. It is typically much weaker than the leading vortex because the fluid upstream and inside of it carries much less momentum.

The vector plots in Figure 3 indicate strong downward velocities across the core of the microburst. Although the directions vary due to smaller perturbations, the magnitudes are fairly uniform. The large velocities lead the primary vortex slightly before it encounters the bottom surface (Figure 3c) and persist after the vortex impingement (Figure 3d). The downward velocity vectors decrease in magnitude as the leading vortex expands. Meanwhile, the horizontal velocities beneath and behind the primary vortex become large. Note also the significant upward velocities ahead of the primary vortex which lift fluid (and secondary structures) away from the wall (Figures 3e, 3f, 4f). These vectors and the resulting vorticity distributions are very similar to the numerical results of Lundgren *et al.* (1992) where wall "friction" was included.

Local velocity magnitudes may be observed more readily in Figure 5 where ensemble averages of velocity vectors for eight separate events are shown. The first four plots depict every third row of velocity vectors computed, while the last two show every third column. (Note that Figures 5d and 5e represent the same time: T/T_0 = 4.96). Since vortex size and speed vary somewhat from burst to burst, the results shown are obviously smoothed. Nevertheless, although irregular smaller scale variations and eddies are suppressed in these plots, the primary structure and general behavior persist. The first four plots emphasize the large downward vectors present until T/T_0 = 4.96, while the last two show the large radial vectors underneath and behind the leading primary vortex ring.

The profiles in the first four plots appear similar to the numerically computed vectors in the inviscid code of Lundgren *et al.* (1992). This result suggests that even though viscous shear is present in the experiment, it's effect is small compared with baroclinic vorticity generation due to density gradients. Two small differences between the current and numerical results are evident, however. First, note that in Figure 5d, the downward velocity magnitude decreases steadily with increasing radius. The numerical result shows uniform velocity magnitudes across this region with slight increases near the vortex core. Figure 6 shows contours of vertical velocity for a single downburst at T/T_0 = 4.96. Here also, the velocity decreases from a maximum at r = 0. The second difference is emphasized in this figure. Note that the maximum downward velocities lie upstream of the primary vortex core near $y = R_0$. At a similar stage in the numerical study, the maximum velocities occur at an axial position closer to the height of the vortex core. These differences could result from either the absence of viscous effects in the numerical study or different initial slug geometries. The contours in Figure 6 exhibit further that strong downflows persist after the downburst impact.

Data from the ensemble-averaged vectors nearest the wall are plotted in Figure 7. These vectors correspond to heights of 3 mm above the wall. Here we see that after the vortex touches down, there is a very sharp rise in velocity between the vortex core and the wall. The velocity maxima occur at radial locations near the vortex centers, but the exact relationships are difficultto pinpoint due to scatter in the data. Typically (also for single burst profiles) the velocity remains high over a range of $1.5R_0$ before decreasing sharply behind the vortex. These plots are similar to those in Figure 13 of Lundgren *et al.* (1992) although the peaks are not as high due to the averaging process. Instantaneous values near the wall rise typically as high as $2.4v_0$ matching well with the numerical values. Note that the numerical results are for surface velocities which should correspond to maxima in the computed field. The experimental values however are averaged over the region y = 0.5 to 5.5 mm. Thus, they do not necessarily represent the maximum values found in the boundary layer. The ensemble averages show that high velocities persist up to the third or fourth row of vectors (Figures 5e, 5f) indicating that the vertical gradient above the bottom row is not particularly sharp.

Figure 7 reveals an important difference between the PIV and numerical data. In the numerical model, the surface velocity under the primary vortex continues to increase until $4T_0$ after touchdown of the downburst. At this time, the vortex core is near $3.5R_0$. In the PIV study, however, the velocity maximum under the primary vortex occurs slightly after touchdown (T/T_0 = 4.96) when the vortex core is at $1.3R_0$. As the vortex expands further, the velocity under the vortex decreases. Hence, as the microburst diverges, the surface velocities calculated in the "friction" model in the numerical flow are not good indicators for near-wall velocities in the experimental flow. In the future, PIV data will be obtained for larger R_0, so that the comparison along the wall can be extended.

4. DISCUSSION AND SUMMARY

In simple dynamical models, downdrafts and horizontal velocity gradients are seen as the largest contributors to decreases in aircraft "energy" or performance (Bowles (1990)). The PIV results indicate that large

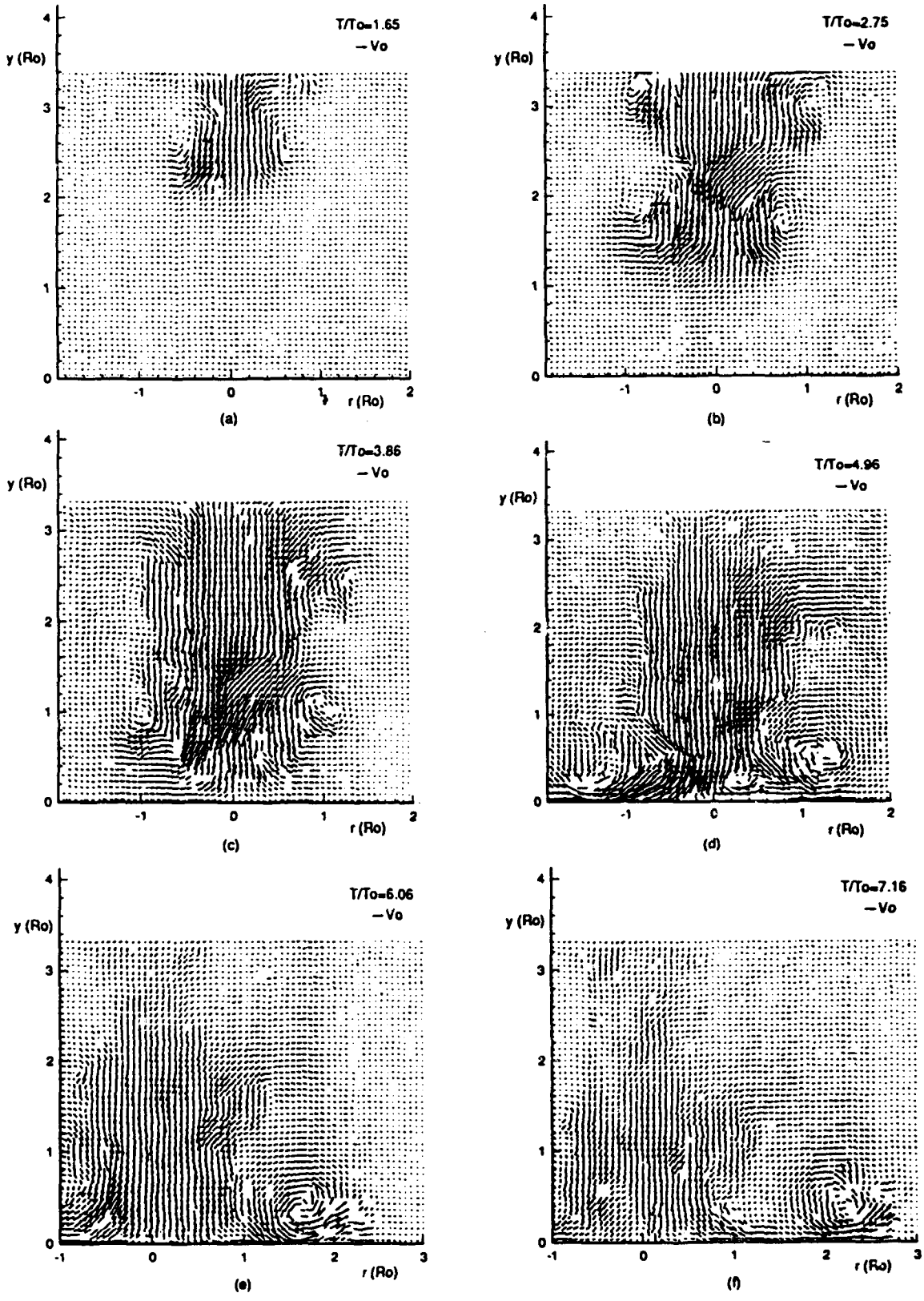

Fig. 3. Instantaneous velocity fields of simulated microburst. Ho/Ro=3.81, Re=3600.

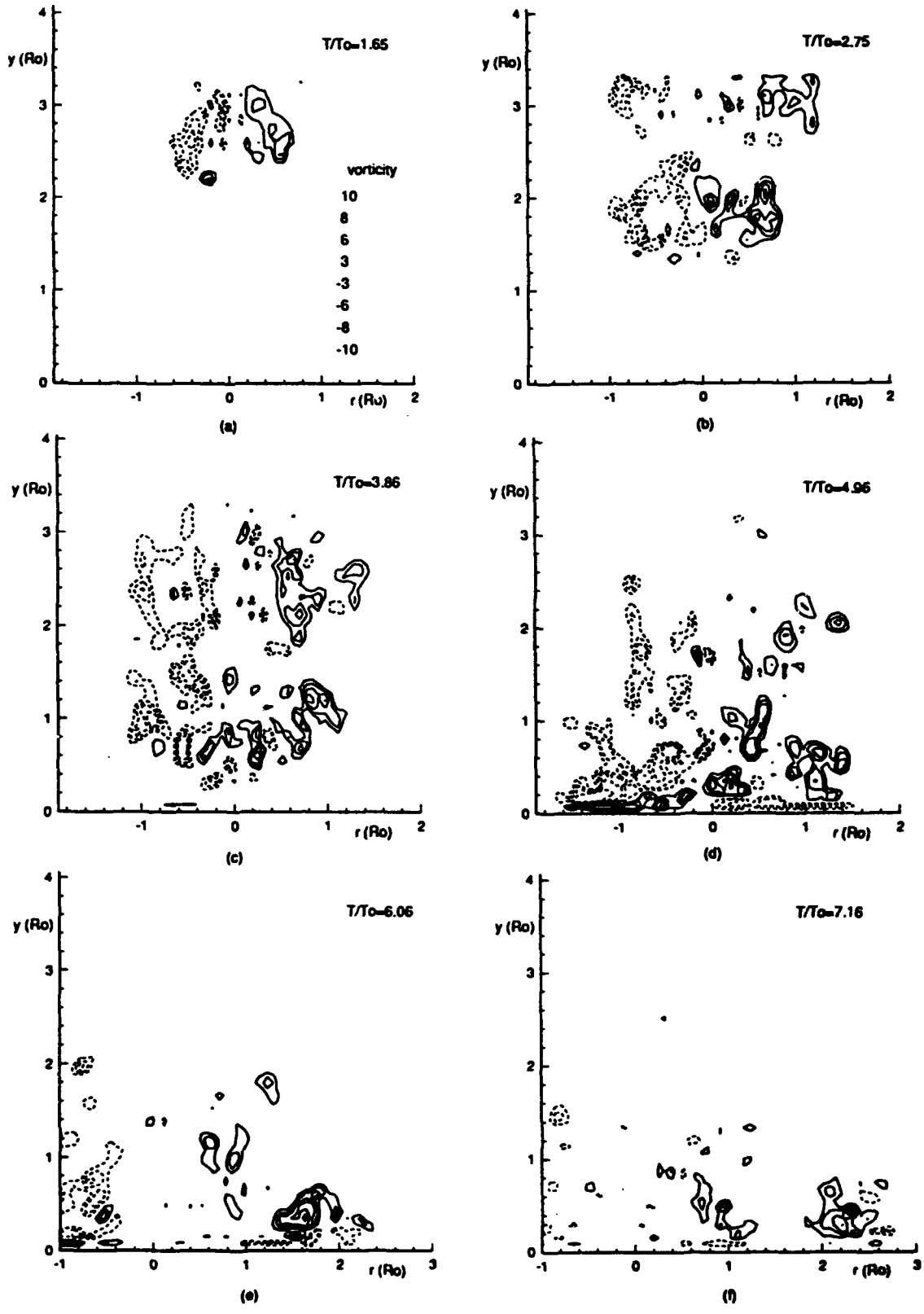

Fig. 4. Vorticity contours of simulated microburst. Dashed contours represent negative values. All levels are same as panel (a).

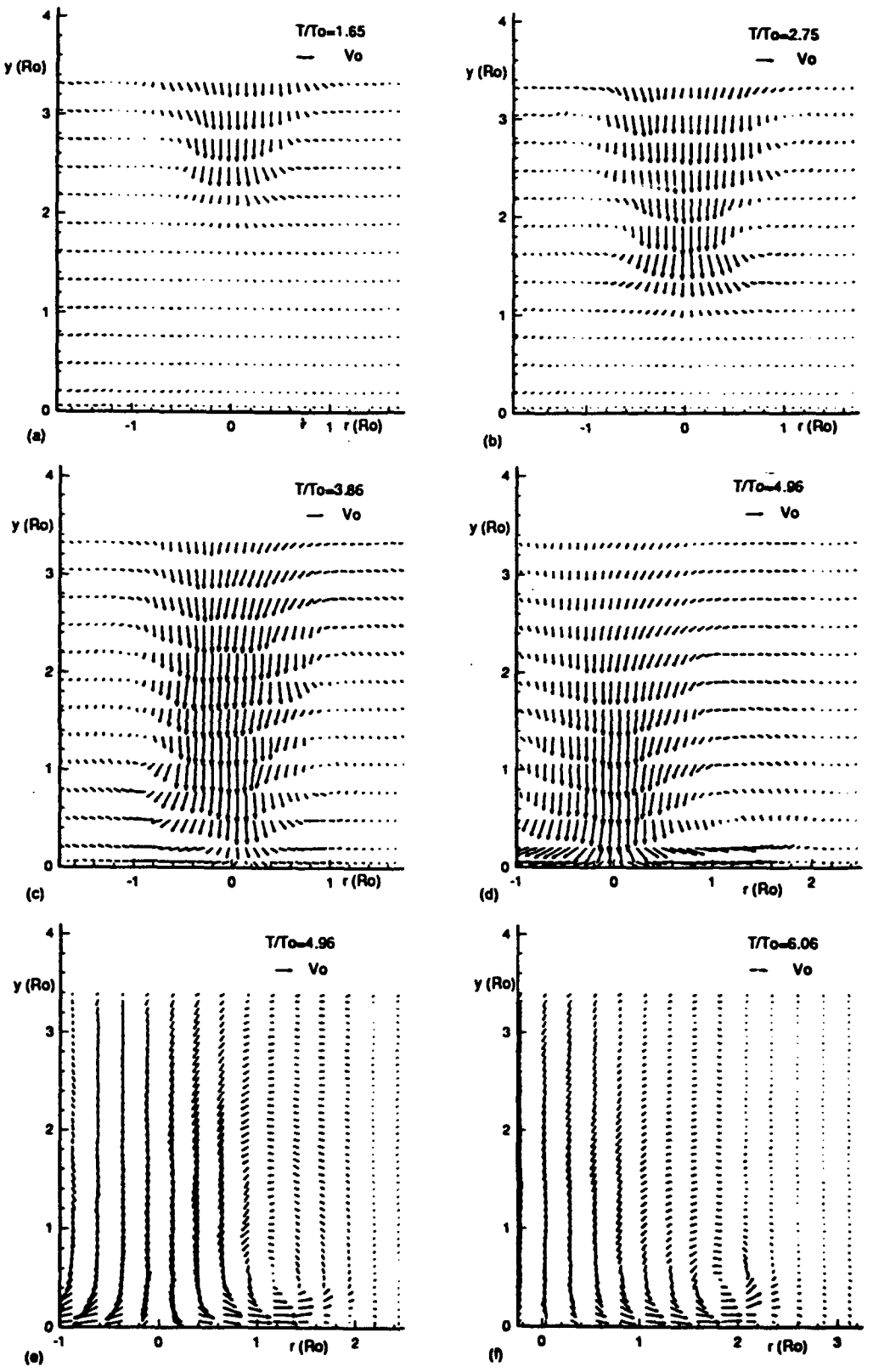

Fig. 5. Ensemble-averaged vector plots of 8 runs. Ho/Ro=3.81, Re=3600.

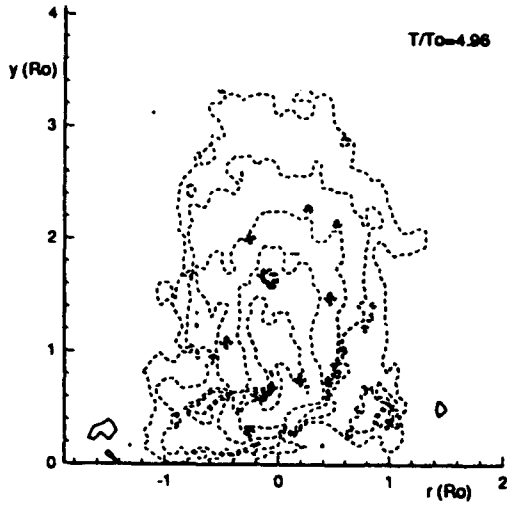

Fig. 6. Contours of vertical velocity for a single microburst at $T/T_0 = 4.96$. Negative contours (dotted) begin at $-0.28v_0$ with succeeding levels representing increases of $-0.45v_0$. Positive contours (solid) begin at $0.61v_0$ with succeeding levels representing increases of $+0.45v_0$.

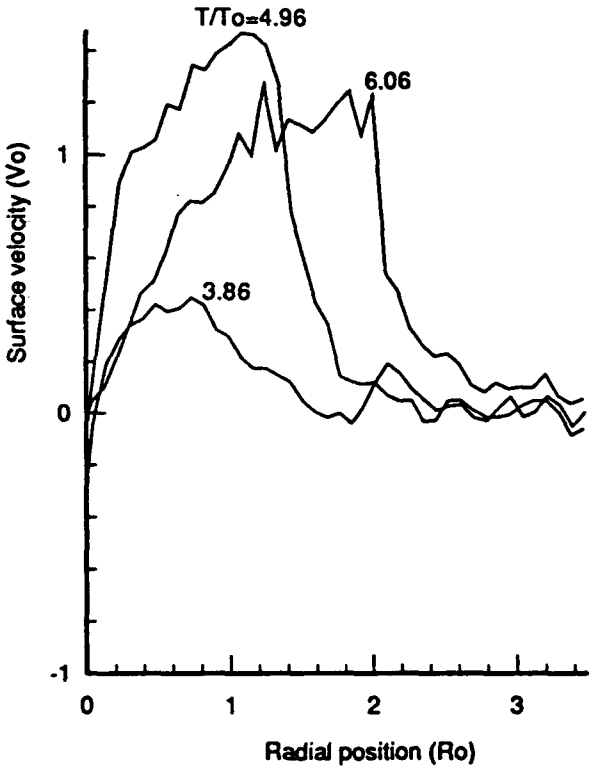

Fig. 7. Ensemble-averaged radial velocities at $y = 0.77R_0$

downdrafts exist across the core of the microburst. Focusing on the region near the ground, strong downdrafts begin before impact of the primary vortex and persist for $1\text{-}2T_0$ before dissipating. After the downburst impact, large horizontal velocity gradients exist. Sharp increases in velocity occur near the radial location of the primary vortex core. Large velocities persist for a radial distance of $1.5R_0$ behind the vortex core. Then, the velocity decreases sharply. The current data suggest that aircraft flying at low altitudes are subject to the greatest danger slightly after microburst touchdown when both contributions can be quite large (i.e. at $T/T_0 = 4.96$). After this time, sharp horizontal velocity gradients and associated windshear persist to at least $7T_0$, the largest time examined with PIV.

The experimental results can be scaled to atmospheric values using existing data from the crash of flight DL 191 at Dallas-Fort Worth airport in 1985. For this downburst, Lundgren *et al.* (1992) found $R_0 = 0.7$ km and $T_0 = 23$ s. Thus, if the PIV results are extrapolated, the maximum downward and horizontal velocities seen just after touchdown are both on the order of 70 m/s. These extremely large velocities would have very severe effects on an aircraft approaching for landing since a normal aircraft approach velocity is also about 70 m/s. The PIV results imply that these large wind speeds should decrease as the microburst diverges. Thus, it is not surprising that the maximum wind speed measured at DFW by ground-based Doppler radar (at $7R_0$) was only 35 m/s.

The PIV measurements in the buoyancy-driven flow show reasonable agreement with previous numerical studies, although some key differences are apparent. Thus far, the method allows the determination of two-dimensional velocity fields in a flow that remains fairly axisymmetric through its evolution. The ensemble-averaged measurements show that the largest flow scales present are repeatable, while examination of results from individual bursts shows that smaller scale structures are also repeatable although their strength and location can vary from case to case. The current setup yields a spatial resolution of 5 mm which corresponds to an atmospheric scale of 90 m. We would like to achieve a finer resolution in future studies to gain a clearer understanding of typical velocity gradients near the wall as well as the size and strength of secondary vortices occurring there. The development and importance of azimuthal instabilities will also be examined in future experiments.

ACKNOWLEDGMENTS

This work was funded by a Research Initiation Award from the National Science Foundation (CTS-9209948). The authors thank Terry Johnson for his assistance in constructing the facility and in software development.

REFERENCES

Adrian, R. J. 1986, Image Shifting Technique to Resolve Directional Ambiguity in Double-Pulsed Velocimetry, J. Applied Optics, vol. 25, pp. 3855-3858.

Bowles, R.L. 1990, Windshear Detection and Avoidance: Airborne Systems Survey, Proc. 29th Conf. on Decision and Control, Honolulu, pp. 708-736.

Droegemeier, K. K. 1988, Simulation of Microburst Vorticity Dynamics, 15th Conference on Severe Local

Storms, American Meteorological Society, Baltimore, Maryland.

Fujita, T. T. 1985, The Downburst, The University of Chicago Press.

Fujita, T. T. 1986, DFW Downburst, The University of Chicago Press.

Lundgren, T. S., Yao, J., Mansour, N. N. 1992, Microburst modeling and scaling, J. Fluid Mech., vol. 239, pp. 461-488.

Proctor, F. H. 1988, Numerical simulations of an isolated Microburst. Part I. J. Atmos. Sci., vol. 45, pp. 3137-3160.

Proctor, F. H. 1989, Numerical simulations of an isolated Microburst. Part II. J. Atmos. Sci., vol. 46, pp. 2143-2165.

Scorer, R.S. 1957, "Experiments on Convection of Isolated Masses of Buoyant Fluid," J. Fluid Mech., vol. 2, pp. 583-594.

Yao, J. 1993, Experiments on Microbursts. Ph.D. Thesis, Dept. of Aerospace Engineering & Mechanics, University of Minnesota, November.

A STUDY OF AN INCLINED CYLINDER WAKE USING DIGITAL PARTICLE IMAGE VELOCIMETRY

L.J.W. Graham[1] & J. Soria[2]

[1]Commonwealth Scientific and Industrial Research Organisation - DBCE, Highett, Vic. 3190, Australia.

[2]Mechanical Engineering Department, Monash University, Clayton, Vic. 3168, Australia.

ABSTRACT

This paper presents results of a preliminary investigation of the wake of an inclined cylinder at a Reynolds number of 391. The structure of the flow in the plane containing the cylinder axis and parallel to the free stream was investigated using flow visualisation and cross-correlation digital particle image velocimetry (DPIV). A cell structure was observed in the flow and the length scale of this structure was extracted from the DPIV data. Instantaneous and fluctuating velocity and vorticity fields were also calculated and show that a vortex pair travels downstream in this plane of visualisation.

1. INTRODUCTION

Wake flows are of considerable interest in engineering, for example in the design of off shore structures and also in designing buildings to withstand wind loadings. The wake of a circular cylinder is of particular interest as it is geometrically simple and also occurs frequently in engineering structures.

The wake of a cylinder normal to the flow has been studied by several authors over many years. Wu *et al.* (1994), Williamson (1988) and others noted the existence of streamwise vortices in addition to the usual von Karman vortex street. By contrast the wake of cylinders inclined to the flow has not been investigated to anywhere near the same extent. Most of the work in this area has been motivated by the application to missiles at angles of attack.

Hanson (1966) investigated the vortex shedding frequencies of cylinders inclined at yaw angles from 0° to 72°. He noted that the Reynolds number (based on the free stream velocity and the diameter of the cylinder) at which shedding started increased with increasing yaw angle. Van Atta (1968) repeated the work of Hanson (1966) to clarify the anomalous behaviour noted. Smith *et al.* (1972) performed experiments to investigate the influence of yaw angle on pressure drag and the near wake characteristics of a circular cylinder. They found that the transition in the wake from laminar to turbulent flow was promoted as the yaw angle increased and that the basing of the behaviour of the wake properties on the normal component of velocity only was incorrect. Knauss *et al.* (1976) came to a similar conclusion in their experiments on circular cylinders.

Ramberg (1983) investigated wake flows for cylinders at yaw angles of 0° to 60° and Reynolds numbers of 150 – 1100. His results were very sensitive to the end conditions used including free ends and end plates. Wardlaw and Yanta (1984) used a laser-Doppler velocimeter to measure the wake flow of a tangent ogive model. The Reynolds number was 1.5×10^5. Surface pressure measurements were also made. Their results showed the existence of two small secondary vortices, one on each side of the model, as well as the primary vortices. Poll (1985) investigated transition in the boundary layer on the windward side of a yawed cylinder and showed that yaw destabilises the laminar flow on the windward surface of the cylinder.

Shirakashi *et al.* (1986) investigated vortex shedding from cylinders inclined at angles of 0°, 30° and 45° and Reynolds numbers from 800 – 55000. They used flow visualisation and a hot-wire to investigate the flow. Their flow visualisation results showed that the flow around a yawed cylinder is highly three-dimensional and that any applicability of the cosine law for vortex shedding was incidental. They also concluded that the secondary flow in the wake behind the cylinder damaged the regularity of the vortex shedding and reduced its frequency.

Van Tuyl (1988) used a vortex filament approach to model the flow past a missile at angles of attack of 10° and 19°. The results showed good agreement with the experimental data. Bull and Dekkers (1989)

examined vortex shedding from cylinders with very large aspect ratios at small yaw angles ($0-10°$). They found that vortices were shed at much smaller angles than previously thought. The same authors (Bull and Dekkers, 1992) showed that as the yaw angle of a long cylinder was decreased from 45° to 8°, rolling up of the separated shear layer was delayed and at 3.5° was in excess of 100 cylinder radii. Suzuki (1991) studied the computed flow field of a high angle of attack cone-cylinder. Topological techniques were used to characterise the flow.

Degani (1992) examined the flow over an ogive cylinder at angles of attack of 40° and 60°. He found that there were at least two main frequencies in the flow; a low frequency associated with the primary vortices and a high frequency associated with fluctuations in the shear layer near the body surface. De Ponte (1992) investigated the flow around a yawed cylinder and showed that the wake vortex structure was different from vortex to vortex. They also noted that the roll-up of the vortex sheets is first dominated by a Kelvin-Helmholtz instability.

Cross-correlation digital particle image velocimetry (DPIV) is a recent development in velocity vector field measurement techniques. The cross-correlation DPIV analysis of single-exposed multiple images allows unambiguous determination of the velocity direction and a better dynamic range than the classical auto-correlation or auto-spectrum DPIV technique (Soria 1994). Auto-correlation or auto-spectrum DPIV is restricted by the particle size at the low end of the dynamic range and typically requires image shifting, during multi-exposure of the image, to determine the flow direction unambiguously.

The present work uses a time resolved cross-correlation DPIV to investigate the spatio-temporal evolution of the near wake of an inclined cylinder. Measurements of mean and fluctuating velocity vector fields and out-of-plane vorticity fields, as well as statistical information and Reynolds stresses, are presented to illustrate the current possibility of this measurement system using presently available image acquisition and computer hardware.

2. EXPERIMENTAL CONDITIONS

2.1 Water Tunnel Set-up

The investigation was conducted in a low-speed closed-circuit water tunnel with a 244 mm × 244 mm × 2000 mm test section as shown in Figure 1. The speed of the water flow is continuously variable up to a maximum of 500 mm/s. The free-stream turbulence level is typically 0.09% with most of the spectral content below 2 Hz.

The smooth, black painted, acrylic cylinder of 12.7 mm diameter was supported at 45° to the oncoming flow from the top of the working section for the visualisations containing the cylinder axis, and horisontally across the working section for the visualisations of the plane at 45° to the cylinder axis. The water tunnel was open at the top. The length-to-diameter ratio of the cylinder was 27. The Reynolds numbers investigated were 391, 889 and 1697 based on the diameter of the cylinder. The quantitative measurements presented here are for a Reynolds number of 391 only. The measurements were performed in the core flow of the water tunnel test section to avoid boundary layer effects near the tunnel walls.

2.2 Image Acquisition

The flow visualisations and image acquisition were undertaken with an argon-ion laser sheet illumination and a Pulnix TM-865 CCD camera and recorded on a Sony Hi-8 video recorder. The CCD exposures per video field were achieved by shuttering the laser beam with a computer-controlled nm Model LS500A mechanical shutter. This shutter has a frequency response up to 500 Hz. A synchronisation signal from the Pulnix camera was detected by a PC and was used to activate the mechanical shutter. This allows single or multiple exposure of the CCD array per video field. The seeding particles used for visualisation of the flow were Q-CEL 570 hollow micro-spheres with an effective specific gravity of 0.7 and with a mean particle size less than 30 μm. Three grams of particles per cubic metre of water were added to the water tunnel.

Frames from the Hi-8 video tape were digitised using Mediasuite Pro running on a Macintosh Quadra 950. The grey images were sent to and analysed on a Silicon Graphics workstation. Figure 2 shows a sketch giving coordinate details and frame positions for the present work.

2.3 Cross-correlation Analysis of Single Exposed Particle Images

The PIV analysis technique applied in this investigation relies on having available two single-exposed sequential images of the seed particles in the flow. If this type of experimental information is available, then it is possible to use a technique of frame-to-frame cross-correlation to obtain the instantaneous local displacement. Cho and Park (1990) have formulated the equations of the image processing associated with the cross-correlation PIV analysis in terms of continuous variables. The PIV analysis used in the present investigation is the discrete formulation of the cross-

correlation analysis and is analogous to the formulation used by Willert and Gharib (1991) in their study of a vortex ring.

Two digital images of seed particles in the flow are acquired with a time separation Δt. These images are represented by rectangular discrete pixel intensity distributions:

$$I_1(i,j) \quad and \quad I_2(i,j) \tag{1}$$

where $0 \leq i \leq M-1$ and $0 \leq j \leq N-1$ and $M \times N$ is the size of the digital pictures. In order to determine the local displacement in a small region of the flow, the two discrete images I_1 and I_2 are sampled using a small interrogation window similar to the more traditional auto-correlation technique (Soria 1993). Although in the present study the sampling location in both images is coincident, this is not necessary. The sub-images of the digitised images I_1 and I_2 are denoted by I_{s1} and I_{s2}, respectively. For an interrogation window of size $m \times n$, the discrete spatial cross-correlation function between both sub-images is defined as:

$$R_{12}(x,y) = \sum_{i=0}^{n-1} \sum_{j=0}^{m-1} I_{s1}(i,j) I_{s2}(i-x, j-y) \tag{2}$$

where $0 \leq x \leq m$ and $0 \leq y \leq n$ (Bracewell 1986). The discrete spatial cross-correlation function contains the information of the average displacement of the particles in the sampled sub-image. The location of the maximum value of the spatial cross-correlation function corresponds to the average displacement of the seed particles in the sampled sub-image. The local average velocity is readily determined by dividing this displacement by the time separation Δt between the capture of both images and dividing by the appropriate magnification [pixels/(unit length)]. In the present analysis algorithm the normalised spatial cross-correlation function defined as:

$$\rho(x,y) = \frac{\sum_{i=0}^{n-1} \sum_{j=0}^{m-1} I_{s1}(i,j) I_{s2}(i-x, j-y)}{\sqrt{R_{11}(0,0)} \sqrt{R_{22}(0,0)}} \tag{3}$$

is used. The value of $\rho(x,y)$ ranges between 0 and 1. A value of $\rho(x,y)$ close to 1 is observed when many particles in sub-image I_{s1} match up with their corresponding spatially shifted partners in sub-image I_{s2}. Smaller cross-correlation peaks are also observed when individual particle images match up with other particle images. The highest correlation peak is considered to represent the best match of particles between both sub-images.

The direct calculation of eq. (3) is computationally expensive. Therefore, in the present analysis algorithm, eq. (2) is calculated by using the two-dimensional discrete Fourier transform (2-d DFT) and the convolution theorem (Bracewell 1986). The calculation of the 2-d DFT is performed via the fast Fourier transform (FFT). The normalised spatial cross-correlation follows easily from eq. (3). Nyquist sampling theorem associated with discrete sampled data limits the maximum measurable spatial displacement in any sampling direction to half the interrogation window in that direction. In practice, a realistic maximum displacement is between 0.2 and 0.3 of the length of the interrogation window (Keane and Adrian 1990).

The peak in the normalised cross-correlation function is initially found by a search. A two-dimensional Gaussian function is then least squares fitted around this peak region. The location of the extremum of the functional fit allows the resolution of the spatial cross-correlation peak to sub-pixel accuracy. This algorithm is capable of resolving displacements of 0.1 ± 0.06 (95% confidence level) pixels.

The accuracy of the cross-correlation analysis algorithm was established by using computer-generated *ideal* images with Gaussian intensity distributions of typical size 1.5 ± 1 pixel. The tests were conducted with a 64^2 interrogation window, as the experiments were designed to be analysed with this size interrogation window. The digital test images were shifted relative to each other and analysed. Overlap analysis was used, hence the 1444 samples of the measured displacement are strictly speaking not independent. However, the resolution capabilities and uncertainty levels still provide a good indication of the measurement capabilities of this system. The typical signal-to-noise ratio of the cross-correlation analysis algorithm is 70 dB.

The quality of the acquired images and the ability of the cross-correlation analysis to determine real displacements accurately can also be established by applying the same procedure to experimentally acquired images. In this case the digital representation of a single-exposed image is shifted relative to itself by a known amount (typically 1–16 pixels). The entire image is then analysed using a 64^2 interrogation window with overlap processing resulting in 2479 samples. Figure 3 includes the results of the accuracy and uncertainty analysis for both horizontal and vertical displacements. Figure 4 shows a histogram for the horizontal and vertical displacements when *ideal* and *real* images were shifted by 8 pixels in both directions.

The automatic cross-correlation analyses of the experimental data yielded typically 90% *good* vectors. A window size of 64^2 with an overlap of 0.8 was used in all analyses. Vectors were automatically rejected during the cross-correlation analysis if their displacement

exceeded 0.25 of the interrogation window size or if the normalised cross-correlation peak did not exceed 0.8. Erroneous vectors were automatically removed in the post-processing. The reasons for erroneous vectors were identified to be due to: (i) lack of particle pairs in the interrogation window; and (ii) the presence of high velocity gradients within the interrogation window. After rejection, vectors were replaced by a new velocity vector which was computed by a least squares interpolation using the neighbouring vectors.

3. RESULTS AND DISCUSSION

The flow visualisations show that in the near wake region the mean flow direction is nearly parallel to the cylinder axis. This indicates that there is a pressure gradient along the cylinder from the leading region of the cylinder to the trailing region.

In the plane containing the cylinder axis and parallel to the free stream, the flow further downstream had an unsteady cell-like structure with alternate bands of fast and slow flow. This was especially noticeable at the lowest Reynolds number. The shear layers separating the fast and slow mean velocity cells became unstable as the downstream distance increased and as the Reynolds number increased. This instability manifested itself by the rolling up of the shear layer.

The quantitative data presented here is only for the case of the Reynolds number equal to 391. Figure 5 shows the mean velocity vector field near the cylinder obtained by averaging 99 instantaneous velocity vector fields. This plot shows clearly the flow induced parallel to the cylinder. At the lower edge of the figure it can be seen that there are two positions along the y direction where the velocity is at a maximum. These peaks are about 30 mm apart. Velocity profiles corresponding to three positions in Figure 5 and three positions in the frame further downstream are shown in Figure 6. The development of the cell structure referred to earlier can be easily seen. The autocorrelation function of the velocity profiles was calculated directly to extract some information regarding the length scale of the cell structure. These curves are shown in Figure 7. The autocorrelation for the profile nearest to the cylinder was not calculated due to the insufficient length of the profile. The length scales are found to decrease from approximately 2.5×diameter (approximately 30 mm) to about 2.1×diameter (approximately 26 mm) further downstream.

Figure 8(a) shows contours of the velocity in the x direction averaged over 199 velocity vector fields taken at the downstream frame position. The mean vorticity was calculated using least squares interpolation and is shown in Figure 8(b). The rms of the fluctuating velocity in the x direction is shown in Figure 9(a) and shows that the maximum values of the fluctuating component occur in the regions between the high velocity cells as would be expected as these are the regions with the highest shear. The jagged appearance of the contours is due to the limited resolution. The Reynolds shear stress contours are shown in Figure 9(b).

An instantaneous velocity vector field at the downstream station is shown in Figure 10(a) and the corresponding velocity vector field with the overall mean velocity removed from the x component of velocity in Figure 10(b). The flow pattern relative to an observer moving with the mean velocity shows the vortical structures in the flow which are not observable from the instantaneous velocity vector field in Figure 10(a). The existence of the vortical structures are corroborated in the corresponding out-of-plane vorticity field shown in Figure 11(a).

The instantaneous fluctuating velocity vector field was also obtained by calculating the mean velocity vector field using 199 instantaneous velocity vector fields and subtracting this mean field from the instantaneous field. The fluctuating velocity vector field at the same instant as Figure 10(a) is shown in Figure 10(c). The instantaneous fluctuating out-of-plane vorticity is shown in Figure 11(b). Comparing the instantaneous vorticity field in Figure 11(a) with the fluctuating vorticity field in Figure 11(b) shows that both contain a clearly observable vortex pair, which from the time evolution for the vorticity field is observed to travel in the x direction, but at an angle to it. The similarity between the instantaneous and fluctuating out-of-plane vorticity fields also indicates the highly unsteady nature of this flow and that the concentrated vorticity regions are highly unsteady.

4. CONCLUSIONS

The near wake of an inclined cylinder was investigated using cross-correlation digital particle image velocimetry. One hundred and ninety-nine frames were analysed to yield statistical information about the flow, including mean and fluctuating velocities and vorticity.

An interesting feature of this flow is the cell structure which was identified qualitatively from the flow visualisations and subsequently quantitatively from DPIV results. This feature has not been observed in the case of cylinders normal to the flow but has been observed previously for the inclined case. The length scale of the cells was extracted from the mean velocity profiles by taking the spatial auto-correlation

normal to the mean flow direction. This length scale was found to decrease with downstream distance. The structure of the wake in the visualised plane was emphasised by subtracting the local mean from each instantaneous velocity vector. The time record of the out-of-plane fluctuating vorticity distribution showed the periodic evolution of a vortex pair which moved downstream. The distance between the two vortex centres of the vortex pair was found to be approximately 1.3 cylinder diameters.

REFERENCES

Bracewell, R. N. 1986, The Fourier Transform and its Applications, p5 .McGraw-Hill.

Bull, M. K. & Dekkers, W. A. 1989, Vortex Shedding from Cylinders in Near Axial Flow, Proc. 10th Australasian Fluid Mechanics Conference, University of Melbourne, (ed. A. E. Perry), pp. 6.41–6.44.

Bull, M. K. & Dekkers, W. A. 1992, Application of Flow Visualisation to the Study of Very Long Cylinders in Near Axial Flow, Proc. 6th Int. Symp. on Flow Visualisation, Yokohama, Japan,.pp. 338–342

Cho, Y.-C. & Park, H. 1990, Instantaneous Velocity Field Measurement of Objects in Coaxial Rotation Using Digital Image Velocimetry, Proc. SPIE Vol. 1346 Ultrahigh- and High-Speed Photography, Videography, Photonics, and Velocimetry '90, San Diego, CA, USA.

Degani, D. 1992, Numerical Simulation of Vortex Unsteadiness on a Slender Body at High Incidence, AIAA Journal, vol. 30, pp. 841–843.

De Ponte, S. 1992, Further Studies on the Asymmetrical Flow Past Yawed Cylinders, ICAS Proc. V. 18 (2), pp. 1201–1207.

Hanson, A. R. 1966, Vortex Shedding from Yawed Cylinders, AIAA Journal, vol. 4, pp. 738-740.

Keane, R. D. & Adrian, R. J. 1990, Optimization of Particle Image Velocimetry. Part I: Double Pulsed Systems, Meas. Sci. Technol., vol. 1, pp. 1202–1215.

Knauss, D. T., John, J. E. A. & Marks, C. H. 1976, The Vortex Frequencies of Bluff Cylinders at Low Reynolds Numbers, J. Hydronautics, vol. 10, pp 121–126.

Poll, D. I. A. 1985, Some Observations of the Transition Process on the Windward Face of a Long Yawed Cylinder, J. Fluid Mech., vol. 150, pp. 329–356.

Ramberg, S. E. 1983, The Effects of Yaw and Finite Length upon the Vortex wakes of Stationary and Vibrating Circular Cylinders, J. Fluid Mech., vol. 128, pp. 81–107.

Shirakashi, M., Hasegawa, A & Wakiya, S. 1986, Effect of the Secondary Flow on Karman Vortex Shedding, Bulletin of JSME, vol. 29, pp. 1124–1128.

Smith, R. A., Moon, W. T. & Kao, T. W. 1972., Experiments on Flow About a Yawed Circular Cylinder, Trans. ASME J. Basic Engineering, vol. 94, pp. 771–776.

Soria, J. 1993, Particle Image Velocimetry, Proc. Workshop on Laser Diagnostics in Fluid Mechanics and Combustion, DSTO Aeronautical Research Laboratory, Melbourne, Australia.

Soria, J. 1994, Digital Cross-correlation Particle Image Velocimetry Measurements in the Near Wake of a Circular Cylinder, Proc. Int. Colloq. on Jets, Wakes and Shear Layers, CSIRO Division of Building, Construction and Engineering, Melbourne, Australia.

Susuki, K. 1991, Topology of a Computed Incompressible Three-dimensional Separated Flow Field Around a High-angle-of-attack Cone-cylinder, Computers Fluids, vol. 19, 315–334.

Van Atta, C. W. 1968, Experiments on Vortex Shedding from Yawed Circular Cylinders, AIAA Journal, vol. 6, 931–933.

Van Tuyl, A. H. 1988, Vortex Filament Model of the Wake Behind a Missile at High Angle of Attack, AIAA Journal, vol. 26, 264–270.

Wardlaw, A. B. Jr., & Yanta, W. J. 1984, Asymmetric Flow Field Development on a Slender Body at High Incidence, AIAA Journal, vol. 22, 242–249.

Williamson, C. H. K. 1988, The Existence of Two Stages in the Transition to Three-dimensionality of a Cylinder Wake, Phys Fluids, vol. 31, pp. 3165–3168.

Willert, C. E. & Gharib, M. 1991, Digital Particle Image Velocimetry, Experiments in Fluids, vol. 10, pp. 181–193.

Wu, J., Sheridan, J., Soria, J. & Welsh, M. C. 1994, An Experimental Investigation of Streamwise Vortices in the Wake of a Bluff Body, Journal of Fluids and Structures, in press.

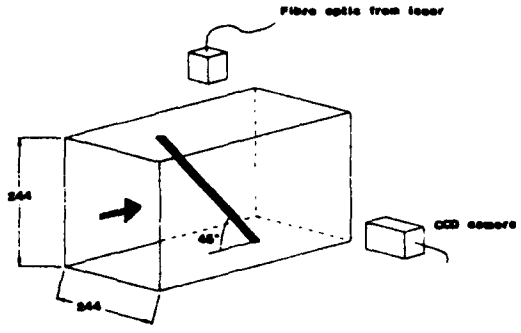

Fig. 1. Arrangement of water tunnel, cylinder and optics.

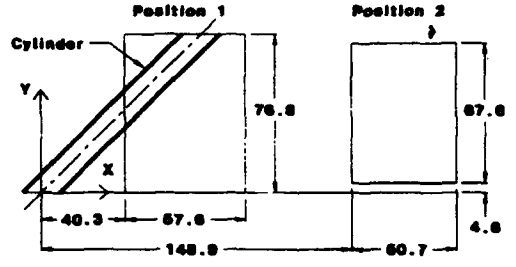

Fig. 2. Coordinate system and positions of frames. Free stream flow is in the x direction.

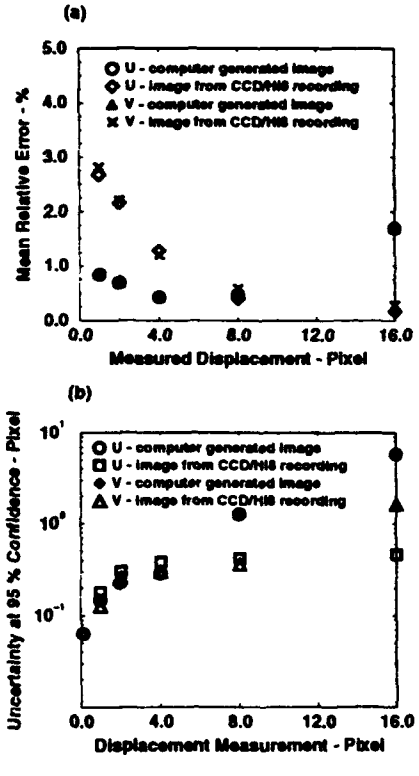

Fig. 3. Cross-correlation PIV analysis accuracy: (a) measurement accuracy; (b) measurement uncertainty.

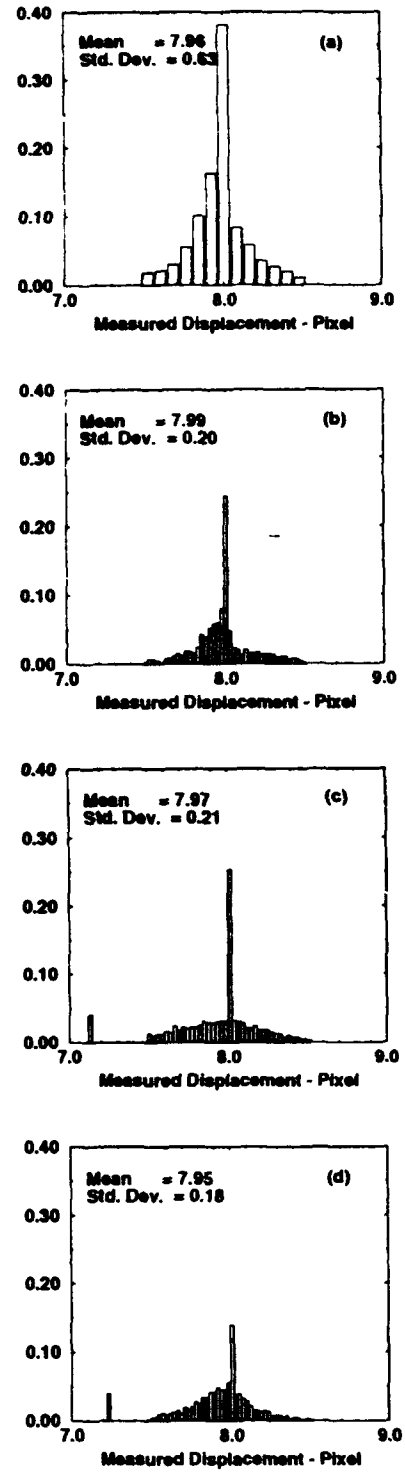

Fig. 4. Probability histogram of the measured displacement distribution using cross-correlation analysis of a uniform 8 pixel shift in the horisontal and vertical directions: (a) and (b) computer-generated *ideal* images; (c) and (d) typical experiment images.

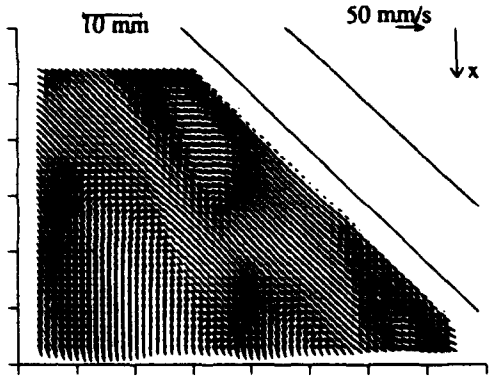

Fig. 5. Mean velocity vector field near cylinder at Re = 391.

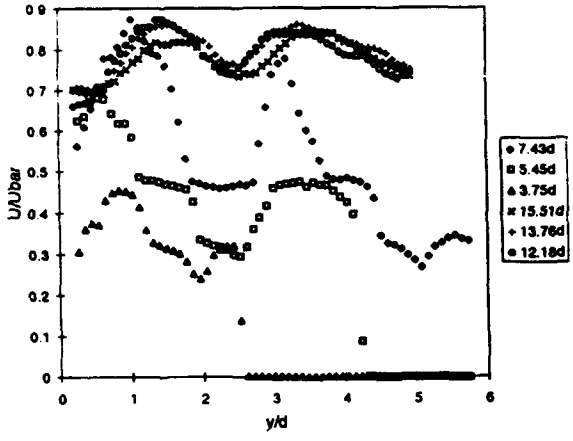

Fig. 6. Mean x-velocity profiles at Re = 391.

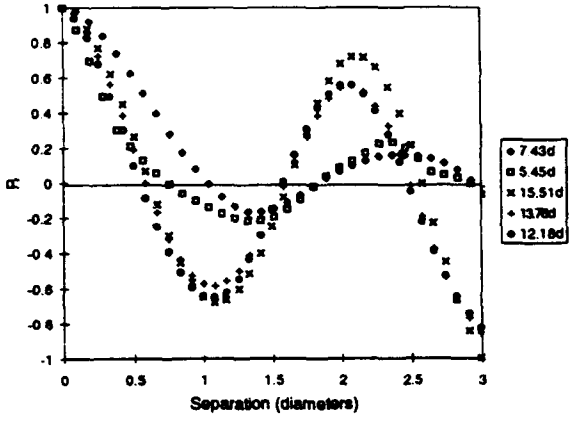

Fig. 7. Auto-correlation functions of mean velocity profiles shown in Fig. 6.

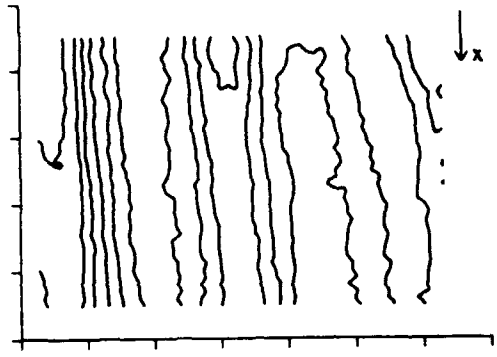

Fig. 8 (a). Contours of mean velocity in the x direction. Contours range from 21–28 mm/s.

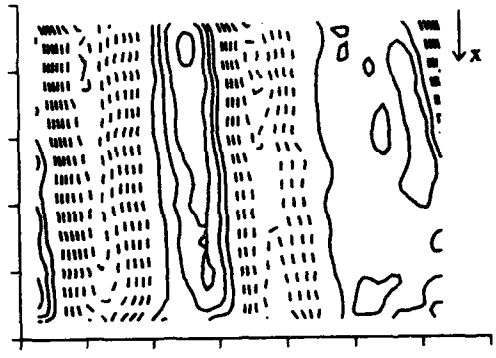

Fig. 8 (b). Contours of mean vorticity. Dashed contours -0.7 to -0.1 s^{-1}, solid 0.1 to 0.7 s^{-1}. Contour level interval 0.1 s^{-1}.

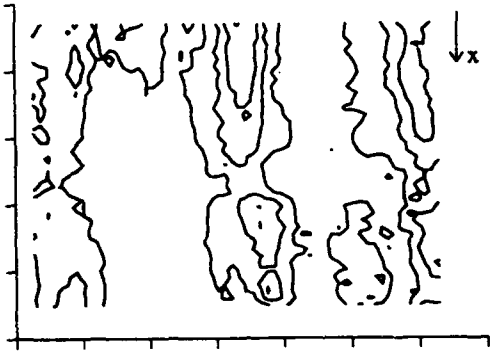

Fig. 9 (a). Contours of rms velocity in the x direction. Contours range from 4 to 7 mm/s.

Fig. 9 (b). Contours of Reynolds shear stress. Dashed contours range from -9 to -1 $(\text{mm/s})^2$, solid contours 1 to 9 $(\text{mm/s})^2$.

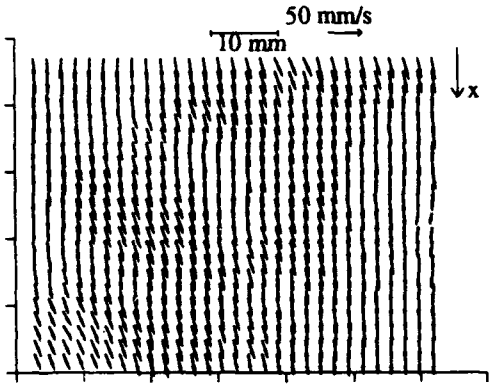

Fig. 10 (a). Instantaneous velocity vector field at position 2 shown in Fig. 2.

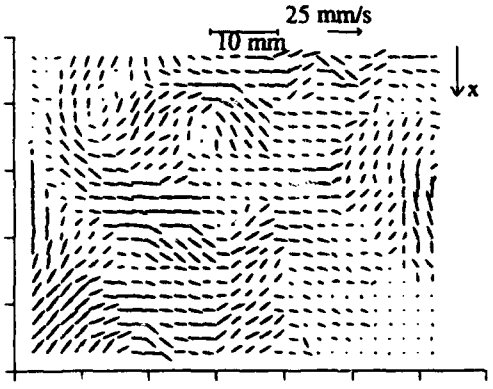

Fig. 10 (b). Velocity vector field shown in Fig. 10 (a) as seen relative to an observer moving in the x direction with a velocity of 25.5 mm/s.

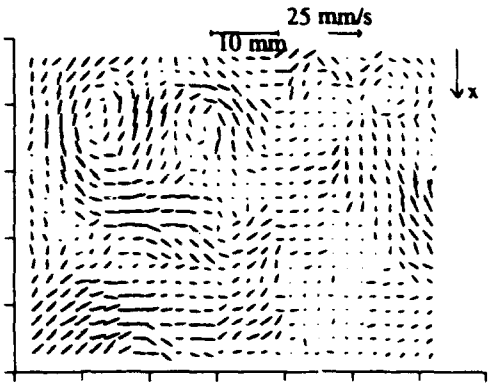

Fig. 10 (c). Fluctuating velocity vector field field corresponding to Fig. 10(a).

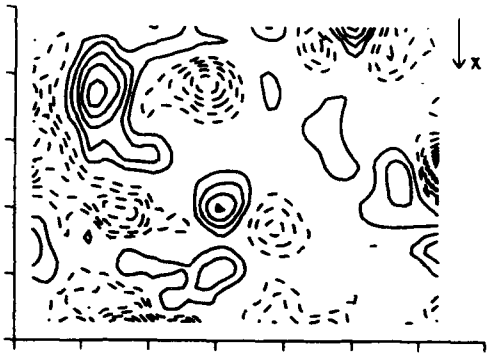

Fig. 11 (a). Instantaneous vorticity contours. Dashed contours range from -4 to -0.5 s^{-1}, solid contours 0.5 to 4 s^{-1}. Contour level interval 0.5 s^{-1}.

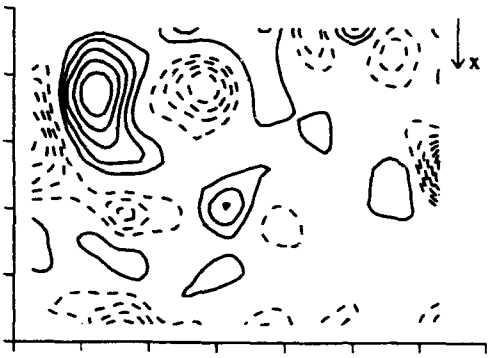

Fig. 11 (b). Fluctuating vorticity contours. Contour levels as for Fig. 11 (a).

INVESTIGATION OF THE LOCAL FLOW TOPOLOGY IN THE VICINITY OF A PROSTHETIC HEART VALVE USING PARTICLE IMAGE VELOCIMETRY

F. Hirt , E. Jud , Z. Zhang

Sulzer Innotec AG, Fluid Mechanics Laboratory
CH-8401 Winterthur, Switzerland

ABSTRACT

A study of the local flow structure of the fluid in a pulsatile flow behind a prosthetic bileaflet heart valve is underway. In a preliminary study the unsteady flow structure of the fully open valve at constant flowrate is investigated. The objective of the research is to develop a better understanding of local flow patterns, in particular the relationship between the local rate of strain and vorticity. With regard to the possibility of mechanical hemolysis (destruction of blood cells) a special focus is directed to the local dissipation of kinetic energy which is for a Newtonian fluid proportional to the second invariant II_s of the rate of strain tensor S.

The present experiments are conducted in a pulse duplication system and the flow structure is analyzed in different view planes by using a particle image velocimetry (PIV) technique. The vector velocity information is extracted from multiply-exposed photographic images of scattered light from seed particles. The illumination source is a continuous argon laser and the pulse duration is controlled by the programmable shutter of a novel video-camera with integrated light amplifier. The optical measurements are conducted in a Newtonian blood analog fluid where the refractive index is matched to the one of the perspex test sections.

1. INTRODUCTION

The application of theories of pulsatile blood flow to the flow in heart chambers or in prosthetic heart valves is very limited. Exact solutions to the Navier-Stokes equations are rarely available because the flowfield related to cardiac prostheses is often in a transitional stage and slightly three-dimensional. The design and development of cardiac prostheses has been mainly by the application of experimental facilities. These range in complexity from a simple column of fluid (cf. Kolff, 1959) to complex pulse duplication systems such as the one reported by Pickard *et al.* (1979). The design of an experimental facility for the simulation of the cardiovascular system involves a thorough analysis of the fluid dynamics of pulsatile flows. Temple *et al.* (1964) applied the principle of dynamic similarity to the design of a pulse duplicator and conducted a significant in vitro study of the flow properties of healthy and diseased human heart valves.

An ideal heart valve replacement can be defined as one that permits the unrestricted, unidirectional flow of blood and when implanted in a human being, will not decrease the quality or length of life. Some of the criteria for ideal performance are: pressure drop, valvular regurgitation, noise, hemolysis and thromboembolism. The latter two are responsible for valve-related mortality. Both are related to non-Newtonian hydrodynamic effects which are poorly understood. From in vitro experiments of hemolysis it is well known that there exists a limit to the stress load of the blood cells. Therefore, knowledge about the magnitude of stresses in the whole flowfield and at the boundaries (valve surface, vessel wall) is very important. The location of points of high stresses depends on the design of a valve. Most of the investigations related to stresses have been conducted by using single point measurements and statistical means. An example concerning these kind of investigations is given by Yoganathan *et al.* (1986) who studied the wall shear stress due to a mechanical valve in the aortic vessel. A recent method for the determination of mean velocity and fluctuations in pulsatile flow has been published by Baldwin *et al.* (1993). In the present work an attempt is made to study the stress on the basis of the local deformation of the flow by using the partial derivatives of the velocity field. The approach is applied to the flow of a bileaflet valve in the symmetry plane at the aortic and the mitral position.

2. PULSE DUPLICATION SYSTEM

According to dimensional analysis the flow of the cardiovascular system can be described by nine independent physical quantities. The condition for physical similarity states that the values of the resulting parameters must be the same for model and original. As a result it follows that physical similarity is fulfilled only with a 1:1 scale of model and original. The intrinsic task for the simulation of the cardiac cycle is to provide a time dependent cardiac output which corresponds to the physiological waveform of a human being. A feedback controlled piston-in-cylinder pump is used to reproduce the cardiac output. The pump is connected to the left heart ventricle, which consists of the aortic and the mitral test sections. Both are manufactured in perspex and in the center of each section a prosthetic heart valve is placed. The contours of the vanes correspond to the vessels of an average human being (cf. Wieting, 1969). The generated

pressure waveform and the pulsewave propagation speed is determined by the compliance of the large blood vessels and the flow resistance of the small capillary vessels. In the present set up this mechanism is modeled by two compliance elements, one each for the arterial and the venous vessels, and by two conventional flow resistors. The compliances consist of a spring loaded piston in a cylinder. Two springs of different stiffness model the arterial and the venous compliances. The fluid capacity of the venous vessels can be adjusted by using a hydraulic reservoir. With the help of a bypassed centrifugal pump the loop can be operated in a steady state mode. The arrangement of the flow loop and its components is seen in the sketch of **Fig.1**. Pulsatile velocity measurements will be conducted in a tuned system defined by the aortic pressure ratio, the flow rate and the frequency (e.g. 120/80 mmHg, 5 l/min and 72 beats per minute). In order to phase lock the optical measurement equipment with the cardiac cycle a pulse generator is coupled with the pulsatile pump which provides an appropriate number of equally spaced pulses over one cardiac cycle. By this means the flow data can be collected at specified times during the flow cycle. The aortic and the mitral test sections of the fluid loop are shown on **Fig.2**. Since both test sections are manufactured of perspex the influence of the flexible walls is ignored. However, an experimental study in the aortic section of Bellhouse & Talbot (1969) has shown that the influence of the flexible wall is of no significance to the flow behaviour.

3. BLOOD ANALOG FLUID

Blood is a type of connective tissue whose cells are suspended in plasma. Whole blood is slightly heavier and three to four times more viscous than water. A blood sample consists usually of about 45% cells by volume. These include red blood cells (erythrocytes), white blood cells (leukocytes) and platelets (thrombocytes) which play an importat role in blood cloth formation. The use of mammalian blood in fluid mechanical experiments is very difficult because of the clot formation in contact with artificial surfaces. Since optical techniques are applied the fluid must be transparent. Therefore, a Newtonian blood analog fluid with the same viscosity as blood has been used. This fluid is a mixture of saturated aqueous sodium iodide and 25% glycerin and possesses a kinematic viscosity of 3.5 cS at 23°C. In order to avoid the application of optical correc-tions the refractive index is matched to n = 1.49 of the perspex test sections by adding aqueous glycerin. The refractive index is measured by a conventional Abbe-Refractometer. By using a Newtonian fluid the influence of the cells on the viscosity is not described correctly. However, it is pointed out by Skalak *et al.* (1989) that the non-Newtonian influence becomes important if the vessel diameter is comparable to the blood cell size. This is the case for the fluid mechanics in capillaries.

4. APPLIED PIV-TECHNIQUE

The applied PIV- technique uses one thin light sheet at 90^{o} to the imaging axis thus illuminating only particles that lie in one plane. This approach provides a planar vector velocity field and effectively filters out particles with a significant velocity perpendicular to the light sheet. The amount of filtering is determined by the thickness of the light sheet. There is a strong dependence of scattered light intensity on particle diameter. This dependence enforces a lower limit on particle diameter since each light pulse must scatter sufficient energy to expose the imaging system. This lower limit is coupled with the magnification of the system and the incident energy provided by the light source. There is also an upper limit to the particle size enforced by the requirement of minimal slip between the particle and the fluid. The resolution of the flowfield in the vicinity of prosthetic heart valves basically requires small particles. The laser light pulse frequency is controlled by the shutter of the video-camera. This shutter is controlled by a software via PC. On the photographic image the particles leave behind their 'foot prints' which consist of two or more different scattered light points (principal and tagged). The flow direction is given from the small tagged and the large principal spots. The spatial separation between tagging and principal spots is choosen large enough to ensure that there is no overlap of the images. Because of the large velocity gradients perpendicular to the mean flow direction several pulse frequencies for the same state of flow were necessary in order to track enough particles in the vortical flowfield. The image is digitized directly by the high density line scan camera and data analysis is carried out from a digital picture of 512 x 512 pixels. The spatial resolution of the flowfield is about 60 μm/pixel. A commercially available algorithm developed by Optimage Ltd. of Edinburgh (cf. Grant & Liu, 1990) is implemented on a PC and used for the data processing and the analysis. This technique allows instantaneous velocity vector fields to be obtained. The instantaneous velocity fields are based on the random location of the seeding particles in the flowfield and are interpolated onto a structured grid for further analysis.

5. DESCRIPTION OF THE LOCAL FLOWFIELD

In the present study the stresses and the energy dissipation due to viscosity are described not in terms of statistical means but in terms of the local deformation of the flowfield. This approach is based on the assumption that the fluid motion is locally describable by the leading terms of a Taylor series expansion for the velocity field in terms of space coordinates. The local deformation of the flowfield is determined by the partial derivatives of the velocity field which form the 3x3 matrix of the local velocity gradient tensor **W** (for details see Batchelor, 1967). The velocity gradient tensor may be decomposed in the usual way into its symmetric and antisymmetric parts by $\mathbf{W} = \mathbf{S} + \mathbf{R}$ where **S** is the rate of strain and **R** is the vorticity tensor respectively. The eigenvalues λ of a second order tensor **A** satisfy the characteristic equation

$$\lambda^3 + I\lambda^2 + II\lambda + III = 0 \qquad (1)$$

where the three matrix invariants are:

$$I = -\,\text{trace}\,\mathbf{A} \qquad (2)$$

$$II = \frac{1}{2}\left(\text{trace}[\mathbf{A}]^2 - \text{trace}\,[\mathbf{A}^2]\right) \qquad (3)$$

$$III = -\det[\mathbf{A}] \qquad (4)$$

The quantities I_s, II_s, III_s denote the invariants of the rate of strain tensor **S** respectively. Associated with the three independent components of the vorticity tensor **R** is the vorticity vector ω. It turns out that a general flowfield is

characterized by fundamental flow patterns which can all be classified in space of matrix invariants. A review of this type of analysis is given by Perry & Chong (1987) and Chong *et al.* (1988). Accordingly the local topology of an incompressible flow at a point is described by the second and third invariants (II-III plane). Thereby the characteristic equation (1) can have either real roots or a pair of conjugate complex roots. For incompressible flow (I = 0) the relation

$$III = \pm \frac{2\sqrt{3}}{9} (-II)^{3/2} \qquad (5)$$

divides real roots from complex roots in the II-III plane. Complex eigenvalues are associated with a focus where local trajectories may spiral outwards (stretched) or inwards (compressed). The real eigenvalues represent a topology in the 3D-space which is a combination of node and saddle (cf. **Fig. 6&7**).

6. DEFORMATION OF A FLUID PARTICLE AND THE LINK TO HEMOLYSIS

The mechanical dissipation of kinetic energy due to viscous friction is expressed in terms of the dissipation function which is defined as

$$\phi = -4\nu II_s \qquad (6)$$

where ν is the kinematic viscosity. In the case of an incompressible fluid and if thermal diffusion is neglected the change of internal energy u of a fluid particle is given by

$$\frac{Du}{Dt} = \phi \ . \qquad (7)$$

It is shown below that this relation also plays an important role for hemolysis. Thereby it is assumed that cell membranes possesse a strain energy function u such that the material derivative of this function is equal to the fluid stress power per unit volume. According to data of different experimenters (cf. Giersiepen, 1988) the maximum shear stress τ which can be applied to blood cells without damaging them is dependent on the loading time Δt. In **Fig. 3** the maximum load of shear stress for the red blood cells (erythrocytes) and the platelets (thrombocytes) are plotted versus the loading time. According to these plots the relation

$$\tau^2 \Delta t = \text{constant} \qquad (8)$$

describes the cell behaviour within the time range of interest in good approximation. Thereby the shear stress, the rate of shear $\dot{\gamma}$, and the second invariant of the rate of strain tensor II_s are related as

$$\tau^2 \sim \dot{\gamma}^2 \sim II_s \ . \qquad (9)$$

The combination of (6), (7), (8) and (9) leads to a relation between the local change of strain energy and the material property of blood cells

$$\left.\frac{Du}{Dt}\right|_{max} \approx \frac{\Delta u_{max}}{\Delta t} \sim \frac{\text{constant}}{\Delta t} \ . \qquad (10)$$

This is an interesting result which indicates that the local maximum tolerated change of internal energy due to viscous stresses is a constant within the time range of interest. The value of the constant depends slightly on the blood cell type (cf. **Fig. 3**).

7. RESULTS

Based on the outlined analysis the flowfield behind the fully opened valve is investigated for one valve geometry in the aortic and the mitral position. The velocity gradients used to construct invariants and vorticity were all scaled with the valve orifice diameter and the average orifice flow speed. The nominal Reynolds number based on these quantities is about Re = 3000 for the experiments reported here. A snapshot of the velocity vector field is shown for the aortic position on **Fig. 4**. This has been obtained by interpolation of PIV-flowfield visualisation onto a structured grid. The topology of this flowfield shows a saddle and two counterrotating large scale vortices. A scatter plot of the magnitudes of vorticity versus the rate of strain is made for each of the grid points. Thereby it is indicated that the small scale motions are confined within a wedge which is defined by the vorticity free potential flow and the pipe flow. Motions with a high rate of strain are in general associated with a high magnitude of vorticity. A weak preference towards rates of strain which are about twice as large as the vorticity is visible. The smallest eddies near the centerline of a pipe flow have for the present Reynolds numbers a length scale which is about 0.07 times the diameter (cf. Bradshaw, 1978). This length represents an upper limit for the size of small scale eddies; it corresponds also to the mesh size of the present data analysis. The measured velocity vector field of the mitral side is presented on **Fig. 5**. This flow is characterized by a separation line and a vortex which is generated near the boundary. The associated scatter plot indicates a strain dominated flow behaviour with rates of strain more than twice those of the aortic flow.

The local change of internal energy u is according to (7) proportional to the second invariant of the rate of strain tensor. The magnitude of this quantity is plotted in **Fig. 6** for the aortic flow at each grid point in the symmetry plane. The peaks correspond to high dissipative motions (equation 7) which are of potential danger with respect to hemolysis. The whole information of such motions is represented by a single scatter plot in the II_s - III_s plane. Thereby the scattered points are bounded by the relationship (5). Following the analysis of Chong *et al.* (1988) the local trajectories of the fluid particles of these small motions can be classified in terms of the invariants. For the present data at the **aortic** position it is found that all the small motions have a 3D-topology of the type stable node/saddle/saddle as sketched on the scatter plot. In this connection it is interesting to note that direct numerical simulations of shear layers by Chen *et al.* (1990) showed that in their flow the local topology of small scale motions with high rate of strain are of the type unstable node/saddle/saddle.

The change of the internal energy at the **mitral** position and at the same flowrate as for the aortic flow is shown in **Fig. 7**. From there it is recognized that the peaks are more than four times higher than in the aortic case. Also the spatial density of the peaks is higher which indicates that the fluid is in a mixed state. The scatter plot in invariant space reflects

the highly dissipative motions of this flow. The maximum negative value of the second invariant is twice as high as that of the aortic flow. Most of the motions of high dissipation have a preference towards the axis where the third invariant vanishes. The topology of these motions is of the type stable line node/unstable line node/no flow.

8. CONCLUSIONS AND OUTLOOK

An attempt is made to describe a part of the 3D-flowfield in the vicinity of a prosthetic heart valve in terms of matrix invariants. These are derived from PIV measurements. As a result, a link between the maximum stresses leading to deformation of the blood cells and the second invariant II_S of the rate of strain tensor S has been made. Based on the investigation the following conclusions can be drawn:

- o A new method of using Laser PIV measurements to quantify the rate of strain in a plane section of the flow downstream of a bileaflet heart valve has been developed.
- o Motions with a large local rate of strain are related to a high dissipation rate of kinetic energy due to viscosity. Locations of high dissipation are of potential danger for the damage of blood cells.
- o A large local rate of strain is associated with a large negative value of the second invariant of the rate of strain tensor.
- o The flow structure at the mitral position is characterized by a high rate of strain which is more than twice as large as the one of the aortic flow.
- o The local 3D-topology of small motions in the aortic and the mitral section is dominated by trajectories of the type node/saddle/saddle or stable line node/unstable line node/ no flow.

The preliminary results show that the large amount of information of small scale motions of the 3D-flowfield can be mapped into a single scatter plot in invariant space. This methodology provides an elegant criterion for the judgement of the performance of prosthetic heart valves with respect to hemodynamics. A complete picture of small motions within the cardiac cycle will be obtained by the application of the present approach to different phase locations.

ACKNOWLEDGEMENTS

The advice and support from T. Baldwin and G. Richard, CarboMedics Inc., Texas, U.S.A., during the building up of the pulse duplicator at Sulzer Innotec AG is gratefully acknowledged.

REFERENCES

Baldwin J.T., Deutsch S., Petrie H.L., Tarbell J.M. 1993, Determination of Principal Reynolds Stresses in Pulsatile Flows After Elliptical Filtering of Discrete Velocity Measurements. Trans. of ASME, J. of Biomechanical Engineering, Vol. 115, pp 396-403.

Batchelor G.K. 1967, An Introduction to Fluid Dynamics. Cambridge University Press.

Bellhouse B.J., Talbot L. 1969, The fluid mechanics of the aortic valve. J. Fluid Mech., **35**.

Bradshaw P. 1978, Turbulence. Topics of Applied Physics Vol 12, Springer.

Chen J.H., Chong M.S., Soria J., Sondergaard R., Perry A.E., Rogers M., Moser R., Cantwell B.J. 1990, A Study of the Topology of Dissipating Motions in Direct Numerical Simulations of Time - Developing Compressible and Incompressible Mixing Layers. Center for Turbulence Research, Proc. Summer Program, Stanford University.

Chong M.S., Perry A.E., Cantwell B.J. 1988, A general classification of three-dimensional flow fields. The Physics of Fluids A 2 (5), pp 765-777.

Giersiepen M. 1988, Ermittlung von Strömungsprofilen und Schubspannungen an Herzklappenprothesen mit Hilfe der Laser-Doppler-Anemometrie in Pulsatiler Strömung. Diss. , Technische Hochschule Aachen.

Grant I., Liu A. 1990, Directional ambiguity resolution in partticle image velocimetry by pulse tagging. Experiments in Fluids, Vol. **10**, pp 71-76.

Kolff W.J. 1959, Mock circulation to test pumps designed for permanent replacement of damaged hearts. Cleveland Clinique Quarterly, **26**, pp 223.

Perry A.E., Chong M.S. 1987, A description of eddying motions and flow patterns using critical-points concepts. Ann. Rev. Fluid Mech., **19**, pp 125-155.

Pickard M.L., O'Bannon WO., Lloyd MJ., De Bakey M.E. 1979, Computer managed in vitro testing of ventricular assist devices. Trans Am Soc Artif Intern Organs, **25**, pp 192.

Skalak R., Özkaya N. 1989, Biofluid Mechanics. Ann. Rev. Fluid Mech., **21**, pp 167-204.

Temple L.J., Serafin R., Calvert N.G., Drabble J.M. 1964, Principle of Fluid Mechanics Applied to Some Situations in the Human Circulation and Particularly to the Testing of Valves in a Pulse Duplicator. Thorax, Vol. **19**, pp 261-267.

Wieting D. 1969, Dynamic Flow Characteristics of Heart Valves. PhD. Thesis, The University of Texas at Austin.

Yoganathan A.P., Woo Y., Sung H. 1986, Turbulent Shear Stress measurements in the Vicinity of Aortic Heart Valve Prostheses. J. Biomechanics, Vol. **19** (6), pp 433.

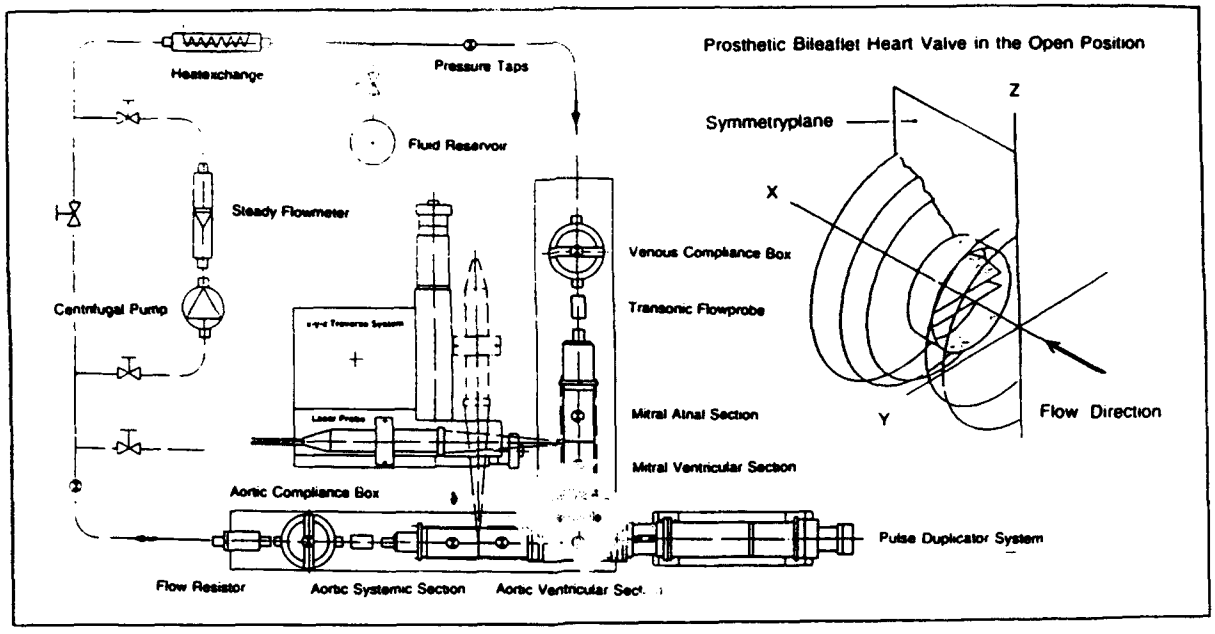

FIGURE 1. Experimental setup of the pulse duplication system 'HEMO' for flow studies in the vicinity of cardiac prostheses. Experiments are conducted by using a Newtonian blood analog fluid for which the refractive index is matched to the one of the perspex test sections.

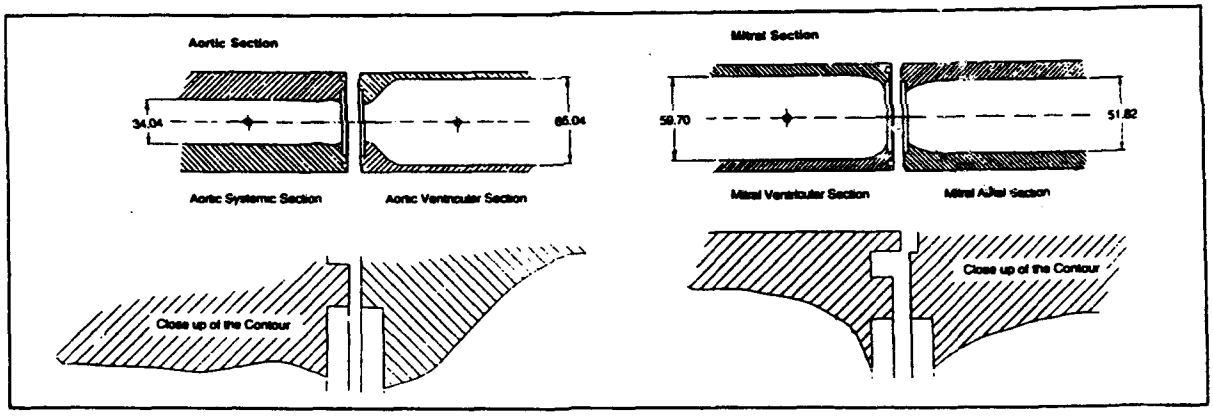

FIGURE 2. Design of the **aortic** and the **mitral** test sections according to Wieting (1969). The heart valves are inserted in the middle of each section. Optical measurements are conducted downsteam of the valves.

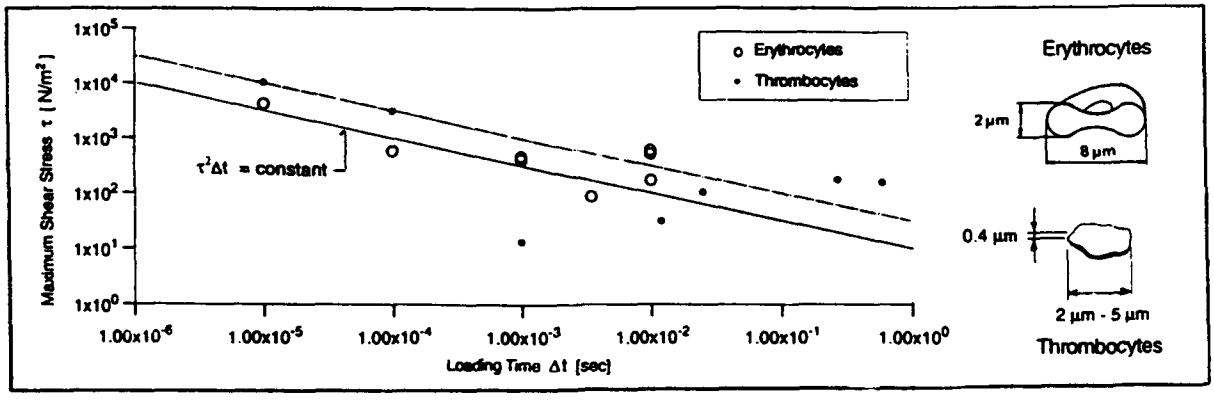

FIGURE 3. Maximum tolerated shear load of blood cells in dependence of the loading time. The data represent results from *in vitro* experiments of different researchers given by Giersiepen (1988).

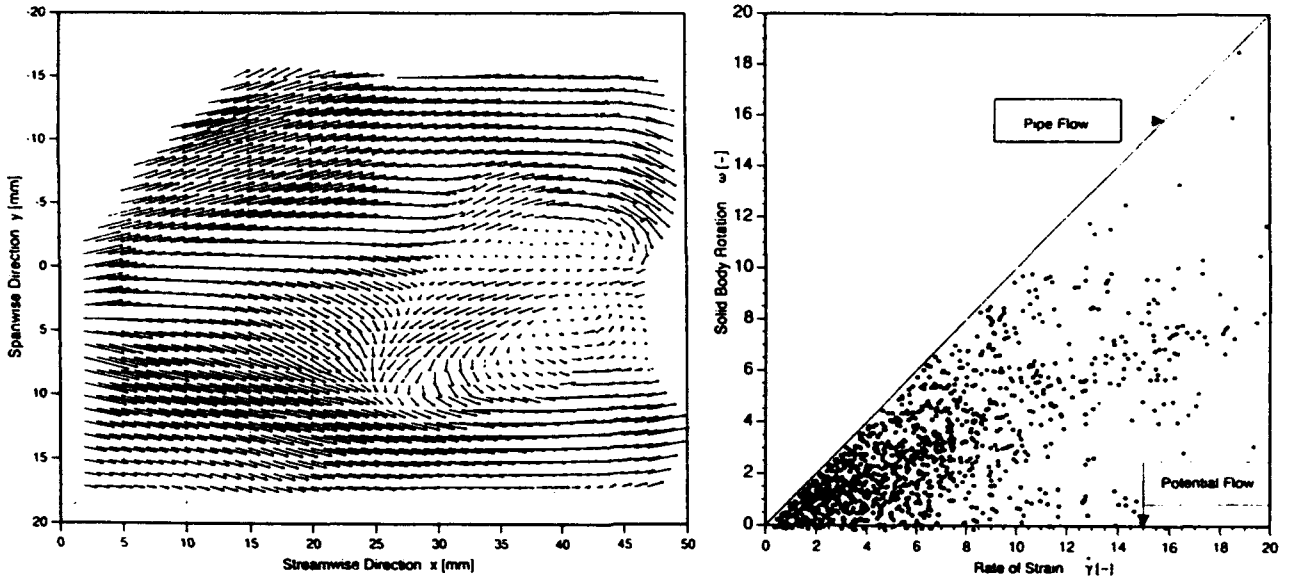

FIGURE 4. Snapshot of the velocity vector field at the fully open bileaflet valve in the symmetry plane of the **aortic** position. The corresponding scatter plot represents the relationship between the magnitude of the rate of strain and the solid body rotation (vorticity) at every grid point. In this case small local motions with a large rate of strain are associated with a large solid body rotation. Large rates of strain lead to high rates of dissipation of kinetic energy due to viscosity and therefore are critical with respect to hemodynamics.

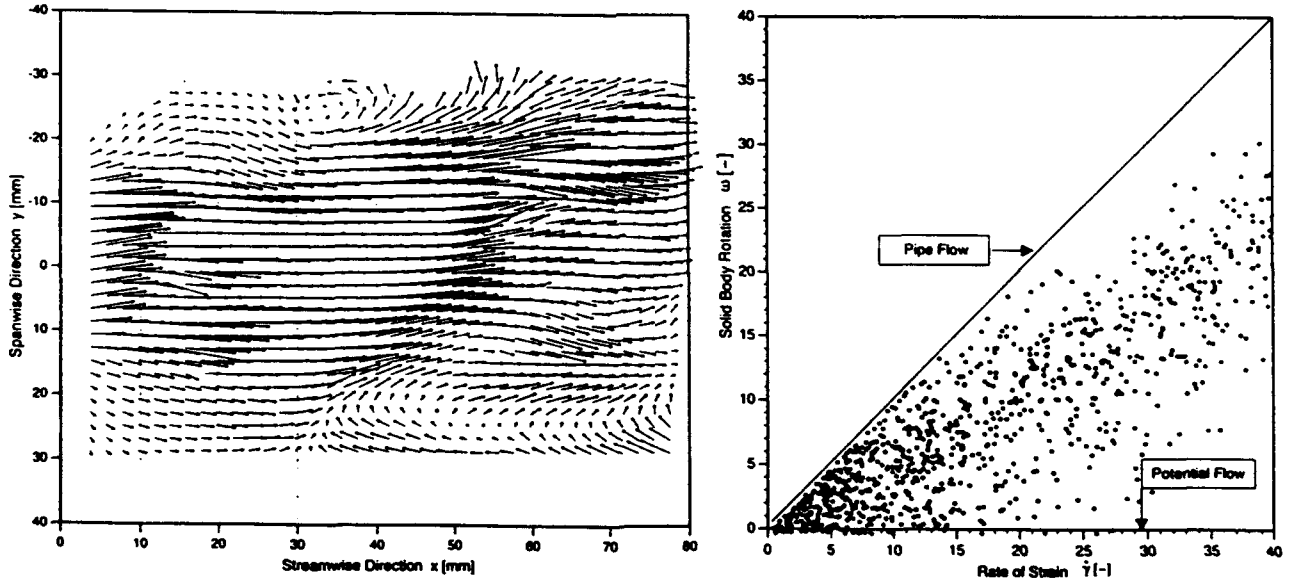

FIGURE 5. Snapshot of the velocity vector field at the fully open bileaflet valve in the symmetry plane of the **mitral** position. The corresponding scatter plot represents the relationship between the magnitude of the rate of strain and the solid body rotation at every grid point. It is noted that the local rate of strain in this case is more than double as large as for the aortic flow. Most of the motions of large rate of strain are associated with a large solid body rotation.

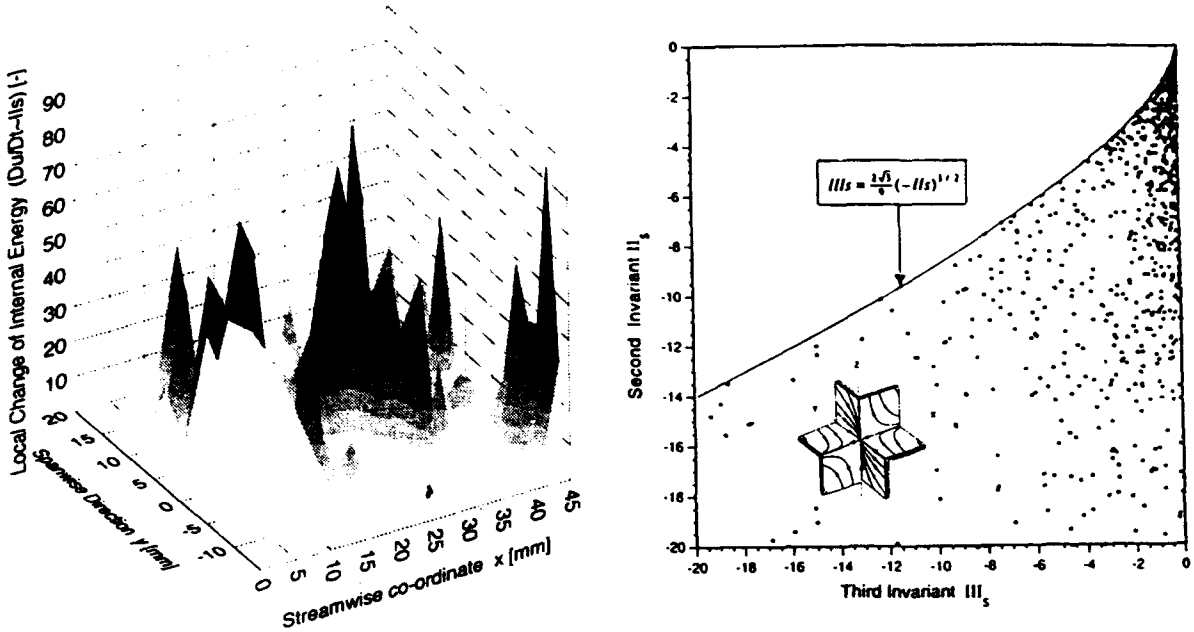

FIGURE 6. The local change of internal energy Du/Dt for the flow state of Fig. 4 at the **aortic** position. The peaks correspond to locations of high dissipation of kinetic energy which means a high shear load of the blood cells. The information of the small motions is represented in a scatter plot in invariant space (II_s - III_s) of the rate of strain tensor S. It is recognized that large negative values of the second invariant II_s are associated with high kinetic energy dissipation. Based on the invariants the local trajectories of the fluid particles of these motions can be classified as demonstrated by Chong, Perry & Cantwell (1988). Accordingly the local 3D-topology of the motions of high dissipation (without solid body rotation) are of the type stable node/saddle/saddle as it is sketched on the plot.

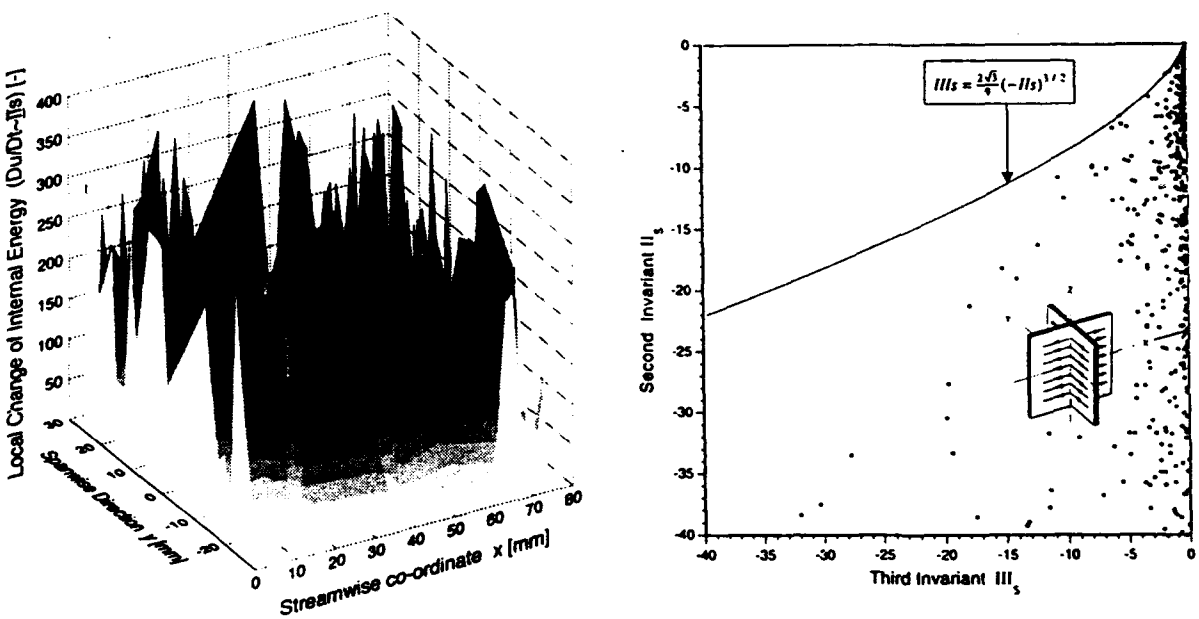

FIGURE 7. The local change of internal energy corresponding to the flow state of Fig. 5 at the **mitral** position. It is noted that the peaks are more than four times higher than in the aortic position at the same flowrate. The scatter plot in invariant space indicates that most of the motions with large rates of strain are concentrated at $III_s = 0$. The local 3D-topology of these motions corresponds to the type stable line node/unstable line node/no flow.

COMPARISON OF PIV DATA WITH HOT-WIRE MEASUREMENTS AND CALCULATIONS OBTAINED FOR INSTABILITIES IN A FLAT PLATE BOUNDARY LAYER

M.Fischer

Institut für Strömungsmechanik
Deutsche Forschungsanstalt für Luft- und Raumfahrt (DLR)
Bunsenstraße 10, 37073 Göttingen, Germany

ABSTRACT

Artificially forced instabilities were studied experimentally in the transition region of a Blasius boundary layer in air by means of Particle Image Velocimetry (PIV) and hot-wire anemometry. Reproducible and constant conditions in the development of the instabilities were achieved by forcing the boundary layer with well controlled disturbances. The arrangement for artificial excitation provides the possibility to generate the fundamental and the subharmonic transition type as well. Out of the instantaneous velocity fields of the PIV recordings integral quantities were obtained by means of data analysis. These integral data were compared with data achieved by the hot-wire measurements and calculations (Numerical Simulation). The procedure itself to obtain integral data out of the PIV recordings and the limiting parameters of this procedure will be presented.

1. INTRODUCTION

PIV is increasingly used to investigate instantaneous two-dimensional velocity fields in a wide domain of fluid mechanical applications, Adrian (1991), Kompenhans et al. (1993, 1994), Lourenço (1988). For the case of a flat plate boundary layer flow in air, Fischer et al. (1993) demonstrated the applicability of PIV for the investigation of instabilities developing within the boundary layer. There are three properties of PIV which motivate the use of this measurement technique for this kind of fluid mechanical research: The fact of working instantaneously, the possibility to obtain information in a complete velocity field at once and the non-intrusive method of operation.

The transitional process in a boundary layer is determined by a mechanism of generation and decomposition of various instabilities. Small disturbances can cause primary instability and lead to the beginning of the transition process. Primary instability of such a boundary layer occurs as two-dimensional travelling waves known as Tollmien-Schlichting waves (TS waves). If the amplitudes of the TS waves grow above a certain threshold value, a new state of the flow is present. This modulated flow is sensitive to three-dimensional disturbances. The amplification of these disturbances leads to a three-dimensional distortion of the TS waves. The following appearance of counter-rotating streamwise vortices is a consequence of the secondary instability. These vortices known as Λ-vortices grow very rapidly and lead to the breakdown within a few wavelengths after onset of three-dimensional distortion. The occurrence of Λ-vortices in a plane parallel to the surface of the flat plate is characterized by two possible types of spanwise periodic arrangements. The so called fundamental transition type is characterized by an aligned streamwise pattern of the Λ-vortices whereas the subharmonic transition type appears with a staggered streamwise pattern. Which type of transition is present depends on the nature and the scale of the three-dimensional disturbances. The extension of the knowledge about this mechanism enables the prediction and control of transition as required for applications in fluid mechanical engineering.

2. EXPERIMENTAL SET-UP

The experiments were conducted in the Low Turbulence Wind Tunnel of DLR, Fig.1. It is an Eiffel type tunnel with a high contraction ratio of 16:1. The measurements were conducted at a free-stream velocity of U_∞ =11 m/s and a turbulence level of 0.065 %.

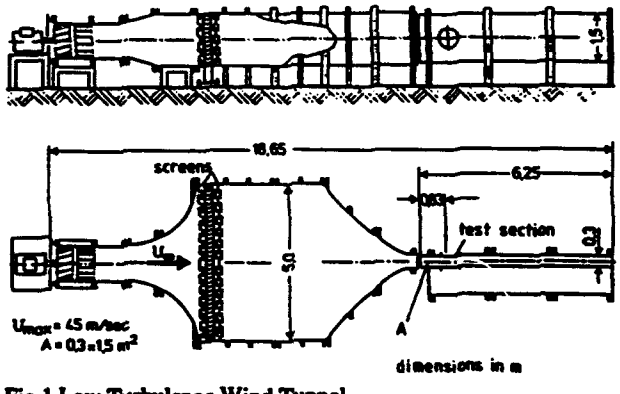

Fig.1 Low Turbulence Wind Tunnel

The dimensions of the closed test section are 0.3 m in width and 1.5 m in height.

The flat plate model was vertically mounted in the test section of the tunnel, Fig.2.

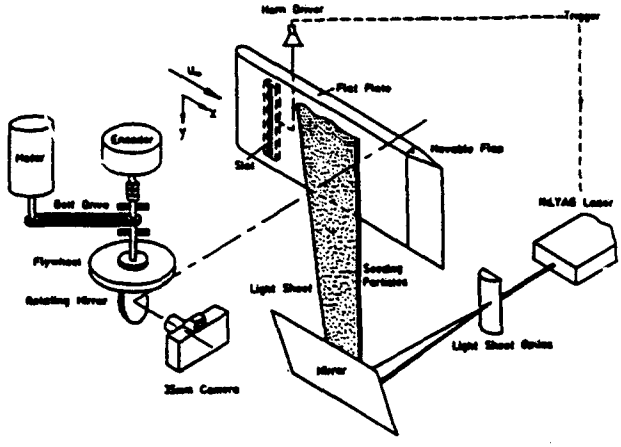

Fig.2 Experimental set-up

In order to get reproducible and constant conditions in the development of the instabilities, well controlled disturbances were excited in the boundary layer by a flush mounted slot in the plate. The disturbances were generated by means of a periodic fluid motion as a result of periodic pressure oscillations generated from a loudspeaker. The excitation level was controlled as Sound Pressure Level (SPL) with a microphone.

For our optical investigations a Nd:YAG laser system was utilized, Kompenhans and Reichmuth (1987). The original wavelength of 1064 nm is converted to the visible 532 nm wavelength via a frequency doubling crystal. The laser emits light pulses of about 16 nsec duration and pulse energies of 70 mJ. The laser was triggered by the excitation signal for the loudspeaker, so that a fixed phase relation among the artificial excitation and the recorded images is guaranteed. The light sheet with constant thickness was aligned parallel to the surface of the flat plate model and its height above the plate was varied between 0.5 and 3.5 mm. The pictures were recorded with a commercial Contax RTS photo camera, a specially corrected objective for short object distances and a highly sensitive film (3200 ASA). The recorded area was 0.18·0.13 m^2. Because of the small fluctuation amplitudes of the instabilities we used a rotating mirror to increase the accuracy of the velocity data (the lowest attainable limit was u'/U_{∞}=0.5 %). This high speed mirror system has been successfully applied to low speed as well to high speed flows, Raffel (1993). The rotation frequency ranges from 0.5 to 50 Hz, thus covering a range of shift velocities from 1 to 500 m/s.

The tracer particles in the flow were olive oil droplets. They were produced by means of a Laskin nozzle. Pressurized air, injected in olive oil, leads to the formation of oil droplets with a mean diameter of 1 µm. The homogeneous seeding of the flow was realized by feeding the particles into the flow upstream of the grid and the screens of the wind tunnel. The particle density in the flow was about 10^2 to 10^3 particles/mm^3 . For the data evaluation of the PIV recordings an optical Fourier processor was utilized for the formation of the Young's fringes. The following second Fourier transformation was performed digitally in an Image Processing Computer, Vogt (1993), Fig.3.

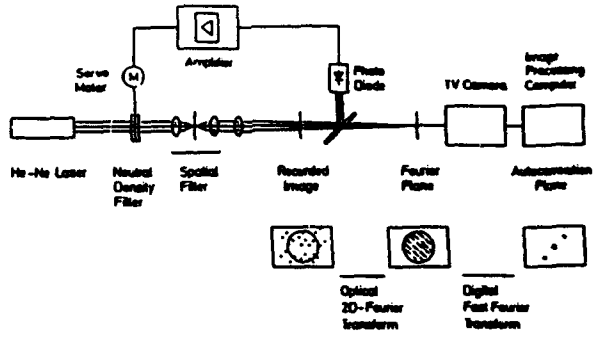

Fig. 3 Data evaluation

3. RESULTS

3.1. PIV measurements

As mentioned above, the height of the light sheet above the plate was varied during the experiments, but in this work only the results for a height of 0.5 mm will be considered. This height corresponds in our case to the height of the inner maximum of the TS wave eigenfunction. For the generation of the fundamental transition type we used a sine wave with a certain amplitude as excitation signal for the loudspeaker. The frequency of the fundamental sine wave was f=154 Hz.

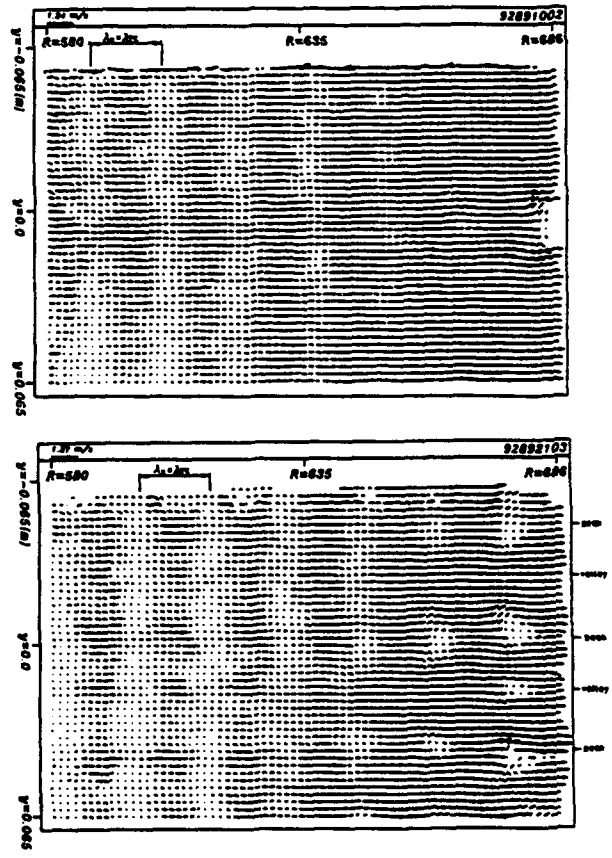

Fig. 4 Field of instantaneous velocity fluctuations (u', v'), fundamental transition type, a) SPL=106.0 dB, b) SPL=108.6 dB

Figure 4a shows for an excitation level of SPL=106.0 dB the fundamental transition type as distribution of instantaneous velocity fluctuations u', v'. The flow direction is, as in all following evaluated PIV recordings, from left to right. R is the square-root of the Reynolds number related to x. Beginning from left one can see the development of a TS wave with increasing amplitude in streamwise direction. The magnitude of the streamwise wavelength is λ_x=2.5 cm. It compares well with the wavelength obtained for this frequency by stability calculations based on the primary, local and linear theory, Ehrenstein (1987). For the same observation area as in the previous Figure, Figure 4b presents due to the higher excitation level of SPL=108.6 dB later stages of transition. At R=580 the onset of three-dimensional distortion of the previously two-dimensional TS wave becomes evident. Moving downstream the three-dimensional distortion becomes intensified and leads finally to the development of Λ-vortices in the typical aligned streamwise pattern. The streamwise wavelength at this stage remains the same as in the TS wave stage. Planes of enhanced (peak) and reduced (valley) amplitude are clearly distinguishable.

For the lower excitation level of SPL=105 dB Figure 5a shows from left to right the sudden development of Λ-vortices appearing in a staggered pattern typical for the subharmonic transition type. It can be more clearly seen in Figure 5b for a higher excitation level, SPL=108.0 dB. It is remarkable that λ_x at the stage of fully developed Λ-vortices has been doubled compared to the wavelength at the TS wave stage.

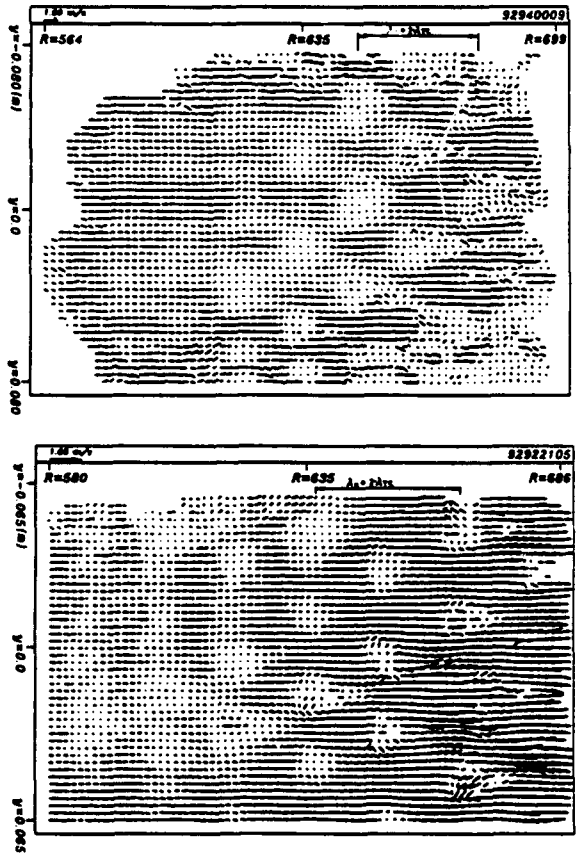

Fig. 5 Field of instantaneous velocity fluctuations (u', v'), subharmonic transition type, a) SPL=105.0 dB, b) SPL=108.0 dB

3.2. Data analysis

In order to compare the achieved PIV data with data obtained by hot-wire anemometry and Numerical Simulation, Kleiser and Zang (1991), a program for data analysis was developed. With this program spatial rms-values (rms i.e. root mean square) were obtained out of the evaluated PIV recordings. Under certain conditions, which will be described a little bit later, it is proper to compare these spatial rms-values of the PIV recordings with temporal rms-values obtained by hot-wire measurements and spatial rms-values obtained by a Numerical Simulation.

The general features of the program presents Figure 6. Each evaluated PIV recording is divided in rows (along R, see Figure 4) and columns (along y). In Figure 6a U (component of the total velocity in streamwise direction) is shown as circles for an arbitrary row of an evaluated PIV recording.

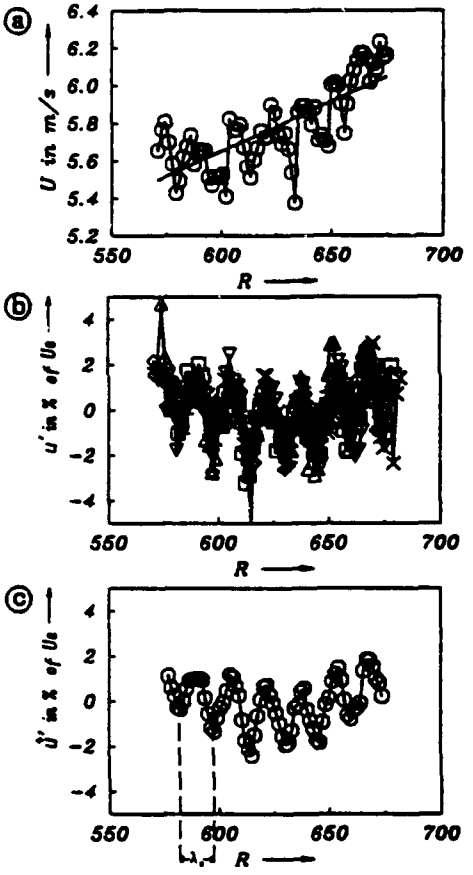

Fig. 6 Program steps for data analysis

In the following this curve will be approximated by a least-square fit (solid line). For each measuring point the value of velocity fluctuation u' can be achieved by subtracting the functional value of the least-square fit from the total velocity. Due to the fact, that the PIV pictures were recorded phase-fixed, it is possible to compare for the same row several PIV recordings of one case of excitation. Figure 6b shows together the curves of u' over R for n=7 PIV recordings. During the data analysis n ranged between 5 and 20. For each measuring point it is now possible to calculate out of the number of n values of u' a statistical velocity fluctuation $\overset{+}{u'}$. Figure 6c presents finally the curve of $\overset{+}{u'}$ over R. In the last step the program calculates

always over the range of one wavelength λ_x a spatial rms-value. Due to the periodical behaviour of the instability development in space and time and furthermore the assumption that the increase or decrease of the amplitude over one wavelength is sufficiently low, it is proper to compare a spatial rms-value obtained for a certain spatial domain with a temporal rms-value obtained at one point within this domain.

3.3. PIV vs. hot-wire

For the fundamental transition type Figure 7a shows for a peak-plane (p) the curves of spatial rms-value ($\tilde{u}_{rms}$, PIV data) and temporal rms-value u_{rms} (hot-wire data) along R. The excitation level was SPL=108.6 dB. Additionally, the curve of $\tilde{u}_{rms}$ (PIV data) along R for a valley-plane (v) can be seen.

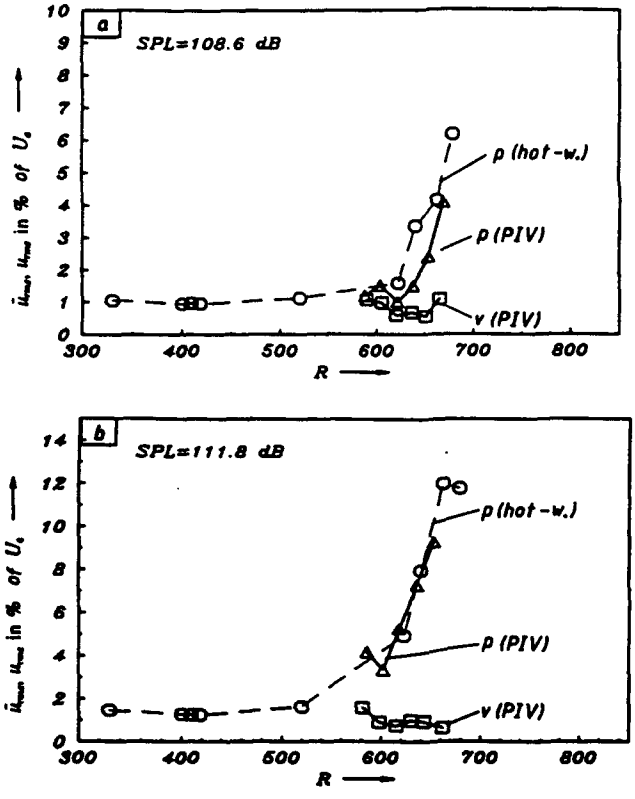

Fig. 7 Comparison of spatial rms-value ($\tilde{u}_{rms}$, obtained from PIV data) with temporal rms-value (u_{rms}, obtained from hot-wire measurements) along R, fundamental transition type, a) SPL=108.6 dB, b) SPL=111.8 dB

Respecting to the peak-plane one can see that both measurement techniques manifest the rapid increase of the rms-value at nearly the same Reynolds number (R=620). At this Reynolds number the onset of splitting in peak-valley-planes becomes evident. In the following $\tilde{u}_{rms}$ deviates in the worst case 35 % from u_{rms}. For a higher excitation level (SPL=111.8 dB) presents Figure 7b a good agreement between both curves in the peak-plane. However, due to missing values at lower Reynolds numbers it is not possible to say something about the beginning of the steep slope of the curve for the spatial rms-value. Further results, which are not presented here, showed that for an excitation level of SPL=114.3 dB the amplitude growth over one wavelength is considerable large, so that the used assumption could not be longer valid. Thus, for this case it makes no longer sense to calculate spatial rms-values out of the PIV recording.

3.4 PIV vs. calculations

Figure 8 shows the curves of $\tilde{u}_{rms}$ over R for peak- and valley-plane obtained from PIV data and a Numerical Simulation (NS). The excitation parameters are the same as in Figure 7a. The starting-conditions and information about the size of the calculation-box were taken from the experiment. In spite of the fact that the corresponded curves in peak- and valley-plane show partly some large deviations from each other, there is qualitative the same behaviour distinguishable in the instability development of experiment and theory. However, the main purpose of this comparison was to get information from the Simulation about the amplitudes of the three-dimensional disturbances, which were completely unknown in the experiment.

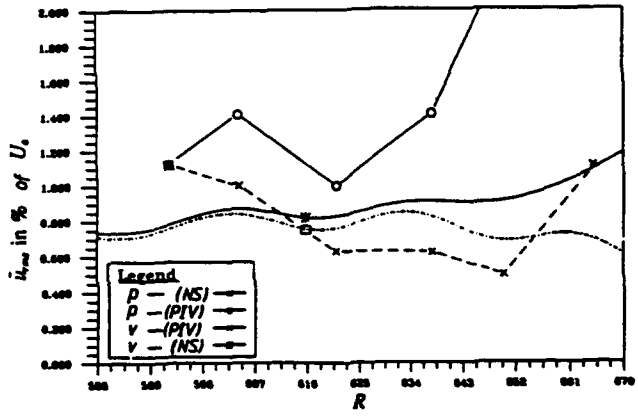

Fig. 8 Spatial rms-value ($\tilde{u}_{rms}$) along R obtained from PIV data and calculations, fundamental transition type, SPL=108.6 dB

4. ACKNOWLEDGEMENTS

The PIV measurements of the development of instabilities in the boundary layer have been carried out in a pleasant team-work together with Dr. Kompenhans, Dr. Raffel and Dr. Vogt. Moreover the author would like to express his gratitude to Dr. Kleiser and Dipl.-Ing. Wintergerste for performing the Numerical Simulation. I would also like to thank Mr. Kühne for his support at the post processing of the PIV recordings.

7. REFERENCES

Adrian, R.J. 1991, Particle-Imaging Techniques for Experimental Fluid Mechanics, Ann. Rev. Fluid Mech., vol. 23, pp.261-304.

Ehrenstein, U. 1987, Rechenprogramm DFVLR-LISA-T, DFVLR-IB 221-87 A12.

Fischer, M., Raffel, M., Vogt, A. & Kompenhans, J. 1993, Combined PIV and visualization experiments on instabilities in a flat plate boundary layer with zero pressure gradient, SPIE

Proc. Optical Diagnostics in Fluid and Thermal Flow, San Diego, vol. 2005, pp.448-456, moreover to be published in Optical Engineering, April 1994.

Kleiser, L. & Zang, T.A. 1991, Numerical simulation of transition in wall-bounded shear flows, Ann. Rev. Fluid Mech., vol. 23, pp.495-537.

Kompenhans, J., Raffel, M., Vogt, A. & Fischer, M. 1993, Aerodynamic investigations in low and high speed wind tunnels by means of Particle Image Velocimetry, ICIASF93 Record, St. Louis, pp. 46-1--46-5.

Kompenhans, J., Raffel, M., Vogt, A. & Fischer, M. 1994, Investigation of unsteady flow fields in wind tunnels at high flow velocities by means of Particle Image Velocimetry, Proc. I.C.E.F.M., Torino.

Kompenhans, J. & Reichmuth, J. 1987, 2-d flow field measurements in wind tunnels by means of Particle Image Velocimetry, Proc. 6th Int. Congress on Applications of Lasers and Electro-Optics, San Diego.

Lourenço, L.M. 1988, Some comments on Particle Image Displacement Velocimetry, Lecture Series, von Karman Institute for Fluid Dynamics, 1988-06.

Raffel, M. 1993, PIV-Messungen instationärer Geschwindigkeitsfelder an einem schwingenden Rotorblatt, Ph.D. thesis, University of Hannover.

Vogt, A. 1993, Optische Auswertung von Particle-Image-Velocimetry-Messungen im Nachlauf eines quer angeströmten Kreiszylinders, Ph.D. thesis, University of Göttingen.

Flow Measurement of a Two - Phase Fluid around Cylinders in a Channel using Particle Image Velocimetry

Y. A. Hassan, R. S. Martinez, O. G. Philip, and W. D. Schmidl

Department of Nuclear Engineering
Texas A&M University
College Station, TX 77843-3133

Abstract

The Particle Image Velocimetry (PIV) flow measurement technique was used to study both single-phase flow and two-phase flow over cylindrical rods inserted in a channel. First, a flow consisting of only a single-phase fluid was studied. The experiment consisted of running a laminar flow over four rods inserted in a channel. The water flow rate was 126 cm^3/s. Then a two-phase flow was studied. A mixture of water and small air bubbles was used. The water flow rate was 378 cm^3/s and the air flow rate was approximately 30 cm^3/s. Then the data was analyzed to obtain the velocity fields for both experiments.

1. Introduction

One of the major concerns with steam generator operation is the tube vibration caused by turbulent flow buffeting. The vibration can cause wear on the tube joints which may eventually lead to ruptures and leaks. This repair procedure can be very costly. Figure 1 shows a typical U-tube steam generator. To help avoid this problem, experimental data is needed to test the empirical correlations which predict the behavior of the turbulent flow around the cylinders, Blake (1987), Hassan (1991), Wu (1994). The PIV flow measurement technique can be used to acquire that experimental data, Adrian (1991).

The use of the PIV flow measurement technique is an improvement over conventional single sensor methods, such as laser doppler anemometry or hot-wire anemometry, because it offers the opportunity of capturing all the in-plane velocities of a spatial velocity field simultaneously. The objective of this study was

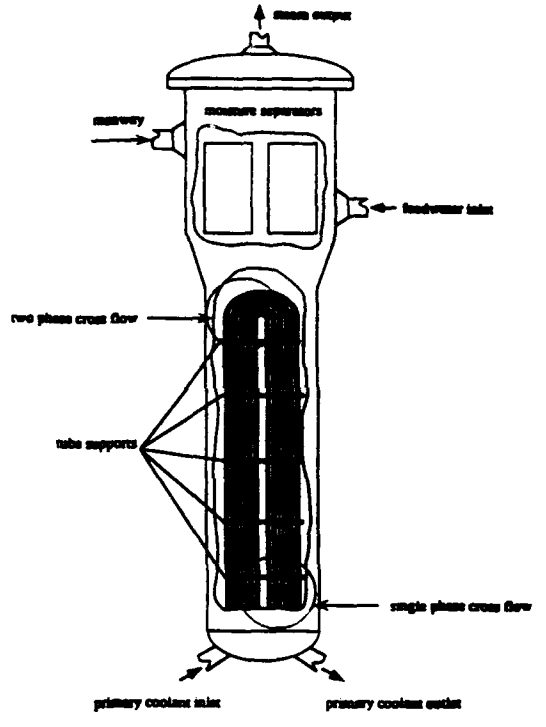

Figure 1. Typical U-tube Steam Generator

to use the PIV technique to study the flow around cylinders in a channel and to find the velocity of both phases in a two-phase flow. This information might be useful for developing or improving computer models which simulate this type of flow field. It may also be useful for understanding the structure of two-phase flows.

2. Experimental setup

The PIV setup for this experiment included two charged coupled device (CCD) cameras, two frame grabber boards, an image

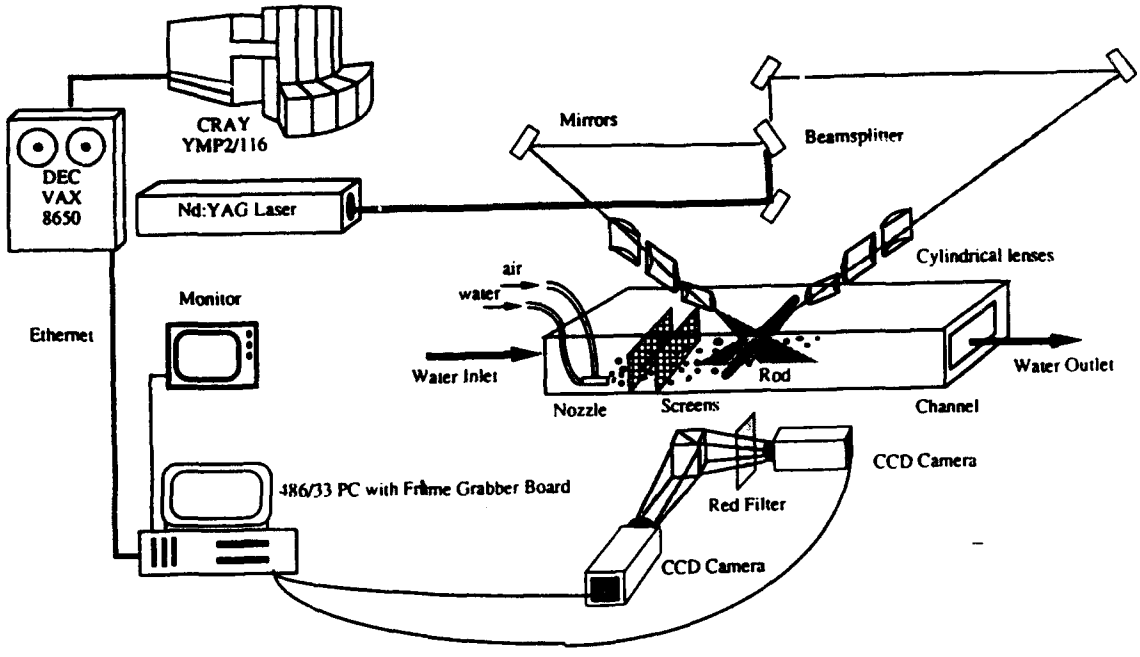

Figure 2. Two-Phase Flow Experimental Setup

intensifier and an Nd-YAG pulsed laser. Figure 2 shows the experimental setup which was used to study the two-phase flow around cylinders in a channel. The setup for the single-phase flow experiment is similar, however, only 1 camera is required. The light source used in the experiment is a frequency doubled Nd-YAG high energy, pulsed laser. The light can be moved into position with high energy mirrors. The light is shaped from a circular beam into a planar sheet with a set of cylindrical lenses, and passed through the moving fluid under study. The lenses shape the light from a 7 mm circular beam into a sheet of light approximately 2 mm thick and 5 cm long.

The Plexiglas channel is 3.05 m long. Its height is 8 cm and its width is 15 cm. The cylindrical rods do not allow light to pass through them. To capture the flow on the far side of the rod, two planes of light were used. This was done by inserting a beam splitter lense in the laser light's path. This was done before the cylindrical lenses.

The first camera was positioned perpendicular to the rod. The second camera was positioned perpendicular to the first camera. A beam splitter prism was used so that both cameras could view the same view plane simultaneously. Fluorescent seeds (fluoresce red when struck by green light) were used in the two-phase flow experiment so they could be differentiated from the air bubbles. A red filter was placed in front of the camera which was capturing the images of the seeds to block the green light reflected by the bubbles. Since the red light which was emitted by the fluorecent seeds was not very intense, an image intensifier had to be used. The camera which acquired images of the bubbles did not acquire images of the seeds because of the low intensity of the light emitted by the fluorescent seeds and the camera's aperture setting. The data from each CCD camera was stored on its respective frame grabber board, before being transferred to hard disk.

The air bubbles for the experiment were generated by positioning a nozzle at the bottom of the channel. The nozzle generated the bubbles by breaking up the inlet flow of air with a stream of water. The flow through the channel consisting of water and entrained air bubbles was then straightened by a set of two screens inserted in the channel. The screens also filtered out the large air bubbles.

The seeds which were used to track the water flow were 6 micron diameter, neutral density (1.02 specific gravity), thermoplastic microspheres for the single-phase experiment. Red fluorescent, 30 micron, neutral density (1.02 specific gravity) microspheres were used for the two-phase flow experiment. Figure 3 shows the flow path of the air bubbles and water around the

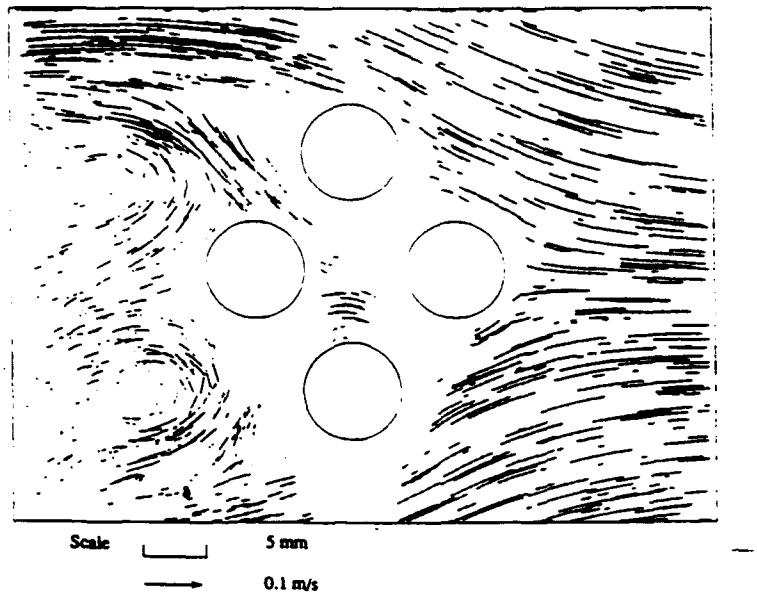

Figure 5. Velocity Vector Track for Single Phase Flow Experiment

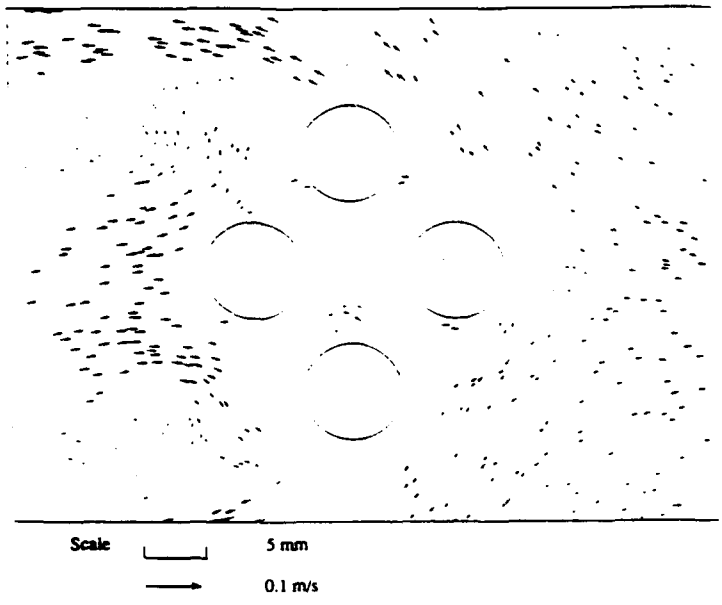

Figure 6. Velocity Vector Track for Single Phase Flow Experiment with 0.65 of Mean Velocity Frame of Reference

water moving around the single cylinder from the two-phase flow experiment (captured by the camera which acquired only the seeds). Figure 9 shows the movement of the air-bubbles around the single cylinder from the two-phase flow experiment (captured by the camera which acquired only the bubbles). The water flow was 378 cm^3/s and the air flow was estimated to be 30 cm^3/s. The results from the experiment showed that the average velocity of both the air bubbles and the water was approximately 0.05 m/s.

4. Conclusion

This study showed that a two-phase

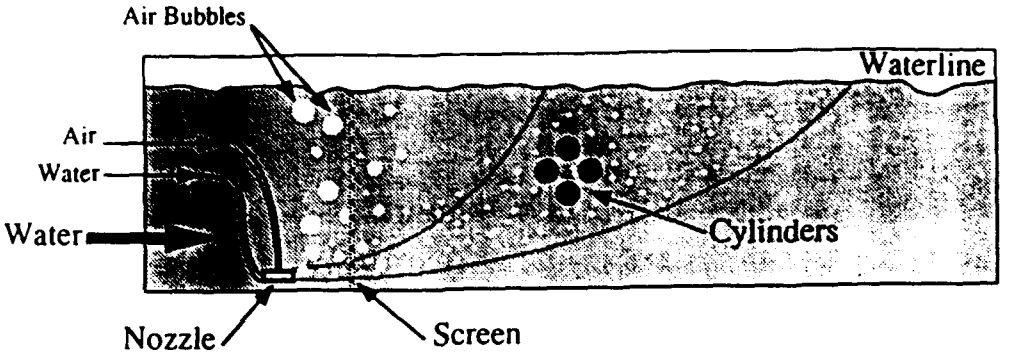

Figure 3. Two-Phase Flow Experiment

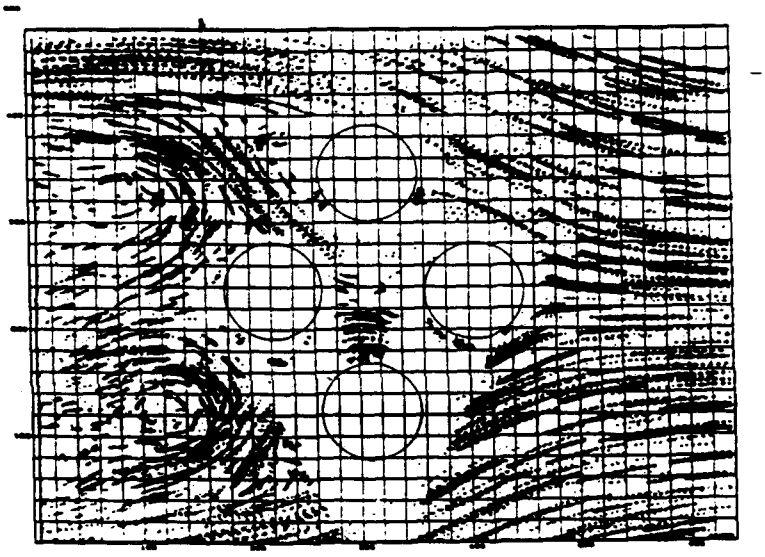

Figure 4. Single-Phase Flow Experiment Binary Overlay

cylinder in the channel.

The data for the experiment was acquired by first establishing a steady flow through the channel. Then the data acquisition sequence was triggered from the computer. The data set was stored to the hard drive of the computer. Then the next set of data was captured.

3. Results

Once the data is acquired, the first step is to convert the gray scale data images to binary images. This was done with a local threshold. Figure 4 shows an overlay of 13 binary images (one dataset) from the single-phase flow experiment around 4 rods. The tracks of the seeds around the rod are clearly visible. There are two recirculation regions behind the rods (an upper and a lower). Then the binary image is converted into an array of tracers by combining the spots in the binary image. This array is input into a tracking algorithm, to produce the velocity vectors, Hassan (1992).

Figure 5 shows the velocity vectors from the movement around the four cylinders in the single-phase experiment. The recirculation regions are visible behind the cylinders. Figure 6 was produced by subtracting 0.65 of the mean velocity from all the vectors in the flow field to enhance the region behind the cylinders. Figure 7 is a plot of the vorticity of this flow field. The water flow rate was 126 cm^3/s. The results from the experiment showed that the average velocity of the water was approximately 0.01 m/s.

Figure 8 shows the velocity field of the

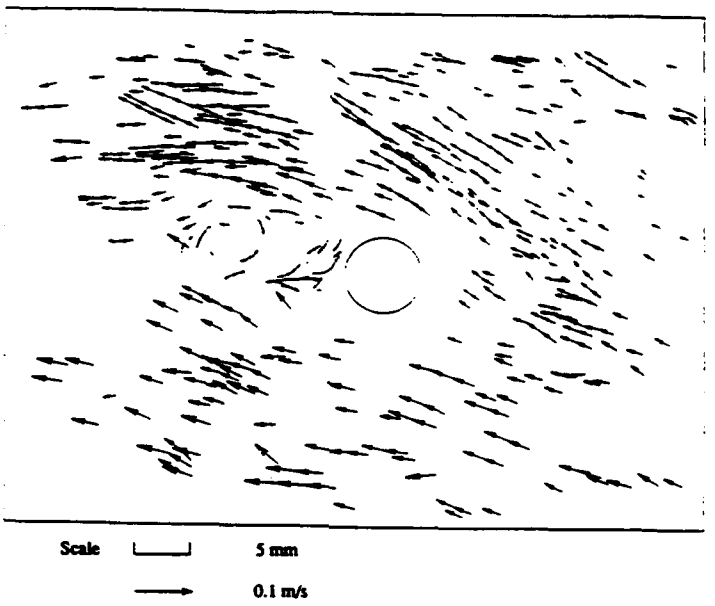

Figure 9. Two-Phase Flow Velocity Vector Track - Air Bubbles

bubbly flow around a cylinder in a channel can be effectively studied using the PIV flow visualization technique. The technique can be used to obtain the velocity field from this type of flow field.

References

Adrian, R.J. 1991, Particle-Imaging Techniques for Experimental Fluid Mechanics, Ann. Rev. Fluid Mech., vol. 23.

Hassan, Y.A. & Canaan, R.E., 1991, Full-field bubbly flow velocity measurements using a multiframe particle tracking technique, Experiments in Fluids, 12,pp. 46-60.

Blake, J. & Gibson, D., 1987, Cavitation Bubbles Near Boundaries, Ann. Rev. Fluid Mech., Vol. 19, pp.97-123.

Wu, J.; Sheridan, J. & Soria, J., 1994, An Investigation of Unsteady Flow Behind A Circular Cylinder Using A Digital PIV Method, ASME FED Summer Meeting.

Hassan, Y.A; Blanchat, T.K. & Seeley, C.H., 1992, PIV Flow Visualization Using Particle Tracking Techniques, Measurement Science and Technology, vol.3 , p. 633-642.

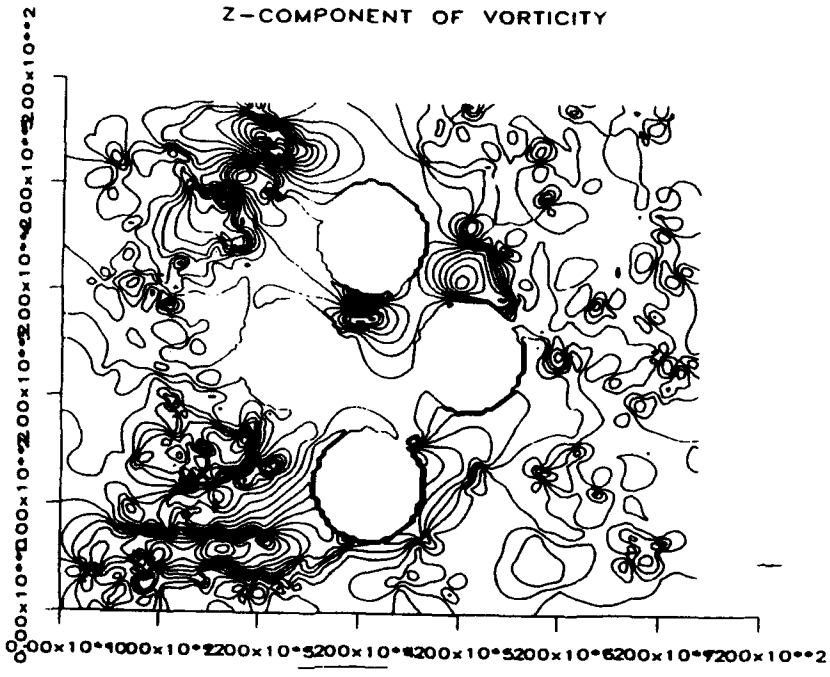

Figure 7. Vorticity Plot of single Phase Flow Experiment

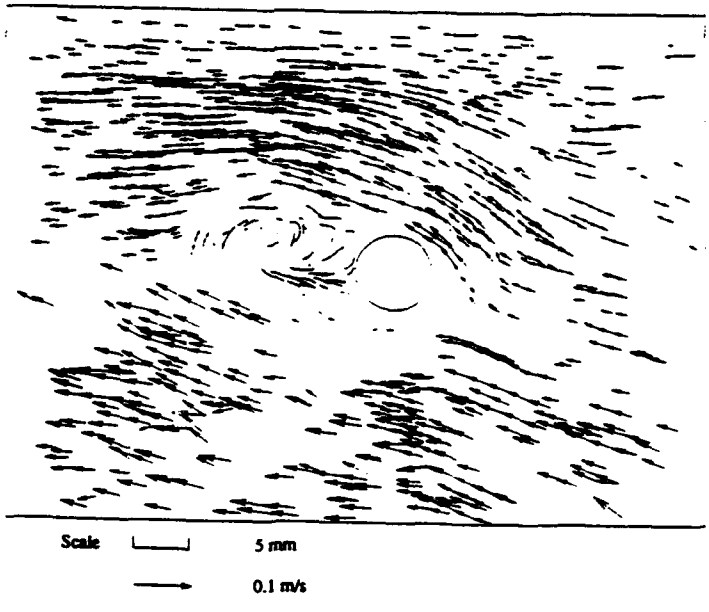

Figure 8. Two-Phase Flow Velocity Vector Track - Water

Session 38.
Aerodynamics

EXPERIMENTAL STUDY OF THE DYNAMIC STALL PROCESS ON A PITCHING AIRFOIL BY MEANS OF PIV MEASUREMENTS AND LASER-SHEET VISUALIZATIONS

P. Wernert, G. Koerber, F. Wietrich
French-German Research Institute of Saint-Louis (ISL)
5, rue du Général Cassagnou, BP 34, F-68301 Saint-Louis, France

M. Raffel, J. Kompenhans
Deutsche Forschungsanstalt für Luft- und Raumfahrt (DLR)
Bunsenstraße 10, D-37073 Göttingen, Germany

ABSTRACT

The unsteady flowfield above a NACA 0012 airfoil pitching under deep dynamic stall conditions has been investigated in a low-speed wind tunnel by means of Particle Image Velocimetry measurements and laser-sheet visualizations. The PIV results show the occurrence of small-scale structures in the separated flowfield and even within the dynamic stall vortex for increasing incidences, and the complex flow behaviour during the downstroke regime. Due to the finite shutter speed of the video camera, the visualization technique cannot record such structures: instead, we obtain a large-scale vortex rolling up in the upstroke. Thus it is seen that PIV allows to better analyze the qualitative visualization pictures obtained when investigating unsteady separated flowfields.

1. INTRODUCTION

Because of the requirement of increased performance and maneuverability, unsteady separated flow phenomena have received, in recent developments of aircraft technology, a great deal of attention. In the particular case of a helicopter in high-speed forward flight, the retreating rotor blades experience a combination of high incidences and low velocities of the oncoming freestream, so that an unsteady stalled flowfield can be obtained over the blade. It is of course of great importance to be able to characterize the flow phenomena involved in this flight configuration.

It has been very soon noticed that the basic effects of this stalled flow could be reproduced in a realistic way by simulating a two-dimensional sinusoidally pitching airfoil (McCroskey and Fisher 1972).This simplification has led to numerous experimental investigations (for example Carr et al. 1977) which have shown the relation between the main features observed on the lift and pitching moment curves (delay of stall to higher incidences and much higher maximum values with respect to the steady case) and the formation, development and subsequent shedding of an organized vortex structure on the airfoil: this phenomenon is widely known under the term "dynamic stall" (McCroskey 1981).

Most of these experimental results were obtained by qualitative flow visualizations and quantitative pressure measurements. The velocity field over a pitching airfoil has also been explored by means of hot wires (De Ruyck and Hirsch 1984) and most recently, by use of the Laser Doppler Anemometry (LDA) technique (Wernert et al. 1992a). However, to study the mechanisms involved in such an unsteady flow, it would be better to have instantaneous data about the whole velocity field at one's disposal: therefore, a global method such as the Particle Image Velocimetry (PIV) technique seems to be best suited.

The purpose of the experiments reported here is to characterize the unsteady separated flowfield over a pitching airfoil oscillating under deep dynamic stall conditions: for this, both PIV and laser-sheet visualization techniques are used.

2. EXPERIMENTAL FACILITY

2.1 Wind Tunnel and Airfoil

The experiments were conducted in the ISL low-speed wind tunnel, described by Jaeggy (1982). This tunnel has an open and rectangular test section of 70 cm width, 90 cm height and 80 cm length. The freestream turbulence is less than 0.25 %.

The airfoil had a NACA 0012 profile of c = 20 cm chord and 56 cm span. It was mounted between two circular end plates of plexiglass (diameter 40 cm) in order to assure a two-dimensional flow in the vertical center plane of the test section. The airfoil oscillated around an axis at 25% chord from the leading edge.

2.2 Driving Mechanism

The airfoil motion to be investigated is provided by a novel system (Wernert et al. 1992b) which includes an automated apparatus (Asea Brown Boveri type Procontic T300) that can be programmed by the user, two variable speed drives, each controlling a brushless motor (this system has been designed to produce two kinds of motions: pitching and heaving motions) and a support system, essentially adapted to transmit the motions from the motors to the airfoil by means of mechanical parts such as: rotating arms, cardans, driving belts, etc (see Fig. 1).

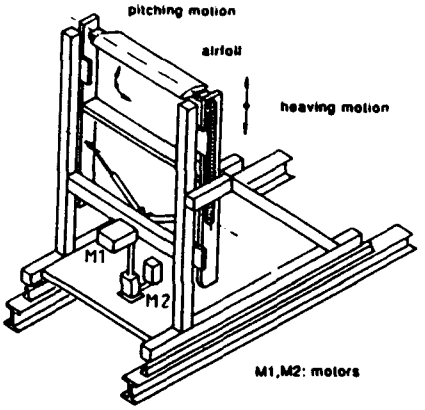

Fig. 1: Schema of the airfoil driving mechanism

The control of these motions is made by comparison of the actual angular position of the motors and the value computed by the automated apparatus. The angular positions of the motors, the pitching incidence and the heaving position of the airfoil are given by incremental rotary and linear encoders. The accuracy of these encoders is respectively 0.09° and 5 µm .

The airfoil motions are programmed on the basis of a point-by-point procedure which allows a large domain of motions to be investigated. Thus, it is possible to obtain periodic motions (harmonic, sawtooth or more complex motions) or transient motions (steps, ramps) with maximal frequency of 15 Hz for pitching motions and 7 Hz for heaving motions. Of course, inertial effects of the mechanical parts limit the actual amplitude and complexity of the motions when frequency increases or rise time decreases.

3. LASER-SHEET VISUALIZATIONS

A complete laser-sheet visualization setup has been installed: it is composed of a continuous argon laser (power used: 3-4 W), a few mirrors in order to lead the laser beam to the top of the wind tunnel test section and finally, a cylindrical and a converging lens which expand the beam into a vertical plane about 1 mm thick, located at airfoil midspan.

Vaporized oil particles were injected in the flow, about 20 cm upstream from the airfoil leading edge.

The airfoil was painted in black to avoid light reflections; white marks were also drawn on the airfoil suction side (at midspan) in order to estimate easily the chordwise location of the vortex structures.

Pictures were taken with a video camera (Sony TR-808) operating at the standard frequency of 25 pictures per second. One important parameter to be defined was the camera shutter speed; a compromise had to be found between a high shutter speed (i.e. a short recording time) in order to freeze the vortex development on the pictures and a low shutter speed (i.e. a longer recording time) to have enough light scattered by the seeded particles: the chosen time was finally 1 ms.

It was also necessary, for a relevant comparison with the PIV results, to obtain visualization pictures at as many incidences as possible; because of the periodicity of both the camera (one picture every 40 ms) and the airfoil motion (period of 150 ms), it appeared that after 4 complete periods (600 ms), the pictures were again taken at the same phases of the airfoil motion. Therefore, we had to take several sequences with interruption of the camera between successive sequences in order to get pictures at random phases of the airfoil motion. With this operating procedure, it became possible to obtain several hundreds of pictures taken at different phases of the airfoil motion.

Of course, it was also essential to know the airfoil incidence for each recorded video frame: therefore, a display system showing the instantaneous incidence of the airfoil measured by an incremental rotary encoder was mounted near the airfoil, in the sight field of the camera; a synchronization system based on the camera output video signal was developed (see Fig. 2) in order to freeze the incidence value displayed at the instant when the CCD-sensor of the camera begins to record the picture. This system allowed us to know the instantaneous incidence of the airfoil for each picture with an accuracy of 0.01°.

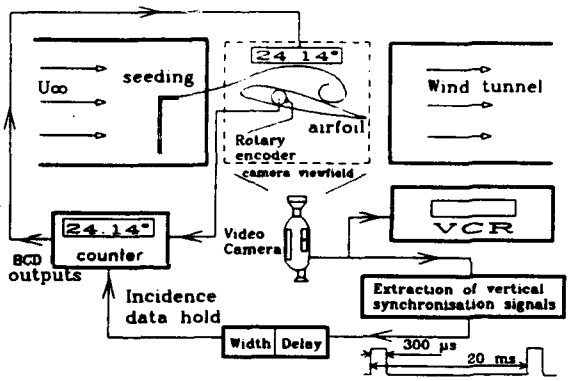

Fig. 2: Simplified schema of the accurate incidence measurement during visualizations

The recorded pictures were then digitized and image processing techniques were employed for two purposes: firstly, to improve the contrast of the pictures by using spatial filters and secondly, to rearrange them in order to obtain a video movie.

All the aspects of the laser-sheet setup, procedure of pictures recording, accurate incidence determination and image processing are described in detail by Wernert et al. (1994).

4. PARTICLE IMAGE VELOCIMETRY SYSTEM

During the last years a PIV system has been developed at DLR, which can be operated under the rough environmental conditions of wind tunnels (Kompenhans et al. 1993 and Fig. 3).

A double oscillator Nd:YAG pulse laser is used for illumination (Kompenhans and Höcker 1988). The output energy is 70 mJ (for each pulse) at 532 nm, the pulse length 20 ns. Typical time delays between the two pulses range from 10 µs to 14 µs for these experiments.

The output energy of our laser was sufficient to illuminate a sheet of 20 cm height and 29 cm length, when using a photographic system with an f-number of 2.8 and a Kodak TMAX 3200 recording material.

The tracer particles have been generated by means of several Laskin nozzles in parallel (Hunter and Nichols 1985): pressurized air, injected in olive oil, leads to the formation of small oil droplets. The aerosol generator was located outside the tunnel. It was connected by a pipe to a specially developed low-disturbance ejection device for homogeneous seeding density, which was mounted in the settling chamber of the tunnel. The mean diameter of the tracer particles (olive oil), measured at the exit of the Laskin nozzle by means of a particle analyzer (Polytec HC-15), is 1.06 µm (Schäfer 1993).

Due to the diffraction limited imaging of the 1 µm tracer particles, the depth of focus could decrease to less than 1 mm (Adrian 1991). In order to save time when aligning the system, the photographic 35 mm camera is equipped with a device for fast focusing (Towers et al. 1991): a CCD sensor has been mounted in the viewfinder of the photographic camera. The position of the CCD sensor is carefully aligned in such a way that the distance between lens and CCD sensor via the mirror is exactly the same as from the lens to the the film plane. The distance between light sheet and film plane can be changed by moving the complete camera system by means of a traversing table.

An image shifting system is necessary in order to be able to investigate flow fields containing reversal flow regions and to adapt the velocity range to the range of optimal evaluation. The high-speed rotating mirror system which was used (Raffel 1993) allowed a high velocity shift without noticeable degradation of the optical quality of the PIV recordings. It consists of the following components: a carefully balanced shaft mounted in a precision bearing, with a mirror mount attached to one end of the shaft and an optical encoder fixed to the other end. The rotating mirror is driven by a stepper motor, which leads to stable rotation frequencies from 1 to 100 Hz. This results in a range of shift velocities from -500 m/s to +500 m/s calculated with the typical distance R = 0.4 m from the observation field to the mirror.

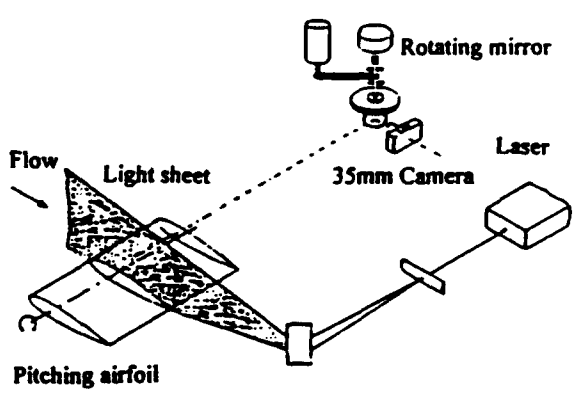

Fig. 3: Experimental PIV setup with pitching airfoil, pulse laser and high-speed rotating mirror system.

The evaluation of the photographic PIV recordings is performed by means of the standard analog-optical / digital method, i.e. by means of the digital Fast Fourier Transform of Young's fringes pattern. The location of the peaks in the 2D autocorrelation plane is determined by means of the grey value weighted 'center of gravity method', applying a variable threshold for clipping in such a way that the area covered by the peaks matches a pre-defined value.

After the automatic evaluation of the PIV recordings a certain number of obviously incorrectly determined velocity vectors can usually be found by visual inspection of the raw data. In order to get rid of these incorrect data the raw flow field data have to be validated. For this purpose special algorithms have to be developed, which must also work automatically (Raffel et al. 1992). It should be emphasized that for all PIV results presented in this paper only this validation algorithm has been applied after automatic evaluation. No smoothing (e.g. by means of gaussian filters or interpolation of missing data) has been carried out.

The absolute overall accuracy of this PIV system depends on many parameters and has to be checked separately for each experiment. No simple method is available to do this: however, it is possible to give a relative accuracy for the present system from other investigations in low turbulence flows: spatial turbulent structures in a flow field with a degree of turbulence of 0.6% as measured by means of a hot wire, could be obtained (Kompenhans et al. 1993). The error sources in PIV investigations are further discussed by Raffel et al. (1992).

The PIV recordings were taken during the upstroke and the downstroke motions of the model in intervals of 1°. Because of the limited pulse rate of the Nd:YAG laser and the performance of the winder of the photocamera (about one picture/second), it was not possible to record the flowfields at many different angles of incidence within one oscillation of the airfoil: therefore, the records were taken in successive cycles, leading to the problem of reproducibility mentioned later.

During the experiments the rotation of the mirror and the pulse rate of the laser were controlled by means of a high-precision pulse generator. This pulse generator was driven with a frequency which was an integer multiple of the frequency of the driving mechanism of the airfoil. Both systems were running in a very stable way. Thus, it was possible to obtain e.g. 6 PIV recordings within about 6 seconds at exactly the same phase of the pitching motion (with each record being taken out of a different cycle), although the absolute value of the incidence could not be measured very accurately. The system was then adjusted to the next pitching angle in a step-by-step procedure.

5. RESULTS AND DISCUSSION

5.1 Airfoil Motion

The selected airfoil motion for this investigation had the following incidence law:

$$\alpha(t) = 15° + 10° \sin 2\pi ft$$

with a frequency f = 6.67 Hz. The freestream velocity

was U_∞ = 28 m/s corresponding to a Reynolds number, based on chord length, of 373000. These values led to a reduced frequency

$$\omega = \frac{2\pi fc}{2U_\infty} = 0.15 \ .$$

The incidence variation of ± 10°, the mean incidence of 15° and the above-mentioned value of reduced frequency correspond to the "deep stall" case according to the description given by McCroskey (1981): thus strong unsteady effects can be expected.

5.2 Presentation of the Results

In order to be able to follow the evolution of the dynamic stall process during a whole cycle, both PIV velocity fields and visualization pictures are shown for nine different phases of the airfoil motion (Fig. 4a to 12b). The flow direction is from left to right. As the video and photographic camera were not exactly located at the same place, a slight parallax effect can occur when comparing the results.

The visualization pictures cannot be considered to be instantaneous ones because of the finite camera shutter speed (i.e. 1 ms) : therefore it is essential to know the incidence interval described by the airfoil during the recording time of 1 ms. By measuring the incidence of the airfoil when the CCD-sensor of the camera begins to record a picture (this value is indicated on the visualization pictures) and knowing the incidence law of the airfoil oscillation, it is easy to calculate the incidence when the CCD-sensor stops the recording of the picture concerned. These two incidences are noted for each visualization picture. The presence of the end plates can also be noticed on these pictures.

It is also necessary to state that the undisturbed freestream is directed 15 ° upwards for the PIV pictures, due to the position of the photographic camera (15 ° is the mean airfoil incidence). For visualization pictures, the freestream is horizontal.

5.3 Comparison of PIV and Visualization Pictures

In general, a good agreement is found between these two sets of data. The basic flow structures are respected: attached flow at low incidences (Fig. 4a and 4b), formation and development of the dynamic stall vortex during upstroke (Fig. 5a to 7b), complex interactions of vortices during downstroke (Fig. 8a to 11b) and finally, reattachment from the leading edge (Fig. 12a and 12b).

However, three phases of the dynamic stall process should be commented: firstly, figures 4a and 4b show a thin layer without seeded particles on the airfoil surface although the flow is fully attached: this can be related to the existence of a "thin reversal flow layer" which is characteristic of unsteady flows (Telionis 1981) and which has been reported in many investigations on dynamic stall (see Carr et al. 1977).

Secondly, the small-scale vortex structures seen on the PIV results are not observed on the visualization pictures. For increasing incidences (Fig. 5b, 6b and 7b), we have instead streaklines showing a large-scale vortex rolling up. These streaklines are recognized to form the separation line between the "external" undisturbed flow and the "internal" dynamic stall vortex. The absence of small-scale vortex structures on the visualization pictures is due to an "integration effect" that can be related to the finite shutter speed of the video camera (1 ms as compared to about 10 µs for PIV measurements). It appears here that a low shutter speed can lead to a too simplified interpretation of this flow phenomenon when the laser-sheet technique is used alone. A higher shutter speed should therefore be used, although more laser energy is required.

The third main difference is obtained for high increasing and decreasing incidences, when the flow remains fully separated over the airfoil: the flow structures observed on both PIV and visualization pictures are not exactly the same. This can be explained by small discrepancies in incidence between the two data sets (it must be remembered that the incidence of the PIV records could not be measured very accurately) and by the fact that the flow is very unsteady (compare Fig. 7a and 7b). Another explanation is related to the problem of reproducibility of this flow phenomenon. The PIV and visualization pictures were not taken at the same time but in successive wind-tunnel runnings: thus, comparing these two kinds of results presupposes that the dynamic stall events are the same for successive cycles, i.e. the process is perfectly reproducible. In fact, the 6 PIV records and the numerous visualization pictures taken for each incidence showed pronounced differences between cycles, for angles of attack greater than 24° on the upstroke and during the complete downstroke part of the airfoil motion : a similar result was established by Shih et al. (1992). This problem is also of importance when trying to make a video movie from visualization pictures taken at different cycles of the airfoil motion. A more detailed discussion is given by Raffel et al. (1994).

5.4 Remark on the PIV Results

Lastly the high quality of the PIV pictures should be emphasized: small-scale vortices can be recognized even within the dynamic stall vortex. However a lack of velocity vectors is observed in some critical flow regions (airfoil surface, leading and trailing edges): this can be explained by the limitations of the experimental techniques (low light intensity at the field boundaries) and by the non-optimal distribution of particles due to aerodynamic phenomena (existence of thin reversal flow regions on the airfoil, possibility of strong velocity gradients within the interrogation spot, possibility of strong three-dimensional velocity components). As these three areas (airfoil surface, leading and trailing edge regions) are essential to the complete understanding of the dynamic stall process, further improvements are required to quantify these missing regions.

6. CONCLUSIONS AND PERSPECTIVES

The unsteady flowfield above a NACA 0012 airfoil pitching under deep dynamic stall conditions has been investigated in a low-speed wind tunnel by means of Particle Image Velocimetry measurements and laser-sheet visualizations. The PIV results have been seen to be of high quality, although velocity data were missing in some critical flow regions.

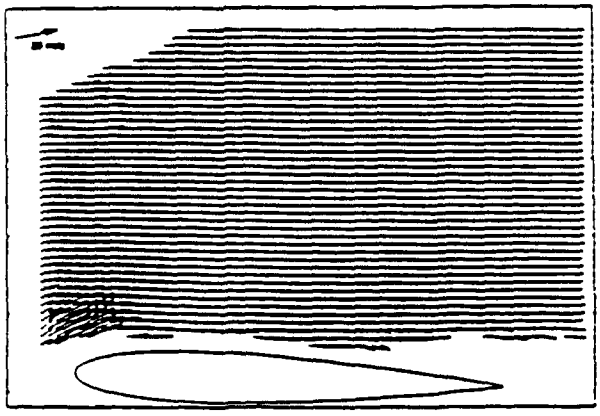

Fig 4a: $\alpha = 17°$ (upstroke)
PIV picture

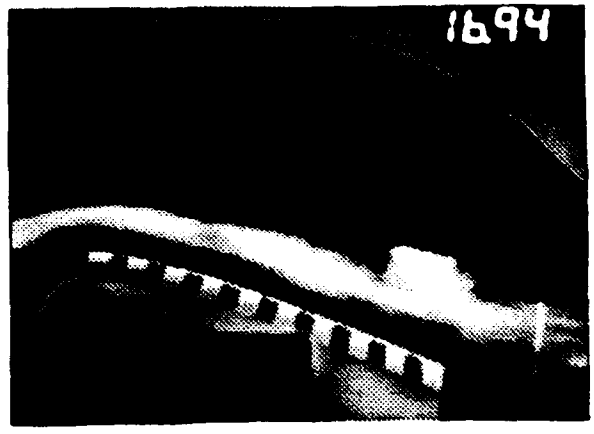

Fig 4b: $16.94° < \alpha < 17.34°$ (upstroke)
Visualization picture

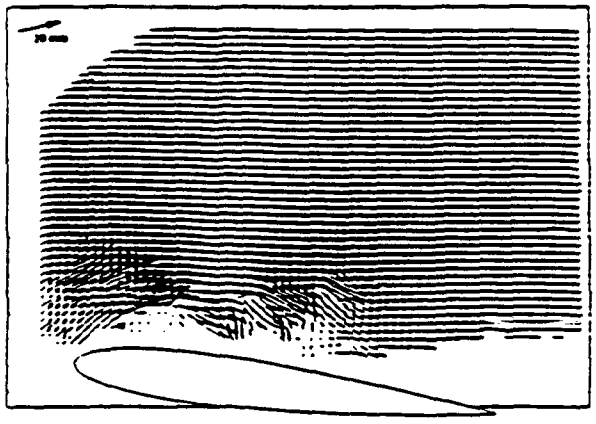

Fig 5a: $\alpha = 22°$ (upstroke)

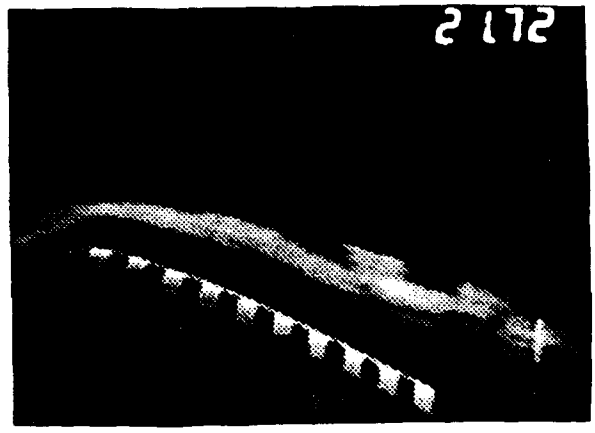

Fig 5b: $21.72° < \alpha < 22.02°$ (upstroke)

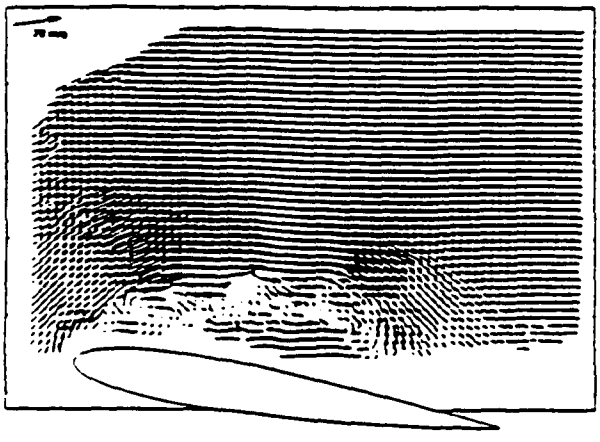

Fig 6a: $\alpha = 24°$ (upstroke)

Fig 6b: $23.33° < \alpha < 23.55°$ (upstroke)

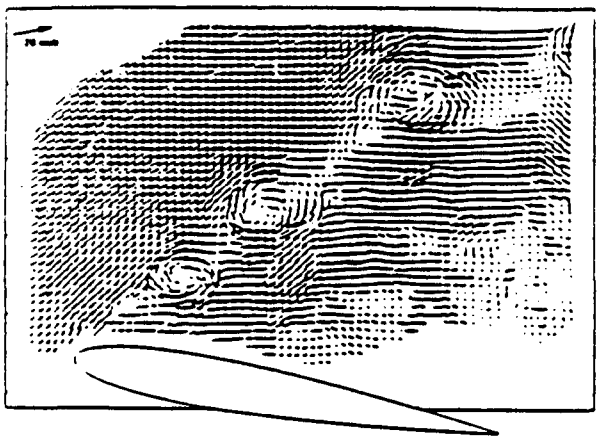

Fig 7a: $\alpha = 25°$

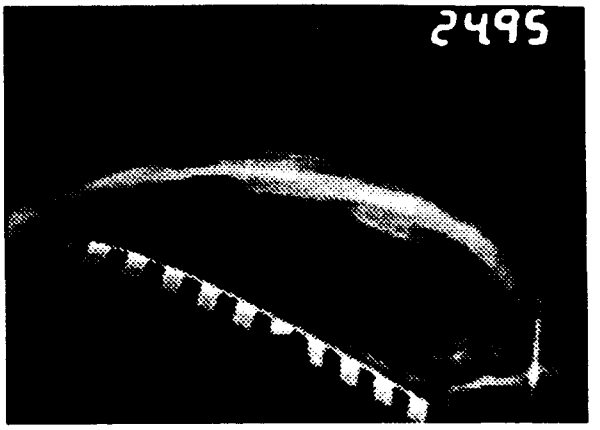

Fig 7b: $24.95° < \alpha < 24.98°$ (upstroke)

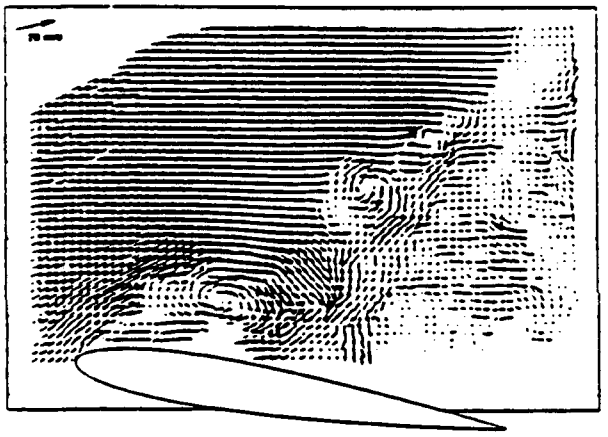

Fig 8a: $\alpha = 24°$ (downstroke)

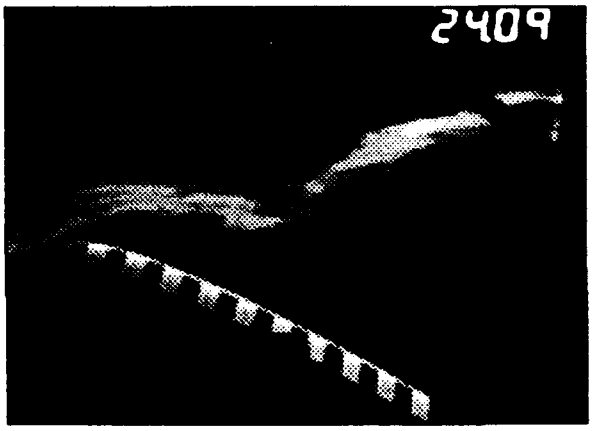

Fig 8b: $24.09° < \alpha < 23.90°$ (downstroke)

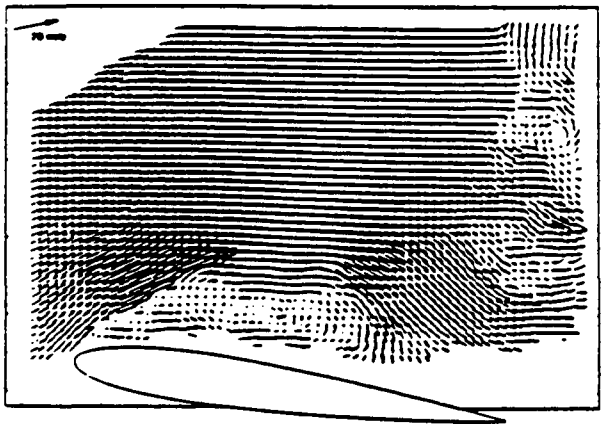

Fig 9a: $\alpha = 23°$ (downstroke)

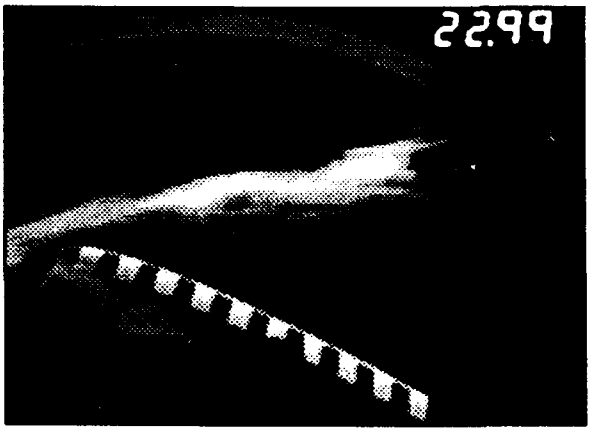

Fig 9b: $22.99° < \alpha < 22.73°$ (downstroke)

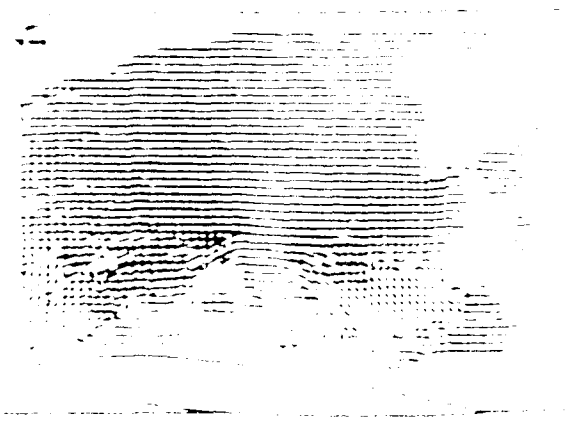

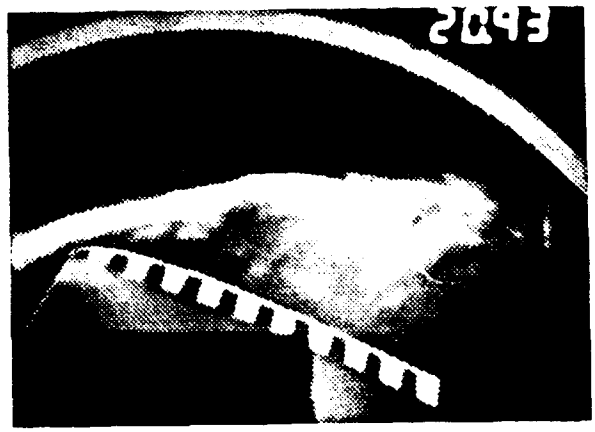
2093

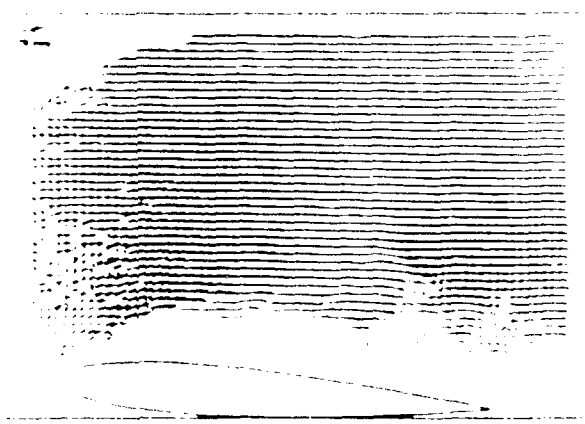

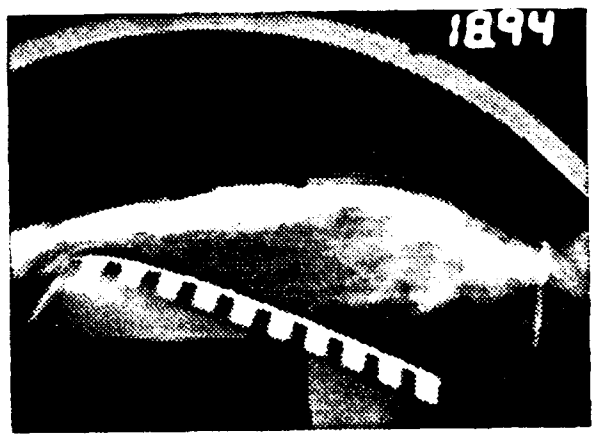
1894

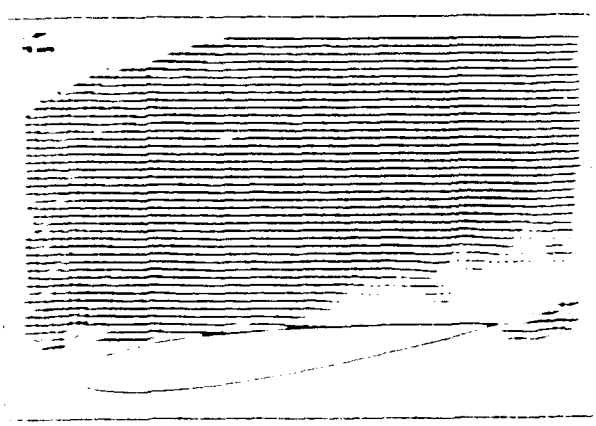

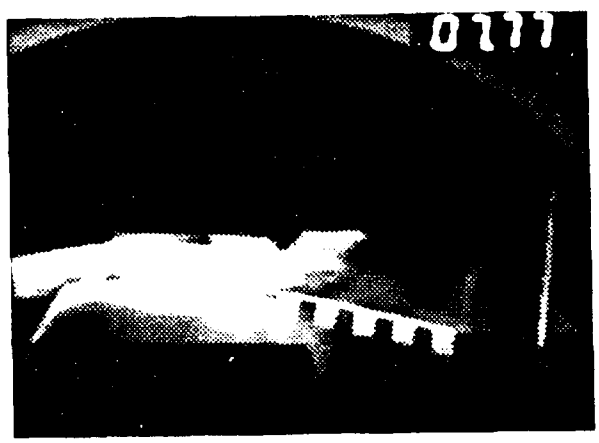
0777

The differences observed between PIV and visualizations pictures have been related to the exposure time of the recording systems, to the discrepancies in airfoil incidences and to the problem of reproducibility of the flow phenomenon. A higher shutter speed for visualizations and a better incidence measurement system for PIV should be used in future experiments. The problem of reproducibility of the flow phenomenon should also be investigated.

ACKNOWLEDGMENTS

The authors would like to thank Dr. Schäfer (ISL) for his support in organizing the cooperative measurements, Mr. Köneke (ISL) for his work on the digitized visualization pictures, Mr. Seyb (DLR) for his help during the PIV measurements, Dr. Bretthauer (DLR) for his assistance during the phase of evaluation of the PIV records and Dr. Geissler (DLR) for helpful discussions on the dynamic stall problem.

REFERENCES

Adrian, R.J. 1991, Particle-Imaging Techniques for Experimental Fluid Mechanics, Ann. Rev. in Fluid Mech., vol. 23, pp. 261-304.

Carr, L.W., McAlister, K.W. & McCroskey, W.J. 1977, Analysis of Dynamic Stall Based on Oscillating Airfoils Experiments, NASA TN D-8382.

De Ruyck, J. & Hirsch, C. 1984, Instantaneous Flow Field Measurements of Stalled Regions on an Oscillating Airfoil, AIAA Paper 84-1565.

Hunter, W.W. & Nichols, C.E. 1985, Wind-Tunnel Seeding Systems for Laser Velocimeters, NASA CP 2393.

Jaeggy, B.C. 1982, Description et Caractéristiques de la Soufflerie Subsonique de 70 cm × 90 cm de l'ISL, ISL-Report N 608/82.

Kompenhans, J. & Höcker, R. 1988, Application of Particle Image Velocimetry to High Speed Flows, Particle Image Displacement Velocimetry, Lecture Series 1988-06, Von Karman Institute for Fluid Dynamics, Brussels, pp. 67-83.

Kompenhans, J., Raffel, M., Vogt, A. & Fischer, M. 1993, Aerodynamic Investigations in Low and High Speed Wind-Tunnels by Means of Particle Image Velocimetry, Proc. 15th ICIASF, ISL, Saint-Louis, France, paper 46.

McCroskey, W.J. & Fisher, R.K. 1972, Detailed Aerodynamic Measurement on a Model Rotor in the Blade Stall Regime, J. of the American Helicopter Society, vol. 17, No 1, pp. 20-30.

McCroskey, W.J. 1981, The Phenomenon of Dynamic Stall, NASA TM 81264.

Raffel, M., Leitl, B. & Kompenhans, J. 1992, Data Validation for Particle Image Velocimetry, Proc. 6th Int. Symp. on Applications of Laser Techniques to Fluid Mechanics, Lisbon, Portugal, Paper 30-1.

Raffel, M. 1993, PIV Messungen Instationärer Geschwindigkeitsfelder an einem Schwingenden Rotorprofil, Thesis, Universitat Göttingen, Germany, and DLR Forschungsbericht 93-50.

Raffel, M., Geissler, W., Kompenhans, J. & Wernert, P. 1994, PIV Measurements, Laser-Sheet Visualizations and Navier-Stokes Calculations of the Dynamic Stall Process on a Pitching NACA 0012 Airfoil, submitted for publication to AIAA J.

Schäfer, H.J. 1993, Private Communication, ISL.

Shih, C., Lourenco, L., Van Dommelen, L. & Krothapalli, A. 1992, Unsteady Flow Past an Airfoil Pitching at a Constant Rate, AIAA J., Vol. 30, No 5, pp. 1153-1161.

Telionis, D.P. 1981, Unsteady Separation, in Unsteady Viscous Flows, Springer Series in Computional Physics, chapter 7, pp. 279-404, ed. Springer Verlag, Berlin.

Towers, C.E., Bryanston-Cross, P.J. & Judge, T.R. 1991, Application of Particle Image Velocimetry to Large-Scale Transonic Wind-Tunnels, Optics and Laser Tech., Vol. 23, No 5, pp. 289-295.

Wernert, P., Koerber, G. & Wietrich, F. 1992a, LDA Measurements of the Unsteady Near Wake Behind an Airfoil Undergoing Transient and Periodic Pitching Motions, Proc. 6th Int. Symp. on Applications of Laser Techniques to Fluid Mechanics, Lisbon, Portugal, Paper 13.1 and ISL-Report CO 215/92, 1992.

Wernert, P., Koerber, G. & Wietrich, F. 1992b, A New Experimental Apparatus for the Study of the Unsteady Flowfield over an Airfoil in Pitching and Heaving Motions Using Laser Doppler Anemometry, Proc. European Forum on Wind-Tunnels and Wind-Tunnel Test Techniques, Southampton, UK, Paper 45 and ISL-Report CO 229/92.

Wernert, P., Wietrich, F., Koerber, G. & Köneke, A. 1994, Visualisation du Phénomène de Décrochage Dynamique sur Profil Oscillant: Dispositif Expérimental, Prises de Vues, Mesure Précise de l'Incidence et Traitement d'Images, ISL Report to be published.

EMBEDDED LDA TECHNIQUE APPLIED TO THE BOUNDARY-LAYER SEPARATION MEASUREMENT ON OSCILLATING AIRFOILS

M. PASCAZIO, D. FAVIER and C. MARESCA
Institut de Mécanique des Fluides
Université d'Aix-Marseille II, UM 34 du CNRS
Les Souffleries de Luminy, 163, Avenue de Luminy, 13009 Marseille, France

ABSTRACT

The embedded optical fibre LDA technique used to investigate the boundary-layer behavior on oscillating models, is a powerful tool to characterize phenomena such as transition, separation and reattachment in unsteady flows. To gain a better understanding of the boundary layer response to unsteadiness, previous works from the present group have been focused on the development of an embedded LDA technique, suited for unsteady boundary-layer measurements on an oscillating flat plate model.

In the present paper, such an embedded LDA technique has been extended to boundary-layer measurements around moving curved walls and oscillating airfoils of arbitrary shape. Moreover, the present extension of the embedded measuring technique also includes the determination of the 2D instantaneous velocity profiles (U, V), tangent and normal to the local wall curvature. The following sections present typical data sets illustrating some aspects of the steady and unsteady boundary-layer behavior specially in the case of a fore-and-aft oscillation, including turbulent separation phenomena. It results from these measurements, a steady and unsteady turbulent separation criteria based on the shape factor H.

INTRODUCTION

The determination of the boundary-layer response to unsteadiness produced by the forced motion of an airfoil, requires nowadays additional investigations on basic unsteady flow phenomena, including unsteady separation which plays a major role in a wide range of aeronautical applications see Telionis (1981), Cousteix & Houdeville (1988), Favier & alii (1988). To gain a better understanding of the boundary layer response to unsteadiness, previous works from the present group, see Favier & alii (1990), Favier & alii (1992), Pascazio & alii (1993), have been focused on the development of an embedded LDA technique, suited for unsteady boundary-layer measurements on an oscillating flat plate model. The measurement principle has been based on a LDA optical fibre option using an optical head embedded inside the oscillating flat plate model. The result was a 1D longitudinal velocity measurement in a reference frame linked with the moving wall.

In the present paper, such an embedded LDA technique has been extended to boundary-layer measurements around moving curved walls and oscillating airfoils of arbitrary shape. As described below, the measurement principle then consists in using a different arrangement of the LDA optical fibres option, which is installed outside the airfoil, but always linked with the oscillating frame and thus with the motion law of the model. Morever, the present extension of the embedded measuring technique also includes the determination of the 2D instantaneous velocity profiles (U, V), see Favier & alii (1994), tangent and normal to the local wall curvature.

The present results concern U and V steady and unsteady boundary-layer measurements performed at different distances from the leading-edge of a NACA 0012 airfoil, and for various conditions of frequency, amplitude and incidence of the airfoil oscillating in fore-and-aft motion (oscillation parallel to the freestream direction with a fixed incidence α_0). Specially the U and V instantaneous velocity profiles will clearly exhibit the powerfull efficiency of the embedded non-intrusive technique in investigating non-steady flow problems, such as the unsteady separation and the unsteady reattachment on the moving surface. This study has also provided suited turbulent separation criteria in steady and unsteady flows, based on the shape factor quantity H.

EXPERIMENTAL SET-UP AND MEASUREMENT PROCEDURE

As sketched in Figure 1, experiments are conducted at I.M.F.M. in the S2-Luminy subsonic wind-tunnel (rectangular cross section : 0.5 x 1.0 m^2 , length : 3m ; velocity $U_\infty \leq 20$ ms^{-1}), by means of an oscillating device located under the wind-tunnel test section. The NACA 0012 airfoil is supported in a vertical position and attached to the oscillating frame by means of a support shaft located at the quarter chord axis. Different kinds of airfoil motions can be simulated : fore-and-aft, plunging, pitching and fore-and-aft coupled to pitching, see Favier & alii (1988).

The airfoil is 30 cm in chord, 49.5 cm in span and 3.6 cm in thickness. As shown in Figure 2, the optical head is mounted on a supporting turntable which is attached to the oscillating frame. The optical head is equipped with a beam-expander to increase the focal distance to f = 400 mm, so that the laser beams are focused at mid-span in the boundary-layer through a 45° mirror. Due to the fact that the supporting turntable is linked with the oscillating frame the U and V velocity profiles are directly obtained in the reference frame in relative motion. Moreover, the optical head is also

installed on a 2D-displacement device mounted itself on the turntable. This teledriven system allows the adequate positionning of the measurement volume at any point of the airfoil surface (30 cm of chordwise displacement). A teledriven angular sector (from 0° to 360° by step of 0.1°) provides the selection of the surveying normal direction, and the measurement volume can then be displaced along the local normal n (from y = 0.2 mm to y = 145 mm with a precision displacement of 0.1 μm), see Favier & alii (1994).

Figure 3 presents the acquisition chain of the bidimensional LDA system operating in the back scatter mode. It includes the Argon laser source (4 W), the beam splitter and the transmitter block where the four beams (2 blue for the U-component, 2 green for the V-component) are connected by means of four optical fibres to the optical head linked with the airfoil motion. The light reception is realized through an additional optical fibre connected to a beam splitter and two photomultipliers PM1 and PM2 (see Figure 3). The main characteristics of such a LDA system are as follows :

- On the blue color, (wavelength : 488 nm) the measurement volume is 0.23 x 0.23 x 5.74 mm^3 ; and the interfringe is i = 6.10 mm.
- On the green color (wavelength : 514.5 nm), the measurement volume is 0.24 x 0.24 x 6.08 mm^3 ; and the interfringe is i = 6.44 μm.

Data acquisition is made on a computer from 2 Burst Spectrum Analyzers delivering for each velocity component (U, V) the Doppler frequencies and the arrival validation time for each frequency measurement (Figure 3). The arrival validation times are counted from a time origin delivered by a photoelectric cell mounted on the oscillating device and providing the airfoil position at each cycle of oscillation. The software (COMBSA) used for acquisition and data reduction is developped at I.M.F.M. under Labview system (National Instruments). The unsteady data reduction technique is made using an ensemble average procedure suited for periodic flows investigation, see Favier & alii (1992), Favier & alii (1994). Due to the periodicity of the flow, each period is considered as a specific sample of the same phenomenon (see Figure 4), so that each velocity component, U(t) or V(t), can be obtained at each phase angle ωt as the averaged value of the velocity samples recorded at the same given phase angle and over a large number (ligher than 50) of cycles of oscillation. The simultaneousness of the 2D measurement is then obtained from the post-synchronisation by software of the data obtained at the same phase during the oscillating period (divided for the present tests into 32 intervals of phase ωt). Fourier series analysis of each velocity component (U, V) are then obtained as sketched in Figure 4.

Concerning the seeding of the flow, rates of data validation of about 500 Hz are obtained using a mixture of alcohol and glycerine. As shown in Figure 1 the freestream flow is seeded by means of a streamlined tube located in the suction chamber of the wind-tunnel.

STEADY BOUNDARY-LAYER MEASUREMENTS WITH SEPARATION

Figure 5 gives a typical example of the U and V velocity profiles measured on the NACA 0012 airfoil in the uniform steady flow (U_∞ = 5 m/s, Rec = 10^5), at a fixed longitudinal distance from the leading edge (s/C = 0,508) and for six different values of the angle-of-attack α_0 = 9° ; 12° ; 12.5° ; 14° ; 16° ; 20°. For the lower values of the airfoil incidence (α_0 = 9°, 12°), the U = U (y) profile indicates that the boundary-layer is turbulent and attached on the forward part of the airfoil (0 ≤ s/C ≤ 0.508), and that its thickness slightly increases with α_0 (δ ≈ 10 mm). The V-component evolution remains strictly positive as a function of y, and its level tends to zero in the region very close to the wall (y < 7 mm). It can be noticed that the data acquisition of the V-component have been no longer realized for y < 7 mm, due to the very weak levels recorded (V < 0.1 m/s) and to the sharp increase in the time validation required to acquire data in this region.

A slight increase of the incidence at α_0 = 12.5° (which is a value close to the stall incidence angle of the NACA 0012 airfoil), produces a significant change on both U and V velocity profiles. The U-component exhibits the occurence of a recirculating zone (10 mm in thickness, at the point where U = 0) where negative values of U are obtained. The V-component also shows negative values in this recirculating zone. As α_0 increases to higher value (α_0 = 14° , 16° , 20°) the thickness of the recirculating zone is significantly increased as well as the thickness of the flow region where viscous effects are present (y ≈ 100 mm at α_0 = 20°). It can be also noticed that the point U = 0 nearly corresponds to the maximum negative values of V. This maximun value is shown to decrease due to the thickening of the recirculating zone as α_0 increases.

Such steady flow experiments performed on the airfoil at rest in the uniform flow, and at different conditions of velocity U_∞ and incidence α_0, have provided suited criteria of transition and separation based on the integral thicknesses of the boundary-layer ($\delta 1$, $\delta 2$, $H = \delta 1/\delta 2$, $\delta 3$, $\delta 3'$) directly deduced from the velocity profiles measurements, see Favier & alii (1994).

In this paper, only the turbulent separation criteria is presented which is based on the shape factor H as follows :

→ the occurence of separation corresponds to $H \geq H^*$, with:

$H = \delta_1/\delta_2$ et $H^* = 2{,}70$; and integral thicknesses are defined by:

$$\delta_1 = \int_0^\delta \left[1 - \frac{U}{U_e}\right] dy \quad \text{and}$$

$$\delta_2 = \int_0^\delta \frac{U}{U_e}\left[1 - \frac{U}{U_e}\right] dy$$

→ the presence of a separated boundary-layer corresponds to $H > H^*$ or $H < 0$,

→ the presence of an attached boundary-layer corresponds to $0 < H < H^*$.

An example for checking the above criterion is shown in Figure 6 which gives thicknesses evolutions of the boundary-layer $\delta 1$, $\delta 2$ and $H = \delta 1/\delta 2$. The white symbols correspond to an attached boundary-layer and the black symbols to a separated boundary-layer. The experimental test conditions are relative to the measurements proposed in Figure 5.

In Figure 6, $\delta 1$ is around 5mm for $\alpha_0 < 12°$ which corresponds to an attached flow. Then $\delta 1$ suddenly increases when the incidence α_0 of the airfoil reaches 12.5°, which gives a separated boundary-layer (see figure 5), so the value of $\delta 1$ is thus beyond 30mm and reaches 80mm at $\alpha_0 = 20°$.

$\delta 2$ increases too when $\alpha_0 = 12.5°$ and takes negative values for greatest incidences which are due to an important recirculating zone.

Finally, the evolution of shape factor H in Figure 6 shows that the separation criterion ($H > H^* = 2.70$) detects clearly the occurence of the boundary-layer separation. When the boundary-layer is attached, for $\alpha_0 = 9°$, 12° , shape factor values are around 1.9 (usual values for turbulent states). The occurence of separation, for $\alpha_0 = 12.5°$, produces an increase of H which grows over 2.70. Greatest incidences intensify the separation level and H has negative values which correspond to the occurence of an important recirculating zone.

UNSTEADY SEPARATION/REATTACHMENT MEASUREMENTS

When the airfoil oscillates in fore-and-aft motion at a fixed high incidence ($\alpha_0 \geq 12.5°$, where the flow separation is generated on the airfoil) one major effect of the unsteadiness is to produce a dynamic reattachment of the boundary-layer as examplified in Figures 7 to 10 for $\alpha_0 = 14°$; s/C = 0.508, $U_\infty = 5$ m/s, ($Rec = 10^5$). The influence of the reduced oscillating parameters (amplitude λ and frequency k) is shown on these Figures by means of the U and V-profiles measured at different phases ωt of the period.

Figures 7 and 8 show the evolution of the U = U (y) and V = V (y) instantaneous profiles at 8 phases of the period $\omega t = 0°$, 45°, 90°, 135° (Figure 7) ; and $\omega t = 180°$, 225°, 270°, 315° (Figure 8), for different values of the reduced amplitude λ and at a fixed reduced frequency k =0.188. The plots clearly exhibit the occurence of the unsteady boundary-layer reattachment during a large fraction of the period ($270° \leq \omega t \leq 360° + 45°$). This reattachment process is only obtained for the higher value of $\lambda = 0{,}377$ (A = 0.30m) and corresponds to positive value of both U and V-component in Figures 7, 8. During the separation process (for instance $\omega t = 135°$ in Figure 6) the recirculation region remains almost the same for all values of λ as well as for the steady flow regime.

This influence of the λ-parameter on the separation-reattachment process of the boundary layer is also shown in Figure 9, which gives the mean unsteady terms (U_0, V_0) of the Fourier series as a function of λ. The results indicate that the mean reattachment ($U_0 > 0$ and $V_0 > 0$) of the boundary layer during the period can only be obtained at the higher λ value ($\lambda = 0.377$ in Figure 9). For $\lambda < 0.377$ the effects of the flow velocity variations are not strong enough to produce the mean reattachment of the flow on the upper side surface.

Figure 10 gives another example of the unsteadiness produced by increasing the frequency parameter (from k = 0.188 to k = 0.288) at a fixed value of $\lambda = 0.377$. In this case the U = U (ωt) velocity profile is plotted at 8 different distances from the wall (varying from y = 0.5 mm to y = 80 mm), at s/C = 0.508 and $\alpha_0 = 14°$. The results indicated that the reattachment process occuring for $\omega t \geq 180°$, is weakly dependent on the k-parameter. On the other hand, the separation process is shown to be delayed when k increases. For instance at y = 0.5 mm the separation is shown to occur at $\omega t = 70°$ for k = 0.188, and at $\omega t = 120°$ for k = 0.288 in Figure 10.

The steady turbulent separation criterion has been also tested in unsteady flow, see Favier & alii (1994), and Figure 11 shows the evolution of the instantaneous shape factor corresponding to the two experimental cases plotted on figures 7, 8 and 9. These cases have common parameters which are $\alpha_0 = 14°$; s/C = 0.508 ; $U_\infty = 5$ m/s ; f=1Hz ; k = 0.188, and they differ only by the value of λ : case A : A=0.30m ; $\lambda = 0.377$ and case B : A=0.10m ; $\lambda = 0.126$

The parameters of case B lead to a complete separated configuration of the boundary layer during the period (see figure 7, 8). So $H(\omega t)$ is at all time out of the range defined by $0 < H(\omega t) < H^*$, with $H^* = 2.70$ (black symbols).

It is also shown that the parameters of case A lead to the separation-reattachment process of the boundary layer. For $0 < \omega t < 70°$, shape factor values are around 1.9 and the unsteady boundary-layer is attached. The instant of separation is at $\omega t = 70°$ and the reattachement occurs at $\omega t = 230°$, (see figure 10, k = 0.188, white symbols at y = 0.5mm), where H recovers values around 1.9. These instants of separation and reattachement are correctly detected by the criterion (see figure 11, white symbols).

Figure 12 shows the corresponding evolution of integral thicknesses of the boundary-layer $\delta 1(\omega t)$, $\delta 2(\omega t)$ and $\frac{\partial \delta 2}{\partial y} = \frac{U}{Ue}(1 - \frac{U}{Ue})$. These results indicate an important increase of $\delta 1(\omega t)$ at the instant of separation ($\omega t = 70°$) and that $\delta 1(\omega t)$ reaches 60mm when the separation is the greatest ($\omega t = 150°$). When ωt increases, $\delta 1(\omega t)$ decreases and recovers moderate values (around 15mm) which correspond to an attached turbulent boundary-layer.

The evolution of $\delta 2(\omega t)$ shows negative values when the flow separation is more important ($\omega t = 150°$). This is due to the evolution of $\frac{\partial \delta 2}{\partial y} = \frac{U}{Ue}(1 - \frac{U}{Ue})$ which provides a negative area greater than the positive area (see $\omega t = 135°$), and corresponds to the devellopement of an important recirculation region whithin the boundary-layer. The

momentum quantity generated from the recirculating flow is, in this case most, important that the one generated from the flow parallel to the freestream direction.

CONCLUSION

The embedded optical fibre LDA technique has been successfully extended in this study to 2D velocity measurements (U,V) around moving curved walls and oscillating airfoils of arbitrary shape. Using this new measurement technique, the boundary-layer dynamic development and the specific local unsteady phenomena such as separation and transition, can be detected over a large range of y (0.2mm < y <145mm).

Concerning the unsteady separation-reattachment process of the boundary layer, the influence of the velocity fluctuations caused by the fore-and-aft motion to create significant mean reattachement of the flow has been confirmed. A well-suited criterion has been formulated as a function of the intantaneous shape factor H. Using such a formulation, the instantaneous separation especially generated in fore-and-aft motion can be fully detected, as well the corresponding reattachement at hight λ values.

This embedded laser velocimetry technique will be applied in future works on airfoils oscillating in translation, pitching or coupled translation/pitching motions in order to provide unique data to investigate more complex flow configurations, like the vortex emission caused by the instantaneous boundary-layer separation during the dynamic stall process generated at different conditions of unsteadiness.

ACKNOWLEDGMENTS

The authors wish to thank the support provided by the "Direction des Recherches, Etudes et Techniques" under Grants 87/272 and 91/158.

NOMENCLATURE

A	amplitude displacement in fore-and-aft motion, (m).
C	chord of the model, (m).
f	frequency of oscillation, (Hz).
H	integral shape factor ($H=\delta 1/\delta 2$).
k	reduced frequency of oscillation, ($C\omega/2U_\infty$).
Re_C	local Reynolds number, ($U_\infty C/\nu$).
Re_s	local Reynolds number, ($Ue(s,t)s/\nu$).
s	curvilinear distance along the wall from the leading edge, (m).
t	time, (sec).
U	boundary-layer velocity parallel to the wall, (ms^{-1}).
$\overline{U}$	unsteady mean velocity, (ms^{-1}).
Ue	local external velocity, (ms^{-1}).
U_∞	freestream velocity, (ms^{-1}).
y	distance normal to the model chord, (m).
α_0	mean incidence of the model, (deg).
δ	boundary-layer thickness, (m)
$\delta 1$	integral displacement thickness, (m).
δ_2	integral momentum thickness, (m).
δ_3	first integral energy thickness, (m).
δ'_3	second integral energy thickness, (m).
λ	reduced amplitude of oscillation, ($A\omega/U_\infty$).
Φ_1	phase angle of the 1^{st} harmonic component, (deg).
ν	kinematic viscosity, (m^2s^{-1}).
ω	angular frequency, ($2\pi f$), ($rads^{-1}$).
ωt	phase of the period, (deg).

REFERENCES

COUSTEIX, J. and HOUDEVILLE, R., 1988, "Effects of unsteadiness on turbulent boundary layers.", Fluid Dynamics Lecture Series of V.K.I.

FAVIER, D., AGNES, A., BARBI, C. and MARESCA, C., 1988, "Combined translation/pitch motion : a new airfoil dynamic stall simulation.", Journal of Aircraft, Vol. 25, N° 9, pp. 805-814.

FAVIER, D., MARESCA, C. and BELLEUDY, J., 1990, "Unsteady flows around an oscillating flat plate model using an embodied technique of fibre optics laser velocimeter.", Proceedings of the 17th Congress of Aeronautical Sciences, I.C.A.S.-A.I.A.A., Stockholm.

FAVIER, D., MARESCA, C., RENON, P. and AUTRIC, J.M., 1992, "Boundary-layer measurements on oscillating models using an optical fibre LDA technique", Proceedings of the 6th International Symposium on Applications of Laser Techniques to Fluid Mechanics, Lisbon.

FAVIER, D., MARESCA, and C...PASCAZIO, M., 1994, "Etude expérimentale et numérique du décollement de la couche limite instationnaire sur un modèle oscillant en écoulement 2D/3D.", D.R.E.T. CONTRACT n° 91/158, Synthesis Report.

PASCAZIO, M., AUTRIC, J.M., FAVIER, D. and MARESCA, C., 1993, "Etude de la couche limite sur une plaque plane oscillant en tangage par vélocimétrie laser emlbarquée", Proceedings du 11ème Congrès Français de Mécanique, Lille-Villeneuve d'Ascq.

TELIONIS, D.P.,1981,"Unsteady viscous flow.", Springer Verlag Editor, N.Y..

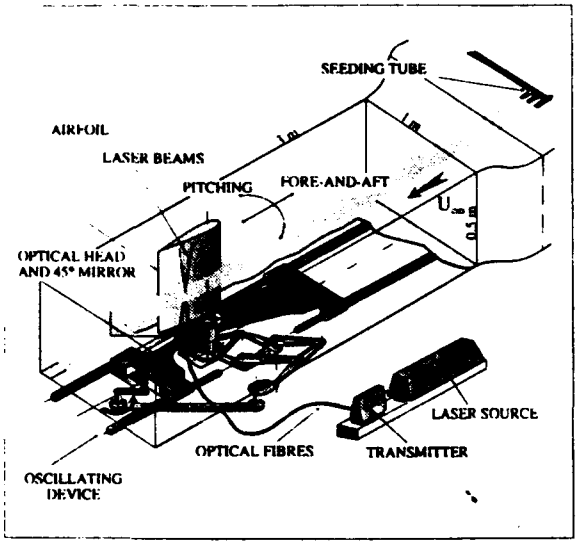

Fig. 1 : Schematics of the experimental set-up

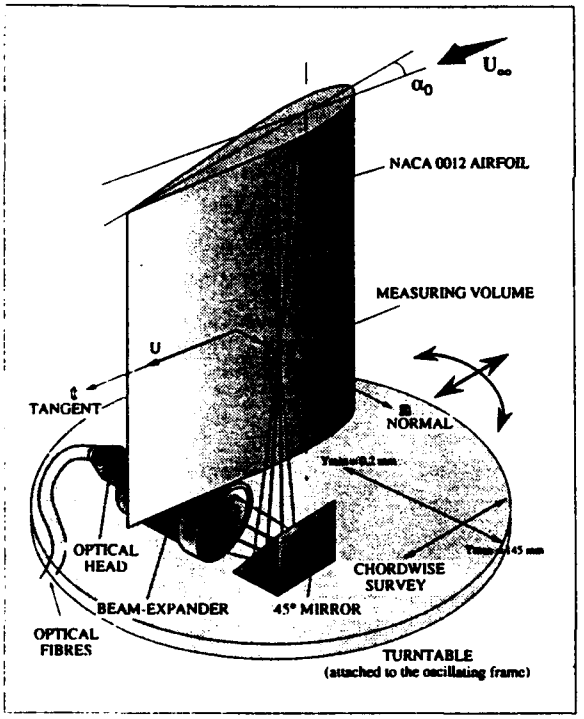

Fig. 2 : Embedded LDA System on oscillating airfoil

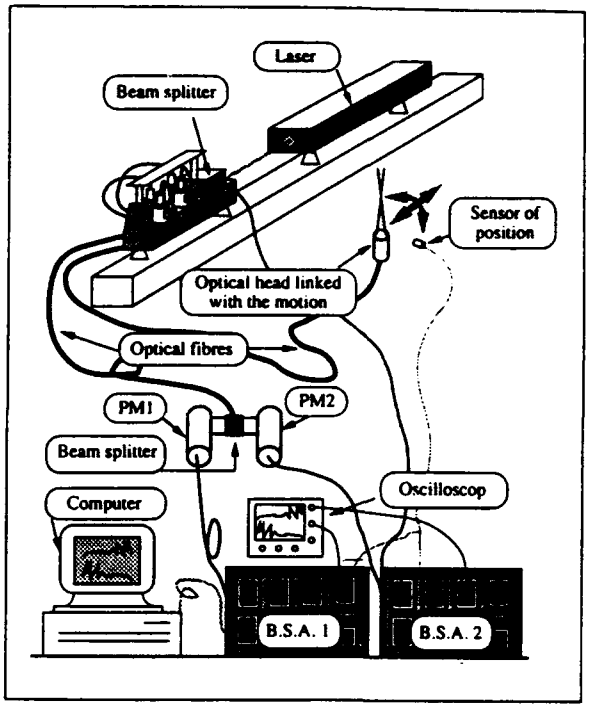

Fig. 3 : 2D-LDA acquisition chain

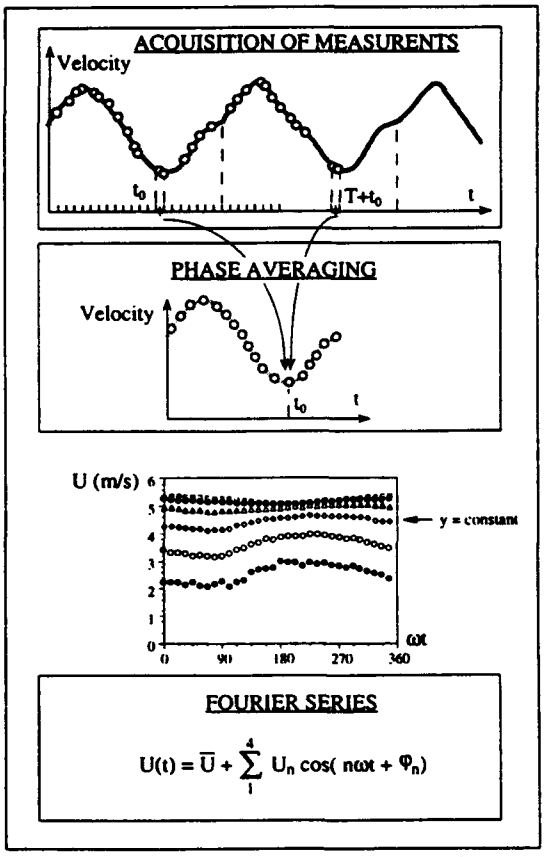

Fig . 4 : Statistical phase averaging technique for each velocity component (U and V)

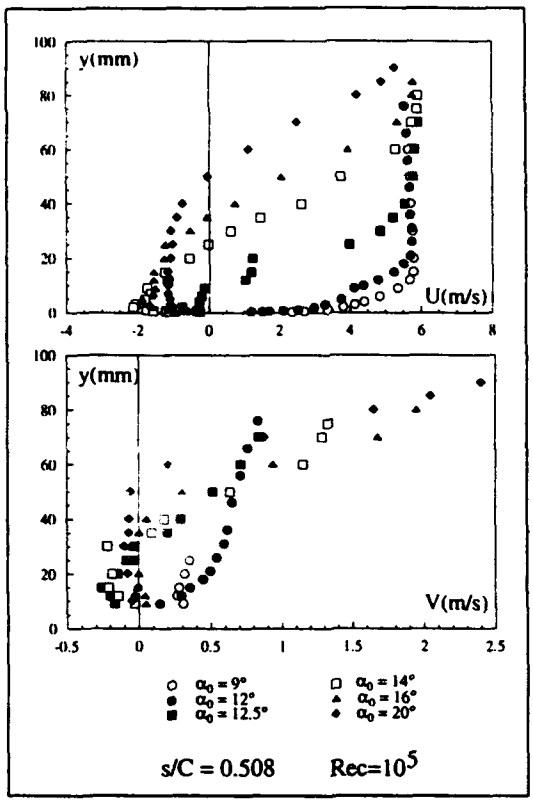

Fig. 5 : Steady velocity profiles (U,V) on the NACA 0012 airfoil

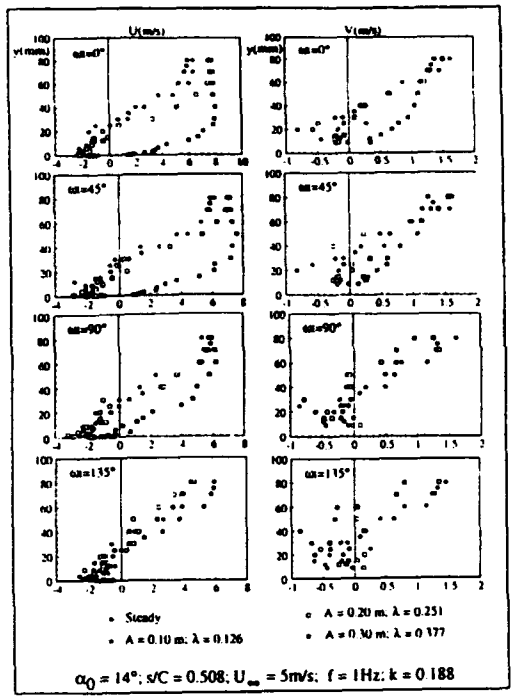

Fig. 7 : Influence of λ on the unsteady velocity profiles (U, V) for ωt = 0° à 135° NACA 0012 : fore-and-aft motion

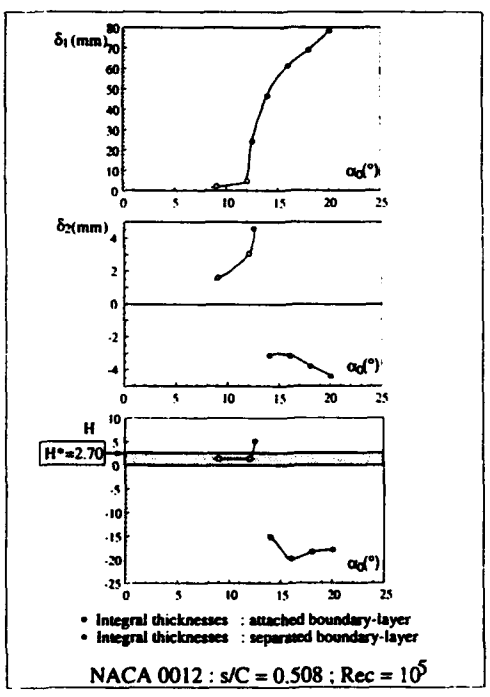

Fig.6 : Evolution of integral thicknesses δ1, δ2, H, steady configuration, separation criteria of boundary-layer

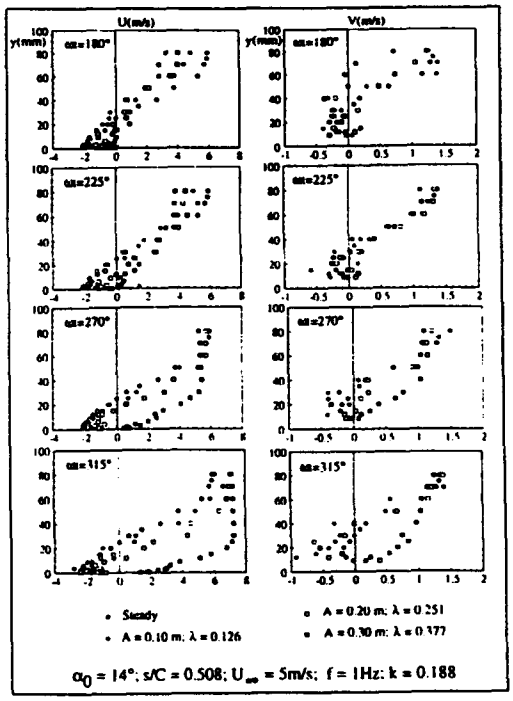

Fig. 8 : Influence of λ on the unsteady velocity profiles (U, V) for ωt = 180° à 315° NACA 0012 : fore-and-aft motion

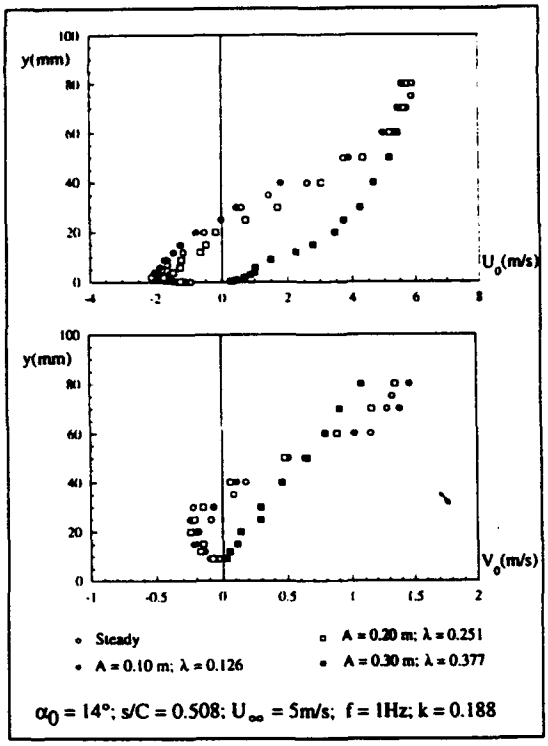

Fig. 9 : Influence of λ on the unsteady velocity mean profiles (U_0, V_0)
NACA 0012 : fore-and-aft motion

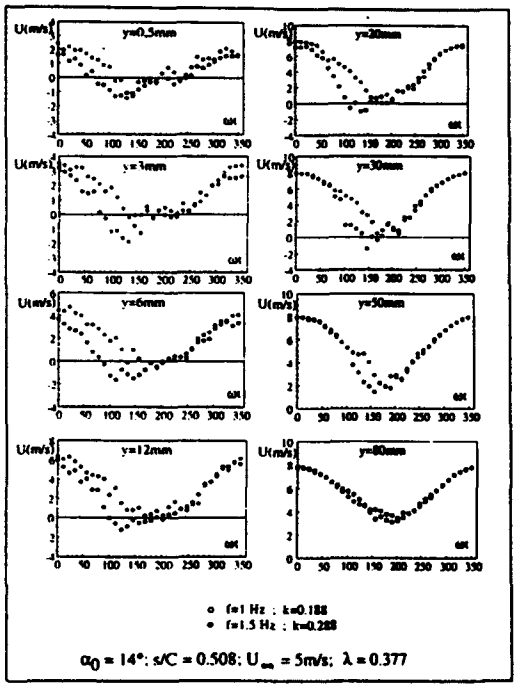

Fig. 10 : Influence of k on the unsteady velocity velocity profiles U = U(ωt) at different altitudes y
NACA 0012 : fore-and-aft motion

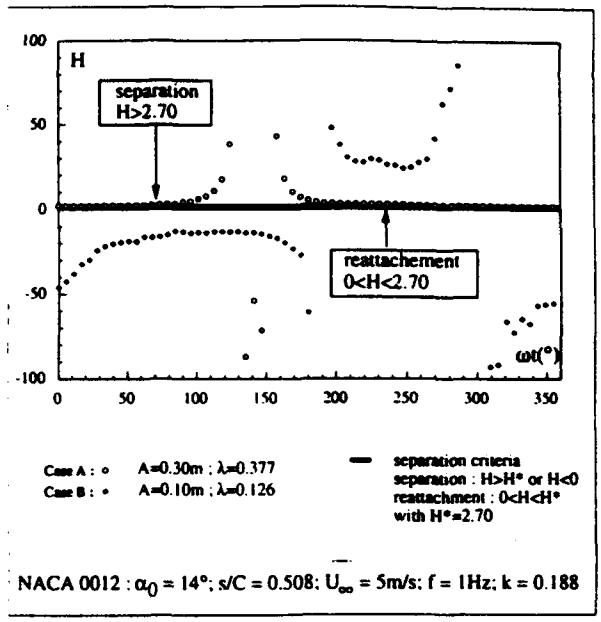

Fig. 11 : Evolution of the shape factor H = H(ωt), fore-and-aft motion

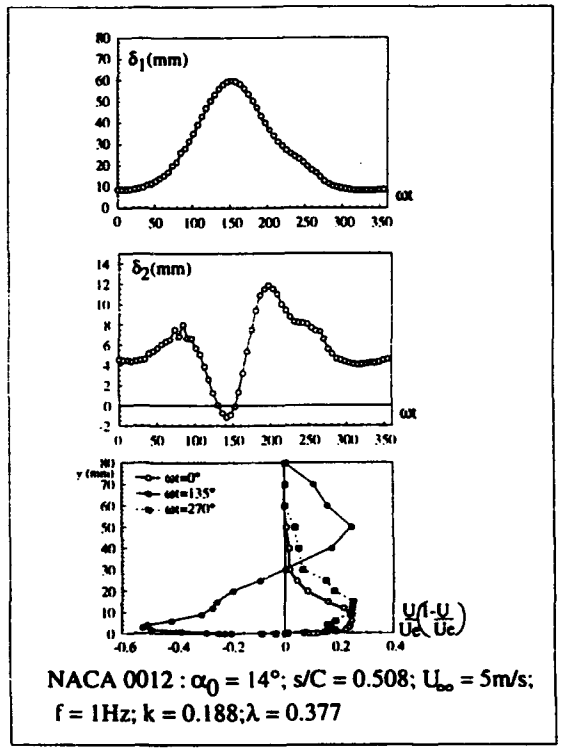

Fig. 12 : Evolution of integral thicknesses δ_1, δ_2, fore-and-aft motion

A PHASE-LOCKED HIGH-SPEED REAL-TIME INTERFEROMETRY SYSTEM FOR LARGE AMPLITUDE UNSTEADY FLOWS

M.S. Chandrasekhara
Navy-NASA Joint Institute of Aeronautics
Department of Aeronautics and Astronautics
Naval Postgraduate School, Monterey, CA 93943, U.S.A.

D.D.Squires
Sverdrup Technology Inc., Moffett Field, CA 94035, U.S.A.

M.C. Wilder
Navy-NASA Joint Institute of Aeronautics and
MCAT Institute, San Jose, CA 95127, U.S.A.

and

L.W. Carr
Aeroflightdynamics Directorate, U.S.Army ATCOM and,
Fluid Dynamics Research Branch
NASA Ames Research Center, Moffett Field, CA 94035-1000, U.S.A.

ABSTRACT

A high-speed phase-locked interferometry system has been designed and developed for real-time measurements of the dynamic stall flow over a pitching airfoil. Point diffraction interferograms of incipient flow separation over a sinusoidally oscillating airfoil have been obtained at framing rates of up to 20 KHz and for free stream Mach numbers of 0.3 and 0.45. The images were recorded on 35mm ASA 125 and ASA 400 films using a drum camera. Special electronic timing and synchronizing circuits were developed to trigger the laser light source from the camera and to initiate acquisition of the interferogram sequence from any desired phase angle of oscillation. The airfoil instantaneous angle of attack data provided by an optical encoder was recorded via a FIFO data buffer into a microcomputer. The interferograms have been analyzed using software developed in-house to get quantitative flow density and pressure distributions.

1. INTRODUCTION

Research on compressibility effects on dynamic stall of pitching airfoils is on-going at the U.S. Navy-NASA Joint Institute of Aeronautics and is being conducted in the Fluid Mechanics Laboratory of NASA Ames Research Center. The phenomenon of dynamic stall pertains to the production of lift at angles of attack well beyond the static stall angle of attack by rapidly pitching an airfoil. The problem is of importance to helicopters and fighter aircraft. Dynamic stall occurs on the retreating blade of a helicopter as it is pitched to high angles of attack during the portion of the blade revolution when it is moving with the wind. A fighter aircraft performing a rapid maneuver also experiences dynamic stall. The process is characterized by the formation of a large vortex at the leading edge (known as the dynamic stall vortex) whose vorticity is responsible for the enhanced lift. However, its convection over the airfoil upper surface needs to be avoided since it produces strong pitching moment variations, which are destructive to the aircraft. The current lack of understanding of the full flow details needed to prevent these undesirable effects has been responsible for the phenomenon remaining unexploited thus far. Another characteristic feature of the flow is the large flow accelerations around the leading edge, resulting in the onset of compressibility effects at a very low free stream Mach number of 0.2. [McCroskey(1981)]. The local flow could become supersonic and form a series of shocks, [Chandrasekhara et al(1994)]. The various fine scale events of the flow that are present for the different flow conditions need to be properly understood before an effective means of controlling the flow can be devised.

As part of this study, a real-time interferometry method known as point diffraction interferometry(PDI) has been developed, [Brock et al (1991), Carr et al (1991)] to map the instantaneous global flow details. This effort has been successful in delivering sharp, high-contrast interferograms of the flow for all conditions of the experiment. The interferograms are obtained as conditionally sampled images and have provided the first insight into the the origination of dynamic stall from the bursting of the laminar separation bubble, flow field pressure distribution and other critical flow details. However, capturing the full flow sequence takes several cycles of motion. The rapid changes that occur in the flow, especially the details of the dynamic stall vortex formation and the shock/boundary layer interactions leading to possible premature flow separation, do not repeat perfectly from cycle to cycle because of the influence of the slight variations in the pitching history for each cycle. Thus, there is a need to obtain the flow details in just one pitching cycle, as they occur. It is this need that prompted the design and development of the very high-speed interferogram recording system being presented in this paper.

2. DESIGN SPECIFICATIONS

The studies are being conducted on a NACA 0012 airfoil with a chord length of 7.62cm in the Compressible Dynamic Stall Facility(CDSF). Two different drive systems could be used in the CDSF to produce either an oscillatory pitching motion or a constant rate transient pitching motion of the airfoil. The angle of attack variation in the former case is given by $\alpha = \alpha_0 + \alpha_m \sin \omega t$ with the mean angle of attack α_0 and the amplitude α_m variable from $0^0 - 15^0$ and $2^0 - 10^0$, respectively. The maximum frequency of oscillation is 100 Hz. The constant rate pitch drive produces a rapid change of angle of attack from $0^0 - 60^0$ at rates as high as 3600 degrees/sec and the motion is completed in 15 millisec. Earlier work by Carr et al (1991) has shown that the events of dynamic stall onset occur rapidly over a small angle of attack range

of about 0.5 to 1.0 degree. Thus, in order to have a resolution of 0.1 degree or better at the limits of operation of either drive system, a camera speed of 36 KHz or more is necessary.

The very large flow acceleration (and concomitant density variations around the airfoil leading edge which could create as many as 60 fringes/millimeter at the airfoil) and the rapidity of the development of the dynamic stall vortex or the shock induced flow events, result in interference fringes that evolve and move at very high frequency ($\approx$ KHz). This necessitates the use of extremely short light pulse duration, typically nanoseconds. These challenges require the use of a laser that produces the necessary energy for each exposure and is externally controllable at the high pulse rates.

The high framing rates, the short duration of the light pulse, and the low light levels preclude the use of video cameras or similar recording devices, limiting the choice to film cameras. Possible blurring of the images due to flow changes eliminates choices such as streak cameras.

It is also necessary to record the airfoil angle of attack corresponding to each frame on the film. Further, the system should be controllable in order to generate an interferogram sequence starting at any desired angle of attack.

3. DETAILS OF THE CAMERA, LASER CONTROL AND RECORDING SYSTEMS

A Qunatronix Series 100 CW/pumped Nd:YAG laser, capable of operating from DC to 50KHz was used in the experiments. It can be externally triggered without any detectable delay at all rates. The pulse duration and the energy output varied nonlinearly from 85ns and 0.14mJ at 500Hz, 420ns and 25μJ at 40KHz and 100ns and 11μJ at 50KHz. At the rates used for the high-speed interferometry experiments being reported, the corresponding numbers were: 140ns and 65μJ at 10KHz and 240ns and 17μJ at 20KHz, at nearly full current settings. The energy density in the laser light pulse at 10 KHz rate was adequate to give proper exposure on ASA 100 T-MAX film; ASA 400 film was necessary at 20 KHz.

A 35 mm, variable speed Cordin drum camera (DYNAFAX Model 350) was used for image recording. A rotating 8-faceted mirror in the camera reflects the incoming light beam onto the film which is rotating in the same direction in the camera drum. Effective shutter times of 1.35μsec can be achieved at 40 KHz framing rate. At 20 KHz, this time was 2.7μsec. The camera recorded two rows of 16mm images images on the film strip, with subsequent exposures being recorded alternately in each row, but displaced 16 frames. A maximum of 224 frames can be recorded at any framing speed.

The laser was triggered by TTL pulses emitted by custom built (in-house) circuitry installed on the camera. Tuning the camera required aligning the mirror facet with the incident light beam. In order to sense the position of the mirror, an infrared (IR) emitter and detector were installed in the camera (see Fig. 1) to "see" the mirror facets as they pass. The IR detection beam was not in the optical path of the camera and the selected film was not sensitive to the 940nm IR wavelength. Each mirror facet accounted for two photo images. To obtain an image in each frame, two delayed pulses were generated from the passing of each mirror facet. Fast rise-time (1$nsec$) photodiodes were selected to ensure adequate signal level as the center of each mirror facet passed the detector. To aid in synchronizing the laser pulses, two additional photo detectors were placed in the camera, one at each frame position. The trigger pulse from the mirror face detection event started a delay sequence which synchronized laser pulsing to subsequent frame positions as shown in Fig. 1. Tuning of the laser-firing pulse train occurred in a circuit attached to the camera. The tuning procedure involved adjusting two delay times with the camera running: T_1, the delay between detecting a mirror facet and emitting the first TTL pulse (the trigger pulse to the laser and for data collection) and T_2, the time between the two TTL pulses. The delay times T_1 and T_2 were adjusted to maximize the laser light detected by the frame photo detectors. Once tuning was properly completed, the photo detectors were moved from the field of view to permit laser light to reach the film plane. The short effective shutter times (of 1.35 μsec at the maximum camera speed)and the high framing speeds required a careful design of the electronic system that included schemes for proper attenuation of noise.

A Nikon 55mm macro, f/2.8 lens was used on the camera. Aligning the camera along the optical axis of the interferometry system required very accurate adjustment.

Both unsteady motion producing drives referred to in section 2 are equipped with an optical encoder that produces 800 counts/cycle of motion (one oscillation cycle or one pitch-up from 0-60 degrees). It is an incremental encoder outputting a quadrature pulse train which is in turn processed by an Oscillating Airfoil Position Interface(OAPI) for phase locking and recording by the data acquisition system. The OAPI could be preset to produce a TTL event pulse (or pulse repetitively) at any desired phase angle by a series of front panel BCD switches. The TTL output pulse was used to trigger the opening of a laser safety shutter and also to initiate encoder data transfer to memory as shown in Fig. 2. The laser is enabled by the first TTL pulse from the OAPI. However, recording the encoder outputs was enabled subsequently when the system was ready. The data was recorded for each camera pulse in a 512 word first-in-first-out(FIFO) buffer. The number of frames acquired by the camera could be controlled from 0 to 224 (camera maximum) by the external electronics built for enabling the handshake between the various devices. Typically, 200 frames of point diffraction interferograms were obtained and the phase angles corresponding for each of the frames were recorded into the FIFO and later downloaded into a microVAX II computer.

4. OPERATION

The interframe pulse delay was tuned to the desired rate and the actual rate of the camera was measured using a frequency counter. The data to be reported were obtained at 11.56 KHz. Interferograms have also been obtained at 19.62KHz. The desired initial phase angle for the interferogram sequence was set using BCD switches on the OAPI front panel. Before the images were acquired, to maintain a consistent pulse energy level, the laser was triggered by an external pulse train at a 40KHz rate. This was necessary to protect the laser crystal from the giant pulse that is normally generated when the laser is pulsed after a

short lapse time. In order to prevent these pulses from exposing the film and for safety reasons, a solenoid actuated laser shutter was set up in front of the laser. A hand switch was used to initiate the controlled laser pulsing sequence. which is schematically described in Fig. 2. The corresponding timing sequence is shown in Fig. 3. After the switch is pressed, the circuitry was activated by an event pulse from the OAPI with an output pulse corresponding to the manually preselected angle of attack. The laser pulsing circuit was then inhibited (for 1.1 msec) until the laser shutter fully opened. The laser was enabled at the expiration of the delay and was actually triggered from the next camera pulse, at which time the encoder was latched and recorded in the FIFO. During this short elapsed time, the laser builds up sufficient charge to cause the first pulse to be a "small-giant" pulse, which over-exposed the first frame. This frame served to determine the first image on the film strip; thus, it was possible to accurately match the interferogram images with the phase angle of motion and to correlate the values in the FIFO buffer. A frame counter, started at the first laser-pulse event, permitted capturing the angles corresponding to each of the 200 laser pulses and hence PDI images that were recorded on film. Following the completion of the imaging, the shutter was closed and the laser returned to the constant 40KHz external triggering. The camera alignment was verified by taking test sequences on a Polapan ASA 125 film and the data was obtained on a higher resolution T-MAX 400 film.

Fig. 4 shows a schematic of the PDI optics and its implementation in the dynamic stall facility. The details of the PDI technique have been described in Brock, et al (1991). It uses one single pass of the laser beam through the test section and depends upon the ability of a pin-hole created *in-situ* in a semi-transparent plate to produce the reference beam. The signal beam passes around this pin-hole to produce interference fringes on a continuous basis in real time. In the experiment, the PDI spot was created with no-flow in the test section and once it was determined to be satisfactory (from single event polaroid pictures), the high speed images were obtained.

5. RESULTS AND DISCUSSION

5.1. Flow Development

Fig. 5 compares typical interferograms obtained with two different imaging techniques. Figures 5a and 5c were taken over a *single cycle* of airfoil motion using the high-speed filming method. Figures 5b and 5d were taken over *different cycles* of airfoil motion using the standard method of single-exposure, phase-locked, realization of the flow events. As stated earlier, the phase-locked images obtained over several cycles contain the *pitch rate history* effects as well. The airfoil was tripped in both cases and was oscillating as $\alpha = 10^0 + 10^0 \sin \omega t$ at a reduced frequency of 0.05. The free stream Mach number of the flow was 0.3. The camera framing rate was $\alpha = 10.07^0$ in the high-speed-images sequence and Fig. 5b represents the result for $\alpha = 10.00^0$ from a single-exposure recording of the event. (The triangles seen in the images are registration markers on the glass windows of the facility which are used to determine the airfoil profile during image processing. The slight dark bulge seen near the leading edge region is due to the light beam being bent away from the leading edge due to the very large local density gradients.) A careful comparison of the pictures shows that for this experimental condition of pre-dynamic stall flow, there are no significant differences between the image recording techniques and the fringe count agrees to within one fringe. Fig. 5c and 5d show the corresponding pictures for $\alpha = 13.99^0$, when the dynamic stall process has just begun, (this is evidenced by the appearance of vertical fringes in the flow immediately above the airfoil upper surface near the leading edge). A casual comparison may not show differences in the number and distribution of the fringes and hence no flow field differences, but as will be discussed later, there are differences in the initiation of the dynamic stall process from cycle to cycle, which affect the overall flow development and stall progression. Similar results were obtained at the higher framing rate of 19.62KHz.

Fig. 6a and Fig. 6b compare the global pressure distributions obtained from the images presented in Fig. 5c and Fig. 5d using custom image processing software developed in-house. It is to be noted that even though the two figures appear to be nearly identical, the corresponding pressure fields are indeed different as can be determined from the lines of constant pressure coefficients shown in the figures. The finer details of the flow in the region of dynamic stall vortex formation, $0 \leq x/c \leq 0.10$ differ measurably; Fig. 7 has been drawn to offer a comparison of these details. These differences are important since the instantaneous adverse pressure gradient development with pitching is different in the two images leading to considerably different dynamic stall developments during each pitch-up cycle, which makes the already challenging task of unsteady flow separation control even more difficult.

Fig. 8 shows the pressure distributions over the airfoil surface obtained from the interferograms presented in Fig. 5a and 5b. The pressure distributions agree for the most part. However, there is a difference of one fringe as already noted, which is the uncertainty of the PDI method itself. But, the pressures around the suction peak are somewhat different between the two cases, causing the adverse pressure gradient following the suction peak to be different, leading to major differences in pressure gradient magnitudes at higher angles of attack.

5.2. Interferogram Imaging Concerns

The image size on the film was 3.5mm in diameter and the images shown in Fig. 5a and 5c have been magnified by nearly 1000 times. Despite the large magnification factor, the quality of the images can be seen to be very good. Attempts to enlarge the original size (using extension rings) of the image met with only partial success owing to the long focal length of the mirrors and the fact that the laser beam has a small divergence angle, unlike white light.

Yet another concern in the use of the high-speed imaging system was the ability of the PDI spot to withstand the rapid exposure to the laser energy that occurred during high speed imaging. In the experiment at 20 KHz the PDI spot was exposed to a total of 3.4mJ in 10 milliseconds. At such large energy levels there was a possibility that the PDI spot could get enlarged or even damaged, thus creating inaccurate interferograms. However, the robustness of the holographic plate film coating material used for the purpose prevented this from happening.

It is worth commenting that acquisition of high speed interferograms using white light has been reported in the literature, [Desse and Pegneaux(1993)]. However, the key differences in the present study - the

requirements of phase locking, controlling the laser from the camera pulses, the need to precisely record the phase angle for each pulse (since the flow undergoes significant changes in a very small angle of attack range), and the very short duration of the pitching motion - all precluded the use other measurement methods.

6. CONCLUSIONS

A novel system for recording real-time phase-locked interferograms at very high rates has been developed for use in study of unsteady separated flows. The rapid nature of the flow changes and the extremely high gradients around the leading edge of an airfoil experiencing dynamic stall in compressible flow requires the use of such a measurement technique. The system uses a laser that can be pulsed at high rates to produce interferograms and record these on film at rates of up to 40KHz. Proper electronic interlocking has enabled precise control of the experiment and accurate recording of the resultant interferograms.

ACKNOWLEDGEMENTS

The project was supported by U.S. Air Force Office of Scientific Research through grants, AFOSR-ISSA-89-0067 and AFOSR-MIPR-92-004. Additional support was received from the Army Research Office grant ARO-MIPR-125-93. The support and encouragement of Dr. S.S.Davis, Chief, Fluid Mechanics Laboratory Branch and the help provided by Mr. N.J.Brock and Mr. B.J.Weber of Aerometrics, Inc. in preparing the laser specifications are gratefully acknowledged.

REFERENCES

1. Brock, N., Chandrasekhara, M.S. & Carr, L.W. 1991, A Real-Time Interferometry System for Unsteady Flow Measurements", ICIASF'91 RECORD, IEEE Publication 91CH3028 – 8, pp. 423-430.

2. Carr, L.W., Chandrasekhara, M.S., Ahmed, S. & Brock, N. 1994, A Study of Dynamic Stall Using Real-Time Interferometry, To appear in AIAA J. Aircraft.

3. Chandrasekhara M.S. & Carr, L.W. 1990, Flow Visualization Studies of the Mach Number Effects on the Dynamic Stall of Oscillating Airfoils, AIAA J. Aircraft, Vol. 27, No. 6, pp. 516-522.

4. Chandrasekhara, M.S., Carr L.W. & Wilder, M.C., 1994, Interferometric Investigations of Compressible Dynamic Stall Over a Transiently Pitching Airfoil, AIAA Journal, Vol. 32, No. 3, pp. 586-593.

5. Desse J.M. & Pegneaux, J.C. 1993, Direct Measurement of the Density Field Using High Speed Differential Interferometry, Expts. in Fluids, Vol. 15, pp. 452-458.

6. McCroskey, W.J. 1981, The Phenomenon of Dynamic Stall, NASA TM-81264, March.

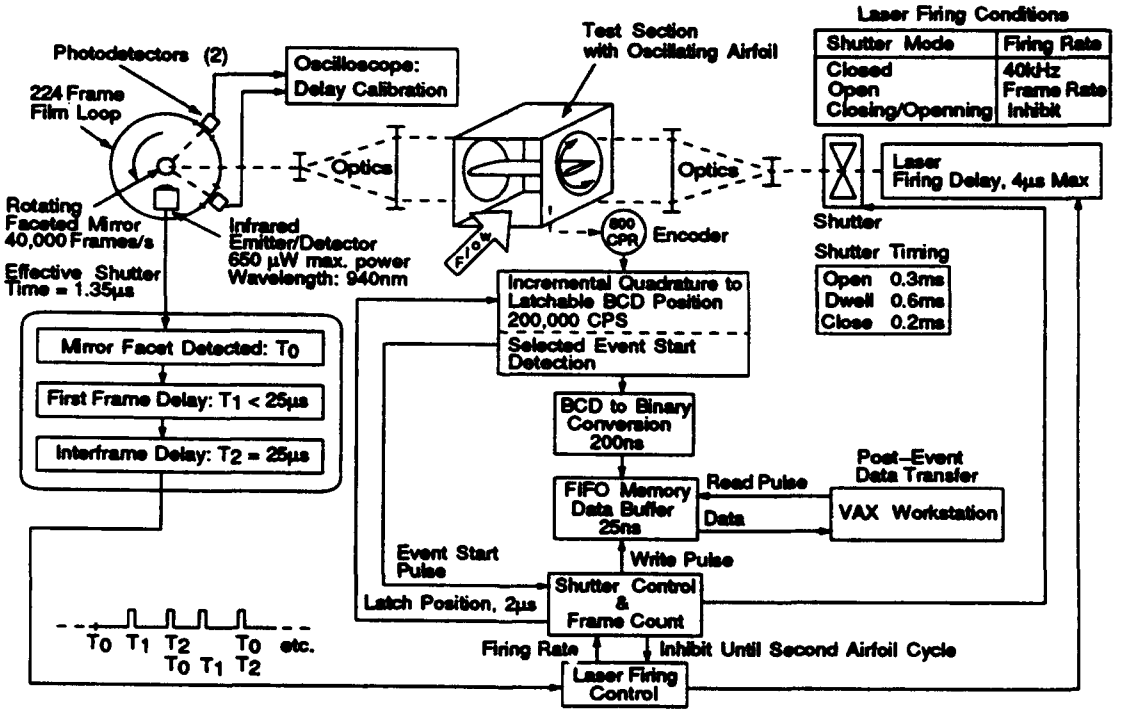

Fig. 1. Block Diagram of Camera/Laser Synchronization for the High Speed Interferometry System

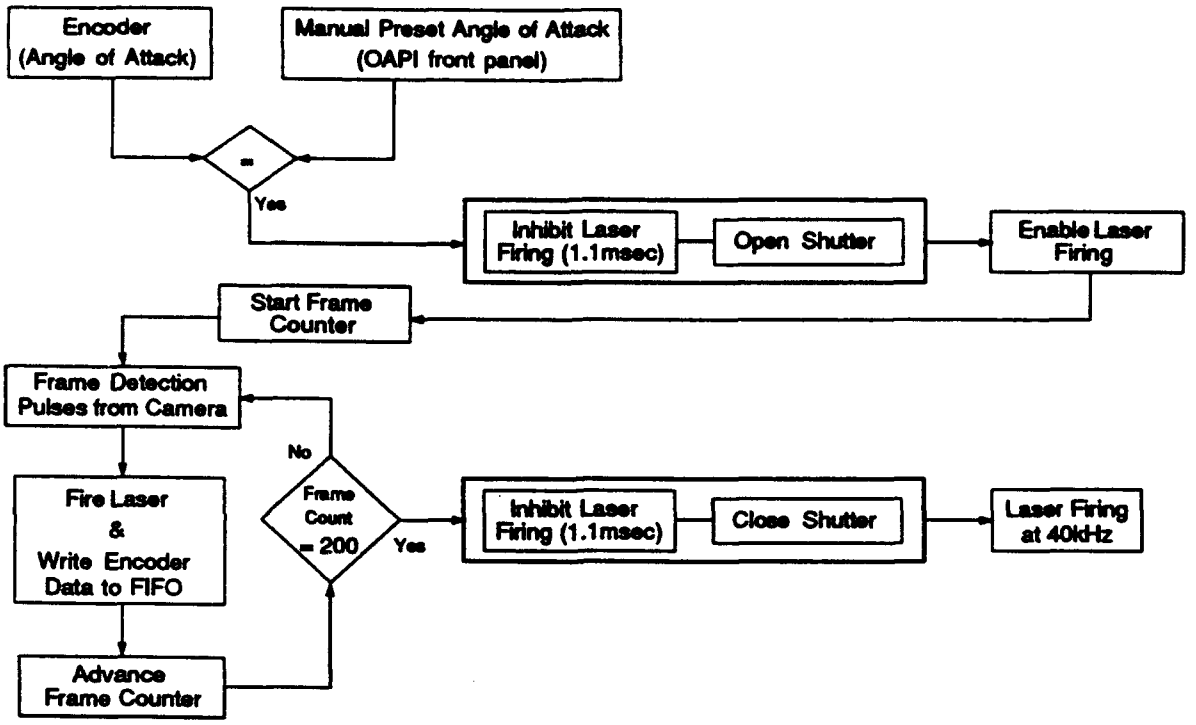

Figure 2. Flowchart of Events Following Handswitch "FIRE" for the High-Speed Interferometry System.

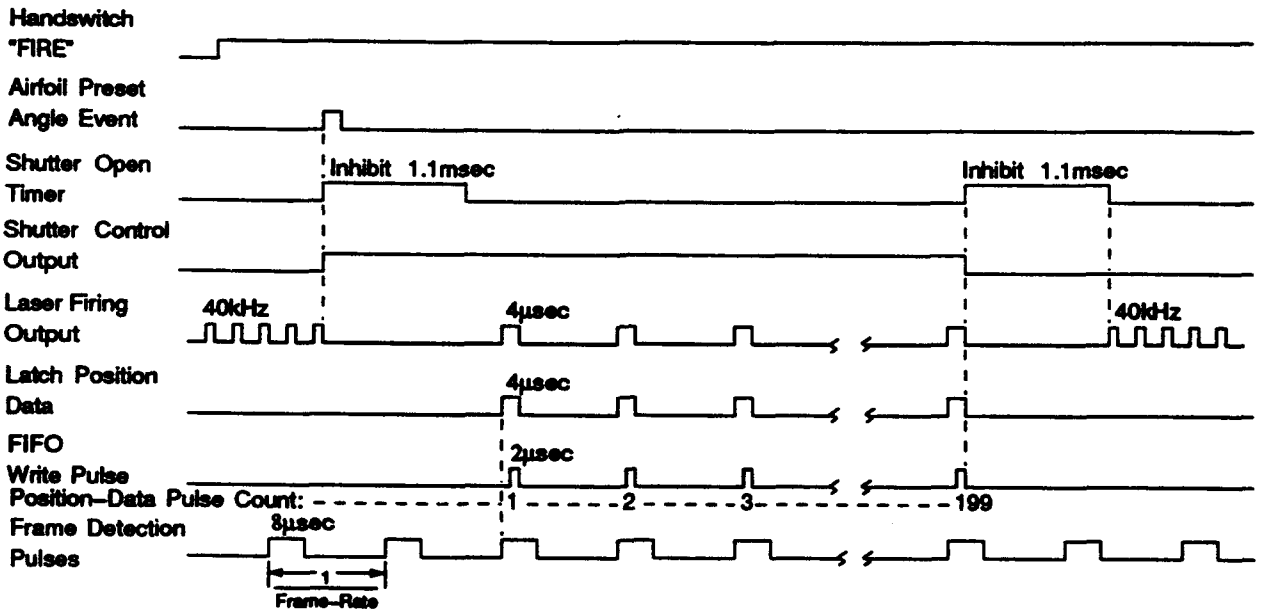

Note: Event edges are shown in proper sequence, but not properly scaled. Refer to the pulse durations shown.

Figure 3. Timing Sequence for the High-Speed Interferometry System.

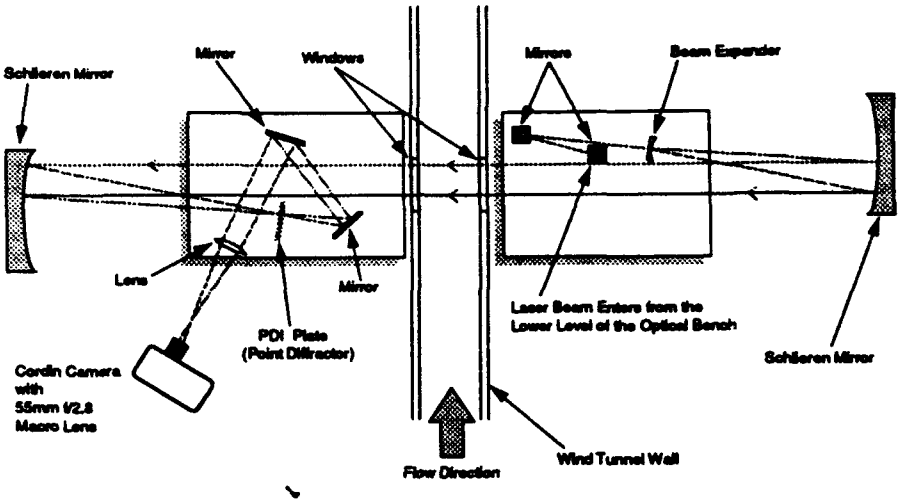

Figure 4. Schematic of the Point Diffraction Interferometry System.

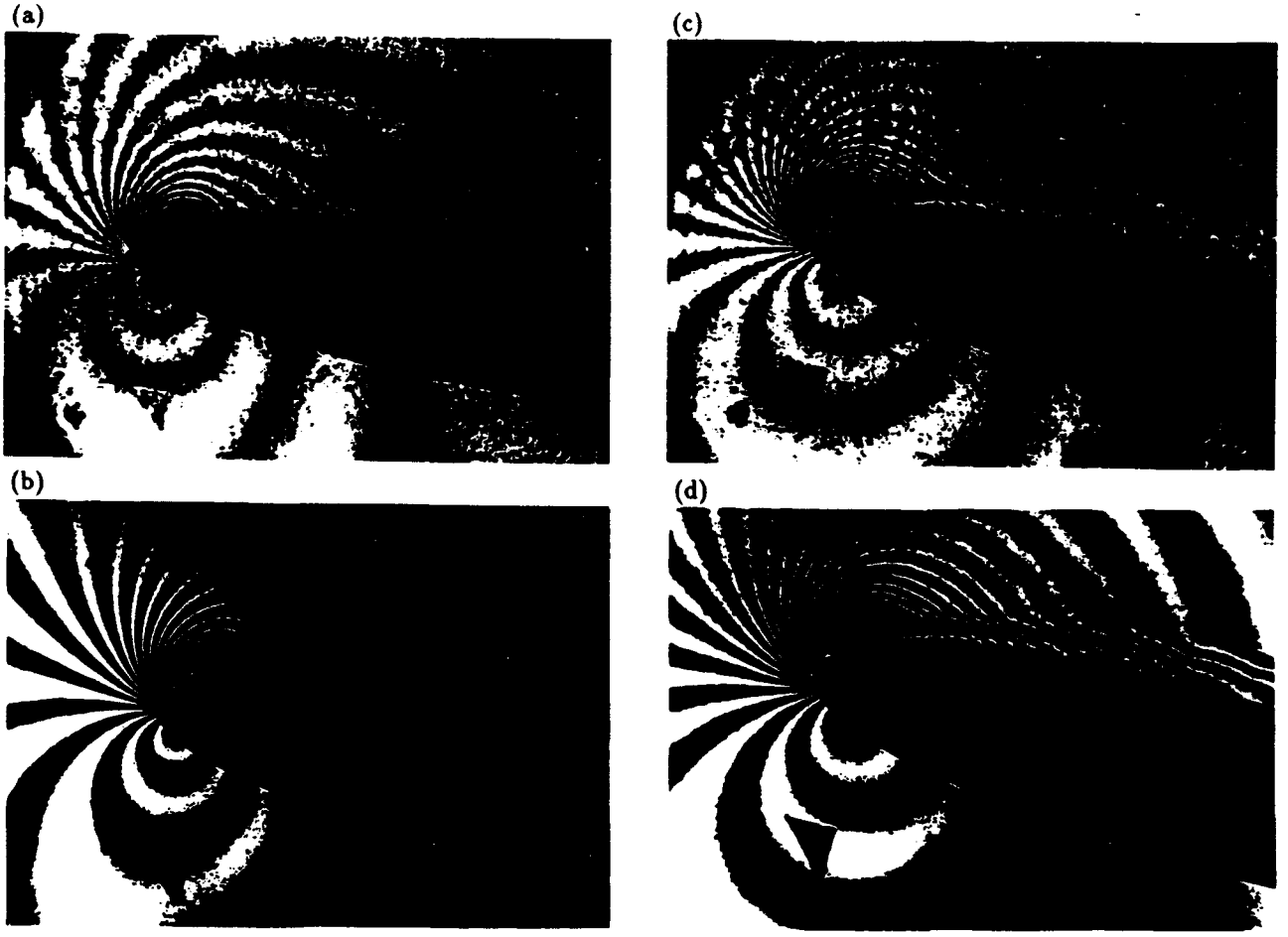

Figure 5. Representative Interferograms of the Flow Field for M = 0.3, k = 0.05. (a) $\alpha = 10.07^0$. High-Speed Camera at 11.56kHz. (b) $\alpha = 10.00^0$, Single-Exposure Camera. (c) $\alpha = 13.99^0$. High-Speed Camera at 11.56kHz. (d) $\alpha = 13.99^0$, Single-Exposure Camera.

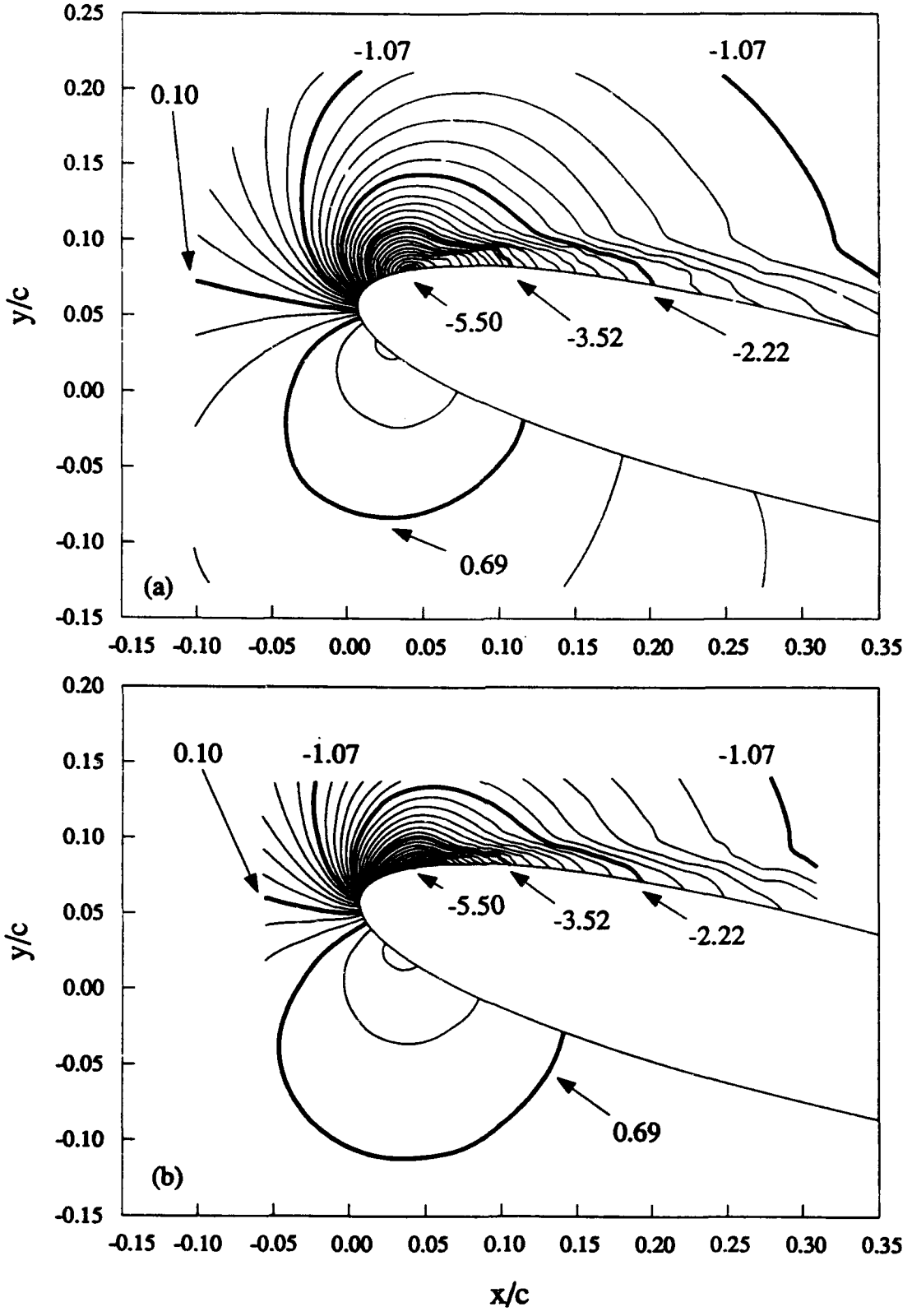

Figure 6. Global Pressure Distributions for M = 0.3, k = 0.05, $\alpha = 13.99^0$. (a) from the High-Speed Camera Image, Fig. 5c. (b) from the Single-Exposure Camera Image, Fig. 5d.

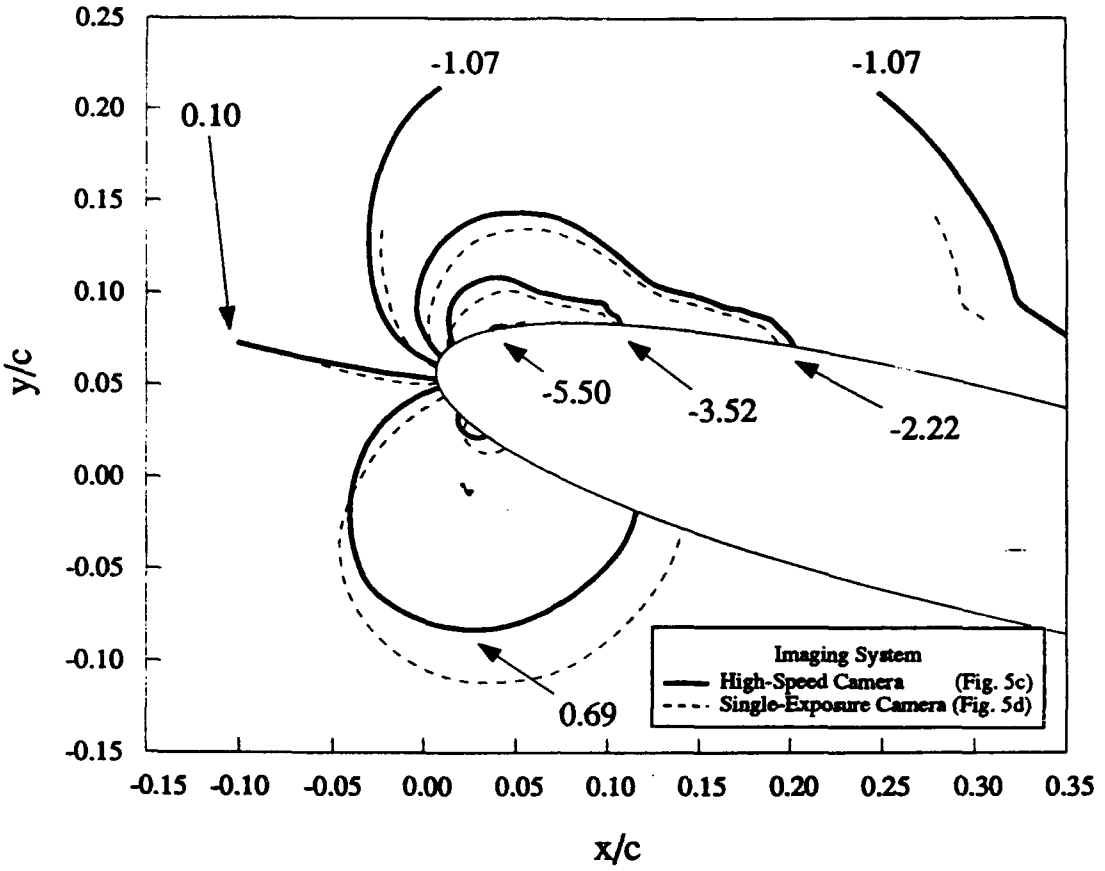

Figure 7. Comparison of the Global Pressure Distributions Obtained with the High-Speed and Single-Exposure Imaging Systems.

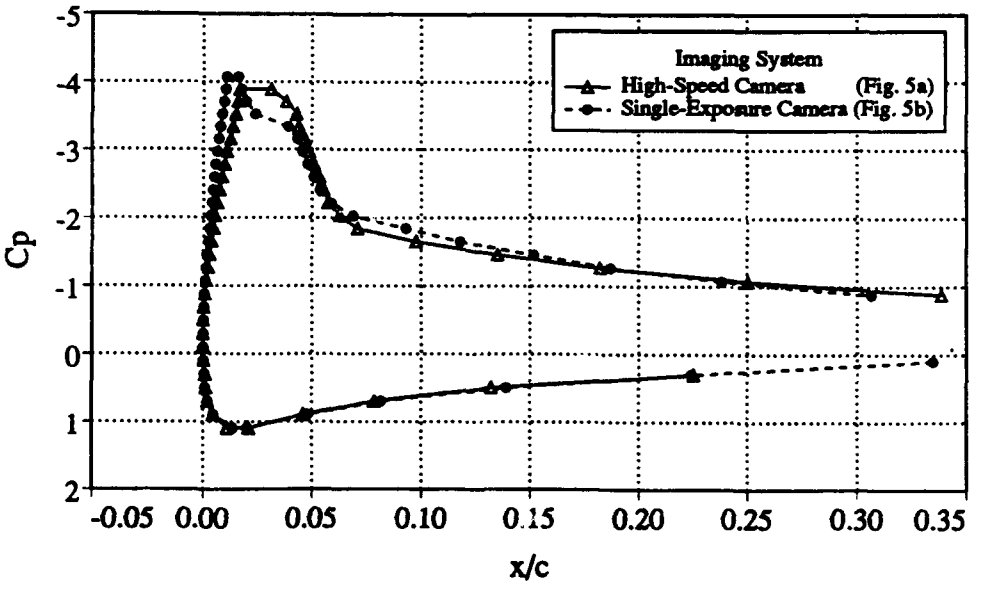

Figure 8. Comparison of the Surface Pressure Coefficient Distributions Obtained with the High-Speed and Single-Exposure Imaging Systems.

INVESTIGATION OF THE UNSTEADY DIFFUSER FLOW IN A RADIAL PUMP

K. Eisele, Z. Zhang and F. Muggli

Sulzer Innotec AG, Fluid Dynamics Laboratory
CH 8401 Winterthur, Switzerland

ABSTRACT

This paper describes the extension of earlier work using Laser anemometry and numerical simulation on the impeller of radial pumps to the flow in a pump diffuser. This earlier investigation showed that the pump characteristic is strongly influenced by the interaction between the impeller and the vaned diffuser. The goal of the current research project is to get a better understanding of the diffuser flow through unsteady measurements and numerical simulations. For this work the test pump was equipped with a special diffuser selected for the Laser anemometry measurements and the numerical simulations. For the measurements Laser Particle Image Velocimetry and Laser Doppler Anemometry were used. In a first step the measurements were compared with steady numerical diffuser simulations. The phase-locked ensemble-averaged 3 dimensional unsteady flow field in the diffuser was animated for better understanding.

NOMENCLATURE

B	width
Cx, Cy, Cz	velocity components
D	diameter
n	speed (rpm)
Δp	pressure difference
Q	flow rate
Q_0	flow rate at best efficiency point
U	circumferential velocity
Δx	fringe spacing
X,Y,Z	coordinates
α	beam crossing angle
ϕ	angle
ρ	density
$\psi = \frac{\Delta p}{\rho/2 \times u_2^2}$	pressure coefficient

INTRODUCTION

A pump characteristic, that is the variation of the head coefficient and efficiency versus flow coefficient, can be improved by optimising the impeller alone, the diffuser alone or the entire pump. In industrial design methods for pumps the impeller and diffuser are considered separately, and the unsteady interaction between the impeller and the diffuser has, until now, not usually been considered in design calculations (Casey 1994). The unsteady flow interaction is, however, very important as it affects not only the pump characteristic but also the acoustic and structural performance of pump components (Gülich and Bolleter 1993). The unsteadiness in the diffuser is generated by viscous blade wakes from the impeller and by potential flow effects.

Due to the importance of the unsteady flow interaction between rotating and stationary blade rows many turbomachinery research projects on this topic have been reported in the literature. Most of these reports deal with axial compressors or axial turbines (Casey 1994, Cho et al. 1993, Saxer 1993, Daniel 1993). Research projects which deal with centrifugal turbomachines are not so numerous although some attention has been given to the interaction between the impeller and the tongue of radial pumps (Chu 1993, Hureau et al. 1993).

This paper describes a new investigation using experimental and numerical tools to get a better understanding of the unsteady interaction between a radial pump impeller and a vaned diffuser. This current work builds on earlier experience gained in applying laser anemometry and numerical methods to pump impellers (Eisele et al 1992, Eisele et al 1993). In the current work the measured data for the flow field in the diffuser are compared with steady Navier-Stokes simulations.

EXPERIMENTAL SET-UP

Test rig

A test rig for a single stage pump has been designed to represent a last stage of a multi stage pump. The details of the design of test rig are described in Eisele et al 1992. The diffuser used in this investigation was optimised to provide good optical access and to improve the specification of the boundary conditions for the numerical simulations (Fig. 1). This diffuser is similar to that in the last stage of a multistage pump diffuser. The advantage of this design lies in the clear definition of the boundary conditions for the simulations and in the well defined measurement planes for comparison between the results of the measurements and of the numerical simulations.

Two diffusers of similar geometry were used in this work. For the flow visualisation and LPIV measurements a perspex model was manufactured and for the LDA measurements an aluminium diffuser was machined. The perspex model was also equipped with pressure transducers for static and dynamic measurements of the wall pressures.

The main dimensions of the impeller and the diffuser section are listed in table 1.

Impeller	Diffuser
D0 = 140 mm	D3 = 364 mm
D1 = 208 mm	D4 = 570 mm
D2 = 350 mm	
B2 = 32.9 mm	B3 = 34.5 mm
n = 1000 rpm	
Vanes: 7	Vanes: 12

Table 1: Main dimensions of the pump

LDA

A two colour Dantec fiber LDA with a PDA processor was used for the measurements in the pump diffuser. A summary of the optical characteristics of the velocimeter is provided in table 2.

Laser type	Innova 90
Laser wave length	488.0/ 514.5 nm
Probe diameter	60 mm
Beam spacing	38 mm
Focal length	400 mm
Fringe spacing	5.14 / 5.42 µm

Table 2: Main dimensions of the LDA

With this LDA, two components of the three dimensional velocity vector can be measured from a single viewing angle. The third component of the 3 dimensional flow was measured by an additional measurement from a second LDA viewing angle. For this approach to be satisfactory special care needs to be taken with regard to the accuracy of the traverse system. This system must ensure that the two measurements are taken at exactly the same point.

The final accuracy of measurement position is determined not only by the accuracy of the traversing system but also by the adjustment of the measurement volume in the diffuser. The measurement volume was checked by using a gold sphere fixed at a defined position in the diffuser. When the measurement volume is focused on the surface or in the centre of the sphere then the reflected beams are such that they follow the reverse path of the incoming beams and provide an exact calibration of position. With this system the accuracy of the positioning system was found to be very high ($\leq \pm 0.05$ mm).

The best measurement results would be obtained if the second viewing angle were perpendicular to the first one, in such a manner that the third component could be measured directly. This was not possible in the existing test pump as the LDA probe had to be mounted in front of the pump (see **Fig. 1**) at an angle less than 90 degrees. The viewing angle was selected on the basis of the LDA data rate and the accuracy of the measurements, to be 26 degrees away from the vertical to the window in the horizontal plane (**Fig. 2**). The selection of a non-perpendicular view angle effects the LDA characteristics of the two beams differently (Zhang 1993). The green and blue laser beams no longer cross at the same position and, as a consequence, only one dimensional measurements are possible with either the blue or green beams. The fringe spacing in the measurement volume is also influenced because the beam intersection angle decreases. The fringe spacing is determined as follows :

$$\Delta x_{\angle} = \frac{\sin(\alpha_1/2)_{\perp}}{\sin(\alpha_1/2)_{\angle}} \times \Delta x_{\perp}$$

If the LDA probe is moved in the axial direction, a purely 1-dimensional movement, the measurement volume describes a 2-dimensional trajectory in the horizontal plane. The relationship between the trajectory of the probe and the measurement volume is given by (**Fig. 2**) (Zhang 1993):

X- co-ordinate:

$$\frac{\Delta X_{MV}}{\Delta X_{Probe}} = \frac{tg\phi_{A0} - tg\phi_{B0}}{tg\phi_{A1} - tg\phi_{B1}}$$

Y-co-ordinate:

$$\frac{\Delta Y_{MV}}{\Delta x_{Probe}} = tg\phi_{A0} + \frac{\Delta x_{MV}}{\Delta x_{Probe}} \times tg\phi_{A1}$$

These equations were used to determine the measurement position in the diffuser. (Δx, Δy) M

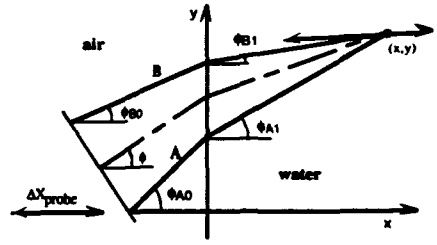

Fig. 2: LDA beam path

LPIV

To obtain 2-dimensional steady and unsteady flow field information a particle image velocimetry technique was applied. The illumination source was a continuous wave argon ion laser with a glass fiber light sheet probe. This fiber probe was mounted in the pump. The measurement zone was illuminated through a window and a perspex diffuser vane. Multiple exposures were realised through a CCD camera with a high speed shutter and with an integrated light amplifier. The shutter of this camera is computer controlled and the PIV parameters could be rapidly optimised. The shutter of the camera and the frame grabber were synchronised with the rotational position of the pump impeller. With a delay box, a phase-averaged velocity field at different impeller positions could be measured. The direction of the velocity vector was determined by tagged particle traces with long and short exposures. The velocity vectors were determined by a particle tracking software from Grant 1990.

NUMERICAL METHODS

A commercially available Navier-Stokes code (TASCflow) was used for both the impeller and the diffuser

simulations. The simulation results at the impeller outlet were used to provide the inlet conditions for the diffuser simulation. The impeller results were averaged in the circumferential direction. The diffuser was discretized with a H-grid with about 50000 nodes. One simulation needed between 10 and 20 hours CPU time on an IBM RS 6000 computer.

RESULTS

The data rate and the SNR were improved by using the Dantec LDA instead of the earlier Sulzer LDA (Eisele 1992). The data rate increased from about 600 HZ to 1500 Hz for the 2-dimensional measurements. For the measurement of the third component a data rate of about 500 Hz was reached.

The 3-D flow field in the diffuser was measured at 5 different flow rates from the BEP (best efficiency point) to deep partload. The main interest of the LDA measurements was to examine the flow in the semi-vaneless region of the diffuser, so the most of the LDA measurement points were localised in this region. The LPIV measurements were used to complement the LDA measurements to obtain a better idea of the flow field in the whole diffuser.

The LDA measurements were first analysed with software from Dantec. This software averaged and arranged the data for one complete revolution with an averaging window of 3 degrees. Afterwards the 3-D velocity vectors were calculated and the data were reduced to single impeller pitch by ensemble-averaging.

Fig. 3 shows the scatter diagrams over several revolutions of the impeller for two flow rates at two points in the diffuser. The blade passing frequency is dominant at the diffuser inlet (B2) for both flow rates. In the diffuser channel the strength of the blade passing influence decreases. At partload other unsteady flow phenomena become important and the turbulence intensity increases. The mean values and the RMS values show the decreasing blade passing frequency and the increasing RMS values along the diffuser (**Fig. 4**). The Rms values for the third component was not analysed because the optical axes of the LDA probe is not perpendicular to the window. The third component is also dependent on the blade passing. The time lag (see the wave maxima in **Fig. 4**) between the blade passing waves between the two measurement points (B2 and F3) correspond with the time which is calculated from the distance of these measurement points and the mean velocity.

Fig. 5 show the velocity vectors in the middle of the diffuser pitch near the diffuser inlet for all 5 flow rates at different impeller positions. These figures show that the recirculation zones near the hub and the shroud depend on the flow rate and the impeller position.

The best method to show and to understand the phase averaged flow is to animate the LDA results. The 224 velocity vectors were animated at 17 different impeller positions. The shape of the diffuser vanes and the position of the impeller vane has also been animated for better understanding of the flow. This animation was realised with the graphic package AVS developed for the visualisation of CFD results. One of these images is shown in **Fig. 6.** This animation shows very clear that not only the velocity vector magnitude but also the vector direction changes, depending on the impeller rotational position.

The main differences between the LDA, LPIV and the TASCflow results are the size of the recirculation zone near the pressure side of the diffuser vane (**Fig. 7**). Due to the positions of the LDA measurement points only the onset of the recirculation zone can be detected. The LPIV results show a much smaller recirculation zone than the simulation. The recirculation is initiated by change in the slope of the diffuser wall. In reality the recirculation zone is unsteady in time and position. These differences also affect the pressure rise in the diffuser (**Fig. 8**). The onset of the recirculation can also be seen as a disagreement between the measured and simulated pressure rise at partload. These differences between the real diffuser flow and the simulation may be the result of using a steady simulation or a result of the $K\varepsilon$ turbulence model being used. This question can be answered by an unsteady diffuser simulation with measured boundary conditions which will follow in the next phase of this work.

CONCLUSIONS

Earlier experience in applying LDA technology to industrial pump impellers, has been extended in such a manner that high quality 3-dimensional unsteady LDA measurements have now been obtained in a pump diffuser. In addition new experience with a LPIV system using a 'pulsed' camera instead of a pulsed laser, has been obtained. For measurements in a pump it is very important to trigger the camera with the rotational position of the impeller.

The measured unsteady flow field in the diffuser could be animated using software developed for CFD flow visualisation. This animation leads to better understanding of the flow.

The comparison of the measured and simulated pressure rise in the diffuser is very encouraging for further numerical studies especially for unsteady Navier-Stokes simulations.

ACKNOWLEDGEMENTS

The authors would like to thank Sulzer Pumps, Sulzer Hydro, Sulzer Turbo and Sulzer Innotec for their financial support of this project.

REFERENCES

Casey, M.V. 1994, The industrial use of CFD in the design of Turbomachinery, AGARD Lecture Series 195, May 1994.

Cho, N.-H., Liu, X., Rodi, W. & Schönung, B. 1993, Calculation of Wake-Induced Unsteady Flow in Turbine Cascade, Journal of Turbomachinery, October 1993, Vol. 115, pp. 675-684.

Chu, S., Dong, R. & Katz, J. 1993, The Effect of Blade-Tongue Interactions on the Flow Structure, Pressure Fluctuations and Noise within a Centrifugal Pump, Proc. of First Int. Symposium: Pump Noise and Vibrations, Clamart, July 1993.

Daniel, J.D &Verdon, M.V.1993, Numerical Simulations of Unsteady Cascade Flows, ASME Symposium: Int. Gas Turbine and Aeroengine Congress and Exposition, Cincinnati, Ohio May 1993.

Eisele, K., Muggli, F. & Schachenmann, A. 1992, Investigations of flow phenomena in multistage pumps, Sixth Int. Symp. on Appl. of Laser Anem. to Fluid Mechanics Lisbon July 1992.

Eisele, K., Muggli, F. et al 1993, Pump Development with Laser and Computer, Technical Review Sulzer, 2 1993 pp. 37-39.

Grant,I & Liu,A 1990 Directional ambiguity resolution in particle image velocimetry by pulse tagging, Experiments in Fluids, Vol 10, pp71-76, reprinted in Selected Papaers on Fluids, SPIE Milestone Volume MS 99 Editor Ian Grant 1994.

Gülich, J.F.&Bolleter, U. 1992, Pressure pulsations in Centrifugal Pumps. Transactions of the ASME 1992 Vol. 114 pp. 272-279.

Hureau, F., Kermarec, D. & Foucher, D. 1993, Etude de l' Ecoulement Instationaire dans une Pompe Centrifuge Fonctionnant a Debit Partiel, Proc. of First Int. Symposium: Pump Noise and Vibrations, Clamart, July 1993.

Saxer, A.P.& Giles M.B. 1993, Predictions of 3-D Steady and Unsteady Inviscid Transonic Stator/Rotor Interaction with Inlet Radial Temperature Non-Uniformity, ASME Symposium: Int. Gas Turbine and Aeroengine Congress and Exposition, Cincinnati, Ohio May 1993.

Zhang, Z. 1993, Theoretische Untersuchungen der Einsatzbedingungen für 3-dimensionale Laser-Doppler-Messunegn in Kanalströmungen.
Sulzer Innotec Report, STT. TB.93.022.

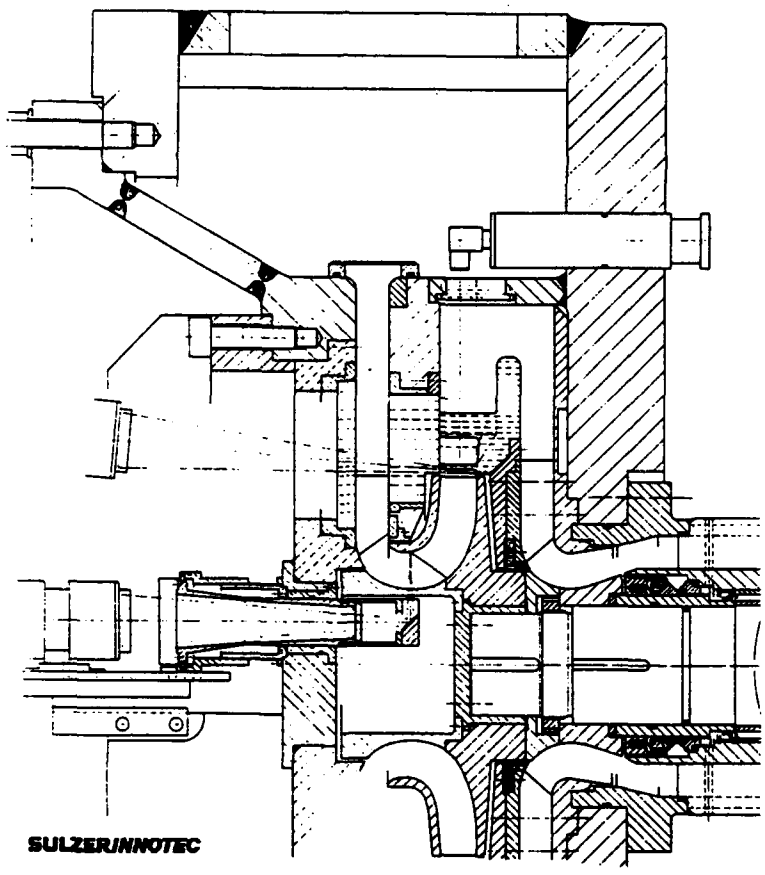

Fig. 1: Pump with vaned diffuser

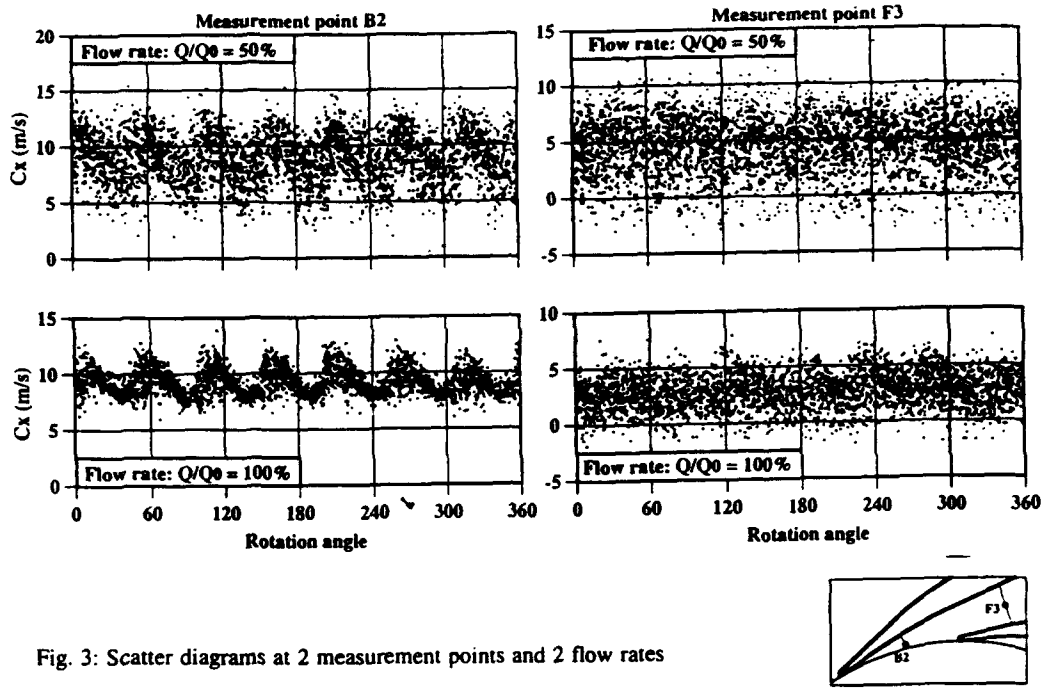

Fig. 3: Scatter diagrams at 2 measurement points and 2 flow rates

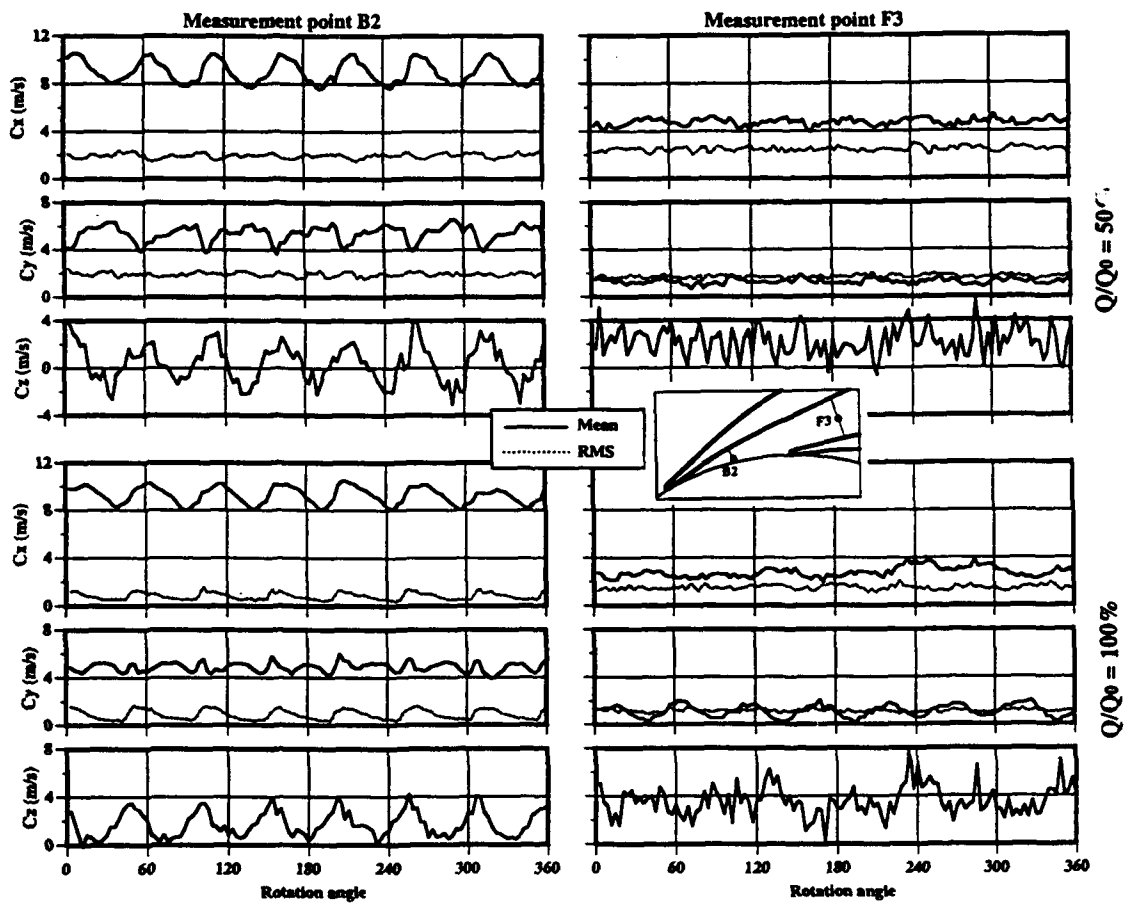

Fig. 4: Phase averaged data at 2 measurement points and 2 flow rates

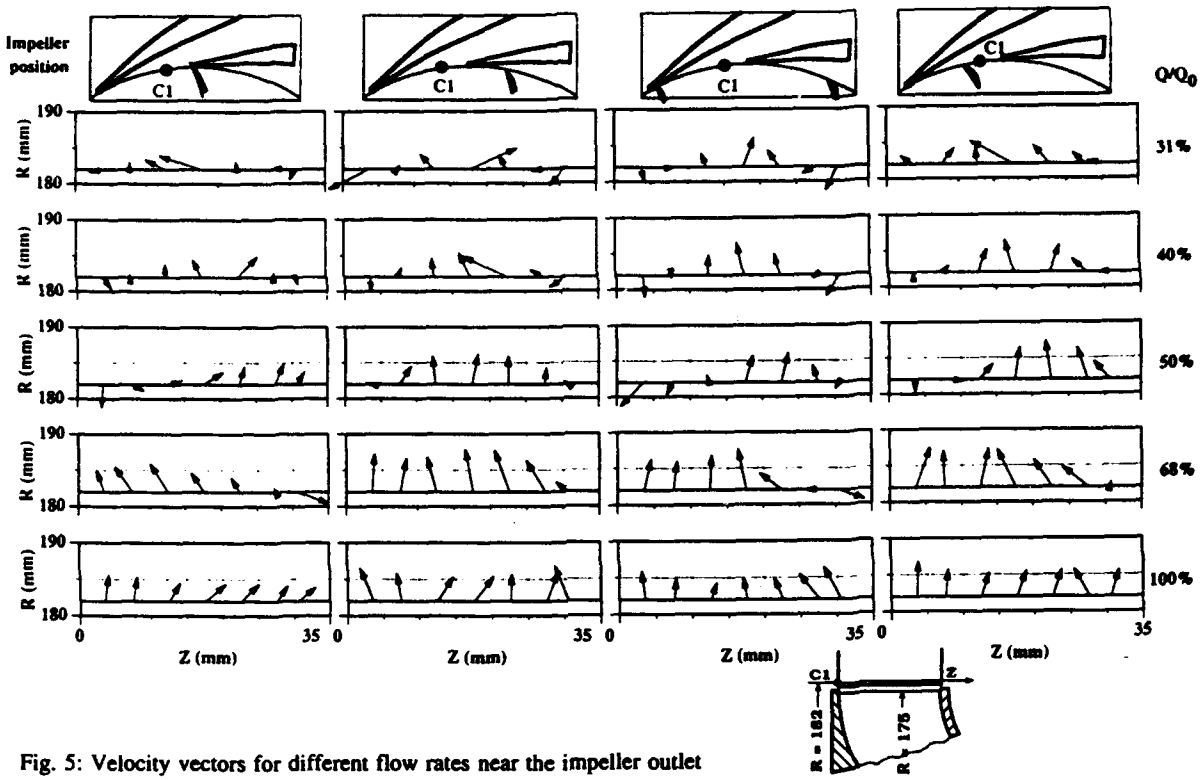

Fig. 5: Velocity vectors for different flow rates near the impeller outlet

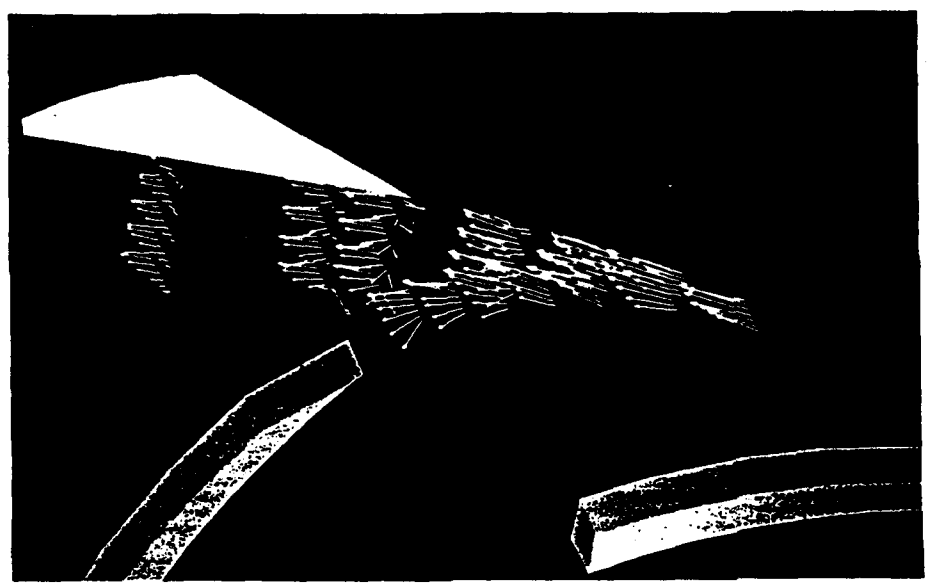

Fig. 6: Snapshot of the computer animation of 3 D velocity field (Q/Q_0 = 50 %)

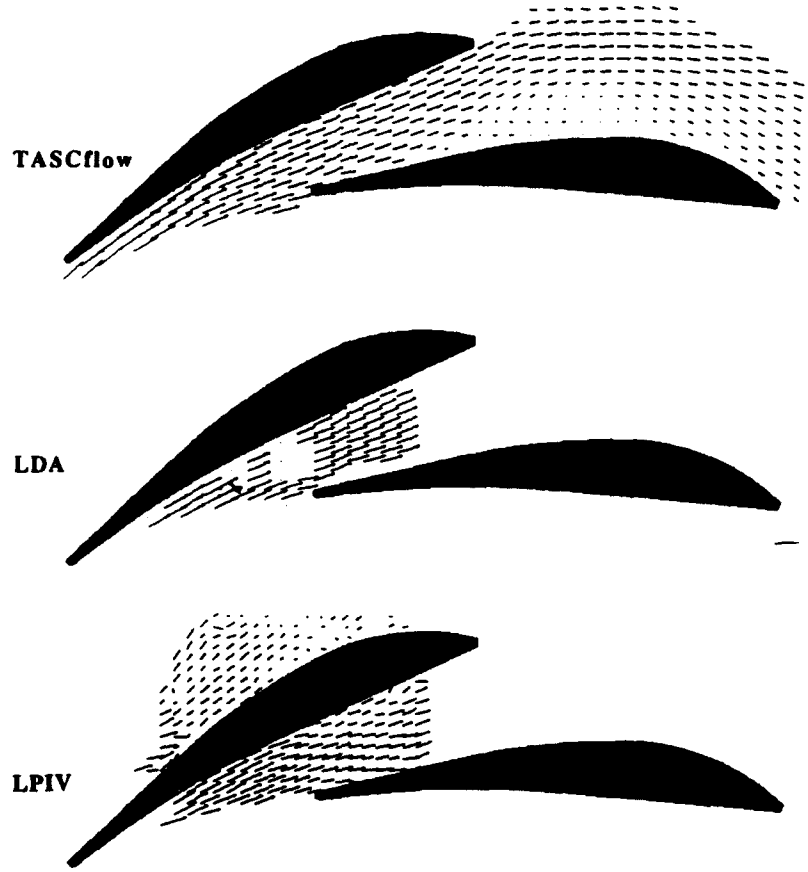

Fig. 7: Velocity comparison in the midplane of the diffuser channel

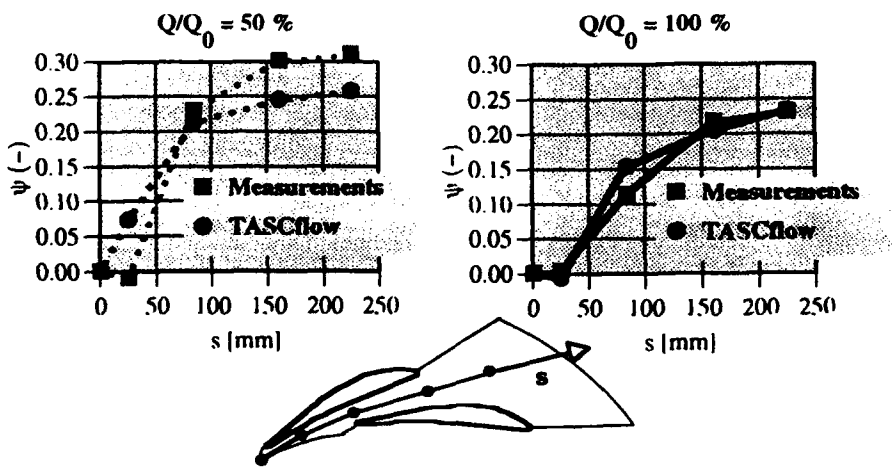

Fig. 8: Comparison of the pressure rise in the diffuser at the shroud side

THE APPLICATION OF 3D LASER DOPPLER ANEMOMETRY TO LARGE SCALE FLOW MEASUREMENTS ON A FORMULA 1 RACING CAR

C.Saunders.
Williams Grand Prix Engineering Limited, England.

J.Rickards, C.Swales, R.V.Barrett.
Department of Aerospace Engineering.
University of Bristol, England.

ABSTRACT

The aim of this work was to map fully the flow field around a half scale Formula one racing car in the Williams low turbulence wind tunnel. Readings of mean velocity, and turbulence intensity with its associated statistical quantities were taken at over 8000 discrete measurement points using a Dantec three dimensional LDA system. The paper outlines the techniques employed to improve the accuracy of the measurements taken, examines the spatial resolution of the system and uses some of the results obtained to illustrate the complex flows encountered. These included very strong vortices, wakes with large RMS velocities and regions of high local velocity. Modifications to the standard traverse gear allowed a wider range of optical configurations to be employed enabling measurements to be taken in regions which would otherwise have been inaccessible. The use of 45 degree mirror boxes to improve optical access by allowing the beams to be projected at a very shallow grazing angle to the tunnel floor is also described.

1. INTRODUCTION

This work was undertaken to provide measurements of velocity, turbulence intensity and RMS velocity covering the entire flow field around the Williams FW16 F1 car. These were intended to provide details of the flow structures present, enabling further optimisation of the aerodynamic performance of the vehicle.

The method of measurement was required to provide three components of velocity to a high degree of accuracy and to be completely non-intrusive. Measurements were required at approximately 5000 points around the main body of the car, divided into twelve lateral traverse planes, and to within 1mm of the surface, with a further 3000 measurements required under the front wing and around the foot-plate. To achieve accurate mean values the measurements were averaged over several complete recirculations of the flow around the tunnel (around 10 seconds). The task was required to be completed in a short time scale to prevent undue interruption to existing test programs. These requirements made 3D laser Doppler anemometry essential to the task.

The measurements were taken in the low turbulence research tunnel at Williams Grand Prix Engineering, Didcot on a half scale model with the tunnel and rolling road running at 40 m/s. This tunnel has a large square working section, very low freestream turbulence intensity and runs at atmospheric pressure in the working section. Electronic feedback control of the rolling road ensures that its speed is accurately matched to the wind speed. Boundary layer suction is used to remove the tunnel wall boundary layer at the start of the test section. The large volume of the tunnel (approx. 2000m^3) necessitated that high levels of seeding would be required in order to achieve acceptable data rates. This was provided by five Dantec type 55118 single jet seeders and two TSI model 9306A six-jet seeders, the seeding being injected through a breather vent downstream of the test section.

The equipment used was a Dantec three component LDA, illustrated schematically in Fig. 1. This consists of two optic heads mounted on a fully automated three-dimensional traverse mechanism, allowing 0.6 metres of movement in each direction, and linked by two 10 metre long fibre optic cables to a Spectra-Physics 5 Watt Argon-ion laser (model 2016). Both optic heads are free to rotate within their gimbal mounts, which, in turn, can be swept and dipped to provide the required optical configuration. Two pairs of beams (green and blue) are emitted from one head (referred to as the 2D head) and a third, violet, pair from the opposing (1D) head. Both heads are able to receive as well as transmit light and consequently either the back-scatter mode, where light is received by the transmitting optic head, or the cross-coupled mode, where scattered light from each pair of beams is received by the non-

transmitting head, can be employed. The frequency information from each channel is processed by separate Dantec Burst Spectrum Analysers (BSAs). These are connected to a 486DX 66MHz PC which controls data acquisition, processing and presentation using the 'Burstware™' software package.

The purpose of this paper is primarily to describe the operational procedures used, and the practical methods developed to improve the accuracy and scope of the measurements. *The reader should be aware that due to the sensitive nature of the results, it was necessary to omit certain details. In particular, the geometry of the car may differ slightly from that shown in the figures.*

2. TRAVERSE MODIFICATIONS

Due to the configuration of current Formula one cars, access was difficult to some areas in which measurements were required. For example, at some traverse positions, measurements close to the wheels were problematic due to the beams impinging on suspension components. In addition, highly swept configurations were required to gain access to some areas around the car, as illustrated by Fig. 2. This figure also shows the axis conventions used. Furthermore measurements under the front wing of the car could only be made using significantly different optical configurations to those conventionally employed. Due to the time constraints applied to this work, rapid repositioning of the traverse gear was necessary whilst maintaining the X-axis (streamwise) parallel to the tunnel working section. To maintain a high degree of alignment it was also necessary to isolate the traverse gear from any wind tunnel vibration. To achieve this, the traverse was fitted with metal wheels and mounted on two steel rails which were accurately aligned with the tunnel axis. These were raised 10mm above the floor and mounted at either end onto a solid concrete base. A clamp mechanism was used to prevent movement of the traverse gear once the desired position had been set.

To enhance the access to the car, through the use of a highly swept optical configuration, a simple turn-table, illustrated in Fig. 3, was designed to enable the optic bench to be rotated about the vertical Z-axis without affecting the direction of motion of the three traverse axes.

As the focal length of the optics were fixed at two metres, it was important that the optic heads, attached to the optic bench, could be moved fore and aft relative to the fixed traverse gear. This was achieved by the design of a forward extension arm, Fig. 3, on which the optic bench was mounted using a sliding junction block. The optic bench could thus be moved forward to compensate for an increase in the sweep angle of the bench, thereby preserving the distance of penetration of the beams into the tunnel whilst still allowing the full range of motion to be used on the traverse gear. To prevent undue strain on the traverse vertical drive motor the additional weight of this structure was relieved by a counterbalance weight. This was mounted onto the back of the vertical section of the traverse gear and connected to the optic bench by means of a steel cable passing over a pulley at the apex of the traverse gear (see Fig. 3). A high quality linear bearing allowed the counterbalance weight to move up and down smoothly thereby preventing backlash in the movement of the traverse.

3. ALIGNMENT AND VELOCITY TRANSFORMATION

A number of operational difficulties arose from the scale of the measurements taken and the large volume of the wind tunnel. The use of two metre focal length optic which was necessary to gain access to all regions of interest on the car, leads to a reduction in performance of the LDA, in terms of both data rate and data validity, compared to that achieved with shorter focal length lenses. In addition, even with the large number of seeding units used, the volume of the wind tunnel meant that a high seeding density could not be achieved. Thus accurate alignment was a prerequisite for this work to compensate for these difficulties and also to enable the system to operate in the cross-coupled mode (simultaneous side-scatter). Cross-coupled operation was used to achieve the spatial resolution needed for measurements close to surfaces and to minimise the effects of velocity biasing in regions of strong velocity gradient. Furthermore, to gain access to all regions of the car and minimise the number of traverse points lost due to impingement of beams on fixed features, such as suspension components, many different optical configurations were needed and thus it was frequently necessary to re-align the system optics. The alignment method used was required to be fast and reliable and to give consistently high performance.

Conventional alignment techniques require the six beams to be passed through an objective lens in order to view their images on a screen some distance beyond the lens. In some areas of the car, and in particular under the front wing, the very limited physical and visual access and confined space makes such techniques impossible. Consequently a quantitative alignment technique, developed at Bristol University, was used throughout the tests. The technique, described in detail in reference 1, uses the voltage output from a light dependent resistor with a 20 micron pin-hole aperture, as illustrated in Fig. 4, to locate the position of peak intensity within a laser beam or collection volume (made visible by passing light down the collection fibre). By

bringing the foci of the two collection volumes, and each of the six beams, separately onto the face of the pin-hole, an extremely accurate alignment is achieved. This method has the main advantage that it uses an entirely quantitative approach and is thus not hindered by the need to make subjective judgements based on visual interpretation of beam images, as is the case for most conventional methods. In addition alignment can be carried out in very confined spaces as there is no need to project the beams beyond the plane of the pin-hole. The highly consistent alignment accuracy achieved by the pin-hole meter method means that routine operation in the stringent cross-coupled mode can be guaranteed, and enables a large number of alignments to be carried out in a short time.

When using a 3D LDA a transformation matrix must be applied to the velocity data in order to convert non-orthogonal velocities into components aligned with the conventional wind tunnel axes. The derivation of this matrix is described by reference 2. It is important when evaluating the matrix to accurately determine the positional geometry of the six laser beams by a fast and reliable method. This was achieved by a simple extension of the pin-hole alignment technique, illustrated in Fig. 5. The pin-hole meter was used to locate the position of the centre of each of the six beams at two positions along its length. This was done by fixing the position of the meter, and moving the beams, one at a time, to the plane of the pin-hole thereby enabling the position of the beam centres could be read from the traverse control software. Having established the vector of each beam in space this geometry was converted into the requisite angles used in the velocity transformation matrix calculation. The same geometry may also be used to evaluate the calibration factor for each channel.

4.1 MEASUREMENTS AROUND THE CAR BODY

The flow around a contemporary Formula 1 racing car provides a wide variety of localised flow structures, each of which requires different approaches in order to achieve the best possible LDA results. These structures include very strong vortices shed from the tips of lifting surfaces such as the front and rear wings, high RMS wake flows shed by bluff bodies such as wheels and suspension components, and both laminar and turbulent boundary layer flows.

Two of the most difficult flow structures in which measurements were required were within boundary layers on the car body and vortices. The main problem posed by the boundary layer measurements was that of surface reflection, as it was necessary for the beams to approach almost perpendicular to the surface. This problem was accentuated in some regions where the curvature of the car body caused light to be reflected directly into the collection optics. The reflections were reduced by painting the measurement surfaces matt black, but this was not sufficient to enable boundary layer measurements. In addition boundary layer flows and vortices contain regions of very strong velocity gradient in which the spatial resolution of the LDA is important. If the LDA is operated in the commonly used back-scatter light collection mode in such regions, the very long, cigar shaped measuring volume obtained, results in strong velocity biasing effects.

To overcome both the above problems the system was operated in the cross-coupled light collection mode, which results in a near spherical measurement volume of significantly reduced dimensions. This is due to the fact that scattered light can only be detected from within the common overlap region of the collection volume path to the collection optic, and the cigar shaped intersection of the transmitted beams, as illustrated by Fig. 6. Fig. 7 illustrates graphically the superiority of the cross-coupled mode of operation compared to the back-scatter mode. The figure compares directly contours of vorticity for the central region of a small wing tip vortex, calculated from velocity components recorded in back-scatter and cross-coupled modes. The oval shaped distribution seen in the back-scatter case is caused by a velocity biasing effect which most strongly influences the vertical velocity component and is due to the length of the back-scatter measuring volume. Furthermore the peak vorticity values recorded in back-scatter mode are artificially high due to the influence of the biased vertical velocity gradient on the vorticity equation. The velocity biasing problem is accentuated in the case of a vortex as the nature of the flow tends to centrifuge the seeding away from the vortex core so that the seeding density increases with distance from the core. The authors consider the cross-coupled mode to be essential for LDA measurements in any flow where strong velocity gradients occur and to be the preferential mode for all other LDA measurements.

Behind the car, and in the regions downstream of the suspension components and the open wheels, wake flows were encountered with characteristically high RMS velocities. In such regions it is necessary to use a large bandwidth in order to capture all the velocity data and obtain accurate mean values. Experience has shown that operating with a high bandwidth, and in particular with a bandwidth significantly larger than that expected from knowledge of the velocity range, does degrade the performance of the LDA, and it is only through good alignment that this can be countered.

Due to the strong three dimensional nature of the flow around the car the vertical and horizontal velocity components can differ widely and may change rapidly with position. Consequently if the LDA processors are set to optimise data collection at one point

in space the settings may be unsuitable at a point only a short distance away resulting in a loss of data. To counter this problem it is possible to use a large bandwidth on all three channels, but only at the expense of velocity definition, data rate and data validity. Ideally the system should be configured so that it operates in a balanced manner with all three channels measuring similar velocities and using the same bandwidth, thereby improving the velocity definition.

This was achieved by the axial rotation of each of the optic heads within their gimbal mounts until each channel measured approximately the same velocity when in freestream flow. When operating in this way the system is more tolerant to sudden changes in velocity or RMS velocity and all channels respond in a similar manner to such changes. Furthermore by rotating the optic heads the configuration of the four beams emitted from the 2D head becomes more compact thereby allowing greater optical access to confined spaces.

To save time during the test program the geometry of the car was accurately measured beforehand using a micrometer, and the data fed into a computer program which generated co-ordinate grids which were shaped to the contours of the car body, as illustrated by Fig. 8.

4.2 RESULTS FROM THE BODY OF THE CAR

One of the most strongly disturbed regions of flow surrounding the car is in the region immediately behind the front wheels, where wakes shed from the rotating wheel and hub, suspension struts and strut/body interfaces interact with wing endplate vortices to produce highly complex three dimensional flows. This is illustrated by Fig. 9, which shows contours of streamwise RMS velocity at a section 20mm downstream of the rear of the front wheel. Immediately behind the wheel, marked by geometry lines, the velocities are much lower than freestream and the RMS velocity is extremely high as may be seen from the high density of contours in this area. By comparison the region between the wheel and the car body has areas of low RMS where the flow is almost undisturbed, and areas of strong localised wake disturbances shed from the suspension and front wing. The flow above the top of the wheel is almost undisturbed and thus high mean velocities and low RMS velocities are seen. The figure serves to illustrate the wide variation in RMS velocities encountered even within a single traverse.

In the region immediately behind the rear wing, two types of flow dominate, vortices and low speed/high RMS flow at the exit of the rear diffuser. The vortices are shed from the top surface of the rear wing end plate and are caused by the flow separating from the top edge of the end plate as it travels from the high pressure region inboard of the end plate to the low pressure area outside. These vortices may be visualised when Formula one cars race in humid conditions. Fig. 10 shows contours of U(streamwise), V(cross-flow) and W(vertical) velocity components and contours of streamwise vorticity taken at a station 170mm downstream of the rear wing end plate. The contours of streamwise velocity show a region of velocity deficit in the area of the vortex and in the lower portion of the plot where the flow exits the rear diffuser. The contours of the V and W velocity components show classical distributions for a vortex structure at the top edge of the end plate. In the region behind the diffuser the cross-flow velocities are very small whilst the vertical component shows a small up-flow.

The flow around the open wheels on a Formula one car has a strong influence on the overall aerodynamics of the car, and generates a large proportion of the aerodynamic drag. Fig. 11 shows a velocity vector plot composed of the V and W velocity components at a station 20mm in front of the rear wheel. This illustrates the strong three dimensional nature of the flow and, as can be seen, the direction of the velocity vector can suddenly reverse in the region of flow stagnation near the centre of the wheel posing considerable difficulties when recording data. It will be noted that this stagnation region is not central to the wheel as the rotation of the wheel causes flow circulation thus displacing the stagnation region downwards.

The strong influence of the open wheels is illustrated by Fig. 13, which shows contours of streamwise RMS at the three previously described stations, and the position of the traverse grids relative to the car. The wake flows from the wheels dominate the flow at all three stations though it is possible to see the trailing vortex from the rear wing.

5.1 MEASUREMENTS UNDER THE FRONT WING

A number of factors make measurements under the front wing of the car particularly difficult. The most obvious of these is that due to the extremely low ride height of the car it is difficult to gain access to the under side of the wing, both for alignment purposes and to take the measurements. The access is limited ultimately by the angular separation of the beams and the angle to the tunnel floor at which they can be projected. Fig. 12 illustrates the difficulties of access to the underside of the front wing. Several methods were developed to increase the level of access to the underwing region. In order to achieve the minimum possible grazing angle to the tunnel floor, thereby maximising the depth of beam penetration under the wing, the beams were projected vertically downwards and a pair of 45 degree mirror boxes were used to turn the beams through 90 degrees. These are

seen in Fig. 3. To allow these mirror boxes to reach the floor the optic bench was mounted on the front of the forward extension arm previously described. Triangulated adjustment of the mirrors enabled fine adjustment of the beam paths to be carried out and the pin-hole meter was used to establish the beam geometries. In addition to the mirror boxes a perspex window was built into the front wing end plate to allow measurements to be taken in the region behind it.

The flow under the wing is strongly accelerated and can reach almost twice the freestream speed. At such speeds, in order to achieve a sufficiently high centre frequency, it is necessary to employ a large bandwidth, and consequently, as discussed previously, the data rate and data validity will be much reduced. Furthermore the enclosed space beneath the wing means that strong reflections are almost unavoidable. Due to these reflections and the presence of regions of very steep velocity gradients and vortical flows the cross-coupled mode of operation was required. The extremely restricted space under the wing meant that conventional alignment techniques were impossible as there was insufficient space to project the beam images, particularly when aligning the beams through the perspex end plate. It was however possible to achieve the required alignment accuracy by the use of the pin-hole meter alignment method, which is not compromised by confined space.

5.2 RESULTS FROM THE FRONT WING

The flow around the front wing of the car is seen to be essentially two dimensional for the majority of the span except at the wing tips and near the centre of the wing where the raised nose causes some spanwise flow. The end of the wing is finished with a large end plate which has the primary function of minimising the 'leakage' of air from the high pressure region on the top surface to the low pressure area on the suction side, and thereby prevent loss of down force (lift) near the end of the wing. The flow around the wing is also further modified by the proximity of the wing to the ground which results in a greater lift force than would be achieved by the same wing in free air, an effect known as ground effect.

Fig. 14 shows a vector plot in the 'V-W' plane from a traverse taken through the vortex shed from the bottom of the wing end plate, which was recorded through the perspex window described above. The vortex is caused by separation of the airflow from the under side of the end plate as air is drawn under it into the low pressure region beneath the wing. Fig. 15 shows a 'U-V' vector plot taken from a horizontal traverse immediately below the wing end plate and illustrates the flow under the end plate which results in the vortex seen in Fig. 14. As can be seen, near the front of the car the U-vector is large, reaching a maximum at the point of peak suction on the wing, and hence the UV vector is predominantly streamwise. As the flow moves downstream the V-component increases, and the flow is impeded by the presence of the front wheel so that the 'U-V' vector tends increasingly towards the V direction, with the effect of increasing the vortex strength.

6. CONCLUSIONS

The successful acquisition of three dimensional velocity data at over 8000 discrete data points around the Williams FW16 formula one car has shown that large scale measurements can be carried out to a high degree of accuracy within a short space of time and encompassing a wide variety of flow structures. The quality of the data, and the high Reynolds number employed, enables the results to be directly related to the flow around the full scale car. It has been shown that in regions of strong velocity gradient where spatial resolution is of paramount importance the cross-coupled mode of light collection is essential and should be the preferred mode of operation for all other LDA measurements.

The quantitative pin-hole alignment technique has been found to consistently provide the alignment accuracy required, enabling routine cross-coupled operation. The method may be applied equally well when optical or visual access is poor. Modifications to the standard traverse gear have been shown to considerably increase the flexibility of the system when applied to a large scale flow problem.

ACKNOWLEDGEMENTS

The authors would like to thank Dantec (UK) for their invaluable advice and technical back-up during the course of this work.

REFERENCES

1. Swales, C. Rickards, J. Brake, C.J. Barrett, R.V. "Development of a Pin-Hole Meter for Aligning 3D LDAs" Dantec Information, No.12, pp2-5, (February 1993)

2. Swales, C. Rickards, J. Brake, C.J. Barrett, R.V. "Derivation of a Global Velocity Transformation Matrix For 3D LDAs" University of Bristol, Dep't of Aerospace Engineering, Report No.462 (November 1992)

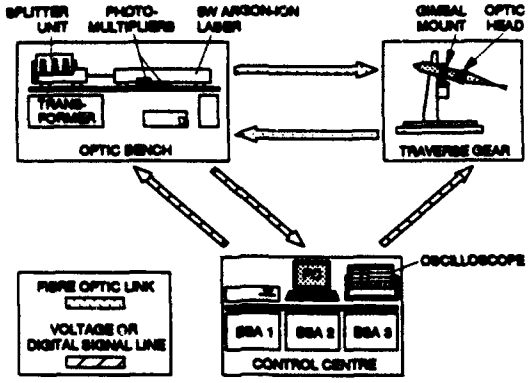

Fig. 1 Schematic diagram of the 3D LDA system.

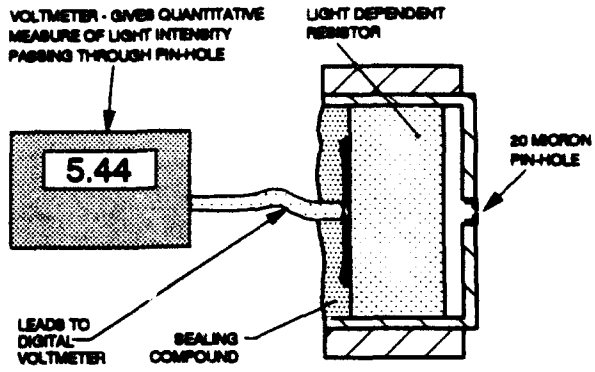

FIG. 4 Section through the pin-hole meter

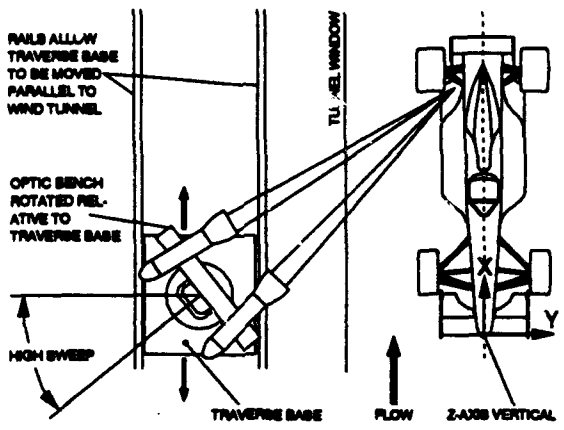

FIG. 2 Example of a typical highly swept optical configuration, also showing the definition of the model axes.

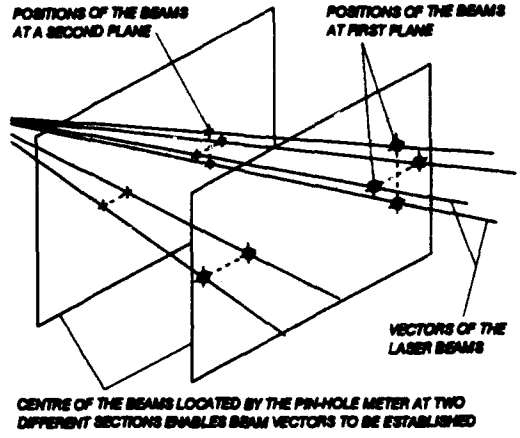

Fig. 5 Illustration of the use of the pin-hole meter to establish the geometry of the beams on a 3D LDA

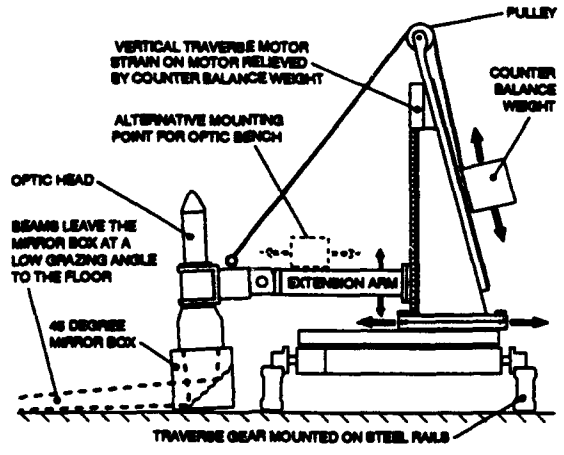

Fig. 3 Diagram showing the traverse gear modifications.

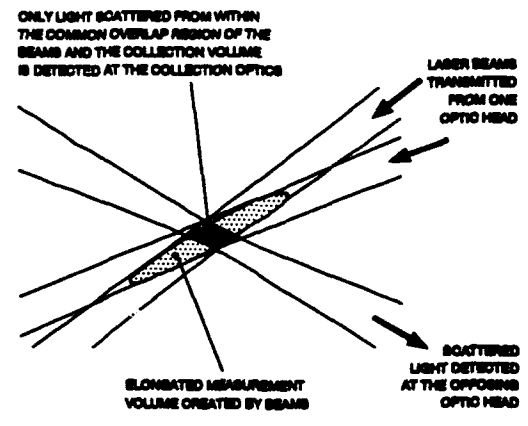

Fig. 6 Illustration of the cross-coupled mode of scattered light collection

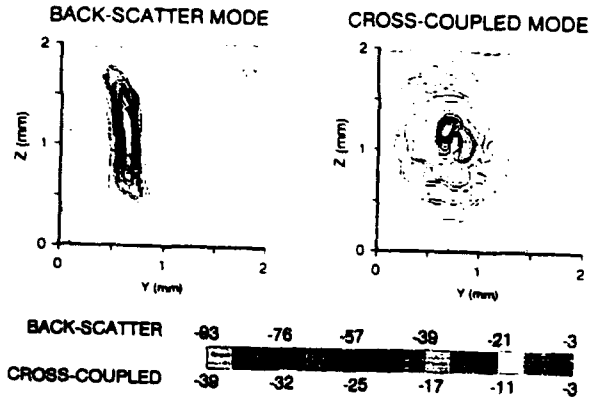

Fig. 7 *Contours of streamwise vorticity, Ωx, for a wing tip vortex, calculated from LDA data recorded in back-scatter and cross-coupled modes*

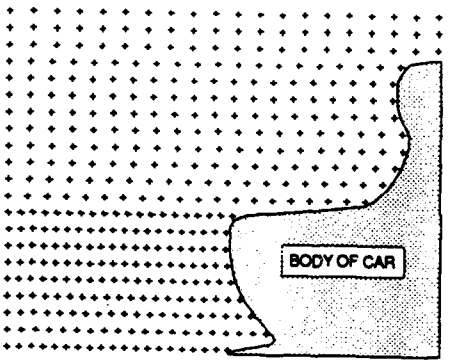

Fig. 8 *Example of a typical traverse grid*

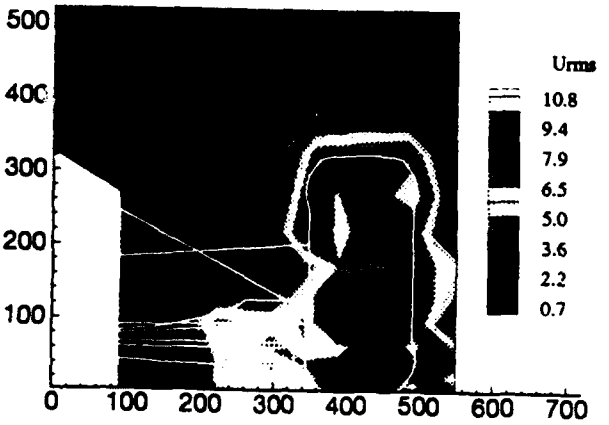

Fig. 9 *Contours of streamwise RMS velocity at a station 20mm downstream of the front wheel*

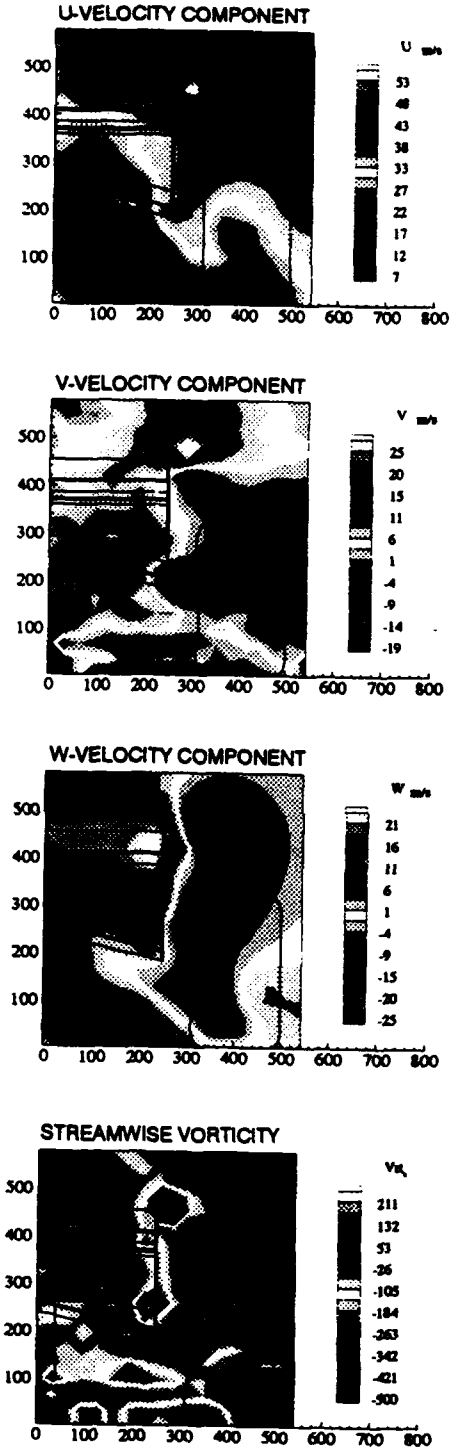

Fig. 10 *Contours of U,V and W velocity components and streamwise vorticity at a station 25mm downstream of the rear wing end plate*

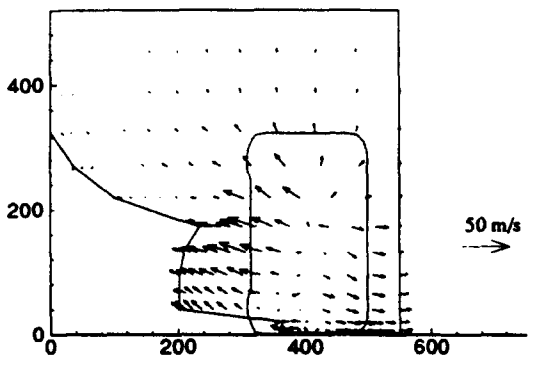

Fig. 11 *Velocity vector plot composed of the V and W components at a station 20mm upstream of the rear wheel*

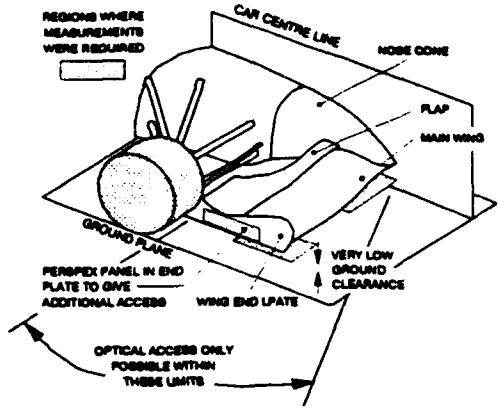

Fig. 12 *Illustration of the problems of access to test traverse sections under the front wing*

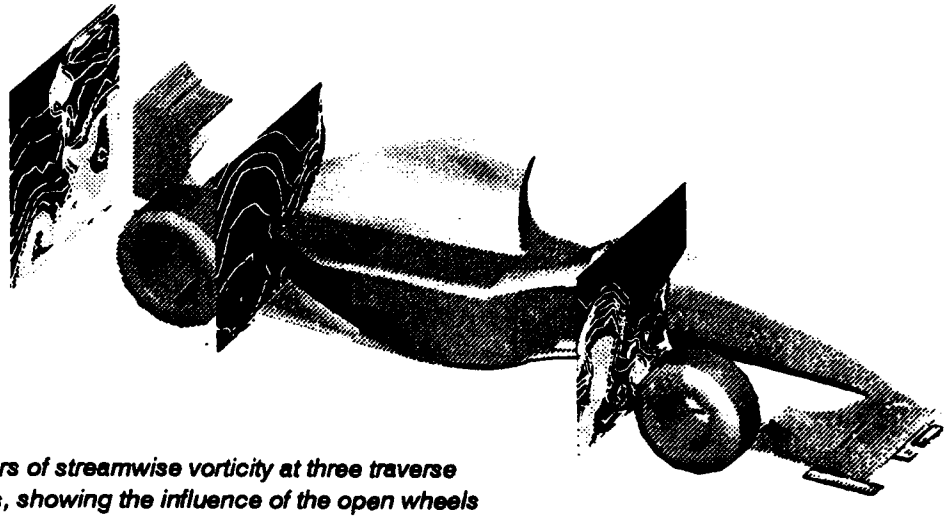

Fig. 13 *Contours of streamwise vorticity at three traverse stations, showing the influence of the open wheels and rear wing vortex*

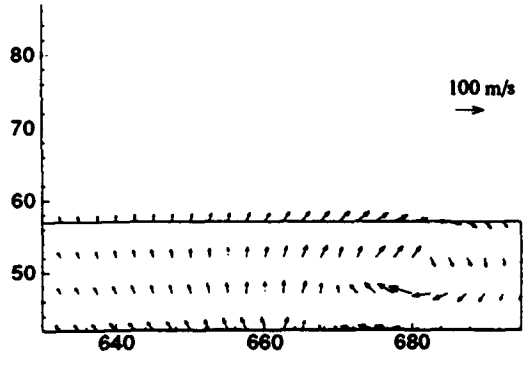

Fig. 14 *Velocity vector plot composed of the V and W components for a section through a vortex shed from the front wing*

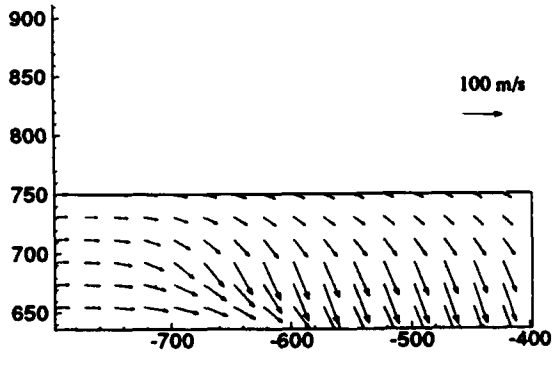

Fig. 15 *Velocity vector plot composed of the U and V components showing the flow under the front wing*

Session 39.
Complex Flows

MEASUREMENTS OF VELOCITY AND A PASSIVE SCALAR IN AN ISOTHERMAL-FLOW MODEL OF A PRESSURISED-COAL COMBUSTOR

A. Moore, A.M.K.P. Taylor and J.H. Whitelaw

Mechanical Engineering Department
Imperial College of Science, Technology and Medicine,
Exhibition Road, London SW7 2BX, England

ABSTRACT

The isothermal flow in a model of an arrangement proposed for the combustion of pulverised coal at high pressure has been examined by a combination of flow visualisation, laser-Doppler velocimetry and probe measurements of the concentrations of a passive scalar. The model comprised a perspex enclosure of 138 mm diameter and 311 mm length, closed at the top and with the lower end joined to a diffuser. Four 19 mm diameter inlet pipes were arranged circumferentially at 90 degree intervals and directed the inlet flows so that they impinged on each other and subsequently on the top surface before turning to form a region of separated flow and passing between the incoming jets and into the diffuser. The results confirm the nature of the flow and quantify the size of the recirculation regions and, therefore the residence times which they provide for particles. The passive scalar, a tracer of helium in air, was added to one inlet flow and the results show that scalar field is dominated by the penetration of the jet.

1. INTRODUCTION

The use of pulverised coal as fuel for a gas-turbine combustor implies that it be burned at high pressure and that particulates be removed from the hot gases before they enter the turbine. These topics have been discussed by, for example Preusser and Spindler (1988) and by Hannes, Reichert and Weber (1989), and particular geometrical arrangements have been proposed by Hannes et al, Hazanov, Goldman and Timnat (1985), Sadakata, Sakai, Tominaga, Yamamoto and Suzuki (1993) and Thambimuthu (1993) and by Mattsson and Stankevics (1985). This paper is concerned with the arrangement of the last two authors in which a number of jets of coal-laden air are directed into a cylindrical furnace so that they impinge and move towards the closed top of the enclosure which causes the formation of a region of recirculation which allows the required residence time for combustion before the hot gases and remaining solids flow towards the bottom of the container where the gases flow through ducting, which causes the solids to remain, and towards the turbine. The investigation is restricted to the flow in the chamber of the furnace in which the primary combustion takes place and so does not address the flow in the lower region where the hot gases are separated from the solid materials. Nevertheless, the results provide a basis for further investigation in that they include the fluid-dynamic boundary condition for the flow at entry to the separating region.

The measurements presented here correspond to isothermal single-phase flow and have been performed to quantify the nature of the flow under these idealised conditions and thereby serve as a foundation upon which to build the complexities associated with two-phase flow and combustion. They have been performed with a combination of flow visualisation, laser-Doppler velocimetry and probe measurements of a tracer of helium gas which quantifies the behaviour of a passive scalar and this instrumentation is described in the following section in the context of the flow configuration and with an assessment of the uncertainties. Two visualisation methods were used, the first based on direct photography of the light scattered from small particles and the second on the dispersion of an oil and paint mixture on a surface within the flow. The first proved to be less quantitative than hoped and the second provided a near-quantitative impression of the flow upon which to base the location and detail of the velocity measurements. The measurements of the passive scalar, with injection of the helium tracer through one of the four entry ducts, are representative of non-dimensional temperature for the particular boundary condition of an adiabatic wall. All measurements have been provided in sufficient detail to support the corresponding computational efforts of Bergeles and Papadakis (1994). The results are presented and discussed in the third section and the paper ends with a summary of the more important conclusions.

2. FLOW CONFIGUATION AND MEASUREMENT TECHNIQUES

The plexiglass model is shown in figure 1 and comprised a cylinder of 138 mm internal diameter, closed at its top end and with four entry ducts of 19 mm internal diameter arranged symmetrically around the circumference to introduce air so that the four jets impinged on the axis of the cylindrical container and moved upwards until forced to reverse by the top surface. The entry ducts were arranged at 60 degrees to the vertical axis with the intersection of the axis of each entry duct with the inside of the enclosure at a distance of 173 mm from the top. The entry ducts were 760 mm long and connected to rotameters to measure and meter the flow and to a central source of compressed air. The lower end of the enclosure was connected to a 45 degree half-angle diffuser so that the exhaust passed through a duct of 38 mm internal diameter. All dimensions were checked and found to be constant within 2 % of those cited above. The surfaces of the perspex enclosure and entry ducts were polished to ensure optical access without major distortion and the various joins were effected with perspex cement. The flow rate of air to the four entry ducts was

maintained constant and equal to each other within 4 % and the consequences of asymmetries due to imposed differences in the four flow rates are discussed in the following section. Experiments were performed with total flow rates of 5.7 and 8.2 x 10^{-3} kg/s, corresponding to Reynolds number in each pipe and in the enclosure of 20,000 and 29,000 and 11,000 and 16,000 respectively. Preliminary tests with visualisation and by measurement of velocity profiles in orthogonal planes indicated symmetry of the flow sufficient to justify subsequent and detailed measurements of half profiles. A single reverse-cyclone arrangment was used to add seeding particles to one of the entry ducts at a time and this was done downstream of the rotameter and 2000 mm upstream of the entrance to the enclosure. Kaolin was the chosen seeding material for the velocity measurements and was supplied to the cyclone in the form of a powder of comprising particles of nominal diameter less than 3. For the visualisation, micro-balloons were added to the cyclone in the form of a powder of comprising particles with a nominal mean diameter within a 40-50 µm distribution. They provided a means to scatter light from a light sheet formed by a cylindrical lens and an argon ion laser operating in the green line with a power of around 0.7 W. Visualisation of these particles proved to be a less satisfactory method than that used by Sivasegaram and Whitelaw (1986) in their box combustor. This method made use of a thin sheet of stainless steel which was introduced into the enclosure along the symmetry planes of zero and 45 degrees after it had been coated with a mixture of kerosene, silicone oil and oleic acid with titainium dioxide particles as pigment. The plate and oil mixture were exposed to the flow for periods up to an hour and depended upon the thickness of the mixture and the wall shear stress in the region of interest. The surface patterns were photographed with a 35mm SLR camera using black and white 100 ASA film.

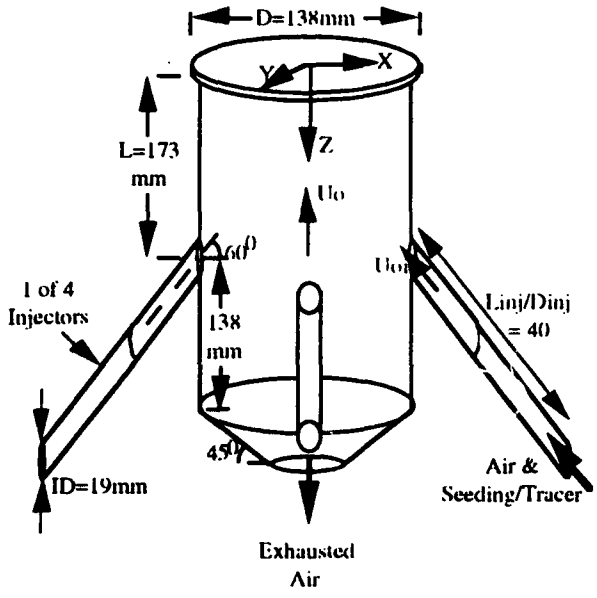

Figure 1 Schematic diagram of combutor geometry and co-ordinate system

The laser-Doppler velocimeter comprised a helium neon laser operated at 632.8 nm and 25 mW with an arrangement of Bragg cells and lenses to divide, focus and combine the light beams and to provide the possibility of frequency shift. Scattered light was collected in the forward direction by a "Tamron" 70-210mm f4.5 zoom lens. Further details of the optical arrangement are provided in table 1.

25 mW He-Ne Laser, Wavelength	632.8 nm
Beam Diameter of Laser at e-2 Intensity	1.25 mm
Focal Length Of :	
Imaging Lens From Laser to Grating	150 mm
Collimating Lens After Grating	200 mm
Imaging Lens to Focus Control Volume	300 mm
No. of Lines on Radial Diffraction Grating	16384
Maximum Frequency Shift	6.55 MHz
Stability of Frequency Shift	0.30%
Beam Spacing	41.8 mm
Half Angle of Beam Intersection Angle	3.991
Width of Control Volume at e-2 Intensity	145.09 µm
Length of Control Volume at e-2 Intensity	2079.6 µm
Fringe Spacing	4.546 µm
No. of Fringes within e-2 Intensity	32
Frequency to Velocity Conversion	0.22 ms /MHz

Table 1. Optical characteristics of laser-Doppler velocimeter

The amplified signal from the photomultiplier was converted into velocity values by a zero-crossing counter, as described by Heitor, Laker, Taylor & Vafidis (1984) and an IBM compatible 486DX personal computer and the minimum number of velocity values used to form averages at each measurement location was 4000. This resulted in statistical uncertainties of ±3% in the mean and ±6% in the rms.

The concentrations of a helium gas tracer added to the air of one of the entry ducts with a volumetric concentration of 10% (2.6% by volume of total air flow rate) were sampled with a probe and measured by a katharometer (Taylor Servomex CG.197) with an uncertainty within ±2% of the maximum value. The probe had external and internal diameters of 3.2 mm and 1.5 mm respectively and entered the enclosure through a series of holes located on the combustor wall. Suction was applied to the probe at a rate determined from experiments performed with a wide range of flow rates which showed that the flow rate had little influence within the range of the present measurements.

3. RESULTS

The photographs of figure 2 provide a near-quantitative impression of the flow. That taken in the plane of two entry ducts and orthogonal to the third shows the jets entering the chamber and directed towards it's axis before which it interacts with the orthogonal jet directed towards the plane of the paper. These three jets merge and move upwards where they reach a stagnation region caused by the top surface of the enclosure, and turn through 180 degrees and towards the exit diffuser. The thickness of the oil-paint mixture distorts the flow in that it suggests a stagnation region close to the top of the enclosure but not as close as the true region of flow reversal. Also, there is a clear tendency for oil to build up in low velocity regions such as that in the left hand edge of the photograph and at the upper edge of incoming jets. The second photograph corresponds to the plane at 45 degrees to that of the first photograph with the impingement of two jets at 45 degrees to the paper, and in the

vicinity of the intersection of the horizontal line and the vertical axis. Again, the flow moves upwards towards a stagnation region where it turns to flow towards the diffuser and exit. The line corresponding to a thick layer of oil represents the division between the flow moving upwards and that moving downwards.

Figures 3 and 4 show the results of measurements by laser-Doppler velocimetry with mean velocities represented by the vectors and stream function contours of figure 3 and turbulence intensities by the contours of figure 4. In each case, results are presented for the two planes of figure 2.

Figure 2. Visualisation of Gaseous Phase along Planes Normal to Injection and at 45 degrees to it.

The mean velocity vectors show the trajectory of the jet entering from the duct at the bottom right and the manner of its turning towards the top of the enclosure with subsequent change of direction close to the top and reversal towards the outlet. There is some acceleration of the jet as close to its upper edge and after it intersects the other three jets with the highest velocities above the location of impingement and reducing towards the top surface. The region of turning of the flow is closer to the top of the enclosure than suggested by figure 2 and the downwards flow widens rapidly as it moves from the region close to the top. In the region of the incoming flow it is clear that the downwards flow has low velocities in the plane of the jet but it can readily be conjectured that the flow moves downwards rapidly between the jets. There is a large region of lower velocities directed towards the exit and coming from the lower surface of the jet and the air passing between it and its neighbours.

Figure 3. Vector Plots of Mean Velocity and Streamfunction Contours in Planes Normal to Injection and at 45 degrees to it.

The vectors in the plane at 45 degrees to that discussed

above suggests near-symmetrical turning of the flow close to the top of the enclosure and the less symmetrical turning below the incoming flows. The contours emphasise the regions of high velocity, show the different shapes of the intersection regions in the two planes and identify the possible existence of a small vortex within the plane of injection underneath the reversed incoming jets.

The turbulence intensities of figure 4, defined as the local rms of velocity fluctuations divided by the bulk velocity of the incoming jet and minima of around 0.12 in the regions of low velocity and shear. The maximum value is around 0.24, close to that of a fully-developed turbulent jet, but occurring a comparatively short distance from the plane of entry to the enclosure and before impingement where the intensities are rather lower, in contrast to the measurements of McGuirk and Palma (1992) which show a high intensity at the location of intersection of normal jets. It may be that the latter are associate with a periodic instability which would be less likely to occur in jets which impinge obliquely as in the present case.

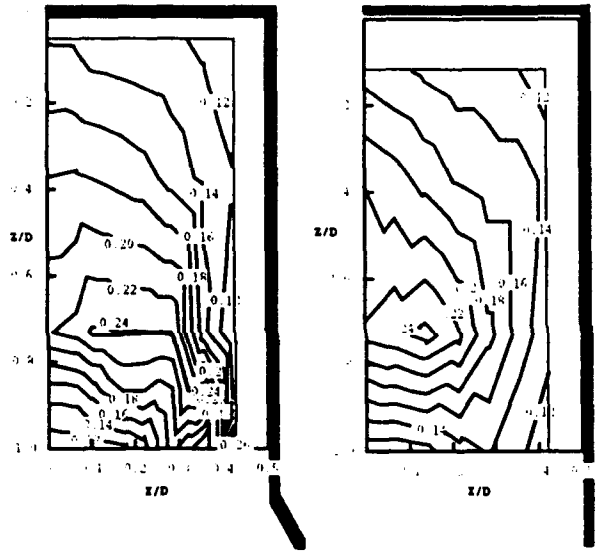

Fig. 4 Contour plots of turbulence intensity within planes normal and at 45 degrees to injection

The mixture fractions of figure 5 are also shown in the two planes of figure 2, here with full view of the vessel rather than a symmetrical half as in figures 3 and 4 and required because the tracer of helium gas was injected into one entering flow as shown. The incoming jet allows the passive scalar to reach almost to the centre line before it concentration begins to decay but the decay from the edges of the contour of the concentration of the incoming gas is rapid, particularly in the downwards and cross-stream directions although it can be expected that the latter would be considerably reduced when all jets contain the same concentration of the scalar. This rapid decay is emphasised by the results in the 45 degree plane where the highest concentration to be seen is less than half that of the incoming gas. The probable reduction in decay is supported by the previous figures which show that the velocity characteristics, which should behave in a manner similar to that of the scalar where the scalar is present in all four entry ducts, decay more gradually.

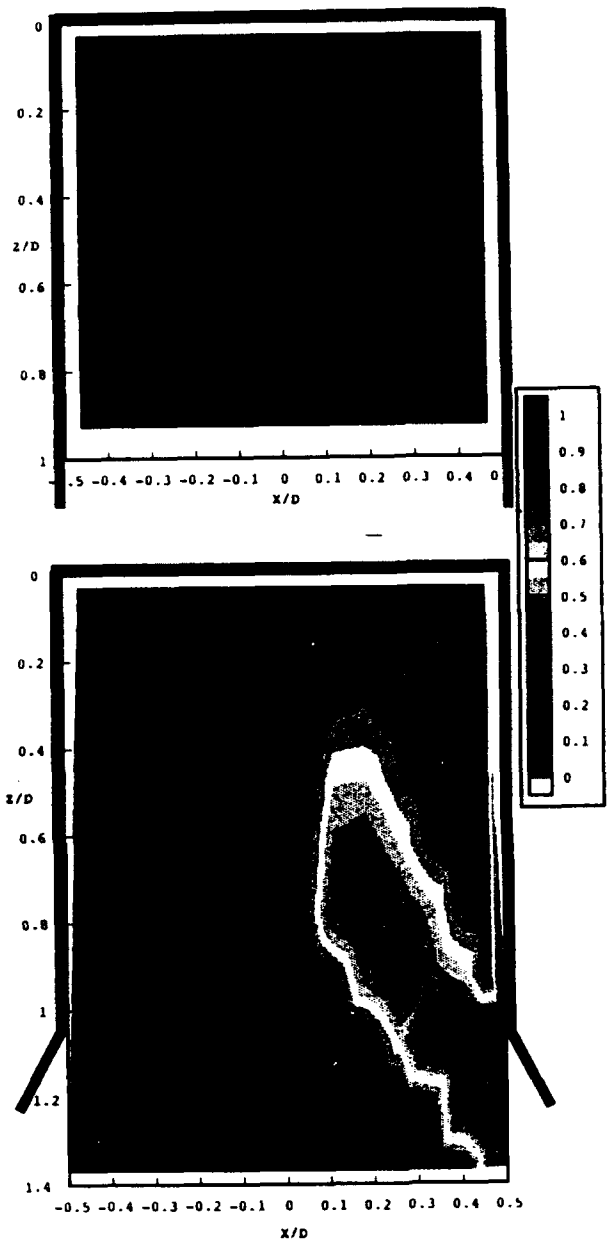

Figure 5 Passive Scalar Mixture Fraction Contours Within Both Planes

4. DISCUSSION AND CONCLUDING REMARKS

The present flow may be compared usefully with that of an aircraft gas-turbine combustor where primary jets are arranged to impinge and to create a toroidal recirculation region in which fuel has time to burn. In the present flow, the jets impinge obliquely and the fuel would be transported by the in-coming air but the two configurations are similar in that they seek to provide residence time for combustion and a flow of hot gases which pass between the incoming jets. There is a further similarity in that experiments have been performed

with isothermal flow in models of gas-turbine combustors and compared with results of flows with combustion and the comparisons show, for example, the much stronger recirculating flows associated with the accelerations of the combusting flows.

The dimensions of the toroidal or near-toroidal region formed by the four jets and the enclosure are similar to those of the model combustor of Heitor and Whitelaw (1985) and the maximum velocity in the enclosure with isothermal flow is also similar with a value of around 15 m/s downstream of the entry ducts. The dimensions may also be compared with the ratio of the area of the entry apertures to that of the enclosure in the present combustor and the gas-turbine combustor equal to 0.075 and 0.109 respectively. However comparison of the strengths of the vortical motions is difficult because of the oblique entry the present geometry and the influence of swirl in the gas-turbine combustor. In the region between the entry ducts and the top of the two combustors, the recirculation zones have characteristic widths and lengths of 0.67D and 0.67D for the gas turbine combustor and 0.3D and 0.75D for the present geometry, where D is the combustor width. Consideration of the residence times provided within both recirculation zones allows comparison of the time available for combustion in each flow. Using the residence time scale derived in Visser and Weber (1992) and Orfanoudakis (1994), we can estimate the residence time within the gas-turbine as 120 ms, assuming the internal recirculation zone to be elliptical in nature. For the present geometry, where the recirculation zone is effectively a torus the residence time is around 190 ms so that the present geometry provides some 50 % more time for combustion and this will assist the complete burn out of char particles within it.

The influence of combustion in the gas-turbine flow reduced the effective residence time by some 25 % primarily due to a 20 % decrease in the width of the recirculation zone and an increase in the axial velocities. Within the geometry of the present paper, similar trends may be inferred and a large increase in the axial velocities, particularly in the region downstream of the entry ducts, will decrease the mean residence time for char particles burn. However it must be rememberred that wall capture of larger particles can increase their effective residence times which are certain to be longer in the real geometry since the dimensions are some three times greater.

The similarity of the two flows is also of assistance in considering the representation of the furnace by the numerical solution of conservation equations in differential form since there is a considerable background of effort in the calculation of gas-turbine flows. In both cases, there are three independent variables, impinging jets, two-phase flows, recirculation and combustion at pressures which require consideration of radiation heat transfer. In the present case, however, the fuel involves devolatilisation and the combustion of gas and solid material with the need for longer times.

ACKNOWLEDGEMENTS

The authours wish to express their gratitude to the Commission of the European Community for their finacial support and to Maurice Bodegom for his assistance.

REFERENCES

Bergeles, G., Mouzakis, F. & Papadakis, G. 1994, Evaluation of Pressurised Pulverised Fuel Combustors, CEC Report No JOU2-CT 92-0015, April 1994

Hannes, K.W., Reichert, G. & Weber. E. 1989, Pressurised Pulverised Coal Combustion With Molton Ash Removal, Conf. on Technologies for Producing Electricity in 21st Century, Nov 1989 pp. 155-173.

Hazanov, Z. Goldman, Y. & Timnat, Y.M. 1985, Opposed Flow Combustion of Pulverised Coal, Comb & Flame, Vol 61, pp. 119-130.

Heitor, M.V. & Whitelaw, J.H. 1986, Velocity, Temperature, and Species Characteristics of the Flow in a Gas-Turbine Combustor, Comb & Flame, Vol 64, pp. 1-32.

Heitor, M.V., Laker, J.R., Taylor, A.M.K.P. & Vafidis, C. 1984, Imperial College Rep. No. FS/84/09

Libis, N., Greenberg, J.B. & Goldman,Y.
1994, A Numerical Investigation of Aspects of Coal Powder Combustion in a Counterflow Combustor, Fuel Vol. 73, no.3, pp. 405-411

Mattsson, A.C.J. & Stankevics, J.O.A. 1985, Development of Retrofit External Slagging Coal Combustor System, 2nd Ann Pittsburgh Coal Conf., Pitts, USA, Sept 1985 pp. 776-784.

McGuirk, J.J, & Palma, J.M.L.M. 1992, Calculation of the Dilution System in an Annular Gas-Turbine Combustor, AIAA Journal, 1992, Vol. 30, No. 4, pp. 963-972.

Orfanoudakis, N.G. 1994, Measurements of Size and Velocity of Burning Coal, Ph.D. thesis, Imperial College, University of London.

Preusser, P. & Spindler, K. 1988, Pressurised Pulverised Coal Combustion, VGB Kraftwerkstechnik, no. 9, pp. 813-817.

Reichert, G., Thelen, F., Schmidt, D. & Weber,E. 1988, Investigations on Pressurised Pulverised Coal Furnaces, VGB Kraftwerkstechnik, No.9, pp. 908-912.

Sivasegarem, S. & Whitelaw, J.H. 19[illegible] Flow Charcteristics of Opposing Rows of Jets in a Confined Space, Proc. Inst. Mech. Eng, Vol. 200, pp. 71-75.

Sadakata, M., Sakai, T., Tominaga, H., Yamamoto, S. & Suzuki, K. 1988, Development of Slag-tap Combustor for High Intensity Pulverised Coal Combustion, Proc. 22nd Int Symposium of Combustion vol. 93, pp. 183-191.

Thambimuthu, K.V. 1993, Gas Cleaning For Advanced Coal-Based Power Generation, IEA Coal Research 1993.

Visser, B.M. & Weber, R. 1992, Mathematical Modelling of Full Industrial-Scale Combustion Equipement, IFRF Doc No F 36/Y/18

INVESTIGATION OF PARTICLE FLOWS IN A TOP-FEED SHELL BOILER USING LASER SHEET ILLUMINATION

J. L. Stroud

British Coal, Coal Research Establishment,
Stoke Orchard, Cheltenham, Gloucestershire, UK

ABSTRACT

Impact erosion by particles is the most common cause of mechanical failure in stoker fired shell boilers. Impact erosion is influenced by the particle/gas flows in the reversal chamber of the shell boiler. Hence the objective of this work was to assess, using laser sheet illumination, the particle flow, for example particle velocity, and particle size, in the reversal chamber of a top-feed shell boiler, and the effect on the flow of changing boiler conditions.

Overall as boiler firing rate was increased, the number of particles increased and the average particle velocity decreased. The highest wear of the smoke tube entrances was estimated to be at the base and the outer edges of the smoke tube bank, and this agreed with previously observed smoke tube bank wear patterns.

1. INTRODUCTION

The aim of this work was to use laser sheet illumination to determine the solid loading, solid velocity and particle size in the rear reversal chamber of a top-feed stoker fired shell boiler and the effect of boiler conditions on these parameters.

In a top-feed shell boiler coal is burnt in a furnace. The grits and hot gases produced by combustion enter the front reversal chamber, turn by 180° and enter the first set of heat exchanger tubes arranged in a half crescent smoke tube bank at the side of the furnace. After exiting these tubes, they enter the rear reversal chamber where their flow is reversed once more and they enter the second set of heat exchanger tubes (or smoke tubes).

These grits travelling at relatively high speed cause impact erosion at the smoke tube entrances. This is the most common cause of mechanical failure in a stoker fired shell boiler. In a survey of sprinkler stoker fired shell boiler plant in the North-West of England, 35% of boilers were reported to have erosion wear problems causing smoke tube failures (British Coal (1993)).

Impact erosion was known to be affected by the mass flow of solids, solids velocity, and particle size, which in turn may be affected by boiler conditions, for example the boiler firing rate. Hence it was important to characterise the solid flow by measuring solid loading, velocity and size in a rear reversal chamber of a top-feed shell boiler, and the effect of boiler conditions on these flows and subsequently on smoke tube wear.

2. LASER SHEET ILLUMINATION

A laser sheet was expanded from a pulsed, high-powered, frequency doubled (wavelength=532nm) Nd:YAG laser with a f=-6mm cylindrical lens and a f=350mm converging lens (Figure 1).

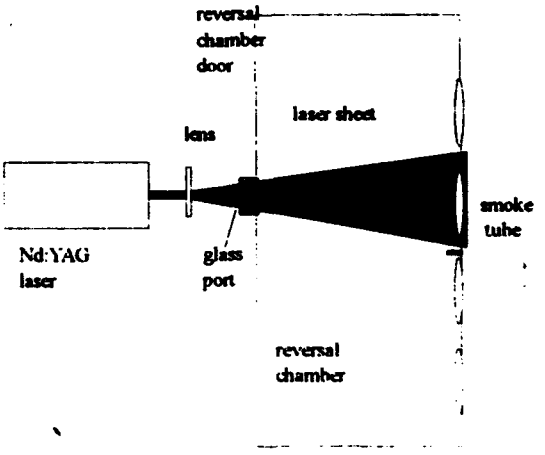

Figure 1 Laser sheet illumination in top-feed shell boiler

The sheet was directed into one of seven ports located in the door of the rear reversal chamber (Figure 2). Each port was in line with a smoke tube exit.

A Sony XC-77/RRCE CCD camera positioned at the top of the reversal chamber viewed the solids in the horizontal laser sheet at 90°. The lens used was either a zoom lens or f=12.5mm lens, depending on the distance between the camera and the laser sheet. The nearest smoke tube (number 5) intersected by the sheet was 35cm away from the camera, while the furthest smoke tube (number 18) was 1.5m away from the camera. The

laser fired 25 pulses a second to ensure particle images appeared on each video frame.

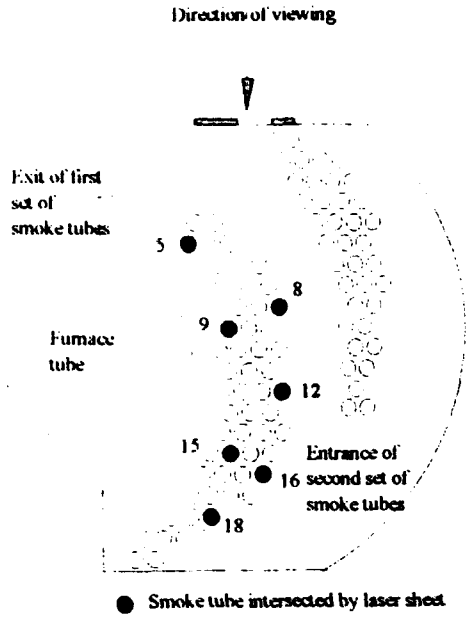

Figure 2 Position of smoke tubes and viewing in top-feed shell boiler

For velocity information (i.e. for Particle Image Velocimetry), the Nd:YAG laser fired 2 pulses 0.5ms apart. Hence a total of 50 pulses a second were fired and 2 images of the same particles were captured on a single video frame.

3. EXPERIMENTAL

Video images were recorded of solid flows in the laser sheet intersecting each of the seven smoke tubes at a low boiler firing rate (48% Maximum Continuous Rating, MCR). In the middle of the test the boiler firing rate was increased to a high rate of 113% MCR. For some tests the rate of grits being refired in the furnace was increased by banging the grit refiring line. This line took the grits collected in the cyclone back into the furnace.

To determine the number of particles and their size and how this was affected by differing boiler conditions, video images of solids around each smoke tube were digitised with a Data Translation DT3852 framegrabber processor into a 486 33MHz computer. Software was used to locate the particles within user defined grey level threshold and then measure the area of the particles.

To determine the velocity of solids in the reversal chamber, and the effect of differing boiler conditions, 2-d velocity maps were compiled from the video images recorded by the CCD camera of solids in the laser sheet intersecting the smoke tubes. The video images were selected and digitised with a Data Translation DT3852 framegrabber processor into the computer. The video frames were then analysed with the software package 'Visiflow'.

The 'Visiflow' software offered a choice of analysis methods to determine velocity vectors from the video images, which were first binarised into a black and white image (black background and white particles). The optimum method for a particular video image depended on the number of particles and their velocity gradient. Manual matching and particle tracking methods were best for low particle concentrations, and high velocity gradients. Autocorrelation was best for high particle concentrations on the video image when particle pairs could not be distinguished.

The optimum analysis method for the video images in this work was a combination of particle tracking and manual matching. The particle tracking algorithm in 'Visiflow' was applied to the binarised image with a user defined maximum velocity. The subsequent data was plotted as a velocity vector map. Manually the vectors were edited; discarding wrong particle pairs, and matching clearly correct particle pairs.

Around some smoke tubes, the number of particle pairs on a single video image was insufficient. Hence several video frames for a certain smoke tube were analysed with 'Visiflow' and the velocity vector data sets summed. The average velocity was calculated and the velocity vector map plotted. This analysis was repeated for all solids in the laser sheet for each of the seven smoke tubes at varying boiler conditions.

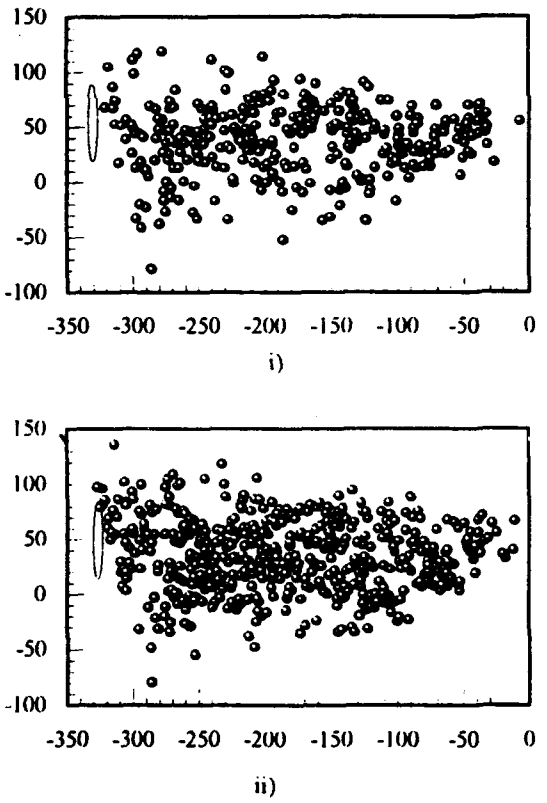

Figure 3 Solid loading at smoke tube 8 with i) low, and ii) high boiler firing

4 SOLID LOADING

The number of particles counted by the software around each smoke tube varied with the location of the smoke tube in the smoke tube bank. There were two regions of high solid loading for all boiler conditions and these were; i) in the upper central region of the smoke tube bank, around smoke tubes 8 and 9, and ii) in the lower part of the bank around smoke tube 16. Previous measurements of grits by British Coal (1993) collected with isokinetic equipment placed through the appropriate port had also detected two regions of high solid loading at smoke tubes 8 and 18.

The number of particles was affected by boiler conditions. Figure 3 shows a typical result for smoke tube 8 with low and high boiler firing. The location of solids is plotted on the grid. The numbers on the axes represent distance in the reversal chamber in millimetres. The number of particles clearly increased with an increase in boiler firing rate.

5. PARTICLE SIZE

The average area varied between 2 and 7mm^2 with a mean area of 4mm^2 across all the smoke tubes. This area was equivalent to a particle diameter of 2.3mm, assuming the particle was a sphere. Previous size analysis by British Coal (1993) of grits had measured an average particle size of between 1 and 1.5mm^2. The close agreement between the 2 size measurements validated the laser sheet determination of particle size. The smaller size measured by sieve analysis was expected because sieve analysis generally measures the smallest dimension of the particle while image analysis measures any of the dimensions of a particle.

Area histograms were drawn from the image analysis area data to show the proportion of large and small particles around each smoke tube at different boiler conditions. Figure 4 shows a typical distribution for smoke tube 12. From the area histograms it was easier to assess how boiler conditions affected the size of particles around the smoke tubes. For instance the number of smaller particles increased with an increase in boiler firing rate and grit refiring rate around smoke tubes 9, 12 and 15 (Figure 4).

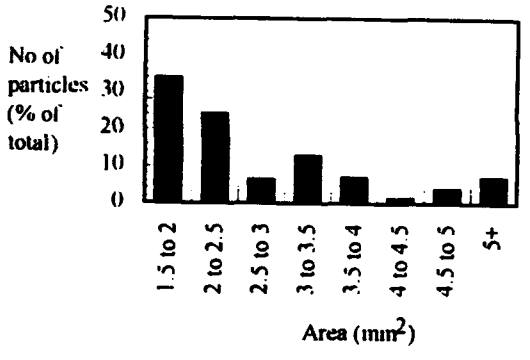

i)

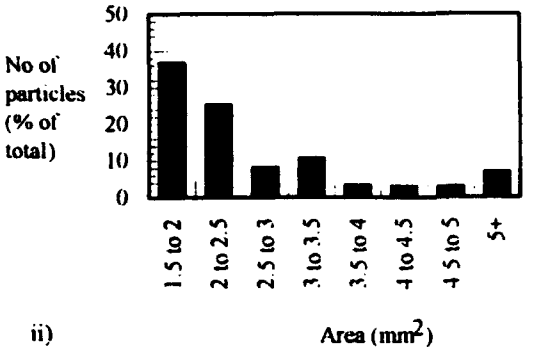

ii)

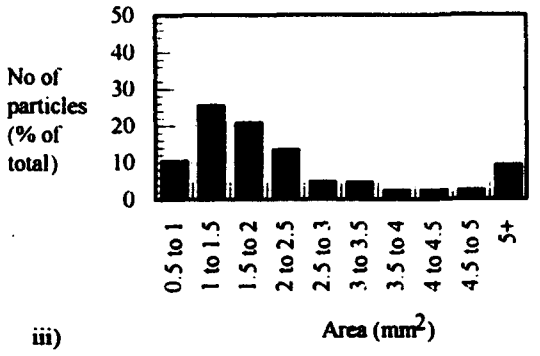

iii)

Figure 4 Area Histogram for solids around smoke tube 12 with; i) low, and ii) high boiler firing, and iii) increase in grit refire

6. SOLID VELOCITY

6.1 Average Velocity

The average solid velocity for the particles around each smoke tube for different boiler conditions was calculated from the velocity vector data (Table 1).

The average solid velocity varied with smoke tube location; the highest average solid velocity was around smoke tubes 8 and 12, and the lowest at smoke tube 9. The solid velocity was consistently lower than a previously calculated gas velocity (British Coal (1993)). This was not surprising because there were a wide range of sizes of particles in the reversal chamber, including larger particles which travelled slower than the gas stream. It was interesting to note the gas velocity was also highest around smoke tubes 8 and 12, and lowest around smoke tube 9.

Increasing the boiler firing rate and grit refire rate decreased the average solid velocity at all smoke tubes except

smoke tube 8 where the average solid velocity increased with a higher boiler firing rate

Table 1 Velocity for top-feed boiler

Tube Number	Gas Velocity (ms^{-1})	Average Solid Velocity (ms^{-1})		
		48% MCR	113% MCR	grit refire
5	11.3	8.74	7.5	no data
8	14.1	9.91	10.24	7.81
9	10.4	6.98	6.06	5.87
12	14.7	9.67	8.56	7.2
15	13	9.6	9.53	8.55

6.1 Velocity maps and solid flow

Velocity maps were plotted for the 2-d solid velocities around each smoke tube at varying boiler conditions. A typical velocity vector map is shown in Figure 5 for the solids in the laser sheet intersecting smoke tube 12 with the boiler at a low firing rate.

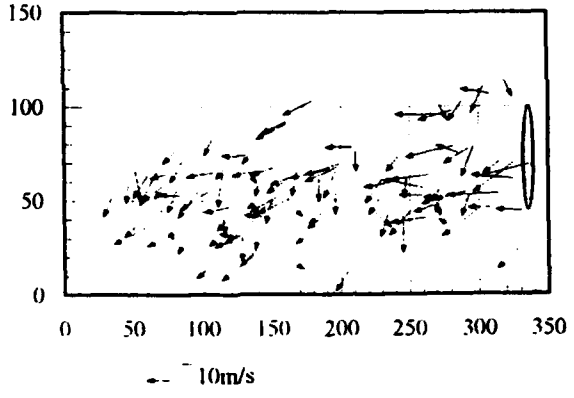

Figure 5 Velocity vector map for solids around smoke tube 12 at a low boiler firing rate

The numbers on the axes represent distance in the reversal chamber in millimetres. The length of the velocity vectors represented the velocity magnitude.

The general solid flow in the reversal chamber could be assessed from the velocity maps because they contained the directional and velocity information of solids.

Solids are seen exiting the first set of smoke tubes and crossing the body of the reversal chamber. A second flow of particles is seen crossing the reversal chamber diagonally. Furthermore, solids are seen turning towards the second set of smoke tubes. These flows were due to the combined effects of gravity and the 180° change in direction within the reversal chamber.

Generally changing boiler conditions did not affect the path of solids in the rear reversal chamber.

7. WEAR OF SMOKE TUBES

Impact wear erosion was known to be affected by the mass flow of solids, solid velocity and particle size. Previous work by British Coal (1993) had predicted the erosion rate of smoke tubes was proportional to the solid velocity cubes multiplied by the mass flow of particles hitting the target area.

Hence the wear around the smoke tubes in the tube bank of the rear reversal chamber was estimated from the experimental data of particle numbers, particle velocity, and particle size (Table 2). The mass of solids was assumed to be proportional to the average solid volume multiplied by the number of particles. The highest rate of wear was at the outer edge of the smoke tube bank at smoke tubes 8 and 15. Past wear surveys by British Coal (1993) had measured high levels of wear in these smoke tubes, i.e at the base of the tube bank and in the outer edges.

Table 2 Wear esimates for top-feed shell boiler

Tube Number	Wear Estimate (m^3/s^2)		
	48% MCR	113% MCR	grit refire
5	18	16	no data
8	135	163	88
9	19	7	6
12	38	26	12
15	84	26	87

The most severe wear occured at the base of the tube bank most likely because of an accumulation of grits at the base which are continuously being entrained into the emerging particle stream. Hence the concentration of particles in the gas flow in the vicinity of the base of the tube bank is increased.

ACKNOWLEDGEMENTS

The assistance of Grahame Cox of British Coal, and Dave Tyson of Evode Ltd are gratefully acknowledged.

Furthermore this work could not have been completed without the financial support of the Department of Trade and Industry, the European Coal and Steel Community, and British Coal.

REFERENCES

British Coal, Coal Research Establishment, 1993, Optimising the aerodynamic design of boilers to improve combustion and reduce erosion, Final report on ECSC project no 7220-ED/827.

VELOCITY CHARACTERISTICS OF THE CROSSFLOW OVER TUBE BUNDLES

S.Balabani†, G. Bergeles*, D. Burry* and M. Yianneskis†

†Centre for Heat Transfer and Fluid Flow Measurement
King's College London, University of London,
United Kingdom.

*Laboratory of Aerodynamics
National Technical University of Athens
Athens, Greece.

ABSTRACT

LDA measurements of the three mean velocity components and the associated turbulence levels were performed in a staggered rod bundle arrangement typical of lignite utility boilers. Measurements were carried out in flow of water at a Re_d of 12,858. The relative transverse and longitudinal pitches were 3.6 and 1.6 respectively. A numerical code was developed based on the well known k-ε turbulence model with and without a curvature modification. Low levels of turbulence were observed behind the first row but they increased downstream of the second row. Comparisons of the flow predictions with the experimental results show that mean velocities are well predicted with some discrepancies in the recirculation zones. Predictions are improved using the curvature modification. However, the turbulence levels are underpredicted as soon as the flow separates from the first cylinder and the discrepancies become larger further downstream.

1. INTRODUCTION

Numerous experimental studies of the fluid flow and heat transfer in tube banks have been conducted due to their wide applications in shell-and-tube heat exchangers. Most of the investigations have been concerned with the pressure drop and heat transfer in tube banks of various arrangements. In recent years, detailed information about the velocity and turbulence characteristics of the tube banks became available utilising the LDA technique. The investigations most relevant to the present work are outlined below; a detailed review of the literature can be found in Balabani and Yianneskis (1993).

Several LDA studies of tube bundle flows have been presented in the LDA conferences held in Lisbon. Halim and Turner (1986) reported detailed experimental data for the mean velocity and turbulence distributions through successive rows of a triangularly pitched staggered tube bank with a pitch to diameter ratio of 1.58 and Re_d ranging from 60,000 to 110,000. Simonin and Barcouda (1986) measured the two velocity components in a square array with a pitch to diameter ratio of 1.47 at Re_d = 20,000 in flow of water. In a later paper (Simonin and Barcouda, 1988), the flow development across the same staggered arrangement up to the sixth row was measured at a Re_d = 18,000 and the results were compared with predictions from a numerical code employing the k-ε turbulence model.

The present work forms part of a JOULE-II research programme investigating the effects of fouling on the efficiency of heat exchangers in lignite utility boilers. A staggered tube bundle configuration typical of the heat exchangers in utility boilers employed by the Public Power Corporation of Greece was examined under subcritical flow conditions. This arrangement is characterised by extremely wide transverse spacing which has not been previously studied. Furthermore, measurements of the third velocity component enabled us to estimate the turbulence kinetic energy based on the three components in contrast to previous investigations.

2. EXPERIMENTAL FACILITY

2.1 Flow rig

A closed-loop flow rig was designed and manufactured to facilitate single-phase and two-phase LDA experiments in flow of water as well as refractive-index matching experiments. A centrifugal pump is used to pump the working fluid from the tank. The flowrate is monitored by means of precision-bore flow-meters. The fluid flows downwards through a straightening section and then enters the test section. A proportional temperature control system consisting of a cooling coil, an immersion heater and a thermocouple was built and installed in the tank in order to maintain the temperature of the working fluid to within ± 0.05°C. The pipework, fluid tank and all components were arranged with their axes vertical and designed so that there are no stagnant regions in the flow; in this way, complete particle re-entrainment into the flow will be ensured every time the experiment is re-started for subsequent two-phase flow studies. Flowrates up to 290 lt/min can be reached corresponding to upstream velocities, U_∞, up to 0.93 m/s.

2.2 Test section

A square cross-sectioned test section (72 mm x 72 mm) was designed and manufactured from transparent cast acrylic material (poly-methyl methacrylate - Perspex). The test section consists of 6 transverse rows of cast acrylic rods, 10 mm in diameter, arranged in a staggered configuration with a relative transverse pitch of 3.6

and relative longitudinal pitch of 1.6 (centre-to-centre distance to diameter ratios). The length to diameter ratio of the rods L/d is 7.2 so that measurements obtained at midspan can be considered free from end effects (Fox and West, 1990). The rods were supported at each end by pressing them into holes drilled on the Perspex plates so that they can be removed and cleaned easily. Half rods were fixed in alternate rows along the side walls to simulate an infinite tube bundle and minimise boundary layer effects. A cross-section of the staggered arrangement under study is shown in Figure 1 together with the coordinate system employed in this study. The origin of the coordinate system is taken at the centre of the cylinder in the first row. All coordinates were expressed in non-dimensional form by dividing them with the rod diameter.

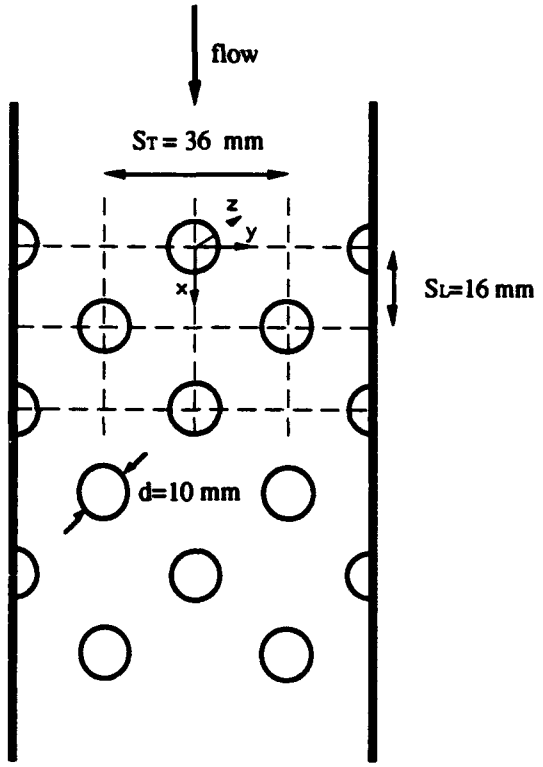

Figure 1 Cross-section of the staggered arrangement investigated.

2.3 Experimental procedures

The first set of experiments reported here were carried out in flow of water using a fringe-type LDA system operating in forward-scatter configuration. The diameter and the length of the control volume were 48.8 μm and 466 μm respectively. The Doppler signal from the photomultiplier was low-pass and high-pass filtered for noise and pedestal removal respectively. It was then amplified and fed to a frequency counter interfaced to a microcomputer and a two-channel oscilloscope which was used to monitor the signal quality. The transmitting and receiving optics were mounted on a three-dimensional traversing mechanism so that the contol volume could be positioned anywhere in the flow field. The positional accuracy in all three directions was 0.05 mm.

The flow was not seeded with particles since the impurities in the water provided good quality signals and high data rates. Measurements were carried out upstream of the first row at x/d = -2.1 in order to ensure that the approaching flow was uniform. The two-dimensionality of the flow was established both upstream and inside the bundle (at x/d = -2.1 and 2.8 respectively) by measuring mean velocity profiles at three different z-planes (z/d = -0.6, 0, 0.6).

The axial velocities (U, u') were measured first, then the diffraction grating and consequently the control volume was rotated through 90° and the transverse velocities (V, v') were measured. All measurements were taken at the plane of symmetry (z/d = 0). Measurements of the axial component in the region $-1.8 \le y/d \le 1.8$ and $0.0 \le x/d \le 6.4$ indicated that the flow was symmetrical. Subsequently, measurements were made in the region $0.0 \le y/d \le 1.8$ and $0.0 \le x/d \le 6.4$. More detailed measurements of the axial velocity were taken along the centerlines of the wakes. In order to measure the third component, (W,w'), the whole test section was rotated by 90 ° around the vertical axis. Measurements of the latter were possible only midway between successive rows due to the restricted optical access. These data enable the estimation of the turbulent kinetic energy. However, more detailed data will be obtained using the refractive index matching technique.

All measurements were carried out at a Reynolds number, based on the velocity and hydraulic diameter upstream of the bundle, of 66,862. The equivalent Re_d defined by tube diameter and gap velocity was 12,858. Under these flow conditions, the flow is subcritical characterised by laminar boundary layer separation (Zukauskas, 1989), in spite of the high turbulence generated by the tube bundle.

3. COMPUTATIONAL MODEL

The basic equations describing the flow field are the Reynolds equations using the Boussinesq hypothesis for the calculation of the Reynolds stresses and the k-ε turbulence model for calculating the turbulent viscocity. These equations all reduce to a single universal form with convection and diffusion terms and a source term (S_Φ) which represents the other terms of each equation. More specifically in orthogonal curvilinear coordinates the equation takes the form:

$$\frac{1}{\ell_\xi \ell_\eta}\frac{\partial}{\partial \xi}(\rho u \ell_\eta \Phi)+\frac{1}{\ell_\xi \ell_\eta}\frac{\partial}{\partial \eta}(\rho v \ell_\xi \Phi)-\frac{1}{\ell_\xi \ell_\eta}\frac{\partial}{\partial \xi}(\Gamma_\Phi \frac{\ell_\eta}{\ell_\xi}\frac{\partial \Phi}{\partial \xi})$$
$$-\frac{1}{\ell_\xi \ell_\eta}\frac{\partial}{\partial \eta}(\Gamma_\Phi \frac{\ell_\xi}{\ell_\eta}\frac{\partial \Phi}{\partial \eta})=S_\Phi \qquad (1)$$

where (Φ)=1 (continuity equation), u (momentum in the ξ direction), v (momentum in the η direction), k (turbulence kinetic energy), ε (turbulence energy dissipation). Details regarding equations (1) can be found in Antonopoulos (1979).

Other variables related to the k-ε turbulence model are de-

fined:

$$\mu = C_\mu \rho \frac{k^2}{\varepsilon} + \mu_\ell \ , \ \Gamma_\phi = \frac{\mu}{\sigma_\phi} \ , \ C_\mu = 0.09 \ , \ \sigma_{(u,v)} = 1 \ ,$$
$$\sigma_k = 0.9, \ \sigma_\varepsilon = 1.3 \qquad (2)$$

where μ_ℓ is the dynamic viscocity of the fluid and μ is the effective viscocity. Finally, ℓ_ξ, ℓ_η are spatially varying metric coefficients that relate the orthogonal-curvilinear coordinate system ξ–η to physical space. These metric coefficients are calculated by the grid generation procedure of Theodoropoulos et al (1985) which ensures orthogonality of the grid system while it is fitted to the calculation domain geometry.

Equations (1) are discretised and solved using the SIMPLE finite method. A detailed description of the whole methodology including grid generation, discretisation etc. can be found in Antonopoulos (1979) and in Mouzakis and Bergeles (1991) and Bergeles (1985). However, the approach presented here differs from that of the previous authors in the way the variables are stored on the grid. In the collocated approach all variables are stored in the center of the grid cells as opposed to the staggered grid arrangement where the u and v velocities are displaced to other positions with relation to the scalar variables. When forming the pressure equations special interpolations must be used for the cell face velocities as suggested by Rhie and Chow (1983). This is done to avoid an oscillating pressure field which originates from the second order difference approximation for the pressure gradients in the momentum equations.

It is well known that the k-ε turbulence model does not include the influence of curvature on the flow. Therefore, in a flow situation such as the flow around a tube where there is a curvature resulting from both recirculation zones and a curved wall, the model will lead to inaccuracies. An attempt was made to overcome this problem by incorporating into the k-ε model the curvature modification proposed by Leschziner and Rodi (1981). They attempt to include curvature effects by linking the C_μ turbulence constant to the shear stresses because as the fluid follows a curved streamline these tend to influence the transfer equations more and more.

C_μ appears in the source term (S_ϕ) for k and ε in (1):

$$S_k = G - C_\mu \rho^2 k^2 / \mu \quad , \quad S_\varepsilon = C_1 C_\mu G \rho k / \mu - C_2 \rho \varepsilon^2 / k \qquad (4)$$

where G is the generation of turbulent kinetic energy by the fluid stresses. More specifically Leschziner and Rodi (1981) propose that:

$$C_\mu = \mathrm{MAX}\{0.02, \ 0.09\,[1 + 8K_1^2 \frac{k^2}{\varepsilon^2}(\frac{\partial u_s}{\partial n} + \frac{u_s}{R_c})\frac{u_s}{R_c}]^{-1}\} \qquad (5)$$

where the s and n subscripts denote directions tangential and normal to the direction of the streamlines respectively and R_c denotes the radius of curvature of the streamline at the specific location. Using the velocities u and v in the cartesian directions:

$$\frac{1}{R_c} = (uv(\frac{\partial v}{\partial y} - \frac{\partial u}{\partial x}) + u^2 \frac{\partial v}{\partial x} - v^2 \frac{\partial u}{\partial y})(u^2 + v^2)^{-1.5}$$
$$\frac{\partial u_s}{\partial n} - \frac{u_s}{R_c} = (\frac{\partial v}{\partial y} - \frac{\partial u}{\partial x})\sin 2\theta + (\frac{\partial u}{\partial y} + \frac{\partial v}{\partial x})\cos 2\theta \qquad (6)$$

where θ is the angle between the stream line coordinates and the cartesian coordinates and $K_1 = 0.266$ is an empirical constant.

4. RESULTS AND DISCUSSION

4.1 Experimental results

Velocity measurements. The mean velocity field is shown in Figure 2. Both the vector length and heads are proportional to the

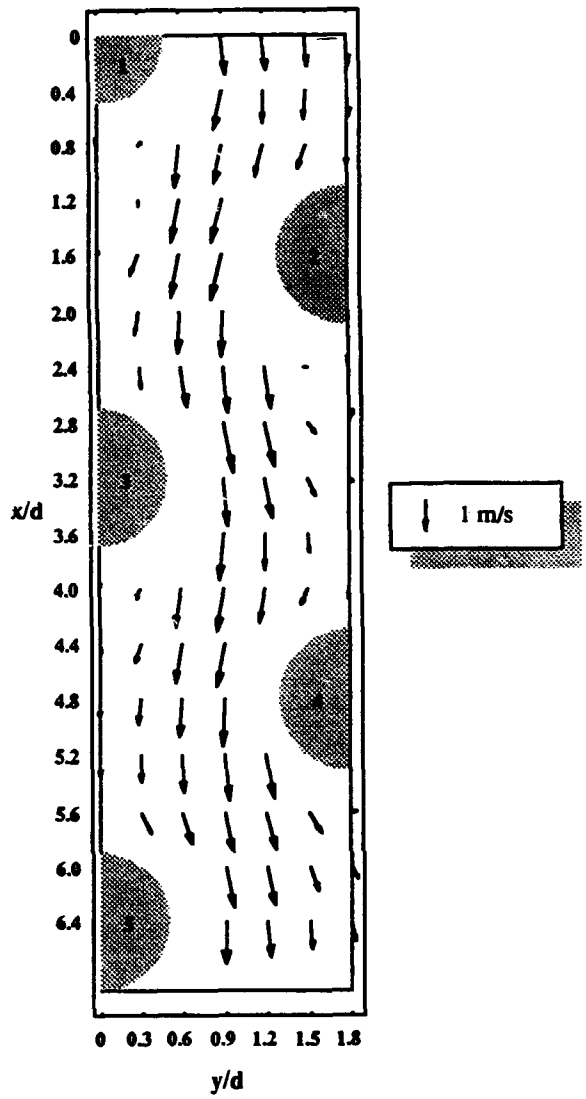

Figure 2 Velocity vectors (Re_d = 12,858).

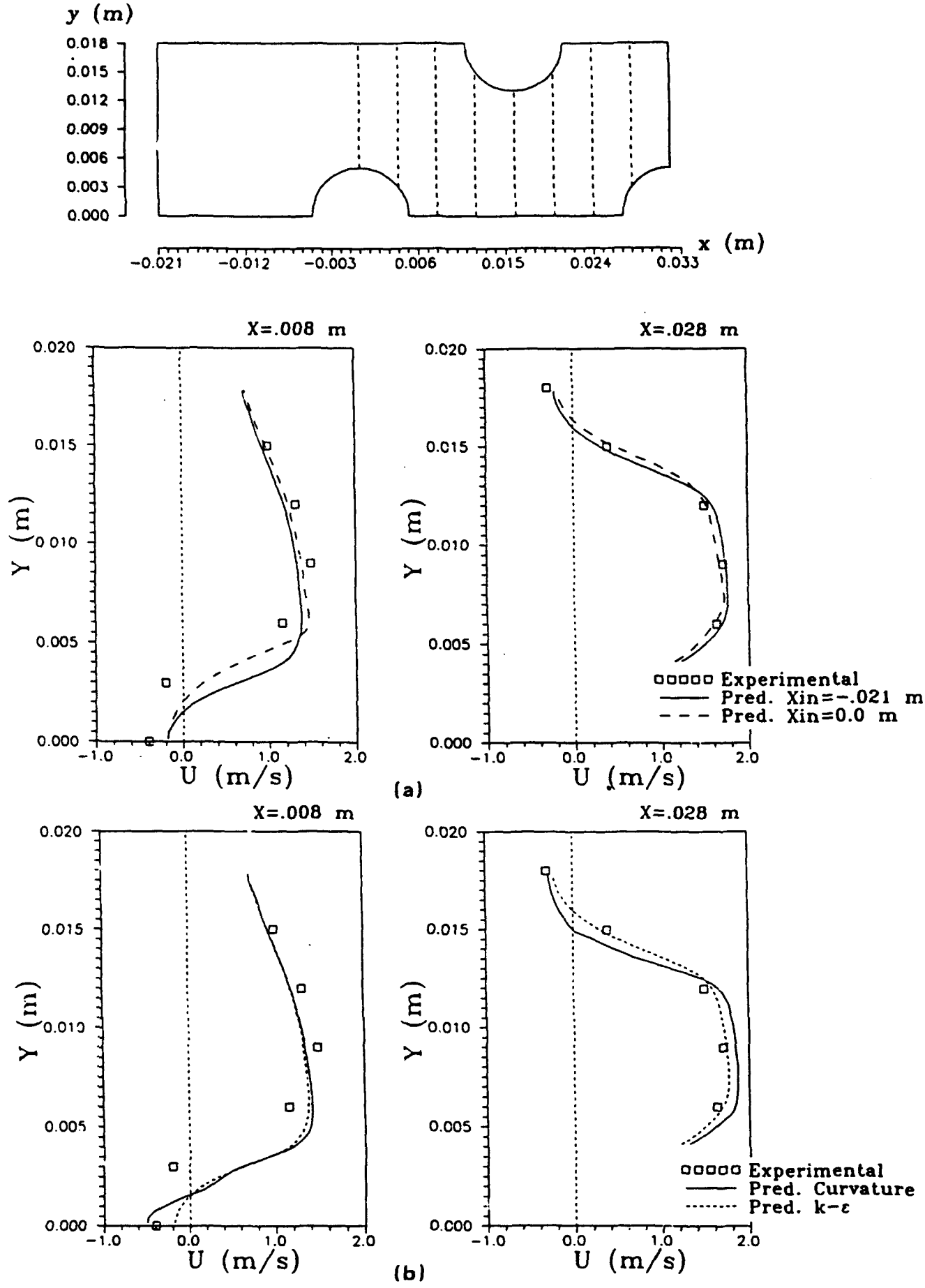

Figure 6 Predictions of the axial mean velocity: (a) using different inlet conditions, (b) using the standard k-ε model and the curvature modification and comparison with the experimental results.

velocity magnitude. The flow field is characterised by areas of high velocity at the flow passages between the rods and flow reversals and low velocities in the wakes. A long recirculation zone is evident behind the first row but the length of the recirculation zones behind the following rows is significantly reduced.

Typical mean axial velocity profiles are shown together with the flow predictions in Figure 6. Flow reversal is pronounced behind the first cylinder with negative velocities reaching up to 50 % of the velocity upstream (U_∞ = 0.93 m/s). The same features can be seen to a lesser extent in the flow behind the second row but tend to dissapear behind subsequent rows. The highest velocities are observed along the centre of the narrow flow passages between successive rows. The velocity decreases as the flow approaches each cylinder. Transverse mean velocities reach higher values at the gaps between successive rows. An interesting observation was made during measurements of this component. The velocities exhibited bimodal distributions probably due to a flapping action of the separated shear layer. Flow instability is a well-known feature of the flow in tube bundles and further investigation is needed to clarify this observation. Measurements of the third mean velocity component (W) confirmed the two-dimensionality of the flow since their values were found equal to zero to within the experimental error.

Measurements of the mean axial velocities along the wake centrelines provided information about the recovery of the axial velocity as well as the length of the recirculation zones. The length of the recirculation zone, l/d, formed behind the first row was found to be 1.15 at the present Re_d. This value is twice the length reported by Halim and Turner (1986) for an equilateral-triangle rod arrangement. However, this value is equal to the length of the recirculation zone behind a circular cylinder (l/d = 1.65) reported by McKillop and Durst (1984) at a similar Re bearing in mind that they measured the length starting from the centre of the cylinder and not from the surface. The length of the recirculation zone behind the third row is less than half its value behind the first row. More detailed measurements were carried out in other Reynolds numbers and the results are reported by Balabani and Yianneskis (1994).

Turbulence characteristics. In order to visualise better the generation of turbulence in the rod bundle, contours of the axial and transverse components of the rms velocities as well as of the turbulence kinetic energy, k, are shown in Figures 3, 4 and 5, respectively. The area adjacent to the rods was left undefined in the contours since interpolation by assuming zero values at the walls of the cylinders led to an unrealistic representation of the distributions in that region.

The axial rms velocities (Figure 3) are relatively low behind the first row but they start rising immediately after the second row. Behind both the first and second rows, the rms values increase with distance from the cylinder and are higher near the end of the recirculation zones. However, behind the third and fourth rows, axial rms velocities are higher in the recirculation zones (0.50-0.55 m/s) and reduce with distance from the surface. A maximum value (0.60 m/s) is reached near the edges of the recirculation zones. Turbulence levels in the main stream flow between the third and fourth rows are almost constant with values between 0.4 - 0.5 m/s.

The distribution of the transverse rms velocities (Figure 4) exhibits slightly different behaviour. Rms velocities are higher after the end of the recirculation zones indicating intense lateral mixing. Again rms velocities are relatively low behind the first row but they increase with distance from the surface and reach higher values (up

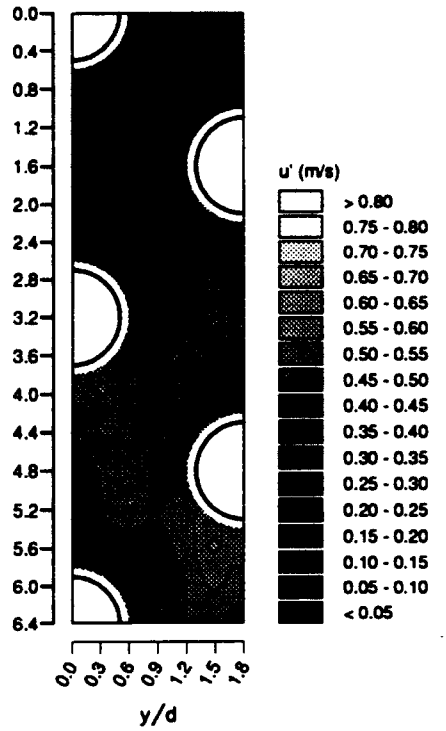

Figure 3 Distribution of the axial rms velocities (Re_d = 12,858).

to 0.60 m/s) after the end of the recirculation zone. Turbulence levels start rising behind the second row reaching a maximum of 0.80 m/s. The same trends can be observed downstream of subsequent rows with higher values after the end of the recirculation zones not exceeding 0.75 m/s. Turbulence levels in the main stream between the third and fifth rows are almost constant with values equal to those of the axial component. On average, the ratio of axial to transverse rms velocities was found to be 1.02 ± 0.3. This, however, cannot be taken as an indication of isotropy as the distributions are not identical.

The third rms velocity component (w') was measured only at 4 transverse planes between successive rows (x/d = 0.8, 2.4, 4.0 and 5.6). The w' profiles at these planes exhibited the same trends with the corresponding v' profiles but the w' values were smaller. The average ratio of v'/w' in these positions was found to be 1.24 ± 0.29. This ratio was used to estimate w' values in other locations and consequently estimates of the turbulence kinetic energy, k. A contour plot of the turbulence kinetic energy is shown in Figure 5. The same trends as those identified in the v' contour plot can be observed. This is expected since the distributions of the two components v' and w' are assumed similar. Turbulence kinetic energy is low behind the first row and starts rising after the second row. Higher values are observed behind the rods whereas lower values of k can be seen in the main flow stream between the rods. The highest values (0.60 m^2/s^2) are reached behind the second row. This effect has been observed by other investigators (Halim and Turner, 1986; Simonin and Barcouda, 1988) but it has not been explained as yet. Almost constant values of the turbulence kinetic energy (0.2-0.3 m^2/s^2) can be observed in the main flow stream between the third and fifth rows.

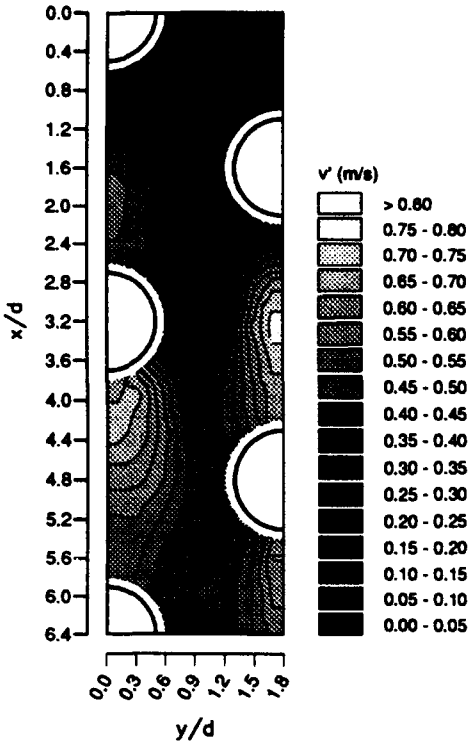

Figure 4 Distribution of the transverse rms velocities (Re_d = 12,858).

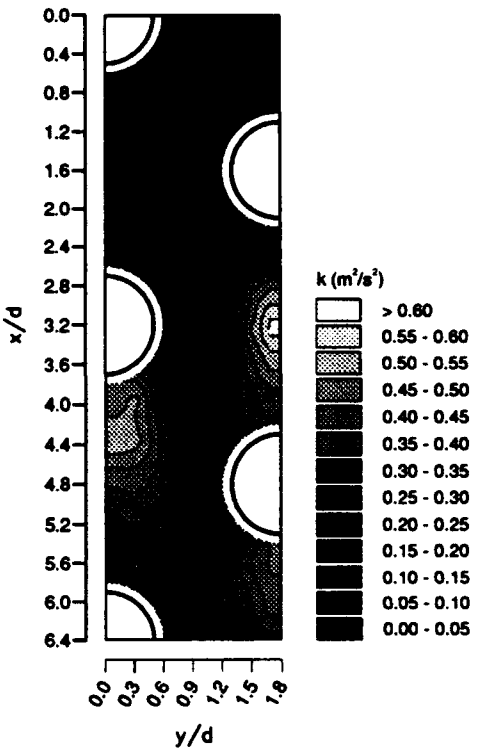

Figure 5 Distribution of the turbulence kinetic energy, k (Re_d = 12,858).

4.2 Numerical predictions

Predictions were made using a 128 x 70 orthogonal curvilinear grid with inlet conditions for the mean and r.m.s. axial velocities specified by experimental measurements. A representative sample of predicted axial mean and rms velocities is shown in Figures 6 and 7, respectively.

For the predictions made with the standard k-ε turbulence model (Figure 6(b)) overall agreement is good. The discrepancies in the areas of the recirculation zones are a result of the well known weakness of the k-ε model. Using the curvature modification provided some improvement in the predictions in these areas.

Another parameter which might influence the prediction of a flow such as the one presented here is that of the developing boundary layer on the front of the cylinder. This is usually transitional in nature and not easy to model especially with the k-ε turbulence model which was developed for fully turbulent flows (having assumed isotropic turbulence). The influence of this parameter was made evident by performing two calculations: the first using as the inlet plane the experimental measurements at the center plane of the first tube (Xin=0.0 m) and the second with the inlet plane 21 mm before the first tube (Xin=-0.021 m) so that the boundary layer developing on the front of the first tube is predicted. The results (Figure 6(a)) are obviously better for the inlet at Xin=0.0 m where the boundary layer development is not modelled but taken from experiment. This emphasizes the need to implement a model that will correctly predict developing and transitional boundary layers if better accuracy is to be achieved.

Axial rms velocities (Figure 7) were predicted using the standard k-ε turbulence model as well as the curvature modification proposed by Leschziner and Rodi (1981). The rms velocities were calculated from the mean velocities, turbulence kinetic energy (k) and its dissipation (ε) using an algebraic Reynolds stress model (Picart et al., 1986). The rms velocities are well predicted at positions where there is no flow separation. At X=0.008 m where the flow separates over the first cylinder discrepancies begin to appear near the separated region and by the time the flow begins to separate over the second cylinder (X = 0.016 m) they spread to the rest of the flow domain. Profiles at positions after the second cylinder are influenced by two separated regions making the discrepancies larger. This is a well known weakness of the k-ε turbulence model which does not perform correctly in separated regions.

5. CONCLUSIONS

Detailed experimental data for the mean and rms velocities were obtained in a staggered tube bundle and a numerical code based on the k-ε turbulence model using a curvature modification was developed.

Mean velocity measurements revealed a flow pattern charac-

terised by a main stream flowing through the gaps between successive rows possessing high velocities that change little in magnitude from row to row and areas of flow reversals and low velocities in the wakes. A large velocity gradient is observed at the separated shear layer from the first cylinder. The gradients are much smaller in subsequent rows. Flow reversal is pronounced behind the first row with negative velocities up to 50 % of the velocity upstream and a long recirculation zone is formed with a length l/d = 1.15 at Re_d = 12,858. The length of the recirculation zone is significantly reduced further downstream with a value of l/d = 0.43 behind the third row.

Turbulence levels are low behind the first row and they start to increase after the second row. The transverse components reach generally higher values than the axial ones at the end of the recirculation zones with a maximum observed downstream of the second row. The third rms component exhibits the same trends as the transverse component but the values are lower. The distribution of the estimated turbulence kinetic energy exhibits maximum levels behind the second row.

Predictions of the mean axial velocities using the standard k-ε model showed good agreement with some discrepancies in the areas of the recirculation zones. Improved predictions were obtained using the curvature modification. Axial rms velocities are well predicted at locations where there is no separation of the flow but discrepancies are present where the flow separates from the first cylinder and they become larger further downstream. In general, predicted values are lower than the experimental ones.

The experimental and computational work is currently being extended to investigate different rod bundle arrangements and two-phase flows.

ACKNOWLEDGEMENT

The authors are pleased to acknowledge financial support from the Commission of the European Union under contract JOU2-CT92-0014 for the work carried out for this paper.

REFERENCES

Antonopoulos K.A. 1979, Prediction of flow and heat transfer in rod bundles, PhD thesis, Imperial College, University of London.

Balabani, S. & Yianneskis, M. 1993, Flow and heat transfer characteristics of tube bundles in crossflow, King's College London, Department of Mechanical Engineering Report EM/93/05.

Balabani, S. & Yianneskis, M. 1994, Wake characteristics of tube bundles in crossflow, Paper submitted to the Eurotherm Seminar No 40: Combined Energy and Water Management in Industry, Thessaloniki, October 1994.

Bergeles G. 1985, Numerical calculation of turbulent flow around two dimensional hills, J.Wind Engineering and Ind.Aerodyn., vol. 21, pp. 307-321.

Fox, T.A. & West, G.S. 1990, On the use of end plates with circular cylinders, Experiments in Fluids, vol. 9, no. 4, pp.237-339.

Halim, M.S. & Turner, J.T. 1986, Measurements of cross flow development in a staggered tube bundle, Proc.3rd Int. Symposium on Applications of Laser Anemometry to Fluid Mech., Lisbon, paper 21.7.

Leschziner, M.A. & Rodi W. 1981, Calculation of annular and twin parallel jets using various discretisation schemes and turbulence model variations, J.Fluids Engng., vol. 103, pp. 352-360.

McKillop, A.A & Durst, F. 1984, LDA experiments of separated flow behind a circular cylinder, 2nd Int. Symposium on Applications of Laser Anemometry to Fluid Mech. Lisbon, paper 14.4.

Mouzakis F. & Bergeles, G. 1991, Numerical prediction of turbulent flow over a two-dimensional ridge, Int.J.Num.Methods in Fluids, vol. 12, pp. 287-296.

Picart, A., Berlemont, A. & Gouesbet, G. 1986, Modelling and predicting turbulence fields and the dispersion of discrete particles transported by turbulent flows, Int.J.Multiphase Flow, vol. 12, no.2, pp. 237-261.

Rhie, C. & Chow, W. 1983, Numerical study of the turbulent flow past an airfoil with trailing edge separation, AIAA Journal, vol. 21, pp. 1525-1532.

Simonin, O. & Barcouda, M. 1986, Measurements of fully developed turbulent flow across tube bundle, 3rd Int. Symposium on Applications of Laser Anemometry to Fluid Mech., Lisbon, paper 21.5.

Simonin, O. & Barcouda, M. 1988, Measurements and prediction of turbulent flow entering a staggered tube bundle, 4th Int. Symposium on Applications of Laser Anemometry to Fluid Mech., Lisbon, paper 5.23.

Theodoropoulos T., Bergeles, G. & Athanasiadis, N. 1985, Orthogonal grid generation in two dimensional space, Proc. 4th Int. Conf. on Num. Meth. in Lam. and Turb. flow, SWANSEA, pp. 1747-1758.

Zukauskas, A. 1989, Crossflow over Tube Bundles, in High Performance single-phase heat exchangers, English ed. J. Karni, pp. 241-264, Hemisphere Publishing Corporation.

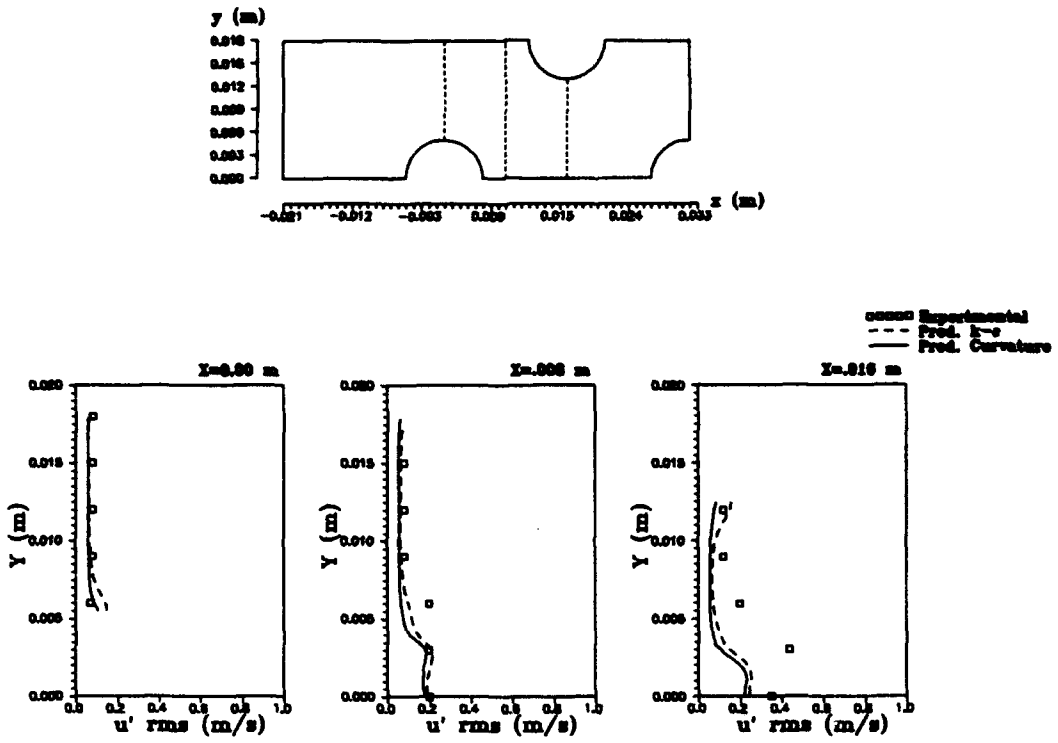

Figure 7 Predictions of the axial rms velocity using the standard k-ε model and the curvature modification and comparison with the experimental results.

LDA STUDY OF TURBULENT FLOW IN A STAGGERED TUBE BUNDLE

K. E. Meyer and P. S. Larsen

Department of Fluid Mechanics, Technical University of Denmark
DK-2800 Lyngby

ABSTRACT

The two-dimensional mean velocity and Reynolds stress fields have been measured in the middle of a staggered tube bundle in cross flow of water. The tube bundle had transverse to longitudinal pitches of 2×2 and the Reynolds number for the flow was $Re = 32\,000$. The measurements did not cover the region close to the tube walls. A recirculation zone extended one diameter behind the axis of each tube. Visualization illustrates the flow further. Numerical solutions based on the "standard" versions of the k-ϵ and the Reynolds stress turbulence models are compared with the measurements.

1 INTRODUCTION

Tube bundles in cross flow appear in many industrial heat transfer processes. In most practical applications the flow downstream of the first or second row is highly turbulent and involves large recirculation regions. Confined flows, such as this, and the associated heat transfer, is difficult to predict by existing turbulence models. Such flows represent good test cases for turbulence models for at least two reasons: The first is that the flow contains several complex features that are found in many other industrial flows; the second is that the flow can be modelled with a periodic boundary condition instead of an inlet condition. In this way, there is no need to estimate model variables that are difficult or impossible to measure. It is the purpose of the present study to provide new data that can be used for the development of improved turbulence models for this class of confined flows. In addition, the study compare these data with predictions based on two standard turbulence models.

A more detailed description of the present study and of heat transfer measurements made in the same geometry can be found in Meyer (1994) . Only few measurements of local flow and turbulence fields have been published. Measurements with hot-wire and similar techniques are unrealiable in the recirculating and highly turbulent zone behind the tubes. Optical methods like laser-Doppler Anemometry (LDA) are probably the best methods for this flow. Halim and Turner (1986) have presented LDA-measurements of the flow development in a staggered tube bundle, but these measurements are only performed between the tube rows. The present study has used a technique that is similar to the LDA-study of Simonin & Barcouda (1988). They presented quite detailed LDA-measurements in a staggered tube bundle that had a closer arrangement than the tube bundle used in the present study.

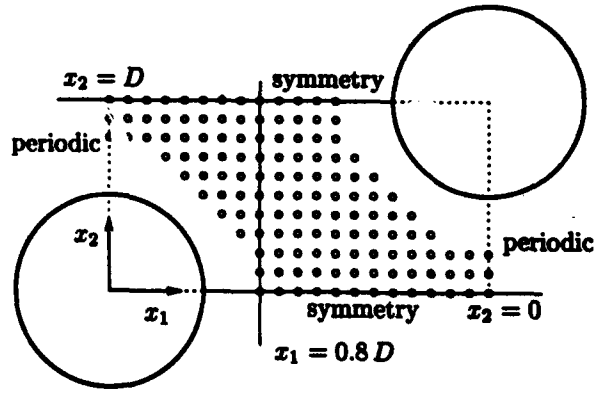

Figure 1: Coordinate system located at the tube center the middle of the seventh row. The symbol o marks measuring positions in one of the unit cells.

It is a general experience in most experiments, e.g. see Žukauskas and Ulinskas (1988), that the flow (and the heat transfer) is fully developed after the first 3–5 rows. This means that inside a tube bundle all features of the flow are represented in a "unit-cell" between two rows, see Figure 1. The present study will only

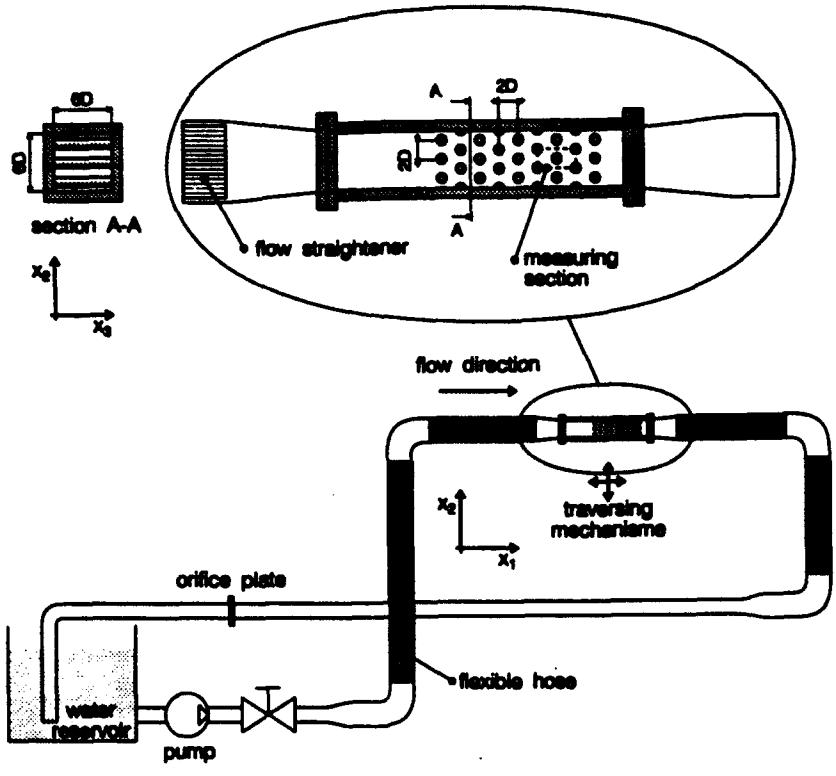

Figure 2: Flow system and test channel used for measurements

investigate the flow in the middle of a tube bundle.

2 EXPERIMENTAL SET-UP

The flow system and the test channel are shown in Figure 2. The test channel consist of rods with a diameter $D = 10\,\text{mm}$ and they are mounted in a box of acryl of good optical quality. The transverse and the longitudinal pitches of the bundle are $a \times b = 2 \times 2$ and the length of each rod is 6 diameters. The test channel is connected to the flow system with flexible hoses and it can be moved by a traversing mechanisme. The error on the positioning is believed to within $\pm 0.15\,\text{mm}$.

In the flow system, tap water is circulated by a centrifugal pump and the flow is regulated with a throttle valve. The mean flow rate is believed to be steady within $\pm 1\,\%$. The Reynolds number is $Re = U_m D/\nu = 32\,000$ and is based on the mean velocity U_m in the minimum flow section, the tube diameter D and the kinematic viscosity ν. The minimum flow section for this tube bundle is located between two tubes in the same row and the mean velocity was found to be $U_m = 2.85\,\text{m/s}$ by measurements in several of these cross sections.

The laser-Doppler anemometer consists of a 1.5 W Argon laser, a 4 beam, two-component optical unit with frequency shift and front lens with a focal length of 160 mm. The two photomultipliers were placed in forward scatter mode and the signals were processed by a frequency shifter (Dantec 55N15) and two counter processors (Dantec 55L96). Some of the parameters for the two data channels are listed in table 1. The setting of frequency shifting and hi- and low-pass filters ensured for both channels and for all measuring positions that all data points were within 5 standard deviations of the mean value were treated correctly.

The counter processors were equipped with a coincidence filter in order to ensure the simultaneity of the signals. The maximal time difference between the two signals was chosen to $50\,\mu\text{s}$. Typical data rates were between 10 and 50 Hz. These data rates give an average time between samples that is significantly larger that the correlation time for the flow. The data from the counters are collected and processed to the final results with a program by Jørgensen & Marxen (1993) running on a personal computer.

direction		x_1	x_2
colour		green	blue
beam intersection angle		12.8°	13.4°
wavelength	[nm]	514.5	488.0
fringe spacing	[μm]	2.300	2.085
frequency shift	[kHz]	2000	3000
high pass filter	[kHz]	64	256
low pass filter	[kHz]	4000	8000

Table 1: Parameters for the two data channels

At each measuring point mean velocity components and Reynolds stresses were computed by residence time averaging of 5000 samples recorded at a mean sampling frequency that was significantly lower that the reciprocal of the integral time scale. Preliminary measurement with different numbers of samples indicated that 5000 samples gave reasonable accurate results although measurements with even more samples could be justified. The uncertainty has been estimated for the velocities to be less than 2% of U_m and for the Reynolds stresses to be less than 5% of their local levels.

3 NUMERICAL METHOD

To illustrate the performance of standard turbulence models in a tube bundle, calculations have been performed with the commercial program CFDS-FLOW3D from Harwell Laboratories, UK (1991). The time-averaged continuity og momentum equations for incompressible flows have been solved together with two of the most used turbulence models: the "standard" k-ϵ (e.g. see Rodi 1980) and the "standard" Reynolds stress model by Gibson & Launder (1978). For the latter, the so-called wall reflection terms have been implemented specially for this geometry.

The equations have been solved with the finite difference method on a curviliniar grid and with all variables located at the center of each cell. The SIMPLE algoritm has been used to ensure continuity and to find the local pressure. The convective terms have been discretized using the hybrid scheme. When the Reynolds stress model is used the momentum equations are discretized with the upwind scheme due to the lack of a diffusive terms in this case.

The wall boundary conditions for the momemtum and the ϵ equations are the modified wall laws described by Launder (1988). For the k-equation and the Reynolds stress equations, a zero gradient condition has been used as boundary condition at walls.

The calculations have been performed in a "unit-cell" located between two tube rows, see Figure 1. Here, a grid of 80×40 cells was used. It could be argued that a grid with more cells should be used. However, since the wall laws are based on the assumption that the first cell node be locaced at a distance $y^+ > 11$ from the wall, it is not justified to refine the grid further.

The boundary conditions for the unit cell are periodic conditions in the up- and downstream boundaries, wall laws at the walls and symmetry conditions on the remaining two sides of the domain. The periodic boundary condition is anti-symmetric and should also take into account the pressure drop over the domain. This special periodic boundary condition has been implemented into the code in the present study.

4 RESULTS AND DISCUSSION

The measurements were performed in a plane normal to the tube axes and located in the middle of the test channel at a distance of 3 D from the side walls. Some measurements were made closer to the side walls; effects of the side walls were found to extend up to about 1 diameter from the wall. The final measurements were performed in a measuring section around the tube in the middle of the seventh row as indicated in Figure 2. The coordinate system is shown in Figure 1.

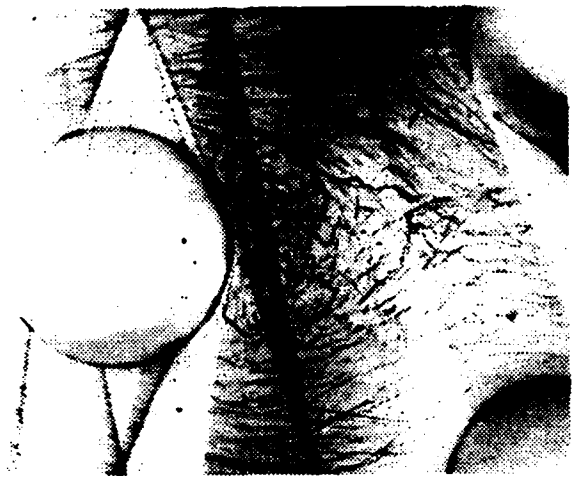

Figure 3: Picture of the flow with exposure time 1/30 second. Flow from left to right.

Figure 3 shows a visualization of the flow. The test section has been turned 90° around the x_1-axis and the two green laser beams produce sheets of laser light in the measuring plane by means of two cylinders lenses. Mirrors were used to give a better distribution of the light. However, due to reflections by the acryl rods, fields of different shading are seen in Figure 3.

Tiny air bubbles were added to the water. The photographs was taken with a standard 35 mm SLR camera with a black and white film and it is shown in negative format, i.e. the traces of the bubbles are shown as black lines. During the exposure time, the main flow has moved about 7 diameters.

The visualization gives an impression of the mean flow. The flow seems to be divided into two regions: The region behind the cylinder with large vortices and the rest of the flow where no vortices can be seem. However, in the latter region, the tracks of the bubbles cross each other indicating that there is a high degree of turbulence in this region also. In the region behind the cylinder the existence of large vortices indicates that flow reversal occurs.

The measuring section contains four unit cells and the results from these have been mapped into the one unit cell shown in Figure 1. This figure also indicates the positions of the single measurements. The measurements were performed on a grid with a spacing of 0.1 mm. Due to the angle of the laser beams it is not possible to make measurements close to the tube walls.

A selection of the measurements are shown in Figures 4–6 as profiles of both velocities and Reynolds stresses along the three lines at respectively $x_1 = 0.8\,D$, $x_2 = 0$ and $x_2 = D$ (see Figure 1). The plots of velocities show that the flow contains a recirculating zone behind the tube and the profil of U_1 in Figure 6 shows that this zone extents to about $x_1 = 1.0\,D$. The levels of the Reynolds stresses in the recirculation zone are about three times higher that the generally quite high levels found in the main flow.

In Figure 4 the measurements from each of the 4 unit cells around the middle tube in the seventh row are transformed to one of the unit cells and are shown together with the mean value of these measurements. In general, the measurements from the different unit cells are close to each other. This supports the use of a unit cell to describe the entire flow in the middle of a tube bundle.

However, at the border of the recirculation zone, there is a systematic difference between the measurements of $\overline{u_2 u_2}$ and $\overline{u_1 u_2}$ that changes sign (shown with the symbols $\times$ and $+$) during the transformation to this unit cell and the other measurements. There is therefore a velocity bias error on the u_2 velocity at this location. This error was found consistently at many corresponding locations in the flow and it is therefore believed that the bias error does not arise from the flow but from the measuring system. It has not been possible to ascertain whether the bias error arises from the optical system or from the processing of the signal.

The results from the calculations are also presented in Figures 4–6. The velocities predicted by the k-ϵ model show only a very little recirculation zone. The level of the turbulent kinetic energy k is predicted too low in the recirculation zone and too high in the rest of the flow. It is a general experience that the k-ϵ model predicts too small recirculation zones and this model is therefore probably too simple to represent the complex flow in a tube bundle.

The velocities predicted by the calculation with the Reynolds stress model are in reasonable agreement with the measurements. The recirculation zone is predicted to be a little too long and a little too narrow. However, the level of the Reynolds stresses are all predicted to be much too low. The reason for this is not clear, but it is likely that this problem is connected to the use of wall laws. Since the cell nodes adjacent to the walls have value of y^+ close to 11 and the flow at the same time is far from the approximations used in the wall laws, it could be argued that the calculation should resolve the wall layer instead of using wall laws. As mentioned earlier it would also be desirable to use a finer grid in order to ensure grid independent results. However, Reynolds stress models that are able to model the low-Reynolds number layer at the wall are still only under development.

5 CONCLUSIONS

Measurements have been made in four unit cells in the middle of a tube bundle. These data fit well with the assumption that all characteristics of the flow are found in each of the unit cells. The measurements show a quite large recirculation zone that extents 1 diameter behind the axis of each tube. The largest levels of the Reynolds stresses are found in the recirculation zone; here they are about 3 times large than the levels found in the main flow.

Numerical results obtained with a commercial CFD-code show that neither the k-ϵ model nor the Reynolds stress model give satisfactory predictions of the flow, when wall laws were used as boundary conditions. The measured data supply valuable data for further development and test of turbulence modelling of industrial flows.

REFERENCES

CFDS (1991). FLOW3D Release 2.4 – Users Manual. CFDS, AEA Industrial Technology, Harwell Laboratory, UK.

Gibson, M. M. & Launder, B. E. (1978). Ground effects on pressure fluxtuations in the atmospheric boundary layer. *Journal of Fluid Mechanics* vol. 86, no. 3, pp. 491–511.

Halim, M. S. & Turner J. T. (1986). Measurements off cross flow development in a staggered tube bundle. In *Proceedings of the 3rd International Symposium on Applications of LDA to Fluid Mechanics*, Lisbon, Portugal.

Jørgensen, O. A. & Marxen, U. (1993). Turbulent strømning over ribber. Report AFM EP 93-06 C, Department of Fluid Mechanics, Technical University of Denmark. Documentation of program for LDA-measurements (in Danish).

Launder, B. E. (1988). On the computation of convective heat transfer in complex turbulent flows. *Journal of Heat Transfer* vol. 110, pp. 1112-1128.

Meyer, K. E. (1994). Experimental and Numerical Investigation of Turbulent Flow and Heat Transfer in Staggered Tube Bundles. Ph. D. thesis, Report AFM 94-03, Department of Fluid Mechanics, Technical University of Denmark.

Rodi, W. (1980). Turbulence models and their application in hydralics. State-of-the-art paper, IAHR, Delft.

Simonin, O. & Barcouda, M. (1988). Measurements and prediction of turbulent flow entering a staggered tube bundle. In *Proceedings of the 4th International Symposium on Applications of LDA to Fluid Mechanics*, Lisbon, Portugal.

Žukauskas, A. & Ulinskas, R. (1988). *Heat Transfer in Tube Banks in Crossflow.* Hemisphere Publishing Corporation.

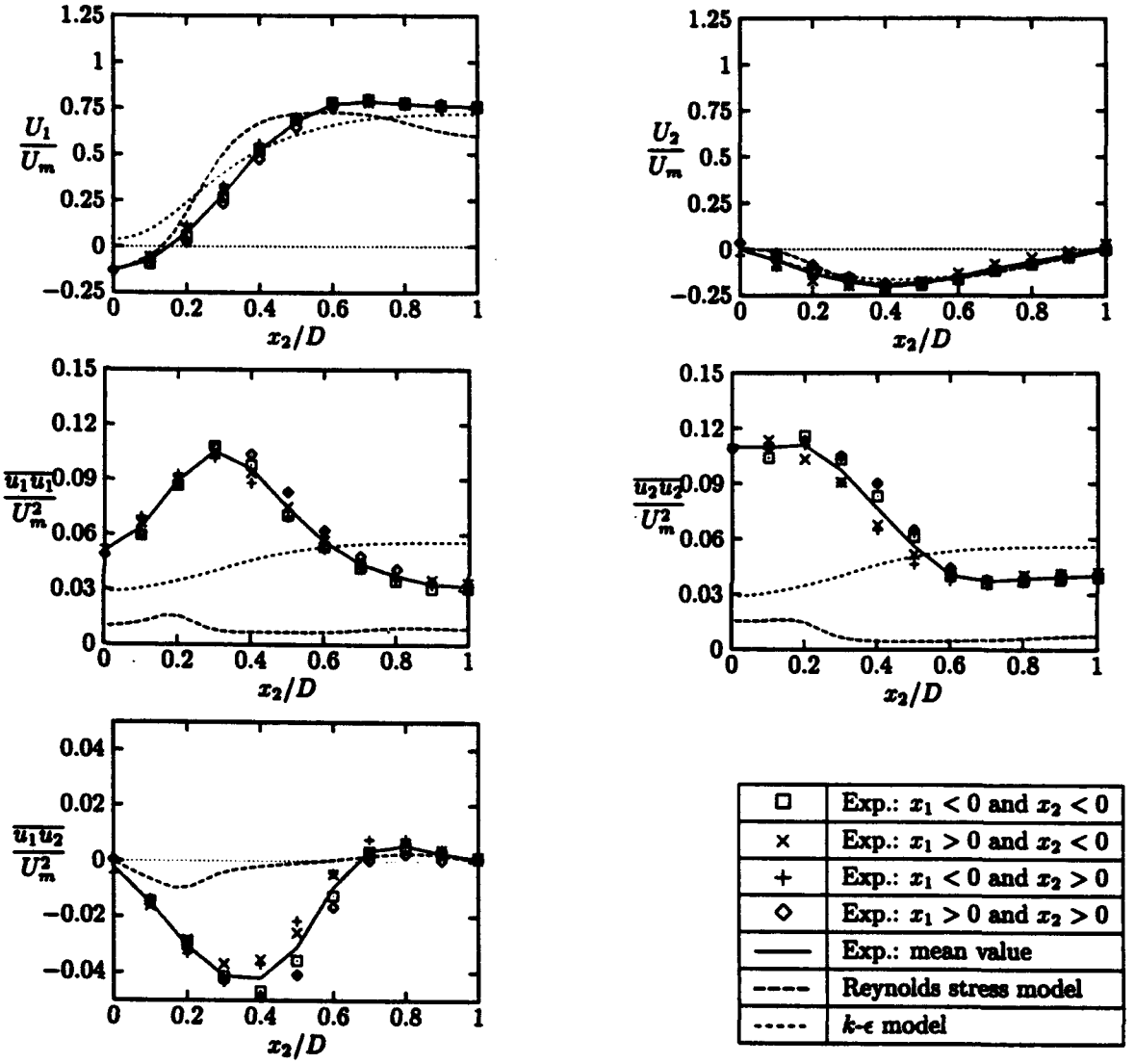

Figure 4: Measurement at $x_1 = 0.8\,D$.

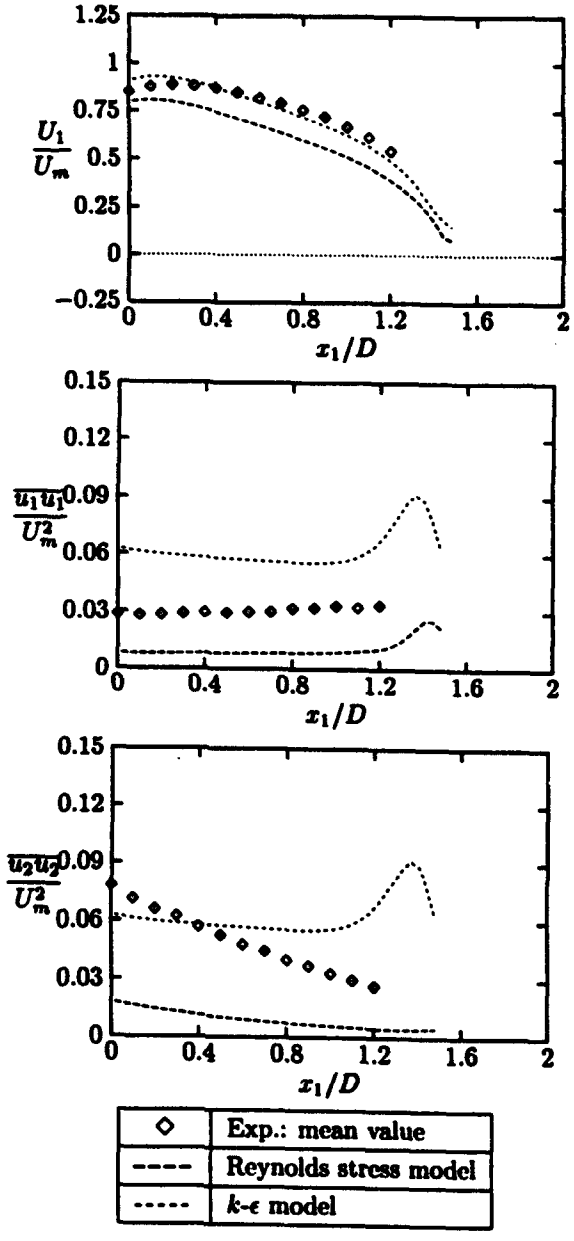

Figure 5: Measurement at impact line ($x_2 = 1.0\,D$).

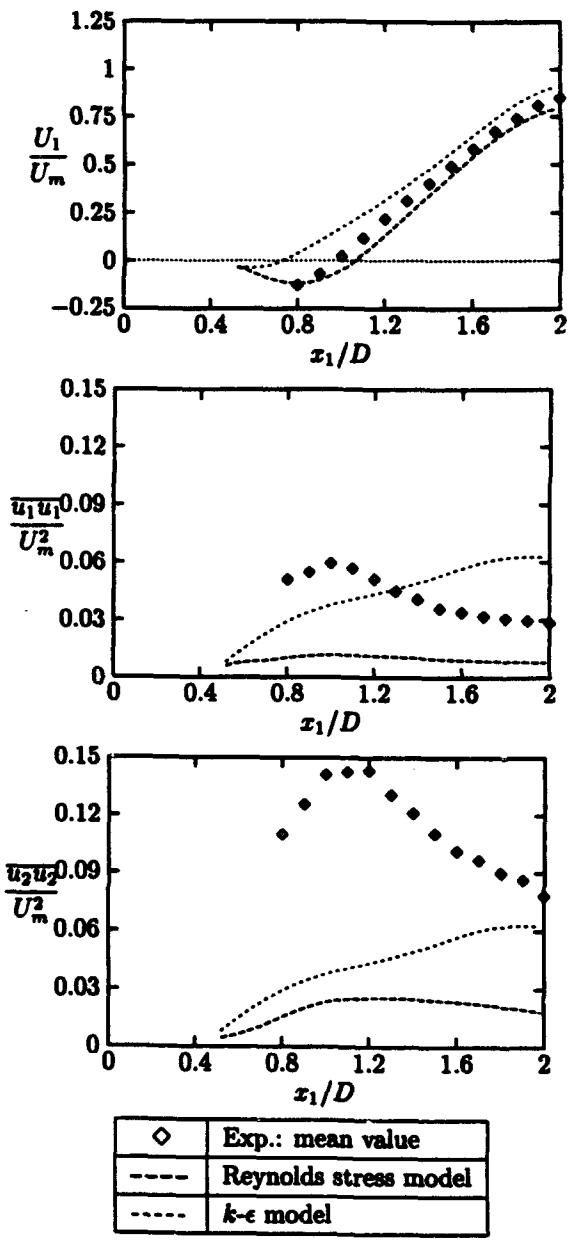

Figure 6: Measurement at wake line ($x_2 = 0.0\,D$).

July 11- 14, 1994 in Lisbon, Portugal

AUTHORS' INDEX

END